Springer Tracts in Modern Physics 280

Demetrios Christodoulides · Jianke Yang
Editors

Parity-time Symmetry and Its Applications

Springer

Springer Tracts in Modern Physics

Volume 280

Springer Tracts in Modern Physics provides comprehensive and critical reviews of topics of current interest in physics. The following fields are emphasized:

– Elementary Particle Physics
– Condensed Matter Physics
– Light Matter Interaction
– Atomic and Molecular Physics
– Complex Systems
– Fundamental Astrophysics

Suitable reviews of other fields can also be accepted. The Editors encourage prospective authors to correspond with them in advance of submitting a manuscript. For reviews of topics belonging to the above mentioned fields, they should address the responsible Editor as listed in "Contact the Editors".

More information about this series at http://www.springer.com/series/426

Demetrios Christodoulides • Jianke Yang
Editors

Parity-time Symmetry and Its Applications

Springer

Editors
Demetrios Christodoulides
College of Optics and Photonics
University of Central Florida
Orlando, Florida, USA

Jianke Yang
Department of Mathematics and Statistics
University of Vermont
Burlington, Vermont, USA

ISSN 0081-3869 ISSN 1615-0430 (electronic)
Springer Tracts in Modern Physics
ISBN 978-981-13-1246-5 ISBN 978-981-13-1247-2 (eBook)
https://doi.org/10.1007/978-981-13-1247-2

Library of Congress Control Number: 2018959871

This Springer imprint is published by the registered company Springer Nature Singapore Pte Ltd.
The registered company address is: 152 Beach Road, #21-01/04 Gateway East, Singapore 189721, Singapore

Preface

Parity-time ($\mathcal{PT}$) symmetry is nowadays an active area of research, having an impact in both science and technology. Parity-time concepts first originated within the framework of quantum mechanical formalisms, when Bender and Boettcher (1998) indicated, for the first time, that if the one-dimensional Schrödinger equation with a complex potential

$$i\frac{\partial}{\partial t}\psi\,(x,t) = -\frac{\partial^2}{\partial x^2}\psi\,(x,t) + V(x)\psi\,(x,t)$$

is $\mathcal{PT}$-symmetric, then the spectrum of the Schrödinger operator $-\partial_{xx} + V(x)$ can be entirely real. In other words, if this equation is invariant under the combined action of the parity $\mathcal{P}\ (x \to\ -x)$ and time-reversal $\mathcal{T}\ (t \to\ -t,\quad i \to\ -i)$, then the energy levels E of the eigenstates $\psi(x,t) = u(x)e^{iEt}$ can in principle be all-real. In this case, one can show that a necessary (albeit not sufficient) condition for this complex potential to be $\mathcal{PT}$-symmetric is

$$V(x) = V^*(-x)\,.$$

While the ramifications of $\mathcal{PT}$ symmetry in actual quantum systems are still to be assessed, the same is not true in classical settings. A decade later, this field started to flourish in earnest, when a series of papers published in the period of 2007–2008 indicated that optics and photonics can provide a fertile ground where $\mathcal{PT}$-symmetric ideas can be investigated. In the optical realm, the complex refractive index function $n(x) = n_R(x) + in_I(x)$ now plays the role of a complex potential $V(x)$, where $n_R(x)$ represents the refractive index distribution while $n_I(x)$ stands for the gain and loss profiles within the medium. In this case, $\mathcal{PT}$ symmetry implies that

$$n_R(x) = n_R(-x)\,, \qquad n_I(x) = -n_I(-x)\,.$$

Hence, the refractive index function must be even, whereas the gain-loss profile should be an odd function of position. What makes optics a natural platform for $\mathcal{PT}$

symmetry is the fact that all these three ingredients (refractive index, gain, and loss) can be readily deployed in photonics. Soon after, this was followed by an explosion of experimental works, all of which corroborating such possibilities. Symmetry breaking was first reported in 2009, and full $\mathcal{PT}$ symmetry was subsequently observed in pairs of coupled waveguides in 2010. Some very exciting applications stemming from optical $\mathcal{PT}$ symmetry have also been demonstrated by a number of groups. These include, for example, the prospect for unidirectional invisibility, ultra-responsive sensors, unidirectional elements, single-mode micro-ring $\mathcal{PT}$-symmetric lasers, and coherent perfect absorbers/lasers, to mention a few. The impact of nonlinearities on optical $\mathcal{PT}$-symmetric arrangements was also extensively investigated in several settings, including topological photonics. Generalizations of $\mathcal{PT}$ symmetry to accommodate more flexible gain-loss profiles have also been proposed. By now, concepts from $\mathcal{PT}$ symmetry have permeated several other branches of physics beyond optics, ranging from nuclear and quantum, to microwave, electronic and mechanical systems. One can also include in this expanding list plasmonics, Bose-Einstein condensates, acoustics, superconductivity, magnetics, and wireless power transport systems.

In this book, theoretical and experimental progresses in diverse areas of $\mathcal{PT}$ symmetry are reviewed by experts in the field. In Chapter "Linear and Nonlinear Experiments in PT-Symmetric Photonic Mesh Lattices", Peschel and collaborators review linear and nonlinear experimental results on light propagation in $\mathcal{PT}$-symmetric photonic mesh lattices made of fiber components, where Bloch oscillations and solitons are demonstrated. In Chapter "PT-symmetry on-a-Chip: Harnessing Optical Loss for Novel Integrated Photonic Functionality", Feng et al. discuss experimental results associated with chip-scale $\mathcal{PT}$-symmetric integrated photonic systems designed for a number of applications. In Chapter "Parity-Time Symmetry in Scattering Problems", Alu and colleagues provide an overreview of $\mathcal{PT}$ symmetry in scattering problems, where scattering from open $\mathcal{PT}$-symmetric systems in coupled waveguide cavity arrangements is analyzed in one and higher dimensions. In Chapter "Scattering Theory and PT-symmetry", Mostafazadeh introduces a one-dimensional scattering theory with $\mathcal{P}$, $\mathcal{T}$, or $\mathcal{PT}$ symmetry and derives mathematical conditions that encourage or forbid reciprocal transmission, reciprocal reflection, and the presence of spectral singularities. In Chapter "Passive PT-symmetry in Laser-Written Optical Waveguide Structures", Szameit and collaborators discuss how $\mathcal{PT}$-symmetric systems can be implemented in a passive fashion, without using gain, by employing modulated waveguide structures. In Chapter "Non-Hermitian Effects Due to Asymmetric Backscattering of Light in Whispering-Gallery Microcavities", Wiersig reviews progress on non-Hermitian effects due to asymmetric backscattering of light in whispering-gallery microcavities and their applications in single-particle detection. In Chapter "Exact Results for a Special PT-symmetric Optical Potential", Jones provides exact analytical results of light propagation in $\mathcal{PT}$-symmetric sinusoidal optical potentials at the phase transition, for both transverse and longitudinal configurations. In Chapter "Parity-time-Symmetric Optical Lattices in Atomic Configurations", Xiao and colleagues provide a roadmap for designing and experimentally implementing exact $\mathcal{PT}$-symmetric opti-

cal lattices with gain and loss in atomic vapors and investigate dynamic behaviors of light propagating in such induced non-Hermitian optical lattices. In Chapter "Effects of Exceptional Points in PT-symmetric Waveguides", Moiseyev et al. discuss physical effects stemming from exceptional points in $\mathcal{PT}$-symmetric waveguides, such as a slowdown of light oscillations and possible group-velocity effects. In Chapter "Higher Order Exceptional Points in Discrete Photonics Platforms", El-Ganainy and collegues introduce a systematic approach based on a recursive bosonic quantization scheme for generating discrete photonic networks that exhibit exceptional points of any arbitrary order and discuss the spectral properties and the extreme dynamics near these singularities. In Chapter "Non-Hermitian Optical Waveguide Couplers", Kivshar and collaborators review $\mathcal{PT}$-symmetric effects in non-Hermitian two-core couplers and trimers and show that their nonlinear response can break $\mathcal{PT}$ symmetry. In Chapter "Parity-Time Symmetric Plasmonics", Dionne et al. provide an overview of nano-photonic $\mathcal{PT}$ devices based on plasmonics, such as ultra-compact perfect absorber/amplifiers, multiplexers, and polarization converters with unity-efficiency. In Chapter "PT-symmetry and Non-Hermitian Wave Transport in Microwaves and RF Circuits", Kottos and colleagues provide a review of recent progress in $\mathcal{PT}$ symmetry and non-Hermitian wave transport in microwaves and radio-frequency circuits, where concepts like coherent perfect absorbers, gain-induced shut-down of lasing, and asymmetric transport naturally emerge. In Chapter "Coupled Nonlinear Schrödinger Equations with Gain and Loss: Modeling PT -symmetry", Konotop considers coupled nonlinear Schrödinger equations with balanced gain and loss and explores various wave transport phenomena in nonlinear $\mathcal{PT}$-symmetric settings such as bright and dark solitons and their interactions with defects, soliton switches, resonant wave interactions, and wave collapse. In Chapter "Making the PT Symmetry Unbreakable", Malomed et al. outline approaches for extending $\mathcal{PT}$ symmetry to very large gain-loss strengths, when dealing with subwavelength-scale waveguides and $\mathcal{PT}$-symmetric solitons in one- and two-dimensional models having self-defocusing nonlinearities. In Chapter "Krein Signature in Hamiltonian and PT -symmetric Systems", Pelinovsky and collaborators discuss the concept of Krein signature in Hamiltonian and $\mathcal{PT}$-symmetric systems such as the one-dimensional Gross–Pitaevskii equation with a real harmonic potential and a corresponding linear imaginary component. In Chapter "Integrable Nonlocal PT Symmetric and Reverse Space-Time Nonlinear Schrödinger Equations", Musslimani and colleagues overview recent advances in integrable nonlocal nonlinear Schrödinger equations having $\mathcal{PT}$, reverse-time and reverse space-time symmetries, both in continuum and discrete settings. In Chapter "Construction of Non-PT –symmetric Complex Potentials with All-Real Spectra", Yang reviews the generalization of $\mathcal{PT}$ symmetry and shows that, in addition to $\mathcal{PT}$-symmetric complex potentials, there are also large classes of non-$\mathcal{PT}$-symmetric complex potentials that allow for more flexible gain-loss profiles and all-real spectra, that can be constructed via symmetry, supersymmetry, and soliton-theory methods. In Chapter "Constant-Intensity Waves in Non-Hermitian Media", Makris and colleagues systematically discuss how to suppress intensity variations and reflections for waves propagating through a nonuniform potential landscape by

judiciously incorporating gain and loss in the potential. In Chapter "Nonlinear Beam Propagation in a Class of Complex Non-PT -symmetric Potentials", Kevrekidis et al. review nonlinear wave propagation in a class of complex non-$\mathcal{PT}$-symmetric potentials and show that the departure from a strict $\mathcal{PT}$-symmetric form does not allow for the numerical identification of true soliton solutions.

The material in this book provides a rather comprehensive survey of recent progress on the theory and applications of $\mathcal{PT}$ symmetry. It could be useful to scientists, engineers, and graduate students, who wish to further explore and advance this active field.

Orlando, Florida, USA — Demetrios N. Christodoulides
Burlington, Vermont, USA — Jianke Yang

Contents

Contributors

Mark J. Ablowitz Department of Applied Mathematics, University of Colorado, Boulder, CO, USA

H. Alaeian Materials Science and Engineering, Stanford University, Stanford, CA, USA

Physikalisches Institut, Universität Stuttgart, Stuttgart, Germany

Andrea Alù Department of Electrical and Computer Engineering, The University of Texas at Austin, Austin, TX, USA

Photonics Initiative, Advanced Science Research Center, City University of New York, New York, NY, USA

Physics Program, Graduate Center, City University of New York, New York, NY, USA

Department of Electrical Engineering, City College of The City University of New York, New York, NY, USA

D. Barton III Materials Science and Engineering, Stanford University, Stanford, CA, USA

B. Baum Materials Science and Engineering, Stanford University, Stanford, CA, USA

Andre Brandstötter Institute for Theoretical Physics, Vienna University of Technology (TU Wien), Vienna, Austria

A. Chernyavsky Department of Mathematics and Applied Mathematics, University of Cape Town, Rondebosch, South Africa

Mahboobeh Chitsazi Department of Physics, Wesleyan University, Middletown, CT, USA

Demetrios Christodoulides CREOL, College of Optics and Photonics, University of Central Florida, Orlando, FL, USA

J. Cuevas-Maraver Departamento de Física Aplicada I, Escuela Politécnica Superior, Grupo de Física No Lineal, Universidad de Sevilla, Sevilla, Spain

Instituto de Matemáticas de la Universidad de Sevilla (IMUS), Sevilla, Spain

J. Dionne Materials Science and Engineering, Stanford University, Stanford, CA, USA

Robert S. Duggan Department of Electrical and Computer Engineering, The University of Texas at Austin, Austin, TX, USA

T. Eichelkraut Carl Zeiss AG, Oberkochen, Germany

R. El-Ganainy Department of Physics, Michigan Technological University, Houghton, MI, USA

Henes Center for Quantum Phenomena, Michigan Technological University, Houghton, MI, USA

F. M. Ellis Department of Physics, Wesleyan University, Middletown, CT, USA

Jingliang Feng Department of Physics, University of Arkansas, Fayetteville, AR, USA

Liang Feng Department of Materials Science and Engineering, University of Pennsylvania, Philadelphia, PA, USA

D. J. Frantzeskakis Department of Physics, National and Kapodistrian University of Athens, Athens, Greece

Er'el Granot Department of Electrical and Electronic Engineering, Ariel University, Ariel, Israel

H. F. Jones Imperial College, London, UK

P. G. Kevrekidis Department of Mathematics and Statistics, University of Massachusetts, Amherst, MA, USA

M. Khajavikhan College of Optics & Photonics-CREOL, University of Central Florida, Orlando, FL, USA

Yuri S. Kivshar Nonlinear Physics Centre, Research School of Physics and Engineering, Australian National University, Canberra, ACT, Australia

Y. Kominis School of Applied Mathematical and Physical Science, National Technical University of Athens, Athens, Greece

Vladimir V. Konotop Departamento de Física and Centro de Física Teórica e Computacional, Faculdade de Ciências, Universidade de Lisboa, Lisboa, Portugal

Tsampikos Kottos Department of Physics, Wesleyan University, Middletown, CT, USA

M. Kremer Institute for Physics, Rostock University, Rostock, Germany

M. Lawrence Materials Science and Engineering, Stanford University, Stanford, CA, USA

Huanan Li Department of Physics, Wesleyan University, Middletown, CT, USA

Vitaly Lutsky Faculty of Engineering, Department of Physical Electronics, School of Electrical Engineering, Tel Aviv University, Tel Aviv, Israel

Eitam Luz Faculty of Engineering, Department of Physical Electronics, School of Electrical Engineering, Tel Aviv University, Tel Aviv, Israel

Alexei A. Mailybaev Instituto Nacional de Matemática Pura e Aplicada – IMPA, Rio de Janeiro, Brazil

Konstantinos G. Makris Department of Physics, University of Crete, Heraklion, Greece

Boris A. Malomed Faculty of Engineering, Department of Physical Electronics, School of Electrical Engineering, Tel Aviv University, Tel Aviv, Israel

Center for Light-Matter Interaction, Tel Aviv University, Tel Aviv, Israel

ITMO University, Saint Petersburg, Russia

Pei Miao Department of Materials Science and Engineering, University of Pennsylvania, Philadelphia, PA, USA

Department of Electrical Engineering, The State University of New York at Buffalo, Buffalo, NY, USA

Mohammad-Ali Miri Department of Electrical and Computer Engineering, The University of Texas at Austin, Austin, TX, USA

Department of Physics, Queens College of the City University of New York, Queens, New York City, NY, USA

Nimrod Moiseyev Schulich Faculty of Chemistry and Faculty of Physics, Technion – Israel Institute of Technology, Haifa, Israel

Ali Mostafazadeh Departments of Mathematics and Physics, Koç University, Sarıyer, Istanbul, Turkey

Ziad H. Musslimani Department of Mathematics, Florida State University, Tallahassee, FL, USA

M. Ornigotti Institute for Physics, Rostock University, Rostock, Germany

Mingsen Pan Department of Materials Science and Engineering, University of Pennsylvania, Philadelphia, PA, USA

Department of Electrical Engineering, The State University of New York at Buffalo, Buffalo, NY, USA

D. E. Pelinovsky Department of Mathematics and Statistics, McMaster University, Hamilton, Canada

Ulf Peschel Institute of Solid State Theory and Optics, Abbe Center of Photonics, Friedrich Schiller University Jena, Jena, Germany

Stefan Rotter Institute for Theoretical Physics, Vienna University of Technology (TU Wien), Vienna, Austria

Jiteng Sheng State Key Laboratory of Precision Spectroscopy, East China Normal University, Shanghai, China

Sergey V. Suchkov Nonlinear Physics Centre, Research School of Physics and Engineering, Australian National University, Canberra, ACT, Australia

Andrey A. Sukhorukov Nonlinear Physics Centre, Research School of Physics and Engineering, Australian National University, Canberra, ACT, Australia

A. Szameit Institute for Physics, Rostock University, Rostock, Germany

M. H. Teimourpour Department of Physics, Michigan Technological University, Houghton, MI, USA

Roney Thomas Department of Physics, Wesleyan University, Middletown, CT, USA

S. Weimann Institute for Physics, Rostock University, Rostock, Germany

Jan Wiersig Institut für Theoretische Physik, Otto-von-Guericke-Universität Magdeburg, Magdeburg, Germany

Martin Wimmer Erlangen Graduate School in Advanced Optical Technologies (SAOT), Erlangen, Germany

Institute of Solid State Theory and Optics, Abbe Center of Photonics, Friedrich Schiller University Jena, Jena, Germany

Min Xiao Department of Physics, University of Arkansas, Fayetteville, AR, USA

National Laboratory of Solid State Microstructures and School of Physics, Nanjing University, Nanjing, China

Jianke Yang Department of Mathematics and Statistics, University of Vermont, Burlington, VT, USA

Yanpeng Zhang Key Laboratory for Physical Electronics and Devices of the Ministry of Education & Shaanxi Key Lab of Information Photonic Technique, Xi'an Jiaotong University, Xi'an, China

Yiqi Zhang Key Laboratory for Physical Electronics and Devices of the Ministry of Education & Shaanxi Key Lab of Information Photonic Technique, Xi'an Jiaotong University, Xi'an, China

Zhaoyang Zhang Department of Physics, University of Arkansas, Fayetteville, AR, USA

Key Laboratory for Physical Electronics and Devices of the Ministry of Education & Shaanxi Key Lab of Information Photonic Technique, Xi'an Jiaotong University, Xi'an, China

Zhifeng Zhang Department of Electrical and Systems Engineering, University of Pennsylvania, Philadelphia, PA, USA

Han Zhao Department of Electrical and Systems Engineering, University of Pennsylvania, Philadelphia, PA, USA

Q. Zhong Department of Physics, Michigan Technological University, Houghton, MI, USA

Linear and Nonlinear Experiments in $\mathcal{PT}$-Symmetric Photonic Mesh Lattices

Martin Wimmer, Demetrios Christodoulides, and Ulf Peschel

Abstract Photonic mesh lattices provide a versatile experimental platform for studying light propagation in a discrete environment. By using standard telecommunication equipment it is possible to influence the evolution of light by actively modulating its amplitude and phase. Fiber components thus offer a ready to use solution for creating a $\mathcal{PT}$-symmetric optical network. Here, we analyze two classes of $\mathcal{PT}$-symmetric networks: those with local $\mathcal{PT}$ symmetry fulfilling the conditions of $\mathcal{PT}$ symmetry in each time step but not globally and those with global $\mathcal{PT}$ symmetry providing completely real eigenvalues. We investigate light propagation in these dissipative media in the linear and nonlinear regime and discuss nonlinear localization as well as the formation of soliton. Furthermore, Bloch oscillations are induced by an external phase modulation and are found to restore pseudo-Hermitian propagation.

1 Introduction

In this chapter, we discuss light propagation through a fiber optical network, which shares the same working principle as the Galton board [1] (see Fig. 1a). Originally proposed as a machine, where particles fall through multiple layers of scatterers, each deflecting the particles either to the left or to the right, it is a prime example for

M. Wimmer
Erlangen Graduate School in Advanced Optical Technologies (SAOT), Erlangen, Germany

Institute of Solid State Theory and Optics, Abbe Center of Photonics, Friedrich Schiller University Jena, Jena, Germany

D. Christodoulides
CREOL, College of Optics and Photonics, University of Central Florida, Orlando, FL, USA

U. Peschel (✉)
Institute of Solid State Theory and Optics, Abbe Center of Photonics, Friedrich Schiller University Jena, Jena, Germany
e-mail: ulf.peschel@uni-jena.de

D. Christodoulides, J. Yang (eds.), *Parity-time Symmetry and Its Applications*, Springer Tracts in Modern Physics 280,
https://doi.org/10.1007/978-981-13-1247-2_1

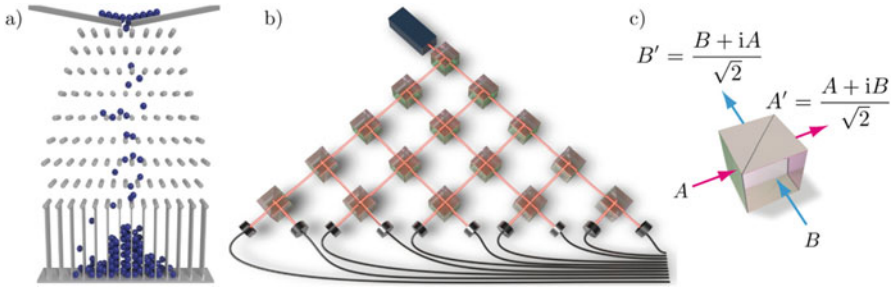

Fig. 1 Schematics of the classical and optical Galton board. (**a**) In case of the classical Galton board, a mechanical walker falls through multiple layers of scatterers, each deflecting the particle either to the left or to the right. (**b**) In the optical analogue, a laser beam is inserted into a pyramid of beam splitters. At each row of beam splitter cubes, the laser beam is divided up into one part going to the left and another going to the right. Photodetectors record the final intensity distribution. (**c**) The output of a standard 50/50 beam splitter is given by the superposition of both input fields, where the reflected path is phase shifted

Random Walks [2]. This stochastic process applied to classical particles reveals a diffusive motion, which is not time reversible. By replacing the mechanic particles by photons and the scatterers by beam splitters, a so-called optical Galton board is realized [3] (see Fig. 1b). Although the idea is the same, interestingly the optical version features a fast ballistic spreading [4] and a reversible evolution [5], providing an interesting ansatz for quantum mechanical search algorithms [6]. In the following, we present an implementation of the optical Galton board, which relies on fiber amplifiers for compensating losses. Therefore, the optical Galton board is discussed in terms of classical optics based on the propagation of coherent wave packets and their mutual interference [7]. At each beam splitter cube (see Fig. 1c), the incoming field amplitudes A and B transform into the fields A' and B' at the output according to

$$\begin{pmatrix} A' \\ B' \end{pmatrix} = \frac{1}{\sqrt{2}} \begin{pmatrix} 1 & i \\ i & 1 \end{pmatrix} \begin{pmatrix} A \\ B \end{pmatrix}, \tag{1}$$

where in this notation the reflected parts acquire a phase shift of $\pi/2$. As amplifiers and classical optical states are used in this project, the optical Galton board is called a Light Walk in order to distinguish it from Quantum Walks based on e.g. single photon states [8, 9] or atoms [5].

The main challenges of implementing the spatial Galton board are the growing number of components with increasing system size and the need for an active stabilization in order to observe a coherent propagation. A clever solution to both problems was demonstrated in [8], where time-multiplexing schemes are adapted to the challenge of realizing an optical Galton board. The working principle is not limited to a single spatial dimension, but even 2D Quantum walks could be realized based on this method [10]. In the following, we first want to discuss the

basics behind time multiplexing of Light Walks and afterwards we explain the experimental setup in detail. Finally, we present results on linear and nonlinear light evolution, even in presence of $\mathcal{PT}$-symmetrical potentials.

2 Light Walks via Time Multiplexing

The Galton board is a typical $1+1$ dimensional system, the rows of which can be interpreted as discrete time steps and the horizontal deflection of the walker as the position, which is discretized as well. For a time-multiplexed implementation of the optical Galton board, pulses are used instead of cw-signals. While in the standard arrangement all beam splitters of a single row are passed at the same time, in [8, 11] a time delay between each beam splitters is introduced by shortening all paths going the left compared to the paths going to the right (compare red and blue paths in Fig. 2a). The system now evolves on two time scales: firstly, each row is separated from the next by the path length $\overline{L} = (L_1 + L_2)/2$ and secondly the length difference $\Delta L = L_1 - L_2$, with $L_1 > L_2$, separates two adjacent beam splitters of the same row. Instead of labelling every beam splitter by its individual row m and column n, it is now possible to identify each beam splitter by a single parameter, which is the arrival time

$$T_{arrival} = \overline{T}m + \frac{\Delta T}{2}n. \tag{2}$$

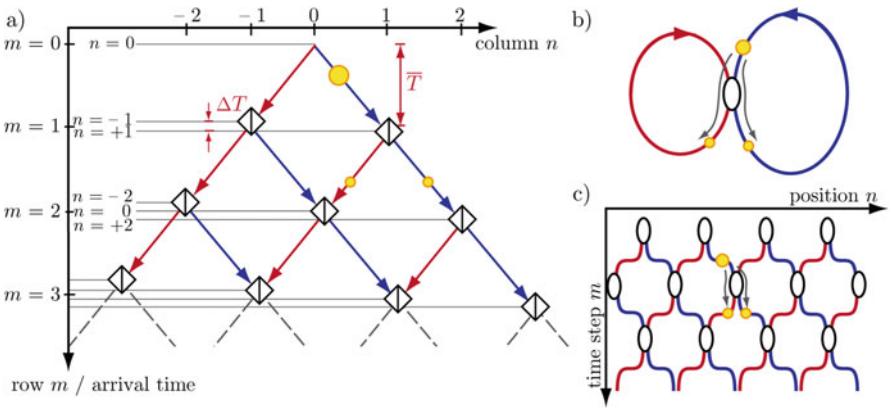

Fig. 2 Time multiplexing used to realize the optical Galton board. (**a**) Coding the spatial distribution of light pulses (yellow circles) by their arrival time: By shortening paths to the left (red), an artificial length difference is introduced, which attributes to each beam splitter in row m and column n a unique arrival time given by Eq. (2). Large time steps separate different rows, while small time steps separate pulses of the same row, but of different columns. (**b**) The pyramid is then reduced to two fiber loops of different length and a 50/50 fiber coupler. Each roundtrip in the short (long) loop equals a step to the left (right). The introduction of the length difference is not altering the dynamics through the pyramid. (**c**) Equivalent mesh lattice consisting of 50/50 fiber couplers. For a better visualization, the length difference between red and blue paths is ignored, since it does not influence the evolution

Here, we introduced the average propagation time $\overline{T}$ and the time difference ΔT between both optical paths. By creating the length imbalance between the short paths to the left and the long paths to the right, a dimensional reduction from 1 + 1D to a single temporal dimension is carried out, which has a crucial impact on the experiment: Not only the coordinate system of the optical Galton board is conflated, but instead also the experiment can be simplified to a short and a long piece of optical fibers connecting the input and output of a 50/50 fiber coupler (see Fig. 2b). A pulse starting in the longer loop is split up at the fiber coupler into two smaller pulses, which propagate in the short and long loop, akin to pulses propagating to the left or right in the pyramid of beam splitters. After each roundtrip they reach the central coupler, where they split up again. While a path through the spatial implementation of the optical Galton board is given by a combination of steps to the left or right, this translates into a specific sequence of short and long loop roundtrips in the temporal implementation. In this sense, each roundtrip of the pulses corresponds to a time step m, and the difference in number of round trips through the long and short loop define the position n.

Obviously, based on time multiplexing only the two fiber loops and the beam splitter are needed, which is the first main advantage. In case of the Galton board [1] the accessible propagation length is limited by the rapidly growing size of the required apparatus. In contrast, the maximum number of round trips realized in the temporal version is restricted to the ratio $N = \overline{T}/\Delta T$ between the average roundtrip time and the time difference. If this limit is exceeded pulses start mixing with those of the previous round trip. In our experimental setup, an average loop length of 4 km is chosen and a length difference of about 45 m. In this case, the spatial size of the optical Galton board extends over approximately 90 positions.

A second advantage of the time multiplexing principle is the intrinsic stability of the setup. Due to the reduction to only three components, the same parts are passed again and again. As a necessary condition for interference, two pulses have to meet at the 50/50 coupler at the same time, which is only possible, if they propagate for the same number of roundtrips through the long and short loop, but do not necessarily pass the loops in the same order. In practice this means, that any fluctuations with a larger time scale than a single measurement, do not influence the evolution as all possible paths are affected in the same way.

3 Experimental Setup

However, in reality more than three components are needed for realizing a time-multiplexed version of the Galton board (see Fig. 3). In the supplementary material of [11–13] detailed descriptions of the experiment are provided. For each measurement, a seed pulse with a length of 25 ns is cut out of the signal of a DFB laser diode ($\lambda_{signal} = 1555$ nm) by a Mach-Zehnder modulator (MZM). For achieving high peak powers, the pulse is amplified by two erbium-doped fiber amplifiers (EDFA) and

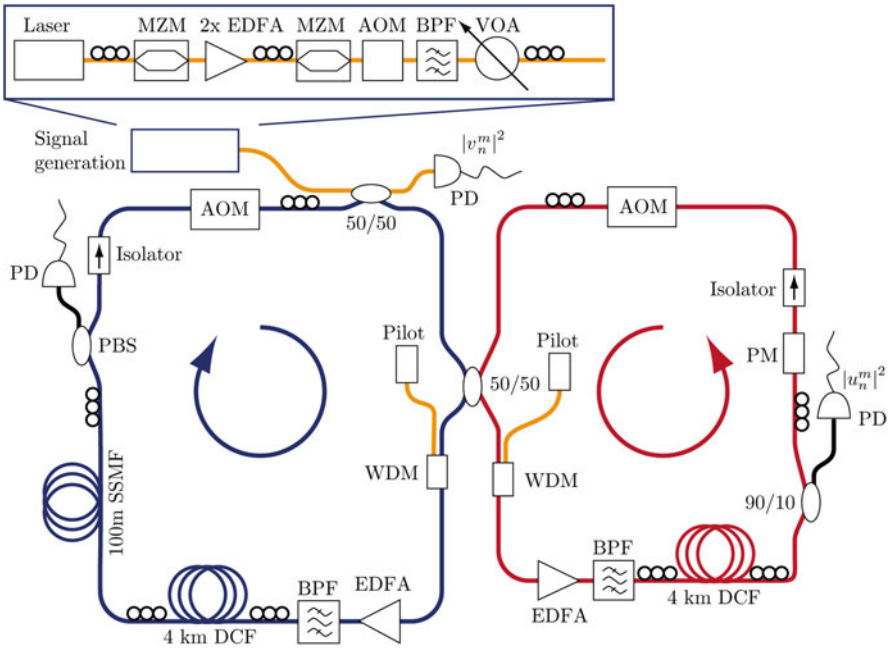

Fig. 3 Experimental setup consisting of the signal generation and the two optical fiber loops. The signal of a DFB laser diode is transformed into pulses by a Mach-Zehnder modulator (MZM) and amplified twice by erbium-doped fiber amplifiers (EDFA). Afterwards, the background is suppressed by another MZM and cleaned by a bandpass filter. The peak power is adjusted via a variable optical screw attenuator and an acousto-optical modulator (AOM). After inserting the seed pulse into the long loop via a 50/50 coupler, it passes a wavelength-division multiplexing coupler (WDM), which adds a pilot signal to each loop. All losses during one roundtrip are compensated by an EDFA followed by a tunable bandpass filter. 4 km of dispersion compensating fibers (DCF) provide a significant nonlinear phase shift already at low power levels. A polarizing beam splitter (PBS) and a phase modulator (PM) with an integrated polarizer in the short loop filter out a single polarization state. This state is adjusted via polarization controllers (denoted by three circles) at numerous positions. At the end of the loops, isolators block back reflections of the AOMs, which are used for a dynamic gain and loss modulation

afterwards reshaped again by a MZM in order to further suppress the dark signal. Before being injected into the long loop through a 50/50 coupler, the spectrum of the pulse is cleaned by a tunable bandpass filter and the peak power is adjusted by a variable optical attenuator and an acousto-optical modulator (AOM). Both fiber loops are built up in a nearly symmetric way, starting with an amplification stage. This consists of an EDFA in each loop, which is adjusted in such a way that any losses during one roundtrip are compensated. For avoiding transients and for adjusting the amplification rate, a continuous pilot signal at $\lambda_{pilot} = 1536$ nm is added via wavelength-division-multiplexing couplers (WDM). After the amplifiers, the pilot signal is filtered out by tunable bandpass filters before the pulses enter

4 km of dispersion compensating fibers (DCF). A DCF has a comparable small core size and thus a higher nonlinear coefficient compared to standard single mode fibers (SSMF) [14]. In combination with the long propagation distance of 4 km, this leads to nonlinear effects already at comparable low peak powers of 100 mW. The dominant nonlinear effect, which is observed in the experiment is self-phase modulation based on the Kerr effect. Based on fiber parameters provided in [14], it is estimated that a nonlinear phase shift of 2π is accumulated at a power level of about 300 mW within a single roundtrip [12]. Besides the two DCFs, a third spool of SSMF fiber is needed for balancing the length difference up to a remaining imbalance of 45 m. For monitoring the pulses, a 90/10 coupler is placed in the short loop after the fiber spools. In the longer loop, the injection coupler is also used for pulse monitoring. For adjusting the polarization in each fiber loop, the signal at the second output port of a polarizing beam splitter in the longer loop is minimized via manual polarization controllers. A phase modulator in the short loop determines the polarization state in the respective loop via an integrated polarizer. Optical isolators prevent any back reflections and the built up of stimulated Brillouin scattering. At the end of each loop, acousto-optical modulators (AOM) in zeroth order are used as intensity modulators. The transmission ratio of the AOM depends on the applied voltage, which is adjusted so, that only 50% of the pulse intensity passes, while the EDFA compensates for this additional loss. In this way, it is possible to either attenuate pulses by lowering the transmission ratio, or amplifying them by increasing the transmission.

4 Mathematical Description of the Evolution

As pulses are much too long to be influenced by the group velocity dispersion of the fiber they are completely characterized by complex amplitudes u_n^m and the pulses v_n^m in the long loop and short loop, respectively [11]. Each roundtrip the time step m of the system advances to $m + 1$, while the position n is either decreased for pulses in the short loop (going to the left) or increased for pulses in the long loop (propagating to the right). In combination with the matrix of a single 50/50 beam splitter in Eq. (1), this leads to the evolution equations [11]

$$u_n^{m+1} = \frac{1}{\sqrt{2}}\left(u_{n+1}^m + i\,v_{n+1}^m\right) \text{ and} \tag{3.1}$$

$$v_n^{m+1} = \frac{1}{\sqrt{2}}\left(v_{n-1}^m + i\,u_{n-1}^m\right). \tag{3.2}$$

The periodic arrangement of beam splitters in the optical Galton board reveals a unit cell, which covers two positions and two time steps. The periodicity itself is reflected in a band structure (see Fig. 4), which is derived by inserting a Floquet-Bloch ansatz [15].

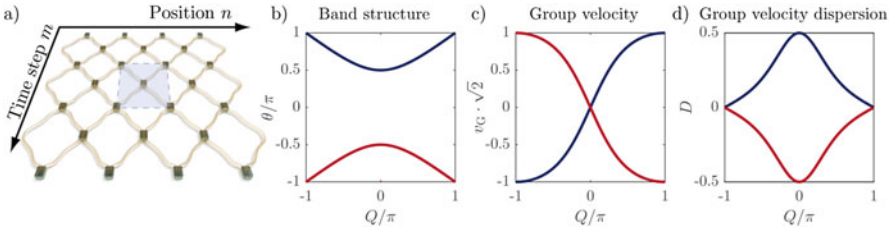

Fig. 4 Unit cell of the mesh lattice and the band structure. (**a**) The mesh lattice consists of unit cells covering two positions and two time steps. (**b**) The two-atom unit cell leads to a splitting of the band structure into two bands [15]. Due to the spatial and temporal discretization, the band structure is not only periodic in the Bloch momentum Q, but also in the propagation constant θ. (**c**) The group velocity vanishes at the center of the Brillouin zone and has maximum absolute values at the edges. (**d**) In the linear regime the second derivative of the dispersion relation determines the dispersive spreading of the wave packets [12, 16]

$$\begin{pmatrix} u_n^m \\ v_n^m \end{pmatrix} = \begin{pmatrix} U \\ V \end{pmatrix} e^{\frac{iQn}{2}} e^{-\frac{i\theta m}{2}} \tag{4}$$

into a double step of the evolution equations (3.1 and 3.2). The resulting dispersion relation

$$\cos\theta = \frac{1}{2}(\cos Q - 1) \tag{5}$$

connects the propagation constant θ with the Bloch momentum Q. As the evolution proceeds in discrete round trips, the band structure is not only periodic in the Bloch momentum Q but also in the propagation constant θ.

A specific point of the dispersion relation is excited by starting with a train of pulses with a Gaussian envelope in one of the loops. In the next round trip when pulses have distributed over both loops amplitudes and phases are tuned according to the desired eigenstate $(U, V)^{\mathrm{t}}$ [12]. However, the task of creating a Gaussian distribution is non-trivial, as the system loses its intrinsic stabilization, if an externally generated pulse sequence is inserted into one of the loops. In this case, pulses may interfere, which did not pass the same number of components. As a consequence, the phase relation between different pulses is no longer fixed and unpredictable fluctuations from one realization to the next may occur. However, it is possible to create internally a Gaussian distribution by blocking every second time step one of the two fiber loops [11]. The resulting evolution equations

$$u_n^{m+2} = \frac{1}{2}\left(u_{n+2}^m + iv_{n+2}^m + iv_n^m - u_n^m\right) \text{ and} \tag{6.1}$$

$$v_n^{m+2} = \frac{1}{2}\left(v_{n-2}^m + iu_{n-2}^m + iu_n^m - v_n^m\right). \tag{6.2}$$

then simplify to a discretized diffusion equation (e.g. if v_n^m is blocked):

$$u_n^{m+2} = \frac{1}{2}\left(u_{n+2}^m - u_n^m\right) \text{ and} \tag{7.1}$$

$$v_n^{m+2} = \frac{i}{2}\left(u_{n-2}^m + u_n^m\right), \tag{7.2}$$

the solution of which is known to be Gaussian for an initial single site excitation. Additional accumulations of phases and drifts of the center-of-mass can be avoided by blocking long and short loop in an alternating way every second time step. At the end, a wave packet is produced in each loop with a Gaussian envelope, where in a final step the phase and amplitude is adjusted through the modulators.

5 Creation of a $\mathcal{PT}$-Symmetric Potential

In their seminal work [17] on $\mathcal{PT}$-symmetric Hamiltonians, Bender and Boettcher considered a one-dimensional Schrödinger equation

$$i\hbar\frac{\partial}{\partial t}\psi(x,t) = -\frac{\hbar^2\partial^2}{2m\partial x^2}\psi(x,t) + V(x)\psi(x,t), \tag{8}$$

which is invariant under simultaneous time reversal $\mathcal{T}$ and inversion of space $\mathcal{P}$, setting up a symmetry condition for the potential

$$V(x) = V^*(-x). \tag{9}$$

Ten years later, the criterion above in Eq. (9) was transferred to the optical regime, where the refractive index distribution $n(x) = n_R(x) + in_I(x)$ replaces the potential $V(x)$ [18]. Consequently, a system fulfills $\mathcal{PT}$ symmetry, if the refractive index obeys the two conditions

$$n_R(x) = n_R(-x) \text{ and } n_I(x) = -n_I(-x) \tag{10}$$

simultaneously. The first successful realization of these symmetry conditions via two coupled waveguides was reported in [19]. While the sign of $n_I(x)$ distinguishes between an amplifying active medium ($n_I(x) < 0$) and a lossy medium ($n_I(x) > 0$), it is also possible to avoid any amplification by symmetrically distributing minor and major losses, e.g. by introducing bending losses in waveguide arrays [20, 21] or by adding absorbing layers [19, 22]. In such systems a global loss can be scaled out, leaving regions of amplification and attenuation [23]. However, the presence

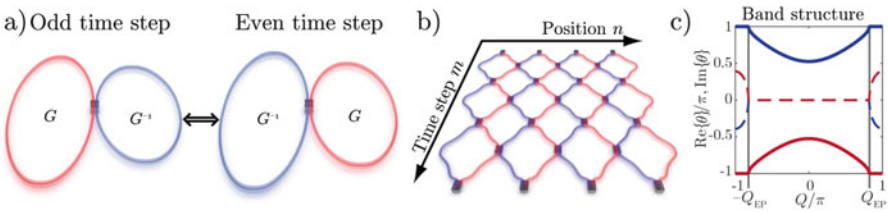

Fig. 5 Creation of an antisymmetric gain and loss distribution. (**a**) At odd time steps the long loop is amplified and the short loop attenuated, a situation, which is reversed for even time steps. (**b**) This alternating amplitude modulation corresponds to a mesh lattice with gain and loss waveguides, which are coupled at discrete time steps. (**c**) Exceptional points (EP) separate the complex part of the band structure from the real valued central part. At the EPs, the eigenvalues and eigenvectors of the system merge. The dash-dotted lines denote the imaginary part of the band structure

of a global loss limits the applicability, since the propagation length of optical signals is reduced. It also renders nonlinear experiments virtually impossible as the action of optical nonlinearities soon becomes negligible. Active systems like doped micro-ring cavities [24, 25] require a more stringent choice of materials, which is traded in for an avoidance of unnecessary losses. In optical fiber networks, commercially available amplifiers provide a convenient solution to this problem. We use a combination of amplitude modulators for dynamical gain and loss regulation and EDFAs for a static compensation of any damping [26–28]. The required symmetric real part of the refractive index distribution is on the other side realized by an appropriate phase modulation.

Starting with the imaginary part of the refractive index, an antisymmetric distribution is achieved by amplifying one loop by G and attenuating the other in a balanced way by $1/G$, which results in the evolution equations

$$u_n^{m+1} = \frac{\sqrt{G^{\pm 1}}}{\sqrt{2}} \left(u_{n+1}^m + i v_{n+1}^m \right) \text{ and} \tag{11.1}$$

$$v_n^{m+1} = \frac{\sqrt{G^{\mp 1}}}{\sqrt{2}} \left(v_{n-1}^m + i u_{n-1}^m \right). \tag{11.2}$$

After each time step, the gain and loss distribution is inverted (denoted by $\pm$), corresponding to the creation of temporally discretized coupled waveguides with gain and loss [26] as depicted in Fig. 5. A reflection of space requires at the same time an exchange of amplification and attenuation in order to restore the original lattice. In this sense, $\mathcal{PT}$ symmetry is already fulfilled by the sole imaginary part of the potential, however the resulting dispersion relation

$$\cos\theta = \frac{1}{2} \left(\cos Q - \cosh\gamma \right), \tag{12}$$

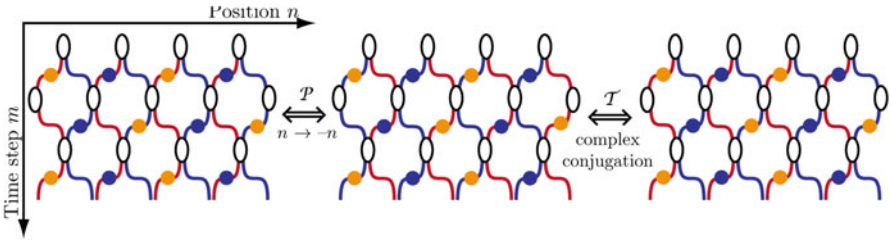

Fig. 6 Symmetry operations of the $\mathcal{PT}$ symmetric mesh lattice including the phase modulation. Parity symmetry leads to a reflection of space, which is equal to mirroring the lattice about a vertical line. Time inversion flips the lattice about the horizontal axis and adds complex conjugation, which is equal to an exchange of gain and loss. To demonstrate that those symmetries are still present in the case of phase modulation we have assumed the operation of a phase modulator in one of the loops. The phase modulation is denoted by blue ($-\varphi_0$) and yellow circles ($+\varphi_0$)

with $\gamma = (\ln G)/2$, shows complex eigenvalues at the edge of the Brillouin zone (see Fig. 5c). These zones are separated from a completely real valued region by exceptional points at

$$Q_{\mathrm{EP}} = \pm \arccos\left(2 + \cosh\gamma\right), \tag{13}$$

where not only the eigenvalues but even the eigenstates merge [29]. The resulting propagation is dominated by the exponential increase of power due to the complex eigenstates (see Fig. 9 third column).

In order to establish full $\mathcal{PT}$ symmetry in the whole Brillouin zone, it is mandatory to include also a phase modulation, which is equivalent to a symmetric real part of the refractive index. Since the gain and loss alternates with each lattice site thus realizing an antisymmetric potential, a symmetric phase modulation

$$\varphi(n) = \begin{cases} +\varphi_0, & \mathrm{mod}\,(n+3,4) < 2 \\ -\varphi_0, & \mathrm{else} \end{cases} \tag{14}$$

is needed with a periodicity of four spatial positions [26] (see Fig. 6). Eq. (14) is experimentally implemented via a phase modulator in the short loop

$$u_n^{m+1} = \frac{\sqrt{G^{\pm 1}}}{\sqrt{2}}\left(u_{n+1}^m + i\,v_{n+1}^m\right) e^{i\varphi(n)}, \tag{15.1}$$

$$v_n^{m+1} = \frac{\sqrt{G^{\mp 1}}}{\sqrt{2}}\left(v_{n-1}^m + i\,u_{n-1}^m\right). \tag{15.2}$$

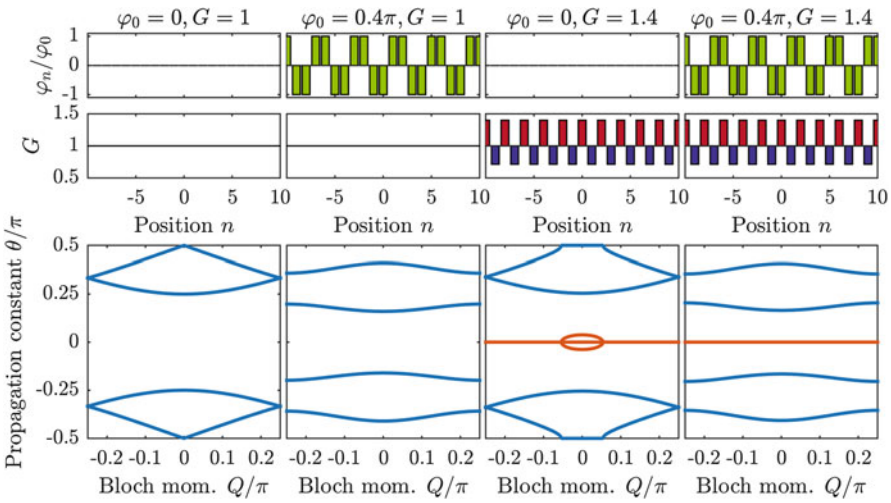

Fig. 7 Band structure of the $\mathcal{PT}$-symmetric lattice. In the case of a passive lattice as shown in the first column, the band structure is completely real valued. Applying a phase modulation increases the size of the unit cell, which leads to a splitting of the dispersion relation into four bands in total (second column). When complex valued (imaginary part is shown in red) and features exceptional points. In the case of a combined amplitude and phase modulation, the band structure is completely real valued again (fourth column). Compared to Figs. 4 and 5, the Floquet-Bloch ansatz in Eq. (16) is used, which leads to a backfolding of the band structure about the horizontal axis

For deriving the band structure (see Fig. 7) [15]

$$\cos 2\theta = -\frac{1}{2}\cos\varphi_0 \cosh 2\gamma \pm \frac{1}{2}\sqrt{\cos^2\varphi_0 \cosh^2 2\gamma + \frac{1}{2}\left[\cos 4Q - \cosh 4\gamma - 4\cos^2\varphi_0 + 4\right]}$$

of this lattice, a Floquet-Bloch ansatz

$$\begin{pmatrix} u_n^m \\ v_n^m \end{pmatrix} = \begin{pmatrix} U \\ V \end{pmatrix} e^{\frac{iQn}{4}} e^{-\frac{i\theta m}{2}} \tag{16}$$

with an increased spatial periodicity of four lattice sites is chosen. Due to the increased size of the unit cell, the original two bands split up in four. In absence of gain and loss ($G = 1$), the pulse spreads while maintaining a constant power level. However, for gain/loss values exceeding the PT threshold, the band structure is complex again (see Fig. 8). The increase and decrease of the phase for pairs of

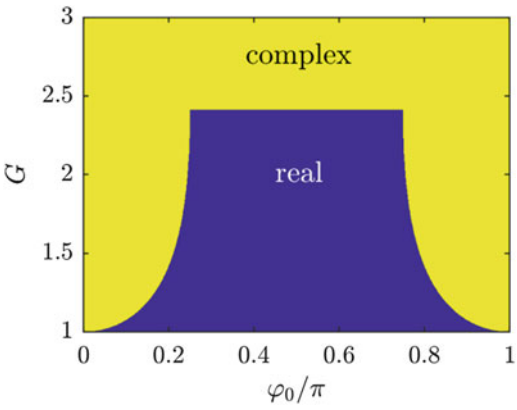

Fig. 8 $\mathcal{PT}$ threshold of the mesh lattice. Even when combining amplitude and phase modulation, $\mathcal{PT}$ symmetry does not guarantee a real-valued dispersion relation. Only below a critical value of the amplification G, the band structure is real, while above it has complex parts. The figure is adapted from the supplementary material accompanying [26]

waveguides leads to an effective decoupling to neighboring pairs and a reduced spreading compared to the passive lattice (see Fig. 9 second column).

6 $\mathcal{PT}$ Bloch Oscillations

Besides the real space propagation in Fig. 9, which illustrated the effects of a complex, but also proves the existence of a completely real valued band structure, further details about the shape of the dispersion relation are revealed by studying Bloch oscillations [11, 22, 28, 31]. The original idea of Bloch [32, 33] goes back to the motion of charge carriers in a crystalline material. In contrast to electrons in free space, charge carriers in a crystalline material cannot propagate freely, but instead their motion is dictated by the underlying band structure [34]. Therefore, by applying an electric field, charge carriers perform Bloch oscillations, which are a mirror image of the periodic band structure. In our optical system, electrical fields can be mimicked by linearly increasing phase gradients [11, 28] reminiscent to a refractive index gradient in waveguide arrays [35, 36].

For convenience we increase the induced phase in one of the loops in each time step

$$u_n^{m+1} = \frac{\sqrt{G^{\pm 1}}}{\sqrt{2}} \left(u_{n+1}^m + i\, v_{n+1}^m \right) e^{i\alpha m} \text{ and} \tag{17.1}$$

$$v_n^{m+1} = \frac{\sqrt{G^{\mp 1}}}{\sqrt{2}} \left(v_{n-1}^m + i\, u_{n-1}^m \right), \tag{17.2}$$

by a fixed amount α , a scheme, which is equivalent to a transverse modulation as demonstrated in [37]. Compared with a modulation in each transverse step n requiring a temporal resolution of $\Delta T \approx 200$ ns, the necessary band width of the

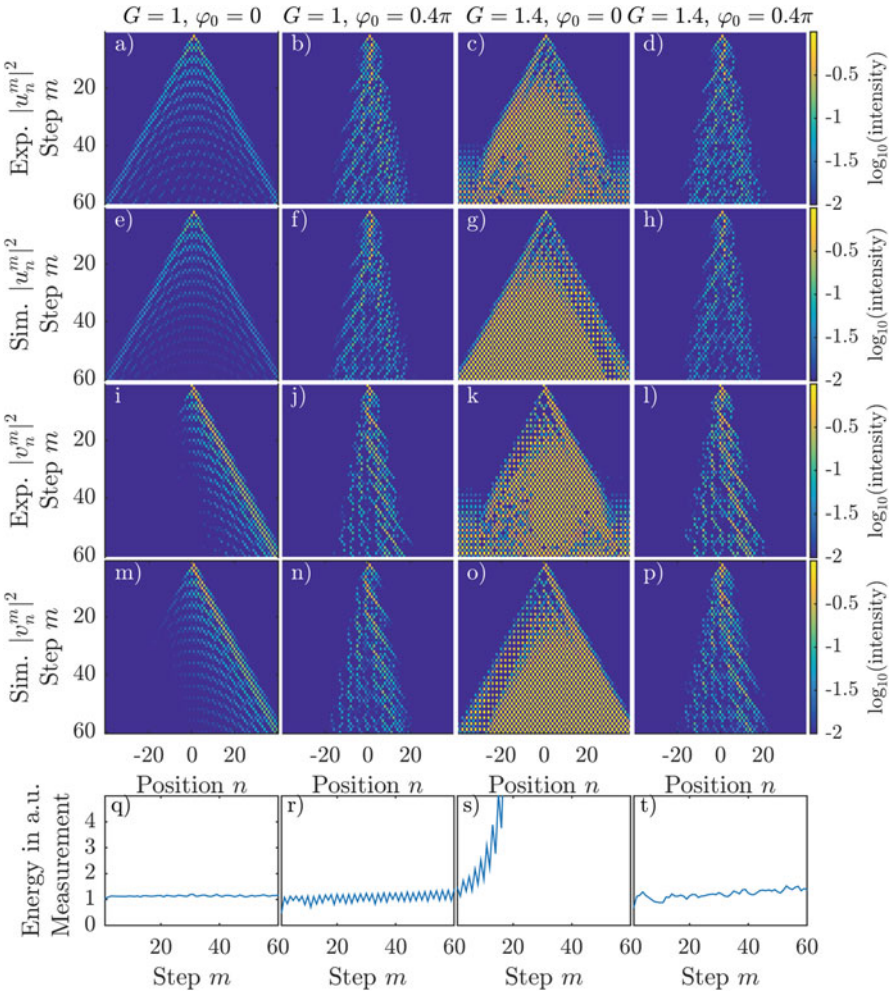

Fig. 9 Experimental and numerical propagation dynamics through the $\mathcal{PT}$ lattice. In absence of any modulation, the pulse distributions in both loops exhibit a classical Light Walk pattern [11] (see first column). By applying the phase potential in Eq. (14), waveguides are pairwise decoupled from each other, which reduces the spreading of a single lattice site excitation (second column). In the presence of a pure amplitude modulation, the complex band structure is reflected in an exponential increase in power (third column). The combination of both modulations restores $\mathcal{PT}$ symmetry for the whole band structure, and as a result power stays on average constant (fourth column). In a)-p) the intensities in the short or long loop are depicted. In q)-t) the total power is shown. This figure is motivated by [26] and depicts results from [28]

electrical signal generator for controlling the phase modulator is much lower in case of a modulation along the evolution direction m amounting to $\overline{T} \approx 20\ \mu$s only. It is also possible to transform the temporal gradient into a spatial gradient

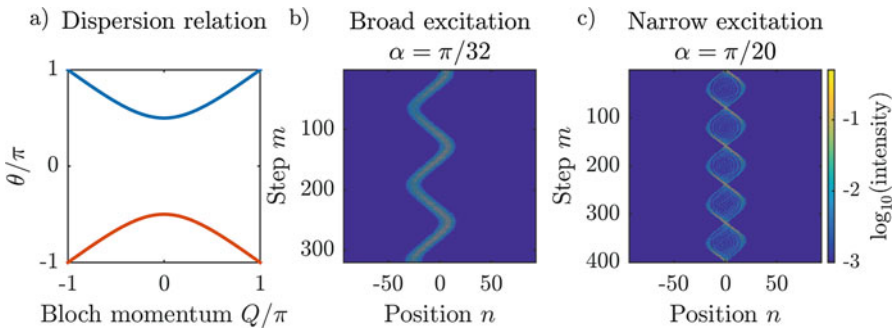

Fig. 10 Bloch oscillations in the passive lattice. By applying a phase gradient $\varphi(m) = m\alpha$, the Bloch momentum $Q = Q_0 + m\alpha/2$ of a spectrally narrow initial state is shifted for each time step. When reaching the edge of the Brillouin zone, the state performs a transition from one band to the other mediated by the Floquet-Bloch nature of the band structure. In real space, the continuous shift of the Bloch momentum is reflected in a periodic oscillation of the wave packet. The figure is adapted from [28] and shows experimental results

$$u_n^{m+1} = \frac{1}{\sqrt{2}} \left(u_{n+1}^m + i v_{n+1}^m \right) e^{\frac{i\varphi_0 n}{2}}, \tag{18.1}$$

$$v_n^{m+1} = \frac{1}{\sqrt{2}} \left(v_{n-1}^m + i u_{n-1}^m \right) e^{\frac{i\varphi_0 n}{2}}, \tag{18.2}$$

by choosing the ansatz

$$u_n^m = \widetilde{u}_n^m e^{-\frac{i\varphi}{2} nm} e^{\frac{im^2\varphi}{4}} e^{-\frac{im\varphi}{4}}, \tag{19.1}$$

$$v_n^m = \widetilde{v}_n^m e^{-\frac{i\varphi}{2} nm} e^{\frac{im^2\varphi}{4}} e^{-\frac{im\varphi}{4}}, \tag{19.2}$$

which however requires a spatial phase gradient in each loop.

Starting with a Gaussian distribution and in absence of gain and loss ($G = 1$), the wave packet performs classical Bloch oscillations (see Fig. 10b). This behavior can be explained by analyzing the evolution of the Bloch wave amplitudes of the system based on the ansatz $u_n^m = \widetilde{u}_m \exp(i\,Qn)$ and $v_n^m = \widetilde{v}_m \exp(i\,Qn)$.

If we assume that these amplitudes evolve from step m to step $m + 1$ by accumulating a phase $\widetilde{u}_{m+1} = \widetilde{u}_m \exp(i\theta(m))$ and $\widetilde{v}_{m+1} = \widetilde{v}_m \exp(i\theta(m))$, the dispersion relation

$$\cos\left(\frac{\theta}{2} + \frac{\alpha m}{2}\right) = \frac{1}{\sqrt{2}} \cos\left(\frac{Q}{2} + \frac{\alpha m}{2}\right) \tag{20}$$

is formally identical to that of a homogenous lattice (see Eq. 5) except for an m-dependent shift in absolute phase, and more importantly in the position in the

Brillouin zone. Each time step, the effective Bloch momentum Q is increased by $\alpha m/2$. When starting at the center of the Brillouin zone $Q_0 = 0$, the edge is reached at $\alpha m/2 = \pi$. At this point, the Floquet-Bloch nature of the system mediates a transition from one band to the other, since the upper left (right) and lower right (left) points of the dispersion relation are pairwise degenerate (see Fig. 10). As a result, the wave packet reenters the Brillouin zone from the opposite site. However, at the same time it changes to the other band and continues there the Bloch oscillation until it reaches again the edge of the Brillouin zone.

For sampling the Brillouin zone via Bloch oscillations we expect the most interesting effects to occur for a band structure consisting of real and complex valued sections being connected by exceptional points at $\pm Q_{EP}$. This is already realized for pure amplitude modulation ($G \neq 1, \varphi_0 = 0$), which we will consider in the following. On its way through the Brillouin zone the wave packet has to pass not only the region of complex eigenvalues but also two exceptional points. In higher dimensions, instead of passing the EP it is also possible to encircle it, which leads to a non-adiabatic transition of the excitation from one band to the other as theoretically discussed in [38] and experimentally demonstrated in [39]. At each exceptional point the two bands merge and respective eigenstates are coupled. In 1D, when crossing such pair of EPs confining a complex section of the band structure the wave packet is not only amplified, but a part of its energy is also transferred to the other band. In real space (see Fig. 11) this splitting is

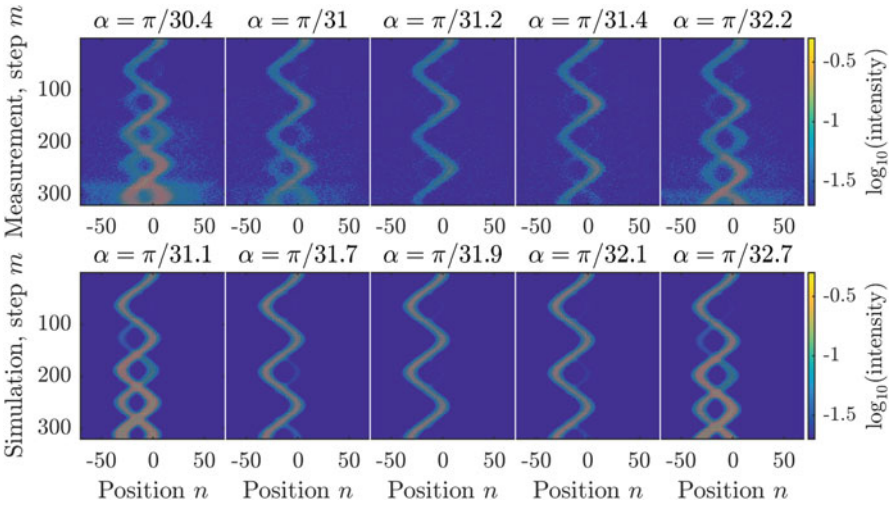

Fig. 11 $\mathcal{PT}$ Bloch oscillations. In presence of $\mathcal{PT}$ amplitude modulation ($G \approx 1.1$), the band structure is partially complex valued and features two exceptional points. The complex propagation constants lead to an increase in power during each Bloch oscillation, while at the exceptional points, a secondary branch is emitted into the opposite direction. However, for a set of magic gradients (here at $\alpha \approx \pi/31.2$), the propagation is pseudo-Hermitian and any emission of a second branch is strongly suppressed. These measurements support the theoretical results from [31] and are shown in [28]

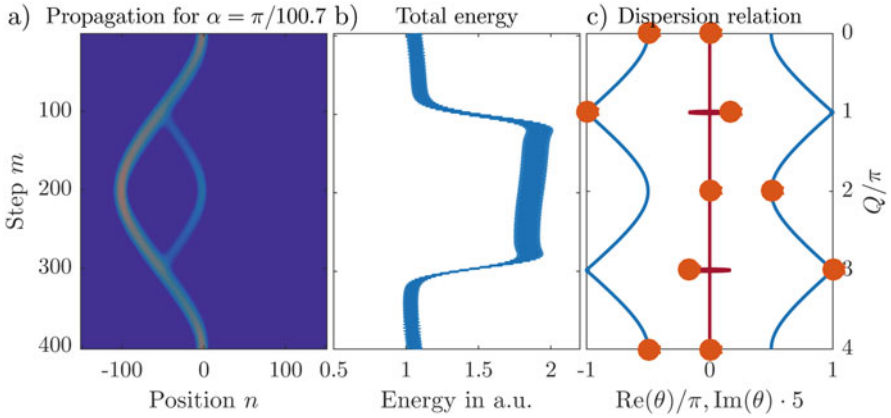

Fig. 12 Detailed numerical analysis of a single $\mathcal{PT}$ Bloch oscillation**. (a)** Real space propagation of a Bloch oscillation in presence of the $\mathcal{PT}$ amplitude modulation ($G = 1.1$). During the first half of the Bloch oscillation, the total energy shown in (**b**) increases, when the wave packet passes the complex region of the band structure. During the second half, the intensity drops again to the original value. (**c**) Dispersion relation with states of the wave packet (orange circles) for specific points during the propagation. Interestingly, even when passing the EPs, not all information is lost but instead the wave packet moves to the other band. The real part of the dispersion relation is shown in blue and the imaginary part in red. The imaginary part is stretched by a factor of five for better visibility

accompanied by the emission of a secondary branch, which counter propagates to the original one. As the wavenumber shift is the same for both bands, the two wave packets meet again at the exceptional points and power is redistributed between the bands. In some cases one of the branches is completely cancelled by destructive interference (see Fig. 12). By performing experimental and numerical sweeps over different Bloch gradients α this fascinating phenomenon is further investigated (see Fig. 11). As theoretically predicted in [31] the emission of the secondary branch is suppressed and the amplification and attenuation during the complex regions of the band structure is exactly balanced for some magic gradients. In simulations an even wider interval of Bloch gradients are accessible, which show a set of such magic gradients, for which the propagation is pseudo Hermitian (see Fig. 13).

7 Bloch Oscillations in the Local $\mathcal{PT}$-Symmetric Lattice

In the previous sections, two different approaches were described for achieving a pseudo-Hermitian propagation, where the total power is on average constant. First a spatial phase modulation was introduced, which completes the amplitude modulation in terms of the symmetry requirements of $\mathcal{PT}$ symmetry in Eq. (10). In the previous section another method based on Bloch oscillations was discussed,

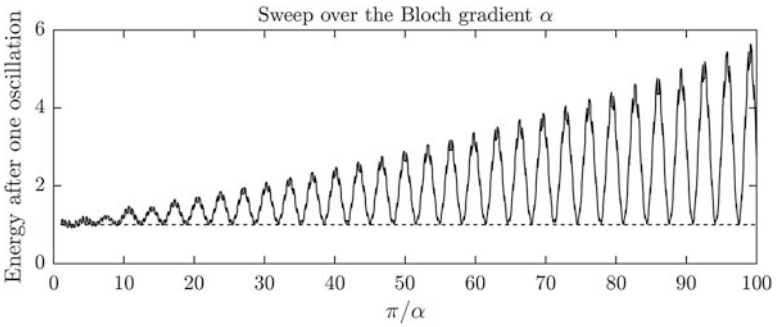

Fig. 13 Numerical parameter sweep of the Bloch gradient. For each Bloch gradient α, a single Bloch oscillation over $\approx 4\pi/\alpha$ time steps is simulated. The initial energy at the first time step is normalized to one, which is marked by the horizontal dashed line as a guide to the eyes. The solid curve depicts the energy after a full Bloch oscillation, which takes the initial value for the magic gradients (intersection points of the dashed and solid curve). By scaling the horizontal axis with the reciprocal value π/α, reveals a nearly equidistant spacing of the magic gradients. The amplification and attenuation rate is set to $G = 1.1$

where special gradients also lead to a pseudo-Hermitian propagation even in absence of the $\mathcal{PT}$ phase modulation. Therefore, the question remains, whether there are simpler ways of realizing a dissipative system with real eigenvalues. In the previous sections, the distribution of amplification and attenuation between the two fiber loops was alternating after each round trip for creating coupled waveguides with gain and loss. However, with respect to experiments, a static distribution of gain and loss is more relevant: A small maladjustment of the amplification rates of the EDFAs either leads to an exponential increase or decrease in power. While in reality, the EDFAs are precisely enough adjusted, so that hardly a change in the total power is visible, in the following a provoked imbalance is discussed. In this case, the long loop is amplified by G and the short loop is attenuated by G^{-1} according to

$$u_n^{m+1} = \frac{1}{\sqrt{2G}} \left(u_{n+1}^m + i v_{n+1}^m \right) \text{ and} \tag{21.1}$$

$$v_n^{m+1} = \frac{\sqrt{G}}{\sqrt{2}} \left(v_{n-1}^m + i u_{n-1}^m \right). \tag{21.2}$$

As a result, pulses moving to the right on the lattice are amplified, while pulses to the left are attenuated.

Also this lattice formally fulfills the requirements of $\mathcal{PT}$ symmetry in Eq. (9) for each time step (see Fig. 14), the dispersion relation

$$\cos\theta = \frac{1}{2} \left[\cos\left(Q + i\gamma\right) - 1 \right] \tag{22}$$

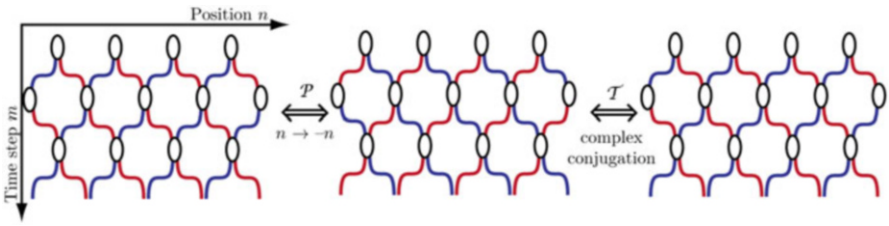

Fig. 14 Symmetry operations of the local $\mathcal{PT}$-symmetric lattice. Similar to Fig. 6, symmetries are analyzed in the local $\mathcal{PT}$ -symmetric lattice: The parity operation requires a left-right flip of the lattice and time reversal complex conjugation. However, here the lattice is not symmetric with respect to an additional vertical flip ($m \to -m$) as for time reversal symmetry in the global $\mathcal{PT}$-symmetric case (see Fig. 6). Therefore, the lattice preserves $\mathcal{PT}$ symmetry for each instantaneous time step, but not globally

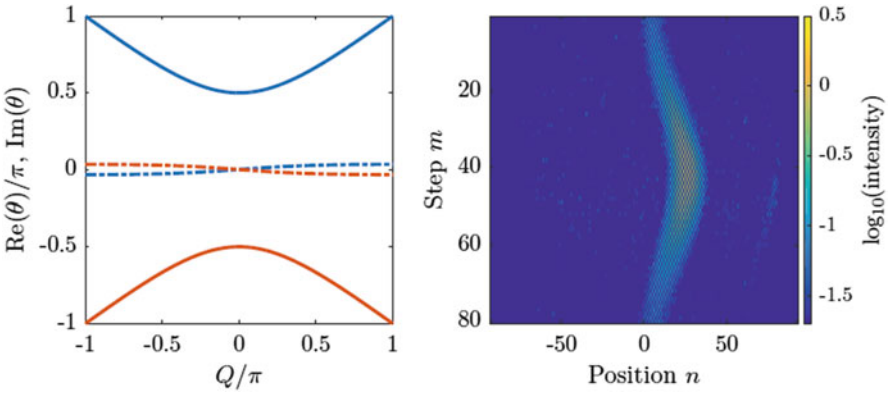

Fig. 15 Band structure of the local $\mathcal{PT}$ symmetric system and real space motion during a full Bloch oscillation**. (a**) The band structure consists of two bands, where only for $Q = 0$, the imaginary part of θ (dash-dotted lines) vanishes. The real part is shown as solid lines. (**b**) During one Bloch oscillation ($\alpha = \pi/30$), the wave packet is amplified ($G = 1.1$), while it propagates along the gain direction. At the edge of the Brillouin zone, it reenters the band structure from the opposite site and changes to the other band. Due to the symmetric imaginary part, the amplitude decays again, when the wave packet returns to its initial position. Figure is adapted from [28]

of this lattice shows complex eigenvalues over the complete Brillouin zone except at $Q = 0$ (see Fig. 15). Even by including the $\mathcal{PT}$ phase modulation, it is not possible to restore real eigenvalues. This highlights the circumstance that fulfilling $\mathcal{PT}$ symmetry does not guarantee completely real eigenvalues. Here, $\mathcal{PT}$ symmetry is fulfilled for each time step, however not for the global lattice when performing the combined operations for time reversal $\mathcal{T}$: $m \to -m$ and $G \to 1/G$ and parity $\mathcal{P}$: $n \to -n$. Therefore, this lattice is referred to as local $\mathcal{PT}$-symmetric [27].

Although the band structure of the lattice shows complex eigenvalues, it is possible to transform the system into a Hermitian counterpart by introducing reflecting

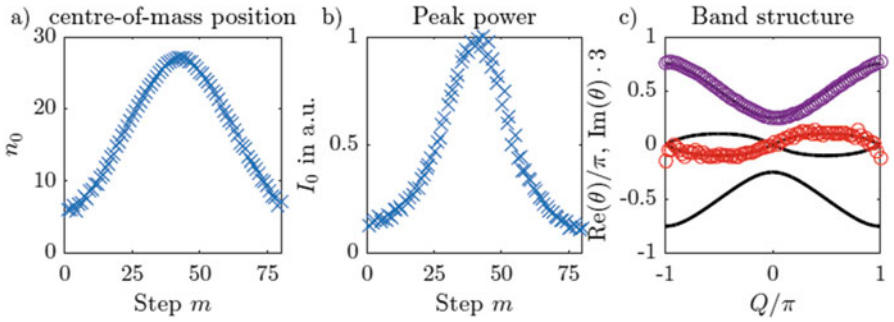

Fig. 16 Reconstruction of a complex band structure based on experimental results on Bloch oscillations. The center-of-mass motion and the evolution of the peak power is extracted by fitting a Gaussian distribution according to Eq. (23) to each row of the propagation in Fig. 15. (**a**) The derivative of the center-of-mass motion follows the group velocity of the system, which is in turn determined by the derivative of the dispersion relation (see Eq. (25)). (**b**) The increase of the amplitude each time step is determined by the imaginary part of θ (see Eq. (28)). (**c**) By evaluating both parameters, the real (violet) and imaginary part (red) of the dispersion relation is reconstructed. The amplification and attenuation rate is set to $G = 1.1$ and the Bloch gradient to $\alpha = \pi/30$. Figure is adapted from [28]

boundaries. In this case, any propagation in the amplified loop is limited by the finite system size, where at the edge the pulses are reflected from the gain direction into the loss one. Despite an initial amplification, no path can be constructed with an unbounded increase in power. Besides this illustrative explanation, also numerical calculations of the finite system indicate real eigenvalues.

In combination with Bloch oscillations an interesting question arises: On the one hand, the amplitude modulation leads to an amplification of pulses tending always into the same direction. On the other hand, applying the Bloch gradient forces wave packets to perform an oscillatory motion. In order to shed light on the question, which mechanism dominates, the temporal phase gradient $\varphi(m) = \alpha m$ is combined with a static amplitude modulation. The propagation of the wave packet starts as expected: The wave propagates analogously to the passive Bloch oscillation depicted in Fig. 15. However at the same time, the wave is amplified as it propagates into the direction of the gain loop. After half of the Bloch period, the Bloch oscillation forces the wave packet to propagate along the lossy direction back to its initial position, where it arrives without a change in the amplitude.

It is even possible to analyze systematically the position $n_0(m)$ and amplitude $A(m)$ of the wave packet at each time step for reconstructing the dispersion relation (see Fig. 16). For this purpose, a Gaussian curve

$$f(n) = Ae^{-\frac{(n-n_0)^2}{\sigma^2}} \tag{23}$$

is fitted to the pulse distribution in each time step. In a semi-classical picture of wave packet propagation, the center-of-mass of the wave packet estimated by n_0 moves at the group velocity

$$v_{\mathrm{G}} = \frac{\partial \theta(Q)}{\partial Q} \approx \frac{\partial n_0(m)}{\partial m}, \tag{24}$$

where $Q = Q_0 + m\alpha/2$. Consequently, the real part of the dispersion relation is given by the discrete summation over the center-of-mass motion

$$\theta_R(Q) = \int_0^{2\pi} dQ v_G(Q) \approx \sum\nolimits_{m=0}^{M} \frac{n_0\,(m+2) - n_0\,(m-2)}{4}. \tag{25}$$

within M time steps of a complete Bloch oscillation. The finite difference in Eq. (25) is evaluated at ± 2 due to the natural size of the unit cell covering two time steps. Complementary to the center of mass motion, the imaginary part of the propagation constant determines the evolution of the amplitude. After M time steps, the amplitude of an eigenstate

$$\psi = \begin{pmatrix} U \\ V \end{pmatrix} e^{iQm} e^{-i\theta_{\mathrm{R}} m} e^{i\theta_{\mathrm{I}} m} \tag{26}$$

is given by

$$|A(m)| = |A(0)| \prod\nolimits_{m=0}^{M} e^{\theta_I(Q(m))} = |A(0)| \exp\left(\sum\nolimits_{m=0}^{m} \theta_I\,(Q(m))\right). \tag{27}$$

In the measurement, the intensity of the wave packet is extracted by fitting the Gaussian distribution in Eq. (23). Therefore, the finite difference of the logarithm of the amplitude reveals the imaginary part of the propagation constant

$$\theta_I = \frac{\ln I\,(m+2) - \ln I\,(m-2)}{8}. \tag{28}$$

8 Nonlinear Light Propagation in the Fiber Network

On the one hand, linear light evolution through the lattice is already capable of depicting numerous phenomena like Bloch oscillations [22, 28, 31], unidirectional invisibility [26, 40–42] and the existence of trivial and topological $\mathcal{PT}$ defect states [20, 43–45]. On the other hand, the use of dispersion compensated fibers in the optical fiber network provides easy access to the nonlinear regime [12, 27]. For the optical Galton board, nonlinear effects were first theoretically studied in [46]. In experiments, the dominant nonlinear effect is the self-phase modulation (SPM) through each fiber loop. Already at comparable low peak powers of 300 mW a

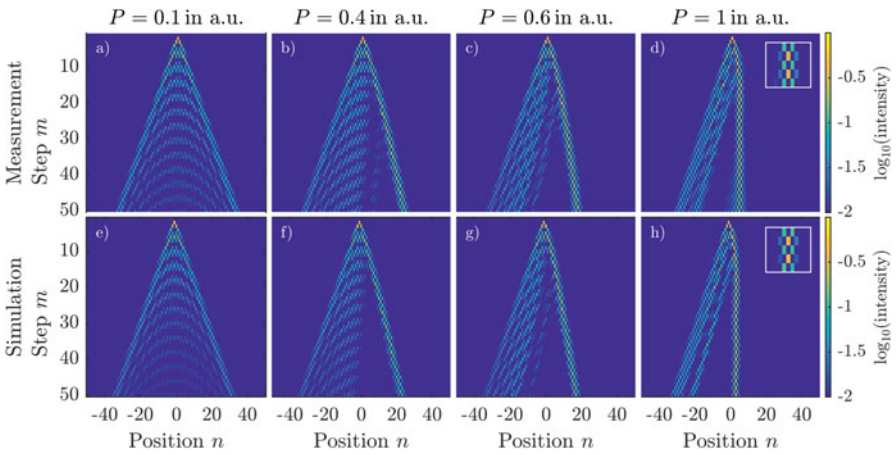

Fig. 17 Experimental observation of a Hermitian soliton in the double discrete mesh lattice. By increasing the initial power of the seed pulse, a soliton is formed, which is discretized in space and position. Figure is adapted from [27]

nonlinear phase shift of 2π is expected to accumulate within a single round trip, an effect which can be easily included in the evolution equations

$$u_n^{m+1} = \frac{\sqrt{G(m)}}{\sqrt{2}} \left(u_{n+1}^m + i\, v_{n+1}^m\right) e^{i\Gamma \left|u_{n+1}^m + i v_{n+1}^m\right|^2} e^{i\varphi(n)}, \tag{29.1}$$

$$v_n^{m+1} = \frac{\sqrt{G(m)}}{\sqrt{2}} \left(v_{n-1}^m + i\, u_{n-1}^m\right) e^{i\Gamma \left|v_{n-1}^m + i u_{n-1}^m\right|^2}. \tag{29.2}$$

In these measurements, the initial peak amplitude is varied via a screw attenuator and an AOM is used for an automatic parameter sweep.

We first discuss nonlinear evolution of the passive optical Galton board ($G = 1$) and $\varphi(n) = 0$. By increasing the power level of the initial seed pulse, the formation of a nonlinear wave is observed, which is bent towards the center of the Light Walk distribution (see Fig. 17). Compared to the initial propagation angle, the nonlinear wave propagates at a lower velocity as it is hindered by an increasing Peierls-Navarro potential [47, 48]. Light, which was originally located at the center of the Light Walk, is simultaneously repelled and shifted away from of the nonlinear wave.

This redistribution of intensities is mediated by the two band system: By starting with a single pulse, the complete Brillouin zone including both bands is excited. The effect of self-phase modulation now depends on the curvature of the respective band, which either leads to self-focusing (upper band) or defocusing (lower band) [16]. Between both bands, a diametric interaction takes place, which leads to a simultaneous attraction and repulsion [12]. At even higher peak powers, which correspond to a nonlinear phase shift of approximately 0.8π, the nonlinear

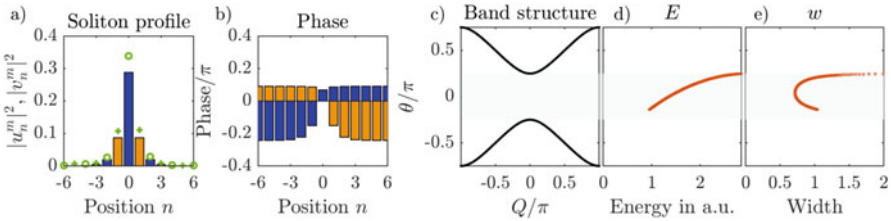

Fig. 18 Numerically determined soliton solutions. (**a**) Comparison between experimentally (crosses and circles) and numerically (bars) determined soliton profiles. The experimental data are extracted from time step $m = 25$. (**b**) Phase distribution across the soliton profile for the short and long loop. (**d**, **e**) Dependency of the soliton energy and width on the propagation constant. Figure is adapted from [27]

wave forms a soliton, propagating stable for approximately 45 time steps in the experiment. The soliton is not only discretized in space but even in time. As a result of the discretization, the main soliton pulse at the center cyclically splits up and reunites during two time steps.

Besides the experimental and simulated soliton formation and propagation, also numerical soliton solutions are found see (Fig. 18). The soliton solver is initialized with a Gaussian distribution for U_n and V_n with a $1/e$ width of 5 positions and an amplitude of 0.2. For a specific propagation constant θ_0 of the soliton within the band gap, the residual error

$$\delta f = \left\| f\left(\overrightarrow{v}\right) - \overrightarrow{v}\, e^{-i\theta} \right\| \tag{30}$$

after one time step is calculated. Here, $\overrightarrow{v} = (U_1, V_1, U_2, V_2, \ldots, U_N, V_N)^{\mathrm{t}}$ denotes a vector, which is constructed out of the soliton profile and f denotes the nonlinear evolution equations. The residual error is then minimized based on Newton's algorithm. For a propagation constant of $\theta = -0.2\pi$, the soliton solver initially converges within numerical precision. The complete branch of solitons is then calculated by choosing the last soliton solution as an initial guess for the soliton with a different propagation constant θ. For each solution, the width

$$w^2 = \frac{\sum_{n=-N_{max}}^{N_{max}} (n - n_0)^2 \left[|U_n|^2 + |V_n|^2\right]}{\sum_{n=-N_{max}}^{N_{max}} \left[|U_n|^2 + |V_n|^2\right]} \tag{31}$$

with

$$n_0 = \frac{\sum_{n=-N_{max}}^{N_{max}} n \left[|U_n|^2 + |V_n|^2\right]}{\sum_{n=-N_{max}}^{N_{max}} \left[|U_n|^2 + |V_n|^2\right]} \tag{32}$$

and energy

$$E = \sum_{n=-N_{max}}^{N_{max}} \left[|U_n|^2 + |V_n|^2 \right] \tag{33}$$

of the soliton are determined.

The stability of the soliton is numerically investigated by perturbing the solution $U_n \rightarrow U_n e^{i\delta_n}$ and $V_n \rightarrow V_n e^{i\delta_n}$ with an equally distributed phase noise δ_n. Below the center of the band gap $\theta_0 < 0$ solitons propagate stable, while above the band gap, even in absence of an initial noise the soliton decays into a stable solution [27]. Besides solitons with a maximum, which is maximum localized on a single lattice site, a second class of solitons is also found with symmetrically distributed maximum on two sites.

9 Solitons in the Local $\mathcal{PT}$ Symmetric Lattice

An interesting situation arises when nonlinearity is combined with a static amplification to the right and the attenuation of pulses propagating to the left, which was discussed before in terms of local $\mathcal{PT}$ symmetry. When injecting a low power pulse, an asymmetric Light Walk arises due to the gain/loss imbalance (see Fig. 19). However, the continuous amplification of the pulses travelling through the long loop (to the right in the optical Galton board) leads to an accumulation of nonlinear

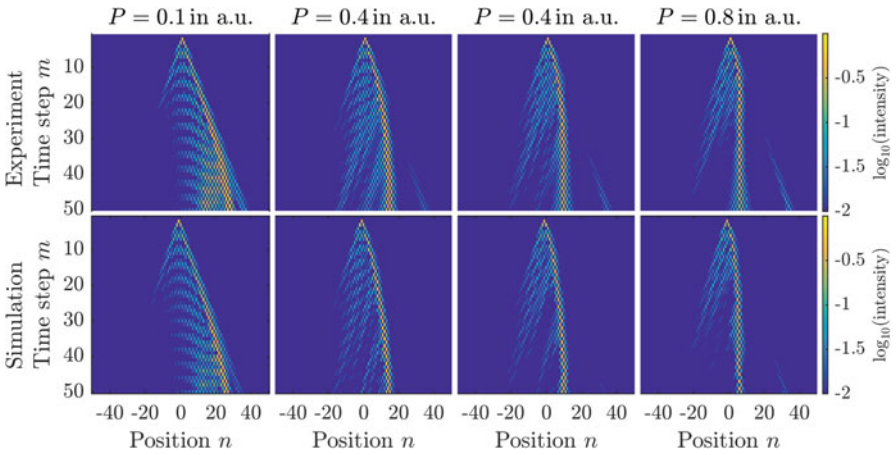

Fig. 19 Dissipative Light Walk in the local $\mathcal{PT}$-symmetric system. At low power levels, the Light Walk shows an asymmetric distribution due to the amplification in the long loop and the attenuation in the short loop ($G = 1.1$). For medium power levels, the initial amplification to the right is sufficient to form the double discrete soliton. The soliton maintains a constant power by equally propagating through the long and short loop. This figure is adapted from [27]

effects even in spite of the initial linear power level. As a consequence of the increase in power, a nonlinear wave is formed, which loses mobility due to its increasing peak power. It bends towards the center of the light walk distribution, where it finally forms a soliton, which manages to propagate in a balanced way through the gain and loss loops, so that no increase or decrease in power takes place. As this soliton on average experiences neither gain nor loss, it closely reproduces the features of its Hermitian counterpart thus forming a one-parameter family, a finding which could be confirmed by numerical simulations. This is different from localized solutions in other dissipative systems, which tend to form fixed point solutions [49], albeit exceptions like e.g. the cubic-quintic Ginzburg-Landau equation that are known to exist (see e.g [49–52].). In fact the directional distribution of gain and loss tends to stabilize the system, as any perturbation of the soliton is radiated away along the gain direction (see Fig. 20).

This internal power management of the soliton also provides the possibility of steering it through an additional global loss L in the evolution equations,

$$u_n^{m+1} = \frac{\sqrt{L}}{\sqrt{2G}} \left(u_{n+1}^m + i v_{n+1}^m\right) e^{i\Gamma \left|u_{n+1}^m + i v_{n+1}^m\right|^2}, \tag{34.1}$$

$$v_n^{m+1} = \frac{\sqrt{LG}}{\sqrt{2}} \left(v_{n-1}^m + i u_{n-1}^m\right) e^{i\Gamma \left|v_{n-1}^m + i u_{n-1}^m\right|^2}. \tag{34.2}$$

In the experiment, typically small gain/loss imbalances of $\gamma = \frac{(\ln G)}{2} \ll 1$ are investigated, where e.g. $G = 1.1$ and thus $\gamma \approx 0.05$. In this case, the real and imaginary parts of the dispersion relation ($\Gamma = 0$) are expanded in Taylor series

$$\mathrm{Re}\,\{\theta\} = \theta(Q)|_{\gamma=0} + \mathcal{O}\left(\gamma^2\right) \text{ and} \tag{35.1}$$

$$\mathrm{Im}\,\{\theta\} = \left.\frac{\partial \theta}{\partial Q}\right|_{\gamma=0} \gamma + \mathcal{O}\left(\gamma^3\right). \tag{35.2}$$

For a positive imaginary part of θ, the amplitude $A(m)$ of an eigenstate increases by

$$\left|\frac{A\,(m+1)}{A(m)}\right| = e^{\theta_{im}} \tag{36}$$

according to the Floquet-Bloch ansatz in Eq. (4). The increase in amplitude then has to overcome the global loss L per roundtrip, which yields with Eq. (35.2) the critical velocity

$$v_{crit} = \frac{\ln L}{\ln G}, \tag{37}$$

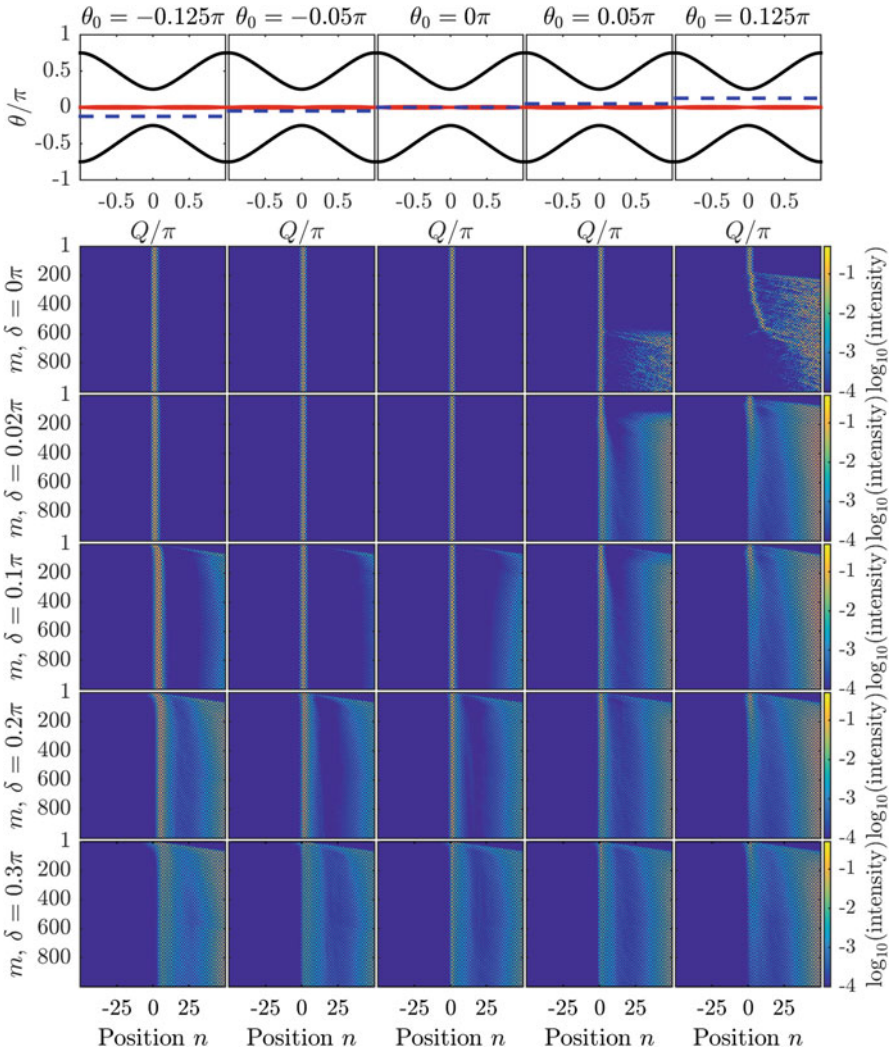

Fig. 20 Numerical test of the stability of dissipative solitons. The stability of the various solitons (different columns) of the local $\mathcal{PT}$-symmetric lattice ($G = 1.1$) is probed by different perturbations of the initial distribution $U_n' = U_n \exp(i\delta_n)$ and $V_n' = V_n \exp(i\delta_n)$ with a random phase noise δ_n (different rows of the figure), which is equally distributed between 0 and δ. The upper row displays the propagation constant of the soliton and its location in the band structure. For propagation constants $\theta_0 < 0$ (left three columns) the soliton is stable. In this case, noise is radiated into the direction of amplification, until it is absorbed at the boundary of the simulation domain. For $\theta_0 > 0$ (two columns on the right), the soliton either decays into a stable solution or vanishes completely. This figure is adapted from the supplementary material of [27]

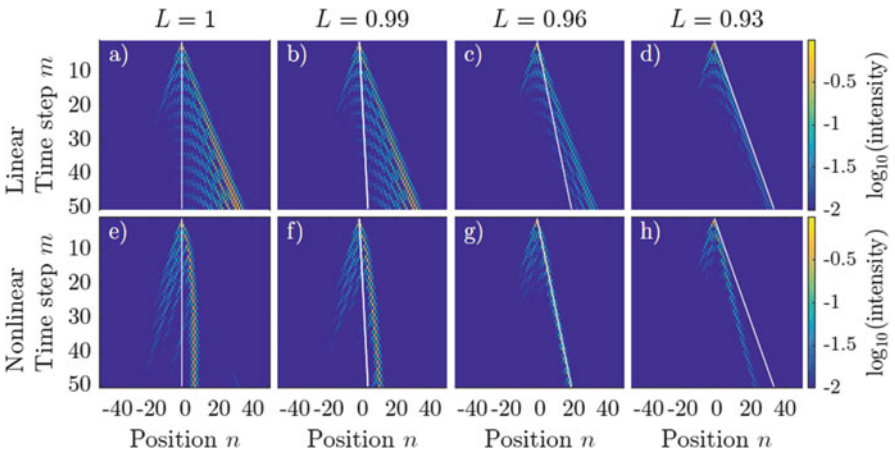

Fig. 21 Simulation of linear and nonlinear Light propagation through the local $\mathcal{PT}$-symmetric lattice with a global loss. In the linear regime, the critical velocity in Eqs. (34.1 and 34.2) separates the attenuated from the amplified parts. In the nonlinear regime ($\Gamma \approx 0.67\pi$), the same velocity is a good measurement for the soliton velocity. However, for large losses as $L = 0.93$ compared to the gain and loss imbalance of $G = 1.1$, the decreased mobility of the soliton impedes the soliton to propagate at the critical velocity, which is necessary to maintain a constant power

at which a wave packet is neither amplified nor attenuated. In the linear regime, this velocity separates the attenuated parts of the Light Walk from the amplified (see Fig. 21), while in the nonlinear regime this velocity is a good approximation of the propagation angle of the dissipative soliton.

10 Solitons in the Global $\mathcal{PT}$-Symmetric Lattice

Already before the first study on linear beam dynamics in $\mathcal{PT}$-symmetrical systems [18], the first manuscript on $\mathcal{PT}$ solitons was published [53]. However, as the stringent requirements of $\mathcal{PT}$ symmetry on the used materials is even more restricted when including materials with a significant nonlinear response, $\mathcal{PT}$ solitons remained an exclusively theoretical topic for a long time[1] [53–66]. In this sense, the fiber network provides a versatile experimental platform for studying $\mathcal{PT}$ solitons [27].

In fact we could demonstrate nonlinearly induced localization and the formation of various solitons in the global $\mathcal{PT}$-symmetric fiber network (see Figs. 22 and 23). However, for a single side excitation as demonstrated in Fig. 22 solitons show a tendency of destabilization often resulting in a slight exponential power increase

[1]The list of references here does by far not provide a complete overview about the theoretical framework of $\mathcal{PT}$ solitons.

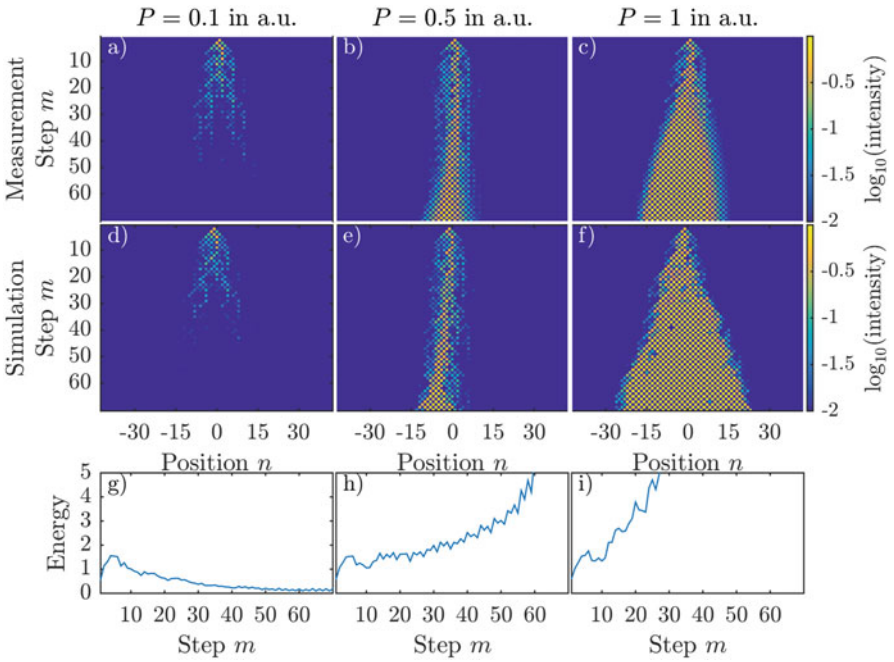

Fig. 22 Localization on the global $\mathcal{PT}$-symmetric lattice. By increasing the initial power, the spreading of a single lattice site excitation is strongly reduced until the wave packet clearly localizes. Due to the intrinsic instability of the $\mathcal{PT}$ lattice ($G = 2$, $\varphi = 0.4\pi$), nonlinear waves exponentially grow during propagation. By adding a global loss of 5% per round trip, the linear propagation is strongly damped, while only nonlinear waves survive, which acts like a saturable absorber. This figure is adapted from [27]

during propagation [26]. This is in stark contrast to an expected stabilizing effect of a focusing nonlinearity as predicted for continuous $\mathcal{PT}$-symmetric systems [66]. This instability seems to be an artifact of the discretization of the propagation in the mesh lattice. In the fiber network, phase and amplitude modulation as well as nonlinear propagation are strictly separated and thus seemingly more vulnerable with respect to perturbations. We utilized this idiosyncrasy in order to implement a saturable absorber. By adding global loss to the system, all linear waves are damped, but the soliton does not only pass the lossy system, but can be even additionally amplified during the propagation (see Fig. 22).

Besides the discrete localization, it is also possible to excite broad solitons in the global $\mathcal{PT}$-symmetric lattice with a Gaussian distribution. For these broad nonlinear waves, no intrinsic instability is visible. When increasing the amplitude of the Gaussian distribution, it self-focuses during the propagation and forms a soliton. As the input field is symmetric with respect to the real valued potential a sign change of the phase modulation $\varphi_0 \rightarrow -\varphi_0$ has a considerable impact on the propagation resulting in a transition from a single to a double hump soliton as shown in Fig. 23.

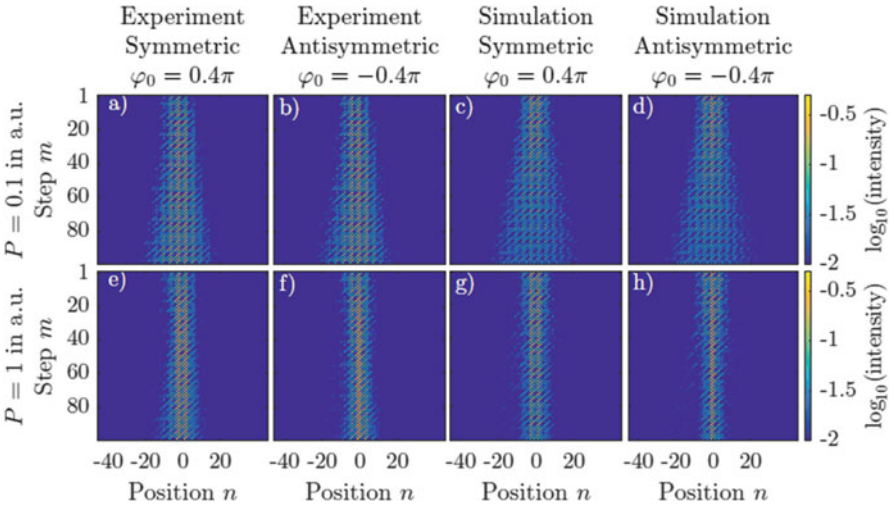

Fig. 23 Excitation of broad $\mathcal{PT}$ solitons in the experiment and simulation. In presence of gain and loss ($G = 1.4$) and a global phase modulation, broad solitons are excited, which show a stable propagation over 100 time steps in the experiment. By inverting the sign of the phase modulation, it is possible to change from a single to a double hump soliton. This figure is adapted from [27]

11 Conclusion

In the previous chapter we discussed linear and nonlinear light evolution in a synthetic photonic mesh lattice, where phase and amplitude modulators are used to establish $\mathcal{PT}$ symmetry. Based on the coupling of two fiber loops with a slight length imbalance, we showed how a double discrete $1 + 1$dimensional temporal system is created. Fiber amplifiers compensate for any losses and even allow, in combination with acousto-optical modulators, for dynamical variations of gain and loss in the network. By meticulously balancing the amplification and a suitable phase modulation, a $\mathcal{PT}$-symmetric lattice is synthesized. Although gain and loss are present, the band structure is completely real valued below the $\mathcal{PT}$ threshold. Furthermore, when combining the amplitude modulation with a phase gradient, Bloch oscillations are induced, which depict the dynamical wave propagation close to exceptional points as well as the existence of Bloch gradients featuring a pseudo-Hermitian propagation. In the local $\mathcal{PT}$-symmetric environment, we showed how to analyze the trajectories and amplitudes of wave packets performing Bloch oscillations in order to reconstruct real and imaginary part of the band structure.

In the limit of high power levels, we observe a clear localization of waves in the mesh lattice. While in the Hermitian system, a double discrete soliton forms, which is locked to a single lattice site, this soliton can be steered in the local $\mathcal{PT}$-symmetric environment via a global loss factor. The directionality of the gain/loss distribution leads to an effective cleaning of the soliton from perturbations as in convectively

stable nonlinear systems [49]. In the global $\mathcal{PT}$-symmetric mesh lattice, broad solitons are found, which propagate in a stable manner for over 100 time steps in the experiment. However, the $\mathcal{PT}$ symmetric mesh lattice seems to be intrinsically unstable with respect to nonlinear perturbations, which is demonstrated for single side excitations. In this case, the amplitudes of nonlinear waves drastically grow, which we in turn suppress by a global loss. In this case, a saturable absorber is formed, where linear waves are damped due to the global attenuation, while nonlinear waves propagate lossless or even with a net gain.

In the future, central topics in this research area will be the expansion to two spatial dimensions, as demonstrated in [10] for Quantum Walks, in combination with $\mathcal{PT}$ symmetry, as well as the merging of geometrical and topological effects with $\mathcal{PT}$ symmetry. For Bloch oscillations in $\mathcal{PT}$-symmetric systems precise measurements of the band structure were demonstrated. In combination with geometrical nontrivial systems [13], the same approach could provide useful insights into a non-Hermitian expansion of the concept of geometric phases. Additionally, higher dimensional systems provide direct access to the physics of exceptional rings [67].

Finally, by combining the phase and amplitude modulations, which both fulfill the requirements of $\mathcal{PT}$ symmetry, a pseudo-Hermitian propagation is established (see Fig. 9 fourth column), where even in the presence of gain and loss the total power stays constant on average. This is also highlighted by the dispersion relation, which is real valued for the entire Brillouin zone and free of any exceptional points [26] (see Fig. 7, fourth column). However, $\mathcal{PT}$ symmetry does not guarantee a real-valued dispersion relation as shown in Fig. 8. The band structure is only real for the gain parameter G below a critical threshold value, which depends on the amplitude φ_0 of the phase modulation. By either decreasing the phase potential φ_0 or by increasing the gain/loss imbalance above a critical value, it is possible to perform a transition across the $\mathcal{PT}$ threshold [26]. While parity and time symmetry are graphically illustrated in Fig. 6, an explicit and rigorous analysis of $\mathcal{PT}$ symmetry in the fiber network is provided in [30].

Acknowledgements We thank Alois Regensburger, Christoph Bersch, Georgy Onishchukov and Mohammad-Ali Miri for fruitful collaborations. Furthermore, we acknowledge financial support from the Erlangen Graduate School of Advanced Optical Technologies and GRK 2101.

References

1. Galton, F.: Natural Inheritance. Macmillan, New York (1889)
2. Kempe, J.: Quantum random walks: an introductory overview. Contemp. Phys. **44**, 307 (2003)
3. Bouwmeester, D., Marzoli, I., Karman, G.P., Schleich, W., Woerdman, J.P.: Optical Galton board. Phys. Rev. A. **61**, 13410 (1999)
4. Schreiber, A., Cassemiro, K.N., Potoček, V., Gábris, A., Jex, I., Silberhorn, C.: Decoherence and disorder in quantum walks: from ballistic spread to localization. Phys. Rev. Lett. **106**, 180403 (2011)

5. Karski, M., Forster, L., Choi, J.-M., Steffen, A., Alt, W., Meschede, D., Widera, A.: Quantum walk in position space with single optically trapped atoms. Science. **325**, 174 (2009)
6. Shenvi, N., Kempe, J., Whaley, K.B.: Quantum random-walk search algorithm. Phys. Rev. A. **67**, 52307 (2003)
7. Knight, P.L., Roldán, E., Sipe, J.E.: Quantum walk on the line as an interference phenomenon. Phys. Rev. A. **68**, 20301 (2003)
8. Schreiber, A., Cassemiro, K.N., Potoček, V., Gábris, A., Mosley, P.J., Andersson, E., Jex, I., Silberhorn, C.: Photons walking the line: a quantum walk with adjustable coin operations. Phys. Rev. Lett. **104**, 50502 (2010)
9. Kitagawa, T., Broome, M.A., Fedrizzi, A., Rudner, M.S., Berg, E., Kassal, I., Aspuru-Guzik, A., Demler, E., White, A.G.: Observation of topologically protected bound states in photonic quantum walks. Nat. Commun. **3**, 882 (2012)
10. Schreiber, A., Gabris, A., Rohde, P.P., Laiho, K., Stefanak, M., Potocek, V., Hamilton, C., Jex, I., Silberhorn, C.: A 2D quantum walk simulation of two-particle dynamics. Science. **336**, 55 (2012)
11. Regensburger, A., Bersch, C., Hinrichs, B., Onishchukov, G., Schreiber, A., Silberhorn, C., Peschel, U.: Photon propagation in a discrete fiber network: an interplay of coherence and losses. Phys. Rev. Lett. **107**, 233902 (2011)
12. Wimmer, M., Regensburger, A., Bersch, C., Miri, M., Batz, S., Onishchukov, G., Christodoulides, D.N., Peschel, U.: Optical diametric drive acceleration through action–reaction symmetry breaking. Nat. Phys. **9**, 780 (2013)
13. Wimmer, M., Price, H.M., Carusotto, I., Peschel, U.: Experimental measurement of the Berry curvature from anomalous transport. Nat. Phys. **13**, 545 (2017)
14. Gruner-Nielsen, L., Wandel, M., Kristensen, P., Jorgensen, C., Jorgensen, L.V., Edvold, B., Palsdottir, B., Jakobsen, D.: Dispersion-compensating fibers. J. Light. Technol. **23**, 3566 (2005)
15. Miri, M.-A., Regensburger, A., Peschel, U., Christodoulides, D.N.: Optical mesh lattices with *PT* symmetry. Phys. Rev. A. **86**, 23807 (2012)
16. Morandotti, R., Eisenberg, H.S., Silberberg, Y., Sorel, M., Aitchison, J.S.: Self-focusing and defocusing in waveguide arrays. Phys. Rev. Lett. **86**, 3296 (2001)
17. Bender, C.M., Boettcher, S.: Real spectra in non-hermitian hamiltonians having *PT* symmetry. Phys. Rev. Lett. **80**, 5243 (1998)
18. Makris, K.G., El-Ganainy, R., Christodoulides, D.N., Musslimani, Z.H.: Beam dynamics in *PT* symmetric optical lattices. Phys. Rev. Lett. **100**, 103904 (2008)
19. Guo, A., Salamo, G.J., Duchesne, D., Morandotti, R., Volatier-Ravat, M., Aimez, V., Siviloglou, G.A., Christodoulides, D.N.: Observation of *PT* -symmetry breaking in complex optical pot entials. Phys. Rev. Lett. **103**, 93902 (2009)
20. Weimann, S., Kremer, M., Plotnik, Y., Lumer, Y., Nolte, S., Makris, K.G., Segev, M., Rechtsman, M.C., Szameit, A.: Topologically protected bound states in photonic parity–time-symmetric crystals. Nat. Mater. **16**, 433 (2016)
21. Eichelkraut, T., Weimann, S., Stützer, S., Nolte, S., Szameit, A.: Radiation-loss management in modulated waveguides. Opt. Lett. **39**, 6831 (2014)
22. Xu, Y.-L., Fegadolli, W.S., Gan, L., Lu, M.-H., Liu, X.-P., Li, Z.-Y., Scherer, A., Chen, Y.-F.: Experimental realization of Bloch oscillations in a parity-time synthetic silicon photonic lattice. Nat. Commun. **7**, 11319 (2016)
23. Ornigotti, M., Szameit, A.: Quasi *PT* -symmetry in passive photonic lattices. J. Opt. **16**, 65501 (2014)
24. Peng, B., Özdemir, Ş.K., Lei, F., Monifi, F., Gianfreda, M., Long, G.L., Fan, S., Nori, F., Bender, C.M., Yang, L.: Parity–time-symmetric whispering-gallery microcavities. Nat. Phys. **10**, 394 (2014)
25. Hodaei, H., Miri, M.-A., Heinrich, M., Christodoulides, D.N., Khajavikhan, M.: Parity-time-symmetric microring lasers. Science. **346**, 975 (2014)
26. Regensburger, A., Bersch, C., Miri, M.A., Onishchukov, G., Christodoulides, D.N., Peschel, U.: Parity–time synthetic photonic lattices. Nature. **488**, 167 (2012)

27. Wimmer, M., Regensburger, A., Miri, M., Bersch, C., Christodoulides, D.N., Peschel, U.: Observation of optical solitons in PT-symmetric lattices. Nat. Commun. **6**, 7782 (2015)
28. Wimmer, M., Miri, M.-A., Christodoulides, D., Peschel, U.: Observation of Bloch oscillations in complex PT-symmetric photonic lattices. Sci. Rep. **5**, 17760 (2016)
29. Heiss, W.D.: The physics of exceptional points. J. Phys. A. Math. Theor. **45**, 444016 (2012)
30. Mochizuki, K., Kim, D., Obuse, H.: Explicit definition of *PT* symmetry for nonunitary quantum walks with gain and loss. Phys. Rev. A. **93**, 62116 (2016)
31. Longhi, S.: Bloch oscillations in complex crystals with *PT* symmetry. Phys. Rev. Lett. **103**, 123601 (2009)
32. Bloch, F.: Über die Quantenmechanik der Elektronen in Kristallgittern. Zeitschrift Für Phys. **52**, 555 (1929)
33. Zener, C.: A theory of the electrical breakdown of solid dielectrics. Proc. R. Soc. A. Math. Phys. Eng. Sci. **145**, 523 (1934)
34. Kittel, C.: Introduction into solid state physics, 8th edn. Wiley, New York (2005)
35. Peschel, U., Pertsch, T., Lederer, F.: Optical Bloch oscillations in waveguide arrays. Opt. Lett. **23**, 1701 (1998)
36. Pertsch, T., Dannberg, P., Elflein, W., Bräuer, A., Lederer, F.: Optical bloch oscillations in temperature tuned waveguide arrays. Phys. Rev. Lett. **83**, 4752 (1999)
37. Matjeschk, R., Ahlbrecht, A., Enderlein, M., Cedzich, C., Werner, A.H., Keyl, M., Schaetz, T., Werner, R.F.: Quantum walks with nonorthogonal position states. Phys. Rev. Lett. **109**, 240503 (2012)
38. Uzdin, R., Mailybaev, A., Moiseyev, N.: On the observability and asymmetry of adiabatic state flips generated by exceptional points. J. Phys. A Math. Theor. **44**, 435302 (2011)
39. Doppler, J., Mailybaev, A.A., Böhm, J., Kuhl, U., Girschik, A., Libisch, F., Milburn, T.J., Rabl, P., Moiseyev, N., Rotter, S.: Dynamically encircling an exceptional point for asymmetric mode switching. Nature. **537**, 76 (2016)
40. Mostafazadeh, A.: Invisibility and *PT* symmetry. Phys. Rev. A. **87**, 12103 (2013)
41. Longhi, S.: Invisibility in *PT* -symmetric complex crystals. J. Phys. A Math. Theor. **44**, 485302 (2011)
42. Lin, Z., Ramezani, H., Eichelkraut, T., Kottos, T., Cao, H., Christodoulides, D.N.: Unidirectional invisibility induced by PT-symmetric periodic structures. Phys. Rev. Lett. **106**, 213901 (2011)
43. Regensburger, A., Miri, M.-A., Bersch, C., Näger, J., Onishchukov, G., Christodoulides, D.N., Peschel, U.: Observation of defect states in *PT* -symmetric optical lattices. Phys. Rev. Lett. **110**, 223902 (2013)
44. Longhi, S.: Zak phase of photons in optical waveguide lattices. Opt. Lett. **39**, 1697 (2014)
45. Schomerus, H.: Topologically protected midgap states in complex photonic lattices. Opt. Lett. **38**, 1912 (2013)
46. Navarrete-Benlloch, C., Pérez, A., Roldán, E.: Nonlinear optical Galton board. Phys. Rev. A. **75**, 62333 (2007)
47. Kivshar, Y.S., Campbell, D.K.: Peierls-Nabarro potential barrier for highly localized nonlinear modes. Phys. Rev. E. **48**, 3077 (1993)
48. Morandotti, R., Eisenberg, H.S., Mandelik, D., Silberberg, Y., Modotto, D., Sorel, M., Stanley, C.R., Aitchison, J.S.: Interactions of discrete solitons with structural defects. Opt. Lett. **28**, 834 (2003)
49. Ankiewicz, A., Akhmediev, N.: Dissipative solitons: from optics to biology and medicine. Springer, Berlin/Heidelberg (2008)
50. Rozanov, N.N.: Dissipative optical solitons. Physics-Uspekhi. **43**, 421 (2000)
51. Akhmediev, N., Ankiewicz, A.: Dissipative solitons, pp. 1–17. Springer, Berlin/Heidelberg (2005)
52. Lederer, F., Stegeman, G.I., Christodoulides, D.N., Assanto, G., Segev, M., Silberberg, Y.: Discrete solitons in optics. Phys. Rep. **463**, 1 (2008)
53. Musslimani, Z.H., Makris, K.G., El-Ganainy, R., Christodoulides, D.N.: Optical solitons in *PT* periodic potentials. Phys. Rev. Lett. **100**, 30402 (2008)

54. He, Y., Zhu, X., Mihalache, D., Liu, J., Chen, Z.: Lattice solitons in *PT* -symmetric mixed linear-nonlinear optical lattices. Phys. Rev. A. **85**, 13831 (2012)
55. Miri, M.A., Aceves, A.B., Kottos, T., Kovanis, V., Christodoulides, D.N.: Bragg solitons in nonlinear PT-symmetric periodic potentials. Phys. Rev. A. **86**, 33801 (2012)
56. Li, C., Liu, H., Dong, L.: Multi-stable solitons in *PT* -symmetric optical lattices. Opt. Lett. **20**, 16823–16831 (2012)
57. Li, C., Huang, C., Liu, H., Dong, L.: Multipeaked gap solitons in PT-symmetric optical lattices. Opt. Lett. **37**, 4543 (2012)
58. Achilleos, V., Kevrekidis, P.G., Frantzeskakis, D.J., Carretero-González, R.: Dark solitons and vortices in *PT* -symmetric nonlinear media: From spontaneous symmetry breaking to nonlinear *PT* phase transitions. Phys. Rev. A. **86**, 13808 (2012)
59. Shi, Z., Jiang, X., Zhu, X., Li, H.: Bright spatial solitons in defocusing Kerr media with *PT* -symmetric potentials. Phys. Rev. A. **84**, 53855 (2011)
60. Abdullaev, F.K., Kartashov, Y.V., Konotop, V.V., Zezyulin, D.a.: Solitons in *PT* -symmetric nonlinear lattices. Phys. Rev. A. **83**, 41805 (2011)
61. Zhong, W.-P., Belić, M.R., Huang, T.: Two-dimensional accessible solitons in PT-symmetric potentials. Nonlinear Dyn. **70**, 2027 (2012)
62. Konotop, V.V., Pelinovsky, D.E., Zezyulin, D.A.: Discrete solitons in *PT* -symmetric lattices. EPL (Europhys. Lett.). **100**, 56006 (2012)
63. Nixon, S., Ge, L., Yang, J.: Stability analysis for solitons in *PT* -symmetric optical lattices. Phys. Rev. A. **85**, 23822 (2012)
64. Alexeeva, N.V., Barashenkov, I.V., Sukhorukov, A.a., Kivshar, Y.S.: Optical solitons in *PT* -symmetric nonlinear couplers with gain and loss. Phys. Rev. A. **85**, 63837 (2012)
65. Nixon, S., Zhu, Y., Yang, J.: Nonlinear dynamics of wave packets in parity-time-symmetric optical lattices near the phase transition point. Opt. Lett. **37**, 4874 (2012)
66. Lumer, Y., Plotnik, Y., Rechtsman, M.C., Segev, M.: Nonlinearly induced *PT* transition in photonic systems. Phys. Rev. Lett. **111**, 263901 (2013)
67. Zhen, B., Hsu, C.W., Igarashi, Y., Lu, L., Kaminer, I., Pick, A., Chua, S.-L., Joannopoulos, J.D., Soljačić, M.: Spawning rings of exceptional points out of Dirac cones. Nature. **525**, 354 (2015)

PT-Symmetry on-a-Chip: Harnessing Optical Loss for Novel Integrated Photonic Functionality

Mingsen Pan, Pei Miao, Han Zhao, Zhifeng Zhang, and Liang Feng

Abstract The development of non-Hermitian parity-time (PT) symmetric quantum mechanics has offered a powerful platform to engineer novel device functionality for integrated photonics. In this chapter, we review the chip-scale applications of PT-symmetry in photonic devices, including the implementation of the unidirectional reflectionless PT metamaterial, coherent asymmetric light-light switching, and orbital angular momentum (OAM) laser on-chip. We study the optical analogy of non-Hermitian PT systems, manipulate the complex refractive index properties such as gain/loss modulation, and investigate the unique wave transport characteristics near the exceptional point (EP) to achieve these intriguing on-chip functionalities.

1 Introduction

As an extension of conventional quantum mechanics into the complex domain, the concept of parity-time (PT) symmetric Hamiltonian has given new understanding to the behaviors of non-Hermitian systems. A system described by the non-Hermitian Hamiltonians can also possess real spectra if it is PT symmetric [1–3], giving rise to discussions and debates in the quantum field theory [3] and open quantum systems

M. Pan · P. Miao
Department of Materials Science and Engineering, University of Pennsylvania, Philadelphia, PA, USA

Department of Electrical Engineering, The State University of New York at Buffalo, Buffalo, NY, USA

H. Zhao · Z. Zhang
Department of Electrical and Systems Engineering, University of Pennsylvania, Philadelphia, PA, USA

L. Feng (✉)
Department of Materials Science and Engineering, University of Pennsylvania, Philadelphia, PA, USA
e-mail: fenglia@seas.upenn.edu

D. Christodoulides, J. Yang (eds.), *Parity-time Symmetry and Its Applications*, Springer Tracts in Modern Physics 280,
https://doi.org/10.1007/978-981-13-1247-2_2

[4]. Although re-searchers are pursuing the impacts of PT symmetry on these fields, it has been realized that optics, due to the equivalence between the wave equation and the Schrödinger equation in quantum mechanics, has provided an ideal platform for studying the fundamentals of PT symmetryboth theoretically and experimentally [5–8].

A Hamiltonian is considered to be PT symmetric when it commutes with PT symmetry operator, $PT\widehat{H} = \widehat{H}PT$, which is the compound symmetry of parity P and time reversal T [2, 9, 10]. For a Hamiltonian $\widehat{H} = \widehat{p}/2m + V(\widehat{x})$, where $\widehat{x}$ and $\widehat{p}$ are position and momentum operator, and m and V are the mass and potential, parity operator P corresponds to $\widehat{p} \to -\widehat{p}, \widehat{x} \to -\widehat{x}$, while the time reversal T corresponds to $\widehat{p} \to -\widehat{p}, \widehat{x} \to \widehat{x}$, and $i \to -i$. We can get a PT symmetry Hamiltonian when its potential is modulated in a complex way, $V(\widehat{x}) = V^*(-\widehat{x})$. In optics, the complex refractive index in the paraxial equations of diffraction plays the role as a complex potential. For a PT symmetry photonic system, the complex refractive index can be $n(x) = n^*(-x)$, where the real part is an even function of x, and the gain/loss modulation is odd.

Another important aspect of such photonic system modulated with absorption and amplification is that the evolution of PT symmetry is measurable from the periodic potential contrast [5, 11, 12]. As the energy spectrum change spontaneously from real to complex values, a PT symmetry threshold can be clearly observed at a certain point in the parametric space, namely the PT symmetry breaking point, or the exceptional point (EP). At this point, the eigenstates in the PT photonic system become degenerate, which creates counter-intuitive wave transport characteristics and thus introduces intriguing properties to the artificial materials (i.e., metamaterials), such as dynamic power oscillations of light propagation [13–16] and coherent perfect absorber-lasers [17].

In our previous study, by carefully engineering the non-Hermitian photonic system with the PT theory, we have achieved versatile functionality of the metamaterials for the new-generation on-chip applications. In this chapter, we mainly go through the fundamentals and technical details of three chip-scale applications [18–20]. The first topic is the unidirectional invisibility metamaterial. We create a non-Hermitian system with a modulated gain/loss structure and confirm that the degenerate states at the EP support for the unidirectional wave transport where reflecting wave from one direction disappears. When we further study this intrinsic asymmetry of the non-Hermitian photonic metamaterials, optical modes working near these EPs can also present coherent perfect absorption states in the degenerate eigenstates. In the second topic, we show that, in such a photonic system, coherent optical absorbing states exist, and a weak control beam can be exploited to control an intense laser signal functioning as a light-light switch. The unidirectional characteristics works not only in waveguides, but also in ring structures where the end meets the start, which gives the idea of our third topic. When working near the EP in a ring resonator, the degenerated eigenstates isolate the two counter-propagating modes, drive unidirectional power flows, and scatter out a twisted helical light beam carrying orbital angular momentum (OAM). To accomplish these novel functionalities, we begin with the analysis using the optical

scattering matrix (S-matrix) and transfer matrix to study the fundamentals of the unique wave characteristics. We will explore the asymmetric wave transport in PT symmetry photonic systems near the EP. To manifest the functionality of the photonic devices, we fabricated on-chip microstructures and experimentally verified the characteristics of the metamaterial.

2 Passive PT Metamaterial and Unidirectional Reflectionless Transport

Materials characterized by unidirectional reflection, or invisibility, can be found in various military applications, where the electromagnetic waves emitted from radar are absorbed in order to hide from detection sources. Here we show the realization of chip-scale unidirectional reflectionless optical metamaterials where reflection from one side is significantly suppressed. Based on the study of the wave properties near its EP in the optical wavelength, we theoretically propose and experimentally realize a silicon-based optical non-Hermitian PT system with only absorptive media on the silicon-on-insulator (SOI) platform.

2.1 EP Characterization of Passive PT Metamaterial

For ease of the fabrication and experimental implementation, the photonic systems are usually designed to be passive, i.e., loss-dominant with only absorptive materials. Here we show that the evolution of PT transition of a passive system is the same as the balanced system in PT theory in quantum mechanics.

To study the reflection and transmission characteristics of material, we choose a model with the optical potential modulated as a second-order Bragg reflector. The spatial distribution of complex dielectric permittivity is $\Delta\varepsilon(z) = cos(qz) - i\delta sin(qz)$, where $q = 2k_1$ is the grating period, z is the distance in the wave propagation direction, δ is the amplitude of loss modulation, and the grating region is $4n\pi/q + \pi/q \leq z \leq 4n\pi/q + 2\pi/q$. In this region, $sin(qz)$ is a negative number to accomplish a system without gain. To obtain the analytical model of the system, the introduced modulation was averaged in an entire period as $\overline{\Delta\varepsilon} = C_q e^{iqz} + C_{-q} e^{-iqz} + C_0$ where the coefficients are $C_0 = \frac{q}{4\pi}\int_{\frac{\pi}{q}}^{\frac{2\pi}{q}} \Delta\varepsilon(z)dz = i\frac{\delta}{2\pi}$, $C_q = \frac{q}{4\pi}\int_{\frac{\pi}{q}}^{\frac{2\pi}{q}} \Delta\varepsilon(z)e^{-iqz}dz = \frac{1-\delta}{8}$, and $C_{-q} = \frac{q}{4\pi}\int_{\frac{\pi}{q}}^{\frac{2\pi}{q}} \Delta\varepsilon(z)e^{iqz}dz = \frac{1+\delta}{8}$.

In this modulated regime, the electrical field can be written as $E(x, y, z) = A(z)E(x, y)\, e^{ik_1 z} + B(z)E(x, y)\, e^{-ik_1 z}$ where $A(z)$ and $B(z)$ are the amplitudes of forward and backward fundamental modes. Under adiabatic approximation, the coupled-mode equations can be derived as

$$\frac{d}{dz}\begin{bmatrix} A(z) \\ B(z) \end{bmatrix} = H \begin{bmatrix} A(z) \\ B(z) \end{bmatrix} \tag{1}$$

If we consider the mode attenuation α and mode coupling strength κ between forward and backward fundamental modes, matrix H can be determined by $\begin{bmatrix} iC_0\alpha & iC_q\kappa \\ -iC_{-q}\kappa & -iC_0\alpha \end{bmatrix}$, which is $\begin{bmatrix} -\frac{\delta}{2\pi}\alpha & i\frac{1-\delta}{8}\kappa \\ -i\frac{1+\delta}{8}\kappa & \frac{\delta}{2\pi}\alpha \end{bmatrix}$ for this specific modulation. Due to the asymmetric gain/loss modulation for fields coming from different directions, the diagonal elements of H become unequal with increasing amplitudes of loss doping in this system. To observe the phase transition characteristics in this passive system, we analyze the evolution solutions to the backward and forward transporting electric fields.

The solutions to this matrix differential equation, in the form of $\frac{d}{dz}\psi = H\psi$, evolves in the z direction as $\psi(z) = e^{Hz}\psi(0) = \mathrm{W}e^{\Gamma z}W^{-1}\psi(0)$. Here Γ and W are the eigenvalue matrix and eigenvector matrix of H respectively. The transfer matrix of the photonic system after propagating a distance of L from $z = 0$ through the modulation region can be derived as

$$\begin{bmatrix} A(z) \\ B(z) \end{bmatrix} = \begin{bmatrix} M_{11} & M_{12} \\ M_{21} & M_{22} \end{bmatrix} \begin{bmatrix} A(0) \\ B(0) \end{bmatrix} \tag{2}$$

where

$M_{11} = \cosh(\gamma L) - \frac{\delta}{2\pi\gamma}\alpha \sinh(\gamma L), M_{12} = i\frac{1-\delta}{8\gamma}\kappa \sinh(\gamma L)$,
$M_{21} = -i\frac{1+\delta}{8\gamma}\kappa \sinh(\gamma L), M_{22} = \cosh(\gamma L) + \frac{\delta}{2\pi\gamma}\alpha \sinh(\gamma L)$, and $\gamma = \sqrt{(\delta\alpha/2\pi)^2 + \left(1-\delta^2\right)(\kappa/8)^2}$ is the eigenvalue of H.

The transfer matrix solutions reveal the evolution of the system for both backward and forward propagating waves. To determine the transmission and reflection of the 'two-port' system, we derived the scattering matrix which relates the outgoing waves to the incoming waves of the system. The scattering matrix of the modulation (i.e. the S-parameter) [21] is

$$S = \begin{bmatrix} t & r_b \\ r_f & \mathrm{t} \end{bmatrix} = \begin{bmatrix} 1/M_{22} & M_{12}/M_{22} \\ -M_{21}/M_{22} & 1/M_{22} \end{bmatrix} = aS' \tag{3}$$

In equation (3), t is the transmission amplitude, r_f and r_b are reflection amplitude from forward and backward directions respectively, and S' is an 'intrinsic' unimodular scattering matrix with an attenuation term $a = \sqrt{1 + M_{12}M_{21}}/M_{22}$. The scattering matrix clearly shows that, when $\delta = 1$ at the exceptional point, the system can be simplified due to $C_q = 0$. The corresponding transmission and reflection coefficients are $t = e^{-\frac{i\alpha L}{\pi}}$, $r_b = 0$, and $r_f = \left(\frac{\pi\kappa}{2\alpha}\right)^2 \sinh^2\frac{2\pi}{\alpha L}e^{-\alpha L/\pi}$. With

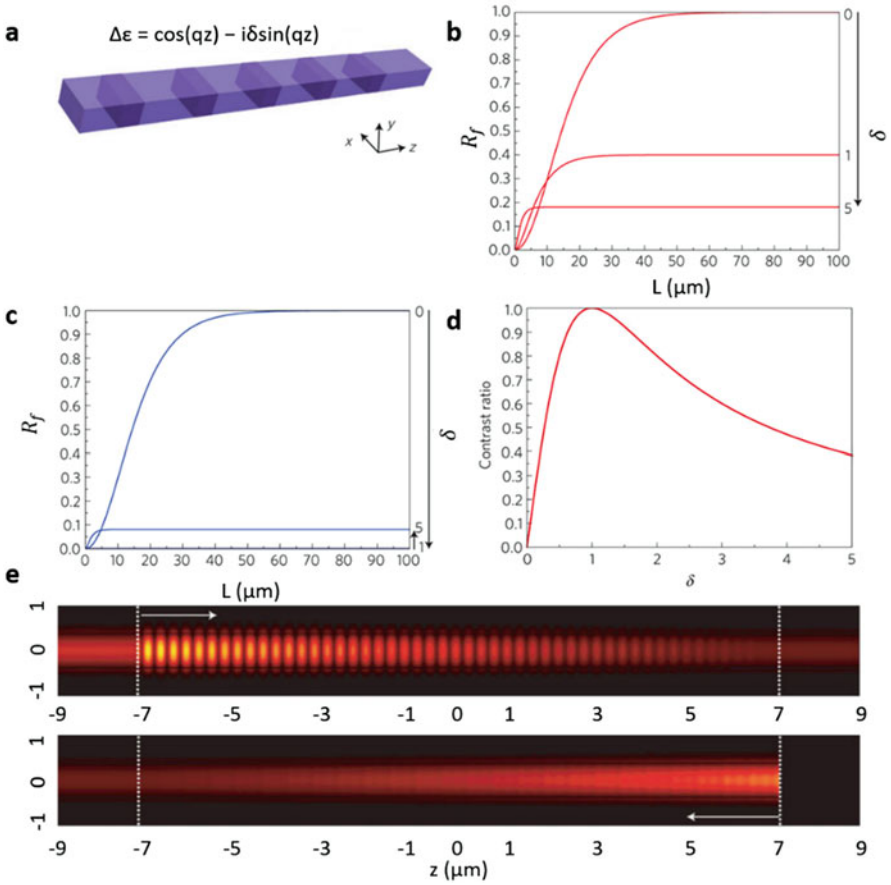

Fig. 1 Characteristics of parity-time symmetry in the proposed passive parity-time metamaterial. (**a**) Schematic of the passive PT metamaterial on a SOI platform, (**b**, **c**) Forward and backward reflectance with different values of δ and the modulation length L at the wavelength of 1550 nm. (**d**) The contrast ratio of reflectivities in both directions at different values of δ. (**e**) Electric field amplitude distribution of light passing through the 25-period PT modulations at its exceptional point from forward (upper) and backward (lower) directions propagating at a wavelength of 1550 nm

these derived analytical formulas for transmission and reflection, the attenuation coefficient and the coupling coefficient can be determined numerically by fitting these analytical calculations into the simulation results (see the supplementary material in [18]). The modulation in the structure of Fig. 1 and Fig. 2 determines $\alpha = 0.61\ \mu m^{-1}$ and $\kappa = 0.49\ \mu m^{-1}$.

In contrast, by the same steps of derivations, the S-matrix in the balanced PT system is

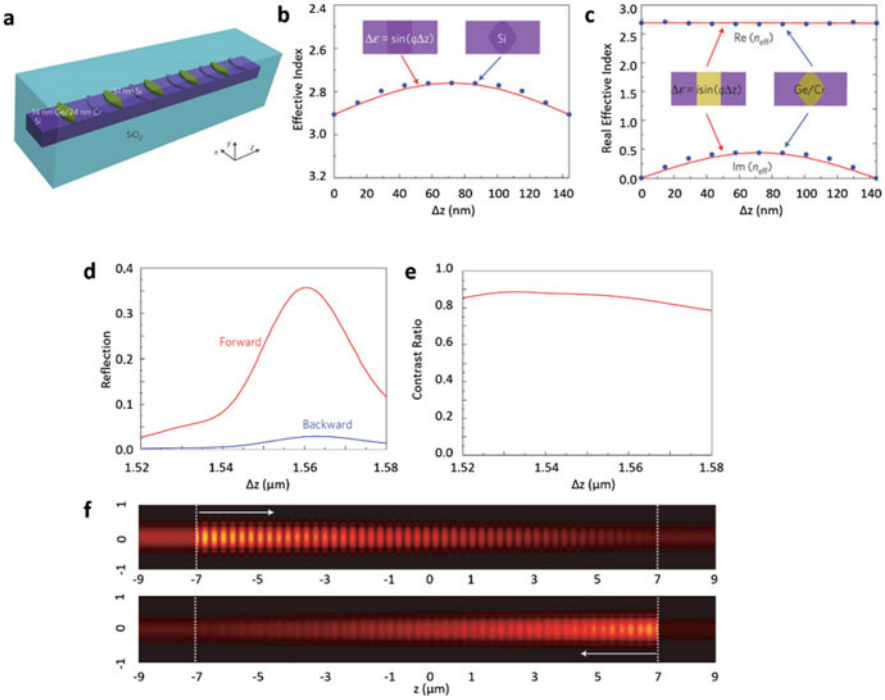

Fig. 2 Optical properties of the designed passive unidirectional reflectionless PT metamaterial. (**a**) Periodically arranged 760-nm-wide sinusoidal shaped combo structures on the top of an 800-nm-wide Si waveguide embedded inside SiO_2 to mimic parity-time optical potentials. The imaginary part modulations are 14-nm Ge/24-nm Cr bi-layer. The real part modulations are 51-nm Si layer. The designed parity-time metamaterial consists of 25 sets of top-modulated combo structures with a period of 575.5 nm and a width of 143.9 nm for each sinusoidal-shaped combo. (**b, c**) Index equivalence of the combo structures (blue dots) to the proposed modulation model (red lines): Real effective index of the dielectric modulation (**b**); Real and imaginary effective index of the loss modulation (**c**). (**d**) Simulated reflection spectra of the device in forward (red) and backward (blue) directions. (**e**) Spectrum of contrast ratio of reflectivities, showing high contrast ratios over the studied wavelength range from 1520 to 1580 nm. (**f**) Simulated electric field amplitude distribution of light in the device, where incidence is set at boundaries of the PT metamaterial from the forward (upper) and backward (lower) directions

$$S = \begin{bmatrix} 1/\cosh(\gamma_0 L) & i\sqrt{\frac{1-\delta}{1+\delta}}\sinh(\gamma_0 L)/\cosh(\gamma_0 L) \\ i\sqrt{\frac{1+\delta}{1-\delta}}\sinh(\gamma_0 L)/\cosh(\gamma_0 L) & 1/\cosh(\gamma_0 L) \end{bmatrix} \quad (4)$$

where $\gamma_0 = \sqrt{1-\delta^2}\,(\kappa/8)$. Here, the dielectric function of the balanced system is the same as the passive system, but without a limitation of the modulation region of $4n\pi/q + \pi/q \leq z \leq 4n\pi/q + 2\pi/q$, so that there will be same amount of gain and loss in the grating (i.e., gain/loss balanced).

Table 1 Evolution of Eigen spectrum $s_n = as_n^{'}$ in a balanced and passive PT system

	Balanced PT system	Passive PT system
$\mathbf{0 \leq \delta < 1}$	$\mathbf{s_n} = \frac{\mathbf{1 \pm \sinh(\gamma_0 L)}}{\cosh(\mathbf{\gamma_0 L})}$, unimodular and exact PT symmetric phase.	$\mathbf{s_n} = \mathbf{a}\frac{\mathbf{1 \pm \frac{i\kappa}{\delta\gamma}\sinh(\gamma L)\sqrt{1-\delta^2}}}{\sqrt{\mathbf{1+M_{12}M_{21}}}}$, unimodular; PT symmetry phase.
$\mathbf{\delta = 1}$	$\mathbf{s_n = 1}$, EP; degenerate.	$\mathbf{s_n = a}$, with $\mathbf{s_n^{'} = 1}$ EP; degenerate.
$\mathbf{\delta > 1}$	$\mathbf{s_n} = \frac{\mathbf{1 \pm \sin\left(\frac{\kappa}{\delta}\sqrt{\delta^2-1}L\right)}}{\cos\left(\frac{\kappa}{\delta}\sqrt{\delta^2-1}\mathbf{L}\right)}$, non-unimodular; broken PT phase.	$\mathbf{s_n} = \mathbf{a}\frac{\mathbf{1 \pm \frac{i\kappa}{\delta\gamma}\sinh(\gamma L)\sqrt{\delta^2-1}}}{\sqrt{\mathbf{1+M_{12}M_{21}}}}$, non-unimodular; broken PT phase.

The eigenvalues of the scattering matrix correspond to the evolution of the PT symmetry of the system, which is efficiently controlled by δ in both the balanced PT system and the passive PT system (Table. 1). It is clear to see that the EP ($\delta = 1$) marks the boundary between PT symmetry and PT broken phase. Apparently, the passive PT symmetry we are studying has the same PT symmetry transition as the balanced PT system, except for the attenuation term $|a|$. At the EP of the passive system ($\delta = 1$), the eigenvalues degenerate and become $s_n = a = \exp(-\alpha L/2\pi)$. The degenerated eigenvalues/eigenstates can be observed from the forward and backward reflection from the Bragg modulation, R_f and R_b.

$$R_f = |M_{21}/M_{22}|^2, R_b = |M_{12}/M_{22}|^2 \tag{5}$$

The underlying physics of EP characteristics in a passive PT system and a gain/loss balanced system are the same for this modulation regime. Therefore, in a passive PT system, the wave characteristics introduced by the EP are similar to that in a balanced PT system. By utilizing the unique wave characteristics near the EP of the passive PT photonic system, we can design novel integrated photonic devices with versatile applications.

2.2 Unidirectional Reflectionless Wave Transport

To achieve the unique wave characteristics near the EP, such as unidirectional reflectionless wave transport, we design a waveguide structure with modulation of its dielectric permittivity using absorptive materials. As shown in Fig. 1a, the passive PT metamaterial embedded inside silicon dioxide (SiO_2) is an 800-nm-wide and 220-nm-thick silicon waveguide with periodically modulated dielectric permittivity (i.e., effective refractive index). The wave number of fundamental mode of the waveguide is $k_1 = 2.69k_0$, where k_0 is the wave number in free space.

Figure 1b,c show the calculated R_f and R_b as a function of modulation length L at several different values of δ. As the material is absorptive, the

reflection curves reach an asymptotic value after enough modulation periods. However, R_f and R_b respond quite differently to the value of δ. Especially when $\delta = 1$ at the EP, the two reflection coefficients become unidirectional with backward reflection R_b diminished, which can be clearly evaluated by the contrast ratio $C = |(R_f - R_b)/(R_f + R_b)| = 2\delta/(1 + \delta^2)$, shown in Fig. 1d, which reaches 1 at the EP.

Moreover, the 3D simulation in Fig. 1e shows the unidirectional wave transport excited by the forward and backward input respectively. The disappearance of the interference patterns in the backward input confirms no wave reflected from the port.

To implement this interesting design of metamaterial, we need to modulate the complex index of a silicon waveguide by attaching additional periodical silicon or metal layer on top of the waveguide. It is important to note that additional deposition can increase the real part index, which may break the balance of real part modulation amplitudes. Thus, we modify the design in Fig. 1a to physically implement the index modulation.

As can be seen in the schematic in Fig. 2a, the index modulations of the real and imaginary part are separated in the z direction. The corresponding cosine modulation in the real part is shifted 5π/2q in the z direction to become a positive sinusoidal modulation ($\Delta\varepsilon_{real} = \cos(qz) = |\sin(qz - 5\pi/2|)$, while the imaginary part modulation remains at the same location ($\Delta\varepsilon_{imag} = i|\sin(qz)|$). Because the modulation is a second-order Bragg reflector, guided light will accumulate the same modulated phase and amplitude after passing through the modulated region.

Additionally, to achieve these sinusoidal optical potentials using microscopically homogeneous materials, sinusoidal-shaped combo structures are deposited on top of the Si waveguide (Fig. 2a). By doping silicon and germanium (Ge)/Chromium (Cr) bilayer combo structures, the effective indices of fundamental modes are consistent with the real and imaginary part modulations, as shown in Fig. 2b and 2c respectively. FDTD simulations with single-wavelength sweeping from 1520 to 1580 nm show that the forward and backward reflections are significantly distinguished with about 11 dB of extinction ratio (Fig. 2d) with high contrast ratio (Fig. 2e). The electric field distribution is shown in Fig. 2f.

In the experiments, we use tapered fiber excitation and on-chip waveguide directional couplers to measure the reflectance as shown in Fig. 3a. The sample was fabricated using overlay electron beam lithography, followed by evaporation and lift-off of Si and Ge/Cr as well as dry etching to form the Si waveguide. The SEM pictures before deposition of the SiO_2 cladding are shown in Fig. 3b, c. The reflection spectra of the device are measured from both forward and backward directions, as shown in Fig. 4a. The reflectivity in the forward direction is about 7.5 dB stronger than that in the backward direction, indicating asymmetric optical properties near the EP. The high contrast ratio of reflections, shown in Fig. 4b, confirms the unique characteristics of unidirectional invisibility of the material. Similar to previously investigated balanced gain/loss systems, our experiments show that PT phase transition in a passive system also has measurable quantities such as the EP.

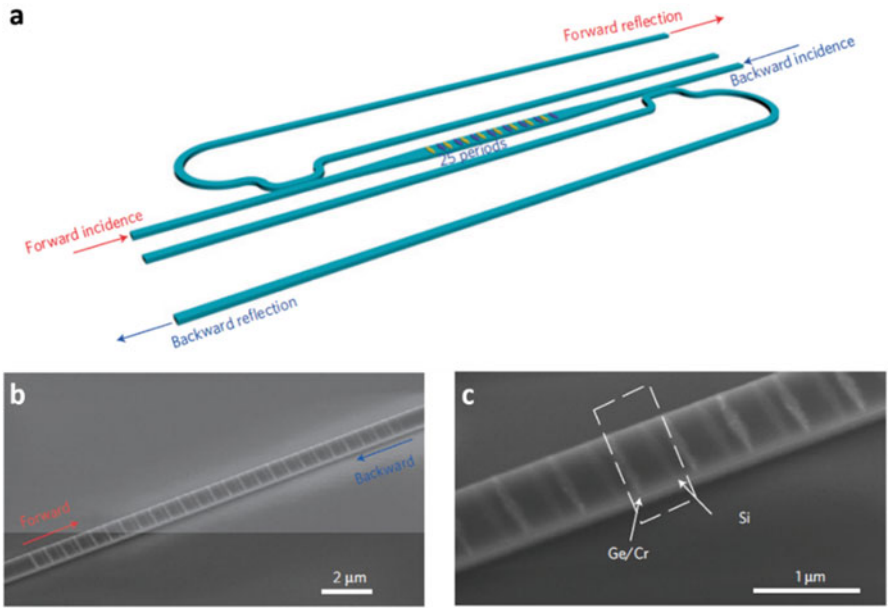

Fig. 3 Experimental implementation of the passive unidirectional reflectionless PT metamaterial. (**a**) Configuration of layout circuit on the SOI platform to measure reflection from the device, (**b**) SEM picture of the whole device before deposition of SiO_2 cladding. The fabricated device consists of 25 periods of Ge/Cr and Si sinusoidal combo structures with a period of 575.5 nm on top of the Si waveguide, (**c**) Zoom-in SEM picture of the device, where the boxed area indicates a unit cell

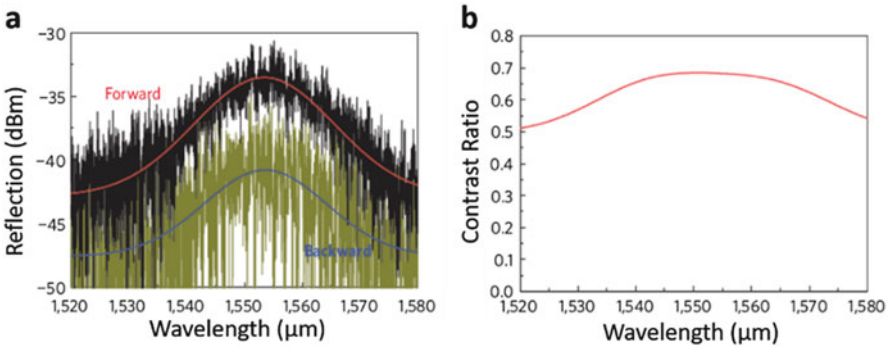

Fig. 4 Measured optical properties of the PT metamaterial in broadband. (**a**) Measured reflection spectra of the device from both directions over a broad band of telecom wavelengths from 1520 to 1580 nm. Red and blue curves are Gaussian fits of raw data in forward (black) and backward (green) directions, respectively, (**b**) Spectrum of contrast ratio of the fitted reflectivities

In this section, we implement the chip-scale PT metamaterial with unidirectional reflectionless properties on the conventional complementary metal-oxide-semiconductor platform. The simulation and experiment results clearly confirm the expected unidirectional and asymmetric characteristics. The novel functionalities of the PT metamaterial can be further enriched by the modulation of the complex refractive index as well as geometric arrangement of these optical potentials. The periodic modulation of the meta-material has created multiple desired wave characteristics for on-chip applications. The general design principle of this unidirectional reflection can be applied to the design of unidirectional invisibility metamaterials, optical isolators [6], and non-reciprocal circuits.

3 Asymmetric Interferometric Light-Light Switching

Following the proposal and implementation of the unidirectional invisible metamaterial, here we demonstrate that the asymmetric reflection can be further utilized to facilitate asymmetric light-light switching in a linear regime. In this novel photonic device, a weak control beam can interferometrically control an intense laser signal by the asymmetric reflection at the EP of the non-Hermitian system.

An effective light-light switching circuit improves on-chip optical information processing for high-speed and energy-efficient optical networks. In recent research, a unique linear scheme of coherent perfect absorption (CPA) utilizing photonics absorption is put forward for this light-light switching by mutually coherent interaction of light beams [22–25]. However, in these works, the control beam still has a similar amount of power as the actual source signal in these previous works. To realize an energy-efficient and effective light-light switching circuit, here we utilize intrinsic asymmetry of a non-Hermitian photonic metamaterials near its EP.

As shown in Fig. 5a, the device is designed on a silicon-on-insulator (SOI) platform. The structure is an 800 nm by 220 nm silicon meta-waveguide embedded in SiO_2 with the signal and control port on each side. The waveguide supports a fundamental mode propagating with an effective wave number of $k_1 = 2.69k_0$ at the wavelength of 1550 nm. The optical potential is modulated along the z direction of the meta-waveguide in the complex refractive index plane

$$\Delta\varepsilon = \Delta\varepsilon_0 \left[\cos(qz) - i\delta \sin(qz)\right] \tag{6}$$

where $\Delta\varepsilon_0 = 0.317$ is the modulation amplitude, and the modulation is in the region $4n\pi/q + \pi/q \leq z \leq 4n\pi/q + 2\pi/q$, $(n = 1, 2, 3 \ldots)$.

Similar with the structure in Sect. 2 in this chapter, such modulated system can be described by equations (1) and (2). The modulation introduces the coupling between forward and backward propagating wave by Bragg reflection, and the meta-waveguide supports two degenerate Bragg modes with different absorption coefficients. To maximize the extinction ratio for switching, the device consists of 38 periods of modulation (approximately 21.9 μm). With enough modulations, we

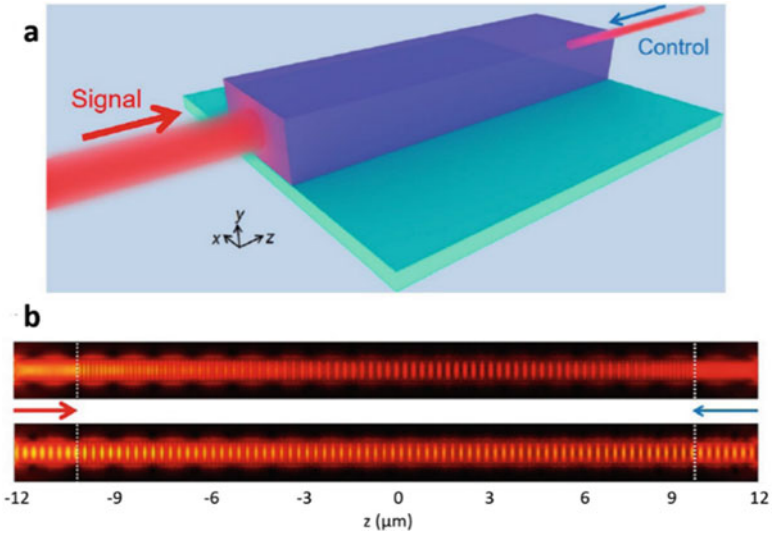

Fig. 5 Asymmetric interferometric light-light switching. (**a**) Schematic of the meta-waveguide with asymmetric reflection to implement asymmetric interferometric light-light switching of a strong source signal (forward input) by a weak control field (backward input), (**b**) Electric field distributions of the light-light switching, where the power ratio of the weak control to the strong source signal is set to 1 : 3. The CPA mode excited with no scattering when the incident phase of the control is $\pi/2$ (upper), and the degenerated mode of less absorption observed when the incident phase of the control is $\pi/2$ (lower)

can find one degenerate mode satisfies the CPA condition (i.e., $M_{11} = 0$) [26] where coherent light inputs from the left and right ports are perfectly absorbed without output scatterings, as shown in the upper panel, Fig. 5b. The other degenerate mode has much less absorption in the lower panel, Fig. 5b.

Because the device works as a light-light switch in the interferometric control regime, the relative phase between the optical waves of the two ports controls the operating mode of the system. Assuming the incident phase of the signal remains 0, efficient switching between these two modes of operation can be achieved by tuning the incident phase of the control field from $\pi/2$ to $-\pi/2$. A relatively small value of $\delta = 2$ was chosen to obtain a reasonable transmission efficiency and ensure that fabrication imperfections do not make the system deviate strongly from the designed CPA condition. As a result, the intensity ratio ξ, given by $(\delta+1)/(\delta-1)$, is 3 between the strong signal beam and the weak control beam.

As illustrated in Fig. 6a, an equivalent optical potential modulation is mimic to the non-Hermitian function in equation (6). The sample was then fabricated using overlay electron beam lithography, followed by electron beam evaporation and lift-off of sinusoidal shaped Cr/Ge combos and dry etching to form the Si waveguide with cosine shaped sidewall modulations, respectively. The SEM pictures of the meta-waveguide before top cladding of SiO_2 are shown in Fig. 6b, c.

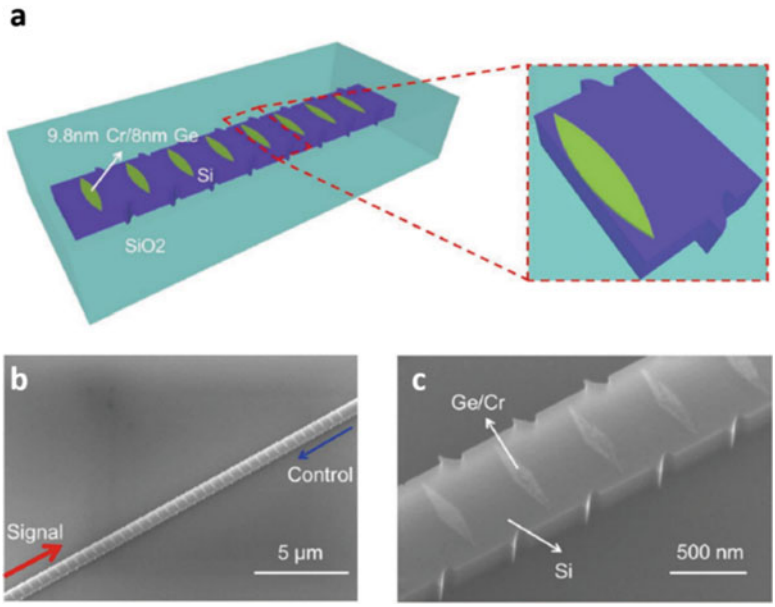

Fig. 6 Modulated structure of the meta-waveguide for asymmetric interferometric light-light switching. (**a**) Schematic of the meta-waveguide to create a spatial modulation equivalent to the periodically modulated refractive index. The real index modulations are transverse waveguide width varying in cosine function from +71 to −48.5 nm. The imaginary index modulations are the bilayer sinusoidal shaped combo structures of 9.8 nm chrome Cr and 8 nm germanium (Ge) deposited on top of the Si waveguide, (**b**) The SEM picture of the device consisting of 38 periods for strong signal light switching by a weak control, (**c**) Zoom-in picture of the modulated combo structures

In the experiments, coherent laser beams, split from the same laser source, were coupled into the waveguide from both ports. As shown in Fig. 7a, two on-chip waveguide directional couplers separate the inputs and outputs and route them to four respective grating couplers. The intensities of coupled light were imaged and integrated for reflection evaluations by a highly sensitive charge-coupled device (CCD) camera, using a function

$$Q_S = 10\log_{10}\left[(O_1 + O_2)\,/\,(I_1 + I_2)\right] + \mathrm{C} \tag{6}$$

where O_1 and O_2 are scattered light intensity from two output grating couplers, I_1 and I_2 are the intensity from two input grating couplers. The constant C is the overall loss of the directional couplers, which can be measured in the experiments as a background loss.

With the incident phase of the control field modified by a motorized optical delay line and the intensity ratio ξ manipulated by different coupling efficiency, the spectra of the output scatterings are shown in Fig. 7b. At the resonant peak (i.e. the wavelength detuning Δ=0), the CPA mode was excited with little output scatterings

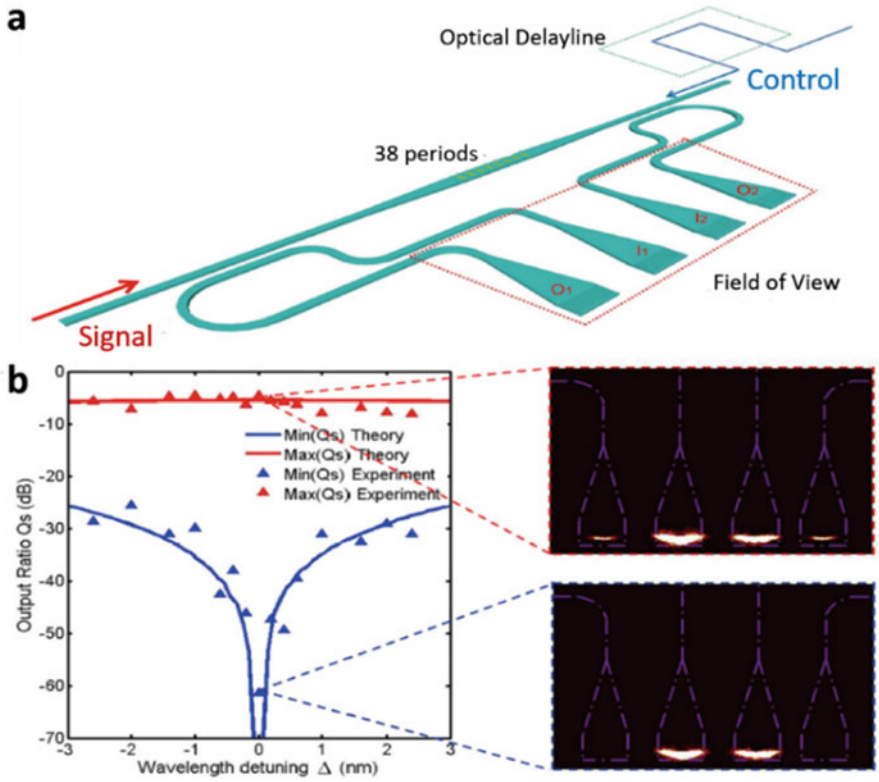

Fig. 7 Characterization of asymmetric interferometric light-light switching. (**a**) Layout circuit to measure the optical switching signals, (**b**) Spectra of maximum (red) and minimum (blue) output scattering coefficients. Insets: microscope snapshots of the scattering (top) and CPA (bottom) modes at the resonance. The experimental results (triangles) of asymmetric interferometric light-light switching shows an extinction ratio of about 60 dB at the resonance

when the phase of the control was $\phi = \pi/2$, as shown in the lower panel inset of Fig. 7b. On the other hand, the mode of less absorption was excited with strong scattered outputs when $\phi = -\pi/2$, upper panel inset of Fig. 7b.

As shown in Fig. 8a, the two output grating couplers manifested consistently in-phase on-off light scatterings for O_1 and O_2. This unique wave characteristic demonstrates a weak-to-intense optical switching with an extinction ratio up to approximately 60 dB in the meta-waveguide. In the out-of-resonant wavelengths, such light-light switch has a different phase response of output scatterings that O_1 and O_2 behave out-of-phase on-off relations. Because the mismatch between the wave numbers of the non-Hermitian modulation and the input wave, an additional phase shift is accumulated, either positive or negative according to the sign of detuning. Hence, output light scatterings showed opposite out-of-phase on-off

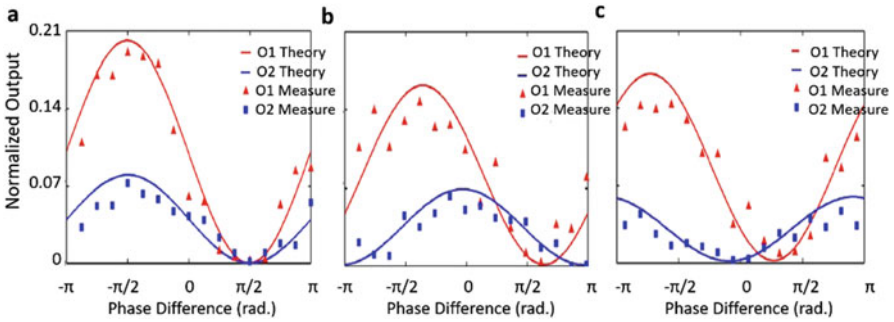

Fig. 8 Phase responses of outputs in interferometric light-light switching. (**a**) At the resonant wavelength, two reflection outputs oscillate in phase and reach their minimum (at $\pi/2$) and the maximum (at $-\pi/2$) simultaneously. (**b**) At the off-resonance wavelength when detuning is -4.2 nm, the output O_2 accumulates more phase than O_1. (**c**) At off-resonance wavelength when detuning is $\Delta = 4.6$ nm, the extra phase shift changes sign and results in a shift of output oscillations in the opposite direction

responses with respect to interferometric control of the control at $\Delta < 0$ (Fig. 8b) and $\Delta > 0$ (Fig. 8c).

In this section, we show the asymmetric interferometric light-light switching by utilizing a non-Hermitian meta-waveguide. Operating near an EP, the meta-waveguide can act as CPA that a weak control light strongly modulates the outputs of a large optical source signal. Such interference-enhanced absorption shows its promising applications to optical information processing.

4 Orbital Angular Momentum Microlaser

The asymmetric wave characteristics introduced by non-Hermitian PT photonics has offered various functionalities to on-chip applications. Inspired by the unidirectional power flow in the modulated waveguide structure, here we realize a microscale orbital angular momentum (OAM) laser.

Because of the angular momentum they may carry, light beams with spatially structured polarization and phase fronts provide additional degrees of freedom for modern optics science and practical applications. Associated with the polarization degree of freedom is the spin angular momentum (SAM), carrying only one of two values $\pm\hbar$. In addition to the SAM, researchers also demonstrated that a light beam could carry OAM [27]. Such beams possess helical phase fronts so that the Poynting vector within the beam twists around the principal axis. The OAM degree of freedom has opened a new branch of optical physics and enabled technological advances [28–30]. In contrast to the SAM that can take only two values, the OAM is unlimited. OAM beams are thus being considered as potential candidates for encoding information in both quantum and classical

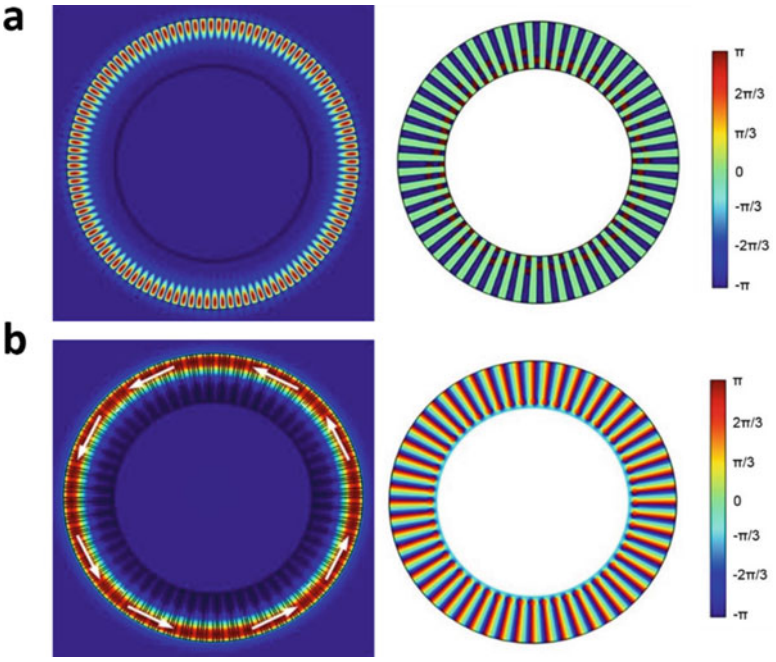

Fig. 9 The formation of unidirectional power flow in a ring resonator. (**a**) Simulation results of the intensity of WGM at the azimuthal order of $N = 56$ in a microring cavity (left panel) and the discontinuous phase distribution observed along the azimuthal direction with phase quantized at either 0 or π (right panel). (**b**) Simulation results of the intensity of WGM at the azimuthal order of $N = 56$ in a microring cavity with combined index and loss/gain modulations at the EP (left panel) and the continuous phase variation observed along the azimuthal direction (right panel), indicating that the WGM carries an effective OAM capable of producing the OAM lasing

systems [31]. The complex OAM beams can be generated by either bulk devices [32], or developed planar optical components [33]. Here we utilize the pronounced changes in light propagation at the EP to realize a scalable and designable micro-OAM source on a complementary metal-oxide-semiconductor (CMOS) compatible platform.

At the micro scale, the whispering gallery modes (WGMs) circulating in an optical micro-ring cavity carries large OAM. However, because of the mirror symmetry of a ring cavity, clockwise and counterclockwise eigen-WGMs coexist, and their carried OAMs consequently cancel each other (Fig. 9a). To isolate and extract the OAM of an individual WGM, it is essential to introduce a mechanism of robust selection of either clockwise or counterclockwise mode. We found that non-Hermitian photonics might help to solve the limitations. A unidirectional power circulation can be achieved by introducing complex refractive-index modulations to form an EP [34, 35]. At the EP of a PT system, multiple eigenstates coalesce into one due to the gain/loss modulations, which is essential to obtaining OAM laser emission.

The micro-ring laser resonator is designed with 500-nm-thick InGaAsP multiple quantum wells on an InP substrate. The complex refractive index grating is the modulation of the complex refractive index ($n^{'} + in^{''}$) along the azimuthal direction (θ)

$$\Delta n = \begin{cases} in'' \; for \; 2\pi p/N < \theta < 2\pi \left(p + \frac{1}{4}\right)/N \\ n' \; for \; 2\pi \left(p + \frac{3}{8}\right)/N < \theta < 2\pi \left(p + \frac{5}{8}\right)/N \end{cases} \tag{8}$$

where N denotes the azimuthal number of the targeted WGM and p takes integer values from the set {0, N – 1}. Such index modulation can be achieved by placing on top of InGaAsP layer periodically alternate single-layer Ge and bilayer Cr/Ge structures. An EP is obtained when the amplitudes of index and gain/loss gratings are set equal (i.e., $n^{'} = n^{''}$). At the EP, the counterclockwise WGM unidirectionally circulates in the cavity carrying large OAM through the azimuthally continuous phase evolution (Fig. 9b).

The OAM associated with the unidirectional power flow is extracted upward into free space by introducing periodic sidewall modulations along the micro-ring perimeter. For M equidistant scatters, the locations of the scatters are given by $\theta_s = 2\pi s/M$, where $s \in \{0, M-1\}$, resulting in the extracted phase $\theta_s = 2\pi sN/M$ of OAM beam. The extracted phase φ_s increases linearly from 0 to $2\pi(N - M)$

$$\varphi_s = 2\pi s\,(N - M)\,/M \tag{9}$$

Under this modulated regime, Fig. 10 shows the modeling result of the vortex laser emission, where $N = 56$ and $M = 57$. The pumping beam was shone from the back of the sample and the emitted beam carries both the pumping and OAM beam. The pumping component was then filtered out from the emitted laser beams (the wavelength of the pumping beam is at 1064 nm and the OAM beam is at about 1474 nm). Circulating a full circle around the center of the vortex, the phase of the scattered electric field changes continuously by 2π. At the center of the beam is the topological phase singularity point. The topological charge of the OAM is $l = -1$, which reveals the number of wave front twists within one wavelength.

The OAM microlaser with periodically arranged Ge and Cr/Ge modulation (Fig. 11) was fabricated by overlay electron beam lithography. In our OAM microlaser, unidirectional power flow forced at the EP modulation enables efficient and stable single-mode lasing with a sideband suppression ratio of 40 dB (Fig. 12). As shown in Fig. 12a, b, with an increasing pumping intensity, the transition from broadband photoluminescence (PL), to amplified spontaneous emission (ASE), and finally to lasing states demonstrates the selection of desired lasing modes. The unidirectional power flow can destroy the interference pattern of two counter-propagating WGMs that may cause undesired spatial hole-burning effects, such as, a decrease in the laser slope efficiency, multi-longitudinal mode operation, and unstable laser emission.

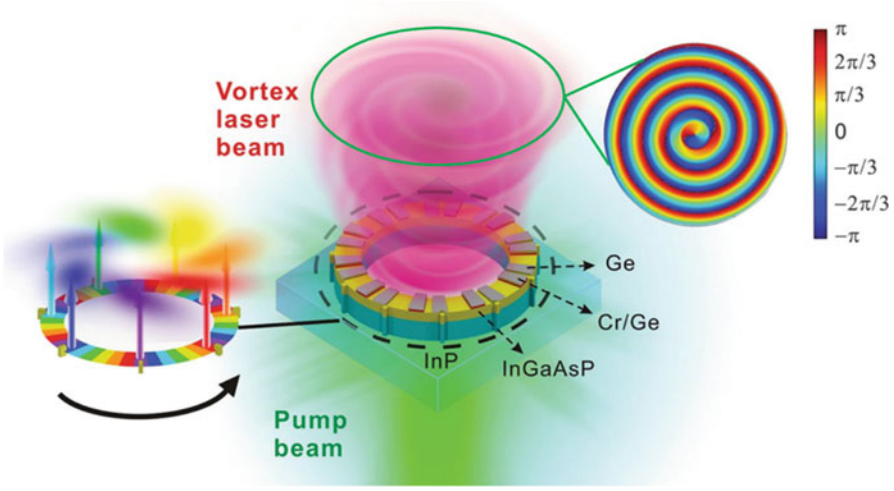

Fig. 10 Design of the OAM laser. Schematic of the OAM microlaser on an InP substrate. The diameter of the resonator is 9 mm, the width is 1.1 mm, and the height is 1.5 mm (500 nm of InGaAsP and 1 mm of InP). The modulations on the ring are 13-nm Ge single-layer and 5-nm Cr/11-nm Ge bilayer structures, periodically arranged in the azimuthal direction to mimic real index and gain/loss parts of an EP modulation and support unidirectional power circulation. The designed topological charge of the vortex beam is -1, realized by an azimuthal order is $N = 56$ at the resonant wavelength of 1472 nm with equidistant sidewall scatters with a total number of $M = 57$, the pumping beam was incident below the structure and the vortex beam was generated upwards. The inset shows the simulated phase distribution of emitted light. A spiral phase distribution of an OAM charge-one vortex

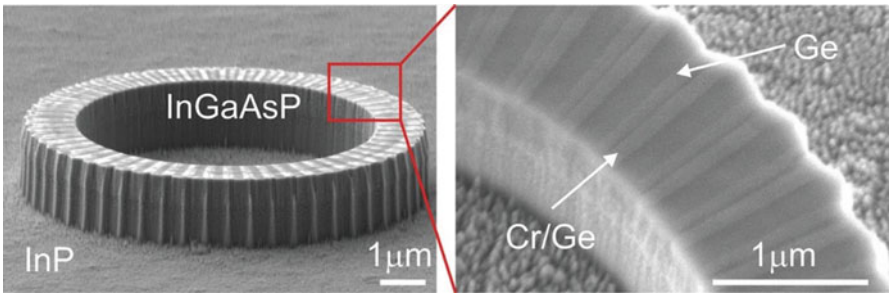

Fig. 11 SEM Pictures of OAM microlaser fabricated on the InGaAsP/InP platform. Alternating Cr/Ge bilayer and Ge single-layer structures were periodically deposited in the azimuthal direction on top of the micro-ring, presenting, respectively, the gain/loss and index modulations required for unidirectional power circulation

As shown in Fig. 12c, the intensity of lasing emission spatially distributed in a doughnut shape with a dark core in the center, formed by topological phase singularity at the beam axis. Figure 12d shows the off-center self-interference

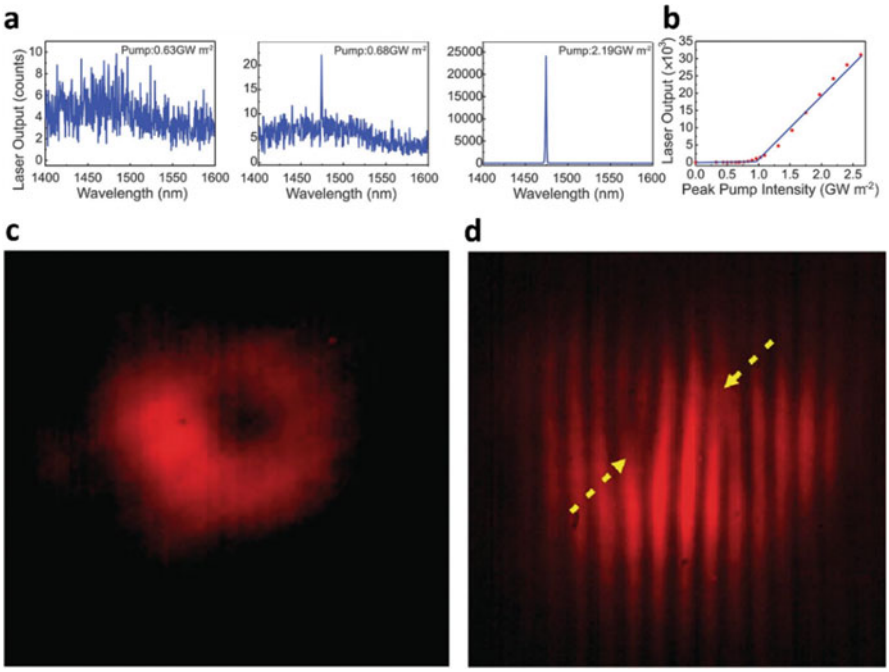

Fig. 12 Characterization of the generated OMA laser beam. (**a**) Evolution of the light emission spectrum from PL, to ASE, and to lasing at 1474 nm, as the peak power density of pump light was increased from 0.63, to 0.68, to 2.19 GWm^{-2}, respectively. (**b**) Input-output laser curve, showing a lasing threshold of about 1 GWm^{-2}. (**c**) Far-field intensity distribution of the laser emission exhibiting a doughnut-shaped profile, where the central dark core is due to the phase singularity at the center of the OAM vortex radiation. (**d**) Off-center self-interference of the OAM lasing radiation, showing two inverted forks (marked with arrows) located at two phase singularities

pattern. Two inverted forks at the center of the two beam axis and parallel fringes away from the centers evidently confirm that the radiation from the OAM laser was an optical vortex of topological charge $l = -1$.

In our micro-ring cavity, the dominant oscillating mode is designed to be a quasi-TM mode which is sensitive to sidewall modulation scatters, leading to the radially polarized OAM lasing. As shown in Fig. 13, the doughnut profile splits into two lobes aligned along the orientation of the polarizer, manifesting pure radially polarized OAM lasing.

In this section, we demonstrated a novel on-chip micro-ring OAM laser producing an optical vortex beam with a designable topological charge and polarization. This is enabled through the unidirectional power oscillation at an EP of the PT non-Hermitian system. The OAM microlaser may have novel applications for the next-generation on-chip optical communications in both classical and quantum regimes.

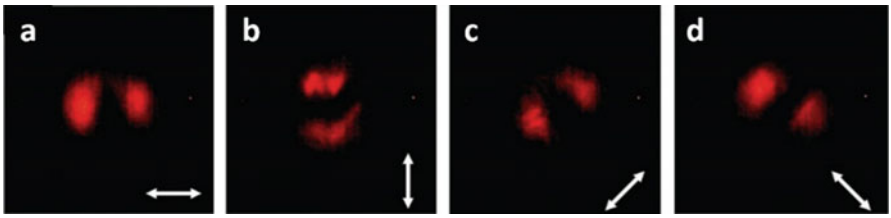

Fig. 13 Polarization state of the OAM field. Measured intensity distributions of the OAM lasing radiation passing through a linear polarizer with different polarization orientations indicated by arrows: (**a**) 0°, (**b**) 90°, (**c**) 45°, and (**d**) −45°. The two-lobe structure rotated with the rotation of the polarizer in the same fashion, confirming radially polarized OAM lasing

5 Conclusion and Outlook

Inspired by the development of non-Hermitian theory, especially the theory of PT symmetry, researchers on photonics has developed various interesting on-chip functionalities. In this chapter, we focus on on-chip implementations of non-Hermitian photonics using the state-of-the-art nanophotonics technology. We found that the asymmetric wave characteristics induced by optical potential modulation leads to the unidirectional reflection and power flow near the EP of the non-Hermitian system.

By utilizing these characteristics appropriately, we achieved novel functionalities of on-chip photonic devices. These discoveries and researches offer additional degrees of freedom and become a driving force for the future research in the field of integrated photonics.

Reference

1. Bender, C.M., Boettcher, S.: Real spectra in non-Hermitian Hamiltonians having PT symmetry. Phys. Rev. Lett. **80**, 5243–5246 (1998)
2. Bender, C.M.: Making sense of non-Hermitian Hamiltonians. Rep. Prog. Phys. **70**, 947–1018 (2007)
3. Bender, C.M., Brody, D.C., Jones, H.F.: Extension of PT-symmetric quantum mechanics to quantum field theory with cubic interaction. Phys. Rev. D. **70**, 025001 (2004)
4. Rotter, I.: A non-Hermitian Hamilton operator and the physics of open quantum systems. J. Phys. A. **42**, 1_51 (2009)
5. Rüter, C.E., et al.: Observation of parity–time symmetry in optics. Nat. Phys. **6**, 192–195 (2010)
6. Chang, L., et al.: Parity-time symmetry and variable optical isolation in active-passive-coupled microresonators. Nat. Photon. **8**, 524–529 (2014)
7. Regensburger, A., et al.: Parity-time synthetic photonic lattices. Nature. **488**, 167–171 (2012)
8. Musslimani, Z.H., et al.: Optical solitons in P T periodic potentials. Phys. Rev. Lett. **100**, 030402 (2008)

9. Ahmed, Z.: Schrödinger transmission through one-dimensional complex potentials. Phys. Rev. A. **64**, 042716 (2001)
10. Mostafazadeh, A.: Pseudo-Hermiticity versus PT symmetry: the necessary condition for the reality of the spectrum of a non-Hermitian Hamiltonian. J. Math. Phys. **43**, 205–214 (2002)
11. Schindler, J., Li, A., Zheng, M.C., Ellis, F.M., Kottos, T.: Experimental study of active LRC circuits with PT symmetries. Phys. Rev. A. **84**, 040101R (2011)
12. Guo, A., et al.: Observation of PT-symmetry breaking in complex optical potentials. Phys. Rev. Lett. **103**, 093902 (2009)
13. Musslimani, Z.H., El-Ganainy, R., Makris, K.G., Christodoulides, D.N.: Optical solitons in PT periodic potentials. Phys. Rev. Lett. **100**, 030402 (2008)
14. Longhi, S.: Bloch oscillations in complex crystals with PT symmetry. Phys. Rev. Lett. **103**, 123601 (2009)
15. Klaiman, S., Guenther, U., Moiseyev, N.: Visualization of branch points in PT symmetric waveguides. Phys. Rev. Lett. **101**, 080402 (2008)
16. Graefe, E.M., Jones, H.F.: PT-symmetric sinusoidal optical lattices at the symmetry-breaking threshold. *Phys. Rev. A*. **84**, 013818 (2011)
17. Ge, L., et al.: Unconventional modes in lasers with spatially varying gain and loss. Phys. Rev. A. **84**, 023820 (2011)
18. Feng, L., et al.: Experimental demonstration of a unidirectional reflectionless parity-time metamaterial at optical frequencies. Nat. Mat. **12**, 108–113 (2013)
19. Zhao, H., et al.: Metawaveguide for asymmetric interferometric light-light switching. Phys. Rev. Lett. **117**, 193901 (2016)
20. Miao, P., et al.: Orbital angular momentum microlaser. Science. **353**, 464–467 (2016)
21. Cannata, F., Dedonder, J.-P., Ventura, A.: Scattering in PT-symmetric quantum mechanics. Ann. Phys. **322**, 397–433 (2007)
22. Fang, X., MacDonald, K.F., Zheludev, N.I.: Controlling light with light using coherent metadevices: all-optical transistor, summator and invertor. Light. Sci. Appl. **4**(5), e292 (2015)
23. Chong, Y.D., et al.: Coherent perfect absorbers: time-reversed lasers. Phys. Rev. Lett. **105**, 053901 (2010)
24. Chong, Y.D., Ge, L., Douglas Stone, A.: PT-symmetry breaking and laser-absorber modes in optical scattering systems. *Phys. Rev. Lett*. **106**, 093902 (2011)
25. Wan, W., et al.: Time-reversed lasing and interferometric control of absorption. Science. **331**, 889–892 (2011)
26. Longhi, S.: PT-symmetric laser absorber. Phys. Rev. A. **82**, 031801 (2010)
27. Allen, L., et al.: Orbital angular momentum of light and the transformation of Laguerre-Gaussian laser modes. Phys. Rev. A. **45**, 8185 (1992)
28. Guo, Q., et al.: Line degeneracy and strong spin-orbit coupling of light with bulk bianisotropic metamaterials. Phys. Rev. Lett. **115**, 067402 (2015)
29. Franke-Arnold, S., et al.: Rotary photon drag enhanced by a slow-light medium. Science. **333**, 65–67 (2011)
30. Franke-Arnold, S., et al.: Uncertainty principle for angular position and angular momentum. New J. Phys. **6**, 103 (2004)
31. Bozinovic, N., et al.: Terabit-scale orbital angular momentum mode division multiplexing in fibers. Science. **340**, 1545–1548 (2013)
32. Yao, A.M., Padgett, M.J.: Orbital angular momentum: origins, behavior and applications. Adv. Opt. Photon. **3**, 161–204 (2011)
33. Lin, D., et al.: Dielectric gradient metasurface optical elements. Science. **345**, 298–302 (2014)
34. Peng, B., et al.: Parity-time-symmetric whispering-gallery microcavities. Nat. Phys. **10**, 394–398 (2014)
35. Brandstetter, M., et al.: Reversing the pump dependence of a laser at an exceptional point. Nat. Commun. **5**, 4032 (2014)

Parity-Time Symmetry in Scattering Problems

Mohammad-Ali Miri, Robert S. Duggan, and Andrea Alù

Abstract The realization that non-Hermitian parity-time (PT) symmetric Hamiltonians can exhibit entirely real spectra has raised considerable interest in the physics and engineering communities. In the context of optics and photonics, in particular, mathematical analogies with quantum mechanical problem have enabled several breakthrough in terms of observing and utilizing PT-symmetry in closed guided-wave systems. On the other hand, less attention has been paid to the scattering behavior of open PT-symmetric systems. In this chapter, we consider canonical PT-symmetric open systems and explore some of the scattering characteristics of coupled waveguide cavity arrangements. In this regard, we show how an open PT-symmetric configuration can be compared to a closed system, and how the scattering properties are related to the spectral properties of the PT-symmetric system and the associated phase transitions. Afterwards, different scattering geometries are

M.-A. Miri
Department of Electrical and Computer Engineering, The University of Texas at Austin, Austin, TX, USA

Department of Physics, Queens College of the City University of New York, Queens, New York City, NY, USA

R. S. Duggan
Department of Electrical and Computer Engineering, The University of Texas at Austin, Austin, TX, USA

A. Alù (✉)
Department of Electrical and Computer Engineering, The University of Texas at Austin, Austin, TX, USA

Photonics Initiative, Advanced Science Research Center, City University of New York, New York, NY, USA

Physics Program, Graduate Center, City University of New York, New York, NY, USA

Department of Electrical Engineering, City College of The City University of New York, New York, NY, USA
e-mail: aalu@gc.cuny.edu

D. Christodoulides, J. Yang (eds.), *Parity-time Symmetry and Its Applications*, Springer Tracts in Modern Physics 280,
https://doi.org/10.1007/978-981-13-1247-2_3

explored in one, two and three dimensions. In addition, we review recent investigations on this topic and highlight opportunities for future research.

1 Introduction

Recently there has been considerable interest in hybrid active-passive optical geometries that utilize balanced regions of gain and loss [1–8]. These activities have been mainly inspired by recent theoretical developments in quantum mechanics, which show that non-Hermitian Hamiltonians can exhibit entirely real spectra as long as they respect the condition of parity-time (PT) symmetry [9–13]. For a non-relativistic quantum mechanical Hamiltonian, $H = -\frac{\hbar^2}{2m}\nabla^2 + V(\boldsymbol{r})$, this condition demands that the complex potential satisfies $V^*(-\boldsymbol{r}) = V(\boldsymbol{r})$, i.e., the real and imaginary parts of $V(\boldsymbol{r})$ should be even and odd functions of position, respectively. In a similar fashion, in the context of optics the condition for PT-symmetry requires that the real and imaginary parts of the dielectric permittivity should be even and odd functions of position. In this case, the imaginary part of the optical potential represents optical gain and loss processes, which should be symmetrically distributed in space.

Figure 1 depicts several examples of PT-symmetric systems, in which gain and loss regions are structured in a balanced manner. In general, these structures can be divided into two main categories, closed and open systems. In the former case, the system is isolated from the surrounding medium and in the absence of gain and loss mechanisms the electromagnetic energy is conserved and is interchanged among a discrete set of bound states. In the latter case, on the other hand, the system can exchange energy with the surrounding environment and the localized states always suffer from leakage to a continuum of radiation states. Therefore, the terminology of modes or states in closed systems is often replaced with leaky-modes or meta-stable states in the case of localized states in open systems. Here, we use the terminology of

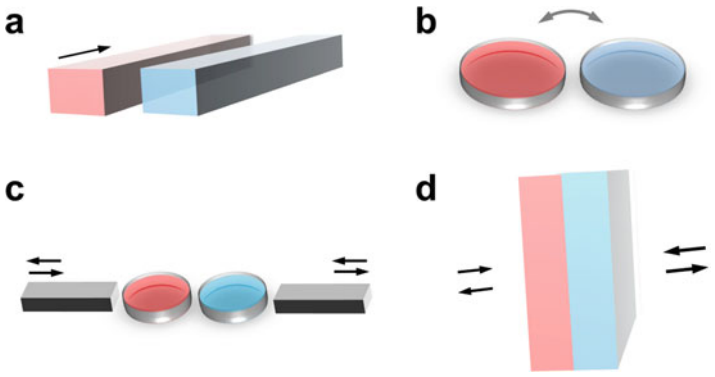

Fig. 1 Examples of closed (**a**, **b**) and open (**c**, **d**) PT-symmetric optical systems: (**a**) coupled optical waveguides, (**b**) coupled cavities, (**c**) waveguide-cavity geometry, (**d**) dielectric slabs. Here, the red and blue colors represent gain and loss regions, respectively

closed and open PT-symmetric systems based on their passive lossless counterparts, i.e., when neglecting any gain or absorption loss. Examples of closed PT-symmetric systems are two coupled optical waveguides and optical resonators with infinite lifetime, as shown in Fig. 1a, b, respectively. Examples of open systems, on the other hand, are waveguides coupled to optical cavities and dielectric slabs, as shown in Fig. 1c, d.

Closed optical PT-symmetric systems, being directly analogous to Hamiltonian systems in quantum mechanics, have been intensely investigated in the context of optics and photonics. On the other hand, open PT-symmetric systems, which are the subject of the present chapter, have been less explored. This is primarily due to the mathematical difficulties of handling open PT-symmetric systems as well as because of the challenges in the experimental realization of such systems. On the other hand, in reality most systems are open systems given that perfect isolation can never be achieved. In this chapter, we overview the main properties of open PT-symmetric systems and review recent progress in the theoretical and experimental investigation of these systems. We start with coupled waveguide-cavity geometries, which provides a good insight into the concept of PT symmetry. We then provide examples of PT-symmetric structures with various dimensionalities and investigate their scattering properties.

2 Scattering in Integrated Photonic Circuits

In this section, we consider a waveguide-cavity geometry, an idealized model that nonetheless involves all the elements of an open scattering problem. Here, we consider single mode cavities, supporting a mode with a finite lifetime. Assuming that the lifetime of the modes in the two optical cavities is large enough, one can utilize a coupled mode formalism in order to describe the temporal evolution of light in the two modes and their coupling to the waveguides, better known as temporal coupled mode theory [14, 15]. Here, we consider $a_{1,2}$ to be the modal amplitudes of the localized resonant states in the two cavities and $s^{\pm}_{1,2}$ as the amplitudes of the incoming $(+)$ and outgoing $(-)$ waves at the two ports. The amplitudes of the localized and traveling waves are assumed to be normalized such that $|a_i|^2$ represents the total energy stored in the modes while $|s_i|^2$ represents the power at the port. In this case, the temporal evolution of the modes is governed by the coupled mode equations:

$$\frac{d}{dt}\begin{pmatrix} a_1 \\ a_2 \end{pmatrix} = -iH\begin{pmatrix} a_1 \\ a_2 \end{pmatrix} + D^T\begin{pmatrix} s_1^+ \\ s_2^+ \end{pmatrix} \tag{1}$$

where, the coupling between the input/output ports and the modes is governed by

$$\begin{pmatrix} s_1^- \\ s_2^- \end{pmatrix} = C\begin{pmatrix} s_1^+ \\ s_2^+ \end{pmatrix} + D\begin{pmatrix} a_1 \\ a_2 \end{pmatrix}, \tag{2}$$

In these relations, H is an evolution matrix, D and its transport D^T model the coupling from modes to ports and from ports to modes, and C is a direct path scattering matrix of the ports. The evolution matrix H can be written as a sum of real and imaginary parts as $H = \Omega - i\Gamma$, where Ω is a matrix involving the resonance frequencies as well as the coupling coefficients while Γ represents the gain and loss mechanisms. In general, one can write $\Gamma = \Gamma_e + \Gamma_i$, where Γ_e is the matrix of external losses, i.e., losses due to coupling to the channels, while Γ_i represents the internal gain or loss processes. Clearly even in the absence of any material gain or loss, this system is not conservative given that energy can always leak into the outside environment through the waveguide channels. It is important to note that time reversal symmetry conditions demands Ω and Γ_i to be symmetric matrices. In addition, the time reversal symmetry and energy conservation considerations require $C D^* = -D$, and $D^\dagger D = 2\Gamma_e$.

For the PT-symmetric system shown in Fig. 1c, one can write the following evolution matrix:

$$H = \begin{pmatrix} \omega_0 - i\gamma_e + ig & -\mu \\ -\mu & \omega_0 - i\gamma_e - ig \end{pmatrix}, \tag{3}$$

where, ω_0 is the resonance frequency of each isolated mode, μ is the coupling rate, γ_e is the rate of dissipation due to leakage to the channels, and $\pm g$ represent the PT-symmetric gain/loss added to each resonator. The C and D matrix can be written as:

$$C = \begin{pmatrix} 1 & 0 \\ 0 & 1 \end{pmatrix}, \tag{4}$$

$$D = i\sqrt{2\gamma_e} \begin{pmatrix} 1 & 0 \\ 0 & 1 \end{pmatrix}. \tag{5}$$

By definition, the condition of PT symmetry is satisfied when $[H, \mathcal{PT}] = 0$, where the parity $\mathcal{P}$ and time $\mathcal{T}$ operators act on an arbitrary state $(a, b)^t$ as $\mathcal{P}(a, b)^t = (b, a)^t$ and $\mathcal{T}(a, b)^t = (a^*, b^*)^t$. According to relation (3), the condition of PT symmetry can only be achieved for $\gamma_e = 0$, i.e., where the two cavities are isolated from the waveguides. On the other hand, in the presence of waveguide leakage, the eigenvalues of the evolution matrix H are given by:

$$\sigma_\pm = \omega_0 - i\gamma_e \pm \sqrt{\mu^2 - g^2}, \tag{6}$$

and therefore exhibit a phase transition at the critical gain-loss contrast of $g_{\text{th}} = \mu$. The two-port waveguide-cavity system is best described through its scattering matrix S, defined as $\left(s_1^-,\ s_2^-\right)^t = S\left(s_1^+,\ s_2^+\right)^t$, which can be written as:

$$S = \begin{pmatrix} r_1 & t \\ t & r_2 \end{pmatrix}. \tag{7}$$

Here, $r_{1,2}$ represents the reflection from ports 1 and 2 respectively and t shows the transmission coefficient. These scattering parameters are found to be:

$$t = \frac{2i\gamma_e\mu}{(\omega-\omega_0+i\gamma_e)^2+g^2-\mu^2}, \tag{8a}$$

$$r_1 = \frac{(\omega-\omega_0)^2+(\gamma_e+g)^2-\mu^2}{(\omega-\omega_0+i\gamma_e)^2+g^2-\mu^2}, \tag{8b}$$

$$r_2 = \frac{(\omega-\omega_0)^2+(\gamma_e-g)^2-\mu^2}{(\omega-\omega_0+i\gamma_e)^2+g^2-\mu^2}, \tag{8c}$$

Relations 8a, 8b and 8c clearly show an asymmetry in the reflection coefficients induced by the gain-loss parameter g, while the transmission is identical. This is consistent with the fact that the presence of gain-loss contrast along the propagation direction of light breaks the left-right symmetry of the reflection coefficient, while it does not violate the reciprocity of light. Another important observation in the scattering coefficients is the appearance of a singularity at $\omega = \omega_0$ for the gain-loss level of $g = \sqrt{\gamma_e^2+\mu^2}$. This point is regarded as the onset of lasing, where the gain in the active cavity overcomes the total losses due to leakage as well as coupling to the lossy cavity. Figure 2 depicts the frequency-dependent scattering coefficients of the PT-symmetric coupled mode system for different values of the gain-loss contrast. According to this figure, by increasing the gain/loss contrast, the asymmetry in the reflection coefficients can be controlled.

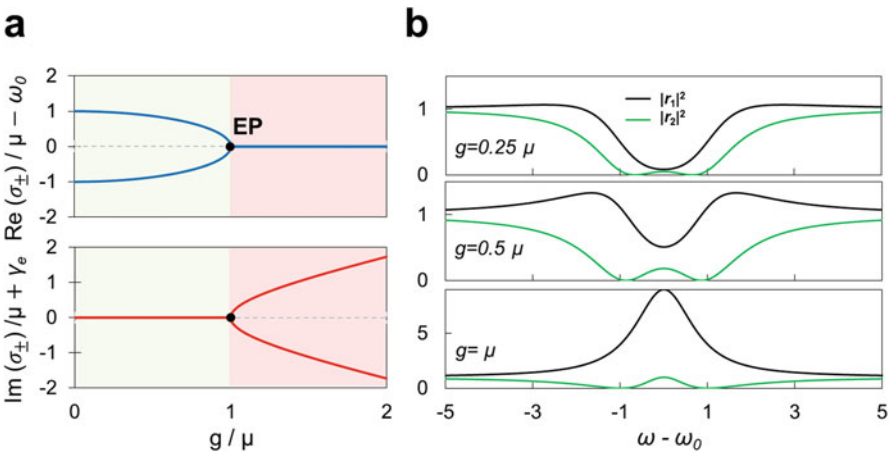

Fig. 2 (**a**) The eigenvalues of the evolution matrix of the PT-symmetric coupled cavity as a function of the gain-loss parameter. (**b**) The scattering parameters for different values of the gain-loss parameter. In all cases we have assumed $\gamma_e = \mu$

Before concluding this section, it is worth stressing that the simplified model investigated in this section involves several interesting properties of open PT-symmetric systems that are also encountered in the structures described in the following sections.

- In a scattering setting, coupling to the continuum of the radiation states creates an additional loss mechanism, but does rule out a phase transition as in a Hermition system.
- The phase transition in the eigenfrequencies is associated with the splitting or merging of the resonance features in the scattering parameters. The visibility of such features depends on the strength of the radiative losses.

In the following sections, the scattering properties of different PT-symmetric systems are investigated while different sections are separated based on the dimensionality of the problem in terms of complexity.

3 Scattering in 1D

Here, we investigate one-dimensional scattering problems involving a PT-symmetric Fabry-Perot resonator. As depicted in Fig. 1d such structure involves two dielectric slabs with equal gain and loss. By considering propagation along the normal direction in this Fabry-Perot, independent from the choice of polarization, one can consider the following 1D wave equation in the frequency domain:

$$\frac{d^2E(x)}{dx^2} + k_0^2\varepsilon(x)E(x) = 0, \tag{9}$$

where, E represents the electric field, k_0 is the free space wavenumber, and $\varepsilon(x)$ represents the relative permittivity of the media involved. Similar to the coupled mode model presented in the previous section, the gain and loss dielectric slab can be considered as individual cavities which are probed through plane waves propagating in the background medium. It should be noted that in this case, the Fabry-Perot cavity supports an infinite number of meta-stable states. However, as it will be discussed in the following, the pairwise coupling and splitting of these states can become visible for proper gain-loss contrasts.

Here, the background medium is assumed to be free space, i.e., $\varepsilon = 1$, while for the gain and loss slabs we assume $\varepsilon = (n \pm ig)^2$ where n and g represent the refractive index and gain-loss coefficients, respectively. Assuming that the electric field in the left region is given by $E_1 = s_1^+ e^{-ik_0x} + s_1^- e^{ik_0x}$, while in the right region is $E_2 = s_2^- e^{-ik_0x} + s_2^+ e^{ik_0x}$, the scattering matrix, defined through $\left(s_1^-,\ s_2^-\right)^t = S\left(s_1^+,\ s_2^+\right)^t$, can be written in terms of the reflection and transmission coefficients as in relation (7). From these it is straightforward to show that the reflection and transmission coefficients are obtained from the following relations:

$$t = \frac{g^2 + n^2}{g^2 \cosh(k_0 L g) - \frac{ig}{2}\left(1 - n^2 - g^2\right)\sinh(k_0 L g) + n^2 \cos(k_0 L n) - \frac{in}{2}\left(1 + n^2 + g^2\right)\sin(k_0 L n)}, \tag{10a}$$

$$r_1 = -i \frac{+gn\cosh(k_0 L g) - gn\cos(k_0 L n) + \frac{g}{2}\left(1 + n^2 + g^2\right)\sinh(k_0 L g) + \frac{n}{2}\left(1 - n^2 - g^2\right)\sin(k_0 L n)}{g^2 \cosh(k_0 L g) - \frac{ig}{2}\left(1 - n^2 - g^2\right)\sinh(k_0 L g) + n^2 \cos(k_0 L n) - \frac{in}{2}\left(1 + n^2 + g^2\right)\sin(k_0 L n)}, \tag{10b}$$

$$r_2 = -i \frac{-gn\cosh(k_0 L g) + gn\cos(k_0 L n) + \frac{g}{2}\left(1 + n^2 + g^2\right)\sinh(k_0 L g) + \frac{n}{2}\left(1 - n^2 - g^2\right)\sin(k_0 L n)}{g^2 \cosh(k_0 L g) - \frac{ig}{2}\left(1 - n^2 - g^2\right)\sinh(k_0 L g) + n^2 \cos(k_0 L n) - \frac{in}{2}\left(1 + n^2 + g^2\right)\sin(k_0 L n)}, \tag{10c}$$

where, L represents the total length of the PT-symmetric slab. In this case, the reflection asymmetry is proportional to the quantity $gn[\cosh(k_0 L g) - \cos(k_0 L n)]$, which is related to both refractive index n and gain-loss coefficient g. The eigenvalues of the scattering matrix can be obtained in terms of the reflection and transmission coefficients as:

$$\sigma_{\pm} = \frac{r_1 + r_2}{2} \pm \sqrt{\left(\frac{r_1 - r_2}{2}\right)^2 + \mathrm{t}^2}, \tag{11}$$

while, the eigenvectors of the system are $v_{\pm} = (1, \ \rho_{\pm})^t$, where, the ratio $\rho_{\pm}$ is:

$$\rho_{\pm} = \frac{r_2 - r_1}{2t} \pm \sqrt{1 + \left(\frac{r_2 - r_1}{2}\right)^2}. \tag{12}$$

The eigenvectors are subject to the normalization condition of $v_m^T v_n = \delta_{mn}$, and the scattering matrix can be expanded in terms of the eigenvalues and eigenvectors as $S = \sigma_+ v_+ v_+^T + \sigma_- v_- v_-^T$. One should notice, however, that this particular representation of the S-matrix is not valid at the exceptional point, where, the scattering matrix can no longer be diagonalized. Figure 3 depicts the eigenvalues of the PT-symmetric Fabry-Perot as a well as the transmission and reflection coefficients versus the incoming wave frequency. As this figure clearly indicates, at a critical frequency the eigenvalues associated with a particular set of modes bifurcate in direct analogy with closed systems. The bifurcation of the eigenvalues is also associated with the merging of two resonance features in the scattering coefficients.

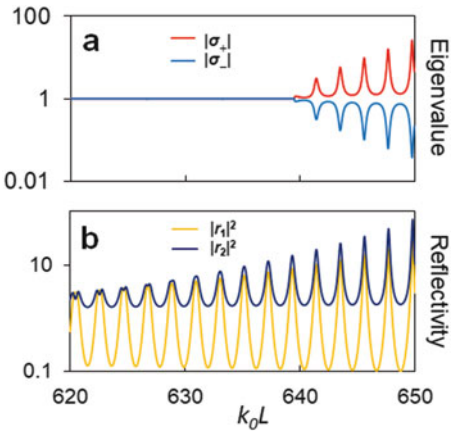

Fig. 3 (**a**) The moduli of the scattering matrix eigenvalues of the PT-symmetric Fabry-Perot. (**b**) The reflection coefficient from left and right

In the asymptotic limit of $k_0L \to \infty$, the eigenvectors evolve as $v_+ \to \begin{pmatrix} 1 \\ 0 \end{pmatrix}$ and $v_- \to \begin{pmatrix} 0 \\ 1 \end{pmatrix}$, thus the S-matrix can be approximated as $S \to \begin{pmatrix} \sigma_+ & 0 \\ 0 & \sigma_- \end{pmatrix}$. Therefore, the reflection coefficients from the left and right directions asymptotically approach the two eigenvalues. This can also be seen from relation (10) for a vanishing transmission coefficient (Fig. 3).

The PT-symmetric Fabry-Perot was first investgated in Ref. [16] and the connection with Hamiltonian systems was explored [17]. The connection with coherent perfect absorber was noted in [18] and demosntrated experimentally in [19]. Other examples of 1D PT-symmetric structures are PT-symmetric Bragg gratings investigated in [20, 21]. Interestingly, it has been shown the reflection coefficients of a PT-symmetric grating can completely vanish from one side while from the other side a large reflection is obtained. This unidirectioanl invisibility has been experimentally observed in gratings incorporated in silicon waveguides [22] as well as in time-domain lattices [23]. In addition, it has been shown that PT-symmetric gratings in the presence of optical Kerr nonlinearities behave in a similar manner and one-way Bragg solitons have been peredicted [24].

With the introduction of additional dimensions, systems with tractable closed-form solutions are limited, especially with the asymmetry of PT-symmetric systems. In the following, we present two canonical examples with enlightening responses: a 2D Janus cylinder and coupled 3D spheres.

4 Scattering in 2D

As mentioned above mathematical analogy of the Schrödinger equation with the scalar wave equation in the frequency domain allows one to treat the refractive

index profile as an effective potential, thus defining the conditions of PT-symmetric symmetry as

$$n^* (-x, -y, -z) = n (x, y, z) . \tag{13}$$

As one would expect, when considering the vectorial nature of the electromagnetic fields the conditions of PT-symmetric symmetry for the material tensors $\bar{\bar{\varepsilon}}$ and $\bar{\bar{\mu}}$ is written as [25]

$$\bar{\bar{\varepsilon}}^* (-x, -y, -z) = \bar{\bar{\varepsilon}} (x, y, z) \;\; ; \;\; \bar{\bar{\mu}}^* (-x, -y, -z) = \bar{\bar{\mu}} (x, y, z) . \tag{14}$$

Given the lack of magnetic gain, and strong magnetic response at all at optical frequencies, we will again focus solely on dielectric properties of materials. In two dimensions, we consider the TE polarization with three field components H_x, H_y, E_z, obeying the wave-equation

$$\frac{\partial^2 E_z}{\partial x^2} + \frac{\partial^2 E_z}{\partial y^2} + k_0^2 \varepsilon (x, y) E_z = 0, \tag{15}$$

A PT-symmetric symmetric potential is formed again when $\varepsilon^*(-x, -y) = \varepsilon(x, y)$. As with most scattering problems, we decompose the electric field into incident and scattered fields. Here, we assume a plane-wave excitation and consider only the far-field scattering such that

$$E_z (x, y) = E_0 \left(e^{i \boldsymbol{k} \cdot \boldsymbol{\rho}} + f (\phi) \frac{e^{ik\rho}}{\sqrt{k\rho}} \right), \tag{16}$$

where (ρ, ϕ) represent the radial and azimuthal polar coordinates and the far-field azimuthal pattern of the scattered field $f(\phi)$ is obtained in terms of the total field inside the scatterer as

$$f (\phi) = \frac{k^2 (1 + i)}{2\sqrt{\pi}} \int \left(\varepsilon \left(\boldsymbol{r}' \right) - 1 \right) E_z \left(\boldsymbol{r}' \right) \exp \left(-ik \hat{\boldsymbol{r}} \cdot \boldsymbol{r}' \right) d^2 \boldsymbol{r}'. \tag{17}$$

This integral equation can be solved numerically, such as by the method of moments. After finding the solution, we note the asymmetry from the difference in imaginary permittivity creates an asymmetric scattering response, more so than an equivalent difference in the real part of permittivity. For dielectric cylinders, the scattering peak actually is directed toward the loss cylinder. In addition, the peak deflection is more pronounced for smaller particles, but the beam is more directive as the particle size is increased [26].

Beyond the direct properties of any individual system, the 2D geometry is useful for deriving a generalized optical theorem. Because the permittivity follows the PT-symmetric condition, through the wave equation we can derive

$$E_z(x, y)\,\nabla^2 E_z^*(-x, -y) - E_z^*(-x, -y)\,\nabla^2 E_z(x, y) = 0, \tag{18}$$

Converting this areal integral to a flux integral over a circle with $r \to \infty$ and considering only the far-field terms, by using the method of steeped descent, one can derive a modified optical theorem as follows

$$\int_0^{2\pi} f(\phi)\, f^*(\phi + \pi)\, d\phi = -2\sqrt{\pi}\,\mathrm{Re}\left[(1 + i)\, f(\pi)\right]. \tag{19}$$

Unlike the passive optical theorem, the integrand in this case is not positive definite, and so the total extinction energy cannot be deduced from a single scattering angle. Instead, the backward scattering is related to the integral of a quasi-energy related to the PT-symmetry. This relation can easily be extended to 3D, and it is inherent to all PT-symmetric systems.

5 Scattering in 3D

In this section we focus on the response of PT-symmetric spherical particle pairs. This simple geometry offers a number of benefits for an initial study of radiative systems. Scattering from a sphere or collection of spheres has been extensively studied, giving us an easy framework to model the system. This includes a number of well-known approximations that allow us to form conclusions while also finding results from more complete models. In general, several approaches to solving the scattering from a collection of spheres exist. Mie theory offers the exact solution to scattering of a plane wave by a single particle as an infinite series of spherical harmonics [27], and is the starting point for the methods extending to multiple particles. A truly rigorous solution should consider the spherical harmonics to all orders. Indeed, with the T-matrix formulation developed one can include the spherical harmonics from any number of scatterers to find the fields with desired precision [28, 29]. In reality, a good approximation is often found by including only a few harmonics in systems of wavelength-scale size. Subwavelength non-magnetic particles in particular have a response dominated by the first transverse-magnetic harmonic, corresponding to the electric dipole moment. We will start our discussion with approximate methods, as the simpler analysis gives semi-analytic solutions and grants more clarity into their origins. We will subsequently add in material dispersion and higher-order harmonics in order to provide a more complete picture.

Consider two spherical dielectric particles with permittivities chosen to meet the PT-symmetric condition ($\varepsilon_1 = \varepsilon_r + i\varepsilon_i = \varepsilon_2^*$) as recently investigated in Ref. [31], and shown in Fig. 4. If the particles have radius a and the excitation wavenumber is $k = 2\pi/\lambda$, the electric dipole mode will dominate the response in the range $ka \ll 1$. The total dipole moment of each particle is related to the local field through a polarizability $\boldsymbol{p}_i = \alpha_i \boldsymbol{E}^{tot}(\boldsymbol{r}_i)$.The field can be divided into the sum of the incident field and the scattered field from the other particle. The total response can be written as a system of equations

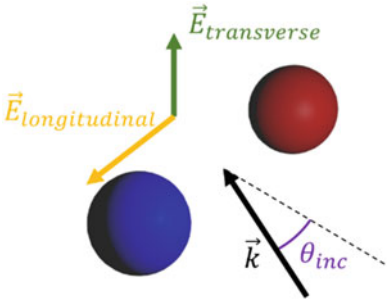

Fig. 4 A schematic of the geometry under consideration with appropriate polarization and angle definitions

$$\begin{bmatrix} \alpha_1^{-1} & -\boldsymbol{G}_{12} \\ -\boldsymbol{G}_{12} & \alpha_2^{-1} \end{bmatrix} \begin{bmatrix} \boldsymbol{p}_1 \\ \boldsymbol{p}_2 \end{bmatrix} = \begin{bmatrix} \boldsymbol{E}^1 \\ \boldsymbol{E}^2 \end{bmatrix} \tag{20}$$

where $\boldsymbol{p}_i$ is the dipole of the ith particle, $\boldsymbol{r}_i$ its position, α_i its polarizability, $\boldsymbol{E}^i$ the incident electric field, and $\boldsymbol{G}$ is the Green's function between the dipoles [30]. The polarizability can be rigorously derived from Mie theory as $\alpha_i = j\frac{6\pi\varepsilon_o\varepsilon_b C_1^{TM}}{k^3}$, but can be simplified in the subwavelength limit as $\alpha_i \approx 4\pi\varepsilon_0\varepsilon_b a^3\left(\frac{\varepsilon_i+2\varepsilon_b}{\varepsilon_i-\varepsilon_b} - j\frac{2(ka)^3}{3}\right)^{-1}$. This is identical to the value derived for a static field, with the addition of the lowest-order imaginary component to account for radiation losses. Note that, similar to the systems investigated in previous sections, balancing materials loss and gain $\varepsilon_1 = \varepsilon_2^*$ does not satisfy the true PT-symmetric symmetry condition as the radiation loss is not "time-reversed". The electric dipole Green's function is well known, and for small particle separations, it can be similarly approximated $G^t \approx \frac{1}{4\pi\varepsilon_0\varepsilon_b}\left(-\frac{1}{d^3} + j\frac{2k^3}{3}\right)$ for a field polarization transverse to the particle separation, and $G^l \approx \frac{1}{4\pi\varepsilon_0\varepsilon_b}\left(\frac{2}{d^3} + j\frac{2k^3}{3}\right)$ for the longitudinal polarization. Considering the scalar version of Eq. (20), and assuming $\boldsymbol{E}^1 \approx \boldsymbol{E}^2$ for our closely-spaced particles, the effective polarizability for the dimer can be expressed as

$$\alpha_{\text{tot}} = \frac{p_1 + p_2}{E} = \frac{\frac{1}{\alpha_1} + \frac{1}{\alpha_2} + 2G}{\left(\frac{1}{\alpha_1\alpha_2}\right) - G^2}. \tag{21}$$

While the above expressions contain a number of approximations, the result gives a semi-analytic result, rather than an infinite coupled transcendental equations. The α_{tot} does not uniquely define the particle's response as in a single dipolar scatterer as there will be higher-order scattering due to the particle separation. However, it does give a general sense of the strength and allows us to easily evaluate the absorption and extinction cross sections, with minimal approximation errors when the particles are illuminated with an equal amplitude and phase.

At this point, we insert the PT-symmetric values for the permittivity, and allow the transverse polarization to exhibit a general behavior. Similar relations to

those below can be derived for the longitudinal polarization as well. One benefit of expressing the response as in Eq. (21) is the ability to find the scattering minima and maxima from the zeros of the numerator and denominator, respectively. Interestingly, the numerator is completely real for all PT-symmetric permittivities, and is zero on the contour defined by

$$\left(\varepsilon_r + \frac{(1+2x)\,\varepsilon_b}{2\,(1-x)}\right)^2 + \varepsilon_i^2 = \frac{9}{4(1-x)^2}\varepsilon_b^2, \tag{22}$$

where, the dimensionless $x = (a/d)^3$ is a measure of the ratio of the relative coupling strength of the particles to the inverse polarizability. This contour is a circle centered on the real axis near $\varepsilon_r = -0.5$ and passes through the trivial result of $\varepsilon_{\mathrm{r}} = 1$ and slightly below $\varepsilon_r = -2$, the single particle plasmonic resonance.

The denominator of relation (21) is in general complex, simplifying to

$$\begin{aligned}\frac{1}{\alpha_1\alpha_2} - G^2 = \frac{1}{a^6}\left(1 - x^2 + \frac{3\varepsilon_b\,(\varepsilon_b + 2\varepsilon_r)}{\varepsilon_i^2 + (\varepsilon_r - \varepsilon_b)^2}\right) \\ - j\frac{4k^3}{3a^3}\left(1 - x + \frac{3\varepsilon_b\,(\varepsilon_b + 2\varepsilon_r)}{\varepsilon_i^2 + (\varepsilon_r - \varepsilon_b)^2}\right).\end{aligned} \tag{23}$$

Unlike the numerator, the denominator only is zero at one point described by $\varepsilon_r = -\frac{\varepsilon_b(2+x)}{x-1}$, $\varepsilon_i = 0$. This point solves Eq. (22) at the same time, and this pole-zero overlap has some interesting behavior associated with it. For now, we return to Eq. (23), and look for minima rather than zeros. The ratio of coefficients of the imaginary and real parts is $\frac{4}{3}(ka)^3$. When $a \ll 1.44\lambda$, the real part of the expression will dominate, and the minima of the magnitude of Eq. (23) can be approximated with the zeros of the real part. By doing so, we derive the "resonance" contour as the curve

$$\left(\varepsilon_r + \frac{\left(2 + x^2\right)\varepsilon_b}{\left(1 - \mathrm{x}^2\right)}\right)^2 + \varepsilon_i^2 = \frac{9x^2}{(1-x)^2}\varepsilon_b^2. \tag{24}$$

Again, the contour is a circle, this time centered near the plasmonic resonance of $\epsilon_r = -2$ with a radius of roughly $3x$. This result is not surprising as resonance splitting in coupled systems is a widely reported and understood phenomenon. Note also that the inclusion of the imaginary parts in α and G, related to power conservation for dynamic fields, prevents the denominator from going exactly to zero, and keeps the response finite.

Numerically, we can easily restore the exact expression for the dipole polarizability and the Green's function. Figure 5 shows the magnitude of α_{tot} under both polarizations, where, in both cases, the two circles as predicted by the quasistatic analysis appear. The permittivity of the plasmonic resonance shifts to more negative

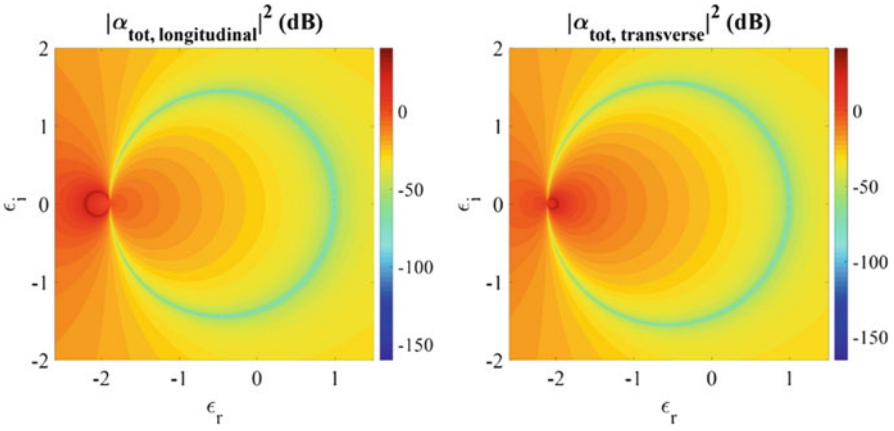

Fig. 5 The total polarizability for dipoles of radius 100 nm with center-to-center spacing of 350 nm under broadside illumination ($\theta_{inc} = 0$) with $\lambda = 5\mu m$. Longitudinal polarization is displayed on the left and transverse on the right. Figures are obtained by numerical calculation of the dynamic Mie theory polarizability and complete dipole Green's function

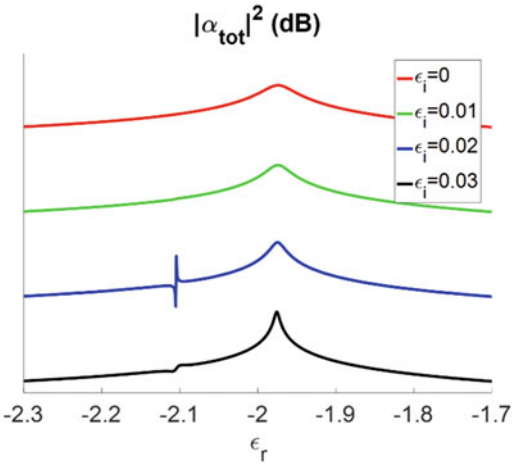

Fig. 6 Total polarizability for two particles, one having permittivity $\varepsilon = \varepsilon_r - j0.01$ and the other with $\varepsilon = \varepsilon_r - j0.01 + j\varepsilon_i$. Note the anticausal Fano feature near $\varepsilon_r = -2.1$ is most prominent when the PT-symmetric symmetry condition is met. The curves are offset for clarity

values as *ka* becomes sufficiently different than zero, explaining the deviation of the center of the resonance curve from $\varepsilon_r = -2$.

An intriguing property of this system is the merging of the scattering maxima and minima near the real axis. This feature is linked to the PT-symmetric case, as shown with Fig. 6. For two slightly lossy particles of $\varepsilon = \varepsilon_r + j0.01$, the anti-causal Fano peak is not present. By adding an additional gain to one particle ($\varepsilon_2 = \varepsilon_r + j(0.01 - \varepsilon_i)$), this peak appears when $\varepsilon_1 = \varepsilon_2^*$ ($\varepsilon_i = 0.02$), and is barely noticeable when more gain is added to the system.

It is worth noting that in the above discussion we have made a number of simplifications. Generally, once the materials and geometry are chosen, the other

degrees of freedom include the frequency, pump power, and incident direction. To start, we account for the finite separation and therefore phase difference of the particles with a non-broadside incident field. The individual dipole moments for a plane wave excitation at incidence angle ϕ_{inc} can be expressed as

$$p_1(\phi_{inc}) = \frac{\frac{1}{\alpha_2} + G\, e^{jkd\sin(\phi_{inc})}}{\frac{1}{\alpha_1}+\frac{1}{\alpha_2}+2G},\ p_2(\phi_{inc}) = \frac{\frac{1}{\alpha_1} e^{jkd\sin(\phi_{inc})} + G}{\frac{1}{\alpha_1}+\frac{1}{\alpha_2}+2G}, \tag{25}$$

The usual parameters of interest are the scattering, extinction, and absorption cross-sections, which for a dimer under transverse excitation can be simplified to

$$\begin{aligned} C_{scat} &= \frac{k^4}{12\pi^2\varepsilon_0^2}\int_0^{2\pi}\left|p_1 + p_2 e^{jkd\sin(\phi_{inc})}\right|^2 d\phi \\ &= \frac{k^4}{6\pi^2\varepsilon_0^2}\left(|p_1|^2 + |p_2|^2 + 2\,\mathrm{Re}\left[p_1 p_2^*\right] J_0(kd)\right) \end{aligned} \tag{26}$$

$$\boldsymbol{C}_{ext}(\phi_{inc}) = \frac{k}{\varepsilon_0}\mathrm{Im}\left[\frac{\frac{\mathbf{1}}{\alpha_1}+\frac{1}{\alpha_2}+2G\cos\left(kd\sin\left(\phi_{inc}\right)\right)}{\left(\frac{1}{\alpha_1\alpha_2}\right)-G^2}\right] \tag{27}$$

$$C_{abs} = \frac{3k\varepsilon_i}{4\pi^3\varepsilon_0^2\left((\varepsilon_r-1)^2+\varepsilon_i^2\right)}\left(\left|p_{gain}\right|^2 - |p_{loss}|^2\right) \tag{28}$$

where $J_0(z)$ is the cylindrical Bessel function and ϕ_{inc} is the angle from broadside of the illuminating plane wave ($\phi_{\text{inc}} = 90^\circ$) when $\overrightarrow{k}_{inc}$ points from loss to gain). From Eq. (27), it is clear that C_{ext} is invariant under the transformation $\phi_{\text{inc}} \rightarrow -\phi_{\text{inc}}$, so the extinguished power will not depend on which particle the field "hits" first. This is not true for the scattered power, and so the scattering and absorption can be drastically altered by "switching" the positions of the particles.

A number of results can be gathered by applying these formulae to this simple model. In Fig. 7c we see that the scattering cross section does not have a zero that extends nearly to the antiparallel resonance. Thus, the particles may oscillate mostly out of phase and therefore they have a small total dipole moment, but radiation into higher order modes must be strong. Also, the calculated absorption cross section is always negative when the incidence is broadside. Physically, the material gain offsets the damping from radiation, and so the gain particle always oscillates with a larger magnitude when equally excited. On the other hand, there can be absorption when incident angle is skewed toward one particle (Fig. 8). The directional dependence in absorption must be matched by a change in the scattering, which is also shown in Fig. 8. Further, the extinction is negative in a region that generally follows the scattering minima. Since a negative extinction implies lasing (the particles supply power into their own driving field), this relationship is intuitive, as radiation losses are low in this regime. Note that lasing only occurs in the region

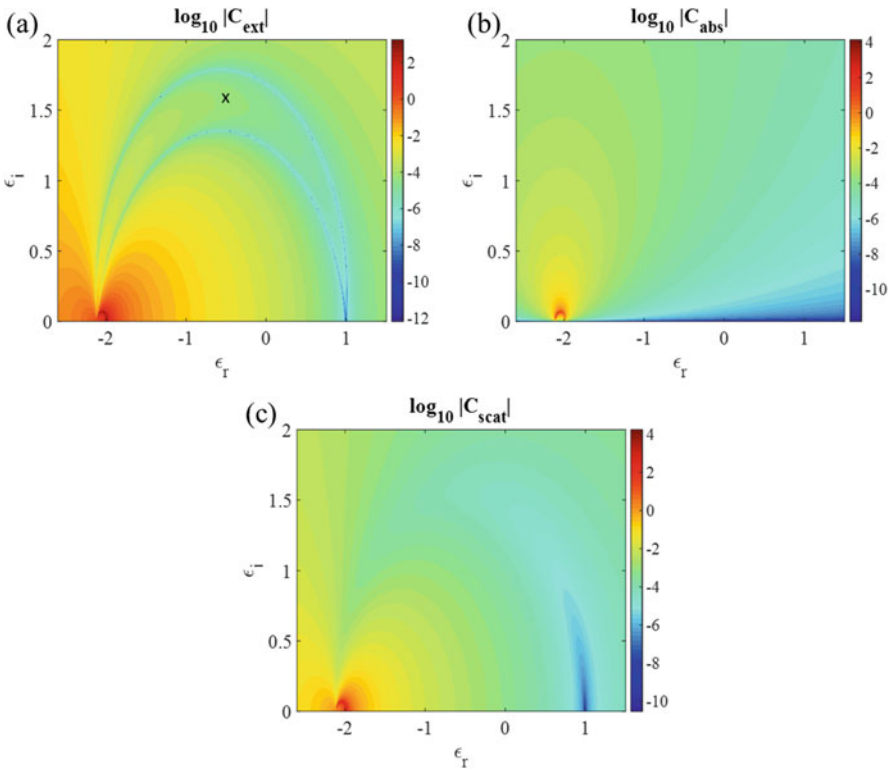

Fig. 7 (**a**) Extinction, (**b**) absorption, and (**c**) scattering cross section magnitudes for the dimer under transverse broadside incidence. The extinction is positive, except for between the two curves of low magnitude that originate at $\varepsilon_r = 1$ and terminate near the $\varepsilon_r \approx -2$ resonance, in the region marked with "x". The absorption cross section is never positive, and it has its largest magnitude along the resonance curve. Contrary to the sharp zero-pole merging for the effective polarizability, the scattering cross section minima change along the "zero" curve

roughly defined by $-2 < \varepsilon_r < 1$. The lasing at $\varepsilon_r = 1$ is thresholdless (the region with negative extinction reaches the real axis), while the gain/loss lasing threshold near $\epsilon_r = -2$ decreases as the dimer's electrical size shrinks.

The frequency dispersion and pump power are more closely coupled, and are best considered in tandem. This aspect has been recently explored, which we draw from here [32]. Conductive materials in general can be modelled as collections of free electrons and the permittivity dispersion follows the well-known Drude model. The dispersion of gain particles, on the other hand, is less understood. A common model for emitters "doped" into background is to add the "gain half" of a Lorentzian, with a coefficient to account for the population inversion produced by the pump [33, 34]. We then consider a dimer similar to two conducting oxide spheres, with one doped to provide gain, as in Ref. [32]. The two permittivities can then be approximated near the gain resonance as

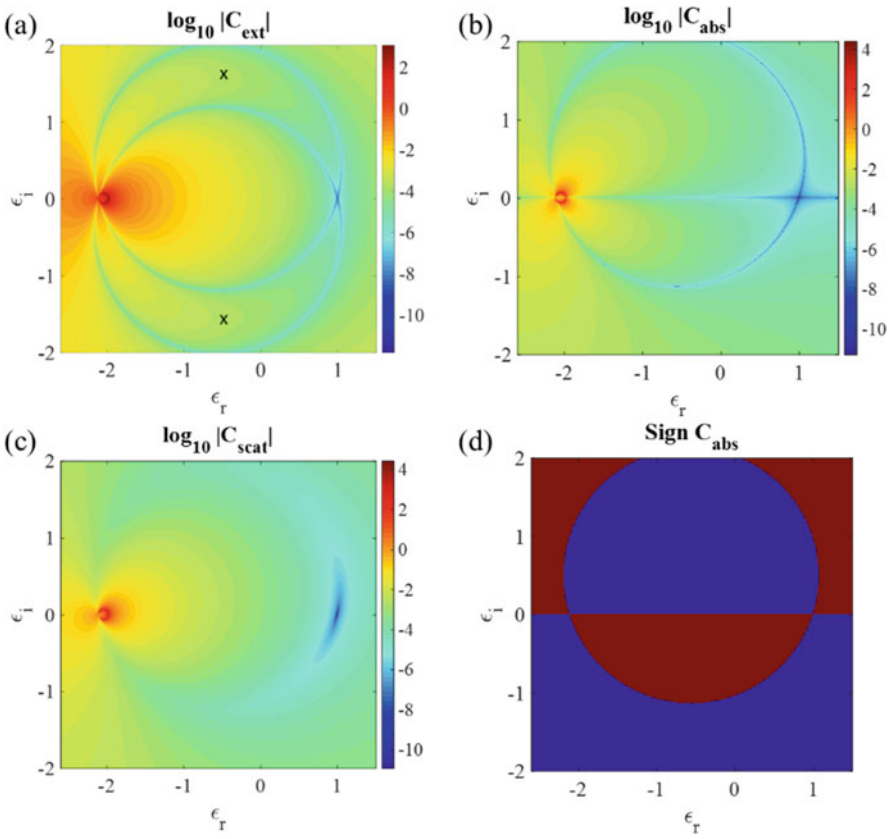

Fig. 8 Cross sections of particles under side incidence ($\theta_{inc} = \pm 90^{\circ}$). Top half plane corresponds to exciting the gain particle first, and bottom half plane to exciting the loss particle first. (**a**) Extinction cross section is positive except in regions marked by "x" as in Fig. 3a. Also, it is symmetric with respect to angle of incidence. The (**b**) absorption and (**c**) scattering cross sections are in general asymmetric, and so the scattered power can depend on the orientation of the particles. Also note that the sign of the absorption cross section (**d**) (red is positive, blue negative) can depend on the direction of incidence

$$\varepsilon_1 = \varepsilon_\infty - \frac{\omega_{plasmon}^2}{\omega^2 + j\omega\gamma_{plasmon}}, \varepsilon_2 = \varepsilon_1 + A\frac{\gamma_{gain}}{\omega - \omega_{gain} + j\gamma_{gain}}. \tag{29}$$

At the gain resonance, the emitter contribution to the permittivity is simply a positive imaginary term, but any difference from this frequency will add a component to the real part of the permittivity as well. As one would expect, increasing the pump power tends to narrow the resonant linewidth of the scattering peak, while providing a large boost to the peak scattering cross section (Fig. 9). The absorption cross section can even become negative, as the gain overcomes the material loss.

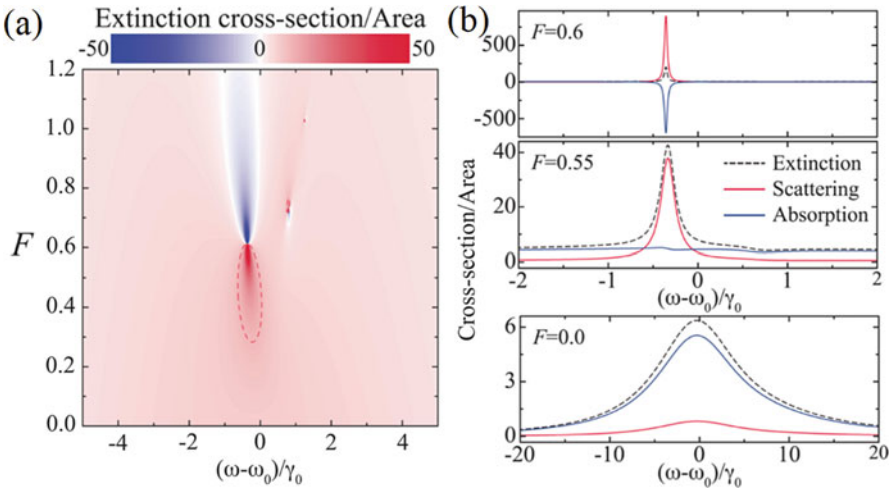

Fig. 9 From [32]. (**a**) The extinction cross section as a function of frequency detuning and gain coefficient. (**b**) The extinction, scattering, and absorption cross sections as a function of frequency detuning and for different pump levels. As the pump reaches a critical level at the appropriate frequency, the scattering linewidth shinks and the absorption cross section becomes negative, cancelling out the scattering losses and mimicking the high Q response of a lossless resonantor

This analysis also gives a good intuition on the effect of gain on the scattering anisotropy. For particles with strictly identical real parts of permittivity, the gain particle will oscillate more strongly as there is less effective damping from material and radiation losses. However, the particles can also experience a significant difference in phase, especially when the antiparallel resonance is significantly excited. The scattering patterns are easily calculated with the discrete dipole approximation, acting identically to an antenna phased array. In general, for broadside incidence, increasing the pump power skews the scattering pattern toward the gain particle, with the anisotropy growing with pump power as shown in Fig. 10. Extending the analysis from merely two particles to a linear array, the scattering anisotropy grows with the array length. In all cases, increasing the gain increases the scattered power, but disproportionately toward the gain direction. For finite PT-symmetric chains, large asymmetric scattering with minimal extinction has been predicted due to edge modes [35].

As mentioned previously, reversing the incident direction will not change the extinguished power, but can alter the scatting and absorption. As shown in Fig. 10, for small pumping (and therefore small anisotropies), the scattering and absorption are roughly the same after reversing the incident field direction. For higher values of gain, the cross sections will be heavily directionally dependent, with the total scattering significantly higher when impinging on the gain particle first.

So far, we have examined only particles near a plasmonic resonance, and only worked with the dipole approximation. In general, PT-symmetric systems are noted for exceptional points and symmetry breaking thresholds, which have not

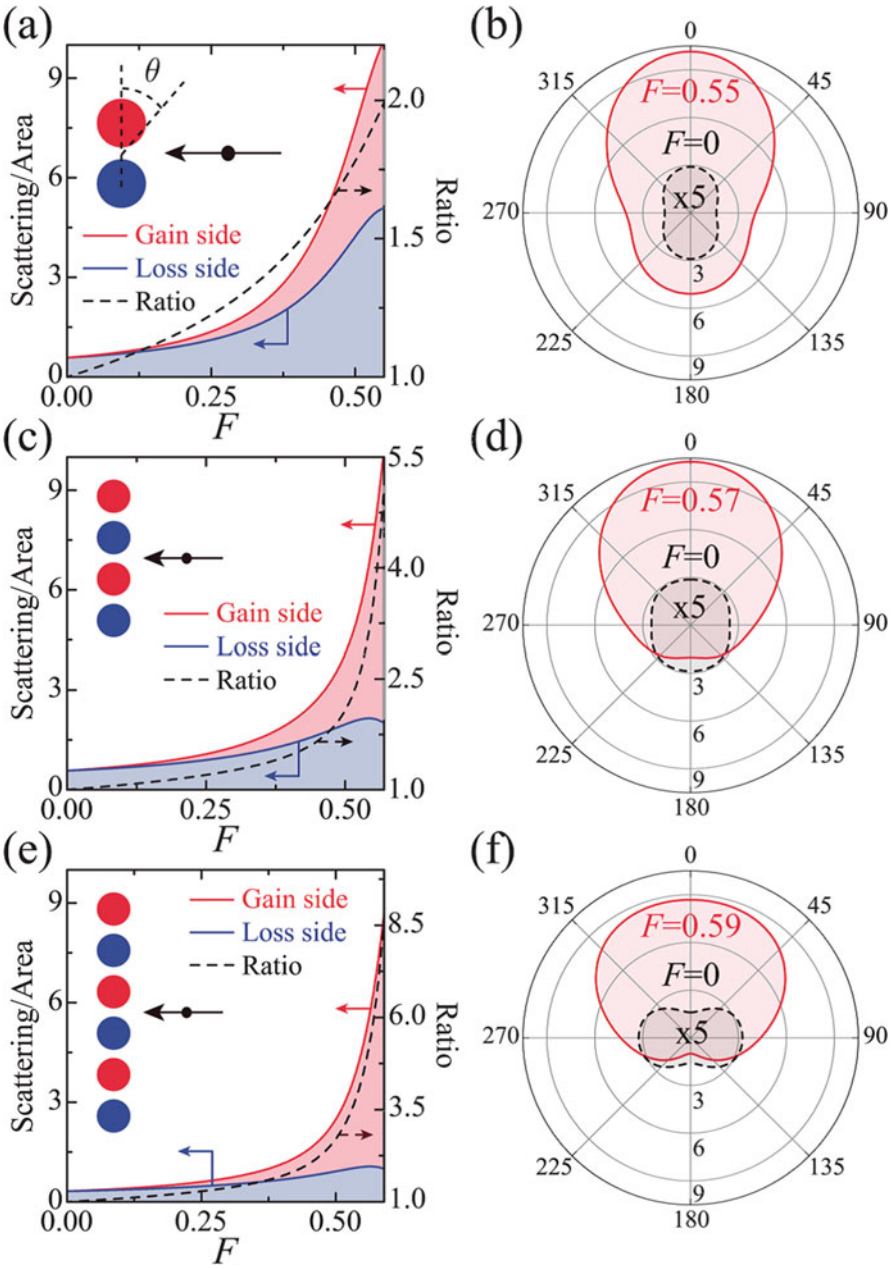

Fig. 10 From [32]. (**a**), (**c**), (**e**) Scattering intensities in the direction of gain particles (0°) and loss particles (180°) as a function of pump strength for various particle array sizes and broadside incidence. As the gain is increased, the scattering is increasingly directed toward the "gain" side of the linear array. (**b**), (**d**), (**f**) show the scattering patters for a highly pumped (red) and non-pumped (dashed black) system. For each array size, the detuning from the resonance frequency is kept constant

been apparent in any observables so far. The symmetry breaking does become mathematically noticeable when the analysis is performed with a scattering matrix. For lossless systems with finite port numbers, the scattering matrix fulfils the unitary condition, i.e., the eigenvalues all have magnitude unity and the input power equals the output power. PT-symmetric systems can break this condition and have complex-conjugate eigenvalues above a certain threshold [16], for which the scattered power can be higher or lower than the incident (net emission or absorption), depending on the incident state. A scattering system can theoretically scatter power into an infinite number of modes (the spherical harmonics). Clusters of spherical scatterers have been extensively studied, with the T-matrix approach mentioned earlier. This technique decomposes the incident and scattered wave into spherical harmonics, including the internal coupling between particles. A derivation of this approach will not be included here, but numerous explanations already exist in the literature. Interestingly, the connection between the scattering matrix eigenvalues and the absorption cross section is not as straightforward as in 1D. As shown for the scattering eigenvalues of a PT-symmetric dielectric ($\epsilon = 1.1 \pm j0.1$) dimer (Fig. 11), the broken symmetry is found only for short wavelengths, when the system is large compared to wavelength [36]. In general, although negative absorption cross sections are found even in the unbroken regimes, the absorption is always negative for broadside incidence, consistent with what is expected in the dipole approximation. For the analogous 1D problem, the scattering is always amplified in the broken phase when the two ports are excited with the same amplitude. Similarly, when the plane wave illuminates the two particles, even with a phase difference due to the incident angle, the absorption is negative for broken-symmetry wavelengths.

The most interesting result from this approach is the disconnection between the matrix analysis and physical behavior. There is no abrupt change in any of the cross sections, or general change in behavior at all when crossing from the broken to the unbroken regimes. Because PT-symmetric systems are inherently non-Hermitian, the eigenvectors are not orthogonal. Thus, although the individual scattering eigenvalues may be unimodular, the actual mode of the system cannot be decomposed onto a higher dimensional unit circle as in the case of orthogonal bases (the dimensionality will be determined by the number of harmonics in the S-matrix expansion). As in the 1D case [16], the unitarity of eigenvalues does not guarantee unitary scattering for a generic excitation. Special care, therefore, must be taken when predicting the physical behavior from mathematical solutions in non-Hermitian systems.

6 Summary

In conclusion, we have shown how PT-symmetry manifests itself in open scattering problems. By providing intuition with simple models, we show many consistent behaviors that are common to these systems in all dimensions. The gain-loss anisotropy can produce highly directional responses, along with scattering

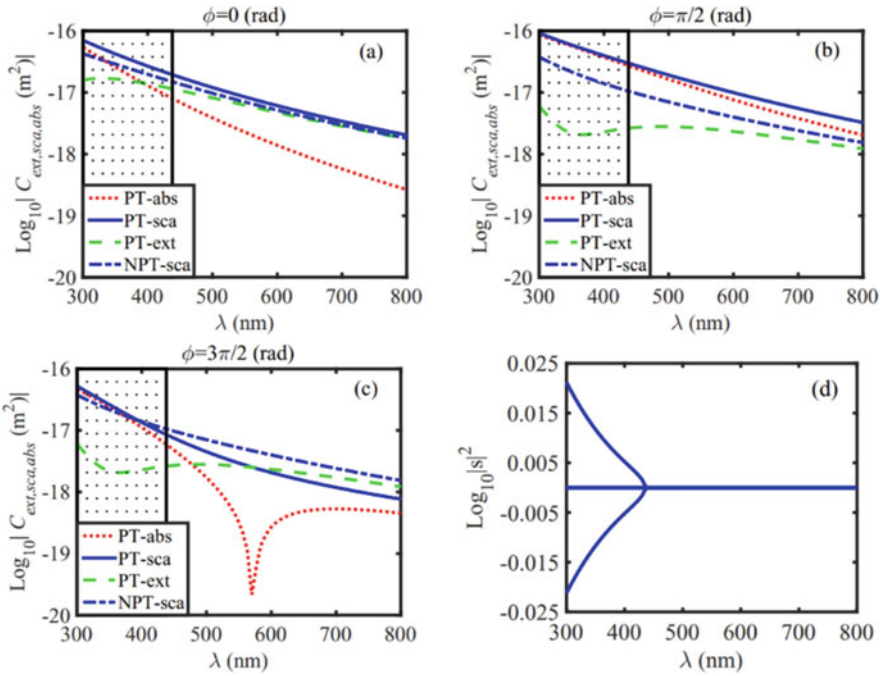

Fig. 11 From [36]. (**a**)–(**c**) Plots of the extinction, scattering and absorption cross sections as a function of wavelength and under three illumination directions. Here, $\theta = \pi/2$ corresponds to the loss sphere being illuminated first (opposite to the angle defined in the text). All absorption cross section values are negative except in (**c**) when $\lambda > 571$ nm. The dotted region indicates the wavelengths associated with the broken symmetry regime. NPT-symmetric refers to a lossless dimer of equal real permittivity, included for comparison. (**d**) Scattering matrix eigenvalue magnitudes as a function of wavelength. Here, the scattering matrix is of dimension 16

enhancement or suppression. Even with radiation loss, a system can move into the lasing regime with purely equal material gain and loss, especially near resonance. However, inherently active PT-symmetric systems exhibit some differences with typical scattering problems, and are subject to different constraints, as illustrated by a new optical theorem.

Acknowledgments This work was partially supported by the Office of Naval Research.

References

1. Makris, K.G., El-Ganainy, R., Christodoulides, D.N., Musslimani, Z.H.: Beam dynamics in PT-symmetric symmetric optical lattices. Phys. Rev. Lett. **100**, 103904 (2008)
2. Klaiman, S., Guenther, U., Moiseyev, N.: Visualization of branch points in PT-symmetric waveguides. Phys. Rev. Lett. **101**, 080402 (2008)

3. Longhi, S.: Bloch oscillations in complex crystals with PT-symmetric symmetry. Phys. Rev. Lett. **103**, 123601 (2009)
4. Rüter, C.E., Makris, K.G., El-Ganainy, R., Christodoulides, D.N., Segev, M., Kip, D.: Observation of parity-time symmetry in optics. Nat. Phys. **6**, 192–195 (2010)
5. Regensburger, A., Bersch, C., Miri, M.-A., Onishchukov, G., Christodoulides, D.N., Peschel, U.: Parity-time synthetic photonic lattices. Nature. **488**, 167–171 (2012)
6. Feng, L., Xu, Y.L., Fegadolli, W.S., Lu, M.H., Oliveira, J.E., Almeida, V.R., Chen, Y.-F., Scherer, A.: Experimental demonstration of a unidirectional reflectionless parity-time metamaterial at optical frequencies. Nat. Mater. **12**, 108–113 (2013)
7. Peng, B., Özdemir, Ş.K., Lei, F., Monifi, F., Gianfreda, M., Long, G.L., Fan, S., Nori, F., Bender, C.M., Yang, L.: Parity–time-symmetric whispering-gallery microcavities. Nat. Phys. **10**, 394–398 (2014)
8. Wong, Z.J., Xu, Y.L., Kim, J., O'Brien, K., Wang, Y., Feng, L., Zhang, X.: Lasing and anti-lasing in a single cavity. Nat. Photon. **10**, 796–801 (2016)
9. Bender, C.M., Boettcher, S.: Real spectra in non-Hermitian Hamiltonians having PT-symmetric symmetry. Phys. Rev. Lett. **80**, 5243–5246 (1998)
10. Lévai, G., Znojil, M.: Systematic search for PT-symmetric potentials with real energy spectra. J. Phys. Math. Gen. **33**, 7165–7180 (2000)
11. Ahmed, Z.: Real and complex discrete eigenvalues in an exactly solvable one-dimensional complex PT-symmetric invariant potential. Phys. Lett. A. **282**, 343–348 (2001)
12. Bender, C.M., Brody, D.C., Jones, H.F.: Complex extension of quantum mechanics. Phys. Rev. Lett. **89**, 270401 (2002)
13. Mostafazadeh, A.: Pseudo-Hermiticity versus PT-symmetric symmetry: the necessary condition for the reality of the spectrum of a non-Hermitian Hamiltonian. J. Math. Phys. **43**, 205–214 (2002)
14. Haus, H.A.: Waves and Fields in Optoelectronics. Prentice-Hall, Englewood Cliffs (1984)
15. Suh, W., Wang, Z., Fan, S.: Temporal coupled-mode theory and the presence of non-orthogonal modes in lossless multimode cavities. IEEE J. Quant. Electron. **40**, 1511 (2004)
16. Chong, Y.D., Ge, L., Stone, A.D.: PT-symmetry breaking and laser-absorber modes in optical scattering systems. Phys. Rev. Lett. **106**, 093902 (2012)
17. Ge, L., Chong, Y.D., Stone, A.D.: Conservation relations and anisotropic transmission resonances in one-dimensional PT-symmetric photonic heterostructures. Phys. Rev. A. **85**, 023802 (2012)
18. Longhi, S.: PT-symmetric laser absorber. Phys. Rev. A. **82**, 031801 (2010)
19. Wong, Z.J., Xu, Y.L., Kim, J., O'Brien, K., Wang, Y., Feng, L., Zhang, X.: Lasing and anti-lasing in a single cavity. Nat. Photon. **10**, 796–801 (2016)
20. Lin, Z., Ramezani, H., Eichelkraut, T., Kottos, T., Cao, H., Christodoulides, D.N.: Unidirectional invisibility induced by PT-symmetric periodic structures. Phys. Rev. Lett. **106**, 213901 (2011)
21. Kulishov, M., Laniel, J.M., Bélanger, N., Azaña, J., Plant, D.V.: Nonreciprocal waveguide Bragg gratings. Opt. Express. **13**, 3068 (2005)
22. Feng, L., Xu, Y.L., Fegadolli, W.S., Lu, M.H., Oliveira, J.E., Almeida, V.R., Chen, Y.-F., Scherer, A.: Experimental demonstration of a unidirectional reflectionless parity-time metamaterial at optical frequencies. Nat. Mater. **12**, 108–113 (2013)
23. Regensburger, A., Bersch, C., Miri, M.-A., Onishchukov, G., Christodoulides, D.N., Peschel, U.: Parity–time synthetic photonic lattices. Nature. **488**, 167–171 (2012)
24. Miri, M.-A., Aceves, A.B., Kottos, T., Kovanis, V., Christodoulides, D.N.: Bragg solitons in nonlinear PT-symmetric periodic potentials. Phys. Rev. A. **86**, 033801 (2012)
25. Castaldi, G., Savoia, S., Galdi, V., Alù, A., Engheta, N.: PT-symmetric metamaterials via complex-coordinate transformation optics. Phys. Rev. Lett. **110**, 173901 (2013)
26. Miri, M.-A., Eftekhar, M.A., Facao, M., Abouraddy, A.F., Bakry, A., Razvi, M.A., Alshahrie, A., Alù, A., Christodoulides, D.N.: Scattering properties of PT-symmetric objects. J. Opt. **18**, 075104 (2016)

27. Bohren, C.F., Huffman, D.R.: Absorption and Scattering of Light by Small Particles, vol. 98. Wiley, London (1983)
28. Waterman, P.C.: Symmetry, unitarity, and geometry in electromagnetic scattering. Phys. Rev. D. **3**, 825–839 (1971)
29. Peterson, B., Ström, S.: T matrix for electromagnetic scattering from an arbitrary number of scatterers and representations of E(3). Phys. Rev. D. **8**, 3661–3678 (1973)
30. Capolino, F. (ed.): Theory and phenomena of metamaterials. CRC Press/Taylor & Francis Group, Boca Raton (2009)
31. Duggan, R., Miri, M.-A., Alu, A. Scattering properties of parity-time symmetric nanoparticle dimers. In: IEEE International Symposium on Antennas and Propagation & USNC/URSI National Radio Science Meeting, 1067, San Diego, CA (2017)
32. Manjavacas, A.: Anisotropic optical response of nanostructures with balanced gain and loss. ACS Photon. **3**, 1301–1307 (2016)
33. Campione, S., Albani, M., Capolino, F.: Complex modes and near-zero permittivity in 3D arrays of plasmonic nanoshells: loss compensation using gain. Opt. Mater. Express. **1**, 1077 (2011)
34. Chua, S.-L., Chong, Y., Stone, A.D., Soljacic, M., Bravo-Abad, J.: Low-threshold lasing action in photonic crystal slabs enabled by Fano resonances. Opt. Express. **19**, 1539–1562 (2011)
35. Ling, C.W., Choi, K.H., Mok, T.C., Zhang, Z.-Q., Fung, K.H.: Anomalous light scattering by topological PT-symmetric -symmetric particle arrays. Sci. Rep. **6**, 38049 (2016)
36. Chen, X., Yue, W., Tao, R., Yao, P., Liu, W.: Scattering phenomenon of PT-symmetric dielectric-nanosphere structure. Phys. Rev. A. **94**, 53829 (2016)

Scattering Theory and $\mathcal{PT}$-Symmetry

Ali Mostafazadeh

Abstract We outline a global approach to scattering theory in one dimension that allows for the description of a large class of scattering systems and their $\mathcal{P}$-, $\mathcal{T}$-, and $\mathcal{PT}$-symmetries. In particular, we review various relevant concepts such as Jost solutions, transfer and scattering matrices, reciprocity principle, unidirectional reflection and invisibility, and spectral singularities. We discuss in some detail the mathematical conditions that imply or forbid reciprocal transmission, reciprocal reflection, and the presence of spectral singularities and their time-reversal. We also derive generalized unitarity relations for time-reversal-invariant and $\mathcal{PT}$-symmetric scattering systems, and explore the consequences of breaking them. The results reported here apply to the scattering systems defined by a real or complex local potential as well as those determined by energy-dependent potentials, nonlocal potentials, and general point interactions.

1 Basic Setup for Elastic Scattering in One Dimension

The theory of the scattering of waves by obstacles or the interactions modelling them rests on the assumption that the strength of the interaction diminishes at large distances, so that in the vicinity of the source and detectors the wave can be safely approximated by a plane wave. A consistent implementation of this assumption requires the existence of solutions of the relevant wave equation that tend to plane waves at spatial infinities. For a time-harmonic scalar wave, $e^{-i\omega t}\psi(x)$, propagating in one dimension, this requirement takes the form of the following asymptotic boundary conditions:

A. Mostafazadeh (✉)
Departments of Mathematics and Physics, Koç University, Istanbul, Turkey
e-mail: amostafazadeh@ku.edu.tr

D. Christodoulides, J. Yang (eds.), *Parity-time Symmetry and Its Applications*, Springer Tracts in Modern Physics 280,
https://doi.org/10.1007/978-981-13-1247-2_4

$$\psi(x) \to \begin{cases} A_-(k)e^{ikx} + B_-(k)e^{-ikx} & \text{for } x \to -\infty, \\ A_+(k)e^{ikx} + B_+(k)e^{-ikx} & \text{for } x \to +\infty, \end{cases} \tag{1}$$

where $A_\pm(k)$ and $B_\pm(k)$ are complex-valued functions of the wavenumber k, which we take to be a positive real variable unless otherwise is clear. The factors e^{ikx} and e^{-ikx} appearing in (1) are related to the solutions, $e^{i(kx-\omega t)}$ and $e^{-i(kx+\omega t)}$, of the wave equation in the absence of the interaction. They represent the right- and left-going waves, respectively.

As a principal example, consider the scattering phenomenon described by the Schrödinger equation,

$$-\psi''(x) + v(x)\psi = k^2\psi(x), \tag{2}$$

where $v(x)$ is a real or complex interaction potential. The existence of the solutions of this equation that satisfy (1) restricts the rate at which $|v(x)|$ decays to zero as $x \to \pm\infty$. We can also consider the more general situations where the potential is energy-dependent. For example consider the Helmholtz equation,

$$\psi''(x) + k^2\hat{\varepsilon}(x,k)\psi(x) = 0, \tag{3}$$

which describes the interaction of polarized electromagnetic waves having an electric field of the form $E_0e^{-i\omega t}\psi(x)$ pointing along the y-axis with an isotropic nonmagnetic media represented by a real or complex relative permittivity profile $\hat{\varepsilon}(x,k)$, [4]. We can express (3) in the form (2) provided that we identify $v(x)$ with the energy-dependent optical potential:

$$v(x,k) = k^2[1 - \hat{\varepsilon}(x,k)]. \tag{4}$$

The scattering setup we have outlined above also applies for the scattering of waves described by nonlocal and nonlinear Schrödinger equations [44, 53, 59, 65],

$$-\psi''(x) + \int_{-\infty}^{\infty} V(x,x')\psi(x')dx' = k^2\psi(x), \tag{5}$$

$$-\psi''(x) + V(x,\psi(x))\psi(x) = k^2\psi(x), \tag{6}$$

if the nonlocal and nonlinear potentials, $V(x,x')$ and $V(x,\psi(x))$ decay sufficiently rapidly as $x \to \pm\infty$ so that (5) and (6) admit solutions satisfying (1). This is clearly the case for confined nonlocal and nonlinear interactions [8, 44], where

$$V(x,x') = v(x)\delta(x-x') + F(x,x')\chi_{[a,b]}(x),$$

$$V(x,\psi(x)) = v(x) + F(x,\psi(x))\chi_{[a,b]}(x),$$

$\delta(x)$ stands for the Dirac delta function, F is a complex-valued function of a pair of real or complex variables, $[a, b]$ is a closed interval of real numbers,

$$\chi_{[a,b]}(x) := \begin{cases} 1 \text{ for } x \in [a, b], \\ 0 \text{ for } x \notin [a, b], \end{cases}$$

and we use the symbol ":=" (respectively "=:") to state that the right-hand (respectively left-hand) side is the definition of the left-hand (respectively right-hand.)

Another class of scattering problems that we can treat using our general framework for scalar-wave scattering in one dimension is that of single- or multi-center point interactions [41]. These correspond to scalar waves $\psi(x)$ that satisfy

$$\begin{aligned} &-\psi''(x) = k^2\psi(x) && \text{for} \quad x \in \mathbb{R} \setminus \{c_1, c_2, \cdots, c_n\}, \\ &\begin{bmatrix} \psi(c_j^+) \\ \psi'(c_j^+) \end{bmatrix} = \mathbf{B}_j \begin{bmatrix} \psi(c_j^-) \\ \psi'(c_j^-) \end{bmatrix} && \text{for} \quad j \in \{1, 2, \cdots, n\}, \end{aligned} \tag{7}$$

where $c_1, c_2, \cdots, c_n$ are distinct real numbers representing the interaction centers, for every function $\phi(x)$ the symbols $\phi(c_j^-)$ and $\phi(c_j^+)$ respectively denote the left and right limit of $\phi(x)$ as $x \to c_j$, i.e., $\phi(c_j^\pm) := \lim_{x\to c_j^\pm} \phi(x)$, and $\mathbf{B}_j$ are possibly k-dependent 2×2 invertible matrices. The point interactions of this type may be used to model electromagnetic interface conditions [50].

The best known example of a single-center point interaction is the delta-function potential $v(x) = \mathfrak{z}\,\delta(x)$ with a coupling constant $\mathfrak{z}$. It corresponds to the choice: $n = 1$, $c_1 = 0$, and

$$\mathbf{B}_1 = \begin{bmatrix} 1 & 0 \\ \mathfrak{z} & 1 \end{bmatrix}. \tag{8}$$

In a scattering experiment, the incident wave is emitted by its source which is located at one of the spatial infinities $\pm\infty$, and the scattered wave is received by the detectors which are placed at one or both of these infinities. If the source is located at $-\infty$, the incident wave travels towards the region of the space where the interaction has a sizable strength. A part of it passes through this region and reaches the detector at $+\infty$. The other part gets reflected and travels towards the detector at $-\infty$. As a result, the incident and transmitted waves are right-going while the reflected wave is left-going. This scenario is described by a solution $\psi_l(x)$ of the wave equation that has the following asymptotic behavior.

$$\psi_l(x) \to \begin{cases} \mathcal{N}\left[e^{ikx} + \mathfrak{r}_l(k)\, e^{-ikx}\right] & \text{for } x \to -\infty, \\ \mathcal{N}\,\mathfrak{t}_l(k)\, e^{ikx} & \text{for } x \to +\infty, \end{cases} \tag{9}$$

where $\mathcal{N}$ is the amplitude of the incident wave, and $\mathfrak{r}_l(k)$ and $\mathfrak{t}_l(k)$ are complex-valued functions of k that are respectively called the *left reflection and transmission amplitudes*. Similarly, we have the solution $\psi_r(x)$ of the wave equation that corresponds to the scattering of an incident wave that is emitted from a source located at $x = +\infty$. This satisfies

$$\psi_r(x) \to \begin{cases} \mathcal{N}\,\mathfrak{t}_r(k)\,e^{-ikx} & \text{for } x \to -\infty, \\ \mathcal{N}\left[e^{-ikx} + \mathfrak{r}_r(k)\,e^{ikx}\right] & \text{for } x \to +\infty, \end{cases} \tag{10}$$

where $\mathfrak{r}_r(k)$ and $\mathfrak{t}_r(k)$ are respectively the *right reflection and transmission amplitudes*.

Scattering experiments involve the measurement of the reflection and transmission amplitudes, $\mathfrak{r}_{l/r}(k)$ and $\mathfrak{t}_{l/r}(k)$, or their modulus square, $|\mathfrak{r}_{l/r}(k)|^2$ and $|\mathfrak{t}_{l/r}(k)|^2$, which are respectively called the *left/right reflection and transmission coefficients*.[1] By solving a scattering problem we mean the determination of $\mathfrak{r}_{l/r}(k)$ and $\mathfrak{t}_{l/r}(k)$. We sometimes call these the "*scattering data*".

If $\mathfrak{r}_{l/r}(k_0) = 0$ for some wavenumber $k_0 \in \mathbb{R}^+$, we say that the scatterer[2] is *reflectionless from the left/right* or simply *left/right-reflectionless* at $k = k_0$. Similarly we call it *left/right transparent* at $k = k_0$, if $\mathfrak{t}_{l/r}(k_0) = 1$. A scatterer is invisible from the left or right if it is both reflectionless and transparent from that direction. In this case we call it *left/right-invisible*. *Unidirectional reflectionlessness* (respectively *unidirectional invisibility*) refers to situations where a scatterer is reflectionless (respectively invisible) only from the left or right [25]. The reflectionlessness, transparency, and invisibility of a scatterer are said to be *broadband* if they hold for a finite or infinite interval of positive real values of k.

If the wave equation is linear, we can scale $\psi_{l/r}$ and work with $\psi_{+/-} := \psi_{l/r}/\mathcal{N}\mathfrak{t}_{l/r}$. These satisfy:

$$\begin{aligned} &\psi_\pm(x) \to e^{\pm ikx} && \text{for } x \to \pm\infty, \\ &\psi_+(x) \to \frac{1}{\mathfrak{t}_l(k)}\,e^{ikx} + \frac{\mathfrak{r}_l(k)}{\mathfrak{t}_l(k)}\,e^{-ikx} && \text{for } x \to -\infty, \\ &\psi_-(x) \to \frac{\mathfrak{r}_r(k)}{\mathfrak{t}_r(k)}\,e^{ikx} + \frac{1}{\mathfrak{t}_r(k)}\,e^{-ikx} && \text{for } x \to +\infty, \end{aligned} \tag{11}$$

and are called the *Jost solutions*. It turns out that the Schrödinger equation (2) admits Jost solutions, if $\int_{-\infty}^{\infty} \sqrt{1+x^2}\,|v(x)|dx < \infty$. This is equivalent to the *Faddeev condition*:

[1] These are occasionally labelled by $T^{l/r}(k)$ and $R^{l/r}(k)$, [44, 59]. Here we refrain from using this notation, because some references use these symbols for the reflection and transmission amplitudes and not their modulus squared [25].

[2] By a scatterer we mean the interaction causing the propagation of a wave differ from that of a plane wave.

$$\int_{-\infty}^{\infty}(1+|x|)|v(x)|dx<\infty. \tag{12}$$

Under this condition the Jost solutions exist not only for real and positive values of k, but also for complex values of k belonging to the upper-half complex plane, i.e., $k\in\{\mathfrak{z}\in\mathbb{C}\mid \mathrm{Im}(\mathfrak{z})\geq 0\}$. Furthermore, in this half-plane they are continuous functions of k, [21].

Faddeev condition clearly holds for *finite-range potentials* which vanish outside a finite interval (have a compact support), and *exponentially decaying potentials* which satisfy

$$e^{\mu_\pm|x|}|v(x)|<\infty \quad \text{for} \quad x\to\pm\infty, \tag{13}$$

for some $\mu_\pm\in\mathbb{R}^+$. Notice that finite-range potentials fulfill this condition for all $\mu_\pm\in\mathbb{R}^+$. Therefore they share the properties of exponentially decaying potentials that follow from (13).

In this article we use the term "*scattering potential* " for real or complex-valued potentials $v(x)$ that satisfy the Faddeev condition (12).

2 Transfer Matrix

Consider a linear scalar wave equation that admits time-harmonic solutions $e^{-i\omega t}\psi(x)$ fulfilling the asymptotic boundary conditions (1). We can identify these solutions by the pairs of column vectors:

$$\begin{bmatrix}A_-(k)\\ B_-(k)\end{bmatrix} \quad \text{and} \quad \begin{bmatrix}A_+(k)\\ B_+(k)\end{bmatrix}.$$

The 2×2 matrix $\mathbf{M}(k)$ that connects these is called the *transfer matrix* [63, 66]. By definition, it satisfies

$$\mathbf{M}(k)\begin{bmatrix}A_-(k)\\ B_-(k)\end{bmatrix}=\begin{bmatrix}A_+(k)\\ B_+(k)\end{bmatrix}. \tag{14}$$

If we demand that the knowledge of the solution of the wave equation at either of the spatial infinities, $x\to\pm\infty$, determines it uniquely, $\mathbf{M}(k)$ must be invertible. In what follows we assume that this is the case, i.e., $\det\mathbf{M}(k)\neq 0$.[3]

We can express the entries of $\mathbf{M}(k)$ in terms of the reflection and transmission amplitudes by implementing (14) for the Jost solutions. This requires the

[3] In Sect. 4, we prove that this conditions holds for the scattering systems described by the Schrödinger equation (2).

identification of the coefficient functions $A_\pm(k)$ and $B_\pm(k)$ for $\psi(x) = \psi_\pm(x)$. Comparing (1) and (11), we see that for $\psi(x) = \psi_+(x)$,

$$A_- = \frac{1}{\mathfrak{t}_l}, \qquad B_- = \frac{\mathfrak{r}_l}{\mathfrak{t}_l}, \qquad A_+ = 1, \qquad B_+ = 0. \tag{15}$$

Here and in what follows we occasionally suppress the k-dependence of $A_\pm(k)$, $B_\pm(k)$, $\mathfrak{r}_{l/r}(k)$, $\mathfrak{t}_{l/r}(k)$, $\mathbf{M}(k)$, and other relevant quantities for brevity. Similarly for $\psi(x) = \psi_-(x)$, we have

$$A_- = 0, \qquad B_- = 1, \qquad A_+ = \frac{\mathfrak{r}_r}{\mathfrak{t}_r}, \qquad B_+ = \frac{1}{\mathfrak{t}_r}. \tag{16}$$

Substituting (15) and (16) in (14) gives

$$\frac{1}{\mathfrak{t}_l}\mathbf{M}\begin{bmatrix}1\\ \mathfrak{r}_l\end{bmatrix} = \begin{bmatrix}1\\ 0\end{bmatrix}, \qquad \mathbf{M}\begin{bmatrix}0\\ 1\end{bmatrix} = \frac{1}{\mathfrak{t}_r}\begin{bmatrix}\mathfrak{r}_r\\ 1\end{bmatrix}. \tag{17}$$

The second of these equations implies

$$M_{12} = \frac{\mathfrak{r}_r}{\mathfrak{t}_r}, \qquad M_{22} = \frac{1}{\mathfrak{t}_r}. \tag{18}$$

Using these relations in the first equation in (17), we find

$$M_{11} = \mathfrak{t}_l - \frac{\mathfrak{r}_l\mathfrak{r}_r}{\mathfrak{t}_r}, \qquad M_{21} = -\frac{\mathfrak{r}_l}{\mathfrak{t}_r}. \tag{19}$$

In view of (18) and (19),

$$\mathbf{M} = \frac{1}{\mathfrak{t}_r}\begin{bmatrix}\mathfrak{t}_l\mathfrak{t}_r - \mathfrak{r}_l\mathfrak{r}_r & \mathfrak{r}_r\\ -\mathfrak{r}_l & 1\end{bmatrix}. \tag{20}$$

In particular,

$$\det\mathbf{M} = \frac{\mathfrak{t}_l}{\mathfrak{t}_r}. \tag{21}$$

We can also solve (18) and (19) for the reflection and transmission amplitudes in terms of M_{ij}. The result is

$$\mathfrak{r}_l = -\frac{M_{21}}{M_{22}}, \qquad \mathfrak{t}_l = \frac{\det\mathbf{M}}{M_{22}}, \qquad \mathfrak{r}_r = \frac{M_{12}}{M_{22}}, \qquad \mathfrak{t}_r = \frac{1}{M_{22}}. \tag{22}$$

Equations (20) and (22) show that *the knowledge of the transfer matrix is equivalent to solving the scattering problem*. It is also instructive to make the k-dependence of

the Jost solutions explicit and note that in light of (22) and (11) their asymptotic expression takes the form

$$\begin{aligned}
&\psi_\pm(k,x) \to e^{\pm ikx} && \text{for } x \to \pm\infty,\\
&\psi_+(k,x) \to \det\mathbf{M}(k)^{-1}\left[M_{22}(k)\,e^{ikx} - M_{21}(k)\,e^{-ikx}\right] && \text{for } x \to -\infty,\\
&\psi_-(k,x) \to M_{12}(k)\,e^{ikx} + M_{22}(k)\,e^{-ikx} && \text{for } x \to +\infty.
\end{aligned} \tag{23}$$

These relations together with the assumption that $\det\mathbf{M}(k) \neq 0$ show that *as functions of k the entries of the transfer matrix, $M_{ij}(k)$, have the same analytic properties as the Jost solutions $\psi_\pm(k,x)$.*

A simple consequence of (21) is that $\det\mathbf{M}$ is a measure of the violation of reciprocity in transmission; *a scattering system has reciprocal transmission if and only if* $\det\mathbf{M}(k) = 1$ *for all* $k \in \mathbb{R}^+$.

An example of a scattering system that has nonreciprocal transmission is a single-center point interaction (7) that is defined by a matching matrix $\mathbf{B}_1$ with $\det\mathbf{B}_1 \neq 1$, [41]. To see this, we set $n = 1$ and drop the subscript 1 in c_1 and $\mathbf{B}_1$ in (7). Clearly for $x \neq c$, every solution of (7) has the form

$$\psi(x) = A_\pm(k)e^{ikx} + B_\pm(k)e^{-ikx} \quad \text{for} \quad \pm(x-c) > 0. \tag{24}$$

We can use this expression to show that

$$\begin{bmatrix} \psi(c^\pm) \\ \psi'(c^\pm) \end{bmatrix} = \mathbf{N}_c \begin{bmatrix} A_\pm \\ B_\pm \end{bmatrix}, \tag{25}$$

where

$$\mathbf{N}_c(k) := \begin{bmatrix} e^{ick} & e^{-ick} \\ ike^{ick} & -ike^{-ick} \end{bmatrix}. \tag{26}$$

If we substitute (26) in (7), we can relate $A_+(k)$ and $B_+(k)$ to $A_-(k)$ and $B_-(k)$. This gives (14) with the following formula for the transfer matrix of the system.

$$\mathbf{M} = \mathbf{N}_c^{-1}\mathbf{B}\,\mathbf{N}_c. \tag{27}$$

In particular $\det\mathbf{M} = \det\mathbf{B}$. Therefore, single-center point interactions that satisfy $\det\mathbf{B} \neq 1$ violate reciprocity in transmission. These are called *anomalous point interactions* in [41], because they cannot be viewed as singular limits of sequences of scattering potentials.

Next, consider a situation that the solutions $\psi(x)$ of our linear wave equation have also the form of a plane wave in a closed interval, $[x_1, x_1+\epsilon]$, where $x_1 \in \mathbb{R}$ and $\epsilon \in \mathbb{R}^+$, i.e., there are coefficient functions $A_1(k)$ and $B_1(k)$ such that for all $x \in [x_1, x_1+\epsilon]$,

$$\psi(x) = A_1(k)e^{ikx} + B_1(k)e^{-ikx}. \tag{28}$$

In the limit $\epsilon \to 0$ this is certainly true for any x_1, because we can satisfy (28) for $x \to x_1$ by setting

$$A_1(k) = \frac{e^{-ikx}}{2}\left[\psi(x_1) + \frac{\psi'(x_1)}{ik}\right], \quad B_1(k) = \frac{e^{ikx}}{2}\left[\psi(x_1) - \frac{\psi'(x_1)}{ik}\right]. \tag{29}$$

We can use x_1 to disect the original scattering problem into two pieces. First, we consider the case where $\psi(x)$ solves the given wave equation for all $x < x_1$ and takes the form (28) for $x \geq x_1$. Then the choice (29) for $A_1(k)$ and $B_1(k)$ ensures the continuity and differentiability of the resulting wave function, namely

$$\psi_1(x) := \begin{cases} \psi(x) & \text{for } x \leq x_1, \\ A_1(k)e^{ikx} + B_1(k)e^{-ikx} & \text{for } x > x_1, \end{cases} \tag{30}$$

at $x = x_1$. We can therefore view $\psi_1(x)$ as the general solution of the wave equation with the interaction terms missing for $x > x_1$. Similarly, we introduce

$$\psi_2(x) := \begin{cases} A_1(k)e^{ikx} + B_1(k)e^{-ikx} & \text{for } x < x_1, \\ \psi(x) & \text{for } x \geq x_1, \end{cases} \tag{31}$$

and identify it with the general solution of the wave equation with the interaction terms missing for $x < x_1$. According to (1), (30), and (31),

$$\psi_1(x) \to \begin{cases} A_-(k)e^{ikx} + B_-(k)e^{-ikx} & \text{for } x \to -\infty, \\ A_1(k)e^{ikx} + B_1(k)e^{-ikx} & \text{for } x \to +\infty, \end{cases} \tag{32}$$

$$\psi_2(x) \to \begin{cases} A_1(k)e^{ikx} + B_1(k)e^{-ikx} & \text{for } x \to -\infty, \\ A_+(k)e^{ikx} + B_+(k)e^{-ikx} & \text{for } x \to +\infty. \end{cases} \tag{33}$$

We can use these relations together with the definition of the transfer matrix to introduce the transfer matrices $\mathbf{M}_j$ for $\psi_j(x)$. These fulfil

$$\mathbf{M}_1\begin{bmatrix} A_- \\ B_- \end{bmatrix} = \begin{bmatrix} A_1 \\ B_1 \end{bmatrix}, \qquad \mathbf{M}_2\begin{bmatrix} A_1 \\ B_1 \end{bmatrix} = \begin{bmatrix} A_+ \\ B_+ \end{bmatrix}. \tag{34}$$

Comparing these equations with (14), we see that the transfer matrix of the original wave equation is given by

$$\mathbf{M} = \mathbf{M}_2\mathbf{M}_1. \tag{35}$$

Now, consider dividing the set of real numbers into $n + 1$ intervals:

$$I_1 := (-\infty, a_1], \quad I_2 := [a_1, a_2], \quad I_3 := [a_2, a_3], \quad \cdots, \quad I_n := [a_{n-1}, a_n],$$
$$I_{n+1} := [a_n, \infty),$$

and let $\mathbf{M}_j$ be the transfer matrix for the scattering of a scalar wave with interactions confined to I_j. Then a repeated use of the argument leading to (35) shows that the transfer matrix for the original scattering problem is given by

$$\mathbf{M} = \mathbf{M}_{n+1}\mathbf{M}_n\mathbf{M}_{n-1}\cdots\mathbf{M}_1. \tag{36}$$

This property, which is known as the *composition rule for the transfer matrices*, allows for reducing the scattering problem with interactions taking place in an arbitrary region of space to simpler scattering problems where the interaction is confined to certain intervals.

For example, if the interaction has a finite range, i.e., it seizes to exist outside an interval $[a, b]$, we can set

$$a_j := a + \frac{(j-1)(b-a)}{n} \quad \text{for} \quad j = 1, 2, \cdots, n.$$

In this way, by taking large values for n we can reduce the initial scattering problem to those whose solution requires solving the wave equation in small intervals. If the interaction is a smooth function of space, we can approximate it by a constant in each of these intervals. This in turn simplifies the calculation of $\mathbf{M}_j$. We can use the result of this calculation together with (36) to find an approximate expression for $\mathbf{M}$. Aside from the technical problems of multiplying a large number of 2×2 matrices, this provides a simple approach for the solution of the scattering problem for finite-range linear interactions.

We can easily implement this procedure to solve the scattering problem for a multi-center point interaction (7). To do this we label the centers of the point interaction so that $c_1 < c_2 < \cdots < c_n$ and compute the transfer matrix for single-center point interactions associated with c_j. As we explained above this has the form

$$\mathbf{M}_j = \mathbf{N}_j^{-1}\mathbf{B}_j\mathbf{N}_j, \tag{37}$$

where $\mathbf{N}_j$ is given by the right-hand side of (26) with c changed to c_j. We can then determine the transfer matrix of the multi-center point interaction by invoking the composition rule (36). The result is

$$\mathbf{M} = \mathbf{N}_n^{-1}\mathbf{B}_n\mathbf{N}_n\mathbf{N}_{n-1}^{-1}\mathbf{B}_{n-1}\mathbf{N}_{n-1}\cdots\mathbf{N}_1^{-1}\mathbf{B}_1\mathbf{N}_1. \tag{38}$$

In particular, we find that

$$\det\mathbf{M} = \det\mathbf{B}_1 \det\mathbf{B}_2 \cdots \det\mathbf{B}_n. \tag{39}$$

Combing this equation with (21), we infer that *a multi-center point interaction violates reciprocity in transmission if and only if it consists of an odd number of anomalous single-center point interactions*.

Next, consider a multi-delta-function potential

$$v(x) = \epsilon \sum_{j=1}^{n} \mathfrak{z}_j \delta(x - c_j), \tag{40}$$

where ϵ is a nonzero real parameter and $\mathfrak{z}_j$ are possibly complex coupling constants. We can identify this with the multi-center point interaction with matching matrices

$$\mathbf{B}_j = \begin{bmatrix} 1 & 0 \\ \epsilon\, \mathfrak{z}_j & 1 \end{bmatrix}. \tag{41}$$

Substituting this relation in (38) we find the transfer matrix $\mathbf{M}$ for (40). This has a unit determinant, because $\det \mathbf{B}_j = 1$ and $\mathbf{M}$ satisfies (39).

It is not difficult to see that the transfer matrix $\mathbf{M}$ of the multi-delta-function potential (40) and hence its entries are polynomials of degree at most n in the parameter ϵ. In view of (23), and the fact that $\det \mathbf{M} = 1$, this implies that the same is true of the Jost solutions of the Schrödinger equation (2) for this potential. This observation shows that if we treat ϵ as a perturbation parameter and perform an n-th order perturbative calculation of the Jost solutions, we obtain their exact expression. In view of (11), this allows for determining the reflection and transmission amplitudes of (40). We therefore have the following result.

Theorem 1 *The n-th order perturbation theory gives the exact solution of the scattering problem for multi-delta-function potentials with n centers.*

In fact, a direct analysis shows that n-th order perturbation theory gives the exact solution of the Schrödinger equation (2) for multi-delta-function potentials (40), [54].

3 Scattering Matrix

By definition, the scattering operator, which is also known as the scattering matrix, maps the waves traveling toward the interaction region (incoming waves) to those traveling away from it (outgoing waves). In one dimension, the boundary conditions (1) at spatial infinities show that the incoming waves have the asymptotic form $A_-(k)e^{ikx}$ (respectively $B_-(k)e^{-ikx}$), if their source is located at $x = -\infty$ (respectively $x = +\infty$), and the outgoing waves tend to B_+e^{-ikx} as $x \to -\infty$ and $A_+(k)e^{ikx}$ as $x \to +\infty$. In light of these observations, we can quantify the scattering operator by a 2×2 matrix $\mathbf{S}(k)$ that connects $A_-(k)$ and $B_+(k)$ to $A_+(k)$ and $B_-(k)$. Clearly there are four different ways of doing so, namely

$$\begin{aligned}
&\mathbf{S}_1\begin{bmatrix}A_-\\ B_+\end{bmatrix}=\begin{bmatrix}A_+\\ B_-\end{bmatrix}, \qquad \mathbf{S}_2\begin{bmatrix}A_-\\ B_+\end{bmatrix}=\begin{bmatrix}B_-\\ A_+\end{bmatrix},\\
&\mathbf{S}_3\begin{bmatrix}B_+\\ A_-\end{bmatrix}=\begin{bmatrix}A_+\\ B_-\end{bmatrix}, \qquad \mathbf{S}_4\begin{bmatrix}B_+\\ A_-\end{bmatrix}=\begin{bmatrix}B_-\\ A_+\end{bmatrix}.
\end{aligned} \tag{42}$$

These correspond to various conventions for defining the **S**-matrix in one dimension. It is easy to see that

$$\mathbf{S}_2=\boldsymbol{\sigma}_1\mathbf{S}_1, \qquad \mathbf{S}_3=\mathbf{S}_1\boldsymbol{\sigma}_1, \qquad \mathbf{S}_4=\boldsymbol{\sigma}_1\mathbf{S}_1\boldsymbol{\sigma}_1, \tag{43}$$

where $\boldsymbol{\sigma}_1$ is the first Pauli matrix,

$$\boldsymbol{\sigma}_1:=\begin{bmatrix}0&1\\ 1&0\end{bmatrix}.$$

Next, let us express the entries of $\mathbf{S}_1$ in terms of the reflection and transmission amplitudes. To do this, we implement the first equation in (42) for the Jost solutions $\psi_\pm(x)$. For $\psi(x)=\psi_+(x)$, $A_\pm$ and $B_\pm$ are given by (15). Substituting these in the first equation in (42) gives

$$\mathbf{S}_1\begin{bmatrix}1\\ 0\end{bmatrix}=\begin{bmatrix}\mathfrak{t}_l\\ \mathfrak{r}_l\end{bmatrix}. \tag{44}$$

Similarly for $\psi(x)=\psi_-(x)$, we use (15) to obtain

$$\mathbf{S}_1\begin{bmatrix}0\\ 1\end{bmatrix}=\begin{bmatrix}\mathfrak{r}_r\\ \mathfrak{t}_r\end{bmatrix}. \tag{45}$$

In view of Eqs. (44) and (45),

$$\mathbf{S}_1=\begin{bmatrix}\mathfrak{t}_l&\mathfrak{r}_r\\ \mathfrak{r}_l&\mathfrak{t}_r\end{bmatrix}. \tag{46}$$

This relation together with (43) imply

$$\mathbf{S}_2=\begin{bmatrix}\mathfrak{r}_l&\mathfrak{t}_r\\ \mathfrak{t}_l&\mathfrak{r}_r\end{bmatrix}, \qquad \mathbf{S}_3=\begin{bmatrix}\mathfrak{r}_r&\mathfrak{t}_l\\ \mathfrak{t}_r&\mathfrak{r}_l\end{bmatrix}, \qquad \mathbf{S}_4=\begin{bmatrix}\mathfrak{t}_r&\mathfrak{r}_l\\ \mathfrak{r}_r&\mathfrak{t}_l\end{bmatrix}. \tag{47}$$

According to Eqs. (46) and (47), we can use any of $\mathbf{S}_1,\mathbf{S}_2,\mathbf{S}_3$, and $\mathbf{S}_4$ to encode the information about the scattering properties of the system. They are therefore physically equivalent. We adopt the convention of identifying the **S**-matrix with $\mathbf{S}_1$, i.e., set

$$\mathbf{S} := \begin{bmatrix} \mathfrak{t}_l & \mathfrak{r}_r \\ \mathfrak{r}_l & \mathfrak{t}_r \end{bmatrix}. \tag{48}$$

This choice has the appealing property of reducing to the 2×2 identity matrix $\mathbf{I}$ in the absence of interactions.

Eigenvalues of the scattering matrix turn out to contain some useful information about the scattering properties of the system. In view of (48), they have the form:

$$\mathfrak{s}_\pm = \frac{\mathfrak{t}_l + \mathfrak{t}_r}{2} \pm \sqrt{\left(\frac{\mathfrak{t}_l - \mathfrak{t}_r}{2}\right)^2 + \mathfrak{r}_l \mathfrak{r}_r}. \tag{49}$$

In particular, whenever $\mathfrak{t}_l = \mathfrak{t}_r =: \mathfrak{t}$,

$$\mathfrak{s}_\pm = \mathfrak{t} \pm \sqrt{\mathfrak{r}_l \mathfrak{r}_r}. \tag{50}$$

Both the transfer and the **S**-matrix contain complete information about the scattering data, but in contrast to the transfer matrix the **S**-matrix does not obey a useful composition rule. An advantage of the **S**-matrix is the simplicity of its higher-dimensional, relativistic, and field theoretical generalizations [76].[4]

4 Potential Scattering, Reciprocity Theorem, and Invisibility

Consider the time-independent Schrödinger equation (2) for a scattering potential $v(x)$ which admits Jost solutions $\psi_\pm$ and defines a valid scattering problem. Being solutions of a second order linear homogeneous differential equation, $\psi_\pm$ are linearly independent if and only if their Wronskian, $W(x) := \psi_-(x)\psi'_+(x) - \psi_+(x)\psi'_-(x)$, does not vanish at some $x \in \mathbb{R}$, [5]. In fact, because the Schrödinger equation (2) does not involve the first derivative of ψ, $W(x)$ is a constant.[5] We can determine this constant using the asymptotic expression (11) for the $\psi_\pm(x)$. Doing this for $x \to -\infty$ and $x \to +\infty$, we respectively find $W(x) = 2ik/\mathfrak{t}_l(k)$ and $W(x) = 2ik/\mathfrak{t}_r(k)$. This proves the following reciprocity theorem.

Theorem 2 (Reciprocity in Transmission) *The left and right transmission amplitudes of every real or complex scattering potential coincide, i.e.,*

$$\mathfrak{t}_l(k) = \mathfrak{t}_r(k). \tag{51}$$

[4] A genuine multidimensional generalization of the transfer matrix has been recently proposed in [31].

[5] This can be easily checked by differentiating $W(x)$ and using (2) to show that $W'(x) = 0$.

In the following we use $\mathfrak{t}(k)$ for the common value of $\mathfrak{t}_l(k)$ and $\mathfrak{t}_r(k)$ whenever a scattering system has reciprocal transmission.

In view of Eqs. (20), (21), (22), (48), and (51), the transfer and scattering matrices and the scattering data associated with real or complex scattering potentials satisfy:

$$\mathbf{M}=\frac{1}{\mathfrak{t}}\begin{bmatrix}\mathfrak{t}^2-\mathfrak{r}_l\mathfrak{r}_r & \mathfrak{r}_r\\ -\mathfrak{r}_l & 1\end{bmatrix},\qquad \det\mathbf{M}=1,\qquad \mathbf{S}=\begin{bmatrix}\mathfrak{t} & \mathfrak{r}_r\\ \mathfrak{r}_l & \mathfrak{t}\end{bmatrix},\tag{52}$$

$$\mathfrak{r}_l=-\frac{M_{21}}{M_{22}},\qquad \mathfrak{r}_r=\frac{M_{12}}{M_{22}},\qquad \mathfrak{t}=\frac{1}{M_{22}}.\tag{53}$$

Another consequence of (51) is that the Wronskian of the Jost solutions take the form

$$W(x)=\frac{2ik}{\mathfrak{t}(k)}.\tag{54}$$

This is a number depending on the value of k. In particular, for $k\in\mathbb{R}^+$ it cannot diverge. This proves the following theorem.

Theorem 3 *Let $v(x)$ be a real or complex scattering potential. Then its transmission amplitude does not vanish for any wavenumber, i.e.,*

$$\mathfrak{t}(k)\neq 0\quad\text{for}\quad k\in\mathbb{R}^+.\tag{55}$$

This theorem shows that real and complex scattering potentials can never serve as a perfect absorber. According to Theorem 2 they cannot even serve as an approximate one-way filter.

Next, we examine the following simple example:

$$v(x)=\mathfrak{z}\chi_{[0,L]}(x)=\begin{cases}\mathfrak{z}\ \text{for}\ x\in[0,L],\\ 0\ \text{for}\ x\notin[0,L],\end{cases}\tag{56}$$

where $\mathfrak{z}$ and L are nonzero complex and real parameters. This is a piecewise constant finite-range potential with support $[0,L]$, which we can identify with a rectangular barrier potential of a possibly complex height $\mathfrak{z}$.

We can easily solve the Schrödinger equation (2) for the barrier potential (56). Its general solution has the form

$$\psi(x)=\begin{cases}A_-(k)e^{ikx}+B_-(k)e^{-ikx} & \text{for}\quad x<0,\\ A_0(k)e^{ik\mathfrak{n}x}+B_0(k)e^{-ik\mathfrak{n}x} & \text{for}\ x\in[0,L],\\ A_+(k)e^{ikx}+B_+(k)e^{-ikx} & \text{for}\quad x\geq L,\end{cases}\tag{57}$$

where $A_j(k)$ and $B_j(k)$, with $j = 0, \pm$, are complex-valued coefficient functions,

$$\mathfrak{n} := \sqrt{1 - \frac{\mathfrak{z}}{k^2}}, \tag{58}$$

and for every complex number w we use $\sqrt{w}$ to label the principal value of $w^{1/2}$, i.e., $\sqrt{w} = \sqrt{|w|}e^{i\varphi}$ with $\varphi \in [0, \pi)$. By demanding ψ to be continuous and differentiable at $x = L$ and $x = 0$, we can respectively express A_+ and B_+ in terms of A_0 and B_0, and A_0 and B_0 in terms of A_- and B_-. This in turn allows us to relate A_+ and B_+ to A_- and B_-. We can write the resulting equations in the form (14) with the transfer matrix given by

$$\mathbf{M}(k) = \begin{bmatrix} [\cos(kL\mathfrak{n}) + i\mathfrak{n}_+ \sin(kL\mathfrak{n})]e^{-ikL} & i\mathfrak{n}_- \sin(kL\mathfrak{n})e^{-ikL} \\ -i\mathfrak{n}_- \sin(kL\mathfrak{n})e^{ikL} & [\cos(kL\mathfrak{n}) - i\mathfrak{n}_+ \sin(kL\mathfrak{n})]e^{ikL} \end{bmatrix}, \tag{59}$$

and $\mathfrak{n}_\pm := (\mathfrak{n} \pm \mathfrak{n}^{-1})/2$.

In view of (53), we can use (59) to read off the expression for the reflection and transmission amplitudes of the barrier potential (56). These have the form:

$$\mathfrak{r}_l(k) = \frac{i\mathfrak{n}_- \tan(kL\mathfrak{n})}{1 - i\mathfrak{n}_+ \tan(kL\mathfrak{n})}, \tag{60}$$

$$\mathfrak{r}_r(k) = \frac{i\mathfrak{n}_- \tan(kL\mathfrak{n})e^{-2ikL}}{1 - i\mathfrak{n}_+ \tan(kL\mathfrak{n})}, \tag{61}$$

$$\mathfrak{t}(k) = \frac{e^{-ikL}}{\cos(kL\mathfrak{n}) - i\mathfrak{n}_+ \sin(kL\mathfrak{n})}. \tag{62}$$

Clearly, $\mathfrak{t}(k) \neq 0$ for all $k \in \mathbb{R}^+$. We can check that indeed $\det \mathbf{M}(k) = 1$, and evaluate the $\mathbf{S}$-matrix and its eigenvalues. In light of (50) the latter are given by

$$\mathfrak{s}_\pm(k) = \left[\frac{1 \pm i\mathfrak{n}_- \tan(kL\mathfrak{n})}{1 - i\mathfrak{n}_+ \tan(kL\mathfrak{n})}\right] e^{-ikL}. \tag{63}$$

According to (60) the barrier potential (56) is left-reflectionless if and only if $\mathfrak{n}$ is real and $k = k_m := \pi m/L\mathfrak{n}$ for a positive integer m.[6] In this case it is also right-reflectionless, but not in general transparent. It is easy to show that for these values of the wavenumber, $\mathfrak{t}(k) = e^{-im\pi(\mathfrak{n}^{-1}+1)}$. This equals unity, i.e., the potential is transparent and hence bidirectionally invisible if and only if there is an integer q such that $\mathfrak{n} = (2q/m - 1)^{-1}$. It is easy to see that this is equivalent to demanding that

[6] Equation (58) implies that $k_m = \sqrt{(\pi m/L)^2 + \mathfrak{z}}$. This in turn means that for $\mathfrak{z} > 0$, m can be any positive integer, and for $\mathfrak{z} < 0$, $m > L\sqrt{-\mathfrak{z}}/\pi$.

$$\mathfrak{z} = \frac{4\pi^2 q(q-m)}{L^2}, \qquad k = \frac{2q-m}{L}.$$

Because $k > 0$, the latter relation implies that $2q > m$.

The entries of the transfer matrix for the barrier potential (56) are smooth functions of the wavenumber k. In fact, we can analytically continue them to the entire complex k-plane. This turns out to be a common feature of all finite-range potentials. To see this first we note that if a potential $v(x)$ decays exponentially as $x \to \pm\infty$, i.e., there are positive numbers $\mu_\pm$ satisfying (13), then the Jost solutions are holomorphic (complex analytic) functions in the strip [3]:

$$\mathcal{S}_{\mu_\pm} := \{k \in \mathbb{C} \mid -\mu_- < \mathrm{Im}(k) < \mu_+\}. \tag{64}$$

In light of (23) and the fact that $\det \mathbf{M} = 1$, this implies that the same holds for the entries of the transfer matrix. We state this result as a theorem:

Theorem 4 *Let $v(x)$ be a real or complex potential satisfying (13) for some $\mu_\pm > 0$. Then the entries $M_{ij}(k)$ of its transfer matrix are holomorphic functions in the strip (64).*

A basic result of complex analysis is that a nonzero holomorphic function can only vanish at a discrete set of isolated points. In view of Theorem 4 this applies to the entries of the transfer matrix of exponentially decaying potentials. In particular, for each choice of i and j in $\{1, 2\}$, either $M_{ij}(k) = 0$ for all $k \in \mathcal{S}_{\mu_\pm}$ or there is a (possibly empty) discrete set of isolated values of $k \in \mathcal{S}_{\mu_\pm}$ at which $M_{ij}(k)$ vanishes. This is particularly important, because $\mathcal{S}_{\mu_\pm}$ contains the positive real axis where the physical wavenumbers reside.

According to (53), the zeros of $M_{12}(k)$ (respectively $M_{21}(k)$) that are located on the positive real axis are the wavenumbers k_0 at which the right (respectively left) reflection amplitude of the potential $v(x)$ vanishes, i.e., $v(x)$ is right- (respectively left-) reflectionless at k_0. Similarly, if $M_{22}(k_0) = 1$, then $\mathfrak{t}(k_0) = 1$, and $v(x)$ is transparent at k_0. Therefore real and positive zeros of $M_{12}(k)$, $M_{21}(k)$, and $M_{22}(k) - 1$ are the wavenumbers at which $v(x)$ is right-reflectionless, left-reflectionless, and transparent. In particular, equations

$$M_{12}(k) = M_{22}(k) - 1 = 0, \tag{65}$$

$$M_{21}(k) = M_{22}(k) - 1 = 0, \tag{66}$$

respectively characterize the invisibility of the potential from the right and left. These results are clearly valid for any scattering system whose scattering features can be described using a transfer matrix.

The following no-go theorem is a simple consequence of Eqs. (53) and the above-mentioned property of the zeros of holomorphic functions.

Theorem 5 *If the entries $M_{ij}(k)$ of the transfer matrix for a scattering system are nonzero functions that are holomorphic on the positive real axis in the complex k-*

plane, then the system cannot display broadband reflectionlessness, transparency, or invisibility from either direction.

According to Theorem 4, the conclusion of this theorem applies to exponentially decaying and finite-range potentials.

The above analysis does not exclude the existence of exponentially decaying potentials that are unidirectionally or bidirectionally reflectionless for all $k \in \mathbb{R}^+$ (fullband reflectionlessness). Such potentials were known to exist since the 1930s. The principal example is the Pöschl-Teller potential:

$$v(x) = -\frac{\zeta}{\cosh(\alpha x)},$$

where ζ and α are positive real parameters. It turns out that the scattering problem for this potential admits an exact solution, and that for integer values of ζ/α^2 it is bidirectionally reflectionless for all $k \in \mathbb{R}^+$, [10]. The Pöschl-Teller potential is a member of an infinite class of real, attractive (negative), exponentially decaying potentials with this property. These were initially obtained in the 1950s as an application of the methods of inverse scattering theory [20]. Their much less-known complex analogs were constructed in the 1990s, [74].[7]

The construction of scattering potentials that are unidirectionally invisible in the entire spectral band is a much more recent development [16, 30]. Before making specific comments about these potentials, we wish to address the problem of the existence of exponentially decaying and finite-range potentials that are unidirectionally reflectionless, transparent, or invisible in the whole spectral band. To do this, first we examine the structure of the transfer matrix $\mathbf{M}(k)$ for negative values of k.

Consider a solution of the Schrödinger equation (2) for a scattering potential $v(x)$. In order to make the k-dependence of this solution explicit, we denote it by $\psi(k,x)$. In particular, we write (1) as

$$\psi(k,x) \to A_+(k)e^{ikx} + B_+(k)e^{-ikx} \qquad \text{for} \qquad x \to \pm\infty. \tag{67}$$

Because the Schrödinger equation (2) is invariant under $k \to -k$,

$$\check{\psi}(k,x) := \psi(-k,x) \tag{68}$$

is also a solution of (2). In view of the fact that $v(x)$ is a scattering potential, $\check{\psi}(k,x)$ must satisfy the asymptotic boundary conditions:

$$\check{\psi}(k,x) \to \check{A}_+(k)e^{-ikx} + \check{B}_+(k)e^{ikx} \qquad \text{for} \qquad x \to \pm\infty, \tag{69}$$

[7] Reflectionless potentials also arise as soliton solutions of nonlinear differential equations [24].

where $\breve{A}_\pm(k)$ and $\breve{B}_\pm(k)$ are some coefficient functions. We can use (67), (68), and (69) to show that for $k \in \mathbb{R}^-$,

$$\breve{A}_\pm(k) = B_\pm(-k), \qquad \breve{B}_\pm(k) = A_\pm(-k). \tag{70}$$

Now, suppose that we can analytically continue $\mathbf{M}(k)$ from $k \in \mathbb{R}^+$ to $k \in \mathbb{R}^-$. Then we can relate $\breve{A}_+(k)$ and $\breve{B}_+(k)$ to $\breve{A}_-(k)$ and $\breve{B}_-(k)$ using $\mathbf{M}(k)$ for $k \in \mathbb{R}^-$. This gives

$$\begin{bmatrix} \breve{A}_+(k) \\ \breve{B}_+(k) \end{bmatrix} = \mathbf{M}(k) \begin{bmatrix} \breve{A}_-(k) \\ \breve{B}_-(k) \end{bmatrix}. \tag{71}$$

Substituting (70) in this equation and using (14), we arrive at

$$\mathbf{M}(k) = \boldsymbol{\sigma}_1 \mathbf{M}(-k) \boldsymbol{\sigma}_1, \tag{72}$$

where $k \in \mathbb{R}^-$. Because this equation is invariant under $k \to -k$, it holds for all $k \in \mathbb{R} \setminus \{0\}$. In terms of the components of $\mathbf{M}(k)$, we can write (72) in the form:

$$M_{11}(-k) = M_{22}(k), \qquad M_{12}(-k) = M_{21}(k), \tag{73}$$

which again hold for all $k \in \mathbb{R} \setminus \{0\}$.

Equations (72) and (73) apply to any scattering system in which the wave equation involves even powers of k and have a transfer matrix that can be analytically continued from the positive to the negative real axis in the complex k-plane. For such systems, we can determine the reflection and transmission amplitudes for $k \in \mathbb{R}^-$, by inserting (73) in (22). This gives

$$\mathfrak{r}_l(-k) = -\frac{\mathfrak{r}_r(k)}{\mathfrak{D}(k)}, \quad \mathfrak{t}_l(-k) = \frac{\mathfrak{t}_l(k)}{\mathfrak{D}(k)}, \quad \mathfrak{r}_r(-k) = -\frac{\mathfrak{r}_l(k)}{\mathfrak{D}(k)}, \quad \mathfrak{t}_r(-k) = \frac{\mathfrak{t}_r(k)}{\mathfrak{D}(k)}, \tag{74}$$

where

$$\mathfrak{D}(k) := \frac{M_{11}(k)}{M_{22}(k)} = \mathfrak{t}_l(k)\mathfrak{t}_r(k) - \mathfrak{r}_l(k)\mathfrak{r}_r(k) = \det \mathbf{S}(k). \tag{75}$$

Again, because Eqs. (74) are invariant under $k \to -k$, they hold for all $k \in \mathbb{R} \setminus \{0\}$. A straightforward consequence of these equations is that if $\mathfrak{r}_{l/r}(k)$ (respectively $\mathfrak{t}_{l/r}(k)$) vanishes for all $k \in \mathbb{R}^+$, then it will also vanish for all $k \in \mathbb{R}^-$. It is important to note that this conclusion relies on the existence of the analytic continuation of $\mathbf{M}_{ij}(k)$ from $k \in \mathbb{R}^+$ to $k \in \mathbb{R}^-$. Certainly, this condition holds for finite-range and exponentially decaying potentials. This together with Theorem 5 prove the following result.

Theorem 6 *Scattering potentials with a finite range or an asymptotic exponential decay cannot display broadband unidirectional reflectionlessness, transparency, or invisibility.*

This theorem shows that as far as finite-range and exponentially decaying potentials are concerned, unidirectional reflectionlessness, transparency, and invisibility can only be achieved at a discrete set of isolated values of the wavenumber.

The principal example of a unidirectionally invisible finite-range potential is

$$v(x) = \begin{cases} \mathfrak{z}\, e^{iKx} & \text{for } x \in [-\frac{L}{2}, \frac{L}{2}], \\ 0 & \text{for } x \notin [-\frac{L}{2}, \frac{L}{2}], \end{cases} \tag{76}$$

where $\mathfrak{z}$, K, and L are nonzero real parameters, and $L > 0$, [13, 23, 25, 61]. This potential is unidirectionally invisible from the left for the wavenumber $k = K/2$, if $K = 2\pi/L$ and $K^2\mathfrak{z} \ll 1$. It belongs to the class of locally periodic finite-range potentials of the form

$$v(x) = \begin{cases} f(x) & \text{for } x \in [-\frac{L}{2}, \frac{L}{2}], \\ 0 & \text{for } x \notin [-\frac{L}{2}, \frac{L}{2}], \end{cases} \tag{77}$$

where

$$f(x) := \sum_{n=-\infty}^{\infty} \mathfrak{z}_n e^{iK_n x}, \tag{78}$$

$\mathfrak{z}_n$ are complex coefficients, and $K_n := 2\pi n/L$. The following theorem, which is proven in Ref. [46], reveals a remarkable property of these potentials.

Theorem 7 *Let $v(x)$ be a potential of the form (77) and suppose that we are interested in the scattering of waves of wavenumber k satisfying $|\mathfrak{z}_n|/k^2 \ll 1$, so that the first Born approximation is valid. If $\mathfrak{z}_n = 0$ for all $n \leq 0$, $v(x)$ is unidirectionally left-invisible for all $k = K_n/2 = \pi n/L$.*[8]

Now, consider taking $L \to \infty$. Then (77) becomes $v(x) = f(x)$, the Fourier series in (78) turns into a Fourier integral, the role of $\mathfrak{z}_n$ is played by the Fourier transform of $v(x)$, i.e., $\tilde{v}(\mathfrak{K}) := \int_{-\infty}^{\infty} e^{-i\mathfrak{K}x} v(x)dx$, and Theorem 7 states that *if the first Born approximation is reliable, then $v(x)$ is unidirectionally left-invisible for all $k \in \mathbb{R}^+$ provided that $\tilde{v}(\mathfrak{K}) = 0$ for $\mathfrak{K} \leq 0$.* A highly nontrivial observation is that the same conclusion may be reached without assuming the validity of the first Born approximation [16, 30]. In other words the following theorem on broadband invisibility holds.

[8] This means that $v(x)$ is unidirectionally left-invisible for $k = K_n/2 = \pi n/L$ provided that we can neglect terms of order $(\mathfrak{z}_n/k^2)^2$ in the calculation of the reflection and transmission amplitudes.

Theorem 8 *A scattering potential $v(x)$ is unidirectionally left-invisible for all wavenumbers $k \in \mathbb{R}^+$, if its Fourier transform $\tilde{v}(\mathfrak{K})$ vanishes for all $\mathfrak{K} \leq 0$.*

Because the hypothesis of this theorem is equivalent to the condition that the real and imaginary part of $v(x)$ are connected by the spatial Kramers-Kronig relations, these potentials are sometimes called Kramers-Kronig potentials.[9] It is well-known that they have a power-law decay at spatial infinities.[10]

The unidirectional invisibility of the potential (76) for $k = K/2 = \pi/L$ is a perturbative result [46]; it is violated for sufficiently large values of $|\mathfrak{z}|$, [18, 29]. This potential does however support exact (nonperturbative) unidirectional invisibility for particular values of $\mathfrak{z}$, [51]. Another example of a finite-range potential with exact unidirectional invisibility is (77) with

$$f(x) := \frac{-2\alpha K^2(3 - 2e^{iKx})}{e^{2iKx} + \alpha(1 - e^{iKx})^2},$$

where α and K are real parameters. It turns out that this potential is unidirectionally right-invisible for $k = K/2 = \pi n/L$ with n being any positive integer provided that $\alpha > -1/4$, [47]. The simplest scattering potential supporting exact unidirectional invisibility are barrier potentials of the form $v(x) = \mathfrak{z}_1\chi_{[-a_1,0)} + \mathfrak{z}_2\chi_{[0,a_2]}$ where $\mathfrak{z}_j$ and a_j are respectively complex and positive real parameters [43]. See also [67].

5 Spectral Singularities, Resonances, and Bound States

In Sect. 4 we show that the Wronskian of the Jost solutions $\psi_\pm$ of the Schrödinger equation for a scattering potential $v(x)$ is given by

$$W(x) = \frac{2ik}{\mathfrak{t}(k)} = 2ikM_{22}(k). \tag{79}$$

This in particular implies that $\psi_\pm$ are linearly dependent solutions of the Schrödinger equation (2) whenever k is a real and positive zero of $M_{22}(k)$. This represents a physical wavenumber k at which $\mathfrak{t}(k)$ blows up. The corresponding value of the energy, $E := k^2$, which belongs to the continuous spectrum of the Schrödinger operator, $-\frac{d^2}{dx^2} + v(x)$, is called a *spectral singularity*[11] of the potential [38].

[9] For a review of basic properties of these potentials, see [15].

[10] This explains why Theorems 6 and 8 do not conflict.

[11] The notion of a spectral singularity was originally introduced in [60] for Schrödinger operators in the half-line. It was subsequently generalized to the case of full-line in [21]. The term "spectral singularity" was originally used to refer to this notion in [69]. For a readable account of basic mathematical facts about spectral singularities and further references, see [14].

If k_0^2 is a spectral singularity, $M_{22}(k_0) = 0$, but because $\det \mathbf{M}(k_0) = 1$, neither of $M_{12}(k_0)$ and $M_{21}(k_0)$ can vanish. In light of (53), this implies that similarly to the transmission amplitude $\mathfrak{t}(k)$, the reflection amplitudes $\mathfrak{r}_{l/r}(k)$ blow up at $k = k_0$. Furthermore, (23) shows that whenever $M_{22}(k) = 0$,

$$\psi_+(x) = -\frac{M_{21}(k)}{M_{12}(k)}\,\psi_-(x) \to \begin{cases} -M_{21}(k)e^{-ikx} & \text{for } x \to -\infty, \\ e^{ikx} & \text{for } x \to +\infty. \end{cases} \tag{80}$$

Application of this relation for $k = k_0$ shows that at a spectral singularity Jost solutions $\psi_\pm(x)$ are scattering solutions of the Schrödinger equation that satisfy outgoing asymptotic boundary conditions. These are also known as the Seigert boundary conditions [70] which provide a standard description of resonances.

Consider a solution $\psi(x)$ of the time-independent Schrödinger equation (2) for a general complex value of the energy k^2 and suppose that it satisfies the outgoing asymptotic boundary conditions:

$$\psi(x) \to N_\pm(k)\, e^{\pm ikx} \quad \text{for } x \to \pm\infty, \tag{81}$$

where $N_\pm(k)$ are nonzero complex coefficients. $\psi(x)$ corresponds to a solution $\psi(x,t)$ of the time-dependent Schrödinger equation, $i\partial_t\psi(x,t) = -\partial_x^2\psi(x,t) + v(x)\psi(x,t)$, namely

$$\psi(x,t) := e^{-ik^2t}\psi(x) = e^{-\Gamma t}e^{-iEt}\psi(x), \tag{82}$$

where

$$E := \mathrm{Re}(k)^2 - \mathrm{Im}(k)^2, \qquad \Gamma := -2\mathrm{Re}(k)\mathrm{Im}(k). \tag{83}$$

If $\Gamma > 0$, $\psi(x,t)$ decays exponentially as $t \to \infty$. In this case, we identify $\psi(x,t)$ with a *resonance*. The quantity Γ which determines its decay rate is called the *width* of the resonance. If $\Gamma < 0$, $\psi(x,t)$ grows exponentially as $t \to \infty$, and we call it an *antiresonance*. It is not difficult to see that resonances and antiresonances are also zeros of $M_{22}(k)$. But the corresponding value of k^2 lie in the lower and upper complex energy half-planes,

$$\mathcal{E}_{\text{lower}} := \{k^2 \in \mathbb{C} \mid \mathrm{Im}(k^2) < 0\}, \qquad \mathcal{E}_{\text{upper}} := \{k^2 \in \mathbb{C} \mid \mathrm{Im}(k^2) > 0\},$$

respectively.

The Jost solutions of the time-independent Schrödinger equation (2) that correspond to a spectral singularity satisfy the above description of a resonance except that for a spectral singularity k is real. This suggests identifying these solutions

with certain *zero-width resonances* [38].[12] Note that spectral singularities lie on the positive real axis in the complex energy plane:

$$\mathcal{E}_+ := \{k^2 \in \mathbb{C} \mid \mathrm{Re}(k^2) > 0 \text{ and } \mathrm{Im}(k^2) = 0\}. \tag{84}$$

There is another way in which we can have a real zero of $M_{22}(k)$ such that $\Gamma = 0$. This is when k is purely imaginary; i.e., $E = k^2 \in \mathbb{R}^-$. Let us set $k = i\sqrt{|E|}$. Then, according to (80), ψ_+ determines a solution of the time-independent Schrödinger equation that decays exponentially at spatial infinities. This solution is clearly square-integrable. Therefore its energy $E = k^2$, which is real and negative, belongs to the point spectrum of the Schrödinger operator $-\frac{d^2}{dx^2} + v(x)$; it is a real and negative eigenvalue of this operator that corresponds to a bound state of the potential $v(x)$. If k is a zero of $M_{22}(k)$ that lies in the upper-half k-plane, i.e., $\mathrm{Im}(k) > 0$, then $|\psi_+(x)|$ is again exponentially decaying as $x \to \pm\infty$. Therefore $\psi_+(x)$ is a square-integrable function and k^2 is a complex eigenvalue of $-\frac{d^2}{dx^2} + v(x)$.

Note that the above discussion of the interpretation of the zeros of $M_{22}(k)$ as spectral singularities, resonances, antiresonances, and eigenvalues of the Schrödinger operator $-\frac{d^2}{dx^2} + v(x)$ applies to any scattering potential. As shown in [21], in this case the Jost solutions $\psi_\pm$ and consequently the entries of the transfer matrix are continuous functions of k for $\mathrm{Im}(k) \geq 0$. They might not however be holomorphic in any region containing the real axis in the complex k-plane. If there is such a region in which $M_{22}(k)$ is a nonzero holomorphic function, then the zeros of $M_{22}(k)$ that lie in this region form a discrete isolated set of points. This in turn implies that one cannot have spectral singularities in an extended interval of real numbers other than the whole positive real axis. In particular we have the following result.

Theorem 9 *If $v(x)$ is a real or complex potential with a finite range or an asymptotic exponential decay, so that (13) holds for some $\mu_\pm \in \mathbb{R}^+$, then either its spectral singularities are isolated points of the positive real axis in the complex energy plane or cover the whole positive real axis.*

Next, we examine the behavior of the eigenvalues $\mathfrak{s}_\pm$ of the $\mathbf{S}$-matrix in the vicinity of a spectral singularity k_0^2. As $k \to k_0$, $\epsilon := M_{22}(k)$ tends to zero. Because the entries of the transfer matrix are continuous functions on the upper half-plane and $\mathrm{Im}(k_0) \geq 0$, none of them blow up at $k = k_0$. We also know that $\det \mathbf{M}(k) = 1$. In view of these observations and (50), we can show that the eigenvalues of the $\mathbf{S}$-matrix for a scattering potential satisfy

[12] Spectral singularities must be distinguished with the solutions of the time-independent Schrödinger equation that correspond to a bound state in the continuum [17, 72] for the following reasons: (1) They define scattering states that do not decay at spatial infinities. (2) They may exist for exponentially decaying and short-range potentials. (3) As we explain in Sect. 8, real potentials cannot have spectral singularities. None of these holds for bound states in the continuum.

$$\mathfrak{s}_\pm(k) \to \frac{1}{\epsilon} \pm \frac{1}{|\epsilon|} \mp \frac{\mathrm{sgn}(\epsilon) M_{11}(k_0)}{2} \qquad \text{for} \qquad k \to k_0. \tag{85}$$

This implies that as k^2 approaches a spectral singularity, one of the eigenvalues of $\mathbf{S}(k)$ diverges while the other attains a finite limit. More specifically we have the following result.

Theorem 10 *Let k_0^2 be a spectral singularity of a scattering potential $v(x)$. Then as $k \to k_0$ the eigenvalues (50) of the* **S***-matrix behave as follows. Either $\mathfrak{s}_-(k) \to -M_{11}(k_0)/2$ and $|\mathfrak{s}_+(k)| \to \infty$, or $|\mathfrak{s}_-(k)| \to \infty$ and $\mathfrak{s}_+(k) \to M_{11}(k_0)/2$.*

Now, suppose that $v(x)$ is a scattering potential such that $\det \mathbf{S}(k)$ is a bounded function of k. Then Theorem 10 implies that $M_{11}(k_0) = 0$ whenever k_0^2 is a spectral singularities of $v(k)$, i.e., k_0 is a common zero of $M_{11}(k)$ and $M_{22}(k)$. Spectral singularities satisfying this condition are said to be *self-dual* [42]. We study these in Sect. 9.

Let us examine the spectral singularities of a couple of exactly solvable potentials.

First, consider a delta-function potential with a complex coupling constant $\mathfrak{z}$, [37],

$$v(x) = \mathfrak{z}\, \delta(x). \tag{86}$$

We can determine its transfer matrix using (8), (26), and (27) with $c = 0$. This gives

$$\mathbf{M}(k) = \begin{bmatrix} 1 - i\mathfrak{z}/2k & -i\mathfrak{z}/2k \\ i\mathfrak{z}/2k & 1 + i\mathfrak{z}/2k \end{bmatrix}. \tag{87}$$

In view of this relation and (53),

$$\mathfrak{r}_l(k) = \mathfrak{r}_r(k) = \frac{-i\mathfrak{z}}{2k + i\mathfrak{z}}, \qquad\qquad \mathfrak{t}(k) = \frac{2k}{2k + i\mathfrak{z}}. \tag{88}$$

The following are consequences of the fact that $M_{22}(k)$ has a single zero, namely $k_0 = -i\mathfrak{z}/2$.

- The delta-function potential has a spectral singularity, if and only if $\mathfrak{z}$ is purely imaginary and $\mathrm{Im}(\mathfrak{z}) > 0$, i.e., $\mathfrak{z} = i\zeta$ for some $\zeta \in \mathbb{R}^+$. In this case, $k_0 = \zeta/2$, the spectral singularity has the value $k_0^2 = \zeta^2/4$, and

$$\psi_+(x) = e^{\pm i k_0 x} \qquad \text{for} \qquad \pm x \geq 0. \tag{89}$$

- It has a single resonance (respectively antiresonance) with a square-integrable position wave function $\psi(x)$ if and only if $\mathrm{Im}(\mathfrak{z}) > 0$ (respectively < 0) and $\mathrm{Re}(\mathfrak{z}) < 0$. In this case $\psi(x)$ is a constant multiple of the right-hand side of (89) with $k_0 = [\mathrm{Im}(\mathfrak{z}) - i\mathrm{Re}(\mathfrak{z})]/2$.

- It has a bound state with a real and negative energy if and only if $\mathfrak{z} \in \mathbb{R}^-$. The position wave function for this state is a constant multiple of the right-hand side of (89) with $k_0 = i|\mathfrak{z}|/2$.

Next, we consider the spectral singularities of the complex barrier potential (56). According to (59), zeros k_0 of $M_{22}(k)$ satisfy

$$\cos(k_0 L \mathfrak{n}_0) - i\mathfrak{n}_{0+} \sin(k_0 L \mathfrak{n}_0) = 0, \tag{90}$$

where

$$\mathfrak{n}_0 := \sqrt{1 - \frac{\mathfrak{z}}{k_0^2}}, \qquad \mathfrak{n}_{0+} := \frac{\mathfrak{n}_0^2 + 1}{2\mathfrak{n}_0}. \tag{91}$$

It is not difficult to express (90) in the form:

$$e^{-2ik_0 L \mathfrak{n}_0} = \left(\frac{\mathfrak{n}_0 - 1}{\mathfrak{n}_0 + 1}\right)^2. \tag{92}$$

k_0^2 is a spectral singularity if and only if k_0 is a positive real number satisfying this relation. For such a k_0, we can write (92) as a pair of real equations for the k_0, $\eta_0 := \mathrm{Re}(\mathfrak{n}_0)$, and $\kappa_0 := \mathrm{Im}(\mathfrak{n}_0)$. Because

$$\mathfrak{n}_0 = \eta_0 + i\kappa_0, \tag{93}$$

evaluating the modulus of both side of (92) we find

$$\kappa_0 = \frac{1}{2k_0 L} \ln\left|\frac{(\eta_0 - 1)^2 + \kappa_0^2}{(\eta_0 + 1)^2 + \kappa_0^2}\right|. \tag{94}$$

Similarly, equating the phase angles of both side of (92), we obtain

$$k_0 = \frac{2\pi m - \varphi_0}{2L\eta_0}, \tag{95}$$

where m is a positive integer, and φ_0 is the principle argument of the right-hand side of (92), i.e.,

$$\varphi_0 = \begin{cases} \arctan(\alpha_0) & \text{for } \eta_0^2 + \kappa_0^2 \geq 1, \\ \arctan(\alpha_0) - \pi & \text{for } \eta_0^2 + \kappa_0^2 < 1, \end{cases} \qquad \alpha_0 := \frac{2\kappa_0}{(\eta_0^2 + 1)^2 + \kappa_0^2}. \tag{96}$$

Next, let us identify the barrier potential (56) with an optical potential (4) that describes the scattering of normally incident polarized electromagnetic waves by an infinite slab of homogeneous nonmagnetic material. We choose a coordinate system

in which the slab occupies the space confined between the planes $x = 0$ and $x = L$, and the wave is polarized along the y-direction and propagates along the x-direction. Then the relative permittivity of the system that enters the Helmholtz equation (3) has the form:

$$\hat{\varepsilon}(x) = \begin{cases} \hat{\varepsilon}_{\rm slab} & \text{for } x \in [0, L], \\ 1 & \text{for } x \notin [0, L], \end{cases} \tag{97}$$

where $\hat{\varepsilon}_{\rm slab}$ is the relative permittivity of the slab. In general this takes a possibly complex constant value. We can identify the Helmholtz equation with the Schrödinger equation (2) provided that $v(x)$ is the barrier potential (56) with $\mathfrak{z} = k^2(1 - \hat{\varepsilon}_{\rm slab})$. Substituting this equation in (58), we find $\mathfrak{n} = \sqrt{\hat{\epsilon}}$. Therefore $\mathfrak{n}$ is the refractive index of the slab.

According to (94) the optical system we have described has a spectral singularity, if the imaginary part of the refractive index of our slab is negative. This is precisely the case where the slab is made out of gain material. To see this we note that the gain coefficient of a homogeneous medium is related to its refractive index according to

$$g = -\frac{4\pi \,\mathrm{Im}(\mathfrak{n})}{\lambda} = -2k\,\mathrm{Im}(\mathfrak{n}), \tag{98}$$

where $\lambda = 2\pi/k$ is the wavelength [71]. If the refractive index of the slab equals $\mathfrak{n}_0$, it emits coherent outgoing radiation of wavelength $\lambda_0 = 2\pi/k_0$, i.e., it acts as a laser. In view of (94), for $k = k_0$ and $\mathfrak{n} = \mathfrak{n}_0$, the gain coefficient (98) is given by [40]:

$$g = \frac{1}{L} \ln \left| \frac{(\eta_0 + 1)^2 + \kappa_0^2}{(\eta_0 - 1)^2 + \kappa_0^2} \right| = \frac{2}{L} \ln \left| \frac{\mathfrak{n}_0 + 1}{\mathfrak{n}_0 - 1} \right|. \tag{99}$$

This relation is known as the *laser threshold condition* in optics [71]. It is usually derived by balancing the energy input of the laser by the sum of its energy output and losses. Here we obtain it using the notion of spectral singularity, i.e., demanding the existence of purely outgoing solutions of the wave equation. Notice that this condition also yields a formula for the available laser modes, namely (95). For typical lasers, $k_0 L \gg 1$. This implies $m \gg 1$ which together with (95) give $k_0 \approx \pi m/L\mathrm{Re}(\mathfrak{n}_0)$. The latter is also a well-known result in optics.

The notion of spectral singularity can be extended to more general scattering problems. This is done by identifying it with the values of k^2 at which the left or right reflection and transmission coefficients blow up. This corresponds to situations where $\psi(x)$ satisfies purely outgoing boundary conditions.[13] For a linear scattering problem, the assumption $\det \mathbf{M}(k) \neq 0$ together with Eqs. (22) imply that spectral

[13]The importance of purely outgoing waves in the laser theory predates the discovery of their connection to the mathematics of spectral singularities. See for example [73].

singularities are given by the real and positive zeros of $M_{22}(k)$ and that they are always bidirectional, i.e., both the left and right reflection and transmission coefficients diverge at a spectral singularity.

Determination of spectral singularities of an optical system having an arbitrary geometry is equivalent to finding its laser threshold condition. This observation has been employed for obtaining laser threshold condition for bilayer [42], cylindrical [57], and spherical [55, 56, 58] lasers. A brief review of the physical aspects of spectral singularities is provided in [49]. For a discussion of the spectral singularities of nonlinear Schrödinger equation and their applications in optics, see [9, 12, 26, 44].

6 Space Reflections and Time-Reversal Transformation

In this section we explore the space reflection and time-reversal transformations in quantum mechanics. This requires the knowledge of unitary and Hermitian operators acting in a Hilbert space. Because a precise definition of a Hermitian operator involves certain notions of functional analysis that are not familiar to most physicists, here we provide a less rigorous description. The interested reader may consult [39, 62] for a more careful treatment of the subject.

Consider a linear operator L acting in a Hilbert space $\mathscr{H}$, and let $\prec \cdot, \cdot \succ$ denote the inner product of $\mathscr{H}$. Then the *adjoint* of L is the operator $L^\dagger : \mathscr{H} \to \mathscr{H}$ that satisfies

$$\prec \cdot, L \cdot \succ = \prec L^\dagger \cdot, \cdot \succ .$$

We call L *Hermitian* or *self-adjoint* if $L^\dagger = L$. We call it a *unitary operator* if its domain is $\mathscr{H}$, it is one-to-one and onto, and $L^{-1} = L^\dagger$. These conditions are equivalent to the requirement that

$$\prec L\phi_1, L\phi_2 \succ = \prec \phi_1, \phi_2 \succ,$$

i.e., L leaves the inner product invariant. Here and in what follows ϕ_1 and ϕ_2 are arbitrary elements of $\mathscr{H}$. It turns out that L is unitary if and only if it preserves the norm of the vectors; $\| L\phi_1 \| = \| \phi_1 \|$ where $\| \phi_1 \| := \sqrt{\prec \phi_1, \phi_1 \succ}$.

In the standard quantum mechanical description of the nonrelativistic motion of a particle on a straight line, we take $\mathscr{H}$ to be the space of square integrable functions $L^2(\mathbb{R})$ endowed with the inner product: $\langle \phi_1 | \phi_2 \rangle := \int_{-\infty}^{\infty} \phi_1(x)^* \phi_2(x) dx$.

Hermitian operators play a basic role in both kinematical and dynamical aspects of quantum mechanics. Observables of quantum systems are described by Hermitian operators not just because they have a real spectrum, but more importantly because their expectation values are real. *Non-Hermitian operators may have a real spectrum and even a complete set of eigenvectors forming a basis of the Hilbert space, but*

there are always states in which their expectation value is not real.[14] Because the calculation of expectation values involves the inner product of the Hilbert space, a non-Hermitian operator can play the role of an observable of a quantum system, only if we can modify the inner product on the space of state vectors or even the space of state vectors itself [45], so that the operator acts in the new Hilbert space as a Hermitian operator.[15] This leads to different representations of quantum mechanics whose structure is identical to the standard representation that we employ here [39]. The Hamiltonian operator is required to be Hermitian not only because it is usually identified with the energy observable, but also because it ensures the unitarity of time-evolution, i.e., the time-evolution operator defined by the Hamiltonian is a unitary operator. A celebrated result of functional analysis, known as Stone's theorem [64], establishes the converse of this statement. Therefore, *the unitarity of dynamics implies the Hermiticity of the Hamiltonian.* This result also disqualifies non-Hermitian operators from serving as the Hamiltonian operator for a unitary quantum system.

Non-Hermitian operators can nevertheless be employed in the study of open quantum systems and a variety of problems in the areas where some of the axioms of quantum mechanics are violated. This has actually turned out to be more fruitful than the attempts to use non-Hermitian operators for invoking the nonstandard representations of quantum mechanics.

Having reviewed the meaning of Hermiticity and unitarity of an operator and their role in quantum mechanics, we return to the study of space reflections and time-reversal transformation.

For each $a \in \mathbb{R}$, the active transformation, $x \to 2a - x$, corresponds to the reflection of the real line about the point a. This transformation induces a mapping of the wave functions $\phi(x)$ according to $\phi(x) \to \phi(2a - x)$. We identify this with the action of a linear operator $\mathcal{P}_a$ in $L^2(\mathbb{R})$, namely $\phi \to \widetilde{\phi} := \mathcal{P}_a\phi$, where

$$(\mathcal{P}_a\phi)(x) := \phi(2a - x). \tag{100}$$

It is easy to show that $\mathcal{P}_a$ is a Hermitian operator. It is also clear that $\mathcal{P}_a^2 = I$, so that $\mathcal{P}_a^{-1} = \mathcal{P}_a$. Combining this with the Hermiticity of $\mathcal{P}_a$ we conclude that $\mathcal{P}_a$ is also a unitary operator.

We can use $\mathcal{P}_a$ to transform linear operators $L(t)$ acting in $L^2(\mathbb{R})$ according to

$$L(t) \to \widetilde{L}(t) := \mathcal{P}_a\, L(t)\, \mathcal{P}_a^{-1} = \mathcal{P}_a\, L(t)\, \mathcal{P}_a. \tag{101}$$

[14] For a proof of this statement see [39, Appendix]. A more detailed discussion is provided in [68].

[15] This is obviously not always possible. A sufficient condition for the existence of such a modified inner product is that the operator L satisfies the pseudo-Hermiticity relation $L^\dagger = \eta\, L\, \eta^{-1}$ for a positive-definite bounded linear operator η with a bounded inverse. For further discussion of these and related issues see [39, 45] and references therein.

For example, let $\hat{x}$, $\hat{p}$, and $H(t)$ be respectively the standard position, momentum, and Hamiltonian operators acting in $L^2(\mathbb{R})$, i.e.,

$$\hat{x}\,\phi(x) := x\phi(x), \qquad \hat{p}\,\phi(x) := -i\phi'(x), \qquad H(t) = \frac{\hat{p}^2}{2m} + v(\hat{x}, t). \tag{102}$$

We can use (100) to show that

$$\{\hat{x}, \mathcal{P}_a\} = 2aI, \qquad \{\hat{p}, \mathcal{P}_a\} = 0, \tag{103}$$

where $\{\cdot, \cdot\}$ stands for the anticommutator of operators. Equations (101), (102), and (103) imply

$$\widetilde{\hat{x}} = 2aI - \hat{x}, \qquad \widetilde{\hat{p}} = -\hat{p}, \qquad \widetilde{H}(t) = \frac{\hat{p}^2}{2m} + v(2aI - \hat{x}, t). \tag{104}$$

The first of these relations justifies the name "space reflection" or "parity operator with respect to a" for $\mathcal{P}_a$.

If $H(t)$ is the Hamiltonian operator for a quantum system $\mathcal{S}$, we call the quantum system defined by $\widetilde{H}$ the "space reflection of $\mathcal{S}$ with respect to a." Equation (101) and the unitarity of $\mathcal{P}_a$ imply that $\widetilde{H}(t)$ is Hermitian if and only if so is $H(t)$. This means that space reflections of a unitary quantum system are unitary.

An operator $L(t)$ is called *parity-invariant with respect to a* if $\widetilde{L}(t) = L(t)$. In particular, a standard Hamiltonian operator (102) is parity-invariant with respect to a if and only if $v(2a - x, t) = v(x, t)$.

The parity operators $\mathcal{P}_a$ can be generated from $\mathcal{P}_0$ using the space-translation operator $T_a := e^{-ia\hat{p}}$ which satisfies:

$$(T_a\,\phi)(x) = \phi(x - a). \tag{105}$$

To see this we use (100) and (105) to show that

$$(\mathcal{P}_a\phi)(x) = \phi(2a - x) = (\mathcal{P}_0\phi)(x - 2a) = (T_{2a}\mathcal{P}_0\phi)(x).$$

Therefore,

$$\mathcal{P}_a = T_{2a}\mathcal{P}_0. \tag{106}$$

We use the symbol $\mathcal{P}$ for $\mathcal{P}_0$ and refer to it as the *parity operator* in $L^2(\mathbb{R})$. According to this terminology a standard Hamiltonian operator (102) is *parity-invariant* or *$\mathcal{P}$-symmetric* if and only if $v(x, t) = v(-x, t)$. For a time-independent potential $v(x)$, this means that it is an even function.

Next, consider the operation of complex-conjugation of complex-valued functions, $\phi(x) \to \phi(x)^*$. This defines a function $\mathcal{T} : L^2(\mathbb{R}) \to L^2(\mathbb{R})$ according to $(\mathcal{T}\phi)(x) := \phi(x)^*$. Because for any pair of complex numbers α_1 and α_2,

$$\mathcal{T}(\alpha_1\phi_1 + \alpha_2\phi_2) = \alpha_1^*\mathcal{T}\phi_1 + \alpha_2^*\mathcal{T}\phi_2,$$

$\mathcal{T}$ is an *antilinear operator*. It is also clear that $\mathcal{T}$ squares to the identity operator I. In particular, it is invertible, and $\mathcal{T}^{-1} = \mathcal{T}$.

Let us apply $\mathcal{T}$ to both sides of the time-dependent Schrödinger equation,

$$i\frac{d}{dt}\psi(x,t) = H(t)\psi(x,t). \tag{107}$$

This gives $-i\frac{d}{dt}\mathcal{T}\psi(x,t) = \mathcal{T}H(t)\psi(x,t)$. We can write this equation in the form

$$i\frac{d}{d(-t)}\mathcal{T}\psi(x,t) = \overline{H}(-t)\mathcal{T}\psi(x,t), \tag{108}$$

where for a time-dependent linear operator $L(t)$,

$$\overline{L}(t) := \mathcal{T}L(-t)\mathcal{T}^{-1} = \mathcal{T}L(-t)\mathcal{T}. \tag{109}$$

If we make the change of variables:

$$t \to \bar{t} := -t, \qquad \psi(x,t) \to \overline{\psi}(x,\bar{t}) := \psi(x,t)^* = (\mathcal{T}\psi)(x,t),$$

Eq. (108) takes the form $i\frac{d}{d\bar{t}}\overline{\psi}(x,\bar{t}) = \overline{H}(\bar{t}))\overline{\psi}(x,\bar{t})$. Because t and $\bar{t}$ take arbitrary real values, this equation is equivalent to

$$i\frac{d}{dt}\overline{\psi}(x,t) = \overline{H}(t)\overline{\psi}(x,t). \tag{110}$$

We can express the solutions of (107) and (110) in terms of the time-evolution operators $U(t)$ and $\overline{U}(t)$ for the Hamiltonians $H(t)$ and $\overline{H}(t)$. For a given initial state vector $\psi_0(x)$, we have

$$\psi(x,t) = U(t)\psi_0(x), \qquad \overline{\psi}(x,t) = \overline{U}(t)\psi_0(x)^*. \tag{111}$$

According to these relations, as we increase the value of the time label t starting from $t = 0$, the evolution operators $U(t)$ and $\overline{U}(t)$ respectively determine $\psi(x,t)$ and $\overline{\psi}(x,t)$ for $t > 0$. In view of the fact that $\psi(x,-t) = \overline{\psi}(x,t)^*$, we can say that $\overline{U}(t)$ determines $\psi(x,t)$ for $t < 0$. For this reason, the systems described by the Hamiltonian operators $H(t)$ and $\overline{H}(t)$ are said to be the time-reversal of one another. This, in particular, suggests identifying the antilinear operator $\mathcal{T}$ with the *time-reversal operator*.

The above argument leaves a crucial question unanswered: Suppose that $H(t)$ is a Hermitian operator so that it determines a unitary quantum system. Does this imply that the time-reversed system is also unitary? Equivalently, is $\overline{H}(t)$ Hermitian? The answer turns out to be in the affirmative, because $\mathcal{T}$ satisfies

$$\langle \mathcal{T}\phi_1|\mathcal{T}\phi_2\rangle = \int_{-\infty}^{\infty} [\mathcal{T}\phi_1(x)]^* \mathcal{T}\phi_2(x)dx = \int_{-\infty}^{\infty} \phi_1(x)\phi_2(x)^* dx = \langle \phi_2|\phi_1\rangle. \tag{112}$$

With the help of this relation and the Hermiticity of $H(t)$, we can show that

$$\begin{aligned}\langle \phi_1|\overline{H}(t)\phi_2\rangle &= \langle \mathcal{T}^2\phi_1|\overline{H}(t)\phi_2\rangle = \langle \mathcal{T}^2\phi_1|\mathcal{T}H(-t)\mathcal{T}\phi_2\rangle = \langle H(-t)\mathcal{T}\phi_2|\mathcal{T}\phi_1\rangle \\ &= \langle \mathcal{T}\phi_2|H(-t)\mathcal{T}\phi_1\rangle = \langle \mathcal{T}\phi_2|\mathcal{T}^2 H(-t)\mathcal{T}\phi_1\rangle = \langle \mathcal{T}H(-t)\mathcal{T}\phi_1|\phi_2\rangle \\ &= \langle \overline{H}(t)\phi_1|\phi_2\rangle.\end{aligned}$$

This concludes the proof of the Hermiticity of $\overline{H}(t)$.

An antilinear operator $\mathfrak{S}$, which by definition satisfies

$$\mathfrak{S}(\alpha_1\phi_1 + \alpha_2\phi_2) = \alpha_1^*\mathfrak{S}\phi_1 + \alpha_2^*\mathfrak{S}\phi_2,$$

is said to be unitary, if

$$\langle \mathfrak{S}\phi_1|\mathfrak{S}\phi_2\rangle = \langle \phi_2|\phi_1\rangle. \tag{113}$$

Unitary antilinear operators are also called "*antiunitary operators*" [76]. Similarly to unitary linear operators they preserve the norm of state vectors.

Equation (112) means that $\mathcal{T}$ is an antiunitary operator. There are other antiunitary operators that square to identity and share the time-reversal property of $\mathcal{T}$.[16] This implies that in general $\mathcal{T}$ is not the only possible choice for a time-reversal operator [35]. In what follows, however, we take $\mathcal{T}$ to implement the time-reversal transformation in $L^2(\mathbb{R})$ and refer to it as the *time-reversal operator*.

A possibly time-dependent linear operator $L(t)$ is said to be *time-reversal-invariat* or *real* if $\overline{L}(t) = L(t)$. It is called an *imaginary operator* if $\overline{L}(t) = -L(t)$. For example, the standard position operator $\hat{x}$ is real, because

$$\overline{\hat{x}}\,\phi(x) = \mathcal{T}\hat{x}\mathcal{T}\phi(x) = [x\phi(x)^*]^* = x\phi(x) = \hat{x}\,\phi(x),$$

while the standard momentum operator $\hat{p}$ is imaginary, because

$$\overline{\hat{p}}\,\phi(x) = \mathcal{T}\hat{p}\mathcal{T}\phi(x) = \mathcal{T}\left[-i\frac{d}{dx}\phi(x)^*\right] = i\mathcal{T}\left[\frac{d}{dx}\phi(x)^*\right] = i\frac{d}{dx}\phi(x) = -\hat{p}\phi(x).$$

[16] A simple examples is $\mathcal{T}_\tau := e^{i\tau}\mathcal{T}$ where $\tau \in \mathbb{R}$.

Clearly $L(t)$ is an imaginary operator if and only if $iL(x)$ is real. In particular, iI is imaginary, because I is a real operator. Note also that time-independent linear operators L_R and L_I are respectively real and imaginary if and only if

$$[L_R, \mathcal{T}] = 0, \qquad \{L_I, \mathcal{T}\} = 0.$$

We can easily show that the real multiples, sums, and products of real operators are real. This for instance implies that $\hat{p}^2 = -(i\hat{p})^2$ is a real operator. In light of this observation, the time-reversal of a standard Hamiltonian operator (102) is given by $\overline{H}(t) = \frac{\hat{p}^2}{2m} + \overline{v(\hat{x}, t)}$, where

$$\overline{v(\hat{x}, t)}\phi(x) = \mathcal{T}v(\hat{x}, -t)\mathcal{T}\phi(x) = \mathcal{T}[v(x, -t)\phi(x)^*] = v(x, -t)^*\phi(x).$$

This shows that $v(\hat{x}, t)$ is a real operator provided that $v(x, -t) = v(x, t)^*$. In particular, for a time-independent standard Hamiltonian,

$$H = \frac{\hat{p}^2}{2m} + v(\hat{x}), \tag{114}$$

we have

$$\overline{H} = \frac{\hat{p}^2}{2m} + v(\hat{x})^*, \tag{115}$$

where $v(\hat{x})^*\phi(x) := \overline{v(x)}\phi(x) = v(x)^*\phi(x)$. The Hamiltonian (114) is therefore real if and only if $v(x)$ is a real-valued potential.

Next, we explore the consequences of the combined action of parity and time-reversal transformations. This is realized in $L^2(\mathbb{R})$ by $\mathcal{PT}$ whose effect on the wave functions $\phi(x)$ and time-dependent linear operators $L(t)$ are give by

$$\phi(x) \longrightarrow \widetilde{\phi}(x) := (\mathcal{PT}\phi)(x) = \phi(-x, t)^*,$$
$$L(t) \longrightarrow \widetilde{L}(t) := \mathcal{P}\Big[\mathcal{T}L(-t)\mathcal{T}^{-1}\Big]\mathcal{P}^{-1} = \mathcal{PT}L(-t)(\mathcal{PT})^{-1} = \mathcal{PT}L(-t)\mathcal{PT}.$$

Here, in the last equality we have used the fact that $\mathcal{P}$ and $\mathcal{T}$ commute and square to identity;

$$[\mathcal{P}, \mathcal{T}] = 0, \qquad \mathcal{P}^2 = \mathcal{T}^2 = I. \tag{116}$$

Because $\mathcal{P}$ and $\mathcal{T}$ are respectively unitary and antiunitary operators,

$$\mathcal{PT}(\alpha_1\phi_1 + \alpha_1\phi_2) = \mathcal{P}(\alpha^*\mathcal{T}\phi_1 + \alpha_2^*\mathcal{T}\phi_2) = \alpha^*\mathcal{PT}\phi_1 + \alpha_2^*\mathcal{PT}\phi_2,$$
$$\langle \mathcal{PT}\phi_1 | \mathcal{PT}\phi_2\rangle = \langle \mathcal{T}\phi_1 | \mathcal{T}\phi_2\rangle = \langle \phi_2 | \phi_1\rangle.$$

These show that $\mathcal{PT}$ is an antiunitary operator. The same is true about $\mathcal{P}_a\mathcal{T}$.

We can use (116) and

$$\begin{aligned} \overline{\hat{x}} &= \mathcal{T}\,\hat{x}\,\mathcal{T}^{-1} = \hat{x}, & \overline{\hat{p}} &= \mathcal{T}\,\hat{p}\,\mathcal{T}^{-1} = -\hat{p}, \\ \widetilde{\hat{x}} &= \mathcal{P}\,\hat{x}\,\mathcal{P}^{-1} = -\hat{x}, & \widetilde{\hat{p}} &= \mathcal{P}\,\hat{p}\,\mathcal{P}^{-1} = -\hat{p}, \end{aligned} \tag{117}$$

to show that

$$\widetilde{\overline{\hat{x}}} = \mathcal{PT}\,\hat{x}\,(\mathcal{PT})^{-1} = -\hat{x}, \qquad \widetilde{\overline{\hat{p}}} = \mathcal{PT}\,\hat{p}\,(\mathcal{PT})^{-1} = \hat{p}. \tag{118}$$

In other words,

$$\{\hat{x}, \mathcal{PT}\} = 0, \qquad [\,\hat{p}, \mathcal{PT}] = 0. \tag{119}$$

Another consequence of (118) and the antilinearity of $\mathcal{PT}$ is that it transforms a standard Hamiltonian operator of the form (114) to

$$\widetilde{\overline{H}} = \frac{\hat{p}^2}{2m} + v(-\hat{x})^*. \tag{120}$$

A linear operator $L(t)$ is said to be $\mathcal{PT}$-*symmetric* if it is invariant under the combined action of $\mathcal{P}$ and $\mathcal{T}$, i.e., $L(t) \to \widetilde{\overline{L}}(t) = L(t)$. For a time-independent operator L, this means

$$[L, \mathcal{PT}] = 0.$$

In particular, $\hat{p}$ is $\mathcal{PT}$-symmetric, and a time-independent standard Hamiltonian H is $\mathcal{PT}$-symmetric if and only if its potential is $\mathcal{PT}$-symmetric, i.e., $v(-x)^* = v(x)$. In terms of the real and imaginary parts of $v(x)$, which we denote by $v_r(x)$ and $v_i(x)$, this condition takes the form

$$v_r(-x) = v_r(x), \qquad v_i(-x) = -v_i(x). \tag{121}$$

Therefore, the real and imaginary parts of a $\mathcal{PT}$-symmetric potential are respectively even and odd functions. Similarly, it follows that H is $\mathcal{P}_a\mathcal{T}$-symmetric if and only if $v(2a - x)^* = v(x)$. This is equivalent to

$$v_r(2a - x) = v_r(x), \qquad v_i(2a - x) = -v_i(x). \tag{122}$$

7 $\mathcal{P}$-, $\mathcal{T}$-, and $\mathcal{PT}$-Transformation of the Scattering Data

Consider the scattering problem for a wave equation in one dimension that admits solutions $\psi(x)$ satisfying the asymptotic boundary conditions (1). Suppose that for $x \to \pm\infty$ the parity, time-reversal, and space translations respectively transform $\psi(x)$ according to:

$$\psi(x) \xrightarrow{\mathcal{P}} \widetilde{\psi}(x) := \psi(-x), \qquad \psi(x) \xrightarrow{\mathcal{T}} \overline{\psi}(x) := \psi(x)^*, \qquad \psi(x) \xrightarrow{T_a} \psi_a(x) := \psi(x-a). \tag{123}$$

It is easy to see that these transformations leave the asymptotic boundary conditions (1) form-invariant. This shows that the transformed wave functions, $\widetilde{\psi}(x)$, $\overline{\psi}(x)$, and $\psi_a(x)$ also define consistent scattering problems. We wish to explore the behaviour of the corresponding reflection and transmission amplitudes. To do this, we confine our attention to situations where we can define a transfer matrix $\mathbf{M}(k)$ and examine the effect of the transformations (123) on $\mathbf{M}(k)$.

Let $\widetilde{\mathbf{M}}(k)$, $\overline{\mathbf{M}}(k)$, and $\mathbf{M}_a(k)$ respectively denote the transfer matrix for $\widetilde{\psi}(x)$, $\overline{\psi}(x)$, and $\psi_a(x)$. We can use (1), (14), and (123) to relate them to $\mathbf{M}(k)$. This requires expressing the asymptotic expression for $\widetilde{\psi}(x)$, $\overline{\psi}(x)$, and $\psi_a(x)$ in the form (1) with $(A_\pm, B_\pm)$ respectively replaced by $(\widetilde{A}_\pm, \widetilde{B}_\pm)$, $(\overline{A}_\pm, \overline{B}_\pm)$, and $(A_{a\pm}, B_{a\pm})$. In this way we find asymptotic formulas for $\widetilde{\psi}(x)$, $\overline{\psi}(x)$ and $\psi_a(x)$ that together with (123) imply:

$$\widetilde{A}_\pm = B_\mp, \qquad \widetilde{B}_\pm = A_\mp, \tag{124}$$

$$\overline{A}_\pm = B_\pm^*, \qquad \overline{B}_\pm = A_\pm^*, \tag{125}$$

$$A_{a\pm} = e^{-iak} A_\pm, \qquad B_{a\pm} = e^{iak} B_\pm. \tag{126}$$

Recalling that the transfer matrices $\widetilde{\mathbf{M}}$, $\overline{\mathbf{M}}$, and $\mathbf{M}_a$ satisfy

$$\begin{bmatrix} \widetilde{A}_+ \\ \widetilde{B}_+ \end{bmatrix} = \widetilde{\mathbf{M}} \begin{bmatrix} \widetilde{A}_- \\ \widetilde{B}_- \end{bmatrix}, \quad \begin{bmatrix} \overline{A}_+ \\ \overline{B}_+ \end{bmatrix} = \overline{\mathbf{M}} \begin{bmatrix} \overline{A}_- \\ \overline{B}_- \end{bmatrix}, \quad \begin{bmatrix} A_{a+} \\ B_{a+} \end{bmatrix} = \mathbf{M}_a \begin{bmatrix} A_{a-} \\ B_{a-} \end{bmatrix}, \tag{127}$$

we can use (14), (124), (125), and (126) to infer:

$$\widetilde{\mathbf{M}} = \boldsymbol{\sigma}_1 \mathbf{M}^{-1} \boldsymbol{\sigma}_1, \qquad \overline{\mathbf{M}} = \boldsymbol{\sigma}_1 \mathbf{M}^* \boldsymbol{\sigma}_1, \qquad \mathbf{M}_a = e^{-iak\boldsymbol{\sigma}_3} \mathbf{M}\, e^{iak\boldsymbol{\sigma}_3}, \tag{128}$$

where

$$\boldsymbol{\sigma}_1 := \begin{bmatrix} 0 & 1 \\ 1 & 0 \end{bmatrix}, \qquad \boldsymbol{\sigma}_3 := \begin{bmatrix} 1 & 0 \\ 0 & -1 \end{bmatrix}, \qquad e^{ia\boldsymbol{\sigma}_3} = \begin{bmatrix} e^{ia} & 0 \\ 0 & e^{-ia} \end{bmatrix}.$$

It is instructive to examine the explicit expression for the entries of $\widetilde{\mathbf{M}}$, $\overline{\mathbf{M}}$, and $\mathbf{M}_a$. According to (128), they have the form:

$$\widetilde{M}_{11} = \frac{M_{11}}{\det \mathbf{M}}, \quad \widetilde{M}_{12} = -\frac{M_{21}}{\det \mathbf{M}}, \quad \widetilde{M}_{21} = -\frac{M_{12}}{\det \mathbf{M}}, \quad \widetilde{M}_{22} = \frac{M_{22}}{\det \mathbf{M}}, \tag{129}$$

$$\overline{M}_{11} = M_{22}^*, \quad \overline{M}_{12} = M_{21}^*, \quad \overline{M}_{21} = M_{12}^*, \quad \overline{M}_{22} = M_{11}^*, \tag{130}$$

$$M_{a11} = M_{11}, \quad M_{a12} = e^{-2iak} M_{12}, \quad M_{a21} = e^{2iak} M_{21}, \quad M_{a22} = M_{22}. \tag{131}$$

We can use these relations together with (22) to compute the reflection and transmission amplitudes for the reflected, time-reversed, and translated waves, $\widetilde{\psi}(x)$, $\overline{\psi}(x)$, and $\psi_a(x)$. These are respectively given by

$$\widetilde{\mathfrak{r}}_l = \mathfrak{r}_r, \qquad \widetilde{\mathfrak{t}}_l = \mathfrak{t}_r, \qquad \widetilde{\mathfrak{r}}_r = \mathfrak{r}_l, \qquad \widetilde{\mathfrak{t}}_r = \mathfrak{t}_l, \tag{132}$$

$$\overline{\mathfrak{r}}_l = -\frac{\mathfrak{r}_r^*}{\mathfrak{D}^*}, \qquad \overline{\mathfrak{t}}_l = \frac{\mathfrak{t}_l^*}{\mathfrak{D}^*}, \qquad \overline{\mathfrak{r}}_r = -\frac{\mathfrak{r}_l^*}{\mathfrak{D}^*}, \qquad \overline{\mathfrak{t}}_r = \frac{\mathfrak{t}_r^*}{\mathfrak{D}^*}, \tag{133}$$

$$\mathfrak{r}_{al} = e^{2iak}\,\mathfrak{r}_l, \qquad \mathfrak{t}_{al} = \mathfrak{t}_l \qquad \mathfrak{r}_{ar} = e^{-2iak}\,\mathfrak{r}_r, \qquad \mathfrak{t}_{ar} = \mathfrak{t}_r, \tag{134}$$

where we recall that $\mathfrak{D} := M_{11}/M_{22} = \mathfrak{t}_l\mathfrak{t}_r - \mathfrak{r}_l\mathfrak{r}_r = \det \mathbf{S}$.

Next, we examine the effect of $\mathcal{P}_a$ on the scattering data. Because in view of (106) we have $\mathcal{P}_a = T_{2a}\mathcal{P}$, $\mathcal{P}_a$ transforms the transfer matrix $\mathbf{M}$ according to

$$\mathbf{M} \xrightarrow{\mathcal{P}_a} \widetilde{M}_{2a} = e^{-i2ak\boldsymbol{\sigma}_3}\boldsymbol{\sigma}_1\mathbf{M}^{-1}\boldsymbol{\sigma}_1 e^{i2ak\boldsymbol{\sigma}_3} = \frac{1}{\det \mathbf{M}}\begin{bmatrix} M_{11} & -e^{-4iak}M_{21} \\ -e^{4aik}M_{12} & M_{22} \end{bmatrix}. \tag{135}$$

Here we have made use of (128) and the identity

$$e^{-i\varphi\boldsymbol{\sigma}_3}\boldsymbol{\sigma}_1 = \boldsymbol{\sigma}_1 e^{i\varphi\boldsymbol{\sigma}_3} = \begin{bmatrix} 0 & e^{-i\varphi} \\ e^{i\varphi} & 0 \end{bmatrix}.$$

Using (22) and (135), we obtain

$$\mathfrak{r}_l \xrightarrow{\mathcal{P}_a} e^{4iak}\mathfrak{r}_r = e^{4iak}\widetilde{\mathfrak{r}}_l, \qquad \mathfrak{t}_l \xrightarrow{\mathcal{P}_a} \mathfrak{t}_r = \widetilde{\mathfrak{t}}_r, \tag{136}$$

$$\mathfrak{r}_r \xrightarrow{\mathcal{P}_a} e^{-4iak}\mathfrak{r}_l = e^{-4iak}\widetilde{\mathfrak{r}}_r, \qquad \mathfrak{t}_r \xrightarrow{\mathcal{P}_a} \mathfrak{t}_l = \widetilde{\mathfrak{t}}_r. \tag{137}$$

These equations show that the effect of a space reflection about a point $a \neq 0$ introduces the extra phase factors $e^{\pm 4iak}$ in the expression for the $\mathcal{P}$-transformed reflection amplitudes. In particular, it does not affect the zeros and singularities of the reflection and transmission amplitudes of the system.

We now study the implication of $\mathcal{PT}$ on the scattering data. According to (128), the $\mathcal{PT}$-transformation of the transfer matrix $\mathbf{M}(t)$ yields

$$\begin{aligned} \mathbf{M} \xrightarrow{\mathcal{PT}} \widetilde{\overline{\mathbf{M}}} &= \boldsymbol{\sigma}_1[\boldsymbol{\sigma}_1\mathbf{M}^*\boldsymbol{\sigma}_1]^{-1}\boldsymbol{\sigma}_1 = \mathbf{M}^{-1*} \\ &= \frac{1}{\det \mathbf{M}^*}\begin{bmatrix} M_{22}^* & -M_{12}^* \\ -M_{21}^* & M_{11}^* \end{bmatrix}. \end{aligned} \tag{138}$$

In particular,

$$\det \mathbf{M} \xrightarrow{\mathcal{PT}} \det \widetilde{\mathbf{M}} = \frac{1}{\det \mathbf{M}^*}, \tag{139}$$

$$M_{11} \xrightarrow{\mathcal{PT}} \widetilde{M}_{11} := \frac{M_{22}^*}{\det \mathbf{M}^*}, \qquad M_{12} \xrightarrow{\mathcal{PT}} \widetilde{M}_{12} := -\frac{M_{12}^*}{\det \mathbf{M}^*}, \tag{140}$$

$$M_{21} \xrightarrow{\mathcal{PT}} \widetilde{M}_{21} := -\frac{M_{21}^*}{\det \mathbf{M}^*}, \qquad M_{22} \xrightarrow{\mathcal{PT}} \widetilde{M}_{22} := \frac{M_{11}^*}{\det \mathbf{M}^*}. \tag{141}$$

With the help of these relations and (22) or alternatively (132) and (133), we can derive the following expressions for the $\mathcal{PT}$-transformed reflection and transmission amplitudes.

$$\widetilde{\mathfrak{r}}_l = -\frac{\mathfrak{r}_l^*}{\mathfrak{D}^*}, \qquad \widetilde{\mathfrak{t}}_l = \frac{\mathfrak{t}_r^*}{\mathfrak{D}^*}, \qquad \widetilde{\mathfrak{r}}_r = -\frac{\mathfrak{r}_r^*}{\mathfrak{D}^*}, \qquad \widetilde{\mathfrak{t}}_r = \frac{\mathfrak{t}_l^*}{\mathfrak{D}^*}. \tag{142}$$

8 $\mathcal{P}$-, $\mathcal{T}$-, and $\mathcal{PT}$-Symmetric Scattering Systems

A physical system that involves the scattering of a scalar wave in one dimension is said to be *$\mathcal{P}$-, $\mathcal{T}$-, and $\mathcal{PT}$-symmetric* if its reflection and transmission amplitudes are respectively invariant under space reflection, time-reversal, and the combined action of space reflection and time-reversal transformation, i.e.,

$$\mathcal{P}\text{-symmetry} := \widetilde{\mathfrak{r}}_{l/r} = \mathfrak{r}_{l/r} \text{ and } \widetilde{\mathfrak{t}}_{l/r} = \mathfrak{t}_{l/r}, \tag{143}$$

$$\mathcal{T}\text{-symmetry} := \overline{\mathfrak{r}}_{l/r} = \mathfrak{r}_{l/r} \text{ and } \overline{\mathfrak{t}}_{l/r} = \mathfrak{t}_{l/r}, \tag{144}$$

$$\mathcal{PT}\text{-symmetry} := \widetilde{\overline{\mathfrak{r}}}_{l/r} = \mathfrak{r}_{l/r} \text{ and } \widetilde{\overline{\mathfrak{t}}}_{l/r} = \mathfrak{t}_{l/r}. \tag{145}$$

We can alternatively state the definition of these symmetries in terms of the invariance of the transfer matrix $\mathbf{M}$ or the scattering matrix $\mathbf{S}$ of the system under the action of $\mathcal{P}$, $\mathcal{T}$, and $\mathcal{PT}$. In this section we explore the consequences of these symmetries.

According to (132), the $\mathcal{P}$-symmetry of a scattering system implies

$$\mathfrak{r}_l = \mathfrak{r}_r, \qquad \mathfrak{t}_l = \mathfrak{t}_r. \tag{146}$$

Substituting the latter equation in (21), we find $\det \mathbf{M} = 1$. Let us also mention that in view of (49) and (146), the eigenvalues of the $\mathbf{S}$-matrix for $\mathcal{P}$-symmetric systems take the simple form: $\mathfrak{s}_\pm = \mathfrak{t} \pm \mathfrak{r}$ where $\mathfrak{t} := \mathfrak{t}_l = \mathfrak{t}_r$ and $\mathfrak{r} := \mathfrak{r}_l = \mathfrak{r}_r$.

Another obvious consequence of (146) is that $\mathcal{P}$-symmetric systems cannot support unidirectional reflection or unidirectional invisibility.

The delta-function potential (86) provides a simple example of a $\mathcal{P}$-symmetric potential that may not be time-reversal-invariant. As demonstrated by (88), it complies with (146).

We can similarly derive the consequences of $\mathcal{P}_a$-symmetry. This symmetry also implies transmission reciprocity and $\det \mathbf{M} = 1$, but breaks the reciprocity in reflection amplitudes as it yields the following generalization of the first relation in (146).

$$e^{-2iak}\mathfrak{r}_l(k) = e^{2aik}\mathfrak{r}_r(k). \tag{147}$$

Notice however that reciprocity in reflection coefficients, $|\mathfrak{r}_l|^2 = |\mathfrak{r}_r|^2$, persists. A simple example of $\mathcal{P}_a$-symmetric scattering system is that of the barrier potential (56) with $L = 2a$. Clearly in this case the expressions (60) and (61) for the reflection amplitudes agree with (147).

The consequences of the $\mathcal{T}$-symmetry are more interesting. Imposing (144), we can use (133) to deduce

$$\mathfrak{r}_r^* = -\mathfrak{D}^*\mathfrak{r}_l, \qquad \mathfrak{r}_l^* = -\mathfrak{D}^*\mathfrak{r}_r, \qquad \mathfrak{t}_{l/r}^* = \mathfrak{D}^*\mathfrak{t}_{l/r}. \tag{148}$$

The first two of these relations indicate that either both $\mathfrak{r}_{l/r}$ vanish or $|\mathfrak{D}| = 1$. This means that there is some real number $\sigma \in \mathbb{R}$ such that $\mathfrak{D} = e^{i\sigma}$. Substituting this in (148), we can show that

$$\mathfrak{r}_r = -e^{i\sigma}\mathfrak{r}_l^*, \qquad \mathfrak{t}_{l/r} = \epsilon_{l/r}|\mathfrak{t}_{l/r}|e^{i\sigma/2}, \tag{149}$$

where $\epsilon_{l/r}$ are some unspecified signs; $\epsilon_{l/r} \in \{-1, 1\}$. In particular,

$$|\mathfrak{r}_l| = |\mathfrak{r}_r|. \tag{150}$$

This equation proves the following result.

Theorem 11 *Time-reversal-invariant systems in one dimension cannot support unidirectional reflection or unidirectional invisibility.*

If we insert (149) in the definition of $\mathfrak{D}$, namely (75), and impose $\mathfrak{D} = e^{i\sigma}$, we find

$$|\mathfrak{r}_l|^2 + \epsilon_l\epsilon_r|\mathfrak{t}_l\mathfrak{t}_r| = 1. \tag{151}$$

The following theorem summarizes the content of Eqs. (150) and (151).

Theorem 12 *The reflection and transmission amplitudes of a time-reversal-invariant scattering system in one-dimension satisfy*

$$|\mathfrak{r}_l(k)|^2 = |\mathfrak{r}_r(k)|^2 = 1 \pm |\mathfrak{t}_l(k)\mathfrak{t}_r(k)|, \tag{152}$$

where $k \in \mathbb{R}^+$ and the unspecified sign on the right-hand side is to be taken negative whenever the system has reciprocal transmission, i.e., $\mathfrak{t}_l(k) = \mathfrak{t}_r(k)$.

If $\mathfrak{t}_r = \mathfrak{t}_l$, which is for example the case for systems that are both $\mathcal{T}$- and $\mathcal{P}$-symmetric or described by a real scattering potential, $\epsilon_l = \epsilon_r$ and we can write (151) as

$$|\mathfrak{r}_{l/r}|^2 + |\mathfrak{t}|^2 = 1, \tag{153}$$

where again $\mathfrak{t} := \mathfrak{t}_l = \mathfrak{t}_r$. Equation (153) is usually derived for real scattering potentials using the unitarity of the time-evolution generated by the corresponding standard Hamiltonian (114). It is therefore often called the *unitarity relation*. The derivation we have offered here is more general, for it relies on the transmission reciprocity and time-reversal-invariance. Removing the first of these conditions, we arrive at (152) which is a mild generalization of the unitarity relation (153). Equation (152) apply, for example, to the scattering problem defined by the time-independent Schrödinger equation for the Hamiltonian operator:

$$H = (I + e^{-\mu\hat{x}^2})\left[\frac{\hat{p}^2}{2m} + v(\hat{x})\right],$$

where μ is a positive real parameter, and $v(x)$ is a real and even scattering potential. Note that this Hamiltonian is both $\mathcal{P}$- and $\mathcal{T}$-symmetric but not Hermitian.[17]

The unitarity relation (153), which holds for time-reversal-invariant systems with reciprocal transmission, in general, and real scattering potentials in particular, implies that the reflection and transmission coefficients of the system cannot exceed 1; $|\mathfrak{r}(k)|^2 \leq 1$ and $|\mathfrak{t}(k)|^2 \leq 1$ for all $k \in \mathbb{R}^+$. This means that *these systems do not amplify the transmitted or reflected waves*. In particular, we have:

Theorem 13 *If a time-reversal-invariant scattering system in one dimension has reciprocal transmission, it cannot have spectral singularities.*

It is for this reason that spectral singularities do not appear in the study of unitary quantum systems described by standard Hamiltonian operators.

Time-reversal-invariant systems violating reciprocity in transmission can have spectral singularities. A simple example is a single-center point interaction (7) with $n = 1$, $c_1 = 0$, and

[17] The scattering problem for this Hamiltonian operator is equivalent to that of the energy-dependent scattering potential $v(x, k) := 2mv(x) + k^2/(1 + e^{\mu x^2})$. This is because we can write $H\psi(x) = E\psi(x)$ in the form $-\psi''(x) + v(x, k)\psi(x) = k^2\psi(x)$ where $k := \sqrt{E}$.

$$\mathbf{B}=\begin{bmatrix}\alpha & \beta\\ \gamma & -\alpha\end{bmatrix},\qquad \alpha,\beta,\gamma\in\mathbb{R},\quad \beta\gamma>0. \tag{154}$$

It is easy to see that the system described by this point interaction is time-reversal-invariant, because $\mathbf{B}$ is a real matrix [41]. Furthermore, we can compute its transfer matrix using (27) and find out that for this system $M_{22}(k)=\beta k^2-\gamma$. Therefore, it has a spectral singular $k_0^2=\gamma/\beta$. Note also that because $\det\mathbf{M}=\det\mathbf{B}=-\alpha^2-\beta\gamma<0$, $\det\mathbf{M}\neq 1$ which shows that it has nonreciprocal transmission.

We can also characterize time-reversal symmetry in terms of the restrictions it imposes on the transfer and scattering matrices. These have the following simple form.

$$\mathbf{M}^*=\boldsymbol{\sigma}_1\mathbf{M}\boldsymbol{\sigma}_1,\qquad\qquad \mathbf{S}^*=\boldsymbol{\sigma}_1\mathbf{S}^{-1}\boldsymbol{\sigma}_1. \tag{155}$$

Because $\det\boldsymbol{\sigma}_1=-1$, the first of these equations implies that $\det\mathbf{M}$ must be real while the second reproduces the result that $\det\mathbf{S}$ is unimodular; $|\det\mathbf{S}|=1$.

Let us examine the eigenvalues of $\mathbf{S}$ for time-reversal-invariant systems. In view of (49), (149), and (151), these are given by

$$\mathfrak{s}_+=(\tau+\sqrt{\tau^2-1})e^{i\sigma/2},\quad \mathfrak{s}_-=(\tau-\sqrt{\tau^2-1})e^{i\sigma/2}=\frac{e^{i\sigma/2}}{\tau+\sqrt{\tau^2-1}}, \tag{156}$$

where

$$\tau(k):=\frac{\epsilon_l|\mathfrak{t}_l(k)|+\epsilon_r|\mathfrak{t}_r(k)|}{2}. \tag{157}$$

It is not difficult to see that $|\mathfrak{s}_\pm|=1$ if and only if

$$|\tau|\leq 1. \tag{158}$$

If $|\tau(k)|\leq 1$ for all $k\in\mathbb{R}^+$, we say that the time-reversal symmetry of the system is *exact* or *unbroken*. If $|\tau|>1$ for some $k\in\mathbb{R}^+$, we say that the system has a *broken time-reversal symmetry*.

To examine the physical meaning of exact time-reversal symmetry, we examine the consequences of (158). First we use (157) to write it in the form

$$|\mathfrak{t}_l|^2+|\mathfrak{t}_r|^2+2\epsilon_l\epsilon_r|\mathfrak{t}_l\mathfrak{t}_r|\leq 4. \tag{159}$$

With the help of (151), we can express this equation as

$$\frac{|\mathfrak{t}_l|^2+|\mathfrak{t}_r|^2}{2}\leq 1+|\mathfrak{r}_l|^2. \tag{160}$$

If $\epsilon_l\epsilon_r = 1$, (151), (150), and (160) imply

$$|\mathfrak{r}_{l/r}|^2 \leq 1, \qquad |\mathfrak{t}_l|^2 + |\mathfrak{t}_r|^2 \leq 4. \tag{161}$$

Therefore similarly to the unitary systems the reflection and transmission amplitudes are bounded functions, and the system cannot involve spectral singularities.

If a system has a broken time-reversal symmetry, there is some $k \in \mathbb{R}^+$ such that $|\tau(k)| > 1$. In this case, (151) implies

$$\frac{|\mathfrak{t}_l(k)|^2 + |\mathfrak{t}_r(k)|^2}{2}| > 1 + |\mathfrak{r}_l|^2 \geq 1. \tag{162}$$

Furthermore because $\sqrt{\tau^2 - 1}$ is real and nonzero, (156) implies $|\mathfrak{s}_\pm| \neq 1$ and $\mathfrak{s}_- = 1/\mathfrak{s}_+^*$.

Equation (151) which reveals various properties of the time-reversal-invariant scattering systems has a rather interesting equivalent that does not involve the unspecified signs $\epsilon_{l/r}$. To derive this, first we use (74) and the fact that $\mathfrak{D}(k) = e^{i\sigma(k)}$ to show that

$$\mathfrak{r}_{l/r}(-k) = -e^{-i\sigma(k)}\mathfrak{r}_{r/l}(k), \qquad \mathfrak{t}_{l/r}(-k) = e^{-i\sigma(k)}\mathfrak{t}_{l/r}(k). \tag{163}$$

These relations have the following straightforward implications:

$$|\mathfrak{r}_{l/r}(-k)| = |\mathfrak{r}_{r/l}(k)|, \qquad |\mathfrak{t}_{l/r}(-k)| = |\mathfrak{t}_{l/r}(k)|, \tag{164}$$

$$\mathfrak{r}_{l/r}(-k)\mathfrak{r}_{l/r} + \mathfrak{t}_{l/r}(-k)\mathfrak{t}_{r/l}(k) = 1, \tag{165}$$

where we have made use of the definition of $\mathfrak{D}(k)$, i.e., (75), and the fact that $\mathfrak{D}(k) = e^{i\sigma(k)}$.

It is important to notice that our derivation of Equations (163), (164), and (165) only uses the fact that $|\mathfrak{D}(k)| = 1$, which is much less restrictive than the time-reversal symmetry of the system. We state this result as a theorem:

Theorem 14 *Equations* (164) *and* (165) *hold for any scattering system whose reflection and transmission amplitudes satisfy* $|\mathfrak{t}_l(k)\mathfrak{t}_r(k) - \mathfrak{r}_l(k)\mathfrak{r}_r(k)| = 1$, *i.e.,* $|\mathfrak{D}(k)| = 1$.[18]

Next, we examine the implications of $\mathcal{PT}$-symmetry. In view of (142) and (145), the reflection and transmission amplitudes of $\mathcal{PT}$-symmetric scattering systems satisfy

$$\mathfrak{r}_{l/r}^* = -\mathfrak{D}^*\mathfrak{r}_{l/r}, \qquad \mathfrak{t}_{l/r}^* = \mathfrak{D}^*\mathfrak{t}_{l/r}. \tag{166}$$

[18] An extension of this theorem to more general scattering systems is given in [52].

If we complex-conjugate both sides of (75) and use (166) in the right-hand side of the resulting equation, we find $\mathfrak{D}^* = \mathfrak{D}^{*2}\mathfrak{D}$, which means $|\mathfrak{D}| = 1$. In view of Theorem 14, this shows that, similarly to time-reversal-invariant systems, $\mathcal{PT}$-symmetric systems satisfy the identities (164) and (165).[19]

Because $|\mathfrak{D}| = 1$, $\mathfrak{D} = e^{i\sigma}$ for some $\sigma \in \mathbb{R}$. Using this relation in (166), we can show that

$$\mathfrak{r}_{l/r} = i\eta_{l/r}e^{i\sigma/2}|\mathfrak{r}_{l/r}|, \qquad \mathfrak{t}_{l/r} = \epsilon_{l/r}e^{i\sigma/2}|\mathfrak{t}_{l/r}|, \tag{167}$$

where $\eta_{l/r}, \epsilon_{l/r} \in \{-1, 1\}$. Now, we substitute these relations in (75) and make use of $\mathfrak{D} = e^{i\sigma}$ to conclude that

$$\epsilon_l\epsilon_r|\mathfrak{t}_l\mathfrak{t}_r| + \eta_l\eta_r|\mathfrak{r}_l\mathfrak{r}_r| = 1. \tag{168}$$

According to this equation, $\epsilon_l\epsilon_r = -1$ implies $\eta_l\eta_r = 1$ and $\eta_l\eta_r = -1$ implies $\epsilon_l\epsilon_r = 1$. These observations prove the following theorem.

Theorem 15 *For all $k \in \mathbb{R}^+$, the reflection and transmission amplitudes of a $\mathcal{PT}$-symmetric scattering system in one-dimension satisfy either*

$$|\mathfrak{t}_l(k)\mathfrak{t}_r(k)| = -1 + |\mathfrak{r}_l(k)\mathfrak{r}_r(k)|, \tag{169}$$

or

$$|\mathfrak{t}_l(k)\mathfrak{t}_r(k)| = 1 \pm |\mathfrak{r}_l(k)\mathfrak{r}_r(k)|. \tag{170}$$

If the system has reciprocal transmission, i.e., $\mathfrak{t}_l(k) = \mathfrak{t}_r(k)$, only the second of these relations holds. In this case, we have

$$|\mathfrak{t}(k)|^2 \pm |\mathfrak{r}_l(k)\mathfrak{r}_r(k)| = 1. \tag{171}$$

If the system has reciprocal reflection, i.e., $\mathfrak{r}_l(k) = \mathfrak{r}_r(k)$, (169) is not excluded but the unspecified sign on the right-hand side of (170) is to be taken negative, i.e., it reads

$$|\mathfrak{t}_l(k)\mathfrak{t}_r(k)| + |\mathfrak{r}(k)|^2 = 1. \tag{172}$$

[19] Equations (164) was originally conjectures in [1] for $\mathcal{PT}$-symmetric scattering potentials based on evidence provided by the study of a complexified Scarf II potential. It was subsequently proven in [48] for general $\mathcal{PT}$-symmetric scattering potentials which respect transmission reciprocity.

For a scattering system defined by a $\mathcal{PT}$-symmetric scattering potential, Theorem 2 ensures the reciprocity in transmission. Therefore, $\mathcal{PT}$-symmetric scattering potentials satisfy (171), [11].

Next, we examine the effect of $\mathcal{PT}$-symmetry on the transfer and scattering matrices. It is easy to show that for $\mathcal{PT}$-symmetric systems,

$$\mathbf{M}^* = \mathbf{M}^{-1}, \qquad \mathbf{S}^\dagger = \boldsymbol{\sigma}_1 \mathbf{S}^{-1} \boldsymbol{\sigma}_1, \tag{173}$$

where $\mathbf{S}^\dagger$ is the conjugate-transpose or Hermitian-conjugate of $\mathbf{S}$. The first of these relations follows from (138) and implies that $\det \mathbf{M}$ is unimodular;

$$|\det \mathbf{M}| = 1. \tag{174}$$

The second is a consequence of (48) and (166). Because $\boldsymbol{\sigma}_1^{-1} = \boldsymbol{\sigma}_1$, we can write it in the form $\mathbf{S}^\dagger = \boldsymbol{\sigma}_1 \mathbf{S}^{-1} \boldsymbol{\sigma}_1^{-1}$. This indicates that $\mathbf{S}$ is a $\boldsymbol{\sigma}_1$-*pseudo-unitary matrix* [36], i.e., if we identify the elements of $\mathbb{C}^2$ with 2×1 matrices and view $\boldsymbol{\sigma}_1$ and $\mathbf{S}$ as linear operators acting on them, then $\mathbf{S}$ preserves the indefinite inner product:

$$\langle \mathbf{a}, \mathbf{b} \rangle_{\boldsymbol{\sigma}_1} := \langle \mathbf{a} | \boldsymbol{\sigma}_1 \mathbf{b} \rangle = \mathbf{a}^\dagger \boldsymbol{\sigma}_1 \mathbf{b} = a_1^* b_2 + a_2^* b_1,$$

where $\mathbf{a} = [a_1\ a_2]^T$ and $\mathbf{b} = [b_1\ b_2]^T$ are arbitrary 2×1 complex matrices, and a superscript "T" on a matrix labels its transpose.[20] Because the $\mathbf{S}$-matrix of every $\mathcal{PT}$-symmetric scattering potential is $\boldsymbol{\sigma}_1$-pseudo-unitary, Eq. (171) is sometimes called the *pseudo-unitarity relation*.

In general, an invertible square matrix $\boldsymbol{\mathcal{U}}$ is said to be *pseudo-unitary*, if there is an invertible Hermitian matrix $\boldsymbol{\eta}$ such that $\boldsymbol{\mathcal{U}}^\dagger = \boldsymbol{\eta} \boldsymbol{\mathcal{U}}^{-1} \boldsymbol{\eta}^{-1}$. Pseudo-unitary matrices have the property that the inverse of the complex-conjugate of their eigenvalues are also eigenvalues, i.e., if $\mathfrak{s}$ is an eigenvalue of a pseudo-unitary matrix, either $|\mathfrak{s}| = 1$ or $1/\mathfrak{s}^*$ is also an eigenvalue [36]. As we show above this condition applies also for the eigenvalues of the $\mathbf{S}$-matrix for time-reversal-invariant systems. We can check its validity for the $\mathbf{S}$-matrix of $\mathcal{PT}$-symmetric systems by a direct calculation of its eigenvalues. Inserting (167) in (49) and making use of (168), we find that the expression for $\mathfrak{s}_\pm$ coincides with the one we obtain for the time-reversal-invariant systems, namely (156). Therefore, again either $|\tau| \leq 1$ in which case $|\mathfrak{s}_\pm| = 1$, or $|\tau| > 1$ in which case $|\mathfrak{s}_\pm| \neq 1$ and $\mathfrak{s}_- = 1/\mathfrak{s}_+^*$.

Following the terminology we employed in our discussion of time-reversal symmetry, we use the sign of $1 - |\tau|$ to introduce the notions of exact and broken $\mathcal{PT}$-symmetry. If for all $k \in \mathbb{R}^+$, $1 - \tau(k)| \geq 0$ so that $|\mathfrak{s}_\pm(k)| = 1$, we say that the system has an *exact or unbroken* $\mathcal{PT}$*-symmetry*. If this is not the case we say that its $\mathcal{PT}$-symmetry is *broken*. This terminology should not be confused with the

[20] For a 2×2 matrix $\mathbf{A}$, the condition of being $\boldsymbol{\sigma}_1$-pseudo-unitary is equivalent to the requirement that $e^{i\pi\boldsymbol{\sigma}_2/4} \mathbf{A} e^{-i\pi\boldsymbol{\sigma}_2/4}$ belong to the pseudo-unitary group $U(1, 1)$, where $\boldsymbol{\sigma}_2$ is the second Pauli matrix.

one employed in the study of $\mathcal{PT}$-symmetric Hamiltonian operators H that have a discrete spectrum. For these systems unbroken $\mathcal{PT}$-symmetry means the existence of a complete set of eigenvectors of H that are also eigenvectors of $\mathcal{PT}$. This in turn implies the reality of the spectrum of H, [2]. Scattering theory for a $\mathcal{PT}$-symmetric Hamiltonian is sensible only if its spectrum contains a real continuous part that covers the positive real axis in the complex plane. In particular it may or may not have nonreal eigenvalues.[21]

If for some $k \in \mathbb{R}^+$, a $\mathcal{PT}$-symmetric system has reciprocal transmission, $\tau(k) = |\mathfrak{t}(k)|$. Therefore the condition $|\tau| \leq 1$ puts an upper bound of 1 on the transmission coefficient $|\mathfrak{t}(k)|^2$. This in turn implies that the unspecified sign in (171) must be taken positive and $|\mathfrak{r}_l(k)\mathfrak{r}_r(k)| \leq 1$. As a result, the system cannot amplify reflected or transmitted waves having wavenumber k. In particular k^2 cannot be a spectral singularity. In summary, *for a system with reciprocal transmission, such as those described by a scattering potential, exactness of $\mathcal{PT}$-symmetry forbids amplification of the reflected and transmitted waves and spectral singularities.*

An important advantage of $\mathcal{PT}$-symmetry over $\mathcal{P}$- and $\mathcal{T}$-symmetries, is that it does not imply the equality of the left and right reflection amplitudes. Therefore *unidirectional reflection and unidirectional invisibility are not forbidden by $\mathcal{PT}$-symmetry*. In fact, it turns out that it is easier to achieve unidirectional reflectionlessness and invisibility in the presence of $\mathcal{PT}$-symmetry than in its absence. This has to do with the following result that is a straightforward consequence of (142).

Theorem 16 *The equations characterizing unidirectional invisibility, namely*

$$\mathfrak{r}_{l/r}(k) = 0 \neq \mathfrak{r}_{r/l}, \qquad \mathfrak{t}_{l/r}(k) = 1, \tag{175}$$

are invariant under the $\mathcal{PT}$-transformation.

For a $\mathcal{PT}$-symmetric system the equations of unidirectional invisibility enjoy the same symmetry as that of the underlying wave equation. This leads to enormous practical simplifications in constructing specific unidirectionally invisible models. It does not however imply that $\mathcal{PT}$-symmetry is a necessary condition for unidirectional reflection or invisibility [43].

9 Time-Reversed and Self-Dual Spectral Singularities

Consider a linear scattering system $\mathcal{S}$ with an invertible transfer matrix $\mathbf{M}(k)$. Then spectral singularities of this system are determined by the real and positive zeros of $M_{22}(k)$. According to (130), $M_{11}(k) = 0$ if and only if $\overline{M}_{22}(k) = 0$. This in

[21] We use the term "eigenvalue" to mean an element of the point spectrum of H which has a square-integrable eigenfunction.

turn means that the real and positive zeros of $M_{11}(k)$ give the spectral singularities of the time-reversed system $\overline{\mathcal{S}}$. We will refer to these as the *time-reversed spectral singularities* of $\mathcal{S}$.

At a time-reversed spectral singularity the Jost solutions of the time-reversed system become linearly dependent and satisfy purely outgoing boundary conditions at $x = \pm\infty$. This suggests the presence of solutions of the wave equation for the system $\mathcal{S}$ that satisfy purely incoming asymptotic boundary conditions. To see this, first we note that according to Eq. (14) whenever $M_{11}(k) = 0$, we can have a solution $\psi(x)$ of the wave equation satisfying (1) with $A_+(k) = B_-(k) = 0$, i.e.,

$$\psi(x) \to N_\pm(k)e^{\mp ikx} \qquad \text{for} \qquad x \to \pm\infty, \tag{176}$$

where $N_\pm(k)$ are nonzero complex coefficients satisfying

$$N_+(k) = M_{21}(k)N_-(k). \tag{177}$$

In other words, $\psi(x)$ satisfies the asymptotic boundary conditions (1) with

$$A_-(k) = N_-(k), \qquad B_-(k) = 0, \qquad A_+(k) = 0, \qquad B_+(k) = N_+(k).$$

If we substitute these in the first equation in (42) and recall that $\mathbf{S}_1 = \mathbf{S}$, we find that

$$\mathbf{S}(k)\begin{bmatrix} N_-(k) \\ N_+(k) \end{bmatrix} = \begin{bmatrix} 0 \\ 0 \end{bmatrix}.$$

This shows that $[N_-(k)\ N_+(k)]^T$ is an eigenvector of $\mathbf{S}(k)$ with eigenvalue zero. In particular, one of the eigenvalues of $\mathbf{S}(k)$ vanishes.

The existence of a solution of the wave equation having the asymptotic expression (176) means that the scatterer will absorb any pair of incident left- and right-going waves whose complex amplitude $N_\pm(k)$ are related by (177). This phenomenon is called *coherent perfect absorption* [6, 27, 75]. In the study of effectively one-dimensional optical systems, spectral singularities correspond to the initiation of laser oscillations in a medium with gain, i.e., a laser, while their time-reversal give rise to perfect absorption of finely tuned coherent incident beams by a medium with loss. The latter is sometimes called an *antilaser*.

It may happen that a particular wavenumber k_0 is a common zero of both $M_{11}(k)$ and $M_{22}(k)$. In this case, we call k_0^2 a *self-dual spectral singularity* [42]. At a self-dual spectral singularity the wave equation admits both purely outgoing and purely incoming solutions. This means that if the system is not subject to any incident wave, it will amplify the background noise and begin emitting outgoing waves of wavenumber k_0. But if it is subject to a pair of left- and right-going incident waves with wavenumber k_0 and complex amplitudes satisfying (177) for $k = k_0$, then it will absorb them completely. In its optical realizations this corresponds to a

special laser that becomes a coherent perfect absorber (CPA) once it is subject to an appropriate pair of incoming waves. Such a device is called a *CPA-laser*.

For a time-reversal-invariant system we have $M_{11}(k) = M_{22}(k)^*$. Therefore every spectral singularity is self-dual. But according to Theorem 13 spectral singularities are forbidden for time-reversal-invariant systems with reciprocal transmission. This excludes real scattering potentials. There are however nonreal potentials that admit self-dual spectral singularities. Principal examples are $\mathcal{PT}$-symmetric scattering potentials [7, 28, 77]. According to (140), for every $\mathcal{PT}$-symmetric scattering system,

$$M_{11}(k) = \det \mathbf{M}(k) M_{22}(k)^*.$$

This proves the following theorem.

Theorem 17 *Spectral singularities of every $\mathcal{PT}$-symmetric scattering system are self-dual.*

This does not however exclude the possibility of having non-$\mathcal{PT}$-symmetric systems with self-dual spectral singularities. Simple examples of the latter are examined in [19, 22, 42].

10 Summary and Concluding Remarks

Scattering of waves can be studied using a general framework where the asymptotic solutions of the relevant wave equation are plane waves. This point of view is analogous to the general philosophy leading to the **S**-matrix formulation of scattering in the late 1930s. In one dimension, the transfer matrix proves to be a much more powerful tool than the **S**-matrix. We have therefore offered a detailed discussion of the transfer matrix and used it to introduce and explore the implications of $\mathcal{P}$-, $\mathcal{T}$-, and $\mathcal{PT}$-symmetry. This is actually quite remarkable, for we could derive a number of interesting and useful quantitative results regarding the consequences of such symmetries without actually imposing them on the wave equation. These results apply to scattering phenomena modeled using local as well as nonlocal potentials and point interactions. The general setup we offer in Sect. 1 can also be used in the study of the scattering of a large class of nonlinear waves that are asymptotically linear. The results we derived using the transfer matrix may not however extend to such waves.

The recent surge of interest in the properties of $\mathcal{PT}$-symmetric scattering potentials has led to the study of remarkable effects such as unidirectional invisibility, optical spectral singularities, and coherent perfect absorption. The global approach to scattering that we have outlined here allows for a precise description of these concepts for a general class of scattering systems that cannot be described using a local scattering potential. In particular, we have derived specific conditions imposed by $\mathcal{P}$-, $\mathcal{T}$-, and $\mathcal{PT}$-symmetry on the presence of nonreciprocal transmission

and reflection, spectral singularities and their time-reversal, and unidirectional reflectionlessness and invisibility.

A recent development that we have not covered in the present text is the construction of a transfer matrix for potential scattering in two and three dimensions [31]. This has led to the discovery of a large class of exactly solvable multidimensional scattering potentials [33], and allowed for the extension of the notions of spectral singularity and unidirectional invisibility to higher dimensions [31, 32]. A particularly remarkable application of the multidimensional transfer matrix is the construction of scattering potentials in two dimensions that display perfect broadband invisibility below a tunable critical frequency [34].

Acknowledgements The author is indebted to Keremcan Doğan, Sasan HajiZadeh, and Neslihan Oflaz for their help in locating a large number of typos in the first draft of the manuscript. This work has been supported by the Scientific and Technological Research Council of Turkey (TÜBİTAK) in the framework of the project no: 114F357 and by Turkish Academy of Sciences (TÜBA).

References

1. Ahmed, Z.: New features of scattering from a one-dimensional non-Hermitian (complex) potential. J. Phys. A Math. Theor. **45**, 032004 (2012)
2. Bender, C.M., Boettcher, S.: Real spectra in non-Hermitian Hamiltonians having $\mathcal{PT}$ symmetry. Phys. Rev. Lett. **80**, 5243–5246 (1998)
3. Blashchak, V.A.: An analog of the inverse problem in the scattering for a non-self-conjugate operator I. J. Diff. Eq. **4**, 1519–1533 (1968)
4. Born, M., Wolf, E.: Principles of Optics. Cambridge University Press, Cambridge (1999)
5. Boyce, W.E., DiPrima, R.C.: Elementary Differential Equations and Boundary Value Problems, 10th edn. Wiley, Hoboken (2012)
6. Chong, Y.D., Ge, L., Cao, H., Stone, A.D.: Coherent perfect absorbers: time-reversed lasers. Phys. Rev. Lett. **105**, 053901 (2010)
7. Chong, Y.D., Ge, L., Stone, A.D.: $\mathcal{PT}$-symmetry breaking and laser-absorber modes in optical scattering systems. Phys. Rev. Lett. **106**, 093902 (2011)
8. Devillard, P., Souillard, B.: Polynomially decaying transmission for the nonlinear Schrödinger equation in a random medium. J. Stat. Phys. **43**, 423–439 (1986)
9. Doğan, K., Mostafazadeh, A., Sarısaman, M.: Spectral singularities, threshold gain, and output intensity for a slab laser with mirrors. Preprint arXiv: 1710.02825, to appear in Ann. Phys. (N.Y.)
10. Flügge, S.: Practical Quantum Mechanics. Springer, Berlin (1999)
11. Ge, L., Chong, Y.D., Stone, A.D.: Conservation relations and anisotropic transmission resonances in one-dimensional $\mathcal{PT}$-symmetric photonic heterostructures. Phys. Rev. A **85** 023802 (2012)
12. Ghaemi-Dizicheh, H., Mostafazadeh, A., Sarısaman, M.: Nonlinear spectral singularities and laser output intensity. J. Opt. **19**, 105601 (2017)
13. Greenberg, M., Orenstein, M.: Irreversible coupling by use of dissipative optics. Opt. Lett. **29**, 451–453 (2004)
14. Guseinov, G.Sh.: On the concept of spectral singularities. Pramana J. Phys. **73**, 587–603 (2009)
15. Horsley, S.A.R., Longhi, S.: One-way invisibility in isotropic dielectric optical media. Am. J. Phys. **85**, 439–446 (2017)
16. Horsley, S.A.R., Artoni, M., La Rocca, G.C.: Spatial Kramers-Kronig relations and the reflection of waves. Nat. Photon. **9**, 436–439 (2015)

17. Hsu, C.W., Zhen, B., Stone, A.D., Joannopoulos, J.D., Soljačić, M.: Bound states in the continuum. Nat. Rev. Mater. **1**, 16048 (2016)
18. Jones, H.F.: Analytic results for a PT-symmetric optical structure. J. Phys. A Math. Theor. **45**, 135306 (2012)
19. Kalozoumis, P.A., Morfonios, C.V., Kodaxis, G., Diakonos, F.K., Schmelcher, P.: Emitter and absorber assembly for multiple self-dual operation and directional transparency. Appl. Phys. Lett. **110**, 121106 (2017)
20. Kay, I., Moses, H.E.: Reflectionless transmission through dielectrics and scattering potentials. J. Appl. Phys. **27**, 1503–1508 (1956)
21. Kemp, R.R.D.: A singular boundary value problem for a non-self-adjoint differential operator. Can. J. Math. **10**, 447–462 (1958)
22. Konotop, V.V., Zezyulin, D.A.: Phase transition through the splitting of self-dual spectral singularity in optical potentials. Opt. Lett. **42**, 5206–5209 (2017)
23. Kulishov, M., Laniel, J.M., Belanger, N., Azana, J., Plant, D.V.: Nonreciprocal waveguide Bragg gratings. Opt. Exp. **13**, 3068–3078 (2005)
24. Lamb, G.L.: Elements of Soliton Theory. Wiley, New York (1980)
25. Lin, Z., Ramezani, H., Eichelkraut, T., Kottos, T., Cao, H., Christodoulides, D.N.: Unidirectional invisibility induced by PT-symmetric periodic structures. Phys. Rev. Lett. **106**, 213901 (2011)
26. Liu, X., Dutta Gupta, S., Agarwal, G.S.: Regularization of the spectral singularity in $\mathcal{PT}$-symmetric systems by all-order nonlinearities: nonreciprocity and optical isolation. Phys. Rev. A **89**, 013824 (2014)
27. Longhi, S.: Backward lasing yields a perfect absorber. Physics **3**, 61 (2010)
28. Longhi, S.: $\mathcal{PT}$-symmetric laser absorber. Phys. Rev. A **82**, 031801 (2010)
29. Longhi, S.: Invisibility in PT-symmetric complex crystals. J. Phys. A Math. Theor. **44**, 485302 (2011)
30. Longhi, S.: Wave reflection in dielectric media obeying spatial Kramers-Kronig relations. EPL **112**, 64001 (2015)
31. Loran, F., Mostafazadeh, A.: Transfer matrix formulation of scattering theory in two and three dimensions. Phys. Rev. A **93**, 042707 (2016)
32. Loran, F., Mostafazadeh, A.: Unidirectional invisibility and nonreciprocal transmission in two and three dimensions. Proc. R. Soc. A **472**, 20160250 (2016)
33. Loran, F., Mostafazadeh, A.: Class of exactly solvable scattering potentials in two dimensions, entangled-state pair generation, and a grazing-angle resonance effect. Phys. Rev. A **96**, 063837 (2017)
34. Loran, F., Mostafazadeh, A.: Perfect broad-band invisibility in isotropic media with gain and loss. Opt. Lett. **42**, 5250–5253 (2017)
35. Messiah, A.: Quantum Mechanics. Dover, New York (1999)
36. Mostafazadeh, A.: Pseudounitary operators and pseudounitary quantum dynamics. J. Math. Phys. **45**, 932–946 (2004)
37. Mostafazadeh, A.: Delta-function potential with a complex coupling. J. Phys. A Math. Gen. **39**, 13495–13506 (2006)
38. Mostafazadeh, A.: Spectral singularities of complex scattering potentials and infinite reflection and transmission coefficients at real energies. Phys. Rev. Lett. **102**, 220402 (2009)
39. Mostafazadeh, A.: Pseudo-Hermitian representation of quantum mechanics. Int. J. Geom. Meth. Mod. Phys. **7**, 1191–1306 (2010)
40. Mostafazadeh, A.: Optical spectral singularities as threshold resonances. Phys. Rev. A **83**, 045801 (2011)
41. Mostafazadeh, A.: Spectral singularities of a general point interaction. J. Phys. A Math. Theor. **44**, 375302 (2011)
42. Mostafazadeh, A.: Self-dual spectral singularities and coherent perfect absorbing lasers without $\mathcal{PT}$-symmetry. J. Phys. A Math. Gen. **45**, 444024 (2012)
43. Mostafazadeh, A.: Invisibility and $\mathcal{PT}$-symmetry. Phys. Rev. A **87**, 012103 (2013)

44. Mostafazadeh, A.: Nonlinear spectral singularities for confined nonlinearities. Phys. Rev. Lett. **110**, 260402 (2013)
45. Mostafazadeh, A.: Pseudo-Hermitian quantum mechanics with unbounded metric operators. Philos. Trans. R. Soc. A **371**, 20120050 (2013)
46. Mostafazadeh, A.: Transfer matrices as non-unitary S-matrices, multimode unidirectional invisibility, and perturbative inverse scattering. Phys. Rev. A **89**, 012709 (2014)
47. Mostafazadeh, A.: Unidirectionally invisible potentials as local building blocks of all scattering potentials. Phys. Rev. A **90**, 023833 (2014)
48. Mostafazadeh, A.: Generalized unitarity and reciprocity relations for $\mathcal{PT}$-symmetric scattering potentials. J. Phys. A Math. Theor. **47**, 505303 (2014)
49. Mostafazadeh, A.: Physics of spectral singularities. In: Proceedings of XXXIII Workshop on Geometric Methods in Physics, Held in Bialowieza, 29 June–5 July 2014, Trends in Mathematics, pp. 145–165. Springer International Publishing, Switzerland (2015); preprint arXiv:1412.0454
50. Mostafazadeh, A.: Point interactions, metamaterials, and $\mathcal{PT}$-symmetry. Ann. Phys. (NY) **368**, 56–69 (2016)
51. Mostafazadeh, A.: Dynamical theory of scattering, exact unidirectional invisibility, and truncated $\mathfrak{z}\, e^{2ik_0x}$ potential. J. Phys. A Math. Theor. **49** 445302 (2016)
52. Mostafazadeh, A.: Generalized unitarity relation for linear scattering systems in one dimension. Preprint arXiv:1711.04003
53. Mostafazadeh, A., Oflaz, N.: Unidirectional reflection and invisibility in nonlinear media withanincoherent nonlinearity. Phys. Lett. A **381**, 3548–3552 (2017)
54. Mostafazadeh, A., Rostamzadeh, S.: Perturbative analysis of spectral singularities and their optical realizations. Phys. Rev. A **86**, 022103 (2012)
55. Mostafazadeh, A., Sarısaman, M.: Spectral singularities of a complex spherical barrier potential and their optical realization. Phys. Lett. A **375**, 3387–3391 (2011)
56. Mostafazadeh, A., Sarısaman, M.: Optical spectral singularities and coherent perfect absorption in a two-layer spherical medium. Proc. R. Soc. A **468**, 3224–3246 (2012)
57. Mostafazadeh, A., Sarısaman, M.: Spectral singularities and whispering gallery modes of a cylindrical gain medium. Phys. Rev. A **87**, 063834 (2013)
58. Mostafazadeh, A., Sarısaman, M.: Spectral singularities in the surface modes of a spherical gain medium. Phys. Rev. A **88**, 033810 (2013)
59. Muga, J.G., Palao, J.P., Navarro, B., Egusquiza, I.L.: Complex absorbing potentials. Phys. Rep. **395**, 357–426 (2004)
60. Naimark, M.A.: Investigation of the spectrum and the expansion in eigenfunctions of a non-selfadjoint differential operator of the second order on a semi-axis. Am. Math. Soc. Transl. **16**, 103–193 (1960). This is the English translation of M. A. Naimark, Trudy Moscov. Mat. Obsc. **3** 181–270 (1954)
61. Poladian, L.: Resonance mode expansions and exact solutions for nonuniform gratings. Phys. Rev. E **54**, 2963–2975 (1996)
62. Prugovečki, E.: Quantum Mechanics in Hilbert Space. Academic, New York (1981)
63. Razavy, M.: Quantum Theory of Tunneling. World Scientific, Singapore (2003)
64. Reed, M., Simon, B.: Methods of Modern Mathematical Physics: Volume 1 Functional Analysis. Academic, San Diego (1980)
65. Ruschhaupt, A., Dowdall1, T., Simón, M.A., Muga, J.G.: Asymmetric scattering by non-Hermitian potentials. EPL **120**, 20001 (2017)
66. Sánchez-Soto, L.L., Monzóna, J.J., Barriuso, A.G., Cariñena, J.F.: The transfer matrix: a geometrical perspective. Phys. Rep. **513**, 191–227 (2012)
67. Sarısaman, M.: Unidirectional reflectionlessness and invisibility in the TE and TM modes of a PT-symmetric slab system. Phys. Rev. A **95**, 013806 (2017)
68. Schechter, M.: Operator Methods in Quantum Mechanics. Dover, New York (2002)
69. Schwartz, J.: Some non-selfadjoint operators. Commun. Pure. Appl. Math. **13**, 609–639 (1960)
70. Seigert, A.J.F.: On derivation of the dispersion formula for nuclear reactions. Phys. Rev. **56**, 750–752 (1939)

71. Silfvast, W.T.: Laser Fundamentals. Cambridge University Press, Cambridge (1996)
72. Stillinger, F.H., Herrick, D.R.: Bound states in the continuum. Phys. Rev. A **11**, 446–454 (1975)
73. Türeci, H.E., Stone, A.D., Collier, B.: Self-consistent multimode lasing theory for complex or random lasing media. Phys. Rev. A **74**, 043822 (2006)
74. Vu, P.L.: Explicit complex-valued solutions of the Korteweg–deVries equation on the half-line and on the whole-line. Acta Appl. Math. **49**, 107–149 (1997)
75. Wan, W., Chong, Y., Ge, L., Noh, H., Stone, A.D., Cao, H.: Time-reversed lasing and interferometric control of absorption. Science **331**, 889–892 (2011)
76. Weinberg, S.: Quantum Theory of Fields, Vol. I. Cambridge University Press, Cambridge (1995)
77. Wong, Z.J., Xu, Y.-L., Kim, J., O'Brien, K., Wang, Y., Feng, L., Zhang, X.: Lasing and anti-lasing in a single cavity. Nat. Photon **10**, 796–801 (2016)

Passive $\mathcal{PT}$-Symmetry in Laser-Written Optical Waveguide Structures

T. Eichelkraut, S. Weimann, M. Kremer, M. Ornigotti, and A. Szameit

Abstract In this chapter we describe how $\mathcal{PT}$-symmetric systems can be implemented in a passive fashion, that is, without using gain, by employing modulated waveguide structures. To this end, we present the underlying theoretical ideas as well as the details of the implementation of such passive structures. As an application, we experimentally demonstrate the transition from ballistic to diffusive transport in passive $\mathcal{PT}$-symmetric waveguide arrays.

1 Introduction

Since $\mathcal{PT}$ symmetric systems entered optics [1, 2], it became evident that loss is not only an unwanted side effect of an optical system, but can introduce a variety of new and exciting physical phenomena, such as unusual beam dynamics [3, 4], $\mathcal{PT}$ symmetric solitons [5, 6], Bloch Oscillations and dynamic localization in complex crystals [7, 8], and even optical tachyons [9]. All this is possible, provided that losses can be introduced in a controllable manner. $\mathcal{PT}$ symmetric optical structures, in fact, are based on platforms, where one is able to introduce well-defined gain and loss, in order to account for an appropriate complex optical potential. As the most natural way of implementing $\mathcal{PT}$ symmetry is by means of systems of evanescently coupled waveguides, loss and gain management in the individual waveguides is therefore a crucial step in the fabrication process. The fact that implementing gain and losses in optical systems requires careful, and sometimes challenging,

T. Eichelkraut
Carl Zeiss AG, Oberkochen, Germany
e-mail: toni@eichelkraut-net.de

S. Weimann · M. Kremer · M. Ornigotti · A. Szameit (✉)
Institute for Physics, Rostock University, Rostock, Germany
e-mail: steffen.weimann@uni-rostock.de; mark.kremer@uni-rostock.de; marco.ornigotti@uni-rostock.de; alexander.szameit@uni-rostock.de

D. Christodoulides, J. Yang (eds.), *Parity-time Symmetry and Its Applications*, Springer Tracts in Modern Physics 280,
https://doi.org/10.1007/978-981-13-1247-2_5

engineering, represents nowadays a bottleneck for the realisation of more complex structures than simple waveguide couplers or arrays.

To overcome this problem, however, it has been recently proposed to use entirely passive structures, whose dynamics are fully equivalent to $\mathcal{PT}$ symmetric systems [10–12]. The advantage of these passive structures relies on the fact that they only present losses and no gain, a feature that makes them simpler to design and experimentally realise. The correspondence between $\mathcal{PT}$ symmetric systems and such passive systems, however, holds only if the passive structure is "quasi"-$\mathcal{PT}$ symmetric around the mean loss of the structure, as it has been formally demonstrated in Ref. [13].

From an experimental point of view, therefore, the problem of realising $\mathcal{PT}$ symmetric structures corresponds to the problem of controlling the losses in a waveguiding system. To be able to realise complex optical structures with passive $\mathcal{PT}$ symmetry, therefore, one needs to achieve a high degree of control over the losses of an optical system. Currently, controlling the losses in a waveguiding system can be done by employing three different techniques. The first one concerns waveguides implemented in an AlGaAs heterostructures (the most popular fabrication technique of waveguides these days); in this system, additional losses can be introduced by adding a thin chromium layer on top of the target waveguides [10]. For the case of waveguides obtained by Ti-indiffusion into LiNb wafers, instead, additional losses can be inserted by optical excitation of electrons from Fe^{2+} color centers to the conduction band [14]. A third possibility to control the losses in an optical waveguide consists in the use of $\mathcal{PT}$ synthetic lattices with time as the "transverse" coordinate. In such a system, losses are obtained by acousto-optical modulation [15]. The first two approaches, however, are inherently planar, and therefore offer no possibility of involving a second transverse dimension. The third approach is instead limited to 1D systems due to practical reasons, and additionally the evolution equations in these systems do not perfectly match the set of coupled Schrödinger-like equations as required in the original proposal of optical $\mathcal{PT}$ symmetry. A fourth, more efficient and controllable, solution for realising controllable losses in optical waveguides consists in introducing radiation losses by sinusoidally bending the longitudinal waveguide profile. This approach, in particular, will be discussed in detail in this chapter, as it represents the core technology to realise passive $\mathcal{PT}$ symmetric and non-Hermitian lattices [12].

This chapter is organised as follows: in Sect. 2, we demonstrate the equivalence of $\mathcal{PT}$ and "quasi"-$\mathcal{PT}$ symmetry, using a simple directional coupler as prototypical example of waveguiding structure. The technique used to fabricate laser-written waveguide structures, together with the one used to characterise the flow of light in such structures, are briefly discussed in Sect. 3.1, and in Sect. 4 it is discussed in detail how to realise controlled losses in such structures. Finally, in Sect. 5 some examples of transport properties of passive $\mathcal{PT}$-symmetric and non-Hermitian systems are discussed.

2 Passive $\mathcal{PT}$-Symmetry

We begin our analysis by considering a monochromatic scalar electric field $\psi(x, z)$ characterized by a frequency ω_0 and a wavelength $\lambda = 2\pi/k$ propagating inside a directional coupler. We assume that the mode field inside the coupler is strongly confined along the y-direction, so that the beam dynamics in such a system can be taken to be one-dimensional in the transverse plane. The evolution of the light field $\psi(x, z)$ inside such a structure can be described by the following adimensional paraxial equation:

$$i\frac{\partial\psi}{\partial z} = -\frac{\partial^2\psi}{\partial x^2} + V(x)\psi \equiv \hat{\mathcal{H}}\psi, \tag{1}$$

where z and x are suitably chosen adimensional coordinates and $V(x) = V_R(x) + iV_I(x)$ is the complex optical potential that implements $\mathcal{PT}$-symmetry in the system [16]. By expanding the scalar electric field $\psi(x, z)$ onto the orthogonal eigenmodes $u_n(x)$ of the coupler as $\psi(x, z) = [a_1(z)u_1(x) + a_2(z)u_2(x)]e^{i\beta z}$, where β is the real (due to $\mathcal{PT}$-symmetry) propagation constant, and $a_n(z)$ is the complex field amplitude in the waveguide n of the coupler, the above equation can be rewritten in the following coupled mode form:

$$i\frac{\mathrm{d}}{dz}\begin{pmatrix} a_1 \\ a_2 \end{pmatrix} = \begin{pmatrix} i\gamma & \kappa \\ \kappa & -i\gamma \end{pmatrix}\begin{pmatrix} a_1 \\ a_2 \end{pmatrix}, \tag{2}$$

where κ is the usual coupling constant, and γ is the shift in the propagation constant due to the presence of gain $(+\gamma)$ in the first waveguide, and an equal amount of losses $(-\gamma)$ in the second one. According to Ref. [10], as long as $\kappa/\gamma > 1$ the $\mathcal{PT}$-symmetry is unbroken and light is periodically exchanged between the two waveguides. On the other hand, $\mathcal{PT}$-symmetry is said to be broken when $\kappa/\gamma < 1$ and the light dynamics become exponentially growing in one waveguide and exponentially damping in the other one [10]. The directional coupler described by Eq. (2) fully implements a $\mathcal{PT}$-symmetric system, and it is realized according to the rule described in Ref. [17], namely to insert gain in one waveguide and losses in the other one in equal measure.

The same physical problem, however, can be obtained by exploiting only passive systems, and create a loss unbalance between the two waveguides instead of a gain and loss structure. To prove this, let us consider a directional coupler in which each waveguide experiences a different level of losses, and no gain is inserted in the system. The coupled mode equations governing this lossy coupler can be derived straightforwardly from Eq. (2) as follows:

$$i\frac{\mathrm{d}}{dz}\begin{pmatrix} a_1 \\ a_2 \end{pmatrix} = \begin{pmatrix} -i\gamma_1 & \kappa \\ \kappa & -i\gamma_2 \end{pmatrix}\begin{pmatrix} a_1 \\ a_2 \end{pmatrix}, \tag{3}$$

where $\gamma_{1,2}$ account for the losses in the first and second waveguide, respectively, and κ has been defined before as the coupling constant. Notice, that while in Eq. (2) the diagonal elements are equal in modulus but differ in sign, here $\gamma_1 \neq \gamma_2$ but the sign is the same. The sign discrepancy is due to the fact that while Eq. (2) describes a gain/loss system, Eq. (3) describes a system with losses only. Note, moreover, that since the diagonal elements of the matrix in Eq. (3) are purely imaginary, they cannot be removed via a simple phase transformation. To remove these diagonal terms, a suitable transformation of coordinates must be found, that brings Eq. (3) in a form which allows to apply a phase transformation to remove the diagonal terms, as it is done in standard Hermitian couple mode theory [18]. To do that, we can apply the so-called Wick rotation [19] to the system, namely we rotate the propagation axis by $\pi/2$ in the complex plane, thus switching from a real to a complex propagation direction.[1] We then define $\zeta = iz$ and substitute this Ansatz into Eq. (3), to obtain

$$-\frac{\mathrm{d}}{d\zeta}\begin{pmatrix} a_1 \\ a_2 \end{pmatrix} = \begin{pmatrix} -i\gamma_1 & \kappa \\ \kappa & -i\gamma_2 \end{pmatrix}\begin{pmatrix} a_1 \\ a_2 \end{pmatrix}. \tag{4}$$

We can now make the phase transformation $(a_1\ a_2)^T = (\tilde{a}_1\ \tilde{a}_2)^T e^{i\gamma_1\zeta}$, and then transform back to the real propagation axis z to obtain

$$i\frac{\mathrm{d}}{dz}\begin{pmatrix} \tilde{a}_1 \\ \tilde{a}_2 \end{pmatrix} = \begin{pmatrix} 0 & \kappa \\ \kappa & -i(\gamma_2 - \gamma_1) \end{pmatrix}\begin{pmatrix} \tilde{a}_1 \\ \tilde{a}_2 \end{pmatrix}. \tag{5}$$

Before proceeding with the analysis of Eq. (5), it is worth spending some words to describe the procedure that lead to Eq. (5). First, to restore the initial amplitudes $\tilde{a}_{1,2}(z)$ from the amplitudes in $a_{1,2}(\zeta)$ in the Wick frame, one needs to multiply the solutions of Eq. (5) by an exponentially damping factor $\exp(-\gamma_1 z)$. While theoretically this only accounts to a gauge transformation in Wick space, experimentally the presence of this extra damping term is not a problem, since once the amount of losses γ_1 is known, this term can be easily eliminated via post processing of the acquired image.

To study the dynamical properties of the system described by Eq. (5), let us calculate the eigenvalues of the Hamiltonian appearing in Eq. (5) and compare them with the ones from Eq. (2). If we call $\mu_{1,2}$ the eigenvalues of the $\mathcal{PT}$-symmetric system (Eq. (2)) and $\lambda_{1,2}$ the ones for the passive system (Eq. (5)), we have the following result:

$$\mu_{1,2} = \pm\sqrt{\kappa^2 - \gamma^2}, \tag{6a}$$

[1] This operation is quite common in quantum field theory (especially in lattice quantum field theory), where it is used to transform the Minkowski metric to an Euclidean one, allowing methods of statistical mechanics to be used for evaluating path integrals on a lattice [20].

$$\lambda_{1,2} = -i\left(\frac{\gamma_2 - \gamma_1}{2}\right) \pm \sqrt{\kappa^2 - \left(\frac{\gamma_2 - \gamma_1}{2}\right)^2}. \tag{6b}$$

If we now choose $\gamma_2 - \gamma_1 = 2\gamma$, where γ is the same value of gain/loss that appears in the $\mathcal{PT}$-symmetric case, then, apart from a common imaginary part (that will result in an exponential damping factor), the dynamics of the passive system is the same of the one of the $\mathcal{PT}$-symmetric case, as $\lambda_{1,2} = i\gamma + \mu_{1,2}$. This holds, provided that the losses of the system are chosen in such a way that $\gamma_2 - \gamma_1 = 2\gamma$. A comparison between the dynamics of a passive system as described by Eq. (5) and the correspondent $\mathcal{PT}$-case is depicted in Fig. 1 for unbroken $\mathcal{PT}$-symmetry, and in Fig. 2 for the broken $\mathcal{PT}$-symmetry case. It is worth noticing, that while below threshold (Fig. 1b) the presence of the exponential damping factor only affects the intensity of the light propagating in the quasi-$\mathcal{PT}$ system, above threshold (Fig. 2b), where the $\mathcal{PT}$-symmetry is broken, the behaviour of the quasi-$\mathcal{PT}$ and the $\mathcal{PT}$ system are profoundly different, and one needs to compensate for the overall damping factor dynamically by performing a z-dependent normalisation of the power evolution inside the system in order to restore the real $\mathcal{PT}$ dynamics.

Last, but not least, let us consider the dynamics in the passive system, for different values of the ratio κ/γ below threshold. As can be seen in Fig. 3, the equivalence between the dynamics is only trivial when $\kappa/\gamma \gg 1$ or, equivalently, $\gamma \ll 1$. In this case, a compensation of the losses in the system is not needed, as the amount of losses is small enough not to disturb the underlying $\mathcal{PT}$-like dynamics. If the losses increase, however, these dynamics start to get obscured by the high losses of the system, and an immediate correspondence between the two cases cannot be established anymore. This is also consistent with the fact that in systems with high losses the light trapped in the waveguides gets quickly absorbed or scattered away, and the characteristic length upon which the dynamics takes place is too small to allow any interesting dynamics to be seen.

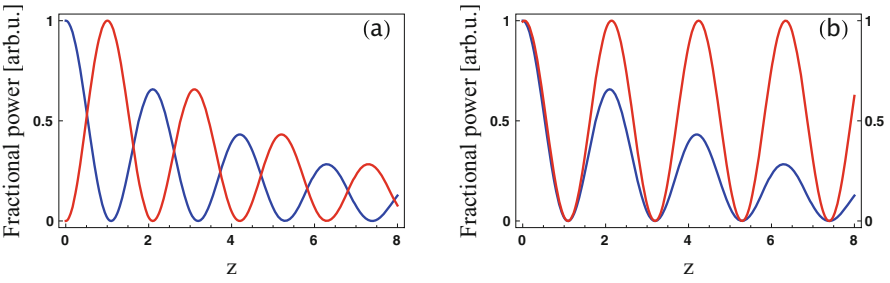

Fig. 1 (**a**) Evolution of the fractional powers $|\tilde{a}_1(z)|^2$ (blue line) and $|\tilde{a}_2(z)|^2$ (red line) for the unbroken quasi-$\mathcal{PT}$-symmetry with $\kappa/\gamma = 15$. (**b**) Comparison between the evolution in the unbroken $\mathcal{PT}$-symmetry regime ($\kappa/\gamma = 15$) of the fractional power for the quasi-$\mathcal{PT}$-symmetric system $|\tilde{a}_1(z)|^2$ (blue line) and the corespondent $\mathcal{PT}$-symmetric system (red line). As can be seen, apart from an exponential damping factor that progressively reduces the intensity along z, the dynamics in the two cases is identical

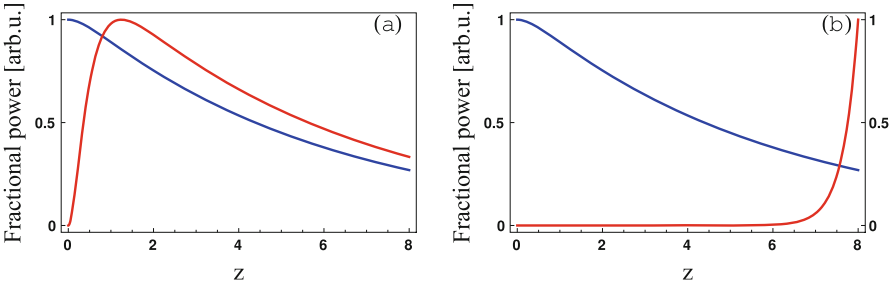

Fig. 2 (**a**) Evolution of the fractional powers $|\tilde{a}_1(z)|^2$ (blue line) and $|\tilde{a}_2(z)|^2$ (red line) for the broken quasi-$\mathcal{PT}$-symmetry with $\kappa/\gamma = 1/3$. (**b**) Comparison between the evolution in the broken $\mathcal{PT}$-symmetry regime ($\kappa/\gamma = 1/3$) of the fractional power for the quasi-$\mathcal{PT}$-symmetric system $|\tilde{a}_1(z)|^2$ (blue line) and the corespondent $\mathcal{PT}$-symmetric system (red line). As can be seen, above the $\mathcal{PT}$-threshold, the presence of the overall damping exponential term makes the dynamics of the quasi-$\mathcal{PT}$ system very different from its $\mathcal{PT}$-counterpart. However, if the exponentially damping term is compensated by a z-dependent power normalization, the two dynamics perfectly coincide

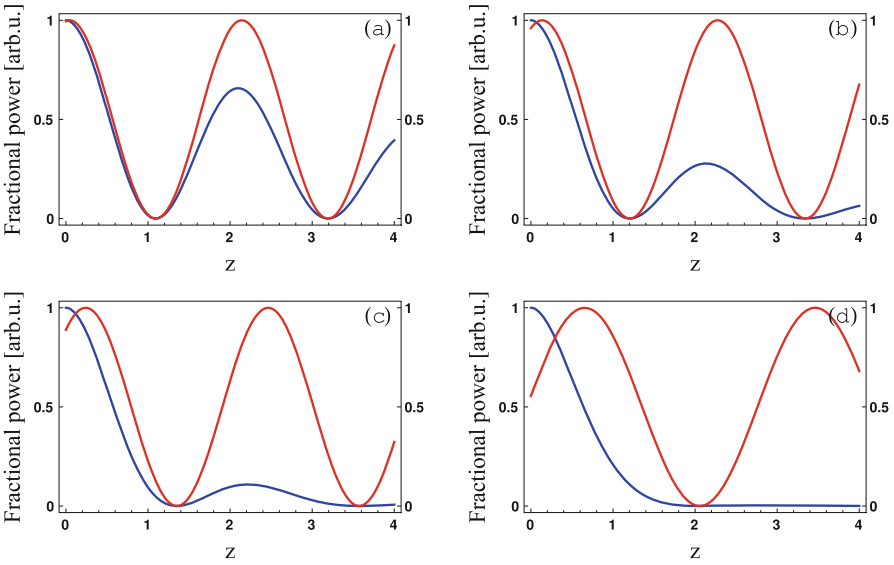

Fig. 3 Comparison of the dynamics of the evolution of the fractional power contained in the first waveguide for the quasi-$\mathcal{PT}$ system $|\tilde{a}_1(z)|^2$ (blue line) and its $\mathcal{PT}$-counterpart (red line) for different values of the losses in the system. For all these graphs, the value of the coupling coefficient is $\kappa = 1.5$. (**a**) $\gamma = 0.1$, (**b**) $\gamma = 0.3$, (**c**) $\gamma = 0.5$ and (**d**) $\gamma = 1$. As can be seen, as the losses increase, the discrepancy between the two curves also increases, and the main effect on the dynamics is that the quasi-$\mathcal{PT}$ system is no longer able to faithfully reproduce the dynamics of its $\mathcal{PT}$-counterpart. This is in particular visible in panels (**c**) and (**d**) where the period of the two curves is not matched

3 Fabrication and Characterisation Technology

3.1 Fabrication Technology

To realise experimentally passive $\mathcal{PT}$ structures in an efficient and controllable way, one can employ a commercially available Coherent Mira/RegA laser system, characterised by a wavelength of 800 nm, a pulse length of 150 fs (full width at half maximum), a repetition rate of 100 kHz, and an energy of approximately 300 nJ. These pulses are tightly focused into fused silica (Corning HPFS 7980) using a 20× microscope objective (NA = 0.35). As the focal spot has a diameter of a few microns, light intensity in the focal region is very high and field ionisation, as well as multiphoton absorption processes, occur. Together with onsetting avalanche ionization, recombination, and restructuring processes, this leads to a permanent modification of the material [21, 22]. In order to fabricate optical waveguides, the silica wafer is moved with respect to the focal spot using a Computer controlled positioning system (Aerotech).

A sketch of the femtosecond laser direct writing (FLDW) technique is shown in Fig. 4a. To tune the propagation constants of the modes of the individual

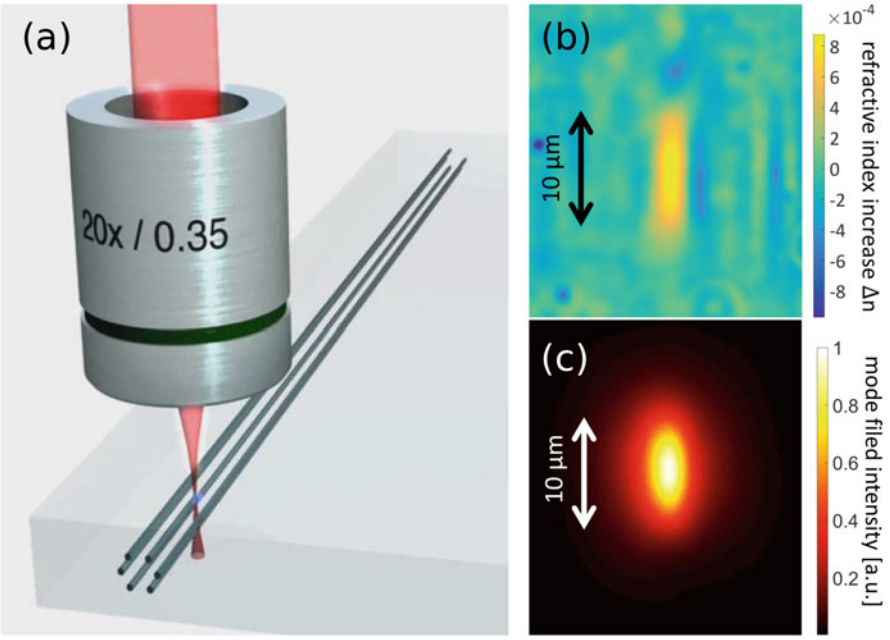

Fig. 4 (**a**) Scheme of the FLDW process. The laser is focused inside the glass sample which is continuously moved in order to fabricate elongated waveguides. (**b**) Transverse cross-section of a fs-LASER-written waveguide. (**c**) Transverse cross-section of the mode supported by the waveguide shown in (**b**)

waveguides, moreover, one can act on the writing speed, i.e., the velocity with which the glass wafer is moved with respect to the laser pulse. This is possible since the writing velocity determines the amount of energy deposited in the glass, and consequentially the refractive index increase. As the writing speed increases, in fact, less energy is deposited in the glass, and the refractive index contrast of the modified region is therefore reduced. A typical writing velocity of 100 mm/min, for example, results in a refractive index increase on the order of $\delta n = 5 \times 10^{-4}$.

Figure 4b displays that the cross section of the resulting waveguides is oval with dimensions of approximately $10 \times 4\,\mu\text{m}$. A comparison with the numerical simulation of the refractive index profile, obtained by numerical inversion of the Helmholtz Equation from the mode profile, is shown in Fig. 4c [23]. As a consequence of the oval cross section, the waveguides are not polarisation degenerate but rather support two linearly polarised eigenmodes. The coupling of these polarisation modes, however, are usually very small and can be therefore neglected.

3.2 Characterisation Technology

To characterise light dynamics in laser written waveguides, it is possible to use a fluorescence measurement technique [24–27], based on the fact that during the writing process, non-bridging oxygen hole color centers are created inside the waveguide region. For this to occur, fused silica with a high content of hydroxide needs to be used. Illuminating the waveguides with a HeNe laser at a wavelength of 633 nm results in an excitation of these color centers, which emit a fluorescence signal at a wavelength of 650 nm. While the excitation light is being guided along the waveguides the fluorescence is being emitted isotropically and can be observed with a CCD-camera from above the glass sample, as depicted in Fig. 5a. The fluorescence measurement technique therefore provides an image of the light evolution inside a waveguide array. An example of a recorded fluorescence image is depicted in Fig. 5b. In order to extract data from fluorescence images, all measured images are post processed numerically, using a dedicated algorithm, whose functioning can be better explained with an example. To do this, let us consider the situation depicted in Fig. 6a, which represents a raw fluorescence image. First, the two main sources of errors in this image, namely the misalignment of the sample and noise, must be individuated and minimised. To compensate for a misalignment of the sample, the figure is first rotated by an angle α.

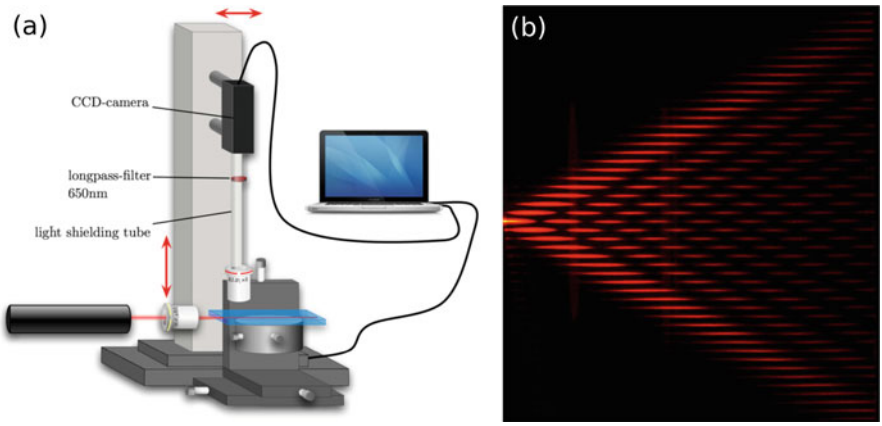

Fig. 5 (**a**) Fluorescence measurement setup. Glass chip with waveguides is being illuminated with a HeNe-laser and a 10×microscope objective. The CCD-camera mounted on a translation stage scans along the sample. The single images are stitched together at the PC after the scanning process. (**b**) Example of fluorescence image retrieved with the setup depicted in panel (**a**). The image refers to the propagation of light in a ballistic array in the single waveguide excitation scheme

The optimal value of the rotation angle is found by calculating $\max_{\alpha}\left[\max_{j}\sum_{l} I_{jl}(\alpha)\right]$, where I_{jl} is the intensity at row j and column l of the fluorescence image, and α is the rotation angle. Figure 6b shows the maximum column sum of (a) as a function of α. Here, the maximum is found at $\alpha_0 = -0.104$, showing that the raw data was rotated by a slight angle. The original image is therefore rotated by α_0 to compensate this error, and the new image is depicted in Fig. 6c. At this point, the image is ready for the noise reducing part of the algorithm. The image is then filtered in both its transverse and longitudinal dimensions. In the transverse direction, the shape of the transverse mode of the waveguide is used as a filter. To approximate this shape, the aligned image is averaged over all columns. From this, the normalised mode profile can be retrieved, as shown in Fig. 6d. Moreover, the averaging procedure yields the central position of the waveguide as well – corresponding to row j_0 in Fig. 6c. Figure 6e shows the filtered image, when the profile depicted in Fig. 6d was used as a transverse filter. The mode amplitude, shown in Fig. 6f, is finally retrieved from (e) by extracting the row j_0. To estimate the noise level in (e), the average signal outside of the waveguide region is calculated. This value is finally subtracted from (f).

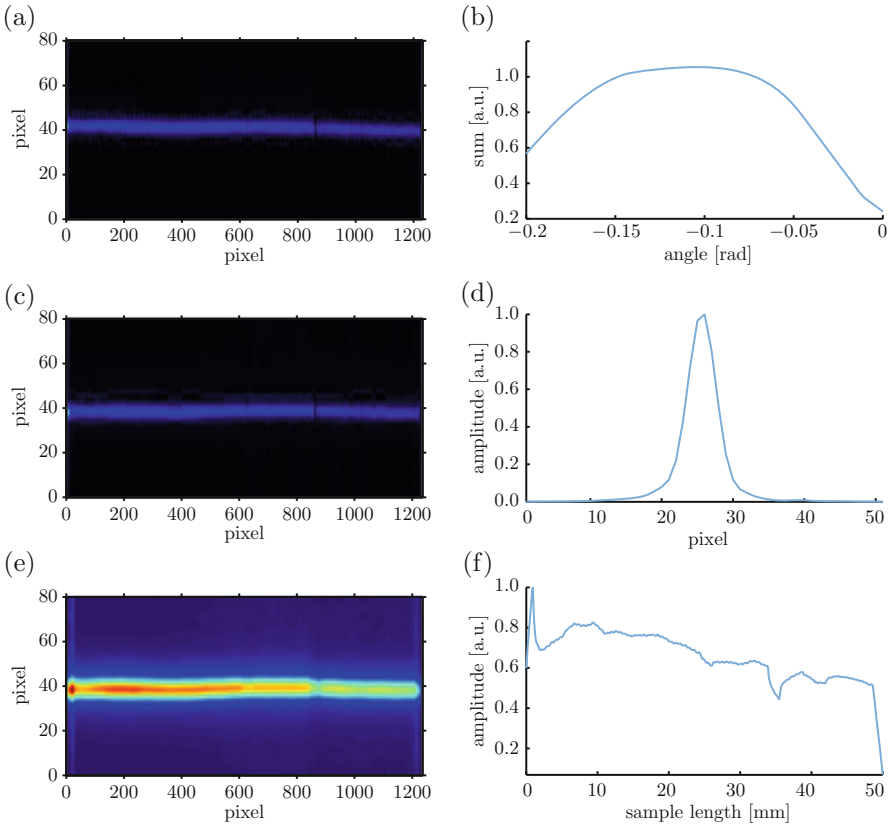

Fig. 6 (**a**) Raw fluorescence image. (**b**) Maximum row sum as a function of rotation angle. (**c**) Rotated image, where the rotation angle is obtained from (**b**). (**d**) Approximated mode profile. Obtained by summing over the rows of (**c**). (**e**) Filtered image, where fig. (**c**) Was horizontally averaged and vertically filtered using the normalised profile given by fig. (**d**). (**f**) Mode amplitude extracted from (**e**)

4 Realising Controllable Losses in Laser-Written Waveguide Structures

In this section, we concentrate our attention on the problem of introducing controllable losses in an optical system. Here, we discuss in detail the case of a sinusoidally modulated single mode waveguide, which we take as prototype model of controllable losses in a waveguiding system. At the end of the section, a suitable generalisation to the of an array of lossy waveguides will also be presented. This will serve as introduction for the study of transport properties in non-Hermitian lattices, which will be the subject of the next session.

4.1 Theoretical Modelling of a Sinusoidally Modulated Waveguide

We consider a single, one-dimensional waveguide with a sinusoidally modulated propagation direction, which can be represented by the following 1D, adimensional, Schrödinger equation with a sinusoidally oscillating step-index potential

$$i\frac{\partial\psi}{\partial z} = -\frac{\partial^2\psi}{\partial x^2} - \Delta n(x - x_0(z))\psi, \tag{7}$$

where

$$x_0 = d\left[1 - \cos\left(\frac{2\pi}{p}z\right)\right], \tag{8}$$

is the sinusoidal bending profile of the waveguide, characterised by an amplitude d and a period p (or, equivalently, by a bending frequency $\nu = 2\pi/p$). For the sake of simplicity, and to guarantee the existence of a simple analytical solution to Eq. (7), we choose $\Delta n(x)$ to be a step-index potential, namely

$$\Delta n = \begin{cases} \delta n_{max} & , \ |x - x_0(z)| < a \\ 0 & , \ \text{elsewhere} \end{cases} \tag{9}$$

where δn_{max} is the maximum refractive index change, and a is the width of the waveguide.[2] If we now apply a Kramers-Henneberger transformation [28, 29] $X = x - x_0(z)$ to switch to a reference frame co-moving with the waveguide bending, we can write Eq. (7) in the following, modified, form[3]:

$$i\frac{\partial\psi}{\partial z} = -\frac{\partial^2\psi}{\partial X^2} - \left[\Delta n(X) + i\nu d\sin(\nu z)\frac{\partial}{\partial X}\right]\psi. \tag{10}$$

The above equation can be solved perturbatively, assuming the amplitude d of the sinusoidal bending to be a small perturbation parameter and expanding the solution ψ in terms of the modes of the unperturbed (straight) waveguide, obtained from the equation above in the limit where $d = 0$. Under these assumptions, we write the field amplitude ψ as superposition of bound and radiation modes as follows

$$\psi(X, z) = c_b(z)u_b(X)e^{i\beta_b z} + \sum_{k=\{a,s\}}\int_0^\infty d\beta_k\, c_k(z)u_k(X)e^{i\beta_k z}, \tag{11}$$

[2]The results presented in this section, although specific to the case of a step-index potential, are valid for any arbitrary (but well defined) refractive index distribution, as it will be discussed at the end of this paragraph.

[3]Notice, that Eq. (10) differs slightly from the one obtained by applying the Kramers-Henneberger transformation, since the extra term appearing in Eq. (10) should be of the form $\nu^2 d\cos(\nu Z)\psi$ instead of $i\nu d\sin(\nu z)\partial\psi/\partial X$. Here, we choose this second form, since it offers a better way to calculate the losses of the system analytically. However, it is not difficult to prove that both versions of the transformed equation lead to equivalent results.

where $u_k(X)$ are the eigenmodes of the straight waveguide (for which the orthogonality relation $\int dX\, u_k^*(X)u_j(X) = \delta_{kj}$ holds), and we assumed, without loss of generality, that the waveguide sustains a single bound mode, with amplitude $c_b(z)$, and we have divided the radiation modes into the symmetric (with amplitude $c_s(z)$) and anti-symmetric (with amplitude $c_a(z)$) ones for later convenience. Inserting the above equation into Eq. (10) and projecting onto each single eigenmode then gives the following set of coupled mode equations:

$$\dot{c}_b(z) = \nu d \sin(\nu z) \int_0^\infty d\beta_a c_a(z)\xi_{ab}(\beta_{ab})e^{i\beta_{ab}z}, \tag{12a}$$

$$\dot{c}_s(z) = \nu d \sin(\nu z) \int_0^\infty d\beta_a c_a(z)\xi_{sa}(\beta_{as})e^{i\beta_{as}z}, \tag{12b}$$

$$\dot{c}_a(z) = \nu d \sin(\nu z) \left[c_b\xi_{ab}e^{i\beta_{ab}z} + \int_0^\infty d\beta_s c_s(z)\xi_{as}(\beta_{as})e^{i\beta_{sa}z} \right], \tag{12c}$$

where the dot denotes derivative with respect to z, $\beta_{mn} = \beta_m - \beta_n$ is the propagation constant mismatch between modes n and m, and the quantity $\xi_{mn}(\beta_{mn}) = \langle u_m|\partial/\partial X|u_n\rangle/\langle u_n|u_m\rangle$ corresponds to the (normalised) expectation value of the differential operator $\partial/\partial X$ over the modes of the straight coupler. In the remaining part of this section, we will prove that the evolution of light inside a sinusoidally bent waveguide follows an exponentially decaying law, i.e., $c_b(z) \propto \exp[-\Gamma z]$. To do so, we first notice that the equations for $c_{a,s}(z)$ can be formally solved using as initial conditions the fact that all light is initially confined in the bound state of the waveguide, namely $c_b(0) = 1$, and $c_a(0) = c_s(0) = 0$. This gives

$$c_s(z) = \nu d \int_0^z d\zeta\ \sin(\nu\zeta) \int_0^\infty d\beta_a\, \xi_{sa}(\beta_{sa})e^{i\beta_{as}\zeta}, \tag{13}$$

$$c_a(z) = \nu d \int_0^z d\zeta\ \sin(\nu\zeta) \left[c_b(\zeta)\xi_{ab}(\beta_{ab})e^{i\beta_{ab}\zeta} + \int_0^\infty d\beta_s\, c_s(\zeta)\xi_{as}(\beta_{as})e^{i\beta_{sa}\zeta} \right]. \tag{14}$$

Substituting these results into the first of Eqs. (12) allows us to write an integro-differential equation for the amplitude $c_b(z)$ of the waveguide bound mode, namely

$$\dot{c}_b(z) = \nu^2 d^2 \sin(\nu z) \int_0^\infty d\beta_a \int_0^z d\zeta\ \sin(\nu\zeta) \Big[c_b(\zeta)\xi_{ab}(\beta_{ab})\xi_{ba}(\beta_{ba})e^{i\beta_{ab}\zeta} + \int_0^\infty d\beta_s\, c_s(\zeta)\xi_{as}(\beta_{as})\xi_{ba}(\beta_{ba})e^{i(\beta_{sa}+\beta_{ab})\zeta} \Big]. \tag{15}$$

A closer inspection on the above equation reveals that the first term on its right-hand-side is quadratic in νd and depends only on the amplitude $c_b(z)$ of the bound mode, while the second term contains also a dependence on the symmetric part of the radiation mode $c_s(z)$. We can eliminate the dependence on $c_s(z)$ by using Eq. (13) again. If we do so, the second term in the above equation will result in a term proportional to $\nu^4 d^4$, which will contain only $c_b(z)$, plus some other terms that

will still depend on $c_s(z)$. Repeating this process ad libitum will result in a power series expansion (with respect to νd) of the right-hand-side of Eq. (15), namely

$$\dot{c}_b(z) = \sin(\nu z) \sum_{k=1}^{\infty} \left[\nu^2 d^2 \int_0^z d\zeta \int_0^{\infty} d\beta_a \, \sin(\nu\zeta)\, c_b(\zeta) \mathcal{K}_{ab}(\beta_a) e^{i(\beta_{ba}\zeta + \beta_{ab} z)} \right]^k, \tag{16}$$

where $\mathcal{K}_{ab}(\beta_a) = \xi_{ab}(\beta_{ab})\xi_{ba}(\beta_{ba})$. Notice, that the above result is, in the framework of coupled mode theory, *exact*. However, without loss of generality, and since we want to obtain a perturbative solution, we can assume that $\nu d \ll 1$ and neglect terms $\mathcal{O}(\nu^4 d^4)$ in the above equation.

From an experimental point of view, the assumption $\nu d \ll 1$ means, that both the amplitude and the frequency of the sinusoidal modulation needs to be small. While choosing a small amplitude d is not a big problem experimentally, realising modulated waveguides with small frequency (i.e., large period of the oscillations) can be a challenging task. In the simple case of a directional coupler, in fact, the coupling strength defines the longitudinal dimension. To implement homogeneous losses in such a system, therefore, one should choose an oscillation period of the modulation, which is smaller than the coupling length. This, ultimately, constitutes a limitation in the choice of "small frequency" of the modulation, in order to satisfy the constraint $\nu d \ll 1$. The validity of this approximation can be tested by comparing the evolution of $c_b(z)$ as given by Eq. (16) with the exact solution obtained by numerically integrating Eqs. (12). As can be seen from Fig. 7, the approximation that we used to arrive at Eq. (16) holds very well. The fact that this approximation holds, moreover, represents the fact that the contribution of the symmetric radiation modes can be neglected.

To find an explicit analytical solution to Eq. (16), we first have to calculate the kernel $\mathcal{K}_{ab}(\beta_a)$. Since we have assumed a step-index waveguide, we can analytically calculate the mode $u_b(X)$ [18] and therefore write the kernel as

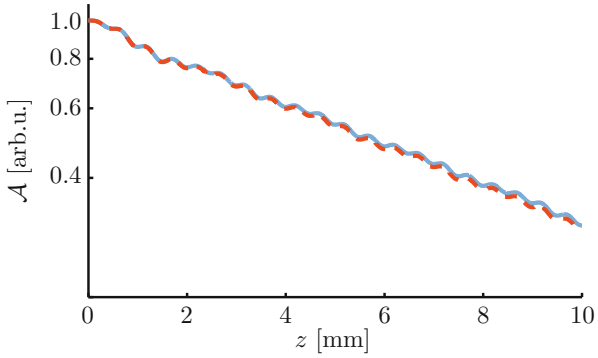

Fig. 7 Amplitude of the bound mode, as calculated by numerically integrating Eqs. (12) (blue line) and calculated using Eq. (16) with only first order terms in $\nu^2 d^2$ (red line). As can be seen, the approximation made to obtain Eq. (16) holds very good. To realise this figure, an oscillation period of 1 mm was assumed

$\mathcal{K}_{ab}(\beta_a) = \alpha S(\beta_a)$, where

$$\alpha = \left[\frac{2\delta n^2(\beta_b + \delta n)}{\pi}\right] \frac{k_2 \cos^2(k_1 a)}{\delta n \cos^2(k_1 a) + (\beta_b + \delta n) k_2 a}, \tag{17}$$

and

$$S(\beta_a) = \left[\frac{1}{(\beta_a - \beta_b)^2}\right] \frac{k_2 \sin^2(k_1 a)}{\beta_a + \delta n \cos^2(k_1 a)}, \tag{18}$$

where $k_{1,2} = k_{1,2}(\beta)$ are the propagation constants inside the waveguide ($k_1 = \sqrt{\beta + \delta n_{max}}$) and outside the waveguide ($k_2 = \sqrt{\beta}$), respectively. With this at hand, we can rewrite the leading term of Eq. (16) as follows:

$$\dot{c}_b(z) = -\alpha \nu^2 d^2 \sin(\nu z) \int_0^z d\zeta \, \sin[\nu(z-\zeta)] c_b(z-\zeta) \int_0^\infty d\beta_a S(\beta_a) e^{i\beta_{ab}\zeta}, \tag{19}$$

where we have used the fact that $\beta_{ab} = -\beta_{ba}$ and employed the change of variables $\zeta' = z - \zeta$ (and renamed $\zeta' \to \zeta$ afterwards for the sake of clarity). The β_a-integral can be calculated numerically as a function of ζ. By doing so, one realises that this integral is nonzero only in a small interval $0 < \zeta < \zeta_c$, and that in this interval, the amplitude of the bound mode $c_b(\zeta)$ is slowly varying, and can then be regarded as constant, i.e., $c_b(z - \zeta) \simeq c_b(z)$. Under this approximation (which is known in literature as Markovian approximation [30]), we can then extend the integration domain of the ζ-integral from $[0, z]$ to $[0, \infty]$ and solve it explicitly using Cauchy theorem [31], thus obtaining

$$\dot{c}_b(z) = -\alpha \nu^2 d^2 \left[\sin^2(\nu z)\mathcal{T}(\beta_b, \nu) + \frac{1}{2}\sin(2\nu z)\mathcal{U}(\beta_b, \nu)\right] c_b(z), \tag{20}$$

where $\mathcal{T}(\beta_b, \nu)$ and $\mathcal{U}(\beta_b, \nu)$ are z-independent quantities, whose explicit expression is given as follows[4]:

$$\mathcal{T}(\beta_b, \nu) = \frac{\pi}{2}\tilde{S}(\beta_b + \nu) - i\mathcal{P}\int_0^\infty d\beta_a \frac{\beta_{ab}}{\beta_{ab}^2 - \nu^2} S(\beta_a), \tag{21a}$$

$$\mathcal{U}(\beta_b, \nu) = i\frac{\pi}{2}\tilde{S}(\beta_b + \nu) + \mathcal{P}\int_0^\infty d\beta_a \frac{\nu}{\beta_{ab}^2 - \nu^2} S(\beta_a), \tag{21b}$$

where $\tilde{S}(\beta_b + \nu) = S(\beta_b + \nu)$ for $\nu \geq |\beta_b|$, and $\tilde{S}(\beta_b + \nu) = 0$ elsewhere, and $\mathcal{P}$ stands for the Cauchy principal value. One last integration with respect to

[4]Notice that, in defining the functions $\mathcal{T}(\beta_b, \nu)$ and $\mathcal{U}(\beta_b, \nu)$, we have neglected a term proportional to $\delta(\beta_a - \beta_b + \nu)$, since it accounts for an off-resonance term.

z yields then the final solution for the amplitude of the bound mode of an oscillating waveguide, which reads

$$c_b(z) = e^{-(\Gamma + i\Phi)z} e^{-\left[\chi \cos^2(\nu z) - \nu\Gamma \sin(2\nu z)\right] - i\left[\eta \cos^2(\nu z) - \nu\Phi \sin(2\nu z)\right]}, \tag{22}$$

where we have defined

$$\Phi = \left(\frac{\alpha\nu^2 d^2}{2}\right) \mathrm{Im}\{\mathcal{T}(\beta_b, \nu)\} = -\left(\frac{\alpha\nu^2 d^2}{2}\right) \mathcal{P} \int_0^\infty d\beta_a \, \frac{\beta_{ab}}{\beta_{ab}^2 - \nu^2}, \tag{23a}$$

$$\Gamma = \left(\frac{\alpha\nu^2 d^2}{2}\right) \mathrm{Re}\{\mathcal{T}(\beta_b, \nu)\} = \left(\frac{\pi\alpha\nu^2 d^2}{4}\right) \tilde{S}(\beta_b + \nu), \tag{23b}$$

$$\chi = \left(\frac{\alpha\nu d^2}{2}\right) \mathrm{Im}\{\mathcal{U}(\beta_b, \nu)\} = \left(\frac{\pi\alpha\nu d^2}{4}\right) \tilde{S}(\beta_b + \nu), \tag{23c}$$

$$\eta = \left(\frac{\alpha\nu d^2}{2}\right) \mathrm{Re}\{\mathcal{U}(\beta_b, \nu)\} = \left(\frac{\alpha\nu d^2}{2}\right) \mathcal{P} \int_0^\infty d\beta_a \, \frac{\nu}{\beta_{ab}^2 - \nu^2} S(\beta_a). \tag{23d}$$

A closer inspection of the above equation reveals that the second exponential only accounts for an amplitude modulation, proportional to χ and Γ, and a complex oscillating z-dependent term, which accounts for a phase modulation proportional to η and Φ. These oscillations, however, are very small and can be therefore neglected, especially in the long term evolutions, as Fig. 8 shows. If we neglect the contribution of the second exponential, we can then write the solution as follows:

$$c_b(z) \simeq e^{-\Gamma z} e^{-i\Phi z} \simeq e^{-\Gamma z}. \tag{24}$$

We have then proved, that the amplitude of the bound mode of a sinusoidally modulated waveguide decays exponentially along the propagation direction, with a decay rate, for the case of a step-index waveguide, given by

$$\Gamma = \left(\frac{\pi\alpha a^2}{4}\right) \frac{k_2 \sin^2(k_1 a)}{\beta_b + \nu + \delta n \cos^2(k_1 a)}, \tag{25}$$

for $\nu \geq |\beta_b|$, and $\Gamma = 0$ otherwise. As can be seen in Fig. 9, this result is in very good agreement with the rigorous result obtained by fully simulating the propagation of light in a bent waveguide using Eq. (10). In particular, one can see how both approaches predict a zero decay rate for large bending periods, i.e., for modulation frequencies smaller than β_b. This behavior can be well understood using the following simple argument: to transfer energy from a bound state of the waveguide (with propagation constant β_b) to a mode in the continuum, one need a perturbation with a modulation frequency $\nu \geq |\beta_b|$. If such perturbation has less energy than $\lambda|\beta_b|$, therefore, the bound mode cannot couple with any mode in the continuum, and it therefore does not decay.

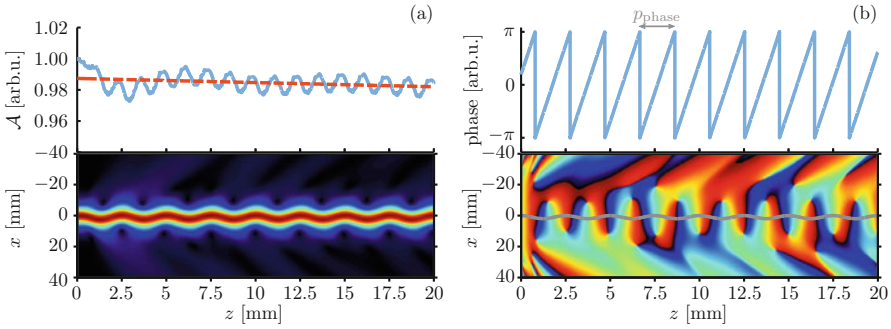

Fig. 8 (**a**) Bottom: Light evolution (amplitude) for sinusoidally bent waveguide with an oscillation period of 1 mm. Top: Amplitude of the light field at the center of the waveguide as a function of propagation distance (blue solid line). The red dashed line corresponds to an exponential decay with a decay rate of 1.16×10^{-1} mm^{-1}. (**b**) Bottom: Phase evolution corresponding to (**a**). Top: Phase at the center of the waveguide. The period length is $p_{\text{phase}} = 2.05$ mm. For these simulations, a refractive index profile corresponding to a super-Gaussian function of order 16, rather than a box function, was employed, to better represent the actual physical refractive index profile generated by the laser-writing technique. The parameters used for this simulations are $\lambda = 633$ nm, $\delta n_{max} = 6 \times 10^{-4}$, and $w_0 = 3/x_0 = 50.71$, where $x_0 = 0.0592$ μm has been assumed. Simulations with the same parameters for the case of a straight waveguide (i.e., $x_0(z) = 0$) leads to a beating period $\Lambda = 1.98$ mm, which corresponds to a propagation constant $\beta = 3.17$ mm^{-1}

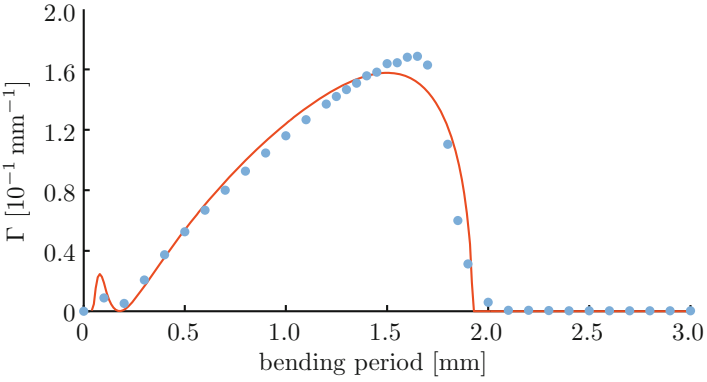

Fig. 9 Exponential decay rate Γ as a function of the waveguide bending period $p = \nu^{-1}$. The solid, red line is the analytical solution as given by Eq. (25), while the dotted, blue line represents the rigorous solution obtained by direct numerical simulation of Eq. (10)

Before proceeding any further, it is worth spending some words on the physical meaning of Eq. (25). Let us firstly recall, that the function $\tilde{S}(\beta_a)$ appearing in the definition of Γ represents the overlap integral between the perturbed bound mode and a given antisymmetric radiation mode. The fact that $\tilde{S}(\beta_b + \nu) = 0$ for $\nu < |\beta_b|$, moreover, represents the fact that only one of the antisymmetric radiation modes is relevant for the dynamics. This means that the coupling takes place only if a certain

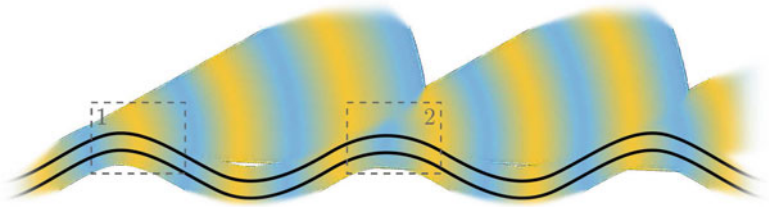

Fig. 10 Schematic illustration of light being radiated away from sinusoidally bent waveguides. In regions 1 and 2 (dashed boxes) light is being emitted and reabsorbed. Light cones from subsequent emission regions overlap and interfere

phase matching condition is met. Even though the bound mode of the waveguide couples with the entire spectrum of antisymmetric radiation modes, there is only one propagation constant $\beta_a = \beta_b + \nu$ for which the light scattered into this mode accumulates constructively during a series of oscillation cycles with period $2\pi/\nu$. To understand this from a qualitative perspective, let us consider the situation depicted in Fig. 10. Light is radiated away from the waveguide at those points, where the curvature of the waveguide is maximal (dashed areas in Fig. 10). The angle $\theta = \sqrt{\beta_b + \nu}/k$ under which this happens, however, is very small, and therefore part of the light radiated away from region 1 in Fig. 10 can re-enter the waveguide at a later position along the propagation axis, say, for example, in region 2. Moreover, the light cones corresponding to radiated light at the maximum bending strongly overlap, thus allowing interference. Depending on the relative phase difference between the light that is been scattered away and the one that is being re-coupled in the waveguide, the net power scattered away from the waveguide can be then either amplified or suppressed.

4.1.1 High Frequency Regime

The result obtained in the previous section is limited to the case of small modulation frequencies ν, such that $\nu d \ll 1$ is fulfilled. In this section, we investigate what happens in the regime of high modulation frequencies, when the approximation $\nu d \ll 1$ does not hold anymore. To do so, we consider again Eq. (7), and we decompose the field amplitude $\psi(x, z)$ in Fourier-components with respect to z as

$$\psi(z) = \int d\beta \, \Psi(\beta) e^{i\beta z} \tag{26}$$

If we assume that the spectral width of $\Psi(\beta)$ is band-limited and there exists a maximum frequency $\beta_{\max}$, for which one has that $A(\beta) \approx 0$ when $|\beta| > |\beta_{\max}|$, then one can find a small longitudinal interval Z with $Z \ll 2/\beta_{max}$, such that

$$\langle \psi(z) \rangle_z = \frac{1}{Z} \int_{z-\frac{Z}{2}}^{z+\frac{Z}{2}} \psi(z')\, dz' \equiv \psi(z)\,. \tag{27}$$

To achieve this result, one can exchange the β-integration coming from the Fourier transform and the z-averaging and then calculate the average for each Fourier component separately. If we apply this averaging process to Eq. (7), we then get

$$i\frac{\partial}{\partial_z}\psi = -\partial_z^2\psi + \langle \Delta n \rangle_z(z)\,\psi \tag{28}$$

where $\langle \partial_z \psi \rangle_z = \partial_z \langle \psi \rangle_z$, and $\langle \delta n \psi \rangle_z = \langle \delta n \rangle_z \psi$ has been used. If the frequency ν with which the potential Δn is oscillating is much larger than $2\pi/Z$, then the mean potential $\langle \Delta n \rangle_z$ is constant along the longitudinal axis. As a consequence, in this high frequency limit the field amplitude ψ only feels a constant potential along the z-direction. In general, however, the shape of the potential changes due to the averaging procedure. Moreover, in general one has that $\langle \Delta n \rangle_z \neq \Delta n \left(x - \langle x_0(z) \rangle_z\right)$. If such an averaged potential is excited with its own bound mode, then, in the high frequency limit the evolution is stationary and $\psi(x, z) = \Phi(x, z) \exp[i\beta_b z]$. In this case, $\beta_{\max}$ can be identified with β_b, and the condition $\beta_b \ll 2/Z < 2\pi/Z \ll \nu$ determines the validity of the high frequency approximation, for which the loss of the bound mode is identically zero, as correctly predicted by numerical simulations shown in Fig. 9.

4.2 Experimental Realisation of Well-Controllable Loss

In this section, we present some experimental results on the realisation of waveguides with well-controllable losses. The main experimental interest resides in obtaining a loss profile $\Gamma(\nu)$ as a function of the bending period, as the one depicted in Fig. 9, which can be then experimentally used, once the geometry of the waveguide (namely, the waveguide width a and the refractive index contrast $\delta n_{\max}$) is fixed, to engineer the amount of losses in the waveguide. To this aim, let us consider as an explicit example, the case of a single 50 mm-long waveguide, fabricated with the laser-writing technique described in Sect. 3.1, whose propagation direction has been bent sinusoidally, with amplitude $d = 1.45\,\mu\text{m}$ and bending period $p = 3.9\,\text{mm}$. The fluorescence image acquired from this waveguide sample is reported in Fig. 11a. The extracted evolution of light amplitude as a function of the (logarithmically scaled) propagation distance is shown in Fig. 11b. After a propagation distance of 12 mm, the graph clearly shows a linear slope, indicating the exponential decay of the light intensity. In this particular example, a measure of the slope gives $\Gamma = -0.42\,\text{cm}^{-1}$ as value for the losses experienced by the bound mode of the waveguide. Initially, for propagation distances smaller

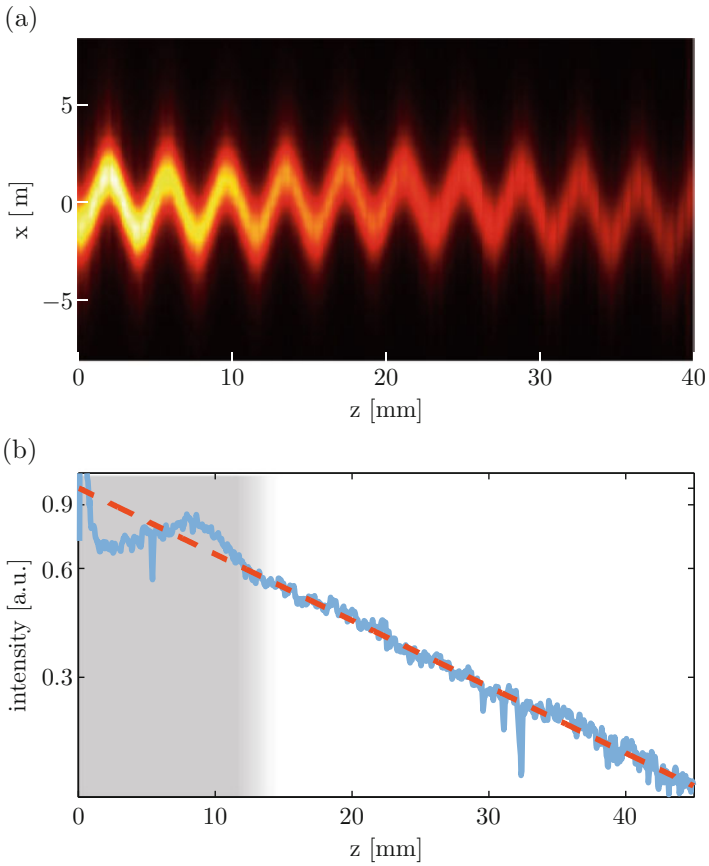

Fig. 11 (**a**) Fluorescence image of a sinusoidally bent waveguide with an oscillation period of $p = 3.9\,\text{mm}$. (**b**) Light intensity extracted from a sinusoidally bent waveguide with a period of $p = 3.9\,\text{mm}$

than 12 mm, the behaviour strongly deviates from an exponential decay. This can be attributed to coupling the free-space laser beam into the glass chip using a microscope objective. As a consequence, therefore, the region $z < 12\,\text{mm}$ can be neglected when evaluating the evolution of light in such a waveguide. Theory and simulations, moreover, not only predict an exponential decay, which is corroborated by the experimental measurements shown in Fig. 11, but also periodic amplitude oscillations. In the measurement data shown in Fig. 11b, however, these oscillations are in the same order of magnitude as the noise level, and therefore not observable.

To obtain experimentally the dependence of the losses $\Gamma(\nu)$ from the bending frequency, one needs to fabricate samples with different period lengths. To each point in Fig. 9, in fact, it corresponds a different waveguide structure.

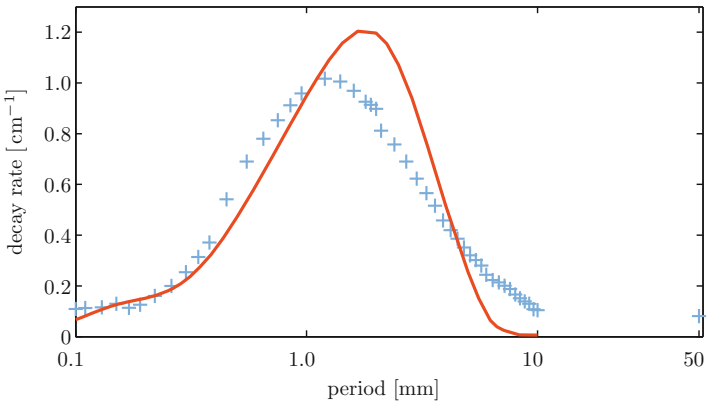

Fig. 12 Experimentally measured intensity decay rate (blue crosses) and decay rate extracted from 2D simulations (red line)

Figure 12 contains the extracted decay rates for different realisations of a sinusoidally bent waveguide, with periods ranging from 100 µm to 50 mm. For large periods, e.g. 50 mm, the experimentally measured decay rate $\Gamma = 0.08\,\mathrm{cm}^{-1}$ differs only minimally from the intrinsic decay of straight waveguides. This behaviour continues for period lengths down to 10 mm, for which the decay only increases by 20% with respect to the intrinsic losses. However, as one moves to smaller periods, a pronounced frequency dependence of the bending-induced decay can be observed (period lengths between 200 µm and 10 mm). The maximum loss $\Gamma_{max} = 1.0\,\mathrm{cm}^{-1}$, is achieved at a period length of $p_{max} = 1.2$ mm. Here, the decay exceeds the intrinsic loss by over an order of magnitude. As it can be seen, the experimentally measured decay rates $\Gamma(\nu)$ agree very well with the theoretical prediction illustrated in Fig. 9. In particular, both graphs show negligible decay for small and large periods, respectively, and exhibit a single pronounced maximum in the range of a few mm of period length.

The sudden drop of $\Gamma(\nu)$ to zero, predicted theoretically to occur around period lengths of the order of 2 mm, however, cannot be confirmed by the measurements. This can be attributed to the dimensionality of the problem; the experimentally realised waveguides, in fact, possesses a two dimensional cross section, whereas the theoretical model is based on a single transverse dimension. If we include these effects in the simulations (red, solid line in Fig. 12), in fact, we are able to predict the same, gradual drop of $\Gamma(\nu)$ shown by the experimental data. This gradual drop, as opposed to the sudden one seen in Fig. 9, originates from the fact that in a 2D environment, the condition of perfect phase matching between the bound mode and a *single* radiation mode is relaxed, as phase matching can be fulfilled by a collection of radiation modes with different transverse momenta.

4.3 Extension to Lossy Waveguide Arrays

In the previous sections, we have considered only the dynamics of a single lossy waveguide. With the same line of reasoning, however, one could also extend the validity of the results given above for the case of an array of lossy waveguides. To do so, let us consider again Eq. (7), where now we use as refractive index profile a discrete superposition of individual lossy waveguides, i.e., $\Delta n(x) = \sum_k \Delta n_k(x)$ (with $\Delta n_k \in \mathbb{C}$, since each single waveguide experiences losses), such that each waveguide supports, when isolated, a single bound mode with $\psi_k = \Phi_k(x) \exp[i\beta_k z]$, where $u_k(x)$ is the mode profile of the k-th waveguide, and β_k its corresponding propagation constant. According to the results obtained in the previous section, the light amplitude decays exponentially in each waveguide. This allows us to write the field in each waveguide as $\psi(x, z) = \sum_k a_k(z) \exp[-\gamma_k z]\psi_k(x, z)$. Substituting this Ansatz into Eq. (7) and using the orthogonality of the transverse modes, i.e., $\langle u_k | u_\ell \rangle = \delta_{k\ell}$, yields the following set of coupled equations for dissipative media

$$i\dot{a}_k = i\gamma_k a_k + C_{k+} a_{k+1} + C_{k-} a_{k-1}, \tag{29}$$

where γ_k are the total loss of each waveguide, and $C_{k\pm}$ are the coupling constants relating the amplitude of the mode in waveguide k, with its two left $(-)$ and right $(+)$ neighbours. For a homogeneous, non-dissipative array, it is not difficult to show that from the conservation of energy, it follows that the coupling constants must all be equal and represented by real numbers [18]. In the case of a homogeneous, dissipative array, on the other hand, although the homogeneity of the array still forces all coupling constants to be equal, these are no longer limited to be real numbers, as no energy conservation condition needs to be applied. Therefore, the coupling constants are, in this case, complex-valued. Hence, the phase of the coupling terms depends on the separation between neighbouring waveguides. This peculiar behaviour, ultimately, is due to the curved, rather than flat, phase front of the lossy waveguide mode. Moreover, as expected from the Hermitian case, the amplitude of the coupling decreases exponentially, whereas its phase increases linearly with the waveguide separation d. As a direct consequence of this, there exists a particular distance for which the coupling constant is purely imaginary. Equivalently, there exists a larger distance at which the coupling is real again, but negative. A rigorous calculation of the coupling constant leads in fact to the following result [32]:

$$C = \frac{\langle u_{k\pm1} | \Delta n_k | u_k \rangle}{\langle u_k | u_k \rangle} \approx e^{-\rho'' d} e^{-i\rho' d}, \tag{30}$$

where ρ' and ρ'' are suitable constants, that depend on the particular problem. From the above result, moreover, we conclude that the dissipative nature of a waveguide does not only manifest itself in a pure amplitude decay rate, as it is the case for

an isolated waveguide discussed in the previous sections, but it also influences the coupling between different waveguides, as they are brought together in an array.

5 Transport in Non-Hermitian Lattices

5.1 *Theoretical Modelling of Transport Properties in Non-Hermitian Lattices*

In this section, we apply the theory developed in Sects. 2 and 4, to study transport properties in non-Hermitian lattices. The model system that we will study here consists of a biatomic lattice, as the one depicted in Fig. 13. The evolution of the on-site amplitudes $a_n(z)$ and $b_n(z)$ can be described by the following, two component, coupled mode equations

$$i\dot{a}_n = (\omega_a + i\Gamma_a)\, a_n + C_i b_n + C_0 b_{n-1}, \tag{31a}$$

$$i\dot{b}_n = (\omega_b + i\Gamma_b)\, b_n + C_i a_n + C_0 a_{n+1}, \tag{31b}$$

where the dot indicates derivation with respect to the adimensional propagation distance ζ, ω_k and Γ_k are the eigenfrequency and decay rate of the two lattice sites, C_i is the intra-site coupling, and C_0 is the inter-site coupling. Introducing the Bloch-Ansatz $(a_{n+1}\ b_{n+1})^T = e^{in\varphi}(a_n\ b_n)^T$ into the above equation leads to

$$i\frac{\mathrm{d}}{d\zeta}\begin{pmatrix} a \\ b \end{pmatrix} = \begin{pmatrix} \omega_a + i\Gamma_a & C_i + C_0 e^{-i\varphi} \\ C_i + C_0 e^{i\varphi} & \omega_b + i\Gamma_b \end{pmatrix}\begin{pmatrix} a \\ b \end{pmatrix}, \tag{32}$$

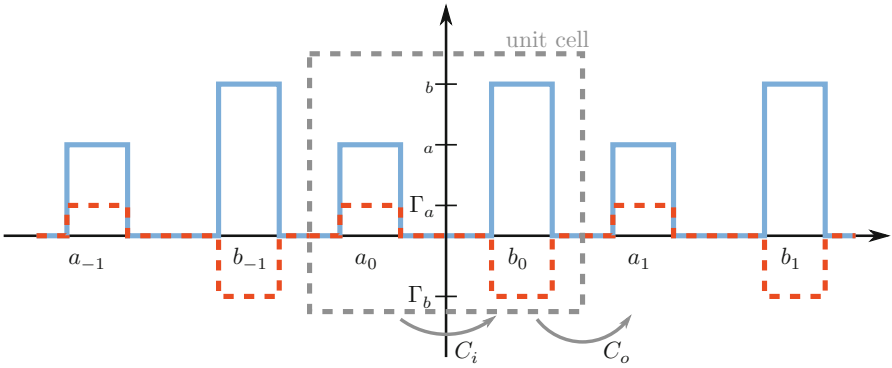

Fig. 13 Schematic illustration of a biatomic lattice. Each unit cell consists of two sites, which couple to each other with strength C_i. The inter-cell coupling is instead given by C_0. Each lattice site is characterised by an eigenfrequency ω, and a decay rate Γ

which reduces the complexity of the problem to study the evolution of a single unit cell. The eigenvalues of the above Hamiltonian give the band structure of the lattice, i.e.,

$$\beta_{\pm} = -\bar{\beta} \pm \sqrt{\delta\beta^2 + C_i^2 + C_0^2 + 2C_i C_0 \cos\varphi}, \tag{33}$$

where $\bar{\beta} = \bar{\omega} + i\bar{\Gamma}$ is the mean propagation constant (written as a function of the mean energy $\bar{\omega} = (\omega_a + \omega_b)/2$ and the mean losses $\bar{\Gamma} = (\Gamma_a + \Gamma_b)/2$), and $\delta\beta = \delta\omega + i\delta\Gamma$, where $\delta\omega = (\omega_a - \omega_b)/2$, and $\delta\Gamma = (\Gamma_a - \Gamma_b)/2$. The above equation, moreover, defines two bands for the system, centered around the mean propagation constant $\bar{\beta}$. Without any loss of generality, one can assume $\bar{\beta} = 0$, (i.e., $\omega_b = -\omega_a$ and $\Gamma_b = -\Gamma_a$).[5] Moreover, we could also assume that $\Gamma_b < \Gamma_a$, which leads to $\delta\Gamma > 0$. With these assumptions, Eq. (33) can be rewritten in the following form:

$$\beta_{\pm} = \pm\sqrt{\omega_a^2 + 2i\omega_a\Gamma_a - \Gamma_a^2 + C_i^2 + C_0^2 + 2C_i C_0 \cos\varphi}. \tag{34}$$

In the Hermitian case, which is recovered in the limit $\Gamma_a = 0$, the spectrum is entirely real, regardless of the specific choice of parameters. Equivalently, the above spectrum is $\mathcal{PT}$-invariant only if $\omega_a = 0$, for which the above band structure reduces to

$$\beta_{\pm} = \pm\sqrt{-\Gamma_a^2 + C_i^2 + C_0^2 + 2C_i C_0 \cos\varphi}. \tag{35}$$

In this case, the spectrum is entirely real, as long as $|C_i - C_0| > \Gamma_a$, and it becomes purely imaginary if $C_i + C_0 > \Gamma_a$. The band structure for the case of $\mathcal{PT}$-invariance is depicted in Fig. 14. Although the above model is well known and has been extensively studied in the framework of $\mathcal{PT}$-symmetry, little is known of its dynamical properties in the regime where $\mathcal{PT}$-symmetry is broken. This regime is controlled only by the ratio $|C_i - C_0|/\Gamma_a$. As it can be seen from Fig. 14c, in fact, Eq. (35) admits purely real solutions for $|\varphi| < 0.45\pi$, whereas for $|\varphi| > 0.45\pi$ the eigenvalues are purely imaginary. These features, however, are not limited to a $\mathcal{PT}$-invariant spectrum, but they also appear in the more general case, when $\omega_a \neq 0$, as Fig. 15 shows. There, in fact, one can see how the spectrum looks qualitatively similar, but smeared, to the one in Fig. 14. Moreover, the sharp transition between purely real and purely imaginary that we observe in Fig. 14 is smoothed out because of the presence of a nonzero ω_a. Moreover, it appears clear from Fig. 15, that the losses that each mode experiences are not constant, but they rather depend on the transverse momentum φ. Hence, eigenmodes in different regions of the Brillouin zone of this diatomic lattice experience different losses. As a direct consequence of this, at the center of the Brillouin zone, each mode experiences intermediate losses

[5] $\bar{\beta}$ can be anyway eliminated by means of a suitable gauge transformation.

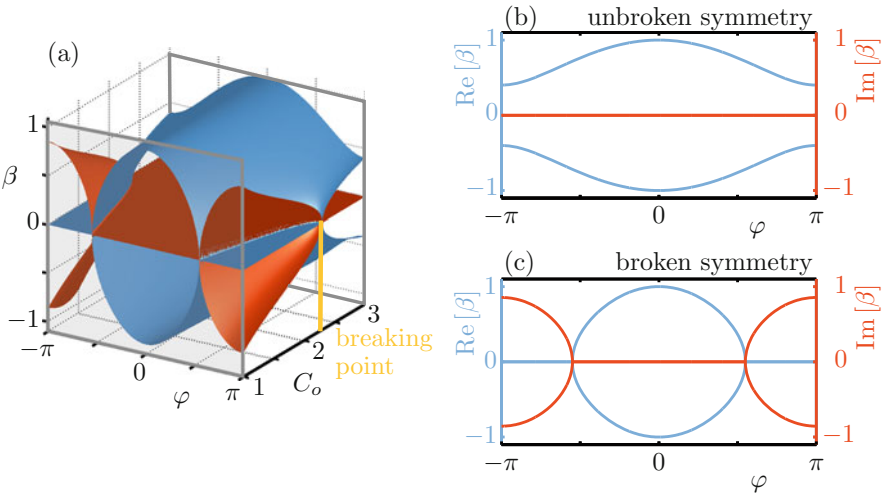

Fig. 14 (**a**) Normalised band structure of a $\mathcal{PT}$-invariant Hamiltonian, like the one described by Eq. (35), with $\Gamma_a = 1.3$, and $C_i = 1$. The blue surface represents the real part, whereas the red surface denotes the imaginary part of the eigenvalue β in Eq. (35). $\mathcal{PT}$-symmetry is broken for $C_0 < 2.3$. (**b**) Normalised band structure of a $\mathcal{PT}$-symmetric Hamiltonian. Eigenvalues are obtained from (**a**) for the specific choice of $C_0 = 3$. (**c**) Normalised band structure for a parameter set, where $\mathcal{PT}$-symmetry is broken. In this case, $C_0 = 1$ has been chosen

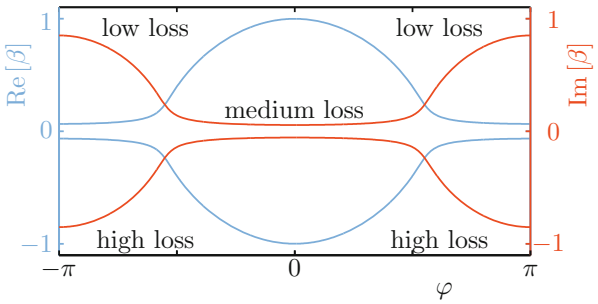

Fig. 15 Normalised band structure of a general dissipative biatomic lattice. The parameter chosen for this figure are almost equivalent to the broken $\mathcal{PT}$ case shown in Fig. 14c, with $\omega_a = 1.3$, and $C_i = C_0 = 1$. In addition, a frequency detuning of $\omega_a = 0.1$ is introduced

(whose value is close to the average losses in the system, i.e., $\bar{\Gamma}$), while at the edges of the Brillouin zone (i.e., around $\varphi = \pm\pi$), the modes in the lower band suffer from much larger losses, than the ones in the upper band. Because of this difference, therefore, the modes in the lower band at the edge will disappear relatively fast, whereas the modes sitting in the upper band will survive longer. For this reason, only a part of the spectrum will contribute to define the transport properties of this system.

To better understand this selective participation of spectral mode to transport properties, let us consider the situation depicted in Fig. 16: panels (a) and (b) depict the evolution of the spectrum in the lower and upper band, respectively, whereas the spatial evolution is plotted in panel (c), for the case of a single-site excitation. Initially, all transverse modes in both bands are excited equally. In this regime, which holds up to $\zeta < 20$ in Fig. 16, the dynamics in real space follows the one of a normal homogeneous lattice, i.e., the evolution dynamics shows strong ballistic lobes, and amplitude oscillations inside each individual waveguide. For longer propagation distances, i.e., when the modes around the edges of the Brillouin zone are predominant, the evolution dynamics deviates significantly from the case of a homogeneous lattice. In fact, as it appears clear from Fig. 16, the intensity is mostly confined within the sub-lattice a_n, and central waveguides possess a larger amplitude than outer ones. Moreover, the amplitude oscillations in the individual waveguides are no longer present. To corroborate these observations, the variance of the wave packet propagating along this structure (i.e., the evolution of its width as a function of ζ) is plotted in Fig. 16d. As it can be seen, two distinct transport regimes are present in this structure. For small distances ($\zeta < 16$, in Fig. 16), the evolution is ballistic, and the variance σ^2 of the wave packet grows quadratically, as expected in a Hermitian homogeneous lattice. For longer distances, however, the evolution is diffusive, i.e., σ^2 grows linearly with ζ. To show this rigorously, one needs to find the solutions to Eq. (31) in terms of superpositions of the eigenstates of the correspondent Hamiltonian as follows

$$\mathbf{A}_n = \frac{\mathcal{N}}{2\pi} \int_{-\pi}^{\pi} d\varphi \left(\alpha_+ \mathbf{A}_+ e^{-i\beta_+ \zeta} + \alpha_- \mathbf{A}_- e^{-i\beta_- \zeta} \right) e^{in\varphi}, \tag{36}$$

where $\mathbf{A}_n = (a_n \; b_n)^T$ (with $\mathbf{A}_\pm$ being the two eigenvectors of the Hamiltonian appearing in Eq. (32), and corresponding to the two eigenvalues $\beta_\pm$, respectively), $\mathcal{N}$ being a suitable normalisation constant, and $\alpha_\pm$ are the coefficients for the two band modes, namely $\alpha_+ = C[1 + \exp(i\varphi)]$ and $\alpha_- = \beta_+ + \bar{\beta} + \delta\beta$ ($C_i = C_0 \equiv C$ has been assumed).

If we limit our analysis to large propagation distances and we consider the contribution of the modes in a narrow region around the band edges $\varphi = \pm\pi$, we can Taylor expand the band structure around such points and take the limit of the correspondent eigenvectors as, say, $\varphi \to \pi$. By doing that we then obtain the following result:

$$\frac{\alpha_-}{\mathcal{N}} \mathbf{A}_- \overset{\varphi \to \pi}{\to} \begin{pmatrix} 1 \\ 0 \end{pmatrix}. \tag{37}$$

This result is consistent with the initial assumption, that the waveguides b_n were lossier than the a_n. As a consequence of this fact, if the mode is confined within the a_n sub-lattice, it only experiences the loss for the a_n waveguides. Moreover, this result is also in agreement with Fig. 16c, where it can be seen, that after a certain

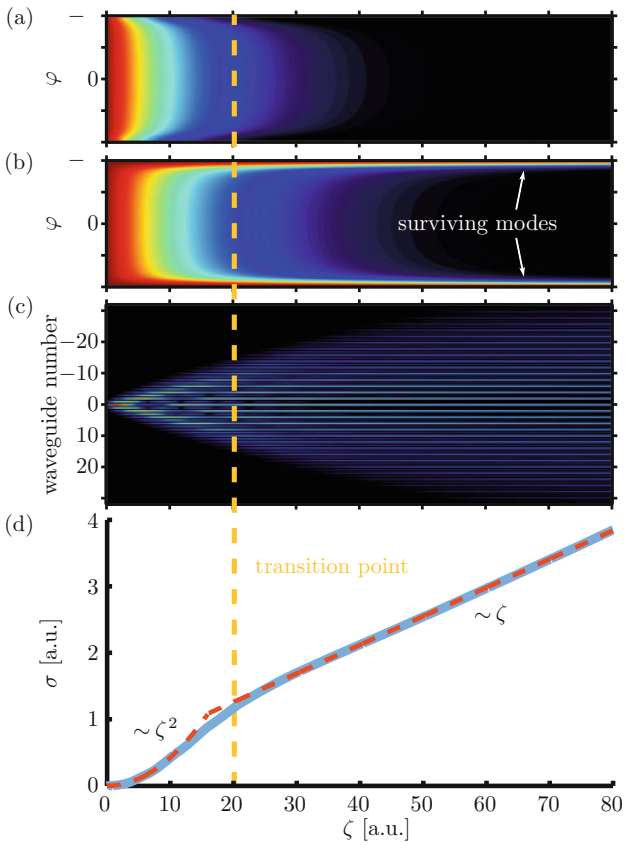

Fig. 16 Evolution of a wave packet inside a lattice described by Eqs. (31), with $\omega_a = \Gamma_a = 0$, $\omega_b = -0.2$, $\Gamma_b = -0.1$, and $C_i = C_0 = 0.3$. Initially, only waveguide a_0 is excited with unit amplitude. (**a**) Evolution of the mode amplitudes in the lower band. (**b**) Evolution of the mode amplitudes in the upper band. (**c**) Evolution dynamics in real space. (**d**) Variance calculated from the evolution shown in panel (**c**). The blue, solid line represents the actual variance σ^2, whereas the red, dashed line has a parabolic profile for $\zeta < 16$ and a straight profile for $\zeta > 16$. The transition region is drawn across all subfigures for clarity

propagation distance, only the a_n waveguides carry nonzero intensity. This argument allows us to simplify Eq. (36), by setting $b_n = 0$ and expanding β around $\varphi - \pi$, thus obtaining

$$a_n = \frac{e^{in\pi}}{2\sqrt{\pi w\zeta}} e^{i(\bar{\beta}-\delta\beta)\zeta} e^{i\frac{n^2}{4w\zeta}}, \tag{38}$$

where $w = C^2\delta\beta^*/(2|\delta\beta|^2)$. It is worth noticing, that the result above is only valid if $\delta\Gamma \neq 0$, i.e., when there is a nonzero loss detuning between the two lattice sites a_n and b_n. When $\delta\Gamma > 0$, in fact, there always exist propagation distance ζ_c,

for which the approximations leading to Eq. (38) hold. This particular propagation distance can be estimated by requiring that, given a certain spectral region ε, all the modes outside this region are damped by a quantity δ, i.e., by imposing that $|\exp(-iw\varepsilon^2\zeta_c)| < e^{-2}$, which leads to $\zeta_c = (4|\delta\beta|^2)/(\varepsilon^2 C^2 \delta\Gamma)$. The spectral range ε, however, cannot be chosen arbitrarily, but it has to be chosen in such a way that Eq. (37) holds, i.e., $\varepsilon^2 < 2|\delta\beta|^2/C^2$. Substituting this condition in the expression for ζ_c leads to the following result:

$$\zeta_c = \frac{2}{\delta\Gamma}, \tag{39}$$

which represents the propagation distance, after which Eq. (38) is valid. Notice, that ζ_c depends only on the loss imbalance between the two lattice sites a_n and b_n, and in the limit $\delta\Gamma = 0$, $\zeta_c \to \infty$, which is consistent with the fact that in such limit, Eq. (38) cannot be used to approximate the dynamics of the system. We can now calculate the variance of a wave packet described by Eq. (38), i.e.,

$$\sigma^2 = \frac{\sum_{n=1}^{\infty} n^2 |a_n|^2}{\sum_{n=1}^{\infty} |a_n|^2} = \frac{C^2}{2\delta\Gamma}\zeta. \tag{40}$$

The above result, indeed, proves that for propagation distances $\zeta > \zeta_c$, the variance grows linearly with the distance, i.e., the wave packet spreads diffusively. For $\zeta < \zeta_c$, instead, the spreading is ballistic, as in the usual case of a lossless homogeneous array.

5.2 *Experimental Observation of Diffusive Transport in Non-Hermitian Lattices*

To implement experimentally a system, whose evolution is described by Eq. (31), we can, once more, employ the laser-writing technique described in Sect. 3.1 to realise a non-Hermitian waveguide array. According to the model developed in the section above, the key feature of this array must be to possess controllable losses. To implement this, according to the results presented in Sect. 4, we apply a sinusoidal bend to the waveguides, to insert controllable losses in the system. In particular, as Fig. 17 shows, each second waveguide composing the array is sinusoidally bent, in order to implement intrinsic losses, whereas the straight waveguides exhibit no losses ($\Gamma_a = 0$). The bending plane, moreover, is chosen as the plane perpendicular to the lattice plane, in order to prevent light which is radiated away from a lossy waveguide, to be reabsorbed by a different waveguide of the lattice. In the experimental setup shown in Fig. 17, the waveguides are separated by a distance $a = 17$ μm, which corresponds to a coupling con-

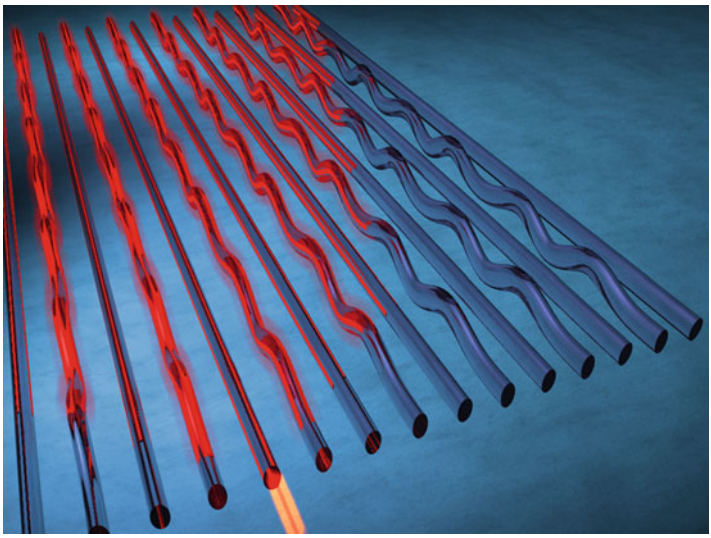

Fig. 17 Schematic illustration of a biatomic waveguide lattice, which models Eq. (31). In order to implement tunable losses, every second waveguide is bent sinusoidally, in the transverse direction, with respect to the lattice plane

stant $C = 1.1\,\mathrm{cm}^{-1}$. Moreover, the amplitude of the sinusoidal modulation is $d = 3\ \mu\mathrm{m}$.[6] To facilitate different intrinsic decay rates, the modulation frequency serves as tuning parameter. The experimental measurements for a range of different loss parameters, i.e., from $\Gamma_b = 0$ for the ballistic case, to a maximum of $\Gamma_b = -2\,\mathrm{cm}^{-1}$ for the lossiest configuration, are shown in Fig. 18. In addition to the evolution of light in such waveguide lattice, Fig. 18 also shows the extracted variance of the wave packet, together with the corresponding numerical simulation. From the measurements presented in Fig. 18, one can then conclude, that the experiments are in agreement with the theoretical prediction given in the previous section. The fluorescence images show that the ballistic characteristics vanish with increasing losses. In the lossless, ballistic case (Fig. 18a), the characteristic lobes of ballistic transport are clearly visible. These lobes, however, already start to vanish in panel (c), and they vanish completely in panel (k), which corresponds to the largest losses. From the measurements presented in Fig. 18, we can also extract the critical distance ζ_c, around which the transition from ballistic to diffusive transport occurs. The correspondent behaviour of the critical distance as a function of the losses Γ_b is shown in Fig. 19, which reveal that, indeed as predicted by Eq. 39, ζ_c is inversely proportional to the loss detuning.

[6]The amplitude of the modulation has chosen to be small, in order to avoid the onset of a z-modulated coupling constant.

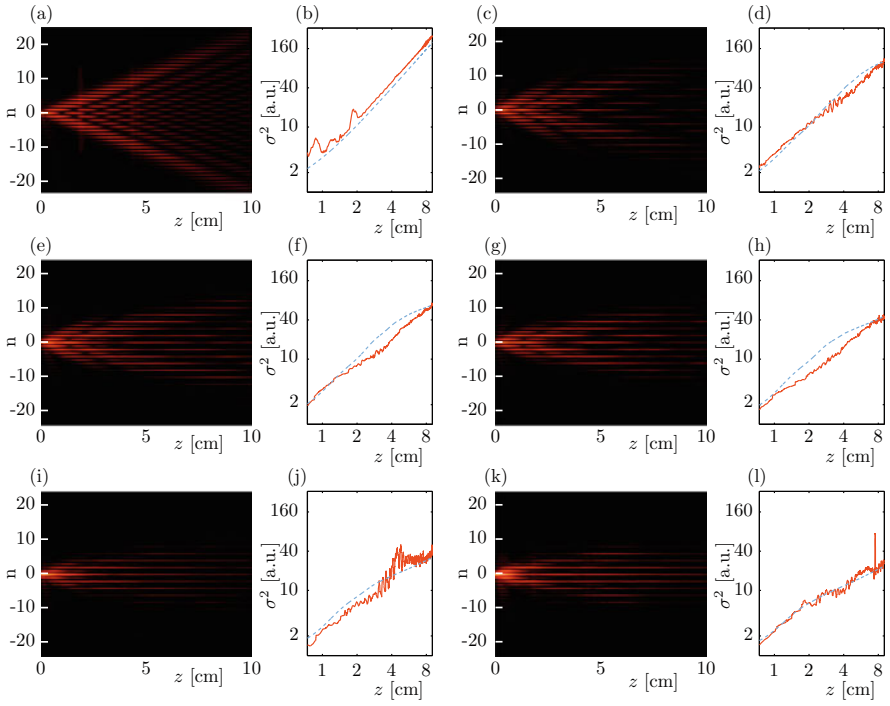

Fig. 18 Panels (**a**), (**c**), (**e**), (**g**), (**i**), and (**k**) show fluorescence microscopy images of the light beams propagating through the lattice. Panels (**b**), (**d**), (**f**), (**h**), (**j**), and (**l**) contain the corresponding variance in a double logarithmic plot, as a function of the propagation distance z. In those graphs, the red solid line represents actual experimental data, whereas the blue, dotted line represents the corresponding simulation. Panels (**a**) and (**b**) depict the purely ballistic case. The correspondent values of Γ_b are given as follows: panels (**a**) and (**b**) correspond to $\Gamma_b = 0$. Panels (**c**) and (**d**) to $\Gamma_b = -0.6\,\mathrm{cm}^{-1}$, panels (**e**) and (**f**) to $\Gamma_b = -0.8\,\mathrm{cm}^{-1}$, panels (**g**) and (**h**) to $\Gamma_b = -1.1\,\mathrm{cm}^{-1}$, panels (**i**) and (**j**) to $\Gamma_b = -1.5\,\mathrm{cm}^{-1}$, and panels (**k**) and (**l**) to $\Gamma_b = -2\,\mathrm{cm}^{-1}$

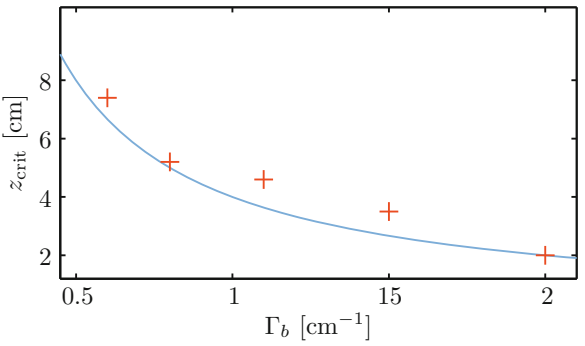

Fig. 19 The red cross represent the critical distance ζ_c extracted from the measurements shown in Fig. 18. In addition, the theoretical prediction given by Eq. (39) is plotted as a solid, blue line. The value of the loss detuning $\delta\Gamma = \Gamma_b$ has also been extracted from the experimental data in Fig. 18

References

1. Bender, C.M., Boettcher, S.: Real spectra in non-Hermitian Hamiltonians having PT symmetry. Phys. Rev. Lett. **80**, 5243–5246 (1998)
2. El-Ganainy, R., Makris, K.G., Christodoulides, D.N., Musslimani, Z.H.: Theory of coupled optical PT-symmetric structures. Opt. Lett. **32**(17), 2632–2634 (2007)
3. Makris, K.G., El-Ganainy, R., Christodoulides, D.N., Musslimani, Z.H.: Beam dynamics in PT symmetric optical lattices. Phys. Rev. Lett. **100**, 103904 (2008)
4. Zheng, M.C., Christodoulides, D.N., Fleischmann, R., Kottos, T.: PT optical lattices and universality in beam dynamics. Phys. Rev. A **82**, 010103 (2010)
5. Musslimani, Z.H., Makris, K.G., El-Ganainy, R., Christodoulides, D.N.: Optical solitons in PT periodic potentials. Phys. Rev. Lett. **100**, 030402 (2008)
6. Dmitriev, S.V., Sukhorukov, A.A., Kivshar, Y.S.: Binary parity-time-symmetric nonlinear lattices with balanced gain and loss. Opt. Lett. **35**(17), 2976–2978 (2010)
7. Longhi, S.: Bloch oscillations in complex crystals with PT symmetry. Phys. Rev. Lett. **103**, 123601 (2009)
8. Longhi, S.: Spectral singularities in a non-Hermitian Friedrichs-Fano-Anderson model. Phys. Rev. B **80**, 165125 (2009)
9. Szameit, A., Rechtsman, M.C., Bahat-Treidel, O., Segev, M.: PT-symmetry in honeycomb photonic lattices. Phys. Rev. A **84**, 021806 (2011)
10. Guo, A., Salamo, G.J., Duchesne, D., Morandotti, R., Volatier-Ravat, M., Aimez, V., Siviloglou, G.A., Christodoulides, D.N.: Observation of PT-symmetry breaking in complex optical potentials. Phys. Rev. Lett. **103**, 093902 (2009)
11. Gräfe, M., Heilmann, R., Keil, R., Eichelkraut, T., Heinrich, M., Nolte, S., Szameit, A.: Correlations of indistinguishable particles in non-Hermitian lattices. New J. Phys. **15**(3), 033008 (2013)
12. Eichelkraut, T., Heilmann, R., Weimann, S., Stützer, S., Dreisow, F., Christodoulides, D.N., Nolte, S., Szameit, A.: Mobility transition from ballistic to diffusive transport in non-Hermitian lattices. Nat. Commun. **4**, 2533 (2013)
13. Ornigotti, M., Szameit, A.: Quasi PT-symmetry in passive photonic lattices. J. Opt. **16**(6), 065501 (2014)
14. Rüter, C.E., Makris, K.G., El-Ganainy, R., Christodoulides, D.N., Segev, M., Kip, D.: Observation of parity-time symmetry in optics. Nat. Phys. **6**, 192–195 (2010)
15. Regensburger, A., Bersch, C., Miri, M.-A., Onishchukov, G., Christodoulides, D.N., Peschel, U.: Parity-time synthetic photonic lattices. Nature **488**, 167–171 (2012)
16. El-Ganainy, R., Makris, K.G., Christodoulides, D.N., Musslimani, H.Z.: Theory of coupled optical pt-symmetric structures. Opt. Lett. **32**, 2632 (2007)
17. Bendix, O., Fleischmann, R., Kottos, T., Shapiro, B.: Optical structures with local pt-symmetry. J. Phys. A Math. Theor. **43**, 263505 (2010)
18. Yariv, A.: Optical Electronics, 3rd edn. CBS College Publishing, New York (1985)
19. Peskin, M.E., Schroeder, D.V.: An Introduction to Quantum Field Theory. Perseus Books, Reading, Massachusetts (1995)
20. Rohe, H.J.: Lattice Gauge Theories: An Introduction. World Scientific Publishing, Singapore (2012)
21. Chan, J.W., Huser, T., Risbud, S., Krol, D.M.: Structural changes in fused silica after exposure to focused femtosecond laser pulses. Opt. Lett. **26**(21), 1726–1728 (2001)
22. Chan, J.W., Huser, T.R., Risbud, S.H., Krol, D.M.: Modification of the fused silica glass network associated with waveguide fabrication using femtosecond laser pulses. Appl. Phys. A **76**(3), 367–372 (2003)
23. Mansour, I., Caccavale, F.: An improved procedure to calculate the refractive index profile from the measured near-field intensity. J. Lightwave Technol. **14**(3), 423–428 (1996)

24. Szameit, A., Dreisow, F., Heinrich, M., Pertsch, T., Nolte, S., Tünnermann, A., Suran, E., Louradour, F., Barthélémy, A., Longhi, S.: Image reconstruction in segmented femtosecond laser-written waveguide arrays. Appl. Phys. Lett. **93**(18), 181109 (2008)
25. Szameit, A., Garanovich, I.L., Heinrich, M., Sukhorukov, A.A., Dreisow, F., Pertsch, T., Nolte, S., Tünnermann, A., Longhi, S., Kivshar, Y.S.: Observation of two-dimensional dynamic localization of light. Phys. Rev. Lett. **104**, 223903 (2010)
26. Heinrich, M., Szameit, A., Dreisow, F., Keil, R., Minardi, S., Pertsch, T., Nolte, S., Tünnermann, A., Lederer, F.: Observation of three-dimensional discrete-continuous X waves in photonic lattices. Phys. Rev. Lett. **103**, 113903 (2009)
27. Naether, U., Meyer, J.M., Stützer, S., Tünnermann, A., Nolte, S., Molina, M.I., Szameit, A.: Anderson localization in a periodic photonic lattice with a disordered boundary. Opt. Lett. **37**(4), 485–487 (2012)
28. Kramers, H.A.: Collected Scientific Papers. North-Holland, Amsterdam (1956)
29. Henneberger, W.C.: Perturbation method for atoms in intense light beams. Phys. Rev. Lett. **21**, 838 (1968)
30. Breuer, H.P.: The Theory of Open Quantum Systems. Oxford University Press, Oxford (2007)
31. Byron, F.W., Fuller, R.W.: Mathematics of Classica and Quantum Physics. Dover, New York (1992)
32. Golshani, M., Weimann, S., Jafari, Kh., Khazaei Nezhad, M., Langari, A., Bahrampour, A.R., Eichelkraut, T., Mahdavi, S.M., Szameit, A.: Impact of loss on the wave dynamics in photonic waveguide lattices. Phys. Rev. Lett. **113**, 123903 (2014)

Non-Hermitian Effects Due to Asymmetric Backscattering of Light in Whispering-Gallery Microcavities

Jan Wiersig

Abstract A whispering-gallery microcavity is an open optical system which supports well confined counterpropagating electromagnetic waves. Deforming the boundary of the cavity or perturbing it by other means, e.g. by placing small scatterers near the boundary, leads to coherent backscattering of these waves inside the cavity. In general, this backscattering is asymmetric, i.e. the strength of scattering from the clockwise to the counterclockwise propagation direction is different from the other way around. This asymmetry is intrinsically tied to the non-Hermiticity of the system including the nonorthogonality of mode pairs and the coalescence of modes at exceptional points. We review and present new results on asymmetric backscattering with emphasis on its non-Hermitian effects. Several types of perturbed whispering-gallery cavities are considered. Different applications, such as single-particle detection with enhanced sensitivity, are discussed.

1 Introduction

Every real physical system is an open system in the sense that it is coupled to its environment or to a measurement apparatus. Therefore, the study of open wave or quantum systems is an important topic in physics for many decades. With the beginning of this century a new focus has emerged: "non-Hermitian physics". The main reason is the observation of interesting and unconventional physics at and near special degeneracies, so-called exceptional points (EPs), of effective non-Hermitian Hamiltonians. In contrast to conventional degeneracies, so-called diabolic points [3] (DPs), at an EP not only eigenvalues but also the corresponding eigenstates coalesce [2, 29, 30, 39]. As in most of the studies in the literature, we here mainly consider EPs of order two, where exactly two

J. Wiersig (✉)
Institut für Theoretische Physik, Otto-von-Guericke-Universität Magdeburg, Magdeburg, Germany
e-mail: jan.wiersig@ovgu.de

D. Christodoulides, J. Yang (eds.), *Parity-time Symmetry and Its Applications*, Springer Tracts in Modern Physics 280,
https://doi.org/10.1007/978-981-13-1247-2_6

eigenstates coalesce. Such EPs are square-root branch points of energy surfaces in their parameter space. A number of experiments have undoubtedly proven the existence of EPs in physical systems, e.g., in microwave cavities [12, 14, 16], optical microcavities [52, 69, 113], coupled atom-cavity systems [9], photonic lattices [68], nonuniformly pumped lasers [4], ultrasonic cavities [79], and exciton-polariton billiards [23]. Furthermore, theoretical investigations revealed that EPs also appear in other systems, such as hydrogen atoms in crossed magnetic and electric fields [6] and coupled-resonator optical waveguides [78]. Finally, EPs are related to symmetry breaking in PT-symmetric non-Hermitian systems [1, 68, 71] which are invariant under a combination of parity (P) and time reversal (T) operations.

Optical microcavities represent an interesting class of open systems which have attracted considerable interest in the recent decades [93]. Important examples of such cavities are microdisks [44, 62, 64, 92], microspheres [11], and microtoroids [34]. Such whispering-gallery mode (WGM) resonators trap light for a long time τ by total internal reflection at the boundary of the resonator. An optical mode in such a resonator therefore has a high quality factor $Q = \omega\tau$, where ω is the resonant frequency of the mode.

All WGM resonators underlie unwanted or wanted perturbations. An unwanted source of perturbation is, for example, surface roughness [105]. A wanted perturbation occurs, for instance, by local scattering at viruses, nanoparticles, or nanofiber tips approaching the outer surface of the resonator, see e.g. Fig. 1a, allowing for single-particle detection by a frequency shift or splitting [94, 95, 114]. Yet another type of wanted perturbation is given by deforming the microcavity's boundary, see Fig. 1b. Suitable deformations result in directional free-space light emission [36, 65, 74, 104], efficient free-space excitation [50], efficient and broadband cavity-waveguide coupling [37], and mode discrimination [22, 76]. Moreover, deformed microcavities serve as model systems for wave chaos and non-Hermitian physics [5]. Another way to perturb a WGM resonator can be realized by introducing a modulation of the (effective) refractive index [63], see e.g. Fig. 1c.

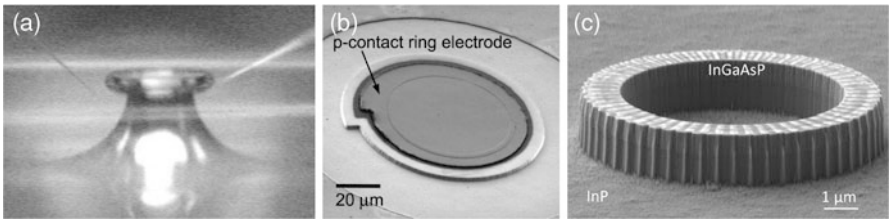

Fig. 1 Microcavities with asymmetric backscattering of light. (**a**) Microtoroid with major and minor diameters of 82 and 8 μm perturbed by two nanofiber tips, (**b**) spiral-shaped microdisk, (**c**) microring with periodic modulation of the effective index of refraction. (Figures in (**a**) and (**c**) are adapted from [66] and [63]. Figure in (**b**) is reproduced from [45] with the permission of AIP Publishing)

The aforementioned perturbations produce coherent backscattering of clockwise (CW) and counterclockwise (CCW) propagating waves inside the resonator. It has been shown that the backscattering is in general asymmetric leading to counterintuitive non-Hermitian effects [106]. The resulting modes do not form standing-wave modes, but partially traveling-wave modes. The fact that a mode has a preferred sense of rotation is called *chirality* (this effect is not related to optical activity). It was first observed in numerical calculations on the spiral cavity (Fig. 1b) without relating it to asymmetric backscattering and non-Hermitian effects [8]. This link was established later by showing the appearance of nearly degenerate pairs of *copropagating* modes [99] which exhibit a strong *nonorthogonality* [106]. The asymmetric backscattering and the resulting copropagation, chirality, and nonorthogonality of mode pairs is a general effect in deformed and perturbed WGM microcavities [41, 66, 100, 106, 107] and in open quantum systems with weakly coupled CW and CCW traveling waves [101]. The chirality has been demonstrated recently in experiments on a microdisk with two small bumps [41], a microtoroid perturbed by two nanofiber tips [66], a microring with periodic index of refraction modulation [63], and in coupled microcavities [112]. The experiment on the microtoroid also confirms directly the asymmetric backscattering [66].

There are a number of potential applications of asymmetric backscattering: microcavity sensors for single- or few particle detection with enhanced sensitivity [7], rotation sensing via output directionality [73], unidirectional lasing operation in (micro)lasers e.g. [88], and orbital angular momentum microlasers [63].

The aim of this chapter is to review and to present new results on asymmetric backscattering in WGM cavities and to explain in detail the resulting non-Hermitian effects including the appearance of EPs. In Sect. 2 we discuss the two-mode model for the isolated and the waveguide-coupled WGM cavity. Sections 3, 4, and 5 deal with deformed microdisk cavities, microdisks which are locally perturbed, and microrings with a modulation of the effective index of refraction. Coupled cavities are the topic of Sect. 6. Applications are overviewed in Sect. 7. Finally, a summary is provided in Sect. 8.

2 The Two-Mode Model for Asymmetric Backscattering

In this section we report on the two-mode model for backscattered light in WGM cavities with broken symmetry. This helps the reader to understand the basic relationship between asymmetric backscattering of counterpropagating waves and the resulting chirality, copropagation, and nonorthogonality of mode pairs.

2.1 The Isolated WGM Cavity

The model discussed here was first phenomenologically introduced for deformed microdisk cavities [106, 107]. The key idea is to model the dynamics in the slowly-varying envelope approximation in the time domain with a Schrödinger-like equation

$$\mathrm{i}\frac{\mathrm{d}}{\mathrm{d}t}\boldsymbol{\psi} = H\boldsymbol{\psi} \,. \tag{1}$$

Here, $\boldsymbol{\psi}$ is the two-component column vector $(\psi_{\mathrm{CCW}}, \psi_{\mathrm{CW}})^T$, where the superscript T indicates the matrix transpose. The complex-valued entry ψ_{CCW} (ψ_{CW}) stands for all the field amplitudes of the CCW (CW) propagating waves. This strong simplification was later justified for open systems in a rather general setting [101].

In the presence of optical losses (radiation/absorption) and/or gain the effective Hamiltonian H is non-Hermitian. In the entire review we restrict ourselves to systems which fulfill Lorentz reciprocity. For such systems there is an orthogonal basis in which H is a complex-symmetric matrix [17, 86]. This basis consists of standing waves (which are invariant under time reversal). Transformed into a basis of traveling waves (which are exchanged under time reversal) the effective Hamiltonian is a 2×2 non-Hermitian matrix

$$H = \begin{pmatrix} \Omega & A \\ B & \Omega \end{pmatrix} \tag{2}$$

where reciprocity requires the diagonal elements to be equal [103]. The real parts of the diagonal elements Ω are the frequencies and the (negative) imaginary parts are the decay rates of the uncoupled traveling waves. The complex-valued off-diagonal elements A and B are the backscattering coupling coefficients. A (B) describes the scattering from the CW (CCW) to the CCW (CW) traveling wave. The backscattering is said to be asymmetric if

$$|A| \neq |B| \,. \tag{3}$$

This is permitted since the Hamiltonian is non-Hermitian and reciprocity does not constrain the coefficients A and B. The possibility of asymmetric backscattering had been excluded for a long time in the microcavity communities, e.g. [43], as it was believed that there must be a detailed balance for the cross-coupling between CW and CCW propagating waves owing to the conservation of energy [42]. This argument is, however, not valid in an open system. Of course, in special cases the backscattering can be symmetric, $|A| = |B|$. For instance, this happens for a closed cavity ($A^* = B$) or a cavity with at least one mirror-reflection symmetry ($A = B$) [107]. For passive (no gain) cavities the inequality

$$2|\mathrm{Im}\,\Omega| \geq |A - B^*| \tag{4}$$

holds [75, 103]. The asterisk stands for complex conjugation.

A short calculation shows that the complex eigenvalues of H are

$$\Omega_\pm = \Omega \pm \sqrt{AB} \tag{5}$$

and the complex (not normalized) right eigenvectors are

$$\boldsymbol{\psi}_\pm = \begin{pmatrix} \sqrt{A} \\ \pm\sqrt{B} \end{pmatrix} . \tag{6}$$

The $\pm$ structure in the eigenvectors is a consequence of reciprocity. Clearly, in the case of asymmetric backscattering (3) one component of a given eigenvector (6) is larger than the other component. Physically, it means that the eigenvectors show an imbalance of CCW and CW components if the backscattering is asymmetric. According to [41, 78] we quantify this imbalance of CCW and CW components in a vector $\boldsymbol{\psi}$ by the chirality

$$\alpha = \frac{|\psi_{\mathrm{CCW}}|^2 - |\psi_{\mathrm{CW}}|^2}{|\psi_{\mathrm{CCW}}|^2 + |\psi_{\mathrm{CW}}|^2} \in [-1, 1] . \tag{7}$$

Obviously, both eigenvectors (6) exhibit the same chirality

$$\alpha = \frac{|A| - |B|}{|A| + |B|} , \tag{8}$$

i.e. they share the main propagation direction in real space. We call this effect copropagation of mode pairs. In contrast to the original definition of the chirality [100, 101, 106, 107], the chirality in Eq. (7) provides information on the sense of rotation. In the case where the CCW (CW) component dominates, $|A| > |B|$ ($|A| < |B|$), the chirality is positive (negative). A balanced contribution of CW and CCW components gives a vanishing chirality.

As a consequence of the non-Hermitian character of the Hamiltonian the eigenvectors (6) can be nonorthogonal. This happens if the backscattering is asymmetric as $\boldsymbol{\psi}_+^* \cdot \boldsymbol{\psi}_- = |A| - |B| \neq 0$, where the inner product $\cdot$ is defined in the usual manner of multiplying the matching components. A natural way to quantify the nonorthogonality of two vectors $\boldsymbol{\psi}_1$ and $\boldsymbol{\psi}_2$ is to calculate the normalized overlap

$$S = \frac{|\boldsymbol{\psi}_1^* \cdot \boldsymbol{\psi}_2|}{|\boldsymbol{\psi}_1||\boldsymbol{\psi}_2|} \in [0, 1] . \tag{9}$$

Straightforwardly, one can show that for the two eigenvectors (6) the overlap (9) and the chirality (7) are connected by the simple formula

$$S = |\alpha| . \tag{10}$$

Nonorthogonality of modes is of particular importance for optical microcavities as it implies excess quantum noise in lasers [51, 77, 81, 82].

It is possible to create fully asymmetry backscattering, i.e. $A = 0$ while $B \neq 0$ or vice versa [100]. This is an EP, as the eigenvalues (5) and eigenvectors (6) coalesce, i.e. the eigenvectors become collinear with the overlap S approaching unity. The eigenvectors of the effective Hamiltonian H no longer form a basis. Note, however, that the set of two ordinary differential equations (1) always has two linearly independent solutions. The time evolution of the two-mode model at an EP is discussed in [107]. It is worth mentioning that fully asymmetric backscattering is related to "unidirectional invisibility" induced by PT-symmetric periodic structures [20, 21, 55]. However, in the latter case, one considers a scattering matrix and focuses on the scattering properties.

At the EP the chirality in Eq. (8) approaches ± 1. In this limit the chirality defined above coincides with the more abstract chirality associated with an EP [13, 31]. It is here useful to define the strength of the EP to be the absolute value of the nonzero off-diagonal element. For an EP with $A = 0$ and $B \neq 0$ the strength of the EP is $|B|$, for the opposite case it is $|A|$. The limiting case of zero strength characterizes a DP.

2.2 Coupling to Waveguides

The extension of the two-mode model to waveguide-cavity systems has been introduced and tested in [46, 66]. Let us consider the situation in Fig. 2 with incoming waves from the upper left with amplitude $a_{1,\mathrm{in}}(t)$ and the upper right with amplitude $a_{2,\mathrm{in}}(t)$. According to coupled mode theory, Eq. (1) is modified such that

$$\mathrm{i}\frac{\mathrm{d}}{\mathrm{d}t}\boldsymbol{\psi} = H\boldsymbol{\psi} + \kappa \begin{pmatrix} a_{2,\mathrm{in}} \\ a_{1,\mathrm{in}} \end{pmatrix} , \tag{11}$$

where the cavity-waveguide coupling coefficient κ is equal for both propagation directions due to reciprocity. The losses due to the coupling of the cavity to the waveguides are included in the diagonal elements Ω of the Hamiltonian (2). The backscattering coupling coefficients A and B do not have to be modified assuming that there is no backscattering of light between the microcavity and the waveguides which is justified when the distances between cavity and waveguides are sufficiently large. By exploiting this assumption, one determines the outgoing amplitudes in the lower waveguide as

$$a_{3,\mathrm{out}} = -\kappa^* \psi_{\mathrm{CW}} , \tag{12}$$

$$a_{4,\mathrm{out}} = -\kappa^* \psi_{\mathrm{CCW}} . \tag{13}$$

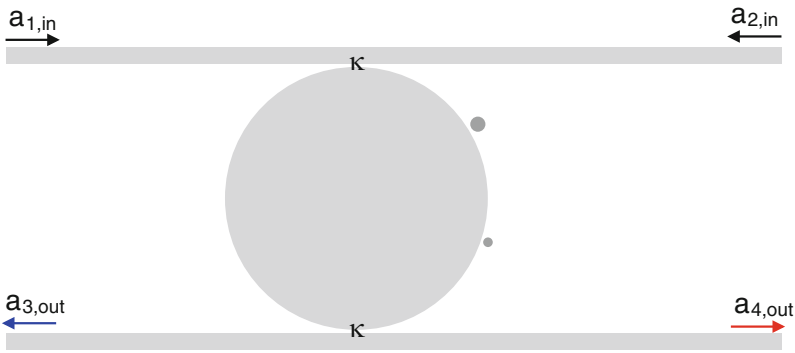

Fig. 2 Sketch of the geometry consisting of two parallel waveguides with two incoming channels with amplitudes $a_{1,\text{in}}, a_{2,\text{in}}$ and the two outgoing channels with amplitudes $a_{3,\text{out}}, a_{4,\text{out}}$, and an asymmetric WGM microcavity (here realized by a disk locally perturbed by two dissimilar scatterers). κ is the cavity-waveguide coupling coefficient which is here for simplicity assumed to be equal for both waveguides

We can choose κ to be real as we are only interested in the absolute values of $a_{3,\text{out}}$ and $a_{4,\text{out}}$.

For an harmonic CW excitation of amplitude $a_{1,\text{in}}$ and real-valued frequency ω_e one finds from Eqs. (11), (12), and (13)

$$a_{3,\text{out}} = \frac{\mathrm{i}\kappa^2(\Omega - \omega_e)}{(\Omega - \omega_e)^2 - AB} a_{1,\text{in}} \,, \tag{14}$$

$$a_{4,\text{out}} = \frac{-\mathrm{i}\kappa^2 A}{(\Omega - \omega_e)^2 - AB} a_{1,\text{in}} \,. \tag{15}$$

Analogously, for a CCW excitation of amplitude $a_{2,\text{in}}$ one finds

$$a_{3,\text{out}} = \frac{-\mathrm{i}\kappa^2 B}{(\Omega - \omega_e)^2 - AB} a_{2,\text{in}} \,, \tag{16}$$

$$a_{4,\text{out}} = \frac{\mathrm{i}\kappa^2(\Omega - \omega_e)}{(\Omega - \omega_e)^2 - AB} a_{2,\text{in}} \,. \tag{17}$$

The asymmetric backscattering expresses itself here by the fact that the numerator in Eq. (15) is proportional to A, whereas the numerator in Eq. (16) is proportional to B.

Of particular interest is the extreme case of fully asymmetric backscattering where the Hamiltonian (2) is at an EP. Let us consider the case with $B = 0$ and $A \neq 0$. The transmission from port 2–3 is zero as there is no backscattering into the CW direction. However, the transmission von port 1–4 is nonzero since there is backscattering into the CCW direction. The strength of the transmission

is determined by the strength of the EP, $|A|$. It is important to note that even at the EP one can couple into both propagation directions (CW and CCW) as can be seen from Eqs. (14) and (17). This is not in contradiction with the fact that the Hamiltonian possesses only one eigenvector. It merely discloses that at an EP of the Hamiltonian H its eigenvectors do not constitute a basis.

3 Deformed WGM Microcavities

In this section we discuss optical modes in deformed microcavities (Fig. 1b). We treat the two-dimensional geometry within the effective index approximation. The solutions of Maxwell's equations with harmonic time dependence $\psi(x, y, t) = \psi(x, y) \exp(-\mathrm{i}\omega t)$ are the optical modes. They fulfill the scalar Helmholtz equations [35]

$$\left[\nabla^2 + \frac{\omega^2}{c^2} n^2(x, y)\right] \psi(x, y) = 0 \,, \tag{18}$$

where ψ is the z-component of either the electric (transverse magnetic polarization—TM) or the magnetic (transverse electric polarization—TE) field, ω is the resonant frequency, c the velocity of light in vacuum and n is the effective refractive index. For TM polarization the wave function ψ and its normal derivative $\partial_\nu \psi$ are continuous across the cavity's boundary. In the case of TE polarization, ψ and $n^{-2}\partial_\nu \psi$ are continuous across the boundary. With Sommerfeld's outgoing-wave condition at infinity the solutions of the mode equation (18) are quasibound states with decay rate $1/\tau = -2\,\mathrm{Im}\,\omega > 0$. The quality factor of the given mode is $Q = -\mathrm{Re}\,\omega/(2\,\mathrm{Im}\,\omega)$. For convenience, we use in the following the dimensionless frequency $\Omega = \omega R/c$.

Here we focus on the cavity whose boundary is given in polar coordinates by

$$\varrho(\phi) = R[1 + \varepsilon_2 \cos 2\phi + \varepsilon_3 \cos(3\phi + \delta)] \tag{19}$$

with $\delta \in [0, 2\pi)$. We call it the asymmetric $(2, 3)$-cavity as only the second and third Fourier-components of the periodic function $\varrho(\phi)$ are nonzero. The symmetric case $\delta = 0$ has been studied in [24]. The even more special case $\varepsilon_3 = 0$ is the well-known quadrupolar shape [65]. For generic ε_2, ε_3, and δ the system does not possess any mirror-reflection symmetry. Note that this shape is different from the asymmetric limaçon [107], which in our nomenclature is a $(1, 2)$-cavity. We choose, rather arbitrarily, $\varepsilon_2 = 0.025$, $\varepsilon_3 = 0.02$, and $\delta = 0.9$. The effective index of refraction is set to $n = 3.3$ (e.g. GaAs) and we only consider TM polarization. The optical modes and their complex frequencies are computed with the boundary element method (BEM) [98]. If not stated otherwise 8,000 discretization points are distributed along the entire boundary.

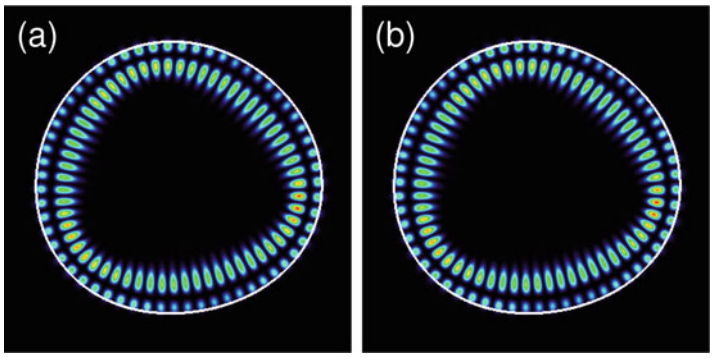

Fig. 3 Intensity $|\psi|^2$ of a nearly degenerate pair of modes in the cavity (19) with parameters specified in the text. Sixteen thousand discretization points have been used for the BEM. (**a**) Dimensionless frequency $\Omega_+ = 12.06033899 - \mathrm{i}3.855 \times 10^{-5}$ and (**b**) $\Omega_- = 12.06033885 - \mathrm{i}3.866 \times 10^{-5}$

Figure 3 depicts an example of a pair of nearly degenerate WGMs in the (2, 3)-cavity. The frequency splitting in the real and the imaginary part is of order 10^{-7}. This indicates a rather weak coupling of CW and CCW propagating waves in the cavity.

A deeper understanding of the mode structure can be gained by expanding the modes inside the cavity in cylindrical harmonics [8, 99],

$$\psi(\varrho, \phi) = \sum_{m=-\infty}^{\infty} \alpha_m J_m(nk\varrho) \exp(\mathrm{i}m\phi) \,, \tag{20}$$

where J_m is the mth order Bessel function of the first kind. Positive (negative) values of the angular momentum index m correspond to CCW (CW) traveling-wave components. Figure 4a shows that for both modes the angular momentum distribution $|\alpha_m|^2$ is dominated by the CCW component. Hence, the two modes are not standing waves but copropagating traveling waves. This is consistent with the eigenvectors (6) of the two-mode model for $|A| \neq |B|$, i.e. for asymmetric backscattering. The definition of the chirality in the two-mode model (7) can be naturally extended to the angular momentum decomposition (20) by

$$\alpha = \frac{\sum_{m=1}^{\infty} |\alpha_m|^2 - \sum_{m=-\infty}^{-1} |\alpha_m|^2}{\sum_{m=1}^{\infty} |\alpha_m|^2 + \sum_{m=-\infty}^{-1} |\alpha_m|^2} \,. \tag{21}$$

For the modes in Fig. 3 we find in both cases $\alpha \approx 0.423$.

The $\pm$ sign in the eigenvectors (6) appears when we look at the real and imaginary parts of α_m in Fig. 4b, c. For negative angular momentum index both the real and the imaginary part of α_m have a different sign for the two modes.

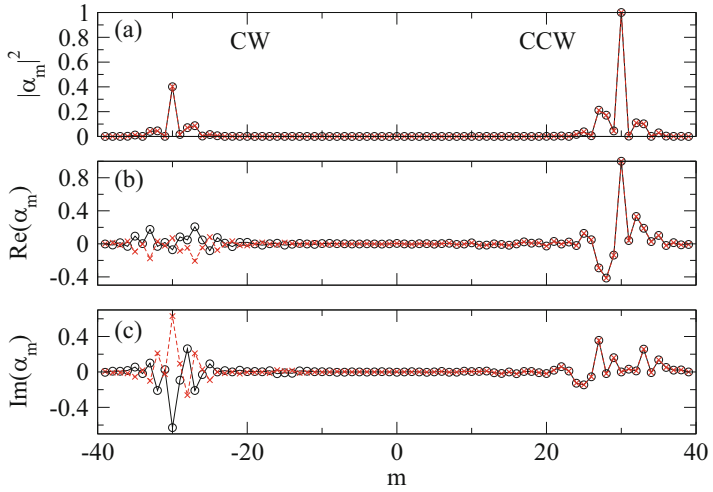

Fig. 4 Angular momentum distributions α_m of the modes in Fig. 3a (circles) and b (crosses). The real part is normalized to 1 at maximum: (**a**) absolute value squared, (**b**) real and (**c**) imaginary part of α_m. The region $m > 0$ ($m < 0$) corresponds to CCW (CW) traveling-wave components. The lines connecting the symbols serve as a guide to the eye

We quantify the nonorthogonality of the modes in analogy to the normalized overlap in the two-mode model (9) by the normalized overlap integral of two modes $\psi_1(x, y)$ and $\psi_2(x, y)$ over the interior of the cavity

$$S = \frac{|\int dxdy\ \psi_1^*\psi_2|}{\sqrt{\int dxdy\ \psi_1^*\psi_1}\sqrt{\int dxdy\ \psi_2^*\psi_2}}\,. \tag{22}$$

For the pair of modes in Fig. 3 we find $S \approx 0.422$ reflecting a significant nonorthogonality. This value together with the values of α reported above is fully consistent with the prediction of the two-mode model in Eq. (10).

Figure 5a shows a region of the complex plane of dimensionless frequencies Ω. It can be clearly seen that modes here always appear in nearly degenerate pairs. As already mentioned, this is due to the rather weak coupling of CW and CCW propagating waves in these open disk-like cavities. Figure 5b compares the chirality and the pairwise nonorthogonality of the modes. It can be seen that most of the modes in this region of the frequency plane have a negative chirality, i.e. they predominantly travel clockwise. Moreover, it also can be observed that the chirality and the overlap are strongly correlated. This correlation is in very good agreement with the result of the effective Hamiltonian of the two-mode model in Eq. (10). The deviations at $S \approx 0.12$ and $S \approx 0.39$ are probably due to coupling of the corresponding mode pairs to other mode pairs. It was shown that mode pair coupling can influence the relation between chirality and nonorthogonality [84].

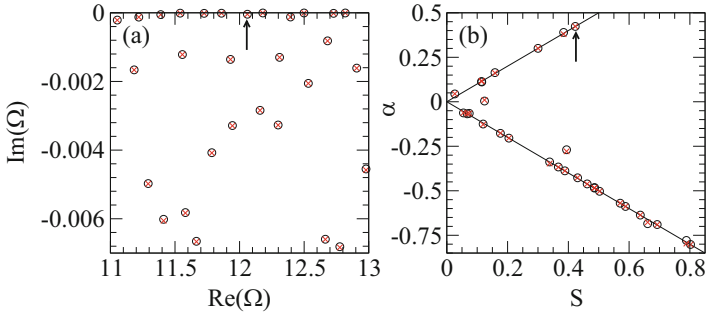

Fig. 5 (**a**) Subset of the complex frequency plane corresponding to the cavity in Eq. (19). Open circles (crosses) mark the slightly higher-Q (lower-Q) mode of a given pair of almost degenerate modes. (**b**) Chirality α versus spatial overlap S of mode pairs in (**a**) calculated from Eqs. (21) and (22). The solid lines show the prediction of the two-mode model in Eq. (10). The arrows mark the mode pair in Fig. 3

The asymmetric backscattering of light in deformed microdisk cavities is a general phenomenon leading to chirality, copropagation, and nonorthogonality. It has been numerically observed in a number of geometries: spiral-shaped cavities [48, 99, 106] (see Fig. 1b), the asymmetric limaçon and cavities of constant width [107], Fourier-truncated spirals [47], double-notched circles [48], rolled-up microcavities [19], and Reuleaux triangular-shaped cavities [72]. It is worth mentioning that surface roughness does not necessarily reduce the asymmetric backscattering. In the case of circular cavities surface roughness even introduces asymmetric backscattering [105].

3.1 Justification of the Two-Mode Model

The fact that the 2×2 Hamiltonian (2) works so well even for strongly deformed microdisk cavities like the one shown in Fig. 3 is surprising because in general many angular momentum components are involved as can be seen in Fig. 4. For other geometries, such as the spiral cavity, even many more angular momentum components contribute [106]. The explanation for this numerical observation is given by the perturbation theory for open quantum/wave systems in [101]. It assumes non-Hermiticity, reciprocity, and weak coupling between CW and CCW propagating waves. The latter reflects the fact that a smooth transition from CW to CCW propagation direction involves waves which do not fulfill the condition for total internal reflection. The coupling within the CW (CCW) propagation direction, however, is allowed to be large, thereby taking into account a possibly strong boundary deformation. In zeroth order the coupling between CW and CCW propagating waves is ignored. The eigenstates of the zeroth-order Hamiltonian come in degenerate pairs with one eigenstate lying in the CW subspace and the other one

lying in the CCW subspace. In the next order the weak coupling between CW and CCW propagating waves couples only the two eigenstates within these pairs. For each such pair the perturbation theory results in the 2×2 Hamiltonian of the form of Eq. (2).

3.2 Perturbation Theory for Weak Deformations

A second-order perturbation theory for TM/TE polarized modes in weakly deformed microcavities had been introduced in [18, 24]. The theory presupposes a boundary shape with at least one mirror-reflection symmetry. In this special case, the modes can be separated into two symmetry classes, leading to two nondegenerate perturbation theories. The generalization to deformations without mirror-reflection symmetry has been developed in [48] for TM polarization. This degenerate perturbation theory is able to determine the complex frequencies, the spatial mode structure including the far-field pattern and the chirality in generic cavities. The theory has been successfully applied to spirals and double-notched circles [48], as well as circles with surface roughness [105]. As expected, deviations between perturbation theory and full numerical calculations appear in close vicinity to EPs.

3.3 Ray Dynamics

The asymmetric backscattering of light waves in deformed microdisks leads to the mode-pair properties such as chirality, copropagation, and nonorthogonality. While the backscattering of light rays should be also asymmetric, obviously in cavities such as the spiral [106], it seems that the above properties, in particular the nonorthogonality, are not possible as they demand the concept of a mode which does not exists for ray dynamics. It was, however, shown that this line of reasoning is untenable. Also for the ray dynamics modes can be defined as the eigenstates of the Frobenius-Perron operator, which is the (discrete) time-evolution operator of densities in phase space. It turns out that for deformed microcavities with chaotic ray dynamics the long-time behavior of such phase-space densities is typically determined by the eigenstates corresponding to two leading, nearly degenerate, real eigenvalues of the Frobenius-Perron operator. This pair of eigenstates also shows chirality, copropagation, and nonorthogonality [47].

4 WGM Cavities with Local Perturbations

In this section we consider cavities with local perturbations. These can be local deformations, such as for the double-notched circle [48] or the disk with two small bumps [41]. It can also be external scatterers, such as small particles [100] (Fig. 6a)

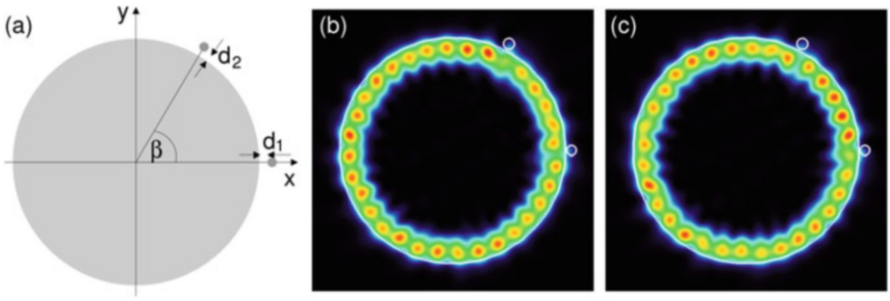

Fig. 6 (**a**) Microdisk with two nanoparticles at distance d_j from the disk's boundary. The azimuthal position of the second nanoparticle is specified by the angle β. (**b**) and (**c**) show intensity patterns of a nearly degenerate mode pair in the perturbed microdisk. (**b**) Dimensionless frequency $\Omega_+ = 9.8781 - \mathrm{i}0.0024$ and (**c**) $\Omega_- = 9.8780 - \mathrm{i}0.0025$

or nanofiber tips [66] (Fig. 1a), or internal scatterers such as holes in the disks [103]. In the following we refer to such a local perturbation simply as scatterer.

For a WGM cavity perturbed weakly by two scatterers the two-mode model appears naturally within a two-mode approximation with fixed angular momentum number m (and $-m$). The matrix elements of H can be analytically determined [100]

$$\Omega = \Omega_0 + V_1 + U_1 + V_2 + U_2 \,, \tag{23}$$

$$A = (V_1 - U_1) + (V_2 - U_2)e^{-2\mathrm{i}m\beta} \,, \tag{24}$$

$$B = (V_1 - U_1) + (V_2 - U_2)e^{2\mathrm{i}m\beta} \,. \tag{25}$$

β is the angular position of the second scatterer. The polar coordinate system is chosen such that the first scatterer is located at the angular position $\phi = 0$. The Eqs. (23), (24), and (25) are not only valid for point scatterers ($U_j = 0$), which is a good approximation in the limit of Rayleigh scattering, but also for finite-size scatterers provided that each scatterer j alone leads to a configuration with a mirror-reflection symmetry. The quantities $2V_j$ and $2U_j$ are given by the complex frequency shifts for positive- and negative-parity modes introduced by scatterer j. These numbers can be calculated for the single-scatterer-microdisk system either numerically, using, e.g., the finite-difference time-domain method [91], the BEM, or approximately using the Green's function approach for point scatterers [15].

In the absence of gain the imaginary parts of Ω_0, V_j, and U_j are nonpositive. A short calculation confirms that the inequality (4) holds. The effective Hamiltonian (2) with matrix elements (23), (24), and (25) is in general non-Hermitian with $A \neq B^*$ if V_j and U_j have a nonzero imaginary part. Interestingly, even though each scatterer alone leads to symmetric backscattering of light, the presence of both scatterers with different $V_j - U_j$ can lead to asymmetric backscattering, $|A| \neq |B|$.

4.1 Microdisk with Two External Scatterers

A microdisk with two nanoparticles as external scatterers (Fig. 6a) has been studied in [100]. Here, we review the main results. If not stated otherwise we fix the parameter as follows. The refractive index of the disk of radius R is set to $n = 2$, the same for the two scatterers. The distances of the scatterers from the cavity's boundary are $d_1/R = 0.01$ and $d_2/R = 0.02$. The scatterers are small circles with radii $r_1/R = 0.043$ and $r_2/R = 0.048325$. The angular position of the second scatterer relative to the first one is $\beta = 1.08468125$ in radian. The mode equation (18) is solved for TM polarization by using the BEM. Figure 6b, c shows the pair of modes corresponding to unperturbed WGMs with azimuthal mode number $m = 16$ and the lowest radial mode number. The traveling-wave character can be already seen in the real-space plot by the lack of a clear nodal line structure. The modes show a strong chirality, $\alpha = -0.976$ and $\alpha = -0.975$, and a strong nonorthogonality, $S = 0.987$, consistent with the prediction of the two-mode model in Eq. (10).

Figure 7 proves that both modes are indeed copropagating traveling waves. The angular momentum distribution $|\alpha_m|^2$ is in both cases dominated by the CW component. Moreover, we can see that just two angular momenta contribute significantly, $m = \pm 16$. We can therefore, in very good approximation, identify these two contributions with the two components in the two-mode model from Sect. 2. Note that in the case of internal scatterers such a direct identification can fail since a significant amount of lower angular momentum components is excited [103]. The results of Fig. 7 are again fully consistent with the eigenvectors (6) of the two-mode model.

By varying the azimuthal position of the second nanoparticle β and its radius r_2 the frequency splitting and the decay rate splitting can be reduced simultaneously to zero, see Fig. 8. This happens at $r_2/R \approx 0.04833$ and $\beta \approx 1.084681$ close to the parameters of the mode pair shown in Fig. 6b, c. Figure 8 clearly demonstrates the complex-square-root topology of a branch point singularity which is usually considered as a proof of the existence of an EP [12, 52]. The coloring in Fig. 8 reveals that near the EP the absolute value of the chirality (21) goes close to unity, consistent with Eq. (10) from the two-mode model. As discussed above the modes of this pair are almost collinear, i.e. effectively one mode is lost.

4.2 Microtoroid with Two Nanofiber Tips

The asymmetric backscattering in perturbed WGM cavities has been experimentally confirmed for a silica microtoroid perturbed by two nanofiber tips [66] as depicted in Fig. 1a. Two waveguides are used to excite and probe the CW and CCW propagation direction independently as illustrated in Fig. 2. When there is no scatterer near the cavity, light coupled into the cavity through the upper waveguide in the CW

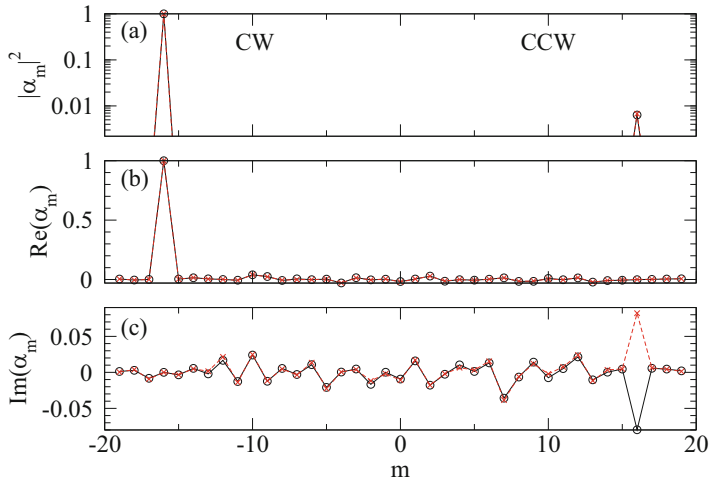

Fig. 7 Angular momentum distributions α_m of the modes in Fig. 6b (circles) and c (crosses). The real part is normalized to 1 at maximum: (**a**) absolute value squared in a semilogarithmic scale, (**b**) real and (**c**) imaginary part of α_m. The lines connecting the symbols serve as a guide to the eye

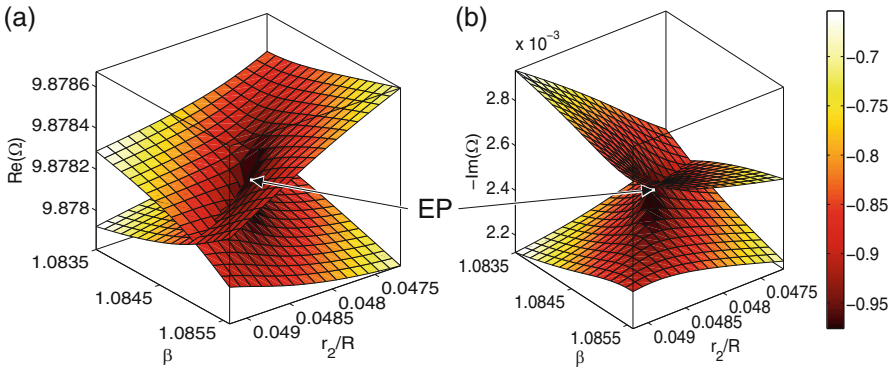

Fig. 8 Complex-square-root topology near an EP in the spectrum of a microdisk perturbed by two external nanoparticles, cf. Fig. 6. Shown is the complex frequency Ω versus the parameters r_2/R and β: (**a**) real and (**b**) imaginary part. The absolute value of the chirality α gradually increases from light to dark and approaches 1 at the EP

(Fig. 9a, i) (or CCW in Fig. 9b, i) propagation direction couples out into the lower waveguide in the CW (or CCW) propagation direction. There is a resonant peak in the transmission and no signal in the reflection. When a first scatterer is placed close to the cavity's boundary (Fig. 9a, ii and b, ii), resonant peaks are observed in both the transmission and the reflection regardless of whether the light is input in the CW or in the CCW direction. When a second scatterer is suitably placed close

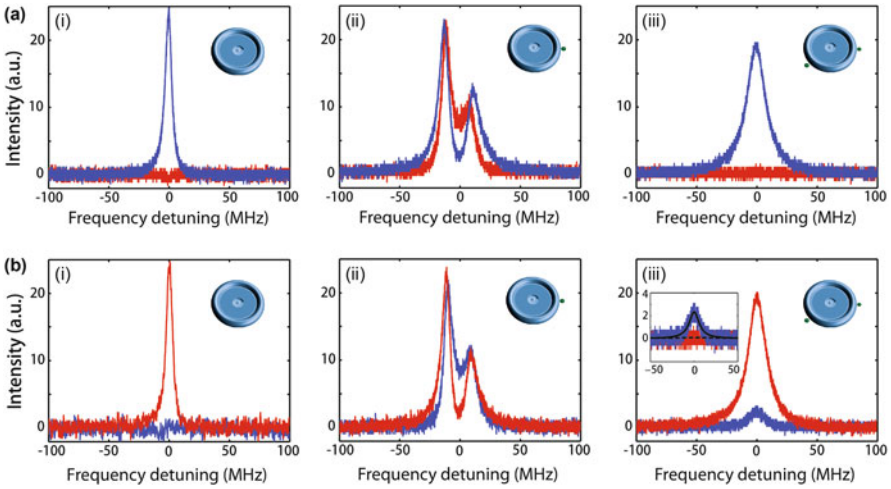

Fig. 9 Experimental confirmation of asymmetric backscattering in a perturbed WGM cavity. (**a**) CW input via port 1 and (**b**) CCW input via port 2; cf. Fig. 2. CW output $|a_{3,\mathrm{out}}|^2$ is shown in blue and CCW output $|a_{4,\mathrm{out}}|^2$ is shown in red. Inset in (**b, iii**) compares the two backscattering peaks in (**a, iii**) and (**b, iii**). (Adapted from [66])

to the boundary of the cavity such that an EP is established (Fig. 9a, iii and b, iii), for the CW input there is no signal in the reflection output port (Fig. 9a, iii), whereas for the CCW input there is a resonant peak in the reflection (Fig. 9b, iii), revealing asymmetric backscattering for the two input directions, cf. Eqs. (15) and (16) with $A = 0$ and $B \neq 0$.

A slightly modified version of the experiment demonstrated the chirality in asymmetric WGM cavities [66]. Again a silica microtoroid is perturbed by two nanofiber tips but now the cavity is doped with erbium ions and is coupled to a single waveguide. Pumping the cavity leads to lasing which, depending on the position of the nanofiber tips, can be directional as demonstrated in Fig. 10. The directionality reveals the underlying chirality of the modes. By moving the nanofiber tips one can go from an EP with chirality $\alpha = +1$ to an EP with $\alpha = -1$. This approach allows to dynamically control the directionality of the light emission. The alternative experiments on a microdisk with two small bumps [41], on a microring with periodic index of refraction modulation [63], and on coupled microcavities [112] also confirm the chirality but do not allow to dynamically control it.

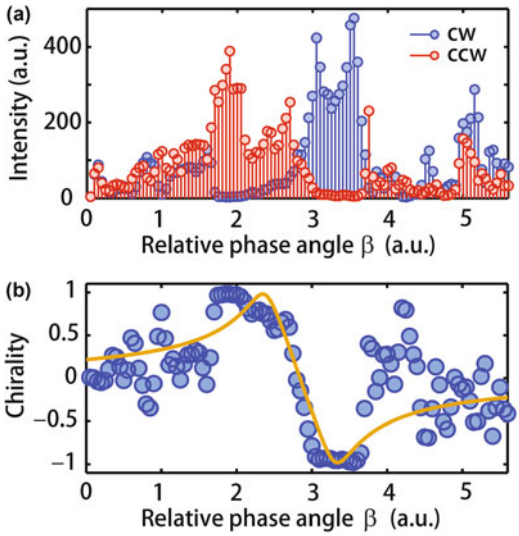

Fig. 10 Experimental confirmation of chirality in a perturbed WGM microlaser coupled to a waveguide. (**a**) Intensity of light outcoupled into a waveguide in the CW and CCW propagation directions as a function of β, the angle between the two nanofiber tips. Regions of bidirectional emission and unidirectional emission can be observed. (**b**) Chirality α as a function of β. Transitions from nonchiral states to states with strong chirality close to EPs are clearly seen. Regions with $\alpha \approx \pm 1$ correspond to unidirectional emission regions in (**a**). The solid curve is the result of the two-mode model with Eqs. (8) and (23), (24), and (25). (Adapted from [66])

5 WGM Cavities with Modulation of the Effective Index of Refraction

Yet another way to render the backscattering in a WGM cavity to be asymmetric is by introducing an asymmetric modulation of the effective index of refraction in the azimuthal direction. This can be achieved by introducing layers of different materials or simply by modulating the height of the cavity, see Fig. 1c. Non-Hermiticity comes in by the coupling to a lossy channel [80] (e.g. the continuum) or by introducing directly loss and gain into the materials [63, 96, 97]. The matrix elements of the Hamiltonian (2) in the two-mode model have not been determined for the case of refractive index modulation but an explicit transfer-matrix approach can be found in [59].

6 Coupled Cavities with Internal Asymmetric Backscattering

This section deals with coupled WGM cavities where at least in one of the cavities the backscattering of light is asymmetric as illustrated in Fig. 11. Song and coworkers [83] suggested to place a circular cavity next to a circular cavity with

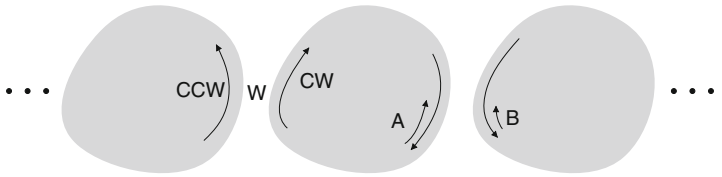

Fig. 11 Sketch of coupled cavities with asymmetric internal backscattering. The coefficient A describes the backscattering of CW traveling waves to CCW traveling waves, while the backscattering from CCW to CW traveling waves is described by B. The parameter W is the inter-cavity coupling coefficient

a spiral-shaped inner boundary. Numerical simulations demonstrated that in such an arrangement a very high Q-factor can be combined with a strong chirality in a robust way. The same setup has been applied for single-nanoparticle detection taking advantage of the sensitivity of the far-field pattern in the presence of strong chirality [111, 112].

Coupled-resonator optical waveguides (CROWs) are waveguides formed by a serial chain of microcavities, which are weakly coupled by their evanescent fields [56, 85, 110]. These exotic waveguides have attracted considerable attention since there is a variety of potential applications such as optical filtering [57], optical buffering [67], nonlinear components [109], and group velocity compensation [40]. Figure 11 illustrates a CROW made of open resonators lacking mirror-reflection symmetry, i.e. each individual resonator can exhibit asymmetric internal backscattering. It has been shown that the asymmetric backscattering in such a periodic system can lead to EPs in the complex band structure $\Omega(k)$, where k is the real-valued Bloch wavenumber [78]. Near an EP of order p, one gets

$$\Omega(k) - \Omega_{\mathrm{EP}} \sim (k - k_{\mathrm{EP}})^{1/p} \,. \tag{26}$$

As a result, the group velocity diverges when the EP is approached,

$$v_g(k) \equiv \frac{d}{dk} \mathrm{Re}\, \Omega(k) \sim (k - k_{\mathrm{EP}})^{(1/p-1)} \,. \tag{27}$$

This is, however, not in contradiction with special relativity. Using a non-Hermitian correction to the Hellmann-Feynman theorem it has been proven in [78] that the intensity transport velocity v_I near an EP remains finite,

$$v_I(k) - v_{I,\mathrm{EP}} \sim (k - k_{\mathrm{EP}})^{1/p} \,. \tag{28}$$

CROWs made of cavities with asymmetric internal backscattering have been used to create topologically protected defect states in a system that is topologically trivial in the closed limit [61].

7 Applications of Asymmetric Backscattering

7.1 EP-Based Sensors

An essential difference between EPs and conventional Hermitian degeneracies, DPs, is the sensitivity to perturbations [39]. Perturbing a DP by a perturbation of strength ε leads to a frequency splitting of order ε. This is in strong contrast to an EP of second order which results in a frequency splitting of order $\sqrt{\varepsilon}$ which is larger for sufficiently small perturbations. In [102] it was suggested to exploit this sensitivity for sensor applications which are based on the detection of frequency (energy level) splittings. Examples are weak magnetic field sensors [70], nanomechanical mass sensors [26], bending curvature sensors [58], optical gyroscopes [10, 90], microcavity sensors for single or few particle detection [27, 94, 114]. For the latter class of systems we explain the scheme of [102] which is based on a two-mode model with fixed azimuthal mode number; a more general approach is provided in [103]. The unperturbed sensor is a WGM sensor described by H_0 as in Eq. (2). It has zero frequency splitting which can be achieved either by using a DP or an EP. A DP is here given by $B = 0$ and $A = 0$, i.e. without any backscattering between CW and CCW traveling waves. An EP results for $B = 0$ or $A = 0$; see Fig. 12a. The EP can be installed by using two scatterers as discussed in Sect. 4. The microcavity sensor together with the target particle are described by

$$H = H_0 + H_1 \,. \tag{29}$$

The perturbation due to the small target particle at angular position β (Fig. 12a) is in the same spirit as in Eqs. (23), (24), and (25) given by

$$H_1 = \begin{pmatrix} V+U & (V-U)e^{-\mathrm{i}2m\beta} \\ (V-U)e^{\mathrm{i}2m\beta} & V+U \end{pmatrix} \,. \tag{30}$$

The disturbance due to the target particle, H_1, induces for the DP the complex frequency splitting

$$\Delta\Omega_{\mathrm{DP}} = 2(V-U) \,. \tag{31}$$

The real part is the conventional frequency splitting observed for instance in [114]. The imaginary part corresponds to a linewidth splitting. In contrast, for the EP ($B = 0$ and $A \neq 0$) one gets

$$\Delta\Omega_{\mathrm{EP}} = \Delta\Omega_{\mathrm{DP}}\sqrt{1 + \frac{Ae^{\mathrm{i}2m\beta}}{V-U}} \,. \tag{32}$$

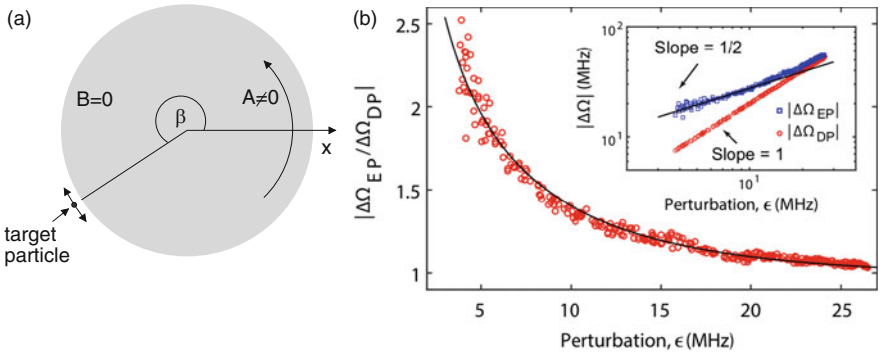

Fig. 12 (**a**) Sketch of a WGM microcavity with fully asymmetric backscattering (indicated by the large single-headed arrow for $A \neq 0$ and $B = 0$) acting as EP-based sensor. The target particle introduces a weak symmetric backscattering (small double-headed arrow) leading to an enlarged frequency splitting. (**b**) Experimental confirmation of the enhanced sensitivity of a microcavity sensor for nanoparticle detection at an EP. Shown is the enhancement factor $|\Delta\Omega_{\mathrm{EP}}/\Delta\Omega_{\mathrm{DP}}|$ as a function of the perturbation strength ε. The solid curve is a fit using Eq. (32). Inset: logarithmic plot of $|\Delta\Omega|$ versus ε. The DP-based sensor shows a slope of 1, whereas the EP-based sensor shows a slope of $1/2$ for sufficiently small perturbations. ((**b**) is adapted from [7])

If the square root in Eq. (32) is larger than unity then the frequency splitting at the EP is larger than the one at the DP even though in both cases the perturbation H_1 is exactly the same. The intuitive explanation is that the intrinsic (and fully asymmetric) backscattering of strength $|A|$ does not lead to a splitting as long as there is no target particle, but in the presence of a target particle it is able to give a significant contribution to the splitting. It might be helpful for the reader to associate the strength of the EP, $|A|$, with the tension of a crossbow. The larger the tension the larger the amplification of the effect of the perturbation (the pulling of the trigger). In this crude analogy, the DP corresponds to an untensioned crossbow.

If the intrinsic backscattering is much larger than the backscattering at the target particle, $|A| \gg |V - U|$, or in other words if the strength of the EP is much larger than the perturbation induced by the target particle, Eq. (32) simplifies to

$$\Delta\Omega_{\mathrm{EP}} = \Delta\Omega_{\mathrm{DP}}\, e^{im\beta} \sqrt{\frac{A}{V-U}}\,. \tag{33}$$

Here, the absolute value of the complex frequency splitting $|\Delta\Omega_{\mathrm{EP}}| \gg |\Delta\Omega_{\mathrm{DP}}|$ is independent from the azimuthal position of the target particle, β. But the corresponding real and imaginary parts do depend on β. It is therefore necessary to measure both the frequency splitting $\mathrm{Re}(\Delta\Omega)$ and the linewidth splitting $-2\,\mathrm{Im}(\Delta\Omega)$. Note that for passive systems, where the inequality (4) applies, it is experimentally difficult to separate the two peaks in the spectrum [103]. This problem can be solved by linewidth reduction due to optical gain in an active microcavity [28].

The presented theory has been confirmed in a recent experiment [7]. As in [66] the WGM cavity is a silica microtoroid coupled to two waveguides. The EP is installed using two nanofiber tips as shown in Fig. 1a. As target particle a third nanofiber or a single polystyrene nanoparticle is used. Figure 12b shows that the enhancement factor is about 2.5 for small perturbations and decays for increasing perturbation. In the logarithmic plot a slope of $1/2$ can be seen which originates from the square-root behavior at the EP. For the DP-based sensor a slope of 1 is present due to the linear behavior at the DP.

The sensitivity enhancement at an EP is not restricted to the discussed scenario of particle detection and asymmetric backscattering [103]. It has also been observed for coupled cavities at an EP [32]. An alternative single-particle detection scheme using asymmetric backscattering has been presented in [112] (see Sect. 6). It is based on the sensitivity of the far-field pattern in the presence of strong chirality. The same effect has been exploited before for rotation sensing as is discussed in the next subsection.

7.2 Rotation Sensing via Output Directionality

The well-known Sagnac effect is the frequency splitting of optical modes in a rotating cavity, see e.g. [89]. It has become the operation principle for ring laser gyroscopes. In the context of this book chapter we focus on cavities without mirror-reflection symmetry. It had been shown in [73] that the quasidegenerate pairs of copropagating modes are transformed by rotation to counterpropagating ones, leading to a striking change of emission directions. This can be understood through the two-mode model Hamiltonian (2). In the case of backscattering with strong asymmetry, e.g. $|A| \ll |B|$, the eigenvectors (6) are very similar, both are dominated by the CW component. This implies that the corresponding two modes have similar properties including the far-field patterns. Figure 13a, b show such a situation for a mode pair in the asymmetric limaçon. Importantly, the small but finite CCW components exhibit very different far-field behavior as shown in Fig. 13c.

The rotation can be modeled as a perturbation with Hamiltonian

$$H_1 = \begin{pmatrix} \Delta & 0 \\ 0 & -\Delta \end{pmatrix} . \tag{34}$$

If the rotation speed is slow enough Δ is proportional to the rotation speed. The Hamiltonian H_1 describes the frequency change of CCW and CW propagating waves induced by the rotation alone. Note that the perturbation (34) is special: in contrast to the perturbation (30) it does not give rise to a square-root behavior when applied to the Hamiltonian (2) at the EP.

In the case $A = 0$ we find for the (not normalized) right eigenvectors of the full Hamiltonian $H + H_1$

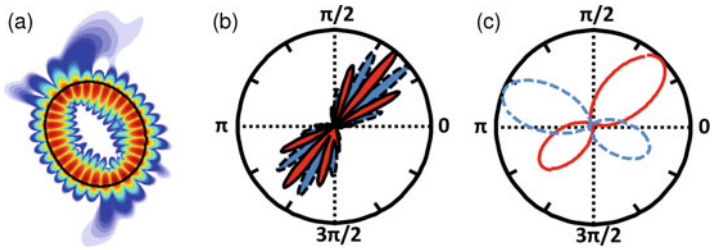

Fig. 13 Near- and far-field intensity patterns of modes in the nonrotating asymmetric limaçon $\varrho(\phi) = R[1 + \varepsilon_1 \cos\phi + \varepsilon_2 \cos(2\phi + \delta)]$ with $R = 591\,\text{nm}$, $\varepsilon_1 = 0.1$, $\varepsilon_2 = 0.075$, and $\delta = 1.94$. The refractive index is $n = 3$ and the wavelength is $\lambda = 598\,\text{nm}$. The TM polarized modes are calculated by the finite-difference frequency-domain method. (**a**) Near-field pattern of one of the quasidegenerate modes. The other mode looks similar. The intensity outside the cavity is enhanced to illustrate the chirality. (**b**) Far-field patterns of both modes, which have similar output directions. (**c**) Far-field patterns of CW (solid curve) and CCW (dashed curve) components of the modes, exhibiting distinct output directions. (Adapted from [73])

$$\boldsymbol{\psi}_1 = \begin{pmatrix} 0 \\ 1 \end{pmatrix}, \quad \boldsymbol{\psi}_2 = \begin{pmatrix} 2\Delta/B \\ 1 \end{pmatrix}. \tag{35}$$

When the rotation speed is increased the eigenvector $\boldsymbol{\psi}_1$ stays the same, whereas $\boldsymbol{\psi}_2$ starts to be dominated by the CCW component for $|\Delta| > |B|/2$. If the CCW and CW components have a significantly different far-field pattern, as in the case of the asymmetric limaçon in Fig. 13, the far-field pattern dramatically changes when the rotation speed is increased. Measuring the rotation with the conventional Sagnac effect requires that the frequency splitting has to overcome the line broadening, i.e. $|\Delta| > 2|\text{Im}(\Omega)|$. Because of the inequality (4) one can expect that the scheme with the far-field pattern performs better. Indeed, numerical simulations have shown a three orders of magnitude stronger effect in comparison to the Sagnac frequency splitting [73].

7.3 Directional Lasing

As discussed in Sect. 4.2 the chirality can be exploited for directional lasing in WGM cavities. The general mechanism is that already below laser threshold there is a preferred propagation direction due to the asymmetric backscattering. There have been several attempts to achieve directional lasing operation in ring lasers, the macroscopic version of WGM cavities, because it offers the advantages of enhanced mode purity and higher single beam power. The first experiment taking advantage of asymmetry was on an "S-shaped" AlGaAs/GaAs ring laser [33]. The unidirectional ratio, defined as the minor directional output to the major directional output, was around 0.05. Another experiment was on triangular AlGaAs/GaAs waveguide lasers

with an asymmetrically modified section, which was termed "optical diode" [54]. The unidirectional ratio was here as small as 0.03. An even better suppression of the minor direction output had been achieved by using a rectangular geometry with "optical diode" [53].

It should be emphasized that the authors of Refs. [33, 53, 54] did not relate their findings to asymmetric backscattering nor to non-Hermitian effects. They believed that the suppression of one propagation direction in the laser dynamics is related to an unequal transmission (as in a diode) coming from unequal losses for the different propagation directions. This interpretation is, however, wrong because it violates reciprocity. Kalagara and coworkers tried to rescue the concept of unequal losses by numerical simulations [38]. But from their simulations of the short-time evolution of many modes no conclusion about individual losses can be drawn. Yet another misinterpretation is that the modes of a given mode pair resulting from asymmetric backscattering have identical quality factors but different spatial mode patterns [49]. This claim was disproved in [99] for the spiral cavity where it was shown that the quality factors are slightly different and the spatial mode patterns are very similar. The latter fact just reflects the strong nonorthogonality [106].

Another approach to achieve unidirectional operation in ring lasers is to introduce an external optical reflector which provides feedback only for one of the propagation directions. In [25] this was modeled by an asymmetric backscattering showing that a strong asymmetry enhances the probability of one propagation mode to lase alone. However, a link to non-Hermitian effects has not been established.

Sui et al. fabricated InP-based spiral-shaped microlasers vertically coupled to a silicon waveguide and demonstrated stable directed light emission [87]. The authors introduced an improved cavity shape, a locally deformed ring, with unidirectional ratio of 0.053 [88].

An analysis based on semiconductor laser rate equations at the EP in ring-like cavities with asymmetric backscattering revealed stable unidirectional operation for not too high current levels [60]. Deviating from the EP can break the unidirectional operation, but for higher currents the unidirectional operation is restored.

7.4 Orbital Angular Momentum Lasers

Once unidirectional lasing operation has been achieved in a WGM microcavity it can be exploited for the effective generation of light with nonzero orbital angular momentum [63, 96, 108]. This has been achieved experimentally in an InGaAsP/InP-microring with periodically modulated complex refractive index to install an EP based on asymmetric backscattering [63] as discussed in Sect. 5. With sidewall modulations periodically arranged along the microring outer boundary laser radiation with an optical vortex of topological charge $l = -1$ was emitted upwards. The topological charge of the vertically emitted light of a mode with azimuthal mode number m depends on the angular momentum contributions α_l with $|l| < |m|$ (Eq. (20)) corresponding to leaky components, see [96]. Another exper-

iment on a silicon microring with asymmetrically deformed inner boundary has shown vertical emission of orbital angular momentum superposition states [108].

8 Summary

This chapter provides a comprehensive overview on the non-Hermitian effects due to asymmetric backscattering of counterpropagating waves in whispering-gallery microcavities. To shed light on the simplicity and the beauty of the physics, the two-mode model for the isolated cavity and the waveguide-coupled cavity has been elaborated first. The non-Hermitian phenomena chirality, copropagation, and nonorthogonality of mode pairs have been discussed. It has been demonstrated that if the backscattering is fully asymmetric an exceptional point in the spectrum is reached; see illustration in Fig. 14.

The non-Hermitian physics of deformed microdisk cavities due to asymmetric backscattering has been demonstrated for the novel (2, 3)-cavity. The chirality, copropagation, and nonorthogonality could be clearly seen in full agreement with the two-mode model. The justification of the latter has been addressed. A perturbation theory for deformed microdisk cavities has been touched. The non-

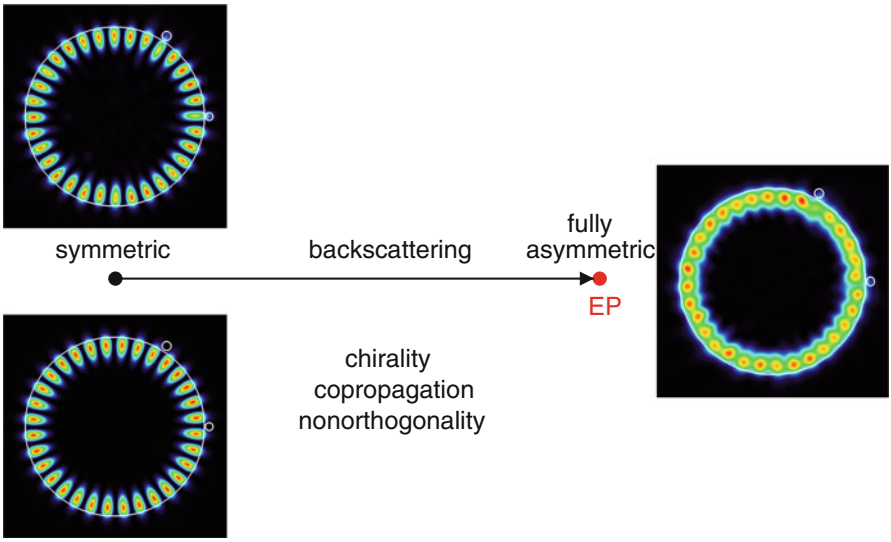

Fig. 14 Asymmetric backscattering of counterpropagating waves in perturbed whispering-gallery microcavities. In the symmetric case on the left-hand side, the optical modes are pairwise orthogonal standing waves. Asymmetric backscattering leads to chirality, copropagation, and nonorthogonality of mode pairs. Raising the asymmetry from left to right increases chirality and nonorthogonality. Fully asymmetric backscattering results in an exceptional point (EP) where the modes coalesce

Hermitian effects can also appear in the ray dynamics when the eigenstates of the time-evolution operator of the phase-space densities are investigated.

Whispering-gallery cavities with local perturbations are another interesting class of systems where asymmetric backscattering is relevant. Here, the dependence of the matrix elements of the two-mode model with respect to the relative angular positions of the local scatterers can be written down explicitly. With proper adjustments of parameters an exceptional point can be installed. The experimental confirmation of the asymmetric backscattering and chirality in a microtoroid perturbed by two nanofiber tips was explained. Microcavities with a modulation of the effective index of refraction were briefly discussed.

Coupled cavities with asymmetric internal backscattering were also considered. Of particular interest are waveguides formed of such cavities as they can exhibit exceptional points in the complex bandstructure. At these points the group velocity diverges but the intensity transport velocity stays finite.

Finally, applications of asymmetric backscattering were outlined. The exceptional point for fully asymmetric backscattering shows a much larger sensitivity with respect to external perturbations if compared to a conventional degeneracy. This can be exploited for sensing of nanoparticles with greatly enhanced sensitivity. Moreover, cavities without mirror-reflection symmetry allow for an alternative scheme of sensing rotations. In contrast to the conventional Sagnac effect which leads to a small frequency splitting, the new approach leads to a dramatic change in the far-field pattern. As another important application, asymmetric backscattering can be exploited to achieve unidirectional laser operation in whispering-gallery and ring-like cavities. Finally, a whispering-gallery or ring-like cavity operating unidirectionally can be utilized as a vertically emitting orbital angular momentum laser.

It would be interesting to extend the study of asymmetric backscattering to deformed microspheres. Because of the higher degeneracy of whispering-gallery modes in the unperturbed sphere it is to be expected that such systems unveil even richer non-Hermitian physics.

Acknowledgements I would like to thank J. Kullig for carefully reading the manuscript, W. Chen and L. Yang for providing Figs. 1a, 9, 10, 12b and L. Feng for providing Fig. 1c. Financial support by the DFG (project WI1986/6-1) is also acknowledged.

References

1. Bender, C.M., Boettcher, S.: Real spectra in non-Hermitian Hamiltonians having PT symmetry. Phys. Rev. Lett. **80**, 5243–5246 (1998)
2. Berry, M.V.: Physics of nonHermitian degeneracies. Czech. J. Phys. **54**, 1039–1047 (2004)
3. Berry, M.V., Wilkinson, M.: Diabolic points in the spectra of triangles. Proc. R. Soc. Lond. A **392**, 15–43 (1984)
4. Brandstetter, M., Liertzer, M., Deutsch, C., Klang, P., Schöberl, J., Türeci, H.E., Strasser, G., Unterrainer, K., Rotter, S.: Reversing the pump dependence of a laser at an exceptional points. Nat. Commun. **5**, 4034 (2014)

5. Cao, H., Wiersig, J.: Dielectric microcavities: model systems for wave chaos and non-Hermitian physics. Rev. Mod. Phys. **87**, 61–111 (2015)
6. Cartarius, H., Main, J., Wunner, G.: Exceptional points in atomic spectra. Phys. Rev. Lett. **99**, 173003 (2007)
7. Chen, W., Özdemir, Ş.K., Zhao, G., Wiersig, J., Yang, L.: Exceptional points enhance sensing in an optical microcavity. Nature **548**, 192–196 (2017)
8. Chern, G.D., Tureci, H.E., Stone, A.D., Chang, R.K., Kneissl, M., Johnson, N.M.: Unidirectional lasing InGaN multiple-quantum-well spiral-shaped micropillars. Appl. Phys. Lett. **83**, 1710–1712 (2003)
9. Choi, Y., Kang, S., Lim, S., Kim, W., Kim, J.R., Lee, J.H., An, K.: Quasieigenstate coalescence in an atom-cavity quantum composite. Phys. Rev. Lett. **104**, 153601 (2010)
10. Chow, W.W., Gea-Banacloche, J., Pedrotti, L.M., Sanders, V.E., Schleich, W., Scully, M.O.: The ring laser gyro. Rev. Mod. Phys. **57**, 61–104 (1985)
11. Collot, L., Lefevre-Seguin, V., Brune, M., Raimond, J., Haroche, S.: Very high-Q whispering-gallery modes observed on fused silica microspheres. Europhys. Lett. **23**, 327–334 (1993)
12. Dembowski, C., Gräf, H.D., Harney, H.L., Heine, A., Heiss, W.D., Rehfeld, H., Richter, A.: Experimental observation of the topological structure of exceptional points. Phys. Rev. Lett. **86**, 787–790 (2001)
13. Dembowski, C., Dietz, B., Gräf, H.D., Harney, H.L., Heine, A., Heiss, W.D., Richter, A.: Observation of a chiral state in a microwave cavity. Phys. Rev. Lett. **90**, 034101 (2003)
14. Dembowski, C., Dietz, B., Gräf, H.D., Harney, H.L., Heine, A., Heiss, W.D., Richter, A.: Encircling an exceptional point. Phys. Rev. E **69**, 056216 (2004)
15. Dettmann, C.P., Morozov, G.V., Sieber, M., Waalkens, H.: Unidirectional emission from circular dielectric microresonators with a point scatterer. Phys. Rev. A **80**, 063813 (2009)
16. Dietz, B., Friedrich, T., Metz, J., Miski-Oglu, M., Richter, A., Schäfer, F., Stafford, C.A.: Rabi oscillations at exceptional points in microwave billiards. Phys. Rev. E **75**, 027201 (2007)
17. Dillon, G., Passatore, G.: The symmetry of the theoretical optical potential and its connection with time reversal and reciprocity. Nucl. Phys. A **114**, 623–628 (1968)
18. Dubertrand, R., Bogomolny, E., Djellali, N., Lebental, M., Schmit, C.: Circular dielectric cavity and its deformations. Phys. Rev. A **77**, 013804 (2008)
19. Fang, Y., Li, S., Mei, Y.: Modulation of high quality factors in rolled-up microcavities. Phys. Rev. A **94**, 033804 (2016)
20. Feng, L., Xu, Y.L., Fegadolli, W.S., Lu, M.H., Oliveira, J.E.B., Almeida, V.R., Chen, Y.F., Scherer, A.: Experimental demonstration of a unidirectional reflectionless parity-time metamaterial at optical frequencies. Nat. Mater. **12**, 108–113 (2013)
21. Feng, L., Zhu, X., Yang, S., Zhu, H., Zhang, P., Yin, X., Wang, Y., Zhang, X.: Demonstration of a large-scale optical exceptional point structure. Opt. Exp. **22**, 1760–1767 (2014)
22. Fujita, M., Baba, T.: Microgear lasers. Appl. Phys. Lett. **80**, 2051–2053 (2002)
23. Gao, T., Estrecho, E., Bliokh, K.Y., Liev, T.C.H., Fraser, M.D., Brodbeck, S., Kamp, M., Schneider, C., Höfling, S., Yamamoto, Y., Nori, F., Kivshar, Y.S., Truscott, A.G., Dall, R.G., Ostrovskaya, E.A.: Observation of non-Hermitian degeneracies in a chaotic exciton-polariton billiard. Nature **526**, 554–558 (2015)
24. Ge, L., Song, Q.H., Redding, B., Cao, H.: Extreme output sensitivity to subwavelength boundary deformation in microcavities. Phys. Rev. A **87**, 023833 (2013)
25. Gelens, L., Beri, S., Van der Sande, G., Verschaffelt, G., Danckaert, J.: Multistable and excitable behavior in semiconductor ring lasers with broken Z_2-symmetry. Eur. Phys. J. D **58**, 197–207 (2010)
26. Gil-Santos, E., Ramos, D., Martínez, J., Fernández-Regúlez, M., García, R., San Paulo, A., Calleja, M., Tamayo, J.: Nanomechanical mass sensing and stiffness spectrometry based on two-dimensional vibrations of resonant nanowires. Nat. Nanotech. **5**, 641–645 (2010)
27. He, L., Özdemir, Ş.K., Zhu, J., Kim, W., Yang, L.: Detecting single viruses and nanoparticles using whispering gallery microlasers. Nat. Nanotech. **6**, 428–432 (2011)
28. He, L., Özdemir, Ş.K., Zhu, J., Yang, L.: Ultrasensitive detection of mode splitting in active optical microcavities. Phys. Rev. A **82**, 053810 (2010)

29. Heiss, W.D.: Repulsion of resonance states and exceptional points. Phys. Rev. E **61**, 929–932 (2000)
30. Heiss, W.D.: Exceptional points of non-Hermitian operators. J. Phys. A Math. Gen. **37**, 2455–2464 (2004)
31. Heiss, W.D., Harney, H.L.: The chirality of exceptional points. Eur. Phys. J. D **17**, 149–151 (2001)
32. Hodaei, H., Hassan, A., Wittek, S., Carcia-Cracia, H., El-Ganainy, R., Christodoulides, D., Khajavikhan, M.: Enhanced sensitivity at higher-order exceptional points. Nature **548**, 187–191 (2017)
33. Hohimer, J.P., Vawter, G.A., Craft, D.C.: Unidirectional operation in a semiconductor ring diode laser. Appl. Phys. Lett. **62**, 1185–1187 (1993)
34. Ilchenko, V.S., Gorodetsky, M.L., Yao, X.S., Maleki, L.: Microtorus: a high-finesse microcavity with whispering-gallery modes. Opt. Lett. **26**, 256–258 (2001)
35. Jackson, J.D.: Classical Electrodynamics. Wiley, New York (1962)
36. Jiang, X.F., Xiao, Y.F., Zou, C.L., He, L., Dong, C.H., Li, B.B., Li, Y., Sun, F.W., Yang, L., Gong, Q.: Highly unidirectional emission and ultralow-threshold lasing from on-chip ultrahigh-Q microcavities. Adv. Mater. **24**, 260–264 (2012)
37. Jiang, X., Shao, L., Zhang, S.X., Yi, X., Wiersig, J., Wang, L., Gong, Q., Loncar, M., Yang, L., Xiao, Y.F.: Chaos-assisted broadband momentum transformation in optical microresonators. Science **358**, 344 (2017)
38. Kalagara, H., Chu, F.H., Smolyakov, G.A., Osiński, M.: Reciprocity principle and nonequivalence of counterpropagating modes in whistle-geometry ring lasers. In: Witzigmann, B., Osiński, M., Arakawa, Y. (eds.) Physics and Simulation of Optoelectronic Devices XXIV. Proceedings of SPIE, vol. 9742, p. 974213. SPIE, Bellingham (2016)
39. Kato, T.: Perturbation Theory for Linear Operators. Springer, New York (1966)
40. Kim, W.J., Kuang, W., O'Brien, J.D.: Dispersion characteristics of photonic crystal coupled resonator optical waveguides. Opt. Exp. **11**, 3431–3437 (2003)
41. Kim, M., Kwon, K., Shim, J., Jung, Y., Yu, K.: Partially directional microdisk laser with two Rayleigh scatterers. Opt. Lett. **39**, 2423–2426 (2014)
42. Kippenberg, T.J.: Nonlinear optics in ultra-high-Q whispering-gallery optical microcavities. PhD thesis, California Institute of Technology (2004)
43. Kippenberg, T.J., Spillane, S.M., Vahala, K.J.: Modal coupling in traveling-wave resonators. Opt. Lett. **27**, 1669 (2002)
44. Kippenberg, T.J., Kalkman, J., Polman, A., Vahala, K.J.: Demonstration of an erbium-doped microdisk laser on a silicon chip. Phys. Rev. A **74**, 051802(R) (2006)
45. Kneissl, M., Teepe, M., Miyashita, N., Johnson, N.M., Chern, G.D., Chang, R.K.: Current-injection spiral-shaped microcavity disk laser diodes with unidirectional emission. Appl. Phys. Lett. **84**, 2485–2487 (2004)
46. Kramer, J.: Zeitaufgelöste Simulationen der asymmetrischen Rückstreuung in einem dielektrischen Mikrodiskresonator. Diplomarbeit, Otto-von-Guericke-Universität Magdeburg (2014)
47. Kullig, J., Wiersig, J.: Frobenius-Perron eigenstates in deformed microdisk cavities: non-Hermitian physics and asymmetric backscattering in ray dynamics. New J. Phys. **18**, 015005 (2016)
48. Kullig, J., Wiersig, J.: Perturbation theory for asymmetric deformed microdisk cavities. Phys. Rev. A **94**, 043850 (2016)
49. Lee, J.Y., Luo, X., Poon, A.W.: Reciprocal transmissions and asymmetric modal distributions in waveguide-coupled spiral-shaped microdisk resonators. Opt. Exp. **15**, 14650 (2007)
50. Lee, S.B., Yang, J., Moon, S., Lee, J.H., An, K., Shim, J.B., Lee, H.W., Kim, S.W.: Chaos-assisted nonresonant optical pumping of quadrupole-deformed microlasers. Appl. Phys. Lett. **90**, 041106 (2007)
51. Lee, S.Y., Ryu, J.W., Shim, J.B., Lee, S.B., Kim, S.W., An, K.: Divergent Petermann factor of interacting resonances in a stadium-shaped microcavity. Phys. Rev. A **78**, 015805 (2008)

52. Lee, S.B., Yang, J., Moon, S., Lee, S.Y., Shim, J.B., Kim, S.W., Lee, J.H., An, K.: Observation of an exceptional point in a chaotic optical microcavity. Phys. Rev. Lett. **103**, 134101 (2009)
53. Lee, J.W., Kim, K.Y., Moon, H.J., Hyun, K.S.: Selection of lasing direction in single mode semiconductor square ring cavities. J. Appl. Phys. **119**, 053101 (2016)
54. Liang, J.J., Lau, S.T., Leary, M.H., Ballantyne, J.M.: Unidirectional operation of waveguide diode ring lasers. Appl. Phys. Lett. **70**, 1192–1194 (1997)
55. Lin, Z., Ramezani, H., Eichelkraut, T., Kottos, T., Cao, H., Christodoulides, D.N.: Unidirectional invisibility induced by PT-symmetric periodic structures. Phys. Rev. Lett. **106**, 213901 (2011)
56. Little, B.E., Chu, S.T., Haus, H.A., Foresi, J., Laine, J.P.: Microring resonator channel dropping filters. J. Lightwave Technol. **15**, 998–1005 (1997)
57. Little, B.E., Chu, S.T., Absil, P.P., Hryniewicz, J.V., Johnson, F.G., Seiferth, F., Gill, D., Van, V., King, O., Trakalo, M.: Very high-order microring resonator filters for WDM applications. IEEE Photon. Technol. Lett. **16**, 2263–2265 (2004)
58. Liu, Y., Zhang, L., Williams, J.A.R., Bennio, I.: Optical bend sensor based on measurement of resonance mode splitting of long-period fiber grating. IEEE Photon. Tech. Lett. **12**, 531–533 (2000)
59. Longhi, S., Feng, L.: PT-symmetric microring laser absorber. Opt. Lett. **39**, 5026–5029 (2014)
60. Longhi, S., Feng, L.: Unidirectional lasing in semiconductor microring lasers at an exceptional point. Photon. Res. **5**, B1–B6 (2017)
61. Malzard, S., Poli, C., Schomerus, H.: Topologically protected defect states in open photonic systems with non-Hermitian charge-conjugation and parity-time symmetry. Phys. Rev. Lett. **115**, 200402 (2015)
62. McCall, S.L., Levi, A.F.J., Slusher, R.E., Pearton, S.J., Logan, R.A.: Whispering-gallery mode microdisk lasers. Appl. Phys. Lett. **60**, 289–291 (1992)
63. Miao, P., Zhang, Z., Sun, J., Walasik, W., Longhi, S., Litchinitser, N.M., Feng, L.: Orbital angular momentum microlaser. Science **353**, 464–467 (2016)
64. Michael, C.P., Srinivasan, K., Johnson, T.J., Painter, O., Lee, K.H., Hennessy, K., Kim, H., Hu, E.: Wavelength- and material-dependent absorption in GaAs and AlGaAs microcavities. Appl. Phys. Lett. **90**, 051108 (2007)
65. Nöckel, J.U., Stone, A.D.: Chaos in optical cavities. Nature (London) **385**, 45–47 (1997)
66. Peng, B., Özdemir, Ş.K., Liertzer, M., Chen, W., Kramer, J., Yilmaz, H., Wiersig, J., Rotter, S., Yang, L.: Chiral modes and directional lasing at exceptional points. Proc. Natl. Acad. Sci. USA **113**, 6845 (2016)
67. Poon, J.K., Scheuer, J., Xu, Y., Yariv, A.: Designing coupled-resonator optical waveguide delay lines. J. Opt. Soc. Am. B **21**(9), 1665–1673 (2004)
68. Regensburger, A., Bersch, C., Miri, M.A., Onishchukov, G., Christodoulides, D.N., Peschel, U.: Parity-time synthetic photonic lattices. Nature **167**, 488 (2012)
69. Richter, S., Michalsly, T., Sturm, C., Rosenow, B., Grundmann, M., Schmidt-Grund, R.: Exceptional points in anisotropic planar microcavities. Phys. Rev. A **95**, 023836 (2017)
70. Rondin, L., Tetienne, J.P., Hingant, T., Roch, J.F., Maletinsky, P., Jacques, V.: Magnetometry with nitrogen-vacancy defects in diamond. Rep. Prog. Phys. **77**, 056503 (2014)
71. Rüter, C.E., Makris, K.G., El-Ganainy, R., Christodoulides, D.N., Segev, M., Kip, D.: Observation of parity-time symmetry in optics. Nat. Phys. **6**, 192–195 (2010)
72. Ryu, J., Lee, J.W., Yi, C.H., Kim, J.H., Lee, I.G., Kim, H.S., Oh K.R., Kim, C.M.: Chirality of a resonance in the absence of backscatterings. Opt. Exp. **25**, 3381 (2017)
73. Sarma, R., Ge, L., Wiersig, J., Cao, H.: Rotating optical microcavities with broken chiral symmetry. Phys. Rev. Lett. **114**, 053903 (2015)
74. Schermer, M., Bittner, S., Singh, G., Ulysee, C., Lebental, M., Wiersig, J.: Unidirectional light emission from low-index polymer microlasers. Appl. Phys. Lett. **106**, 101107 (2015)
75. Schlederer, B.: Description of a bottle resonantor evanescently coupled to a waveguide. Diploma thesis, Vienna University of Technology, supervised by S. Rotter (2013)

76. Schlehahn, A., Albert, F., Schneider, C., Höfling, S., Reitzenstein, S., Wiersig, J., Kamp, M.: Mode selection in electrically driven quantum dot microring cavities. Opt. Exp. **21**, 15951–15958 (2013)
77. Schomerus, H.: Excess quantum noise due to mode orthogonality in dielectric microresonators. Phys. Rev. A **79**, 061801(R) (2009)
78. Schomerus, H., Wiersig, J.: Non-Hermitian-transport effects in coupled-resonator optical waveguides. Phys. Rev. A **90**, 053819 (2014)
79. Shin, Y., Kwak, H., Moon, S., Lee, S.B., Yang, J., An, K.: Observation of an exceptional point in a two-dimensional ultrasonic cavity of concentric circular shells. Sci. Rep. **6**, 38826 (2016)
80. Shu, F.J., Zou, C.L., Zou, X.B., Yang, L.: Chiral symmetry breaking in a microring optical cavity by engineered dissipation. Phys. Rev. A **91**, 013848 (2016)
81. Siegman, A.E.: Excess spontaneous emission in non-Hermitian optical systems. I. Laser amplifiers. Phys. Rev. A **39**, 1253–1263 (1989)
82. Siegman, A.E.: Excess spontaneous emission in non-Hermitian optical systems. II. Laser oscillators. Phys. Rev. A **39**, 1264–1268 (1989)
83. Song, Q.H., Zhang, N., Zhai, H., Liu, S., Gu, Z., Wang, K., Sun, S., Chen, Z., Meng, L., Xiao, S.: The combination of high Q factor and chirality in twin cavities and microcavity chain. Sci. Rep. **4**, 6493 (2014)
84. Song, Q.H., Gu, Z., Zhang, N., Wang, K., Yi, N., Xiao, S.: Improvement of the chirality near avoided resonance crossing in optical microcavity. Sci. China-Phys. Mech. Astrom. **58**, 114210 (2015)
85. Stefanou, N., Modinos, A.: Impurity bands in photonic insulators. Phys. Rev. B **57**, 12127 (1998)
86. Stöckmann, H.J., Persson, E., Kim, Y.H., Barth, M., Kuhl, U., Rotter, I.: Effective Hamiltonian for a microwave billiard with attached waveguide. Phys. Rev. E **65**, 066211 (2002)
87. Sui, S.S., Tang, M.Y., Yang, Y.D., Xiao, J.L., Du, Y., Huang, Y.Z.: Hybrid spiral-ring microlaser vertically coupled to silicon waveguide for stable and unidirectional output. Opt. Lett. **40**, 4995–4998 (2015)
88. Sui, S.S., Huang, Y.Z., Tang, M.Y., Weng, H.Z., Yang, Y.D., Xiao, J.L., Du, Y.: Locally deformed-ring hybrid microlasers exhibiting stable unidirectional emission from a Si waveguide. Opt. Lett. **41**, 3928–3931 (2016)
89. Sunada, S., Harayama, T.: Sagnac effect in resonant microcavities. Phys. Rev. A **74**, 021801(R) (2006)
90. Sunada, S., Harayama, T.: Design of resonant microcavities: application to optical gyroscopes. Opt. Exp. **15**, 16245–16254 (2007)
91. Taflove, A., Hagness, S.C.: Computational Electrodynamics the Finite-Difference Time-Domain Method. Artech House, London (2000)
92. Tamboli, A.C., Haberer, E.D., Sharma, R., Lee, K.W., Nakamura, S., Hu, E.L.: Room-temperature continuous-wave lasing in GaN/InGaN microdisks. Nat. Photon. **1**, 61–64 (2007)
93. Vahala, K.J.: Optical microcavities. Nature (London) **424**, 839–846 (2003)
94. Vollmer, F., Yang, L.: Label-free detection with high-Q microcavities: a review of biosensing mechanisms for integrated devices. Nanophotonics **1**, 267–291 (2012)
95. Vollmer, F., Arnold, S., Keng, D.: Single virus detection from the reactive shift of a whispering-gallery mode. Proc. Natl. Acad. Sci. USA **105**, 20701–20704 (2008)
96. Wang, X.Y., Chen, H.Z., Li, Y., Li, B., Ma, R.M.: Microscale vortex laser with controlled topological charge. Chin. Phys. B **25**, 124211 (2016)
97. Wang, X.Y., Chen, H.Z., Wang, S., Zhang, S., Ma, R.M.: Vortex radiation from a single emitter (2017). ArXiv:1707.01055
98. Wiersig, J.: Boundary element method for resonances in dielectric microcavities. J. Opt. A Pure Appl. Opt. **5**, 53–60 (2003)
99. Wiersig, J.: Reciprocal transmissions and asymmetric modal distributions in waveguide-coupled spiral-shaped microdisk resonators: comment. Opt. Exp. **16**, 5874–5875 (2008)
100. Wiersig, J.: Structure of whispering-gallery modes in optical microdisks perturbed by nanoparticles. Phys. Rev. A **84**, 063828 (2011)

101. Wiersig, J.: Chiral and nonorthogonal eigenstate pairs in open quantum systems with weak backscattering between counterpropagating traveling waves. Phys. Rev. A **89**, 012119 (2014)
102. Wiersig, J.: Enhancing the sensitivity of frequency and energy splitting detection by using exceptional points: application to microcavity sensors for single-particle detection. Phys. Rev. Lett. **112**, 203901 (2014)
103. Wiersig, J.: Sensors operating at exceptional points: general theory. Phys. Rev. A **93**, 033809 (2016)
104. Wiersig, J., Hentschel, M.: Combining directional light output and ultralow loss in deformed microdisks. Phys. Rev. Lett. **100**, 033901 (2008)
105. Wiersig, J., Kullig, J.: Optical microdisk cavities with rough sidewalls: a perturbative approach based on weak boundary deformations. Phys. Rev. A **95**, 053815 (2017)
106. Wiersig, J., Kim, S.W., Hentschel, M.: Asymmetric scattering and nonorthogonal mode patterns in optical microspirals. Phys. Rev. A **78**, 053809 (2008)
107. Wiersig, J., Eberspächer, A., Shim, J.B., Ryu, J.W., Shinohara, S., Hentschel, M., Schomerus, H.: Nonorthogonal pairs of copropagating optical modes in deformed microdisk cavities. Phys. Rev. A **84**, 023845 (2011)
108. Xiao, Q., Klitis, C., Li, S., Chen, Y., Cai, X., Sorel, M., Yu, S.: Generation of photonic orbital angular momentum superposition states using vortex beam emitters with superimposed gratings. Opt. Exp. **24**, 3168–3176 (2016)
109. Xu, Y., Lee, R.K., Yariv, A.: Propagation and second-harmonic generation of electromagnetic waves in a coupled-resonator optical waveguide. J. Opt. Soc. Am. B **17**, 387–400 (2000)
110. Yariv, A., Xu, Y., Lee, R.K., Scherer, A.: Coupled-resonator optical waveguide: a proposal and analysis. Opt. Lett. **24**, 711–713 (1999)
111. Zhang, N., Liu, S., Wang, K., Gu, Z., Meng, L., Yi, N., Xiao, S., Song, Q.H.: Single nanoparticle detection using far-field emission of photonic molecule around an exceptional point. Sci. Rep. **5**, 11912 (2015)
112. Zhang, N., Gu, Z., Liu, S., Wang, Y., Wang, S., Duan, Z., Sun, W., Xiao, Y.F., Xiao, S., Song, Q.H.: Far-field single nanoparticle detection and sizing. Optica **4**, 1151–1156 (2017)
113. Zhu, J., Özdemir, Ş.K., He, L., Yang, L.: Controll manipulation of mode splitting in an optical microcavity by two Rayleigh scatterers. Opt. Exp. **18**, 23535 (2010)
114. Zhu, J., Özdemir, Ş.K., Xiao, Y.F., Li, L., He, L., Chen, D.R., Yang, L.: On-chip single nanoparticle detection and sizing by mode splitting in an ultrahigh-Q microresonator. Nat. Photon. **4**, 46 (2010)

Exact Results for a Special *PT*-Symmetric Optical Potential

H. F. Jones

Abstract We present exact analytical results for the sinusoidal optical potentials $\upsilon(x) \propto \cos Kx + i\lambda \sin Kx$, particularly for the special case $\lambda = 1$. This is at the borderline between broken and unbroken PT symmetry, and propagation through such an optical lattice exhibits many remarkable properties. There are two main configurations for light largely propagating in the longitudinal (z) direction: (a) where the modulation of the refractive index is in the transverse (x) direction and (b) where the modulation is in the longitudinal direction. In the first case one encounters such properties as non-reciprocity, power oscillations, beam splitting and phase dislocations, while the second case is characterized by unidirectional invisibility, that is, almost total transparency and zero reflection from one side, but with a large, highly peaked, reflection from the other side. The latter property can be exploited in lasing cavities.

1 Introduction

The explosion of interest in the use and exploitation of PT-symmetry in optics arguably began with the pioneering paper of Makris et al. [1], who showed the remarkable properties of light propagation in a periodic structure whose refractive index varied sinusoidally, with loss and gain balanced according to the PT-symmetric condition $n^*(x) = n(-x)$. This paper was concerned with transverse modulation, i.e. propagation primarily in the z-direction, in the context of the paraxial approximation. The parameter λ governing the magnitude of the gain-loss modulation relative to that of the real index modulation was kept in the region $\lambda < 1$ of unbroken PT-symmetry, where, in spite of the presence of gain and loss, the propagation constant remains real and there is no exponential growth or decay. Later the special case $\lambda = 1$ was considered, particularly in the case of longitudinal

H. F. Jones (✉)
Imperial College, London, UK
e-mail: hfj@ic.ac.uk

D. Christodoulides, J. Yang (eds.), *Parity-time Symmetry and Its Applications*, Springer Tracts in Modern Physics 280,
https://doi.org/10.1007/978-981-13-1247-2_7

modulation; that is, in the direction of propagation, z. Again, remarkable properties were found, in particular the phenomenon of unidirectional invisibility [2, 3].

Many of these calculations involved approximations, among which are the paraxial approximation and the coupled-wave approximation. However, in many cases an analytic solution is possible, particularly for the case $\lambda = 1$, so it is of interest to present those analytic results and compare them, where possible, with the approximate calculations.

In Sect. 2 we discuss transverse modulation, where for $\lambda < 1$ (Sect. 2.1) the Bloch functions relevant for the calculation of wave-packet propagation within the paraxial approximation are given by Mathieu functions. For $\lambda = 1$ (Sect. 2.2) the relevant functions are modified Bessel functions, but because $\lambda = 1$ is an exceptional point, where eigenfunctions and eigenvalues merge, one also has to consider their associated Jordan functions. These can also be expressed in terms of modified Bessel functions, and may have a significant effect on beam propagation. In order to consider Fresnel reflection at boundaries we need to go beyond the paraxial approximation (Sect. 2.3). Because of the special nature of the $\lambda = 1$ optical potential the coupled-mode (Bragg) series gives exact results for successive diffraction orders.

In Sect. 3 we discuss longitudinal modulation, $n = n(z)$, for the case $\lambda = 1$, where an analytic solution for normal incidence exists, again in terms of modified Bessel functions (Sect. 3.1). Within a certain range of parameters the original results obtained by the coupled-mode approximation prove to be remarkably accurate. In Sect. 3.2 we extend the analytic solution to deal with non-normal incidence and Fresnel reflection at the boundaries of the grating. These results can be used to display angular distributions and to consider the use of such a grating in optical cavities leading to lasing. In the latter context the highly-peaked reflectivity of the grating for right incidence can be exploited to eliminate competing longitudinal modes.

Finally, in Sect. 4 we summarize the physical properties and the various mathematical analyses of this special optical potential.

2 Transverse Modulation

In this section we consider propagation predominantly in the z direction through a medium whose refractive index depends on the transverse distance x in a PT-symmetric fashion. For the first two subsections the calculations are formulated in terms of the paraxial approximation. In the third subsection we take account of Fresnel refraction at boundaries.

The set-up is shown schematically in Fig. 1, where a beam is incident in the z-direction on a slab of material (volume grating) whose refractive index varies periodically in the x direction. The incident beam can be a plane wave or a wave packet and may or may not be at normal incidence. Propagation of the wave is, of course, governed in the first instance by Maxwell's equations. For H-polarization, in

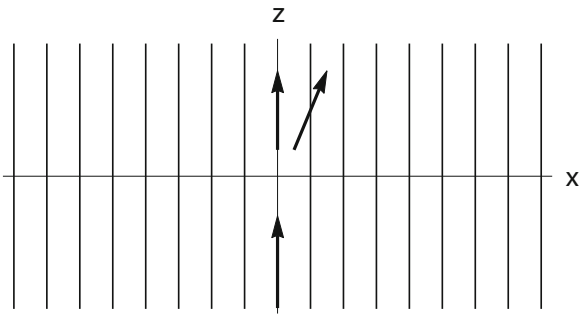

Fig. 1 Schematic of a beam of light incident on a volume grating in which the refractive index is modulated in a PT-symmetric way in the transverse x direction. Among other exotic phenomena the beam will be diffracted asymmetrically, because the grating is not symmetric under P ($x \to -x$) but rather under P combined with T (complex conjugation)

which the electric field is in the y direction, the equation for this tangential electric field is the scalar Helmholtz equation

$$\left(\frac{\partial^2}{\partial z^2} + \frac{\partial^2}{\partial x^2} + k^2\right) E_y(x, z) = 0, \tag{1}$$

where $k = n(x)\omega/c$ for a wave of angular frequency ω. Most treatments of this problem have been in the framework of the paraxial, or slowly-varying, approximation. This is derived under the assumption that the main z-dependence of the wave, of angular frequency ω, is $e^{ik_0 z}$, where $k_0 = n_0\omega/c$ and n_0 is the background index, on which there are small grating modulations, that is

$$n(x) = n_0(1 + \upsilon(x)) \tag{2}$$

where $\upsilon(x)$ is small. Then, writing $E_y(x, z)$ as $E_y(x, z) = e^{ik_0 z}\psi(x, z)$, the resulting equation for the *envelope* ψ is

$$\left(\frac{\partial^2}{\partial z^2} + 2ik_0\frac{\partial}{\partial z} + \frac{\partial^2}{\partial x^2} + (k^2 - k_0^2)\right)\psi(x, z) = 0, \tag{3}$$

in which, because of the assumed smallness of $\upsilon(x)$, we can approximate $k^2 - k_0^2$ as $k^2 - k_0^2 \approx 2\upsilon(x)k_0^2$. The paraxial approximation is based on the assumption that the main z-dependence of $E(x, z)$ is given by $e^{ik_0 z}$ so that the second-derivative term $\partial^2\psi/\partial z^2$ is small compared with the first-derivative term and may be dropped. The resulting *paraxial equation* for ψ is

$$\left(i\frac{\partial}{\partial z} + \frac{1}{2k_0}\frac{\partial^2}{\partial x^2} + k_0\,\upsilon(x)\right)\psi(x, z) = 0, \tag{4}$$

which by a suitable rescaling of x and z can be recast as

$$\left(i\frac{\partial}{\partial z}+\frac{\partial^2}{\partial x^2}+\upsilon(x)\right)\psi(x,z)=0. \tag{5}$$

We have chosen the terminology ψ for the envelope function for a reason, namely that this paraxial equation has the same form as the time-dependent Schrödinger equation in quantum mechanics, but with the longitudinal distance z taking the role of time and $\upsilon(x)$, which we recall measures the additional refractive index due to the grating, taking the role of (minus) the quantum-mechanical potential $V(x)$.

The importance of this observation [4, 5] is that all the ideas, techniques and results developed in the context of PT-symmetry in quantum mechanics [6–9] can be taken over to classical optics. Most importantly, the central idea of PT-symmetry, that the potential $V(x)$ does not have to be real in order to ensure real energy eigenvalues, is extremely relevant to optics. In that context a complex refractive index is entirely natural, with the imaginary part corresponding to either gain or loss. The lesson of PT-symmetry is that when gain and loss are balanced in a PT-symmetric way, wave propagation may still proceed without exponential decay or growth. The phenomenon of PT symmetry-breaking, whereby eigenvalues cease to be real when the imaginary part of V becomes too large, is of potential importance in switching applications.

2.1 Unbroken PT Symmetry: $\lambda < 1$

The first paper to analyze the set-up of Fig. 1 in detail was that of Makris et al. [1], with the PT-symmetric ($n^*(x) = n(-x)$) optical potential

$$\upsilon(x)=\frac{1}{2}\xi(\cos Kx+i\lambda\sin Kx), \tag{6}$$

up to an additive constant, and with $K = 2$, $\xi = 4$. To calculate the electric field distribution starting from an initial distribution at $z = 0$ one can, of course, integrate Eq. (4) numerically, the most efficient method being the split-operator method appropriate for a Hamiltonian of the standard form $H = p^2 + V(x)$, but a semi-analytical method is to use the method of *stationary states*, borrowed from quantum mechanics.

In quantum mechanics the time-dependent Schrödinger equation

$$i\frac{d\psi(x,t)}{dt}=H\psi(x,t) \tag{7}$$

can be solved in principle by expanding $\psi(x, 0)$ in a complete set $\{\psi_m(x)\}$ of eigenstates of H, with eigenvalues E_m:

$$\psi(x,0) = \sum_m c_m \psi_m(x). \tag{8}$$

Then at a later time $\psi(x,t)$ is given by the sum

$$\begin{aligned}\psi(x,t) &= \sum_m c_m \psi_m(x,t) \\ &= \sum_m c_m e^{-iE_m t} \psi_m(x),\end{aligned} \tag{9}$$

which in practice will have to be truncated at some large value of m.

The crux of this method is to find the eigenstates. Since we have a periodic potential with periodicity $a = 2\pi/K$, the boundary conditions are that $\psi(x)$ should also be periodic up to a phase, i.e. $\psi_m(x+a) = e^{ik_m a}\psi_m(x)$, where the k_m are the *Bloch momenta*. The band structure of the lattice gives the relation between the Bloch momentum k_m and the energy E_m, or in this case the coefficient β_m in the z-dependence $e^{i\beta_m z}$ of each eigenstate.[1]

In standard Hermitian situations E is guaranteed to be real, and the band structure (E versus k) consists of bands, where k is real, and gaps, where it is not. A typical figure would look like that in Fig. 2a. In PT symmetry the eigenvalues are either all real, when the symmetry is unbroken, or some may become complex conjugate pairs, when the symmetry is broken. When the symmetry is unbroken the band structure is of the standard form, shown in Fig. 2a. However, when the symmetry

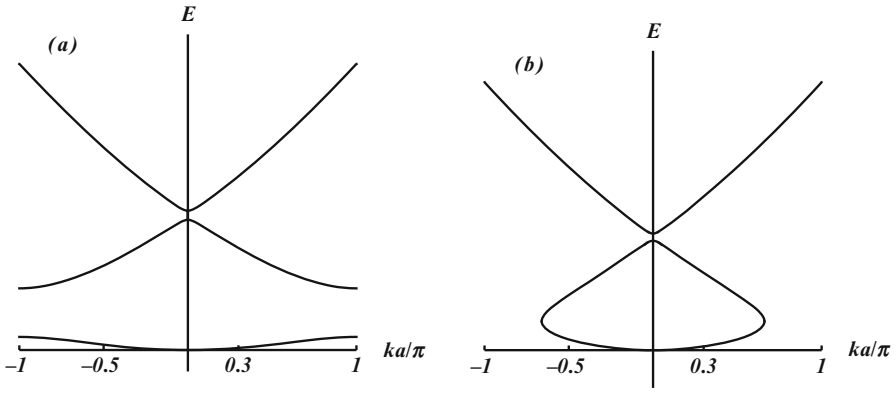

Fig. 2 Schematic band structure (E versus k) for the potential of Eq. (6): (**a**) in the regime of unbroken symmetry $\lambda < 1$ and (**b**) in the broken-symmetry regime $\lambda > 1$. In panel (**b**) only real values of E are shown

[1] Here we have considered the system in a large interval in x with periodic boundary conditions so that the k_m are discrete.

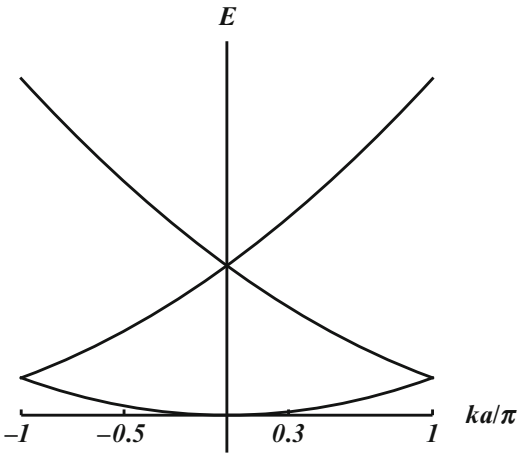

Fig. 3 Schematic band structure for the potential of Eq. (6) precisely at the symmetry-breaking point $\lambda = 1$. The gaps of Fig. 2a have now closed. At the Brillouin-zone boundaries $k = \pm\pi/a$ two eigenvalues and their associated eigenfunctions coalesce

is broken, which for the potential of Eq. (6) occurs when $\lambda > 1$, the bands where E is real close in on themselves and do not reach the Brillouin zone boundaries at $k = \pm\pi/a$, as shown in Fig. 2b. The most interesting situation occurs right at the symmetry-breaking point $\lambda = 1$, when the bands of Fig. 3 come together at $k = 0$ and $k = \pm\pi/a$, so that the gaps disappear. At the Brillouin-zone boundaries two eigenvalues and their associated eigenfunctions coalesce, which requires special treatment and has interesting consequences. Two of the unexpected intensity patterns of the kind first observed in [1] by the optical potential (6) are shown in Fig. 4 for values of $\lambda < 1$ and differing initial conditions. In Fig. 4a it is clearly seen that a secondary beam develops to the right and in Fig. 4b the power oscillations, which are also present in Fig. 4a, are extremely marked. As previously remarked, the handedness of the beam intensity is not altogether surprising, as the potential itself is not left-right symmetric. PT-symmetry implies that a beam incident from the other direction would instead bifurcate to the left. With the benefit of hindsight the power oscillations are again not surprising. In the first place the medium is an active one with both gain and loss, and secondly, in PT symmetry the quantity that is conserved is not the total intensity $\int dx|\psi(x,z)|^2$ but rather the non-local quantity $\int dx\psi^*(x,z)\psi(-x,z)$.

One of the insights gained in PT-symmetric quantum mechanics [8] was that an unbroken PT-symmetric Hamiltonian $H = p^2 + V(x)$ could be mapped onto a Hermitian one h by a similarity transformation, i.e.

$$h = e^{-\frac{1}{2}Q} H e^{\frac{1}{2}Q} \tag{10}$$

In particular just such a mapping can transform the potential (6) into the equivalent Hermitian potential [10]

$$\upsilon'(x) = \frac{1}{2}\xi\sqrt{1-\lambda^2}\cos Kx. \tag{11}$$

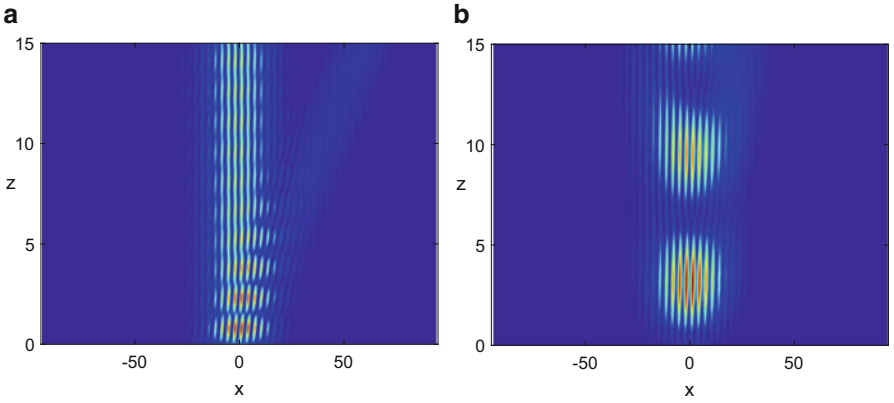

Fig. 4 Intensity patterns, $|\psi(x, z)|^2$, produced by the optical potential (6) in the unbroken regime $\lambda < 1$ for differing wave-packet inputs, exhibiting beam bifurcation and power oscillations

The particular mapping is $Q = -i\theta d/dx$, which effects the shift $x \to x + \frac{1}{2}i\theta$, where $\theta = \text{arctanh}\lambda$. Note that υ' ceases to be a real function of x for $\lambda > 1$, and that the transformation becomes singular ($\theta \to \infty$) as $\lambda \to 1$. The resultant equation for the transformed function $\varphi_k(x) = \psi_k(x - \frac{1}{2}i\theta)$ is the Mathieu equation ($K = 2$):

$$\left[d^2/dx^2 + (a - 2q\cos 2x)\right]\varphi_k(x) = 0, \tag{12}$$

where $a = -\beta$ and $q = \frac{1}{4}\xi\sqrt{1-\lambda^2}$.

Reference [10] was primarily concerned with the band structure associated with $\upsilon(x)$. In particular, using the correspondence with the Mathieu equation, the authors were able to show that there is a second critical point in λ beyond which all of the eigenvalues become complex. However, the correspondence can also be used [11] to calculate the Bloch eigenfunctions for $\lambda \leq 1$.

The standard Floquet procedure for determining the Bloch functions requires two independent solutions $u_1(x)$, $u_2(x)$ satisfying $u_1(0) = u_2'(0) = 1$ and $u_1'(0) = u_2(0) = 0$. In fact these can be identified, up to normalization factors, with the even and odd Mathieu functions $ce(a, q, x)$ and $se(a, q, x)$ respectively. Then for a given value of β the Bloch functions are appropriate linear combinations of u_1 and u_2 with Bloch momentum k given by $k = (1/\pi)\cos^{-1} D$, where D is the discriminant[2] $D(\beta) = \frac{1}{2}(u_1(\pi) + u_2'(\pi))$. This discriminant is what determines the band structure: a real value of k requires $|D| < 1$.

In this way we can calculate the intensity pattern for the Hermitian problem of Eq. (12). Using the same parameters as those in Fig. 4a we obtain Fig. 5, in

[2]Recall that we are now dealing with $K = 2$, as in Ref. [1], so the Brillouin-zone boundaries are at $x = \pm\pi$.

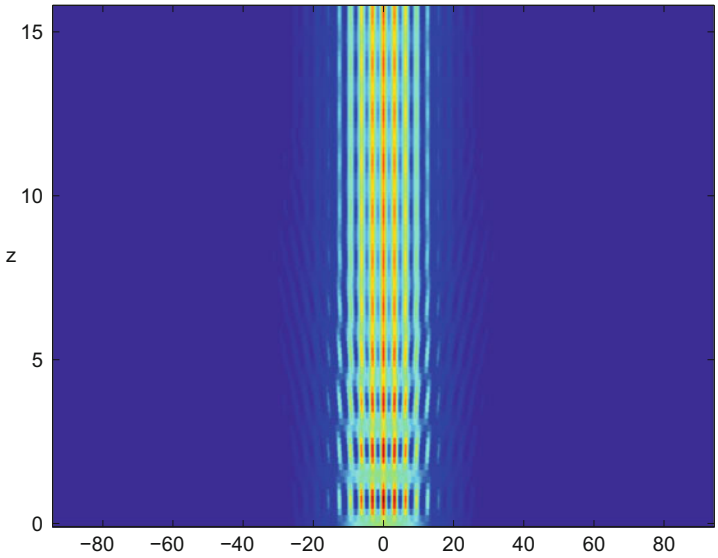

Fig. 5 Intensity patterns, $|\varphi(x,z)|^2$, produced by the equivalent Hermitian optical potential (11)

which the initial Gaussian input for $\varphi(x,0)$ produces power oscillations, but no bifurcation. We can use this equivalent Hermitian formulation to solve the original PT-symmetric problem. However, in that case we need to give the initial conditions for $\psi(x,0) \equiv \varphi(x - \frac{1}{2}i\theta, 0)$ rather than for $\varphi(x,0)$, and the intensity pattern is governed by $|\psi(x,z)|^2$ rather than $|\varphi(x,z)|^2$, reproducing Fig. 4a. The details are given in [11].

2.2 *Symmetry-Breaking Threshold:* $\lambda = 1$

The most interesting features of the potential (6), both physical and mathematical, occur for the special value $\lambda = 1$, when the potential becomes the pure imaginary exponential $\upsilon(x) = \frac{1}{2}\xi e^{iKx}$. For $\lambda < 1$, when PT-symmetry is conserved, we obtain oscillatory behaviour, while for $\lambda > 1$, when the symmetry is broken, we obtain exponential behaviour. At the boundary between the two we may expect secular growth, $\psi(x,z) \propto z$; however, careful analysis [12, 13] shows that the situation is rather subtle.

As already mentioned, the special feature of the case $\lambda = 1$ is that the gaps in the band structure disappear, and there are degenerate eigenvalues, together with their associated eigenfunctions where the bands come together. The stationary-state method requires the initial wavefunction or envelope function to be expanded in a complete set of eigenfunctions. However, in such a situation, which can only occur

for a non-Hermitian Hamiltonian, the set of eigenfunctions is no longer complete, and needs to be supplemented in some way.

Very generally, if a particular eigenfunction ψ_n satisfying $(H - E_n)\psi_n = 0$ is degenerate, it needs to be supplemented by the associated Jordan function χ_n, which satisfies $(H - E_n)\chi_n = \psi_n$. In the 2×2 subspace spanned by ψ_n and χ_n, the matrix $H - E_n$ would be represented by the Jordan-block form

$$H - E_n \leftrightarrow \begin{pmatrix} 0 & 1 \\ 0 & 0 \end{pmatrix}, \tag{13}$$

while ψ_n would be represented by the column vector $(1, 0)$ and χ_n by the missing column vector $(0, 1)$, satisfying indeed $(H - E_n)\chi_n = \phi_n$. This equation does not specify χ_n uniquely; it is satisfied by $\chi_n + c\psi_n$, where c is any constant. A particular solution for χ_n is obtained by differentiation of the eigenvalue equation. Thus

$$0 = \frac{d}{dE}[(H - E)\psi_n] = (H - E)\frac{d\psi_n}{dE} - \psi_n, \tag{14}$$

showing that $\chi_n = d\psi_n/dE$ up to a multiple of ψ_n. The expansion (9) now has to be supplemented by terms involving the $\chi_n(x, t)$, whose time-dependence (z-dependence in optics) is not just the simple phase $e^{-iE_n t}$. Instead

$$\begin{aligned} \chi(x,t) &= e^{-iHt}\chi(x,t) \\ &= e^{-iEt}\left(e^{-i(H-E)t}\chi(x,t)\right) \\ &= e^{-iEt}\left(1 - i(H-E)t + \dots\right)\chi(x,t) \\ &= e^{-iEt}\left(\chi(x,t) - it\psi(x,t)\right), \end{aligned} \tag{15}$$

which has an additional linear[3] growth in t. Thus in the optical context we would expect to see a linear z-dependence of the amplitude, or a quadratic growth of the intensity, provided that the initial input is such that one or more associated Jordan functions are excited.

For $\lambda = 1$ we actually have explicit expressions for the ψ_n and χ_n. In that case the paraxial equation takes the form (recall that $K = 2\pi/a$)

$$\left(\frac{d^2}{dx^2} + \frac{1}{2}\xi e^{2i\pi x/a}\right)\psi = -\beta\psi, \tag{16}$$

[3]There are no higher-order terms for this 2×2 Jordan block because $(H - E)^2\chi(x, t) = 0$.

which can be transformed into the modified Bessel equation

$$y^2\frac{d^2\psi}{dy^2}+y\frac{d\psi}{dy}-(y^2+q^2)\psi=0 \tag{17}$$

by the substitutions $y = y_0 e^{i\pi x/a}$, $y_0^2 = (\xi/2)(a/\pi)^2$, $q^2 = \beta(a/\pi)^2$. For $q \equiv ka/\pi$ not an integer, the equation has the two linearly-independent solutions $\psi_k(x) = I_q(y)$ and $\psi_{-k} = I_{-q}(y)$, which are directly the Bloch functions, as they have the correct periodicity $\psi_k(x + a) = e^{ika}\psi_k(x)$. However, at the Brillouin-zone boundaries, where $q \equiv ka/\pi = n$ is an integer, the two solutions become degenerate: $I_n(y) = I_{-n}(y)$, and we are in precisely the situation outlined above. The Jordan function associated with the eigenfunction I_n is most easily found by differentiation of the eigenvalue equation (16), remembering that for $\lambda = 1$ the dispersion relation is $\beta = k^2$. Thus

$$\chi_k = \frac{1}{2k}\frac{d\psi_k}{dk} = \left(\frac{a}{\pi}\right)^2\frac{1}{2q}\frac{dI_q}{dq}\bigg|_{q=n} \quad , \tag{18}$$

modulo solutions of the homogeneous equation (16). Derivatives of the modified Bessel function with respect to the order are given by the formula (9.6.44) of Ref. [14]:

$$(-1)^n\frac{\partial}{\partial\nu}I_\nu(y)\bigg|_{\nu=n} = -K_n(y)+\frac{1}{2}n!\left(\frac{2}{y}\right)^n\sum_{k=0}^{n-1}(-1)^k\frac{(\frac{1}{2}y)^k I_k(y)}{(n-k)k!}\ , \tag{19}$$

from which, for the purposes of calculating $\chi_n(y)$, we should subtract the term $-K_n(y)$, which does not have the correct periodicity.

Whether or not we get secular behaviour in the beam intensity as a function of z depends on whether any associated Jordan functions are excited, i.e. whether in the expansion (8) of the initial distribution $\psi(x, 0)$, which should now be written out more fully as

$$\psi(x,0) \equiv f(x) = \sum_{k\neq n\pi/a} c_k\psi_k(x) + c_0 I_0(y) + \sum_{n>0}[\alpha_n I_n(y) + \beta_n\chi_n(y)], \tag{20}$$

at least one of the coefficients β_n is non-zero. This in turn is governed by the overlap integral:

$$\beta_n \propto \int_0^a dx\ I_n(y)F_n(x), \tag{21}$$

where

$$F_n(x) = \sum_{m=-N}^{N-1} e^{-i\pi mn} f(x + ma), \tag{22}$$

where we have discretized the system by putting it in a large interval $|x| < Na$ with periodic boundary conditions, so that $k \to k_r = r\pi/(aN)$.

In common with Refs. [1] and [12] we consider the initial beam to be a Gaussian wave-packet of width $w \gg a$ and a possible offset k_0, corresponding to incidence at an angle. That is,

$$f(x) = e^{-(x/w)^2 + ik_0 x}. \tag{23}$$

In order to obtain a non-zero value of F_n it is easily seen [13] that the scaled offset momentum $q_0 \equiv k_0 a/\pi$ must be an integer m, with $m \equiv n \pmod 2$. Then, because of the expansion

$$I_n(y) = \left(\frac{1}{2}y\right)^n \sum_{s=0}^{\infty} \frac{(\frac{1}{2}y)^{2s}}{s!\Gamma(n+s+1)}, \tag{24}$$

the integral (21) vanishes unless m is negative and $|m| \geq n$.

So for $q_0 = 0$, i.e. normal incidence, no Jordan function is excited. However, $\chi_1(y)$ is excited for $q_0 = -1$, which was the parameter chosen in [12], and the distribution of $|\psi(x, z)|$ for this case is shown in Fig. 6a. What is surprising from this figure is that, although $|\psi(x, z)|$ shows the initial linear increase expected from our previous analysis, in particular Eq. (15), it subsequently flattens off. This saturation is shown more clearly in Fig. 6b, where the maximum value of $|\psi(x, z)|$ is plotted as a function of z.

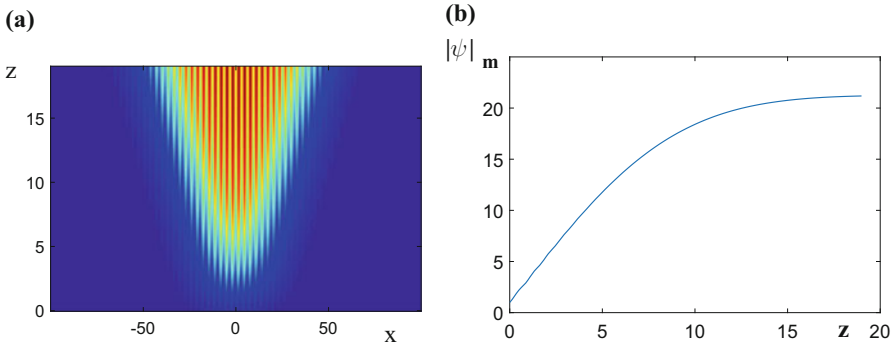

Fig. 6 (**a**) Colour map of amplitude $|\psi(x, z)|$ for $\lambda = 1$ when a Jordan mode is excited. (**b**) Graph of the maximum value of $|\psi(x, z)|$ versus z, showing an initial linear growth, which is subsequently saturated

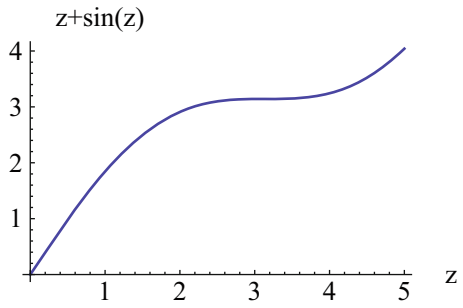

Fig. 7 An example of temporary cancellation between a linear and an oscillatory function, providing a plateau-like behaviour in a limited range of z

How can we understand this phenomenon? The contribution of the Jordan function to $|\psi(x, z)|$ is definitely linear, so what must be happening is some sort of cancellation between that contribution and those of the nearby Bloch functions. It is understandable that their coefficients may be closely related to that of $\chi_1(y)$, but nonetheless their contribution is oscillatory, and it is far from clear how such oscillatory contributions can cancel a linear term. The details of how this comes about are given in [13] and depend on the properties of the Jacobi ϑ function, but a simple example serves to illustrate how such a cancellation is possible mathematically. That is, if we consider the function $z + \sin z$, a combination of a linear and an oscillatory term, it exhibits an initial linear rise, followed by a plateau-like behaviour, as shown in Fig. 7. However, it eventually rises again, as it must: the cancellation is temporary, and the linear term eventually dominates. In the context of our optical problem, firstly the plateau is much wider, and secondly the eventual rise is unphysical, since at such values of z the beam has spread beyond the confines of the finite grating $|x| < Na$. Nonetheless, although $|\psi(x, z)|$ itself does not exhibit the expected linear dependence on z, the total power $\int dx|\psi(x, z)|^2$ does rise linearly, because of the linear spread of the beam in x.

2.3 Reflection and Diffraction

In this subsection we continue to treat the special case $\lambda = 1$, but go beyond the paraxial approximation. The paraxial approximation deals with propagation within a medium with small, smooth variations in the refractive index and results in a linear differential equation in the longitudinal variable z. It cannot deal with an abrupt change in the refractive index such as occurs at a boundary, which produces both reflection and transmission. To deal with that situation we need to use the full Helmholtz equation. Assuming a plane-wave input, the solution of the equation is expanded in a Bragg series, a series of plane waves with different periodic x-dependence. The special feature of the optical potential $\upsilon = \frac{1}{2}\xi e^{iKx}$ is that the coupled equations linking the different modes have a one-sided nature, meaning that they can be solved iteratively to give exact results for successive orders of reflection

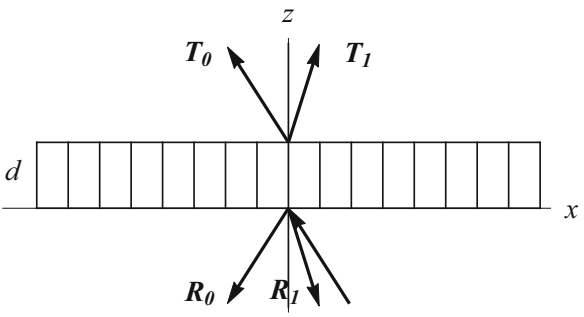

Fig. 8 Schematic of reflection and diffraction from a slab of material of thickness d with the optical potential $\upsilon = \frac{1}{2}\xi e^{iKx}$. We show only the zeroth and first Bragg orders. Note that there are no negative orders, so that the deflections from the zeroth order are one-sided

and diffraction. This one-sided nature of the coupled equations, albeit within the framework of the paraxial approximation, i.e. neglecting reflections, was first noted by Berry [4].

In general we consider an incident wave with angle of incidence θ_1 in a material with refractive index n_1, giving a wave vector of magnitude $k_1 = n_1 k_0$, where $k_0 = \omega/c$ is the vacuum value. Within the slab the background refractive index is n_2, giving a wave-vector of magnitude $k_2 = n_2 k_0$, and finally the transmitted beams emerge in a material of refractive index n_3, corresponding to a wave-vector of magnitude $k_3 = n_3 k_0$. In the absence of the grating we would just have geometrical refraction, with the Snell's law relation $k_1 \sin\theta_1 = k_2 \sin\theta_2$, so that the transverse dependence is the same along the boundary. However, with the periodic modulation of the refractive index the transverse dependences need only match up to an integer multiple of K, the reciprocal lattice vector.

This gives rise to the Bragg series for the incident and reflected waves:

$$E_1(x,z) = \exp\left[-ik_1(x\sin\theta_1 + z\cos\theta_1)\right] + \sum_{m=-\infty}^{\infty} r_m \exp\left[-ik_2((\sin\theta_2 - 2m\sin\theta_B)x - \alpha_m z)\right], \tag{25}$$

in which the first line represents the incident wave, while the second line represents the reflected waves of order m. Here we have written K in terms of the (first) Bragg angle θ_B as $K = 2k_2\sin\theta_B$, while the quantity α_m is given by $\alpha_m = [n_1^2/n_2^2 - (\sin\theta_2 - 2m\sin\theta_B)^2]^{\frac{1}{2}}$.

The transmitted waves are similarly given by

$$E_3(x,z) = \sum_{m=-\infty}^{\infty} t_m \exp\left[-ik_2((\sin\theta_2 - 2m\sin\theta_B)x - \beta_m(z-d))\right], \tag{26}$$

where $\beta_m = [n_3^2/n_2^2 - (\sin\theta_2 - 2m\sin\theta_B)^2]^{\frac{1}{2}}$. Finally, the electric field in the interior takes the form

$$E_2(x,z) = \sum_{m=-\infty}^{\infty} S_m(z)\exp\left[-ik_2(\sin\theta_2 - 2m\sin\theta_B)x\right]. \tag{27}$$

The Helmholtz equation is automatically satisfied by E_1 and E_3, but imposing it on E_2 results in the system of coupled equations

$$\frac{1}{k_2^2}\frac{d^2S_m(z)}{dz^2} + \eta_m^2\, S_m(z) + \frac{1}{2}\,\xi\, S_{m-1}(z) = 0, \tag{28}$$

where $\eta_m^2 = 1 - (\sin\theta_2 - 2m\sin\theta_B)^2$. In particular $\eta_0 = \cos\theta_2$.

The special feature of the optical potential $\upsilon(x) \propto e^{iKx}$ is that the inhomogeneous term in the equation for $S_m(z)$ involves S_{m-1} but not S_{m+1}. Then there is a consistent solution to the coupled equations in which $S_m(z) = 0$ for $m < 0$ and the $S_m(z)$ for positive m can be generated exactly by successive iteration, starting from $S_0(z)$. Each successive order brings in an additional power of ξ, so higher orders are progressively suppressed.

In conjunction with (28) the various orders have to satisfy the boundary conditions at the two interfaces, namely continuity of the tangential electric and magnetic fields. As already mentioned, we are considering H-polarization, in which the electric field is in the y-direction, and so purely tangential. The tangential component of the magnetic field is in the x direction, and is given by the Maxwell equation $i\mu_0\omega H_x = \partial E_y/\partial z$.

The zeroth-order mode function $S_0(z)$ satisfies the homogeneous equation

$$\frac{1}{k_2^2}\frac{d^2S_0(z)}{dz^2} + \eta_0^2\, S_0(z) = 0, \tag{29}$$

with solution $S_0 = A_0e^{i\eta_0 u} + B_0e^{-i\eta_0 u}$, where we have introduced the dimensionless variable $u \equiv k_2 z$. The four boundary conditions, which we take at $z = 0$ and $z = d$, then determine the unknown constants A_0, B_0, and the amplitudes for reflection and transmission r_0 and t_0. The precise expressions are

$$t_0 = \frac{4\alpha_0\eta_0}{(\alpha_0+\eta_0)(\beta_0+\eta_0)e^{i\eta_0 u_d} - (\alpha_0-\eta_0)(\beta_0-\eta_0)e^{-i\eta_0 u_d}} \tag{30}$$

$$r_0 = \frac{(\alpha_0-\eta_0)(\beta_0+\eta_0)e^{i\eta_0 u_d} + (\alpha_0+\eta_0)(\beta_0-\eta_0)e^{-i\eta_0 u_d}}{(\alpha_0+\eta_0)(\beta_0+\eta_0)e^{i\eta_0 u_d} - (\alpha_0-\eta_0)(\beta_0-\eta_0)e^{-i\eta_0 u_d}} \tag{31}$$

$$A_0 = \frac{T_0}{2}\left(\frac{\eta_0-\beta_0}{\eta_0}\right)e^{-i\eta_0 u_d} \qquad B_0 = \frac{T_0}{2}\left(\frac{\eta_0+\beta_0}{\eta_0}\right)e^{i\eta_0 u_d}, \tag{32}$$

where $u_d = k_2 d$, and we recall that $\eta_0 = \cos\theta_2$.

The differential equation for $S_1(z)$ is the inhomogeneous equation

$$\frac{1}{k_2^2}\frac{d^2 S_1(z)}{dz^2} + \eta_1^2 S_1(z) + \frac{1}{2}\xi S_0(z) = 0, \tag{33}$$

in which the inhomogeneous term is the already-determined $S_0(z)$. The solution has the form

$$S_1(z) = C_1 e^{i\eta_1 u} + D_1 e^{-i\eta_1 u} + A_1 e^{i\eta_0 u} + B_1 e^{-i\eta_0 u}, \tag{34}$$

in which the first two terms constitute the general solution of the homogeneous equation and the remaining terms a particular solution of the inhomogeneous equation. The coefficients of these latter terms are determined in terms of A_0 and B_0 as $A_1 = x_1 A_0$ and $B_1 = x_1 B_0$, where

$$x_1 = \frac{\frac{1}{2}\xi}{4\sin\theta_B(\sin\theta_B - \sin\theta_2)}. \tag{35}$$

The remaining parameters, C_1, D_1, r_1 and t_1 are then fixed by the four boundary conditions. The rather lengthy expressions are given in [15]. The process can obviously be continued, each order building on the expressions already obtained for the previous orders. In this way explicit analytic expressions were obtained in [15] for the second-order reflection and transmission amplitudes r_2 and t_2. We emphasize again that these are exact results for the different orders, which occur at different angles of reflection and transmission.

Although these calculations have been designed to accommodate differing values of the background refractive indices n_1, n_2 and n_3, it is instructive to consider the simple case where all three are equal, when we might expect the result to correspond closely to those of the paraxial equation. In this $\alpha_0 = \beta_0 = \eta_0$, and the expressions for t_0 and r_0 in (30) become simply $t_0 = e^{-i\eta_0 u_d}$ and $r_0 = 0$, while those for t_1 and r_1 simplify to

$$\begin{aligned} t_1 &= x_1 \frac{\eta_1 + \eta_0}{2\eta_1}(e^{-i\eta_1 u_d} - e^{-i\eta_0 u_d}) \\ r_1 &= x_1 \frac{\eta_1 - \eta_0}{2\eta_1}(1 - e^{-i(\eta_1+\eta_0)u_d}). \end{aligned} \tag{36}$$

These quantities are sharply peaked, but finite, at $\theta_2 = \theta_B$. The pole in x_1 (see Eq. (35)) is cancelled by a zero in the numerator, since $\theta_2 \to \theta_B$ implies that $\eta_1 \to \eta_0$. Their values at the peak are given by

$$t_1|_{\theta_2=\theta_B} = -i\frac{\xi u_d}{4\eta_0} e^{-i\eta_0 u_d}$$

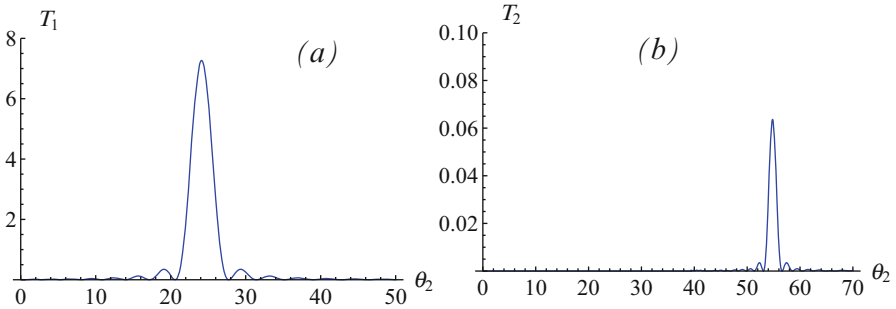

Fig. 9 Transmission coefficients $T_1 = |t_1|^2$ and $T_2 \equiv |t_2|^2$ for the first and second Bragg orders in the case when the background refractive indices n_1, n_2 and n_3 are all equal ($\varepsilon_1 = \varepsilon_2 = \varepsilon_3 = 2.4$). The other parameters are the free-space wavelength $\lambda_0 = 0.633\,\mu\text{m}$, the lattice spacing $\Lambda = 0.5\,\mu\text{m}$ and the width of the grating $d = 8\,\mu\text{m}$

$$r_1|_{\theta_2=\theta_B} = -i\frac{\xi\,\sin(\eta_0 u_d)}{4\eta_0}e^{-i\eta_0 u_d} \tag{37}$$

r_1 is typically very small, but t_1 can become appreciable because of its linear dependence on u_d characteristic of a PT-symmetric structure at the symmetry-breaking threshold.

In Fig. 9a, b we show plots of $T_1 \equiv |t_1|^2$ and $T_2 \equiv |t_2|^2$ versus θ_2. The second-order transmission coefficient, T_2, which peaks at $\theta_2 = \arcsin(2\sin\theta_B)$, is much smaller than T_1 for reasonable parameters. When the refractive indices differ, for example when the volume grating is inscribed in a slab of refractive index of relative permeability $\varepsilon_2 = 2.4$, while $\varepsilon_1 = \varepsilon_3 = 1$, the principal change is in the zeroth-order (i.e. non-diffracted) waves. T_0 differs significantly from 1, and R_0 from 0, because of Fresnel reflections at the boundaries. There is now also significant reflection in first and second orders. This configuration and other asymmetric configurations are considered in detail in Ref. [15].

3 Longitudinal Modulation

In this section we consider the situation in which the index modulation is in the longitudinal (z) direction rather than the transverse (x) direction. Initially we will take the beam to be incident normally, so that it is always in the z-direction, but will later generalize the set-up to incidence at an angle. With the special optical potential $\upsilon(z) = \frac{1}{2}\xi e^{iKz}$ the most striking property is that of (approximate) *unidirectional invisibility*, or *unidirectional transparency*, whereby light incident from one side is transmitted perfectly, with no reflection. The potential has a left-right sense, so the situation is different for incidence from the right, where there is a strong, highly-peaked reflection. These properties were first noticed by Kulishov et al. [2] and later

linked to PT-symmetry and popularized by Lin et al. [3]. In what follows we will set $K = 2\beta$ to conform with the notation of those papers. Thus the optical potential is $\upsilon(z) = \frac{1}{2}\xi e^{2i\beta z}$. Additionally we initially consider the background refractive index to be 1 inside and outside the grating and write k for k_0.

3.1 Normal Incidence

When the index modulation is in the direction of propagation the scalar Helmholtz equation becomes the ordinary differential equation

$$\left(\frac{d^2}{dz^2} + k^2(1 + 2\upsilon(z))\right) E_y(z) = 0, \tag{38}$$

which now corresponds to the one-dimensional time-*independent* Schrödinger equation in quantum mechanics. Note that we no longer need the paraxial approximation, but the optical potential $\upsilon(z)$, and correspondingly ξ, must still be considered small, in order to neglect the $\upsilon(z)^2$ term in the expansion of $(1 + \upsilon(z))^2$. Even this restriction could be dropped if we were to consider a modification of the permittivity rather than the refractive index according to $\varepsilon(z) = \varepsilon_0(1 + 2\upsilon(z))$.

The quantities of interest are the reflection and transmission amplitudes for a wave incident on the grating. Because the grating has a directionality we must consider left and right incidence separately. The general form of the equation ensures that the transmission coefficients are the same from either side, but the respective reflection coefficients are expected to be different, and can indeed be very different. The set-up for incidence from the left is shown in Fig. 10. In both [2] and [3] the scattering coefficients were calculated keeping only the zeroth and first Bragg orders within the slowly-varying envelope approximation, so that the problem is reduced to a pair of coupled linear differential equations. The results are that for left incidence, illustrated in Fig. 10,

$$t_L = 1, \qquad r_L = 0 \tag{39}$$

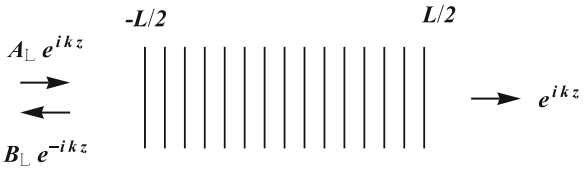

Fig. 10 Schematic of a beam of light incident normally from the left on a volume grating of length L in which the refractive index is modulated in a PT-symmetric way in the longitudinal z direction. The transmission amplitude is $t_{\rm L} = 1/A_{\rm L}$ and the reflection amplitude is $r_{\rm L} = B_{\rm L}/A_{\rm L}$

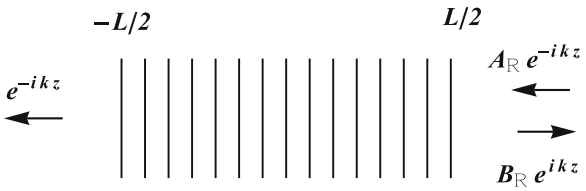

Fig. 11 Schematic of a beam of light incident normally from the right on a volume grating of length L in which the refractive index is modulated in a PT-symmetric way in the longitudinal z direction. The transmission amplitude is $t_{\rm R} = 1/A_{\rm R}$ and the reflection amplitude is $r_{\rm R} = B_{\rm R}/A_{\rm R}$

for k near the Bragg wave-vector β. This is the invisibility or transparency mentioned above.

On the other hand, for right incidence, illustrated in Fig. 11, it was found that[4]

$$t_R = t_L, \qquad r_R = \frac{1}{2} i\xi kL \frac{\sin(\delta L)}{\delta L}, \tag{40}$$

where δ is the detuning, defined by $\delta = \beta - k$. The reflection coefficient $r_{\rm R}$ has the form of a sinc function, with peak value $\frac{1}{2} i\xi kL$. The linear dependence of this peak value on L is again a signal of the exceptional point $\lambda = 1$. The right reflection coefficient $R_{\rm R} = |r_{\rm R}|^2$ is illustrated as a function of δ in Fig. 13 below. The original equation can be transformed into the modified Bessel equation, so this problem can be solved exactly in terms of the modified Bessel functions I_ν and K_ν, and it is of great interest to see how accurately the approximate results of (39) and (40) compare with the exact results. This has been done in Refs. [16] and [17] by slightly different methods. Reference [16] used the transfer-matrix method and expressed the results in terms of the independent functions I_ν and $I_{-\nu}$ with real arguments. Reference [17] treated left and right incidence separately, expressing the coefficients $A_{\rm L}$, $B_{\rm L}$, $A_{\rm R}$ and $B_{\rm R}$ in terms of I_ν and K_ν with complex arguments. It should be noted that Ref. [16] did not treat precisely the same problem as [3], since the factor k^2 in Eq. (38) was replaced by the constant value β^2. This amounts to taking y_0 below as α rather than $k\alpha/\beta$. Since all the interesting structure occurs in the close vicinity of $k = \beta$ this is a very small change.

The transformation to the modified Bessel equation is effected by changing the independent variable z to $y \equiv y_0 e^{i\beta z}$, where $y_0 = k\alpha/\beta$ and α is defined as $\alpha = \sqrt{\xi}$. Writing $E_y(z) = \psi(y)$, the equation then becomes

$$y^2 \frac{d^2\psi}{dy^2} + y\frac{d\psi}{dy} - (y^2 + k^2/\beta^2)\psi = 0. \tag{41}$$

[4]The phase of r_R depends on the origin of the grating. The phase in (40) is for the explicitly PT-symmetric situation where the grating extends from $z = -L/2$ to $z = L/2$.

This is indeed the modified Bessel equation, with index $\nu = k/\beta$. The general solution is $\psi(y) = CI_\nu(y) + DK_\nu(y)$, and tuning ($k = \beta$, or $\delta = 0$) corresponds to $\nu = 1$. In accordance with [17] we take the grating from $z = -L/2$ to $z = L/2$. Changing the range to $z = 0$ to $z = L$, for example, would affect only the phases of the reflection amplitudes, but not their absolute magnitudes.

Applying the continuity conditions on ψ and $d\psi/dz$ at $z = -L/2$ and $z = L/2$, we obtain the amplitudes A_L, B_L, $A_\mathrm{R} = A_\mathrm{L}$ and B_R:

$$\begin{aligned} e^{-ikL}A_\mathrm{L} &= \frac{y_+y_-}{2\nu}[K_{\nu+1}(y_+)I_{\nu-1}(y_-) - I_{\nu+1}(y_+)K_{\nu-1}(y_-)] \\ B_\mathrm{L} &= \frac{y_+y_-}{2\nu}[-K_{\nu+1}(y_+)I_{\nu+1}(y_-) + I_{\nu+1}(y_+)K_{\nu+1}(y_-)] \\ B_\mathrm{R} &= \frac{y_+y_-}{2\nu}[-K_{\nu-1}(y_+)I_{\nu-1}(y_-) + I_{\nu-1}(y_+)K_{\nu-1}(y_-)], \end{aligned} \tag{42}$$

where $y_\pm = y_0 e^{\pm i\beta L/2}$. Care is needed in the evaluation of the modified Bessel functions at $y_\pm$ because they are defined with a cut along the negative real axis, and in going from y_- to y_+ the complex argument $y(z) = y_0 e^{i\beta z}$ encircles the origin and crosses the cut N times. How the functions continue onto subsequent sheets is given by the continuation formulas[14]:

$$\begin{aligned} I_\nu(y_0 e^{im\pi}) &= e^{im\pi\nu} I_\nu \\ K_\nu(y_0 e^{im\pi}) &= e^{-im\pi\nu} K_\nu - i\pi \frac{\sin(m\pi\nu)}{\sin(\pi\nu)} I_\nu. \end{aligned} \tag{43}$$

With the expressions in (42) we can now plot the exact transmission and reflection coefficients. First we plot $T \equiv |1/A_\mathrm{L}|^2$ and $R_L \equiv |B_\mathrm{L}/A_\mathrm{L}|^2$ in Fig. 12. As can be seen, the simple results $T = 1$ and $R_\mathrm{L} = 0$ resulting from the coupled-wave approximation are remarkably good. T is very close to 1 and R_L is very small, of the order of 10^{-7}. It is worth noting that these two features are closely related because PT-symmetry implies the pseudo-unitarity relation [18].

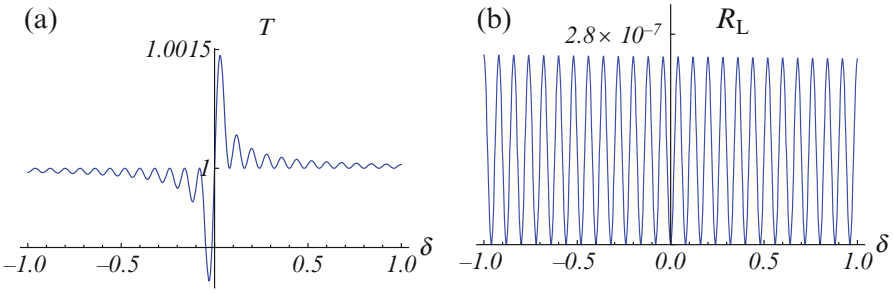

Fig. 12 Exact transmission and reflection coefficients $T \equiv |1/A_\mathrm{L}|^2$ and $R_\mathrm{L} \equiv |B_\mathrm{L}/A_\mathrm{L}|^2$ as functions of the detuning, $\delta = \beta - k$. The parameters are those of Ref. [3]

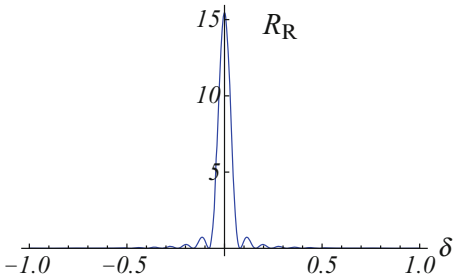

Fig. 13 Exact reflection coefficient $R_R \equiv |B_R/A_L|^2$ as functions of the detuning, $\delta = \beta - k$. The parameters are those of Ref. [3]

$$T \pm \sqrt{R_L R_R} = 1 \tag{44}$$

Thus $R_L \ll 1$ implies $T \approx 1$.

The plot of R_R, given in Fig. 13, is essentially indistinguishable from that of $|r_R|^2$ as given by the simple formula of Eq. (40). It is interesting to note that in the case of a wave-packet input the very large value of the reflectivity near $\delta = 0$ arises not from the height of the reflected pulse, but rather from its increased length [17]. This is a similar phenomenon to the saturation observed in Sect. 2.2. While the expressions given above for A_L, B_L and B_R are rather simple and compact it is by no means clear how they give rise to the phenomenon of (approximate) unidirectional invisibility. In particular, we may ask how the sinc function in the approximate expression for r_R in Eq. (40) arises. The answer lies in the continuation formulas (43), which we can use to reduce all the arguments of the Bessel functions in (42) to the real quantity y_0. This was essentially done in Ref. [19], where there are, however, some misprints, and the expressions were not fully simplified. If that is done the expressions for the scattering amplitudes become

$$\begin{aligned} e^{-ikL} A_L &= \cos(N\pi\nu) \\ &\quad - \frac{1}{2} i\xi\nu \frac{\sin(N\pi\nu)}{\sin(\pi\nu)} \left[(K_{\nu+1} I_{\nu-1} + I_{\nu+1} K_{\nu-1}) \sin(\pi\nu) - \pi I_{\nu+1} I_{\nu-1} \right] \end{aligned} \tag{45}$$

and

$$\begin{aligned} B_L &= \frac{1}{2} i\xi\nu \frac{\sin(N\pi\nu)}{\sin(\pi\nu)} I_{\nu+1} \left[2K_{\nu+1} \sin(\pi\nu) - \pi I_{\nu+1} \right] \\ B_R &= \frac{1}{2} i\xi\nu \frac{\sin(N\pi\nu)}{\sin(\pi\nu)} I_{\nu-1} \left[2K_{\nu-1} \sin(\pi\nu) - \pi I_{\nu-1} \right], \end{aligned} \tag{46}$$

where now all the Bessel functions have argument $y_0 = \alpha\nu$, and N is the number of grating periods, which we take to be even: $N = L/\Lambda = \beta L/\pi$. Given that y_0 is very small we can now use the small-argument approximations [14] to I_μ and K_μ, namely

$$I_\mu(z) \sim \frac{(\frac{1}{2}z)^\mu}{\Gamma(\mu+1)}, \qquad K_\mu(z) \sim \frac{\frac{1}{2}\Gamma(\mu)}{(\frac{1}{2}z)^\mu}. \tag{47}$$

We are concerned with ν very close to 1, so in the expression for A_L the dominant term in the square bracket is $K_{\nu+1}I_{\nu-1}\sin(\pi\nu) \approx (2/\xi)\sin(\pi\nu)$, finally resulting in $A_\mathrm{L} \approx 1$. In the expression for B_L the dominant term in the square bracket is $2K_{\nu+1}\sin(\pi\nu)$, which means that B_L remains small.[5] Finally, in the expression for B_R the dominant term is $-\pi I_{\nu-1}$, so that the prefactor $\sin(N\pi\nu)/\sin(\pi\nu)$ mimics the sinc function in (40).

It should be mentioned that the formulas (45) and (46) are essentially those of Ref. [16]. Indeed the combinations $2K_{\nu+1}\sin(\pi\nu) - \pi I_{\nu+1}$ and $2K_{\nu-1}\sin(\pi\nu) - \pi I_{\nu-1}$ can be written as $-\pi I_{-\nu-1}$ and $-\pi I_{1-\nu}$ respectively. Finally, the transfer matrix, constructed as $M_{22} = e^{-ikL}A_\mathrm{L}$, $M_{11} = M_{22}^*$, $M_{12} = B_\mathrm{R}$ and $M_{21} = -B_\mathrm{L}$, conforms to the iteration formula

$$M = m^N = \cos N\theta + (\sin N\theta/\sin\theta)(m - \cos\theta) \tag{48}$$

where the unimodular matrix $m = \cos\theta + i\sigma.n\sin\theta$ is the single-cell transfer matrix.

3.2 Extended Analytic Solution

The analytic results given above were limited to normal incidence and a uniform background refractive index, but they can be extended [19] to deal with incidence at an angle and different background indices to the left and right of the grating and in the grating itself. This allows one to explore to what extent the invisibility property is affected by Fresnel reflection and to consider the use of this special PT-symmetric grating in lasing cavities.

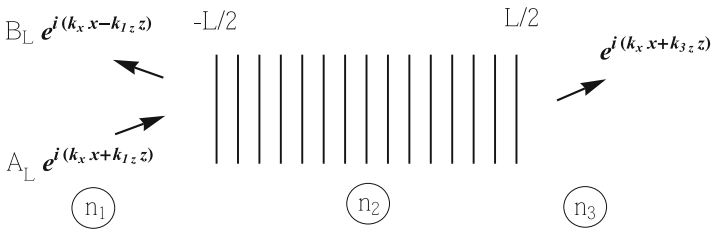

Fig. 14 Set-up for light incident at an angle from the left on the PT-symmetric volume grating, whose background refractive index is n_2. The refractive indices to the left and right of the grating are n_1 and n_3 respectively. All the waves have a common x-dependence $\exp(ik_x x)$

[5] As Longhi has pointed out [16], this is no longer true if N becomes sufficiently large, because of the neglected last term $-\pi I_{\nu+1}$.

The set-up of Fig. 10 for left incidence is now generalized as shown in Fig. 14. For incidence at an angle, there is an overall x-dependence component of the wave, of the form $e^{ik_x x}$. So in Eq. (38) we can write E_y as $E_y(x, z) = e^{ik_x x}\psi(z)$, and the equation for $\psi(z)$ becomes

$$\frac{d^2\psi}{dz^2} + \left[k_2^2(1 + \xi e^{2i\beta z}) - k_x^2\right]\psi = 0. \tag{49}$$

Here $k_2 = n_2 k_0$, where k_0 is the free-space wave-vector. In order to transform this to the modified Bessel equation the appropriate definition of y is $y = (k_2\alpha/\beta)e^{i\beta z}$, which gives

$$y^2\frac{d^2\psi}{dy^2} + y\frac{d\psi}{dy} - (y^2 + \nu^2)\psi = 0, \tag{50}$$

where ν is now defined by

$$\nu^2 = \frac{k_2^2 - k_x^2}{\beta^2} \tag{51}$$

That is, $\nu = k_{2z}/\beta = (k_2\cos\theta_2)/\beta$, where θ_2 is the internal angle of refraction. Thus we can write y as

$$y = \left(\frac{\nu\alpha}{\cos\theta_2}\right)e^{i\beta z}. \tag{52}$$

The boundary conditions are that ψ and ψ' are continuous, as before. However, when $n_2 \neq n_1$ and/or $n_2 \neq n_3$ the longitudinal wave-vectors in the three regions are unequal. Thus, given that $k_1\sin\theta_1 = k_2\sin\theta_2$, it is straightforward to show that $k_{1z} = \gamma_1\nu\beta$ and $k_{3z} = \gamma_3\nu\beta$, where $\gamma_r = \sqrt{\left(n_r^2/n_2^2 - \sin^2\theta\right)}/\cos\theta$. In the previous case of equal background refractive indices these reduce to $\gamma_1 = \gamma_3 = 1$.

After some algebra we obtain the following expressions for A_L and B_L:

$$\begin{aligned} e^{-i(k_{1z}+k_{3z})L/2}A_\mathrm{L} = {} & \left(\frac{y_+y_-}{2\gamma_1\nu}\right)[I_{\nu-1}(y_-)K_{\nu+1}(y_+) - I_{\nu+1}(y_+)K_{\nu-1}(y_-)] \\ & + \left(\frac{\delta_1 y_+}{2\gamma_1}\right)[I_\nu(y_-)K_{\nu+1}(y_+) + I_{\nu+1}(y_+)K_\nu(y_-)] \\ & + \left(\frac{\delta_3 y_-}{2\gamma_1}\right)[I_{\nu-1}(y_-)K_\nu(y_+) + I_\nu(y_+)K_{\nu-1}(y_-)] \\ & + \left(\frac{\delta_1\delta_3\nu}{2\gamma_1}\right)[I_\nu(y_-)K_\nu(y_+) - I_\nu(y_+)K_\nu(y_-)] \end{aligned} \tag{53}$$

$$e^{i(k_{1z}-k_{3z})L/2}B_\mathrm{L} = -\left(\frac{y_+y_-}{2\gamma_1\nu}\right)[I_{\nu+1}(y_-)K_{\nu+1}(y_+) - I_{\nu+1}(y_+)K_{\nu+1}(y_-)]$$

$$+\left(\frac{\delta_1 y_+}{2\gamma_1}\right)[I_\nu(y_-)K_{\nu+1}(y_+) + I_{\nu+1}(y_+)K_\nu(y_-)]$$
$$-\left(\frac{\delta_3 y_-}{2\gamma_1}\right)[I_{\nu+1}(y_-)K_\nu(y_+) + I_\nu(y_+)K_{\nu+1}(y_-)]$$
$$+\left(\frac{\delta_1\delta_3\nu}{2\gamma_1}\right)[I_\nu(y_-)K_\nu(y_+) - I_\nu(y_+)K_\nu(y_-)]$$

where $\delta_r = \gamma_r - 1$. In the general case $\delta_r \neq 0$, so that each expression now has potentially three additional terms. Similar expressions for A_R and B_R are given in [19], but will not be listed here.

3.2.1 Angular Distributions

Up to now we have plotted reflection and transition coefficients as functions of frequency for normal incidence. But we are now in a position to explore how unidirectional invisibility manifests itself as a function of the incident angle for a fixed frequency. We can also explore how these features are degraded by Fresnel reflections in the case of unequal background refractive indices. Such calculations were previously done [20] in the framework of the Bragg series analogous to Eqs. (25), (26), and (27). The difference here is that the different orders add coherently, as they occur at the same angle. So in this case the series is a perturbation series in ξ, in which only the first three orders were calculated. However, for the small value considered ($\xi = 0.02$) the truncated series agrees very well with the exact results presented here (from Ref. [19]).

In Fig. 15 we show the transmission coefficient T and the left reflection coefficient R_L as functions of the internal angle of refraction θ_2 (degrees) for fixed k in the case when all three regions have the same background permittivity. The distributions are even in θ_2, and show the same general features as those of Fig. 12,

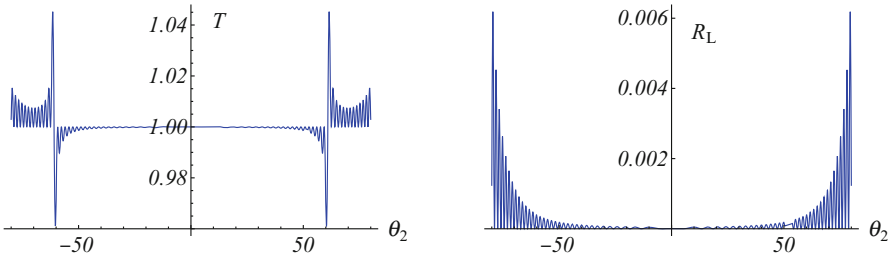

Fig. 15 Transmission coefficient T and left reflection coefficient R_L as functions of the internal angle of refraction θ_2 for fixed k and equal background refractive indices. The parameters are $\varepsilon_1 = \varepsilon_2 = \varepsilon_3 = 2.4$, $\xi = 0.02$, $L = 8.4\,\mu\mathrm{m}$, $\Lambda = 0.42\,\mu\mathrm{m}$ and $\lambda_0 = 0.633\,\mu\mathrm{m}$. Left invisibility is well satisfied for $\theta_2 \lesssim 50^\mathrm{o}$. For larger values of θ_2 the violations, while still small, are greater than in the case of normal incidence and varying λ_0 (Fig. 12)

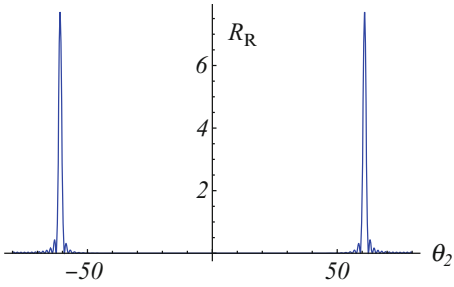

Fig. 16 Right reflection coefficient R_R as functions of the internal angle of refraction θ_2 for fixed k and equal background refractive indices. The parameters are the same as in Fig. 15. As can be seen, R_R is very highly peaked at $\pm\theta_B$, corresponding to $\nu = 1$

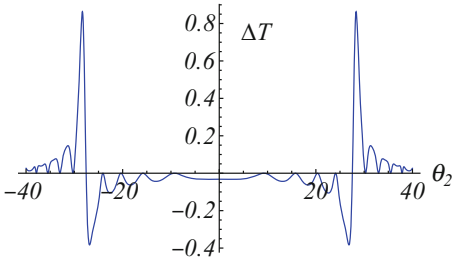

Fig. 17 Contrast $\Delta T \equiv T - T_0$ as a function of the internal angle of refraction θ_2 for fixed k and $\varepsilon_1 = \varepsilon_3 = 1$, $\varepsilon_2 = 2.4$. The effect of the grating is small for $\theta_2 \lesssim 20^o$, but becomes considerable for larger values of θ_2, particularly near $\theta_B \approx 27^o$

where k varied for fixed $\theta_2 = 0$. For $\theta_2 \lesssim 50^o$ the invisibility property holds well, but for larger values of θ_2 the violations are considerably larger than those in Fig. 12. The transition from $T < 1$ to $T > 1$ occurs very close to the Bragg angle $\theta_B = \cos^{-1}(\beta/k_2) \approx 60^o$, the value at which $\nu = 1$. The corresponding right reflection coefficient is shown in Fig. 16. It exhibits a very sharp peak at $\theta_2 = \pm\theta_B$. Details of many more configurations are given in [20]. We show here just one case, showing the extent to which the invisibility is degraded by Fresnel reflections when the background refractive indices are not all equal. What is shown in Fig. 17 is the *contrast* ΔT, that is, the transmission coefficient T minus the corresponding quantity T_0 in the absence of the grating. This is small for small angles, but shows large deviation for larger angles, particularly near the Bragg angle, which in this case is $\theta_B \approx 27^o$. The graph of ΔR_L is similar but the maximum is approximately an order of magnitude smaller. In Fig. 17 the range of θ_2 is restricted to $|\theta_2| \leq 40^o$, since total internal reflection occurs shortly thereafter.

3.2.2 Lasing Cavities

While much attention has focussed on the left invisibility property of the special grating with index profile $e^{2i\beta z}$, the concomitant property, namely the highly-peaked reflectivity on the other side, can potentially be put to use in the context of optical cavities. When such a grating is inserted into a standard cavity, which has many competing longitudinal lasing modes, it can select a single longitudinal mode while eliminating the others. It can also act as a lasing cavity itself if a mirror is placed at the reflective right side.

Fig. 18 Sketch of a resonant cavity formed by two standard Bragg gratings at either end, into which the PT-symmetric grating with index profile $e^{2i\beta z}$ is inserted. The highly-selective right reflectivity of the PT-grating can serve to eliminate competing modes of the original cavity

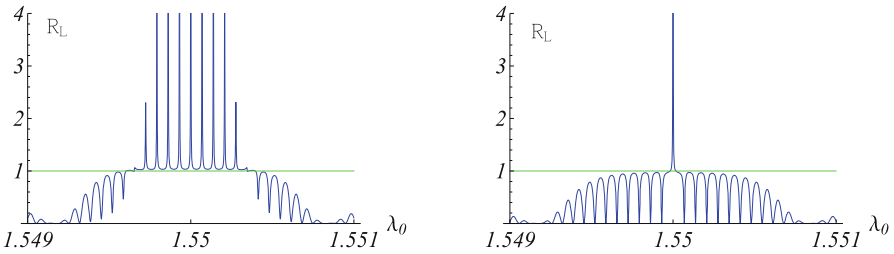

Fig. 19 Left panel: left reflection coefficient R_L of the pumped cavity of Fig. 18 in the absence of the PT-symmetric grating as a function of wavelength λ_0 (μm). Right panel: R_L with insertion of the PT-symmetric grating with parameters adjusted appropriately (see Eq. (54) and Ref. [21] for details)

The first of these configurations, illustrated in Fig. 18, was considered in detail in Ref. [21], using the transfer-matrix approach and the simple form of the transfer matrix of the grating given by the coupled-mode approximation. As we have seen, this is a very good approximation provided that the length of the grating is not too large. In the left panel of Fig. 19 we show the left reflection coefficient of the pumped cavity in the absence of the PT-symmetric grating. The sharp peaks indicate the several competing modes, which would lase once the pumping reaches a threshold value. However, with the PT grating in place it is possible to tune the various parameters, namely the length L and strength κ of the standard Bragg gratings, the length L_{PT} and strength $\kappa_{PT} \equiv \frac{1}{2}\xi$ of the PT-grating, and the separations d_1, d_2. Among various possibilities for the lengths the simplest is that d_1 is an integral multiple of Λ, while d_2 is a half-integral multiple. L_{PT} is always taken as an integral multiple of Λ, which we recall is π/β. The condition for the onset of lasing, which occurs when the element M_{22} of the transfer matrix of the entire cavity equals zero, is then

$$\kappa_{PT} L = \coth(\kappa L) - \tanh(\kappa L). \tag{54}$$

In the right panel of Fig. 19 we show an example of how, when this condition is satisfied, the left reflection coefficient has a single sharp peak. Thus the insertion of the PT-grating has resulted in the elimination of competing longitudinal modes. This result can be attributed to the highly-selective reflectivity of the PT-grating, which singles out one wavelength.

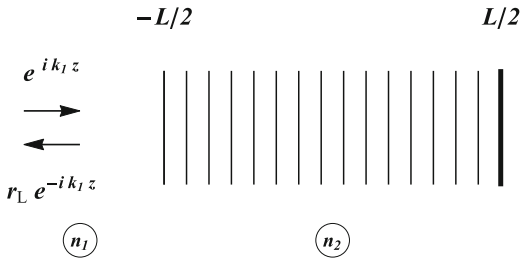

Fig. 20 Resonant cavity obtained by terminating the ideal PT grating with a highly-reflective mirror at its reflective end

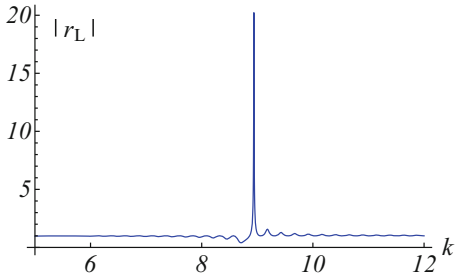

Fig. 21 Modulus of the left reflection amplitude $r_{\rm L}$ of the mirror cavity of Fig. 20, showing that the value of ξ is close to the threshold for lasing. The parameters are $\varepsilon_1 = 1$, $\varepsilon_2 = 2.4$, $\xi = 0.02$, $\Lambda = 0.23$ and $L = 36\Lambda$

The desired property of lasing in a single longitudinal mode can be achieved by a much simpler set-up, obtained by terminating the PT grating with a highly-reflective mirror at its reflective end, as illustrated in Fig. 20. We can obtain the relevant formulas for $A_{\rm L}$ and $B_{\rm L}$ from (53) for normal incidence by taking the limit $n_3 \to \infty$. In that case both $A_{\rm L}$ and $B_{\rm L}$ go to infinity like δ_3. The precise formulas are

$$e^{-i(k_1+k_3)L/2}A_{\rm L} \sim \frac{\delta_3}{2\gamma_1}\Big\{\ y_-[I_{\nu-1}(y_-)K_\nu(y_+) + I_\nu(y_+)K_{\nu-1}(y_-)] + \delta_1\nu[I_\nu(y_-)K_\nu(y_+) - I_\nu(y_+)K_\nu(y_-)]\Big\} \tag{55}$$

$$e^{i(k_1-k_3)L/2}B_{\rm L} \sim \frac{\delta_3}{2\gamma_1}\Big\{\ -y_-[I_{\nu+1}(y_-)K_\nu(y_+) + I_\nu(y_+)K_{\nu+1}(y_-)] + \delta_1\nu[I_\nu(y_-)K_\nu(y_+) - I_\nu(y_+)K_\nu(y_-)]\Big\}$$

The overall factors of δ_3 cancel out when considering $r_L \equiv B_{\rm L}/A_{\rm L}$, so we define $\hat{A}_{\rm L} \equiv A_{\rm L}/\delta_3$ and $\hat{B}_{\rm L} \equiv B_{\rm L}/\delta_3$. Then $r_{\rm L} = \hat{B}_{\rm L}/\hat{A}_{\rm L}$. The onset of lasing is marked by a pole of $r_{\rm L}$, or equivalently a zero of $\hat{A}_{\rm L}$, for real k. In Fig. 21 we give an example of a very sharp peak in $|r_L|$, which would become a pole by fine-tuning the grating strength ξ.

The situation can be most transparently analyzed by using the continuation formulas of Eq. (43) to express $\hat{A}_{\rm L}$ in terms of Bessel functions of argument y_0, as was done for $A_{\rm L}$ in (45), and then using the small-argument approximations of (47). The resulting expression is

$$2\gamma_1 e^{-i(k_1+k_3)L/2}\hat{A}_{\mathrm{L}} \sim \cos(k_2 L) - i\gamma_1 \sin(k_2 L) + \frac{1}{4}(1+\gamma_1) i k_2 \xi \frac{\sin(L\delta)}{\delta}. \quad (56)$$

This was obtained independently in [22] using the transfer-matrix approach. It turns out that the real part of the expression on the RHS of (56), namely $\cos(k_2 L)$, is exact.

Assuming that ξ is real, as we have always done till now, the real part of the lasing condition $\hat{A}_{\mathrm{L}} = 0$ is just $\cos(k_2 L) = 0$, which gives the possible values of k_2 as $k_2 = (n + 1/2)\pi/L$. For any given value of L, the imaginary part of the lasing condition then gives the threshold value of ξ. However, there are many possible modes, and when we are above threshold, the lasing action can hop from one mode to another, something we would like to avoid.

A simple way of obtaining single-mode lasing is to shift the phase of the potential by $\pi/2$. This is equivalent to shifting the origin of the potential by $\Lambda/4$, and amounts to taking ξ to be pure imaginary: $\xi = i|\xi|$. In that case k_2 is now fixed by the *imaginary* part of the lasing condition, namely $\sin(k_2 L) = 0$, giving $k_2 = n\pi/L$, while the real part becomes

$$\cos(k_2 L) = k_2 |\xi| \frac{1}{4}(1+\gamma_1) \frac{\sin(L\delta)}{\delta}. \quad (57)$$

The important thing is that this equation now only has a solution if $\delta = 0$, corresponding to $n = L/\Lambda$, irrespective of the value of $|\xi|$. The other possible modes are excluded because of the zeros of $\sin L\delta$.

4 Summary and Conclusions

As we have seen, the optical potential $\upsilon(x) = \frac{1}{2}\xi e^{iKx}$ is special both physically and mathematically. We have discussed two main set-ups: one where the modulation of the refractive index is perpendicular to the surface of the grating, commonly known as a transmission grating, and the other where the modulation is parallel to the surface of the grating, usually referred to as a reflection grating.

The first case was the subject of Sect. 2. Physically the novel features, first observed in [1], include non-reciprocity, beam splitting and power oscillations. Diffraction of a plane wave from such a grating [15] is one-sided, with negative Bragg orders missing. Mathematically this set-up has many interesting features.

In the context of the paraxial approximation (Sect. 2.2) the equation of propagation is equivalent to a time-dependent Schrödinger equation, whose eigenfunctions, the Bloch waves, are modified Bessel functions [13]. However, because $\lambda = 1$ is an exceptional point for the potential (6), at the boundary for PT-symmetry breaking, a complete set of functions must include associated Jordan functions, which physically give rise to secular behaviour in z, albeit with the subtleties discussed in that section, and in more detail in [13].

The analysis in terms of the Bragg series for diffraction of plane waves for $\lambda = 1$, discussed in Sect. 2.3, has the special feature that the equations coupling the different orders are one-sided, with the result that successive orders can be calculated exactly, although the explicit expressions become very unwieldy beyond second order. In that section we gave explicit expressions for the zeroth and first orders: those for second order can be found in [15].

The second case was dealt with in Sect. 3. There there is an exact solution in terms of modified Bessel functions, both for normal incidence and for incidence at an angle.

In the case of normal incidence (Sect. 3.1), the previous analysis [2, 3] using the coupled-wave approximation turns out to be extremely accurate, at least for the parameters chosen. However, as previously pointed out in [16], the approximation, and indeed the phenomenon of unidirectional invisibility, breaks down if the length of the grating becomes too large.

The analysis was extended in Sect. 3.2 to cover both non-normal incidence and different diffractive indices on either side of the grating. The solutions are still in terms of modified Bessel functions. The distributions in k for normal incidence are mirrored in the angular distributions (Sect. 3.2.1). Finally, in Sect. 3.2.2 we showed how the enhanced reflection from the right-hand side, which comes hand in hand with the left invisibility, could be used to eliminate all but one longitudinal mode in a lasing cavity.

In conclusion, this particular optical potential shows a variety of unusual physical phenomena, which inspired the current intense research on the application of the ideas of PT symmetry to optics. Mathematically it is also unusual in being amenable to exact analytic solutions, which can be used in their own right or to check the validity of the simpler expressions arising from various approximations.

References

1. Makris, K.G., El-Ganainy, R., Christodoulides, D.N.: Beam dynamics in PT symmetric optical lattices. Phys. Rev. Lett. **100**, 103904-1–4 (2008)
2. Kulishov, M., Laniel, J.M., Bélanger, N., Azaña, J., Plant, D.V.: Nonreciprocal waveguide gratings. Opt. Exp. **13**, 3068–3078 (2005)
3. Lin, Z., Ramezani, H., Eichelkraut, T., Kottos, T., Cao, H., Christodoulides, D.N.: Unidirectional invisibility induced by PT-symmetric structures. Phys. Rev. Lett. **106**, 213901-1–4 (2011)
4. Berry, M.V.: Lop-sided diffraction by absorbing crystals. J. Phys. A Math. Gen. **31**, 3493–3502 (1998)
5. El-Ganainy, R., Makris, K.G., Christodoulides, D.N., Musslimani, Z.H.: Theory of coupled optical PT-symmetric structures. Opt. Lett. **32**, 2632–2634 (2007)
6. Bender, C.M., Boettcher, S.: Real spectra in non-Hermitian Hamiltonians having PT symmetry. Phys. Rev. Lett. **80**, 5243–5246 (1998)
7. Bender, C.M., Brody, D.C., Jones, H.F.: Complex extension of quantum mechanics. Phys. Rev. Lett. **89**, 270401-1–4 (2002); **92**, 119902(E) (2004)

8. Mostafazadeh, A.: Pseudo-Hermiticity versus PT symmetry: the necessary condition for the reality of the spectrum of a non-Hermitian Hamiltonian. J. Math. Phys. **43**, 205–214 (2002); Exact PT-symmetry is equivalent to Hermiticity. J. Phys. A **36**, 7081–7091 (2003)
9. Bender, C.M.: Introduction to PT-symmetric quantum theory. Contemp. Phys. **46**, 277 (2005); Making sense of non-Hermitian Hamiltonians. Rep. Prog. Phys. **70**, 947–1018 (2007)
10. Midya, B., Roy, B., Roychoudhury, R.: A note on the PT invariant periodic potential $V(x) = 4\cos^2 x + 4iV_0 \sin 2x$. Phys. Lett. A **374**, 2605–2607 (2010)
11. Jones, H.F.: Use of equivalent Hermitian Hamiltonian for PT-asymmetric sinusoidal lattices. J. Phys. A Math. Theor. **44**, 34302 (2011)
12. Longhi, S.: Spectral singularities and Bragg scattering in complex crystals. Phys. Rev. A **81**, 022102-1–6 (2010)
13. Graefe, E.-M., Jones, H.F.: PT-symmetric sinusoidal optical lattices at the symmetry-breaking threshold. Phys. Rev. A **84**, 013818-1–8 (2011)
14. Abramowitz, M., Stegun, I.A.: Handbook of Modern Analysis, 4th edn. Cambridge University Press, Cambridge (1990)
15. Kulishov, M., Jones, H.F., Kress, B.: Analysis of PT-symmetric volume gratings beyond the paraxial approximation. Opt. Exp. **23**, 9347–9362 (2015)
16. Longhi, S.: Invisibility in PT-symmetric optical structures. J. Math. Phys. A **44**, 485302 (16pp) (2011)
17. Jones, H.F.: Analytic results for a PT-symmetric optical structure. J. Math. Phys. A **45**, 135306 (10pp) (2012)
18. Ge, L., Chong, Y.D., Stone, A.D.: Conservation relations and anisotropic transmission resonances in one-dimensional PT-symmetric photonic heterostructures. Phys. Rev. A **85**, 023802-1–10 (2012)
19. Jones, H.F., Kulishov, M.: Extension of analytic results for a PT-symmetric structure. J. Opt. **18**, 055101-1–8 (2016)
20. Kulishov, M., Jones, H.F., Kress, B.: Analysis of unidirectional non-paraxial invisibility of purely reflective PT-symmetric volume gratings. Opt. Exp. **23**, 18694–18711 (2015)
21. Kulishov, M., Kress, B., Jones, H.F.: Novel optical characteristics of a Fabry-Perot resonator with embedded PT-symmetrical grating. Opt. Exp. **22**, 23164–23181 (2014)
22. Jones, H.F., Kulishov, M., Kress, B.: Parity time-symmetric vertical cavities: intrinsically single-mode regime in longitudinal direction. Opt. Exp. **24**, 17125–17137 (2016)

Parity-Time-Symmetric Optical Lattices in Atomic Configurations

Zhaoyang Zhang, Yiqi Zhang, Jingliang Feng, Jiteng Sheng, Yanpeng Zhang, and Min Xiao

Abstract In this chapter, we show how to theoretically design and experimentally construct exact parity-time (PT) symmetric optical lattices with gain and loss in atomic configurations. By making use of the advantages of light-induced atomic coherence in multi-level atomic systems, spatially extended gain and loss arrays with real-time reconfigurability and multiple-parameter tunability can be effectively obtained in hot atomic vapors. We have constructed periodically alternative gain-loss structures with two very different schemes based on spatially-arranged optical induction techniques. With the required symmetric/antisymmetric spatial distributions for the real/imaginary parts of the refraction index satisfied, PT-symmetric optical lattices can be achieved with easy controllability. The dynamic behaviors of light propagating inside the induced non-Hermitian optical lattices are investigated by measuring the relative phase difference between two adjacent gain and loss channels.

Z. Zhang
Department of Physics, University of Arkansas, Fayetteville, AR, USA

Key Laboratory for Physical Electronics and Devices of the Ministry of Education & Shaanxi Key Lab of Information Photonic Technique, Xi'an Jiaotong University, Xi'an, China

Y. Zhang · Y. Zhang (✉)
Key Laboratory for Physical Electronics and Devices of the Ministry of Education & Shaanxi Key Lab of Information Photonic Technique, Xi'an Jiaotong University, Xi'an, China
e-mail: ypzhang@mail.xjtu.edu.cn

J. Feng
Department of Physics, University of Arkansas, Fayetteville, AR, USA

J. Sheng
State Key Laboratory of Precision Spectroscopy, East China Normal University, Shanghai, China

M. Xiao (✉)
Department of Physics, University of Arkansas, Fayetteville, AR, USA

National Laboratory of Solid State Microstructures and School of Physics, Nanjing University, Nanjing, China
e-mail: mxiao@uark.edu

D. Christodoulides, J. Yang (eds.), *Parity-time Symmetry and Its Applications*, Springer Tracts in Modern Physics 280,
https://doi.org/10.1007/978-981-13-1247-2_8

1 Introduction

Artificial optical lattices provide a fertile ground for molding the flow of optical waves, which is a fundamental issue with scientific and practical importance for optical information processing. When lights travel in such a periodic environment, the propagating behaviors can be modulated due to the induced spatially periodic refractive index of the media [1, 2]. Generally, photonic lattices are composed of equally spaced identical coupled waveguides, which can effectively discretize the incident fields. The presented discrete optical dynamics, which are not possible in homogeneous bulk media, include discrete diffraction [3], discrete solitons [4], and optical Bloch oscillation [5], to name a few.

In the past few years, PT symmetry has been implemented in the frameworks of electronics [6, 7], acoustics [8, 9] and, particularly, optics [10]. In the optical field, the experimental observations of exact parity-time (PT) symmetry have been mainly achieved in pairs of coupled optical elements (such as waveguides and micro-resonators) with elaborated gain and loss [11] in solid-state materials. Considering that many unconventional optical features were demonstrated in single PT cells (one pair of coupled gain-loss elements) [12–16], interesting exotic behaviors are expected in the extended non-Hermitian optical lattices [17–39]. The proposed effects for light propagation through such lattices include non-Hermitian optical solitons [19–22], non-Hermitian Bloch oscillation [23, 24], unidirectional invisibility [25, 26], PT-symmetric Talbot effect [32], double refraction, and nonreciprocal characteristics [35], etc. Studying these novel effects may provide new routes for exploring useful applications in non-Hermitian synthetic materials, and enlighten novel ideas in producing on-chip optical integrated devices.

Even though various fascinating theoretical proposals have been reported, the experimental generation of PT-symmetric lattice with gain and loss is not easy to realize due to various restrictions in material properties, including the limitation on engineering required gain (one of the most important parameters for implementing exact PT symmetry) in certain solid-state materials as well as the relationship between the real and imaginary parts of the index as imposed by Kramers-Kronig relations [40]. Different from solid-state systems, atomic media provide an ideal ground for easily and efficiently constructing desired refractive index profiles [41]. By making use of the laser-induced atomic coherence, particularly with the electromagnetically induced transparency (EIT) [42–44] technique, one can easily construct controllable and desired linear (dispersion, gain/loss) and nonlinear properties are easily acquirable in multi-level atomic media [45]. As a result, the schemes based on multi-level coherent atomic gases have been recently proposed to synthesize periodical non-Hermitian optical potentials [37–39, 46]. The constructed non-Hermitian optical lattices in atomic media can possess certain distinguished features. First, with due to the various tunable parameters, the non-Hermitian system in atomic configurations allows real-time reconfigurability and easy tunability (especially for the periodicity and structure of the established lattice) without the requirement of specific fabrication technologies and making large

number of samples. This advantage provides a new platform to demonstrate non-Hermitian Hamiltonians under different parametric mechanisms. Second, many interesting effects, including nonlinear non-Hermitian defect modes [47], solitons in non-Hermitian nonlinear lattices [22] and unidirectional light transmission [48], have been predicted recently by taking advantage of the interactions between the PT-symmetric potential and Kerr nonlinearity. Such phenomena might be relatively easy to be realized in EIT-modulated atomic systems with enhanced/controllable nonlinearity, which opens the door for future experimental studies of non-Hermitian properties in nonlinear optics. Third, the investigations of PT-symmetric optics in multi-level EIT atomic configurations can be potentially extended to atomic-like solid materials [49], such as prototypical NV-center diamond and Pr^{3+}:Y_2SiO_5 crystal where the EIT-related effects are already effectively generated. In the following, we will demonstrate how to effectively construct PT-symmetric lattices both theoretically and experimentally based on atomic coherence in detail.

The organization of this Chapter is as following. In Sect. 2, we show the experimental setup for constructing PT-symmetric lattices in a four-level atomic medium. According to this experimental setup, the corresponding theoretical model is established in Sect. 3. In the theoretical section, we begin from the density-matrix equations to solve for the susceptibility, and then we derivate the coupled mode equations. In Sect. 4, we show the experimental results and corresponding analysis in detail. In Sect. 5, PT symmetry based on alternating three- and four-level atomic configurations is proposed, and some basic experimental results are displayed. We conclude the chapter in Sect. 6.

2 Experimental Setup

Figure 1(a) schematically depicts the experimental setup for constructing a PT-symmetric lattices with a four-level atomic configuration. The signal field and two sets of standing-wave fields are injecting into the medium along the same direction to drive the N-type four-level ^{85}Rb atomic configuration [see Fig. 1(b)], which involves two hyperfine states F = 2 (level $|1\rangle$) and F=3 ($|2\rangle$) of the ground state $5S_{1/2}$, and two excited states $5P_{1/2}$ ($|3\rangle$) and $5P_{3/2}$ ($|4\rangle$). Two coupling beams $\boldsymbol{E}_c$ and $\boldsymbol{E}_c{}'$ (of wavelength λ_c=794.97 nm, frequency ω_c, Rabi frequencies Ω_c and $\Omega_c{}'$, respectively) from the same external cavity diode laser (ECDL2) are symmetrically arranged with respect to the z direction and intersect at the center of the vapor cell with an angle of $2\theta \approx 0.4°$ to form a standing-wave field. The coupling beams with vertical polarization are coupled by two polarization beam splitters (PBSs). The half-wave plates placed in front of the corresponding PBSs can adjust the powers of $\boldsymbol{E}_c$ and $\boldsymbol{E}_c{}'$. As a result, an optical lattice can be established along the transverse direction x inside the vapor cell. The 7 cm long atomic vapor cell is wrapped with μ-metal sheets to shield outside magnetic field and heated by a heat tape to provide an atomic density of 2.0×10^{12} cm^{-3} at 75 °C. Similarly, two pump beams $\boldsymbol{E}_p$ and $\boldsymbol{E}_p{}'$ (λ_p=780.24 nm, ω_p, Ω_p and $\Omega_p{}'$), partially overlapped with $\boldsymbol{E}_c$ and $\boldsymbol{E}_c{}'$,

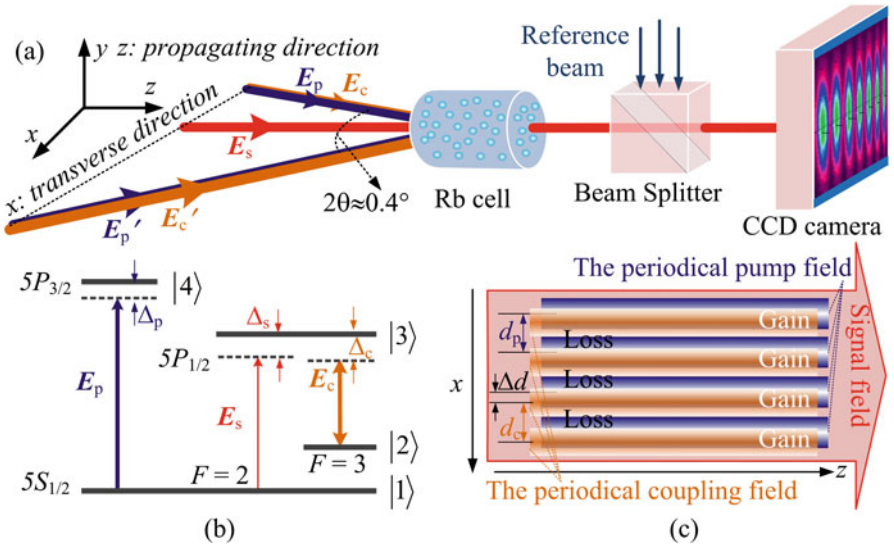

Fig. 1 (**a**) Experimental setup. Three external cavity diode lasers (ECDLs), which are not shown in the diagram, are applied to establish the experimental system. Pump beams $\boldsymbol{E}_{\mathrm{p}}'$ and $\boldsymbol{E}_{\mathrm{p}}$ are from the third laser ECDL3, while the coupling beams $\boldsymbol{E}_{\mathrm{c}}'$ and $\boldsymbol{E}_{\mathrm{c}}$ come from the second laser ECDL2. The reference beam intersects with $\boldsymbol{E}_{\mathrm{S}}$ (from the first laser ECDL1) to generate the reference interference (along the *y* direction) at the position of the CCD camera. (**b**) The energy-level diagram of the four-level *N*-type configuration in ^{85}Rb atoms. (**c**) The spatial arrangements of the signal field, coupling-field lattice, and pump-field lattice. *x* and *z* represent the transverse and longitudinal directions of beam propagation, respectively. Δd marks the displacement between the two lattices

respectively, enter the cell at the almost same angle 2θ to form a pump-field optical lattice. The two pump beams $\boldsymbol{E}_{\mathrm{p}}$ and $\boldsymbol{E}_{\mathrm{p}}'$ (with horizontal polarization) from the same ECDL3 are coupled into the vapor cell by two reflective mirrors and build the standing-wave pump field. The four laser beams ($\boldsymbol{E}_{\mathrm{c}}$&$\boldsymbol{E}_{\mathrm{c}}'$ and $\boldsymbol{E}_{\mathrm{p}}$&$\boldsymbol{E}_{\mathrm{p}}'$) are shaped as ellipses with approximate axial diameters of 1.5 mm and 4.5 mm, respectively, by two pairs of anamorphic prisms. The Gaussian signal beam $\boldsymbol{E}_{\mathrm{s}}$ (λ_{s}=794.97 nm, ω_{s}, Ω_{s}) propagating along the *z* direction travels through the two sets of induced optical lattices, as shown in Fig. 1c. The size of the signal beam is large enough to cover the two induced lattices and its diffraction pattern is monitored at the output surface of the cell.

By properly adjusting the experimental parameters, the required active Raman gain for implementing exact PT symmetry can be generated on the signal field [50–53]. As a consequence, desired periodic gain and loss profiles (along the *x* direction) are generated after the near-parallel signal beam passing through the two sets of partially-overlapping optical lattices. The discretized signal beam with a periodic gain-loss profile then interferes with a reference beam (from the same ECDL as $\boldsymbol{E}_{\mathrm{s}}$ and injected long the *y* direction) to exhibit the induced phase difference between two adjacent gain and loss waveguides/channels. The Gaussian-

shaped reference beam is introduced into the optical path via a 50/50 beam splitter to intersect with the $\boldsymbol{E}_{\mathrm{s}}$ beam at the position of a charge coupled device (CCD) camera [see Fig. 1a], which is used to monitor both the output signal beam and the relative phase difference. Figure 1c shows the spatial arrangement for the two sets of optical lattices and the signal beam inside the cell. The spatial periodicity of the coupling lattice is $d_{\mathrm{c}} = \lambda_{\mathrm{c}}/2\sin\theta \approx 114\ \mu\mathrm{m}$, and the spatial-shift distance Δd between the two sets of lattices can be modified to effectively control the real and imaginary parts of the susceptibility experienced by the signal field.

3 Theoretical Model

Under the rotating-wave approximation, the density-matrix equations for theoretically describing the four-level N-type atomic system are given as [38].

$$
\begin{aligned}
&\dot{\rho}_{22} = \Gamma_{42}\rho_{44} + \Gamma_{32}\rho_{33} - \Gamma_{21}\rho_{22} + \tfrac{i}{2}\left(\rho_{32} - \rho_{23}\right)\Omega_c,\\
&\dot{\rho}_{33} = \Gamma_{43}\rho_{44} - \Gamma_{32}\rho_{33} - \Gamma_{31}\rho_{33} + \tfrac{i}{2}\left[\left(\rho_{23} - \rho_{32}\right)\Omega_c + \left(\rho_{13} - \rho_{31}\right)\Omega_s\right],\\
&\dot{\rho}_{44} = -\left(\Gamma_{43} + \Gamma_{42} + \Gamma_{41}\right)\rho_{44} + \tfrac{i}{2}\left(\rho_{14} - \rho_{41}\right)\Omega_p,\\
&\dot{\rho}_{21} = -\tilde{\gamma}_{21}\rho_{21} + \tfrac{i}{2}\left(\rho_{31}\Omega_c - \rho_{24}\Omega_p - \rho_{23}\Omega_s\right),\\
&\dot{\rho}_{31} = -\tilde{\gamma}_{31}\rho_{31} + \tfrac{i}{2}\left[\rho_{21}\Omega_c - \rho_{34}\Omega_p + \left(\rho_{11} - \rho_{33}\right)\Omega_s\right],\\
&\dot{\rho}_{41} = -\tilde{\gamma}_{41}\rho_{41} + \tfrac{i}{2}\left[-\rho_{43}\Omega_s + \left(\rho_{11} - \rho_{44}\right)\Omega_p\right],\\
&\dot{\rho}_{32} = -\tilde{\gamma}_{32}\rho_{32} + \tfrac{i}{2}\left[\rho_{12}\Omega_s + \left(\rho_{22} - \rho_{33}\right)\Omega_c\right],\\
&\dot{\rho}_{42} = -\tilde{\gamma}_{42}\rho_{42} + \tfrac{i}{2}\left(\rho_{12}\Omega_p - \rho_{43}\Omega_c\right),\\
&\dot{\rho}_{43} = -\tilde{\gamma}_{43}\rho_{43} + \tfrac{i}{2}\left(\rho_{13}\Omega_p - \rho_{42}\Omega_c - \rho_{41}\Omega_s\right),\\
&\rho_{11} + \rho_{22} + \rho_{33} + \rho_{44} = 1.
\end{aligned}
\tag{1}
$$

Here, $\Omega_{\mathrm{s}} = d_{13}E_{\mathrm{s}}/\hbar$, $\Omega_{\mathrm{c}}{=}d_{23}E_{\mathrm{c}}/\hbar$ and $\Omega_{\mathrm{p}}{=}d_{14}E_{\mathrm{c}}/\hbar$ represent the Rabi frequencies corresponding to the signal, coupling and pump fields, respectively, and d_{ij} is the dipole momentum between levels $|i\rangle$ and $|j\rangle$. Γ_{ij} is the decaying rate between $|i\rangle$ and $|j\rangle$, and $\gamma_{ij} = (\Gamma_i{+}\Gamma_j)/2$ is the decoherence rate. $\tilde{\gamma}_{21} = \gamma_{21} - i\left(\Delta_s - \Delta_c\right)$, $\tilde{\gamma}_{31} = \gamma_{31} - i\Delta_s$, $\tilde{\gamma}_{41} = \gamma_{41} - i\Delta_p$, $\tilde{\gamma}_{32} = \gamma_{32} - i\Delta_c$, $\tilde{\gamma}_{32} = \gamma_{32} - i\Delta_c$, $\tilde{\gamma}_{32} = \gamma_{32} - i\Delta_c$, $\tilde{\gamma}_{42} = \gamma_{42} - i\left(\Delta_c + \Delta_p - \Delta_s\right)$, $\tilde{\gamma}_{43} = \gamma_{43} - i\left(\Delta_p - \Delta_s\right)$. $\Delta_{\mathrm{s}}{=}\omega_{\mathrm{s}}{-}\omega_{31}$, $\Delta_{\mathrm{c}} = \omega_{\mathrm{c}}{-}\omega_{32}$ and $\Delta_{\mathrm{p}} = \omega_{\mathrm{p}}{-}\omega_{41}$ are the frequency detunings of the signal, coupling and pump fields, respectively. The corresponding susceptibility can be obtained by numerically solving ρ_{31} in Eq. (1) under steady-state approximation by considering the relation $2N\mu_{13}\rho_{31} = \varepsilon_0\chi E_{\mathrm{s}}$. As a consequence, the real and imaginary parts of the refractive index can be written as $n_R \approx \frac{1}{2}\chi' = \frac{N\mu_{13}}{\varepsilon_0 E_s}\,\mathrm{Re}\left(\rho_{31}\right)$ and $n_I \approx \frac{1}{2}\chi'' = \frac{N\mu_{13}}{\varepsilon_0 E_s}\,\mathrm{Im}\left(\rho_{31}\right)$, according to $n = \sqrt{1+\chi} \approx 1 + \chi/2$, $\chi = \chi' + i\chi''$, and $n = n_0 + n_R + in_I$. Here $n_0 = 1$ is the background index of the atomic vapor. The initially calculated susceptibility versus the signal-field detuning Δ_{s} at different coupling intensity Ω_{c} is shown in Fig. 2. By looking through Fig. 2b and d, one can conclude that the pump field can surely give rise to both gain and

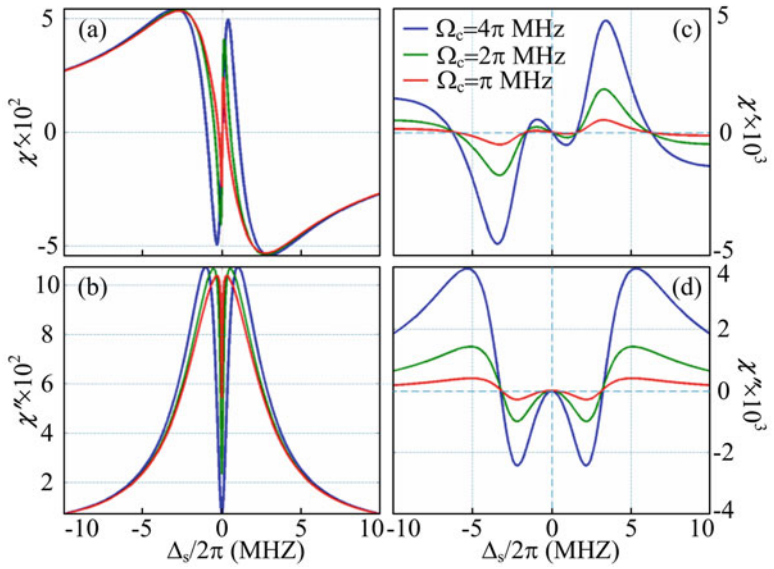

Fig. 2 Theoretical susceptibility χ versus Δ_s. (**a**) Real part and (**b**) imaginary part of the χ versus Δ_s with $\Omega_p = 0$. (**c**) The real and (**d**) imaginary parts of χ versus Δ_s with $\Omega_p = 2\pi \times 6$ MHz. The presence of the pump field can result in positive and negative imaginary susceptibility at different Δ_s. Other parameters are $\Omega_s = 2\pi \times 0.1$ MHz and $\Delta_p = \Delta_c = 0$. Adapted from Ref. [52]

loss in the system, and the zero point of the imaginary part keeps constant at these Ω_c values.

In another view, we show the calculated real and imaginary parts of the susceptibility versus the transverse x coordinate in Fig. 3. In principle, when the values of the real part versus Δ_s at $\Omega_p = 0$ and $\Omega_p \neq 0$ are the same and the corresponding imaginary parts have equivalent absolute value but opposite signs, the periodic PT-symmetric conditions can be achieved in this periodic environment. According to the results in Fig. 3a and b, with the parameters set as $\Delta_s \approx 2\pi \times 15$ MHz, $\Delta_c = -100$ MHz, $\Delta_p \approx 40$ MHz, $\Omega_s = 2\pi \times 0.2[1 + \cos(\pi x/2)]$ MHz and $\Omega_c = 2\pi \times 0.2$ MHz, the real and imaginary parts of the susceptibility can meet the requirements for periodic PT-symmetric potential, i.e. the real part χ' has a symmetric profile while the corresponding imaginary part χ becomes antisymmetric along the x direction [see Fig. 3c and d], which shows that an exact PT-symmetric structure with alternating gain and loss can indeed be established in such an N-type atomic configuration.

According to the Maxwell's equations and considering the paraxial approximation, the above calculated complex spatial index refraction (susceptibility) that represents the potential $V(x)$ can be described by the Schrödinger-like equation [11, 28, 35, 54]

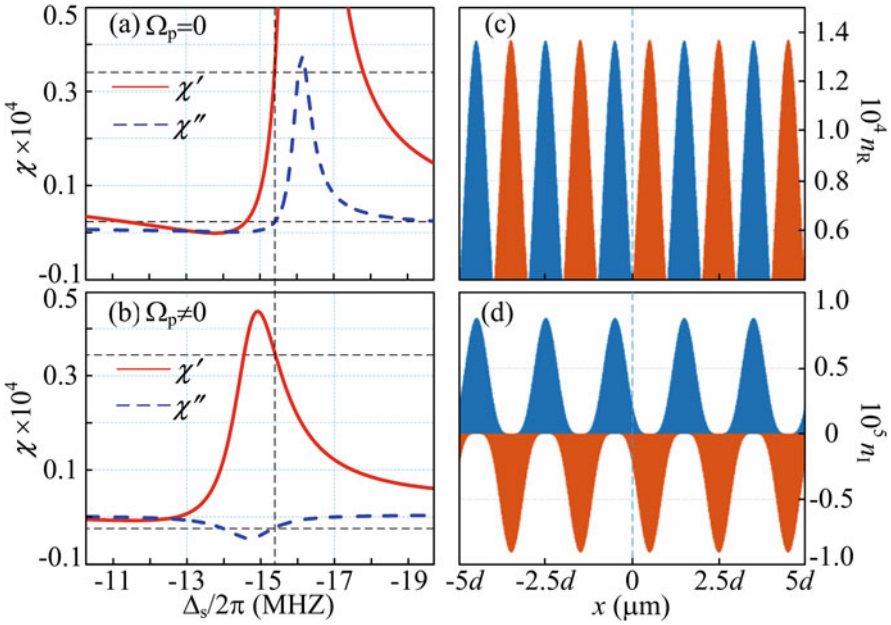

Fig. 3 (**a**) Real (dispersion) and (**b**) imaginary parts of the susceptibility versus Δ_s under the conditions of turning the pump field (**a**) off and (**b**) on, respectively. (**c**) Real and (**d**) imaginary (gain or absorption) parts of the refractive index (experienced by the signal field) as a function of position x with the coupling intensities spatially modified. Adapted from Ref. [52]

$$i\frac{\partial E}{\partial z}+\frac{\partial^2 E}{\partial x^2}+V(x)E=0. \tag{2}$$

Considering that the potential is uniform along the propagation direction, the PT-symmetric potential describes a periodic coupled-waveguide structure. In the potential, the electric field can be written as [54]

$$\begin{aligned}E(x,z,t)=\exp(i\beta z)\Big[&A_1(x)E_1(z)+A_2(x)E_2(z)+A_3(x)E_3(z)+A_4(x)E_4(z)\\&+A_5(x)E_5(z)+A_6(x)E_6(z)+A_7(x)E_7(z)+A_8(x)E_8(z)\\&+A_9(x)E_9(z)+A_{10}(x)E_{10}(z)\Big],\end{aligned} \tag{3}$$

where $A_m(x)$ is the eigenmode of each waveguide and $E_m(z)$ is the amplitude of the mode, $m=1, 2, \ldots, 10$ represents the number of the coupled waveguides. As a consequence, a coupled-mode (tight-binding) set of equations with 10 waveguides involved are given as [12, 27]

$$
\begin{aligned}
&i\frac{dE_1}{dz} - i\frac{\gamma_G}{2}E_1 + \kappa E_2 = 0,\\
&i\frac{dE_2}{dz} + i\frac{\gamma_L}{2}E_2 + \kappa\,(E_1 + E_3) = 0,\\
&i\frac{dE_3}{dz} - i\frac{\gamma_G}{2}E_3 + \kappa\,(E_2 + E_4) = 0,\\
&i\frac{dE_4}{dz} + i\frac{\gamma_L}{2}E_4 + \kappa\,(E_3 + E_5) = 0,\\
&i\frac{dE_5}{dz} - i\frac{\gamma_G}{2}E_5 + \kappa\,(E_4 + E_6) = 0,\\
&i\frac{dE_6}{dz} + i\frac{\gamma_L}{2}E_6 + \kappa\,(E_5 + E_7) = 0,\\
&i\frac{dE_7}{dz} - i\frac{\gamma_G}{2}E_7 + \kappa\,(E_6 + E_8) = 0,\\
&i\frac{dE_8}{dz} + i\frac{\gamma_L}{2}E_8 + \kappa\,(E_7 + E_9) = 0,\\
&i\frac{dE_9}{dz} - i\frac{\gamma_G}{2}E_9 + \kappa\,(E_8 + E_{10}) = 0,\\
&i\frac{dE_{10}}{dz} + i\frac{\gamma_L}{2}E_{10} + \kappa E_9 = 0,
\end{aligned}
\tag{4}
$$

where γ_G and γ_L are the gain and loss coefficients experienced by two adjacent waveguides [for example, the fifth ($A_5(x)$) and sixth ($A_6(x)$) waveguides] and κ is the coupling coefficient. The three coefficients in Eq. (4) can be explicitly given as:

$$
\begin{aligned}
\gamma_G &= \frac{\int V_6(x)A_5(x)A_6^*(-x)dx}{\int A_5(x)A_6^*(-x)dx},\\
\gamma_L &= \frac{\int V_5(x)A_6(x)A_5^*(-x)dx}{\int A_6(x)A_5^*(-x)dx},\\
\kappa &= \frac{\int V_5(x)A_6(x)A_6^*(-x)dx}{\int A_5(x)A_6^*(-x)dx}.
\end{aligned}
\tag{5}
$$

Also, the eigenmodes obey the following relations:

$$
\begin{aligned}
&A_1(x) = A_{10}^*(-x)\,,\ A_2(x) = A_9^*(-x)\,,\\
&A_3(x) = A_8^*(-x)\,,\ A_4(x) = A_7^*(-x)\,,\\
&A_5(x) = A_6^*(-x)\,,
\end{aligned}
\tag{6}
$$

and

$$
\begin{aligned}
&A_1(x - 4x_0) = A_3(x - 2x_0) = A_5(x) = A_7(x + 2x_0) = A_9(x + 4x_0)\,,\\
&A_2(x - 4x_0) = A_4(x - 2x_0) = A_6(x) = A_8(x + 2x_0) = A_{10}(x + 4x_0)\,.
\end{aligned}
\tag{7}
$$

Here, x_0 is the space between two adjacent waveguides. According to the coupling equations in Eq. (4), we can obtain the corresponding band structures (under balanced gain/loss case $\gamma_G{=}\gamma_L{=}\gamma$) as shown Fig. 4.

The band structure of this lattice reveals an interesting property which has not been observed in other periodic lattices, i.e., by increasing the gain/loss contrast,

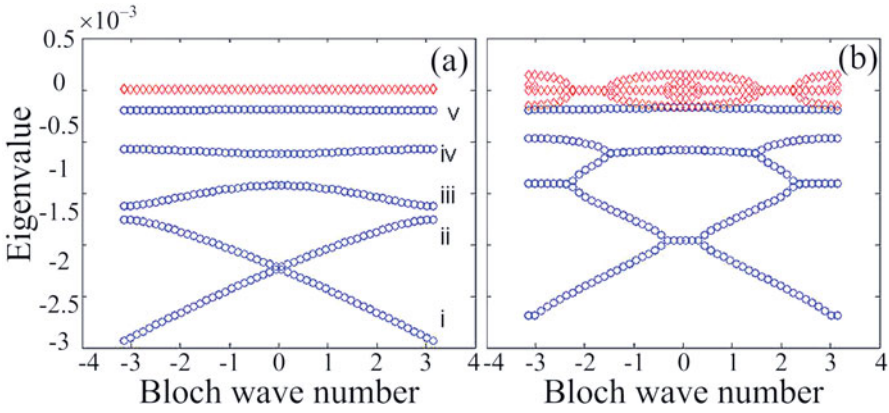

Fig. 4 Band structures for the cases (**a**) below and (**b**) above PT-symmetric threshold, respectively. The blue circles are the real parts of the first five bands and the red diamonds are for the imaginary parts

the first band [curve i in Fig. 4a] remains intact from symmetry breaking, as shown in Fig. 4. When the imaginary part n_{I} of the refractive index is zero, the bands (i)&(ii) and (ii)&(iii) have already touched each other. With n_{I} gradually increased to operate the system above the threshold, the first band keeps unchanged and the third (iii) and fourth (iv) bands start to merge obviously. This is due to the fact that the gain and loss regions are mostly confined to the two sides of each waveguide channel and thus have a minimum overlap with the lowest-order Floquet-Bloch mode of the first band (that is mostly confined to the center of each channel). On the other hand, the second-band Floquet-Bloch wave functions overlap more effectively with these gain and loss regions and therefore this band is the first one to break the PT symmetry. The major difference between the cases below [Fig. 4a] and the above [Fig. 4b] PT-symmetric threshold can be seen from the corresponding imaginary parts. In Fig. 4a, the imaginary parts are always zero for all the eigenvalues, while in Fig. 4b, non-zero values appear in the imaginary parts.

The relation between the coupling efficiency and the separation of adjacent channels was studied in Ref. [54] for coupled waveguide systems. One can reduce the separation between the two coupled waveguides to get a stronger coupling efficiency. In such a case, the imaginary part displays a discontinuity between the induced gain and absorption regions [55], as shown in Fig. 5.

By setting different numbers of coupled waveguides, we can obtain the corresponding band structures (under the balanced gain/loss case) as shown in Fig. 6, which clearly gives the exception point as about $\gamma_L/2\kappa \approx 0.284$ if $N_{\mathrm{waveguide}}=10$ waveguides are involved. Also, according to Fig. 6, the exception point value decreases with increasing the number of coupled waveguides.

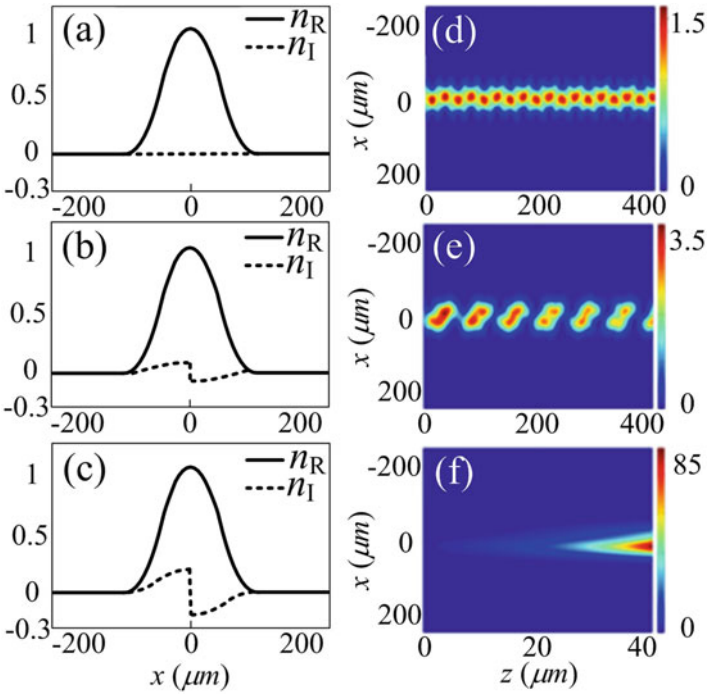

Fig. 5 Real (solid black curves) and imaginary (dashed blue curves) refractive indices as a function of position x for (**a**) passive waveguide, (**b**) PT-symmetric waveguide operating below symmetry breaking threshold, (**c**) PT-symmetric waveguide above threshold. (**d**)–(**f**) Beam dynamics for each case

4 Experimental Results

In the experiment, we first explore proper parameters (mainly including the frequency detuning and intensities of corresponding laser fields, and the atomic density) to generate the required Raman gain based on EIT in the N-type four-level system in the frequency domain. The observed EIT (generated by the signal and coupling fields) and gain spectra, corresponding to the transition ^{85}Rb, $F{=}3{\rightarrow}F'$, are demonstrated in Fig. 7a. Next, we periodically modulate the refractive index distribution based on the EIT scheme [56] and then establish the periodic gain-loss profiles (by adding the standing-wave pump field) along the x direction. With the Gaussian signal beam [as shown in Fig. 7b] launched into the coupling lattice (with the pump fields blocked), we observed the discrete diffraction pattern, which can manifest the periodic modification of the signal-field refractive index. Such discrete diffraction patterns appear within a frequency detuning window of about 50 MHz near the two-photon resonance that satisfies $\Delta_s - \Delta_c = 0$ [57, 58]. With the signal-field detuning set as $\Delta_s = -100$ MHz, the diffraction image shown in Fig. 7c is

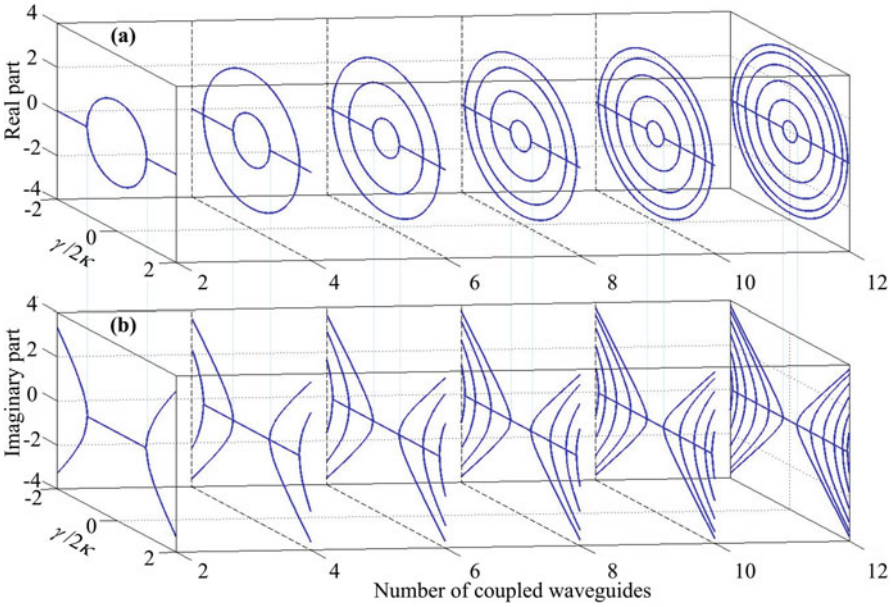

Fig. 6 Band structures of the (**a**) real and (**b**) imaginary parts with $N_{\text{waveguide}}$(=2, 4, 6, 8, 10, 12) gain-loss waveguides coupled in an array. The PT-symmetry breaking threshold decreases as $N_{\text{waveguide}}$ increases

obtained by carefully adjusting the coupling-field period d_c to match the maximum refractive index contrast at $\Delta_s - \Delta_c = 10$ MHz.

The pump-field lattice can lead to an amplification on $\boldsymbol{E}_s$. With the two sets of lattices turned on concurrently, the gain and loss regions with a high and controllable contrast on $\boldsymbol{E}_s$ can be simultaneously obtained by carefully modifying the displacement Δd between the two established optical lattices [see Fig. 1c] and other experimental controlling parameters, e.g., the field intensities, frequency detunings, and the temperature of atoms, etc. As shown in Fig. 7d, two adjacent channels in the probe lattice experience alternative gain and loss, which can be determined by comparing the intensity profile of the modulated signal beam with its original Gaussian intensity profile [Fig. 7b].

By taking the advantages of atomic media, the intensity ratio of the generated gain and loss can be effectively manipulated. Figure 8a demonstrates the evolution of the gain/loss ratio as a function of the detuning Δ_p of the pump field. Figure 8b and c present the observed gain-loss modulated probe intensity profiles at $\Delta_p = 20$ MHz and 40 MHz, respectively. In the current atomic configuration, the intensity for the detected signal field can be written as $I = I_0 - I_0 e^{-aL} \approx I_0 - I_0(1 - aL)$, where $a = (2\pi/\lambda_s)\chi''$ and I_0 is defined as the initial intensity of the signal field and L as the cell length. The loss or gain is determined

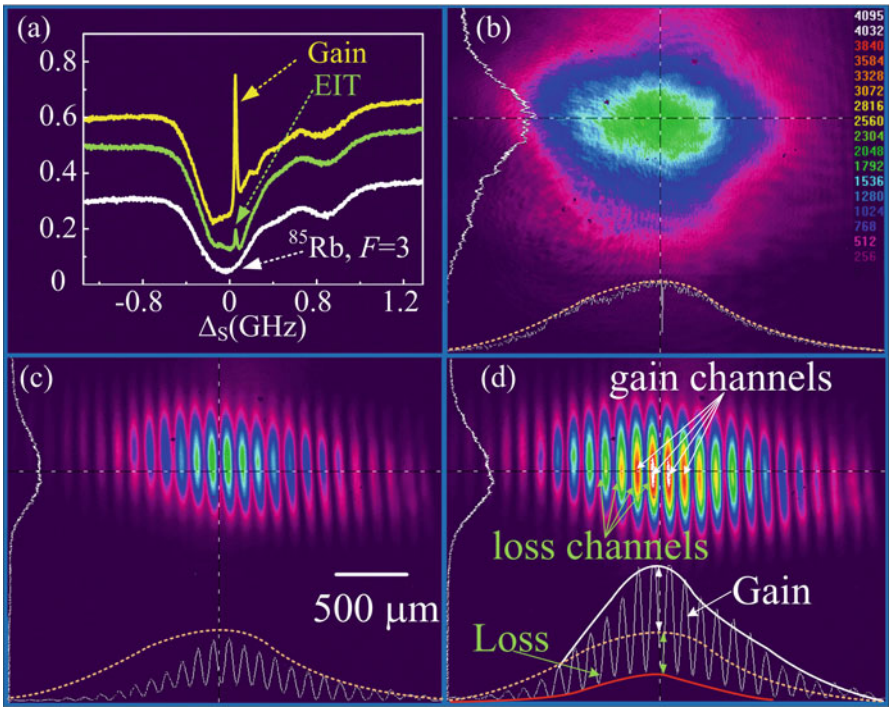

Fig. 7 (**a**) Observed Raman gain signal in the frequency domain. The upper, middle and lower curves are the generated gain, EIT signal and the absorption spectrum corresponding to the transition of ^{85}Rb, F=3→F', respectively, versus the detuning of the signal field. (**b**) Image and intensity profile of $\boldsymbol{E}_s$ without interacting with atoms. (**c**) Diffraction patterns of the signal beam after propagating through the coupling lattice. (**d**) Simultaneous gain and loss profiles on $\boldsymbol{E}_s$ with both lattices turned on

by the sign of χ'', namely, the negative (positive) n_I represents the gain (loss). Consequently, we have $I \propto \chi'' = 2n_I$, which means that the ratio of gain and loss intensity profiles in current atomic setting can be equivalent to the coefficient ratioγ_G/γ_L.

In a PT-symmetric system, the evolution of eigenvalues is the most reliable criterion to determine whether the system is below or above the symmetry-breaking threshold. For such an induced non-Hermitian gain/loss-modulated array, the behaviors of its eigenvectors can be unveiled by the changes in the relative phase difference v (which represents the internal phase difference of the eigenvectors) between the adjacent gain and loss channels [10]. The phase difference is experimentally measured with the assistance of the reference interference (generated by the signal beam and the reference beam) along the y direction, as shown in Fig. 9. To quantitatively determine the phase difference, we define the distance (along the y direction) between the adjacent interference fringes as 2π (the length of the double-sided arrow between the two solid lines), as shown in Fig. 9a. The black dotted

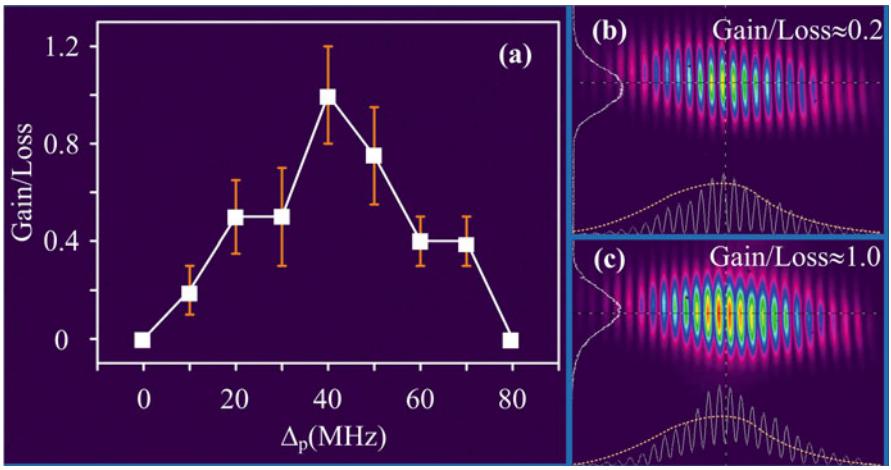

Fig. 8 (**a**) Dependence of the gain/loss ratio on the frequency detuning Δ_p of the pump field. The squares are experimental observations and the solid curve is the guide for eyes to demonstrate the evolution of gain/loss. The observed gain-loss profiles are presented at (**b**) $\Delta_p = 10$ MHz and (**c**) $\Delta_p = 40$ MHz

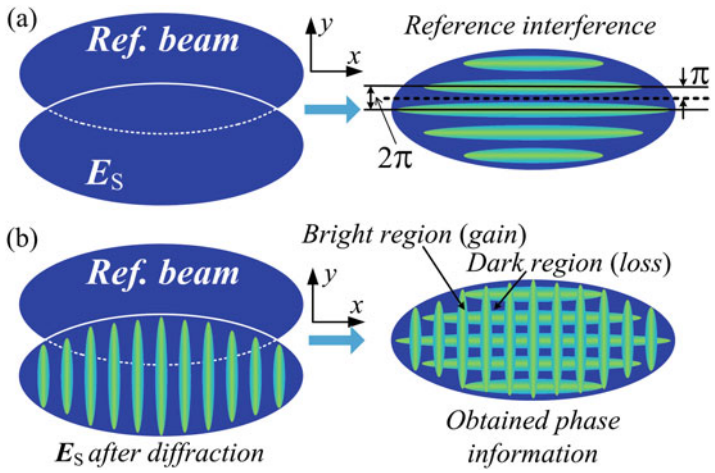

Fig. 9 Schematic diagram for measuring the relative phase difference between the gain/loss channels. (**a**) Interference between the signal field $\boldsymbol{E}_S$ and a reference beam (both of which are from the same laser) in the y direction. The phase difference between the two solid lines is defined as 2π. The phase difference between the black dotted line (located at the center of the two solid lines) and one of the two solid lines is π. (**b**) Interference pattern between the intensity modulated $\boldsymbol{E}_S$ field (after diffraction) and the reference beam, so that the square-like lattice is obtained and the phase difference can then be measured

line gives the center of the two solid lines, so phase π can be described by distance (marked by a pair of one-way arrows) between one of the two solid lines and the dotted line. With the $\boldsymbol{E}_{\mathrm{S}}$ spatially discretized by the induced lattices, the interference pattern divides the "bright" gain regions and "dark" loss regions into a net-like square lattice, as shown in Fig. 9b.

Figure 10 shows the measured phase difference between two adjacent gain and loss waveguides. By carefully tuning the experimental parameters to generate the gain and loss with high contrast (the loss should be more than 60% of the original signal-field intensity), we can observe a clear relative distance/shift (along the y direction) between the bright square and dark square (corresponding to the gain and loss channels, respectively) through the reference interference. The values of the distance/shift can be proportionally referred to as the relative phase difference. Figure 10a is the observed reference interference, in which the phase 2π and π are marked by corresponding arrows. A red dotted line is drawn along the center of a "dark" square in one row of the lattice to label its position. The relative distance [marked by a pair of one-way arrows in Fig. 10c–e] between the red dotted line and black dotted line represents the relative phase difference between two neighboring gain and loss channels [10]. Figure 10b shows the case that no phase difference (the black dotted line and red dotted line overlap) is detected between the gain and loss channels when the gain is zero. Several relative phase differences (ν) are measured in Fig. 10c–e as the gain/loss ratio $\gamma_{\mathrm{G}}/\gamma_{\mathrm{L}}$ increases but still below the PT-symmetry breaking threshold. Considering that the measured ν is consistently zero under low and no gain conditions, there are no error bars for the first two data points. Figure 10f illustrates the situation above the symmetry breaking point, in which the phase difference is constantly $\nu = \pi/2$ even the ratio $\gamma_{\mathrm{G}}/\gamma_{\mathrm{L}}$ continuously increases from 1 to 1.2. The measured phase-difference dependence on $\gamma_{\mathrm{G}}/\gamma_{\mathrm{L}}$, as shown in Fig. 10g, can be qualitatively explained by the theoretical predictions given in Fig. 10h, which illustrates that the value of $\gamma_{\mathrm{L}}/2\kappa$ can indeed affect the dynamics behaviors of a coupled waveguide array system with a certain $\gamma_{\mathrm{G}}/\gamma_{\mathrm{L}}$. The vertical axis $\gamma_{\mathrm{L}}/2\kappa$ represents the evolution of $n_{\mathrm{I}}/n_{\mathrm{R}}$ since the coupling coefficient κ directly relates to the real part n_{R} of the index.

Actually, for the established non-Hermitian optical lattice, most of the demonstrated cases possess an unbalanced gain/loss ratio. In principle, these unbalanced cases can be still mathematically transformed into a PT-symmetry-like configuration [10]. This then establishes a "quasi-PT symmetry" system [59], in which the characteristic eigenvalue pattern is simply offset with respect to the original zero line [60]. Note that the dynamical behaviors of the exact PT-symmetry system and its quasi-PT-symmetry counterparts are essentially identical if the PT symmetry is unbroken, while their dynamics are different when the PT symmetry is broken [59].

For the experimental point at $\gamma_{\mathrm{G}} = \gamma_{\mathrm{L}}$, the phase difference can vary from 0 to π below PT-symmetry breaking threshold and jumps to a fixed value of $\pi/2$ above threshold by increasing $\gamma_{\mathrm{L}}/2\kappa$ [10]. Actually, Fig. 10f shows the exact PT-symmetry breaking point with $\gamma_{\mathrm{G}}/\gamma_{\mathrm{L}} = 1$ and $\gamma_{\mathrm{L}}/2\kappa > 0.284$ simultaneously realized. Here the threshold $\gamma_{\mathrm{L}}/2\kappa = 0.284$ is theoretically obtained with 10 waveguides coupled. In

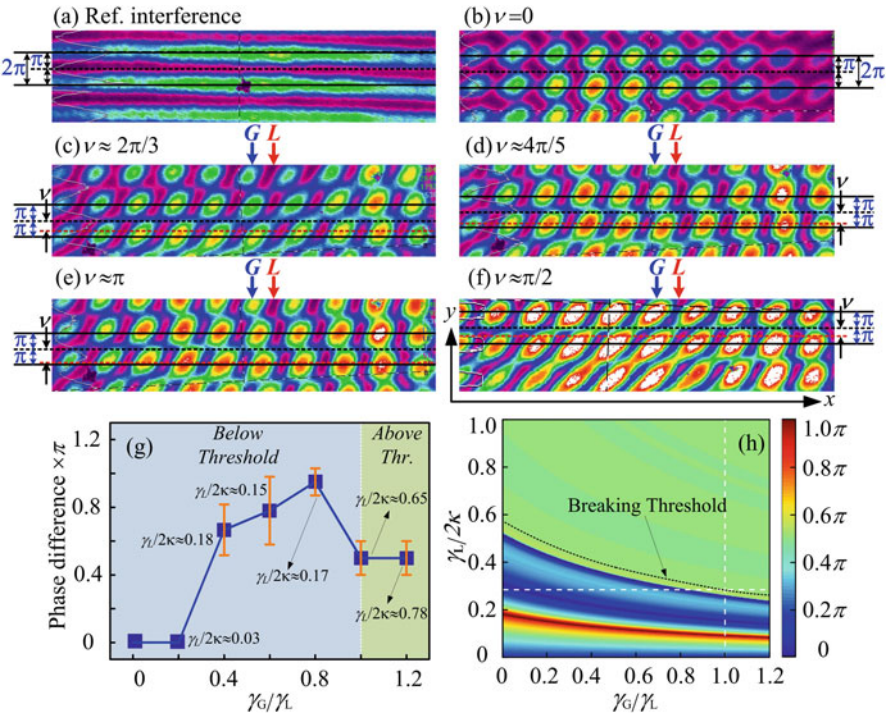

Fig. 10 Selected gain and loss channels for measurements are marked with *G* and *L*, respectively. (**a**) Reference interference fringes generated by the reference beam and the Gaussian signal beam. The two solid lines mark the centers of two adjacent fringes. (**b**−**f**) Observed phase differences (marked by the pair of one-way arrows) between the neighboring gain and loss channels with γ_G/γ_L setting as 0, 0.4, 0.6, 0.8, and 1.0, respectively. (**g**) Measured dependence of phase difference on γ_G/γ_L. (**h**) Theoretical simulations of phase difference according to the coupled equations for 10 waveguides at a propagation distance of z=10, and the breaking threshold (the dotted curve) decreases with the increase of gain/loss ratio. The dimensionless z is scaled by the Rayleigh range kx_0^2 ($k = 2\pi/\lambda$, and x_0 is the waveguide width). Adapted from Ref. [52]

principle, infinite number of coupled waveguides can be considered. However, due to the limited beam size and the periodicity of the waveguide, we use 10 effective waveguides in theory to mimic the experiment.

For the cases of $\gamma_G \neq \gamma_L$, the coupled gain and loss waveguides can still have phase differences in the same way as the case of $\gamma_G = \gamma_L$. It is worth mentioning that the PT-symmetry breaking threshold value for $\gamma_L/2\kappa$ can change with the value of gain/loss ratio as indicated by the dotted curve shown in Fig. 10h. Giving the experimental parameters at certain gain-loss ratio in Fig. 10g, we can calculate the $\gamma_L/2\kappa$ value and determine whether the system operates below or above the PT-symmetry breaking threshold according to the coupling equations Eq. (4).

5 PT-Symmetric Optical Lattice with Alternating Three- and Four-Level Atomic Configurations

The establishment of such PT-symmetric optical lattice with gain and loss based on discrete diffractions and EIT can be an exciting progress in the fields of both non-Hermitian optics and AOM physics. As an improvement of the current work, we further construct a PT-symmetric lattice based on alternating three- and four-level atomic configurations, which can also provide respective gain and loss with easy accessibility and better tunability [61]. The four-level system providing Raman gain is driven by a signal field, a coupling field and a pump field, as shown in Fig. 11a, which is the same as the energy-level structure in Fig. 1b. With the intensity of the pump field set to be zero, the four-level system reduces down to a three-level system [with only subsystem $|1\rangle \rightarrow |2\rangle \rightarrow |3\rangle$ in Fig. 11a involved], which provides a modifiable loss under the EIT condition.

To be specific, we inject two elliptically-shaped signal beams $\boldsymbol{E}_s$ and $\boldsymbol{E}_s'$ (wavelength of λ_s=794.97 nm, horizontal polarization) from a same ECDL into the rubidium cell symmetrically with respect to the z axis. They intersect at the center of the rubidium cell with an angle of $2\theta \approx 0.4°$ to establish a periodical signal field in the x direction. The small-angle arrangement can make the signal beam be a standing-wave field for a relatively long distance (over 20 cm) along the z direction. Considering the requirement of loss in a PT-symmetric system, the intensities of fields $\boldsymbol{E}_s$ and $\boldsymbol{E}_s'$ are different, and the minimum intensity of the established standing wave is non-zero. The strong Gaussian coupling beam (λ_c=794.97 nm, vertical polarization) is introduced into the medium at the same propagation direction of $\boldsymbol{E}_s$. With the frequency of the coupling beam $\boldsymbol{E}_c$ tuned to be near resonant with the transition $|2\rangle \leftrightarrow |3\rangle$, a Λ-type EIT configuration is achieved in this $|1\rangle \leftrightarrow |2\rangle \leftrightarrow |3\rangle$ subsystem. Considering that the coupling beam is large enough, the spatially periodical EIT (along the x direction) can be observed on the output signal field. Furthermore, the two pump beams $\boldsymbol{E}_p$ and $\boldsymbol{E}_p'$ (λ_p=780.24 nm, vertical

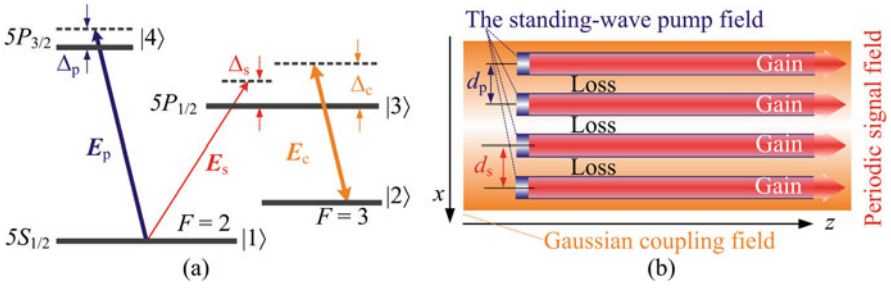

Fig. 11 (**a**) Four-level N-type energy-level configuration for introducing gain. The subsystem $|1\rangle \rightarrow |2\rangle \rightarrow |3\rangle$ is responsible for adjustable loss. (**b**) Spatial arrangement of the laser fields inside the medium. The symbol z represents the propagation direction of light. The intensity of the pump field at the points near the interference valley is zero while the signal field at the valley is non-zero

polarization) partially overlapped with $\boldsymbol{E}_{\mathrm{s}}$ and $\boldsymbol{E}_{\mathrm{s}}'$, respectively, are incident into the cell with almost the same angle of 2θ to build the periodical pump field. The angle between the two pump beams should be carefully adjusted to make the pump-field lattice fully overlaps with the signal-field lattice. The presence of the pump field can introduce an alternating Raman gain on the signal field under the four-level N-type configuration [51, 53]. The schematic diagram for the spatial arrangement of the three fields inside the cell is shown as Fig. 11b, where the signal array completely overlaps with the pump array. Such standing-wave structure can realize the alternative on/off of pump field. The pump field intensity has its maximum and minimum (basically zero) at the interference peak and valley, respectively. As a result, the detected signal profile exhibits interference pattern with peak experiencing gain due to the four-level Raman process and valley experiencing loss due to three-level EIT (without the pump field). Since the signal field has orthogonal polarization from the pump and coupling fields, we reject the pump and coupling fields with a polarization beam splitter and monitor the signal field on a CCD camera.

Such periodic gain-loss pairs can be exploited to construct a spatially distributed PT-symmetric refractive index by appropriately tuning the gain/loss ratio, which can be easily manipulated by adjusting the pertinent parameters including the atomic density, the periodicity of the standing waves, and the frequency detunings and Rabi frequencies of the corresponding fields. One of the key advantages of the current system is that the gain and loss channels can be adjusted more independently, which will be easier to balance the gain and loss to realize PT-symmetric condition and study some related effects. With the gain-loss modulated periodic signal field obtained, we similarly introduce a reference beam (from the same ECDL as $\boldsymbol{E}_{\mathrm{s}}$) to interfere with the signal beam and demonstrate non-Hermitian properties of the system by measuring the relative phase difference between the gain and loss channels.

Figure 12 depicts the detected signal field on the CCD camera under different conditions. First, with the frequency detuning of the signal field $\boldsymbol{E}_{\mathrm{s}}$ set away from the atomic resonance, one sees the simple interference fringe in Fig. 12a. As the signal frequency tuned to be near resonant with the transition $|1\rangle \leftrightarrow |3\rangle$, it can be dramatically absorbed [Fig. 12b]. When the large-size Gaussian coupling field $\boldsymbol{E}_{\mathrm{c}}$ is turned on, it induces EIT on the signal field and reduces its absorption [Fig. 12c] under the two-photon resonance satisfying $\Delta_{\mathrm{s}} - \Delta_{\mathrm{c}} = 0$. Here the detuning Δ_{s} and Δ_{c} are same as the definition in Sect. 3. The amount of residual absorption is controlled by the coupling beam parameters. Then, by injecting the pump field into the cell, we can obtain simultaneous gain and loss channels with a controllable contrast on the signal field by carefully arranging the coupling- and pumping-field parameters. For the bright fringe regions (maximum intensity), the presence of the pump field can couple a four-level N-type system and therefore can lead to an amplification on the signal field without population inversion ($\rho_{11} > \rho_{33}$) [51]. As shown in Fig. 12d, one can clearly find the alternative gain and loss in the middle region of the periodical field by comparing it with the original intensity profile of the signal field shown in Fig. 12a. The dark fringes (minimum intensity) represent the loss

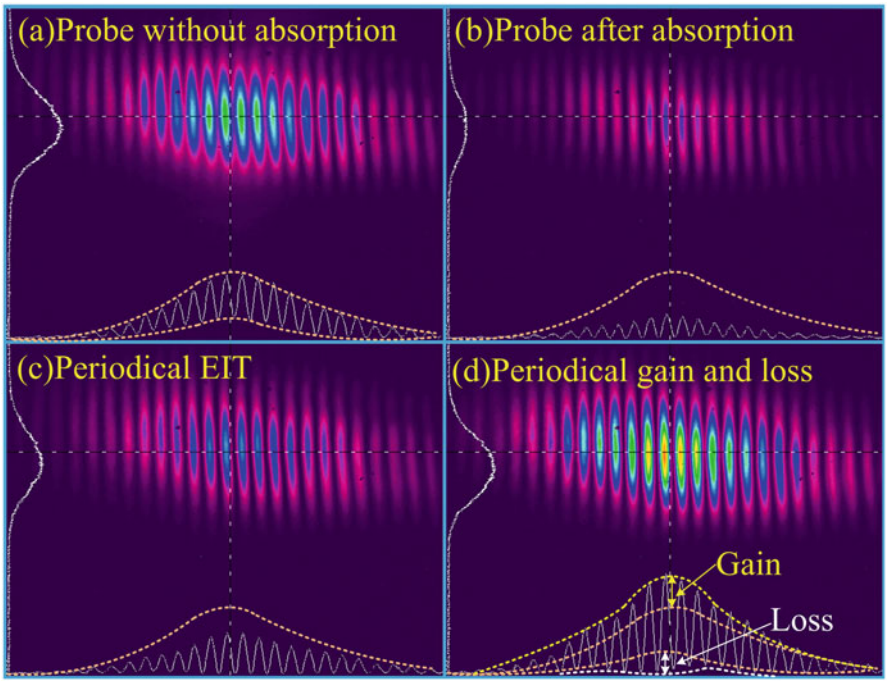

Fig. 12 Detected signal field under various conditions. (**a**) Observed image and intensity profiles of the signal field $\boldsymbol{E}_{\mathrm{s}}$ without interacting with atoms. (**b**) Signal field after propagating through the atomic medium under the resonant condition (simple atomic absorption). (**c**) Reduced absorption with generated EIT when the Gaussian coupling field $\boldsymbol{E}_{\mathrm{c}}$ turned on. (**d**) Simultaneous alternative gain and loss profiles on $\boldsymbol{E}_{\mathrm{s}}$ with both $\boldsymbol{E}_{\mathrm{c}}$ and pump field $\boldsymbol{E}_{\mathrm{p}}$ turned on

region with only EIT, where the intensity of the pump filed is nearly zero. By taking advantages of the atomic coherence, the ratio between the induced gain and loss can be easily manipulated by controlling the experimental parameters. Actually, the ratio $\gamma_{\mathrm{G}}/\gamma_{\mathrm{L}}$ can be in the range of 0 to 1.5 by adjusting the coupling detuning Δ_{c} over approximately 40 MHz.

With the periodical gain-loss region effectively generated, the dynamics behaviors of the system below and above the threshold are demonstrated by the relative phase difference ν between two neighboring gain and loss channels. The measuring method is the same as the one we adopted in Sect. 4. As a result, the relative phase difference can increase from 0.16π to π with the gain/loss ratio adjusted from 0.1 to 1, which advocates again that the relative phase difference ν, for the case below the phase-transition point, can increase (from the initial values 0) with the gain/loss ratio. When the ratio $\gamma_{\mathrm{G}}/\gamma_{\mathrm{L}}$ is increased to 1.2, the phase difference jumps to $\nu = \pi/2$. With the ratio further increased to $\gamma_{\mathrm{G}}/\gamma_{\mathrm{L}} = 1.5$, the measured phase difference can still be $\pi/2$. This also supports the previous conclusion that, for the

cases at and above the phase-transition point, the phase differences can constantly be $\pi/2$ even increasing the gain.

6 Summary and Outlook

In summary, we have experimentally demonstrated the PT-symmetric optical lattices with controllable gain/loss ratio by utilizing two different coherently-prepared multi-level atomic configurations. The required index modulation and the anti-symmetric gain/loss profiles are introduced by exploiting the modified absorption (or EIT) and induced active Raman gain, which is fully reconfigurable and all-optically controllable with various experimental parameters. The presence of a well-defined breaking-phase threshold was experimentally verified by observing the abrupt change of relative phase difference between the gain and loss channels.

The constructed PT-symmetric atomic lattices can be used to study a variety of effects related to PT symmetry and other non-Hermitian Hamiltonians, including anti-PT-symmetric lattice and PT-symmetric Talbot effect [32] as well as intriguing beam dynamical features [35] such as double refraction, power oscillation, and nonreciprocal diffraction patterns. Further, owning to the versatile nature of the coherently prepared multi-level atomic media in easily synthesizing desired linear dispersion/absorption, Raman gain, and nonlinearities, the demonstrated work can provide an ideal platform for exploiting novel effects in gain/loss modulated optical lattice systems, such as non-Hermitian nonlinear optics (PT-symmetric solitons, vortices, *etc*.) and condensed-matter physics effects (defect states, surface states, *etc*.), to bridge a connection between non-Hermitian physics and atomic physics.

Acknowledgements This work was supported in part by National Key R&D Program of China (2017YFA0303703), National Natural Science Foundation of China (61605154, 11474228), Natural Science Foundation of Shaanxi Province (2017JQ6039, 2017JZ019), China Postdoctoral Science Foundation (2016M600776, 2016M600777, and 2017T100734) and Postdoctoral Science Foundation of Shaanxi Province (2017BSHYDZZ54, 2017BSHTDZZ18).

References

1. Garanovich, I.L., Longhi, S., Sukhorukov, A.A., Kivshar, Y.S.: Light propagation and localization in modulated photonic lattices and waveguides. Phys. Rep. **518**, 1–79 (2012)
2. Christodoulides, D.N., Lederer, F., Silberberg, Y.: Discretizing light behaviour in linear and nonlinear waveguide lattices. Nature. **424**, 817–823 (2003)
3. Sheng, J., Wang, J., Miri, M.A., Christodoulides, D.N., Xiao, M.: Observation of discrete diffraction patterns in an optically induced lattice. Opt. Express. **23**, 19777–19782 (2015)
4. Fleischer, J.W., Carmon, T., Segev, M., Efremidis, N.K., Christodoulides, D.N.: Observation of discrete solitons in optically induced real time waveguide arrays. Phys. Rev. Lett. **90**, 023902 (2003)

5. Zhang, Y., Zhang, D., Zhang, Z., Li, C., Zhang, Y., Li, F., Belić, M.R., Xiao, M.: Optical Bloch oscillation and zener tunneling in an atomic system. Optica. **4**, 571–575 (2017)
6. Schindler, J., Li, A., Zheng, M.C., Ellis, F.M., Kottos, T.: Experimental study of active LRC circuits with PT symmetries. Phys. Rev. A. **84**, 040101R (2011)
7. Bender, N., Factor, S., Bodyfelt, J.D., Ramezani, H., Christodoulides, D.N., Ellis, F.M., Kottos, T.: Observation of asymmetric transport in structures with active nonlinearities. Phys. Rev. Lett. **110**, 234101 (2013)
8. Zhu, X., Ramezani, H., Shi, C., Zhu, J., Zhang, X.: PT-Symmetric acoustics. Phys. Rev. X. **4**, 031042 (2014)
9. Fleury, R., Sounas, D., Alù, A.: An invisible acoustic sensor based on parity-time symmetry. Nat. Commun. **6**, 5905 (2015)
10. Ruter, C.E., Makris, K.G., EI-Ganainy, R., Christodoulides, D.N., Segev, M., Kip, D.: Observation of parity-time symmetry in optics. Nat. Phys. **6**, 192–195 (2010)
11. Christodoulides, D.N., Miri, M.A.: PT symmetry in optics and photonics. Proc. SPIE. **9162**, 91621P (2014)
12. Guo, A., Salamo, G.J., Duchesne, D., Morandotti, R., Volatier-Ravat, M., Aimez, V., Siviloglou, G.A., Christodoulides, D.N.: Observation of PT-symmetry breaking in complex optical potentials. Phys. Rev. Lett. **103**, 093902 (2009)
13. Chong, Y.D., Ge, L., Cao, H., Stone, A.D.: Coherent perfect absorbers: time-reversed lasers. Phys. Rev. Lett. **105**, 053901 (2010)
14. Longhi, S., Feng, L.: PT-symmetric microring laser-absorber. Opt. Lett. **39**, 5026–5029 (2014)
15. Peng, B., Özdemir, S.K., Lei, F., Monifi, F., Gianfreda, M., Long, G.L., Fan, S., Nori, F., Bender, C.M., Yang, L.: Parity-time-symmetric whispering-gallery microcavities. Nat. Phys. **10**, 394–398 (2014)
16. Chang, L., Jiang, X., Hua, S., Yang, C., Wen, J., Jiang, L., Li, G., Wang, G., Xiao, M.: Parity-time symmetry and variable optical isolation in active-passive-coupled microresonators. Nat. Photon. **8**, 524–529 (2014)
17. Makris, K.G., El-Ganainy, R., Christodoulides, D.N., Musslimani, Z.H.: PT-symmetric optical lattices. Phys. Rev. A. **81**, 063807 (2010)
18. Dmitriev, S.V., Sukhorukov, A.A., Kivshar, Y.S.: Binary parity-time-symmetric nonlinear lattices with balanced gain and loss. Opt. Lett. **35**, 2976–2978 (2010)
19. Musslimani, Z.H., Makris, K.G., El-Ganainy, R., Christodoulides, D.N.: Optical solitons in PT periodic potentials. Phys. Rev. Lett. **100**, 030402 (2008)
20. He, Y., Zhu, X., Mihalache, D., Liu, J., Chen, Z.: Lattice solitons in PT-symmetric mixed linear-nonlinear optical lattices. Phys. Rev. A. **85**, 013831 (2012)
21. Wimmer, M., Regensburger, A., Miri, M.A., Bersch, C., Christodoulides, D.N., Peschel, U.: Observation of optical solitons in PT-symmetric lattices. Nat. Commun. **6**, 7782 (2015)
22. Abdullaev, F.K., Kartashov, Y.V., Konotop, V.V., Zezyulinm, D.A.: Solitons in PT-symmetric nonlinear lattices. Phys. Rev. A. **83**, 041805R (2011)
23. Longhi, S.: Bloch oscillations in complex crystals with PT symmetry. Phys. Rev. Lett. **103**, 123601 (2009)
24. Wimmer, M., Miri, M.A., Christodoulides, D.N., Peschel, U.: Observation of Bloch oscillations in complex PT-symmetric photonic lattices. Sci. Rep. **5**, 17760 (2015)
25. Yin, X.B., Zhang, X.: Unidirectional light propagation at exceptional points. Nat. Mater. **12**, 175–177 (2013)
26. Lin, Z., Ramezani, H., Eichelkraut, T., Kottos, T., Cao, H., Christodoulides, D.N.: Unidirectional invisibility induced by PT-symmetric periodic structures. Phys. Rev. Lett. **106**, 213901 (2011)
27. Feng, L., Xu, Y.L., Fegadolli, W.S., Lu, M.H., Oliveira, J.E.B., Almeida, V.R., Chen, Y.F., Scherer, A.: Experimental demonstration of a unidirectional reflectionless parity-time metamaterial at optical frequencies. Nat. Mater. **12**, 108–113 (2013)
28. Regensburger, A., Bersch, C., Miri, M.A., Onishchukov, G., Christodoulides, D.N., Peschel, U.: Parity-time synthetic photonic lattices. Nature. **488**, 167–171 (2012)

29. Eichelkraut, T., Heilmann, R., Weimann, S., Stützer, S., Dreisow, F., Christodoulides, D.N., Nolte, S., Szameit, A.: Mobility transition from ballistic to diffusive transport in non-Hermitian lattices. Nat. Commun. **4**, 2533 (2013)
30. Wu, J.H., Artoni, M., La Rocca, G.C.: Parity-time-antisymmetric atomic lattices without gain. Phys. Rev. A. **91**, 033811 (2015)
31. Miri, M.A., Regensburger, A., Peschel, U., Christodoulides, D.N.: Optical mesh lattices with PT symmetry. Phys. Rev. A. **86**, 023807 (2012)
32. Ramezani, H., Christodoulides, D.N., Kovanis, V., Vitebskiy, I., Kottos, T.: PT-symmetric Talbot effects. Phys. Rev. Lett. **109**, 033902 (2012)
33. Bendix, O., Fleischmann, R., Kottos, T., Shapiro, B.: Exponentially fragile PT symmetry in lattices with localized eigenmodes. Phys. Rev. Lett. **103**, 30402 (2009)
34. Regensburger, A., Miri, M.A., Bersch, C., Näger, J., Onishchukov, G., Christodoulides, D.N., Peschel, U.: Observation of defect states in PT-symmetric optical lattices. Phys. Rev. Lett. **110**, 223902 (2013)
35. Makris, K.G., El-Ganainy, R., Christodoulides, D.N., Musslimani, Z.H.: Beam dynamics in PT-symmetric optical lattices. Phys. Rev. Lett. **100**, 103904 (2008)
36. Zheng, M.C., Christodoulides, D.N., Fleischmann, R., Kottos, T.P.T.: Optical lattices and universality in beam dynamics. Phys . Rev. A. **82**, 010103R (2010)
37. Wu, J.H., Artoni, M., La Rocca, G.C.: Non-Hermitian degeneracies and unidirectional reflectionless atomic lattices. Phys. Rev. Lett. **113**, 123004 (2014)
38. Sheng, J.T., Miri, M.A., Christodoulides, D.N., Xiao, M.: PT-symmetric optical potentials in a coherent atomic medium. Phys. Rev. A. **88**, 041803R (2013)
39. Hang, C., Kartashov, Y.V., Huang, G., Konotop, V.V.: Localization of light in a parity-time-symmetric quasi-periodic lattice. Opt. Lett. **40**, 2758–2761 (2015)
40. Horsley, S.A.R., Artoni, M., La Rocca, G.C.: Spatial Kramers–Kronig relations and the reflection of waves. Nat. Photon. **9**, 436–439 (2015)
41. Scully, M.O.: Enhancement of the index of refraction via quantum coherence. Phys. Rev. Lett. **67**, 1855–1858 (1991)
42. Li, H.J., Dou, J.P., Huang, G.: PT symmetry via electromagnetically induced transparency. Opt. Express. **21**, 32053–32062 (2013)
43. Harris, S.E.: Electromagnetically induced transparency. Phys. Today. **50**, 36–42 (1997)
44. Gea-Banacloche, J., Li, Y.Q., Jin, S.Z., Xiao, M.: Electromagnetically induced transparency in ladder-type inhomogeneously broadened media: theory and experiment. Phys. Rev. A. **51**, 576–584 (1995)
45. Xiao, M., Li, Y., Jin, S., Gea-Banacloche, J.: Measurement of dispersive properties of electromagnetically induced transparency in rubidium atoms. Phys. Rev. Lett. **74**, 666–669 (1995)
46. Wu, J., Artoni, M., La Rocca, G.C.: Parity-time-antisymmetric atomic lattices without gain. Phys. Rev. A. **91**, 033811 (2015)
47. Hang, C., Zezyulin, D.A., Konotop, V.V., Huang, G.: Tunable nonlinear parity–time-symmetric defect modes with an atomic cell. Opt. Lett. **38**, 4033–4036 (2013)
48. Ramezani, H., Kottos, T., El-Ganainy, R., Christodoulides, D.N.: Unidirectional nonlinear PT-symmetric optical structures. Phys. Rev. A. **82**, 043803 (2010)
49. Childress, L., Walsworth, R., Lukin, M.: Atom-like crystal defects: from quantum computers to biological sensors. Phys. Today. **67**, 38–43 (2014)
50. Pei, L., Lu, X., Bai, J., Miao, X., Wang, R., Wu, L., Ren, S., Jiao, Z., Zhu, H., Fu, P., andZuo, Z.: Resonant stimulated Raman gain and loss spectroscopy in Rb atomic vapor. Phys. Rev. A. **87**, 063822 (2013)
51. Kang, H.S., Wen, L.L., Zhu, Y.F.: Normal or anomalous dispersion and gain in a resonant coherent medium. Phys. Rev. A. **68**, 063806 (2003)
52. Zhang, Z., Zhang, Y., Sheng, J., Yang, L., Miri, M.-A., Christodoulides, D.N., He, B., Zhang, Y., Xiao, M.: Observation of parity-time symmetry in optically induced atomic lattices. Phys. Rev. Lett. **117**, 123601 (2016)

53. Zhang, Z., Feng, J., Liu, X., Sheng, J., Zhang, Y., Zhang, Y., Xiao, M.: Controllable photonic crystal with periodic Raman gain in a coherent atomic medium. Opt. Lett. **4**, 919–922 (2018)
54. El-Ganainy, R., Makris, K.G., Christodoulides, D.N., Musslimani, Z.H.: Theory of coupled optical PT-symmetric structures. Opt. Lett. **32**, 2632–2634 (2007)
55. Sheng, J.T., Miri, M.A., Christodoulides, D.N., Xiao, M.: PT symmetry in coherent atomic media. CLEO: 2013 Technical Digest. QTu1E. **5**,
56. Ling, H.Y., Li, Y.Q., Xiao, M.: Electromagnetically induced grating: homogeneously broadened medium. Phys. Rev. A. **57**, 1338–1344 (1998)
57. Sheng, J., Wang, J., Miri, M.A., Christodoulides, D.N., Xiao, M.: Observation of discrete diffraction patterns in an optically induced lattice. Opt. Express. **23**, 19777–19782 (2015)
58. Zhang, Z.Y., Liu, X., Zhang, D., Sheng, J.T., Zhang, Y.Q., Zhang, Y.P., Xiao, M.: Observation of electromagnetically induced Talbot effect in an atomic system. Phys. Rev. A. **97**, 013603 (2018)
59. Marco, O., Alexander, S.: Quasi PT-symmetry in passive photonic lattices. J. Opt. **16**, 065501 (2014)
60. Lupu, A., Benisty, H., Degiron, A.: Switching using PT symmetry in plasmonic systems: positive role of the losses. Opt. Express. **21**, 21651–21668 (2013)
61. Zhang, Z., Yang, L., Feng, J., Sheng, J., Zhang, Y., Zhang, Y., Xiao, M.: Parity-Time-Symmetric Optical Lattice with Alternating Gain and Loss Atomic Configurations. Laser Photon. Rev. 12, 1800155 (2018)

Effects of Exceptional Points in PT-Symmetric Waveguides

Nimrod Moiseyev and Alexei A. Mailybaev

Abstract We start with a general theoretical introduction to $\mathscr{P}\mathscr{T}$-symmetric systems. Quantum systems with gain and loss can be modeled by non-Hermitian Hamiltonians, and $\mathscr{P}\mathscr{T}$-symmetry is a property that can be achieved, e.g. by a coupling with the laser field. The resulting $\mathscr{P}\mathscr{T}$-symmetric Hamiltonians possess a real spectrum (when the gain and loss are not too strong) and can be considered as a special case of pseudo-Hermitian Hamiltonians. The transition from a real to a complex spectrum occurs at the exceptional point (EP), where two eigenmodes coalesce both in eigenvalue and eigenvector. The $\mathscr{P}\mathscr{T}$-symmetric Hamiltonian can be realized experimentally in a system of two coupled waveguides with loss and gain. We describe in detail two physical effects related to the EPs in such a system. First, we show that light oscillations between two waveguides are suppressed by approaching the EP condition. Second, we prove that the group velocity of a light pulse decreases to zero as the system is tuned to be at the EP.

1 Introduction

Recently there has been an explosion of interest to $\mathscr{P}\mathscr{T}$-symmetric properties of non-Hermitian Hamiltonians, as first introduced by Bender and Boettcher [6]; see also [5, 14] and references therein. This symmetry is achieved when the parity transformation, $\mathscr{P}$, interchanges the system elements experiencing gain and loss, such that the system returns to its original form after the subsequent time reversal, $\mathscr{T}$. Under certain conditions $\mathscr{P}\mathscr{T}$-symmetric Hamiltonians can have a completely real

N. Moiseyev (✉)
Schulich Faculty of Chemistry and Faculty of Physics, Technion – Israel Institute of Technology, Haifa, Israel
e-mail: nimrod@technion.ac.il

A. A. Mailybaev
Instituto Nacional de Matemática Pura e Aplicada – IMPA, Rio de Janeiro, Brazil
e-mail: alexei@impa.br

D. Christodoulides, J. Yang (eds.), *Parity-time Symmetry and Its Applications*, Springer Tracts in Modern Physics 280,
https://doi.org/10.1007/978-981-13-1247-2_9

spectrum and, thus, can serve, under the appropriate inner product, as Hamiltonians of unitary quantum systems [28]. We should stress that although we focus on $\mathscr{P}\mathscr{T}$-symmetric systems, $\mathscr{P}\mathscr{T}$ symmetry is neither a necessary nor a sufficient condition for a non-Hermitian Hamiltonian to have a real spectrum [27, 28].

Why are the $\mathscr{P}\mathscr{T}$ properties of non-Hermitian Hamiltonians relevant to realistic physical systems? The realization of $\mathscr{P}\mathscr{T}$-symmetric "Hamiltonians" has been studied most recently for optical waveguides with complex refractive indices [13, 21, 22, 30]. The equivalence of the Maxwell and Schrödinger equations in certain regimes provides a physical system in which the properties of $\mathscr{P}\mathscr{T}$-symmetric operators can be studied and exemplified. In this chapter we will focus on the special effects of exceptional points (EPs) on the dynamical properties of $\mathscr{P}\mathscr{T}$-symmetric waveguides with complex index of refraction. The EP is a special type of a non-Hermitian degeneracy between two (or more) eigenstates formed by the coalescence of both eigenvalues and eigenvectors.

Quantum mechanics deals with matter waves and the effects of EPs in atomic and molecular systems have not been observed until now in experiments. Consider two atomic or molecular resonances, which are coupled by a CW-laser field (i.e., AC-electromagnetic field) to have the structure of the non-Hermitian Hamiltonian

$$\hat{H}_{NH} = \begin{pmatrix} E_1^{res} + \hbar\omega_L & d \\ d & E_2^{res} \end{pmatrix}, \tag{1}$$

where E_1^{res} and E_2^{res} are two complex autoionization or predissociation decay resonances; ω_L is fundamental frequency of the laser field; the off-diagonal elements d are proportional to the maximum amplitude of the laser field and describe the dipole transitions between the two metastable states. The imaginary parts of the complex eigenvalues E_1^{res} and E_2^{res} determine the decay rates, which are inversely proportional to the lifetimes of the corresponding metastable states [25]. In a special case, when the laser frequency is at the exact resonance

$$\hbar\omega_L = \mathrm{Re}\left(E_2^{res} - E_1^{res}\right), \tag{2}$$

a simple rewrite of the Hamiltonian (1) brings it to the form

$$\hat{H}_{NH} = \hat{H}_{\mathscr{P}\mathscr{T}} - i\frac{\Gamma_0}{2}\hat{I}, \tag{3}$$

where $\hat{I}$ is a identity operator and

$$\hat{H}_{\mathscr{P}\mathscr{T}} = \begin{pmatrix} E_0 + i\Gamma/2 & d \\ d & E_0 - i\Gamma/2 \end{pmatrix} \tag{4}$$

with $E_0 = \mathrm{Re}\, E_2^{res}$, $\Gamma = \mathrm{Im}\left(E_1^{res} - E_2^{res}\right)$ and $\Gamma_0 = -\mathrm{Im}\left(E_1^{res} + E_2^{res}\right)$. Here Γ_0 features the mean decay rate of both states. Due to Eq. (2), the diagonal elements

of $\hat{H}_{\mathscr{P}\mathscr{T}}$ have equal real parts and opposite imaginary parts. In this case the contribution $\hat{H}_{\mathscr{P}\mathscr{T}}$ to the full non-Hermitian Hamiltonian (3) is $\mathscr{P}\mathscr{T}$-symmetric; see Sect. 2 below. This observation provides a constructive way to design the $\mathscr{P}\mathscr{T}$ symmetry and EPs in realistic quantum systems.

In Sect. 2, we discuss basic features of $\mathscr{P}\mathscr{T}$-symmetric and pseudo-Hermitian Hamiltonians. These Hamiltonians possess real spectrum for the interval of parameters bounded by the EPs described in Sect. 3. Section 4 studies light propagation in a $\mathscr{P}\mathscr{T}$-symmetric system of coupled waveguides. Section 5 investigates the propagation of light pulses in the same system showing that light stops (the group velocity vanishes) exactly at the EP.

2 $\mathscr{P}\mathscr{T}$ Symmetry and Pseudo-Hermitian Hamiltonians

A quantum system is described by a Hermitian Hamiltonian $\hat{H}_0$. In the absence of magnetic field, this Hamiltonian is real and symmetric. Evolution of open quantum systems, when particles can be injected into or removed from the system, can be modeled by introducing a non-Hermitian part into the Hamiltonian, which describes the respective gain and loss. This non-Hermitian Hamiltonian part is given by $i\hat{V}$, where $\hat{V}$ is a real symmetric operator and i is the imaginary unit. In general, the resulting non-Hermitian Hamiltonian $\hat{H} = \hat{H}_0 + i\hat{V}$ has complex eigenvalues, $E = E_0 - i\Gamma/2$, where the real part is the energy and the imaginary part describes the rate of decay ($\Gamma > 0$) or growth ($\Gamma < 0$) of the respective metastable quantum state.

The spectrum of a non-Hermitian Hamiltonian may become real in a robust way when the system possesses an extra symmetry that accurately balances the gain and loss [6, 7, 21]. This can be understood using the example of a two-level system, where the first state $|1\rangle$ has energy E_0 and experiences gain, while the second state $|2\rangle$ has the same energy E_0 but decays; the gain and loss having exactly the same rates. The corresponding Hamiltonian, analogous to (4), can be written as

$$\hat{H} = \begin{pmatrix} E_0 + i\Gamma/2 & d \\ d & E_0 - i\Gamma/2 \end{pmatrix}, \tag{5}$$

where the real parameter d denotes coupling between the two states. Such Hamiltonians are called $\mathscr{P}\mathscr{T}$-symmetric, because they remain invariant under the combined action of parity interchanging the two states, $|1\rangle \leftrightarrow |2\rangle$, and of time reversal interchanging the gain with loss, $\Gamma \leftrightarrow -\Gamma$.

Computing eigenvalues and eigenvectors of the matrix (5), we obtain

$$E_\pm = E_0 \pm \sqrt{d^2 - \Gamma^2/4}, \qquad |\psi_\pm\rangle = \begin{pmatrix} 1 \\ \pm\sqrt{1 - (\Gamma/2d)^2} - i\Gamma/2d \end{pmatrix}. \tag{6}$$

We see that both eigenvalues are real if the intensity of gain and loss is not large, namely, $|\Gamma| < 2d$. In this case $| \pm \sqrt{1-(\Gamma/2d)^2} - i\Gamma/2d| = 1$ and, hence, the eigenvector is equally distributed between the gain $|1\rangle$ and loss $|2\rangle$ states. As a result, the loss balances gain and the mode amplitude stays constant. Otherwise, if $|\Gamma| > 2d$, both eigenvalues in (6) are complex: One of the eigenmodes decays and the other grows with time, because the eigenvectors are not distributed equally between the gain and loss states. At $|\Gamma| = 2d$, a non-Hermitian degeneracy is obtained, the so-called exceptional point, which will be described in the next section in more detail.

The fact that $\mathscr{P}\mathscr{T}$-symmetric Hamiltonians have a real spectrum follows from a more general concept of pseudo-Hermitian Hamiltonians [27]. The Hamiltonian $\hat{H}$ is called pseudo-Hermitian if there is an invertible Hermitian operator $\hat{\eta}$ such that

$$\hat{H}^\dagger \hat{\eta} = \hat{\eta}\hat{H}. \tag{7}$$

Such Hamiltonians are in general non-Hermitian, but they conserve the quantity

$$\langle \hat{\eta} \rangle = \langle \Psi(t)|\hat{\eta}|\Psi(t)\rangle, \tag{8}$$

where $\Psi(t)$ satisfies the Schrödinger equation $i\dot{\Psi} = \hat{H}\Psi$. This conservation property follows from (7) after differentiating $\langle \hat{\eta} \rangle$ with respect to time.

It is not difficult to see that the property of having a real spectrum is robust under small perturbations, as long as the Hamiltonian satisfies condition (7) and all its eigenvalues are non-degenerate. Indeed, let E be a non-degenerate real eigenvalue with the right eigenvector $|\psi_R\rangle$ and left eigenvector $\langle \psi_L|$:

$$\hat{H}|\psi_R\rangle = E|\psi_R\rangle, \qquad \langle \psi_L|\hat{H} = E\langle \psi_L|. \tag{9}$$

Note that, for non-Hermitian Hamiltonians, right and left eigenvectors are generally different, $|\psi_R\rangle \neq |\psi_L\rangle$; here we use the Dirac bra-ket notation and the definition of bra-states includes the conjugation $|\psi_L\rangle = \langle \psi_L|^\dagger$. In the case of a non-degenerate eigenvalue, the scalar product of left-right eigenvectors is nonzero, $\langle \psi_L|\psi_R\rangle \neq 0$, see e.g. [25, 33]. Using the properties $\hat{\eta}^\dagger = \hat{\eta}$, relation (7) written as $\hat{\eta}^{-1}\hat{H}^\dagger = \hat{H}\hat{\eta}^{-1}$ and the second equation in (9), we derive:

$$\hat{H}\hat{\eta}^{-1}|\psi_L\rangle = \left(\langle \psi_L|\hat{\eta}^{-1}\hat{H}^\dagger\right)^\dagger . = \left(\langle \psi_L|\hat{H}\hat{\eta}^{-1}\right)^\dagger = \left(E\langle \psi_L|\hat{\eta}^{-1}\right)^\dagger = E^*\hat{\eta}^{-1}|\psi_L\rangle. \tag{10}$$

We just have shown that, for any eigenvalue E, the complex conjugate E^* is the eigenvalue with the right eigenvector

$$|\psi_R'\rangle = \hat{\eta}^{-1}|\psi_L\rangle. \tag{11}$$

For a non-degenerate real eigenvalue, we have $E = E^*$, which implies the relation between the right and left eigenvectors as $|\psi_R\rangle \propto \hat{\eta}^{-1}|\psi_L\rangle$ (equality up to a

complex factor). Now we can see that a non-degenerate real eigenvalue cannot become complex under a small perturbation of the Hamiltonian, because otherwise a real eigenvalue E would split into a complex conjugate pair E and E^*; this is clearly in the contradiction to the assumption that E is non-degenerate. We see that the spectrum of the pseudo-Hermitian Hamiltonian remains real with a change of parameters until the point with a spectral degeneracy. As we will see in the next section, a typical degeneracy appearing in this case is the EP.

Let us define the parity operator as

$$\hat{P} = \begin{pmatrix} 0 & 1 \\ 1 & 0 \end{pmatrix}, \tag{12}$$

which interchanges the states $|1\rangle$ and $|2\rangle$ and, thus, its square $\hat{P}^2 = \hat{I}$ is the identity matrix. For the 2×2 matrix (5), condition (7) holds for $\hat{\eta} = \hat{P}$ as one can easily verify. In this case the conserved quantity (8) becomes $\langle\hat{\eta}\rangle = \varphi_1^*\varphi_2 + \varphi_2^*\varphi_1$, where $|\Psi(t)\rangle = \varphi_1(t)|1\rangle + \varphi_2(t)|2\rangle$. Note that $\langle\hat{\eta}\rangle$ is not positive definite, thus, its conservation does not necessarily imply that the solution is bounded. In fact, exponential growing or decaying solutions appear when $\Gamma > 2d$. Since the Hamiltonian (5) is complex and symmetric, Eqs. (9) for the right and left eigenvectors are transposed to each other and, hence, the eigenvectors are complex conjugate, $|\psi_L\rangle = |\psi_R^*\rangle$. From relation (11) we see that the eigenvector $|\psi_R'\rangle = \hat{P}|\psi_L\rangle = \hat{P}|\psi_R^*\rangle$ with the eigenvalue E^* describe the mode that is $\mathscr{P}\mathscr{T}$-symmetric to $|\psi_R\rangle$ and E.

For a complex symmetric Hamiltonian, let us introduce the c-product of two vectors ψ_1 and ψ_2 denoted by $(\psi_1|\psi_2)$ as [25, Ch. 6 and 9]

$$(\psi_1|\psi_2) = \langle\psi_1^*|\psi_2\rangle. \tag{13}$$

Here the complex conjugation in the first vector implies that $\langle\psi_1^*| = |\psi_1^*\rangle^\dagger = |\psi_1\rangle^T$ is only transposed, instead of Hermitian transposed. It is convenient to normalize the eigenvector of a non-degenerate eigenmode with this c-product as $(\psi_R|\psi_R) = 1$, which yields the eigenvector $|\psi_R\rangle$ defined up to a sign; note that this normalization is not possible for a degenerate eigenvalue, see Sect. 3. From the results of the previous paragraph it follows that the mode with a non-degenerate real eigenvalue $E = E^*$ is $\mathscr{P}\mathscr{T}$-symmetric, with the eigenvector satisfying the relation $|\psi_R\rangle = \pm\hat{P}|\psi_R^*\rangle$, where the sign distinguishes symmetric and anti-symmetric modes. In such a case (when the spectrum of the Hamiltonian is real), $\mathscr{P}\mathscr{T}$-symmetry is called exact. When eigenvalues of the Hamiltonian are complex, $\mathscr{P}\mathscr{T}$-symmetry is broken: each eigenmode with complex E is $\mathscr{P}\mathscr{T}$-symmetric to the complex conjugate mode with E^*.

Expression (5) provides a subset of all pseudo-Hermitian Hamiltonians for the choice $\hat{\eta} = \hat{P}$. This is, of course, not the only type of Hamiltonians that possess a real spectrum. For example, the Hamiltonian

$$\hat{H}' = \begin{pmatrix} -E_0 & id \\ id & E_0 \end{pmatrix}, \qquad d, E_0 \in \mathbb{R}, \tag{14}$$

is pseudo-Hermitian with $\hat{\eta} = \hat{P}'$, where

$$\hat{P}' = \begin{pmatrix} 1 & 0 \\ 0 & -1 \end{pmatrix}, \qquad (\hat{P}')^2 = \hat{I}. \tag{15}$$

This Hamiltonian is $\mathscr{P}\mathscr{T}$-symmetric with respect to the parity defined by $\hat{P}'$ (changing sign of the second state $|2\rangle$) and the time reversal interchanging the gain and loss, $ig \mapsto -ig$. At the same time, this Hamiltonian is anti-$\mathscr{P}\mathscr{T}$-symmetric with the parity operator (12) interchanging the states $|1\rangle$ and $|2\rangle$. We refer to [15, 29, 42] for physical applications of anti-$\mathscr{P}\mathscr{T}$-symmetric systems.

Furthermore, the relation between $\mathscr{P}\mathscr{T}$-symmetric and pseudo-Hermitian Hamiltonians extends in exactly the same form to multiple-state systems. The respective Hamiltonians are defined as $\hat{H} = \hat{H}_0 + i\hat{V}$ with the real symmetric matrices (or operators) $\hat{H}_0$ and $\hat{V}$, where $\hat{H}_0$ describes the Hermitian system and $\hat{V}$ provides the contribution due to gain and loss. The $\mathscr{P}\mathscr{T}$-symmetry imposes the additional conditions that $\hat{H}_0$ is symmetric and $\hat{V}$ is anti-symmetric under the parity transformation $\hat{P}$, i.e.,

$$\hat{P}\hat{H}_0 = \hat{H}_0\hat{P}, \qquad \hat{P}\hat{V} = -\hat{V}\hat{P}. \tag{16}$$

Such $\mathscr{P}\mathscr{T}$-symmetric Hamiltonians are also pseudo-Hermitian with $\hat{\eta} = \hat{P}$, since condition (7) with the complex symmetric operator $\hat{H} = \hat{H}_0 + i\hat{V}$ and real operator $\hat{P}$ reduces to the (anti-)commutation relations (16).

We stress again that $\mathscr{P}\mathscr{T}$-symmetry is only one of many ways to impose a real spectrum in a structurally stable way. For example, consider $\hat{H} = \hat{H}_0 + i\hat{V}$ with real symmetric operators $\hat{H}_0$ and $\hat{V}$. If $\hat{H}_0$ is invertible, one can take $\hat{\eta} = \hat{H}_0$. Then, condition (7) for the operator $\hat{H}$ to be pseudo-Hermitian reduces to the anticommutation relation $\hat{H}_0\hat{V} + \hat{V}\hat{H}_0 = 0$.

3 Exceptional Point at the Transition from a Real to a Complex Spectrum

Let us analyze the transition from a real to a complex spectrum for a simple $\mathscr{P}\mathscr{T}$-symmetric Hamiltonian (5). Its eigenvalues and eigenvectors are found explicitly in Eq. (6). Let us denote $\Gamma_{EP} = 2d$. For $\Gamma < \Gamma_{EP}$ the spectrum is real, while for $\Gamma > \Gamma_{EP}$ the spectrum is complex. At the transition point $\Gamma = \Gamma_{EP}$, the two eigenvalues and two eigenvectors coalesce at $E_+ = E_- = E_{EP}$ and $|\psi_+\rangle = |\psi_-\rangle = |\psi_{EP}\rangle$, where

$$E_{EP} = E_0, \qquad |\psi_{EP}\rangle = \begin{pmatrix} 1 \\ -i \end{pmatrix}. \tag{17}$$

The point with such properties (full coalescence of two eigenmodes both in their eigenvalues and eigenvectors) is called the *exceptional point* (EP). At the EP, the spectrum is incomplete in the sense that the eigenvectors do not constitute a full basis for the wave function. It is easy to see that the unique eigenvector at the EP is self-orthogonal with respect to the c-product (13):

$$(\psi_{EP}|\psi_{EP}) = 0. \tag{18}$$

In the language of linear algebra, the EP implies that the canonical Jordal form of the Hamiltonian contains a Jordan block [33]. The well-known property of the Jordan block is that its right and left eigenvectors (9) are orthogonal. For a symmetric Hamiltonian $\hat{H}$, this property is equivalent to the c-product self-orthogonality condition (13) because, at the EP, one has $|\psi_R\rangle = |\psi_{EP}\rangle$ and $\langle\psi_L| = |\psi_{EP}\rangle^T$.

The EP plays important role for the representation of spectrum in the form of Taylor series. Let us rewrite the Hamiltonian (5) in the form

$$\hat{H}(\lambda) = \hat{H}_0 + i\lambda\hat{V}, \tag{19}$$

where $\hat{H}_0 = E_0\hat{I} + d\hat{\sigma}_x$ and $\hat{V} = \hat{\sigma}_z$ with the Pauli matrices $\hat{\sigma}_x$ and $\hat{\sigma}_z$. The factor $\lambda = \Gamma/2$ describing the gain and loss will be considered as a perturbation parameter, with $\lambda = 0$ corresponding to the Hermitian Hamiltonian $\hat{H}(0) = \hat{H}_0$. Eigenvalues (6) of the Hamiltonian (19) can be written as

$$E_{\pm}(\lambda) = E_{EP} \pm \sqrt{\lambda_{EP}^2 - \lambda^2}, \qquad \lambda_{EP} = \Gamma_{EP}/2 = d. \tag{20}$$

They are analytic functions of λ with the branch point singularities at $\lambda = \pm\lambda_{EP}$. These functions can be expanded in the Taylor series

$$E_j(\lambda) = \sum_{n=0}^{\infty} C_j^{(n)}\lambda^n, \tag{21}$$

where $j = \pm$. The branch point λ_{EP} defines the radius of a circle in the complex parameter plane, $|\lambda| < \lambda_{EP}$, where the Taylor series (21) converges.

In the neighborhood of the EP, dependence of the eigenvalues on a parameter λ is shown in Fig. 1. According to expressions (20), the leading term of this dependence near λ_{EP} can be written as

$$E_{\pm}(\lambda) \approx E_{EP} \pm a\sqrt{\lambda - \lambda_{EP}}, \tag{22}$$

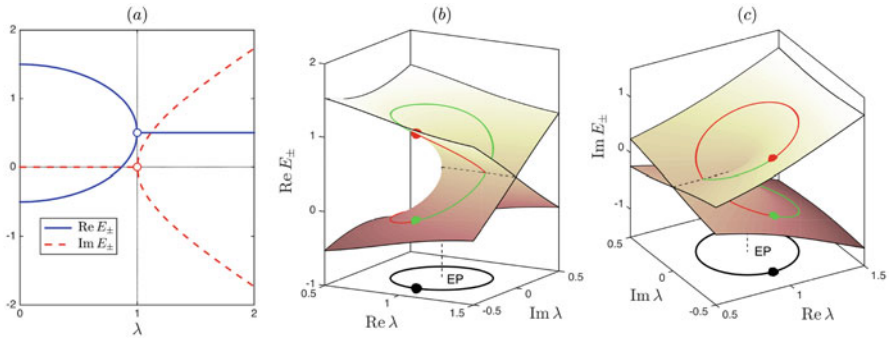

Fig. 1 (**a**) Real and imaginary parts of eigenvalues $E_\pm$ from (20) as functions of the real parameter λ; the numerical values are taken as $E_{EP} = 1/2$ and $\lambda_{EP} = 1$. Same graphs but as functions of the complex parameter λ are shown for (**b**) $\mathrm{Re}\, E_\pm$ with the intersection corresponding to $\mathrm{Re}\,\lambda > \lambda_{EP}$, $\mathrm{Im}\,\lambda = 0$ and (**c**) $\mathrm{Im}\, E_\pm$ with the intersection corresponding to $\mathrm{Re}\,\lambda < \lambda_{EP}$, $\mathrm{Im}\,\lambda = 0$. In horizontal projection, the black line describes the change of λ along a cycle around the EP. The corresponding change of two eigenvalues leading to the switch between two states is shown by the red and green curves. In one cycle of λ, the state E_- (green ball) is transported to the state E_+ (red ball), and vice versa

with the purely imaginary prefactor $a = i\sqrt{2\lambda_{EP}}$. Thus, the eigenvalues as functions of the real parameter λ have the square root singularity for both real and imaginary parts at λ_{EP}, see Fig. 1a. When extended to the complex values of λ, the local dependence is described by the two-sheet Riemann surface (branch point singularity) as shown in Fig. 1b, c.

One of the implications of the branch point singularity in Eq. (22) is that the two eigenmodes are interchanged when λ is changed continuously in the complex plane around the EP, see Fig. 1b, c. After the second cycle around the EP, the eigenvalues and eigenvectors return to their original values. This effect is known as the switch of eigenmodes for the parametric encircling of the EP, and it was observed experimentally in a microwave system [11]. In this experiment, the switch characterizes the eigenstates at different time-independent values of λ rather than the evolution of a wavefunction with λ changing in time. In fact, this switch mechanism does not work if the parameter λ is changed in time, i.e. for the dynamic encircling of the EP, because one of the transitions is always broken due to non-adiabatic effects. Although the adiabatic theorem does not hold, the topological property of the EP is manifested. When encircling the EP, the transitions acquire a chiral property: the final state depends on the direction in which the EP is encircled. We refer to [16, 17, 37] for the theory and physical applications, and to [12, 43] for the experimental observations of this effect. We stress that the system is not $\mathscr{PT}$-symmetric for complex values of λ. In general, a second-order degeneracy requires two real parameters in order to satisfy the single complex constraint, $E_1 = E_2$, at the EP. However, in $\mathscr{PT}$-symmetric systems, the EP can be found conveniently by tuning a single parameter, due to the reality of the spectrum below the symmetry-breaking point.

The described local properties of the EP extend similarly to systems with more than two states, when the $\mathscr{P}\mathscr{T}$-symmetric Hamiltonian has the form (19) with real symmetric operators $\hat{H}_0$ and $\hat{V}$ satisfying the (anti-)symmetry relations (16). In this case a large variety of spectral singularities may appear, including EPs (branch points) of higher order and eigenvalue crossings with distinct eigenvectors (so-called diabolic points); see e.g. [8, 25, 34]. For the higher-order EP, expansions for eigenvalues and eigenvectors of non-Hermitian Hamiltonians contain fractional powers like $(\lambda - \lambda_{EP})^{1/p}$ (the so-called Puiseux series), where p is the number of eigenvalues and eigenvectors that coalesce at the EP [25, Sections 7.7 and 9.1.1]; see also [24, 33] for the general perturbation theory and numerical methods. It should be stressed, however, that singularities in the spectrum of the generic (typical) $\mathscr{P}\mathscr{T}$-symmetric Hamiltonian with a single real parameter λ appear at discrete values, $\lambda = \lambda_j^{EP}$ $(j = 1, 2, \ldots)$, and have the form of the EPs with only two coalescent eigenvalues and eigenvectors [2]. In this case, the local behavior of eigenvalues and eigenvectors near the EP is equivalent (and in fact can be reduced) to the case of 2×2 Hamiltonian studied above. Note that such EPs must exist whenever the matrices $\hat{H}_0$ and $\hat{V}$ do not commute [26].

Finally, let us describe some properties of the Taylor expansions (21) for the eigenvalue E_j $(j = 1, \ldots, n)$ in the general case of $\mathscr{P}\mathscr{T}$-symmetric Hamiltonian operator (19). This expansion can be written as

$$E_j(\lambda) = \sum_{n=0}^{\infty} c_j^{(n)} \Lambda^n, \qquad c_j^{(n)} = (-i)^n C_j^{(n)}, \tag{23}$$

where $\Lambda = i\lambda$, $\hat{H} = \hat{H}_0 + \Lambda\hat{V}$, and we redefined the coefficients of (21) to include powers of the imaginary unit. Let us show that in $\mathscr{P}\mathscr{T}$-symmetric systems, all the odd coefficients vanish and all the even coefficients are real; therefore, the spectrum is real as long as the series converges. Since $\hat{H}_0$ and $\hat{V}$ are real symmetric matrices, one can use the Hermitian perturbation theory for real Λ, which is extended analytically to $\mathscr{P}\mathscr{T}$-symmetric Hamiltonians for purely imaginary Λ. From this argument, we immediately conclude that all the perturbational coefficients $c_j^{(n)}$ are real. Furthermore, from the Wigner $(2n + 1)$-rule [40] we express the odd-order coefficients as

$$c_j^{(2n+1)} = \langle \psi_j^{(n)} | \hat{V} | \psi_j^{(n)} \rangle, \tag{24}$$

where the real vector $|\psi_j^{(n)}\rangle$ is the nth-order correction in the expansion for the eigenvector

$$|\psi_j\rangle = \sum_{n=0}^{\infty} \Lambda^n |\psi_j^{(n)}\rangle. \tag{25}$$

Applying the parity operator to the equality $E|\psi_j\rangle = (\hat{H}_0 + \Lambda\hat{V})|\psi_j\rangle$, we obtain

$$E\,\hat{P}|\psi_j\rangle = \hat{P}(\hat{H}_0 + \Lambda\hat{V})|\psi_j\rangle = (\hat{H}_0 - \Lambda\hat{V})\hat{P}|\psi_j\rangle, \tag{26}$$

where we used the (anti-)symmetry assumptions (16). We see that $\hat{P}|\psi_j\rangle$ is the eigenvector corresponding to the parameter value $-\Lambda$. This means that the coefficients in the expansion (25) for Λ and $-\Lambda$ should match such that

$$P|\psi_j^{(n)}\rangle = \pm(-1)^n|\psi_j^{(n)}\rangle, \tag{27}$$

where the first sign depends whether the unperturbed real state $|\psi_j^{(0)}\rangle$ (at $\Lambda = 0$) is $\mathscr{P}$-symmetric or anti-symmetric (even or odd). Using the relations $\hat{P}^2 = \hat{I}$, (16) and (27) in (24), we obtain

$$c_j^{(2n+1)} = \langle\psi_j^{(n)}|\hat{V}|\psi_j^{(n)}\rangle = \langle\psi_j^{(n)}|\hat{P}^2\hat{V}\hat{P}^2|\psi_j^{(n)}\rangle = -c_j^{(2n+1)}, \tag{28}$$

i.e., all odd-order coefficients $c_j^{(2n+1)}$ vanish. With this property, we showed explicitly that the spectrum of the $\mathscr{P}\mathscr{T}$-symmetric Hamiltonian $\hat{H}$ is real as long as the series (23) is convergent, i.e.

$$|\lambda| < \min_j |\lambda_j^{EP}| \tag{29}$$

for the minimum among all EPs.

4 $\mathscr{P}\mathscr{T}$−Symmetric System of Coupled Waveguides Near the EP

We will show in this section that a system of two coupled waveguides (WGs) can be made $\mathscr{P}\mathscr{T}$-symmetric if the gain in one WG is accurately balanced by the loss in the second WG. In this setup, the EP appears for a specific value of the gain-loss parameter. In our description we follow the theoretical work of one of us together with Shachar Klaiman and Uwe Günter [21]. The effects we describe were first observed in the experiments conducted in the Laboratory of Detlef Kip together with Mordechai Segev and members of the group of Demetrios N. Christodoulides [31].

A $\mathscr{P}\mathscr{T}$-symmetric optical system can be easily realized with a symmetric index guiding profile and an antisymmetric gain and loss profile, i.e., $n(x) = n^*(-x)$ [13]. We consider two coupled planar WGs depicted in Fig. 2 for which the refractive index varies only in the x-direction. The direction of propagation in the WGs is taken to be the z-axis. The wave equation for the transverse-electric (TE) modes (derived from the full Maxwell equations) reads [20]:

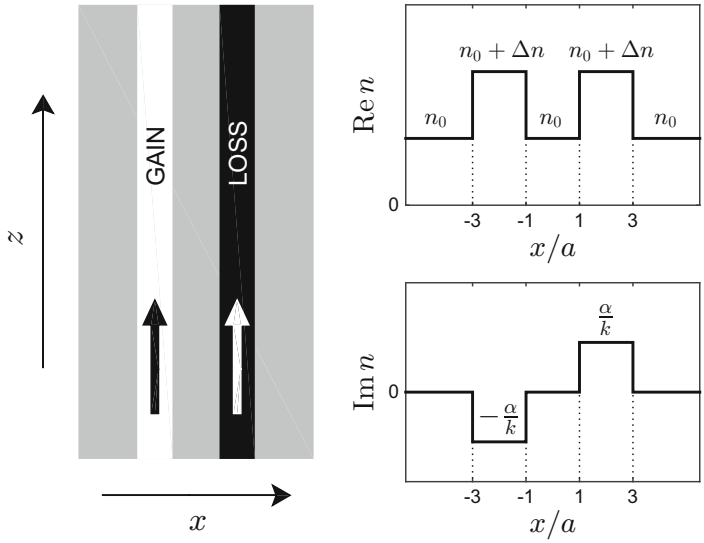

Fig. 2 Coupling between the gain guided mode and the loss guided mode provides a $\mathscr{PT}$-symmetric system with the refractive index profile such that $n(x) = n^*(-x)$. A control parameter α defines the gain and loss strength in the WGs as $\mathrm{Im}\, n = \pm\alpha/k$. The refractive index only varies in the x direction

$$\frac{\partial^2\psi}{\partial x^2} + \left(\frac{n(x)^2\omega^2}{c^2} - \beta^2\right)\psi = 0, \tag{30}$$

where the y-component of the electric field is given by

$$E_y(x, z, t) = \psi(x)e^{i(\omega t - \beta z)}. \tag{31}$$

Here β is the propagation constant and ω is the frequency. The vacuum wavelength is equal to $2\pi/k$ with $k = \omega/c$. Clearly, the wave equation (30) for the y-component of the electric field is analogous to the one-dimensional Schrödinger equation:

$$\left(-\frac{1}{2}\frac{\partial^2}{\partial x^2} + V(x)\right)\psi(x) = E\psi(x), \tag{32}$$

identifying $V(x) = -k^2n^2(x)/2$ as the potential, $E = -\beta^2/2$ as the energy, and $\psi(x)$ as the wave function.

As shown in Fig. 2, we couple between one gain-guiding WG (negative imaginary part of the refractive index) and one loss-guiding WG (positive imaginary part of the refractive index) in order to create the $\mathscr{PT}$-symmetric structure [35]. For simplicity we take the separation between the two coupled WGs to be the same as the their width, i.e., $2a$. Note that in our case the imaginary part of refractive

index (the complex part of potential) vanishes as $x \to \pm\infty$. For propagating modes (bound states), we impose the boundary conditions $\psi(x) \to 0$ as $x \to \pm\infty$.

For the numerical illustration, we choose the following parameters for the WG structure shown in Fig. 2. The background index is taken to be $n_0 = 3.3$, the vacuum wavelength $2\pi/k = 1.55\,\mu\text{m}$, the real index difference between the WGs and the background material $\Delta n = 10^{-3}$, and the separation between the WGs, which equals the WGs width, $2a = 5\mu\text{m}$. The imaginary part of the refractive index in the WGs is chosen as $\text{Im}\, n = \pm\alpha/k$, where α is a parameter. The parameters are chosen such that each WG contains only a single guided mode before we couple them. The coupled guided modes are calculated by diagonalizing the matrix representation of Eq. (30) in a sine basis. The resulting "Hamiltonian" matrix is non-Hermitian and one needs to take care when normalizing the eigenvectors. We choose to normalize our eigenvectors according to the c-product (13), i.e., $(\psi_n|\psi_m) = \langle\psi_n^*|\psi_m\rangle = \delta_{n,m}$.

The coupled waveguides support two guided modes. The propagation constants of the two modes are plotted in Fig. 3 as functions of the gain-loss parameter α. Increasing α causes the propagation constants of the two modes to move towards each other and coalesce at $\alpha_{EP} \approx 8.4\,\text{cm}^{-1}$. As long as $\mathscr{P}\mathscr{T}$ symmetry remains exact, i.e. $\alpha < \alpha_{EP}$, the power of each guided mode is distributed equally between the two WGs. The critical value α_{EP} is the EP, where the two modes coalesce: both the propagation constants and the corresponding electric fields become equal. Therefore, one can study the EP in a $\mathscr{P}\mathscr{T}$-symmetric WG system by varying only a single gain-loss parameter α. Past the critical value, $\alpha > \alpha_{EP}$, the propagation

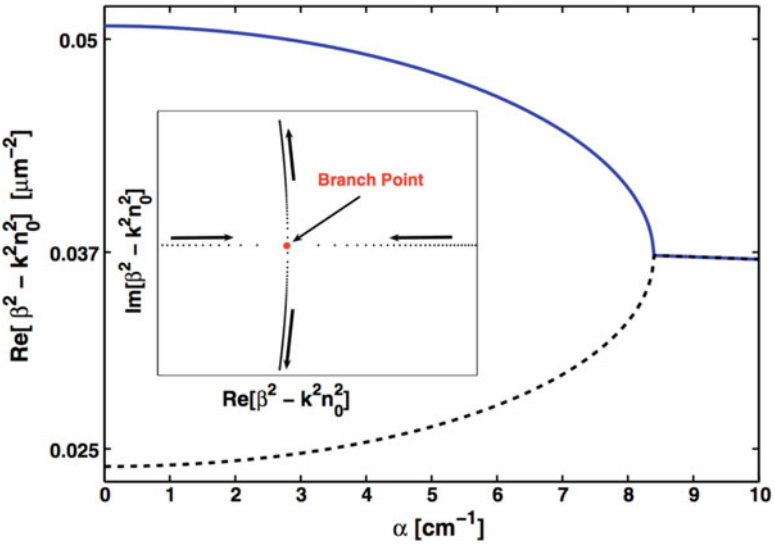

Fig. 3 Two trapped modes of the WGs of Fig. 2 as functions of the gain-loss parameter α. The eigenmodes approach each other on the real axis as α increases until a critical value of $\alpha_{EP} \approx 8.4\,\text{cm}^{-1}$. The critical value is the EP (branch point), where the two modes coalesce. Beyond the EP, the directional coupler sustains one gain guiding mode and one loss guiding mode

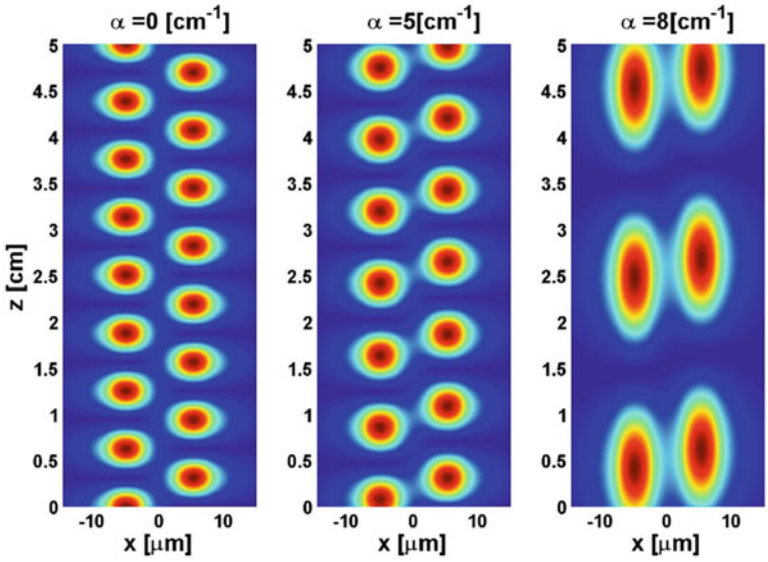

Fig. 4 The power distribution for a propagating sum field consisting of the two guided modes, see Eq. (33) for three values of α. As can be readily observed, the beat length (analogous to the beat time period in quantum mechanics) increases as the value of α approaches the critical value $\alpha_{EP} \approx 8.4\,\mathrm{cm}^{-1}$

constants become complex conjugate to each other. Then the WGs support one gain-guiding mode and one loss-guiding mode. The corresponding transverse field no longer retains the symmetry properties of the $\mathscr{P}\mathscr{T}$ operator, but rather each of the two modes becomes localized in one of the waveguides.

The advance of two real propagation constants towards the EP can be visualized by observing the beat length of the sum field for two equally populated modes:

$$E_y(x,z,t) = \frac{1}{\sqrt{2}}\left(\psi_1(x)e^{-i\beta_1 z} + \psi_2(x)e^{-i\beta_2 z}\right)e^{i\omega t}. \tag{33}$$

Figures 4 and 5 display the power distribution $|E_y(x,z,t)|^2$ for three values of α. One can see that the beat length, which is equal to $L = 2\pi/|\beta_2 - \beta_1|$, increases as α approaches the EP. At the EP, the sum field no longer oscillates between the two waveguides but rather travels in both waveguides simultaneously. This fact can be used for a direct observation of the EP: the propagation constants approach when the gain-loss parameter α is increased to the value at the EP. Recall that the critical value α_{EP} characterizes the maximum antisymmetric index profile, which can still be treated within perturbation theory; see Sect. 3.

Although propagation constants of the studied $\mathscr{P}\mathscr{T}$-symmetric WGs are real, the system is non-Hermitian. This can be most readily observed by looking at the integrated intensity, $\int_{-\infty}^{\infty}|E_y(x,z)|^2dx$. This intensity is not conserved as one can

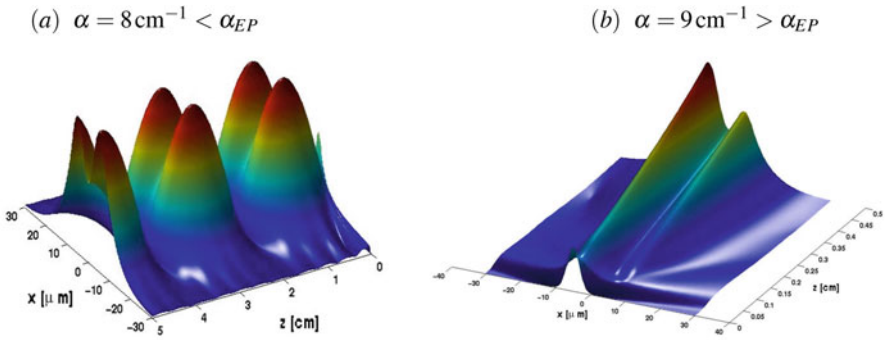

Fig. 5 3D representation of the power distribution for a propagating sum field (33). (**a**) The exact $\mathscr{P}\mathscr{T}$ symmetry with $\alpha = 8\,\mathrm{cm}^{-1} < \alpha_{EP}$. The light power oscillates, with the beat length increasing as the system approaches the EP at $\alpha_{EP} \approx 8.4\,\mathrm{cm}^{-1}$. (**b**) The broken $\mathscr{P}\mathscr{T}$ symmetry with $\alpha = 9\,\mathrm{cm}^{-1} > \alpha_{EP}$. The light power increases along the propagation axis, because the signal occupies primarily the WG with a gain-guiding mode

easily see from Figs. 4 and 5a: the intensity drops almost to zero between oscillations for $\alpha = 8\,\mathrm{cm}^{-1}$. In the case of $\mathscr{P}\mathscr{T}$-symmetric system, one can find a different conserved quantity instead of the integrated intensity; see Eq. (8) in Sect. 2. In our system, this conserved quantity takes the form of the c-product as

$$\int_{-\infty}^{\infty} E_y^*(-x, z) E_y(x, z) dx = const. \tag{34}$$

Yet another effect can be observed in the suggested experiment: the maximum intensity reached by the initially normalized sum field (33) increases as the EP is approached. This can be understood by observing that as one approaches the self-orthogonal state the overlap between the two functions comprising the sum field increases. Finally, Fig. 5b gives an insight on the dramatic change of light propagation when the gain-loss parameter exceeds the EP and the propagation constant gets a nonzero imaginary part.

It is important to note that the manifestation of $\mathscr{P}\mathscr{T}$ symmetry and its resulting properties is not (theoretically) restricted to optical systems. To date, however, optical systems seem to be the most readily applicable and $\mathscr{P}\mathscr{T}$ symmetry in optics was quoted among top 10 physics discoveries of the last 10 years by Nature Physics [10]. One could easily envision a setting using matter waves in which a condensate is placed in a double well potential, where in one well particles are injected into the condensate whereas in the second well particles are removed from the condensate. Here attention should be given to the non-linearity of the Gross-Pitaevskii equation. In order to keep the dynamics similar to that described in the optics experiment, the non-linearity should be made small. This can be achieved either by tuning the interaction between the atoms to zero or by using a very dilute sample. The experiment would also require accurate and independent control over

the rates of particles injected or removed from the system. Hopefully, experimental methods will improve to allow such experiments to be done.

5 Vanishing Group Velocity at the Exceptional Point

In this section, following our work with Tamar Goldzak [18], we extend the study of $\mathscr{P}\mathscr{T}$-symmetric WGs to the case of isolated wave pulses. We consider two-dimensional WGs with the propagation axis z described in the previous section. In a $\mathscr{P}\mathscr{T}$-symmetric system, the gain and loss are balanced and satisfy the condition $n(x) = n^*(-x)$, where the complex conjugation corresponds to the time reversal that interchanges the gain and loss. Equation (30) for transverse electric modes (31) is equivalent to the one-dimensional stationary Schrödinger equation (32) for the complex (non-Hermitian) potential, and the propagating modes correspond to bound states [25].

As long as the strength of gain and loss is below a problem dependent critical value (see Sect. 2), non-decaying modes exist with real propagation constants β. The corresponding complex eigenfunctions (by selecting a proper complex pre-factor) can be taken $\mathscr{P}\mathscr{T}$-symmetric, $\psi(x) = \psi^*(-x)$. Thus, the phase speed of each mode is defined as $v_p = \omega/\beta$, while the group speed is $v_g = (d\beta/d\omega)^{-1}$. For a nondegenerate bound-state solution, differentiating equation (30) with respect to ω yields

$$\left(\frac{\partial^2}{\partial x^2} + \frac{n^2\omega^2}{c^2} - \beta^2\right)\frac{\partial\psi}{\partial\omega} + \left(\frac{\partial(n^2\omega^2/c^2)}{\partial\omega} - \frac{\partial\beta^2}{\partial\omega}\right)\psi = 0. \tag{35}$$

Following the classical perturbation theory [23, 25], one multiplies this expression by $\psi(x)$ and integrates with respect to x. The terms with $\partial\psi/\partial\omega$ cancel in the resulting expression after integrating by parts and using (30). The remaining terms yield expression for the group speed as

$$v_g = (d\beta/d\omega)^{-1} = \frac{2c^2\beta\int\psi^2 dx}{\int[\partial(n^2\omega^2)/\partial\omega]\psi^2 dx}. \tag{36}$$

By the derivation, this formula takes into account that the index of refraction may be frequency dependent in general.

The numerator in (36) represents the c-product (13) of the right eigenfunction $|\psi_R\rangle = \psi(x)$ with itself. Due to the $\mathscr{P}\mathscr{T}$-symmetry, $\psi(x) = \psi^*(-x)$, the full integral $\int\psi^2 dx$ is real but not necessarily positive. For the same reason, the denominator is real too. It follows from Eq. (36) that the group speed vanishes if and only if $\int\psi^2 dx = 0$, provided that the integral in the denominator is nonzero. The latter condition is generic and can be easily verified in each specific problem. The c-product self-orthogonality of the propagating mode is the well-known condition for the exceptional point (EP); see Eq. (18). At the EP, two propagating modes coalesce

both in propagation constants β and corresponding functions $\psi(x)$. This proves that *the group speed in a $\mathscr{P}\mathscr{T}$-symmetric WG vanishes at (and only at) an exceptional point*. Such a simple and universal condition provides a link from $\mathscr{P}\mathscr{T}$-symmetric systems to the rapidly developing field of slow light; see [3, 4, 9, 19] for other ways to stop/slow light such as the electromagnetically induced transparency (EIT).

According to Sect. 3, expansion of eigenvalues near the EP starts with a square root term

$$\beta - \beta_{EP} \propto \sqrt{\omega - \omega_{EP}}, \tag{37}$$

which implies that $d\beta/d\omega = \infty$ and $v_g = (d\beta/d\omega)^{-1} = 0$ at the EP. This provides a simple explanation of our phenomenon, because a steep slope in the dispersion curve (large derivative $d\beta/d\omega$) corresponds to a small group velocity. This argument relies exclusively on the presence of the EP, with no reference of $\mathscr{P}\mathscr{T}$-symmetry. The problem is that in conventional systems this effect will also lead to losses. The balance between gain and loss in a $\mathscr{P}\mathscr{T}$ symmetric system eliminates this problem: the light intensity remains constant because the spectrum is real (before reaching the EP). Also, the real spectrum of the $\mathscr{P}\mathscr{T}$ symmetric system simplifies a definition of the group speed, which is a nontrivial issue for a general system with gain and loss. The direct link between the EP and zero group speed makes the proposed effect robust to various imperfections, as the proximity to the EP can be effectively controlled by tuning two arbitrarily chosen parameters of the system [25, 33]. The stopping condition is limited to a very well defined EP frequency ω_{EP}. Its value can be effectively controlled by changing the parameters of the index of refraction.

We mention also that the EPs may appear in a different context: at the coalescing frequencies of Bloch modes for the (time-periodic) Schrödinger equation. Such EPs can be associated with the infinite group speed in corresponding optical systems [32]; see [38, 41] for physical interpretation of the superluminal effect.

A specific device with desired properties can be constructed by attaching layers of materials with different indices of refraction. The refractive index can be engineered, e.g., via the photorefractive nonlinearity or effective index as in metamaterials, while the spectrum of gain/loss can be engineered by using quantum well structures. The $\mathscr{P}\mathscr{T}$-symmetry is achieved if one gain guided mode (negative $\mathrm{Im}\, n$) couples with an exactly balanced loss guided mode (positive $\mathrm{Im}\, n$) [21, 35], with a profile of the refractive index shown in Fig. 2. Note that the standard gain media are dispersive, i.e., the index of refraction is frequency dependent. This frequency dependence may break the $\mathscr{P}\mathscr{T}$ symmetry due to a finite gain bandwidth.

Let us describe the effective light intensities of the two (gain and loss) modes by two complex variables (φ_1, φ_2). Then one obtains a simple model in the form of 2×2 $\mathscr{P}\mathscr{T}$-symmetric non-Hermitian system

$$\begin{pmatrix} \beta_w^2 - i\widetilde{\alpha}k & \delta \\ \delta & \beta_w^2 + i\widetilde{\alpha}k \end{pmatrix} \begin{pmatrix} \varphi_1 \\ \varphi_2 \end{pmatrix} = \beta^2 \begin{pmatrix} \varphi_1 \\ \varphi_2 \end{pmatrix}, \tag{38}$$

where the Hamiltonian has the same structure, up to notation, as in Eq. (5). Here $\beta_w = n_w k$ is the real propagation constant of each separate WG with the effective index of refraction n_w and $k = \omega/c$, δ describes the coupling, and $\widetilde{\alpha} = 2n_w\alpha$ determines the gain in one WG and the loss in the other. The system with no gain/loss ($\widetilde{\alpha} = 0$) has one symmetric and one antisymmetric mode, with $\beta^2 = \beta_w^2 \pm \delta$ and $(\varphi_1, \varphi_2) = (\pm 1,\ 1)$. When gain and loss are taken into account, one finds $\beta^2 = \beta_w^2 \pm \sqrt{\delta^2 - \widetilde{\alpha}^2 k^2}$. With increasing $\widetilde{\alpha}$, the real propagation constants come closer and coalesce at the EP given by $\widetilde{\alpha}_{EP} = \delta/k$. The corresponding two eigenvectors coalesce too, with the resulting vector $(\varphi_1, \varphi_2) = (1, i)$ satisfying the c-product self-orthogonality condition $\varphi_1^2 + \varphi_2^2 = 0$.

The full-stop of a Gaussian pulse can be accomplished by an adiabatic increase of the gain-loss parameter to the value $\widetilde{\alpha}_{EP}$, as was also proposed in the context of photonic-crystal waveguides [36, 44]. Varying the gain-loss parameter in our non-Hermitian system would be best done via parametric nonlinear gain, which separates the variation in the gain from affecting the real part of refractive index, avoiding restrictions imposed by the Kramers–Kronig relations. Nonlinear parametric interactions operating at ultrafast rates [39] can be engineered using synchronously-pumped optical parametric oscillators, where the nonlinear medium is in a cavity and pumped with a pulse at repetition rate matched to cavity, or optical parametric amplifiers pumped without a cavity by femtosecond pulse. Usually these utilize $\chi^{(2)}$ crystals, which are commercial technologies. Another choice is $\chi^{(3)}$ materials, through non-degenerate four-wave-mixing interactions, where the pumps serve as gain for the signal beams [1].

Time-dependent solutions for the simplified model (38) can be found using the system of coupled wave equations

$$\begin{aligned} \frac{n_w^2}{c^2}\frac{\partial^2\Phi_1}{\partial t^2} - \frac{\widetilde{\alpha}}{c}\frac{\partial\Phi_1}{\partial t} - \delta\,\Phi_2 - \frac{\partial^2\Phi_1}{\partial z^2} = 0, \\ \frac{n_w^2}{c^2}\frac{\partial^2\Phi_2}{\partial t^2} + \frac{\widetilde{\alpha}}{c}\frac{\partial\Phi_2}{\partial t} - \delta\,\Phi_1 - \frac{\partial^2\Phi_2}{\partial z^2} = 0. \end{aligned} \tag{39}$$

It is straightforward to check that this system is equivalent to Eq. (38) for a single-mode solution

$$(\Phi_1, \Phi_2) = (\varphi_1, \varphi_2)\, e^{i\beta z - i\omega t}. \tag{40}$$

Furthermore, it is easy to see that the model is $\mathscr{P}\mathscr{T}$-symmetric under the transformation:

$$\Phi_1(z,t) \to \Phi_2(-z,-t), \qquad \Phi_2(z,t) \to \Phi_1(-z,-t). \tag{41}$$

System (39) was simulated numerically using the pseudo-spectral method in a large periodic domain. Initial condition at $t = 0$ was taken in the form of a Gaussian pulse corresponding to the antisymmetric mode of the system with no gain and loss,

$$(\Phi_1, \Phi_2) = (-1, 1)\, A \int \exp\left(-\frac{(\beta-\beta_0)^2}{2\sigma^2} + i\beta z\right) d\beta, \tag{42}$$

with mean propagation constant $\beta_0 = 0.8$, standard deviation $\sigma = 0.01$ and arbitrary prefactor A. This value $\beta_0 = 0.8$ corresponds to the EP at the final time when $\widetilde{\alpha}_{EP} = 1$, see Fig. 6a. In simulations, we used a finite window $0.75 \leq \beta \leq 0.85$ to avoid instabilities, which occur for some propagation constants outside this interval. In practical applications, such instabilities (if they appear) must be suppressed for efficient operation of the system.

Numerical simulation of such time-dependent dynamics with the model (39) is presented in Fig. 6, where a Gaussian pulse is prepared initially in the antisymmetric mode of the system with no gain and loss. In full agreement with our theoretical prediction, with the increase of the gain-loss parameter in time, the pulse slows down and stops at the EP (graphs at latest times collapsed to a single curve). A backward change of the gain-loss parameter brings the signal to its original mobile form.

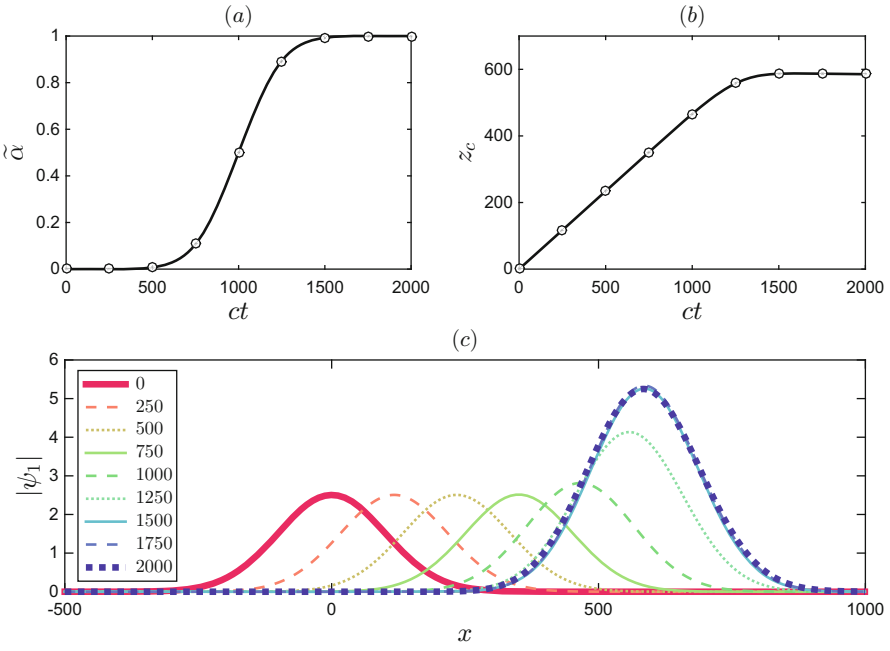

Fig. 6 (**a**) Adiabatic change of the gain-loss parameter from $\widetilde{\alpha} = 0$ at $t = 0$ to $\widetilde{\alpha}_{EP} = 1$ at final time $t = 2000/c$ in a system with representative parameters $k = 0.5$, $n_w = 1.6$, and $\delta = 0.5$ (arb. unit). (**b**) Temporal evolution of the center z_c of the Gaussian pulse, stopping when $\widetilde{\alpha}$ reaches the value $\widetilde{\alpha}_{EP} = 1$ at EP. The pulse is prepared initially in anti-symmetric mode of the system with no gain and loss with the mean propagation number $\beta = 0.8$ and standard deviation $\sigma = 0.01$. (**c**) Pulse envelope $|\Phi_1|$ in the first WG at times $ct = 0, 250, \ldots, 2000$, which correspond to circles in the upper figures. At the three latest times, the group speed vanishes and the corresponding graphs collapse to a single curve demonstrating the full-stop of a pulse. A backward change of the gain-loss parameter brings the optical signal to its original mobile form

Conclusions based on the effective model (38) are further confirmed by numerical computation for the full Eq. (30). Here the propagation constants β and eigenfunctions $\psi(x)$ are calculated numerically for given frequency ω by diagonalizing the non-Hermitian Hamiltonian in a matrix representation using a particle in a box basis set. We use specific values of the WG width $a = 1.25\,\mu\text{m}$ and the same distance between them. The two modes coalesce at the EP for specific values of k and β in the presence of gain and loss, and one can see from Fig. 7a that the derivative $d\beta/dk$ becomes infinite at the EP giving the vanishing group velocity $v_g = c\,(d\beta/dk)^{-1}$. The corresponding self-orthogonal eigenfunction is given in panel (b).

Finally, Fig. 8 shows the propagation of Gaussian wave packets, comparing the power spectrum $|E_y(x, z, t)|^2$ at the initial time $t = 0$ vs. the final time of 10 picoseconds. Here the Gaussian solution for a constant gain-loss parameter α is written as

$$E_y(x, z, t) = A \int \exp\left(-\frac{(\beta - \beta_0)^2}{2\sigma^2} + i\beta z - i\omega t\right) \psi(x) d\beta, \tag{43}$$

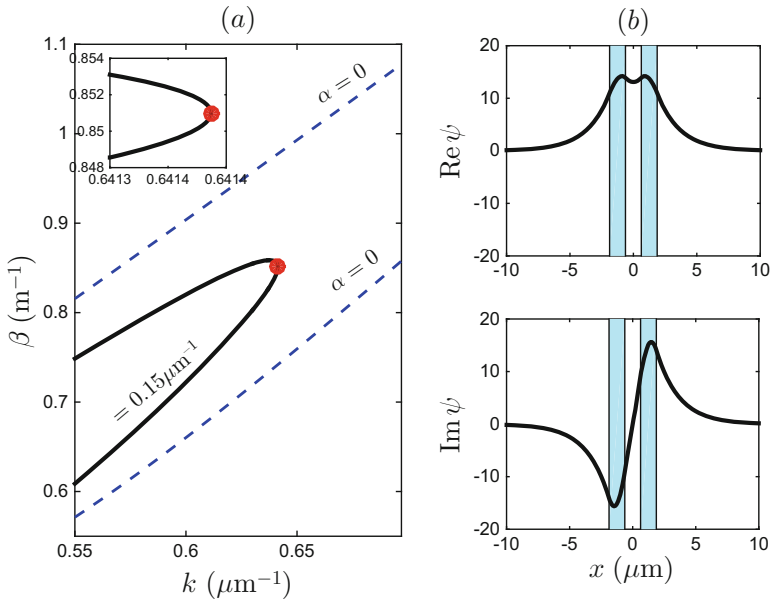

Fig. 7 (**a**) The propagation constant β as a function of $k = \omega/c$ for two different values of the gain-loss parameter: Hermitian system with $\alpha = 0$ (dashed black lines: upper symmetric and lower antisymmetric modes) and non-Hermitian $\mathscr{P}\mathscr{T}$-symmetric system with $\alpha = 0.15\,\mu\text{m}^{-1}$ (solid blue line). Two modes of the $\mathscr{P}\mathscr{T}$-symmetric system coalesce at the EP marked with a red circle. Inset shows enlarged vicinity of the EP at $k_{EP} = 0.6414\,\mu\text{m}^{-1}$ and $\beta_{EP} = 0.851\,\mu\text{m}^{-1}$. The infinite derivative $d\beta/dk$ at the EP yields the vanishing group velocity $v_g = c\,(d\beta/dk)^{-1}$. (**b**) Real and imaginary parts of the complex eigenfunction for the $\mathscr{P}\mathscr{T}$-symmetric system at the EP. This mode satisfies the self-orthogonality condition $\int \psi^2 dx = 0$. Colored vertical regions in the background show positions of the two coupled WGs

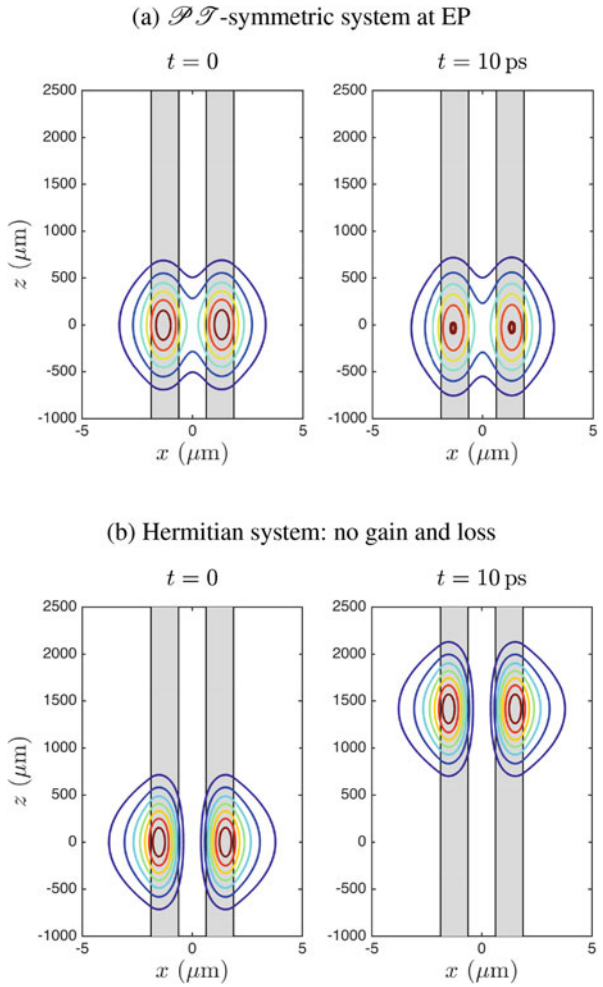

Fig. 8 Contour plot of the light power $|E_y(x, z, t)|^2$ for the Gaussian wave packets at the initial time $t = 0$ and the final time $t = 10\,\mathrm{ps}$. In both plots the pulse has the mean propagation constant $\beta = 0.851\,\mu\mathrm{m}^{-1}$ with standard deviation $\sigma = 0.002\,\mu\mathrm{m}^{-1}$. Grey regions in the background show positions of the two coupled WGs. (**a**) Fully stopped pulse centered exactly at the EP in the $\mathscr{P}\mathscr{T}$-symmetric system for $\alpha = 0.15\,\mu\mathrm{m}^{-1}$. (**b**) The antisymmetric mode in the Hermitian case with no gain and loss ($\alpha = 0$). One can see that the pulse is displaced by about 1.4 mm in the Hermitian case, while it does not move at all when prepared at the EP in the $\mathscr{P}\mathscr{T}$-symmetric system. (**a**) $\mathscr{P}\mathscr{T}$-symmetric system at EP. (**b**) Hermitian system: no gain and loss

where both ω and $\psi(x)$ should be expressed as functions of β. Note that the Gaussian pulse at the EP contains the contributions from both sides of β_{EP}, which correspond to two different modes coalescing at the EP in Fig. 7a. In numerical computations, we used $\beta_0 = 0.851\,\mu\text{m}^{-1}$, $\sigma = 0.002\,\mu\text{m}^{-1}$ and the overall interval $0.845 \le \beta \le 0.857\,\mu\text{m}^{-1}$. In Fig. 8a, the pulse parameters are chosen exactly at the EP, while figure (b) corresponds to a similar pulse but for the system far from the EP (no gain and loss, $\alpha = 0$). The latter pulse has the large group speed $v_g/c = 0.47$ and the phase speed $v_p/c = 0.82$, demonstrating a considerable displacement of about 1.4 mm in 10 ps, while the full-stop is confirmed for the pulse designed at the EP. We used illustrative values of physical parameters in these simulations, which provide a larger frequency window near the EP than those studied experimentally in [31]. Note that the dispersion curve in Fig. 7a exhibits a round shape including also a point with infinite group velocity [38, 41], where $d\beta/dk = 0$. This point is outside the operation window for our protocol.

The stopped signal in our system has the phase velocity $v_p/c = 0.75$, which is only weakly affected as the group velocity is reduced to zero under the EP mechanism. Furthermore, the phase speed demonstrates a slight decrease compared to the system with no gain and loss, contrary, e.g., to the well-known relation $v_p \propto 1/v_g$ in special relativity or in optics at the mode-opening.

The major advantages of the proposed protocol is its non-resonant nature, in which the EP can be adjusted to any frequency by tuning the coupling or gain-loss parameters. There is also a benefit of using the time-dependent variation of parameters. In this case an optical pulse is expanded in spatial Fourier modes with the frequency evolving adiabatically along the real dispersion curve in Fig. 7a. In this way our protocol avoids the instability related to complex modes at frequencies above the EP, as confirmed by our numerical tests in Fig. 6.

We see that the full-stop of a light pulse is possible at the exceptional point in $\mathscr{P}\mathscr{T}$-symmetric coupled waveguides by varying the gain-loss parameter in time. This allows to "freeze" and then release the light pulse preserving the carried coherent information. The use of $\mathscr{P}\mathscr{T}$-symmetry has practical advantages of keeping a constant intensity of propagating modes and providing a robust protocol that brings the system to the EP. The non-resonant mechanism of the proposed phenomenon, due to large flexibility of controlling the EP position, is an important technological advantage, with potential applications for short optical pulses. Specifically, one can engineer this effect in a $\mathscr{P}\mathscr{T}$-symmetric system of two waveguide channels. This approach is not limited only to light but can be extended, e.g., to acoustic waves or other fields in physics related to the $\mathscr{P}\mathscr{T}$-symmetry.

6 Conclusion

The transition from a real to a complex spectrum of non-Hermitian $\mathscr{P}\mathscr{T}$-symmetric Hamiltonians occurs at the exceptional point (EP), where two eigenmodes coalesce both in eigenvalue and eigenvector. In spite of the fact that EPs are accidental non-

Hermitian degeneracies they are not rare and not mathematical objects but physical ones. We have described in detail how light oscillations between two waveguides are suppressed by approaching the EP condition. We also prove that the group velocity of a light pulse decreases to zero as the system is tuned to be at the EP and propose a way how to observe it experimentally. Last but not least, the findings and conclusions presented in this Chapter are relevant to any two atomic or molecular metastable states, which are resonantly coupled by a laser field, because their non-Hermitian Hamiltonian can be simply transformed to have the $\mathscr{P}\mathscr{T}$-symmetric structure.

Acknowledgements The authors thank Adi Pick for most helpful comments. N.M. acknowledges the financial support of I-Core: The Israeli Excellence Center "Circle of Light", and of the Israel Science Foundation Grant No. 1530/15. A.A.M. was supported by the CNPq Grant No. 302351/2015-9.

References

1. Agrawal, G.P.: Nonlinear Fiber Optics. Academic, Amsterdam (2013)
2. Arnold, V.I.: Geometrical Methods in the Theory of Ordinary Differential Equations. Springer Science & Business Media, New York (2012)
3. Baba, T.: Slow light in photonic crystals. Nat. Photonics **2**(8), 465–473 (2008)
4. Bajcsy, M., Zibrov, A.S., Lukin, M.D.: Stationary pulses of light in an atomic medium. Nature **426**(6967), 638–641 (2003)
5. Bender, C.M.: Making sense of non-Hermitian Hamiltonians. Rep. Prog. Phys. **70**(6), 947 (2007)
6. Bender, C.M., Boettcher, S.: Real spectra in non-Hermitian Hamiltonians having PT symmetry. Phys. Rev. Lett. **80**(24), 5243 (1998)
7. Bender, C.M., Berry, M.V., Mandilara, A.: Generalized PT symmetry and real spectra. J. Phys. A **35**(31), L467 (2002)
8. Berry, M.V., Dennis, M.R.: The optical singularities of birefringent dichroic chiral crystals. Proc. R. Soc. A **459**(2033), 1261–1292 (2003)
9. Boyd, R.W., Gauthier, D.J.: Controlling the velocity of light pulses. Science **326**(5956), 1074–1077 (2009)
10. Cham, J.: Top 10 physics discoveries of the last 10 years. Nat. Phys. **11**(10), 799 (2015)
11. Dembowski, C., Gräf, H.D., Harney, H.L., Heine, A., Heiss, W.D., Rehfeld, H., Richter, A.: Experimental observation of the topological structure of exceptional points. Phys. Rev. Lett. **86**(5), 787–790 (2001)
12. Doppler, J., Mailybaev, A.A., Böhm, J., Kuhl, U., Girschik, A., Libisch, F., Milburn, T.J., Rabl, P., Moiseyev, N., Rotter, S.: Dynamically encircling an exceptional point for asymmetric mode switching. Nature **537**(7618), 76–79 (2016)
13. El-Ganainy, R., Makris, K.G., Christodoulides, D.N., Musslimani, Z.H.: Theory of coupled optical PT-symmetric structures. Opt. Lett. **32**(17), 2632–2634 (2007)
14. El-Ganainy, R., Makris, K.G., Khajavikhan, M., Musslimani, Z.H., Rotter, S., Christodoulides, D.N.: Non-Hermitian physics and PT symmetry. Nat. Phys. **14**(1), 11 (2018)
15. Ge, L., Türeci, H.E.: Antisymmetric PT-photonic structures with balanced positive-and negative-index materials. Phys. Rev. A **88**(5), 053810 (2013)
16. Gilary, I., Moiseyev, N.: Asymmetric effect of slowly varying chirped laser pulses on the adiabatic state exchange of a molecule. J. Phys. B **45**(5), 051002 (2012)

17. Gilary, I., Mailybaev, A.A., Moiseyev, N.: Time-asymmetric quantum-state-exchange mechanism. Phys. Rev. A **88**(1), 010102 (2013)
18. Goldzak, T., Mailybaev, A.A., Moiseyev, N.: Light stops at exceptional points. Phys. Rev. Lett. **120**, 013901 (2018)
19. Hau, L.V., Harris, S.E., Dutton, Z., Behroozi, C.H.: Light speed reduction to 17 metres per second in an ultracold atomic gas. Nature **397**(6720), 594–598 (1999)
20. Jackson, J.D.: Classical Electrodynamics. Wiley, Chichester (1999)
21. Klaiman, S., Günther, U., Moiseyev, N.: Visualization of branch points in PT-symmetric waveguides. Phys. Rev. Lett. **101**(8), 080402 (2008)
22. Kottos, T.: Optical physics: broken symmetry makes light work. Nat. Phys. **6**(3), 166–167 (2010)
23. Landau, L.D., Lifshitz, E.M.: Quantum Mechanics, Non-relativistic Theory. Pergamon, Oxford (1991)
24. Mailybaev, A.A.: Computation of multiple eigenvalues and generalized eigenvectors for matrices dependent on parameters. Numer. Linear Algebra Appl. **13**(5), 419–436 (2006)
25. Moiseyev, N.: Non-Hermitian Quantum Mechanics. Cambridge University Press, Cambridge/New York (2011)
26. Moiseyev, N., Friedland, S.: Association of resonance states with the incomplete spectrum of finite complex-scaled Hamiltonian matrices. Phys. Rev. A **22**(2), 618–624 (1980)
27. Mostafazadeh, A.: Pseudo-Hermiticity versus PT symmetry: the necessary condition for the reality of the spectrum of a non-Hermitian Hamiltonian. J. Math. Phys. **43**(1), 205–214 (2002)
28. Mostafazadeh, A.: Quantum brachistochrone problem and the geometry of the state space in pseudo-Hermitian quantum mechanics. Phys. Rev. Lett. **99**(13), 130502 (2007)
29. Peng, P., Cao, W., Shen, C., Qu, W., Wen, J., Jiang, L., Xiao, Y.: Anti-parity-time symmetry with flying atoms. Nat. Phys. **12**(12), 1139–1145 (2016)
30. Ruschhaupt, A., Delgado, F., Muga, J.G.: Physical realization of-symmetric potential scattering in a planar slab waveguide. J. Phys. A **38**(9), L171–L176 (2005)
31. Rüter, C.E., Makris, K.G., El-Ganainy, R., Christodoulides, D.N., Segev, M., Kip, D.: Observation of parity–time symmetry in optics. Nat. Phys. **6**(3), 192–195 (2010)
32. Schomerus, H., Wiersig, J.: Non-Hermitian-transport effects in coupled-resonator optical waveguides. Phys. Rev. A **90**(5), 053819 (2014)
33. Seyranian, A.P., Mailybaev, A.A.: Multiparameter stability theory with mechanical applications. World Scientific, Singapore (2003)
34. Seyranian, A.P., Kirillov, O.N., Mailybaev, A.A.: Coupling of eigenvalues of complex matrices at diabolic and exceptional points. J. Phys. A **38**(8), 1723–1740 (2005)
35. Siegman, A.E.: Propagating modes in gain-guided optical fibers. J. Opt. Soc. Am. A **20**(8), 1617–1628 (2003)
36. Tanaka, Y., Upham, J., Nagashima, T., Sugiya, T., Asano, T., Noda, S.: Dynamic control of the Q factor in a photonic crystal nanocavity. Nat. Mater. **6**(11), 862–865 (2007)
37. Uzdin, R., Mailybaev, A.A., Moiseyev, N.: On the observability and asymmetry of adiabatic state flips generated by exceptional points. J. Phys. A **44**(43), 435302 (2011)
38. Wang, L.J., Kuzmich, A., Dogariu, A.: Gain-assisted superluminal light propagation. Nature **406**(6793), 277–279 (2000)
39. Weiner, A.: Ultrafast Optics. Wiley, New York (2011)
40. Wigner, E.: On a modification of the Rayleigh–Schrdinger perturbation theory. Math. Natur. Anz. (Budapest) **53**, 477–482 (1935)
41. Withayachumnankul, W., Fischer, B.M., Ferguson, B., Davis, B.R., Abbott, D.: A systemized view of superluminal wave propagation. Proc. IEEE **98**(10), 1775–1786 (2010)
42. Wu, J.H., Artoni, M., La Rocca, G.C.: Parity-time-antisymmetric atomic lattices without gain. Phys. Rev. A **91**(3), 033811 (2015)
43. Xu, H., Mason, D., Jiang, L., Harris, J.G.E.: Topological energy transfer in an optomechanical system with exceptional points. Nature **537**(7618), 80–83 (2016)
44. Yanik, M.F., Suh, W., Wang, Z., Fan, S.: Stopping light in a waveguide with an all-optical analog of electromagnetically induced transparency. Phys. Rev. Lett. **93**(23), 233903 (2004)

Higher Order Exceptional Points in Discrete Photonics Platforms

M. H. Teimourpour, Q. Zhong, M. Khajavikhan, and R. El-Ganainy

Abstract The introduction of parity-time (PT) symmetry in optics and photonics has initiated intense activities exploring the exotic properties of these structures, eventually leading to the more general notion of non-Hermitian photonics. Efforts to understand the behavior of these systems have revealed a host of distinct features originating from the unusual character of their eigenspectra and eigenstates. These include for example, spontaneous symmetry breaking, bandgap merging, laser self-termination, unidirectional invisibility, and ultra-sensitivity to external perturbations. A central notion pertinent to all these effects is the concept of exceptional points (EPs). Also known as branch points, EPs are non-Hermitian spectral singularities that arise when two (or more) eigenvalues and their corresponding eigenstates become identical. While exceptional points of order two have been studied thoroughly at both the theoretical and experimental level, higher order EPs are attracting attention only recently. Here we discuss a systematic approach based on a recursive bosonic quantization scheme for generating discrete photonic networks that exhibit exceptional points of any arbitrary order. We also discuss the spectral properties and the extreme dynamics near these singularities as well as their physical implementation in various photonic platforms.

M. H. Teimourpour · Q. Zhong
Department of Physics, Michigan Technological University, Houghton, MI, USA

M. Khajavikhan
College of Optics & Photonics-CREOL, University of Central Florida, Orlando, FL, USA

R. El-Ganainy (✉)
Department of Physics, Michigan Technological University, Houghton, MI, USA

Henes Center for Quantum Phenomena, Michigan Technological University, Houghton, MI, USA
e-mail: ganainy@mtu.edu

D. Christodoulides, J. Yang (eds.), *Parity-time Symmetry and Its Applications*, Springer Tracts in Modern Physics 280,
https://doi.org/10.1007/978-981-13-1247-2_10

1 Introduction

Branch points (BPs) are peculiar singularities that arise in dealing with multi-valued complex functions [1]. The singular behavior of these points is manifested by the failure of the Taylor series expansion of the associated function at their locations. Another seemingly different context where branch points appear is non-Hermitian physics [2, 3]. The spectra of non-Hermitian Hamiltonians are in general complex, and for certain sets of parameters, they may contain a special type of degeneracy where not only the eigenvalues but also their corresponding eigenvectors become identical. The points at which this occur are known as exceptional points (EPs). From the mathematical point of view EPs are a special type of BPs associated with solutions of complex polynomials.

While EPs have been studied previously in the context of complex-valued Hamiltonians [4–6], the discovery by Bender et al. that parity-time- (PT-) symmetric Hamiltonian might contain real spectra [7, 8] has rekindled the interest of these peculiar degeneracies. As it turned out, in PT-symmetric systems, EPs mark the transition between two different phases: (1) PT phase with real eigenvalues and PT-symmetric eigenstates; and (2) broken PT phase with complex conjugate eigenvalues and eigenstates that do not respect PT symmetry.

Later on, the introduction of PT symmetry in optics [9–14] has opened a host of new opportunities for engineering new optical structures having novel functionalities and offering unprecedented control over light generation, transport and trapping [2, 3]. Some of the exotic effects observed in PT photonics structures are bandgap merging [10], laser self-termination [15–18], unidirectional invisibility [19–21]. On the practical front, optical isolation [22–24], single mode microlasers [25, 26], ultra-responsive sensors [27, 28], supersymmetric laser arrays [29, 30] and light sources based on non-Hermitian wave-mixing [31, 32] are some of the emerging applications of non-Hermitian photonics. Interestingly, all these phenomena are linked to the unusual features of EPs. Particularly, as a non-Hermitian Hamiltonian is parametrically steered along a trajectory to bring the system towards an EP, two or more eigenstates approach each other until they coalesce exactly at the location of the EP. This means that the relevant eigenvalues become the same and their corresponding eigenvectors become "parallel", thus signaling a reduction in the eigenstate space dimensionality. The order of the EP can be defined as the number of coalescing modes. While the mathematical construction of EPs of order two (see [2, 3] for several theoretical and experimental examples) and three [33–37] is relatively straightforward, the situation is different for higher order EPs. Few years ago, our group introduced a systematic mathematical approach based on bosonic algebra, known as the recursive bosonic quantization (RBQ), that can achieve this task [38].

In this chapter, we review the essential ingredients of the RBQ method, discuss the extreme power oscillations near higher order EPs and present possible strategies for implementing them in various photonic platforms.

2 Recursive Bosonic Quantization

The starting point for the RBQ method is a non-interacting (i.e. without nonlinear terms) PT-symmetric two-site Bose-Hubbard Hamiltonian:

$$\hat{H}_2^{(1)} = -i\hbar\frac{\gamma}{2}(\hat{a}_1^\dagger\hat{a}_1 - \hat{a}_2^\dagger\hat{a}_2) + \hbar\kappa(\hat{a}_1^\dagger\hat{a}_2 + \hat{a}_1\hat{a}_2^\dagger) \tag{1}$$

where $\hat{a}_{1,2}^\dagger$ and $\hat{a}_{1,2}$ are the bosonic creation and annihilation operators of site 1 and 2, respectively and they obey $[\hat{a}_i, \hat{a}_j] = [\hat{a}_i^\dagger, \hat{a}_j^\dagger] = 0$, $[\hat{a}_i, \hat{a}_j^\dagger] = \delta_{ij}$ with δ_{ij} being the Kronecker delta function. The parameter γ represents the gain/loss factor while κ is the hopping constant between the two sites. The superscript in $\hat{H}_2^{(1)}$ refers to the fact that this is the first iteration as obtained by quantizing the classical PT coupled waveguide/cavity structures, while the subscript denotes the number of sites. Before we proceed, we emphasize that the Bose-Hubbrard model of Eq. (1) is used to generate classical configurations with higher order EPs rather than representing actual quantum systems. A closed form expression for the eigenvalue spectrum of Eq. (1) can be obtained by diagonalizing $\hat{H}_2^{(1)}$ (see Appendix). This diagonalization process gives two eigenstates having even-like and odd-like symmetries. If now assume that the former is populated by m bosons and the latter by $M-m$ bosons, the resultant expression for the eigenvalues $\lambda_{M,m}$ (as defined by the time dependency $\exp(-i\lambda_{M,m}t/\hbar)$) is:

$$\lambda_{M,m} = (M-2m)\hbar\sqrt{\kappa^2 - (\gamma/2)^2}, \quad m = 0, 1, 2, \ldots, M. \tag{2}$$

The spectrum $\lambda_{M,m}$ has an exceptional point of order $M+1$ at $\gamma = 2\kappa$. Note that, despite the higher order of the EP, the eigenvalues of Eq. (2) are expressed in terms of a square root. This peculiar observation will be discussed in more details later. This non-Hermitian degeneracy of Hamiltonian $\hat{H}_2^{(1)}$ was noted before in [39] and independently studied in details later in [40] using the angular momentum algebra. Here we take a different route by using the bosonic algebra combined with Fock space representation of $\hat{H}_2^{(1)}$. While these two approaches are mathematically equivalent, the latter has two advantages: (1) It lends itself naturally to photonic implementations; (2) It can be applied iteratively to generate complex PT-symmetric networks with higher order EPs of arbitrary order.

Essentially, one can construct a non-Hermitian photonic network having an identical spectrum as that given in Eq. (2) by employing the Fock space representation of the Hamiltonian $\hat{H}_2^{(1)}$. To demonstrate this and without any loss of generality, we will consider the case of $M = 2N$ and use the symmetrized bases $|n_{2N}\rangle = \frac{(\hat{a}_1^\dagger)^{N-n}(\hat{a}_2^\dagger)^{N+n}}{\sqrt{(N-n)!(N+n)!}}|vac\rangle = |N-n, N+n\rangle$, with $N \mp n$ being the number of bosons in sites 1 and 2, respectively and $|vac\rangle$ is the vacuum state. In contrast to quantum systems, these bases are used here only to generate

PT-symmetric arrays and thus both integers and half integers are valid choices for N. The dynamical evolution of any arbitrary wavefunction inside this subspace is given by $|\psi(t)\rangle = \sum_{n=-N}^{N} c_n(t)\,|n_{2N}\rangle$ where the time dependent amplitudes $c_n(t)$ are completely determined by their initial conditions $c_n(0)$ and the coupled ordinary differential equations (ODEs):

$$i\frac{d\mathbf{c}}{dt} = \Omega\mathbf{c}, \quad \Omega = \begin{bmatrix} -i\gamma N & \kappa g_{-N+1} & & & & \\ \cdots & \cdots & \cdots & \cdots & \cdots & \\ & \kappa g_n & i\gamma n & \kappa g_{n+1} & & \\ \cdots & \cdots & \cdots & \cdots & \cdots & \\ & & & \kappa g_N & i\gamma N & \end{bmatrix}, \tag{3}$$

where $\mathbf{c} = (c_{-N}, \ldots, c_{N-1}, c_N)^T$ with the superscript T indicating matrix transpose. Note that the coupling coefficients $g_n = \sqrt{(N+n)(N-n+1)}$ are symmetric around $n = 0$ while the gain/loss profile (determined by the diagonal elements of Ω) is antisymmetric. In other words, the system exhibits PT symmetry. Importantly, in the bases $|n_{2N}\rangle$, the eigenvalue spectrum of Eq. (3) is given by $\mu_{2N,n} = 2n\sqrt{\kappa^2 - (\gamma/2)^2}$, $|n| \leq N$, featuring time dependency of the form $\exp(-i\mu_{N,n}t)$. Here again, a square root expression is associated with higher order EPs. As it turned out, this occurs because of the correlation between the matrix elements (i.e. all the diagonal elements vary with γ and the off-diagonals depend on κ). If the elements of the matrix Ω are allowed to change independently, one recovers the more common higher $(M+1)$th root. More detailed analysis about perturbations around EPs can be found in [41].

The advantage of our approach for optics applications is evident from the form of Eq. (3): a system of first order coupled differential equations that can be emulated by using coupled photonic structures. For example, Fig. 1a, b depict a schematic of an arrays that can be used to emulate Eq. (3) when $N = 1$ and $N = 3/2$, featuring third and fourth order EPs respectively. The waveguides/cavities are represented by the nodes and the network connectivity (diagonal/off diagonal values of Ω) is indicated in the figure. These structures can be realized using current photonic technology as we will discuss shortly.

Interestingly, more complicated PT-symmetric networks having nonlinear topology (i.e. with quasi-two dimensional network connectivity as shown in Fig. 2) can be generated by successive application of the bosonic quantization method. Moreover, as we will show, these structures exhibit degenerate spectral features that do not exist in the spectrum of $\hat{H}_2^{(1)}$. To do so, we simply replace the c-numbers c_n in Eq. (3) by a bosonic annihilation operators $\hat{a}_n$:

$$i\frac{d\hat{\mathbf{a}}}{dt} = \Omega\hat{\mathbf{a}}, \tag{4}$$

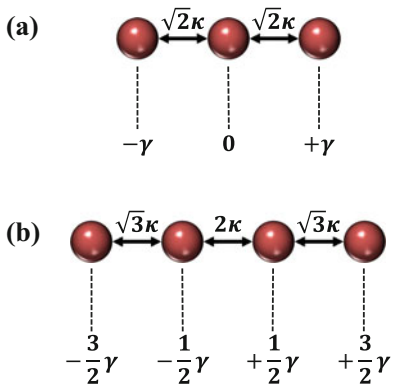

Fig. 1 (**a**) and (**b**) depict a schematic of discrete networks (made of waveguide or cavity elements) that can be used to emulate Eq. (3) when $N = 1$ and $N = 3/2$, respectively. The diagonal and off-diagonal values of Ω corresponding to these structures are indicated in the figure

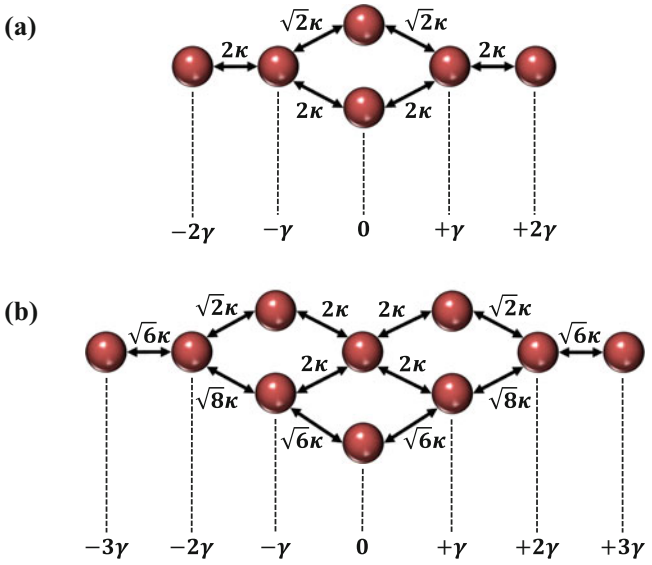

Fig. 2 A schematic of discrete network structures that correspond to 2 and 3-boson representations of $\hat{H}_3^{(2)}$ are shown (**a**) and (**b**), respectively. The diagonal and off diagonal elements are also indicated in the figure

where $\hat{\mathbf{a}} = (\hat{a}_{-N}, \ldots, \hat{a}_n, \ldots, \hat{a}_N)^T$ and the formal solution of Eq. (4) is given by $\hat{\mathbf{a}}(t) = \exp(-i\Omega t)\hat{\mathbf{a}}(0)$. Viewed from a different perspective, Eq. (4) is the Heisenberg equation of motion associated with the Hamiltonian:

$$\hat{H}_{2N+1}^{(2)} = i\hbar\gamma \sum_{n=-N}^{N} n\hat{a}_n^{\dagger}\hat{a}_n + \hbar\kappa \left(\sum_{n=-N+1}^{N} g_n \hat{a}_n^{\dagger}\hat{a}_{n-1} + \sum_{n=-N}^{N-1} g_{n+1}\hat{a}_n^{\dagger}\hat{a}_{n+1} \right). \quad (5)$$

Expanding $\hat{H}_{2N+1}^{(2)}$ in its Fock space generates higher hierarchy PT-symmetric structures. This recursive second quantization can be applied indefinitely to generate higher hierarchy of complex PT-symmetric networks.

As an example, the second quantization of the PT-symmetric configuration of Fig. 1a is given by $\hat{H}_3^{(2)} = -i\hbar\gamma(\hat{a}_1^{\dagger}\hat{a}_1 - \hat{a}_3^{\dagger}\hat{a}_3) + \sqrt{2}\hbar\kappa(\hat{a}_1^{\dagger}\hat{a}_2 + \hat{a}_1\hat{a}_2^{\dagger} + \hat{a}_2^{\dagger}\hat{a}_3 + \hat{a}_2\hat{a}_3^{\dagger})$. The Hamiltonian $\hat{H}_3^{(2)}$ can be diagonalized by means of linear transformations and its eigenvalue spectrum is given by $\lambda_{M,m_1,m_2} = 2(M - 2m_1 - m_2)\hbar\sqrt{\kappa^2 - (\gamma/2)^2}$, $m_{1,2} = 0, 1, 2, \ldots M$ with the condition $m_1 + m_2 \leq M$. Here $m_{1,2}$ are the occupation numbers of the two lowest supermodes of $\hat{H}_3^{(2)}$ while $M - m_1 - m_2$ represents the population of the third mode. Figure 2a, b depict the 2 and 3-boson representations of $\hat{H}_3^2$, featuring PT-symmetric networks with nonlinear topology and multiple degeneracies. For instance, the PT-symmetric array of Fig. 2a has two degenerate eigenmodes associated with the stationary states $|1, 0, 1\rangle_D$ and $|0, 2, 0\rangle_D$, where the subscript D indicates a representation in the diagonal bases (where the numbers represent the occupation of the system's supermodes) as opposed to those defined by the site numbers. These degenerate modes have null eigenvalue and never undergo PT phase transition regardless of the values of γ. The network depicted in Fig. 2b exhibits even a larger set of degenerate eigenstates. Here the supermodes corresponding to the states $|1, 1, 1\rangle_D$ and $|0, 3, 0\rangle_D$ have zero eigenvalue and they never experience PT phase transition, while each of the two sets of eigenstates $\{|0, 2, 1\rangle_D, |1, 0, 2\rangle_D\}$ and $\{|1, 2, 0\rangle_D, |2, 0, 1\rangle_D\}$ is doubly degenerate and their eigenvalues are complex conjugate. Higher order symmetries can be also found in higher hierarchy networks.

These degeneracies do not arise from the network invariance under geometric transformations (rotation, reflection, etc.) nor are they related to the EPs but are rather an outcome of hidden symmetries which can be characterized by a set of operators $\{\hat{A}_i\}$ where $[\hat{H}, \hat{A}_i] = 0$ and $[\hat{A}_i, \hat{A}_j] \neq 0$ [42]. In our system, these operators can be easily identified in the diagonal bases. For example, the diagonal form of $\hat{H}_3^{(2)}$ can be written as $\hat{H}_{D,3}^{(2)} = -\hbar\sqrt{4\kappa^2 - \gamma^2}(\hat{b}_1^{+}\hat{b}_1 - \hat{b}_3^{+}\hat{b}_3)$, where $\hat{b}_i^{+}$ and $\hat{b}_i$ are the creation and annihilation operators associated with the supermodes and as before, the subscript D denotes a diagonal representation. Note that we use the symbol $\hat{b}_i^{+}$ instead of $\hat{b}_i^{\dagger}$ to emphasize that $\hat{b}_i^{+}$ are not the Hermitian conjugates of $\hat{b}_i$ (see Appendix). It is now straightforward to show that the operators $\hat{A}_1 = \hat{b}_1^{+}\hat{b}_2\hat{b}_2\hat{b}_3^{+}$ and $\hat{A}_2 = \hat{b}_1\hat{b}_2^{+}\hat{b}_2^{+}\hat{b}_3$ satisfy the above relations and thus give rise to degeneracy in the spectrum. For example, $\hat{A}_1 |0, 3, 0\rangle_D = |1, 1, 1\rangle_D$ and $\hat{A}_2 |1, 1, 1\rangle_D = |0, 3, 0\rangle_D$ while $\hat{A}_1 |0, 2, 1\rangle_D = |1, 0, 2\rangle_D$ and $\hat{A}_2 |1, 0, 2\rangle_D = |0, 2, 1\rangle_D$. In order to better understand the origin of these degeneracies from a more intuitive perspective, we consider Fig. 3 which depicts the bosons occupation numbers for three pairs of degenerate states associated with the Hamiltonian $\hat{H}_{D,3}^{(2)}$.

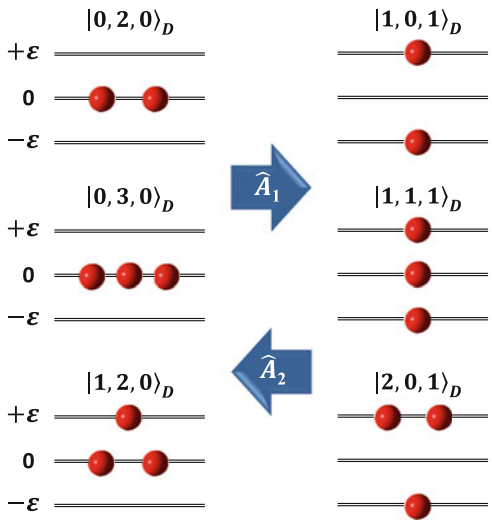

Fig. 3 Depicts bosons occupation numbers for some degenerate eigenstates (each degenerate pair is schematically shown in one row) associated with the Hamiltonian $\hat{H}^{(2)}_{D,3} = -\varepsilon(\hat{b}_1^+\hat{b}_1 - \hat{b}_3^+\hat{b}_3)$, where $\varepsilon = \hbar\sqrt{4\kappa^2 - \gamma^2}$. The eigenvalue levels (analogous to energy levels in atoms) are shown by black lines while individual bosons are represented using red spheres. For instance, it is clear that bosonic occupation configurations shown in the first row have null eigenvalue. The action of hidden symmetry operators $\hat{A}_{1,2}$ is also indicated in the figure. Evidently even higher order degeneracies will arise for Hamiltonians associated with more than three sites

Here the eigenvalue levels (analogous to energy levels in atoms) are shown by double lines while individual bosons are represented using red spheres. Evidently, these degeneracies arise from the existence of different possible boson distribution profiles that share the same eigenvalue. Clearly, higher order Hamiltonians will even have more bosonic distribution configurations that share the same eigenvalues and thus more degeneracies are expected for networks generated by using higher iterations.

3 Conservation Laws

In this section, we briefly present a systematic approach for deriving the conservation laws associated with light transport in linear PT-invariant networks having higher order EPs. The simple case of two coupled PT-symmetric waveguides were previously treated using Stokes parameters [22]. However, these calculations become cumbersome for complicated configurations. Here we present an alternative route for obtaining the system's constants of motion using standard matrix algebra. In quantum mechanics, conservation laws arise from symmetry operators that commute with the Hermitian Hamiltonian. For a more general non-Hermitian

Hamiltonian $\hat{H}$, the conserved quantities Q_i are associated with operators $\hat{S}_i$ that satisfy the relation $\hat{S}_i\hat{H} - \hat{H}^\dagger\hat{S}_i = 0$ [43]; and are given by $Q_i = \langle\hat{S}_i\rangle$. For discrete systems, the above operators reduce to matrices and the conserved quantities can be obtained by solving the above modified commutation relation for the unknown elements of the matrix S_i. To better illustrate the advantage of this approach, we consider the PT-symmetric network described by Eq. (3) when $\gamma \neq 0$ and we treat the case of $N = 1$ (Fig. 1a). Applying the above procedure leads to the following condition $s_{11} = s_{33}$, where s_{ij} represents that elements of matrix S. In addition, we find that the linear system of equations is of rank five and we choose s_{12}, s_{22} and s_{32} as free parameters. We then obtain the independent solutions by identifying three different vectors that span the parameter space (s_{12}, s_{22}, s_{32}). One particular choice of these bases gives: $S_1 = \begin{bmatrix} 0 & 0 & 1 \\ 0 & 1 & 0 \\ 1 & 0 & 0 \end{bmatrix}$, $S_2 = \begin{bmatrix} 0 & 1 & i\gamma/\sqrt{2}\kappa \\ 1 & 0 & 1 \\ -i\gamma/\sqrt{2}\kappa & 1 & 0 \end{bmatrix}$, $S_3 = \begin{bmatrix} 1 & i\gamma/\sqrt{2}\kappa & -(\gamma^2/2\kappa^2+1) \\ -i\gamma/\sqrt{2}\kappa & 0 & i\gamma/\sqrt{2}\kappa \\ -(\gamma^2/2\kappa^2+1) & -i\gamma/\sqrt{2}\kappa & 1 \end{bmatrix}$, and the associated conserved quantities $Q_{1,2,3} = \mathbf{c}^\dagger S_{1,2,3}\mathbf{c}$ are $Q_1 = (c_1^*c_3 + c_1c_3^*) + |c_2|^2$, $Q_2 = (c_1^*c_2 + c_1c_2^*) + (c_3^*c_2 + c_3c_2^*) + \frac{i\gamma}{\sqrt{2}\kappa}(c_1^*c_3 - c_1c_3^*)$ and $Q_3 = |c_1|^2 + |c_3|^2 + \frac{i\gamma}{\sqrt{2}\kappa}(c_1^*c_2 - c_1c_2^*) - \frac{i\gamma}{\sqrt{2}\kappa}(c_3^*c_2 - c_3c_2^*) - (\frac{\gamma^2}{2\kappa^2} + 1)(c_1^*c_3 + c_1c_3^*)$. Evidently, the above calculation is straightforward and can be generalized to any PT-symmetric network of any complexity and dimensionality.

4 Extreme Dynamics Near Higher Order Exceptional Points

So far we have discussed how new topologies for photonic networks having higher order exceptional points can be generated using the RBQ scheme along with the conservation laws associated with these systems and their optical implementation strategies. Another interesting feature of these systems is their dynamical evolution when the system parameters approach the exceptional point from the PT phase. As it turned out [44], the system experiences oscillatory dynamics which, for certain inputs, undergoes extreme amplification cycles.

To illustrate this behavior, let us consider the system described by the discrete Hamiltonian Ω which is generated from $\hat{H}_2^{(1)}$ by populating the latter with M bosons (corresponding to a discrete system having an exceptional point of order $M + 1$). We now focus on the $\hat{H}_2^{(1)}$ and consider the following normalized input state (as expressed in the two-sites bases) at $t = 0$: $|I(q_1, q_2)\rangle = \frac{1}{\sqrt{M!}}(q_1\hat{a}_1^\dagger + q_2\hat{a}_2^\dagger)^M |0, 0\rangle$ with $|q_1|^2 + |q_2|^2 = 1$. This state can be also cast in the form $|I(q_1, q_2)\rangle = \sum_{m=0}^{M} c_m |M - m, m\rangle$ with the expansion coefficients given by

$c_m = \sqrt{\frac{M!}{(M-m)!m!}} q_1^{M-m} q_2^m$. Although this particular construction of $|I(q_1, q_2)\rangle$ does not span all the vector space when $M > 1$, we will see later that it suffices for our calculations.

The output state at time t can be written as [44]:

$$\begin{aligned} |O\rangle &= e^{-i\hat{H}_2^{(1)}t/\hbar} |I\rangle \\ &= \frac{1}{\sqrt{M!}} [q_1(t)\hat{a}_1^\dagger + q_2(t)\hat{a}_2^\dagger]^M |0,0\rangle \\ &= \sum_{m=0}^{M} c_m(t) |M-m, m\rangle , \end{aligned} \tag{6}$$

where $c_m(t) = \sqrt{\frac{M!}{(M-m)!m!}} [q_1(t)]^{M-m} [q_2(t)]^m$ with the t dependent quantities $q_1(t) = q_1 U_{11}(t) + q_2 U_{21}(t)$ and $q_2(t) = q_1 U_{12}(t) + q_2 U_{22}(t)$ and the elements of $U(t)$ are:

$$U(t) = \begin{bmatrix} \cos(\mu t) - \frac{\gamma}{2\mu}\sin(\mu t) & -\frac{i\kappa}{\mu}\sin(\mu t) \\ -\frac{i\kappa}{\mu}\sin(\mu t) & \cos(\mu t) + \frac{\gamma}{2\mu}\sin(\mu t) \end{bmatrix}, \tag{7}$$

where $\mu = \sqrt{\kappa^2 - (\gamma/2)^2}$.

Note that within the coupled mode formalism of waveguides (or cavities) arrays, the states $|M-m, m\rangle$ represents waveguide number m while the coefficients $c_m(t)$ describe the associated field amplitudes (see [38] for more details). Therefore, the total power is given by $P(t) = \sum_{m=0}^{M} |c_m(t)|^2$. When the input power is taken to be unity, the expression for the amplification thus becomes $G = \max[P(t)]$.

For the case of $M = 1$ (second order EP), it is easy to show that, apart from a phase factor, the initial optimal vector leading to the maximum amplification is $\mathbf{c}_I^{\text{opt}} = (q_1, q_2)^T = \frac{1}{\sqrt{2}}(1, -i)^T$. Under these condition, the power oscillations dynamics are given by:

$$P_2^{\text{opt}}(t) = 1 + \frac{2\tilde{g}}{1-\tilde{g}} \sin^2(\mu t), \tag{8}$$

where $\tilde{g} = \frac{\gamma}{2\kappa}$, and this initial condition let $G_2 = \frac{1+\tilde{g}}{1-\tilde{g}}$, where the subscript in P and G indicates the order of EPs.

The general case for $M > 1$ is more subtle. In principle, one has to choose the optimal initial vector that results in the maximum amplification from the set of all initial conditions $|I'\rangle = \sum_{m=0}^{M} q_m (\hat{a}_1^\dagger)^{M-m} (\hat{a}_2^\dagger)^m |0,0\rangle$. The input state $|I\rangle$ however describes only a subset of all initial states. Within this subspace, it is straightforward

to show that even when $M > 1$, the optimal vector still corresponds to $|I(q_1, q_2)\rangle$ with $(q_1, q_2) = \frac{1}{\sqrt{2}}(1, -i)$. In that case, the power dynamics and the maximum G_{M+1} are given by:

$$P_{M+1}^{\text{opt}}(t) = [1 + \frac{2\tilde{g}}{1-\tilde{g}} \sin^2(\mu t)]^M, \tag{9}$$

and

$$G_{M+1}(\tilde{g}) = \max[P_{M+1}^{\text{opt}}(t)] = (\frac{1+\tilde{g}}{1-\tilde{g}})^M. \tag{10}$$

Note that here also $\mathbf{c}_I^{\text{opt}}$ is perpendicular to the exceptional vector $\mathbf{v}_e$ which in higher dimensions can be generated from the expression for $|I(q_1, q_2)\rangle$ by substituting $(q_1, q_2) = \frac{1}{\sqrt{2}}(1, i)$.

Equation (10) shows that when the system operates in the PT phase in vicinity of an EP of order $M + 1$ (i.e., when $\tilde{g}$ approaches unity from below) certain initial conditions will undergo extreme amplification that scales with the power of M. Thus, systems having higher order EPs can exhibit extreme dynamics and violent events even in the PT phase.

5 Photonic Implementation

In this section, we discuss several possible implementations of the PT-symmetric networks of Figs. 1 and 2. We note that the structure in Fig. 1 is one dimensional and can be implemented using planar waveguide technology in different material systems. For instance, a possible realization of the fourth-order exceptional point of Fig. 1b is shown in Fig. 4a.

In these arrangements, silicate ridge waveguides are fabricated on top of an Er/Yb layer that provides the gain under proper pumping. Recently, the optical properties of 2.4 μm wide and 7.8 mm long Er/Yb silicate strip loaded waveguides have been investigated and experimentally measured [45]. It was shown that these structures can provide of up to 5.5 dB of signal amplification at 1530 nm. The coupling constants between waveguides can be controlled by adjusting the distances $d_{1,2}$ and the gradient loss can be achieved by several methods. For example, similar to the work in [13], loss can be introduced through periodic thin metal film stripes (not shown in Fig. 4a) with varying duty cycles on top of each waveguides. Another possibility is to imprint diffraction grating on top of the waveguides to provide loss through the coupling to the continuum. The grating parameters will be then designed to provide exactly the desired loss for each guiding channel. We note that introducing losses by either one of the aforementioned techniques can perturb the effective index of the guided modes. This effect can be offset by varying the ridge width and/or high.

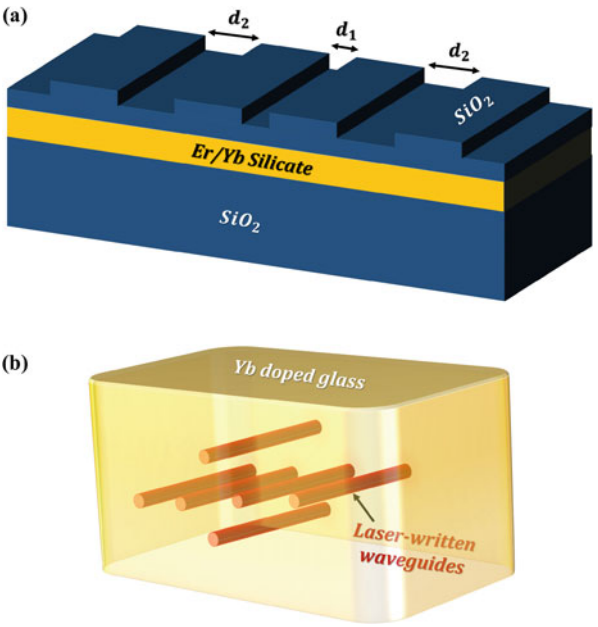

Fig. 4 Schematics of possible implementation of PT networks using (**a**) Er/Yr planar waveguide technology, (**b**) Two dimensional Er/Yr laser written waveguide channels. Details about material systems and principle of operations are presented in the text

The implementation of the two dimensional topologies of Fig. 2 in waveguide systems is more challenging but is still possible through laser writing technology. For example, Taccho et al. have fabricated Er/Yb doped waveguide in a host bulk glass by using femtosecond laser pulses [46]. In these systems, the substrate was made of phosphate glass doped with Er_2O_3 and Yr_2O_3. The operating wavelength was 1533.5 nm and the optical gain was 4 dB. The gradient optical losses in these geometries can be achieved by introducing small curvature in each waveguide channel [47]. Figure 4b shows a schematic of such arrangements where again the distances between waveguides can be engineered to produce the desired coupling coefficients.

Another attractive alternative for implementing higher order exceptional points is by using coupled resonators. This option was recently employed to build photonic networks having a third order exceptional point [27] (see Fig. 5) and demonstrating their ultrasensitivity for external perturbation [48, 49]. While in principle, the same strategy can be utilized to implement the PT network of Fig. 2b, due to its more complexity, undesirable cross coupling might present a real obstacle. Under these circumstances, long distance coupling such as demonstrated by Sato et al. [50] can provide a solution. In all these mircoring implementations, gradient loss can be introduced by a judicious deformation of the ring structure to tune the quality factor. Alternatively, one can keep the radiation loss constant and instead vary the optical gain by controlling the intensity gradient of the pump beam [50]. Finally we note that other platforms such as electric circuits [51] for instance can be also used to implement and experimentally investigate the PT-symmetric networks presented in this work.

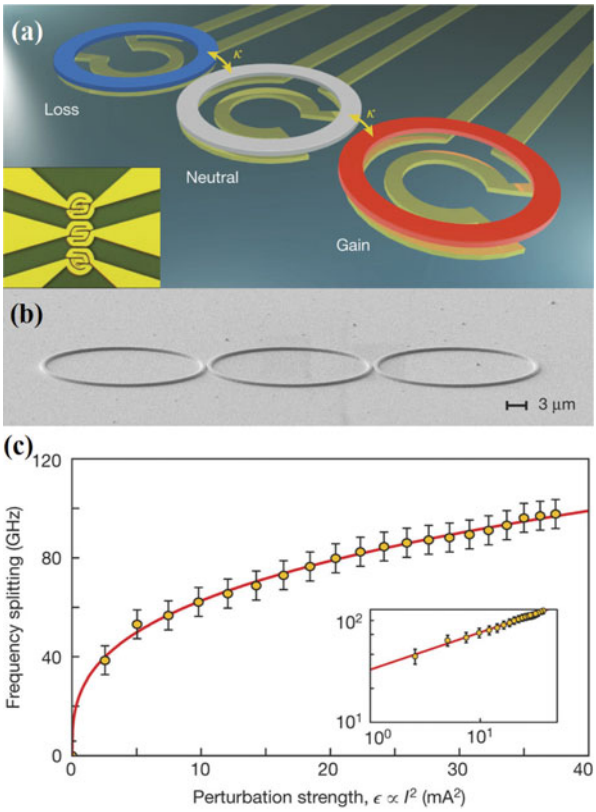

Fig. 5 (**a**) A PT-symmetric ternary microring system with equidistantly spaced cavities. The two edge resonators experience equal gain and loss while the central one is neutral. Each ring (radius, 10 μm; width, 500 nm; height, 210 nm) consists of six quantum wells and the whole structure is fabricated on an InP wafer. The ability to fine-tune the resonant frequency of each cavity is achieved via three gold microheaters (thickness, approximately 150 nm). Additionally, the microheaters are also used to introduce thermal perturbations. (**b**) An SEM image of the structure at an intermediate fabrication step. (**c**) The splitting between two neighbouring lasing lines as a function of the perturbation applied to the mircoheaters though the current I^2. Inset shows a line with a slope of 1/3 on a logarithmic scale. The solid lines are the simulated cube-root behaviour, the filled circles denote experimental data, and the error bars indicate the uncertainty in frequency measurements due to the spectrometer

6 Conclusion

In conclusion, we reviewed the recursive bosonic quantization scheme and how it can be used to construct discrete networks having higher order exceptional points. We have also examined the conservation laws associated with these structures as well as their extreme oscillatory dynamics when operating in the PT phase near a higher order EP. Finally we have discussed possible implementations for higher

order EPs using waveguide arrays and the recent experimental demonstration of an optical sensor based on an EP of order three using microcavity arrays. Future experiments achieving more control over the design parameters can open the door for building even more responsive sensors for applications in industry and health care.

Acknowledgements R. El-Ganainy acknowledges support from Henes Center for Quantum Phenomena at Michigan Technological University.

Appendix

Here we present more details on the diagonalization of the Bose-Hubbard Hamiltonian in Eq. (1). Essentially, this can be done by using the following two transformations:

$$\begin{pmatrix}\hat{b}_e\\ \hat{b}_o\end{pmatrix} = R\begin{pmatrix}\hat{a}_1\\ \hat{a}_2\end{pmatrix},\ \begin{pmatrix}\hat{b}_e^{+}\\ \hat{b}_o^{+}\end{pmatrix} = R\begin{pmatrix}\hat{a}_1^{\dagger}\\ \hat{a}_2^{\dagger}\end{pmatrix},\ R = \begin{bmatrix}\cos(\alpha/2) & \sin(\alpha/2)\\ -\sin(\alpha/2) & \cos(\alpha/2)\end{bmatrix}, \tag{11}$$

where $\tan\alpha = -\frac{2\kappa}{i\gamma}$. It is important here to note that since α is a complex number, the operators $\hat{b}_{e,o}^{+}$ and $\hat{b}_{e,o}$ are not Hermitian conjugate (hence the use of the superscript '+' instead of '†'). As will see, this however does not affect the diagonlization scheme which relies mainly on the commutation algebra.

In terms of the new operators, the Hamiltonian $\hat{H}_2^{(1)}$ in Eq. (1) takes the form $\hat{H}_2^{(1)} = -\varepsilon(\hat{b}_e^{+}\hat{b}_e - \hat{b}_o^{+}\hat{b}_o)$, with $\varepsilon = \hbar\sqrt{\kappa^2 - (\gamma/2)^2}$. Additionally, from Eqs. (11) , it is straightforward to show that $[\hat{b}_i, \hat{b}_j] = [\hat{b}_i^{+}, \hat{b}_j^{+}] = 0$, $[\hat{b}_i, \hat{b}_j^{+}] = \delta_{ij}$. Thus, $\hat{b}_{e,o}^{+}$ and $\hat{b}_{e,o}$ can be still interpreted as the creation and annihilation operators for the non-orthogonal supermodes of the non-Hermitian system. The eigenvalues can be then obtained by populating these supermodes by certain boson numbers as explained in details in the main text.

References

1. Needham, T.: Visual Complex Analysis. Clarendon Press, Oxford (1998)
2. Feng, L., El-Ganainy, R., Ge, L.: Non-Hermitian photonics based on parity-time symmetry. Nat. Photonics **11**(12), 752 (2017)
3. El-Ganainy, R., Makris, K.G., Khajavikhan, M., Musslimani, Z.H., Rotter, S., Christodoulides, D.N.: Non-Hermitian physics and PT symmetry. Nat. Phys. **14**, 11 (2018)
4. Heiss, W.D.: Exceptional points of non-Hermitian operators. J. Phys. A Math. Gen. **37**(6), 2455 (2004)
5. Müller, M., Rotter, I.: Exceptional points in open quantum systems. J. Phys. A Math. Theor. **41**(24), 244018 (2008)

6. Dembowski, C., Gräf, H.D., Harney, H.L., Heine, A., Heiss, W.D., Rehfeld, H., Richter, A.: Experimental observation of the topological structure of exceptional points. Phys. Rev. Lett. **86**(5), 787 (2001)
7. Bender, C.M., Boettcher, S.: Real spectra in non-Hermitian Hamiltonians having PT symmetry. Phys. Rev. Lett. **80**(24), 5243 (1998)
8. Bender, C.M.: Making sense of non-Hermitian Hamiltonians. Rep. Prog. Phys. **70**, 947 (2007)
9. El-Ganainy, R., Makris, K.G., Christodoulides, D.N., Musslimani, Z.H.: Theory of coupled optical PT-symmetric structures. Opt. Lett. **32**(17), 2632 (2007)
10. Makris, K.G., El-Ganainy, R., Christodoulides, D.N., Musslimani, Z.H.: Beam dynamics in PT symmetric optical lattices. Phys. Rev. Lett. **100**(10), 103904 (2008)
11. Musslimani, Z.H., Makris, K.G., El-Ganainy, R., Christodoulides, D.N.: Optical solitons in PT periodic potentials. Phys. Rev. Lett. **100**(3), 030402 (2008)
12. Makris, K.G., El-Ganainy, R., Christodoulides, D.N., Musslimani, Z.H.: PT-symmetric optical lattices. Phys. Rev. A **81**(6), 063807 (2010)
13. Guo, A., Salamo, G.J., Duchesne, D., Morandotti, R., Volatier-Ravat, M., Aimez, V., Siviloglou, G.A., Christodoulides, D.N.: Observation of PT-symmetry breaking in complex optical potentials. Phys. Rev. Lett. **103**(9), 093902 (2009)
14. Rüter, C.E., Makris, K.G., El-Ganainy, R., Christodoulides, D.N., Segev, M., Kip, D.: Observation of parity-time symmetry in optics. Nat. Phys. **6**(3), 192 (2010)
15. Liertzer, M., Ge, L., Cerjan, A., Stone, A.D., Treci, H.E., Rotter, S.: Pump-induced exceptional points in lasers. Phys. Rev. Lett. **108**(17), 173901 (2012)
16. Brandstetter, M., Liertzer, M., Deutsch, C., Klang, P., Schöberl, J., Türeci, H.E., Strasser, G., Unterrainer, K., Rotter, S.: Reversing the pump dependence of a laser at an exceptional point. Nat. Commun. **5**, 4034 (2014)
17. Peng, B., Özdemir, S.K., Rotter, S., Yilmaz, H., Liertzer, M., Monifi, F., Bender, C.M., Nori, F., Yang, L.: Loss-induced suppression and revival of lasing. Science **346**(6207), 328 (2014)
18. El-Ganainy, R., Khajavikhan, M., Ge, L.: Exceptional points and lasing self-termination in photonic molecules. Phys. Rev. A **90**(1), 013802 (2014)
19. Lin, Z., Ramezani, H., Eichelkraut, T., Kottos, T., Cao, H., Christodoulides, D.N.: Unidirectional invisibility induced by PT-symmetric periodic structures. Phys. Rev. Lett. **106**(21), 213901 (2011)
20. Longhi, S.: Half-spectral unidirectional invisibility in non-Hermitian periodic optical structures. Opt. Lett. **40**, 1117–1120 (2015)
21. Feng, L.: Experimental demonstration of a unidirectional reflectionless parity-time metamaterial at optical frequencies. Nat. Mater. **12**, 108 (2013)
22. Ramezani, H., Kottos, T., El-Ganainy, R., Christodoulides, D.N.: Unidirectional nonlinear PT-symmetric optical structures. Phys. Rev. A **82**(4), 043803 (2010)
23. Peng, B., Özdemir, S.K., Lei, F., Monifi, F., Gianfreda, M., Long, G.L., Fan, S., Nori, F., Bender, C.M., Yang, L.: Parity-time-symmetric whispering-gallery microcavities. Nat. Phys. **10**(5), 394 (2014)
24. Aleahmad, P., Khajavikhan, M., Christodoulides, D.N., LiKamWa, P.: Integrated multi-port circulators for unidirectional optical information transport. Sci. Rep. **7**, 2129 (2017)
25. Hodaei, H., Miri, M.A., Heinrich, M., Christodoulides, D.N., Khajavikhan, M.: Parity-time-symmetric microring lasers. Science **346**(6212), 975 (2014)
26. Feng, L., Wong, Z.J., Ma, R.M., Wang, Y., Zhang, X.: Single-mode laser by parity-time symmetry breaking. Science **346**(6212), 972 (2014)
27. Hodaei, H., Hassan, A.U., Wittek, S., Garcia-Gracia, H., El-Ganainy, R., Christodoulides, D.N., Khajavikhan, M.: Enhanced sensitivity at higher-order exceptional points. Nature **548**(7666), 187 (2017)
28. Chen, W., Özdemir, S.K., Zhao, G., Wiersig, J., Yang, L.: Exceptional points enhance sensing in an optical microcavity. Nature **548**(7666), 192 (2017)
29. El-Ganainy, R., Ge, L., Khajavikhan, M., Christodoulides, D.N.: Supersymmetric laser arrays. Phys. Rev. A **92**(3), 033818 (2015)

30. Teimourpour, M.H., Ge, L., Christodoulides, D.N., El-Ganainy, R.: Non-Hermitian engineering of single mode two dimensional laser arrays. Sci. Rep. **6**, 33253 (2016)
31. El-Ganainy, R., Dadap, J.I., Osgood, R.M.: Optical parametric amplification via non-Hermitian phase matching. Opt. Lett. **40**(21), 5086 (2015)
32. Zhong, Q., Ahmed, A., Dadap, J.I., Osgood, R.M., Jr., El-Ganainy, R.: Parametric amplification in quasi-PT symmetric coupled waveguide structures. New J. Phys. **18**(12), 125006 (2016)
33. Gilles, D., Eva-Maria, G., Demange, G., Graefe, E.M.: Signatures of three coalescing eigenfunctions. J. Phys. A Math. Theor. **45**(2), 025303 (2012)
34. Lin, Z., Pick, A., Lončar, M., Rodriguez, A.W.: Enhanced spontaneous emission at third-order Dirac exceptional points in inverse-designed photonic crystals. Phys. Rev. Lett. **117**(10), 107402 (2016)
35. Heiss, W.D., Wunner, G.: A model of three coupled wave guides and third order exceptional points. J. Phys. A Math. Theor. **49**(49), 495303 (2016)
36. Jing, H., Özdemir, S.K., Lü, H., Nori, F.: High-order exceptional points in optomechanics. Sci. Rep. **7**(1), 3386 (2017)
37. Schnabel, J., Cartarius, H., Main, J., Wunner, G., Heiss, W.D.: PT-symmetric waveguide system with evidence of a third-order exceptional point. Phys. Rev. A **95**(5), 053868 (2017)
38. Teimourpour, M.H., El-Ganainy, R., Eisfeld, A., Szameit, A., Christodoulides, D.N.: Light transport in PT-invariant photonic structures with hidden symmetries. Phys. Rev. A **90**(5), 053817 (2014)
39. Hiller, M., Kottos, T., Ossipov, A.: Bifurcations in resonance widths of an open Bose-Hubbard dimer. Phys. Rev. A **73**(6), 063625 (2006)
40. Graefe, E.M., Günther, U., Korsch, H.J., Niederle, A.E.: A non-Hermitian PT symmetric Bose-Hubbard model: eigenvalue rings from unfolding higher-order exceptional points. J. Phys. A Math. Theor. **41**(25), 255206 (2008)
41. Ma, Y., Edelman, A.: Nongeneric eigenvalue perturbations of Jordan blocks. Linear Algebra Appl. **273**(1), 45 (1998)
42. Emil, A.Y., William, H., Boris, L.A., Sriram, B.S.: Extracting hidden symmetry from the energy spectrum. J. Phys. A Math. Gen. **36**(10), 2577 (2003)
43. Mostafazadeh, A.: Extracting hidden symmetry from the energy spectrum. Pseudo-Hermitian representation of quantum mechanics. Int. J. Geom. Meth. Mod. Phys. **07**(07), 1191 (2010)
44. Zhong, Q., Christodoulides, D.N., Khajavikhan, M., Makris, K.G., El-Ganainy, R.: Power-law scaling of extreme dynamics near higher-order exceptional points. Phys. Rev. A **97**(2), 020105 (2018)
45. Guo, R., Wang, X., Zang, K., Wang, B., Wang, L., Gao, L., Zhou, Z.: Optical amplification in Er/Yb silicate strip loaded waveguide. Appl. Phys. Lett. **99**(16), 161115 (2011)
46. Taccheo, S., Della Valle, G., Osellame, R., Cerullo, G., Chiodo, N., Laporta, P., Svelto, O., Killi, A., Morgner, U., Lederer, M., Kopf, D.: Er:Yb-doped waveguide laser fabricated by femtosecond laser pulses. Opt. Lett. **29**(22), 2626 (2004)
47. Zeuner, J.M., Rechtsman, M.C., Plotnik, Y., Lumer, Y., Nolte, S., Rudner, M.S., Segev, M., Szameit, A., Observation of a topological transition in the bulk of a non-Hermitian System: Phys. Rev. Lett. **115**(4), 040402 (2015)
48. Wiersig, J.: Enhancing the sensitivity of frequency and energy splitting detection by using exceptional points: application to microcavity sensors for single-particle detection. Phys. Rev. Lett. **112**(20), 203901 (2014)
49. Wiersig, J.: Sensors operating at exceptional points: General theory. Phys. Rev. A **93**(3), 033809 (2016)
50. Sato, Y., Tanaka, Y., Upham, J., Takahashi, Y., Asano, T., Noda, S.: Strong coupling between distant photonic nanocavities and its dynamic control. Nat. Photonics **6**, 56 (2011)
51. Schindler, J., Li, A., Zheng, M.C., Ellis, F.M., Kottos, T.: Experimental study of active LRC circuits with PT symmetries. Phys. Rev. A **84**(4), 040101 (2011)

Non-Hermitian Optical Waveguide Couplers

Sergey V. Suchkov, Andrey A. Sukhorukov, and Yuri S. Kivshar

Abstract We discuss the PT symmetry effects in non-Hermitian waveguiding geometries starting from a classical example of a two-core coupler with gain and loss. We demonstrate that a nonlinear response can break the PT symmetry in a coupler, and discuss the regimes of parametric amplification and nonlocality associated with such systems. Then, we analyse non-Hermitical trimers and also a PT-symmetric system embedded into an array of waveguides. Finally, we demonstrate the existence of nontrivial modes in non-Hermitian waveguiding structures with asymmetric layers of gain and loss.

1 Introduction

As demonstarated by Bender and Boettcher [1], there exists a class of parity-time (PT) invariant non-Hermitian Hamiltonians that can possess a real eigenspectrum. Due to a similarity between the Schrödinger equation in quantum mechanics and the equation for the slowly varying mode amplitude in optics, it was revealed that the PT effects can be realized and have significant importance on the dynamics of non-conservative optical structures with symmetrically distributed gain and loss regions [2–4]. In particular, optical systems can feature a transition between a *PT-symmetric phase*, when all eigenvalues are real and there is no net amplification, and a *broken phase*, when some of the eigenvalues become complex and some of the associated modes get amplified. This transition enables, in particular, the development of new types of single-mode lasers [5, 6]. The phase transitions are associated with exceptional points [7, 8] in the parameter space where eigenvalues and eigenvectors merge, and which also appear under more general conditions in non-PT-symmetric systems [9–11]. Furthermore, it was shown that PT-symmetry is

S. V. Suchkov (✉) · A. A. Sukhorukov · Y. S. Kivshar
Nonlinear Physics Centre, Research School of Physics and Engineering, Australian National University, Canberra, ACT, Australia

D. Christodoulides, J. Yang (eds.), *Parity-time Symmetry and Its Applications*, Springer Tracts in Modern Physics 280,
https://doi.org/10.1007/978-981-13-1247-2_11

neither sufficient nor necessary condition to have a real spectrum [12], which can also occur in a more general class of pseudo-Hermitian systems.

In this chapter we consider different non-Hermition structures composed of several optical waveguides, determine necessary conditions for their spectrum to be real, and outline the potential of these systems for light control. In Sect. 2, we discuss the specific features of nonlinear interactions and nonlocal effects associated with non-conservative coupled waveguides. We firstly showcase rich physics and phenomena due to the interplay of nonlinearity and PT-symmetry in Sect. 2.1. Next, in Sect. 2.2 we analyse nonlinear parametric amplification and the emergence of anti-PT symmetry in spectral domain. Then, in Sect. 2.3 we show that a PT-symmetric coupler incorporated into a chain of conservative waveguides exhibits nonlocal sensitivity to the type of boundaries. And in Sect. 2.4, we outline the features of light dynamics in the PT-symmetric dimer modulated along the propagation direction. In Sect. 3 we consider trimer structures and compare the PT-symmetric and pseudo-Hermitian configurations. We describe general properties of pseudo-Hermitian trimer configuration, formulate a necessary condition for the spectrum to be real, and analyze wave scattering by a pseudo-Hermitian trimer in the chain of conservative waveguides. In the following Sect. 4, we study guided modes in a three-layer non-Hermitian optical coupler with gain and loss regions which are not necessarily distributed symmetrically. We show that this structure possesses greater functionality than conventional PT-symmetric optical waveguides. Finally, we present conclusions and outlook in Sect. 5.

2 Nonlinear Coupled Waveguides

A pair of coupled waveguides with gain and loss represents the simplest configuration of a PT-symmetric optical system, as sketched in Fig. 1a. However, such a system can already showcase rich physics and phenomena associated with the interplay of nonlinearity and PT-symmetry. In the following, we first discuss the effect of nonlinearity on the optical modes and the phenomenon of nonlinearly-induced PT symmetry breaking, and then outline the effects of nonlocality and modulation which have a potential to lead to new nonlinear interaction regimes.

2.1 Nonlinear Coupler and Symmetry Breaking

The effect of nonlinearity on the beam dynamics in directional couplers composed of waveguides with gain and loss was originally described theoretically already two decades ago [13, 14]. It was predicted that such structures can offer benefits for all-optical switching in the nonlinear regime, lowering the switching power and attaining a sharper switching transition. In the last decade, the renewed interest in

such structures as realizations of PT symmetric optical systems has led to a series of extensive theoretical and more recently experimental studies.

We consider the effect of Kerr-type nonlinearity, which can modify the refractive index in each of the waveguides, depending on the optical intensity [13–18]. This effect can be modeled by including nonlinear terms in the coupled-mode equations as follows [16],

$$\begin{aligned} i\frac{da_1}{dz} + i\rho a_1 + Ca_2 + G(|a_1|^2)a_1 = 0, \\ i\frac{da_2}{dz} - i\rho a_2 + Ca_1 + G(|a_2|^2)a_2 = 0, \end{aligned} \tag{1}$$

where z is the propagation distance, a_1 and a_2 are the mode amplitudes in the first and second waveguide, respectively, the function G characterizes the nonlinear response (we assume it to be real-valued), C is the coupling coefficient between the modes of two waveguides, and $\rho > 0$ is the loss/gain coefficient in the first and second waveguides. We consider here the regime below the linear PT-symmetry breaking threshold, when $\rho < C$.

It was found that nonlinear solutions belong to *two classes* [16]: (i) periodic solutions, where the intensities and relative phases in two waveguides are exactly restored after each period ($z \rightarrow z + z_p$) (Fig. 1b), or (ii) solutions where the total intensity grows without bound due to nonlinearly-induced symmetry breaking (Fig. 1c). This classification is valid for arbitrary Kerr-type nonlinearities with smooth response functions $G(I)$. Quite remarkably, in case of cubic nonlinear response with $G(I) = \gamma I$, Eqs. (1) were shown to be integrable and their solutions can be formulated analytically [15, 17–21]. The dependence of the minimal input intensity I_{cr}, required for nonlinear switching, on gain/loss coefficient is shown in Fig. 1d, which illustrates that the threshold for nonlinear switching is drastically reduced for larger gain/loss coefficients.

It is convenient to represent the mode amplitudes in the following form,

$$\begin{aligned} a_1 = \sqrt{I(z)}\cos[\theta(z)]\exp[+i\varphi(z)/2]\exp[i\beta(z)], \\ a_2 = \sqrt{I(z)}\sin[\theta(z)]\exp[-i\varphi(z)/2]\exp[i\beta(z)], \end{aligned} \tag{2}$$

where I is the total intensity, θ and φ define the relative intensities and phases between the two input waveguides, and β is the overall phase. Then, the initial conditions corresponding to different solution types (oscillating or growing) can be conveniently visualized on a phase plane, see an example in Fig. 1e. This plot illustrates that even for high intensity above the threshold, the type of dynamics depends on the relative amplitudes and phases in the two waveguides. Interestingly, the type of nonlinear dynamics remains the same if we swap the intensities between the two waveguides, which corresponds to a transformation $\theta \rightarrow \pi/2 - \theta$. In particular, we could couple light at the input just to the waveguide with loss, or to the waveguide with gain, and the type of dynamics would be the same. This

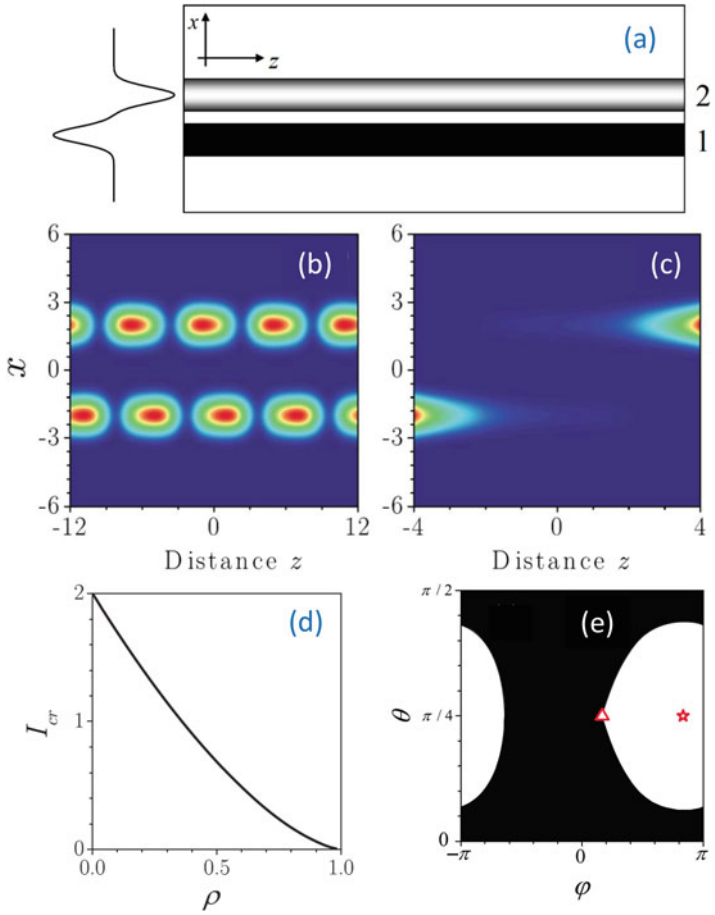

Fig. 1 (**a**) Scheme of nonlinear PT-symmetric directional coupler with balanced loss in waveguide 1 and gain in waveguide 2. (**b**,**c**) Intensity evolution along the propagation direction. Shown are the regimes of (**b**) periodic oscillations and (**c**) nonlinear localization and amplification in the waveguide with gain. (**d**) Minimum critical intensity required for nonlinear PT-symmetry breaking vs. the gain/loss coefficient. (**e**) Regions of PT symmetry (white shading) and symmetry breaking with nonlinear switching (black shading) in the plane of initial conditions. Star and triangle mark stable and unstable stationary solutions, respectively. Parameters are $G(I) = \gamma I$, $\gamma = 1$, $C = 1$, (**b**,**c**,**e**) $\rho = 0.5$ and $I = 2.2$, (**b**) $\varphi = \pi/6 - \pi/20$, (**c**) $\varphi = \pi/6 + \pi/20$. (Adopted from [16])

is a counter-intuitive result, since in the first case the total intensity will initially decrease, whereas in the second case the total intensity will be growing. However, in both cases the type of dynamics will be determined only by the initial intensity level. This is a consequence of linear PT-symmetry in the strongly nonlinear regime.

Whereas in general solutions are oscillating or growing, for particular initial conditions the wave intensities can remain constant. Such a regime corresponds to the excitation of *stationary nonlinear modes*, which can be viewed as a

generalization of linear supermodes. They are positioned at the phase space points $(I = I_0, \theta = \pi/4, \varphi = \varphi_\pm)$ and $\beta = \beta_\pm z$, where $\beta_\pm = G(I_0/2) + C\cos(\varphi_\pm)$, $\sin(\varphi_\pm) = \rho/C$, and $\cos(\varphi_\pm) = \mp[1 - (\rho/C)^2]^{1/2}$. The fixed point in phase space is a stable center if (i) $\tilde{\gamma} < \tilde{\gamma}_{\rm cr}$ and $\varphi = \varphi_-$ or (ii) $\tilde{\gamma} > -\tilde{\gamma}_{\rm cr}$ and $\varphi = \varphi_+$, where $\tilde{\gamma}_{\rm cr} = |\cos(\varphi_\pm)|$ and $\tilde{\gamma} = G'(I_0/2)I_0/(2C)$ (prime stands for the derivative). If these conditions are not satisfied, then the fixed point is a saddle, which indicates an instability. In case of self-focusing Kerr nonlinearity, $G(I) = \gamma I$ with $\gamma > 0$, the stationary point at φ_+ is always stable at arbitrarily high intensities, whereas at φ_- the instability appears for $I_0 > I_{0\rm cr} = 2[1 - \rho^2]^{1/2}$. The stable point at φ_+ is indicated in Fig. 1e by a star, and unstable at φ_- – by a triangle. We note that the unstable point is located at a boundary between the domains of periodic or growing solutions.

Nonlinear PT couplers can have applications for efficient all-optical signal manipulation with reduced switching power and the possibility to perform intensity-dependent amplification. Additionally, such couplers can operate as unidirectional optical valves [15] when nonlinearity breaks PT symmetry, as in this case the output beam becomes localized in the gain channel, irrespective of initial conditions. It was suggested that switching performance can be enhanced with application of Bragg gratings, involving specially engineered modulation of the real and imaginary parts of the optical refractive index [22]. These concepts can be extended to other physical systems beyond optics, including electrical circuits [23, 24].

A PT-symmetric coupler with additional gain and loss proportional to nonlinear terms has been studied in Refs. [25–27]. If such nonlinear PT-symmetric coupler is embedded into a linear chain, it may give rise to new types of nonlinear Fano resonances, with entirely suppressed or greatly amplified transmission [26]. A PT coupler with nonlinear saturation was also formulated based on Wick rotation, which introduces imaginary-time propagation [28].

2.2 *Anti-PT-Symmetry and Parametric Amplification*

Nonlinear modes in PT potentials can also be supported by quadratic ($\chi^{(2)}$) optical nonlinearity [29–31]. Compared to the case of Kerr-type nonlinearity discussed above, quadratic nonlinear response involves parametric coupling of the fundamental and second-harmonic optical waves. Such interactions give rise to a rich family of localized solitons.

Quadratic nonlinearity can also facilitate a fundamentally important regime of parametric amplification, which is efficiently realized through difference-frequency generation [32]. Here the amplification rate is determined by the pump, enabling ultrafast all-optical tunability. Quadratic nonlinear PT-symmetric systems can, on one hand, realize ultrafast spatial signal switching through pump-controlled breaking of PT symmetry, and, on the other hand, they enable spectrally-selective mode amplification [33]. The process of optical parametric amplification in a PT coupler based on nonlinear mixing between a strong pump, and signal and idler

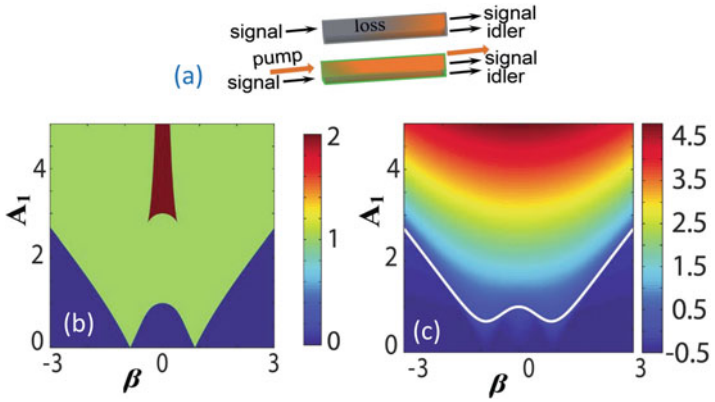

Fig. 2 PT parametric amplifier: (**a**) scheme of wave mixing in a quadratic nonlinear coupler with linear absorption in one waveguide. (**b**) Number of spectrally anti-PT symmetric mode pairs, (**c**) the largest mode gain (white line marks zero), vs. the input pump amplitude in the first waveguide and the phase-mismatch. (Adopted from Ref. [33])

waves is illustrated in Fig. 2a. The evolution of near-degenerate (with close similar frequencies) signal and idler waves in the undepleted pump regime is modelled by coupled-mode equations, which can be represented in a Hamiltonian form:

$$i\frac{\partial \mathbf{a}}{\partial z} = \mathbf{H}\mathbf{a}, \tag{3}$$

where $\mathbf{a}(z) = \left(a_{s1}(z), a_{s2}(z), a_{i1}^*(z), a_{i2}^*(z)\right)^T$ is a vector of wave amplitudes in the two waveguides, the subscripts stand for signal ('s') and idler ('i') waves in two waveguides ('1' and '2'),

$$\mathbf{H} = \begin{pmatrix} \beta - i\gamma_1 & -C & iA_1 & 0 \\ -C & \beta - i\gamma_2 & 0 & iA_2 \\ iA_1^* & 0 & -\beta - i\gamma_1 & C \\ 0 & iA_2^* & C & -\beta - i\gamma_2 \end{pmatrix}, \tag{4}$$

β defines the phase mismatch of parametric wave mixing, $\gamma_{1,2}$ are the linear loss coefficients, C is the mode coupling coefficient between the waveguides, and $A_{1,2}$ are the normalized input pump amplitudes.

Remarkably, the Hamiltonian possesses a *spectral anti-PT symmetry*, corresponding to a negative sign on the right-hand side of the following equality,

$$\mathbf{P}_{1,+}\mathbf{P}_{2,+}\mathbf{T}\mathbf{H} = -\mathbf{H}\mathbf{P}_{1,+}\mathbf{P}_{2,+}\mathbf{T}. \tag{5}$$

Here $\mathbf{T}$ is a usual time-reversal operator which changes $z \rightarrow -z$ and performs a complex conjugation. The *parity operators act in spectral domain*, interchanging the signal and idler waves,

$$\mathbf{P}_{1,\pm} = \left\{a_{s1} \leftrightarrow \pm a_{i1}^{*}\right\}, \ \mathbf{P}_{2,\pm} = \left\{a_{s2} \leftrightarrow \pm a_{i2}^{*}\right\}. \tag{6}$$

The Hamiltonian is linear, and the properties of its solutions are defined by the spectrum of its four eigenmodes. Overall, there can be *three possible symmetry regimes*: (i) two mode pairs with broken spectral anti-PT symmetry, (ii) one pair of PT-broken modes and a pair of anti-PT symmetric modes, or (iii) two pairs of anti-PT symmetric modes. Characteristic dependence of the number of PT-symmetric mode pairs on the pump amplitude in the first waveguide and the phase-mismatch is shown in Fig. 2b, and the largest mode gain is presented in Fig. 2c. Remarkably, the established relations of mode symmetry and gain/loss are reversed in comparison to previously discussed spatial PT-symmetry in directional couplers, due to the spectral *anti*-PT symmetry of parametric wave mixing. Specifically, when all modes have broken spectral PT symmetry (blue shaded regions in Fig. 2b), the pairs of eigenmodes exhibit the same amount of gain/loss, and effectively the amounts of gain and loss are averaged out between the eigenmodes. However, upon transition to the region with spectrally PT-symmetric modes (green and red shaded regions in Fig. 2b), there appears an unequal redistribution of gain and loss between the modes. One PT-symmetric eigenmode exhibits gain much larger than all other modes, while the latter experience stronger loss. Such sensitivity of amplification to PT-breaking threshold could be used to discriminate between multiple spectral modes, analogous to the concept of PT-lasers [5, 6].

In case of perfect phase-matching, $\beta = 0$, and pump amplitudes of the same phase $\mathrm{Im}(A_1) = \mathrm{Im}(A_2) = 0$, the Hamiltonian also features *spatial PT symmetry*. Both the spatial and spectral PT-symmetry breaking occurs simultaneously at the threshold $|\gamma_1 - \gamma_2 - \eta(A_1 + A_2)| = 2C$. However, the spatial and spectral symmetries are opposite: a mode pair is spatially PT-symmetric and has spectrally broken symmetry below threshold, whereas the situation is reversed above the threshold. Numerical simulations reveal a strong connection between spectral symmetry and spatial dynamics even for non-zero phase mismatches. Specifically, an increase of pump amplitude can control the period of mode coupling between the waveguides, while the oscillations get suppressed close to the spectral PT threshold. It is expected that due to the universality of parametric amplification processes, these concepts can be extended to different physical mechanisms including four wave mixing in media with Kerr-type optical nonlinearity.

2.3 Nonlocal Effects

PT-symmetric potentials appear in many physical contexts, and one feature actively investigated in the context of quantum theories is the property of *nonlocality*, where PT-defect dynamics can be sensitive to potential profile at distant locations, raising

questions about the observability of such behavior in real physical systems [34, 35]. In the following, we present a classical analogue of quantum nonlocality in optical PT-symmetric structures with gain and loss where beam dynamics can depend on arbitrarily distant boundaries.

To demonstrate the phenomenon of nonlocality in optical structures, we compare arrays of coupled optical waveguides with planar and circular geometries as illustrated in Fig. 3a, b. The beam profile is determined by the mode amplitudes a_n at individual waveguides, and mode overlap between waveguides is characterized by coupling coefficients: C_2 between the central waveguides $n = 0, 1$, and C_1 between all other neighboring waveguides. We consider PT-symmetric structure composed of waveguide with loss at location $n = 0$ and with gain at the adjacent waveguide $n = 1$. The absolute magnitudes of gain/loss should be equal to satisfy the PT-symmetry condition. We use the coupled-mode equations [4, 36, 37] to model the beam propagation:

$$i\frac{da_n}{dz} + C_1 a_{n-1} + C_1 a_{n+1} = 0, \quad n \neq 0, 1 \tag{7}$$

$$i\frac{da_0}{dz} + i\rho a_0 + C_1 a_{-1} + C_2 a_1 = 0, \tag{8}$$

$$i\frac{da_1}{dz} - i\rho a_1 + C_2 a_0 + C_1 a_2 = 0, \tag{9}$$

where n is the waveguide number, z is the propagation distance, a_n are the mode amplitudes at waveguides, $\rho > 0$ defines the rate of loss at 0-th and gain at 1-st waveguides, and $C_{1,2}$ are the coupling coefficients between the modes of waveguides. The boundary conditions are zero for a planar structure (Fig. 3a),

$$a_{N+2} \equiv 0, \quad a_{-N-1} \equiv 0, \tag{10}$$

and periodic for a circular configuration (Fig. 3b),

$$a_{N+2} \equiv a_{-N}, \quad a_{-N-1} \equiv a_{N+1}. \tag{11}$$

The Eqs. (7), (8), and (9) are linear, since we consider weak optical intensities when the gain saturation and nonlinearity can be neglected. Then, the beam dynamics can be described by analyzing the eigenmodes $a_n = A_n \exp(i\phi_n + i\beta z)$, where $A_n \geq 0$ and real ϕ_n are constant amplitude and phase profiles and β is an eigenvalue (propagation constant).

The analytical expressions for PT-symmetry breaking thresholds in case of planar and circular array configurations were derived in Ref. [38], considering the total number of waveguides $2N$ to be rather large but finite. For a *planar configuration*, the condition of PT-symmetry breaking is

$$|\rho| > \rho_{\mathrm{p}} = |C_2|, \tag{12}$$

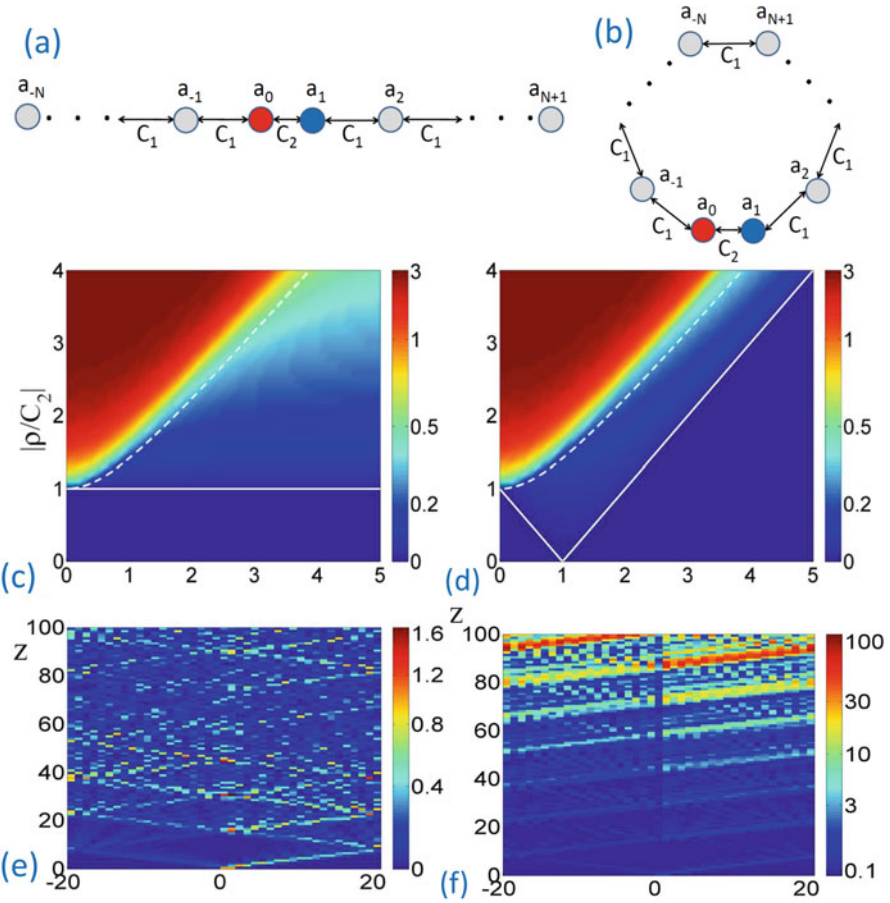

Fig. 3 (**a**, **b**) Schematic of (**a**) planar and (**b**) circular waveguide array with a pair of PT-symmetric waveguides at sites $n = 0, 1$ with balanced gain and loss. (**c**, **d**) Fastest mode amplification rate in parameter plane $|\rho/C_2|$ and $|C_1/C_2|$ for (**c**) planar and (**d**) circular arrays with $N = 20$ waveguides. Solid lines show analytical instability threshold according to (**c**) Eq. (12) and (**d**) Eq. (13), and dashed lines indicate instability threshold for infinitely large structures according to Eq. (14). (**e**, **f**) Optical beam dynamics in (**e**) planar and (**f**) circular waveguide arrays for $\rho/C_2 = 0.8$, $C_1/C_2 = 1.5$, and $N = 20$. (Adopted from Ref. [38])

and the threshold is the same as for an isolated coupler [4], independent on the coupling coefficient in the rest of the array (C_1). This is a surprising result, for example boundaries can have nontrivial effect on stability for planar structures with periodically placed gain and loss elements [39]. The threshold is shown with the solid line in Fig. 3c.

For a *circular configuration*, the threshold condition nontrivially depends on all the structure parameters,

$$|\rho| > \rho_c = ||C_1| - |C_2||\,, \tag{13}$$

and this threshold is shown with solid lines in Fig. 3d. Most remarkably, the PT-symmetry conditions separating fundamentally different cases of real spectrum, when the power is conserved on average, and complex spectrum, when some guided modes experience amplification, are always different for planar and circular arrays of arbitrary size (N) – and this is a manifestation of nonlocality.

From a physical point of view, we should expect that if the *structure size is increased towards infinity*, $N \to \infty$, the type of boundaries should not matter. In this case the PT-symmetry breaking would be associated with the amplification at the waveguide with gain, leading to generation of waves propagating away from the central region, when

$$|\rho| > \rho_{\text{inf}} = \sqrt{C_1^2 + C_2^2}. \tag{14}$$

We show the instability threshold with dashed lines in Fig. 3c, d. When $\rho_{\text{p,c}} < |\rho| < \rho_{\text{inf}}$ for planar ('p') or circular ('c') waveguide arrays, respectively, then there appear unstable modes in arrays of finite length, however their growth rate reduces to zero as $O(N^{-1})$.

As an example, we consider the beam coupled to waveguide number $n = 1$ at the input, and choose the structure parameters $\rho/C_2 = 0.8$ and $C_1/C_2 = 1.5$ such that they correspond to a stable region for planar but an unstable region for circular configuration. The plot of beam dynamics presented in Fig. 3e shows that the power is conserved on average for the planar structure. For the circular geometry, Fig. 3f demonstrates that power grows exponentially as the beam circulates around.

These results suggest an experimental path towards observation of the fundamental property of the PT-symmetric systems associated with their nonlocality, which is an analogue of nonlocality effects raised in the context of quantum theories [34, 35]. Furthermore, new features of nonlinear interactions in presence of PT nonlocality are expected.

2.4 Modulated Waveguide Couplers

Modulation of structure parameters along the propagation direction of coupled optical waveguides with gain and loss can open new opportunities for optical signal control in both linear [40–42] and nonlinear [43–49] regimes. Interestingly, the first studies of couplers with modulated loss and gain were carried out without a consideration of PT symmetry [50–53]. In these studies, it was shown that unidirectional energy transfer between co-propagating optical modes can be achieved in waveguides with longitudinally modulated gain and loss regions. This phenomenon relies on the breaking of the time-reversal symmetry through the modulation of the complex optical refractive index.

When the structural parameters are modulated such that underlying system is not PT-symmetric at any modulation cross-section, the overall dynamics can still

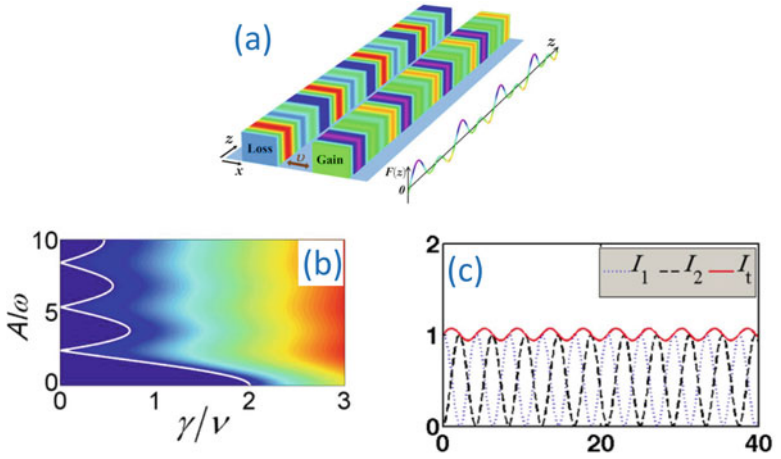

Fig. 4 Quasi-PT symmetry in an aperiodically modulated coupler. (**a**) Schematic of a coupler with symmetric gain and loss, but with asymmetric modulation of the propagation constants. (**b**) The mode growth rate vs. the normalized gain/loss amplitude (horizontal axis) and the modulation strength (vertical axis), for fast modulations. White line marks the boundary of quasi-PT transition. (**c**) Example of almost periodic evolution with very small growth rate in quasi-PT symmetric regime. (Adopted from Ref. [54])

demonstrate the features of pseudo-PT symmetry [54, 55]. The concept of pseudo-PT symmetry corresponds to the PT-symmetry in the effective system, which manifests as quasi-stationary propagation. Such regime can be achieved under high-frequency periodic modulation, when the modulated system can be mapped into an effectively unmodulated one with rescaled parameters. Following Ref. [54], we consider a coupler with balanced gain and loss and modulated propagation constants. For a biharmonic modulation, as illustrated in Fig. 4a, the corresponding Hamiltonian is not PT-symmetric. Nevertheless, the effective system obtained after averaging the high-frequency modulations features PT symmetry. There exists a spontaneous PT-symmetry-breaking transition in the effective system when the imaginary part of quasi-energies, $\mathrm{Im}(\epsilon)$, changes from zero to nonzero, as illustrated in Fig. 4b. It appears surprising that the quasi-energies can be real even when the modulated system is non-PT-symmetric, however the numerical analysis reveals that the eigenvalues of the original modulated structure have a very small but nonzero imaginary part. Accordingly, at intermediate propagation distances the dynamics can be almost exactly periodic in the quasi-PT symmetric regime, as shown in Fig. 4c.

Further interesting possibilities can arise in the case of an aperiodic driving. It was found that a phase diagram analogous to Hofstadter's butterfly spectrum can emerge in PT Hamiltonians [42]. Another example of modulated systems is a PT-symmetric coupler with fluctuating parameters [56]. In such a structure statistically averaged intensity of the field grows independently of the PT symmetry phase of the underlying deterministic system and for any type of fluctuations.

3 Pseudo Hermitian Trimer

In contrast to the PT-symmetric dimer considered in Sect. 2, a system composed of three coupled waveguides has more degrees of freedom and allows different geometric realisations possessing real spectra. Generally, PT-symmetry is not a necessary condition for a spectrum to be real. A concept of pseudo-Hermiticity was introduced in [12] and it states that a Hamiltonian $\mathbf{H}$ is pseudo-Hermitian, if it is non-Hermitian and possesses real eigenspectrum. It can be represented as $\mathbf{H} = \mathbf{A}^{-1}\mathbf{H}'\mathbf{A}$, where $\mathbf{H}'$ is a Hermitian Hamiltonian and $\mathbf{A}$ is an invertible matrix. Thus, when a system is composed of several non-conservative waveguides, there might be various non-PT configurations possessing real eigenspectrum.

We compare the features of a general pseudo-Hermitian (PH) trimer to a PT-symmetric trimer. A PH trimer possesses spatially inhomogeneous gain and dissipation, and generally speaking is not PT-symmetric. The PT-symmetric trimer belongs to the class of PH trimers, but hereinafter when referring to the PH timer we will imply that it is not PT invariant. We determine conditions under which PH and PT trimers possess entirely real spectra, and reveal new opportunities of PH structures to flexibly tailor modes' properties. We will also investigate a behaviour of PT and PH trimers in the chain of conservative waveguides.

3.1 Necessary Conditions for Real Spectrum

We consider a system of three coupled non-conservative waveguides, schematically shown in Fig. 5. Propagation of light through such a system can be described in terms of the coupled mode theory:

$$i\frac{\mathrm{d}}{\mathrm{d}z}\begin{pmatrix} a_{-1} \\ a_0 \\ a_1 \end{pmatrix} + \begin{pmatrix} i\rho & C_{-1} & 0 \\ C_{-1} & i\rho_0 & C_0 \\ 0 & C_0 & i\rho_1 \end{pmatrix}\begin{pmatrix} a_{-1} \\ a_0 \\ a_1 \end{pmatrix} = 0, \tag{15}$$

here a_j is the mode amplitude in the j-th waveguide, $j = -1, 0, 1$, z is the direction of propagation, C_{-1} and C_0 are coupling coefficients between -1-st and 0-th waveguides and 0-th and 1-st waveguides, respectively, $\rho_j > 0$ or $\rho_j < 0$

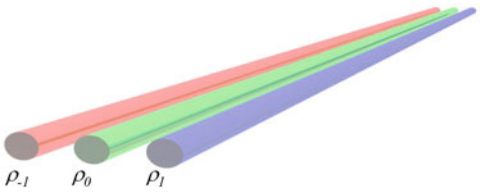

Fig. 5 Schematic of a non-Hermitian trimer with gain/loss strength denoted by ρ_{-1}, ρ_0, and ρ_1

corresponds to loss or gain, respectively. Eigenmodes of such a system can be sought as $a_j = A_j^{(n)} \exp(i\beta_n z)$, where $A_J^{(n)}$ are the constant amplitudes, β_n are the propagation constants, n is the mode index. In this section we determine particular configurations of the non-Hermitian trimer, which provide balance between gain and loss, and feature a real eigenspectrum.

We use a property that a trace of any square matrix equals to the sum of its eigenvalues. Thus, from Eq. (15) we obtain $\sum_j i\rho_j = \sum_n \beta_n$, which means

$$\sum_j \rho_j = 0, \tag{16}$$

if all β_n are real. It should be noted, however, that a more general and practically important situation is when all modes have the same spatially averaged gain/loss $\Delta\rho$ [57], i.e. when $\mathrm{Im}(\beta_n) \equiv \Delta\rho$ for all n. In this case the gauge transformation can be applied, and the system can be reduced to the pseudo-Hermitian or PT-symmetric one.

To determine the next necessary condition of the real spectrum, we consider an eigenmode, $a_j(z)$, of the system. Then it can be shown that $a_j^*(z)(-1)^j$ is also an eigenmode. The latter means that if β_n is a propagation constant, then $-\beta_n^*$ is also a propagation constant. Thus, there are two possible cases: (i) $\beta_k = -\beta_k^*$ for some k, which leads to $\beta_k = 0$ if we assume that the system has an entirely real spectrum; or (ii) $\beta_n = -\beta_m^*$ for a pair of modes with $n \neq m$. Since the total number of modes is equal to the number of waveguides, it follows that for an odd number of waveguides in the system there should always be a mode with zero propagation constant, while all other modes should have counterparts with opposite propagation constants.

We conclude that in the considered case of non-Hermitian trimer, one of the eigenmodes should have a zero propagation constant, $\beta_1 = 0$. It can be shown [58] that the trimer system (15) supports the mode with zero propagation constant if

$$\rho_0 + \frac{C_{-1}^2}{\rho_{-1}} + \frac{C_0^2}{\rho_1} = 0. \tag{17}$$

Condition (17) is another necessary one (but not sufficient) for the whole spectrum to be real-valued. Substituting $a_j = A_j^{(n)} \exp(i\beta_n z)$, $j = -1, 0, 1$ into Eq. (15) and taking to account Eq. (17), we find

$$\beta_1 = 0, \quad \beta_{2,3} = \pm\sqrt{-\rho_1^2 + C_{-1}^2 + C_0^2 + \rho_{-1}\rho_0}, \tag{18}$$

We now use the condition in Eq. (16) to express the three loss/gain coefficients through two independent parameters ρ and θ:

$$\rho \equiv \rho_{-1}, \quad \rho_0 = -\theta\rho, \quad \rho_1 = -(1-\theta)\rho. \tag{19}$$

We analyze Eqs. (18) and determine that the spectrum of Eq. (15) is entirely real under the following conditions:

$$C_0 = \sqrt{(1-\theta)\left(C_{-1}^2 - \theta\rho^2\right)}, \tag{20}$$

$$|\rho| \le \rho_{\text{crit}} = \sqrt{2-\theta}C_{-1}. \tag{21}$$

Since we consider conservative couplings with real coefficients C_{-1} and C_0, then we have an additional restriction on the gain/loss parameter:

$$|\rho| < \rho_{\text{struc}} \equiv C_{-1}/\sqrt{\theta}. \tag{22}$$

Note that condition (21) is stronger than condition (22).

From Eqs. (20) and (21) it follows that system (15) can have an entirely real spectrum if and only if $\theta \le 1$. This means that two waveguides of the trimer, which are of the same type (both with gain or loss) should not be separated by a waveguide of other type (loss or gain, respectively). This interesting result stems from the geometric mode symmetry ($\beta_1 = 0$) and specific gain/loss distribution providing energy balance.

3.2 Eigenmodes of the Pseudo-Hermitian Trimer

Without loss of generality, we consider the case $0 \le \theta < 1$ corresponding to the right and middle waveguides of the same type and the left waveguide of the opposite type. The case $\theta = 1$ corresponds to the uncoupled system of a dimer and a single waveguide (C_0=0). Note that another limiting case $\theta = 0$ corresponds to the PT-symmetric trimer [25].

In what follows, we compare the basic properties of the PT-trimer ($\theta = 0$) with the properties of the PH trimer at $\theta = 0.5$. The latter means that the PH trimer consists of one lossy waveguide (ρ) and two active waveguides with the same gain ($-\rho/2, -\rho/2$).

Using Eqs. (19) and (20), the propagation constants defined in Eq. (18) can be written as

$$\beta_1 = 0, \quad \beta_{2,3} = \pm\sqrt{(2-\theta)C_{-1}^2 - \rho^2}. \tag{23}$$

It is interesting to note that the dependence of the propagation constants β_n on the gain/loss strength does not have a qualitative difference between the PT and PH trimers.

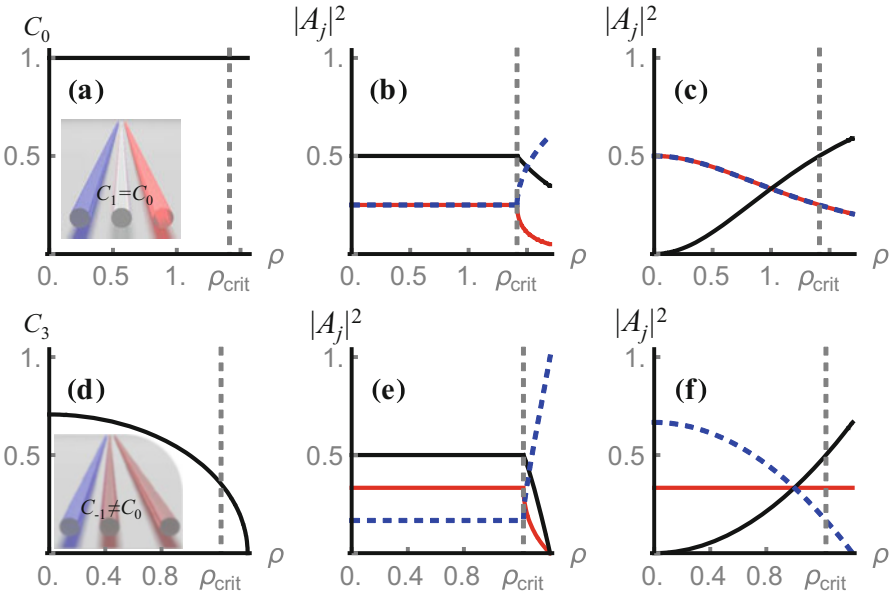

Fig. 6 Characteristic mode properties depending on the gain/loss strength (ρ) in a PT trimer ($\theta = 0$) – top row, and the PH trimer ($\theta = 0.5$) – bottom row. (**a**, **d**) Dependence of the coupling parameter C_0 providing balance between gain and loss. (**b**, **c**, **e**, **f**) Eigenmode profiles: red, black, and dashed blue curves show the intensities in the left, middle, and right waveguides, respectively. Vertical dashed line marks the critical value ρ_{crit} of gain/loss parameter ρ. (**b**, **e**) correspond to the propagation constant β_1, and (**c**, **f**) correspond to β_2 and β_3. (Adapted from Ref. [58])

We illustrate the features of trimers in Fig. 6, where the top row corresponds to the PT-trimer, while the bottom row – to the PH trimer. Figures 6a, d show how the coupling parameter C_0 must be adjusted depending on the gain/loss strength ρ to establish the balance between gain and loss. Panels (b, e) and (c, f) show the relative intensity distribution between the waveguides for the propagation constants $\beta_1 = 0$ and $\beta_{2,3}$, respectively. Here red, black, and dashed blue curves represent the light intensity in the left, middle, and right waveguides, respectively, while the total mode intensity is normalized to unity. Interestingly, the intensities of modes with the zero propagation constant do not depend on the gain/loss strength up to the critical value ρ_{crit} (see Fig. 6b, e), while for $\beta_{2,3}$ we observe redistribution of the intensity between the waveguides (see Fig. 6c, f). Note that for the PT-trimer the energy is distributed equally between the waveguides with gain and loss in contrast to the PH-trimer. Another finding is that at the critical point ρ_{crit}, the propagation constants and complex amplitude profiles of all three modes coincide.

We see that the pseudo-Hermitian trimer can have an entirely real spectrum as well as a phase transition point denoted as ρ_{crit}, which is usually associated with PT-symmetric systems. However, for the PT symmetric trimer the coupling parameter C_0 does not depend on gain/loss parameter ρ, and it is found as $C_0 = C_{-1}$, while

for the PH trimer C_0 depends on not only C_{-1}, but on ρ and gain/loss distribution between the waveguides (θ) as well. We note that the condition (22) is always satisfied for the PT trimer.

Next, we investigate the behaviour of a non-Hermitian trimer embedded into a chain of conservative waveguides in order to reveal its potential for signal manipulation propagating through optical networks.

3.3 *Pseudo-Hermitian Trimer in a Chain of Conservative Wavegudies*

Active elements, incorporated into conservative structures, can demonstrate beneficial effects such as non-reciprocity, signal amplification, suppressed reflection, and invisibility [59–62]. Here we investigate propagation of light in a long array of conservative waveguides including the non-Hermitian trimer.

As we have discussed in Sect. 2.3, when a PT-symmetric coupler is embedded into a chain of conservative waveguides, a symmetry of the structure can be broken and the growing modes can appear [38]. Therefore, it is important to determine a range of trimer model parameters, when the system does not possess exponentially growing and lasing modes. In this regime the PH trimer can be used for active control of propagating signals, i.e. for amplification, filtering, and switching. We note that the balance relation (16) is not a necessary condition for absence of lasing modes in the system due to additional radiation losses through the chain. In what follows, we consider a general case with $\rho_{-1} + \rho_0 + \rho_1 \neq 0$ and introduce the additional gain/loss $\Delta\rho$ for the trimer waveguides. This shifts the spectrum of the isolated trimer by the value $i\Delta\rho$ according to the gauge transformation. When the trimer is embedded into a chain of conservative waveguides, the governing equations take the form

$$\begin{aligned}
i\frac{\mathrm{d}a_j}{\mathrm{d}z} + C_A a_{j+1} + C_A a_{j-1} &= 0, \ \text{for } j \neq -1, 0, 1,\\
i\frac{\mathrm{d}a_{-1}}{\mathrm{d}z} + i(\rho - \Delta\rho)a_{-1} + C_{-1}a_0 + C_A a_{-2} &= 0,\\
i\frac{\mathrm{d}a_0}{\mathrm{d}z} - i(\theta\rho + \Delta\rho)a_0 + C_{-1}a_{-1} + C_0 a_1 &= 0,\\
i\frac{\mathrm{d}a_1}{\mathrm{d}z} - i[(1-\theta)\rho + \Delta\rho]a_1 + C_A a_2 + C_0 a_0 &= 0.
\end{aligned} \tag{24}$$

Here C_A is the coupling coefficient between the conservative waveguides.

Solving the scattering problem [58] we find the scattering coefficients with singularities determined by the roots of a function D:

$$D = e^{ik}\bar{C}_0{}^2\left[\bar{C}_1 - i(\Delta\rho + \bar{\rho})e^{ik}\right] - ie^{2ik}\left[i\bar{C}_A e^{-ik} + \Delta\rho + (\theta - 1)\bar{\rho}\right] \times \left[1 + (2i\bar{C}_A\cos(k) + \Delta\rho - \theta\bar{\rho})(i\bar{C}_A e^{-ik} + \Delta\rho + \bar{\rho})\right], \tag{25}$$

where k is the wavenumber of an incident wave, $\bar{\rho} \equiv \rho/C_{-1}$, $\bar{C}_A \equiv C_A/C_{-1}$, $\bar{C}_0 \equiv C_0/C_{-1}$, and $\Delta\bar{\rho} \equiv \Delta\rho/C_{-1}$.

We now fix the parameters C_A, C_{-1}, θ, and ρ and consider $\Delta\rho = \Delta\rho_{\min} \equiv \min[\rho, -\rho\theta, -(1-\theta)\rho]$. In this case there is no gain in the system and thus no lasing modes can occur. Next, we gradually increase $\Delta\rho$ until it reaches some critical value $\Delta\rho_{\text{crit}}$, at which D turns to zero for some wavenumber k_{crit}. This means that the wave with the wavenumber k_{crit} is a lasing mode and the energy of the system can grow without any incident light for $\Delta\rho > \Delta\rho_{\text{crit}}$.

In Fig. 7a, we plot $\Delta\bar{\rho}_{\text{crit}} \equiv \Delta\rho_{\text{crit}}/C_{-1}$ as a function of $\bar{\rho}$ and θ for $\bar{C}_A = 0.5$. In Fig. 7b we show the corresponding wavenumber k_{crit}. The black dashed line bounds the range of possible structural parameters according to Eq. (22) and black solid line separates regions where $\Delta\bar{\rho}_{\text{crit}} > 0$ and $\Delta\bar{\rho}_{\text{crit}} < 0$. A complex behaviour of $\Delta\bar{\rho}_{\text{crit}}$ in the region $\theta > 0.8$ and $\bar{\rho} \approx 0.9$ results from bifurcations of roots of the equation $D = 0$ at particular parameters θ, $\bar{\rho}$ and $\bar{C}_A$.

Remarkably, the value of $\Delta\rho_{\text{crit}}$ can be either negative or positive. If $\Delta\rho_{\text{crit}} < 0$, then for the range $\Delta\rho_{\text{crit}} < \Delta\rho < 0$ the overall gain/loss balance is shifted into loss; however, lasing modes are present in the system. On the other hand, if $\Delta\rho_{\text{crit}} > 0$, then for the range $0 < \Delta\rho < \Delta\rho_{\text{crit}}$ the overall gain/loss balance is shifted into gain, but no lasing modes are observed.

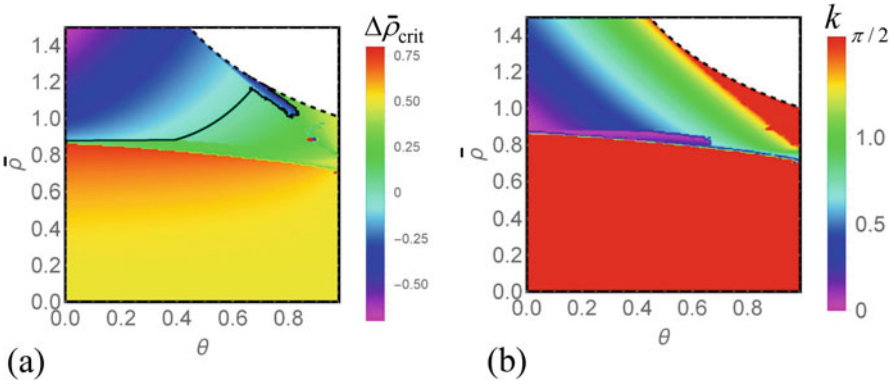

Fig. 7 (**a**) The minimum value of gain/loss imbalance, $\Delta\bar{\rho}_{\text{crit}}$, at which a lasing mode occurs in the chain of conservative waveguides with the embedded trimer as a function of $\bar{\rho}$ and θ. (**b**) A wavenumber of the corresponding lasing mode. Dashed black curve bounds the range of possible structural parameters according to Eq. (22), and black solid line separates regions where $\Delta\bar{\rho}_{\text{crit}} > 0$ and $\Delta\bar{\rho}_{\text{crit}} < 0$. Parameter $\bar{C}_A$=0.5. (Adopted from Ref. [58])

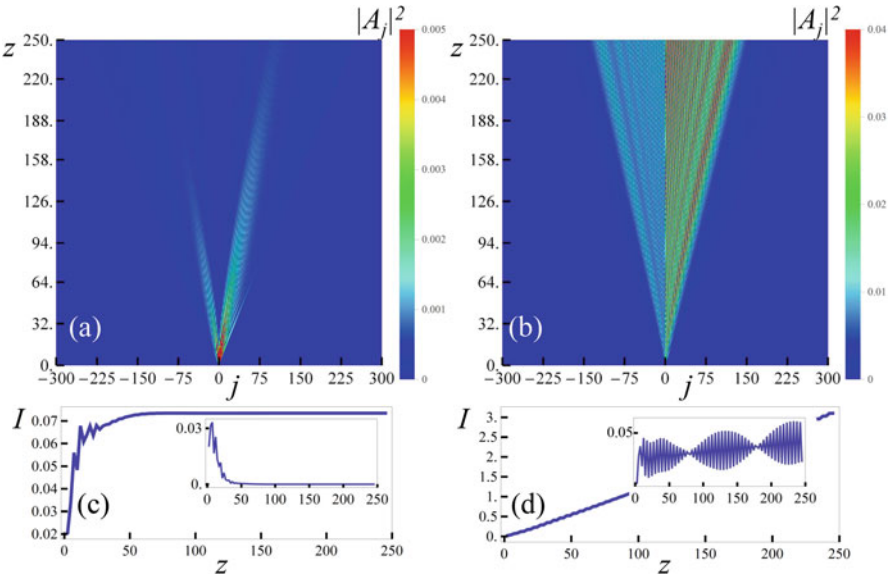

Fig. 8 Noise dynamics in the chain of conservative waveguides with the embedded PH trimer for (**a**) $\bar{\rho} = 0.85$ and (**b**) $\bar{\rho} = 1$. (**c**), (**d**) Evolution of the total energy of the system, I, corresponding to (**a**) and (**b**), respectively. Insets show evolution of the energy concentrated in the waveguides of the PH trimer only. Parameters are $\theta = 0.5$, $\bar{C}_A = 0.5$, and $\Delta\rho = 0$. (Adopted from Ref. [58])

We simulate the dynamics of input noisy conditions in the chain of conservative waveguides with the PH trimer ($\theta = 0.5$). Although the total number of waveguides in the considered case is 601, we emulate an infinite long chain by introducing perfectly matched layers (PML) at the structure boundaries. The noise is introduced only in the trimer waveguides and it is chosen randomly. We simulate light dynamics for several realisations of initial conditions and a representative example for $\bar{C}_A = 0.5$ and $\Delta\rho = 0$ is shown in Fig. 8. For $\bar{\rho} = 0.85$, which is below the black curve in Fig. 7a and corresponds to $\Delta\rho_{\text{crit}} > 0$, we observe that after initial relaxation the total system energy $I = \sum_j |A_j|^2$ is preserved (see Fig. 8c) and the system does not lase. However, if $\bar{\rho} = 1$, then $\Delta\rho_{\text{crit}} < 0$ (see Fig. 7a) and the system lases (see Fig. 8b) with growing total energy as shown in Fig. 8d.

A nonlinear regime of the PT-symmetric trimer was first discussed in [63] and revisited in [25, 64]. We note that an experimental realization of dissipative trimer having "gain-loss-gain" profile was reported in [64]. Although such a trimer does not possess PT-symmetry, this experimental setup serves as a first step towards realization of PT-symmetric trimer.

4 Guided Modes in Waveguides

In optics, the topic of PT-symmetry is closely related to the studies of various waveguiding structures with gain. For example, from the conventional point of view, it is reasonable to expect that by adding gain to the waveguiding structure one can control the characteristics of the propagating modes, as was shown in Ref. [65]. In plasmonic structures, waveguiding is suppressed by losses particularly strongly. There is a search in either optimizing the geometry for these structures [66], or using novel materials [67]. Clearly, such approaches try to minimize losses, and one needs gain materials to compensate losses in plasmonic structures [68–70].

In a convectional approach, it is assumed that the propagating waves are monochromatic, $\exp(-i\omega t)$ time convention, and positive imaginary part of the refractive index describes lossy media, while negative values of this quantity correspond to gain media. For TE guided modes, which have one non-trivial electric field component (E_y) and two magnetic field components (H_x, H_z), the modes of the structure have the form $E_y = E(x)\cdot\exp(i\beta z)$, where β is the mode wavenumber, and the mode profile E is described by the equation

$$\frac{d^2E}{dx^2} + \frac{\omega^2}{c^2}\left[\varepsilon(x) - \beta^2\right]E = 0. \tag{26}$$

A majority of the studies followed the original proposal of a two-layer coupler, and studied similar or dissimilar directional waveguide couplers showing PT-symmetric behavior [71–74]. In particular, it was shown that directional couplers built of dissimilar waveguides that do not fulfill the PT symmetry, can demonstrate the behavior similar to the one observed in PT symmetric systems [74].

Generally, as discussed above, pseudo-Hermitian optical couplers have the properties more advanced in comparison with the true PT-symmetric couplers [58], and the mode spectrum can be entirely real even without PT symmetry, provided the waveguides in a coupler are placed in a special order.

As an example of a non-Hermitian waveguiding structure, we study three-layer non-Hermitian dielectric waveguides with gain and/or loss shown schematically in Fig. 9a. We follow the original paper [75], and consider a three-layer structure to achieve a wider range of regimes as compared to two-layer structures. For the case of three-layer waveguides, Turitsyna et al. [75] demonstrated the stationary regimes when gain and loss compensate each other globally but not locally.

We consider a three-layer waveguide placed in a free space, as shown schematically in Fig. 9a. Each layer i has a thickness d_i, and can have an arbitrary complex index of refraction. In the examples given below we assumed that layers are of the same thickness, $d_i = d$.

In general, Eq. (26) cannot be solved analytically; therefore, in what follows we solve it numerically in order to find the mode wavenumbers β. To find regimes when conservative modes exist in this structure, we fix parameters of the first layer, $n_1 = 2{+}0.1i$, and also fix the real parts of the refractive indices of the two remaining

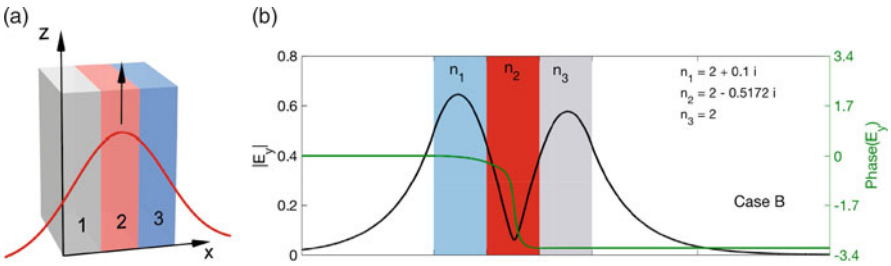

Fig. 9 (**a**) Schematics of a three layer non-Hermitian waveguide. Each layer can be either passive or exhibit gain/loss. For visual identification, we use red tint to denote gain layers (layer 2), blue – loss (layer 3), and grey – passive layers (layer 1 in this scheme). (**b**) Mode structure shown for the electric field amplitudes and phases, when one of the layers is passive. Parameters of the structures are shown in the panel. (Adopted from Ref. [75])

layers at 2. Then, we scan the plane of parameters of imaginary parts of the layers 2 and 3 ($\mathrm{Im}(n_2)$, $\mathrm{Im}(n_3)$) in order to find points at which there is a solution to Eq. (26) with real β.

The example shown in Fig. 9b is quite remarkable, and it suggests a new mechanism for controlling the required balance between gain and loss in two non-conservative layers. Indeed, if we have two layers of the same thickness, then the condition of usual PT symmetry requires that the amount of gain in one of the layers is equal to the loss in another layer. Now, we can attach the third layer to the structure, and due to a change in the mode profile the amount of the required gain can be smaller or larger (for the latter, see Fig. 9b). In a more general case, the modes have a complicated structure.

Thus, the guiding properties of non-Hermitian multi-layered dielectric waveguides with gain and loss revealed that the functionalities of conventional PT-symmetric optical waveguides can be expanded substantially by adding an additional dielectric layer and extending the structure into a broader class of non-Hermitian systems to control a ratio of gain and loss required to support propagating and non-decaying guided modes.

5 Conclusion

In this chapter, we discussed the unique features of non-Hermitian optical couplers composed of several waveguides and their possible applications for effective light control. We formulated the necessary conditions for the spectrum to be real for different optical systems: PT-symmetric dimers, pseudo-Hermitian trimers and chains of conservative waveguides including non-Hermitian defects. We investigated an interplay between nonlinearity and PT-symmetry of a dimer system, analysed nonlinear parametric amplification and the emergence of anti-PT symmetry in spectral domain. We demonstrated how the non-Hermitian defects embedded into

a chain of conservative waveguides can affect the system spectrum, giving rise to nonlocal effects. We also studied guided modes in a three-layer non-Hermitian optical coupler with gain and loss regions.

Acknowledgements The authors acknowledge support by the Australian Research Council (ARC), including Discovery Project DP160100619.

References

1. Bender, C.M., Boettcher, S.: Real spectra in non-Hermitian hamiltonians having PT symmetry. Phys. Rev. Lett. **80**, 5243–5246 (1998)
2. El Ganainy, R., Makris, K.G., Christodoulides, D.N., Musslimani, Z.H.: Theory of coupled optical PT-symmetric structures. Opt. Lett. **32**, 2632–2634 (2007)
3. Makris, K.G., El Ganainy, R., Christodoulides, D.N., Musslimani, Z.H.: Beam dynamics in PT symmetric optical lattices. Phys. Rev. Lett. **100**, 103904–4 (2008)
4. Ruter, C.E., Makris, K.G., El Ganainy, R., Christodoulides, D.N., Segev, M., Kip, D.: Observation of parity-time symmetry in optics. Nat. Phys. **6**, 192–195 (2010)
5. Feng, L., Wong, Z.J., Ma, R.M., Wang, Y., Zhang, X.: Single-mode laser by parity-time symmetry breaking. Science **346**, 972–975 (2014)
6. Hodaei, H., Miri, M.A., Heinrich, M., Christodoulides, D.N., Khajavikhan, M.: Parity-time-symmetric microring lasers. Science **346**, 975–978 (2014)
7. Kato, T.: Perturbation Theory for Linear Operators, 2nd edn. Springer, Berlin (1995)
8. Klaiman, S., Guenther, U., Moiseyev, N.: Visualization of branch points in PT-symmetric waveguides. Phys. Rev. Lett. **101**, 080402–4 (2008)
9. Heiss, W.D.: Exceptional points of non-hermitian operators. J. Phys. A **37**, 2455–2464 (2004)
10. Muller, M., Rotter, I.: Exceptional points in open quantum systems. J. Phys. A **41**, 244018–15 (2008)
11. Mostafazadeh, A.: Self-dual spectral singularities and coherent perfect absorbing lasers without PT-symmetry. J. Phys. A **45**, 444024–10 (2012)
12. Mostafazadeh, A.: Pseudo-hermiticity versus PT symmetry: the necessary condition for the reality of the spectrum of a non-Hermitian Hamiltonian. J. Math. Phys. **43**, 205–214 (2002)
13. Chen, Y.J., Snyder, A.W., Payne, D.N.: Twin core nonlinear couplers with gain and loss. IEEE J. Quantum Electron. **28**, 239–245 (1992)
14. Malomed, B.A., Peng, G.D., Chu, P.L.: Nonlinear-optical amplifier based on a dual-core fiber. Opt. Lett. **21**, 330–332 (1996)
15. Ramezani, H., Kottos, T., El Ganainy, R., Christodoulides, D.N.: Unidirectional nonlinear PT-symmetric optical structures. Phys. Rev. A **82**, 043803–6 (2010)
16. Sukhorukov, A.A., Xu, Z.Y., Kivshar, Y.S.: Nonlinear suppression of time reversals in PT-symmetric optical couplers. Phys. Rev. A **82**, 043818–5 (2010)
17. Kevrekidis, P.G., Pelinovsky, D.E., Tyugin, D.Y.: Nonlinear dynamics in PT-symmetric lattices. J. Phys. A **46**, 365201–17 (2013)
18. Barashenkov, I.V.: Hamiltonian formulation of the standard PT-symmetric nonlinear Schrödinger dimer. Phys. Rev. A **90**, 045802–4 (2014)
19. Barashenkov, I.V., Jackson, G.S., Flach, S.: Blow-up regimes in the PT-symmetric coupler and the actively coupled dimer. Phys. Rev. A **88**, 053817–8 (2013)
20. Pickton, J., Susanto, H.: Integrability of PT-symmetric dimers. Phys. Rev. A **88**, 063840–8 (2013)
21. Barashenkov, I.V., Pelinovsky, D.E., Dubard, P.: Dimer with gain and loss: integrability and PT-symmetry restoration. J. Phys. A **48**, 325201–28 (2015)

22. Lupu, A., Benisty, H., Degiron, A.: Using optical PT-symmetry for switching applications. Photonics Nanostruct. Fundam. Appl. **12**, 305–311 (2014)
23. Schindler, J., Li, A., Zheng, M.C., Ellis, F.M., Kottos, T.: Experimental study of active LRC circuits with PT symmetries. Phys. Rev. A **84**, 040101–5 (2011)
24. Cuevas, J., Kevrekidis, P.G., Saxena, A., Khare, A.: PT-symmetric dimer of coupled nonlinear oscillators. Phys. Rev. A **88**, 032108–11 (2013)
25. Duanmu, M., Li, K., Horne, R.L., Kevrekidis, P.G., Whitaker, N.: Linear and nonlinear parity-time-symmetric oligomers: a dynamical systems analysis. Philos. Trans. R. Soc. A **371**, 20120171–19 (2013)
26. Miroshnichenko, A.E., Malomed, B.A., Kivshar, Y.S.: Nonlinearly PT-symmetric systems: spontaneous symmetry breaking and transmission resonances. Phys. Rev. A **84**, 012123–4 (2011)
27. Zezyulin, D.A., Kartashov, Y.V., Konotop, V.V.: Stability of solitons in PT-symmetric nonlinear potentials. Europhys. Lett. **96**, 64003–6 (2011)
28. Longhi, S.: Phase transitions in wick-rotated PT-symmetric optics. Ann. Phys. **360**, 150–160 (2015)
29. Moreira, F.C., Abdullaev, F.K., Konotop, V.V., Yulin, A.V.: Localized modes in $\chi^{(2)}$ media with PT-symmetric localized potential. Phys. Rev. A **86**, 053815–7 (2012)
30. Li, K., Zezyulin, D.A., Kevrekidis, P.G., Konotop, V.V., Abdullaev, F.K.: PT-symmetric coupler with $\chi^{(2)}$ nonlinearity. Phys. Rev. A **88**, 053820–11 (2013)
31. Abdullaev, F.K., Umarov, B.A.: Exact solitonic solutions for optical media with $\chi^{(2)}$ nonlinearity and PT-symmetric potentials. J. Phys. Conf. Ser. **553**, 012001–6 (2014)
32. Boyd, R.W.: Nonlinear Optics, 3rd edn. Academic, San Diego (2008)
33. Antonosyan, D.A., Solntsev, A.S., Sukhorukov, A.A.: Parity-time anti-symmetric parametric amplifier. Opt. Lett. **40**, 4575–4578 (2015)
34. Jones, H.F.: Scattering from localized non-hermitian potentials. Phys. Rev. D **76**, 125003–5 (2007)
35. Znojil, M.: Scattering theory using smeared non-Hermitian potentials. Phys. Rev. D **80**, 045009–12 (2009)
36. Dmitriev, S.V., Sukhorukov, A.A., Kivshar, Y.S.: Binary parity-time-symmetric nonlinear lattices with balanced gain and loss. Opt. Lett. **35**, 2976–2978 (2010)
37. Zheng, M.C., Christodoulides, D.N., Fleischmann, R., Kottos, T.: PT optical lattices and universality in beam dynamics. Phys. Rev. A **82**, 010103–4 (2010)
38. Sukhorukov, A.A., Dmitriev, S.V., Suchkov, S.V., Kivshar, Y.S.: Nonlocality in PT-symmetric waveguide arrays with gain and loss. Opt. Lett. **37**, 2148–2150 (2012)
39. Longhi, S., Cannata, F., Ventura, A.: Spontaneous PT symmetry breaking in dirac-kronig-penney crystals. Phys. Rev. B **84**, 235131–8 (2011)
40. Moiseyev, N.: Crossing rule for a PT-symmetric two-level time-periodic system. Phys. Rev. A **83**, 052125–5 (2011)
41. Joglekar, Y.N., Marathe, R., Durganandini, P., Pathak, R.K.: PT spectroscopy of the Rabi problem. Phys. Rev. A **90**, 040101–4 (2014)
42. Gong, J.B., Wang, Q.H.: Stabilizing non-Hermitian systems by periodic driving. Phys. Rev. A **91**, 042135–6 (2015)
43. Driben, R., Malomed, B.A.: Stability of solitons in parity-time-symmetric couplers. Opt. Lett. **36**, 4323–4325 (2011)
44. Driben, R., Malomed, B.A.: Stabilization of solitons in PT models with supersymmetry by periodic management. Europhys. Lett. **96**, 51001–5 (2011)
45. Horne, R.L., Cuevas, J., Kevrekidis, P.G., Whitaker, N., Abdullaev, F.K., Frantzeskakis, D.J.: PT-symmetry management in oligomer systems. J. Phys. A **46**, 485101–19 (2013)
46. D'Ambroise, J., Malomed, B.A., Kevrekidis, P.G.: Quasi-energies, parametric resonances, and stability limits in ac-driven PT-symmetric systems. Chaos **24**, 023136–10 (2014)
47. Battelli, F., Diblik, J., Feckan, M., Pickton, J., Pospisil, M., Susanto, H.: Dynamics of generalized PT-symmetric dimers with time-periodic gain-loss. Nonlinear Dynam. **81**, 353–371 (2015)

48. Martinez, A.J., Molina, M.I., Turitsyn, S.K., Kivshar, Y.S.: Nonlinear multicore waveguiding structures with balanced gain and loss. Phys. Rev. A **91**, 023822–8 (2015)
49. Liu, J.B., Xie, X.T., Shan, C.J., Liu, T.K., Lee, R.K., Wu, Y.: Optical bistability in nonlinear periodical structures with PT-symmetric potential. Laser Phys. **25**, 015102–5 (2015)
50. Greenberg, M., Orenstein, M.: Irreversible coupling by use of dissipative optics. Opt. Lett. **29**, 451–453 (2004)
51. Greenberg, M., Orenstein, M.: Unidirectional complex gratings assisted couplers. Opt. Express **12**, 4013–4018 (2004)
52. Greenberg, M., Orenstein, M.: Optical unidirectional devices by complex spatial single sideband perturbation. IEEE J. Quantum Electron. **41**, 1013–1023 (2005)
53. West, B.R., Plant, D.V.: Transfer matrix analysis of the unidirectional grating-assisted codirectional coupler. Appl. Opt. **46**, 8052–8060 (2007)
54. Luo, X.B., Huang, J.H., Zhong, H.H., Qin, X.Z., Xie, Q.T., Kivshar, Y.S., Lee, C.H.: Pseudo-parity-time symmetry in optical systems. Phys. Rev. Lett. **110**, 243902–5 (2013)
55. Yuce, C.: Pseudo PT symmetric lattice. Eur. Phys. J. D **69**, 11–5 (2015)
56. Konotop, V.V., Zezyulin, D.A.: Stochastic parity-time-symmetric coupler. Opt. Lett. **39**, 1223–1226 (2014)
57. Guo, A., Salamo, G.J., Duchesne, D., Morandotti, R., Volatier-Ravat, M., Aimez, V., Siviloglou, G.A., Christodoulides, D.N.: Observation of PT-symmetry breaking in complex optical potentials. Phys. Rev. Lett. **103**, 093902–4 (2009)
58. Suchkov, S.V., Fotsa-Ngaffo, F., Kenfack-Jiotsa, A., Tikeng, A.D., Kofane, T.C., Kivshar, Y.S., Sukhorukov, A.A.: Non-Hermitian trimers: PT-symmetry versus pseudo-Hermiticity. New J. Phys. **18**, 065005–9 (2016)
59. Lin, Z., Ramezani, H., Eichelkraut, T., Kottos, T., Cao, H., Christodoulides, D.N.: Unidirectional invisibility induced by PT-symmetric periodic structures. Phys. Rev. Lett. **106**, 213901–4 (2011)
60. Dmitriev, S.V., Suchkov, S.V., Sukhorukov, A.A., Kivshar, Y.S.: Scattering of linear and nonlinear waves in a waveguide array with a PT-symmetric defect. Phys. Rev. A **84**, 013833–5 (2011)
61. Mostafazadeh, A.: Invisibility and PT symmetry. Phys. Rev. A **87**, 012103–8 (2013)
62. Feng, L., Xu, Y.L., Fegadolli, W.S., Lu, M.H., Oliveira, J.E.B., Almeida, V.R., Chen, Y.F., Scherer, A.: Experimental demonstration of a unidirectional reflectionless parity-time metamaterial at optical frequencies. Nat. Mater. **12**, 108–113 (2013)
63. Li, K., Kevrekidis, P.G.: PT-symmetric oligomers: analytical solutions, linear stability, and nonlinear dynamics. Phys. Rev. E **83**, 066608–7 (2011)
64. Li, K., Kevrekidis, P.G., Frantzeskakis, D.J., Ruter, C.E., Kip, D.: Revisiting the PT-symmetric trimer: bifurcations, ghost states and associated dynamics. J. Phys. A **46**, 375304–12 (2013)
65. Siegman, A.E.: Propagating modes in gain-guided optical fibers. J. Opt. Soc. Am. A **20**, 1617–1628 (2003)
66. Dastmalchi, B., Tassin, P., Koschny, T., Soukoulis, C.M.: A new perspective on plasmonics: confinement and propagation length of surface plasmons for different materials and geometries. Adv. Opt. Mater. **4**, 177–184 (2016)
67. Boltasseva, A., Atwater, H.A.: Low-loss plasmonic metamaterials. Science **331**, 290–291 (2011)
68. Stockman, M.I.: Spaser action, loss compensation, and stability in plasmonic systems with gain. Phys. Rev. Lett. **106**, 156802–4 (2011)
69. Wuestner, S., Pusch, A., Tsakmakidis, K.L., Hamm, J.M., Hess, O.: Overcoming losses with gain in a negative refractive index metamaterial. Phys. Rev. Lett. **105**, 127401–4 (2010)
70. Fang, A., Koschny, T., Soukoulis, C.M.: Self-consistent calculations of loss-compensated fishnet metamaterials. Phys. Rev. B **82**, 121102–4 (2010)
71. Lupu, A., Benisty, H., Degiron, A.: Switching using PT symmetry in plasmonic systems: positive role of the losses. Opt. Express **21**, 21651–21668 (2013)

72. Alaeian, H., Dionne, J.A.: Non-Hermitian nanophotonic and plasmonic waveguides. Phys. Rev. B **89**, 075136–9 (2014)
73. Savoia, S., Castaldi, G., Galdi, V.: Non-Hermiticity-induced wave confinement and guiding in loss-gain-loss three-layer systems. Phys. Rev. A **94**, 043838–10 (2016)
74. Walasik, W., Ma, C.C., Litchinitser, N.M.: Dissimilar directional couplers showing PT-symmetric-like behavior. New J. Phys. **19**, 075002–8 (2017)
75. Turitsyna, E.G., Shadrivov, I.V., Kivshar, Y.S.: Guided modes in non-Hermitian optical waveguides. Phys. Rev. A **96**, 033824–4 (2017)

Parity-Time Symmetric Plasmonics

D. Barton III, M. Lawrence, H. Alaeian, B. Baum, and J. Dionne

Abstract Plasmons are hybrid photon-electron waves bound between conducting and dielectric materials. They have enabled strongly enhanced light-matter interactions for light emission and sensing, sub-wavelength structuring of photonic devices, and exotic optical phenomena such as optical-frequency magnetism. To date, most control over plasmon dispersion has been achieved through structuring of the real part of the refractive index, while losses have been viewed as detrimental. Photonic Parity-Time (PT) symmetry takes advantage of these inherent losses, utilizing them in conjunction with balanced gain media to control eigenmode evolution. In this chapter, we review progress in PT-symmetric plasmonics, focusing on planar and coaxial geometries. We show how inclusion of balanced loss and gain gives rise to exceptional points, enabling a multitude of phenomena including: (1) subwavelength mode multiplexing; (2) chiral molecule sensing and discrimination; (3) subwavelength polarization conversion; and (4) nonreciprocal, nonlinear optical metamaterials. We also show a route towards thresholdless symmetry breaking. These results provide a foundation for ultra-compact optical components with almost complete control over scattering, reflection, and transmission by tuning the PT potential.

1 Introduction

Surface plasmons are hybrid electronic and photonic excitations supported between conducting and dielectric materials [1]. Their unique dispersion enables small wavelengths and high electromagnetic field intensities at optical frequencies,

D. Barton III · M. Lawrence · B. Baum · J. Dionne (✉)
Materials Science and Engineering, Stanford University, Stanford, CA, USA
e-mail: jdionne@stanford.edu

H. Alaeian
Materials Science and Engineering, Stanford University, Stanford, CA, USA

Physikalisches Institut, Universität Stuttgart, Stuttgart, Germany

D. Christodoulides, J. Yang (eds.), *Parity-time Symmetry and Its Applications*, Springer Tracts in Modern Physics 280,
https://doi.org/10.1007/978-981-13-1247-2_12

effects which have been utilized to realize subwavelength waveguides [2], efficient light-emitting diodes [3], thresholdless nanoscale lasers [4], and lenses that beat the diffraction limit [5]. Since plasmonic effects generally take advantage of the real part of a material's refractive index, losses (which arise from the imaginary component of the index) are seen as detrimental. However, the concept of Parity-time (PT) symmetry in optics has cast the imaginary component of the refractive index in a more favorable light. PT-symmetric media allow for control over electromagnetic field distributions with careful structuring of the imaginary index, which depending on sign, encompasses both optical attenuation and amplification.

In general, PT-symmetric systems require that the refractive index fulfills $n\left(\overrightarrow{r}\right) = n^*\left(-\overrightarrow{r}\right)$[6]. Accordingly, spatially-symmetric distributions of loss and gain are inherent to these non-Hermitian systems. Fulfilling this condition on the refractive index guarantees the existence of a so-called exceptional point, where two distinct eigensolutions coalesce to the same values; beyond this point, the electromagnetic properties of a system significantly shift.

PT-symmetric potentials have emerged as a new scheme to control field distributions in loss and gain media, so that light propagation can be asymmetric and even unidirectional. They have enabled loss-induced optical transparency [7, 8], lossless Talbot revivals [9], unidirectional invisibility [10] and perfect cavity absorber-lasers [11, 12]. Combined with non-linear media, PT-symmetric potentials have also been suggested for optical diodes, isolators and circulators.

While most optical components have been constructed from wavelength-scale components, here we describe novel nanophotonic PT elements based on plasmonics. Combining the tunable properties from plasmonic nanostructures with the asymmetric and exceptional point behavior of PT media, wholly new devices can be constructed which overcome fundamental limits in traditional optics. In this chapter, we first develop our understanding of PT-symmetric plasmonic structures by considering both planar and coaxial waveguide geometries. We solve for the waveguide modes with varying PT potentials, and then use this understanding to design ultra-compact perfect absorber-amplifiers, compact multiplexers, and unity-efficiency polarization converters. Placing emitters near these structures leads to other unconventional behavior, including extremely high Purcell enhancements near exceptional points and spectral regimes where emitters act as perfect absorbers and vice versa. Finally, we explore metamaterials constructed from these plasmonic building blocks, developing bulk synthetic media with tunable optical properties. In particular, we show how in the linear regime, such metamaterials can enable unity efficiency Veselago lensing, and in the non-linear regime, broadband and wide-angle nonreciprocity.

Taken together, this suite of PT-plasmonic structures can lay the foundation of novel devices throughout optical engineering, from lasing, sensing, and communication, all within deeply subwavelength footprints whose lengthscales compete with their electronic counterparts.

2 Section 1: Plasmonic Waveguides [13]

Perhaps one of the simplest, yet most fundamental, PT-symmetric plasmonic building blocks is a 5-layer Metal-Insulator-Metal (MIMIM) waveguide. As seen in Fig. 1, it is composed of deeply subwavelength metallic layers separated by dielectric containing either loss or gain in equal magnitude. Using exact solutions of Maxwell's equations to investigate the dispersion, propagation, field distribution, and power evolution as a function of the loss/gain parameter, we will understand the impact of a Parity-Time symmetric potential, and in particular the exceptional point, has on the optical properties. First, we determine the transverse-magnetic (TM) modes of this plasmonic waveguide. This will illustrate eigenmode evolution and the crossing of the mode propagation constants with increasing non-Hermiticity parameter. Then, we demonstrate how tuning the coupling between the metallic and dielectric layers of the MIMIM waveguide impacts state coalescence and propagation constant merging. We note that, while our discussion focuses on waveguide geometries, these derivations and results can be extended to other coupled PT-symmetric systems, such as coupled resonators and quantum wells.

Figure 1a illustrates the five-layer plasmonic waveguide studied here. We consider silver as the metallic layer, with a permittivity described by a lossless Drude model: $\epsilon_{Ag} = 1 - \left(\frac{\omega_p}{\omega}\right)^2$, with ω_p (the bulk plasma frequency of silver) equal to 8.85×10^{15} rad/sec. We consider a lossless Drude model to highlight the emergent features of PT potentials in plasmonic waveguide systems, but note that similar effects can be obtained with a lossy metal. The dielectric layers are assumed to be TiO_2 with $real\left(\epsilon_{Ti0_2}\right) = 10.2$ (real(n) = 3.2). Parameter κ corresponds to the amount of loss or gain in the dielectric layers, and is hereafter called the non-Hermiticity parameter. Note that loss and gain are always balanced in the system, regardless of the value of κ. This system can be viewed as two MIM plasmonic waveguides, each supporting a symmetric and antisymmetric plasmon mode, coupled through the metallic spacer layer. The transverse-magnetic (TM) modes of this five-layer system are described by

$$\left(\frac{d^2}{dx^2} + k_0^2\epsilon_l - k_z^2\right) H_{y_l}(x) = 0, \tag{1}$$

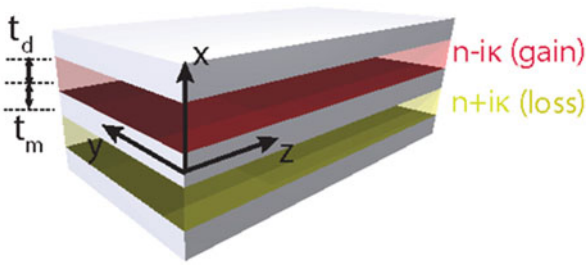

Fig. 1 Structure of plasmonic waveguide system. A layered structure with dielectric thickness t_d and metal thickness t_m is considered, where the dielectric layers have equal and opposite inclusions of loss (+iκ) or gain (−iκ)

where k_z is the wave vector along the propagation direction z, $H_{yl}(x)$ is the magnetic field, and the subscript l denotes the lth layer.

The dispersion of this waveguide system can be determined with the Transfer matrix method, which can be found in other texts [14]. First, we consider metallic and dielectric layer thicknesses of $t_m = t_d = 30$ nm. Figure 2a shows the dispersion curves of the four lowest order modes (labeled B_1–B_4), of the structure as a function of normalized frequency (ω/ω_p) for $\kappa = 0$ (i.e., a lossless waveguide). As seen in Fig. 2a, all modes have divergent wave vectors at a free-space energy of 1.73 eV (0.3 ω_p), which corresponds to the surface plasmon resonance frequency (ω_{sp}) of Ag and TiO_2. Such divergent wave vectors are typical for lossless plasmonic systems. For a non-Hermiticity parameter $\kappa = 0$, $(x) = (-x)$, and all distinct modes have definite magnetic field parities with respect to x: modes B_1 and B_3 are odd with respect to $x = 0$ (the midpoint between the five-layer MIMIM waveguide), while modes B_2 and B_4 are even. Note that modes below ω_{sp} are positive index modes, while modes above ω_{sp} are negative index modes, as evidenced by the slope of the dispersion.

One simple way of rationalizing these four MIMIM modes is through the concept of coupled systems. The five-layer MIMIM waveguide is effectively a system of two coupled three-layer MIM waveguides. For $t_d = 30$ nm, each MIM waveguide supports only two plasmonic modes: an even parity mode below ω_{sp} and an odd parity mode above ω_{sp}. When these two waveguides are coupled together to form the five-layer waveguide of Fig. 1a, even and odd superpositions of the two lowest order plasmonic modes form four distinct branches B_1–B_4. This feature can be clearly observed in panels b–e of Fig. 2, which plot the real part of H_y (x) and z component of the mode Poynting vector (side panels) for each branch. For modes B1 and B2, the fields are indeed in- or out-of-phase superpositions of even MIM modes, while modes B3 and B4 are superpositions of odd modes.

As the non-Hermiticity parameter κ is increased, the wave vectors begin to move into the complex plane. For example, Fig. 3a shows the dispersion curves of the MIMIM structure for $\kappa = 0.2$. Below the surface plasmon resonance, modes B_1 and B_2 appear to coalesce at an energy of 1.34 eV (0.23 ω_p), while above the surface resonance frequency, B_3 and B_4 merge at 1.8 eV (0.31 ω_p). Beyond these "exceptional points" (EP), the wave vectors become complex conjugate pairs. Therefore, they can be distinguished in the imaginary plane: One mode corresponds to an exponentially-growing mode along the propagation axis (z), while the other exhibits exponential decay. It should be noted that the propagation constant is complex beyond the exceptional point, even though the loss and gain values in the dielectric layers are always balanced.

The bottom panels of Fig. 3b–e, show the distribution of H_y for $\kappa = 0.2$. As in Fig. 2, field profiles are shown for wavelengths of 1165 and 615 nm, corresponding to energies less than and greater than the exceptional point energies, respectively. As seen, the distributions of the fields are not symmetric. Notably, the fields become skewed compared to their lossless counterparts, and begin to appear more similar to each other as the exceptional point is approached. However, the power is still distributed symmetrically with respect to x, which is consistent with having a real propagation constant in these regions. As the symmetry of the power is still

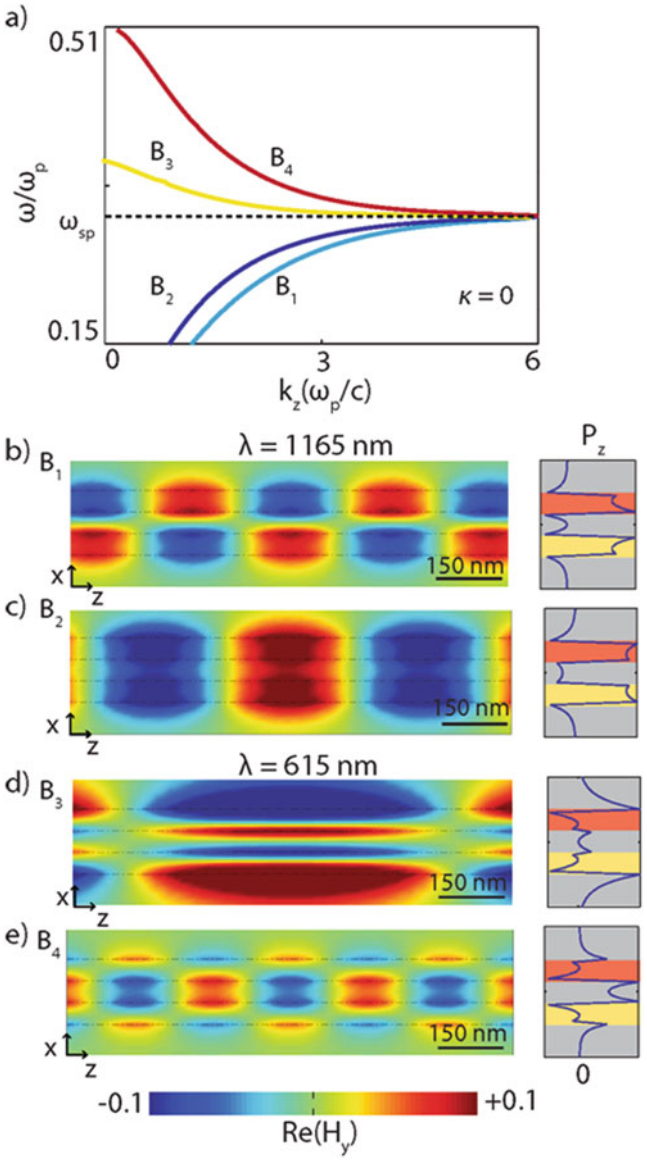

Fig. 2 Dispersion and fields in passive plasmonic waveguides. (**a**) Dispersion curve for $\kappa = 0$. Fields from two different branches for modes with free-space wavelengths of 1165 (**b**, **c**) and 615 (**d**, **e**) nm. These fields demonstrate alternating, but definite, parity of the waveguiding modes

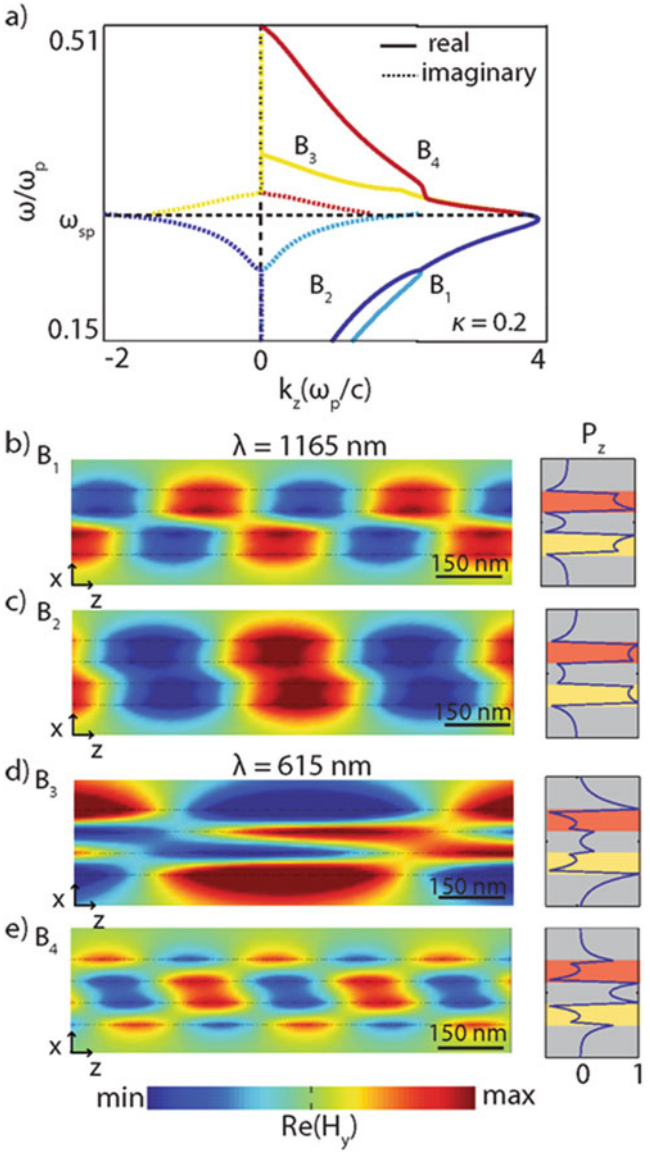

Fig. 3 Dispersion and fields in PT-symmetric waveguides. (**a**) Dispersion curve for $\kappa = 0.2$. Fields from two different branches for modes with free-space wavelengths of 1165 (**b**, **c**) and 615 (**d**, **e**) nm. Note the asymmetric field profiles

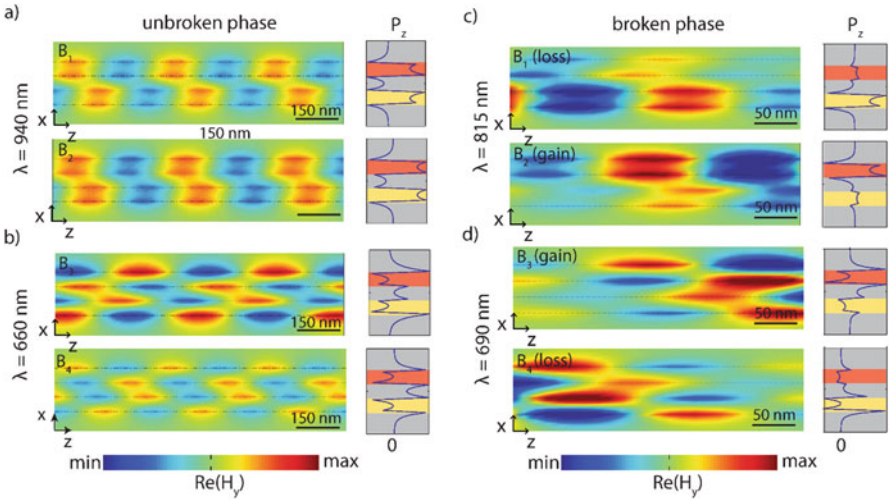

Fig. 4 Exceptional point symmetry breaking. Field profiles for bands B_1, B_2 and bands B_3, B_4 in the unbroken (**a** and **b**, respectively) and broken (**c** and **d**, respectively) phases. Balanced field amplitude in the loss and gain channels are observed in the unbroken phase, while enhanced fields in either the loss or gain are seen in the broken phase. Power distribution displayed on the right side of each field plot

preserved with respect to x, these regions are called "unbroken" phases of the PT system.

Figure 4a and b shows the distribution of the real part of $H_y(x)$ at frequencies very close to, but still within, the unbroken phase regime. Here, it can be clearly observed that the distribution of B1 approaches that of B2 while that of B3 evolves toward B4. Similarly, while the modal energy is distributed symmetrically with respect to the x axis, it becomes quite similar for the two merged modes. These features indicate that the crossing of the branches is not a simple degeneracy of states with multiplicity of 2 (i.e., having two different field profiles with the same energy), but instead a coalescence of two states.

In contrast, Fig. 4c and d illustrate the fields and power profiles for frequencies in the merged region of the dispersion curves. Here, the modes again become distinguishable, both in their complex wave vector and in their field localization. While they have the same phase velocity, they are either growing or decaying in amplitude as they propagate along the waveguide. Accordingly, the fields concentrate exclusively in either the gain region (modes B_2, B_3) or the loss region (modes B_1, B_4) of the waveguide. Further, this asymmetric field concentration is accompanied by an asymmetric power distribution: For the decaying/growing modes, power is concentrated in the loss/gain regions, respectively. Due to this asymmetry, this region is termed a "broken" phase of the system.

Next, we explore the effect of coupling between the gain and loss regions of the MIMIM waveguide, controlled via the metal thickness t_m. As will be shown,

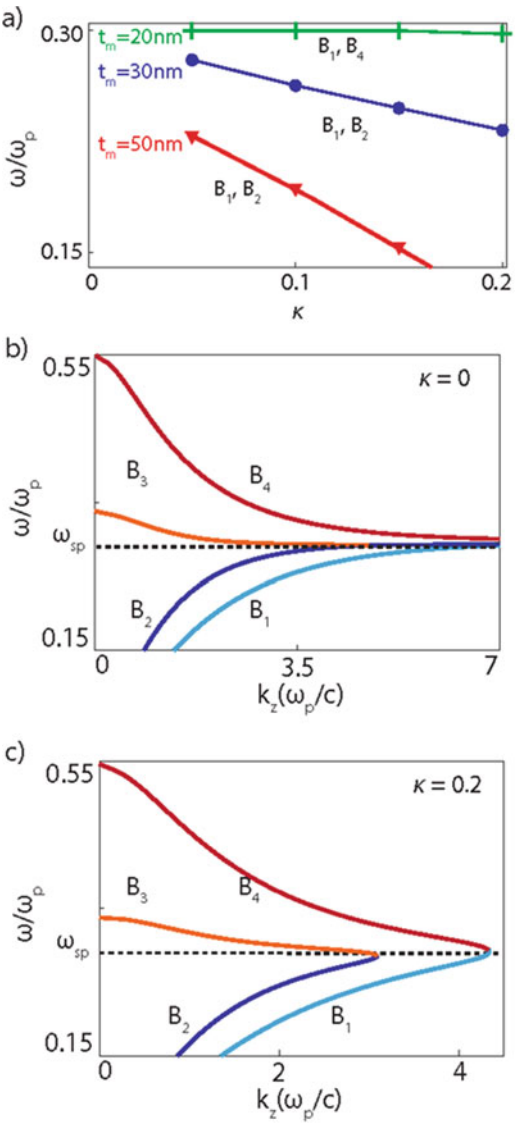

Fig. 5 Exceptional point frequencies with non-Hermiticity. (**a**) Calculated exceptional point frequency for metal spacer thickness of 20 nm (green), 30 nm (blue), and 50 nm (red), for bands indicated. In general, the exceptional point frequency red-shifts with increasing non-Hermiticity. Dispersion plots for a metal thickness $t_m = 20$ nm and dielectric thickness of $t_d = 30$ nm when (**b**) $\kappa = 0$ and (**c**) $\kappa = 0.2$

such coupling not only determines the exceptional point energy, but also which modes coalesce. We consider $t_m = 20$, 30, and 50 nm. As before, we keep the dielectric layer thicknesses fixed at $t_d = 30$ nm to maintain the same number of waveguide modes. Figure 5 plots the exceptional point energy as a function of the non-Hermiticity parameter κ. As seen, for fairly large thicknesses, $t_m = 30$ nm and 50 nm, this mode merges with B_2. Increasing κ or increasing the metal thickness (i.e., decreasing the coupling) shifts the exceptional point to lower energies.

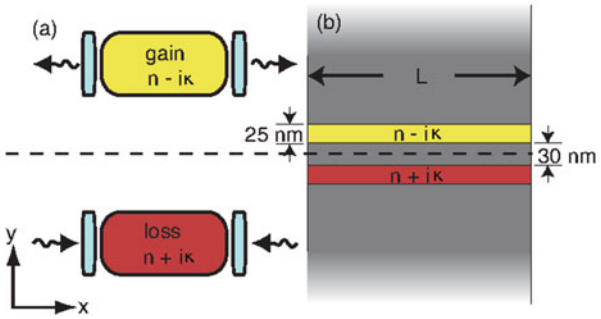

Fig. 6 (**a**) Schematic diagram of a laser cavity and it's time reverse, a coherent perfect absorber. The two devices are PT-symmetric if positioned as in (**a**). (**b**) Schematic diagram of designed absorber-amplifier. Dielectric channels are 25 nm thick with a 30 nm spacer between them. Balanced inclusions of loss and gain in the dielectric channels renders this structure PT symmetric

As the metal thickness is reduced to 20 nm, mode B1 no longer merges with mode B2, but rather with mode B4. The merging of a positive and negative index mode is illustrated in the dispersion diagrams of Fig. 6. For a zero non-Hermiticity parameter, four distinct modes exist, similar to the dispersion for waveguides with $t_m = 30$ nm. As the non-Hermiticity parameter is increased, modes B_1 and B_4 merge together while B_2 and B_3 merge. As seen in Fig. 5, this exceptional point energy is along the surface plasmon resonance frequency (ω_{sp}), and is approximately constant with increasing κ.

3 Section 2: Finite Plasmonic Waveguides for Phase-Controlled Amplification and Absorption [15]

With the modal properties of planar PT plasmonic waveguide structures established, we can exploit their unique properties in new, ultra-compact structures which could enable small-footprint and high-speed signal modulation. Modulation of optical signals typically requires wavelength-scale devices, since most materials have relatively weak optical nonlinearities or electro-optic coefficients. Such large dimensions ensure that the optical signal has sufficient interaction volume with the active material. However, recent advances have enabled compact, subwavelength optical modulators based on the strongly enhanced near fields afforded by surface plasmons. While plasmonic losses play an important role in some of these devices, for example by aiding signal absorption, they generally limit the maximum signal modulation that can be achieved. Indeed, in many plasmonic modulators, it is challenging to completely extinguish losses, resulting in signal attenuation even when the device should be in a transmissive or amplifying state. Accordingly, ohmic losses are often treated as a detriment, reducing propagation lengths or siphoning energy into heating.

Loss, however, plays a beneficial role in PT-symmetric optical systems. Such PT -symmetric optical systems will exhibit real eigenvalues below a critical magnitude of the loss and gain ($|\kappa|_{crit}$), and complex eigenvalues above. Importantly, below κ_{crit}, optical modes will neither become amplified nor attenuated as the loss and gain perfectly balance one another. Above κ_{crit}, however, new optical modes emerge which preferentially interact with either the gain or loss and exhibit either strong amplification or attenuation. This transition plays an important role in enabling unidirectional and even non-reciprocal propagation in these optical devices.

For active signal modulation, no greater contrast exists than that between perfect absorption and lasing, which represent zeros and poles in a scattering matrix. While lasing produces a coherent beam of emitted light, a coherent perfect absorber (CPA) uses the interference of two incoming coherent sources to trap all light in a cavity that contains a threshold amount of loss until it is completely absorbed. If the phase between the two sources is offset, the interference effect is modified and total absorption is lost. The processes therefore represent the time-reverse of one another, ($t \rightarrow -t$), as illustrated in Fig. 6a. Furthermore, note that in lasers, gain ($-\kappa_{crit}$) provides amplification and ultimately stimulated emission, while in CPAs, perfect absorption is achieved via equal but opposite loss ($+\kappa_{crit}$). The relationship between time, loss, and gain in both devices motivates the combination of perfect absorption and lasing in one device based on PT-symmetry. The output of a CPA-laser is determined by its illumination: two coherent illumination sources with the correct phase relation result in CPA, while all other illumination phases produce amplification and lasing.

Inspired by this, we theoretically demonstrate a nanoscale PT-symmetric modulator capable of both strong coherent absorption and amplification. The device design is based on a subwavelength plasmonic aperture composed of deeply subwavelength plasmonic waveguides. As shown in Fig. 6b, we consider two 25 nm-thick dielectric channels separated by a 30 nm metal spacer layer and embedded in a semi-infinite metallic cladding. The length of the aperture is L. The dielectric channels are modeled as materials with a Lorentzian dispersion that have an approximate real refractive index of $n \approx 1.44$ corresponding to SiO_2, while the imaginary component is varied for different simulations but always kept equal in magnitude and opposite in sign for the two channels. The metal is a lossy Drude model representative of silver. Note that we call the aperture PT-symmetric in describing the dielectric channels; the cladding and separating metallic layer do not maintain PT-symmetry and are uniformly lossy.

We first explore this PT-symmetric system for the case of a large aperture length (L), with $L \rightarrow \infty$, to determine the dependence of the modal dispersion on the non-Hermiticity factor (κ). Using both an analytic transfer matrix method and a finite difference time domain (FDTD) mode solver (Lumerical), we determine the complex wavevectors and the |E| field profiles for different values of κ at a fixed near-infrared wavelength, $\lambda = 1662$ nm, for the infinite waveguide. This wavelength corresponds to the peak transmission through a 300 nm long, finite length, absorber-amplifier described in later sections and is near wavelengths of interest to telecom applications. Our analytic and FDTD methods produce highly corroborating results

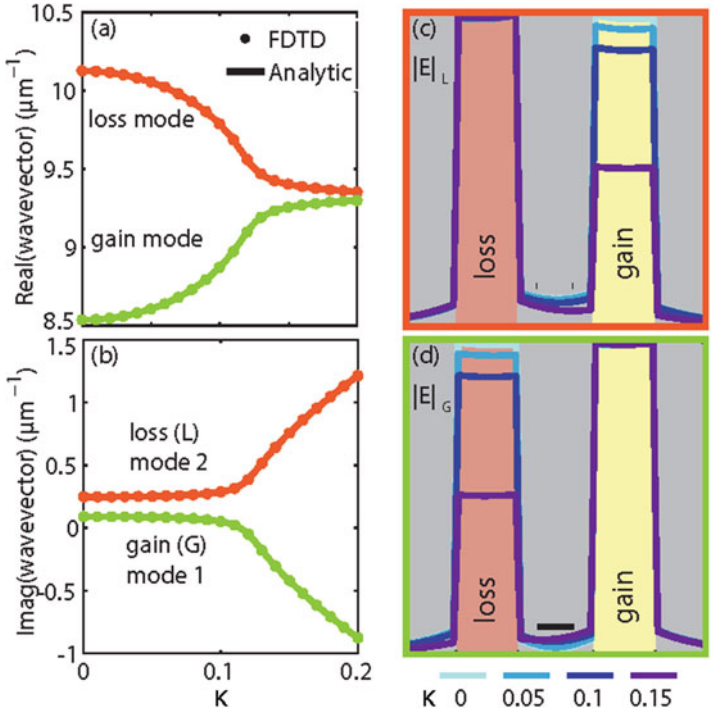

Fig. 7 Dispersion and field profiles in dielectric channels. Real (**a**) and imaginary (**b**) wavevectors for the two modes considered. FDTD simulations (dots) match analytical model (line). Loss (**c**) and gain (**d**) modal field profiles for $\kappa = 0$, 0.05, 0.1, and 0.15. All fields are normalized to either the loss or gain channel, respectively

for modes supported by the structure from $\kappa = 0$ to $\kappa = 0.2$, which encompasses a range of experimentally accessible values.

As seen in Fig. 7a and b, the two lowest order modes in the passive ($\kappa = 0$) structure have imaginary wavevectors of a similar magnitude but distinct real wavevectors, since they represent the even and odd magnetic field (H_y) distributions in a structure. The green point represents the even mode of the five-layer metal-insulator-metal structure, while the red point represents the odd mode of the $\kappa = 0$ structure. For $\kappa > 0$, the modes lose their definite parity, and we simply refer to mode 1 (green trace) and mode 2 (red trace). As the non-Hermiticity factor is increased, the real components of the wavevectors approach the same value, while the imaginary components begin to diverge. Above $\kappa = 0.1$ mode 2 becomes increasingly lossy while mode 1 evolves into a gain mode. This is the transition from unbroken- to broken-symmetry. At $\kappa = 0.11$, mode 1 crosses the zero point in Fig. 7b and becomes lossless, and for greater κ, it experiences amplification.

Figure 7c and d display the time averaged |E|-field profiles for the two modes for selected values of κ. At $\kappa = 0$, the field intensity is greatest within the dielectric

channels, with the odd mode possessing slightly greater field intensity in the metal spacer layer. This profile results in the larger imaginary part of the wavevector. For larger values of κ, the field profiles in the loss and gain channels become unequal for the two modes with greater intensity in the gain channel for mode 1 and greater intensity in the loss channel for mode 2. Note that in our Figure, the magnitude of |E| is normalized such that the intensity remains constant in the dominant channel and is diminished in the other channel. As κ increases, the reduction of intensity in the non-dominant channel becomes more pronounced, and at $\kappa = 0.15$, it is half the intensity of the dominant channel. The unequal field distribution and clearly defined loss and gain modes indicate a transition to broken-symmetry and a unidirectionality of power flow between the two channels in the structure.

For ideal PT-symmetric optical systems, a singular exceptional point marks the transition between the unbroken- and broken-symmetry regimes of the device. In other words, this exceptional point marks the splitting of the imaginary components of the mode wavevectors and the merging of the real components. Correspondingly, the distribution of the power remains perfectly symmetric up to the exceptional point and becomes asymmetric beyond. Our system does not exhibit such a sharp exceptional point because we include a lossy Drude model for the metal, and thus our system is not perfectly PT-symmetric. However, we note that ideal PT-symmetric behavior could be restored through "healing" the device [16] by altering the real part of the index in one or both of the waveguides.

We next consider a finite-length resonator with $L = 300$ nm for both $\kappa = 0$ and $\kappa = 0.1$. Using FDTD simulations, the resonator is illuminated with a single plane wave at normal incidence and the transmitted and reflected intensities are collected. Figure 8 shows the transmission and reflection of both the $\kappa = 0$ and $\kappa = 0.1$ resonators. As seen, the maximum transmission of the passive resonator peaks at a wavelength of 1542 nm and is approximately 6% of the incident intensity. A minimum in reflection occurs at slightly blue-shifted wavelengths (1470 nm) and dips below 3%. Except at this minimum, the passive structure reflects substantially more than it transmits, reaching a maximum of 50% of the incident intensity at a wavelength of 1770 nm.

In contrast to the $\kappa = 0$ configuration, peak transmission through the cavity with $\kappa = 0.1$ is 40 times greater than the peak with $\kappa = 0$, exhibits substantial line-width narrowing, and reaches a maximum at 1662 nm. The reflection and transmission peaks also occur at 1662 nm, and for both reflection and transmission, the signal is amplified by more than two times. In other words, the cavity with $\kappa = 0.1$ has greater-than-unity reflection and transmission coefficients on resonance. For wavelengths longer than the peak transmission, much of the incident intensity is reflected. However, for wavelengths shorter than the peak transmission, there is little reflection or transmission (< 30%) with a minimum in reflection of less than 4% at 1645 nm. From these simulations, we see that the $\kappa = 0.1$ configuration shows unique transmission and reflection properties from $\kappa = 0$, holding promise as a device with signal amplification.

To realize phase-modulated absorption and amplification, we illuminate the resonator with two plane wave sources of equal intensity. As illustrated in Fig. 9a,

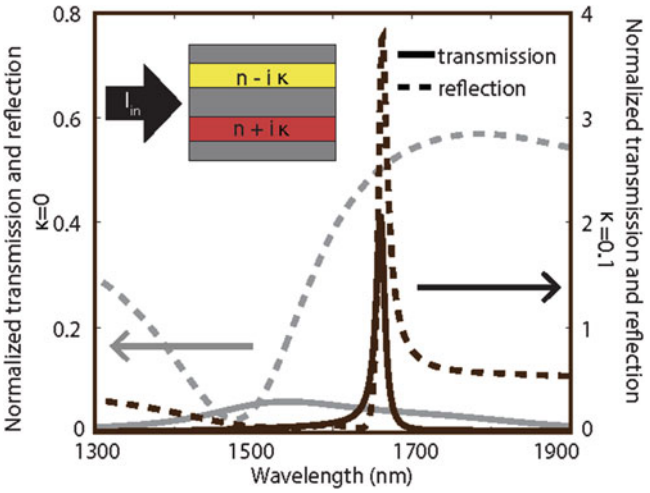

Fig. 8 Normalized Transmission and reflection from the aperture with $\kappa = 0$ (grey, left) and $\kappa = 0.1$ (black, right). Illumination condition is indicated by the inset

two sources of intensity I_{in} impinge on the aperture from opposite sides. The right side source possesses a phase lead, ϕ, between 0° and 360°. The scattering from the aperture is collected as $I_{out,l}$ and $I_{out,r}$, with $I_{out,r}$ corresponding to the side with the variable phase lead. As shown in Fig. 3, the $\kappa = 0$ and $\kappa = 0.1$ resonators have different spectral profiles, and therefore exhibit different phase-dependent behavior at different wavelengths. For $\kappa = 0$, we consider a wavelength of $\lambda = 1767$ nm, which is the reflection peak. We leave out the transmission peak wavelength for $\kappa = 0$ from this discussion as the transmission intensity is far less than the reflection intensity and the phase dependent behavior is accordingly similar but less remarkable. For $\kappa = 0.1$, we look at the peak transmission and reflection wavelengths, $\lambda = 1662$ nm, as well as the minimum reflection wavelength, $\lambda = 1645$ nm. The peak transmission wavelength exhibits large modulation depths, while the minimum in reflection wavelength shows strong directionality. The total intensity scattered from the structures, as well as $I_{out,l}$ and $I_{out,r}$, is plotted as a function of phase offset for these wavelengths in Fig. 9b–d.

The phase dependent scattering for $\kappa = 0$ at $\lambda = 1767$ nm is shown in Fig. 9b. The total scattering and directional scattering are normalized to the combined amplitudes of the two plane waves constructively interfering in free space. The total scattering ($I_{out,l} + I_{out,r}$) reaches a maximum of 63% when the two sources are perfectly out of phase and a minimum of 47% when both sources are in-phase. Between these two extremes, the aperture exhibits minimal directionality, with the difference in scattering between both sides differing by no more than 10% of the incident intensity.

The device's scattering when $\kappa = 0.1$ for $\lambda = 1662$ nm is shown in Fig. 9c. Sweeping the phase offset reveals far greater modulation in the total scattered

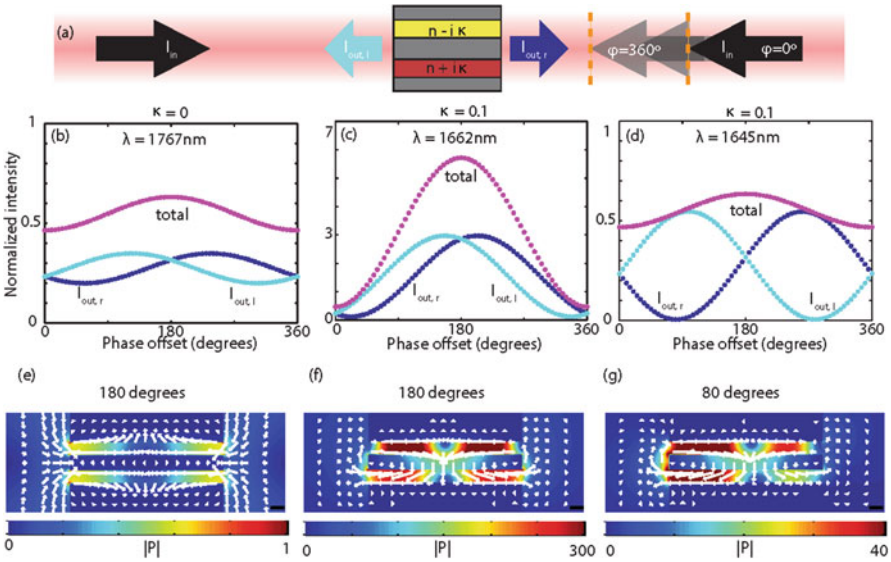

Fig. 9 Phase-dependent absorption and amplification. (**a**) Broadband plane wave illumination from both directions with equal intensity I_{in}. The right side input has a phase lead phi which varies between 0 and 360° relative to the left side input. $I_{out,l}$ and $I_{out,r}$ represent the combined reflection and transmission scattered normal to the aperture. (**b–d**) Scattering intensity exiting the aperture while illuminated from both directions as a function of phase offset. (**b**) shows peak intensity for the passive aperture, while (**c**) and (**d**) show maximum amplification and differential output intensity for the $\kappa = 0.1$ aperture. (**e–g**) Cross sections of the pointing vectors for the same wavelength and κ values of (**b–d**). (**e**) Power profile through a $\kappa = 0$ aperture with 180° offset at a free-space wavelength of 1767 nm. (**f**) Maximum pointing vector magnitude for 1662 nm illumination of a $\kappa = 0.1$ aperture occurs at 180° offset. (**g**) Strongly directional output intensity observed for 80° offset at 1645 nm with $\kappa = 0.1$ aperture. Poynting vector maps are normalized to the passive aperture. Scale bar represents 25 nm

intensity compared to the $\kappa = 0$ configuration. Notably, a phase offset near 0° generates a total output that is less than half of the input intensity, while a phase offset of 180° generates a total output that amplifies the input intensity by 5.7 times. Alternatively, the output from each side ($I_{out,l}$ or $I_{out,r}$) can also vary between roughly three times to less than 15% of the input intensity. Furthermore, the devices with $\kappa = 0.1$ also exhibit more pronounced directionality than an aperture with $\kappa = 0$. Almost complete directional absorption of the incident field is observed at a wavelength of $\lambda = 1645$ nm, shown in Fig. 4d. With an incident phase offset of 80°, the scattering from $I_{out,r}$ can be reduced to a minimum of 0.46% of the incident intensity. Maximum scattering occurs at a phase offset of 260° with $I_{out,r}$ reaching 55% of the input intensity. The modulation depth at this wavelength is therefore greater than 99%.

To better illustrate how far-field modulation arises from near-field properties, Fig. 9e–g plot 2D near-field maps of the Poynting vector for the $\kappa = 0$ and $\kappa = 0.1$ resonators at the same wavelengths in Fig. 9b–d. The overlaid arrows indicate the

direction of the Poynting vector and the underlying color maps show the magnitude of the Poynting vector and are normalized such that the maximum magnitude in the $\kappa = 0$ plot is unity. As seen in Fig. 9e, when $\kappa = 0$ and the structure is illuminated by a phase offset of 180°, the Poynting vector from each aperture facet is symmetric. The Poynting vector points towards the aperture and into the metal with generally low intensities as would be expected for a structure without gain. When $\kappa = 0.1$ and the structure is illuminated with a phase offset of 180°, the Poynting vector behavior is again symmetric along the y-axis (Fig. 9f). However, the maximum intensity is more than two orders of magnitude greater than the $\kappa = 0$ aperture and the distribution is no longer symmetric along the x-axis. The Poynting vector in the gain (top) and loss (bottom) channels now differs by roughly a factor of 1.5, and point from the gain channel to the loss channel. Since the aperture is near but not beyond the exceptional point at $\kappa = 0.1$ and the length of the aperture is small in comparison to the wavelength, we expect this directionality between the two channels. The arrows in Fig. 9f also show that the scattering from the aperture is dominated by the loss channel, indicating that the destructive interference at the ends of the channel necessary for complete CPA is not present although nascent intensity nodes do appear at the ends of the gain channel.

A near-field Poynting vector map is also plotted at a phase offset of 80° (Fig. 9g) for $\lambda = 1645$ nm. As with the 180° phase offset at $\lambda = 1662$ nm, the Poynting vector points from the gain channel to the loss channel inside of the aperture, while on the aperture's left, the Poynting vector mainly emerges from the loss channel. Unlike panels (e) and (f), the color map indicates an unequal distribution of the magnitude of the Poynting vector at the two ends of the aperture. Intensity is greater on the left side and the scattering from the right side is hindered by interference effects visible as a more pronounced node in intensity in the gain channel. The right side of the loss channel does not possess an equally apparent node, but intensity is still substantially reduced in comparison to the intensity from the left side matching the asymmetry in Fig. 9d.

4 Section 3: Thresholdless Symmetry Breaking with Coaxial Plasmonic Geometries [17]

Our analysis of planar plasmonic waveguides provides a foundation to understand modal evolution under a PT symmetric potential which can be applied to other novel systems with more complex configurations. While the waveguides exhibit translational symmetry, PT-symmetric systems can be designed with rotational symmetry. As we will show, azimuthally arranged loss and gain with rotational symmetry leads to new phenomena. Most interestingly, thresholdless exceptional points can be deterministically designed, greatly reducing the materials requirements for this sort of system. The addition of loss and gain can lift the degeneracy between clockwise and counterclockwise modes, which can be used in mode-division multiplexing.

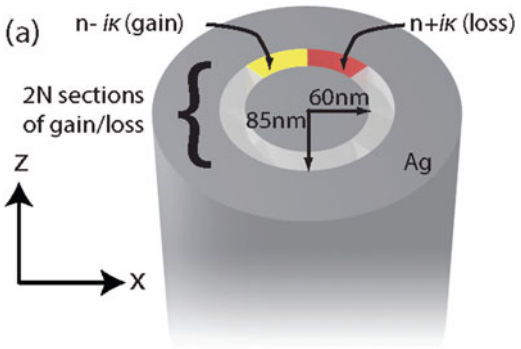

Fig. 10 Schematic of the PT-symmetric coaxial waveguide where the channel includes alternating sections of loss (red) and gain (yellow)

As shown in Fig. 10, our structure is a three-layer coaxial waveguide consisting of a dielectric ring and silver core embedded in a silver cladding. The silver core has a radius of 60 nm and the permittivity is described with a Drude model as $\epsilon_{Ag} = 1 - \left(\frac{\omega_p}{\omega}\right)^2$, where $\omega_p = 8.85 \times 10^{15}$ Hz. The dielectric channel is 25 nm thick and characterized by a real refractive index of n = 1.5. The channel is filled with alternating sections of gain and loss, which can be represented as

$$\Delta n = \begin{cases} n_{gain} = -i\kappa, & l\pi/n \le \phi \le (l+1/2)\,\pi/N \\ n_{loss} = +i\kappa, & (l+1/2)\,\pi/N \le \phi \le (l+1)\,\pi/N \end{cases} \tag{2}$$

Here, κ is the magnitude of the gain/loss, 2N is the number of loss (or gain) segments, ϕ is the azimuthal angle around the coaxial channel, and l is an integer spanning 0,1,...,2 N − 1. The presence of gain and loss makes the system non-Hermitian, so κ can be considered the non-Hermiticity parameter. In this geometry, the parity operator is defined as P(ϕ) → −ϕ. The refractive index profile and permittivity of the coaxial waveguide therefore satisfy the PT-symmetry condition ($\epsilon(r,\phi) = \epsilon^*(r,-\phi)$). While a closed-form solution to this PT coaxial waveguide does not exist, a Hamiltonian formulation and degenerate perturbation theory can be used to investigate the modal properties.

Due to the axial symmetry of the waveguide, the modes vary azimuthally as $e^{im\phi}$; in other words, they have well-defined angular momenta parametrized by m. For a periodic refractive index distribution as in Eq. 2, the index can also be expanded in the harmonic basis of $e^{im\phi}$. The overall symmetry of the waveguide's cross section can be categorized based on whether N is an integer or half integer.

N (*half-integer*): the distribution possesses anti-symmetry with respect to the center of the coaxial waveguide ($\epsilon(r,\phi) = \epsilon^*(r,\phi+\pi)$), so *even*-order Fourier coefficients vanish.

N (*integer*): the distribution has inversion symmetry with respect to the center of the coaxial waveguide ($\epsilon(r,\phi) = \epsilon^*(r,\phi+\pi)$), so *odd*-order Fourier coefficients vanish.

The transverse electric and magnetic fields, E_t and H_t, and corresponding propagation constants β of the waveguide modes are determined via

$$\widehat{H}\begin{bmatrix}\overrightarrow{E_t}\\ \overrightarrow{H_t}\end{bmatrix}=\beta\begin{bmatrix}0 & \widehat{z}\times\\ \widehat{z}\times & 0\end{bmatrix}\begin{bmatrix}\overrightarrow{E_t}\\ \overrightarrow{H_t}\end{bmatrix} \tag{3}$$

Here, the subscript t refers to the transverse components of the fields and $\widehat{z}$ is the direction of propagation. The Hamiltonian $\widehat{H}$ depends on the waveguide geometry, as well as the material properties, and is given by

$$\widehat{H}=\begin{bmatrix}\omega\epsilon_0\epsilon-\frac{1}{\omega\mu_0}\nabla_t\times[\widehat{z}(\widehat{z}\cdot\nabla_t\times)] & 0\\ 0 & \omega\mu_0-\frac{1}{\omega\epsilon_0}\nabla_t\times[\widehat{z}(\widehat{z}\cdot\nabla_t\times)]\end{bmatrix} \tag{4}$$

where ε_0 and μ_0 are the permittivity and permeability of free space, ε is the material permittivity, and ω is the angular frequency. By choosing a complete basis $|\overrightarrow{F_n}\rangle$, the matrix elements of the Hamiltonian $\widehat{H}$ can be determined as

$$\begin{aligned}H_{mn}=\left\langle\overrightarrow{F_n}|\widehat{H}|\overrightarrow{F_n}\right\rangle&=\omega\epsilon_0\int_{WG}\epsilon(r)\,\overrightarrow{E}^*_{mt}\cdot\overrightarrow{E}_{mt}ds\\&+\omega\mu_0\int_{WG}\overrightarrow{H}^*_{mt}\cdot\overrightarrow{H}_{mt}ds-\omega\epsilon_0\int_{WG}\epsilon(r)^*E^*_{mz}E_{nz}ds\\&-\omega\mu\int_{WG}H^*_{mz}H_{nz}ds\end{aligned} \tag{5}$$

where subscripts m and n refer to the mth and nth modes, respectively; subscript z denotes the longitudinal direction; and the integral $\int_{WG}ds$ indicates an integration over the cross section of the waveguide. From this last equation it can be inferred that $\widehat{H}$ is Hermitian if and only if ε(r) is real, i.e., all the materials are lossless.

For $\kappa\neq 0$, the Hamiltonian can be written as $\widehat{H}=\widehat{H}_R+i\widehat{H}_I$. When $\kappa\ll$ n, $\widehat{H}_R$ of the PT-symmetric and the uniform waveguide are nearly equal—hence $\widehat{H}_R$ is diagonal in the basis of the homogeneous waveguide modes. Using Eq. 4 we have

$$\begin{aligned}H_{mn}&=\left\langle\overrightarrow{F}_m\mid\widehat{H}_R+i\widehat{H}_I\mid\overrightarrow{F}_n\right\rangle=\left\langle\overrightarrow{F}_m\mid\widehat{H}_R\mid\overrightarrow{F}_n\right\rangle+i\left\langle\overrightarrow{F}_m\mid\widehat{H}_I\mid\overrightarrow{F}_n\right\rangle\\&=\beta_n\delta_{mn}+i\left\langle\overrightarrow{F}_m\mid\widehat{H}_I\mid\overrightarrow{F}_n\right\rangle\end{aligned} \tag{6}$$

The matrix elements of the perturbing Hamiltonian are determined as

$$H_{Imn}=\left\langle\overrightarrow{F}_m\mid\widehat{H}_I\mid\overrightarrow{F}_n\right\rangle=\omega\varepsilon_0\int_{WG}\epsilon_i(r)\,\overrightarrow{E}^*_m\cdot\overrightarrow{E}_n ds \tag{7}$$

Here $\epsilon_i(r)$ is the imaginary part of the dielectric constant spatially modulated as in Eq. 1. Considering the azimuthal variation of the modes in a uniform waveguide, the above equation can be simplified to

$$H_{Imn} = \left\langle \overrightarrow{F}_m \mid \widehat{H}_I \mid \overrightarrow{F}_n \right\rangle = \omega\varepsilon_0 \int_{R_{in}}^{R_{out}} dr\, r\, \overrightarrow{R}^*_m(r) \cdot \overrightarrow{R}_n(r) \times \int_0^{2\pi} d\phi\, \epsilon_i(\phi)^{i(n-m)\phi} = 2\pi\omega\varepsilon_0 C_{m-n} \times \int_{R_{in}}^{R_{out}} dr\, r\, \overrightarrow{R}^*_m(r) \cdot \overrightarrow{R}_n(r), \tag{8}$$

where $\overrightarrow{R}(r)$ is the radial distribution of the modes and C_{m-n} is the (m − n)th Fourier coefficient of the gain/loss arrangements in the channel given in Eq. 4. Since C_{m-n} describes the gain and loss, it is linearly proportional to κ. The Fourier coefficients can be largely controlled via N. The modal properties of each case can be determined by solving for the eigenvalues and eigenfunctions of the H matrix given by Eq. 6.

We first apply this formalism to a coaxial waveguide with a uniform channel ($\kappa = 0$). Figure 16a plots the dispersion for this coaxial structure, where mode orders up to $m = 6$ are found below 3 eV. Note that the dispersions of all modes diverge for energies close to the surface resonance frequency of the silver-dielectric interface ($\omega_{sp} \approx 3.1$ eV). The modes of the uniform waveguide ($\kappa = 0$) form a complete set, so they can be used as a basis $|\overrightarrow{F_n}\rangle$ to find the modes of the PT-symmetric waveguides of Fig. 10b. Figure 11b shows the distribution of the longitudinal power P_z of the zeroth-, first-, and second-order modes. Note that these modes all have azimuthally symmetric power distributions as a result of possessing well-defined angular momenta.

To investigate the effect of loss and gain inclusions on the modal properties, we consider a fixed energy, E = 2 eV. As seen in Fig. 11, the uniform waveguide supports five modes at this energy, namely, β_0, $\beta_{\pm1}$, and $\beta_{\pm2}$. $\beta_\pm$ represents a pair of degenerate modes, corresponding to CW and CCW OAM. Utilizing these modes as the basis of expansion in Eq. (2), one can investigate the mode morphology as a function of both N and κ. Fig. 17a shows the modal properties of a coaxial waveguide with N = 0.5 at E = 2 eV. Panels (a) and (b) show the variation of the real and imaginary parts of the propagation constants of the five lowest order modes as a function of κ. To differentiate the new modes that appear when $\kappa \neq 0$ from the $\kappa = 0$ modes, superscript indexing has been used. At $\kappa = 0$ in Fig. 12, all modes possess the same propagation constants as in Fig. 11, and the superscript notation eigenvalues can therefore be matched to the unperturbed subscript eigenvalues. The $\beta^{(0)}$ branch has the largest propagation constant and at $\kappa = 0$ corresponds to the $m = 0$ mode β_0. The degenerate pair $\beta_{\pm1}$ becomes $\beta^{(1)}$ and $\beta^{(2)}$ for $\kappa \neq 0$. Similarly, the degenerate pair $\beta \pm 2$ becomes $\beta^{(3)}$ and $\beta^{(4)}$ for $\kappa \neq 0$.

As κ increases, the real(β) of degenerate modes separate from one another (i.e., $\beta^{(1)}$ from $\beta^{(2)}$, $\beta^{(3)}$from $\beta^{(4)}$) and at $\kappa = 0.05$, $\beta^{(0)}$ and $\beta^{(1)}$ reach an EP and real(β) coalesce. $\beta^{(2)}$ and $\beta^{(3)}$ form a similar pair and coalesce at an EP at $\kappa = 0.13$. The

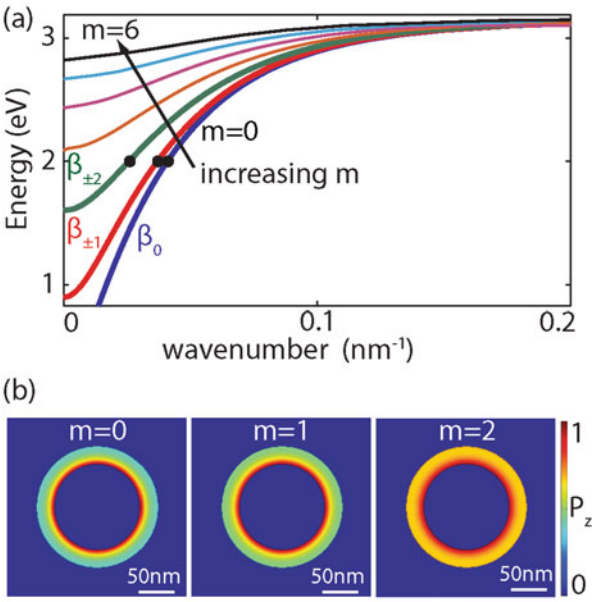

Fig. 11 (**a**) Modes of the passive coaxial waveguide numbered based on their azimuthal order. For the rest of our discussion, we will focus on a photon energy of 2 eV, marked by the three stars. (**b**) Poynting vector distributions for the m = 0, 1, and 2 modes at an energy of 2 eV

propagation constants of the PT-symmetric waveguide's modes are always either real or complex conjugates of each other. To clarify this feature, the imaginary parts of the propagation constants are plotted in Fig. 12a. Note that where real wave vectors converge when the imaginary parts diverge.

Figure 12c shows the spatial distribution of the longitudinal component of the Poynting vector P_z of the modes at small and large values of κ. For small values of non-Hermiticity and before all EPs (κ = 0.02), the propagation constants of all the modes are real, since the power is symmetrically distributed in the gain and loss sections. As seen in Fig. 12a, the power distributions of all modes are symmetric with respect to the x axis; however, in contrast to the uniform waveguide, the power is no longer azimuthally symmetric. When the non-Hermiticity factor is increased to a value beyond both EPs (κ = 0.2), new complex conjugate modes are formed. These modes, on display in Fig. 12c, lose their symmetry with respect to the x axis and are either localized mainly to the loss or gain half of the waveguide. The only mode of this set which does not lose its x-axis symmetry is $\beta^{(4)}$. At higher values of κ and for E > 2 eV, this mode would also eventually reach an EP and lose its symmetry.

The results for N = 0.5 are reminiscent of classical EP behavior in one-dimensional systems: namely, a finite value of κ is required to induce mode coalescence and enter the broken-phase regime. However, because the coaxial waveguide supports degenerate modes, thresholdless behavior can be achieved provided the PT symmetry is engineered. Such behavior requires that the mode symmetry match the distribution of loss and gain—a condition that can be met when N = 1, but which can also be satisfied for higher order modes with higher values of

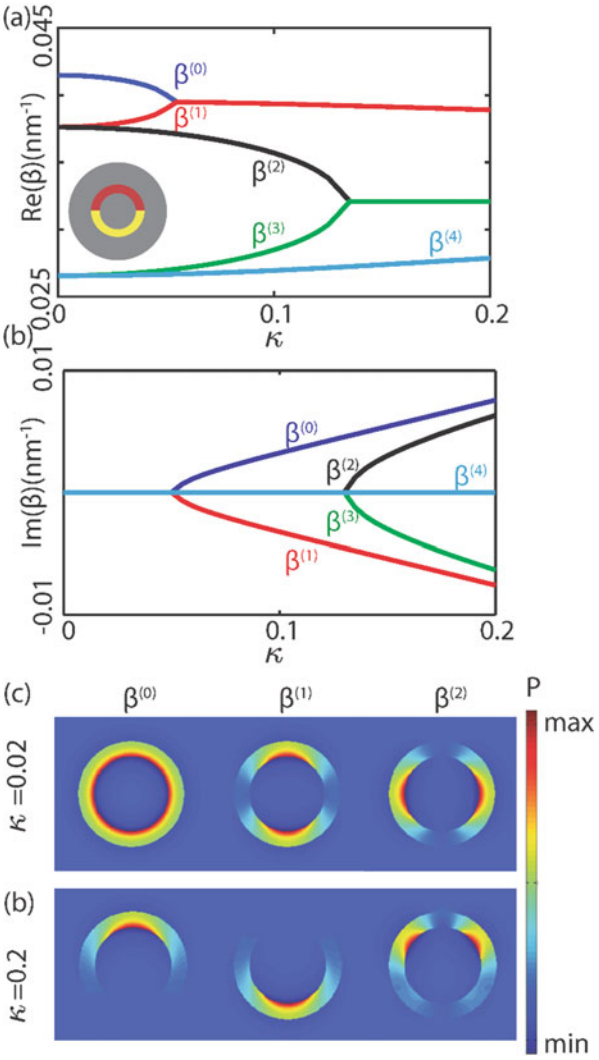

Fig. 12 (**a**) Real and (**b**) imaginary wavevectors for the first 5 modes of the coaxial structure under consideration with N = 0.5 as a function of non-Hermiticity for photon energy E = 2 eV. Inset shows cross section of waveguide. (**c**) Out of plane power distribution of the first 3 modes of the structure for $\kappa = 0.02$ and $\kappa = 0.2$

N. The variations of the propagation constants as well as the corresponding power distributions for this structure are given in Figs. 5 and 6 for E = 2 eV. For this case, modes $\beta^{(1)}$ and $\beta^{(2)}$ possess a constant real propagation constant. The imaginary parts of these modes separate from each other for $\kappa \neq 0$ and therefore have no EP. This behavior exists for all energies above cutoff for $\beta^{(1)}$ and $\beta^{(2)}$ at approximately 0.9 eV. We also observe a new pairing between $\beta^{(0)}$ and $\beta^{(3)}$, which reach an EP at $\kappa = 0.175$. We note this EP occurs at a higher κ than both the pairing of $\beta^{(0)} - \beta^{(1)}$ and $\beta^{(2)} - \beta^{(3)}$ for the N = 0.5 coaxial waveguide because $\beta_0 - \beta_{\pm 2}$ have a greater separation than $\beta_0 - \beta_{\pm 1}$ and $\beta_{\pm 1} - \beta_{\pm 2}$. The mode with the smallest wave vector

remains unaffected by the inclusion of gain and loss and possesses a constant real propagation constant with no imaginary part.

Figure 13 shows the power distribution for this N = 1 coaxial waveguide, again at $\kappa = 0.02$ (a) and 0.2 (b). Unlike the N = 0.5 geometry, $\beta^{(1)}$ and $\beta^{(2)}$ show an unbalanced power distribution even at the small value of $\kappa = 0.02$. The splitting of these two modes is thresholdless (i.e., $\kappa th = 0$), and for any non-Hermiticity parameter greater than zero the power of these modes will be unequally distributed in the gain and loss sections. This phenomenon can be considered spontaneously broken PT symmetry without a regime of unbroken PT symmetry, as the propagation constant becomes complex for any nonzero value of κ. Two additional modes ($\beta^{(0)}$ and $\beta^{(3)}$) reach the broken phase, but these modes possess a classic EP. One can see the power is amplified and attenuated for $\beta^{(1)}$ and $\beta^{(2)}$ in Fig. 13c, while all other modes show no variation in magnitude along the propagation direction for $\kappa = 0.02$.

5 Section 4: Nanoscale Coaxial Polarizers [18]

With the understanding of degenerate modes in PT systems, we apply coaxial structures to finite devices for active polarization control. While high-quality polarizers exist at the nanoscale, they typically reduce transmission. An unpolarized source can be transformed into linearly polarized light with the use of filters, which reduces transmission by 50%. Metasurfaces can spatially modify the outgoing phase of incident light and convert light to another polarization without loss, but these systems are not reconfigurable. Thus, tunable and active polarization conversion in small footprints could be very useful for optical modulation and on-chip light sources. Further, reconfigurability should be more than binary operations, which may occur with electrical or mechanical biasing of phase change materials, liquid crystals, etcetera. To accomplish all of this, we will theoretically demonstrate active polarization conversion in a PT-symmetric plasmonic coaxial structure based on the structures developed in the previous section.

A schematic of the aperture is shown in Fig. 14a. The coaxial aperture is within a 300 nm thick silver film modeled with empirical data from Johnson and Christy. The core's radius is 60 nm, and the dielectric channel is 25 nm across—for a total coaxial cross section of 170 nm. The real part of the refractive index of the dielectric channel is n = 1.5, while the imaginary part, $\pm\kappa$, is dynamically adjusted from 0 to 0.0187 during device operation. These values are achievable with traditional sources of gain media including quantum dots and dopant dyes that could be introduced into a SiO_2 host. The distribution of positive or negative κ is azimuthally defined as four alternating quadrants of gain and loss, producing two-fold mirror symmetry.

The transmission spectra of the finite coaxial aperture is highly dependent on the addition of gain and loss when illuminated with an incident plane wave. Figure 14b shows that the lowest order Fabry-Perot resonance of the aperture occurs at a wavelength of 1117 nm. The transmission is normalized to that of the $\kappa = 0$ aperture and becomes ten times greater when $\kappa = 0.018$ for linear polarized light

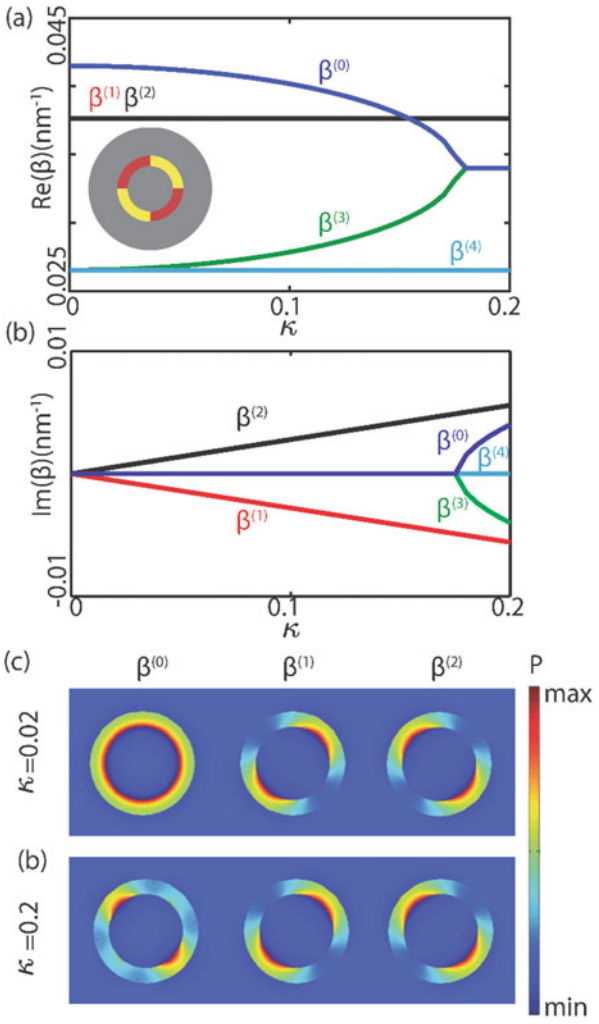

Fig. 13 (**a**) Real and (**b**) imaginary wavevectors for the first 5 modes of the coaxial structure under consideration with N = 1 as a function of non-Hermiticity for photon energy E = 2 eV. Inset of (**a**) shows a cross section of the waveguide. (**c**) Out of plane power distribution for the first 3 modes of the structure for $\kappa = 0.02$ and $\kappa = 0.2$

aligned between the gain and loss sections. The inset of this Figure shows a cross section of the field profile at 1117 nm to confirm this is the lowest order Fabry-Perot resonance. Because only the imaginary part of the index of the dielectric is being modulated, the resonance wavelength changes by less than a nanometer—a distinct advantage of this design over other phase-change material approaches. Alternative dielectric fillers and metals could also tune the response of the resonator and would be particularly useful in regions of the electromagnetic spectrum where silver's losses are too great.

The total transmission for the PT -symmetric coaxial aperture increases with κ, but different output polarization states in the far field will evolve differently. This effect produces the polarization control we explore in this section. We consider two

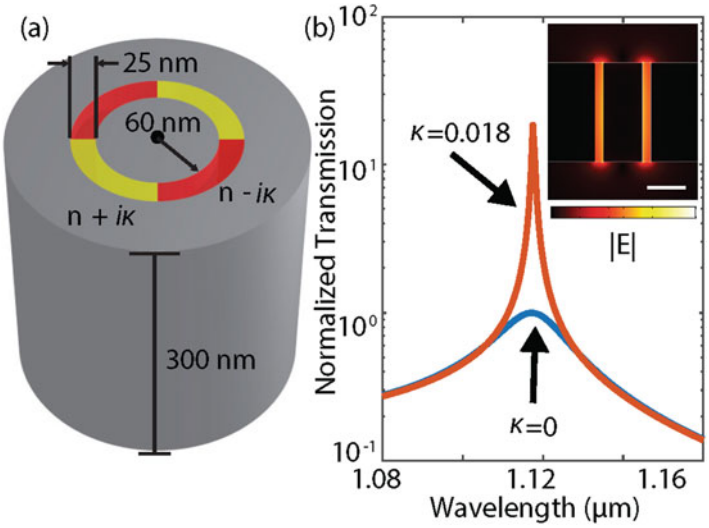

Fig. 14 (**a**) schematic of the coaxial waveguide with alternating sections of gain (yellow) and loss(red). Labels give the specified geometry. (**b**) Transmission spectra of the 300 nm long coaxial aperture when $\kappa = 0$ and $\kappa = 0.018$. (**c**) dispersion of the imaginary wavevectors of the infinitely-long coaxial waveguide as a function of non-Hermiticity at 1117 nm

orthogonal linear polarizations, one aligned to the loss sections and one aligned to the gain sections, as a basis from which all polarizations can be built through variations in phase or amplitude. The loss-aligned polarization ($-45°$) experiences enhanced absorption as κ is increased, and the gain aligned polarization ($+45°$) experiences less absorption or even amplification. Variations in the orthogonal polarizations allow the coaxial aperture to effectively pull an input polarization state towards a linear polarization state aligned with the gain sections.

Our first example of polarization control is conversion from circularly polarized light (CPL) to linearly polarized light (LPL), schematically illustrated in Fig. 15a. Self-normalized near-fields at the end of the aperture are displayed in Fig. 15b for select values of κ. The peak fields are found along the core of the coaxial channel for all values of κ, but the azimuthal distribution differs. When $\kappa = 0.006$, the peak fields near the core interface are altered first, and the fields in the loss sections drop by roughly a factor of two compared to the peak fields in the gain sections. A node starts to appear in the middle of the loss sections for $\kappa = 0.012$ and reaches near-minimum fields at $\kappa = 0.018$. Throughout the full range of operation, the gain regions appear largely unchanged because of the self-normalization but experience well over a two-times amplification. The changes in the near-fields can be relevant for directional or locationally dependent near field coupling applications. To confirm the transmitted polarization state, we propagate the forward scattered light to the far-field, in the direction normal to the film surface, and analyze the transverse electric field components.

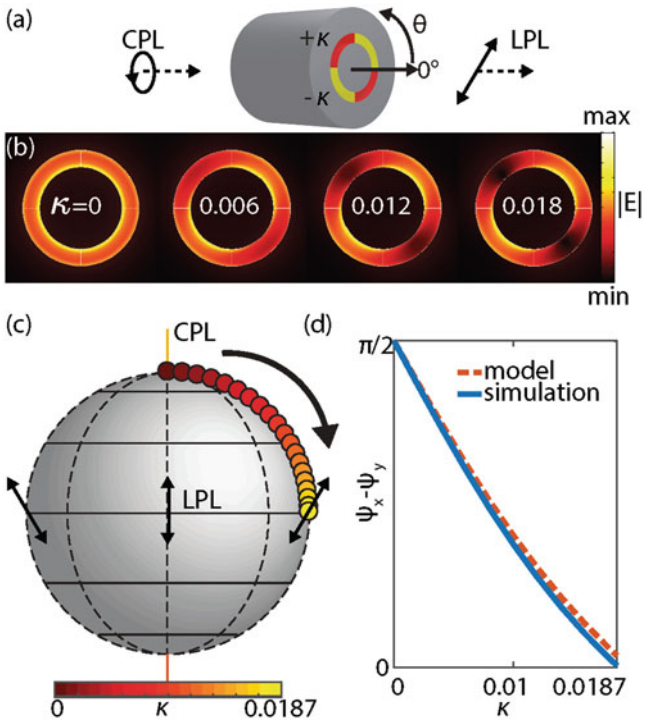

Fig. 15 (**a**) Schematic of illumination conditions considered. (**b**) Evolution of output electric field intensity with increasing non-Hermiticity. Linear polarization characteristic evolves with κ. (**c**) Poincare sphere of the transmitted polarization state in the far field, showing a transition from circularly polarized light to linearly polarized light. (**d**) Far-field phase difference between E_x and E_y

Figure 15c shows the polarization state of the coaxial aperture's far-field transmission for a range of κ when illuminated with CPL; we consider the fields normal to the coaxial aperture. The Poincare sphere is oriented such that the north and south poles correspond to CPL, while the equator is LPL. The polarization is marked with circles for $\kappa = 0$ through $\kappa = 0.0187$, as indicated by the colormap. Each point represents a $\kappa = 0.001$ increment, aside from the last, which represents a 0.0007 increment. The points show a smooth progression from CPL, through varying degrees of ellipticity, to linear polarization. The polarization angle is approximately 45°, the angle corresponding to the center of the gain region.

To explain the rate of change of ellipticity as a function of κ, we consider the anisotropic amplitude modification and investigate the change in phase of the orthogonal polarizations. Figure 15d shows that the difference in phase between the electric field in x and y drops from π/2 to zero as the polarization transitions

from circular to linear. We consider E_x and E_y aligned between the gain and loss sections such that their total magnitudes will remain constant for all κ, but the weight between the gain and loss mode will change considerably. As seen, there is a sublinear drop from $\pi/2$ phase difference to effectively 0 phase difference when $\kappa = 0.0187$, the value at which the loss mode is killed off and the gain mode sufficiently amplified in this geometry.

Selective amplification and absorption can also be used to smoothly achieve polarization rotation of linearly polarized light by adjusting the relative amplitudes of the orthogonal components. The coaxial aperture is capable of up to 80° polarization rotation while maintaining a high degree of linearity. Rotation always occur in the direction with the shortest path of rotation to the gain-orientation defined as 45°, as noted in Fig. 15a. The electric field intensity at the end of the coaxial aperture is shown in Fig. 16b when the structure is illuminated with −35° linearly polarized light for four values of κ. −35° corresponds to 10° away from the loss axis, and so the electric fields are localized to the loss sections while field nodes exist in the gain sections. As κ is increased, the hot spots and nodes rotate counter-clockwise around the dielectric ring. Beyond $\kappa = 0.012$, the rotation increment per κ increases; by $\kappa = 0.018$, the hot spots have aligned with the gain sections, and the weaker nodes are aligned with the loss sections. The fact that the minima are slightly elevated hint that the polarization has taken on some minor ellipticity for this full 80° rotation. For input polarizations beyond 85° offset from the gain-angle, we see the coaxial aperture functions as a polarization filter and increasingly absorbs light for higher values of κ; LPL inputs between −40° and − 50° will therefore lose some intensity when passed through the coaxial aperture.

The progression of the normal far field polarization rotation is expanded on for two input linear polarizations, −5° and −35°, in Fig. 16b. The Poincare spheres are rotated such that the perimeter corresponds to linear polarized outputs equator. For both inputs, we see that for $\kappa = 0.0187$ the polarization is pulled to 45°, the angle corresponding to the gain sections. When the input is −5°, the points are relatively equally spaced and lie directly on the perimeter. In fact, for the final 45° output, the ellipticity ratio between the gain aligned polarization and the loss aligned polarization (major axis and minor axis) is over 550. Conversely, when the input polarization is −35°, the spacing between the equal steps in κ appears nonlinear, and for the maximum degree of rotation the point lies slightly off the perimeter, indicating some ellipticity. For this maximum range of 80° rotation, the elliptical contrast ratio between the gain and loss axis (major axis and minor axis) is approximately 25.

A complete range of input polarizations and their resulting far-field output polarizations is shown in Fig. 16c for four select values of κ. All input polarizations <80° offset are fully rotated to 45°. We see the polarizations are pulled down to the gain axis at 45° with nonlinear rates that vary both as a function of input polarization and κ. The nonlinearity of the polarization rotation is explored more thoroughly in Fig. 16d. For −5° and −15° inputs, we see roughly linear polarization rotation

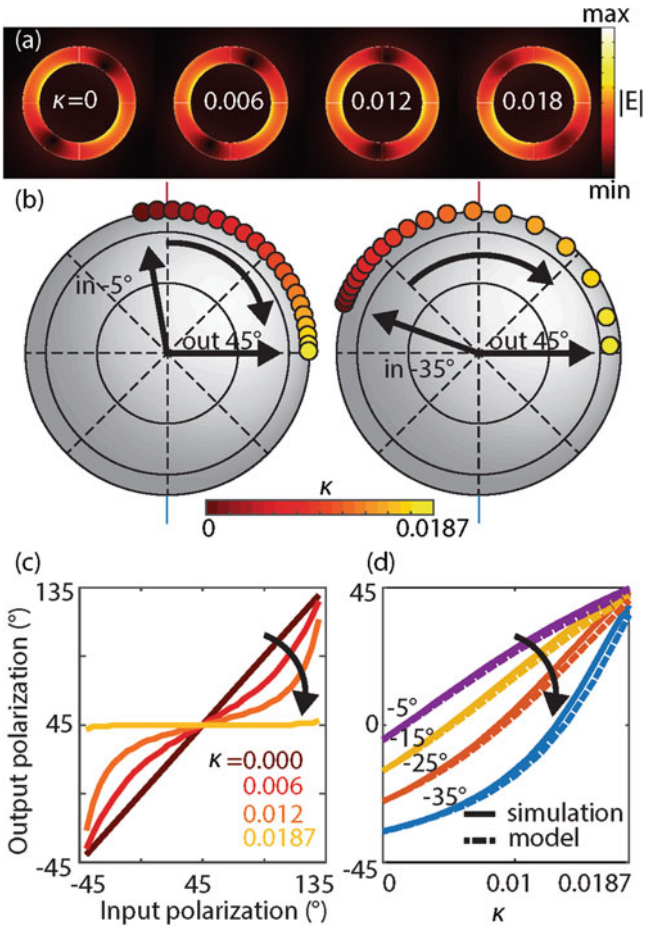

Fig. 16 (**a**) Electric field intensity at the output of the aperture when illuminated with LPL aligned to −35°. Field intensity rotates around the coaxial structure with increasing non-Hermiticity. (**b**) Poincare sphere representation oriented to show linear polarization conversion for two different illumination conditions. (**c**) Output polarization angle as a function of input angle with increasing non-Hermiticity. (**d**) Simulation and model of output polarization as a function of κ

as a function of κ in both the simulation and the model. As the total distance of rotation is increased, as in the case of −25° and −35° inputs, we see the sensitivity of the output polarization to κ increases with κ in both the simulation and the model. This nonlinearity arises from the inverse relationship between the transmitted fields and κ.

6 Section 5: Parity-Time Symmetric Plasmonic Metamaterials [19]

All of the properties we have described thus far result from the strongly confined fields inherent in plasmonic nearfields, which allow us to build materials with deeply subwavelength length scales. Because of this, effective properties can be defined and we can construct metamaterials from these building blocks. As we will see, the exceptional point has a dramatic impact on the optical properties of the metamaterial, with mode coalescence leading to dramatic changes in refractive index, reflection, and transmission. Myriad interesting effects such as a negative refractive index, elliptical to hyperbolic dispersion, double refraction, and others can be tuned by the modifying the non-hermiticity parameter. Due to the large modulation in the bandstructure achievable in this system, we will further demonstrate nonreciprocal transmission over a large bandwidth in the visible with simple assumptions about the saturation of loss and gain media.

We again consider a planar plasmonic metamaterial with five layers of alternating metal and dielectric, with the unit cell period indicated by Λ. Within each unit cell, the thicknesses of the metal t_m and dielectric t_d are deeply subwavelength, with $t_m = t_d = 30$ nm. We consider silver as the metal, described by a lossless Drude model with dielectric constant $\varepsilon_{Ag} = 1 - (\omega_p/\omega)^2$; the bulk plasma frequency of Ag is again assumed to be 8.85×10^{15} s^{-1}. We consider the dielectric layers to be TiO_2 with $n = 3.2 \pm i\kappa$. PT-symmetric potentials require balanced loss and gain, so the magnitude of the imaginary index of TiO_2 (κ) is identical for alternating dielectric layers. With these materials, the surface plasmon resonance ω_{sp} occurs at 1.73 eV ($\omega_{sp}/\omega_p = 0.29$), and negative index modes are observed between this frequency and ω_p. Here we theoretically investigate the evolution of the optical bands of this metamaterial upon varying the non-Hermiticity parameter.

Using the transfer matrix approach, we solve for the dispersion curves of the five-layer unit-cell plasmonic waveguide for transverse-magnetic (TM) polarized illumination. To determine the band diagrams of the periodic metamaterial, the wave vector along the z direction is swept in the first Brillouin zone $(0,\pi/\Lambda)$, and the characteristic equation is minimized to find the propagation constant along the x direction at each frequency. The results are shown in Fig. 17b–e for $\kappa = 0$, 0.2, 0.3, and 0.5, respectively, reflecting gain coefficients achievable with current ($\kappa \leq 0.2$) and next-generation gain media. Note that the colormap indicates purely real values of k_x, corresponding to lossless propagation along the metamaterial. For a non-Hermiticity parameter $k = 0$, four different branches are observed: two below ω_{sp} (B_1 and B_2) and two above (B_3 and B_4). Because all constituents are lossless, the wave vectors diverge at ω_{sp}. B_1 and B_2 are characterized by positive slopes and hence positive refractive mode indices. In contrast, B_3 and B_4 are characterized by negative slopes and hence negative refractive mode indices.

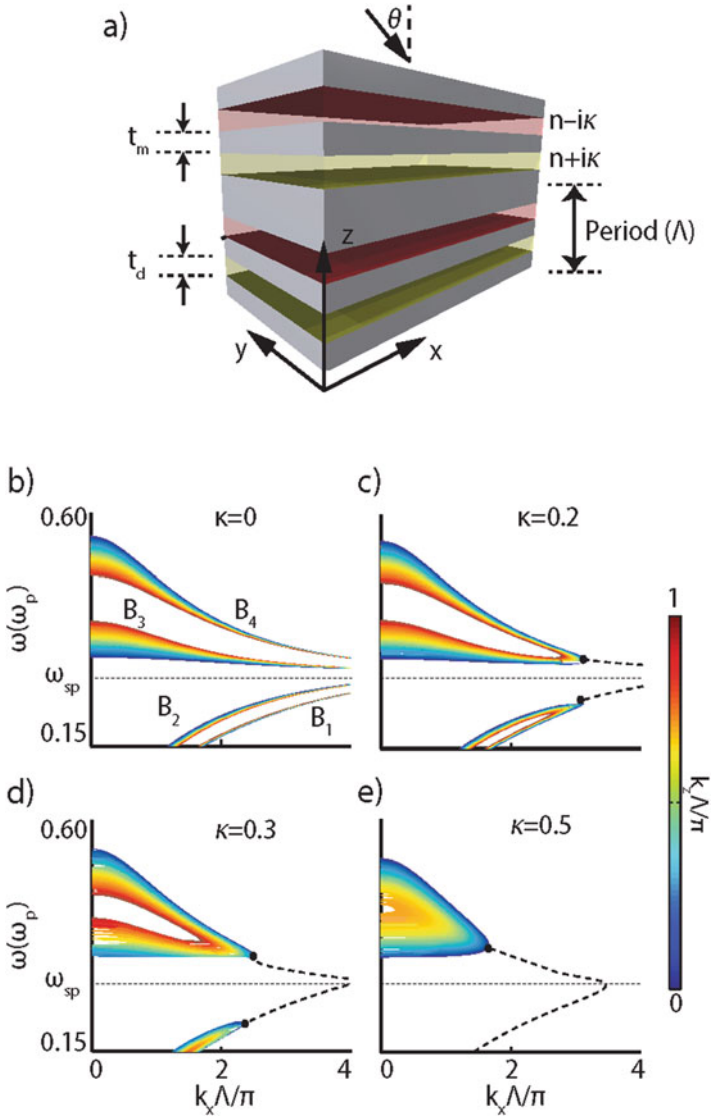

Fig. 17 (**a**) schematic of metamaterial considered in this section. (**b–e**) band diagrams through the first Brillouin zone for the metamaterial with $\kappa = 0$, 0.2, 0.3, and 0.5, respectively. Exceptional points are denoted with black dots, where eigenvalues cease to be real and enter the complex plane (path beyond the EP is traced out with dashed lines)

When κ is increased, the modes merge together at the exceptional points of the dispersion, denoted by black circles in Fig. 17c–e. Beyond these exceptional points, the two distinguishable lossless modes below and above ω_{sp} (i.e., B_1 and B_2 or B_3 and B_4, respectively) evolve to a gain mode and a loss mode with the same phase

velocity. Due to their complex wave vectors, we denote these modes as black, dashed lines in Fig. 17c–e.

To understand these loss and gain modes, note that the transfer matrix of the PT-symmetric metamaterial possesses the following symmetry property:

$$T\left(\omega, k_z, k_x^*\right) T^*\left(\omega, k_z, k_x\right) = I, \tag{9}$$

where I is the identity matrix. The Bloch modes of the metamaterial are eigenvalues of T and satisfy

$$\left| T\left(k_x\right) - e^{i\Lambda k_z} I \right| = 0. \tag{10}$$

Taking the complex conjugate of Eq. 12 and using the symmetry property of Eq. 11, the following relation is obtained:

$$\left| T\left(k_x^*\right) - e^{i\Lambda k_z} I \right| = 0. \tag{11}$$

Equation 11 means that if k_x admits a real solution for the Bloch wave vector, k^*_x is also a solution. Accordingly, the bands are centrosymmetric in the complex (k_x,k_z) plane. Also note that the loss and gain modes of Fig. 17c–e coalesce at ω_{sp} and their wave vectors at ω_{sp} remain finite.

While real periodic spatial refractive index profiles lead to the appearance of an infinite number of band gaps, complex periodic index profiles result in complex dispersion curves and no complete band gap across the entire frequency range. However, if the refractive index profile satisfies the condition for PT symmetry ($n(z) = n^*(-z)$), real propagation constants and complete band gaps can exist provided $\kappa \leq \kappa_{th}$. Here κ_{th} is the threshold value at which the Hamiltonian and the PT operator no longer commute, and consequently, real-valued solutions cease to be supported by the complex potential. Fig. 17c–e illustrate this feature for increasing non-Hermiticity parameter. For example, for $\kappa = 0.2$ and $\kappa = 0.3$ purely real wave vectors and band gaps are observed for all bands both above and below ω_{sp}. However, for $\kappa = 0.5$, purely real eigenmodes below ω_{sp} do not exist across visible and near-infrared frequencies. Furthermore, the band gap between B_3 and B_4 merges for large k_z, and these bands only exist over a very limited wave vector and wavelength range.

The non-Hermiticity parameter not only changes the propagation constant and band gap of the metamaterial, but also the band curvature. Figure 18 plots the equifrequency contours of bands B_1–B_4 at wavelengths of $\lambda = 954$ nm ($\omega/\omega_p = 0.22$) for B_1 and B_2, $\lambda = 604$ nm ($\omega/\omega_p = 0.35$) for B_3, and $\lambda = 445$ nm ($\omega/\omega_p = 0.48$) for B_4. As seen in Fig. 18, for a non-Hermiticity parameter $\kappa = 0$, bands B_1 and B_4 are elliptical (i.e., $n^2_x n^2_z \geq 0$) while bands B_2 and B_3 are hyperbolic (i.e., $n^2_x n^2_z \leq 0$). Moreover, B_4 is characterized by a nearly perfect circular equifrequency contour and almost equal values of effective refractive

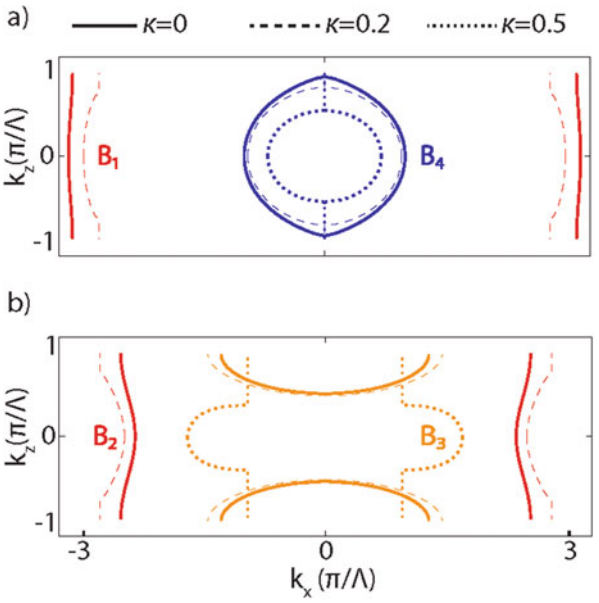

Fig. 18 Equifrequency contours of the metamaterial with increasing non-Hermiticity parameter. (**a**) Bands B_1 and B_4 are plotted at 954 nm and 445 nm, respectively. (**b**) Bands B_2 and B_3 are plotted at 954 nm and 604 nm, respectively. Band B_4 is isotropic for zero and small non-Hermiticity, while B_3 undergoes a hyperbolic to elliptical transition with increasing non-Hermiticity

indices in both the x and z directions. Accordingly, this metal-insulator-metal metamaterial is isotropic at $\lambda = 445$ nm.

For increasing non-Hermiticity parameter, B_1 and B_4 remain elliptical while B_2 remains hyperbolic. However, band B_3 undergoes a hyperbolic to elliptical transition for $\kappa = 0.5$. Such hyperbolic-to-elliptic transitions could enable dynamic tuning of Purcell enhancements for emitters near the metamaterial. Furthermore, they could modulate Talbot revivals or the formation and resolution of images generated by hyperbolic metamaterial superlenses.

The results of Fig. 18 imply that with increasing non-Hermiticity parameter, the material can evolve from an isotropic metamaterial to an anisotropic one. The structure can also become highly directional. This property cannot be derived from the band diagrams, but can be understood by considering the transfer matrix:

$$T = \begin{bmatrix} a & b \\ c & a^* \end{bmatrix}. \tag{12}$$

Here the parameters a, b, and c are related to the reflection and transmission coefficients r and t as $r_L = -c/a^*$, $r_R = b/a^*$, and $t_L = t_R = 1/a^*$, where the subscripts L and R denote illumination from the left and right, respectively. As these equations indicate, an optical system composed of linear and reciprocal materials is nondirectional provided the components are lossless. In other words, the transmitted and reflected powers $T = |t|^2$ and $R = |r|^2$ sum to unity and are independent of illumination direction, since $T_L = T_R = T$ and $T + R_R = 1 = T + R_L$, so $R_L = R_R$. When loss or gain is introduced into the system, the transmission coefficient remains

the same for both directions of illumination. However, the reflection coefficient need not be symmetric, as power can be attenuated or generated within the structure. The asymmetry is obtained at the price of losing propagating Bloch modes. However, asymmetric responses can be obtained in a PT-symmetric potential where purely real bands exist as well.

To illustrate this directional behavior, Fig. 19 plots plane-wave refraction of light from vacuum (n = 1) through a metamaterial composed of 10 unit cells. We consider TM-polarized illumination of wavelength $\lambda = 445$ nm impinging on the metamaterial at an angle of $\theta = 45°$ in the (x,z) plane. The colormap of Fig. 3 plots the H_y component of the fields. The arrows of Fig. 19 indicate the direction of illumination and transmission, each determined by spatially averaging the Poynting vector in each region.

For $\kappa = 0$ (Fig. 19a) the power is negatively refracted with an angle of $\sim -32°$. This result is in excellent agreement with our band structure calculations, which yield a refracted angle from Snell's law of $\sim -31°$. The refractive index $n = -\sqrt{1.87} = -1.36$ at this non-Hermiticity value is independent of the illumination angle and direction. Indeed, for illumination in the (x,z) plane, or an "endfire configuration," the same refraction angle is observed (see Fig. 20a). The same refraction angle is also observed for illumination from all sides of the metamaterial (i.e., illumination from $\pm$x, $\pm$y, and $\pm$ z).

Upon increasing the non-Hermiticity parameter of the metamaterial, the material becomes highly directional. Fig. 19b and c illustrate the field profiles in a 10-layer PT-symmetric metamaterial when illumination is from the loss and gain side (i.e., illumination in the +z or −z directions, respectively). As a particular example we consider $\kappa = 0.445$. As seen, field profiles and refraction angles are completely different for illumination from +z (loss side) versus −z (gain side). Illumination from +z yields negative refraction at an angle of $-81°$ (Fig. 19b). In contrast, illumination from −z yields negative refraction at an angle of $\sim -43°$ (Fig. 19c).

Furthermore, this structure is characterized by tunable reflection and transmission coefficients that can range from zero to at or above unity. This characteristic is illustrated in the lower panels of Fig. 21, which plot the normalized-to-incidence power at each position along the direction of propagation. For example, for illumination from the −z direction (Fig. 20c) power flows backward toward the source in the illumination region ($P_z = -1$), and away from the metamaterial on the transmission side ($P_z = +1$). Therefore, the metamaterial is completely transparent, in that the metamaterial can transmit all of the incident power, even though light is emitted back towards the source.

Complementarily, for illumination from the +z direction (Fig. 20b) this metamaterial can also achieve unidirectional invisibility. As seen, the power is unity on both sides of the metamaterial, indicating complete suppression of reflection on the illumination side and complete transmission on the other. Formally, perfect invisibility requires that the transmitted phase (ϕ_t) equal the phase of a plane wave propagating in free-space (ϕ_{FS}). For the 10-layer metamaterial of Fig. 20b, $(\phi_{FS} - \phi_t)/2\pi = 2.75$, so the object could be identified through the interference with a reference plane wave. However, perfect unidirectional invisibility, i.e.,

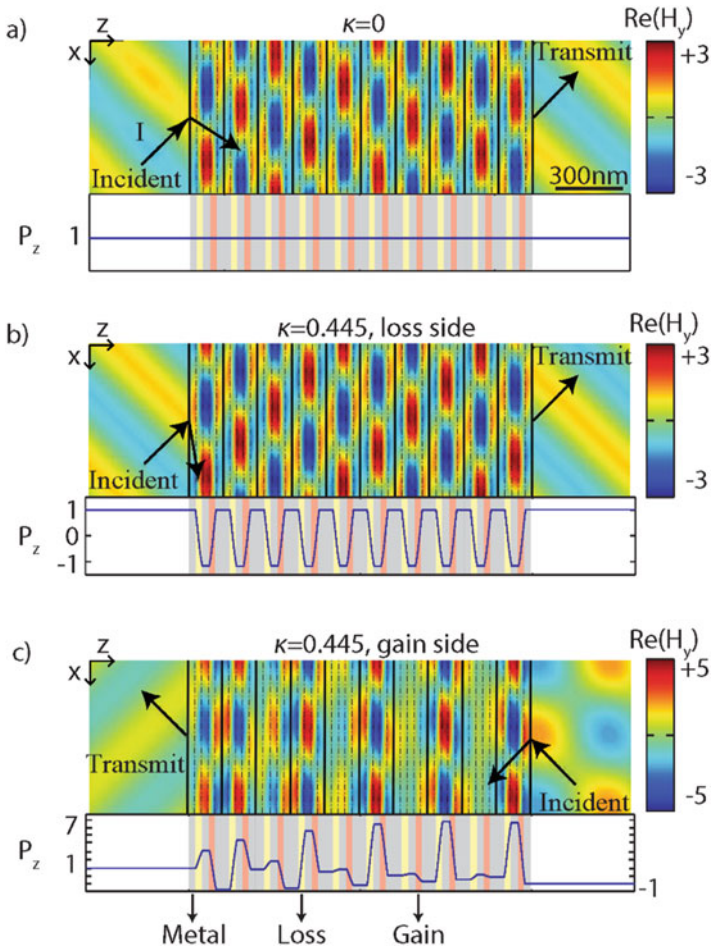

Fig. 19 Transmission and Reflection from structure. Magnetic field values for free-space light with wavelength 445 nm is incident on the structure at 45° from the layer normal for $\kappa = 0$ (**a**) and $\kappa = 0.445$ (**b** and **c**). Light incident from the loss side (**b**) and gain side (**c**) lead to substantially different reflected intensity

$\phi_{FS} - \phi_t = 2m\pi$, where m is an integer, can be achieved when the number of periods is increased to 55, 74, and 91.

The directional scattering properties of the metamaterial can be rationalized by considering the power as light propagates through the array. For $\kappa = 0$, power remains constant throughout the metamaterial (Fig. 19a). However, with increasing κ, power begins to oscillate within the metamaterial, with power increasing in the gain regions and decreasing in the loss regions.

As a final visual example of the unusual unidirectional properties of this metamaterial, Figure 20 plots the fields and refracted angles for illumination along the +x

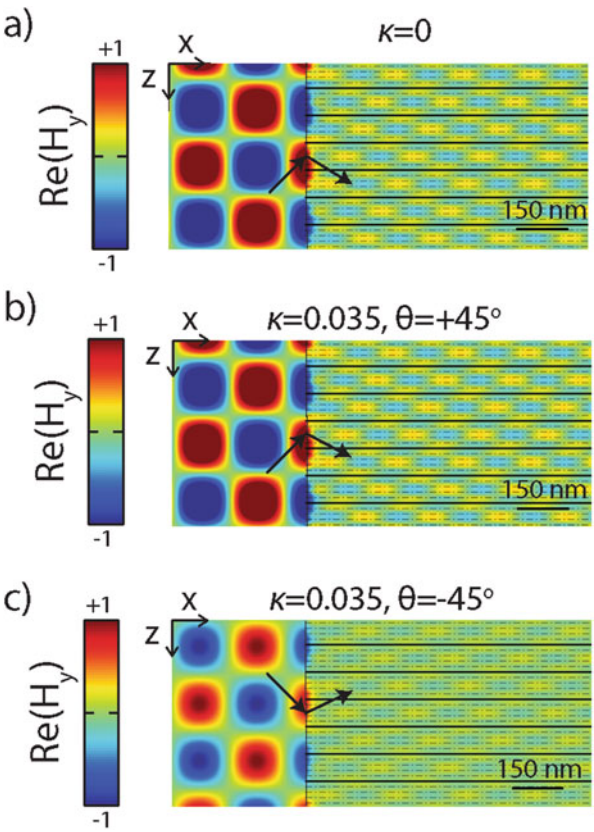

Fig. 20 (**a**) 445 nm light incident on passive structure with angle of +45°, with the magnetic field values 1 micron from the interface plotted on the right. (**b**) and (**c**) plot fields for light incident at +45° or −45°, respectively, for metamaterial with $\kappa = 0.445$

direction (endfire illumination). For a non-Hermiticity parameter $k = 0$, illumination at $\theta = \pm 45°$ yields refraction at $\mp 30°$, respectively, in good agreement with the previously determined value of $\mp 31°$. With increasing non-Hermiticity parameter, however, illumination at $+\theta$ yields markedly different results than illumination at $-\theta$. For example, for $\kappa = 0.445$, illumination at +45° yields a refracted angle of −11°, while illumination at −45° yields refraction along the metamaterial interface at an angle of −90°. This double refraction does not just manifest itself in the intensity of the transmitted beam, but also in the profile of the fields, as seen in the right panels of Fig. 20.

We now consider the effect of varying the non-Hermiticity parameter on the scattering properties of the metamaterial. As before, we consider TM-polarized illumination with a 45° tilted plane wave at $\lambda = 445$ nm. We limit our analysis to illumination along either +z or −z. Based on equation 9, a generalized energy conservation formula can be derived as $|T-1| = \sqrt{R_R R_L}$, where T is the transmitted power and R_R and R_L are the reflected powers from the right and left sides, respectively.

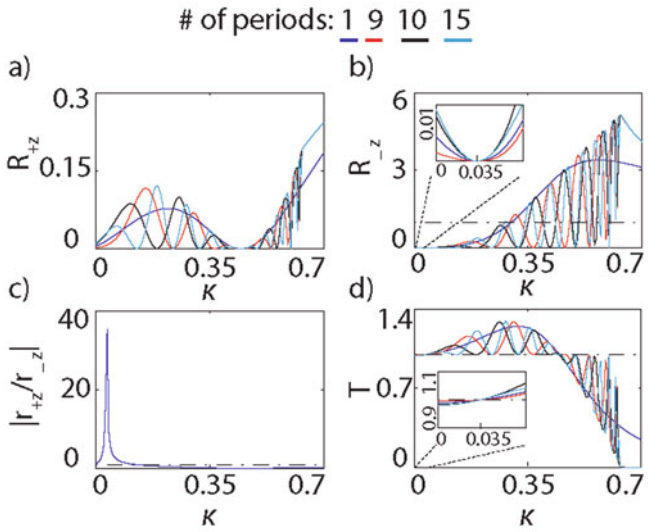

Fig. 21 Reflected and transmitted powers of the metamaterial with increasing k and varying numbers of periods. (**a**) Reflected power upon illumination from the left (loss) side of the metamaterial; (**b**) reflected power upon illumination from the gain (right) right side; (**c**) quotient of reflected powers; and (**d**) transmitted power. In all panels the incident angle is $\theta = 45°$ and the illumination wavelength is $\lambda = 445$ nm. The inset in (**b**) and (**d**) show the behavior of the reflected and transmitted powers around $\kappa = 0.035$, where R_R vanished and $T = 1$ independent of the number of periods

Figure 21 plots the reflection and transmission coefficients as a function of k. As seen, for $\kappa = 0.035$, the transmitted power equals unity independent of the number of layers. Correspondingly at this point r_R, shown in Fig. 21b, vanishes for any number of layers. This property manifests itself as a peak in Fig. 21c, where the quotient of relative reflection coefficients is plotted. Importantly, for $\kappa = 0.035$, this PT-symmetric metamaterial is still isotropic, characterized by circular equifrequency contours. Therefore, this PT-symmetric optical potential could enable lossless and far-field Vesalago lensing, where PT symmetry significantly suppresses reflection.

For larger non-Hermiticity parameters ($\kappa > 0.035$), T exceeds unity. While the transmitted power varies with k and the number of unit cells, it never drops below 1 up through $\kappa = 0.445$. At this non-Hermiticity value, the reflected power from the left/loss side (RL) vanishes, as shown in Fig. 21a. For larger k, T remains at or below unity. Non-Hermiticity parameters κ above 0.63 yield purely imaginary k_z, so no propagation is allowed through the metamaterial. This property is accompanied by a rapid drop in T and strong increase in the reflectance for any number of layers.

7 Section 6: Tunable Purcell Enhancement Near PT-symmetric Potentials [20]

So far, our discussion has focused primarily on the propagating modes of these structures. However, evanescent modes are also of great interest for near-field interactions, such as nearfield scanning optical microscopy (NSOM), coupling and energy transfer between different structures, and countless other topics. Here, we will focus on the reflection and transmission of light from a quantum emitter in the vicinity of this material. This represents a complete discussion of evanescent waves and coupling between an emitter and cavity. Further, this may inform design of non-hermitian local density of states, which may open new avenues for work in quantum optics, strong coupling, and polaritonic-based metastructures.

The spontaneous emission and radiated power of an emitter can be dramatically modified by interaction of a quantum emitter with its surroundings. Optical cavities modify the local density of optical states which an emitter can decay into, which may increase or decrease the radiative and nonradiative pathways. The enhanced rate of radiative decay is encapsulated in the Purcell factor, a measure of the decay rate relative to a dipole emitting into free space. Parity-Time symmetry in these cavities will strongly modify the LDOS due to the guaranteed confluence of optical modes with either increasing loss and gain, or by exceptional points in frequency-wavevector space. As such, it is informative to understand the role that non-hermitian optics has on quantum emitters. The strongly varying reflection coefficients from a planar PT structure will lead to dramatic changes in the emission of electric and magnetic dipoles, which may be used to determine chirality and increase absorption of enantiomers of particular handedness. We begin by exploring achiral emitters, showing how both the magnitude and sign of the radiated power can be tuned. Depending on the strength of κ, the dipole can act either as a strong optical source or an efficient absorber, with positive or negative radiated powers. Further, the emitted power can be increased by several orders of magnitude at the exceptional point, where the eigenstates coalesce and increase the LDOS. Subsequently, we explore the radiation of chiral emitters near PT-symmetric metamaterials. Through appropriate design of PT-symmetric potentials, we show how enantiomers can be distinguished by their decay rates, with maximum differences observed at the exceptional point.

We consider the same planar plasmonic metamaterial (shown in Fig. 22a) as in prior sections, composed of a five-layer stack of alternating metallic and dielectric films. The metal and dielectric thicknesses, t_m and t_d, are deeply subwavelength and are taken to be 30 nm. The metal is modeled as a lossless Drude material with a permittivity $\varepsilon = 1 - (\omega_p/\omega)^2$. The plasma frequency ω_p is taken to be 8.85×10^{15} s^{-1}, similar to bulk plasma frequency of Silver. The dielectric layers have a refractive index $n \pm i\kappa$, with one layer corresponding to loss media ($+\kappa$) and the other corresponding to gain media ($-\kappa$). For concreteness, we consider $n = 3.2$, corresponding to the refractive index of TiO_2 in the frequency range of interest. The imaginary part of the refractive index κ is variable, but it is always identical in each

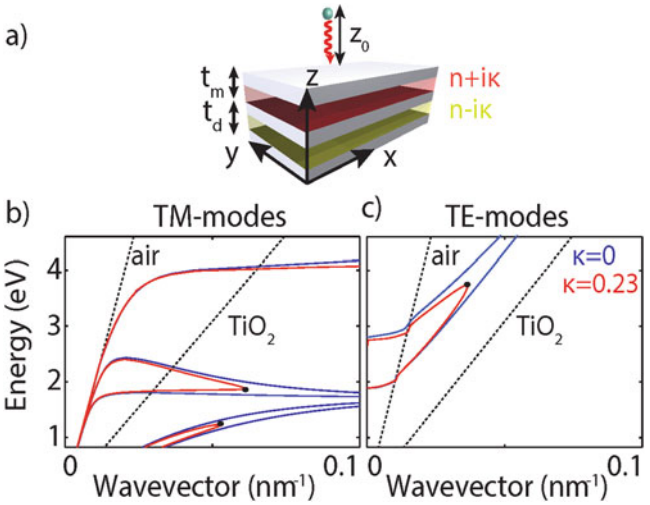

Fig. 22 (**a**) Schematic of Purcell factor calculations. The same plasmonic waveguide structure is considered, with a quantum emitter placed z_0 away from the surface. Dispersion of TM (**b**) and TE (**c**) modes for this structure

dielectric layer to satisfy the PT-symmetric condition of $\varepsilon(z) = \varepsilon^*(-z)$. The dipole emitter is assumed to be a distance z_0 away from the first vacuum/metal interface of the structure.

Figure 22 shows the dispersion curves for the structure, indicating that both transverse-magnetic (TM) and transverse-electric (TE) modes are supported. Each panel includes calculations for two values of the non-Hermiticity parameter, $\kappa = 0$ and $\kappa = 0.23$. At $\kappa = 0$, the in-plane wave vector k_x diverges for TM modes (Fig. 22b) at the Ag-TiO_2 and Ag-vacuum surface plasmon resonance frequencies (E = 1.7 and 4 eV, respectively). Wavevectors remain finite and smaller than the TiO_2 light line for TE modes. As the non-Hermiticity parameter is increased, modes converge toward the same energy and wave vector and coalesce at the exceptional points (EPs), denoted by black circles. The exceptional point is of particular importance as it shows a phase transition in the modal behavior of the waveguide. Before this EP, the modes have real propagation constants, and field distributions have a definite symmetry. After the EP, however, the propagation constants move into the complex plane, and the fields lose their symmetry. This region beyond the exceptional phase is called the broken phase. In the broken phase, one mode is localized almost exclusively in the gain media, while the other is confined to the lossy region.

To determine how these modes impact dipolar emission, we calculate the power radiated by a dipole P normalized to its radiated power in free space P_0. For an electric dipole the normalized radiated power of the dipole is given by [21]

$$\frac{P}{P_0} = 1 + \frac{3}{4}\frac{\left|\overrightarrow{p}_{\rho}\right|^2}{\left|\overrightarrow{p}\right|^2}\int_0^{\infty} \mathrm{Re}\left[\frac{k_{\rho}}{k_z}\left(r_{TE} - r_{TM}k_z^2\right)e^{i2k_z z_0}\right]dk_{\rho} + \frac{3}{2}\frac{\left|\overrightarrow{p}_{z}\right|^2}{\left|\overrightarrow{p}\right|^2}\int_0^{\infty} \mathrm{Re}\left[\frac{k_{\rho}^3}{k_Z}r_{TM}e^{i2k_z z_0}\right]dk_{\rho} \tag{13}$$

whereas for a magnetic dipole, the radiated power is given by

$$\frac{P}{P_0} = 1 + \frac{3}{4}\frac{\left|\overrightarrow{m}_{\rho}\right|^2}{\left|\overrightarrow{m}\right|^2}\int_0^{\infty} \mathrm{Re}\left[\frac{k_{\rho}}{k_z}\left(r_{TM} - r_{TE}k_z^2\right)e^{i2k_z z_0}\right]dk_{\rho} + \frac{3}{2}\frac{\left|\overrightarrow{m}_{z}\right|^2}{\left|\overrightarrow{m}\right|^2}\int_0^{\infty} \mathrm{Re}\left[\frac{k_{\rho}^3}{k_Z}r_{TE}e^{i2k_z z_0}\right]dk_{\rho} \tag{14}$$

In Eq. 13, $\overrightarrow{p}$, $\overrightarrow{p}_{\rho}$, and $\overrightarrow{p}_{z}$ denote the electric dipole moment and its transverse and normal components, respectively [with the same scheme for Eq. 14]. Likewise, k_{ρ} is the transverse momentum in the x-y plane ($k_{\rho} = \sqrt{k_x^2 + k_y^2}$), and r_{TE} and r_{TM} are the reflection coefficients from the structure for TE and TM polarizations.

In general, these equations imply three features of dipolar emission near a PT plasmonic structure: First, the power strongly depends on the modal wave vector. Therefore, at the surface plasmon resonance frequencies where mode momenta diverge and a flat band appears, the LDOS increases and a significant modification of the Purcell factor is expected. Second, the Purcell factor strongly depends on the reflection coefficient. As discussed later, the reflection coefficient can be modified with increasing the non-Hermiticity parameter. An abrupt change in the behavior of the reflection coefficient at the exceptional point noticeably enhances the Purcell factor, essentially giving rise to a new system resonance. Lastly, Eq. 13 suggests that the reflection coefficient can control the sign of the power as well. The reflection coefficients of evanescent components ($k_{\rho} \geq k_0$) interacting with the gain or loss side of PT media are always complex conjugate of each other: $r_G = r^*_L$. For these evanescent components, k_z is purely imaginary; thus, the exponential term $e^{i2k_z z_0}$ is real, and the power spectrum is directly proportional to the imaginary part of the reflection coefficients. Accordingly, the nonradiative power changes sign when the dipole is repositioned from the loss to the gain side. Ultimately, whenever the nonradiative contribution is dominant (i.e., when the dipole is close to the structure), this feature can change the sign of the total power P. This intriguing result complements the reports of asymmetric reflections of propagating plane waves from PT structures when illuminated from the loss or the gain side. In the following sections, we present the numerical results particular to the structure depicted in Fig. 22.

Since the power emitted by a dipole is directly related to the reflected fields, we start by investigating the reflection coefficients. Figure 23a plots the variation of

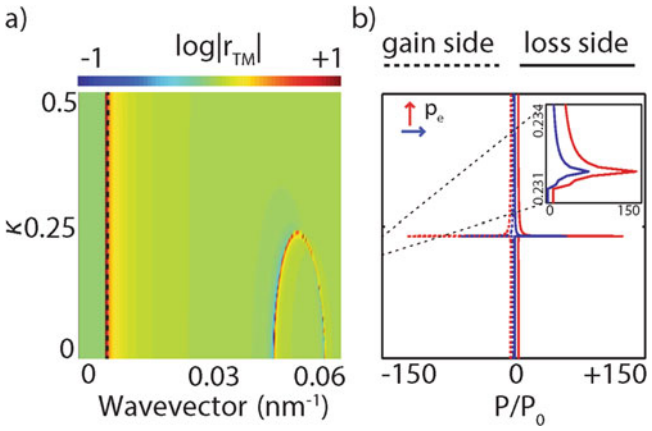

Fig. 23 (**a**) Reflection coefficients of 1.2 eV light as a function of in-plane wavevector and non-hermiticity. A resonant loop is observed. (**b**) Purcell factor for vertical (red) and horizontal (blue) electric dipoles 20 nm above the metamaterial on the gain side dashed line) or loss side (solid line)

the reflection coefficient with non-Hermiticity parameter κ and in-plane momentum k_ρ. We consider TM-polarized illumination and set the energy to E = 1.2 eV. At this energy, all modes supported by the structure lie below the vacuum light line and have real momenta exceeding that of free space (Fig. 22b). As seen, the reflection coefficient diverges for wave vectors corresponding to the guided modes. For $\kappa = 0$, this divergence occurs for three wave. As the non-Hermiticity parameter is increased, the mode with the lowest wave vector exhibits minimal variation. For better clarification the vacuum light line is added to Fig. 23a as well (black dashed line). Referring to Fig. 22b, one can clearly see that at low energies some of the TM modes closely follow the light line and only detach from when the energy increases. However, the higher-momentum modes have reflection coefficients that begin to coalesce and form a loop in the $k_\rho\kappa$ plane, terminating at the exceptional point, $\kappa \approx 0.23$ in Fig. 23a. For larger values of κ, the reflection coefficient at these larger wave vectors decreases due to the lack of momentum matching between guided modes and incident plane waves.

Figure 23b indicates that the sign of the total power changes based on whether the dipole is located on the gain side (dashed lines) or loss side (solid lines) of the metamaterial. As described before, the nonradiative part of the power spectrum experiences complex-conjugated reflection coefficients from the gain and loss sides. This result implies that the nonradiative part of the power changes sign as the dipole is relocated from the gain side to the loss side. Here, the dipole's close proximity to the interface means that the nonradiative contribution dominates the radiative contribution by about two orders of magnitude. Therefore, if the sign of the nonradiative part is changed, the sign of the total power can also be changed. While the large positive power from the loss side means that the dipole behaves

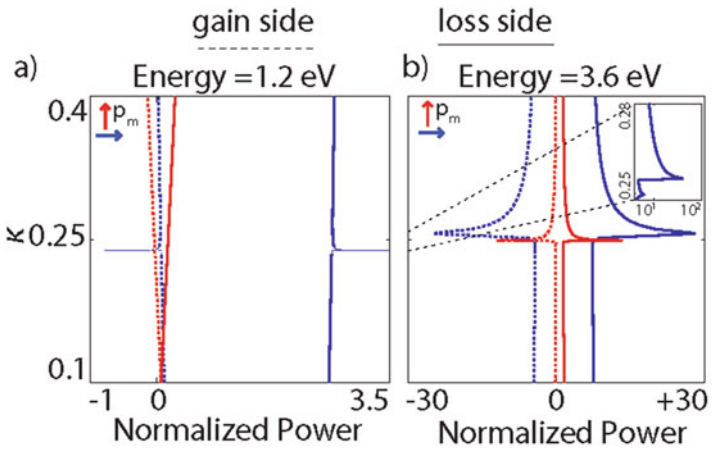

Fig. 24 Purcell factor for vertical (red) and horizontal (blue) magnetic dipoles 20 nm away from structure on the gain side (dashed) or loss side (solid). Incident photon energy of 1.2 eV (**a**) and 3.6 eV (**b**). At higher energies, exceptional points emerge for both TM and TE polarizations, leading to much more enhanced emission

as an efficient emitter, the negative sign on the gain side implies that the dipole efficiently absorbs the power reflected back from the structure.

To understand this behavior further, we investigate the effect of the dual TE modes and calculate the emitted power from a magnetic dipole. Figure 24a plots the normalized power for both horizontal and vertical magnetic dipoles as a function of κ at a fixed energy of E = 1.2 eV. Here, unlike electric dipoles, dipole orientation leads to significant differences. While the horizontal magnetic dipole shows a maximum at the exceptional point ($\kappa \approx 0.23$) like the electric dipole case, the vertical magnetic dipole has no resonant features. Based on the symmetry of emitted fields from these dipoles, it is clear that a horizontal magnetic dipole excites both TE and TM polarizations, while a vertical dipole exclusively couples to TE modes. Since the structure supports no TE modes here, neither an EP nor a significant resonant feature will be observed at E = 1.2 eV for TE modes. Accordingly, the powers remain small for vertically oriented dipoles. Further, the total power for horizontal magnetic dipoles is not symmetric. This asymmetry is a general feature for all dipoles near PT media due to their directional scattering properties, but it is magnified for this particular case since the ratio between nonradiative and radiative contributions is small. While the nonradiative part still contributes dominantly to the total power at this short dipole-structure separation, it only is about three times larger than the radiative part.

As the energy increases, the structure supports both TM and TE modes. For example, at E = 3.6 eV, the TE reflection coefficient in the $k_\rho\kappa$ plane shows a loop at $\kappa \approx 0.25$. Therefore, unlike E = 1.2 eV, at 3.6 eV both TE and TM modes have exceptional points in their spectra. Figure 24b shows the total power radiated by both vertical and horizontal magnetic dipoles at this energy. Unlike

lower energies, resonant features in the dipole power are observed for both dipole orientations. In particular, the vertical magnetic dipole has a resonant peak at $\kappa = 0.25$, corresponding to the exceptional point of these modes at this energy. The horizontal dipole, on the other hand, has two resonance features: one due to the TM-mode coalescence and another due to the TE-mode coalescence. Note that the latter coincides with the resonance features of the vertical magnetic dipole at the EP of the TE modes. For better clarification, the inset shows the zoomed-in version of the power radiated by a horizontal magnetic dipole in the vicinity of the TE and TM exceptional points.

Figures 23 and 24 imply that mode coalescence at the exceptional points significantly modifies the power dissipation spectrum (the integrand of equation 13) and the total power. The poles of the reflection coefficients (or S-matrix) provide a deeper understanding of this phenomenon. Before the exceptional point, the two simple poles, corresponding to the two slow modes below the TiO_2 light line in Fig. 22b, contribute oppositely to the integral and hence the total power. At the exceptional point, these modes coalesce and form a double pole, and this opposite behavior vanishes. Therefore, a marked increase in the power is obtained. After the exceptional point, only one simple pole contributes. However, the contribution of this pole monotonically decreases as the pole moves away from the real axis into the complex plane (larger κ); hence, the total power decreases again. The spectral variation of the radiated power as a function of energy is shown in Fig. 25. Both vertical electric and magnetic dipoles are included. As seen for a dipole 20 nm above the surface of the metamaterial, peaks in the normalized power appear at both frequencies of the exceptional point as well as the surface plasmon resonance frequencies. For example, a vertical electric dipole couples exclusively to TM modes and exhibits local maxima in the Purcell factor for energies of 1.2 and 1.9 eV (the exceptional points for the four lowest-order branches) and at 2.3 and 4 eV. In contrast, magnetic dipole radiation cannot couple to TM modes at E = 1.2 eV. However, its power spectrum has a resonance feature at E = 3.8 eV, where an

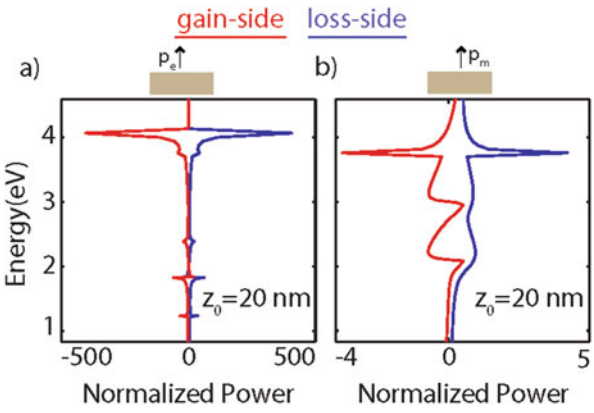

Fig. 25 Vertical (**a**) electric and (**b**) magnetic dipoles 20 nm above metamaterial surface on the gain (red) or loss (blue) side. The non-Hermiticity parameter κ is set to 0.23. The incident photon energy is varied from less than 1 eV to greater than 4 eV.

exceptional point arises for $\kappa = 0.23$. Variation of the normalized power at lower energies is due to the appearance of the two TE modes around 1.9 and 2.7 eV.

While the above results pertain to electric and magnetic dipoles, the effect of the exceptional point on the radiated power is a general property of the structure and its modal features. Therefore, the results can be extended to more complicated sources, including chiral emitters. The emergence of chirality is largely attributed to the interaction of simultaneous electric and magnetic dipoles. Consequently, as with achiral emitters, the decay rate and radiated power of chiral molecules can be modified through their surrounding environment. It has been shown that enantiomers exhibit enantiospecific coupling to the modes of a chiral scatterer and that chiral structures can substantially modify the decay rate and radiation pattern of chiral molecules. Here, we consider the radiation of a chiral molecule in the vicinity of our PT-symmetric structure, which, importantly, contains no chiral constituents. As will be shown, even this achiral structure can significantly modify the radiation of chiral emitters.

Equation 1 can be extended to include the simultaneous radiation of the electric and magnetic dipoles. Doing so, the normalized power radiated by a chiral source composed of electric and magnetic dipoles is given by

$$\frac{P}{P_0} = 1 + \frac{\omega}{2P_0}\mathrm{Im}\left[\vec{p}_e^{\,*} \cdot \vec{E}^{\,s}\left(\vec{r}_0\right) + \vec{p}_m^{\,*} \cdot \vec{B}^{\,s}\left(\vec{r}_0\right)\right]. \tag{14}$$

In this equation, $\vec{p}_e$ and $\vec{p}_m$ are the electric and magnetic dipole moments of the molecule, while $\vec{E}^{\,s}$ and $\vec{B}^{\,s}$ are the scattered electric and magnetic fields at the position of the molecule $\vec{r}_0$. P_0 is the power radiated by a chiral source in free space. Since the magnetic moment is purely imaginary for a two-level system, a $\pi/2$ phase difference exists between the electric and magnetic dipoles. With this phase difference it can be shown that P_0 is given by the summation of the power emitted by each dipole in free space individually. More complex chiral molecules are characterized by a variable phase relationship and the possible need for quadrupolar terms. For simplicity, we consider only dipolar terms here. We use the common naming convention based on the sign of $\vec{p}_e \cdot \vec{p}_m$, where a right-handed enantiomer refers to a positive product, while a left-handed enantiomer refers to a negative dot product.

The electric and magnetic dipoles are located 20 nm away from the interface in the x-y plane with an angle θ between them. We assume that the ratio between the magnetic and electric dipoles is $\xi = 0.1c$, where c is the speed of light. From Figs. 3 and 4, we know achiral emitters will exhibit an increased power emission at the exceptional point. Is it possible to utilize the same LDOS enhancement at the exceptional point to manipulate the emitted power of the chiral source near PT-symmetric potentials? More importantly, do differences in the decay rates of enantiomers emerge, and can they be used to distinguish enantiomers?

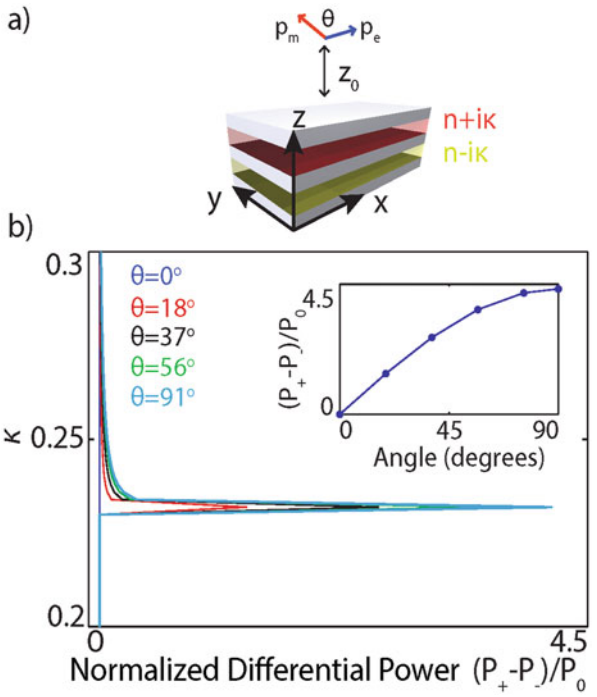

Fig. 26 Chiral emitter discrimination with a PT symmetric metamaterial. (**a**) molecule enantiomers, which can be considered as electric and magnetic dipolar emitters with differing $\overrightarrow{p_e} \cdot \overrightarrow{p_m}$. (**b**) Calculated difference in radiative rates between enantiomers as a function of non-hermiticity parameter

For chiral selectivity, there must be an effect from the electric dipole at the position of the magnetic dipole and vice versa. Otherwise, the power radiated by each enantiomer would be the same. Since state coalescence at the exceptional point manifests itself in all of the scattering parameters, an enhancement in the normalized power of the chiral emitters is expected as well. Figure 26b plots the difference between the normalized emitted powers (decay rates) of the right (+) and left (−) enantiomers as a function of κ. The energy again is fixed at 1.2 eV, where an exceptional point appears at $\kappa \approx 0.23$. The parameters for the left enantiomer have been calculated by substituting $\overrightarrow{p}_m$ with $-\overrightarrow{p}_m$, while $\overrightarrow{p}_e$ is always fixed along the x direction. While the difference between decay rates is minimal below the exceptional point, at this exceptional point the decay rates are markedly different. This difference monotonically increases by increasing the angle between the dipoles. Note that an x-directed electric dipole at r_0 produces only nonzero H_y at this point. Therefore, as the angle between the dipoles approaches 90°, the magnetic field scattered by an electric dipole along the magnetic dipole increases. At $\theta \approx 90°$, the difference between enantiomer decay rate is maximized to 4.5.

8 Section 7: Broadband Nonreciprocity with PT-symmetric Plasmonic Metamaterials [22]

In a final demonstration of the versatility of these materials, we consider the nonreciprocal transmission of light through this metamaterial. For all linear and time-invariant systems, Lorentz reciprocity guarantees identical transmission upon exchange of emitter and detector. In a two-port configuration, this means that, regardless of reflection, transmission is the same when illuminated from the front or the back. This complicates the design of optical diodes and active camouflage, among others. Especially at small length scales (on the order of the incident wavelength), nonreciprocal devices are exceptionally challenging to make due to the weak magneto-optic and nonlinear couplings in typical materials. However, we have just shown dramatic modification of the bandstructure in the visible as a function of non-hermiticity. We can use this to our advantage by adding nonlinearities to the loss and gain, which we will show below.

Given the bandstructure of an infinitely large material (Fig. 17), we next investigate the transmission of a 10 unit cell metamaterial, which has a total thickness of 1.5 μm, approximately three times the wavelengths considered. Figure 27 shows the transmission of $\theta = 45°$ light from free space through this material as a function of wavelength for $\kappa = 0$ and $\kappa = 0.37$. For the passive metamaterial ($\kappa = 0$), the bandgap is readily apparent as a 100 nm wavelength region of low transmission. Upon increasing κ to 0.3734, the bandgap completely disappears, and transmission near unity is seen throughout the entire range (dashed black line). Considering a wavelength of 500 nm, we can observe the impact κ has on the transmission (Fig. 27b). For a passive ($\kappa = 0$) material, the transmission is $\approx 10^{-7}$ and increases super-exponentially until a value of $\kappa = 0.3734$, where transmission is unity. Here, the reflection from the forward direction is zero, while reflection from the backward direction is not (10^{-5}), corresponding to an exceptional point in the scattering parameters. Beyond this value transmission stays at or greater than 1, but is no longer a monotonically increasing function of κ.

At the exceptional point, the field intensity distribution in the material is markedly different when illuminated from the forward or backward directions, as shown in Fig. 27c. When illuminated from the gain side (forward direction), the intensity pattern for each unit cell is approximately the same, with maximum normalized magnetic field intensities of approximately 8 at the interface between metal and dielectric. Conversely, when illuminated from the loss side (backward direction), the field intensities are larger in magnitude than their corresponding value from the gain side, with a maximum in the center. Indeed, intensities near the center of the material are enhanced by over a factor of 80 compared to the incident field. This asymmetry is a direct consequence of the asymmetric loss-gain distribution in this PT-symmetric structure. Here, the material is perfectly impedance matched in the forward direction with no reflection, while a cavity mode is excited from the backwards direction. Note that, while the internal field distributions and reflected intensities are different, the transmission when illuminated from either direction

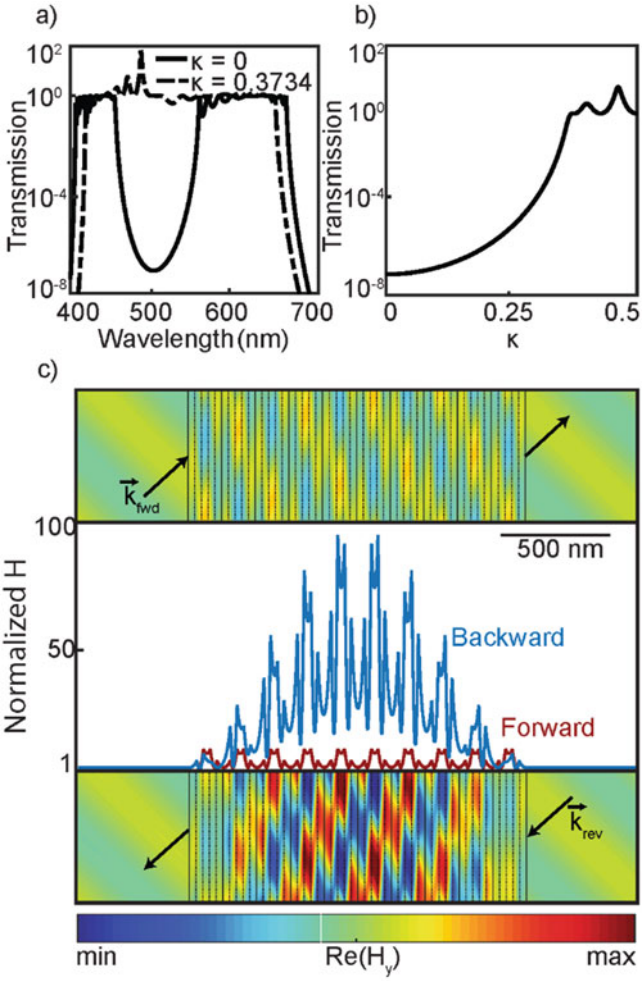

Fig. 27 (**a**) Transmission through a 10 unit cell metamaterial as a function of wavelength for $\kappa = 0$ (solid line) and 0.3734 (dashed line). (**b**) Transmission versus non-Hermiticity parameter for 500 nm light through this structure. (**c**) Magnetic field profiles through the structure for 500 nm light incident at 45° in the forward (top) and backward (bottom) directions, showing strongly enhanced internal field intensities. The middle shows the normalized magnetic field intensities for these directions

is the same, as this material is still reciprocal. In order to break reciprocity, nonlinearities or some form of time modulation is still required.

Considering the asymmetry inherent in PT systems and nonresonant field enhancements inherited from plasmonics, nonlinearities are an attractive route towards nonreciprocity. Since the internal field intensity is enhanced from the backward direction, the nonlinear response of this material will be more pronounced

from this direction. Further, since the loss-gain parameter κ modulates the band-structure over a 100 nm range, modification of this will have dramatic impact on the optical properties. In the linear regime, when no saturation effects are present, the permittivity of the dielectric regions are described as $\epsilon_r = 1 + \chi_{TiO_2} + \chi_{PT}$, where ϵ_r is the relative permittivity, χ_{TiO_2} is the susceptibility of the host dielectric (and hence $1 + \chi_{TiO_2} = n^2$), and χ_{PT} is the susceptibility of the added loss or gain. As the intensity in the dielectric increases, saturation modifies the contribution of the PT susceptibility as: $\chi_{PT}\ \left(|E|^2\right) = \frac{\chi_{PT}^{\infty}}{1+\frac{|E|^2}{|Esat|^2}}$ Here, χ_{PT}^{∞} is the linear susceptibility, |E| is the electric field within the medium, and $|E_{sat}|^2$ is the saturation electric field intensity, a materials parameter. The plasmonic fields inherent in this system mean that the nonlinear permittivity of the dielectric layers will be a strong function of position through the layer; as such, the nonlinear metamaterial is in general non-Hermitian, rather than PT symmetric. For the dielectric layers defined by a refractive index n and loss or gain component κ, the full description of the permittivity with saturation reads as: $\epsilon_r\left(|E|^2\right) = n^2 + \frac{-\kappa^2 \pm 2in\kappa}{1+\frac{|E|^2}{|Esat|^2}}$, where the ± indicates whether the material is the loss or gain layer, respectively. While the gain or loss susceptibility, and hence κ is a strong function of position and intensity, we will show that this non-Hermitian material can be homogenized to a linear PT-metamaterial whose non-Hermiticity parameter is uniformly tuned by the incident intensity.

To understand the nonlinear response of this metamaterial, nonlinear simulations are performed using a Finite Element solver. For these, we consider an initial $\kappa = 0.3734$. First, we consider illumination of 500 nm light incident at $\theta = 45°$ as a function of incident intensity normalized to the saturation intensity. Figure 28a shows the transmission through the metamaterial when illuminated in the forward or backward direction. In both cases, unity transmission is seen at low intensities, corresponding to the linear, reciprocal metamaterial. As the incident intensity increases, transmission is reduced regardless of illumination direction. However, backward illumination leads to lower transmission, consistent with the enhanced internal intensities seen in the linear material. At 3.5% $|E_{sat}|^2$, transmission is below 10% in the backward direction, while approximately 50% in the forward direction. Plotting the ratio between the forward and backward directions, we can see the transmission or isolation ratio as a function of incident intensity in Fig. 28b. As expected, low incident intensity leads to a transmission ratio of 1, where the material acts reciprocally. As the incident intensity increases, the transmission ratio monotonically increases to approximately 6.5 at 3.5% $|E_{sat}|^2$.

Figure 28c shows transmission from the forward or reverse direction as a function of wavelength ($\theta = 45°$) for three different incident intensities. We choose to study wavelengths in a 50 nm range centered on 500 nm, as the transmission is relatively flat and near unity within this range in the linear regime. At a relatively low incident intensity (0.35% $|E_{sat}|^2$), transmission is maintained at approximately unity when incident in the forward direction, while a parabolic depression of the transmission is seen in the backward direction, an indication of the opening bandgap. As intensity increases, this region of reduced transmission increases, and we see transmission

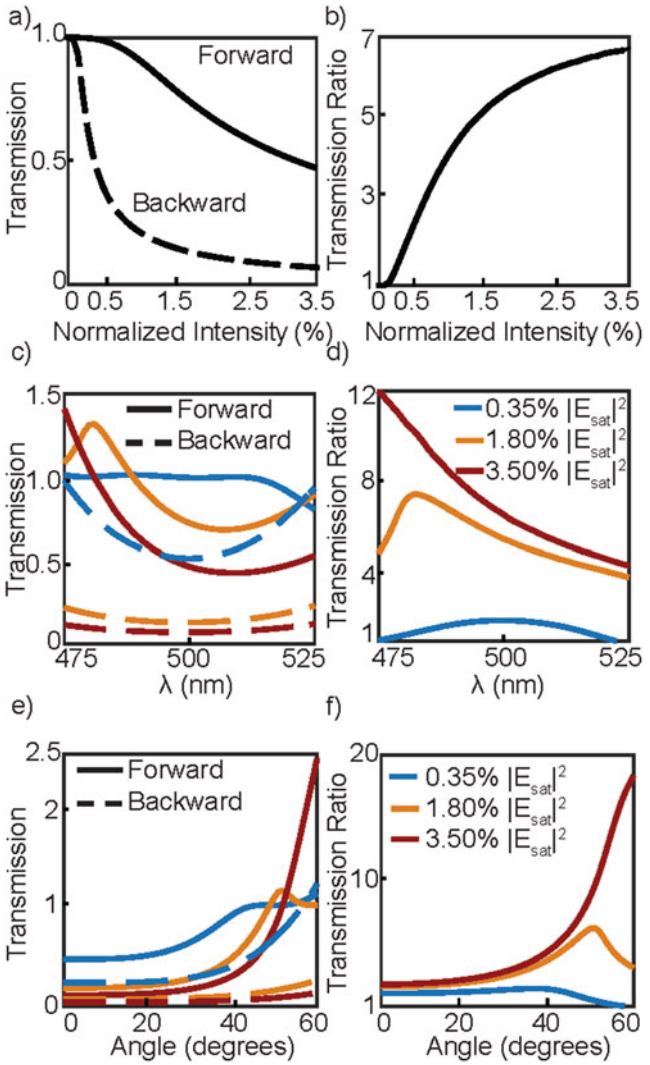

Fig. 28 Nonlinear and Nonreciprocal transmission with initial $\kappa = 0.3734$. (**a**, **b**) Transmission of 500 nm light as a function of normalized incident intensity. (**c**, **d**) Transmission over a 50 nm bandwidth in the visible. (**e**, **f**) Transmission through a 60° angular spectra for 500 nm light. The left column plots the transmission in the forward (solid) and backward (dashed) directions, while the right column plots the transmission ratio T_{fwd}/T_{back}

uniformly decreases in both the forward and backward cases, while the transmission ratio throughout the wavelength range monotonically increases. At the maximum intensity studied ($3.5\%|E_{sat}|^2$), the transmission ratio varies between 5 and 12 within the studied wavelength range. Thus, nonreciprocal transmission is observed over at

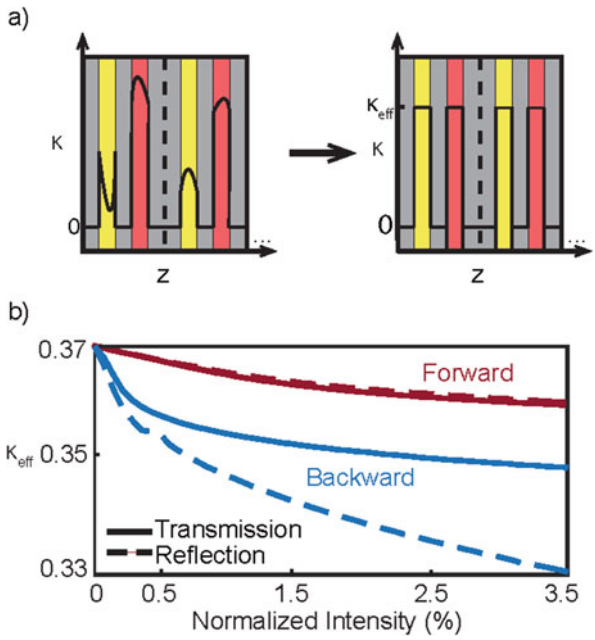

Fig. 29 Retrieval of effective non-Hermiticity. (**a**) schematic of retrieval procedure. (**b**) retrieved nonlinear effective non-Hermiticity for the forward (red) and backward (blue) directions when considering the transmission (solid) and reflection (dashed) intensities as a function of incident intensity

least a 50 nm bandwidth. In principle this bandwidth is limited only by the initial bandgap size and the incident intensity on the structure. Both increasing the number of unit cells and increasing incident intensity can enhance the transmission ratio and bandwidth of operation.

We additionally consider nonreciprocal transmission when the metamaterial is illuminated from differing angles. Figure 28e and f show the transmission for the same incident intensities as 28c and 28d, but consider illumination of 500 nm light incident at an angle ranging $\theta = 0°$ to 60°. In general, transmission increases with increasing angle, corresponding to a greater degree of coupling to plasmonic modes. As intensity increases, transmission decreases at lower incident angles, but transmission greater than 1 is seen at 60° for $3.5\%|E_{sat}|^2$. Here the transmission ratio spans 3–18 with incident angle. Because the wavelengths studied here are above the surface plasmon frequency and the refractive index is negative, this may lead to the development of novel nonreciprocal optical elements such as a nonreciprocal Veselago lens, given suitable gain materials.

To better understand the underlying mechanism of nonreciprocity, we consider the transmission and reflection as a function of power. Remarkably, while the nonlinear metamaterial has in general a spatially varying permittivity in the dielectric, both the reflection and transmission coefficients for a given direction can be well correlated with a uniform and linear value of the loss-gain parameter κ_{eff} . In doing so, this metamaterial can be homogenized to an intensity- and directionally dependent PT-symmetric metamaterial. A schematic of this homogenization scheme is given in Fig. 29a. Figure 29b gives the retrieved κ_{eff} from the forward (left panel)

or backward (right panel) direction. κ_{eff} is determined by separately considering the reflection and transmission values, and both results are plotted for each direction. In the forward direction, almost identical values of κ_{eff} are retrieved from the reflection and transmission parameters. The agreement is not as exact in the backward direction (within 5% relative error), likely due to the induced cavity mode and strongly varying field intensity. This homogenization, possible because of the metamaterial structure, means that the bandstructure is directly modified by the incident intensity, and a spatially varying material can be treated as an effective homogenized nonlinear material.

9 Conclusion

Clearly, these plasmonic structures are of great interest in nanophotonics by virtue of the strong electromagnetic confinement and unique dispersion. By adding in judicious inclusions of loss and gain, we have shown that these properties are highly tunable. Further, there are phenomena which can only be achieved by the non-hermitian structuring, such as reflection and transmission simultaneously greater than unity. By understanding the underlying modal properties of these structures we may better design future devices which could enable ultra-compact optical modulators, diodes, light-emitters, polarizers, and waveguides. These structures could also provide a foundation for compact, ultra-sensitive free-space molecular sensors. All of these rely on the tunability from the additional loss and gain, as well as the dynamics of exceptional points, which are guaranteed to exist on the real line in PT-symmetric media.

References

1. Maier, S.: Plasmonics: Fundamentals and Applications. Springer, New York (2007)
2. Dionne, J.A., Sweatlock, L.A., Atwater, H.A., Polman, A.: Plasmon slot waveguides: towards chip-scale propagation with subwavelength-scale localization. Phys. Rev. B. **73**(3), 035407 (2006)
3. Vuckovic, J., Loncar, M., Scherer, A.: Surface plasmon enhanced light-emitting diode. IEEE J. Quantum Electron. **36**(10), 1131–1144 (2000)
4. Khajavikhan, M., Simic, A., Katz, M., Lee, J.H., Slutsky, B., Mizrahi, A., Lomakin, V., Fainman, Y.: Thresholdless nanoscale coaxial lasers. Nature. **482**(7384), 204–207 (2012)
5. Fang, N., Lee, H., Sun, C., Zhang, X.: Sub–diffraction-limited optical imaging with a silver superlens. Science. **308**(5721), 534–537 (2005)
6. Rüter, C.E., Makris, K.G., El-Ganainy, R., Christodoulides, D.N., Segev, M., Kip, D.: Observation of parity–time symmetry in optics. Nat. Phys. **6**(3), 192 (2010)
7. Guo, A., Salamo, G.J., Duchesne, D., Morandotti, R., Volatier-Ravat, M., Aimez, V., Christodoulides, D.N.: Observation of P T-symmetry breaking in complex optical potentials. Phys. Rev. Lett. **103**(9), 093902 (2009)
8. Peng, B., Özdemir, Ş.K., Rotter, S., Yilmaz, H., Liertzer, M., Monifi, F., Yang, L.: Loss-induced suppression and revival of lasing. Science. **346**(6207), 328–332 (2014)

9. Ramezani, H., Christodoulides, D.N., Kovanis, V., Vitebskiy, I., Kottos, T.: P T-symmetric Talbot effects. Phys. Rev. Lett. **109**(3), 033902 (2012)
10. Lin, Z., Ramezani, H., Eichelkraut, T., Kottos, T., Cao, H., Christodoulides, D.N.: Unidirectional invisibility induced by P T-symmetric periodic structures. Phys. Rev. Lett. **106**(21), 213901 (2011)
11. Chong, Y.D., Ge, L., Stone, A.D.: P t-symmetry breaking and laser-absorber modes in optical scattering systems. Phys. Rev. Lett. **106**(9), 093902 (2011)
12. Wong, Z.J., Xu, Y.L., Kim, J., O'Brien, K., Wang, Y., Feng, L., Zhang, X.: Lasing and anti-lasing in a single cavity. Nat. Photonics. **10**(12), 796–801 (2016)
13. Alaeian, H., Dionne, J.A.: Non-Hermitian nanophotonic and plasmonic waveguides. Phys. Rev. B. **89**(7), 075136 (2014)
14. Dionne, J.A., Verhagen, E., Polman, A., Atwater, H.A.: Are negative index materials achievable with surface plasmon waveguides? A case study of three plasmonic geometries. Opt. Express. **16**(23), 19001–19017 (2008)
15. Baum, B., Alaeian, H., Dionne, J.: A parity-time symmetric coherent plasmonic absorber-amplifier. J. Appl. Phys. **117**(6), 063106 (2015)
16. Benisty, H., Yan, C., Degiron, A., Lupu, A.: Healing near-PT-symmetric structures to restore their characteristic singularities: analysis and examples. J. Lightwave Technol. **30**(16), 2675–2683 (2012)
17. Alaeian, H., Baum, B., Jankovic, V., Lawrence, M., Dionne, J.A.: Towards nanoscale multiplexing with parity-time-symmetric plasmonic coaxial waveguides. Phys. Rev. B. **93**(20), 205439 (2016)
18. Baum, B., Lawrence, M., Barton, D., Alaeian, H., Dionne, J.: Active Polarization Control with a Parity-Time Symmetric Plasmonic Resonator. arXiv preprint arXiv:1712.05383. (currently under review) (2017)
19. Alaeian, H., Dionne, J.A.: Parity-time-symmetric plasmonic metamaterials. Phys. Rev. A. **89**(3), 033829 (2014)
20. Alaeian, H., Dionne, J.A.: Controlling electric, magnetic, and chiral dipolar emission with PT-symmetric potentials. Phys. Rev. B. **91**(24), 245108 (2015)
21. Novotny, L., Hecht, B.: Principles of Nano-Optics. Cambridge University Press, Cambridge (2012)
22. Barton III, D.R., Alaeian, H., Lawrence, M., Dionne, J.: Broadband and wide-angle nonreciprocity with a non-Hermitian metamaterial. Phys. Rev. B. **97**(4), 045432 (2018)

PT-Symmetry and Non-Hermitian Wave Transport in Microwaves and RF Circuits

Huanan Li, Mahboobeh Chitsazi, Roney Thomas, F. M. Ellis, and Tsampikos Kottos

Abstract Many novel concepts in $\mathscr{P}\mathscr{T}$-symmetric wave transport were initially explored and demonstrated in the conceptually simpler and experimentally more accessible framework of active electronic circuits. These include eigenmode analysis and spatio-temporal dynamics of the stored energy in static and in periodically driven (Floquet) $\mathscr{P}\mathscr{T}$-symmetric circuits, and $\mathscr{P}\mathscr{T}$-symmetric scattering in both the linear and nonlinear regime. We review several of these advances – often stretching the borders of investigation to the most general area of non-Hermitian wave transport where concepts like coherent perfect absorbers, gain-induced lasing shut-down, and asymmetric transport are naturally emerging.

1 Introduction

While gain mechanisms have been always considered an important component in signal processing, this is not the case for its time-reversal i.e. physical mechanisms that are associated with attenuation of signals and energy loss. The latter are typically considered an "anathema" – an undesirable feature which is (unfortunately) abundant in nature and have to be contained at all costs. It is perhaps for this particular reason that researchers have never intentionally explored the possibility to utilize loss as a useful ingredient whose manipulation can lead to the realization of devices with non-conventional properties.

Recently, however, an alternate viewpoint has emerged advocating for the importance of loss and the possibility to utilize it together with a delicately balanced amplification mechanism, in order to realize a new class of novel materials and structures that demonstrate unconventional wave transport characteristics and unprecedented functionalities. The technological aspect together with an unveiled

H. Li · M. Chitsazi · R. Thomas · F. M. Ellis · T. Kottos (✉)
Department of Physics, Wesleyan University, Middletown, CT, USA
e-mail: hli01@wesleyan.edu; mchitsazi@wesleyan.edu; rthomas03@wesleyan.edu; fellis@wesleyan.edu; tkottos@wesleyan.edu

D. Christodoulides, J. Yang (eds.), *Parity-time Symmetry and Its Applications*, Springer Tracts in Modern Physics 280,
https://doi.org/10.1007/978-981-13-1247-2_13

wealth of the underlying mathematical structures of these systems, led to a blooming of the field, which during the last few years has reached a climax. Undoubtedly, among the various areas of physics, optics and photonics has been the tip of the spear for these new developments [50, 62, 63]. Consequently, new concepts based on the sole manipulation of loss, like loss-induced transparency [28], perfect absorbers [10, 47], $\mathscr{P}\mathscr{T}$ [21, 31] and chiral-symmetric lasers [59, 68], hypersensitive sensors [7, 32, 75, 78] etc. have been generated, realized and flourished in the photonics framework. It turns out, as it is evident from the various contributions appearing in this book, that this approach has far reaching benefits to a vast range of wave systems including, radio-frequency (RF) [4, 9, 39, 46, 60, 65, 66] and microwaves systems [15–17, 19, 42, 70], acoustics [22, 67], and even cold atoms [30, 36, 57, 58, 69] and magnonics [40].

Our main contribution to the development of non-Hermitian and $\mathscr{P}\mathscr{T}$-symmetric wave transport was in the RF and microwave domain. In Ref. [65] (see also [4, 9, 39, 46, 60, 66]), we have demonstrated that a pair of coupled LRC circuits with active elements, one with amplification and the other with equivalent amount of attenuation, provide an experimental realization of a wide class of systems where gain/loss mechanisms break the Hermiticity while preserving parity-time ($\mathscr{P}\mathscr{T}$) symmetry. Our set-up [65], being the first experimental investigation of $\mathscr{P}\mathscr{T}$-symmetric systems in the *spatio-temporal* domain, allowed for the experimental exploration of many new fundamental concepts associated with $\mathscr{P}\mathscr{T}$-symmetric structures. Coupling the isolated system to external leads (transmission lines) allowed us to perform the first experimental demonstration of $\mathscr{P}\mathscr{T}$-symmetric scattering [46, 66] and show the phenomena of unidirectional invisibility [45] and CPA-lasing [47]. We have also demonstrated, for the first time, asymmetric transport due to the interplay of non-linearities and gain/loss [4] or extending the notion of $\mathscr{P}\mathscr{T}$-symmetry to generalized anti-linear structures which involve gyrotropic elements [39]. Recently we have extended these studies to the case of Floquet $\mathscr{P}\mathscr{T}$-symmetric circuits [9], thus providing the first experimentally accessible example of this class of systems.

In this chapter we provide a concise review of our results on $\mathscr{P}\mathscr{T}$-symmetric RF and microwave domain. Although we have tried to make the presentation self-sufficient, some of the technical details on the design of $\mathscr{P}\mathscr{T}$-symmetric circuits and theoretical derivations were left out and we have simply provided the appropriate references for the interested reader. In the next Sect. 2 we provide the general electronic considerations associated with the design and implementation of $\mathscr{P}\mathscr{T}$-symmetric RLC circuits. Then in Sect. 3 we examine the structure of the normal modes and the associated dynamics using a prototype $\mathscr{P}\mathscr{T}$-symmetric circuit, the $\mathscr{P}\mathscr{T}$-dimer. We theoretically derive its properties and experimentally demonstrate that this simple circuit displays all the novel features encountered in $\mathscr{P}\mathscr{T}$-symmetric systems. We further extend the study to circuitry with broken time-reversal symmetry due to the presence of a gyrotropic element. In the same section we also discuss a microwave implementation of the $\mathscr{P}\mathscr{T}$-symmetric dimer. In the next Sect. 4 we couple the $\mathscr{P}\mathscr{T}$-symmetric dimer with transmission lines and analyze its scattering properties. A generalized conservation relation is derived

theoretically and tested experimentally. We demonstrate that a direct consequence of this relation is the existence of specific parameters (frequencies, gain/loss values) for which the system exhibits unidirectional invisibility. We furthermore show, using our $\mathscr{P}\mathscr{T}$-symmetric dimer, that appropriately prepared incoming waveforms can be completely absorbed at specific frequencies. At the same frequencies and gain/loss values the structure can act as an amplifier if the incoming wave does not satisfy specific conditions. The counter-intuitive possibility to "shut-down" the amplification action by further increasing the gain at one of the nodes of the circuit is also discussed in this section and a simple theoretical explanation is provided based on circuit theory. Finally, in the same section, we discuss the effects of gyrotropy in the scattering process. We demonstrate the existence of a giant non-reciprocal transport in the neighborhood of spectral singularities associated with exceptional points. We also propose the use of such gyrotropic $\mathscr{P}\mathscr{T}$-symmetric structures for the realization of unidirectionally lasing action. In Sect. 5 we analyze the presence of non-conservative nonlinearities in the scattering process and demonstrate a highly asymmetric transport due to the interplay of gain/loss and nonlinearities. Finally in the last Sect. 6 we present our recent efforts to realize a periodically driven $\mathscr{P}\mathscr{T}$-symmetric system. This is a new class of system where driving can act as an extra control parameter in order to induce a cascade of exceptional point singularities. Our conclusions and outlook is given in the last Sect. 7.

2 General Electronic Considerations

One of the most convenient advantages of an electronic approach is that, at least in the low frequency domain, where the wavelength is significantly greater than the dimensions of the circuit, all spatial symmetry considerations can be reduced to a matter of network topology defined through the application of Kirchoff's laws. Physical symmetry is irrelevant as long as the network has the desired node topology and the connecting elements are appropriately valued. Analogous to the familiar case of a $\mathscr{P}\mathscr{T}$-symmetric potential, the parity operation is equivalent to the interchange of labels corresponding to pairs of associated circuit components.

The usual $\mathscr{P}\mathscr{T}$-symmetric potential has a symmetric real part and an antisymmetric imaginary part, as required by the invariance of the combined parity and time reversal operations. Translating this to the realm of discrete electronics implies that the simple non dissipative elements – that is the reactive components, capacitors and inductors – are unchanged by time reversal. The sign reversal imposed on the device current is restored to the identical Kirchhoff relation due to the sign reversal associated with the reactive time derivative.

This is not the case for the dissipative conduction of a resistor. Here, the reversed current transforms to a charge flow *uphill* with respect to the potential drop. Mathematically, this is Ohm's law with a negative resistance. Practically, this cannot be a passive device, but has to be actively motivated, essentially an amplifier. The time reversed resistor is the conceptually simplest form of amplification, a device

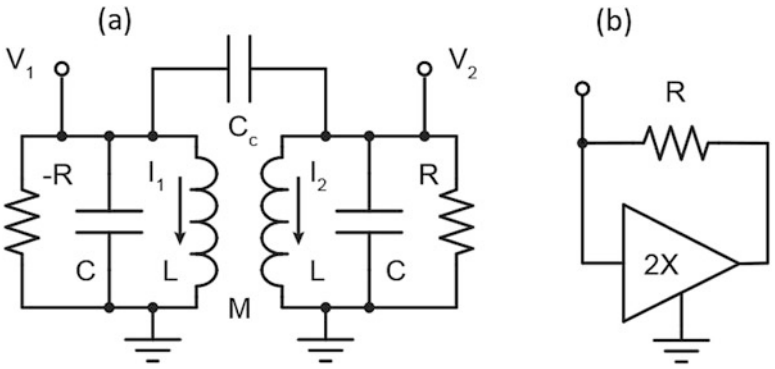

Fig. 1 (**a**) Simplified schematic of the $\mathscr{P}\mathscr{T}$-symmetric electronic dimer. Both mutual inductance coupling and capacitive coupling are included for generality. (**b**) Ground referenced negative resistance. This is the simplest electronic element contributing physical gain, always implemented in reality by positive feedback as shown with the ideal amplifier equivalent

having Ohmic gain. Figure 1b illustrates how an ideal linear amplifier can be configured to achieve negative resistance. The schematic implementation shown results in a single, ground-referenced node completely equivalent to a negative resistance. A similar circuit involving two amplifiers can achieve a two-terminal floating version [66].

With these principles in mind, the simplest, and conceptually most straightforward $\mathscr{P}\mathscr{T}$ system is illustrated in Fig. 1a. Two identical simple harmonic oscillators, in the electronic form of LC resonators are coupled either capacitively or inductively. The non-Hermitian dissipation on the right is paired with its negative resistance counterpart on the left. The convention in this figure will be maintained throughout this chapter: left/right or (1)/(2) will always refer to the gain/loss sides respectively, if not explicitly labeled as such.

There are two aspects of such systems – not unique to electronic circuits – that need to be kept in mind, both relating to practical implementation.

First is that any actual source of gain requires careful management of bandwidth. The negative resistance illustrates this concept. As an ideal, stand-alone device, it is inherently unstable [66] without any additional bandwidth limitation imposed either explicitly, as in the parallel RLC combination of Fig. 1a, or implicitly as a limitation of the actual source of the gain, i.e, the non ideal bandwidth limitation of a real amplifier used in Fig. 1b.

Second is that in any real system, it is important to realize that all physical electronic elements deviate from their ideal intended function. They all have unintentional (stray) impedances – resistive and reactive components – that can become significant in different situations. This is what makes microwave electronics particularly challenging. Electronic elements, particularly amplifiers, are also subject to both linearity and stability limitations, the later most critical in the vicinity of exceptional points.

In summary, ideal $\mathscr{P}\mathscr{T}$-symmetric circuits incorporating these basic elements require that (1) all reactive elements either have representation in parity-associated network pairs, or directly connect parity inverted network nodes, (2) all Ohmic elements are paired with opposite sign, and (3) each negative Ohmic element has an associated parallel capacitance, for bandwidth limitation, as part of the circuit. Valid $\mathscr{P}\mathscr{T}$-circuits of arbitrary complexity can be built up using these simple rules, though their overall stability needs to be independently determined. Note that the long-wave approximation of electronics can be relaxed with an appropriate inclusion of waveguide elements and connections. Waveguide elements also allow a conceptual transition from the electronic regime to the optical, with microwave systems positioned in the middle.

Finally, to complete the toolbox of fundamental electronic devices, we finish with a discussion of the gyrator. Although these devices have no known passive physical implementation approaching ideal in the long-wave electronic regime, some electro-mechanical-magnetic coupled devices can exhibit significant gyrotropic properties, and, due to their availability in the microwave and optical regime, it is nevertheless useful to consider their implementation in electronics as another approach toward simplifying the analysis of certain wave systems.

The ideal gyrator is defined as a four pole device where each of its two-pole ports a, b accepts a voltage difference $V_{a,b}$ and passes a current $I_{a,b}$ through the poles of that port according to the conductance relation

$$\begin{pmatrix} I_a \\ I_b \end{pmatrix} = \begin{pmatrix} 0 & G \\ -G & 0 \end{pmatrix} \begin{pmatrix} V_a \\ V_b \end{pmatrix} \tag{1}$$

where, in spite of the gyrator being characterized by a conductance G, it is a Hermitian (energy conserving) element. The gyrator is complementary to mutual inductance in that, while mutual inductance has equal off-diagonal terms (see the M terms in the mutual inductance parts of Eqs. 2 and 3) the gyrator has opposite off-diagonal terms. The gyrator has a transconductance with equal magnitudes in both directions, like mutual inductance, but *opposite phase* in one direction compared to the other.

A two port, two-pole schematic symbol shown in Fig. 2a, references the voltages, and responds by producing the ideal currents into a common ground shared by lower poles of each port. Figure 2b shows an active-electronic implementation where negative feedback imposed by the op-amps require that the voltages V_a and V_b applied to the op-amp positive inputs force V_a and V_b on the corresponding negative inputs. With these voltages determined, the voltages on the series string of four resistances R can be deduced by moving up the string from ground. The port currents can found from Ohm's law.

A similar circuit for the fully floating two-port, four-pole gyrator can be built up from four op-amps. Although these op-amp gyrators are implemented experimentally as active circuits, they could, in principle, be physically passive devices. In practice, such passive devices have yet to be engineered in the long-wave electronics regime.

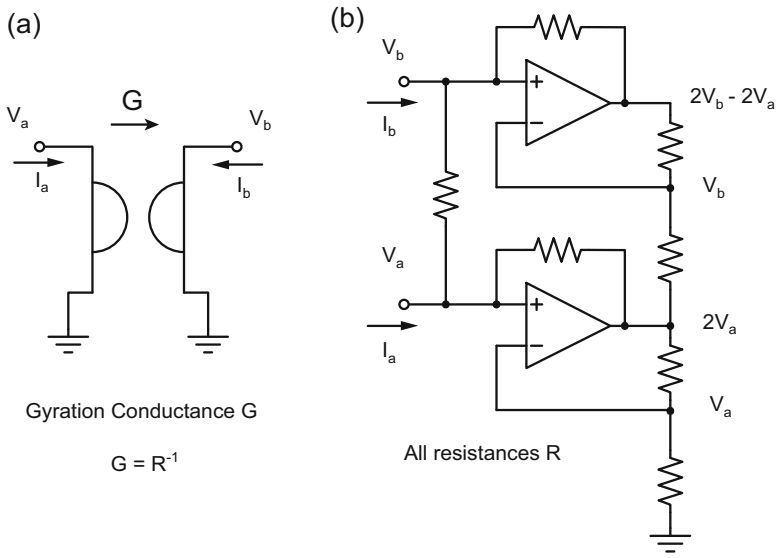

Fig. 2 (**a**) Gyrator symbol and definitions used for Eq. 1, similar to a mutual inductance, but with an opposite sign that imposes a 180° phase depending on direction. (**b**) Ground based op-amp gyrator circuit equivalent. All resistances are R as is the gyration resistance, with $R = 1/G$

Later we associate a mirror-time reversal ($M\mathscr{T}$) symmetry with electromagnetic systems having chiral properties (such as gyrotropic materials) exhibiting a symmetry analogous to $\mathscr{P}\mathscr{T}$ systems. This is discussed in detail in Sect. 4.4.

3 Closed Dimer

The analysis of the simple dimer circuit presented earlier in Fig. 1a shows the characteristic $\mathscr{P}\mathscr{T}$-symmetric behavior associated with the pseudo-Hermitian spectrum and modes. We include both capacitive and mutual inductive coupling for generality, although the experimental results presented throughout this work are exclusively one or the other. Kirchoff's laws in the frequency domain are given below for the gain side (Eq. (2)) and loss side (Eq. (3)) [33].

$$V_1 = i\omega(LI_1 + MI_2) \qquad I_1 - \frac{V_1}{R} + i\omega C V_1 + i\omega C_c(V_1 - V_2) = 0 \tag{2}$$

$$V_2 = i\omega(LI_2 + MI_1) \qquad I_2 + \frac{V_2}{R} + i\omega C V_2 + i\omega C_c(V_2 - V_1) = 0 \tag{3}$$

Eliminating the currents from the relations, scaling frequency and time by $\omega_0 = 1/\sqrt{LC}$, and taking $\mu = M/L$ and $c = C_c/C$ gives the matrix equation:

$$\begin{pmatrix} \frac{1}{\omega(1-\mu^2)} - \omega(1+c) - i\gamma & \omega c - \frac{\mu}{\omega(1-\mu^2)} \\ \omega c - \frac{\mu}{\omega(1-\mu^2)} & \frac{1}{\omega(1-\mu^2)} - \omega(1+c) + i\gamma \end{pmatrix} \begin{pmatrix} V_1 \\ V_2 \end{pmatrix} = 0. \quad (4)$$

At this point, it is obvious that the system is $\mathscr{P}\mathscr{T}$ symmetric: swapping the indices and changing the sign of i leaves the equations unchanged. This linear, homogeneous system has four normal mode frequencies, as required to fulfill any arbitrary initial condition for voltage and current, given by

$$\omega_{1,2} = \pm\frac{\sqrt{\gamma_c^2 - \gamma^2} + \sqrt{\gamma_{PT}^2 - \gamma^2}}{2\sqrt{1+2c}}; \quad \omega_{3,4} = \pm\frac{\sqrt{\gamma_c^2 - \gamma^2} - \sqrt{\gamma_{PT}^2 - \gamma^2}}{2\sqrt{1+2c}}; \quad (5)$$

with the $\mathscr{P}\mathscr{T}$ symmetry breaking point identified as

$$\gamma_{PT} = \left|\frac{1}{\sqrt{1-\mu}} - \sqrt{\frac{1+2c}{1+\mu}}\right| \quad (6)$$

and the upper critical point by

$$\gamma_c = \frac{1}{\sqrt{1-\mu}} + \sqrt{\frac{1+2c}{1+\mu}}. \quad (7)$$

Note that the given forms explicitly show all of the relationships among the critical points and the real and imaginary parts of the frequencies. The exact phase, $0 < \gamma < \gamma_{PT}$, is characterized by four purely real eigenfrequencies coming in two pairs of positive ($\omega_1, \omega_3 > 0$) and negative ($\omega_2, \omega_4 < 0$) values, while in the broken phase below the upper critical point, $\gamma_{PT} < \gamma < \gamma_c$ the eigenfrequencies are coming in complex conjugate pairs with non-vanishing real parts, and above γ_c, as two purely imaginary complex conjugate pairs. The broken phase of the $\mathscr{P}\mathscr{T}$ dimer is unstable, in that it is ultimately dominated by an exponentially growing mode.

The normal modes in the exact phase are characterized by equal magnitudes for the voltage oscillations in the gain and loss sides, which in the $+\omega$, real part convention allowed by the real eigenfrequencies, are given by

$$\begin{pmatrix} V_1 \\ V_2 \end{pmatrix}_{\pm} = \frac{1}{\sqrt{2}} \begin{pmatrix} 1 \\ -\exp(i\phi_{\pm}) \end{pmatrix} \quad (8)$$

with a phase $\phi_\pm$ of the loss side

$$\phi_\pm = \pi/2 - \tan^{-1}\left[\frac{1}{\gamma}\left(\frac{1}{(1-\mu^2)\omega_\pm} - (1+c)\omega_\pm\right)\right]. \tag{9}$$

As the gain/loss parameter traverses the exact region, $0 \leq \gamma \leq \gamma_{PT}$, the phase progresses from the in- and out-of-phase configuration of a Hamiltonian coupled oscillator, to a mode coalescence at γ_{PT} with $\phi_\pm \sim \pi/2$ with the real frequency

$$\omega_+ = \omega_- = \left[(1-\mu^2)(1+c)\right]^{-1/4} \tag{10}$$

Examination of the inductor currents,

$$\begin{pmatrix} I_1 \\ I_2 \end{pmatrix}_\pm = \begin{pmatrix} \frac{1}{1-\mu^2} & -\frac{\mu}{1-\mu^2} \\ -\frac{\mu}{1-\mu^2} & \frac{1}{1-\mu^2} \end{pmatrix} \begin{pmatrix} V_1 \\ V_2 \end{pmatrix}_\pm \tag{11}$$

reveal phase shifts, relative to the corresponding voltages, that advance on the gain side and retard on the loss side within either mode. This is as required for the net transfer of electrical energy from the gain side to the loss side as the gain/loss parameter increases. This evolutionary behavior is helpful in understanding the spectral and dynamical behavior of the dimer.

These modes are plotted in Fig. 3 along with experimental points [65] obtained from an electronic implementation of the circuit in Fig. 1a constructed according to the principles discussed in Sect. 2. The circuit was based on a pair of 30 kHz inductively coupled LC resonators, with the negative resistance feedback amplifier of Fig. 1b based on an LF356 op-amp. The experimental circuit reproduces both the complex eigenfrequencies of the $\mathscr{P}\mathscr{T}$ system and the phases of Eqs. 5, 6, 7, 8, 9, and 10.

Similar results from a COMSOL [12] investigation of a model microwave system [42] illustrate that the modes of a PT dimer are relatively independent of a dramatic redistribution of where the gain and loss are located within the system, as long as the required spatial parity is respected. Figure 4 illustrates the evolution of the isolated eigenfrequencies as a function of the gain/loss parameter for three different configurations involving a coupled pair of half-wave microstrip resonators. Both the gain and loss are implemented via an imaginary part to the dielectric constant of the supporting substrate. In Fig. 4a the gain and loss are collapsed into a localized patch at the resonator ends, as shown schematically in the inset. In Fig. 4b the gain and loss is uniformly distributed over the left and right sides of the whole substrate, and in Fig. 4c, the gain and loss are confined directly beneath the individual resonator striplines.

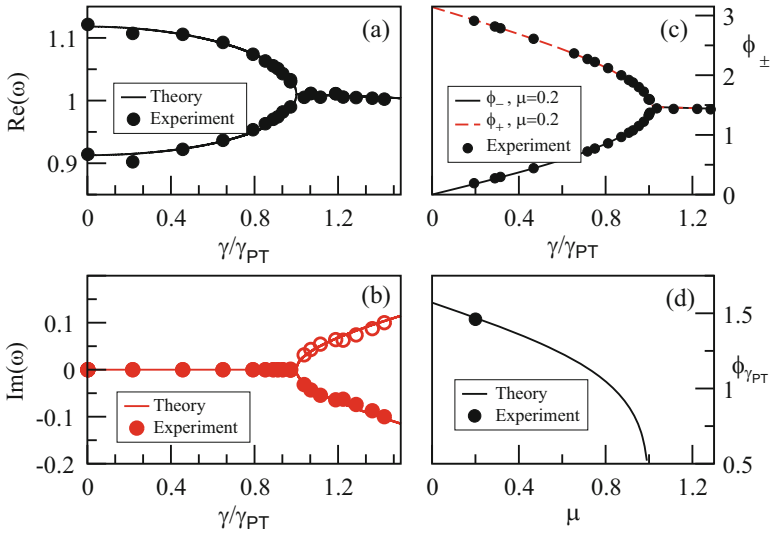

Fig. 3 Parametric evolution of the (**a**) real and (**b**) imaginary part of the eigenmodes of the $\mathscr{PT}$-symmetric dimer versus the normalized gain/loss parameter $\gamma/\gamma_{\mathscr{PT}}$. The experimental data are shown as filled circles while the theoretical predictions are shown as continous lines. In all cases we show the eigenfrequencies associated with $\mathscr{R}e(\omega) > 0$. The open circles in (**b**) are reflections of the experimental values of $\mathscr{I}m(\omega)$ with respect to $\mathscr{I}m(\omega) = 0$. In (**c**) we report the experimental (filled circles) and theoretical results (continous and dashed lines) for the relative phase $\phi_{\pm}$ versus the normalized gain/loss parameter. In (**d**) we report the theoretical (line) prediction for $\phi_{\mathscr{PT}}$ versus μ together with an experimental measurement (filled circle). (After Ref. [65])

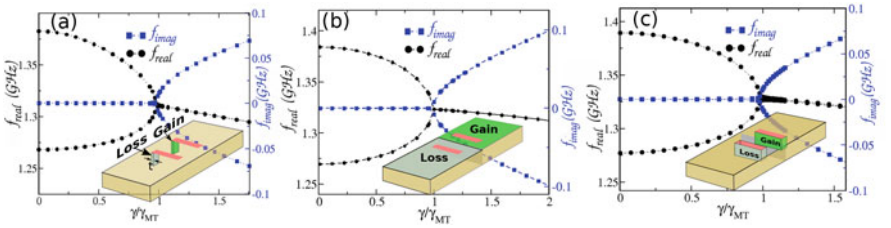

Fig. 4 Parametric evolution of the eigenmodes of a microwave circuit consisting of two $\mathscr{PT}$-symmetric microwave cavities (see inset). In each of the three cases the balanced gain/loss has been included in different ways: (**a**) In localized manner (with $\gamma_{M\mathscr{T}} = 1.6742$); (**b**) in distributed manner (with $\gamma_{M\mathscr{T}} = 0.095$); and (**c**) the gain and loss is confined directly beneath the individual resonator striplines (with $\gamma_{M\mathscr{T}} = 0.26$). (After Ref. [42])

While the latter two scenarios could be realized in the optics framework by appropriately distributed gain and loss media, case (i) is more relevant to the microwave domain. Concentrating the gain and loss into a small patch at the anti-nodes of the half-wave electric potential oscillations in the microstrip resonator mimics the action of discrete electronic gain or loss elements such as transistors or resistors. All cases demonstrate the appropriate transition from the exact phase

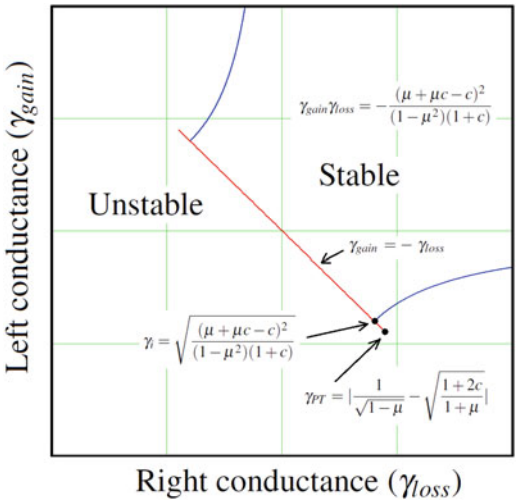

Fig. 5 Stability map for coupled LRC dimer illustrating the regions of exponential decaying solutions (stable) and exponentially growing solutions (unstable). The PT line, $\gamma_2 = \gamma_1$, follows a line of neutral stability until near the PT point, $|\gamma_{1,2}| = \gamma_{PT}$, where the stable region peels off toward the asymptotic region $\gamma_2 > 0, \gamma_1 > 0$

to the broken phase, as seen by the critical behavior of both the real and imaginary parts of the frequencies upon passing through γ_{PT}.

The PT symmetric relation Eq. 4 has real eigenvalues for gain/loss parameter $\gamma < \gamma_{PT}$. From an experimental perspective, it is useful to understand the stability of the dimer when the conductances deviate from the $\mathscr{P}\mathscr{T}$ balanced condition. To this end, we present a map of the character of the eigenfrequencies for arbitrary conductances of either sign, γ_1 on the left side of Fig. 1a and γ_2 on the right, with positive scaled conductance corresponding to loss (Fig. 5). The map is separated into an exponentially decaying (stable) domain, roughly in the first quadrant, and an exponentially growing (unstable) domain elsewhere. Separating these two domains are lines of oscillation threshold.

The straight line along the diagonal $\gamma_2 = -\gamma_1$ with $|\gamma_1| < \gamma_{PT}$ is the $\mathscr{P}\mathscr{T}$ symmetric condition in the exact phase. The separation curves elswhere lead away toward the asymptotes $\gamma_1 > 0, \gamma_2 = 0$ and $\gamma_2 > 0, \gamma_1 = 0$ respectively. There are several notable features pertaining to these threshold lines. First, is the intrusion of the stable domain into regions of individual oscillator gain. This behavior is necessary in order to meet up with the exact $\mathscr{P}\mathscr{T}$ situation. Second, the exact $\mathscr{P}\mathscr{T}$ line, and only this line, is simultaneously the threshold for both modes. This feature is crucially useful for balancing the experimental system. Finally, extending inward from γ_{PT} along the exact phase line is a small segment with zero imaginary part completely surrounded by unstable domain. This is not a threshold – separating stable from unstable – but rather a segment of marginal stability and an extremely difficult region to experimentally explore.

An alternate analysis of the dimer is necessary for a proper analytical consideration of the dynamics, and is accomplished by recasting time-domain version of Kirchoff's laws, Eqs. (2) and (3) into a "rate equation" form by making use of a Liouvillian formalism [60]

$$\frac{d\Psi}{d\tau} = \mathscr{L}\Psi; \quad \mathscr{L} = \begin{pmatrix} 0 & 0 & 1 & 0 \\ 0 & 0 & 0 & 1 \\ -\alpha\beta & \alpha\zeta & \gamma\frac{1+c}{1+2c} & -\gamma\frac{c}{1+2c} \\ \alpha\zeta & -\alpha\beta & \gamma\frac{c}{1+2c} & -\gamma\frac{1+c}{1+2c} \end{pmatrix} \tag{12}$$

where $\alpha = 1/(1-\mu^2)$, $\beta = \frac{1+c-c\mu}{1+2c}$, $\zeta = \frac{-c+\mu+c\mu}{1+2c}$ and $\Psi \equiv (Q_1, Q_2, \dot{Q}_1, \dot{Q}_2)^T$ with $Q_n = CV_n$. This formulation opens new exciting directions for applications [60] of generalized $\mathscr{P}\mathscr{T}$-mechanics [53] as it can be interpreted as a Schrödinger equation with non-Hermitian effective Hamiltonian $H_{\text{eff}} = i\mathscr{L}$. This Hamiltonian is symmetric with respect to generalized $\mathscr{P}_0\mathscr{T}_0$ transformations [60], i.e. $[\mathscr{P}_0\mathscr{T}_0, H_{\text{eff}}] = 0$, where

$$\mathscr{P}_0 = \begin{pmatrix} \sigma_x & 0 \\ 0 & \sigma_x \end{pmatrix}; \quad \mathscr{T}_0 = \begin{pmatrix} \mathbf{1} & 0 \\ 0 & -\mathbf{1} \end{pmatrix}\mathscr{K} \tag{13}$$

and σ_x is the Pauli matrix, $\mathbf{1}$ is the 2×2 identity matrix, and $\mathscr{K}$ denotes the operation of complex conjugation. By a similarity transformation $\mathscr{R}$ [60],

$$\mathscr{R} = \begin{pmatrix} \mu_+ & \mu_+ & \imath\sqrt{1+2c} & -\imath\sqrt{1+2c} \\ \mu_- & -\mu_- & \imath & \imath \\ -\mu_- & \mu_- & \imath & \imath \\ \mu_+ & \mu_+ & -\imath\sqrt{1+2c} & \imath\sqrt{1+2c} \end{pmatrix} \tag{14}$$

$H_{\text{eff}} = \mathscr{R}^{-1}H\mathscr{R}$ can be related to a transposition symmetric, $\mathscr{P}\mathscr{T}-$symmetric Hamiltonian $H = H^T = \mathscr{P}H^\dagger\mathscr{P}$, $\mathscr{T} = \mathscr{K}$ where $\mathscr{P} = \mathscr{R}P_0\mathscr{R}^{-1} = \begin{pmatrix} 0 & \sigma_x \\ \sigma_x & 0 \end{pmatrix}$. The matrix H is then

$$H = \begin{pmatrix} 0 & b_+ + \imath r & b_- + \imath r & 0 \\ b_+ + \imath r & 0 & 0 & b_- - \imath r \\ b_- + \imath r & 0 & 0 & b_+ - \imath r \\ 0 & b_- - \imath r & b_+ - \imath r & 0 \end{pmatrix} \tag{15}$$

where $b_\pm = \frac{1}{2}\left(\mu_+ \pm \frac{\mu_-}{\sqrt{1+2c}}\right)$, $\mu_\pm = 1/\sqrt{1\pm\mu}$ and $r = \frac{1}{2}\frac{\gamma}{\sqrt{1+2c}}$. The frequencies and normal modes within this framework are identical to Eqs. (5) and (11).

The dynamical behavior typical of the exact phase region for an inductively coupled dimer has been observed in electronic circuits [66] and demonstrated to have the expected beat superposition associated with two real frequencies. The beat

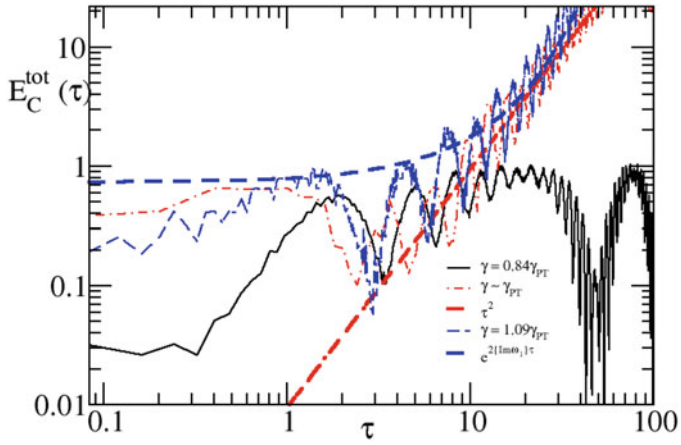

Fig. 6 Temporal evolution of the capacitance energy $E_c^{\text{tot}}(\tau)$ of the whole dimer for gain/loss values below the exceptional point (black line); above the exceptional point (blue line); and at the exceptional point (red line). The dashed red line indicates a τ^2 growth while the dashed blue line indicates an exponential growth $exp(2\mathscr{I}m(\omega_1)\tau)$. (After Ref. [65])

is asymmetric between the gain side and the loss side nodal times, with oscillatory activity spending more time between gain side nodal points as energy grows to a significantly larger size before decaying and growing between the loss side nodal points. However, unlike traditional coupled-oscillator beats, instead of "sloshing" between both sides during the course of the beats, a growth and decay energy dance occurs with both sides more or less equally represented except in the vicinity of the nodal points. This behavior is a direct result of the non-orthogonal phase relationships that become more pronounced as $\gamma \rightarrow \gamma_{PT}$. A Hamiltonian dimer would exhibit a perfect half-beat offset between the left and right voltage beat envelopes.

These energy dance features have also been traced by studying the time-dependence of the total capacitance energy:

$$E_C^{\text{tot}}(\tau) = \frac{Q_1^2(\tau) + Q_2^2(\tau)}{2C}. \tag{16}$$

With the initial condition used in the experiment, we expect power oscillations which are due to the unfolding of the non-orthogonal eigenmodes [3, 50, 63, 79]. This universal feature is evident in the temporal behavior of $E_C^{\text{tot}}(\tau)$ as can be seen in Fig. 6. On the other hand, for $\gamma > \gamma_{\mathscr{PT}}$ the dynamics is unstable and $E_C^{\text{tot}}(\tau)$ grows exponentially with a rate given by the maximum imaginary eigenvalue $\max\{\mathscr{I}m(\omega_l)\}$ (see Fig. 6).

The most interesting behavior appears at the spontaneous $\mathscr{PT}$-symmetry breaking point $\gamma = \gamma_{\mathscr{PT}}$. At this point the matrix $\mathscr{L}$ has a defective eigenvalue. In this case, the evolution $U = \exp(\mathscr{L}\tau)$ can be calculated from the Jordan

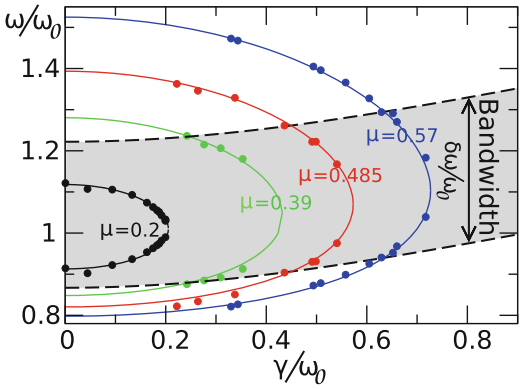

Fig. 7 Parametric evolution of the eigenfrequencies of a $\mathscr{PT}$-symmetric dimmer versus the rescaled gain/loss parameter γ/ω_0 for various mutual inductances μ. The borders of the highlighted area (marked with a black dashed line) indicate a constant bandwidth path with $\delta\omega/\omega_0 = 0.36$. (After Ref. [60])

decomposition of $\mathscr{L}$ as $\mathscr{J} = S\mathscr{L}S^{-1}$. Having in mind the form of the exponential of a Jordan matrix, it follows immediately that linear growing terms appear in the evolution of the charge vector $(Q_1(\tau), Q_2(\tau))^T$ [26]. This results in a quadratic increase of the capacitance energy i.e. $E_C^{\text{tot}}(\tau) \sim \tau^2$. Although all systems typically becomes very sensitive to parameters near a critical point, we are able to control the circuit elements sufficiently well to observe the approach to the predicted τ^2 behavior of the energy.

Figure 7 shows both theoretical and experimental results for the exact phase eigenfrequencies for various values of the coupling μ. The black dashed lines bounding the shaded region illustrate a path of fixed bandwidth, $\delta\omega/\omega_0 = 0.36$, through the families of eigenfrequencies.

Equation (12) can be solved either analytically or via direct numerical integration in order to obtain the temporal behavior of the capacitor charge $Q_n(\tau)$ and the displacement current $I_n(\tau)$ in each of the two circuits of the $\mathscr{PT}$-symmetric dimer. For the investigation of the tachistochrone wave evolution, we consider an initial displacement current in one of the circuits with all other dynamical variables zero. The first passage time τ_{fpt} is then defined as the time interval needed to reach an orthogonal state. In our experiments this corresponds to the condition that the envelope function of the current at the initially excited circuit is zero. We find that the first passage time is asymmetric with respect to the initially excited circuit [60]. Specifically we have that

$$\tau_{\text{fpt}} = \frac{1}{\delta\omega}\left[\pi \pm \arccos\left(\frac{\delta\omega^2 - \gamma^2}{\delta\omega^2 + \gamma^2}\right)\right] \tag{17}$$

where the $+$ sign corresponds to an initial condition starting from the gain side while the $-$ sign corresponds to an initial condition starting from the lossy side. For $\gamma \gg \delta\omega$, Eq. (17) takes the limiting values $\tau_{\text{fpt}} \approx 2\pi/\delta\omega$ and $\tau_{\text{fpt}} \approx 2/\gamma$ respectively. The latter case indicates the possibility of transforming an initial state to an orthogonal final one, or in more practical terms, transferring energy from one side to the other, in an *arbitrarily* short time interval. In the opposite limit of $\gamma = 0$,

we recover for both initial conditions the Anandan-Aharonov lower bound for the first passage time $\tau_{\text{fpt}} = \pi/\delta\omega$ [1]. This is the time for which energy is transferred from the initial circuit to its partner according to the constraint of the Bandwidth theorem.

Geometrically, one can understand the relation (17) in the following way: the time required for the evolution between two states induced by a Hermitian Hamiltonian is proportional to the length of the shortest geodesic connecting the two states in projective Hilbert space [1]. Non-Hermitian $\mathscr{P}\mathscr{T}$-symmetric Hamiltonians in the exact $\mathscr{P}\mathscr{T}$-symmetric domain can be similarity mapped to equivalent Hermitian Hamiltonians. Under such a similarity mapping the corresponding projective Hilbert space undergoes a deformation obtaining a nontrivial metric. This results in an effective contraction or dilation of the corresponding geodesic and with it of the corresponding evolution time [25, 27, 54].

In Fig. 8 we present some typical measurements for the temporal behavior of the displacement currents. In Fig. 8a we show $|I_1(\tau)|$ for an initial condition corresponding to the case $I_1(0) = 1$ with all other dynamical variables zero. The case where the initial current excitation is at the lossy side i.e. $I_2(0) = 1$, is shown for contrast in Fig. 8b. In both cases, agreement between the experiment (circles) and the simulations (lines) is observed. For comparison, we also report with black line the temporal behavior of the displacement current for the case of a passive circuit (i.e. $\gamma = 0$) with the same $\delta\omega$-constraint. We observe that the orthogonal target state is reached faster (or slower) depending on whether the initial excitation is applied to the lossy (or gain) side.

The above results can be verified in more cases by changing the inductive coupling μ and gain/loss parameter γ, while keeping the frequency difference $\delta\omega = \omega_2 - \omega_1$ constant. A summary of our measured τ_{fpt} versus γ is presented in Fig. 8c. The experimental data show agreement with the theoretical prediction Eq. (17).

A parallel analysis pertains directly to the study of the energy transport from one side to another. Using the same initial conditions as above we investigate the temporal behavior of the energies

$$E_n(\tau) = \frac{1}{2}\frac{Q_n^2}{C} + \frac{1}{2}LI_n^2 \tag{18}$$

of each $n = 1, 2$ circuit. The first passage time can be defined as the time for which the two energies become equal for the first time i.e. $E_1(\tau_{\text{fpt}}^E) = E_2(\tau_{\text{fpt}}^E)$. For passive (i.e. $\gamma = 0$) coupled circuitry, this time is half of the beating time $\tau_{\text{fpt}}^E = \tau_{\text{fpt}}(\gamma = 0)/2$ and it is insensitive to the initial preparation. In contrast, for the active $\mathscr{P}\mathscr{T}$-symmetric dimer of Fig. 1a, we find that the energy transfer from the lossy (gain) side to the gain (lossy) one, is faster (slower) than the corresponding passive system with the same $\delta\omega$. In Fig. 8d, we summarize our measurements for the τ_{fpt}^E versus γ under the constraint of fixed frequency bandwidth $\delta\omega$. A similar behavior as the one found for the displacement current is evident.

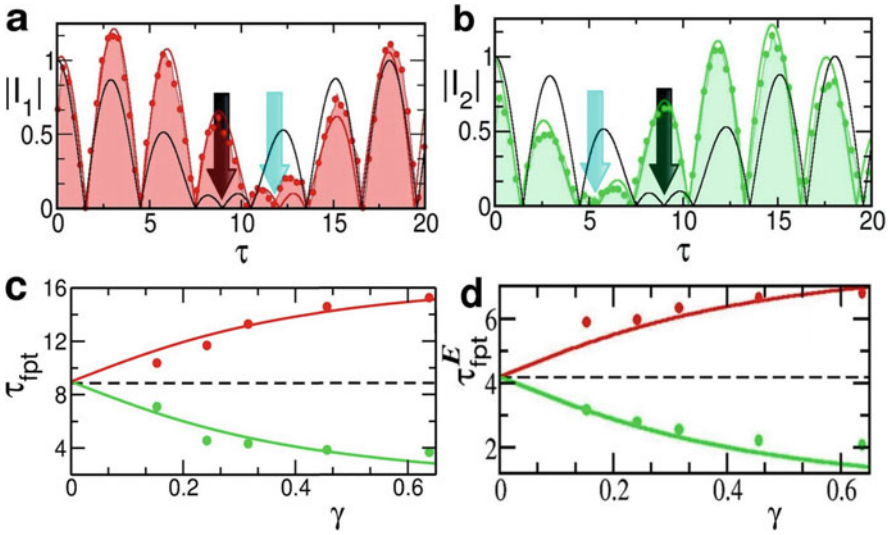

Fig. 8 A typical temporal evolution of the displacement current (**a**) $I_1(\tau)$ for the case that the initial excitation occurs at the gain side ($n = 1$) and for (**b**) $I_2(\tau)$ when the initial excitation occurs at the loss side ($n = 2$). In both cases the bandwidth constraint is $\delta\omega/\omega_0 = 0.36$. The red/green lines indicate the results of the simulations for a circuit with $\gamma = 0.24$ and $\mu = 0.39$. The black line is drawn for reference and correspond to the simulations for the case where $\gamma = 0$. The measurements are indicated with circles. The cyan (black) arrow indicates the first passage time τ_{fpt} for the case of the active (passive) circuit. (**c**) The measured τ_{fpt} (versus γ) when it is extracted using the displacement currents. The red circles correspond to the case that the initial excitation occurs at the gain side ($I_1(0) = 1$) while the green circles correspond to the case that the initial excitation occurs at the lossy side ($I_2(0) = 1$). Equation (17) is reported as a solid line and the beat time corresponding to a circuit with $\gamma = 0$ is reported as black dashed line. (**d**) The same as in (**c**) but now the first passage time τ^E_{fpt} is extracted using the energy exchange condition. Lines correspond to the theoretical prediction $\tau^E_{\text{fpt}} = \tau_{\text{fpt}}/2$. The black dashed line denotes τ^E_{fpt} for $\gamma = 0$. (After Ref. [60])

3.1 Gyration Eigenmodes

We now discuss how gyration influences the normal modes of isolated $\mathscr{PT}$ balanced dimer. For simplicity, we consider only mutual inductance coupling along with a coupling through the gyrator of Fig. 2a between the two oscillators of the dimer. With $c = 0$, the equivalent of Eq. 4 for Kirchhoff's laws in the frequency domain leads to a similar form for the eigenvalue equation,

$$\left(\tilde{\omega}^2 - \frac{1}{1-\mu}\right)\left(\tilde{\omega}^2 - \frac{1}{1+\mu}\right) - (g^2 - \gamma^2)\tilde{\omega}^2 = 0 \tag{19}$$

where the gyration strength $g = G\sqrt{L/C}$ is seen to trade off with the gain/loss parameter γ. The eigenvalues of the antisymmetric and symmetric modes follow the same structure

$$\tilde{\omega}^0_{a/s}(\gamma) = \frac{\sqrt{\gamma_c^2 - \gamma^2} \pm \sqrt{\gamma_{MT}^2 - \gamma^2}}{2} \tag{20}$$

along with their redundant negatives, which are again defined in terms of two critical points for the gain/loss parameter, i.e., an $M\mathscr{T}$ symmetry breaking point

$$\gamma_{MT} = \sqrt{g^2 + \left[\sqrt{\frac{1}{1+\mu}} - \sqrt{\frac{1}{1-\mu}}\right]^2} \tag{21}$$

and an upper critical point

$$\gamma_c = \sqrt{g^2 + \left[\sqrt{\frac{1}{1+\mu}} + \sqrt{\frac{1}{1-\mu}}\right]^2}. \tag{22}$$

Note that the given forms explicitly show all of the relationships among the analogous exceptional points and the real and imaginary parts of the frequencies.

The normal modes in the exact phase are again characterized by equal magnitudes for the voltage oscillations in the gain and loss sides, given by

$$\begin{pmatrix} V_g \\ V_l \end{pmatrix}_{a/s} = \frac{1}{\sqrt{2}} \begin{pmatrix} 1 \\ \exp(i\phi_{a/s}) \end{pmatrix} \tag{23}$$

with a phase $\phi_{a/s}$ of the loss side relative to the gain side of

$$\phi_{a/s} = arg\left((\frac{1}{1-\mu^2} - \left(\tilde{\omega}^0_{a/s}\right)^2 - i\gamma\tilde{\omega}^0_{a/s})(\frac{\mu}{1-\mu^2} + ig\tilde{\omega}^0_{a/s}) \right). \tag{24}$$

It is here that we observe how the gyration qualitatively changes the character of the normal modes in a new way. With mutual inductance alone, as the gain/loss parameter traverses the exact region, $0 \leq \gamma \leq \gamma_{MT}$, the phase progresses from the in- and out-of-phase configuration of a Hamiltonian coupled oscillator pair, to a mode coalescence at γ_{MT} with a real frequency $\tilde{\omega}^0_a = \tilde{\omega}^0_s = (1-\mu^2)^{-1/4}$, where both the magnitudes and phases of the voltage oscillations are identical. The role of the gyration strength g is subtle: it acts in an orthogonal sense to the mutual inductance coupling because of its inherent non-reciprocal coupling of current and voltage, and results in mode phasers initially related by $\pi/2$ usually indicative of dissipation. However, in spite of the gyration being characterized by a real conductance, it is actually a non-dissipative element. Figure 9 schematically

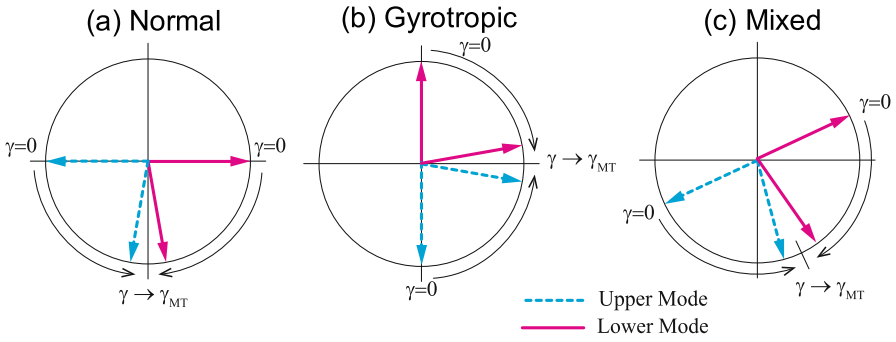

Fig. 9 Loss side voltage phasors relative to the gain side ($+x$ axis) for the low frequency (solid) and high frequency (dashed) isolated dimer modes. Phasors in (**a**) are for pure mutual inductance coupling; (**b**) is for pure gyration coupling; and (**c**) mixed coupling. In all cases, the high and low modes coalesce to identical relations as γ approaches $\gamma_{M\mathscr{T}}$

illustrates the evolution of the left and right voltage mode phasers for pure mutual inductance coupling in (a); pure gyration coupling in (b); and a combination of the two in (c). In all cases, the high and low mode coalesce as γ increases, approaching $\gamma_{M\mathscr{T}}$.

We note that the gyration is thus imposing a non-dissipative quadrature normal mode character to the electronic circuit analogous to the circularly polarized eigenstates of free electromagnetic waves in a gyromagnetic medium. The combination of the gyrotropic coupling with normal reactive coupling allows simple electronic circuits to embody many of the important features of gyrotropically coupled resionators, such as a microstrip dimer on a biased magnetic substrate.

4 Open Dimer (Scattering)

We have seen how the closed $\mathscr{P}\mathscr{T}$ systems have a phase relation between the modes that, as a function of the gain/loss parameter, γ, is not accessible with a normal Hermitian system. This additional dimension of control extends to systems incorporating gyration. We now discuss how the unique properties of the normal modes can be used to create novel scattering systems with useful engineering applications.

4.1 Single Lead Case

We start by comparing two reciprocal geometries where a single scattering lead is attached to either the gain or loss side of the previously isolated $\mathscr{P}\mathscr{T}$ dimer. As before, the qualitative features of generic systems are most easily analyzed and

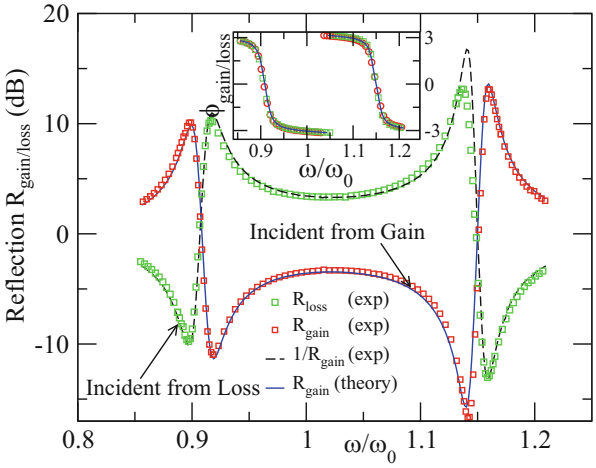

Fig. 10 Experimental (red and green squares) and theoretical (continous blue line) reflectances versus the rescaled incident frequency ω/ω_0. The black dashed line indicate the experimental data associated with $1/R_{\text{gaim}}$ and fall nicely on top of the experimental data for the R_{loss} – thus confirming the generalized conservation relation $R_{\text{gain}}R_{\text{loss}} = 1$. In the inset we report the experimental values of the phases of the corresponding gain/loss (red circles/green circles) reflection amplitudes together with the theoretical prediction (solid line) versus the rescaled frequency. The parameter used are $\gamma = 0.188875$, $\mu = 0.29$ and $\eta = 0.0305$. (After Ref. [46])

understood through the electronics case. The lower right and left insets of Fig. 10 respectively show the transmission line connected to either of the parity-associated nodes in the circuit.

Experimentally, the equivalent of a TEM transmission line with characteristic impedance Z_0 is a Thevenin voltage source attached to the LC circuit node. The Thevenin source resistance with $R_{th} = Z_0$ sets the equivalent transmission line impedance, and the source voltage, V_{th}, determines the incoming wave amplitude. Thus knowledge of the source voltage and measuring the LC node voltage, V_{LC}, allows determination of the incoming, $V_{in} = V_0/2$, and reflected, $V_{refl} = V_{LC} - V_0/2$, complex wave voltage amplitudes for either configuration of Fig. 10.

The simplicity of the circuit allows a straight-forward algebraic analysis. We are interested in the behavior of the reflectance $R_{gain/loss} \equiv |r_{gain/loss}|^2$, and nodal potential $V_{gain/loss}$ inside the gain or loss sides of the scattering domain, as the gain/loss parameter γ, and the frequency ω changes.

For $\mathscr{P}\mathscr{T}$-symmetric structures, the corresponding scattering signals satisfy *generalized unitarity relations* which reveal the symmetries of the scattering target. Specifically, in this single-port set up this information is encoded solely in the reflection. To unveil it, we observe that the lower left set-up of Fig. 10 is the $\mathscr{P}\mathscr{T}$-symmetric replica of the lower right one. Assuming therefore that a potential wave at the gain-side lead (lower right inset) has the form $V_{gain}(x) = \exp(ikx) + r_{gain}\exp(-ikx)$ (we assume unit incoming amplitude), we conclude that the form

of the wave at the loss-side lead associated with the lower left set-up of Fig. 10, is $V_{loss}(x) = \exp(-ikx) + r_r \exp(ikx) = V^*_{gain}(-x)$. Direct comparison leads to the relation

$$r_{gain} \cdot r^*_{loss} = 1 \rightarrow R_{gain} = 1/R_{loss} \quad \text{and} \quad \phi_{gain} = \phi_{loss} \tag{25}$$

where $\phi_{gain/loss}$ are the reflection phases from the gain or loss sides. Note that Eq. (25) differs from the more familiar conservation relation $R = 1$, which applies to unitary scattering processes as a result of flux conservation. In the latter case left and right reflectances are equal. Instead, in the $\mathscr{P}\mathscr{T}$-symmetric case we have in general that $R_{gain} \neq R_{loss}$.

For the specific case of the $\mathscr{P}\mathscr{T}$-symmetric dimer, the exact expression for the reflection coefficients are

$$\begin{aligned} r_{gain}(\omega) &= -f(-\eta, -\gamma)/f(\eta, -\gamma) \\ r_{loss}(\omega) &= -f(-\eta, \gamma)/f(\eta, \gamma) \\ f &= 1 - [2 - \gamma m(\gamma + \eta)]\,\omega^2 + m\omega^4 - i\eta\omega(1 - m\omega^2) \end{aligned} \tag{26}$$

with $m = 1/\sqrt{1-\mu^2}$ and $\eta = Z_0^{-1}\sqrt{L/C}$. In the limiting case of $\omega \rightarrow 0, \infty$ the reflections becomes $r_{gain} = r_{loss} \rightarrow \mp 1$ and thus unitarity is restored.

The main panel of Fig. 10 shows a representative measurement of the reflection signals for the two scattering configurations with their comparison to Eq. (26). The measured reflectances R_{gain}, and R_{loss} satisfy the generalized conservation relation $R_{gain} \cdot R_{loss} = 1$[1] while for the reflection phases, shown in the upper inset, have that $\phi_{gain} = \phi_{loss}$ as expected from Eq. (25). Therefore, our experiment demonstrates that a $\mathscr{P}\mathscr{T}$-symmetric load is a simple electronic Janus device that, for the same values of the parameters ω, μ, γ acts as a signal absorber as well as a signal amplifier, depending on the direction of incident signal.

The (ω, γ) parameter space can then be partitioned into a *sub-unitary* domain for which $R < 1$ (flux is diminished), and a *super-unitary* domain for which $R > 1$ (flux is enhanced). At the transition between the two domains $R_{gain} = R_{loss} = 1$, in which case the scattering from either side conserves flux. Such a *reflectance degeneracy* (RD) occurs along the continuous boundary between the two domains, defined by $|r| = 1$, giving

$$\gamma_{RD}(\omega) = \sqrt{\frac{-1 + 2\omega^2 - (1-\mu^2)\omega^4}{(1-\mu^2)\omega^2}} \quad \text{and} \quad \frac{|\omega^2 - 1|}{\omega^2} \leq \mu \leq 1 \tag{27}$$

A panorama of theoretical $R_{loss}(\omega, \gamma)$ are shown in Fig. 11. The transition line $\gamma_{RD}(\omega)$ where the reflectance degeneracy occurs. Inside this domain, a singularity

[1]The slight deviation from reciprocity in the vicinity of largest reflectance in Fig. 10 is attributed to nonlinear effects.

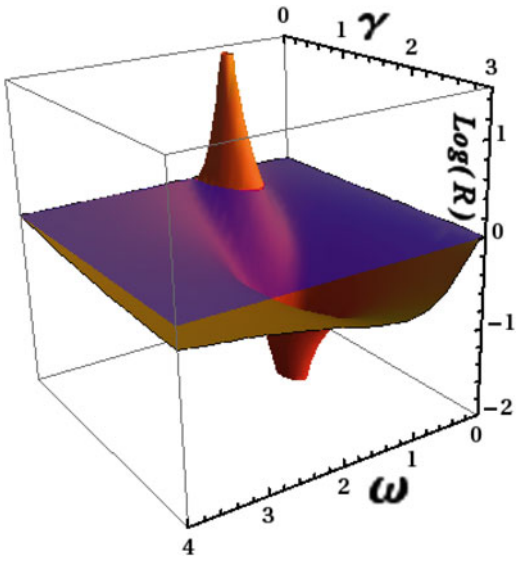

Fig. 11 The R_{loss} versus the gain/loss parameter and the rescaled frequency ω/ω_0 for the case of a $\mathscr{P}\mathscr{T}$-symmetric dimer with one TL attached to the lossy element. The super-unitary ($\log_{10}(R_{\text{loss}}) > 0$) and the sub-unitary ($\log_{10}(R_{\text{loss}}) < 0$) domains are separated via the violet plane at $\log_{10}(R_{\text{loss}}) = 0$. The boundary, in the $\gamma - \omega$ parameter space that defines the transition from super-unitary to sub-unitary scattering is also shown as a red line. The inductive coupling in this case is $\mu = 0.57$. (After Ref. [46])

point appears for which $R_{loss} \to \infty$, while a reciprocal point for which $R_{loss} = 0$ is found in the complementary domain. The corresponding $(\omega_s; \gamma_{\infty,0})$ are found from Eq. (26) to be $\gamma_{\infty,0} = \frac{1}{2}\left(\sqrt{\eta^2 + \frac{4\mu^2}{(1-\mu^2)}} \mp \eta\right)$; $\omega_s = \frac{1}{\sqrt{1-\mu^2}}$ Obviously via Eq. (25) we have the reverse scenario for R_{gain}.

The sub-unitary to super-unitary $\mathscr{P}\mathscr{T}$-symmetric transition is also manifest in the gain/loss nodal voltages inside the dimer, where

$$\begin{aligned} V_{gain} &= 2\eta\omega\left[1 - m\omega(\omega - i\gamma)\right]/D \\ V_{loss} &= -2\eta\mu\omega/D \\ D &= \eta\omega(1 - m\omega^2) + i\left(1 - \omega^2\left[2 - m(\omega^2 + \gamma\omega + \gamma^2)\right]\right) \end{aligned} \tag{28}$$

Typical potential magnitudes $|V_{gain}|$ and $|V_{loss}|$, for the transmission line attached to the loss side (lower left inset of Fig. 10) versus the frequency ω are shown in Fig. 12. In general, the potentials are asymmetric. In the super-unitary domain, the gain side is characterized by a larger potential amplitude $|V_{gain}| > |V_{loss}|$ while in the sub-unitary domain the scenario is reversed and $|V_{gain}| < |V_{loss}|$. The latter configuration ensures that more power is being consumed than compensated by the gain circuit, while the inverse argument applies for the former configuration. At frequencies where the reflection degeneracy occurs, the nodal voltages are spatially symmetric. This is consistent with the intuitive expectation that in order to conserve flux the excitation must on average spend equal amounts of time in the loss and gain circuits of the structure. Obviously, the reverse scenario occurs if we couple the transmission into the $\mathscr{P}\mathscr{T}$-dimer from the gain side.

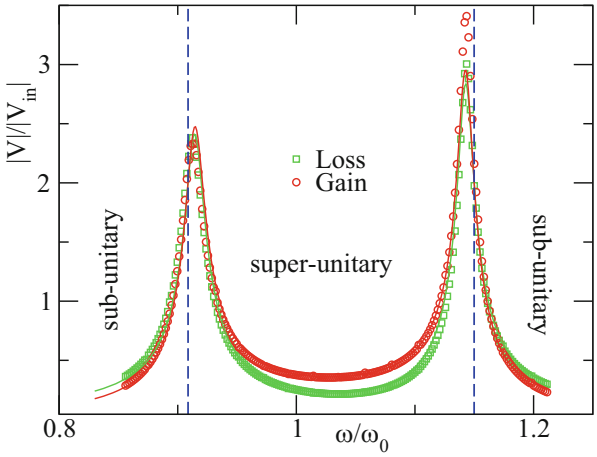

Fig. 12 The distribution of experimentally measured potentials inside the $\mathscr{P}\mathscr{T}$-symmetric dimer versus the frequency ω. The potential and the loss (gain) side is indicated with a green square (red circle). The dimer is coupled to one transmission line attached at the lossy node. The parameter used are $\gamma = 0.188875$, $\mu = 0.29$ and $\eta = 0.0305$. The theoretical predictions for the potential at the loss (gain) side are shown with continuous green (red) lines. The blue dashed lines indicate the boundaries between sub-unitary to super-unitary scattering. (After Ref. [46])

4.2 Stability with Leads

We momentarily turn to a discussion of the stability of a $\mathscr{P}\mathscr{T}$ system with "leads" attached. As discussed in the context of Fig. 5, the closed, but unbalanced gain/loss dimer is equivalent to a balanced, but open system. The radiative dissipation associated with the leads generally shifts the effective operating point of the system into the stable regime, but surprisingly, this is not always the case. It is possible, by monotonically increasing the gain in the parameter space of Fig. 5, to experience reentrant stable/unstable transitions [8].

This behavior is a generic property of systems with spatially distributed gain that includes a $\mathscr{P}\mathscr{T}$-symmetric configuration. Figure 13 shows such a path in a 1D optical gain/loss laser cavity, Fig. 14 shows a similar reentrance path in a tight-binding $\mathscr{P}\mathscr{T}$ dimer model with leads, and Fig. 15 shows an experimental demonstration.

Figure 13b shows the evolution of $\mathscr{I}m(\omega)$ for the dominant pole of the scattering matrix for a specific path of the gain parameters γ_1, γ_2 associated with the left and right portions of the cavity shown in Fig. 13a. The dominant pole is the only one to experience the stability-instability transitions within the frequency range assumed for the γ_1 and γ_2 gain curves. Initially, we assume that both the left and right regions of the optical cavity have the same intrinsic loss $\gamma_0 < 0$ as described earlier. The left part of the cavity is then pumped with increasing gain, $\gamma_0 < \gamma_1 < \gamma_1^{\max}$, until the dominant pole crosses the real axis ($\mathscr{I}m(\omega) = 0$) at some critical gain $\gamma_1^* < \gamma_1^{\max}$.

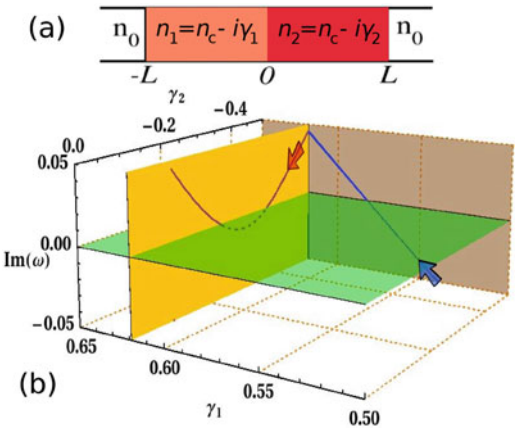

Fig. 13 (**a**) An one-dimensional lasing cavity occupying a space $[-L, L]$ with asymmetrically distributed gain determined by the imaginary part of the index of refraction $\mathscr{I}m(n(-L < z < 0) = -\gamma_1$ and $\mathscr{I}m(n(-L < z < 0) = -\gamma_2$ with $\gamma_1 \neq \gamma_2$. (**b**) The evolution of the dominant pole as the gain $\gamma_{1,2}$ in each of the compartments of the lasing cavity is changing. (After Ref. [8])

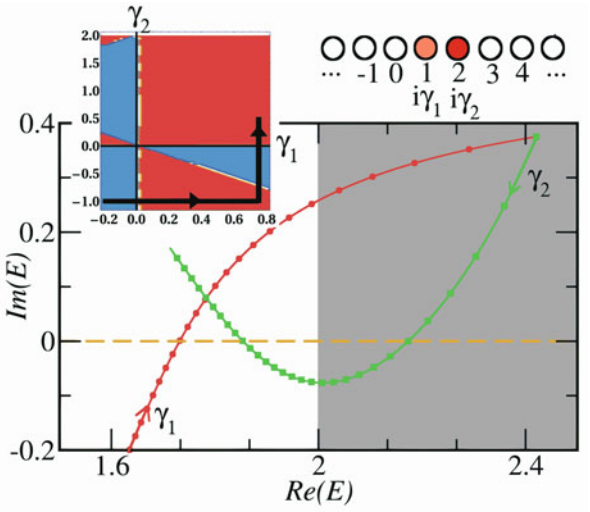

Fig. 14 Right inset: a representation of the simple tight-binding (TB) model that we have used in the text. The two sites at positions $n = 1$ and $n = 2$ in the middle of the TB chain model the couple lasing cavities and have imaginary on-site potential $\gamma_1 \neq \gamma_2$. The sites on the left/right of the active dimer model the leads. Left inset: the $\gamma_1 - \gamma_2$ parameter space of the TB model. Red areas indicate unstable domains while blue areas indicate stable domains. The black line indicates the pumping path. Main panel: the parametric evolution of one resonance as γ_1 and γ_2 changes (see left inset). The other resonance is not reported since its motion is symmetric, with respect to the origin of the axis $\mathscr{R}e(\mathscr{E})$, to the one reported here. (After Ref. [8])

At this point, a lasing state in the cavity is created. For $\gamma_1^* < \gamma_1 < \gamma_1^{\max}$ the pole continues to travel upwards in the positive ($\mathscr{I}m(\omega) > 0$) plane indicating unstable dynamics. In this regime, any physical system ultimately becomes non-linear and the scattering approach fails. However, we may infer from our low amplitude linear analysis the presence or absence of the lasing instability. The pumping on the

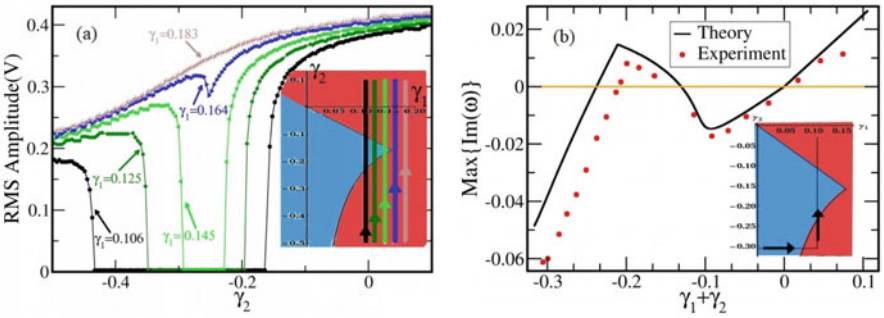

Fig. 15 (Left) Experimental values of the steady-state voltage (measured at side-1 LC node) versus γ_2 for the paths indicated in the inset. Note that although the overall gain increases, the width of the "lasing death" response diminishes. (Right) The maximum imaginary part of the eigenvalues $Max[\mathscr{I}m(\omega)]$ versus the total gain for the pumping path shown in the inset. The theoretical results are indicated with a continuous black line while the measurements are shown as red filled circles. The lasing death phenomenon occurs when the path traverses a protrusion in the stability map the most positive imaginary part momentarily dips back into the negative region. (After Ref. [8])

left partition is now kept constant at $\gamma_1 = \gamma_1^{\max}$, while additional pumping, via increasing γ_2 is applied to the right partition of the cavity. Surprisingly, this results in reversing the evolution of the pole back towards $\mathscr{I}m(\omega) = 0$. At some critical value $\gamma_2 = \gamma_2^*$, the pole re-crosses the real axis returning to $\mathscr{I}m(\omega) < 0$. Such transitions indicate that the system returns to stability, i.e. the laser shuts off despite the fact that the overall pump power provided to the system has been increased. Further increase of γ_2 once again reverses the direction of the motion of the pole which moves upwards and crosses into $\mathscr{I}m(\omega) > 0$. At this new critical value, $\gamma = \gamma_2^{**}$, the mode once again becomes unstable signifying a second turn-on of the laser.

It is instructive to point out that it is possible to express the S-matrix at an arbitrary wavenumber k in terms of all eigenvalues and eigenfunctions of the corresponding closed cavity. This is achieved by employing the so-called reaction matrix formalism which has been developed in the frame of nuclear physics by Wigner and Eisenbud [76]. Specifically we have that

$$S = \frac{\hat{1} - iK}{\hat{1} + iK}; \quad K = \pi W^{\dagger} G_{\text{in}} W \tag{29}$$

where K is the so-called reaction matrix and $(G_{\text{in}})_{n,n'} = \left[k^2(\delta_{n,n'} - i\hat{\Gamma}_{n,n'}) - k_n^2\delta_{n,n'}\right]^{-1}$ is the Green's function of the closed active cavity. The gain matrix, $\hat{\Gamma}$ denotes the gain distribution inside the cavity and the matrix $\hat{W}(k)$ denotes the coupling of the internal level n to the scattering channel j. Equation (29) can be

further expressed [23] in terms of an effective non-Hermitian Hamiltonian $\mathscr{H}_{\text{eff}}$ which contains the dynamics of the closed system and the coupling to the scattering channels:

$$S = \hat{1} - 2i\pi W^{\dagger} G_{\text{eff}} W; \quad G_{\text{eff}} = [\mathscr{E} - H_{\text{eff}}]^{-1} \tag{30}$$

where $(\mathscr{H}_{\text{eff}})_{n,n'} = k_n^2 \delta_{n,n'} - i\pi (W W^{\dagger})_{n,n'}$ and $\mathscr{E} = k^2(\hat{1} - \hat{\Gamma})$. We see therefore that the poles of the scattering matrix are the complex eigenvalues of an effective Hamiltonian. It is useful at this point to keep in mind the equivalence between the various forms of the scattering matrix.

The universality of lasing death via asymmetric pumping can also be illustrated within a simple two-level model (dimer) coupled to two leads. The system is shown in the inset of Fig. 14. The Hamiltonians of the dimer H_d and of the leads H_{leads} read:

$$\begin{aligned} H_d &= \sum_{n_N=1,2} \epsilon_{n_N} |n_N\rangle\langle n_N| + (|n_N\rangle\langle n_N + 1| + c.c.) \\ H_{\text{leads}}^{L,R} &= \sum_{n=n_L,n_R} \epsilon_n |n\rangle\langle n| + (|n\rangle\langle n+1| + c.c.) \end{aligned} \tag{31}$$

where $n_L = 0, \cdots, -\infty$, $n_R = 3, \cdots, \infty$ and $\{|n\rangle\}$ is the Wannier basis of the tight-binding Hamiltonian. The on-site potentials are $\epsilon_n = V_n + i\gamma_n$ with $\gamma_n = 0$, for $n \neq 1, 2$. We note that, unlike the case of optical cavity that we discuss previously, $\mathscr{I}m(\epsilon_n) > 0$ represents gain while $\mathscr{I}m(\epsilon_n) < 0$ represents loss. Furthermore, without loss of generality we will assume that $V_n = 0$ for all n. The complex zeros $\mathscr{E}$ of the secular equation $\det[M_{22}(\mathscr{E})] = 0$ can be calculated analytically:

$$\mathscr{E} = \frac{i[\gamma_1\gamma_2(\gamma_1 + \gamma_2) \pm (2 + \gamma_1\gamma_2)\sqrt{(\gamma_1 - \gamma_2)^2 - 4}]}{2(1 + \gamma_1\gamma_2)} \tag{32}$$

Figure 14 shows the parametric evolution of the poles $\mathscr{E}$ for a pumping path (see left inset) analogous to the previous discussion: an initial increase of γ_1 until the lasing threshold is reached, followed by an increase of γ_2. As before, during the second section of the path the system is first driven back towards stability (lasing death) while later on returning to instability at a second lasing threshold. It should be noted that the pumping path within the shaded region of Fig. 14 has to be excluded from the analysis. Here, the poles have $\mathscr{R}e(\mathscr{E}) > 2$ and the scattering modes fall outside of the propagation band $E(k) = 2\cos(k)$ of the leads.

The generality of the lasing death phenomenon calls for a universal formulation for its explanation. Using standard methods [49] we write the scattering matrix elements in the form [38, 51]

$$S_{\alpha,\beta}(E) = \delta_{\alpha,\beta} - i\sqrt{4 - E^2}\, \mathscr{W}_{\alpha}^{T} (E - \mathscr{H}_{\text{eff}})^{-1} \mathscr{W}_{\beta}\,, \tag{33}$$

where $\alpha, \beta = 1, 2$ and $\mathscr{H}_{\text{eff}}$ is a 2×2 effective non-hermitian Hamiltonian given by

$$\mathscr{H}_{\text{eff}}(E) = H_d + \Sigma(E) \sum_{\alpha} \mathscr{W}_{\alpha} \bigotimes \mathscr{W}_{\alpha}^{T} \tag{34}$$

The two-dimensional vectors $\mathscr{W}_1 = \delta_{\alpha,1}$ and $\mathscr{W}_2 = \delta_{\alpha,2}$ describe at which site we couple the leads with our sample while $\Sigma(E) = \frac{E - i\sqrt{4-E^2}}{2}$ is the so-called self-energy.

The poles of the S-matrix are equal to the complex zeros $\mathscr{E}$ of the following secular equation

$$\det[\mathscr{E} - H_{\text{eff}}(\mathscr{E})] = 0. \tag{35}$$

Solving Eq. (35) is (in general) a difficult task. However, there are circumstances such as the RLC circuit previously discussed, for which one can neglect the dependence of H_{eff} on energy. In such cases the second term in Eq. (34) results in a simple constant shift of the on-site potential of the Hamiltonian H_d.

Results from the experimental electronic version is shown in Fig. 15. In order to make contact with saturable laser dynamics and insure graceful behavior above threshold, a simple conductance nonlinearity was included in the form of parallel of back-to-back diodes in parallel with each of the LRC resonators in the basic dimer. This forces a dominant positive conductance (loss) at high voltage amplitudes, and assures a well behaved limit cycle when the system is unstable, above any oscillation threshold. The linear regime occurs for voltages below approximately 150 mV, where the diodes have negligible conductance.

In the electronic circuit, the equivalent of both "pumping" and output coupling are achieved simply as a re-interpretation of the resistances R_1 and R_2 of Fig. 1: a transmission line output equivalently modifies the resistance of the attachment node by its characteristic impedance in parallel, and pumping similarly is equivalent to a parallel negative conductance. Thus, effective combinations of leads and pumping determine particular paths through the γ_{gain} γ_{loss} parameter map of Fig. 5. These paths are shown on the insets of Fig. 15. The curves in the main portion of Fig. 15a show the corresponding RMS voltage amplitudes vs. the gain, which fall to zero during the stable (lasing death) values for gain, and grow to a level determined by the saturation dynamics otherwise.

In all cases the total gain $\gamma_1 + \gamma_2$ provided to the system is increased. It is seen that depending on the value of γ_1 the system either undergoes a transition from instability to stability or it remains unstable all the time. The former case corresponds to the phenomenon of lasing death found numerically in Ref. [44] and is achieved only for the leftmost three pumping paths shown in the inset of Fig. 15a.

To understand which pumping paths can result in lasing death we see that the paths are associated with the existence of reentrant stability domains in the (γ_1, γ_2) plane of Fig. 5 which are traversed by the specific pumping schemes. In this respect,

every time that a path crosses a boundary between an unstable to stable domain we have a suppression of lasing action and thus the emergence of lasing death.

Figure 15b shows the evolution of experimental values for $\mathcal{I}m(\omega)$ as a function of total gain, defined as $\gamma_1 + \gamma_2$ obtained along the path in the (γ_1, γ_2) stability map shown in the inset. The color scheme used is the same as that of Fig. 15a. Experimental frequencies were obtained by imposing a momentary $V = 0$ on both sides of the dimer and then recording the subsequent transients to obtain the most positive imaginary part of the of the two eigenfrequencies. The comparison to theory is also shown.

4.3 Two Lead Case

We return to the linear two-lead scattering and describe the additional consequences of a transmission channel, as shown in the inset of Fig 16. This system has also been analytically and experimentally studied and reveal generalized conservation relations. Specifically, for 1D geometries, it was found [6, 11, 45, 47] that while the reflectances for left (gain) and right (loss) incident waves might be different (as in the single-port case), the corresponding transmittances must be the same, i.e. $T_{gain} = T_{loss} = T$. Moreover, the following conservation relation was shown to hold [11]:

$$\sqrt{R_{gain} R_{loss}} = |T - 1| \tag{36}$$

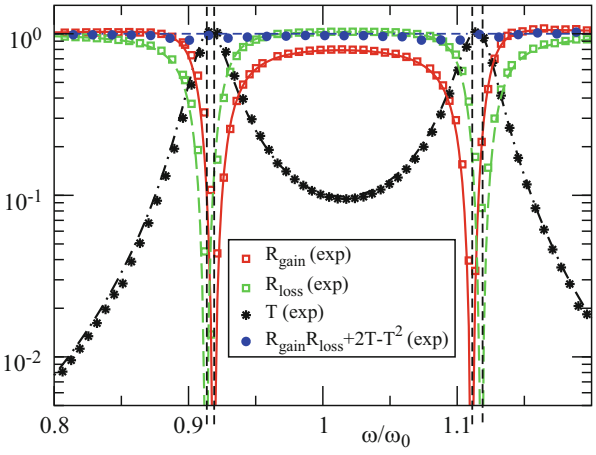

Fig. 16 Measurements (symbols) and numerics (lines of corresponding color) of T, $R_{L/R}$ for the two-port scattering set-up. The vertical black dashed lines indicate the frequencies where unidirectional transparency occurs. The conservation relation Eq. (36) is also evaluated using the experimental data. The horizontal dashed blue line is drawn for the eye and indicates the value 1. The parameter used for the $\mathcal{PT}$-symmetric dimer are $\gamma = 0.188875$, $\mu = 0.29$ and $\eta = 0.0305$. (After Ref. [46])

Note that Eq. (36) is an intriguing generalization of the more familiar conservation relation $R + T = 1$, which applies to unitary processes. In the $\mathscr{P}\mathscr{T}$-symmetric case, the geometric mean of the two reflectances, $\sqrt{R_{gain}R_{loss}}$, replaces the single reflectance R .[2]

Measurements for $R_{gain/loss}$ and T are shown in Fig. 16. The quantity $R_{gain}R_{loss} + 2T - T^2$ (blue circles) is evaluated from the experimental data and it is found to be 1 as it is expected from Eq. (36). An interesting result of the analysis is that at specific $\omega-$values (marked with vertical dashed lines), the transmittance becomes $T = 1$, while at the same time one of the reflectances vanishes. Hence, the scattering for this direction of incidence is flux conserving and the structure is *unidirectionally transparent*. It is interesting to note that a periodic repetition of such a $\mathscr{P}\mathscr{T}$-symmetric unit it will result in the creation of unidirectionally transparent frequency bands. This phenomenon was first predicted in [45] and its generalization was discussed in [11].

Figure 17 illustrates another interesting feature of two-port $\mathscr{P}\mathscr{T}$-symmetric scattering, a so-called simultaneous coherent perfect absorber-amplifier, or CPA-laser [47]. This functionality was first implemented [66] in the capacitively coupled version of the electronic dimer scatterer shown in the inset of Fig. 17a. With $\mu = 0$, Kirchhoff's laws in terms of the traveling wave components in the leads can be recast into a transfer matrix giving the gain-side wave components from the loss-side components:

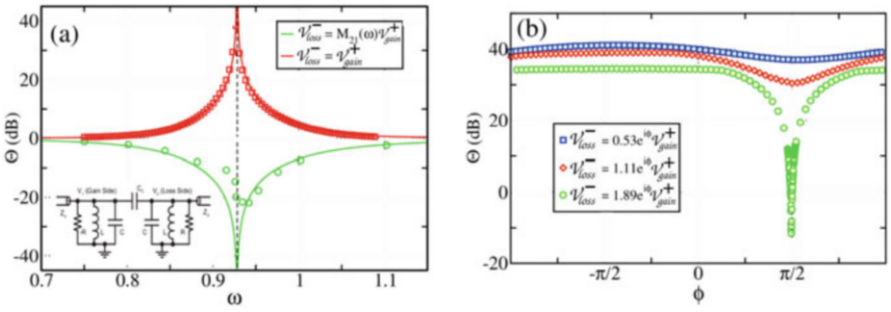

Fig. 17 (**a**) The overall output coefficient $\Theta(\omega)$ versus frequency ω near the amplification/attenuation frequency ω_J (vertical dashed line). The $\mathscr{P}\mathscr{T}$-symmetric electronic circuit is coupled to two ports and has $\eta = 0.110$, $\gamma = 0.186$ and $c = 0.161$. At $\omega = \omega_J$, the system acts as a perfect absorber when the input signal satisfies the coherent attenuation relation $V_R^- = \mathscr{M}_{21}(\omega)V_L^+$. For any other incident signal (e.g. see the blue line corresponding to $V_R^- = V_L^+$) the system acts as an amplifier. The dots are experimental values while the lines are numerical results. (**b**) Plots of experimental $\Theta(\omega_J)$ versus the relative phase ϕ of the signal entering the structure from the lossy node. Various curves correspond to different excitation amplitudes. Note the extremely sharp dependence at the Janus condition. (After Ref. [66])

[2]Equation (25) is a special case of Eq. (36) once it is recognized that in the single port case, the transmittance $T = 0$.

$$\begin{pmatrix} V_{loss}^{+} \\ V_{loss}^{-} \end{pmatrix} = \mathscr{M} \begin{pmatrix} V_{gain}^{+} \\ V_{gain}^{-} \end{pmatrix}; \quad \mathscr{M} = \frac{1}{2\omega c\eta} \begin{pmatrix} A + iB & iC \\ -iD & A - iB \end{pmatrix} \tag{37}$$

where the transfer matrix elements $\mathscr{M}$ are $A = 2\eta\Omega$, $B = \Omega^2 - \eta^2 - \omega^2 c^2 + \gamma^2$, $C = (\gamma - \eta)^2 + \Omega^2 - \omega^2 c^2$, and $D = (\gamma + \eta)^2 + \Omega^2 - \omega^2 c^2$, with $\Omega = \omega(1+c) - 1/\omega$. The transmission and reflection coefficients for gain-side, or loss-side incidence can now be expressed in terms of the transfer matrix elements as [6, 55]

$$t_{gain} = t_{loss} \equiv t = \frac{1}{\mathscr{M}_{22}}, \quad r_{gain} = -\frac{\mathscr{M}_{21}}{\mathscr{M}_{22}}, \quad r_{loss} = \frac{\mathscr{M}_{12}}{\mathscr{M}_{22}} \tag{38}$$

where we have used the identity that $\det(\mathscr{M}) = 1$. Note that these relations result in the conservation relation stated earlier for the inductively coupled case, Eq. 36, illustrating the independence of these results from the form of the internal dimer coupling.

Using an equivalent scattering matrix language [66] one can derive conditions allowing the $\mathscr{P}\mathscr{T}$-symmetric structure to act either as an amplifier or as a perfect absorber. For a laser oscillator without an injected signal, the boundary conditions $V_{gain}^{+} = V_{loss}^{-} = 0$. In contrast, for a perfect absorber the boundary conditions, $V_{gain}^{-} = V_{loss}^{+} = 0$, corresponding to zero reflected waves, hold. In general, the condition for an amplifier/laser system is not satisfied simultaneously with the condition for a perfect absorber. However for any $\mathscr{P}\mathscr{T}$-symmetric structure, one can show that at a real "Janus" frequency $\omega = \omega_J$ the amplifier/laser condition exists simultaneously with the absorber condition satisfied by $\mathscr{M}_{22}(\omega_J) = \mathscr{M}_{11}(\omega_J) = 0$ along with the incident wave condition $V_{loss}^{-} = \mathscr{M}_{21}(\omega) V_{gain}^{+}$. Hence the two-port $\mathscr{P}\mathscr{T}$-symmetric dimer can behave simultaneously as a perfect absorber and as an amplifier. This property can be explored using an overall output coefficient Θ defined as [47]

$$\Theta = \frac{|V_{loss}^{+}|^2 + |V_{gain}^{-}|^2}{|V_{gain}^{+}|^2 + |V_{loss}^{-}|^2} \tag{39}$$

Note that in the case of a single-port scattering set-up discussed earlier, the Θ-function collapses to the left/right reflectances. The Θ-function (Eq. 39) can be re-expressed directly in terms of the incident wave amplitudes and the transfer matrix elements giving

$$\Theta(\omega) = \frac{|\frac{V_{loss}^{-}}{V_{gain}^{+}} \mathscr{M}_{12}(\omega) + 1|^2 + |\frac{V_{loss}^{-}}{V_{gain}^{+}} - \mathscr{M}_{21}(\omega)|^2}{(1 + \frac{|V_{loss}^{-}|^2}{|V_{gain}^{+}|^2})|\mathscr{M}_{22}(\omega)|^2}. \tag{40}$$

At the singularity frequency $\omega = \omega_J$ and for a generic ratio V^-_{loss}/V^+_{gain}, the $\Theta(\omega)$-function diverges as $\omega \to \omega_J$ and the circuit acts as an amplifier/laser. If on the other hand, if the perfect absorption condition $V^-_{loss} = \mathscr{M}_{21}(\omega)V^+_{gain}$ is applied, we get $\Theta(\omega_J) = 0$.

In the context of the actual electronic circuit (Fig. 17a inset), the two port simultaneous laser/absorber presents a delicate balance of the driven, marginally stable circuit. The singular behavior of the theoretical Θ in Fig. 17a, solid curves, illustrate that at the Janus frequency ω_J the injected signals can result in either amplification or complete attenuation, depending on the relative amplitude and phase of the injected signals. The perfect absorption condition is particularly sensitive to the injection parameters: the deviation of the experimental data, Fig. 17a dots, is characteristic of component imbalance of less than 1%. In fact, the minimally absorbing experimental points near the dip in the attenuation curve of Fig. 17a can only be obtained by an independent determination of the minimal reflectance condition at each frequency. Figure 17b shows this extreme sensitivity to the phase of the right input signal near ω_J and illustrates practical limits to the achievement of the CPAA condition.

4.4 $M\mathscr{T}$ Symmetry, Two-Port Circuit, Stripline Structure

We now turn to discussion of systems which incorporate gyration in order to achieve highly directional transmission. Since a one-dimensional linear transmission structure – including gyration – is only capable of a direction dependent phase shift, in addition to the gyration, there are two other requirements for linear, directional transmission: (1) there must be at least two parallel paths, introducing the possibility of (even perfect) interference, and (2) there must be a dissipative component within the structure to avoid complete impedance mismatch as the signal splits and recombines within the scattering system. $\mathscr{P}\mathscr{T}$-symmetric scattering systems provide, through the gain/loss parameter, another engineering tool to help achieve these conditions.

$\mathscr{P}\mathscr{T}$ symmetry have been generalized to include systems with generic gyrotropy such as biased magnetic structures [70]. Here, the symmetry operations have been more carefully accounted for by introducing the notion of $M\mathscr{T}$ symmetry to include a mirroring operation appropriate for the dynamical chirality. The parity in this case is extended through the mirroring operation that preserves an antilinear mirror-time reversal symmetry. The linear mirror-symmetry operator $\mathscr{M}$ performs a reflection $(x, y, z) \to (-x, y, z)$ with respect to the mirror yz-plane at $x = 0$ and reverses the direction of the magnetic field $\mathbf{H}_0 \to -\mathbf{H}_0$. The antilinear time-reversal operator $\mathscr{T}$, performs a complex conjugation $i \to -i$ together with an inversion of the direction of the magnetic vectors i.e. $\mathbf{H}_0 \to -\mathbf{H}_0$. For the generic gyrator of Fig. 2a, both the mirror operation and the time reversal operation applied to this device change

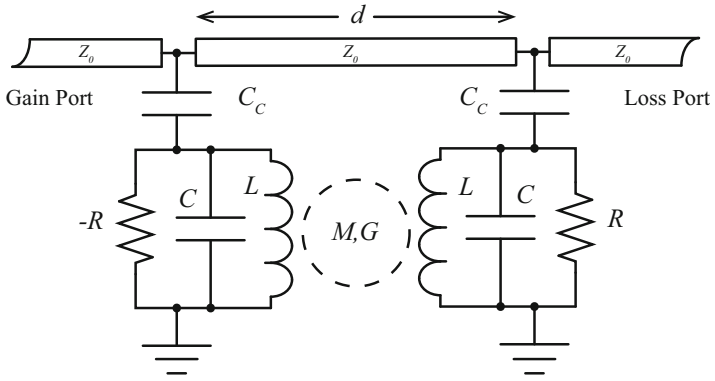

Fig. 18 Equivalent electronic circuit. The full circuit show in (**a**) has reduces the stripline resonators to a lumped equivalent RLC pair with mutual coupling that includes both inductive and gyrotropic components. The transmission line coupling is reduced to single capacitances spaced at d along the ideal TEM transmission lines. The isolated resonator pair is then further reduced to its equivalent conductance matrix, G_{dimer}, shown in (**b**)

the sign of the gyration conductance G in Eq. 1. As before, in the specific case of gain and loss elements, the complex conjugation operation is also equivalent to the exchange of the gain and loss.

Once again, we return to an electronic circuit analog that maintains the essence of the desired physics while also allowing a significantly simplified path toward both analytic and numeric analysis. Figure 18 shows an $M\mathscr{T}$-symmetric lumped element dimer circuit coupled in parallel with a TEM mode transmission line. The dimer is internally coupled with a parallel combination of mutual inductance and gyration. Since the mutual inductance and the gyrator are both pure transconductances – i.e., the current on the left of Fig. 2a depend only on the voltage on the right – Kirchhoff's laws given in Eqs. 2 and 3 for the two-port dimer of Fig. 1a, can immediately be incorporated as effective inductor currents defined through

$$\begin{pmatrix} I_1 \\ I_2 \end{pmatrix} = \frac{1}{i\omega} \begin{bmatrix} L & M \\ M & L \end{bmatrix}^{-1} \begin{pmatrix} V_1 \\ V_2 \end{pmatrix} + \begin{bmatrix} 0 & G \\ -G & 0 \end{bmatrix} \begin{pmatrix} V_1 \\ V_2 \end{pmatrix}. \tag{41}$$

The gain and loss are implemented by negative and positive parallel resistances, which could be of slightly different magnitude to include the small inherent loss discussed earlier.

In the frequency domain, Kirchoff's Laws for this circuit are easily expressed, though transcendental due to the trigonometric wave components in the transmission line section. All seven elements of the circuit (L, C, R_1, R_2, M, G, C_c, and d) represent essential features of the original structure that can contribute to the enhancement of the transmission nonreciprocity. Note that in this circuit, C_c is the individual resonator coupling to points on the transmission line and that the diagonal terms in Eq. 41 are the only means of direct coupling.

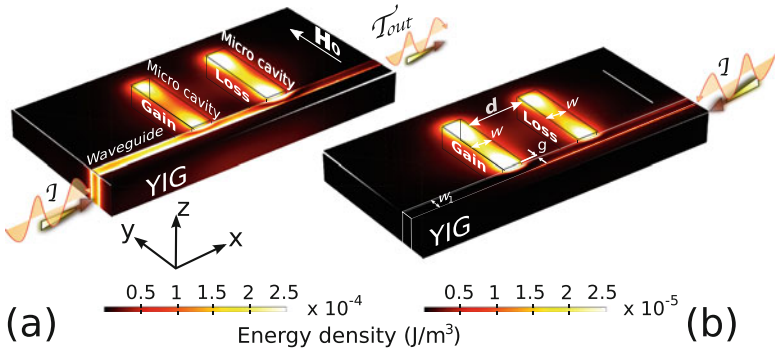

Fig. 19 The microwave structure that we have studied consists of two half-wave microstrip resonators which are end-coupled to a bus waveguide. The substrate consists of YIG which is exposed to an external bias field H_0 along the y-direction. A balanced gain/loss is distributed uniformly beneath each of the two resonators. When the gain/loss parameter γ aquires a specific value (close to $\gamma_{\mathscr{P}\mathscr{T}}$) the transmittance in the forward direction (**a**) is approximately unity while it becomes almost zero in the backward direction (**b**). (After Ref. [70])

Noting that the gyration G plays a similar role as a static magnetic field H_0 in a gyrotropic substrate [42], this circuit was specifically considered to serve as an electronic analog of the model structure shown in Fig. 19 consisting of a pair of half-wave microwave strip-line resonators forming the dimer, in close proximity to a perpendicular bus transmission line passing by their ends. The substrate is a ferrite such as Yttrium Iron Garnet, with a ground plane on the lower surface. A static magnetic field parallel to the resonator axis ($\mathbf{H_0}$ in Fig. 19) lends a gyration component to the inter-resonator proximity coupling, and the end-coupling of the resonators to the bus transmission line completes a second signal path between the resonators.

In the model structure, gain and loss are confined to the spatial domain beneath each of the microstrip resonators and implemented by introducing an imaginary part to the permittivity defined as $\epsilon = \epsilon_r \epsilon_0 (1 \pm i\gamma)$, where γ assumes the role of the gain and loss parameter. The structure was targeted for approximately 1.3 GHz and a 56 Ω port impedance.

Analysis of the transmission properties of this two-port set-up is straightforward based on the scattering parameters returned by the simulation software. To quantify the dependence of the non-reciprocal effect on various system parameters, a nonreciprocity strength NR (here expressed dB) is defined as

$$NR(\gamma) = 10 \times \max_{\omega} \left\{ \left| \log_{10} \frac{T_B}{T_F} \right| \right\}, \tag{42}$$

where T_F and T_B are the transmittances obtained for the forward (gain-to-loss) or backward (loss-to-gain) respective cases. Both the numerical investigations of this system and the electronic analog indicate that the maximum values of NR are

achieved in the proximity of the symmetric mode resonant frequency ω_s, so this mode will be the focus of our subsequent discussion.

A theoretical analysis of the function $NR(\gamma)$ can be understood within the framework of temporal coupled-mode theory. The calculation scheme breaks down the effect of the magnetic field (gyration) into two parts. First, the effect to the resonant frequency of the individual resonators separately (for $\gamma = 0$) in a magnetic substrate is separately considered. Next, the effect of gain and loss γ in each of these resonances, now considered as a two level system and coupled via a non-magnetic substrate with a coupling constant Ω_0 (evaluated with $H_0 = 0$) is added.The resulting symmetric $\omega_s^{(0)}$ and antisymmetric $\omega_a^{(0)}$ resonant modes of the isolated composite structure are then:

$$\omega_{s/a}^{(0)} = \omega_0 \mp \sqrt{\Omega_0^2 - (\rho\gamma)^2} \tag{43}$$

where ρ is a scaling parameter. All parameters, including the exceptional point position $\gamma_{M\mathscr{T}}^0 = \Omega_0/\rho$ are extracted from the simulation analysis of the set-up of Fig. 19.

The second part of our analysis considers the consequences of the magnetic field (gyration) in the coupling between $\omega_{s/a}^{(0)}$. Specifically, the resonances $(\omega_{s/a}^{(0)})$ are coupled via the magnetized substrate between the two microstrip cavities and indirectly via the presence of the bus wave-fields. In general, this additional coupling constant λ is a function of the geometric properties of the two stripline resonators, the applied magnetic field, H_0, and the wavenumber k_x of the bus field. Based on symmetry considerations [70] it is assumed that up to a linear approximation, $\lambda = \lambda_0 + \imath\,(b_0 k_x + c_0 H_0)$ where λ_0, b_0, c_0 are real parameters. When an incident electromagnetic radiation with frequency ω in the vicinity of one of these two resonances enters the bus waveguide, in either direction, it will primarily excite the closer mode in frequency without being (to a good approximation) affected by the presence of the other resonance. Again, it is assumed that $\omega \approx \omega_s$, where maximum non-reciprocity is observed, and that the incident wave is coupled directly only with the symmetric mode.

Under these assumptions, the temporal evolution of the symmetric (a_s) and antisymmetric (a_a) modal amplitudes is described by the following equations

$$\begin{aligned}
\frac{\mathrm{d}a_s}{dt} &= \imath\omega_s^{(0)} a_s - \frac{1}{\tau} a_s - \lambda^* a_a + \kappa_1 S_1^{in} + \kappa_2 S_2^{in} \\
\frac{\mathrm{d}a_a}{dt} &= \imath\omega_a^{(0)} a_a + \lambda a_s \\
S_-^{out} &= S_2^{in} - \kappa_2^* a_s; \quad S_+^{out} = S_1^{in} - \kappa_1^* a_s
\end{aligned} \tag{44}$$

where $\frac{1}{\tau} = \frac{1}{\tau_-} + \frac{1}{\tau_+}$ is the radiative coupling of the symmetric mode to a left-going $(\frac{1}{\tau_-})$ or a right-going $(\frac{1}{\tau_+})$ output wave, and $\{\kappa_1, \kappa_2\}$ indicate the coupling constants between the symmetric mode and the incoming or outgoing waves. We have that

$|\kappa_1|^2 = \frac{2}{\tau_+}$ and $|\kappa_2|^2 = \frac{2}{\tau_-}$. The modal amplitudes are normalized in such a way that $|a_s|^2$ ($|a_a|^2$) correspond to the energy stored at the specific mode, while $\left|S_1^{in}\right|^2$ and $\left|S_2^{in}\right|^2$ ($\left|S_-^{out}\right|^2$ and $\left|S_+^{out}\right|^2$) are the powers carried by incoming (outgoing) waves from (to) two different directions of the bus waveguide.

The forward $T_F \equiv \frac{|S_+^{out}|^2}{|S_1^{in}|^2}$ and backward $T_B \equiv \frac{|S_-^{out}|^2}{|S_2^{in}|^2}$ transmittance for a left $S_1^{in} \propto e^{t\omega t}$ and right $S_2^{in} \propto e^{t\omega t}$ incident monochromatic field can be calculated from Eq. (44) by imposing the appropriate boundary conditions $S_2^{in} = 0$ and $S_1^{in} = 0$ respectively. We obtain that

$$T_{\mathrm{F/B}}(\omega) = \left| \frac{i\left(\omega - \omega_s^{(0)} - \frac{|\lambda_{\mathrm{F/B}}|^2}{(\omega-\omega_a^{(0)})}\right) \mp \Delta\epsilon}{i\left(\omega - \omega_s^{(0)} - \frac{|\lambda_{\mathrm{F/B}}|^2}{\left(\omega-\omega_a^{(0)}\right)}\right) + \left(\frac{1}{\tau}\right)} \right|^2 \tag{45}$$

where $\Delta\varepsilon = \frac{1}{\tau_+} - \frac{1}{\tau_-} \neq 0$ due to gyrotropy and $\lambda_{F/B}$ is the coupling between $\omega_s^{(0)}$ and $\omega_a^{(0)}$ for forward and backward propagation.

These theoretical results compare nicely with the COMSOL simulations as shown in Fig. 20 in the domain of $\omega \approx \omega_s^B$. A non-linear least square fit has been used in order to fit Eq. (45) to the data for T_{B}. The parameters that we have obtained are $\Delta\epsilon \approx -0.0075$, $\frac{1}{\tau} \approx 0.05215$, $\eta \approx 4.9 \times 10^{-3}$ (all measured in nsec^{-1}) and $|\lambda_B|^2 \approx 0.111\ \mathrm{nsec}^{-2}$. All these parameters, apart from $|\lambda_F|^2$, have been kept fixed for the forward transmission T_F, see Eq. (45). The fitting value of T_F indicated that $|\lambda_F|^2 \approx |\lambda_B|^2\ \mathrm{nsec}^{-2}$. Finally, using Eq. (45) together with Eq. (42) we have calculated NR versus γ. These theoretical results are shown in Fig. 20 together with the simulations of COMSOL. Note particularly that the sharp maximum in $NR(\gamma)$ occurs just below the exceptional point at $\gamma_{M\mathscr{T}}$. The physics of this offset will be discussed later.

In order to enhance our understanding of the origin of the giant nonreciprocal effect we have further approximated NR at $\omega = \omega_s^B$. Guided by the numerics, which indicates that $T_F(\omega_s^B) \sim \mathscr{O}(1)$ in this frequency domain, we have assumed that $\log_{10} T_{\mathrm{F}}\left(\omega_s^{\mathrm{B}}\right)$ is negligible when compared to $\log_{10} T_{\mathrm{B}}\left(\omega_s^{\mathrm{B}}\right)$. Therefore $NR(\gamma) \approx 10|\log_{10} T_B(\omega_s^{\mathrm{B}})|$. This approximation leads us to the following expression up to leading order in η, $\Delta\epsilon$ and $\epsilon \equiv 1/(2\tau)$:

$$\mathrm{NR} = \begin{cases} 20\log_{10}\frac{1+\frac{\varepsilon}{\eta}\left(1+\frac{\sqrt{\beta}}{\sqrt{1+\beta}}\right)}{1+\frac{\Delta\varepsilon}{2\eta}\left(1+\frac{\sqrt{\beta}}{\sqrt{1+\beta}}\right)}; & 0 < \gamma < \gamma_{M\mathscr{T}}^0 \\ 10\log_{10}\frac{(\eta+\varepsilon)^2+\beta\eta(\eta+2\varepsilon)}{(\eta+\Delta\varepsilon/2)^2+\beta\eta(\eta+\Delta\varepsilon)}; & \gamma_{M\mathscr{T}}^0 < \gamma < \gamma_{M\mathscr{T}} \end{cases} \tag{46}$$

where $\beta \equiv \frac{\Omega_0^2-(\rho\gamma)^2}{|\lambda_{\mathrm{B}}|^2}$.

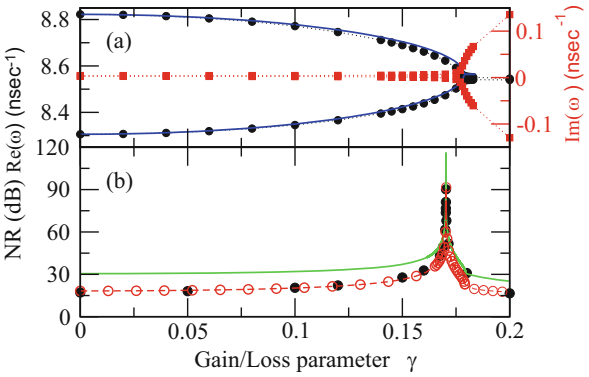

Fig. 20 (**a**) The parametric evolution of resonant modes ($\mathscr{R}e(\omega)$, •/$\mathscr{I}m(\omega)$, ■) vs. the gain/loss parameter γ for the set-up of Fig. 19 with $H_0 = 0$ only in the domain between the two micro-cavities (simulations). A fitting with the theoretical expression Eq. (43) (solid line) gives $\omega_0 \approx 8.545$, $\Omega_0 \approx 0.2576$ and $\rho \approx 1.445$ (all measured in nsec^{-1}) corresponding to $\gamma^0_{\mathscr{PT}} \approx 0.178$. (**b**) Non-reciprocity (NR) obtained by calculating the difference between the FWD and BWD transmittance T from the simulations (•) and from the theoretical expressions Eqs. (45) (○). The green line is the approximated expression for NR, see Eq. (46). (After Ref. [70])

A further analysis of Eq. (46), indicates that when $\frac{\Delta\varepsilon}{2\eta} < \min\left\{-\frac{\Omega}{\Omega_0+\Omega}, -\frac{\varepsilon}{2\varepsilon+\eta}\right\}$, then $NR(\gamma)$ has a single maximum in the exact phase i.e. $0 \le \gamma \le \gamma_{M\mathscr{T}}(H_0)$ which occur at some critical value $\gamma = \gamma_{\rm NR}$. In case $\frac{\Delta\varepsilon}{2\eta} < -1$, we have $\gamma_{\rm NR} = \gamma^0_{M\mathscr{T}}$ while for $-1 < \frac{\Delta\varepsilon}{2\eta} < \min\left\{-\frac{\Omega}{\Omega_0+\Omega}, -\frac{\varepsilon}{2\varepsilon+\eta}\right\}$ we have $\gamma_{\rm NR} = \sqrt{(\gamma^0_{M\mathscr{T}})^2 - \frac{|\lambda_B/\rho|^2}{\left(\frac{\Delta\varepsilon}{2\eta}/\left(1+\frac{\Delta\varepsilon}{2\eta}\right)\right)^2-1}}$. Thus we conclude that the existence and position of the NR is strongly dictated by $\gamma^0_{M\mathscr{T}}$ and $|\lambda_B|^2$, i.e., this giant non-reciprocal behavior is a consequence of an interplay between the EP degeneracy and the interaction of fields within the gyrotropic substrate.

The parameter space affecting the position and strength of the nonreciprocal transmission, as described by $NR\,(\gamma)$, is best explored with the parameters of the lumped electronic system of Fig. 18 where Kirchhoff's laws, transcendental as they are with the central transmission line segment, can be solved significantly more efficiently than a 3D model simulation.

Figures 21 and 22 illustrate numerical results exploring the NR with gain/loss and gyration strengths, $\gamma = \frac{1}{2}(R_1^{-1} + R_2^{-1})\sqrt{L/C}$ and $g = G\sqrt{L/C}$ respectively, to a detail that is not only computationally expensive in the COMSOL simulation, but somewhat abstract in the theoretical analysis. The NR density plot shown in Fig. 21 is separated into two regions by the black solid line representing the position of the isolated system exceptional point, with the exact $M\mathscr{T}$ phase above and the broken phase below. The singular NR is seen as the bright swath *within the unbroken region* just above. Figure 22b, below) shows cuts of the NR at several fixed values of the gyration strength g along with the corresponding isolated dimer eigenfrequencies

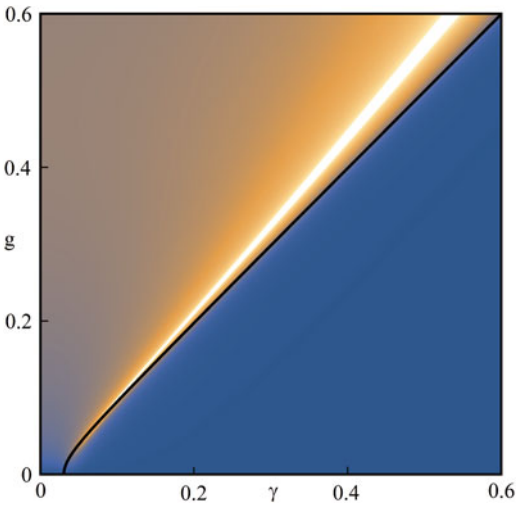

Fig. 21 A density plot of the non-reciprocity NR versus the gain/loss $\gamma = \frac{1}{2}(R_1^{-1} + R_2^{-1})\sqrt{L/C}$ and gyration strength $g = G\sqrt{L/C}$ associated with the lumped circuit shown in Fig. 18. (After Ref. [70])

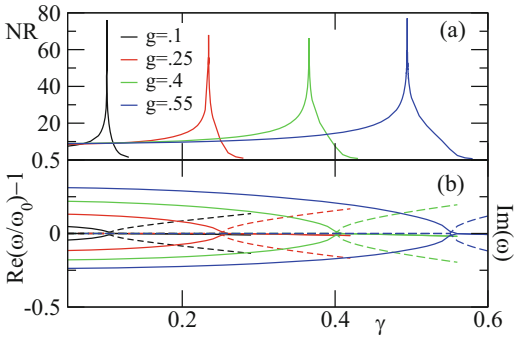

Fig. 22 (**a**) The non-reciprocity for the circuit of Fig. 18 for several gyration strengths g versus the gaon/loss parameter γ. The parameters used are $Z_0\sqrt{C/L} = 0.82$, $kd \approx \pi$ at the LC resonant frequency, $C_c/C = 0.3$, $M/L = 0.03$, and $\eta = \frac{1}{2}(R_2^{-1} - R_1^{-1})\sqrt{L/C} = 0.03$ for the intrinsic loss. (**b**) The real and imaginary parts of the balanced, isolated ($\eta = C_c = 0$) dimer mode frequencies versus the gain/loss parameter. All other values of the circuit are the same as in (**a**). An one-to-one relation between the exceptional points and the singularities of the giant non-reciprocity is evident. The solid line through the NR density plot shows the position of the isolated system exceptional point, slightly beyond the singularity. (After Ref. [70])

(a, above). Note again that the maximum NR occurs below the isolated exceptional points. The similarities with Fig. 4 associated with the photonic structure is striking, thus indicating the shared NR mechanism. Specifically for $\gamma = 0$ we again observe a moderate non-reciprocal behavior which is dramatically enhanced at γ-values close to $\gamma_{M\mathcal{T}}$. This can be better appreciated by analyzing the parametric evolution of the eigenfrequencies of the isolated circuit. The isolated system in this electronic analog includes all of the effects of the resonator coupling, such as the gyration, fulfilling the inequality expressed in Eq. 46.

This universal nature of the giant non-reciprocal response near the EP calls for an intuitive explanation. First we have to realize that the structure constitutes an effective ring since the two cavities are directly coupled to one-another while at the same time they are coupled indirectly via the bus waveguide. At the EP the two supermodes of the effective ring structure are degenerate having a definite chirality [70]. The presence of the magnetic field breaks the spectral degeneracy, while weakly preserving the (common) chiral nature of the modes. As a result the two modes are coupled differently with a left and a right incident wave. Assuming, for example, that the chirality of the modes is clockwise (CW) we conclude that due to phase matching such a mode will be coupled only to a left incident wave but not to a right incident one. Accordingly, the left incident wave will excite the CW supermode while at the same time can exploit a direct optical path associated with a transmission via a direct process between the incident and transmitted channels. These optical paths can interfere destructively at the output channel (depending on the propagation phase associated with the length of the bus waveguide and the gyrotropy) leading to a Fano effect and consequently to a (near) zero transmittance. An important condition here is that the internal losses of the cavities are small so that the two interfering waves have the same amplitudes. On the other hand, a right incident wave, because of phase mismatch, does not couple to the CW chiral supermode of the effective ring. As a result it does not experience the internal losses inside the cavity and consequently the (direct) transmission is high.

It is now clear why the non-reciprocity could be enhanced by the $M\mathscr{T}$ symmetric behavior. As the gain/loss parameter γ progresses toward the exceptional point, $\gamma_{M\mathscr{T}}$, both the frequencies of the modes and their phases coalesce. The novel eigenfrequency and eigenmode behavior present in these systems introducing new parameter distinctly capable of tuning the device in unusual ways to enable the gyrotropic coupling.

We now examine a system demonstrating a related nonreciprocal lasing phenomenon [39], experimentally explored in a different radio-frequency domain $M\mathscr{T}$-symmetric RLC circuit without the need for transmission line coupling. The basis is a generic lasing cavity system shown in Fig. 23a consists of a gyrotropic element sandwiched between two active elements, one with gain and the other one with an equal amount of loss. The total structure is invariant under the generalized $M\mathscr{T}$-symmetry which enforces a new set conservation relations, analogous to Eq. 36 discussed earlier, but now modified by the gyration. Under these conditions one can get unidirectional amplification which can turn to lasing at a critical value of the gain/loss parameter. Furthermore, we show that reversing the gain/loss switches the direction of lasing thus achieving a reconfigurable lasing action. The applicability of these ideas was demonstrated using the $M\mathscr{T}$-symmetric RLC circuit shown in Fig. 23b. Elimination of the transmission line coupling, fundamentally serving both as a parallel path and an impedance matching element, is replaced in the electronic circuit analog by the gyrotropically coupled *pairs* of resonators. It also has the advantage of removing the transcendental relations introduced by a transmission line. To our knowledge, this was the first experimental demonstration of a system that belongs in the $M\mathscr{T}$-symmetry class.

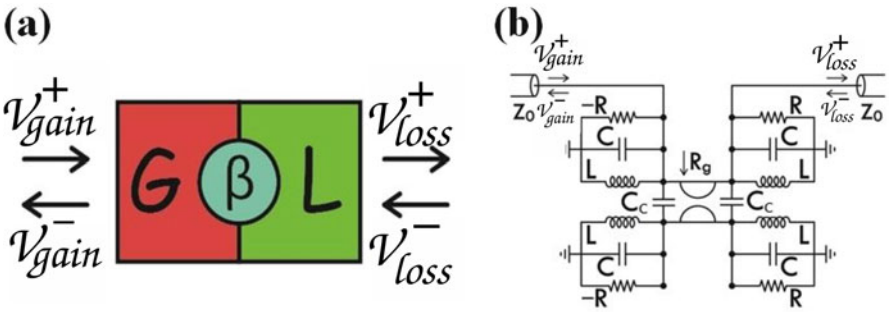

Fig. 23 (**a**) A sketch of a $M\mathscr{T}$ symmetric cavity consisting of a gain (G) and a loss (L) domains which are indicated by red and green respectively. The gyrotropic element is placed symmetrically between the gain and loss domains and it is indicated by β. (**b**) The equivalent $M\mathscr{T}$ -symmetric electronic circuit. R_g indicates the gyrator. (After Ref. [39])

For clarity of the presentation we concentrate on one-dimensional scattering setups which allows us to illuminate the basic principles without the unnecessary algebraic complications of higher dimensions. A conceptual visualization of a $M\mathscr{T}$-symmetric scattering setup is shown in Fig. 23a. The red area indicates a gain domain (G) while the green a balanced loss (L) element. The cyan area in the middle indicates the existence of a gyrotropic element. A monochromatic wave (with wavevector k) on the right of the scattering domain $V_R = V_R^+ \exp(ikx) + V_R^- \exp(-ikx)$ is related to the wave on the left of the scattering domain $V_L = V_L^+ \exp(ikx) + V_L^- \exp(-ikx)$ via the 2×2 transfer matrix $\mathscr{M}$,

$$\begin{pmatrix} V_R^+ \\ V_R^- \end{pmatrix} = \mathscr{M} \begin{pmatrix} V_L^+ \\ V_L^- \end{pmatrix}. \tag{47}$$

Note that this transfer matrix is different than the one used in Eq. 37 due to the different circuit details (compare the circuit of Fig. 23b with that in the inset of Fig. 17a). The transmission and reflection coefficients for left (L) and right (R) incident waves can be found using the boundary conditions $V_R^- = 0$ and $V_L^+ = 0$ respectively. These can be expressed in terms of the transfer matrix elements as follows

$$r_L = \frac{-\mathscr{M}_{21}}{\mathscr{M}_{22}}, t_L = \frac{\det \mathscr{M}}{\mathscr{M}_{22}}, t_R = \frac{1}{\mathscr{M}_{22}}, r_R = \frac{\mathscr{M}_{12}}{\mathscr{M}_{22}}. \tag{48}$$

The associated transmittances and reflectances are then defined as $T_{L/R} \equiv |t_{L/R}|^2$ and $R_{L/R} \equiv |r_{L/R}|^2$.

Next, we define the conditions at which a $M\mathscr{T}$-symmetric system behaves as a unidirectional laser. We request that the output field in one direction, say the left, be amplified while attenuated in the opposite direction. In terms of transmissions and reflections, the above condition reads as

$$r_L \to \infty; \qquad t_L \to 0; \qquad t_R \to \infty; \qquad r_R \to 0. \tag{49}$$

Equations (49) are written in terms of $\mathscr{M}$-matrix elements using Eq. (48). We get

$$\begin{aligned} &\mathscr{M}_{22}(\omega, \beta, \gamma) = 0 \quad \text{(lasing condition)} \\ &\mathscr{M}_{12}(\omega, \beta, \gamma) = 0 \quad \text{(unidirectionality condition)}. \end{aligned} \tag{50}$$

In this framework, the complex frequencies ω for which $\mathscr{M}_{22}(\omega, \beta, \gamma) = 0$, correspond to the poles of the scattering matrix. Due to flux conservation and causality relations they lie on the lower part of the complex plane when a parameter γ that controls the degree of gain/loss strength of the two active elements is equal to zero. As γ is increased, the poles move towards the real axis. Lasing action is achieved at a critical γ_{cr}, at which the first of these poles ω_{cr} crosses the real axis. If the second condition in Eq. (50) is also satisfied at ω_{cr}, we get $\det \mathscr{M} \to 0 \neq 1$ which characterizes non-reciprocal transport in $M\mathscr{T}$-symmetric systems (see Eqs. (48) and [61]).

Application of circuit laws at the transmission line contacts yields the following expressions for the current/voltages amplitudes in the transmission line leads:

$$\begin{aligned} &i[\gamma V_L - \beta(V_1 - V_2)] - \omega[V_L + \kappa(V_L - V_1)] + \frac{V_L}{\omega} = -i\eta Z_0 I_L \\ &i[\gamma V_R - \beta(V_1 - V_2)] + \omega[V_R + \kappa(V_R - V_2)] - \frac{V_R}{\omega} = -i\eta Z_0 I_R \\ &i[\gamma V_1 - \beta(V_L - V_R)] - \omega[V_1 - \kappa(V_L - V_1)] + \frac{V_1}{\omega} = 0 \\ &i[\gamma V_2 - \beta(V_L - V_R)] + \omega[V_2 - \kappa(V_R - V_2)] - \frac{V_2}{\omega} = 0 \end{aligned} \tag{51}$$

where ω is a dimensionless frequency in units of ω_0 and $\eta = \sqrt{L/C}/Z_0$ with Z_0 the impedance of the transmission line. Note that Eqs. (51) are invariant under combined $\mathscr{P}$ ($L \leftrightarrow R$, $1 \leftrightarrow 2$) and a modified $\tilde{\mathscr{T}}$ ($i \leftrightarrow -i$, $\beta \leftrightarrow -\beta$) reversal. The resulting $\mathscr{M}$-matrix takes the form

$$\mathscr{M} = \begin{pmatrix} (a + ib) & i(c - d) \\ i(c + d) & (a - ib) \end{pmatrix} / A. \tag{52}$$

where a, b, c, d, A are polynomials in ω and their exact form is given in [39].

As discussed previously, the condition $\det \mathscr{M} \to 0$ is a necessary (but not sufficient) condition for unidirectional lasing. Assuming constant coupling κ, we

get

$$\det \mathscr{M} = \frac{\beta(1-\omega^2(1+\kappa)) - \gamma\kappa\omega^2}{\beta(1-\omega^2(1+\kappa)) + \gamma\kappa\omega^2} = 0 \rightarrow \beta = \frac{\gamma\kappa\omega^2}{1-\omega^2(1+\kappa)}. \tag{53}$$

Next we find the set of $\omega_{\rm cr}, \gamma_{\rm cr}, \beta_{\rm cr},$ values for which $\mathscr{M}_{22}(\gamma_{\rm cr}, \beta_{\rm cr}, \omega_{\rm cr}) = 0$ and $\mathscr{M}_{12}(\gamma_{\rm cr}, \beta_{\rm cr}, \omega_{\rm cr}) = 0$ are simultaneously satisfied. The latter is achieved by substituting Eq. (53) in these two relations. In Fig. 24 we plot the evolution of complex zeros of $\mathscr{M}_{22}(\omega, \gamma; \beta = \beta_{\rm cr})$ as the gain/loss parameter γ increases and for a fixed value of the magnetic field $\beta_{\rm cr}$. At a critical value $\gamma = \gamma_{\rm cr}$ the first resonance crosses the real axes at $\omega = \omega_{\rm cr}$ and a unidirectional lasing is achieved.

We confirm the existence of a unidirectional lasing mode by introducing an overall left/right outgoing coefficient $\Theta_{L/R}(\omega, \gamma, \beta)$, defined as the ratio of the left/right outgoing field intensity to the total incident intensity:

$$\Theta_L = \frac{|V_L^-|^2}{|V_L^+|^2 + |V_R^-|^2}; \quad \Theta_R = \frac{|V_R^+|^2}{|V_L^+|^2 + |V_R^-|^2} \tag{54}$$

Whenever $\Theta_L \gg 1$ ($\Theta_R \gg 1$) while $\Theta_R \approx 0$ ($\Theta_L \approx 0$) a left (right) unidirectional laser has been achieved. At $\omega = \omega_{\rm cr}$, the outgoing coefficient $\Theta(\omega_{\rm cr})$ diverges, i.e. $\Theta_L \rightarrow \infty$ ($\Theta_R \rightarrow \infty$), signalling the transition to left (right) lasing action. Typical behavior of $\Theta_{L/R}$ near a left unidirectional lasing mode (associated with the parameter values of Fig. 24) is shown in the inset of Fig. 24. We see that around

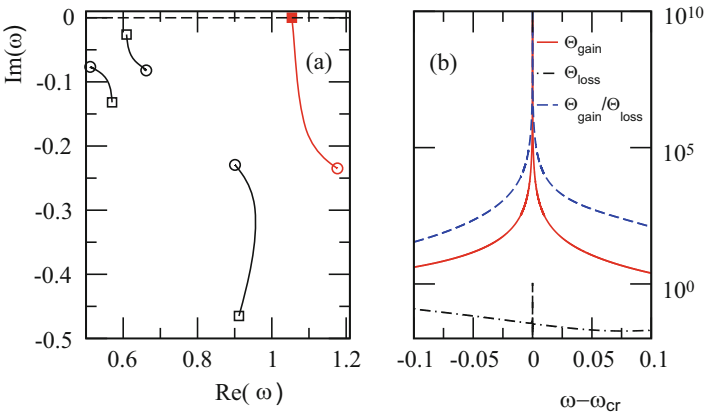

Fig. 24 (**a**) Evolution of resonances ω vs. γ. The starting point of the evolution is indicated with a circle and the ending point with a square. Different colors indicate different resonances. The parameters used are $\beta = \beta_{\rm cr} = -0.50609$, $k = 0.8$, and $\eta = 0.9$. The unidirectional lasing frequency (red square) is $\omega_{\rm cr} = 1.05394$ and it occurs at $\gamma_{\rm cr} = 0.56919$. (**b**) The overall left/right outgoing coefficient $\Theta_{\rm gain/loss}$. A divergence of $\Theta_{\rm gain}$ at $\omega_{\rm cr}$ indicates a left unidirectional lasing action. In the same subfigure we also report the ratio $\Theta_{\rm gain}/\Theta_{\rm loss}$. (After Ref. [39])

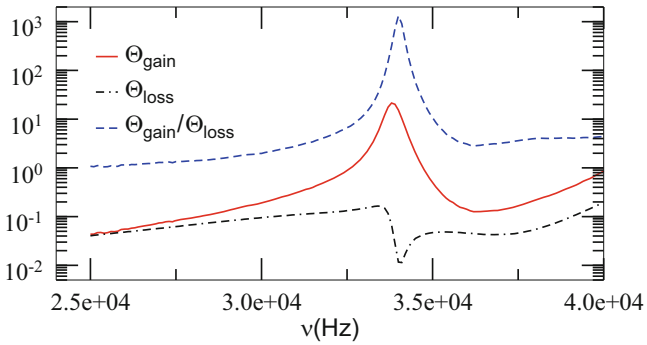

Fig. 25 Experimental results for the overall left/right outgoing coefficient $\Theta_{gain/loss}$. A divergence of Θ_{gain} (Θ_{loss}) at ω_{cr} signifies a left (right) unidirectional lasing action. For completeness we also report theratio $\Theta_{\text{gain}}/\Theta_{\text{loss}}$. The parameters used in the experiment are $L = 1.4\,\text{mH}$; $C = 10\,\text{nF}$; $C_c = 3\,\text{nF}$, $R = 2.7\,\text{kW}$, $Z_0 = 1:35\,\text{kW}$ and $R_g = 4.7\,\text{kW}$. (After Ref. [39])

$\omega = \omega_{\text{cr}}$, the Θ_L is very large while it diverges at $\omega = \omega_{\text{cr}}$. At the same time, Θ_R acquires a small constant value $\mathcal{O}(10^{-2})$ around ω_{cr} while it becomes zero at $\omega = \omega_{\text{cr}}$.

Figure 25 shows experimental results for the left/right outgoing coefficients $\Theta_{L/R}\,(\omega, \gamma, \beta)$ of Eq. (54) for a circuit based on four LRC resonators. The two negative resistances are based on positive feedback with $LM356$ op-amps [65]. Experimentally, the values used (see caption of Fig. 25) were based primarily on the limitations of the op-amps used for the gyrator and negative resistances, with the exact transmission line impedance carefully adjusted to just below the circuit instability (lasing) threshold. Under this condition, scattering parameters used for $\Theta_{L/R}(\omega)$ were deduced from circuit voltages captured by a four-channel oscilloscope. The corresponding scaled parameters for the data shown were $\gamma = 0.23875$; $\beta = 0.765$; $\kappa = 0.356$; and $\eta = 0.38$. Above threshold, the circuit exhibits self-oscillatory exponential growth of the single linear mode at ω_{cr}, ultimately leading to complex saturation dynamics beyond the scope of this investigation.

The proximity in parameter space to a system instability threshold is responsible for two near-threshold modes corresponding to those in Fig. 24 imposed by the $M\mathscr{T}$ symmetry. Figure 25 shows the left unidirectional mode associated with the experimental parameters used. The asymmetric phase inversion that characterizes the gyrator transmission combined with the coupled oscillator phases is ultimately responsible for the expression of asymmetry in the left/right mode amplitudes shown.

This analysis shows that $M\mathscr{T}$-symmetric structures combined with gyrotropic components are capable of directionally controlled power output. Furthermore we show that reversing the gain/loss results in reconfiguring the lasing action. The experimental demonstration of the phenomenon in an electronic circuit illustrates

the physics, emphasizing the crucial role of phase-reversed coupling provided by the gyrator. It will be interesting to implement these ideas in the optics framework using, for example, $M\mathscr{T}$-symmetric structures like the ones discussed in Ref. [61]. Potential applications of such $M\mathscr{T}$-symmetric laser include optical ring gyroscopes in which a beat frequency between two oppositely directed $M\mathscr{T}$ lasers is detected to measure the rotation rate, optical logic elements in which the direction of lasing in a ring is the logic state of the device etc.

5 Circuit Nonlinearity

In Ref. [4] we investigated the transport properties of a class of nonlinear $\mathscr{P}\mathscr{T}$-symmetric systems whose anharmonic parts contain judiciously balanced gain and loss. The electronic circuit consisted on a pair of coupled Van der Pol oscillators [73], each with complementary anharmonic gain and loss conductances, see Fig. 26a, b. The respective nonlinear I–V curves for the gain (red) and loss (blue) elements are shown in the right panel of Fig. 26c. In the same figure we also report the modeled behaviour of the individual (gain or loss) circuit elements using an NGSPICE simulator. The gain and loss arrangement in the combined dimer was such that the whole circuitry preserved a parity-time $\mathscr{P}\mathscr{T}$-symmetry. The system was turned to a scattering set-up when two transmission lines (TL) were coupled on its left and right side, see Fig. 26b.

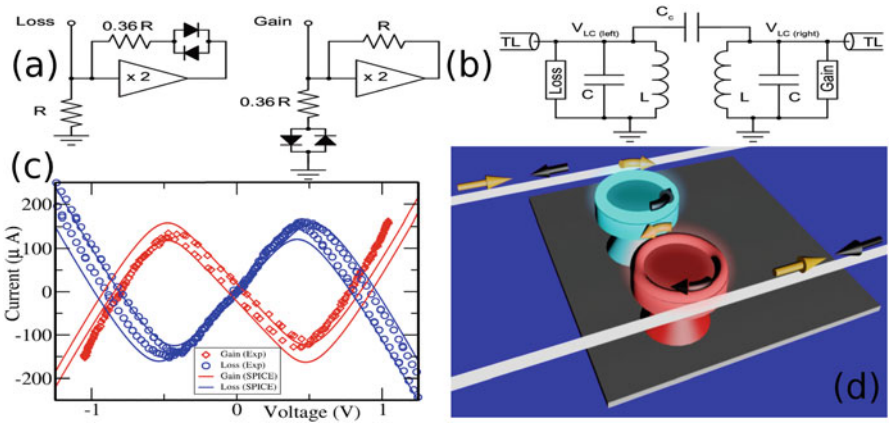

Fig. 26 (**a**) Gain and loss circuits of the van der Pol $\mathscr{P}\mathscr{T}$-symmetric dimer. The elements shown above are incorporated as parallel conductances in the capacitively coupled LC resonators making up the dimer. (**b**) The non-linear $\mathscr{P}\mathscr{T}$-symmetric dimmer. (**c**) Experimental I–V response (circles) for the gain (red) and loss (blue) elements along with the corresponding NGSPICE simulations (solid), taken at a frequency of 30 kHz, typical of the active range of the VDP dimer. (**d**) An equivalent optical circuit. (After Ref. [4])

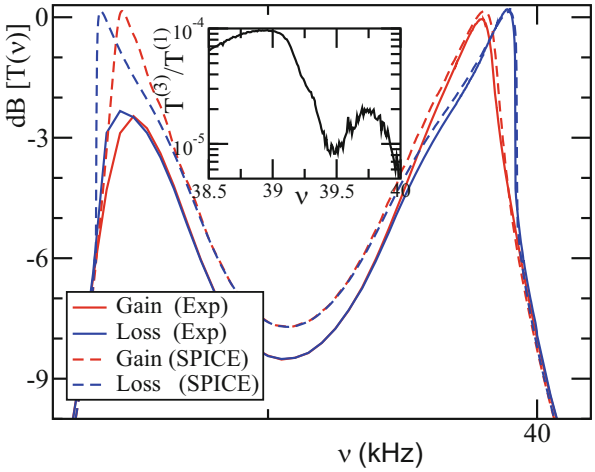

Fig. 27 (Color online) Measured T_L and T_R transmittances for a left (solid blue line) and right (solid red line) incident waves. The NGSPICE simulated $T_L(T_R)$ transmittances are shown as dashed blue (red) lines. Inset: The ratio between the transmittance amplitudes associated with the third harmonic $T^{(3)}$ and the fundamental frequency $T^{(1)}$. The parameter used are $\eta = 0.031$ and $\gamma = 0.15$. (After Ref. [4])

The analysis of the $\mathscr{P}\mathscr{T}$-symmetric dimer indicated that, the left and right transmittances were different indicating a high degree of asymmetric transport which is accompanied with a strong transmitted signal. The physical mechanism has been traced to the presence of amplitude-dependent (nonlinear) resonances which are excited differently, depending if the incident wave interacts first with the gain or the loss element of the $\mathscr{P}\mathscr{T}$-symmetric dimer. Importantly, in contrast to conservative nonlinearities, the outgoing signal was found to be relatively unpoluted from higher harmonics. Such systems, can also be implemented in optics circuitry (see Fig. 26d) using, for example, optical amplifiers, saturable absorbers [35] and two-photon losses to realize the nonlinear $\mathscr{P}\mathscr{T}$-symmetry.

In Fig. 27 we show the measured left (right) transmittances $T_L(\nu)$ $(T_R(\nu))$ versus the driving frequency ν. We found that the degree of asymmetry, i.e. $T_L(\nu) \neq T_R(\nu)$, is more pronounced in the frequency regime near the resonances of the corresponding linear dimer. At the same figure we report the simulated transmittances using NGSPICE. The slight deviations were associated with a small parasitic inductive coupling that was not modeled efficiently by NGSPICE. Our direct measurements indicated clearly that the asymmetric transport is not associated with the generation of higher harmonics. For example, the ratio $T^{(3)}/T^{(1)}$ is found to be less than 10^{-4} (see inset of Fig. 27). For higher harmonics the ratios $T^{(n)}/T^{(1)}$ were below the noise level of our measurements. This behavior has to be contrasted with typical non-linear based, asymmetric transport schemes, where the observed asymmetric transport is due to the high harmonics generation [24, 41, 56, 64].

The transport features of the system of Fig. 26b have been theoretically modeled using a lump theory [4]. Using the first and second Kirchoff's laws at the TL-dimer contacts we derive the following set of coupled differential equations for the current/voltage wave amplitudes I, V at the left (L) and right (R) contact equations

$$\eta\frac{d\mathscr{I}_L}{d\tau} = \gamma(1-\mathscr{V}_L^2)\frac{d\mathscr{V}_L}{d\tau} + \mathscr{V}_L + (1+c)\frac{d^2\mathscr{V}_L}{d\tau^2} - c\frac{d^2\mathscr{V}_R}{d\tau^2}, \tag{55}$$
$$\eta\frac{d\mathscr{I}_R}{d\tau} = \gamma(1-\mathscr{V}_R^2)\frac{d\mathscr{V}_R}{d\tau} - \mathscr{V}_R - (1+c)\frac{d^2\mathscr{V}_R}{d\tau^2} + c\frac{d^2\mathscr{V}_L}{d\tau^2}$$

where all the quantities above are expressed in terms of their dimensionless vadiables: the current (voltage) amplitudes $\mathscr{I}(\mathscr{V})$ at the lead-dimer contacts $I_{L/R} = \frac{V_0}{Z_0}\mathscr{I}_{L/R}$ ($V = V_0\mathscr{V}_{L/R}$); the dimensionless time $\tau = t/\sqrt{LC}$; the dimensionless TL conductance $\eta = \sqrt{L/C}/Z_0$; and the dimensionless coupling capacitance $c = C_c/C$.

Furthermore, the forward $\mathscr{V}^+_{L/R}$ and backward traveling wave amplitudes $\mathscr{V}^-_{L/R}$, and the voltage $\mathscr{V}_{L/R}$ and current $\mathscr{I}_{L/R}$ at the TL-dimer contacts satisfy the continuity relation

$$\mathscr{V}_{L/R} = \left(\mathscr{V}^+_{L/R} + \mathscr{V}^-_{L/R}\right)e^{-i\omega\tau} + cc; \tag{56}$$
$$\mathscr{I}_{L/R} = \left(\mathscr{V}^+_{L/R} - \mathscr{V}^-_{L/R}\right)e^{-i\omega\tau} + cc.$$

Substituting Eqs. (56) into Eqs. (55) and keeping in mind that the output signal is mainly carried by the fundamental frequency we evaluate the transmittances $T \equiv |\mathscr{V}_{\text{out}}/\mathscr{V}_{in}|^2$ using the so-called backward map [29]. The initial conditions utilized in this approach involve the output signal $\mathscr{V}_{\text{out}} = \mathscr{V}^+_R(\mathscr{V}^-_L)$ and the scattering boundary conditions $\mathscr{V}^-_R = 0(\mathscr{V}^+_L = 0)$ corresponding to a left (right) incoming wave. Specifically, for the left transmittance we have

$$T_L = \left|\frac{2\omega\eta c}{\eta\alpha + \alpha\left(\gamma(1-|\frac{\alpha\mathscr{V}_{\text{out}}}{c\omega}|^2) + \frac{i}{\omega} - i\omega(1+c)\right) + (c\omega)^2}\right|^2, \tag{57}$$

where $\alpha = \left(\eta - \gamma(1-|\mathscr{V}_{out}|^2) + \frac{i}{\omega} - i\omega(1+c)\right)$. The transmittance T_R associated with a right incident wave is $T_R(\gamma) = T_L(-\gamma)$ and it is different than $T_L(\gamma)$ (compare blue dashed and red solid lines in Fig. 28b). To further highlight the importance of the interplay between nonlinearity and $\mathscr{PT}$-symmetry, we also report in the inset of Fig. 28 the transmittances for a nonlinear VDP dimer with both elements having gain or loss and for a linear $\mathscr{PT}$-symmetric dimer. In contrast to the nonlinear $\mathscr{PT}$-symmetric structure, the transmission in all these cases is symmetric.

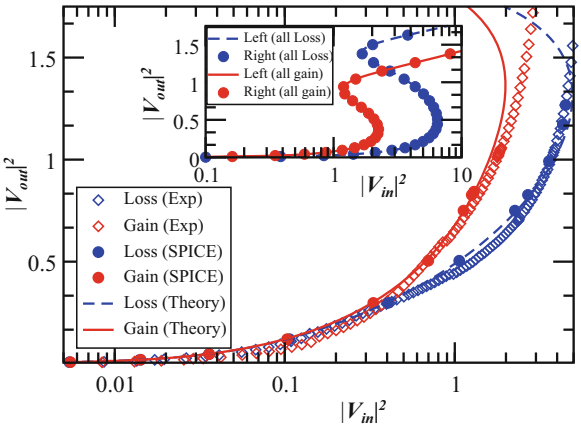

Fig. 28 (Color online) Left T_L and right T_R transmission curves for a nonlinear $\mathscr{P}\mathscr{T}$-symmetric VDP dimer with $\gamma = 0.14$, $\eta = 0.03$, $\omega = 0.98$, and $c = 0.27$. Inset: Theoretical transmission curves for the nonlinear all-gain (red solid line) and all-loss (blue solid line) VDP dimer where reciprocal transport $T_L = T_R$ is found. (After Ref. [4])

6 Floquet-Driven Coupling

Recently, activities related to time-dependent $\mathscr{P}\mathscr{T}$-symmetric systems have started to attract increasing attention [13, 14, 20, 34, 37, 43, 48, 52, 71, 74, 77]. For $\mathscr{P}\mathscr{T}$-symmetric systems one hopes that the use of periodic driving schemes can allow for management of the spontaneous $\mathscr{P}\mathscr{T}$-symmetry breaking for *flexible values of the gain and loss parameter*. Essentially the periodic driving can lead to a renormalization of the coupling and a consequent tailoring of the position of the EPs. In this section, we discuss an experimental example where periodically driven $\mathscr{P}\mathscr{T}$ symmetric systems can be investigated [9]. The set-up is similar to Fig. 1, consisting of two coupled LC resonators with balanced gain and loss. In addition, the capacitance that couples the two resonators is parametrically modulated with a network of varactor diodes. In order to calibrate both the resonator frequency balance and the gain/loss balance in the experimental system, the experimental unmodulated $\mathscr{P}\mathscr{T}$ diagram, shown with the color-map in Fig. 29a, is used to match theoretical results. The coupling is then modulated, directly comparing each calibrated point with and without the modulation. Signal transients are measured by chopping the gain in the system and capturing the resonator responses on both the gain and loss sides. The captured signals are frequency-analyzed to obtain the modulated (or unmodulated) spectrum, shown in Fig. 29b, c.

Theoretically, the driven capacitive coupling is given as $c \equiv \frac{C_c}{C} = c_0 + \varepsilon \cos(\omega_m \tau)$ with respect to the rescaled time $\tau = \omega_0 t$ and $\omega_0 = \frac{1}{\sqrt{LC}}$. Using Kirchoff's laws, the dynamics for the voltages V_1 (V_2) of the gain (loss) side of the driven dimer is:

$$\frac{d^2}{d\tau^2} V + A \frac{d}{d\tau} V + BV = 0; \quad V \equiv (V_1, V_2)^T, \tag{58}$$

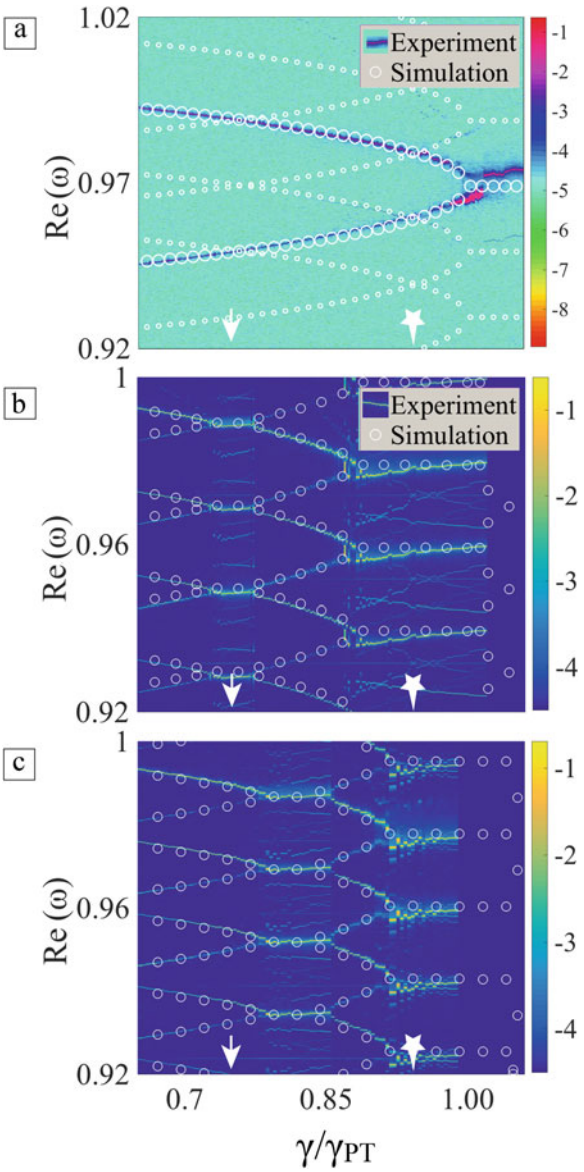

Fig. 29 Spectral density plots for $\mathscr{R}e\,(\omega)$ of a driven $\mathscr{P}\mathscr{T}$-symmetric dimer with $c_0 = 0.0671$ and $\epsilon = 0.01$: (**a**) Undriven dimer $\epsilon = 0$. The Floquet ladder $\omega_{1,2} + n\omega_m$ associated with the eigenfrequencies of $H_{F,0}$ is indicated by the white circles (here $\omega_m = 0.0198$); (**b**) The crossing points "evolve" to flat regions when the system is driven; (**c**) Different driving frequency $\omega_m = 0.01745$ leads to a shift of the flat regions to different γ-domains. The white circles in (**b**, **c**) indicate numerical data. (After Ref. [9])

where

$$A = \frac{1}{\beta}\begin{bmatrix} -\gamma\,(1+c) + 2\,\dot{c} & \gamma c - 2\,\dot{c} \\ -\gamma c - 2\,\dot{c} & \gamma\,(1+c) + 2\,\dot{c} \end{bmatrix}$$

$$B = \frac{1}{\beta}\begin{bmatrix} 1 + c + \ddot{c} & c - \ddot{c} \\ c - \ddot{c} & 1 + c + \ddot{c} \end{bmatrix}. \tag{59}$$

Above $\beta = 1 + 2c, \gamma = R^{-1}\sqrt{L/C}$ is the rescaled gain/loss parameter, and $\dot{c}$ ($\ddot{c}$) denotes the first (second) derivative of the scaled capacitive coupling c with respect to the scaled time τ. Equation (58) is invariant under joint parity $\mathscr{P}$ and time $\mathscr{T}$ operations, where $\mathscr{T}$ performs the operation $\tau \to -\tau$ and $\mathscr{P}$ is the Pauli matrix σ_x.

In the absence of driving, i.e., $\varepsilon = 0$, the eigenfrequencies ω_α ($\alpha = 1, 2$) of system Eq. (58) are given as

$$\omega_\alpha = \frac{1}{2\sqrt{1+2c_0}}\left(\sqrt{\gamma_c^2 - \gamma^2} + (-1)^\alpha \sqrt{\gamma_{PT}^2 - \gamma^2}\right) \tag{60}$$

where $\gamma_{\mathscr{PT}} = \sqrt{1+2c_0} - 1$ for the spontaneous $\mathscr{PT}$-symmetry breaking point and $\gamma_c = \sqrt{1+2c_0} + 1$ for the upper critical point, which are both determined by the strength of the (capacitance) coupling c_0 between the two elements of the dimer. As shown in Fig. 29a, where the open circles represent Eq. (60) and the color map for the experimental results, the spectrum of the undriven dimmer is divided into two domains of exact ($\gamma < \gamma_{\mathscr{PT}}$) and broken ($\gamma > \gamma_{\mathscr{PT}}$) $\mathscr{PT}$-symmetry phase.

We move to the Floquet picture to study the effects of driving. To this end, we employ a Liouvillian formulation of Eq. (58), which takes the form

$$\frac{d\psi}{d\tau} = \mathscr{L}\psi, \quad \mathscr{L} = \begin{bmatrix} 0 & I_2 \\ -B & -A \end{bmatrix}, \quad \psi = \begin{pmatrix} V \\ \dot{V} \end{pmatrix} \tag{61}$$

and allows us to identify a non-Hermitian effective Hamiltonian $H_{eff} = \imath\mathscr{L}$ through time-dependent Schrödinger-like equation. The general solution of Eq. (61) is given by Floquet's theorem which in matrix notation reads $F(\tau) = \Phi(\tau)\, e^{-\imath Q\tau}$ with $\Phi\left(\tau + \frac{2\pi}{\omega_m}\right) = \Phi(\tau)$, Q a Jordan matrix and $F(\tau)$ a 4×4 matrix consisting of four independent solutions of Eq. (61). The eigenvalues of Q are the characteristic exponents (quasi-energies) which determine the stability properties of the system: namely the system is stable (exact $\mathscr{PT}$ phase) if all the quasi-energies are real and it is unstable (broken $\mathscr{PT}$ phase) otherwise. We can evaluate the quasi-energies by constructing the evolution operator $U(\tau, 0) = F(\tau)F^{-1}(0)$ via numerical integration of Eq. (64) (or of Eq. (58)). Then the quasi-energies are the eigenvalues of $\frac{1}{-\imath 2\pi/\omega_m} \ln U(\tau = 2\pi/\omega_m, 0)$.

Our numerical findings together with the experimentally measured values of the quasi-energies versus the gain/loss parameter are reported in Figs. 29, 30, and 31. The unmodulated situation is shown in Figs. 29a and 30a, while Figs. 29b and 30b show the behavior at modulation frequency $\omega_m = 0.0198$ and modulation amplitude $\epsilon = 0.01$. Finally, Figs. 29c and 30c show the evolution of the spectrum with a small change in modulation frequency ω_m for fixed ϵ.

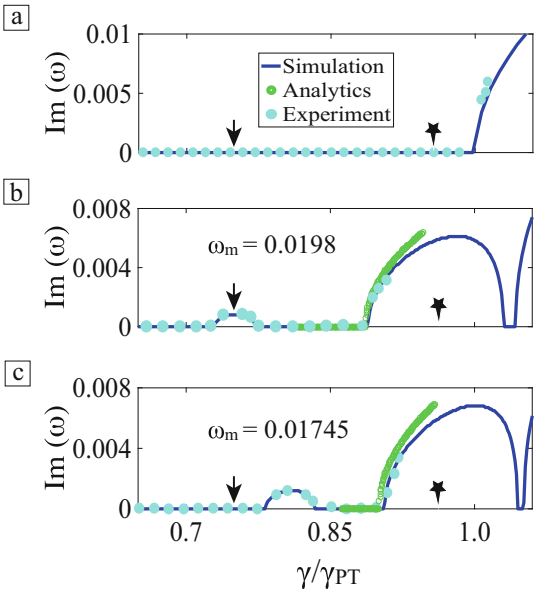

Fig. 30 The imaginary part of the Floquet eigenfrequencies $\mathscr{I}m\,(\omega)$ versus the rescaled gain/loss parameter $\gamma/\gamma_{\mathscr{PT}}$ for: (**a**) an undriven; and (**b**, **c**) driven dimers, with ω_m shown. The arrows and stars correspond to the fixed crossing points in Fig. 29a for reference. The experimental data are shown as aqua circles, the numerics as blue lines and the results from the perturbation theory Eq. (69) as green circles. (After Ref. [9])

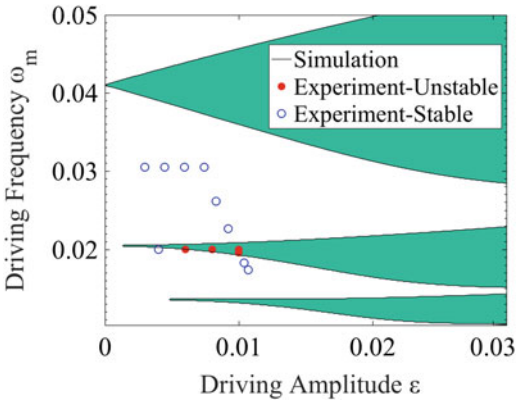

Fig. 31 The (ϵ, ω_m) parameter space for fixed $\gamma/\gamma_{\mathscr{PT}}$ at the position of the arrows in Fig 30. The domains where the system is in the exact PT-symmetric phase are indicated as white while the domains where the system is in the broken $\mathscr{PT}$-symmetric phase are shaded. (After Ref. [9])

There are several new features in the spectrum of the driven $\mathscr{PT}$-symmetric systems. First we see that there exist a cascade of domains for which the system is in the broken $\mathscr{PT}$-phase. These domains emerge as shown in Fig. 29b, c where the real parts of eigenfrequencies have merged in the vicinity of the crossing points (indicated by the arrows and stars) and in Fig. 30a–c the non-zero imaginary parts (the so-called unstable "bubbles") appear. Both the size and position of the unstable "bubbles" can be controlled by the values of the driving amplitude ϵ, compare Figs. 29a and 30a with Figs. 29b and 30b or by the driving frequency ω_m, compare Figs. 29b and 30b with Figs. 29c and 30c. Between the nearest bubbles, there exist

γ-domains where the system is in the exact (stable) $\mathscr{P}\mathscr{T}$-phase. Through the typical EP degeneracy (notice the square -root singularities in Fig. 30a–c), the transition between stable and unstable domains occurs. Beyond some critical gain/loss value $\gamma_{\max}$, the system eventually becomes unstable. The $\gamma_{\max}$ is defined as the maximum value of the gain/loss parameter, above which there are no further stability domains. Generally $\gamma_{\max}$ depends on both ϵ and ω_m. However, in the limit of $\epsilon = 0$, it becomes equal to $\gamma_{\mathscr{P}\mathscr{T}}$. In Fig. 31 we report the numerically determined PT-exact (white) and broken (shaded) phases, when γ is fixed at the position of the arrows in the accompanying plots.

We utilize the notion of Floquet Matrix H_F to understand the spectral metamorphosis from a single exact/broken phase to multiple regions of broken and preserved $\mathscr{P}\mathscr{T}$-symmetry, when ϵ increases from zero. First, we introduce a time-dependent similarity transformation $\mathscr{R}$, which brings the effective Hamiltonian matrix H_{eff} that dictates the evolution in the Schrodinger-like equation Eq. (61) to a symmetric form. We shall see below that the symmetric form is inherited in the Floquet matrix(up to the first order perturbation in ε and $\omega_m \sim \mathscr{O}(\varepsilon)$). Consequently the bi-orthogonal Floquet eigenmodes of the unperturbed Floquet matrix are transpose of each other – a property that greatly simplifies the analytical process for the evaluation via first-order theory of the Floquet eigenmodes. First we observe that H_{eff} satisfies the property, i.e., $P_0 T_0 H_{eff}(\tau) P_0 T_0 = H_{eff}(-\tau)$ with

$$P_0 = \begin{bmatrix} \sigma_x & 0 \\ 0 & \sigma_x \end{bmatrix}, \; T_0 = \begin{bmatrix} I_2 & 0 \\ 0 & -I_2 \end{bmatrix} \tilde{\mathscr{K}}, \tag{62}$$

where σ_x is the Pauli matrix, I_2 is the 2×2 identity matrix and $\tilde{\mathscr{K}}$ denotes the operation of complex conjugation together with setting $\tau \to -\tau$. To determine the similarity transformation $\mathscr{R}$, we impose the transposition symmetry of $R H_{eff} R^{-1}$ together with the requirements $T = \tilde{K} = R T_0 R^{-1}$ and $P = \begin{bmatrix} 0 & \sigma_x \\ \sigma_x & 0 \end{bmatrix} = R P_0 R^{-1}$. Therefore the similarity transformation $\mathscr{R}$ follows:

$$R(\tau) = \begin{bmatrix} 1 & 1 & \imath\sqrt{\beta} & -\imath\sqrt{\beta} \\ \sqrt{1+2\ddot{c}} & -\sqrt{1+2\ddot{c}} & \imath & \imath \\ -\sqrt{1+2\ddot{c}} & \sqrt{1+2\ddot{c}} & \imath & \imath \\ 1 & 1 & -\imath\sqrt{\beta} & \imath\sqrt{\beta} \end{bmatrix}. \tag{63}$$

Under this transformation $R(\tau)$, Eq. (61) takes the form

$$\imath \frac{d}{d\tau}\tilde{\psi} = \tilde{H}\tilde{\psi}; \quad \tilde{H} \equiv \mathscr{R} H_{eff} \mathscr{R}^{-1} - \imath \mathscr{R} \frac{d}{d\tau} \mathscr{R}^{-1} \tag{64}$$

which dictates the evolution of the transformed state $\tilde{\psi} = \mathscr{R}\psi$. The matrix $\tilde{H}$ has the form

$$\tilde{H} = \tilde{H}^T = \begin{bmatrix} -\frac{3}{2}\frac{\imath\dot{c}}{\beta} & c_+ + \frac{\imath\gamma}{2\sqrt{\beta}} & c_- + \frac{\imath\gamma}{2\sqrt{\beta}} & \frac{3}{2}\frac{\imath\dot{c}}{\beta} \\ c_+ + \frac{\imath\gamma}{2\sqrt{\beta}} & \frac{\imath c^{(3)}}{2(1+2\ddot{c})} & -\frac{\imath c^{(3)}}{2(1+2\ddot{c})} & c_- - \frac{\imath\gamma}{2\sqrt{\beta}} \\ c_- + \frac{\imath\gamma}{2\sqrt{\beta}} & -\frac{\imath c^{(3)}}{2(1+2\ddot{c})} & \frac{\imath c^{(3)}}{2(1+2\ddot{c})} & c_+ - \frac{\imath\gamma}{2\sqrt{\beta}} \\ \frac{3}{2}\frac{\imath\dot{c}}{\beta} & c_- - \frac{\imath\gamma}{2\sqrt{\beta}} & c_+ - \frac{\imath\gamma}{2\sqrt{\beta}} & -\frac{3}{2}\frac{\imath\dot{c}}{\beta} \end{bmatrix}, \tag{65}$$

where $c_\pm = \frac{1}{2} \pm \frac{1}{2}\frac{\sqrt{1+2\ddot{c}}}{\sqrt{\beta}}$ and $c^{(3)}$ denotes the third derivative of the capacitive coupling with respect to the scaled time τ. In addition we can easily show that $PT\tilde{H}PT = \tilde{H}$.

Now in component form, the Floquet Matrix H_F is given as

$$\langle \alpha, n | H_F | \beta, l \rangle = \tilde{H}_{\alpha\beta}^{(n-l)} + n\omega_m \delta_{\alpha\beta}\delta_{nl}, \tag{66}$$

where the subscripts $\alpha, \beta = 1, 2, 3, 4$ label the components of $\tilde{H}$, see Eq. (65), n, l are any integers and $\tilde{H}_{\alpha\beta}^{(n)} = \frac{1}{2\pi/\omega_m}\int_0^{2\pi/\omega_m} \tilde{H}_{\alpha\beta}(\tau)\, e^{-\imath n\omega_m \tau} d\tau$. In this picture the quasi-energies are simply the eigenvalues of the Floquet Matrix H_F. Equation (66) defines a lattice model [5] with connectivity given by the off-diagonal elements of H_F and an on-site gradient potential $n\omega_m$.

Generally the Floquet Matrix H_F in Eq. (66) is not transposition symmetric since $H(\tau) \neq H(-\tau)$. However, within the first order approximation to the strength of the driving amplitude ε and the modulation frequency $\omega_m \sim \mathscr{O}(\epsilon)$, the Floquet Hamiltonian is symmetric and takes the block-tridiagonal form $H_F = H_{F,0} + \varepsilon H_{F,1} + O(\varepsilon^2)$ where $\langle n | H_{F,0} | n \rangle = \tilde{H}^{(0)}|_{\varepsilon=0} + n\omega_m I_4$ consists of the diagonal blocks of H_F while $\langle n+1 | H_{F,1} | n \rangle = \langle n | H_{F,1} | n+1 \rangle = X$ consist of off-diagonal blocks of H_F. The 4×4 matrix X has the form

$$X = \frac{\imath}{4(1+2c_0)^{3/2}} \begin{bmatrix} 0 & \imath - \gamma & -\imath - \gamma & 0 \\ \imath - \gamma & 0 & 0 & -\imath + \gamma \\ -\imath - \gamma & 0 & 0 & \imath + \gamma \\ 0 & -\imath + \gamma & \imath + \gamma & 0 \end{bmatrix}. \tag{67}$$

The analytical evaluation of the quasi-energies is shown as follows. First, we diagonalize the leading term $H_{F,0}$. Specifically we can construct a similarity transformation $P_0^{-1}\tilde{H}^{(0)}|_{\varepsilon=0} P_0 = diag\{\omega_2, \omega_1, -\omega_1, -\omega_2\}$. Then the eigenvalues of $H_{F,0}$ are given as $\{\omega_2 + n\omega_m, \omega_1 + n\omega_m, -\omega_1 + n\omega_m, -\omega_2 + n\omega_m\}$ i.e. the spectrum resembles a ladder of step ω_m with the basic unit associated with the

eigenfrequencies of the undriven dimer Eq. (60). The resulting ladder spectrum (white circles) is shown in Fig. 29a versus the gain/loss parameter γ. We notice that level crossing occurs at some specific values of $\gamma^{(j)} < \gamma_{\mathscr{PT}}$, i.e., $\omega_2\big|_{\gamma^{(j)}} = \omega_1\big|_{\gamma^{(j)}} + j\omega_m$.

After we turn on the driving amplitude ε, the crossing points evolve to broken $\mathscr{PT}$-symmetry regions with respect to gain/loss parameter γ. The centers of the instability bubbles are associated with $\gamma^{(j)}$ which is controlled by ω_m (see Fig. 29b, c). In addition, the real part of the eigenfrequencies become degenerate for a range of γ-values around $\gamma^{(j)}$, Fig. 29b, while an instability bubble emerges for the imaginary part – see Fig. 30b for numerical (blue solid lines) and experimental data (filled aqua circles). The transition points from stable to unstable regions have all the characteristic features of an EP. To understand this phenomenon, we consider the effect of the off-diagonal term $\varepsilon H_{F,1}$. For simplicity, we focus on the unstable region around the crossing point at $\gamma^{(1)}$. Application of degenerate perturbation theory to the nearly degenerate levels ω_2 and $\omega_1 + \omega_m$ gives

$$\omega = \frac{(\omega_2 + \omega_1 + \omega_m) \pm \sqrt{(\omega_2 - \omega_1 - \omega_m)^2 + 4\varepsilon^2 \tilde{X}_{12}\tilde{X}_{21}}}{2}, \tag{68}$$

where $\tilde{X} = P_0^{-1} X P_0$ and the subscripts of $\tilde{\mathrm{X}}$ indicate the corresponding matrix components. Around the EP, ω can be written as

$$\mathrm{Re}\,(\omega) \approx \omega_2\big|_{\gamma^{(1)}}\,,\ \ \mathrm{Im}\,(\omega) = \pm\, C_m\sqrt{\gamma - \gamma_0},\ \ \gamma > \gamma_0 \tag{69}$$

which has the characteristic square-root singularity of EP degeneracies. The constant C_m depends on ϵ, ω_m and is given as

$$C_m = \frac{1}{2}\sqrt{\frac{1}{\gamma_{PT}^2 - \gamma_0^2}\frac{\varepsilon\gamma_0}{1+2c_0}\left[\left(\frac{2}{\sqrt{1+2c_0}} - \frac{\omega_m}{\sqrt{\gamma_{PT}^2 - \gamma_0^2}}\right)\gamma_0 + \frac{\varepsilon}{2\,(1+2c_0)}\right]}, \tag{70}$$

where γ_0 is the solution of the equation $(\omega_2 - \omega_1 - \omega_m)^2 + 4\varepsilon^2 \tilde{X}_{12}(\gamma)\tilde{X}_{21}(\gamma) = 0$ (see Eqs. (67) and (68)). For the experiment, where $\gamma_0 \to \gamma_{\mathscr{PT}}$ and $\gamma_{\mathscr{PT}} \to 0$, we estimate that

$$\gamma_0 \approx \gamma_{\mathscr{PT}}\left(1 - \left(\frac{\sqrt{2}\omega_m + \sqrt{2\omega_m^2 + \varepsilon\,(4\gamma_{PT} + \varepsilon)}}{4\gamma_{PT} + \varepsilon}\right)^2\right). \tag{71}$$

Equation (69) imply that both ω_m, ϵ are responsible for a renormalization of the coupling between the two levels (compare with Eq. (60)). We see that predictions

(69) are in agreement with the numerical and experimental data (see green line in Fig. 30b, c). Additionally, higher orders of EPs $\gamma^{(j)}$ can be analyzed in a similar manner if we incorporate higher order perturbation theory corrections. In Fig. 31 we report a summary of $\mathscr{PT}$-exact and broken domains in the parametric (ϵ, ω_m) space [18, 72] where $\gamma/\gamma_{\mathscr{PT}} = 0.74$ (indicated by white arrow in Fig. 29a–c).

It is interesting to observe the revival of the exact $\mathscr{PT}$ phase around $\gamma/\gamma_{PT} = 1.07$, see Fig. 30b, c. To understand this phenomenon, we realize that for constant ω_m (determining the center of the bubble), the edges of the instability domain are pushed away when ϵ increases, which can be deduced from Eq. (71). Furthermore, the broken $\mathscr{PT}$-symmetric regimes can be even broaden beyond the $\gamma_{\mathscr{PT}}$ border. At the same time $\gamma_{\max}$ moves beyond $\gamma_{\mathscr{PT}}$. In fact in the high frequency limit, one can average out the time dependence and recover a "static" $\mathscr{PT}$-symmetric dimmer with renormalized coupling constants [34, 77] and predict the $\gamma_{\max}$. Finally the stability domain between the upper border of the $\gamma^{(1)}$-bubble and $\gamma_{\max}$, originating from the unbroken γ-region between $\gamma^{(1)}$ and the $\gamma_{\mathscr{PT}}$ in the undriven case, appear around $\gamma/\gamma_{PT} = 1.07$.

The management of the exact and broken $\mathscr{PT}$ symmetry phase, either via the driving amplitude ϵ or via the frequency ω_m, also has direct implications to the dynamics of the system. In Fig. 32 we report the total capacitance energy of the dimer for the same $\gamma = 0.0483$ and $\epsilon = 0.01$ values but different driving frequencies $\omega_m = 0.01745$ (left) and $\omega_m = 0.0198$ (right). In the latter case the energy grows exponentially with a rate given by the imaginary part of the eigenfrequencies (see Fig. 30b) while in the former case we have an oscillatory (stable) dynamics (see Fig. 30c).

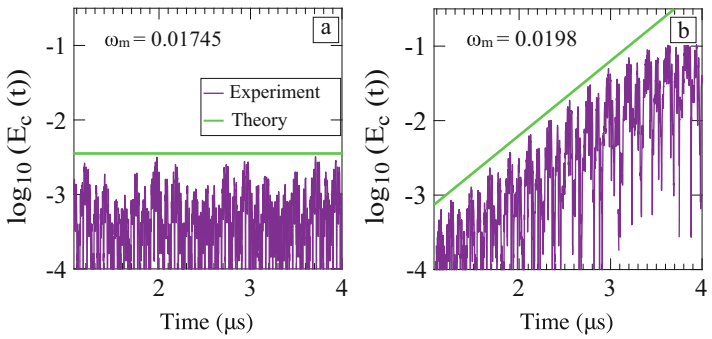

Fig. 32 Measured (cyan lines) time-dependence of the total capacitance energy of the whole circuit $E_c(t) = \left(V_1^2(t) + V_2^2(t)\right)$ (in units of Volt^2) for driving frequencies (**a**) $\omega_m = 0.01745$ and (**b**) $\omega_m = 0.0198$, and for the same driving amplitude and gain/loss paramater γ (indicated by black arrow in Fig. 30b, c). The green lines indicate the theoretical predictions (from simulations) for the slope of the envelope of $E_c(t)$. (After Ref. [9])

7 Conclusions

The aim of the RF circuit and microwave project that we have carried over the last seven years was/is to develop a new circuit design that exploits fundamental $\mathscr{P}\mathscr{T}$ concepts using active electronic circuitry as a working framework. The implemented circuits are experimentally simple, mathematically transparent, and display all the universal phenomena encountered in systems with generalized $\mathscr{P}\mathscr{T}$-symmetries. In fact, in many occasions they have provided a validation to theoretical approximations which due to the non-Hermitian nature of the systems under investigation can be subtle.

On the one hand, we expect that the circuit architectures and concepts that have and will emerge from these studies can also find direct applications in RF systems. A recent example in this direction is the implementation of $\mathscr{P}\mathscr{T}$-circuitry for the realization of robust wireless power transfer [2]. Another example is the utilization of $\mathscr{P}\mathscr{T}$-circuitry for the realization of invisible acoustic sensors [22].

On the other hand, we believe that the development of $\mathscr{P}\mathscr{T}$-circuitry will allow us to better predict the behavior of more complicated structures currently proposed, such as coupled optical micro-resonators or exotic split-ring metamaterial arrays, as they inevitably migrate into the realm of active elements. These ultimate applications, which will undoubtedly be very difficult and expensive to develop, will become significantly less challenging if the fundamental theory and consequent design is well grounded by this more transparent experimental contact.

Acknowledgements This research was partially supported by an AFOSR grant No. FA 9550-10-1-0433, and by NSF grants EFMA-1641109 and DMR-1306984. Many of the results that we have reported in this contribution are the outcome of collaborative research with N. Bender, S. Factor, Z. Lin, H. Ramezani, J. Schindler and M. C. Zheng which we acknowledge for the stimulating discussions and for making this project an exciting adventure.

References

1. Anandan, J., Aharonov, Y.: Geometry of quantum evolution. Phys. Rev. Lett. **65**, 1697 (1990)
2. Assawaworrarit, S., Yu, X., Fan, S.: Robust wireless power transfer using a nonlinear parity-time-symmetric circuit. Nature **546**, 387 (2017)
3. Bender, C.M., Boettcher, S.: Real spectra in Non-Hermitian Hamiltonians having PT symmetry. Phys. Rev. Lett. **80**, 5243 (1998)
4. Bender, N., Factor, S., Bodyfelt, J.D., Ramezani, H., Christodoulides, D.N., Ellis, F.M., Kottos, T.: Observation of asymmetric transport in structures with active nonlinearities. Phys. Rev. Lett. **110**, 234101 (2013)
5. Bender, N., Li, H., Ellis, F.M., Kottos, T.: Wave-packet self-imaging and giant recombinations via stable Bloch-Zener oscillations in photonic lattices with local PT symmetry. Phys. Rev. A **92**, 041803(R) (2015)
6. Cannata, F., Dedonder, J.-P., Ventura, A.: Scattering in PT-symmetric quantum mechanics. Ann. Phys. **322**, 397 (2007)

7. Chen, W., Özdemir, Ş.K., Zhao, G., Wiersig, J., Yang, L.: Exceptional points enhance sensing in an optical microcavity. Nature **548**, 192 (2017)
8. Chitsazi, M., Factor, S., Schindler, J., Ramezani, H., Ellis, F.M., Kottos, T.: Experimental observation of lasing shutdown via asymmetric gain. Phys. Rev. A **89**, 043842 (2014)
9. Chitsazi, M., Li, H., Ellis, F.M., Kottos, T.: Experimental realization of Floquet PT-symmetric systems. Phys. Rev. Lett. **119**, 093901 (2017)
10. Chong, Y.D., et al.: Coherent perfect absorbers: time-reversed lasers. Phys. Rev. Lett. **105**, 053901 (2010)
11. Chong, Y.D., Ge, Li., Stone, A.D.: PT-symmetry breaking and laser-absorber modes in optical scattering systems. Phys. Rev. Lett. **106**, 093902 (2011)
12. COMSOL Multiphysics, version 5.2. www.comsol.com. COMSOL AB, Stockholm, Sweden
13. D'Ambroise, J., Malomed, B.A., Kevrekidis, P.G.: Quasi-energies, parametric resonances, and stability limits in ac-driven PT-symmetric systems. Chaos **24**, 023136 (2014)
14. Della Valle, G., Longhi, S.: Spectral and transport properties of time-periodic PT-symmetric tight-binding lattices. Phys. Rev. A **87**, 022119 (2013)
15. Dembowski, C., Gräf, H.D., Harney, H.L., Heine, A., Heiss, W.D., Rehfeld, H., Richter, A.: Experimental observation of the topological structure of exceptional points. Phys. Rev. Lett. **86**, 787 (2001)
16. Dembowski, C., Dietz, B., Gräf, H.D., Harney, H.L., Heine, A., Heiss, W.D., Richter, A.: Observation of a chiral state in a microwave cavity. Phys. Rev. Lett. **90**, 034101 (2003)
17. Dietz, B., et al.: Exceptional points in a microwave billiard with time-reversal invariance violation. Phys. Rev. Lett. **106**, 150403 (2011)
18. Dohnal, F.: Suppressing self-excited vibrations by synchronous and time-periodic stiffness and damping variation. J. Sound Vib. **306**, 136 (2007)
19. Doppler, J., Mailybaev, A.A., Bohm, J., Kuhl, U., Girschik, A., et al.: Dynamically encircling an exceptional point for asymmetric mode switching. Nature **537**, 76–79 (2016)
20. El-Ganainy, R., Makris, K.G., Christodoulides, D.N.: Local PT invariance and supersymmetric parametric oscillators. Phys. Rev. A **86**, 033813 (2012)
21. Feng, L., Wong, Z.J., Ma, R.M., Wang, Y., Zhang, X.: Single-mode laser by parity-time symmetry breaking. Science **346**, 972 (2014)
22. Fleury, R., Sounas, D.L., Alú, A.: An invisible acoustic sensor based on parity-time symmetry. Nat. Commun. **6**, 5905 (2015)
23. Fyodorov, Y., Sommers, H.-J.: Statistics of resonance poles, phase shifts and time delays in quantum chaotic scattering: random matrix approach for systems with broken time-reversal invariance. J. Math. Phys. **38**, 1918 (1997)
24. Gallo, K., et al.: All-optical diode in a periodically poled lithium niobate waveguide. Appl. Phys. Lett. **79**, 314 (2001)
25. Giri, P.R.: Lower bound of minimal time evolution in quantum mechanics. Int. J. Theor. Phys. **47**, 2095 (2008)
26. Godunov, S.K.: Ordinary Differential Equations with Constant Coefficients. American Mathematical Society, Providence (1997)
27. Günther, U., Samsonov, B.F.: PT-symmetric brachistochrone problem, Lorentz boosts, and nonunitary operator equivalence classes. Phys. Rev. A **78**, 042115 (2008)
28. Guo A., et al.: Observation of PT-symmetry breaking in complex optical potentials. Phys. Rev. Lett. **103**, 093902 (2009)
29. Hennig, D., Tsironis, G.: Wave transmission in nonlinear lattices. Phys. Rep. **307**, 333 (1999)
30. Hiller, M., Kottos, T., Ossipov, A.: Bifurcations in resonance widths of an open Bose-Hubbard dimer. Phys. Rev. A **73**, 063625 (2006)
31. Hodaei, H., et al.: Parity-time-symmetric microring lasers. Science **346**, 975 (2014)
32. Hodaei, H., Hassan, A.U., Wittek, S., Garcia-Gracia, H., El-Ganainy, R., Christodoulides, D.N., Khajavikhan, M.: Enhanced sensitivity at higher-order exceptional points. Nature **548**, 187–191 (2017)
33. Horowitz, P., Hill, W.: The Art of Electronics, ch. 1. Cambridge University Press, New York (1989)

34. Joglekar, Y.N., Marathe, R., Durganandini, P., Pathak, R.: The first paper in citation 37 has the title: "PT spectroscopy of the Rabi problem"; The second paper in citation 37 has the title: "PT-symmetric Rabi model: perturbation theory". Phys. Rev. A **90**, 040101(R) (2014); Lee, T.E., Joglekar, Y.N., Phys. Rev. A **92**, 042103 (2015)
35. Keller, U., et al.: Semiconductor saturable absorber mirrors (SESAM's) for femtosecond to nanosecond pulse generation in solid-state lasers. IEEE J. Sel. Top. Quantum Electron. **2**, 435 (1996)
36. Keller, C., Oberthaler, M.K., Abfalterer, R., Bernet, S., Schmiedmayer, J., Zeilinger, A.: Tailored complex potentials and Friedel's law in atom optics. Phys. Rev. Lett. **79**, 3327 (1996)
37. Konotop, V.V., Zezyulin, D.A.: Stochastic parity-time-symmetric coupler. Opt. Lett. **39**, 1223 (2014)
38. Kottos, T., Weiss, M.: Statistics of resonances and delay times: a criterion for Metal-Insulator transitions. Phys. Rev. Lett. **89**, 056401 (2002)
39. Lee, J.M., Factor, S., Lin, Z., Vitebskiy, I., Ellis, F.M., Kottos, T.: Reconfigurable directional lasing modes in cavities with generalized PT symmetry. Phys. Rev. Lett. **112**, 253902 (2014)
40. Lee, J.M., Kottos, T., Shapiro, B.: Macroscopic magnetic structures with balanced gain and loss. Phys. Rev. B **91**, 094416 (2015)
41. Lepri, S., Casati, G.: Asymmetric wave propagation in nonlinear systems. Phys. Rev. Lett. **106**, 164101 (2011)
42. Li, H., Thomas, R., Ellis, F.M., Kottos, T.: Four-port photonic structures with mirror-time reversal symmetries. New J. Phys. **18**, 075010 (2016)
43. Lian, X., Zhong, H., Xie, Q., Zhou, X., Wu, Y., Liao, W.: PT-symmetry-breaking induced suppression of tunneling in a driven non-Hermitian two-level system. Eur. Phys. J. D **68**, 189 (2014)
44. Liertzer, M., Li Ge, Cerjan, A., Stone, A.D., Türeci, H.E., Rotter, S.: Pump-induced exceptional points in lasers. Phys. Rev. Lett. **108**, 173901 (2012)
45. Lin, Z., Ramezani, H., Eichelkraut, T., Kottos, T., Cao, H., Christodoulides, D.N.: Unidirectional invisibility induced by PT-symmetric periodic structures. Phys. Rev. Lett. **106**, 213901 (2011)
46. Lin, Z., Schindler, J., Ellis, F.M., Kottos, T.: Experimental observation of the dual behavior of PT-symmetric scattering. Phys. Rev. A **85**, 050101(R) (2012)
47. Longhi, S.: PT-symmetric laser absorber. Phys. Rev. A **82**, 031801 (2010)
48. Luo, X., Huang, J., Zhong, H., Qin, X., Xie, Q., Kivshar, Y.S., Lee, C.: Pseudo-parity-time symmetry in optical systems. Phys. Rev. Lett. **110**, 243902 (2013)
49. Mahaux, C., Weidenmüller, H.A.: Shell Model Approach in Nuclear Reactions. North-Holland, Amsterdam (1969)
50. Makris, K.G., et al.: Beam dynamics in PT symmetric optical lattices. Phys. Rev. Lett. **100**, 103904 (2008)
51. Mendez-Bermudez, J.A., Kottos, T.: Probing the eigenfunction fractality using Wigner delay times. Phys. Rev. B **72**, 064108 (2005)
52. Moiseyev, N.: Crossing rule for a PT-symmetric two-level time-periodic system. Phys. Rev. A **83**, 052125 (2011)
53. Mostafazadeh, A.: Pseudo-Hermiticity and generalized PT- and CPT-symmetries. J. Math. Phys. **44**, 974 (2003)
54. Mostafazadeh, A.: Quantum Brachistochrone problem and the geometry of the state space in pseudo-Hermitian quantum mechanics. Phys. Rev. Lett. **99**, 130502 (2007)
55. Mostafazadeh, A.: Hamiltonians generating optimal-speed evolutions. Phys. Rev. A **79**, 014101 (2009)
56. Nesterenko, V.F., et al.: Anomalous wave reflection at the interface of two strongly nonlinear granular media. Phys. Rev. Lett. **95**, 158702 (2005)
57. Oberthaler, M.K., Abfalterer, R., Bernet, S., Schmiedmayer, J., Zeilinger, A.: Atom waves in crystals of light. Phys. Rev. Lett. **77**, 4980 (1996)
58. Oberthaler, M.K., Abfalterer, R., Bernet, S., Keller, C., Schmiedmayer, J., Zeilinger, A.: Dynamical diffraction of atomic matter waves by crystals of light. Phys. Rev. A **60**, 456 (1999)

59. Peng, B., Ozdermir, S.K., Liertzer, M., Chen, W., Kramer, J., Yilmaz, H., Wiersig, J., Rotter, S., Yang, L.: Chiral modes and directional lasing at exceptional points. Proc. Natl. Acad. Sci. **113**, 6845–6850 (2016)
60. Ramezani, H., Schindler, J., Ellis, F.M., Guenther, U., Kottos, T.: Bypassing the bandwidth theorem with PT symmetry. Phys. Rev. A **85**, 062122 (2012)
61. Ramezani, H., et al.: Taming the flow of light via active magneto-optical impurities. Opt. Express **20**, 26200 (2012)
62. Regensburger, A., Bersch, Ch., Miri, M.-A., Onishchukov, G., Christodoulides, D.N., Peschel, U.: Parity-time synthetic photonic lattices. Nature **488**, 167 (2012)
63. Rüter, C.E., et al.: Observation of parity-time symmetry in optics. Nat. Phys. **6**, 192 (2010)
64. Scalora, M., et al.: The photonic band edge optical diode. J. Appl. Phys. **76**, 2023 (1994)
65. Schindler, J., Li, A., Zheng, M.C., Ellis, F.M., Kottos, T.: Experimental study of active LRC circuits with PT symmetries. Phys. Rev. A **84**, 040101(R) (2011)
66. Schindler, J., Lin, Z., Lee, M.J., Ramezani, H., Ellis, F.M., Kottos, T.: PT-symmetric electronics. J. Phys. A Math. Theor. **45**, 444029 (2012)
67. Shi, C., Dubois, M., Chen, Y., Cheng, L., Ramezani, H., Wang, Y., Zhang, X.: Accessing the exceptional points of parity-time symmetric acoustics. Nat. Commun. **7**, 11110 (2016)
68. Shu, F.-J., Zou, C.-L., Zou, X.-B., Yang, L.: Chiral symmetry breaking in a microring optical cavity by engineered dissipation. Phys. Rev. A **94**, 013848 (2016)
69. Stutzle, R., Gobel, M.C., Horner, Th., Kierig, E., Mourachko, I., Oberthaler, M.K., Efremov, M.A., Fedorov, M.V., Yakovlev, V.P., van Leeuwen, K.A.H., Schleich, W.P.: Observation of nonspreading wave packets in an imaginary potential. Phys. Rev. Lett. **95**, 110405 (2005)
70. Thomas, R., Li, H., Ellis, F.M., Kottos, T.: Giant nonreciprocity near exceptional-point degeneracies. Phys. Rev. A **94**, 043829 (2016)
71. Tsironis, G.P., Lazarides, N.: PT-symmetric nonlinear metamaterials and zero-dimensional systems. Appl. Phys. A Mat. Sci. Proc. **115**, 449 (2014)
72. van der Burgh, A.H.: A linear differential equation with a time-periodic damping coefficient: stability diagram and an application. J. Eng. Math. **49**, 99 (2004)
73. van der Pol, B.: On "relaxation-oscillations". Lond. Edinb. Dublin Philos. Mag. J. Sci. **2**, 978 (1927)
74. West, C.T., Kottos, T., Prosen, T.: PT-symmetric wave chaos. Phys. Rev. Lett. **104**, 054102 (2010)
75. Wiersig, J.: Enhancing the sensitivity of frequency and energy splitting detection by using exceptional points: application to microcavity sensors for single-particle detection. Phys. Rev. Lett. **112**, 203901 (2014)
76. Wigner, E.P., Eisenbud, L.: Higher angular momenta and long range interaction in resonance reactions. Phys. Rev. **72**, 29 (1947)
77. Wu, Y., Zhu, B., Hu, S.-F., Zhou, Z., Zhong, H.: Floquet control of the gain and loss in a PT-symmetric optical coupler. Front. Phys. **12**, 121102 (2017)
78. Zhang, N., Liu, S., Wang, K.Y., Gu, Z.Y., Li, M., Yi, N.B., Xiao, S., Song, Q.: Single nanoparticle detection using far-field emission of photonic molecule around the exceptional point. Sci. Rep. **5**, 11912 (2015)
79. Zheng, M.C., et al.: PT optical lattices and universality in beam dynamics. Phys. Rev. A **82**, 010103 (2010)

Coupled Nonlinear Schrödinger Equations with Gain and Loss: Modeling $\mathscr{P}\mathscr{T}$ Symmetry

Vladimir V. Konotop

Abstract Coupled nonlinear Schrödinger (NLS) equations is an ubiquitous model describing wave propagation in diverse physical systems. In combination with gain and loss exactly balanced with each other, this model allows for modeling parity ($\mathscr{P}$) and time ($\mathscr{T}$) symmetries in frameworks beyond the non-Hermitian quantum mechanics, where they have been introduced originally. Being open, i.e. not conserving energy, such systems nevertheless bear many properties which are characteristic for conservative models. This allows one to explore various wave phenomena in $\mathscr{P}\mathscr{T}$-symmetric settings, including bright and dark solitons and their interactions with defects, soliton switches, resonant wave interactions, wave collapse, etc. In this Chapter an overview of some recent results on these processes is presented. The outcomes are interpreted in contexts of nonlinear optics and matter wave theory.

1 Introduction

The nonlinear Schrödiner (NLS) equation is a fundamental model which describes propagation of weakly non-linear and weakly dispersive waves. It is used for theoretical description of wave processes in systems having different physical, and not only physical, nature, like optics, atomic physics, acoustics, hydrodynamics, biology, economy, etc. As its name indicates, the NLS equation represents a nonlinear generalization of the well-known Schrödinger equation which describes a non-relativistic particle in quantum mechanics. This mathematical analogy served as the background for extension of the ideas of parity ($\mathscr{P}$) and time ($\mathscr{T}$) symmetric

V. V. Konotop (✉)
Departamento de Física and Centro de Física Teórica e Computacional, Faculdade de Ciências, Universidade de Lisboa, Lisboa, Portugal
e-mail: vvkonotop@fc.ul.pt

D. Christodoulides, J. Yang (eds.), *Parity-time Symmetry and Its Applications*, Springer Tracts in Modern Physics 280,
https://doi.org/10.1007/978-981-13-1247-2_14

systems from non-Hermitian quantum mechanics [6, 7], first to optics [23, 39, 45, 52], and later to many other branches of physics (see e.g. [33] for review).

In application to wave processes in media with gain and loss, the $\mathscr{P}\mathscr{T}$ symmetry implies existence of exact balance between domains where a wave is amplified and where it is attenuated. These non-conservative effects are described by complex coefficients of the respective wave equations or by complex potentials. For observation of stable wave propagation, the balance between nonlinearity and dispersion (or diffraction) must be verified simultaneously with the balance between gain and loss. This is also typical for dissipative systems [3], where however, both balance conditions can be satisfied only for specific values of the wave parameters. Presence of $\mathscr{P}\mathscr{T}$ symmetry completely changes the situation enabling those conditions for the whole, or at least for a continuous, range of the wave parameters. In this way the $\mathscr{P}\mathscr{T}$ symmetry provides conditions for existence of families of nonlinear wave solutions, which can be stable, in spite of the presence of gain and loss.

A simple way of modeling a nonlinear $\mathscr{P}\mathscr{T}$-symmetric system is to consider two optical waveguides (or two subsystems, in a general case) one of which amplifies the wave and another one absorbs it [53]. If the waveguides are linearly coupled, such that the energy can be transmitted from the waveguide with gain to the one with loss, it is natural to expect that balance necessary for stable wave propagation can be achieved if the coupling is strong enough. In optical applications such a system represents a dispersive coupler, supporting propagation of wavepackets.

Coupled NLS equations with gain and loss have been studied already for many years [41] (see also [40] for a recent review). A decade ago, a linear coupler (without dispersion) which obeys $\mathscr{P}\mathscr{T}$-symmetry was introduced in [23] and later implemented experimentally in [53]. These works initiated studies of the discrete $\mathscr{P}\mathscr{T}-$symmetric optics. Soon after that, the idea of a $\mathscr{P}\mathscr{T}$-symmetric (dispersionless) coupler was formulated for the waveguides with Kerr nonlinearity [51, 54]. Study of dispersive (i.e. allowing for propagation of wavepackets) couplers obeying $\mathscr{P}\mathscr{T}$-symmetry was initiated by the works [1, 20–22].

There exists special interest in modeling $\mathscr{P}\mathscr{T}$ symmetry by coupled NLS equations. Implementation of this symmetry in optical media is constraint by the causality principle, mathematically expressed by the Kramers-Kronnig relations. Required delicate balance between gain and loss can be realized only for isolated frequencies, rather than for a continuous frequency range [60]. This does not affect modeling of the paraxial $\mathscr{P}\mathscr{T}-$symmetric optics, initiated by works [23, 39, 45], since the paraxial optics deals with monochromatic beams. However, this becomes relevant for study of short pulses, obeying finite-band frequency spectra. Indeed, by creating gain and loss domains in different media, similarly to the first suggestion on implementation of $\mathscr{P}\mathscr{T}$ symmetry in optics [52], which are coupled with each other, one can consider dynamics of pulses with relatively broad spectra.

In this Chapter we overview some recent results on coupled NLS equations with $\mathscr{P}\mathscr{T}$-symmetric gain and loss. The results are interpreted in the contexts of nonlinear optics and of theory of matter waves in two-component mixtures of spinor Bose-Einstein condensates (BECs). We start with a short summary of the

basic concepts in Sect. 2 which includes the formulations of the model (Sect. 2.1), definition of the symmetries (Sect. 2.2), and the notions of broken and unbroken $\mathscr{P}\mathscr{T}$-symmetric phases (Sect. 2.3). In Sect. 3 we review some results on the existence of solutions of two coupled $\mathscr{P}\mathscr{T}$-symmetric equations of the NLS-type. In the subsequent sections we study the modulational instability of plane-wave solutions (Sect. 4), as well as bright (Sect. 5) and dark (Sect. 6) vector solitons. Interaction of symmetric and anti-symmetric bright solitons with localized defects is described in Sect. 7. Section 8 is devoted to the phenomenon of four-wave mixing in the coupled $\mathscr{P}\mathscr{T}$-symmetric NLS equations. In the next Sect. 9 two physical systems, whose symmetries involve three operators (time reversion as well as, space and "charge" inversions) are described. These systems are Bose-Einstein condensates with spin-orbit coupling (Sect. 9.1) and optical coupler with dispersive coupling (Sect. 9.2). In Sect. 10 we describe evolution of $\chi^{(2)}$ solitons in a $\mathscr{P}\mathscr{T}$-symmetric coupling in the cascading limit resulting in coupled NLS equations with nonlinear $\mathscr{P}\mathscr{T}$-symmetric terms. In Sect. 11 $\mathscr{P}\mathscr{T}$-symmetric coupled NLS equations allowing for Hamiltonian formulation are introduced. Some results on multi-dimensional models are listed in Sect. 12. The last Sect. 13 contains concluding remarks.

2 Basic Concepts

2.1 The Model

In order to introduce the main model of this Chapter, let us consider one of the pairs of coupled waveguides illustrated in Fig. 1. These are either one-dimensional (1D) two-core waveguides along which optical pulses can propagate (Fig. 1a, c), or planar waveguides (Fig. 1b, d) where diffraction of monochromatic beams can be considered. In all the cases z-axis coincides with the direction of light propagation. The second independent variable is either time $\tau = t - v_g z$, where v_g is the group velocity of the carrier wave (Fig. 1a, c), or spatial coordinate x (Fig. 1b, d). The waveguides are considered having homogeneous gain and loss characterized by the strengths $+\gamma$ and $-\gamma$, respectively (Fig. 1a, b, d), and/or homogeneous coupling κ (Fig. 1a–c). Hereafter we fix $\gamma > 0$. We will also consider a coupler with segments of active and absorbing media, i.e. with $\gamma = \gamma(z)$ (Fig. 1c), or having varying coupling $\kappa = \kappa(z)$ (Fig. 1d). If variations of gain and loss strengths or change of the coupling constant are localized along z, they are referred to as defects. An important requirement in all the cases considered below, is that the gain and loss are exactly balanced, i.e. have equal strengths at any value of the coordinate z (any instant of time). It will also be assumed that the waveguides obey Kerr nonlineary (either focusing or defocusing).

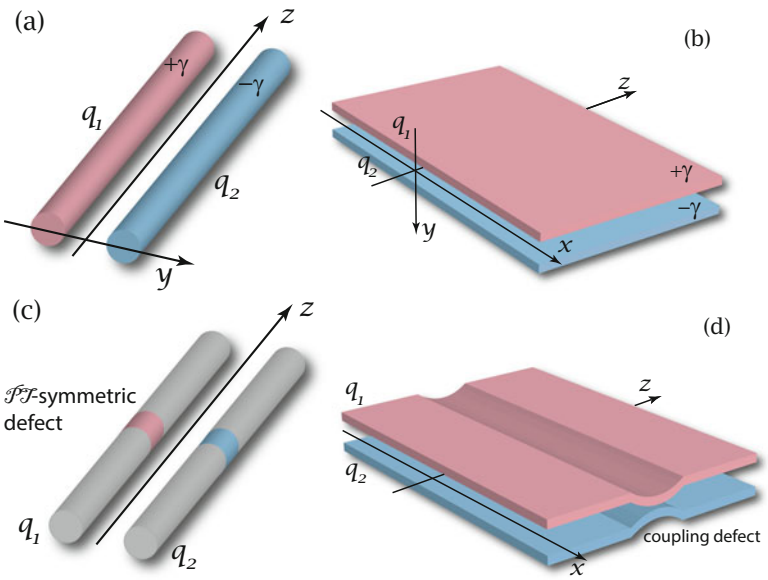

Fig. 1 Schematic illustration of dispersive couplers which in the presence of the nonlinearity are described by coupled NLS equations (1). (**a**) Coupled waveguides one with gain and another with loss; (**b**) planar waveguides with gain and loss; (**c**) transparent waveguides with a localized gain-and-loss defect; (**d**) planar waveguides with a defect of coupling

Collecting the above assumptions, choosing x as a second independent variable (for the sake of definiteness only), and denoting the dimensionless fields in the waveguides with gain and loss by q_1 and q_2, respectively, one can write down the system of equations describing a coupler, as follows

$$\begin{aligned} i\frac{\partial q_1}{\partial z} &= -\frac{\partial^2 q_1}{\partial x^2} + i\gamma q_1 + \kappa q_2 + (g|q_1|^2 + \tilde{g}|q_2|^2)q_1\,, \\ i\frac{\partial q_2}{\partial z} &= -\frac{\partial^2 q_2}{\partial x^2} - i\gamma q_2 + \kappa q_1 + (g|q_2|^2 + \tilde{g}|q_1|^2)q_2\,. \end{aligned} \tag{1}$$

Here g and $\tilde{g}$ describe self-phase modulation (SPM) and cross-phase modulation (XPM), respectively. For the waveguide models shown in Fig. 1a, c, the variable x must be substituted by τ, while for the examples shown in Fig. 1b and Fig. 1d one should consider z-dependent functions $\gamma(z)$ and $\kappa(z)$.

In what follows it will be convenient to use also a vectorial form of Eqs. (1), where the field is written in a form of the column-vector, $\mathbf{q} = (q_1, q_2)^T$ (hereafter the superscript T stands for transpose). Introducing the operator

$$\mathscr{H} = -\sigma_0\partial_x^2 + \kappa\sigma_1 + i\gamma\sigma_3 \tag{2}$$

where σ_0 and $\sigma_{1,2,3}$ are respectively the 2×2 identity and the Pauli matrices, i.e.,

$$\sigma_0 = \begin{pmatrix} 1 & 0 \\ 0 & 1 \end{pmatrix}, \quad \sigma_1 = \begin{pmatrix} 0 & 1 \\ 1 & 0 \end{pmatrix}, \quad \sigma_2 = \begin{pmatrix} 0 & -i \\ i & 0 \end{pmatrix}, \quad \sigma_3 = \begin{pmatrix} 1 & 0 \\ 0 & -1 \end{pmatrix},$$

as well as the 2×2 diagonal nonlinearity matrix

$$F(\mathbf{q}) = \mathrm{diag}(g|q_1|^2 + \tilde{g}|q_2|^2, g|q_2|^2 + \tilde{g}|q_1|^2)\,, \tag{3}$$

equations (1) can be rewritten in a compact matrix form:

$$i\mathbf{q}_z = \mathscr{H}\mathbf{q} + F(\mathbf{q})\mathbf{q}. \tag{4}$$

2.2 Symmetries

At $F(\mathbf{q}) \equiv 0$, system (4) formally coincides with the simplest form of the dimensionless Schrödinger-Pauli equation for a spinor wavefunction of a quantum particle with spin, except that now z plays the role of time t. Respectively, $\mathscr{H}$ can be viewed as a non-Hermitian Hamiltonian acting on the two-component spinor $\mathbf{q}$ (this justifies the names for $\mathscr{H}$ and $\mathbf{q}$ used below). Bearing in mind this analogy we recall the basic symmetry operators (they can be found in textbooks on quantum mechanics, see e.g. [43]). The space inversion in 1D case (4) is given by $\mathscr{P}_x\mathbf{q}(x,z) = \mathbf{q}(-x,z)$ (the subscript x here specifies the coordinate which is inverted). In our case $\mathscr{P}_x$ commutes with the Hamiltonian (2): $[\mathscr{H}, \mathscr{P}_x] = 0$. The anti-linear time-reversal operator, which in the quantum mechanics corresponds to particles with integer-spin (i.e. to bosons), acts as $\mathscr{T}\mathbf{q}(x,z) = \mathbf{q}^*(x,-z)$. For stationary (i.e. $z-$independent) solutions it is simply $\mathscr{T} = \mathscr{K}$ where $\mathscr{K}$ is the complex conjugation: $\mathscr{K}\mathbf{q} = \mathbf{q}^*$. Both operators $\mathscr{P}_x$ and $\mathscr{T}$ have the properties $\mathscr{P}_x^2 = \mathscr{T}^2 = 1$.

The operator of complex conjugation $\mathscr{K}$ (and thus $\mathscr{T}$) defined above does not commute with $\mathscr{H}$. Meantime, an anti-linear operator commuting with the Hamiltonian can be constructed. Indeed, one verifies that $\sigma_1\mathscr{K}$ commutes with the Hamiltonian: $[\sigma_1\mathscr{K}, \mathscr{H}] = 0$. In order to give an interpretation of the symmetry defined by $\sigma_1\mathscr{K}$, we notice that σ_1 applied to $\mathscr{H}$ results in flipping of the waveguides $q_1 \leftrightarrow q_2$. This is the same as inversion of $y-$ coordinate: $y \to -y$ (see Fig. 1). Hence, one can identify σ_1 with the parity operator: $\mathscr{P}_y = \sigma_1$. Then the Hamiltonian $\mathscr{H}$ becomes $\mathscr{P}_y\mathscr{T}$-symmetric: $[\mathscr{P}_y\mathscr{T}, \mathscr{H}] = 0$, although it is not $\mathscr{P}_x\mathscr{T}$ symmetric, $[\mathscr{P}_x\mathscr{T}, \mathscr{H}] \neq 0$. The action of the operator $\mathscr{P}_x$ on the Hamiltonian (2) is trivial. Thus, in terms of the complete spatial inversion operator $\mathscr{P} = \mathscr{P}_x\mathscr{P}_y$ the Hamiltonian is also $\mathscr{P}\mathscr{T}$-symmetric: $[\mathscr{P}\mathscr{T}, \mathscr{H}] = 0$.

The inversion operator $\mathscr{P}_x$, however, acquires nontrivial meaning at least in two general cases. First, adding a term $V(x)\mathbf{q}$, where $V(x)$ is a scalar or matrix potential, to the Hamltonian, yields the equation

$$i\mathbf{q}_z = \mathscr{H}\mathbf{q} + V(x)\mathbf{q} + F(\mathbf{q})\mathbf{q}. \tag{5}$$

The added term breaks the $\mathscr{P}_x$ symmetry, unless $V(x)$ is an even function, i.e. unless $V(x) = V(-x)$. A real potential $V(x)$ does not break time reversal symmetry. Thus, if $V(x)$ is either scalar function or commute with σ_1, it does not break $\mathscr{P}_y$-symmetry, and model (5) remains partially $\mathscr{P}_y\mathscr{T}$ symmetric, but it is not fully $\mathscr{P}\mathscr{T}$-symmetric anymore. In such cases the symmetry is referred to as *partial-*$\mathscr{P}\mathscr{T}$ symmetry [29, 33, 58].

In the second case, the $\mathscr{P}_x$ symmetry is broken by the coupling. Two such systems will be considered in Sect. 9, where also there will be given another physical interpretation for the operator σ_1. In the first example of a spin-orbit coupled BEC (Sect. 9.1), $q_{1,2}(t)$ stand for macroscopic wavefunctions of different atomic states. In that case flipping $q_1 \leftrightarrow q_2$ is not related to inversion of spatial coordinates. Then σ_1 has close analogy with the charge operator $\mathscr{C}$ [30]. It appears more convenient to introduce separately three symmetry operators $\mathscr{P}$, $\mathscr{C}$, and $\mathscr{T}$ (rather than to define $\mathscr{C}\mathscr{P}$ as a new parity inversion operator, although this is possible too) and consider $\mathscr{C}\mathscr{P}\mathscr{T}$ symmetry. Each of the introduced symmetries can be broken without affecting the remaining ones, giving origin to $\mathscr{P}\mathscr{T}$, $\mathscr{C}\mathscr{T}$, and $\mathscr{C}\mathscr{P}$ models.

Finally, we have to clarify the formal meaning of $\mathscr{T}$ operator for a Cauchy problem, defined for $z > 0$, with initial condition at $z = 0$. This can be done by considering a map $\mathscr{T}\mathbf{q}(z) = \mathbf{q}^*(-z)$, provided that a solution existing in an interval $[0, z_0]$ with some $z_0 > 0$, can be extended to the symmetric interval $Z_0 = [-z_0, z_0]$. Then one can define a new vector-function $\mathbf{q}_{\mathscr{P}\mathscr{T}}(z) := \sigma_1\mathbf{q}^*(-z)$. The model (1) (or (4)) is said to obey $\mathscr{P}\mathscr{T}$-symmetry if for any its solution $\mathbf{q}(z)$ defined on the interval Z_0, the spinor $\mathbf{q}_{\mathscr{P}\mathscr{T}}(z)$ is a solution, as well [49].

2.3 Unbroken and Broken $\mathscr{P}\mathscr{T}$-Symmetric Phases

For experimental feasibility of a physical system, it is necessary to require that it is stable in the absence of perturbations, i.e. in the background state. For coupled NLS equations, from the mathematical point of view, this means that the zero solution is stable. Therefore, we start with the linear limit of (1), letting $g = \tilde{g} = 0$ (i.e. $F(\mathbf{q}) \equiv 0$ in Eqs. (4)). Without loss of generality we consider $\gamma, \kappa > 0$. To distinguish solutions of the linear system, below the respective fields and spectral parameters will be denoted by tildes. Thus we consider the system $i\tilde{\mathbf{q}}_z = \mathscr{H}\tilde{\mathbf{q}}$. Substitution of the ansatz $\tilde{\mathbf{q}} \sim e^{ibz+ikx}\mathbf{s}$, where $\mathbf{s}$ is a constant two-component column-vector, in this equation gives two branches $\tilde{b} = b_\pm$ of the dispersion (diffraction) relation:

$$b_\pm(k) = -k^2 \pm \sqrt{\kappa^2 - \gamma^2} = -k^2 \pm \kappa\cos\delta, \tag{6}$$

were the parameter δ is defined by the relations:

$$\sin\delta = \frac{\gamma}{\kappa}, \quad \cos\delta = \sqrt{1-\frac{\gamma^2}{\kappa^2}}, \qquad \delta \in \left[0, \frac{\pi}{2}\right]. \tag{7}$$

The respective eigenvectors $\mathbf{q}_\pm$ read:

$$\mathbf{q}_\pm \equiv \mathbf{s}_\pm e^{ib_\pm(k)z+ikx}, \quad \mathbf{s}_- = \frac{1}{\sqrt{2}}\begin{pmatrix} e^{i\delta} \\ 1 \end{pmatrix}, \quad \mathbf{s}_+ = \frac{1}{\sqrt{2}}\begin{pmatrix} -e^{-i\delta} \\ 1 \end{pmatrix}. \tag{8}$$

The background is stable, and hence supports propagation of linear waves, if $b_\pm(k)$ are real for all k, what happens if $\kappa > \gamma$. If $\kappa < \gamma$, $b_\pm(k)$ become a complex conjugate pair and the zero solution becomes unstable. These two cases are referred to as *unbroken* (real eigenvalues) and *broken* (complex eigenvalues) $\mathscr{P}\mathscr{T}$-symmetric phases, respectively, [6, 7]. The limiting case $\kappa = \gamma$ at which the phase transition occurs is called the *exceptional point* (EP) [31]. The latter is characterized by coalescence of the eigenvalues $b_\pm$ and eigenvectors $\mathbf{q}_\pm$. Indeed, in the EP $\delta = \pi/2$ and we obtain $b_\pm = -k^2$ and $\mathbf{s}_\pm = (i, 1)$.

At $\delta = 0$ the coupler is conservative. In that case, the eigenvectors $\mathbf{q}_-$ and $\mathbf{q}_+$ represent field distributions in the coupler arms which are correspondingly *symmetric* (in-phase, "−") and *antisymmetric* (out-of-phase "+"). Extending this terminology, accepted for conservative couplers [56], to $\mathscr{P}\mathscr{T}$-symmetric systems at $\delta > 0$ [10, 20, 21], the modes $\mathbf{q}_+$ and $\mathbf{q}_-$ will be referred to as antisymmetric and symmetric, respectively. (Note, that this terminology makes sense only for a fixed sign of the coupling; change $\kappa \to -\kappa$ is equivalent to multiplication of one of the field component by -1, or to the transformation $\mathbf{q} \to \sigma_3\mathbf{q}$, which changes the relative phase of the modes by π.)

For a nonzero δ, the non-Hermitian nature of the eigenvalue problem manifests itself in the non-orthogonality of the linear modes: $\mathbf{q}_+^\dagger\mathbf{q}_- \neq 0$. This enables energy transfer among modes during the propagation. In the EP the modes are self-orthogonal, meaning that $\mathbf{s}_\pm^T\mathbf{s}_\pm = 0$ at $\kappa = \gamma$.

The described scenario of the phase transition through the EP is most typical and is verified for majority of physical systems. However it is not the only one. A singular phase transition was found in Ref. [30] (it is described below in Sect. 9.1). Recently, a novel scenario of $\mathscr{P}\mathscr{T}$-symmetry breaking occurring through emergence of complex eigenvalues from continuous spectrum was discovered numerically in Ref. [59] and explained as splitting self-dual spectral singularity in Ref. [34].

Eigenvalues (8) can be obtained also by using the global rotation. To this end we consider the unbroken phase and introduce vector $\mathbf{Q}$ through the relation

$$\mathbf{q} = U\mathbf{Q}, \qquad U = \begin{pmatrix} e^{i\delta/2} & -e^{-i\delta/2} \\ e^{-i\delta/2} & e^{i\delta/2} \end{pmatrix}. \tag{9}$$

It is straightforward to verify that $\mathbf{Q}$ solves the system of equations

$$\begin{aligned} i\frac{\partial Q_1}{\partial z} &= -\frac{\partial^2 Q_1}{\partial x^2} + \kappa\cos(\delta)Q_1 + F_1(\mathbf{Q}), \\ i\frac{\partial Q_2}{\partial z} &= -\frac{\partial^2 Q_2}{\partial x^2} - \kappa\cos(\delta)Q_2 + F_2(\mathbf{Q}) \end{aligned} \tag{10}$$

where the nonlinearities are given by

$$\begin{aligned} F_1 &= \left[(g+\tilde{g})|Q_1|^2 + 2g|Q_2|^2\right]Q_1 \\ &\quad +(g-\tilde{g})Q_1^*Q_2^2 + 2i\sin(\delta)\left[\tilde{g}|Q_1|^2Q_2 - gQ_2^*Q_1^2\right], \\ F_2 &= \left[(g+\tilde{g})|Q_2|^2 + 2g|Q_1|^2\right]Q_2 \\ &\quad +(g-\tilde{g})Q_2^*Q_1^2 - 2i\sin(\delta)\left[\tilde{g}|Q_2|^2Q_1 - gQ_1^*Q_2^2\right]. \end{aligned}$$

System (10) has two advantages as compared with the original equations (4) for $\mathbf{q}$. First, its linear part is governed by the Hermitian Hamiltonian (it does not have gain or loss). This is a manifestation of the equivalence of a $\mathscr{P}\mathscr{T}$-symmetric Hamiltonian in the unbroken phase to a Hermitian Hamiltonian [44]. Second, linear coupling is absent in Eqs. (10). Thus one can readily find linear solutions. Even more importantly, in the nonlinear case one can look for "one-component" solutions $\mathbf{Q}_1 = (Q_1, 0)$ and $\mathbf{Q}_2 = (0, Q_2)$ with Q_j solving the standard NLS equation ($j = 1, 2$)

$$i\frac{\partial Q_j}{\partial z} = -\frac{\partial^2 Q_j}{\partial x^2} - (-1)^j\kappa\cos(\delta)Q_j + (g+\tilde{g})|Q_j|^2Q_j \tag{11}$$

In terms of the original variables $\mathbf{q}$, the solutions $\mathbf{Q}_{1,2}$ describe the symmetric and antisymmetric spinors

$$\mathbf{q}_- = \sqrt{2}e^{-i\delta/2}Q_1\mathbf{s}_-, \qquad \mathbf{q}_+ = \sqrt{2}e^{i\delta/2}Q_2\mathbf{s}_+. \tag{12}$$

3 On Global Existence of Solutions

Since we are dealing with a non-conservative nonlinear system, the first question to be addressed is the existence of solutions for a given class of initial data. Using the standard notation for the H^1-norm: $\|\mathbf{q}\|_{H^1} = \left[\int_{\mathbb{R}}\left(\mathbf{q}_x^\dagger\mathbf{q}_x + \mathbf{q}^\dagger\mathbf{q}\right)dx\right]^{1/2}$, one can prove the existence theorem (see [49], where a more general statement extending the result to non-$\mathscr{P}\mathscr{T}$-symmetric coupled NLS equations with gain and loss can be found, as well):

Theorem 1 *For any spinor* $\mathbf{q}^0 \in H^1(\mathbb{R}) \times H^1(\mathbb{R})$ *there exists a unique global solution* $\mathbf{q}(z) \in C(\mathbb{R}, H^1(\mathbb{R}) \times H^1(\mathbb{R}))$ *of system* (1) *with* $\kappa =$*const and* $\gamma =$*const, such that* $\mathbf{q}(z=0) = \mathbf{q}^0$.

This Theorem ensuring boundness of both components of the field $\mathbf{q}$ and of their derivatives at any finite distance z, however, does not forbid infinite growth of a solution on the semi-infinite real axis. It turns out, that subject to the additional requirement of equal SPM and XPM, i.e. at $g = \tilde{g}$, which often is referred to as Manakov nonlinearity [42]: $F(\mathbf{q}) \equiv g\mathbf{q}^\dagger\mathbf{q}$, boundness of the field at infinite propagation distance can be established. Using the definition of the L^2-norm

$$S_0 = \|\mathbf{q}\|_{L^2}^2 = \int_{\mathbb{R}} \mathbf{q}^\dagger\mathbf{q}dx = \int_{\mathbb{R}} \left(|q_1|^2 + |q_2|^2\right) dx, \tag{13}$$

the following statement can be proven [49]:

Theorem 2 *At* $g = \tilde{g}$, $\gamma =$*const,* $\kappa =$*const, and* $\gamma < \kappa$ *(unbroken* $\mathscr{P}\mathscr{T}$ *symmetry), for any global solution* $\mathbf{q}(z) \in C(\mathbb{R}, H^1(\mathbb{R}) \times H^1(\mathbb{R}))$ *of Theorem 1, there exists a constant* $S_{\max} > 0$ *such that* $\sup_{z\in\mathbb{R}} S_0(z) \leq S_{\max}$. *For* $\gamma \geq \kappa$ *(broken* $\mathscr{P}\mathscr{T}$ *symmetry), there exists a global solution of Theorem 1 such that* $\lim_{z\to\infty} S_0(z) = \infty$.

For the next consideration it is convenient to introduce the Stokes variables $S_j := \int_{\mathbb{R}} \mathbf{q}^\dagger\sigma_j\mathbf{q}dx$, or in the explicit form

$$\begin{aligned} S_1 &= \int_{\mathbb{R}} \left(q_1^* q_2 + q_2^* q_1\right) dx, \\ S_2 &= i\int_{\mathbb{R}} \left(q_2^* q_1 - q_1^* q_2\right) dx, \\ S_3 &= \int_{\mathbb{R}} \left(|q_1|^2 - |q_2|^2\right) dx. \end{aligned} \tag{14}$$

Proof (of Theorem 2) For $\kappa =$const, $\gamma =$const and $g = \tilde{g}$, using definitions (14), one straightforwardly computes from (1) that the Stokes component S_1 and the sum $\kappa S_0 + \gamma S_2 = Q$ are integrals of motion, i.e. they are z-independent quantities: $dS_1/dz = 0$ and $dQ/dz = 0$. The norm S_0 solves the equation

$$\frac{d^2 S_0}{dz^2} + 4(\kappa^2 - \gamma^2)S_0 = 4\kappa Q. \tag{15}$$

Thus, if $\kappa > \gamma$ (unbroken phase), S_0 oscillates with the "frequency" $2\kappa\cos\delta$. The amplitude of oscillations of $S_0(z)$ is computed from the initial conditions giving

$$S_{\max} = \left[\kappa Q + \sqrt{\left[S_0(0)(\kappa^2 - \gamma^2) - \kappa^2 Q\right]^2 + (\kappa^2 - \gamma^2)S_3^2(0)/4}\right] / (\kappa^2 - \gamma^2).$$

□

Growth of the norm S_0 is observed in the EP $\kappa = \gamma$ and in the broken phase $\kappa < \gamma$. However the character of the z-dependence is different: it is algebraic in the former case and exponential in the last case.

Thus the Manakov nonlinearity plays a special role. This can be understood by noting that such nonlinearity is $\mathscr{P}\mathscr{T}$-symmetric in accordance with the definition [62]:

$$[\mathscr{P}\mathscr{T}, F(\mathbf{q})] = 0 \quad \text{for any } \mathbf{q}. \tag{16}$$

In this case the balance between gain and loss, which is verified in the linear limit, is not broken by the nonlinear terms, unlike this happens for a general situation where $g \neq \tilde{g}$. We emphasize that in (16) the parity operator is applied to the matrix $F(\mathbf{q})$ as a whole, without affecting the components of $\mathbf{q}$ individually, in particular, $\mathscr{P}F(\mathbf{q})$ should not be confused with $\mathscr{P}F(\mathscr{P}\mathbf{q})$ where simultaneous $\mathscr{P}$ transformation of the column-vector $\mathbf{q}$ occurs. If

$$\mathscr{P}\mathscr{T}F(\mathbf{q})\mathbf{q} = F(\mathbf{q})\mathbf{q} \quad \text{for all } \mathscr{P}\mathscr{T}\text{ −symmetric } \mathbf{q} : \mathscr{P}\mathscr{T}\mathbf{q} = \mathbf{q} \tag{17}$$

the nonlinearity is termed *weakly* $\mathscr{P}\mathscr{T}$ symmetric. Clearly, if a nonlinearity is $\mathscr{P}\mathscr{T}$-symmetric, it is also weakly $\mathscr{P}\mathscr{T}$ symmetric.

4 Modulational Instability

Let us start the discussion of particular solutions of (1) with stability properties of a nonlinear plane wave having a finite amplitude ρ. Below this solution is referred to as a carrier wave (CW). From (12) one concludes that there exist symmetric and antisymmetric CWs. Here we address the modulational instability (MI) of these solutions, following Refs. [10, 12] (analysis of a more general case of CWs having different amplitudes can be found in [12]).

By noting that $\mathbf{s}_+(\pi - \delta) = \mathbf{s}_-(\delta)$, one can extend the interval of δ, beyond the one defined in (7), and consider $\delta \in [0, \pi]$. This allows to limit the investigation to only one spinor, say $\mathbf{q}_+$. To reduce the number of parameters in this Section we set $\kappa = 1$ (without loss of generality). Then the CW solution can be written down as follows

$$\mathbf{q}^{(\mathrm{cw})} = \rho\mathbf{s}_+ e^{ibz+ikx}, \qquad b = -k^2 - \rho^2(g + \tilde{g}) + \cos\delta. \tag{18}$$

Following the standard procedure, in order to study the stability of the CW one has to consider the evolution of its perturbation, i.e. the anstaz

$$\mathbf{q} = \mathbf{q}^{(\mathrm{cw})} + \left(\mathbf{u}e^{-i(\beta z-\lambda x)} + \mathbf{v}^* e^{i(\beta^* z-\lambda x)}\right) e^{ibz+ikx} \tag{19}$$

where the spinor components **u** and **v** are considered small constants: $|u_{1,2}|, |v_{1,2}| \ll \rho$, and λ and β are real and complex constants, respectively. Substituting (19) into system (1) and linearizing with respect to **u** and **v** one obtains *four* branches of the dispersion relation for the linear waves against the CW: $\beta = \beta_{1,2}^{\pm}$ where

$$\beta_1^{\pm}(\lambda) = 2k\lambda \pm \lambda\sqrt{\lambda^2 + 2\rho^2(g+\tilde{g})}, \tag{20}$$

$$\beta_2^{\pm}(\lambda) = 2k\lambda \pm \lambda\sqrt{\left(\lambda^2 + 2\cos\delta\right)\left[\lambda^2 + 2\cos\delta + 2\rho^2(g-\tilde{g})\right]}. \tag{21}$$

The first conclusion follows form Eq. (20). The CW is unstable if

$$g + \tilde{g} < 0, \tag{22}$$

i.e. both $\beta_1^{\pm}(\lambda)$ become complex for $|\lambda| < \sqrt{2}\rho|g+\tilde{g}|$. Condition (22) is not affected by presence of gain and loss. Thus it represents the conventional MI observed also for two coupled conservative NLS equations. The obtained result is expectable in view of the reduction (9), (10).

In presence of gain and loss new instability domains appear. It follows from (21) that $\beta_2^{\pm}(\lambda)$ are complex at sufficiently small λ if the system parameters are chosen such that

$$\cos\delta < \max\left\{0, \rho^2(\tilde{g}-g)\right\}. \tag{23}$$

Thus, independently on other parameters, the symmetric solutions, that now correspond to the parameter interval $\delta \in [\pi/2, \pi]$, are unstable. This instability is only due to gain and loss introduced in the system. Antisymmetric solution, $\delta \in [0, \pi/2]$, do not display this type of instability if the repulsive SPM is strong enough, compared with XPM, i.e. at $g > \tilde{g}$. Thus the MI of antisymmetric solutions is induced by the gain and loss only if $g < \tilde{g}$. A peculiarity of the instability in domain (23) is that for a given gain-and-loss coefficient γ (respectively, for a fixed δ) unstable waves have large amplitudes above some threshold, i.e. $\rho^2 > \cos(\delta)/(\tilde{g}-g)$, while MI in domain (22) occurs for arbitrary amplitude of the background (due to long-wavelength excitations). Meantime, there is overlap of instability domains (22) and (23) for the antisymmetric solutions, where both scenarios of MI can be observed. Figure 2 summarizes the analysis of MI domains on the plane $(g, \tilde{g})$. An interesting property, clearly seen the figure, is that the $\mathscr{P}\mathscr{T}$-symmetric nonlinearity, i.e. the Manakov nonlinearity $g = \tilde{g}$, similarly to an EP in the linear case, separates the regions of stable and unstable solutions (provided no conservative MI occurs, i.e. outside the domain (22)). This feature also correlates with the peculiar role of the Manakov nonlinearity in existence of nonlinear solutions discussed in Theorem 2 in the preceding Section. More detail description of different dynamical scenarios of MI can be found in Ref. [12].

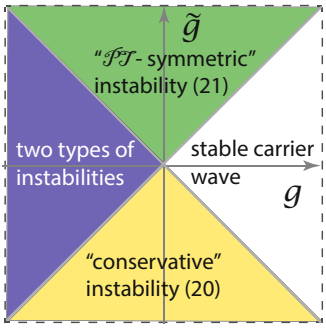

Fig. 2 Domains of MI of the antisymmetric carrier wave in the plane $(g, \tilde{g})$. Different colors denote "conservative" MI determined by (20), instability described by (21) and induced by $\mathscr{PT}$-symmetric gain and loss, as well as the domain where instabilities of both types exist. The empty domain corresponds to stable CWs

5 Vector Bright Soliton

Instability of a CW background indicates on possibility of existence of bright solitons. Particular solutions of this type in the "one-component" form (12) can be readily found in terms of the rotated variables (9), (10). Such solutions were studied for the case of zero XPM [2, 20, 21], $\tilde{g} = 0$, when it is necessary to require $g < 0$ to ensure (22), and in more general cases when both types of the nonlinearity are present [10]. Symmetric and anti-symmetric bright solitons in the last case, when condition (22) for MI is satisfied, are given by

$$\mathbf{q}_{\pm} = \frac{\eta\sqrt{2}}{\sqrt{|g+\tilde{g}|}\cosh\left(\eta x/\sqrt{2}\right)} e^{i\left(\cos\delta - \delta/2 + \eta^2/2\right)z}\mathbf{s}_{\pm}. \tag{24}$$

Here η is a positive constant which determines amplitudes and widths of the solitons.

Explicit expression (24) reveals an important feature: although the system is not conservative its localized nonlinear solutions belong to *continuous families*, like this usually happen in Hamiltonian systems and contrasting to typical dissipative systems (in the latter case dissipative solitons appear as isolated fixed points). For solution (24) such a family is parametrized by η. This is a general property of nonlinear $\mathscr{PT}$-symmetric systems (it will be obtained below also for other types of soliton solutions, including dark solitons (26) and solitons in the presence of dispersive coupling (49)).

Figure 3 shows examples of unstable (panels a and b) and stable (panel c) dynamics of solitons obtained in [10] by the direct numerical simulations of Eqs. (1). The stationary regime, shown in Fig. 3c, is achieved at very short distances even if a soliton is initially perturbed. Stable vector solitons do not display any energy transfer between the fields, since now $|q_1| = |q_2|$ (see Eq. (24)). Oppositely, energy transfer between the components q_1 and q_2 exists if an input pulse corresponds to

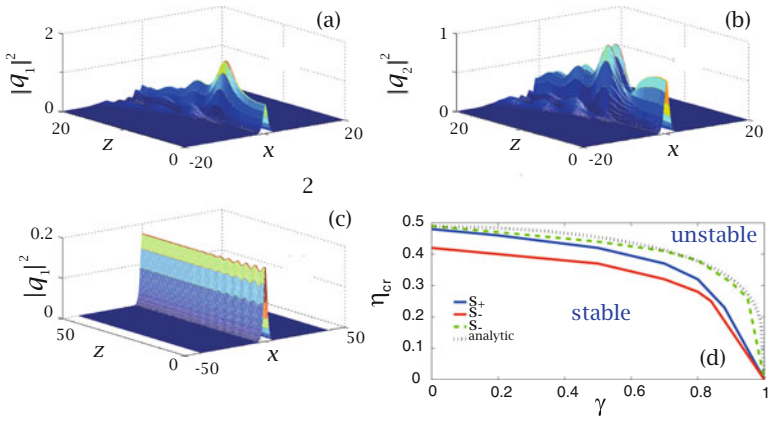

Fig. 3 Evolution of symmetric solitons. (**a**) and (**b**) Field intensities of an unstable soliton with $\eta = 0.6$ and $\delta = \arcsin(0.2)$. (**c**) Intensity of the first component of a stable soliton at $\eta = 0.3$ and $\delta = \arcsin(0.2)$ (after stabilization the second component has the intensity equal to that of the first component). The results are shown for $\tilde{g} = 1$, $g = -1.5$. (**d**) Boundaries of stability domains, denoted by $S_{\pm}$, for antisymmetric $\mathbf{q}_+$ and symmetric, $\mathbf{q}_-$ solitons (24) (blue and red lines respectively), as well as analytic curve (black dotted) for the stability estimate of $\mathbf{q}_+$ soliton, obtained for $\tilde{g} = -1$, $g = 0.5$. The green dashed line S_- shows the stability domain for $\mathbf{q}_-$ soliton for $\tilde{g} = 1$, $g = -1.5$. Solitons are stable (unstable) below (above) the respective curves

an unstable soliton. Intensities of such pulses can acquire values greatly exceeding the intensity of the input pulse, what is a consequence of the system to be not conservative (Fig. 3a, b).

Detail analysis of the stability has to be done numerically. Examples of the stability domains corresponding to different choices of SPM and XPM were obtained in [12]. They are shown in Fig. 3d. Solitons are stable for sufficiently small amplitudes. The threshold between stable and unstable domains decreases with the intensity of gain and loss. Thus, non-conservative effects (i.e. growing γ) reduce the domain of soliton stability. At the linear EP, i.e. at $\gamma = 1$ (recall that in this Section we have set $\kappa = 1$), solutions become unstable due to the instability of the zero background.

All curves displayed in Fig. 3d have similar shapes (the same is valid also for attractive SPM and XPM [10] and for zero XPM $\tilde{g} = 0$ [2, 21]). The numerical curves are also qualitatively similar and quantitatively close to the analytical estimate of the stability domain boundary (black dotted line in Fig. 3d). The latter was obtained by analyzing only perturbations which break the symmetry (e.g. antisymmetric solitons subject to symmetric perturbations) [21]. In the case at hand such analysis gives [10]

$$\eta_{cr}^2 = \frac{16(g+\tilde{g})\cos\delta}{\left(3\sqrt{-g-\tilde{g}}-\sqrt{7\tilde{g}-25g}\right)\left(\sqrt{-g-\tilde{g}}+\sqrt{7\tilde{g}-25g}\right)}. \tag{25}$$

Solitons are expected to be stable at $\eta < \eta_{cr}$. The curve $\eta_{cr}(\gamma)$ is illustrated in Fig. 3d (by the dotted line). It is situated above the actual stability domains. This is expectable, because expression (25) does not account for effect of perturbations that have the same symmetry as the symmetry of the soliton itself, and can become additional sources of instability.

Since in terms of the variables $\mathbf{Q}$, introduced by (9), the one-component solution is described by the conservative NLS equation, the system also possesses the whole set of solutions known for the NLS equation (see e.g. [24]). They include, breathers, multisoliton solutions, rogues waves (i.e. Peregrine solitons [50] studied for $\mathscr{P}\mathscr{T}$-symmetric coupled NLS equations in [10, 16]), etc. All these solutions are characterized by absence of energy exchange between the waveguides. More sophisticated "two-component" solutions where both $Q_{1,2} \neq 0$, in particular, breathers can also be constructed [5]. Such breathers can be stable and appear to be ubiquitous in problems of soliton interaction with localized defects as it is illustrated below in Sect. 7.

6 Vector Dark Solitons

If a finite amplitude CW background is stable, one can look for dark soliton solutions against it. For the backgrounds having equal amplitudes ρ of both components, these are solutions satisfying nonzero boundary conditions $|q_{1,2}| \to \rho$ at $x \to \pm\infty$. Like for stability of bright solitons it was necessary for a system to be in unbroken $\mathscr{P}\mathscr{T}$-symmetric phase, stability of dark solitons is possible only if the CW background is stable. Results of the respective analysis are shown in Fig. 4a in the plane $(g, -b)$. The CW background is stable either at $g > \tilde{g}$ (Fig. 4a) or at sufficiently small amplitudes $\rho < \rho^* = \cos(\delta)/2\tilde{g}$ (shown in the inset). In both regions the stability does not depend on a specific value of g. If $g < \tilde{g}$ or $\rho > \rho^*$ there appear instability domains (white regions in Fig. 4) either at small enough b (notice that the diagrams are shown for $-b$) or for sufficiently large amplitudes.

Considering stable backgrounds only, symmetric and antisymmetric vector dark solitons of the $\mathscr{P}\mathscr{T}$-symmetric NLS equations can be written in the form

$$\mathbf{q}_{\pm} = \frac{1}{\sqrt{2(g+\tilde{g})}}\left[iv - w\tanh\left(\frac{w}{2}(x - vz)\right)\right]e^{ibz}\mathbf{s}_{\pm} \tag{26}$$

where the velocity v and the depth of the background modulation w are related with the nonlinearity parameters: $w^2 + v^2 = 2(g+\tilde{g})\rho^2$.

The results of linear stability of a dark soliton at zero velocity $v = 0$, are shown in Fig. 4b (more detail discussion can be found in [12]). The whole domains shown in the main panel b and in the inset, correspond only to stable backgrounds. The stability of a soliton in the case of repulsive XPM in the region determined by $-\tilde{g} \leq g \leq g^*$, where g^* is some critical value (it is obtained numerically) shown by the vertical dashed line, coincides with the stability of the background. At $g > g^*$ there appears an instability domain whose size increases with g. Interestingly, the lower

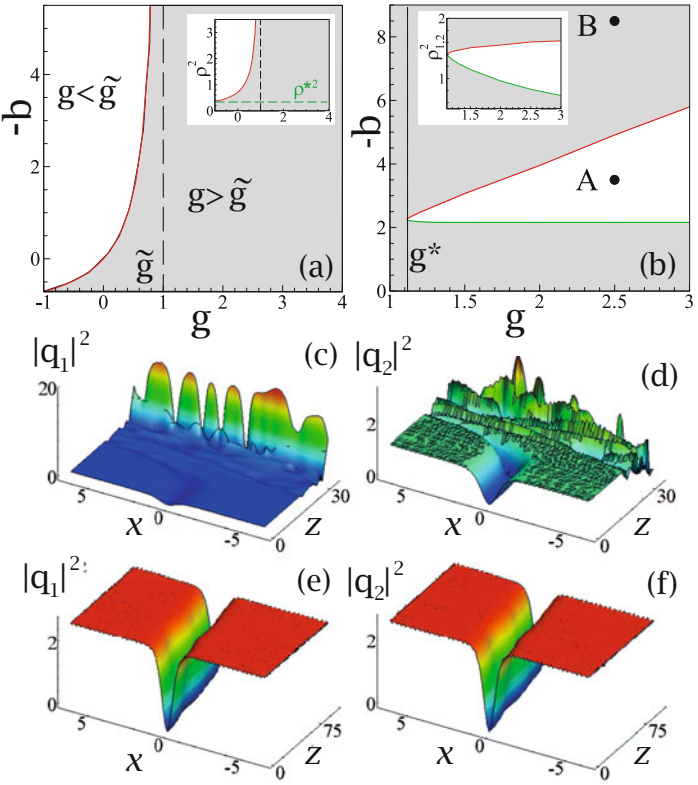

Fig. 4 (**a**) Domains of stability (shaded) and MI (white) of the CW with equal amplitudes of the components. The vertical dashed line shows the case $g = \tilde{g}$ while the left edge of the panels corresponds to $g + \tilde{g} = 0$ according to (22). The bottom edge is defined by $b = \cos\delta$. (**b**) The stability (shaded) and instability (white) domains for the zero velocity dark solitons against stable backgrounds. Both diagrams are shown in $(-b, g)$ plain, and in the (ρ, g) plane in the insets. In the inset of panels (**a**) and (**b**) $\tilde{g} = 1$. The vertical dashed line at g^* in panel (**b**) corresponds to the left edge of the inset. Panels (**c**) and (**d**) show the evolution of an unstable dark soliton for $g = 2.5$, $\tilde{g} = 1$, $b = -3.5$ and $\rho^2 \approx 1.2$ [indicated by point A in panel (**b**)]. Panels (**e**) and (**f**) show the evolution of a stable dark soliton for $g = 2.5$, $\tilde{g} = 1$, $b = -8.5$, and $\rho^2 \approx 2.633$ [indicated by point B in panel (**b**)]. In all panels $\gamma = \sin\delta = 0.7$.

edge on the instability domain (the green line) depends on the nonlinearity very weakly. Unstable solitons correspond to small propagation constants (large values of $-b$).

An example of the dynamics of an unstable dark soliton is shown in Figs. 4c, d. The instability of the soliton leads to growing irregular excitations of almost entire background, although the same background being homogeneous is modulationally stable. Figure 4e,f shows evolution of a stable dark soliton. Remarkably, the soliton can be viewed as stable even if dissipation and gain are not exactly balanced (say given by $-\gamma_1$ and γ_2, respectively, with $\gamma_1 \neq \gamma_2$). Then the system is not exactly

$\mathscr{P}\mathscr{T}$-symmetric any more, but it has net dissipation or gain, depending on the sign of $\gamma_1 - \gamma_2$. At initial stages of the evolution, such dissipation (or gain) leads only to weak decay (or growth) of the CW amplitude, nearly preserving the shape of a dark soliton [12].

7 Interaction of Solitons of $\mathscr{P}\mathscr{T}$-Symmetric NLS Equations with Defects

Now we turn to dynamics of solitons of coupled $\mathscr{P}\mathscr{T}$-symmetric NLS equations with varying parameters. As a first general comment, we notice, that if the nonlinearity in model (5) is given by $F(\mathbf{q}) = g\mathbf{q}^\dagger\mathbf{q}$, the term $V(x)\mathbf{q}$ with a scalar function $V(x)$, does not change the properties of the model with respect to rotations (9). Hence one-component solutions, of the type $\mathbf{Q} = (Q, 0)$, can be obtained from the single NLS equation. If additionally $V(x)$ is real, model (5) obeys $\mathscr{P}_y\mathscr{T}$-symmetry. Furthermore, if $\mathscr{H}$ in (5) is Hermitian and $V(x) = V^*(-x)$ the model obeys partial $\mathscr{P}_x\mathscr{T}$ symmetry (vector solitons in such model with periodic $V(x)$ were considered in [28]). If $\mathscr{H}$ and $V(x)$ obey the above symmetries, the system becomes fully $\mathscr{P}\mathscr{T}$-symmetric with $\mathscr{P} = \mathscr{P}_x\mathscr{P}_y$ (see Sect. 2.2).

In this Section we address two cases where the parameters are varying along the propagation direction, i.e. along $z-$axis. First, we consider gain and loss localized along $z-$axis, as illustrated in Fig. 1c. Second, we address interaction of a soliton with the localized defect of coupling like in the example shown in Fig. 1d. In literature, such problems were studied for localized modulations [1, 11], as well as, for periodic ones [20, 35]. For all cases considered below, an important requirement will be that in spite of spatial modulations locally, at a given z, the system obeys $\mathscr{P}_y\mathscr{T}$-symmetry.

7.1 Soliton Switch Using $\mathscr{P}\mathscr{T}$-Symmetric Defects

Consider a conservative coupler with gain and loss segments embedded in the first and second arms, respectively (as it is sketched in Fig. 1c). Such $\mathscr{P}\mathscr{T}$-symmetric defect is described by $z-$dependent gain-and-loss function $\gamma(z)$. It is centered a some propagation distance z_0 from the input and has length ℓ. The evolution equations for a pulse propagating along such coupler read [cf. (1)]:

$$\begin{aligned} i\frac{\partial q_1}{\partial z} &= -\frac{\partial^2 q_1}{\partial \tau^2} + i\gamma(z)q_1 + q_2 - |q_1|^2 q_1, \\ i\frac{\partial q_2}{\partial z} &= -\frac{\partial^2 q_2}{\partial \tau^2} - i\gamma(z)q_2 + q_1 - |q_2|^2 q_2. \end{aligned} \tag{27}$$

Without loss of generality, the coupling coefficient is set to be one: $\kappa = 1$.

We concentrate on the problem of switching of a localized input pulse between the coupler arms resulting from the interaction of the pulse with the defect [1]. To this end we consider the input signals for q_1 and q_2 fields to be different and having solitonic shapes

$$q_j^{(s)} = (-1)^j A_j \,\mathrm{sech}\,(\tau/T)\, e^{i\phi_j}, \qquad j = 1, 2. \tag{28}$$

The amplitudes $A_{1,2}$, the duration T (considered equal for both solitons), and the phases $\phi_{1,2}$ are treated as slow functions of the propagation distance z. Approximate equations governing these functions can be obtained using the Lagrangian approach, known for solitons in a conservative coupler [48]. The result is conveniently expressed in terms of the renormalized Stokes components $\tilde{S}_3 = -S_3(z)/S_0(z)$ and $\tilde{S}_0 = S_0(z)/S_0(z=0)$ [1]:

$$\begin{aligned} \frac{d\tilde{S}_3}{dz} &= -2\gamma(z)(1-\tilde{S}_3^2) + 2\sin(\phi)\sqrt{1-\tilde{S}_3^2}, & \frac{d\tilde{S}_0}{dz} &= -2\gamma(z)\tilde{S}_0\tilde{S}_3, \\ \frac{d\phi}{dz} &= \frac{S_0(z=0)}{3T}\tilde{S}_3\tilde{S}_0 - 2\tilde{S}_3\frac{\cos(\phi)}{\sqrt{1-\tilde{S}_3^2}}, & \frac{dT}{dz} &= 0. \end{aligned} \tag{29}$$

Figure 5 illustrates switch of an input signal $q_1(z=0) = 5/\cosh(5\tau/\sqrt{2})$, $q_2(z=0) = -20/\cosh(10\sqrt{2}\tau)$, which interacts with the defect $\gamma(z) = \gamma_0\{\arctan[5(z-3)] - \arctan[5(z-1.5)]\}$. The shown results are obtained from system (29) (the red dashed line) and from the direct numerical simulations of (27) (blue solid line) [1]. In terms of the Stokes variable switching corresponds to the change of sign of the sign $\tilde{S}_3$ (the lower curves) after interaction of the pulse with the defect (marked by the gray stripe). The normalized integral intensity $\tilde{S}_0$ changes slightly only in the defect region and remains practically unchanged, $\tilde{S}_0 \approx 1$, in the conservative parts of the coupler before and after the interaction. Thus, in terms of the original Stokes components, the solitonic switch performs the operation $[S_3]_{\text{input}} \to [-S_3]_{\text{output}}$.

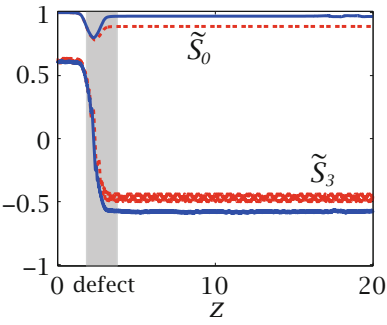

Fig. 5 Switching of an input solitonic signal (28) between the arms of coupler (27). The position of the defect is indicated by the vertical shaded stripe. The blue solid and red dashed curves show respectively the results of direct simulations of Eqs. (27) and the results obtained from approximate Eqs. (29)

The obtained switching is characterized by nonzero signals applied to both arms and, what is more important, accounts for dispersive effects. This distinguishes it from conventional linear switches using $\mathscr{P}\mathscr{T}$ symmetry but based on dispersionless couplers (i.e. τ-independent in our case) [37, 46]. The letter usually operates with the so-called bar and cross states [32], i.e. with the modes of the types $\mathbf{q}_{\rm bar} = (q, 0)^T$ and $\mathbf{q}_{\rm cross} = (0, q)^T$. Unlike in the cases of linear dispersionless switches, determining input characteristics of a signal which would result in a desired output signal, remains an unexplored subject. In this context, it is interesting to mentioned, that for a linear dispersionless $\mathscr{P}\mathscr{T}$-symmetric coupler it is possible to formulate an optimization problem, which leads to a quite unexpected prediction. For implementation of a linear switch with the minimal energy costs, the latter measured by the integral $\int_{z_0-\ell/2}^{z_0+\ell/2} \gamma(z)dz$, the coupler must operate in the EP regime [38]. In our case EP means that the $\mathscr{P}\mathscr{T}$-symmetric defect is characterized by $\gamma(z) = 1$, i.e. has much larger value than the one explored in the example shown in Fig. 5. For solitonic switches optimization problem was not considered, so far. However, the effect of a soliton scattering by an EP defect, achieved by modulation of the coupling, was already studied; it is described in the next subsection.

7.2 *Interaction of a Soliton with a Defect of Coupling*

Interaction of a vector soliton propagating in a $\mathscr{P}\mathscr{T}$-symmetric coupler with a localized defect of coupling, $\kappa_{\rm d}(z)$ (similar to one illustrated in Fig. 1d) is described by the following $\mathscr{P}\mathscr{T}$-symmetric NLS equations

$$\begin{aligned} i\frac{\partial q_1}{\partial z} &= -\frac{\partial^2 q_1}{\partial x^2} + iq_1 + \kappa_{\rm d}(z)q_2 - |q_1|^2 q_1, \\ i\frac{\partial q_2}{\partial z} &= -\frac{\partial^2 q_2}{\partial x^2} - iq_2 + \kappa_{\rm d}(z)q_1 - |q_2|^2 q_2. \end{aligned} \tag{30}$$

Below it will be assumed that the defect has the minimal value $\kappa_{\rm min}$ at $z = 0$, i.e. $\kappa_{\rm min} = \min_z\{\kappa_{\rm d}(z)\} = \kappa_{\rm d}(0)$, and tends to a constant value κ at $z \to \pm\infty$. Following Ref. [11] here we present the results of numerical simulations performed for the coupling of the from $\kappa_{\rm d}(z) = \kappa - (\kappa - \kappa_{min})\, e^{-z^2/\ell^2}$, where ℓ characterizes the width of the defect. In Fig. 6a, b and in Fig. 7a–d, illustrating the main results, location of the defect is outlined by the two horizontal lines. Respectively, the coupler input is located at negative z: $z_{\rm in} = -10$. The difference $\kappa - \kappa_{min}$ can be interpreted as the strengths of the defect, which can be either positive or negative depending on the local increase or decrease of the distance between the waveguides. In (30) without loss of generality we set $\gamma = 1$, i.e. $\kappa_{min} = 1$ corresponds to the EP.

If the defect is located far form the input of the coupler, one can launch a soliton (symmetric, $-$, or antisymmetric, $+$) $\mathbf{q}_\pm = 2\eta e^{i(\eta^2 \pm \kappa^2 \cos\delta)z} \mathrm{sech}(\eta x)\mathbf{s}_\pm$ having amplitude η, which freely propagates in absence of the defect.

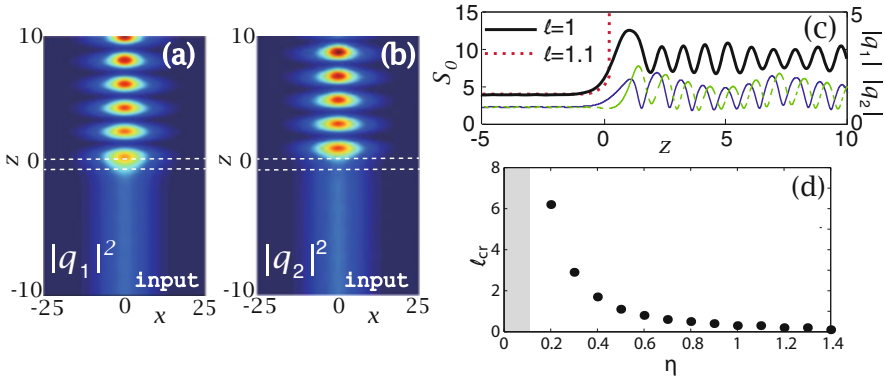

Fig. 6 (**a**), (**b**) Interaction of an antisymmetric soliton with the impurity for $\eta = 0.15$, $\kappa = 2$, and $\ell = 1$. The coupler input is situated at $z = -10$. (**c**) Evolution of the Stokes component S_0 for $\eta = 0.5$, $\kappa = 4$. Excitation of a breather at $\ell = 1 < \ell_{cr}$ and fast growth of the intensity at the critical length $\ell_{cr} = 1.1$ are shown by solid and dotted red lines, respectively. Amplitudes $|q_1|$ and $|q_2|$ are shown by solid blue and dashed green lines. (**d**) Dependence of the critical lengths of the defect on the soliton amplitude. In the gray domain at $\eta < \eta_{cr} \approx 0.1$ no "blow-up" solutions were found. In all cases $\kappa_{min} = 1$

Interaction of the antisymmetric soliton $\mathbf{q}_+$ with the EP defect is illustrated in Fig. 6a, b. The shown behavior is typical for dynamics when the length of the defect is below some critical value ℓ_{cr} (for the shown dynamics $\ell < \ell_{cr} \approx 7$), or alternatively if the soliton width $1/\eta$ is large enough, i.e. at $\eta < \eta_{cr}$ (for a given defect length). In these cases a soliton passes through the defect. However the interaction with the defect transforms it into a breather. Such breather is characterized by almost complete periodic energy transfer between the waveguides (cf. the intensity distributions in panels (a) and (b) of Fig. 6). The period is well approximated by $\pi/\sqrt{\kappa^2 - \gamma^2}$, that is the frequency of oscillations of S_0 obtained in (15). This last estimate is predictable since having passed the defect the pulse propagates in the homogeneous $\mathscr{P}\mathscr{T}$-symmetric coupler (this corresponds also to the breather frequency derived in [5]). If however, for a given soltion width η, the length of the defect is above ℓ_{cr}, i.e. $\ell > \ell_{cr}$, the soliton cannot overcome the defect; the field amplitude starts to grow very rapidly. This is reported in Fig. 6c. The solid (black) and dotted (red) lines show the evolution of $S_0(z)$ slightly below the critical length of the defect and at (numerically found) critical length ℓ_{cr}. While in the former case one observes creation of a breather, in the unstable case increase of the energy resembles collapsing behavior (which however is not the authentic blow up, see Sect. 3). Exchange of the energy between waveguides in the breather solution is also shown by solid blue and dashed green lines describing the field amplitudes Fig. 6c. Numerically obtained critical length ℓ_{cr} is a decaying function on the soliton amplitude (Fig. 6b). All solutions tested numerically for sufficiently small incident amplitudes, $\eta < \eta_{cr} \approx 0.1$, overpassed the defect and were transformed into breathers.

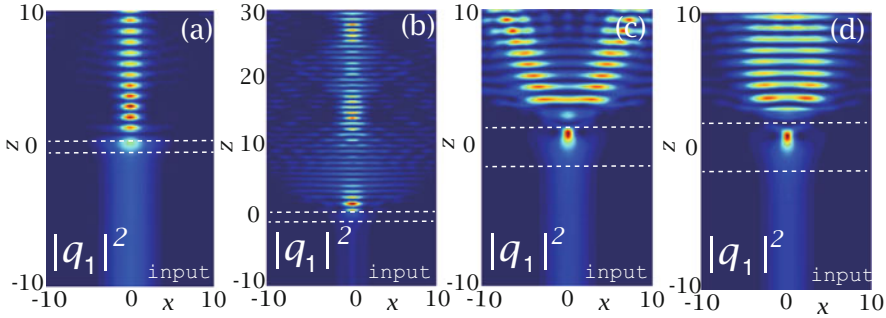

Fig. 7 Evolution of the intensity of the first field $|q_1|^2$ for $\eta = 0.5$ and (**a**) $\ell = 1.1$, (**b**) $\ell = 2.2$, (**c**) $\ell = 2.7$, and (**d**) $\ell = 3.4$. In all panels $\kappa_{\min} = 1$, $\kappa = 4$, and the horizontal dashed lines indicate the position of the defect having the length ℓ (corresponds to the distance between the dashed lines). For the chosen parameters $\ell_{cr} \approx 3.4$. The coupler input is located at $z = -10$

The existence of a critical length of a defect and a critical soliton amplitude, which separate dynamical regimes of breather excitations and growing amplitudes, are also obtained for symmetric solitons. Excitation of breathers, however, now has more different scenarios. In particular, four different types of patterns emerging from interaction of a soliton with the defect were found in [11]. They are shown in Fig. 7. By increasing the length of the defect one can observe generation of a single breather Fig. 7a (similar to one observed in Fig. 6a, b), a breather-like solution with repeating broadening in the transverse direction (Fig. 7b), soliton splitting in two out-propagating breathers (Fig. 7c), as well as a diffracting breather (Fig. 7d).

8 Four-Wave Mixing

An important features of $\mathscr{P}\mathscr{T}$-symmetric systems in the unbroken $\mathscr{P}\mathscr{T}$-symmetric phase, is the possibility of modifying dispersion relation (6) by varying the gain-and-loss coefficient γ. This opens novel possibilities for obtaining matching conditions necessary for resonant wave interactions. Thus, resonantly interacting waves can be manipulated by the strengths of gain and losses. In this section, following [57], we consider an example of four-wave mixing (FWM) in a $\mathscr{P}\mathscr{T}-$symmetric coupler described by the system

$$\begin{aligned} i\frac{\partial q_1}{\partial z} &= -\frac{\partial^2 q_1}{\partial x^2} + i\gamma q_1 + q_2 + |q_1|^2 q_1\,, \\ i\frac{\partial q_2}{\partial z} &= -\frac{\partial^2 q_2}{\partial x^2} - i\gamma q_2 + q_1 + |q_2|^2 q_2\,. \end{aligned} \tag{31}$$

Observation of FWM requires matching conditions for wavenumbers, k, $k_1 + k_2 = k_3 + k_4$, and for propagation constants, $b(k_1) + b(k_2) = b(k_3) + b(k_4)$,

which have to be satisfied simultaneously. It follows from dispersion relation (6) that coupler (31) admits three possibilities for both matching conditions to be satisfied. These cases (the left column) and the respective four-wave processes (the right column) can be summarized as follows:

$$b_-(k_1)+b_-(k_2)=b_+(k_3)+b_+(k_4),\quad \mathbf{q}_-[k_1]+\mathbf{q}_-[k_2]\leftrightarrow\mathbf{q}_+[k_3]+\mathbf{q}_+[k_4], \tag{32}$$

$$b_+(k_1)+b_+(k_2)=b_-(k_3)+b_+(k_4),\quad \mathbf{q}_+[k_1]+\mathbf{q}_+[k_2]\leftrightarrow\mathbf{q}_-[k_3]+\mathbf{q}_+[k_4], \tag{33}$$

$$b_-(k_1)+b_-(k_2)=b_-(k_3)+b_+(k_4),\quad \mathbf{q}_-[k_1]+\mathbf{q}_-[k_2]\leftrightarrow\mathbf{q}_-[k_3]+\mathbf{q}_+[k_4]. \tag{34}$$

Here the wavenumbers are indicated explicitly in the notation for the fields $\mathbf{q}$ (in square brackets) since they play an important role in the analysis and "$\leftrightarrow$" indicates modes which are converted in the FWM process.

Each of the processes in (32), (33), (34) involves energy transfer between two branches b_+ and b_-, since at least one symmetric and one antisymmetric modes have to be involved. Let $k_{1,2}$ are the input wavevectors. Then setting $\kappa=1$, one obtains the matching conditions for the emergent waveves (they correspond to (32), (33) and (34)):

$$k_3=\bar{k}\pm\sqrt{\Delta k^2+2\cos\delta}\,,\quad k_4=\bar{k}\mp\sqrt{\Delta k^2+2\cos\delta}, \tag{35}$$

$$k_3=\bar{k}\pm\sqrt{\Delta k^2-\cos\delta}\,,\quad k_4=\bar{k}\mp\sqrt{\Delta k^2-\cos\delta}\,, \tag{36}$$

$$k_3=\bar{k}\pm\sqrt{\Delta k^2+\cos\delta}\,,\quad k_4=\bar{k}\mp\sqrt{\Delta k^2+\cos\delta}\,. \tag{37}$$

where $\bar{k}=(k_1+k_2)/2$ and $\Delta k=(k_1-k_2)/2$. Importantly, $k_{3,4}$ in each of the processes involve the parameter δ. Thus by changing gain and loss one can change the wavenumbers of the outgoing waves. In the EP $\delta=\pi/2$ ($\gamma=1$) all these conditions degenerate because of coalescence of the eigenvectors. From (36) one can conclude that process (33) has a threshold: it is possible only for sufficiently large mismatch of the wavevectors of the input beam, i.e. at $|k_1-k_2|^2\geqslant 4\cos\delta$. No threshold exists for other two processes.

For the sake of illustration let us consider *degenerate* FWM process (32), $k_1=k_2=\bar{k}$. It corresponds to the transformation $2\mathbf{q}_-[\bar{k}]\rightarrow\mathbf{q}_+[k_3]+\mathbf{q}_+[k_4]$ (see [57] for more details and other examples). Due to Galilean invariance one can fix $\bar{k}=0$. Then the wavenumbers of output waves are computed as $k_4=-k_3=\sqrt{2\cos\delta}$, as it follows from (35).

In Fig. 8a it is shown how the mode $\mathbf{q}_-[k_1=0]$ having a slow Gaussian envelope $\sqrt{0.9\,u_0/(\sqrt{2\pi}\sigma)}\exp[-x^2/(4\sigma^2)]$, with $u_0=177$ and $\sigma=44$, at the input splits into two outgoing wavepackets, which emerge in process (32). To trigger the FWM,

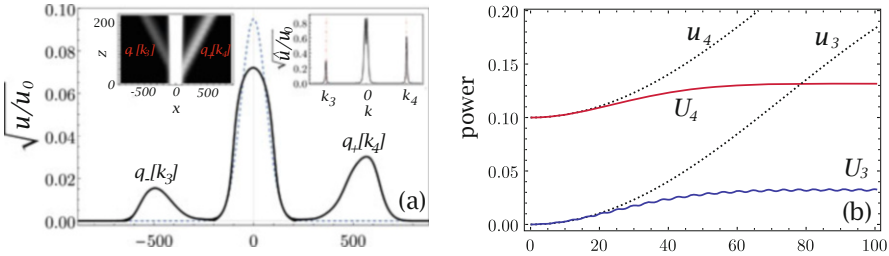

Fig. 8 (**a**) Split of an input source-beam with Gaussian envelope obtained numerically from (31). The central panel shows the normalized intensity, $u = |q_1|^2 + |q_2|^2$, with the input value $u_0 = 177$, at distance $z = 235$ in the direct space. Left upper inset shows the evolutions of beams in the direct space. Right inset shows the intensity distribution in the Fourier space, $\tilde{u}(k)$, at $z = 235$. Vertical red dashed-doted lines in the right inset indicate wavevectors of the generated beams: $k_3 = -\sqrt{\cos\delta}$ and $k_4 = \sqrt{\cos\delta}$. (**b**) Powers of the output beams U_3 and U_4 (solid blue and red lines) obtained by direct integration of Eqs. (31) are compared with the respective intensities obtained from the equations of the slowly varying approximations (39) (dotted lines). All results are obtained for $\gamma = 0.7$ ($\delta \approx \pi/4$). Note that the primary beam is not shown here

shown in the figure, one of the output beams was seeded with an input: $\mathbf{q}_+[\sqrt{2\cos\delta}]$ having the same Gaussian profile as the primary beam, but the amplitude of an order of magnitude smaller. The main panel of Fig. 8a shows the total beam intensity in the real space, $u(x) \equiv |q_1(x)|^2 + |q_2(x)|^2$, at some distance after the separation of the beams k_3 and k_4. The intensities in the Fourier space, $\hat{u}(k) \equiv |\hat{q}_1(k)|^2 + |\hat{q}_2(k)|^2$, where $\hat{q}_j(k)$ is the Fourier transform of the field $q_j(x)$, are shown in the right inset. The left inset illustrates the dynamics of beam splitting.

The initial stages of the evolution of a FWM can be qualitatively described in the approximation of slowly varying amplitudes. In our case this corresponds to the ansatz

$$\mathbf{q}(z, x) = 2a_1(z)e^{-i\delta}\mathbf{q}_-[k_1] + a_3(z)\mathbf{q}_+[k_3] + a_4(z)\mathbf{q}_+[k_4], \tag{38}$$

where $a_{1,3,4}(z)$ are slowly varying amplitudes. Substituting this expression in Eqs. (31) and projecting over $\mathbf{q}_\pm^*$ we derive the equations for the amplitudes:

$$\begin{aligned} i\frac{da_1}{dz} &= a_3a_4a_1^* + \left(\frac{u_1}{2} + u_3 + u_4\right)a_1, \\ i\frac{da_3}{dz} &= 2a_1a_1a_4^* + \left(u_1 + \frac{u_3}{2} + u_4\right)a_3, \\ i\frac{da_4}{dz} &= 2a_1a_1a_3^* + \left(u_1 + u_3 + \frac{u_4}{2}\right)a_4. \end{aligned} \tag{39}$$

It follows from Eqs. (39) that in degenerate FWM process (32) the total power, given by $u_{\text{tot}} = u_1 + u_3 + u_4$, where $u_1 = 4|a_1|^2$ and $u_{3,4} = |a_{3,4}|^2$, is conserved, $du_{\text{tot}}/dz = 0$. However, this conservation, representing the well-known Manley-Rowe relation, is a result of the slowly varying amplitude approximation. Equations (39) describe well only the initial stage of the evolution; they fail for

short pulses considered at longer times. This is illustrated in Fig. 8b where the evolution of the intensities $u_{3,4}$ obtained from system (39) is compared with the evolution of the total normalized energies of the generated beams computed as $U_j = \int |q_j|^2 dx / \int \left(|q_1|^2 + |q_2|^2\right) dx$ from the coupled $\mathscr{PT}$-symmetric NLS equations (31).

9 $\mathscr{CPT}$-Symmetric Coupled NLS Equation

In all examples considered so far, coupled NLS equations were $\mathscr{P}_y\mathscr{T}$-symmetric. Since such systems possess also the trivial $\mathscr{P}_x$ symmetry, they were also $\mathscr{PT}$ symmetric (see discussion in Sect. 2.2). Now we consider two examples of fully $\mathscr{PT}$-symmetric models which do not obey $\mathscr{P}_y\mathscr{T}$ and $\mathscr{P}_x$ symmetries. In alternative interpretation, such systems are $\mathscr{CPT}$-symmetric.

9.1 Spin-Orbit Coupled Bose-Einstein Condensate

First, we consider a spin-orbit (SO) coupled BEC [26, 36] which is described by the spinor $\Psi = (\Psi_\uparrow, \Psi_\downarrow)^T$, where $\Psi_\uparrow$ and $\Psi_\downarrow$ are macroscopic wavefunctions of the hyperfine atomic states. It is assumed that atoms are permanently added in the state $\Psi_\downarrow$, and simultaneously removed from the state $\Psi_\uparrow$. Such SO-BEC is governed by a non-Hermitian Hamiltonian whose linear part reads

$$\mathscr{H}_{\rm SOC} = -\frac{1}{2}\frac{\partial^2}{\partial x^2} + \omega\sigma_1 + i\kappa\sigma_1\frac{\partial}{\partial x} + i\gamma\sigma_3 + V(x). \tag{40}$$

Here ω is the strength of the linear coupling resulting from the Zeeman field, κ is the strength of the SO coupling, $\gamma > 0$ accounts for loading and eliminating atoms, and $V(x)$ is the trap potential. The two-body interactions are modeled by the Manakov nonlinearity $F(\mathbf{\Psi}) \equiv g\mathbf{\Psi}^\dagger\mathbf{\Psi}$ [36]. The Gross-Pitaevskii equation describing SO-BEC acquires the form (4), which in the new variables reads $i\mathbf{\Psi}_t = \mathscr{H}_{\rm SOC}\mathbf{\Psi} + F(\mathbf{\Psi})\mathbf{\Psi}$. Below we overview some of the results on this model obtained in [30].

When dissipation and gain are absent, $\gamma = 0$, Hamiltonian (40) is $\mathscr{P}_x\mathscr{T}$ symmetric. When there is no SO coupling, $\kappa = 0$, Hamiltonian (40) is $\sigma_1\mathscr{T}$ symmetric. Flipping of the spinor components, $\Psi_\uparrow \leftrightarrow \Psi_\downarrow$, executed by the matrix σ_1, corresponds to inversion of population of the hyperfine states, rather than to space inversion discussed in Sect. 2.2. Interpreting the states $\Psi_\uparrow$ and $\Psi_\downarrow$ as having positive, ϵ, and negative, $-\epsilon$, energies with respect to average chemical potential μ (i.e. having chemical potentials $\mu \pm \epsilon$), one observes that σ_1, has similarity with the charge operator. Therefore, one can refer to σ_1 as to a $\mathscr{C}$ operator, denoting $\mathscr{C} = \sigma_1$. So defined $\mathscr{C}$ operator obeys the basic properties of the charge: $\mathscr{C}^2 = 1$, $[\mathscr{C}, \mathscr{PT}] = 0$, and the eigenvalues of $\mathscr{C}$ are ± 1.

There is an additional reason to use separately $\mathscr{C}$ and $\mathscr{P}$ operators (rather than redefine the parity operator $\mathscr{P} \to \sigma_1 \mathscr{P}$ corresponding to $\mathscr{P} = \mathscr{P}_x \mathscr{P}_y$ discussed above for optical systems). In typical experimental setups with SO-BECs the coefficients ω, κ, and γ, as well as the external trap $V(x)$, are controlled by laser beams. Any of this factors can be excluded from the dynamics, and thus, the symmetry $\mathscr{C}\mathscr{P}\mathscr{T}$ can be transformed in $\mathscr{P}\mathscr{T}$ or in $\mathscr{C}\mathscr{T}$ symmetries. At all parameters γ, ω and κ different from zero, the system does not posses partial symmetries, but is $\mathscr{C}\mathscr{P}\mathscr{T}-$symmetric: $[\mathscr{C}\mathscr{P}\mathscr{T}, \mathscr{H}_{\rm SOC}] = 0$. For discussion of a different definition of the operator $\mathscr{C}$ used for the internal product in the proper Hilbert space see [6]. Yet another definition of the $\mathscr{C}$ operator for a two-component system with gain and losses was used in [19].

One of the most interesting features, introduced by $\mathscr{C}\mathscr{P}\mathscr{T}$-symmetry is a novel scenario of $\mathscr{C}\mathscr{P}\mathscr{T}$-symmetry phase breaking. In order to describe this phenomenon, let us consider the linear eigenvalue problem $\tilde{\mu}\tilde{\boldsymbol{\psi}} = \mathscr{H}_{\rm SOC}\tilde{\boldsymbol{\psi}}$ where $\tilde{\mu}$ is the spectral parameter. Unlike in the cases described above, where the $\mathscr{P}\mathscr{T}$-symmetry breaking was determined by only one parameter which was the relation between gain (loss) and the coupling, the $\mathscr{C}\mathscr{P}\mathscr{T}$-symmetric Hamiltonian (40) is characterized by *two* parameters controlling the phase transition. The first parameter, ω/γ describes atom transformation between two hyperfine states due to the linear coupling ω. This type of coupling was present in all above examples. SO coupling κ, introduces a new parameter $\kappa/(\gamma\ell)$. A peculiarity of this second parameter is that the SO coupling depends on the characteristic scale of the wave-function ℓ determined by the relation: $|\partial\Psi_{\uparrow,\downarrow}/\partial x| \sim |\Psi_{\uparrow,\downarrow}|/\ell$. This has important consequences, which we illustrated below on an exactly solvable example [30].

Consider a SO-BEC loaded in a toroidal trap without any additional potential, $V(x) \equiv 0$. Assume that the trap is sufficiently narrow in the transverse direction and has the length ℓ. Thus $\boldsymbol{\psi}(x) = \boldsymbol{\psi}(x+\ell)$. This cyclic boundary condition plays the role of an external trap which limits the length of the condensate in space. Now the chemical potential can be computed exactly as $\tilde{\mu} = \mu_{n,\pm}$ where

$$\mu_{n,\pm} = 4\pi^2 n^2/(2\ell^2) \pm \sqrt{(\omega - 2\pi n\kappa/\ell)^2 - \gamma^2}, \qquad n = 0, \pm 1, \ldots \tag{41}$$

Since the sign of ω is irrelevant, we consider it positive. If $\omega < \gamma$ the zero mode $\mu_{0,\pm}$ is unstable at least for $n = 0$. Thus, the unbroken phase may exist only for $\omega > \gamma$, what in articular, is verified for $\kappa = 0$. However, for nonzero SO coupling the spontaneous phase breaking can occur if $\kappa > 0$. More specifically, the $\mathscr{C}\mathscr{P}\mathscr{T}$ symmetry is broken if there exists an integer n belonging to the interval: $(\omega - \gamma)\ell/2\pi\kappa < n < (\omega + \gamma)\ell/2\pi\kappa$. This means that arbitrarily small $\kappa > 0$ results in the symmetry breaking, provided all other parameters remain unchanged. Moreover, at $\kappa \to 0$ the number of unstable modes, i.e. number of integers in the above interval, tends to infinity. In Ref. [30] this phenomenon was termed as a *singular phase transition*.

Let now SO coupling κ is fixed. For sufficiently large κ, such that $\kappa > \gamma\ell/\pi$, and varying ω there appear *alternating domains* of broken and unbroken $\mathscr{C}\mathscr{P}\mathscr{T}$ symmetry. Broken symmetry domains correspond to $2\pi n\kappa/\ell - \gamma < \omega < 2\pi n\kappa/\ell +$

γ, $(n = 1, 2, \ldots)$. Thus when linear coupling grows the system subsequently enters and leaves the unbroken phase. This phenomenon is referred to as the *re-entrant* $\mathscr{CPT}$-symmetric phase.

The described properties of $\mathscr{CPT}$-symmetric phases of the SO-BEC in a toroidal trap are generic and can also be observed for other types of trap potentials $V(x)$, say in parabolic traps. For detail study of this latter case, as well as for description of the properties of the nonlinear modes in $\mathscr{CPT}-$symmetric systems we refer to [30].

9.2 Dispersive Coupled Waveguides

An analog of SO coupling in BECs can be obtained in optical waveguide systems. Consider a coupler illustrated in Fig. 1a with coupling characterized by the intermodal dispersion [15]. Such coupling can be modeled by the operator [14]

$$K = \kappa_0 + i\kappa_1\partial_\tau - \kappa_2\partial_\tau^2, \tag{42}$$

with real constants $\kappa_{0,1,2}$ characterizing dispersionless coupling (κ_0), as well as first (κ_1) and second (κ_2) orders of dispersion of coupling. The equations describing pulse propagation in such device read (cf. Eq. (1))

$$\begin{aligned} i\frac{\partial q_1}{\partial z} &= -\frac{\partial^2 q_1}{\partial \tau^2} + i\gamma q_1 - Kq_2 - 2|q_1|^2 q_1, \\ i\frac{\partial q_2}{\partial z} &= -\frac{\partial^2 q_2}{\partial \tau^2} - i\gamma q_2 - Kq_1 - 2|q_2|^2 q_2. \end{aligned} \tag{43}$$

$\mathscr{CPT}$-symmetric system (43) was introduced and studied in Ref. [61]. Here we recall some of the obtained results focusing only on the case $\kappa_{0,1} > 0$.

The dispersion relation for the linear modes of Eq. (43) has two branches (obtained by the ansatz $\tilde{\mathbf{q}} \propto e^{ib_z - i\omega\tau}\mathbf{s}$ where $\mathbf{s}$ is a constant column-vector):

$$\tilde{b}_{1,2} = -\omega^2 \pm (\hat{K}^2(\omega) - \gamma^2)^{1/2}, \qquad \hat{K}(\omega) = \kappa_2\omega^2 + \kappa_1\omega + \kappa_0. \tag{44}$$

An example of these brunches is shown in Fig. 9a.

The $\mathscr{CPT}$ symmetry is unbroken if $\gamma < \kappa_0 - \kappa_1^2/(4\kappa_2)$. This condition can be satisfied only for sufficiently strong dispersion of the coupling: $\kappa_2 > \kappa_1^2/(4\kappa_0)$, allowing one to consider rotation (cf. (9))

$$\hat{\mathbf{p}} = S^{-1}\hat{\mathbf{q}}, \qquad S(\omega) = \begin{pmatrix} e^{-i\alpha(\omega)} & -e^{i\alpha(\omega)} \\ e^{i\alpha(\omega)} & e^{-i\alpha(\omega)} \end{pmatrix}, \quad \alpha(\omega) = \frac{1}{2}\arcsin\left[\frac{\gamma}{\hat{K}(\omega)}\right], \tag{45}$$

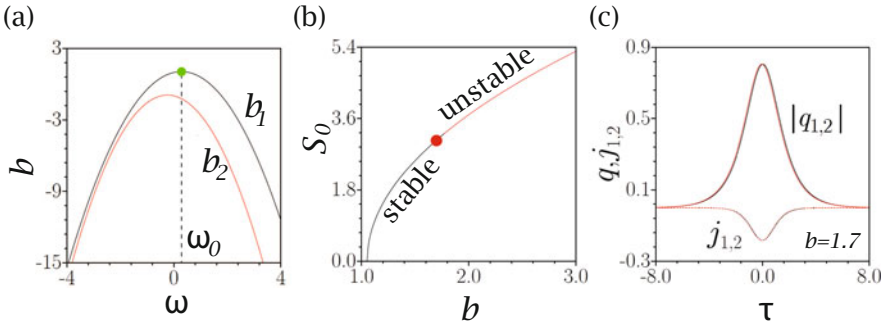

Fig. 9 (**a**) Two branches of the dispersion relation (44) in the unbroken phase. The green dot indicates the maximum of b at ω_0 from which small amplitude solitons (49) bifurcate. (**b**) A family of solutions on the diagram (b, S_0) (where S_0 is defined in (13)). Stable (black) and unstable (red) parts are indicated. The red dot corresponds to the soliton shown in (**c**). (**c**) Example of a quiescent soliton at $b = 1.7$. The amplitudes of the components and currents are shown. In all panels $\kappa_{\{0,1,2\}} = \{1, 0.5, 0.1\}$ and $\gamma = 0.2$

which is applied now to the Fourier transform of the field: $\hat{q}_n = \int_{-\infty}^{\infty} q_n e^{i\omega\tau} d\tau$. In the case at hand, the Fourier space is more convenient because of the nonlocality of the coupling. If the matching conditions for resonant FWM are not satisfied, i.e. no resonant excitations of higher harmonics occurs, one can look for an (approximate) solution in the "one-component" form $\hat{p}_j(\omega) \neq 0$ and $\hat{p}_{3-j}(\omega) \equiv 0$ where $j = 1, 2$ (by analogy with one-component **Q** solutions considered in the previous sections). In this approximation one obtains the integral NLS equation in the Fourier space (presented here for $j = 1$)

$$\frac{\partial \hat{p}_1(\omega)}{\partial z} = ib_1 \hat{p}_1(\omega) + i \iint d\omega_1 d\omega_2 G(\omega, \omega_1, \omega_2) \hat{p}_1(\omega_1) \hat{p}_1(\omega_2) \hat{p}_1^*(\omega_1 + \omega_2 - \omega), \tag{46}$$

where

$$G(\omega, \omega_1, \omega_2) = \frac{\cos\left[\alpha(\omega_1) + \alpha(\omega_2) - \alpha(\omega_1 + \omega_2 - \omega) + \alpha(\omega)\right]}{2\pi^2 \cos[2\alpha(\omega)]}.$$

It is to be mentioned that Eq. (46) remains valid for a more general nonlocal coupling of the form $Kq = \int \mathscr{K}(\tau - t) q(t) dt$ where $\mathscr{K}(\tau)$ is a localized function.

In spite of the approximate character Eq. (46) allows to obtain an *exact* solution of the original system (43): $\hat{p}_1 = \sqrt{2}\pi A e^{i[b_1(\Omega) + |A|^2]z} \delta(\omega - \Omega)$ where A and Ω are arbitrary amplitude and frequency. This solution is the plane wave

$$q_{1,2} = \frac{A}{\sqrt{2}} e^{i[b_1(\Omega) + |A|^2]z - i\Omega\tau \mp i\alpha(\Omega)} \tag{47}$$

in the real space.

Turning to spatially localized solutions, *families* of quiescent solitons, $q_n = e^{ibz}w_n(\tau)$, which are characterized by the continuous dependence of the total power S_0 on the propagation constant b, they can be obtained numerically (definition of S_0 given in (13) remains valid here, with substitution of x by τ). In Fig. 9b we show an example of a soliton family. A representative shape of a stable soliton solution is shown in Fig. 9c. The shown family is stable for sufficiently small amplitudes of solitons (they correspond to small propagation constants b). When soliton amplitude increases, instability emerges from the continuous spectrum. For the example in Fig. 9b this occurs at $b \approx 1.78$. An interesting effect of the dispersive coupling is the existence of the internal energy flow (current) $j_n = |q_n|^2(\arg q_n)_\tau$ accompanying solitons in each waveguide. An example of such currents is illustrated in Fig. 9c.

Bifurcations of soliton families from the linear spectrum occurs from the top of the upper branch of the spectrum, denoted below as ω_0 (it is shown by the green dot in Fig. 9a), such that $b_1'(\omega_0) = 0$ (hereafter $b_j'(\omega) \equiv \partial b_j/\partial\omega$). In order to construct small-amplitude solitons one considers $\hat{p}_1(\omega)$ to be a small function well-localized around $\omega = \omega_0$. Expanding Eq. (46) in powers of $\omega - \omega_0$ and calculating the inverse Fourier transform, one obtains the NLS equation in the real space

$$\frac{\partial p_1}{\partial z} = i\left(b_1 + \frac{\omega_0^2 b_1''}{2}\right)p_1 + \omega_0 b_1''\frac{\partial p_1}{\partial \tau} - \frac{ib_1''}{2}\frac{\partial^2 p_1}{\partial \tau^2} + 2i|p_1|^2 p_1. \tag{48}$$

The soliton solution of Eq. (48) has the form $q_n = e^{ibz}w_n(\tau)$ and is characterized by the amplitude η:

$$q_{1,2} = \eta\frac{\exp\left\{i[\eta^2 + b_1(\omega_0)]z - i\omega_0\tau \mp i\alpha(\omega_0)\right\}}{\cosh\left[\eta(2/|b_1''(\omega_0)|)^{1/2}\,(\tau \pm \alpha'(\omega_0))\right]}. \tag{49}$$

From this expression we conclude that the combined effect of the gain, loss, and dispersive coupling introduces temporal shift $2\alpha'(\omega_0)$ between the soliton components, as well as non-zero energy currents j_n in the soliton components (Fig. 9c) which can be estimated from Eq. (49) as $j_n \approx -\omega_0|q_n|^2$.

10 Coupled NLS Equations as a Cascading Limit of a $\mathscr{P}\mathscr{T}$-Symmetric $\chi^{(2)}$ Coupler

Further extension of the $\mathscr{P}\mathscr{T}$-coupled NLS models can be obtained as the cascading limit [55] of the $\chi^{(2)}$-coupler, studied in [47]:

$$
\begin{aligned}
i\frac{\partial u_1}{\partial z} &= -\frac{\partial^2 u_1}{\partial x^2} + \kappa_1 u_2 - 2u_1^* v_1 + i\gamma_1 u_1,\\
i\frac{\partial v_1}{\partial z} &= -\frac{1}{2}\frac{\partial^2 v_1}{\partial x^2} + \kappa_2 v_2 - u_1^2 - \beta v_1 + i\gamma_2 v_1,\\
i\frac{\partial u_2}{\partial z} &= -\frac{\partial^2 u_2}{\partial x^2} + \kappa_1 u_1 - 2u_2^* v_2 - i\gamma_1 u_2,\\
i\frac{\partial v_2}{\partial z} &= -\frac{1}{2}\frac{\partial^2 v_2}{\partial x^2} + \kappa_2 v_1 - u_2^2 - \beta v_2 - i\gamma_2 v_2.
\end{aligned}
\tag{50}
$$

Here u_j and v_j are the dimensionless field components of the fundamental fields (FFs) and second harmonics (SHs), respectively, in the j-th arm of the coupler ($j = 1, 2$), κ_1 and κ_2 are the coupling coefficients of the FFs and SHs, respectively, γ_1 and γ_2 are the gain (loss) coefficients of the FF and SH in the first (second) waveguides, and β is the mismatch of the propagation constants. System (50) describes the diffraction in a planar coupler, similar to one illustrated in Fig. 1b, where each of the slabs possesses $\chi^{(2)}$ nonlinearity.

The $\mathscr{P}\mathscr{T}$-symmetry of systems (50) is described by the transformations of the four-component column-vector $\psi = (u_1(x,z), v_1(x,z), u_2(x,z), v_2(x,z))^T$ defined by the time reversal operator $\mathscr{T}$: $\mathscr{T}\psi(x,z) = \psi^*(x,-z)$ and by the "permutation" operator

$$
\mathscr{P} = \sigma_1 \otimes \sigma_0 = \begin{pmatrix} 0&0&1&0\\ 0&0&0&1\\ 1&0&0&0\\ 0&1&0&0 \end{pmatrix}. \tag{51}
$$

The latter can be viewed as a generalization of $\mathscr{P}_y$ and $\mathscr{C}$ operators introduced in Sect. 2.2 and in Sect. 9.1, respectively.

$\mathscr{P}\mathscr{T}$-symmetric solutions of system (50) of a general type, i.e. modes satisfying $\mathscr{P}\mathscr{T}\psi = \psi$, are described in [47]. Here we concentrate on the cascading limit, which in conservative $\chi^{(2)}$ systems is defined by the requirement $|\beta| \gg 1$ [55]. In the $\mathscr{P}\mathscr{T}$-symmetric case, due to presence of gain and loss, the condition for cascading limit is more general; it reads $|\Delta| \gg 1$, where $\Delta = \beta^2 + \gamma_2^2 - \kappa_2^2$. Thus the cascading limit can be achieved not only by means of a large mismatch of the propagation constants, but also at strong coupling κ_2 or at a large gain-and-loss coefficient γ_2 of the SHs. In this limit, one can neglect the second derivatives of the SHs, and express the functions $v_{1,2}$ through the FFs:

$$
v_1 \approx -\frac{(\beta + i\gamma_2)u_1^2 + \kappa_2 u_2^2}{\Delta}, \qquad v_2 \approx -\frac{(\beta - i\gamma_2)u_2^2 + \kappa_2 u_1^2}{\Delta}. \tag{52}
$$

Using these relations in the equations for the FFs one obtains coupled $\mathscr{P}\mathscr{T}$-symmetric NLS equations

$$\begin{aligned} iu_{1,z} &= -u_{1,xx} + \kappa_1 u_2 + i\gamma_1 u_1 + \frac{2(\beta + i\gamma_2)}{\Delta}|u_1|^2 u_1 + \frac{2\kappa_2}{\Delta}u_1^* u_2^2, \\ iu_{2,z} &= -u_{2,xx} + \kappa_1 u_1 - i\gamma_1 u_2 + \frac{2(\beta - i\gamma_2)}{\Delta}|u_2|^2 u_2 + \frac{2\kappa_2}{\Delta}u_2^* u_1^2. \end{aligned} \tag{53}$$

This is a $\mathscr{P}\mathscr{T}$-symmetric coupler with effective complex SPM and additional FWM term resulting from the coupling of the FFs with SHs. It is to be emphasized that the nonlinearity in (53) is weakly $\mathscr{P}\mathscr{T}$-symmetric according to definition (17).

An interesting feature of system (53) is that the sign of its effective Kerr-like nonlinearity is determined by the coefficient β/Δ and hence can be either focusing ($\beta/\Delta < 0$) or defocusing ($\beta/\Delta > 0$). Thus the "conservative" nonlinearity depends on the gain and loss. The considered $\chi^{(2)}$ coupler is not the unique system obeying such property; similar phenomenon was recently reported in [9] for a non-$\mathscr{P}\mathscr{T}$-symmetric waveguide with active core and absorbing boundaries.

A soliton solution of (53) can be found subject to constraints

$$\kappa_1^2\gamma_2 = 2\kappa_2\gamma_1\sqrt{\kappa_1^2 - \gamma_1^2} < \beta < \kappa_2\cos(2\delta_1) \quad \text{where} \quad \delta_1 = \arcsin\frac{\gamma_1}{\kappa_1}. \tag{54}$$

It reads

$$\begin{pmatrix} u_1 \\ u_2 \end{pmatrix} = \eta\,\mathrm{sech}\left(\frac{\eta x}{\sqrt{\kappa_2\cos(2\delta) - q}}\right)\mathbf{s}_{\pm}, \tag{55}$$

where η is the soliton amplitude. It was found in the direct numerical simulations [47], that the soliton (55) represents an initial condition for launching sufficiently robust $\chi^{(2)}$ solitons of original system (50).

11 Hamiltonian $\mathscr{P}\mathscr{T}$-Symmetric Coupler

For the models considered in previous sections, integrals of motion are not known. This is a typical situation for nonlinear $\mathscr{P}\mathscr{T}$-symmetric wave equations. Some exceptions, however can be found. A Hamiltonian coupler with balanced gain and loss for which there exist several integrals of motion was reported in [63]. The evolution equations read

$$\begin{aligned} i\frac{\partial q_1}{\partial z} &= -\frac{\partial^2 q_1}{\partial x^2} + i\gamma q_1 + \kappa q_2 + ge^{-i\phi}|q_1|^2 q_1 + 2ge^{-i\phi}|q_2|^2 q_1 + ge^{i\phi}q_1^* q_2^2, \\ i\frac{\partial q_2}{\partial z} &= -\frac{\partial^2 q_2}{\partial x^2} - i\gamma q_2 + \kappa q_1 + ge^{i\phi}|q_2|^2 q_2 + 2ge^{i\phi}|q_1|^2 q_2 + ge^{-i\phi}q_1^2 q_2^*. \end{aligned} \tag{56}$$

Here ϕ is a real constant characterizing the relative strength of the nonlinear gain and loss. System (56) can be viewed as a generalization of the cascading limit equations (53) where additional XPM terms are added. On the other hand, without dispersion, i.e. for x-independent solutions $\mathbf{q}(t)$, it is reduced a $\mathscr{P}\mathscr{T}$-symmetric Hamiltonian dimer. A theory of dimers with cubic nonlinearities was developed in [4]. General discussion of the role of $\mathscr{P}\mathscr{T}$-symmetry of nonlinearity for existence of the integrals of motions for systems of $\mathscr{P}\mathscr{T}$-symmetric ordinary differential equations can be found in [62].

System (56) is obtained from the Hamiltonian equations

$$i\frac{\partial q_2}{\partial z}=\frac{\delta H}{\delta q_1^*},\quad i\frac{\partial q_1}{\partial z}=\frac{\delta H}{\delta q_2^*},\quad i\frac{\partial q_2^*}{\partial z}=-\frac{\delta H}{\delta q_1},\quad i\frac{\partial q_1^*}{\partial z}=-\frac{\delta H}{\delta q_2} \tag{57}$$

with the Hamiltonian

$$H=\int_{-\infty}^{\infty}\left[\frac{\partial q_1^*}{\partial x}\frac{\partial q_2}{\partial x}+\frac{\partial q_2^*}{\partial x}\frac{\partial q_1}{\partial x}+i\gamma(q_1q_2^*-q_1^*q_2)+\kappa(|q_1|^2+|q_2|^2)\right.$$
$$\left.+g(|q_1|^2+|q_2|^2)(e^{i\phi}q_1^*q_2+e^{-i\phi}q_1q_2^*)\right]dx. \tag{58}$$

Equations (57) have a cross-gradient structure, previously explored for $\mathscr{P}\mathscr{T}$-symmetric coupled linear oscillators [8]. Remarkably, in addition to Hamiltonian (58), which does not depend on z, system (57) has two more real integrals of motion. These are the Stokes component S_1 defined in (14), i.e. $dS_1/dz=0$, and the quasi-momentum P [63]:

$$P=i\int_{-\infty}^{\infty}\left(\frac{\partial q_1}{\partial x}q_2^*-\frac{\partial q_1^*}{\partial x}q_2\right)dx,\qquad \frac{dP}{dz}=0. \tag{59}$$

Exact soliton solutions of (56) can be found in both unbroken and broken $\mathscr{P}\mathscr{T}$-symmetric phases, provided the linear and nonlinear gain and loss are related in a special way. If in the unbroken phase ($\gamma<\kappa$) the parameter ϕ is equal to one of two values $\phi_{1,2}=\mp\arctan\left(\frac{\gamma\kappa\sqrt{\kappa^2-\gamma^2}}{\kappa^2+\gamma^2}\right)$ then transformation (9) leads to a conservative NLS equation for one of the components of the vector $\mathbf{Q}$. For example,

$$i\frac{\partial Q_1}{\partial z}=-\frac{\partial Q_1}{\partial x^2}\pm\sqrt{\kappa^2-\gamma^2}Q_1+\frac{4g\kappa}{\sqrt{3\gamma^2+\kappa^2}}|Q_1|^2Q_1,\qquad Q_2=0. \tag{60}$$

If $\mathscr{P}\mathscr{T}$ symmetry is broken ($\gamma>\kappa$), one can introduce another "angular" parameter $\tilde{\delta}$, according to $\sin\tilde{\delta}=\kappa/\gamma$, and use modified transformation (cf. (9))

$$\mathbf{q}=\tilde{U}U_1\mathbf{Q},\qquad \tilde{U}=\begin{pmatrix}e^{i\tilde{\delta}/2} & -e^{-i\tilde{\delta}/2}\\ e^{-i\tilde{\delta}/2} & e^{i\tilde{\delta}/2}\end{pmatrix},\quad U_1=\frac{1}{\sqrt{2}}\begin{pmatrix}1 & -1\\ 1 & 1\end{pmatrix} \tag{61}$$

[notice that $\tilde{U}$ is defined similarly to U in (9) but with δ substituted by $\tilde{\delta}$]. Now the one-component solution $\mathbf{Q} = (Q, 0)$ is obtained from the NLS equation

$$i\frac{\partial Q}{\partial z} = -\frac{\partial^2 Q}{\partial x^2} + i\kappa \cot(\tilde{\delta})Q + 2g|Q|^2 Q \tag{62}$$

with either gain, if $\tilde{\delta} \in (0, \pi)$, or loss, if $\tilde{\delta} \in (-\pi, 0)$. In the EP, $\gamma = \kappa$, equations (60) and (62) coincide.

Detail analysis of the soliton stability and interactions of system (56), as well generalization of the model to Hamiltonian non-$\mathscr{P}\mathscr{T}$-symmetric coupler can be found in [63].

12 On Multidimensional $\mathscr{P}\mathscr{T}$-Symmetric NLS Equations

Finally, we briefly discuss more general, but less explored models, where two (or more) coupled NLS equations with gain and losses are considered in $\mathbb{R}^N$, i.e. to $\mathscr{P}\mathscr{T}$-symmetric N-dimensional models. Direct ND generalization of Eqs. (1) reads

$$\begin{aligned} i\frac{\partial q_1}{\partial t} &= -\Delta q_1 + i\gamma q_1 + \kappa q_2 - (g_1|q_1|^2 + \tilde{g}|q_2|^2)q_1, \\ i\frac{\partial q_2}{\partial t} &= -\Delta q_2 - i\gamma q_2 + \kappa q_1 - (\tilde{g}|q_1|^2 + g_2|q_2|^2)q_2. \end{aligned} \tag{63}$$

Here $x \in \mathbb{R}^N$, $t \geq 0$, Δ is the N-dimensional Laplacian. The Cauchy problem for (63) is formulated with the initial conditions: $q_{1,2}(x, 0) = q_{1,2}^{(0)}(x)$, $q_{1,2}^{(0)} \in H^1(\mathbb{R}^N)$, $|x|q_{1,2}^{(0)}(x) \in L^2(\mathbb{R}^N)$.

Sufficient conditions for supercritical collapse in this Cauchy problem in different ranges of the nonlinear coefficients, were established in [18]. Apart from the technical details, like the possibility of exponential growth of $S_0(z)$ and non-conserved energy functional, the main results of the mentioned analysis are similar to those known for the supercritical collapse of two NLS equations with linear coupling, whose comprehensive analysis can be found in [27]. In particular, sufficient conditions for blow up have been established for the cases $g_{1,2} > 0$, $\sqrt{g_1 g_2} + \tilde{g} > 0$ and $g_1 > 0$, $g_2 \leq 0$, and $g \leq 0$. Results on the critical blow up can be found in Ref. [17].

For existence of solitons in 2D $\mathscr{P}\mathscr{T}$-symmetric NLS equations, strong instabilities must be suppressed, what is possible by adding to the system repulsive quintic nonlinearity. For two coupled 2D $\mathscr{P}\mathscr{T}$-symmetric NLS equations this problem was studied in [13]. A diversity of two-dimensional solitons in three coupled $\mathscr{P}\mathscr{T}$-symmetric NLS equations (such model describes triple-core nonlinear optical waveguides with balanced gain and loss) in presence of quintic nonlinearity were reported in [25].

13 Concluding Remarks

In this Chapter we described a variety of nonlinear phenomena modeled by coupled nonlinear Schrödinger equations with gain and loss which are exactly balanced with each other. The reported systems describe wave propagation in dispersive optical couplers, diffraction in planar waveguides, matter waves in spin-orbit-coupled condensates, etc. In optical applications the gain and loss are introduced by active and absorbing elements, while in the matter wave applications, they can be achieved by adding atoms in and eliminating atoms from the required hyperfine states. It was shown that such systems allow one to model full and partial $\mathscr{PT}$ symmetries, as well as $\mathscr{CPT}$ symmetry. It was shown how to introduce $\mathscr{PT}$-symmetric defects in such systems. We also discussed the conventional scenario of the $\mathscr{PT}$ symmetry breaking through the exceptional point, as well as less common singular phase transitions.

From the point of view of wave propagation, $\mathscr{PT}$-symmetric NLS equations allow to investigate existence and stability of bright and dark solitons, breathers, as well as other solutions familiar from the theory of the nonlinear Schrödinger equation. Interaction of solitons with defects can also be described by the model. In the reported systems it is possible to achieve matching conditions for resonant wave processes, in particular for four-wave mixing in one-dimensional setting.

It was shown that, a special version of coupled $\mathscr{PT}$-symmetric equations of the nonlinear Schrödinger type allows for a Hamiltonian formulation and may posses integrals of motion.

Several results on multidimensional coupled $\mathscr{PT}$-symmetric NLS equations were also mentioned.

Acknowledgements Author is grateful to D. A. Zezyulin, B. A. Malomed, F. Kh. Abdullaev, Y. V. Bludov, G. Huang, C. Hang, Y. V. Kartashov, M. Trippenbah, M. Ögren, R. Driben, D. E. Pelinovsky, J.-P. Dias, M. Figueira, T. Wasak, and P. Szańkowski, for fruitful collaboration on the results reported in this chapter.

References

1. Abdullaev, F.Kh., Konotop, V.V., Ögren, M., Sørensen, M.P.: Zeno effect and switching of solitons in nonlinear couplers. Opt. Lett. **36**, 4566 (2011)
2. Alexeeva, N.V., Barashenkov, I.V., Sukhorukov, A.A., Kivshar, Yu.S.: Optical solitons in PT-symmetric nonlinear couplers with gain and loss. Phys. Rev. A **85**, 063837 (2012)
3. Akhmediev, N., Ankiewicz, A.: Dissipative solitons in the complex Ginzburg-Landau and Swift-Hohenberg equations. In: Akhmediev, N., Ankiewicz, A. (eds.) Dissipative Solitons. Springer, Berlin (2005)
4. Barashenkov, I.V., Pelinovsky, D.E., Dubard, P.: Dimer with gain and loss: integrability and $\mathscr{PT}$-symmetry restoration. J. Phys. A: Math. Theor. **48**, 325201 (2015)
5. Barashenkov, I.V., Suchkov, S.V., Sukhorukov, A.A., Dmitriev, S.V., Kivshar, Yu.S.: Breathers in $\mathscr{PT}$-symmetric optical couplers. Phys. Rev. A **86**, 053809 (2012)
6. Bender, C.M.: Making sense of non-Hermitian Hamiltonians. Rep. Prog. Phys. **70**, 947 (2007)

7. Bender, C.M., Boettcher, S.: Real spectra in mon-Hermitian Hamiltonians having $\mathscr{P}\mathscr{T}$ symmetry. Phys. Rev. Lett. **80**, 5243 (1998)
8. Bender, C.M., Gianfreda, M., Özdemir, Ş.K., Peng, B., Yang, L.: Twofold transition in $\mathscr{P}\mathscr{T}$-symmetric coupled oscillators. Phys. Rev. A **88**, 062111 (2013)
9. Midya, B., Konotop, V.V.: Waveguides with absorbing boundaries: nonlinearity controlled by an exceptional point and solitons. Phys. Rev. Lett. **119**, 033905 (2017)
10. Bludov, Yu.V., Driben, R., Konotop, V.V., Malomed, B.A.: Instabilities, solitons and rogue waves in -coupled nonlinear waveguides. J. Opt. **15**, 064010 (2013)
11. Bludov, Yu.V., Hang, C., Huang, G., Konotop, V.V.: $\mathscr{P}\mathscr{T}$-symmetric coupler with a coupling defect: soliton interaction with exceptional point. Opt. Lett. **39**, 3382 (2014)
12. Bludov, Yu.V., Konotop, V.V., Malomed, B.A.: Stable dark solitons in PT-symmetric dual-core waveguides. Phys. Rev. A **87**, 013816 (2013)
13. Burlak, G., Malomed, B.A.: Stability boundary and collisions of two-dimensional solitons in $\mathscr{P}\mathscr{T}$-symmetric couplers with the cubic-quintic nonlinearity. Phys. Rev. E **88**, 062904 (2013)
14. Chiang, K.S.: Coupled-mode equations for pulse switching in parallel waveguides. IEEE J. Quantum Electron. **33**, 950 (1997)
15. Chiang, K.S., Chow, Y.T., Richardson, D.J., Taverner, D., Dong, L., Reekie, L.: Experimental demonstration of intermodal dispersion in a two-core optical fiber. Opt. Comm. **143**, 189 (1997)
16. Dai, C.-Q., Huang, W.-H.: Multi-rogue wave and multi-breather solutions in -symmetric coupled waveguides. Appl. Math. Lett. **32**, 35 (2014)
17. Destyl, E., Nuiro, S.P., Poullet, P.: Critical blowup in coupled parity-time-symmetric nonlinear Schrödinger equations. AIMS Math. **2**, 195 (2017)
18. Dias, J.-P., Figueira, M., Konotop, V.V., Zezyulin, D.A.: Supercritical blowup in coupled parity-time-symmetric nonlinear Schrödinger equations. Stud. Appl. Math. **133**, 422 (2014)
19. Dana, B., Bahabad, A., Malomed, B.A.: $\mathscr{C}\mathscr{P}$ symmetry in optical systems. Phys. Rev. A **91**, 043808 (2015)
20. Driben, R., Malomed, B.A.: Stabilization of solitons in PT models with supersymmetry by periodic management. EPL **96**, 51001 (2011)
21. Driben, R., Malomed, B.A.: Stability of solitons in parity-time-symmetric couplers. Opt. Lett. **36**, 4323 (2011)
22. Driben, R., Malomed, B.A.: Dynamics of higher-order solitons in regular and $\mathscr{P}\mathscr{T}$ -symmetric nonlinear couplers. EPL **99**, 54001 (2012)
23. El-Ganainy, R., Makris, K.G., Christodoulides, D.N., Musslimani, Z.H.: Theory of coupled optical PT-symmetric structures. Opt. Lett. **32**, 2632 (2007)
24. Faddeev, L.D., Takhtadjan, L.A.: Hamiltonian Methods in the Theory of Solitons. Springer, Berlin (1987)
25. Feijoo, D., Zezyulin, D.A., Konotop, V.V.: Two-dimensional solitons in conservative and parity-time-symmetric triple-core waveguides with cubic-quintic nonlinearity. Phys. Rev. A **92**, 062909 (2015)
26. Galitski, V., Spielman, I.B.: Spin-orbit coupling in quantum gases. Nature **494**, 49 (2013)
27. Jüngel, A., Weishäupl, R.-M.: Blow-up in two-component nonlinear Schrödinger systems with an external driven field. Math. Mod. Method Appl. Sci. **23**, 1699 (2013)
28. Kartashov, Y.V.: Vector solitons in parity-time-symmetric lattices. Opt. Lett. **38**, 2600 (2013)
29. Kartashov, Y.V., Konotop, V.V., Torner, L.: Topological states in partially-$\mathscr{P}\mathscr{T}$-symmetric Azimuthal potentials. Phys. Rev. Lett. **115**, 193902 (2015)
30. Kartashov, Y.V., Konotop, V.V., Zezyulin, D.A.: $\mathscr{C}\mathscr{P}\mathscr{T}$ -symmetric spin–orbit-coupled condensate. EPL **107**, 50002 (2014)
31. Kato, T.: Perturbation Theory for Linear Operators. Springer, Berlin (1966)
32. Kogelnik, H., Schmidt, R.V.: Switched directional couplers with alternating $\Delta\beta$. IEEE J. Quantum. Electron. **12**, 396 (1979)
33. Konotop, V.V., Yang, J., Zezyulin, D.A.: Nonlinear waves in $\mathscr{P}\mathscr{T}$-symmetric systems. Rev. Mod. Phys. **88**, 35002 (2016)

34. Konotop, V.V., Zezyulin, D.A.: Phase transition through the splitting of self-dual spectral singularity in optical potentials. Opt. Lett. **42**, 5206 (2017)
35. Li, X., Xie, X.-T.: Solitons in $\mathscr{P}\mathscr{T}$-symmetric nonlinear dissipative gratings. Phys. Rev. A **90**, 033804 (2014)
36. Lin, Y.J., Jiménez-García, K., Spielman, I.B.: Spin–orbit-coupled Bose–Einstein condensates. Nature **427**, 83 (2011)
37. Lupu, A., Benisty, H., Degiron, A.: Switching using $\mathscr{P}\mathscr{T}$-symmetry in plasmonic systems: positive role of the losses. Opt. Expr. **21**, 21651 (2013)
38. Lupu, A., Konotop, V.V., Benisty, H.: Optimal $\mathscr{P}\mathscr{T}$-symmetric switch features exceptional point. Sci. Rep. **7**, 13299 (2017)
39. Makris, K.G., El-Ganainy, R., Christodoulides, D.N., Musslimani, Z.H.: Beam dynamics in $\mathscr{P}\mathscr{T}$ symmetric optical lattices K. Phys. Rev. Lett. **100**, 103904 (2008)
40. Malomed, B.A.: A variety of dynamical settings in dual-core nonlinear fibers. In: Peng, G.-D. (ed.) Handbook of Optical Fibers. Springer, Singapore (2018)
41. Malomed, B.A., Winful, H.G.: Stable solitons in two-component active systems. Phys. Rev. E **53**, 5365 (1996)
42. Manakov, S.V.: On the theory of two-dimensional stationary self-focusing of electromagnetic waves. Zhurn. Eksp. Teor. Fiz. **65**, 505 (1973)
43. Messiah, A.: Quantum Mechanics, vol. II. Wiley, New York (1966)
44. Mostafazadeh, A.: Pseudo-Hermiticity versus PT-symmetry. II. A complete characterization of non-Hermitian Hamiltonians with a real spectrum. J. Math. Phys. **43**, 2814 (2002)
45. Musslimani, Z.H., Makris, K.G., El-Ganainy, R., Christodoulides, D.N.: Optical solitons in $\mathscr{P}\mathscr{T}$ periodic potentials. Phys. Rev. Lett. **100**, 30402 (2008)
46. Nazari, F., Nazari, M., Moravvej-Farshi, M.K.: A 2×2 spatial optical switch based on $\mathscr{P}\mathscr{T}$-symmetry. Opt. Lett. **36**, 4368 (2011)
47. Ögren, M., Abdullaev, F.Kh., Konotop, V.V.: Solitons in a $\mathscr{P}\mathscr{T}$-symmetric $\chi^{(2)}$ coupler. Opt. Lett. **42**, 4079 (2017)
48. Pare, C., Florjanczyk, M.: Approximate model of soliton dynamics in all-optical couplers. Phys. Rev. A **41**, 6287 (1990)
49. Pelinovsky, D.E., Zezyulin, D.A., Konotop, V.V.: Global existence of solutions to coupled $\mathscr{P}\mathscr{T}$-symmetric nonlinear Schrödinger equations. Int. J. Theor. Phys. **54**, 3920 (2015)
50. Peregrine, D.H.: Water waves, nonlinear Schrödinger equations and their solutions. J. Aust. Math. Soc. B **25**, 16 (1983)
51. Ramezani, H., Kottos, T., El-Ganainy, R., Christodoulides, D.N.: Unidirectional nonlinear $\mathscr{P}\mathscr{T}$-symmetric optical structures. Phys. Rev. A **82**, 043803 (2010)
52. Ruschhaupt, A., Delgado, F., Muga, J.G.: Physical realization of $\mathscr{P}\mathscr{T}$-symmetric potential scattering in a planar slab waveguide. J. Phys. A Math. Theor. **38**, L171 (2005)
53. Rüter, C.E., Makris, K.G., El-Ganainy, R., Christodoulides, D.N., Segev, M., Kip, D.: Observation of parity-time symmetry in optics. Nat. Phys. **6**, 192 (2010)
54. Sukhorukov, A.A., Xu, Z., Kivshar, Yu.S.: Nonlinear suppression of time reversals in $\mathscr{P}\mathscr{T}$-symmetric optical couplers. Phys. Rev. A **82**, 043818 (2010)
55. Stegeman, G.I., Hagan, D.J., Torner, L.: $\chi^{(2)}$ cascading phenomena and their applications to all-optical signal processing, mode-locking, pulse compression and solitons. Opt. Quantum Electron. **28**, 1691 (1996)
56. Wright, E.M., Stegeman, G.I., Wabnitz, S.: Solitary-wave decay and symmetry-breaking instabilities in two-mode fibers Phys. Rev. A **40**, 4455 (1989)
57. Wasak, T., Szankowski, P., Konotop, V.V., Trippenbach, M.: Four-wave mixing in a parity-time ($\mathscr{P}\mathscr{T}$)-symmetric coupler. Opt. Lett. **40**, 5291 (2015)
58. Yang, J.: Partially $\mathscr{P}\mathscr{T}$-symmetric optical potentials with all-real spectra and soliton families in multidimensions. Opt. Lett. **39**, 1133 (2014)
59. Yang, J.: Classes of non-parity-time-symmetric optical potentials with exceptional-point-free phase transitions. Opt. Lett. **42**, 4067 (2017)
60. Zyablovsky, A.A., Vinogradov, A.P., Dorofeenko, A.V., Pukhov, A.A., Lisyansky, A.A.: Causality and phase transitions in $\mathscr{P}\mathscr{T}$-symmetric optical systems. Phys. Rev. A **89**, 033808 (2014)

61. Zezyulin, D.A., Kartashov, Y.V., Konotop, V.V.: $\mathscr{CPT}$ -symmetric coupler with intermodal dispersion. Opt. Lett. **42**, 1273 (2017)
62. Zezyulin, D.A., Konotop, V.V.: Stationary modes and integrals of motion in nonlinear lattices with a $\mathscr{PT}$-symmetric linear part. J. Phys. A Math. Theor. **46**, 415301 (2013)
63. Zezyulin, D.A., Konotop, V.V.: Solitons in a Hamiltonian $\mathscr{PT}$-symmetric coupler. J. Phys. A Math. Theor. **51**, 015206 (2018)

Making the $\mathcal{PT}$ Symmetry Unbreakable

Vitaly Lutsky, Eitam Luz, Er'el Granot, and Boris A. Malomed

Abstract It is well known that typical $\mathcal{PT}$-symmetric systems suffer symmetry breaking when the strength of the gain-loss terms, i.e., the coefficient in front of the non-Hermitian part of the underlying Hamiltonian, exceeds a certain critical value. In this article, we present a summary of recently published and newly produced results which demonstrate various possibilities of extending the $\mathcal{PT}$ symmetry to arbitrarily large values of the gain-loss coefficient. First, we recapitulate the analysis which demonstrates a possibility of the restoration of the $\mathcal{PT}$ symmetry and, moreover, complete avoidance of the breaking in a photonic waveguiding channel of a subwavelength width. The analysis is necessarily based on the system of Maxwell's equations, instead of the usual paraxial approximation. Full elimination of the $\mathcal{PT}$-symmetry-breaking transition is found in a deeply subwavelength region. Next, we review a recently proposed possibility to construct stable one-dimensional (1D) $\mathcal{PT}$-symmetric solitons in a paraxial model with arbitrarily large values of the gain-loss coefficient, provided that the self-trapping of the solitons is induced by self-defocusing cubic nonlinearity, whose local strength grows sufficiently fast from the center to periphery. The model admits a particular analytical solution for the fundamental soliton, and provides full stability for families of fundamental and dipole solitons. It is relevant to stress that this model is nonlinearizable, hence the concept of the $\mathcal{PT}$ symmetry in it is also an essentially nonlinear one. Finally, we

V. Lutsky · E. Luz
Faculty of Engineering, Department of Physical Electronics, School of Electrical Engineering, Tel Aviv University, Tel Aviv, Israel

E. Granot
Department of Electrical and Electronic Engineering, Ariel University, Ariel, Israel

B. A. Malomed (✉)
Faculty of Engineering, Department of Physical Electronics, School of Electrical Engineering, Tel Aviv University, Tel Aviv, Israel

Center for Light-Matter Interaction, Tel Aviv University, Tel Aviv, Israel

ITMO University, Saint Petersburg, Russia
e-mail: malomed@post.tau.ac.il

D. Christodoulides, J. Yang (eds.), *Parity-time Symmetry and Its Applications*, Springer Tracts in Modern Physics 280,
https://doi.org/10.1007/978-981-13-1247-2_15

report new results for unbreakable $\mathcal{PT}$-symmetric solitons in 2D extensions of the 1D model: one with a quasi-1D modulation profile of the local gain-loss coefficient, and another with the fully-2D modulation. These settings admit particular analytical solutions for 2D solitons, while generic soliton families are found in a numerical form. The quasi-1D modulation profile gives rise to a stable family of single-peak 2D solitons, while their dual-peak counterparts tend to be unstable. The soliton stability in the full 2D model is possible if the local gain-loss term is subject to spatial confinement.

1 Introduction

A fundamental principle of the quantum theory is that, while the underlying wave function may be complex, eigenvalues of energy and other physically relevant quantities must be real, which is provided by the condition that the respective Hamiltonian is self-conjugate (Hermitian) [1]. On the other hand, the condition of the reality of the entire energy spectrum does not necessarily imply that it is generated by a Hermitian Hamiltonian. Indeed, it had been demonstrated, about twenty years ago, that non-Hermitian Hamiltonians obeying the parity-time ($\mathcal{PT}$) symmetry may also produce entirely real spectra [2–8]. In terms of the usual single-particle Hamiltonian, which includes potential $U(\mathbf{r})$, the $\mathcal{PT}$ symmetry implies that the potential is complex, $U(\mathbf{r}) = V(\mathbf{r}) + iW(\mathbf{r})$ (the usual Hermitian Hamiltonian contains a strictly real potential), its real and imaginary parts being, respectively, even and odd functions of coordinates [2]:

$$V(\mathbf{r}) = V(-\mathbf{r}),\ W(-\mathbf{r}) = -W(\mathbf{r}),\ \text{i.e.,}\ U(-\mathbf{r}) = U^*(\mathbf{r}), \tag{1}$$

where $*$ stands for the complex conjugate. For a given real part of the potential, the spectrum of $\mathcal{PT}$-symmetric models remains completely real, i.e., physically relevant, as long as the strength of the imaginary component of the potential is kept below a certain critical value, which is a threshold of the $\mathcal{PT}$-symmetry breaking, above which the system becomes unstable. The loss of the $\mathcal{PT}$ symmetry may be preceded by the onset of the jamming anomaly, which means transition from increase to decreases of the power flux between the gain and loss elements in the system following the increase of the gain-loss coefficient [9, 10]. It is relevant to mention that some relatively simple $\mathcal{PT}$-symmetric systems may be explicitly transformed into an alternative form admitting a representation in terms of an Hermitian Hamiltonian [11, 12].

While the concept of $\mathcal{PT}$-symmetric Hamiltonians remained an abstract one in the framework of the quantum theory per se, theoretical works had predicted a possibility to emulate this concept in optical media with symmetrically placed gain and loss elements [13–26], making use of the commonly known similarity between the Schrödinger equation in quantum mechanics and the classical equation governing the paraxial light propagation in classical waveguides. These predictions were followed by the implementation in optical waveguiding settings of various

types [27–30], as well as in metamaterials [31], lasers [32] (and laser absorbers [33]), microcavities [34], optically induced atomic lattices [35], exciton-polariton condensates [36–38], and in other physically relevant contexts. In particular, the transitions from unbroken to broken $\mathcal{PT}$ symmetry was observed in many experiments. One of prominent experimentally demonstrated applications of the $\mathcal{PT}$ symmetry in optics is unidirectional transmission of light [39].

Other classical waveguiding settings also admit emulation of the $\mathcal{PT}$ symmetry, as demonstrated in acoustics [40] and predicted in optomechanical systems [41]. Also predicted were realizations of this symmetry in atomic Bose-Einstein condensates [42], magnetism [43], mechanical chains of coupled pendula [44], and electronic circuits [45] (in the latter case, the prediction was also demonstrated experimentally). In terms of the theoretical analysis, $\mathcal{PT}$-symmetric extensions were also elaborated for Korteweg – de Vries [46, 47], Burgers [48], and sine-Gordon [49] equations, as well as in a system combining the $\mathcal{PT}$ symmetry with the optical emulation of the spin-orbit coupling [50].

While the $\mathcal{PT}$ symmetry is a linear property of the system, it may be naturally combined with intrinsic nonlinearity of the medium in which the symmetry is realized, such as the ubiquitous Kerr nonlinearity of optical waveguides. Most typically, these settings are modelled by nonlinear Schrödinger equations (NLSEs) with the $\mathcal{PT}$-symmetric potentials, subject to constraint (1), and cubic terms. Such models may give rise to $\mathcal{PT}$-symmetric solitons, which were considered, chiefly theoretically, in a large number of works (see, in particular, theoretical papers [15, 19–25] and recent reviews [51, 52]), and experimentally demonstrated too [30]. While most of these works were dealing with one-dimensional (1D) models, stable $\mathcal{PT}$-symmetric solitons were also found in some two-dimensional (2D) models [23, 50, 53–58]. A characteristic feature of solitons in $\mathcal{PT}$-symmetric systems is that, although these systems model, generally speaking, dissipative dynamics (the systems have no dynamical invariants), their solitons form continuous families like in conservative systems (defined by usual Hermitian Hamiltonians) [59], while traditional dissipative nonlinear systems normally give rise to isolated solutions in the form of dissipative solitons, which do not form families (if a dissipative soliton is stable, it plays the role of an attractor in the system's dynamics [60–62]).

Similar to their linear counterparts, soliton states are also subject to destabilization via the breaking of the $\mathcal{PT}$ symmetry at a critical value of the strength of the gain-loss terms [63]. Nevertheless, there are specific models which make the solitons' $\mathcal{PT}$ symmetry *unbreakable*, extending it to arbitrarily large values of the gain-loss strength, i.e., the coefficient in front of the non-Hermitian part of the respective Hamiltonian [64–66]. The particular property of those models is that self-trapping of solitons is provided not by the usual self-focusing sign of the cubic nonlinearity, but by the opposite defocusing sign, with the local strength of the self-defocusing growing fast enough from the center to periphery. For conservative systems (in the absence of gain and loss), this scheme of the self-trapping of stable 1D, 2D, and 3D solitons was elaborated previously in a number of works [67–77].

The objective of the present article is to provide a brief survey of systems which may support unbreakable $\mathcal{PT}$ symmetry, as this property is quite promising for

potential applications, and is interesting in its own right. It was recently elaborated in two completely different settings. One is the above-mentioned model with the solitons supported by the spatially growing strength of local self-defocusing. On the other hand, a possibility of creating the $\mathcal{PT}$ symmetry persisting up to indefinitely large values of the gain-loss coefficient was also discovered in the context of nanophotonics, considering light propagation in structures combining refractive, amplifying, and attenuating elements at a subwavelength scale [78]. This setting was theoretically analyzed in a purely linear form, with an essential peculiarity that the corresponding model is, naturally, based on the full system of Maxwell's equations, rather than on the paraxial-propagation equation of the Schrödinger type, which was used in an absolute majority of works dealing with the $\mathcal{PT}$ symmetry in optical media. Basic findings for the restoration of the $\mathcal{PT}$ symmetry, and a possibility of making it completely unbreakable in the linear nanophotonic model are presented below in Sect. 2.

The results for unbreakable 1D $\mathcal{PT}$-symmetric solitons in the model based on the paraxial-propagation NLSE with the spatially growing strength of the self-defocusing nonlinearity are summarized in Sect. 3. It is followed by Sect. 4, which reports *new results* for 2D extensions of the unbreakable $\mathcal{PT}$ symmetry in a nonlinear model of a similar type. We consider two different versions of the 2D system, with the quasi-one-dimensional or fully two-dimensional $\mathcal{PT}$ symmetry, the former meaning that the gain and loss are swapped by reflection $x \Leftrightarrow -x$, while the reflection in the perpendicular direction, $y \Leftrightarrow -y$ leaves the gain-loss pattern invariant. The main issue is the stability of the 2D $\mathcal{PT}$-symmetric solitons, which turn out to be essentially more stable in the case of the quasi-1D symmetry than in the framework of the full 2D scheme. An essential asset of the 1D, quasi-1D, and full 2D models is that a number of soliton solutions can be obtained in an exact analytical form, even if not all of them are stable.

2 Restoration and Persistence of the $\mathcal{PT}$ Symmetry in the Photonic Medium with a Subwavelength Structure

Following Ref. [78], we here consider the propagation of monochromatic light beams with the TM (transverse-magnetic) polarization , which include only $\mathcal{E}_x$, $\mathcal{E}_z$, and $\mathcal{H}_y$ components of the electric and magnetic fields. The propagation is considered along the z axis in an effectively 2D medium whose dielectric permittivity is modulated in the transverse direction, x. The spatial evolution of the field components is governed by the reduced system of the Maxwell's equations:

$$i\frac{\partial E_x}{\partial z} = -\frac{1}{\varepsilon_0\omega}\frac{\partial}{\partial x}\left(\frac{1}{\varepsilon_{\rm rel}}\frac{\partial \mathcal{H}_y}{\partial x}\right) - \mu_0\omega\mathcal{H}_y,$$
$$i\frac{\partial \mathcal{H}_y}{\partial z} = -\varepsilon_0\varepsilon_{\rm rel}\omega\mathcal{E}_x, \tag{2}$$

$$\mathcal{E}_z = \frac{i}{\varepsilon_0 \varepsilon_{\rm rel} \omega} \frac{\partial \mathcal{H}_y}{\partial x},$$

where ω is the frequency of the monochromatic carrier, ε_0 and μ_0 are the vacuum permittivity and permeability, and $\varepsilon_{\rm rel} = \varepsilon_{\rm bg} + \varepsilon^{\rm re}(x) + i\varepsilon^{\rm im}(x)$ is the complex relative permittivity of the $\mathcal{PT}$-symmetric structure, with x-dependent real and imaginary parts, added to the background permittivity, $\varepsilon_{\rm bg}$.

Two different modulation patterns were considered in Ref. [78], corresponding, respectively, to a single waveguiding channel or a periodic guiding structure in the (x, z) plane. In this article, we focus on solitary (localized) modes, therefore only the former pattern is explicitly considered. It is defined by the following transverse (x-dependent) profile:

$$\varepsilon_{\rm rel}(x) = \varepsilon_{\rm bg} + \mathrm{sech}^2\left(\frac{x}{d}\right)\left[p + i\alpha \sinh\left(\frac{x}{d}\right)\right], \tag{3}$$

where d and $p > 0$ represent, severally, the width and depth of the guiding channel, while $\alpha > 0$ is the strength of the gain-loss term. In accordance with the general definition of the $\mathcal{PT}$ symmetry, the real and imaginary parts of the profile are even and odd functions of x, respectively, cf. Eq. (1).

Eigenmodes for subwavelength beams with propagation constant b are looked for as solutions to Eq. (2) in the form of

$$\left\{\mathcal{E}_x(x,z), \mathcal{H}_y(x,z), \mathcal{E}_z(x,z)\right\} = e^{ibz}\left\{E_x(x) H_y(x), E_z(x)\right\}. \tag{4}$$

Numerical solution of Eq. (2) with modulation profile (3) has produced three types of the solutions [78]: (i) ones with real $b > \sqrt{\varepsilon_{\rm bg}}$ represent stable $\mathcal{PT}$-symmetric beams guided by the channel; (ii) solutions with a complex propagation constant, which has $\mathrm{Re}(b) > \sqrt{\varepsilon_{\rm bg}}$, $\mathrm{Im}(b) \neq 0$ represent, as it follows from Eq. (4), exponentially growing (unstable) channel-guided modes with broken $\mathcal{PT}$ symmetry, and (iii) delocalized modes, which are not actually guided by the channel, have $\mathrm{Re}(b) < \sqrt{\varepsilon_{\rm bg}}$.

The situation which occurs in a majority of previously studied models is that, with the increase of the gain-loss strength, α, the $\mathcal{PT}$ symmetry of the guided states suffers breaking at a critical value, $\alpha_{\rm cr}$. This is indeed observed in the present case in the nearly-paraxial regime, namely, at $d/\lambda \gtrsim 1/5$, where λ is the underlying wavelength of the optical beam (below, following Ref. [78], particular results are displayed for $\lambda = 632.8$ nm (visible red), and $\varepsilon_{\rm bg} = 2.25$). In particular, at $d = 120$ nm, the breaking of the $\mathcal{PT}$ symmetry takes place at $\alpha_{\rm cr} \approx 1.95$, see Fig. 1a (in Fig. 1, the $\mathcal{PT}$ symmetric modes exist at a single value of the propagation constant, as the underlying wavelength is fixed). However, in the deeply subwavelength situation, corresponding to essentially smaller channel's widths, such as $d = 60$ nm $\simeq \lambda/10$ and 30 nm $\simeq \lambda/20$ (see Fig. 1b, c), a drastically different situation is observed: in the former case, the breaking of the $\mathcal{PT}$ symmetry is followed by its

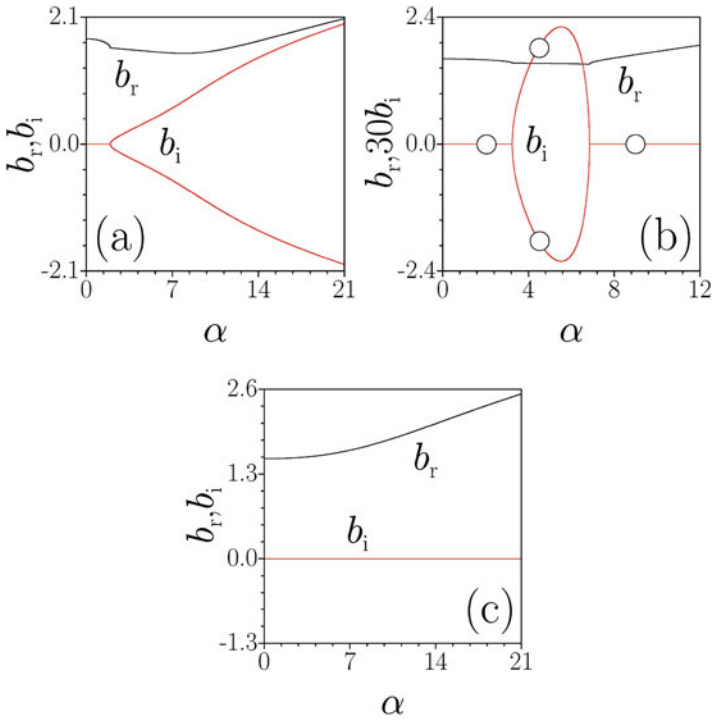

Fig. 1 Real and imaginary parts of the propagation constant, b_r and b_i, versus the gain-loss strength, α, in Eq. (3), for the guiding channel with depth $p = 1.7$, and widths $d = 120\,\text{nm}$ (**a**), $d = 60\,\text{nm}$ (**b**), and $d = 30\,\text{nm}$ (**c**) (as per Ref. [78]). Circles in panel (**b**) designate examples of the eigenmodes displayed in Fig. 2. The underlying wavelength is $\lambda = 632.8\,\text{nm}$, and the background dielectric permeability is $\varepsilon_{\text{bg}} = 2.25$. The emergence of b_i in panels (**a**) and (**b**) signals the breaking of the $\mathcal{PT}$ symmetry, while the disappearance of b_i in (**b**) implies the *restoration* of the symmetry. In the case shown in (**c**), the $\mathcal{PT}$ symmetry is *never broken*

restoration at still larger values of α, and in the latter case the breaking *does not happen* at all.

It is relevant to mention that a similar effect of the spontaneous restoration of the $\mathcal{PT}$ symmetry, although not the full elimination of the symmetry breaking, was reported too in some other models (based on the paraxial, rather than subwavelength, equations), including a linear discrete system of the Aubry-André type [79], and a nonlinear model based on the NLSE in 1D [80]. Examples of unbreakable $\mathcal{PT}$ symmetry are known too in simple models with few degrees of freedom, such as a $\mathcal{PT}$ dimer [11].

A set of typical eigenmodes of the electromagnetic fields, which correspond, respectively, to the unbroken, broken, and restored $\mathcal{PT}$ symmetry, are displayed in Fig. 2. It is clearly seen that, in the case of the unbroken and restored symmetry, each field component is either spatially even or odd, while the modal spatial (anti)symmetry is broken too when the $\mathcal{PT}$ symmetry does not hold.

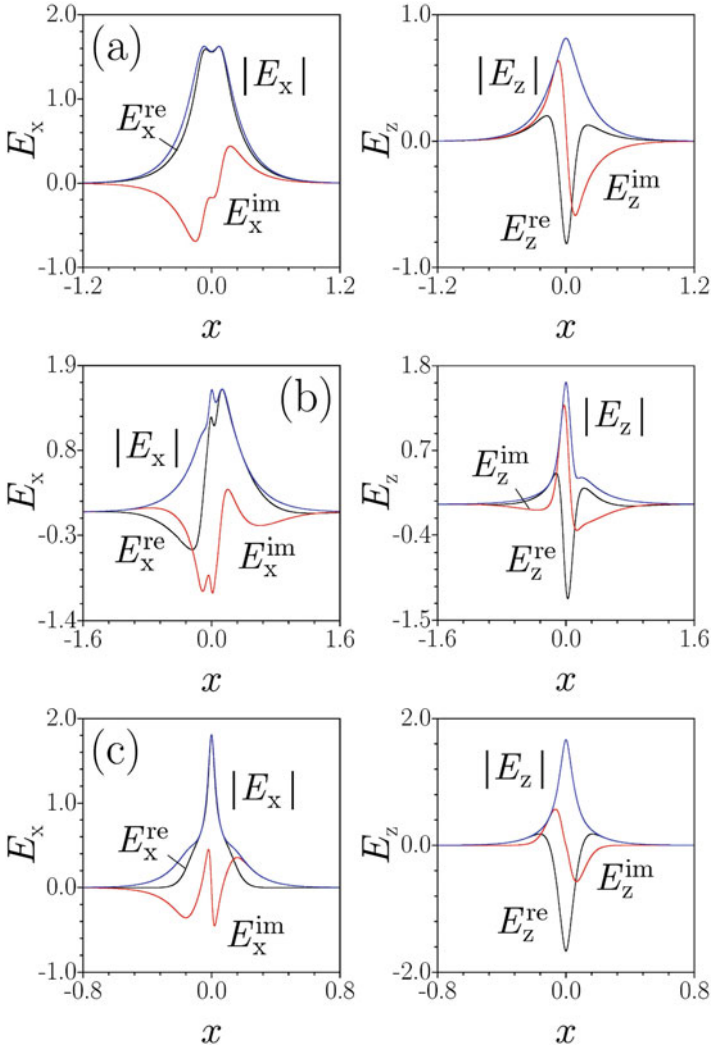

Fig. 2 Profiles of the guided modes designated by circles in Fig. 1, at $\alpha = 2.0$ (**a**), 4.5 (**b**), and 9.5 (**c**), which are typical modes with unbroken, broken, and *restored* $\mathcal{PT}$ symmetry, respectively (as per Ref. [78]). The fields are plotted in dimensionless units, while transverse coordinate x is measured in μm

Finally, the results of the consideration of the model are summarized in Fig. 3, which shows regions of the unbroken, broken, and restored $\mathcal{PT}$ symmetry in the plane of the essential control parameters, viz., the gain-loss coefficient, α, and the width of the guiding channel, d. Relatively small areas where no guided modes exist (in the latter case, the optical beam coupled into the channel waveguide suffers delocalization, spreading out into the entire (x, z) plane) are shown too.

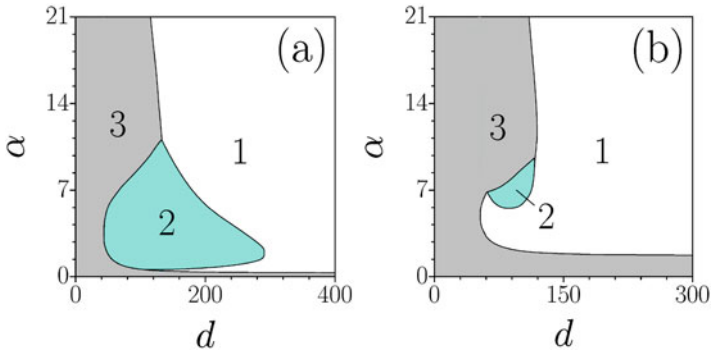

Fig. 3 Domains of the existence and stability of the $\mathcal{PT}$-symmetric modes guided by channel (3), in the plane of the channel's width, d, and gain-loss coefficient, α (as per Ref. [78]). The depth of the channel is $p = 0.3$ in (**a**), which represents a shallow conduit, and $p = 1.7$ in (**b**), representing a deep one. The symmetry is broken in region **1**, and unbroken *or restored* in region **3**, respectively, while region **2** does not support any localized mode

The conclusion suggested by Fig. 3 is quite clear: in the near-paraxial regime, corresponding to a relatively broad guiding channel, with $d \gtrsim 120$ nm, the usual scenario of the $\mathcal{PT}$-symmetry breaking, following the increase of α, is observed. However, in the deeply subwavelength region, the symmetry (hence, the stability of the guided modes too) is either readily *restored* with the further increase of α, or is *never broken*. Figure 3 demonstrates that region **3** of the unbroken and restored stability tends to expand, although not very dramatically, with the increase of the channel's depth, p (see Eq. 3), while, quite naturally, the delocalization area **2** shrinks.

3 Unbreakable $\mathcal{PT}$-Symmetric Solitons in One Dimension

The 1D model which is capable to support solitons with unbreakable $\mathcal{PT}$ symmetry by means of the self-defocusing nonlinearity with the local strength, $S(\eta)$, growing from the center to infinity, as a function of coordinate η, is based on the NLSE for the amplitude of the electromagnetic field, u [64]:

$$i\frac{\partial u}{\partial \xi} + \frac{1}{2}\frac{\partial^2 u}{\partial \eta^2} - S(\eta)|u|^2 u = -iR(\eta)u, \tag{5}$$

where ξ is the propagation coordinate, and $S(\eta)$ provides for the self-trapping of 1D solitons under that condition that $S(\eta)$ grows faster than $|\eta|$ at $|\eta| \to \infty$ [68, 71]. Here, following Ref. [64], we adopt a steep anti-Gaussian modulation profile,

$$S(\eta) = \left(1 + \sigma\eta^2\right) \exp\left(\frac{1}{2}\eta^2\right), \tag{6}$$

where coefficients equal to 1 and 1/2 may be fixed to these values by means of rescaling of a more general expression. Further, the spatially-odd gain-loss modulation profile is adopted also as it was done in Ref. [64]:

$$R(\eta) = \beta\eta \exp\left(-\Gamma\eta^2\right), \tag{7}$$

with $\beta > 0$ and $\Gamma \geq 0$.

An advantage of fixing the profiles in the form of Eqs. (6) and (7) is that they admit a particular exact solution for the self-trapped $\mathcal{PT}$-symmetric soliton [64], provided that $\Gamma = 0$ is set in Eq. (7):

$$u(\eta, \xi) = \frac{1}{2\sqrt{2\sigma}} \exp\left(ib\xi - 2i\beta\eta - \frac{1}{4}\eta^2\right), \tag{8}$$

at a single value of the propagation constant:

$$b = -\left(2\beta^2 + \frac{1}{4} + \frac{1}{8\sigma}\right). \tag{9}$$

The availability of the exact solution is principally important for establishing the concept of the *unbreakability* of the $\mathcal{PT}$ symmetry: obviously, the solution given by Eqs. (8) and (9) exist for *arbitrarily large* values of the gain-loss strength, β, there being no critical value beyond which solitons cannot be found. Moreover, in Ref. [64] it was checked, at least in a part of the parameter plane (β, σ), that the exact solitons are stable.

It is relevant to stress that the model with the sufficiently quickly growing nonlinearity coefficient $S(\eta)$ is *nonlinearizable*: the form of decaying tails of generic self-trapped modes can be investigated analytically (it turns out to be the same as in the particular exact solution (8)), but it is necessary to keep the nonlinear term in Eq. (5) for this purpose [67, 68]. Accordingly, the linear spectrum of the present model cannot be defined, the respective concept of the $\mathcal{PT}$ symmetry and its breaking or unbreakability being a nonlinear one too. The same pertains to the 2D model considered in the next section.

Numerical solution of Eq. (5) produces many families of complex solitons with real propagation constant b, in the form of

$$u(\eta, \xi) = \exp(ib\xi)\left[w_{\mathrm{r}}(\eta) + iw_{\mathrm{i}}(\eta)\right], \tag{10}$$

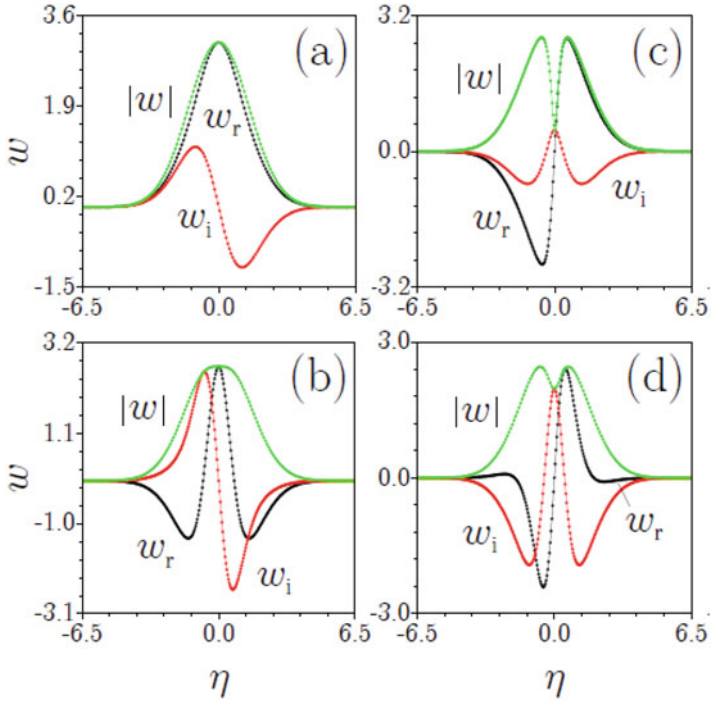

Fig. 4 Profiles of fundamental (**a**),(**b**) and dipole (**c**),(**d**) stable one-dimensional solitons, found as numerical solutions of Eq. (5) with $\sigma = 0$ and $\gamma = 1/2$, for a fixed value of the propagation constant, $b = -10$ (as per Ref. [64]). Panels (**a**), (**c**) and (**b**), (**d**) pertain, severally, to $\beta = 1.04$ and 3.47

which may be naturally identified as fundamental solitons, dipoles, tripoles, quadrupoles, and so on. These solution types feature profiles of $|w(\eta)| \equiv \sqrt{w_r^2(\eta) + w_i^2(\eta)}$ with, respectively, one, two, three, etc. peaks (local maxima). Solitons are characterized by their integral power,

$$U = \int_{-\infty}^{+\infty} |w(\eta)|^2 \, d\eta. \tag{11}$$

Characteristic examples of stable fundamental and dipole solutions are displayed in Fig. 4 (they were obtained for $\sigma = 0$, in which case exact soliton (8) does not exist, but numerically found solitons are available and may be stable). It is seen that the increase of the gain-loss coefficient, β, makes the shape of the solitons more complex, but the fundamental and dipole solitons remain fully stable as long as they exist, while higher-order tripoles and quadrupoles have both stability and instability areas [64], as shown in Fig. 5b.

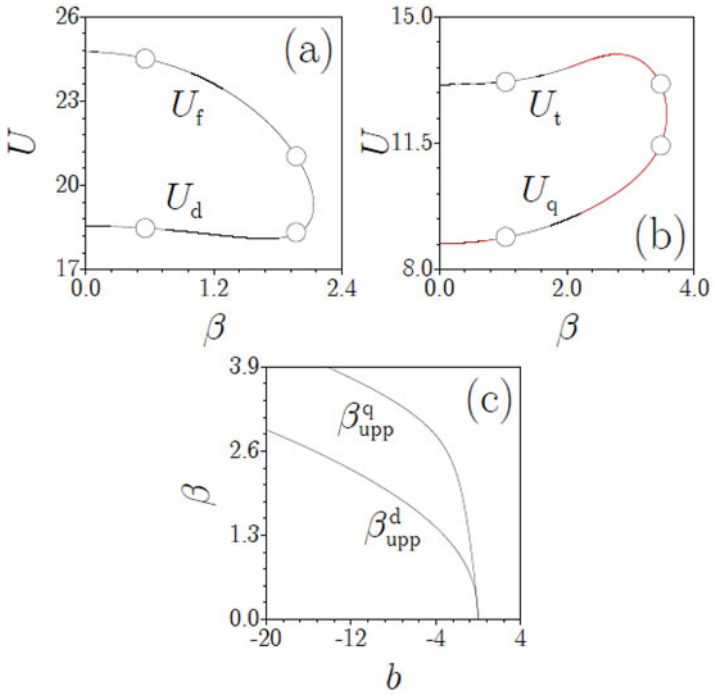

Fig. 5 The solitons' integral power, defined in Eq. (11), vs. the gain-loss strength, β, for branches of the fundamental and dipole solitons (**a**), and ones of the tripole and quadrupole types (**b**) (as per Ref. [64]). In (**b**), black and red segments designate stable and unstable solitons, respectively (the fundamental and dipole solitons are completely stable in their existence areas). Circles in (**a**) correspond to examples of the solutions shown in Fig. 4 (circles in (**b**) correspond to examples of stable and unstable tripole and quadrupole solitons which can be found in Ref. [64], but are not shown here). The families are produced for $\sigma = 0$ in Eq. (6), $\gamma = 1/2$ in Eq. (7), and fixed propagation constant, $b = -10$. The fundamental and dipole families merge at $\beta \approx 2.135$, while the tripole and quadrupole ones merge at $\beta \approx 3.565$. (**c**) The critical ("upper") value, $\beta^{\rm d}_{\rm upp}$, at which the fundamental and dipole branches merge, vs. the propagation constant, b. Curve $\beta^{\rm q}_{\rm upp}$(**b**) shows the same for the merger of the tripole and quadrupole branches

Most essential results characterizing the behavior of solitons in the present model are collected in Fig. 5. In particular, Fig. 5a shows that, at fixed b, branches of the fundamental and dipole solitons, remaining completely stable, merge and disappear, with the increase of the gain-loss coefficient, β, at a critical ("upper") value, which is $\beta_{\rm upp} \approx 2.135$ in Fig. 5a. However, stable fundamental and dipole soliton can be found at arbitrarily high values of β, as demonstrated by the lower curve in Fig. 5c, which shows the critical value $\beta_{\rm upp}$ vs. b: obviously, β may become indefinitely large with the increase of $|b|$. In addition, the upper curve shows the growth with $|b|$ of a similar critical ("upper") value at which another pair of solitons, viz., tripoles and quadrupoles, merge, as can be seen in Fig. 5b (however, unlike the fundamental and dipole modes, the tripole and quadrupole branches become unstable prior to the merger, as seen in Fig. 5b).

4 Unbreakable $\mathcal{PT}$-Symmetric Solitons in Two Dimensions

4.1 The Model and Analytical Solutions

Results presented in the above sections summarize findings originally published in Refs. [78] and [64], respectively. Here we report previously unpublished analytical and numerical results obtained for 2D generalizations of the model based on Eq. (5). The 2D model with transverse coordinates (x, y) and propagation distance z is based on the following NLSE for the amplitude of the electromagnetic field, $w(x, y, z)$:

$$i\frac{\partial w}{\partial z} + \frac{1}{2}\left(\frac{\partial^2 w}{\partial x^2} + \frac{\partial^2 w}{\partial y^2}\right) - S(r)|w|^2 w = iR(x, y)\, w, \tag{12}$$

where $r \equiv \sqrt{x^2 + y^2}$ is the radial coordinate, and the nonlinearity-modulation profile is chosen similar to its 1D counterpart (6):

$$S(r) = \left(1 + \sigma r^2\right)\exp\left(r^2\right), \tag{13}$$

with $\sigma \geq 0$.

Here we consider two different versions of the gain-loss spatial profile: a quasi-1D one, symmetric only with respect to x:

$$R(x, y) = \beta_0 x \exp\left(-\Gamma r^2\right), \tag{14}$$

and a profile symmetric with respect to x and y, which may be called a fully 2D one:

$$R(x, y) = \beta_0 xy \exp\left(-\Gamma r^2\right), \tag{15}$$

with constants $\Gamma \geq 0$ and $\beta_0 > 0$. Strictly speaking, the fully 2D gain-loss profile, unlike its quasi-1D counterpart, cannot be called a $\mathcal{PT}$-symmetric one, but it is completely relevant as the physical model.

Stationary solutions with a real propagation constant, b, are looked for as

$$w(x, y) = \exp(ibz)\, W(x, y), \tag{16}$$

with complex function $W(x, y)$ satisfying the following equation:

$$bW = \frac{1}{2}\left(\frac{\partial^2 W}{\partial x^2} + \frac{\partial^2 W}{\partial y^2}\right) - S(r)|W|^2 W - iR(x, y)\, W. \tag{17}$$

In the case of $\Gamma = 0$ in Eqs. (14) and (15), Eq. (17), with σ and $R(x, y)$ taken in the form of Eqs. (13) and (14), gives rise to an exact analytical solution:

$$W(x, y) = W_0 \exp\left(-\frac{1}{2}r^2 - i\beta_0 x\right), \tag{18}$$

(cf. the 1D solution (8)), with

$$W_0^2 = \frac{1}{2\sigma}, \; b = -\left(1 + \frac{\beta_0^2}{2} + \frac{1}{2\sigma}\right). \tag{19}$$

This solution exists for all values of the control parameters, β_0 and σ, except for $\sigma = 0$. Further, Eq. (11) with σ and $R(x, y)$ taken in the form of Eqs. (13) and (15), where $\Gamma = 0$ is again fixed, also gives rise to an exact solution:

$$W(x, y) = W_0 \exp\left(-\frac{1}{2}r^2 - \frac{1}{2}i\beta_0 xy\right), \tag{20}$$

this time with

$$W_0^2 = \frac{1}{2\sigma}\left(1 - \left(\frac{\beta_0}{2}\right)^2\right), \; b = -\left[1 + \frac{1}{2\sigma}\left(1 - \left(\frac{\beta_0}{2}\right)^2\right)\right]. \tag{21}$$

This solution exists if Eq. (21) yields $W_0^2 > 0$, i.e., $\beta_0 < 2$ and $\sigma > 0$.

Another exact solution of Eq. (11), with σ and $R(x, y)$ again taken in the form of Eqs. (13) and (15), exists under the special condition,

$$\beta_0 = 2, \sigma = 0, \Gamma = 0. \tag{22}$$

This solution is also found in the form of ansatz (20), precisely with $\frac{1}{2}\beta_0$ replaced by 1, as per Eq. (22). However, unlike the solution represented by Eqs. (20) and (21), this time it is not a single one, but a *continuous family* of exact solutions, with *arbitrary amplitude* W_0, and propagation constant

$$b = -\left(1 + W_0^2\right). \tag{23}$$

The possibility to obtain the continuous family of the exact 2D solitons, instead of an isolated one, is a compensation for selecting the special values of the parameters, as fixed by Eq. (22).

The exact solutions clearly suggest that the quasi-1D model, based on Eq. (14), features the unbreakable $\mathcal{PT}$ symmetry, as the respective solution, given by Eqs. (18) and (19), exists for an arbitrarily large strength of the gain-loss term, β_0. On the other hand, the full 2D model, based on Eq. (15), gives rise to the exact solutions, in the form of Eqs. (20), (21) or (22), (23), which exist only at $\beta_0 \leq 2$, hence the unbreakability of the $\mathcal{PT}$ symmetry is not guaranteed in the latter case.

4.2 Numerical Results

4.2.1 The Quasi-1D Model

The exact solution of the model with the quasi-1D gain-loss modulation, given by Eqs. (18) and (19), can be embedded into a family of solitons produced by a numerical solution of Eq. (17), with $S(r)$ and $R(x, y)$ taken as per Eqs. (13) and (14), respectively (the latter is taken here with $\Gamma = 0$). The stationary 2D solutions were constructed by means of the Newton conjugate gradient method [81]. Then, the stability of the stationary states was identify by numerical computation of eigenvalues of small perturbations, using linearized equations for perturbations around the stationary solitons. This computation was performed with the help of the spectral collocation method. Finally, the stability prediction, based on the eigenvalues, was verified through direct simulations of the perturbed evolution of the solitons.

Generic examples of numerically found stable and unstable solitons, which may have single- and dual-peak shapes, are shown in Fig. 6. In accordance with these examples, all the double-peak solitons are unstable, and almost all the single-peak ones are stable. In particular, all the exact solutions, given by Eqs. (18) and (19), are found to be stable.

Results of the stability analysis for the $\mathcal{PT}$-symmetric solitons in the model with the quasi-1D shape of the gain-loss term, based on the eigenvalue computation, are summarized by the stability chart in the plane of (b, β_0), i.e., the soliton's propagation constant and strength of the gain-loss term in Eq. (14), which is displayed in Fig. 7. Direct simulations completely corroborate the predictions produced by the stability eigenvalues. In particular, the solitons which are predicted to be unstable get destructed, decaying in the course of the perturbed evolution. This figure corroborates the unbreakable character of the $\mathcal{PT}$ symmetry in the model, as the stability region does not exhibit a boundary at large values of β_0.

The stability chart, drawn in Fig. 7 for $\sigma = 1$ in Eq. (13), is quite similar to its counterparts produced at other values of $\sigma > 0$. The situation is different in the case of $\sigma = 0$, when the exact solution given by Eqs. (18) and (19) does not exist. The respective stability chart, is displayed in Fig. 8, all unstable solutions, as well as stable ones, featuring the single-peak shape.

4.2.2 The Full 2D Model

A drastic difference produced by the stability analysis for exact solutions of the full 2D model, given by Eqs. (20) and (21) for $\sigma > 0$, $\Gamma = 0$ and arbitrary β_0, and by Eq. (23) for the special case (22), is that these solutions are completely *unstable*. Furthermore, all numerical solutions found in the full 2D model with $\Gamma = 0$ in Eq. (15) are unstable too. The stabilization in this model may be provided by $\Gamma > 0$, i.e., by confining the spatial growth of the local gain and loss in Eq. (15). For fixed

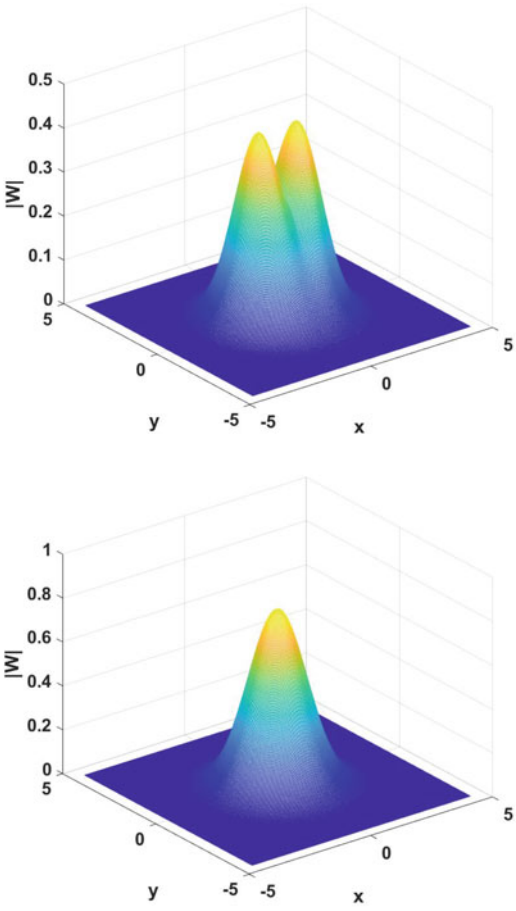

Fig. 6 Typical examples of 2D $\mathcal{PT}$-symmetric solitons produced by the model with the quasi-1D gain-loss profile defined by Eq. (14). The bottom and top panels display, severally, a stable single-peak soliton with propagation constant $b = -2$, and an unstable dual-peak one with $b = -2.7$. In both cases, other parameters are $\beta_0 = 0.8$, $\sigma = 1$, and $\Gamma = 0$

σ, there is a minimum value $\Gamma_{\min}$ of Γ which provides for the stabilization. In fact, $\Gamma_{\min}$ depends on the size of the solution domain: in an extremely large domain, one may find very broad stable solitons, i.e., ones with very small b (see Eq. (17)), at any $\Gamma > 0$. Practically speaking, the size of the domain is always finite, as the steep growth of $S(r)$, defined as per Eq. (13), cannot extend to infinity. As shown in Refs. [67–76], it is sufficient to secure the adopted modulation profile of $S(r)$ on a scale which is essentially larger than a characteristic size of the soliton supported by this profile. Thus, we have concluded that, for instance, in the domain of size $|x|, |y| \leq 9$ the solitons are stable in the model with $\sigma = 1$ in Eq. (13) at $\Gamma \geq 0.2$ in Eq. (15), being explicitly unstable, e.g., at $\Gamma = 0.1$. Typical examples of the stability charts for the $\mathcal{PT}$-symmetric solitons, numerically produced in the full 2D model with $\beta > 0$, are displayed in Fig. 9. Naturally, the stability area expands with the increase of Γ. It is worthy to note that Fig. 9b clearly suggests that the $\mathcal{PT}$

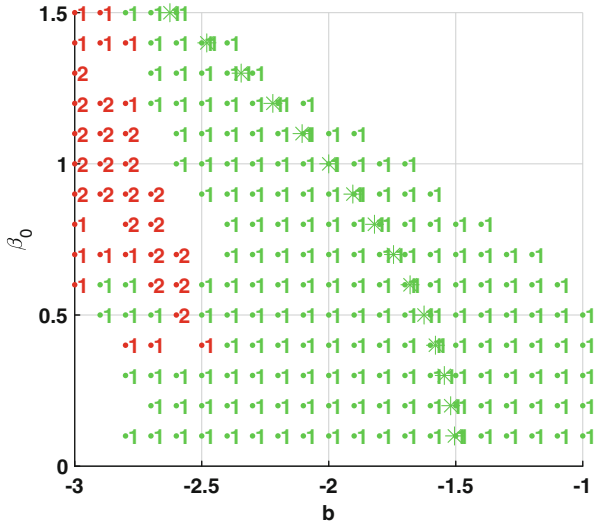

Fig. 7 (Color online) The stability chart for the solitons supported by quasi-1D $\mathcal{PT}$-symmetric gain-loss profile (14) with $\Gamma = 0$, in the case of $\sigma = 1$ in Eq. (13). Exact soliton solutions, given by Eqs. (18) and (19), are indicated by stars (they all are stable), while stable and unstable numerically found solitons are shown by green and red dots, respectively. Numbers near the dots denote the number of peaks in each soliton (one or two). No soliton solutions were found in white areas

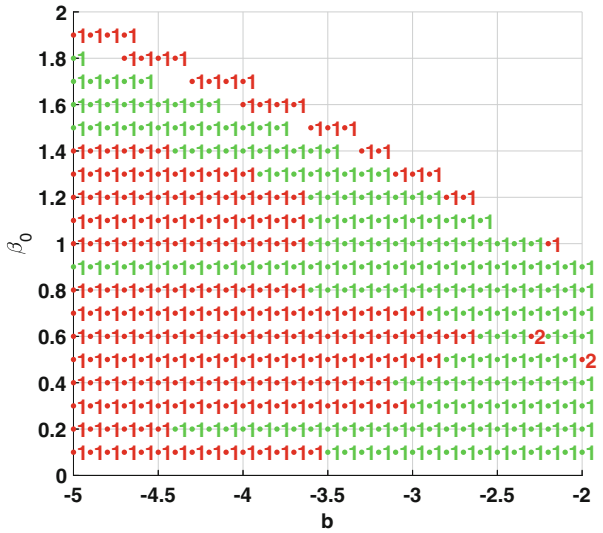

Fig. 8 The same as in Fig. 7 (the stability chart for $\mathcal{PT}$-symmetric solitons), but for $\sigma = 0$ in Eq. (13)

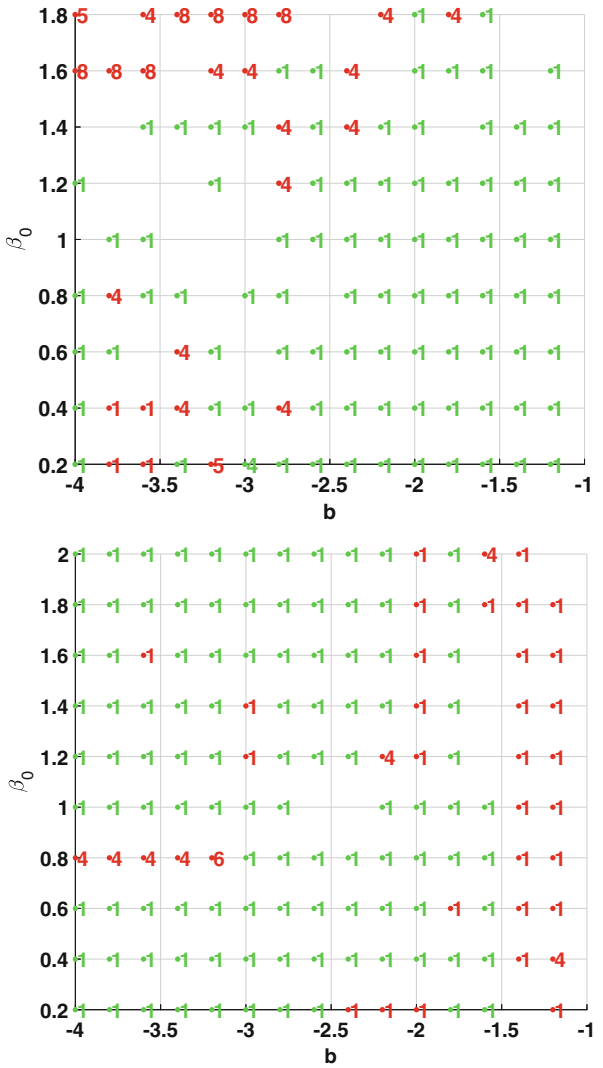

Fig. 9 The same (stability charts) as in Figs. 7 and 8, but for the full 2D model based on Eq. (15), with $\Gamma = 0.5$, $\sigma = 1$ and $\sigma = 0$ in the top and bottom panels, respectively

symmetry in the model with the full 2D modulation of the gain-loss term may also be unbreakable, as the stability chart does features no upper boundary.

These charts include unstable and (very few) stable solitons with multi-peak shapes. Indeed, taking larger Γ, i.e., stronger confinement of the gain and loss in Eq. (15), it is possible to find *stable* multi-peak solitons with rather complex shapes, an example being a stable four-peak soliton displayed in Fig. 10 for $\Gamma = 0.5$.

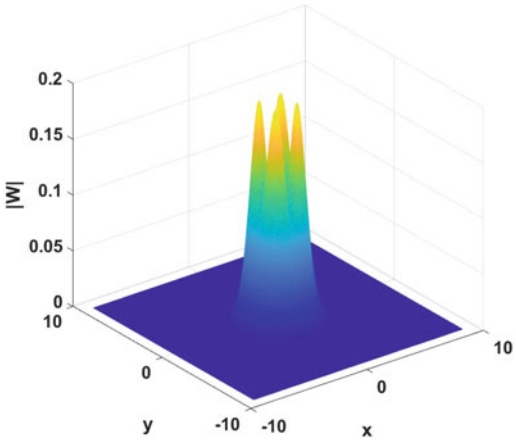

Fig. 10 An example of a stable $\mathcal{PT}$-symmetric four-peak soliton with propagation constant $b = -3$, found in the full 2D models with $\sigma = 1$ in Eq. (13) and $\Gamma = 0.5$ in Eq. (15)

The results for the quasi-1D and full 2D systems, reported in this section, do not provide an exhaustive analysis of these models. A comprehensive analysis, including, in particular, the consideration of possible solitons with embedded vorticity, will be presented elsewhere.

5 Conclusion

The objective of this article is to summarize theoretical results which demonstrate the stabilization of the $\mathcal{PT}$ symmetry in both linear and nonlinear systems, making it possible to produce $\mathcal{PT}$-symmetric states at arbitrarily large values of the strength of the gain-loss terms in the system, i.e., of the coefficient in front of the non-Hermitian part of the underlying $\mathcal{PT}$-symmetric Hamiltonian. In Sects. 2 and 3, we have surveyed previously reported results obtained in two altogether different settings. Namely, the possibility of the restoration and complete stabilization of the $\mathcal{PT}$ symmetry in the linear nanophotonic model of the waveguiding channel with a subwavelength width, the analysis of which is based on the full system of the Maxwell's equations, was recapitulated in Sect. 2. The full stabilization, i.e., removal of the symmetry-breaking transition, takes place in the deeply subwavelength region. In Sect. 3 we have summarized results concerning the possibility of finding stable 1D solitons supported by the model with arbitrarily large values of the gain-loss coefficient, where the self-trapping of the solitons is provided by the self-defocusing nonlinearity with the local strength growing fast enough from the center to periphery. The model admits a particular exact solution for the fundamental soliton, the families of both fundamental and dipole modes being entirely stable.

Section 4 has presented new results for the unbreakable $\mathcal{PT}$-symmetric solitons in two 2D extensions of the 1D model, viz., with the quasi-1D and full 2D modulation profiles of the local gain-loss coefficient. These models also admit

particular exact solutions, this time for 2D solitons. As a result, it is found the quasi-1D model readily gives rise to the stable family of fundamental (single-peak) 2D solitons for an arbitrarily large strength of the gain-loss term, while dual-peak ones are unstable. On the other hand, the stability of the solitons in the model with the full 2D gain-loss profile requires to impose spatial confinement on the gain-loss term. Further results for the 2D models will be presented elsewhere.

Acknowledgements This work was supported, in part, by Grant No. 2015616 from the joint program in physics between the NSF and Binational (US-Israel) Science Foundation, and by Grant No. 1286/17 from the Israel Science Foundation.

References

1. Landau, L.D., Lifshitz, E.M.: Quantum Mechanics. Nauka Publishers, Moscow (1974)
2. Bender, C.M., Boettcher, S.: Real spectra in non-Hermitian Hamiltonians having $\mathcal{PT}$ symmetry. Phys. Rev. Lett. **80**, 5243–5246 (1998).
3. Dorey, P., Dunning, C., Tateo, R.: Spectral equivalences, Bethe ansatz equations, and reality properties in $\mathcal{PT}$-symmetric quantum mechanics. J. Phys. A Math. Gen. **34**, 5679–5704 (2001)
4. Bender, C.M., Brody, D.C., Jones, H.F.: Complex extension of quantum mechanics. Phys. Rev. Lett. **89**, 270401 (2002)
5. Bender, C.M.: Making sense of non-Hermitian Hamiltonians. Rep. Prog. Phys. **70**, 947–1018 (2007)
6. Bender, C.M.: Rigorous backbone of $\mathcal{PT}$-symmetric quantum mechanics. J. Phys. A Math. Theor. **49**, 401002 (2016)
7. Makris, K.G., El-Ganainy, R., Christodoulides, D.N., Musslimani, Z.H.: $\mathcal{PT}$-symmetric periodic optical potentials. Int. J. Theor. Phys. **50**, 1019–1041 (2011)
8. Moiseyev, N.: Non-Hermitian Quantum Mechanics. Cambridge University Press, Cambridge (2011)
9. Zezyulin, D.A., Barashenkov, I.V., Konotop, V.V.: Stationary through-flows in a Bose-Einstein condensate with a PT-symmetric impurity. Phys. Rev. A **94**, 063649 (2016)
10. Barashenkov, I.V., Zezyulin, D.A., Konotop, V.V.: Jamming anomaly in $\mathcal{PT}$-symmetric systems. New J. Phys. **18**, 075015 (2016)
11. Barashenkov, I.V., Gianfreda, M.: An exactly solvable $\mathcal{PT}$-symmetric dimer from a Hamiltonian system of nonlinear oscillators with gain and loss. J. Phys. A **47**, 282001 (2014)
12. Barashenkov, I.V.: Hamiltonian formulation of the standard $\mathcal{PT}$-symmetric nonlinear Schrödinger dimer. Phys. Rev. A **90**, 045802 (2014)
13. Ruschhaupt, A., Delgado, F., Muga, J.G.: Physical realization of $\mathcal{PT}$-symmetric potential scattering in a planar slab waveguide. J. Phys. A Math. Gen. **38**, L171–L176 (2005)
14. El-Ganainy, R., Makris, K.G., Christodoulides, D.N., Musslimani, Z.H.: Theory of coupled optical $\mathcal{PT}$-symmetric structures. Opt. Lett. **32**, 2632–2634 (2007)
15. Musslimani, Z.H., Makris, K.G., El-Ganainy, R., Christodoulides, D.N.: Optical solitons in $\mathcal{PT}$ periodic potentials. Phys. Rev. Lett. **100**, 030402 (2008)
16. Berry, M.V.: Optical lattices with $\mathcal{PT}$-symmetry are not transparent. J. Phys. A Math. Theor. **41**, 244007 (2008)
17. Klaiman, S., Günther, U., Moiseyev, N.: Visualization of branch points in $\mathcal{PT}$-symmetric waveguides. Phys. Rev. Lett. **101**, 080402 (2008)
18. Longhi, S.: Bloch oscillations in complex crystals with $\mathcal{PT}$ symmetry. Phys. Rev. Lett. **103**, 123601 (2009)

19. Zezyulin, D.A., Kartashov, Y.V., Konotop, V.V.: Stability of solitons in $\mathcal{PT}$-symmetric nonlinear potentials. EPL **96**, 64003 (2011)
20. Driben, R., Malomed, B.A.: Stability of solitons in parity-time-symmetric couplers. Opt. Lett. **36**, 4323–4325 (2011)
21. Alexeeva, N.V., Barashenkov, I.V., Sukhorukov, A.A., Kivshar, Y.S.: Optical solitons in $\mathcal{PT}$-symmetric nonlinear couplers with gain and loss. Phys. Rev. A **85**, 063837 (2012)
22. Miri, M.-A., Aceves, A.B., Kottos, T., Kovanis, V., Christodoulides, D.N.: Bragg solitons in nonlinear $\mathcal{PT}$-symmetric periodic potentials. Phys. Rev. A **86**, 033801 (2012)
23. Nixon, S., Ge, L., Yang, J.: Stability analysis for solitons in $\mathcal{PT}$-symmetric optical lattices. Phys. Rev. A **85**, 023822 (2012)
24. D'Ambroise, J., Kevrekidis, P.G., Malomed, B.A.: Staggered parity-time-symmetric ladders with cubic nonlinearity. Phys. Rev. E **91**, 033207 (2015)
25. Alexeeva, N.V., Barashenkov, I.V., Kivshar, Y.S.: Solitons in $\mathcal{PT}$-symmetric ladders of optical waveguides. New J. Phys. **19**, 113032 (2017)
26. Kominis, Y., Bountis, T., Flach, S.: Stability through asymmetry: modulationally stable nonlinear supermodes of asymmetric non-Hermitian optical couplers. Phys. Rev. **95**, 063832 (2017)
27. Guo, A., Salamo, G.J., Duchesne, D., Morandotti, R., Volatier-Ravat, M., Aimez, V., Siviloglou, G.A., Christodoulides, D.N.: Observation of $\mathcal{PT}$-symmetry breaking in complex optical potentials. Phys. Rev. Lett. **103**, 093902 (2009)
28. Rüter, C.E., Makris, K.G., El-Ganainy, R., Christodoulides, D.N., Segev, M., Kip, D.: Observation of parity-time symmetry in optics. Nat. Phys. **6**, 192–195 (2010)
29. Regensburger, A., Bersch, C., Miri, M.A., Onishchukov, G., Christodoulides, D.N., Peschel, U.: Parity-time synthetic photonic lattices. Nature **488**, 167–171 (2012)
30. Wimmer, M., Regensburger, A., Miri, M.A., Bersch, C., Christodoulides, D.N., Peschel, U.: Observation of optical solitons in $\mathcal{PT}$-symmetric lattices. Nat. Commun. **6**, 7782 (2015)
31. Castaldi, G., Savoia, S., Galdi, V., Alù, A., Engheta, N.: $\mathcal{PT}$ metamaterials via complex-coordinate transformation optics. Phys. Rev. Lett. **110**, 173901 (2013)
32. Hodaei, H., Miri, M.A., Heinrich, M., Christodoulides, D.N., Khajavikhan, M.: Parity-time-symmetric microring lasers. Science **346**, 975–978 (2014)
33. Longhi, S.: $\mathcal{PT}$-symmetric laser absorber. Phys. Rev. A **82**, 031801 (2010)
34. Peng, B., Özdemir, Ş. K., Chen, W., Nori, F., Yang, L.: Parity-time-symmetric whispering gallery microcavities. Nat. Phys. **10**, 394–398 (2014)
35. Zhang, Z., Zhang, Y., Sheng, J., Yang, L., Miri, M.A., Christodoulides, D.N., He, B., Zhang, Y., Xiao, M.: Observation of parity-time symmetry in optically induced atomic lattices. Phys. Rev. Lett. **117**, 123601 (2016)
36. Lien, J.-Y., Chen, Y.-N., Ishida, N., Chen, H.-B., Hwang, C.-C., Nori, F.: Multistability and condensation of exciton-polaritons below threshold. Phys. Rev. B **91**, 024511 (2015)
37. Gao, T., Estrecho, E., Bliokh, K.Y., Liew, T.C.H., Fraser, M.D., Brodbeck, S., Kamp, M., Schneider, C., Höfling, S., Yamamoto, Y., Nori, F., Kivshar, Y.S., Truscott, A.G., Dall, R.G., Ostrovskaya, E.A.: Observation of non-Hermitian degeneracies in a chaotic exciton-polariton billiard. Nature **526**, 554–558 (2015)
38. Chestnov, I.Yu., Demirchyan, S.S., Alodjants, A.P., Rubo, Y.G., Kavokin, A.V.: Permanent Rabi oscillations in coupled exciton-photon systems with $\mathcal{PT}$-symmetry. Sci. Rep. **6**, 19551 (2016)
39. Ramezani, H., Kottos, T., El-Ganainy, R., Christodoulides, D.N.: Unidirectional nonlinear $\mathcal{PT}$-symmetric optical structures. Phys. Rev. A **82**, 043803 (2010)
40. Zhu, X., Ramezani, H., Shi, C., Zhu, J., Zhang, X.: $\mathcal{PT}$-symmetric acoustics. Phys. Rev. X **4**, 031042 (2014); Fleury, R., Sounas, D., Alú, A.: An invisible acoustic sensor based on parity-time symmetry. Nat. Commun. **6**, 5905 (2015)
41. Xu, X.-W., Liu, Y.-X., Sun, C.-P., Li, Y.: Mechanical $\mathcal{PT}$ symmetry in coupled optomechanical systems. Phys. Rev. A **92**, 013852 (2015)
42. Schwarz, L., Cartarius, H., Musslimani, Z.H., Main, J., Wunner, G.: Vortices in Bose-Einstein condensates with $\mathcal{PT}$-symmetric gain and loss. Phys. Rev. **95**, 053613 (2017)

43. Lee, J.M., Kottos, T., Shapiro, B.: Macroscopic magnetic structures with balanced gain and loss. Phys. Rev. B **91**, 094416 (2015)
44. Destyl, E., Nuiro, S.P., Pelinovsky, D.E., Poullet, P.: Coupled pendula chains under parametric $\mathcal{PT}$-symmetric driving force. Phys. Lett. A **381**, 3884–3892 (2017)
45. Schindler, J., Lin, Z., Lee, J.M., Ramezani, H., Ellis, F.M., Kottos, T.: $\mathcal{PT}$-symmetric electronics. J. Phys. A: Math. Theor. **45**, 444029 (2012)
46. Bender, C.M., Brody, D.C., Chen, J.-H.: $\mathcal{PT}$-symmetric extension of the Korteweg-de Vries equation. J. Phys. A Math. Theor. **40**, F153-F160 (2007)
47. Fring, A.: $\mathcal{PT}$-symmetric deformations of the Korteweg-de Vries equation. ibid. **40**, 4215–4334 (2007)
48. Yan, Z.Y.: Complex $\mathcal{PT}$-symmetric nonlinear Schrödinger equation and Burgers equation. Phil. Trans. R. Soc. A Math Phys. Eng. Sci. **371**, 20120059 (2013)
49. Cuevas-Maraver, J., Malomed, B., Kevrekidis, P.: A $\mathcal{PT}$-symmetric dual-core system with the sine-Gordon nonlinearity and derivative coupling. Symmetry **8**, 39 (2016)
50. Sakaguchi, H., Malomed, B.A.: One- and two-dimensional solitons in $\mathcal{PT}$-symmetric systems emulating spin-orbit coupling. New J. Phys. **18**, 105005 (2016)
51. Konotop, V.V., Yang, J., Zezyulin, D.A.: Nonlinear waves in $\mathcal{PT}$-symmetric systems. Rev. Mod. Phys. **88**, 035002 (2016)
52. Suchkov, S.V., Sukhorukov, A.A., Huang, J.H., Dmitriev, S.V., Lee, C., Kivshar, Y.S.: Nonlinear switching and solitons in $\mathcal{PT}$-symmetric photonic systems. Laser Photonics Rev. **10**, 177–213 (2016)
53. Zhu, X., Wang, H., Li, H., He, W., He, Y.: Two-dimensional multipeak gap solitons supported by parity-time-symmetric periodic potentials. Opt. Lett. **38**, 2723–2725 (2013)
54. Burlak, G., Malomed, B.A.: Stability boundary and collisions of two-dimensional solitons in $\mathcal{PT}$-symmetric couplers with the cubic-quintic nonlinearity. Phys. Rev. E **88**, 062904 (2013)
55. Yang, J.: Partially $\mathcal{PT}$-symmetric optical potentials with all-real spectra and soliton families in multidimensions. Opt. Lett. **39**, 1133–1136 (2014)
56. Ren, X., Wang, H., Wang, H., He, Y.: Stability of in-phase quadruple and vortex solitons in the parity-time-symmetric periodic potentials. Opt. Exp. **22**, 19774–19782 (2014)
57. Chen, Z., Liu, J., Fu, S., Li, Y., Malomed, B.A.: Discrete solitons and vortices on two-dimensional lattices of $\mathcal{PT}$-symmetric couplers. Opt. Exp. **22**, 29679–29692 (2014)
58. Wang, H., Shi, S., Ren, X., Zhu, X., Malomed, B.A., Mihalache, D., He, Y.: Two-dimensional solitons in triangular photonic lattices with parity-time symmetry. Opt. Commun. **335**, 146–152 (2015)
59. Yang, J.: Necessity of $\mathcal{PT}$ symmetry for soliton families in one-dimensional complex potentials. Phys. Lett. A **378**, 367–373 (2014)
60. Malomed, B.A.: Evolution of nonsoliton and "quasiclassical" wavetrains in nonlinear Schrödinger and Korteweg – de Vries equations with dissipative perturbations. Phys. D **29**, 155–172 (1987)
61. Vanin, E.V., Korytin, A.I., Sergeev, A.M., Anderson, D., Lisak, M., Vázquez, L.: Dissipative optical solitons. Phys. Rev. A **49**, 2806–2811 (1994)
62. Tsoy, E.N., Ankiewicz, A., Akhmediev, N.: Dynamical models for dissipative localized waves of the complex Ginzburg-Landau equation. Phys. Rev. E **73**, 036621 (2006)
63. Yang, J.: Symmetry breaking of solitons in one-dimensional parity-time-symmetric optical potentials. Opt. Lett. **39**, 5547–5550 (2014)
64. Kartashov, Y.V., Malomed, B.A., Torner, L.: Unbreakable $\mathcal{PT}$ symmetry of solitons supported by inhomogeneous defocusing nonlinearity. Opt. Lett. **39**, 5641–5644 (2014)
65. Soloman Raju, T., Ashok Hedge, T., Kumar, C.N.: Unbreakable $\mathcal{PT}$ symmetry of exact solitons in inhomogeneous nonlinear optical media. J. Opt. Soc. Am. B **33**, 35–40 (2016)
66. Guo, D., Xia, J., Gu, L., Jin, H., Dong, L.: One- and two-dimensional bright solitons in inhomogeneous defocusing nonlinearities with an antisymmetric periodic gain and loss. Phys. D **343**, 1–6 (2017)
67. Borovkova, O.V., Kartashov, Y.V., Malomed, B.A., Torner, L.: Algebraic bright and vortex solitons in defocusing media. Opt. Lett. **36**, 3088–3090 (2011)

68. Borovkova, O.V., Kartashov, Y.V., Torner, L., Malomed, B.A.: Bright solitons from defocusing nonlinearities. Phys. Rev. E **84**, 035602 (R) (2011)
69. Tian, Q., Wu, L., Zhang, Y., Zhang, J.-F.: Vortex solitons in defocusing media with spatially inhomogeneous nonlinearity. Phys. Rev. E **85**, 056603 (2012)
70. Wu, Y., Xie, Q., Zhong, H., Wen, L., Hai, W.: Algebraic bright and vortex solitons in self-defocusing media with spatially inhomogeneous nonlinearity. Phys. Rev. A **87**, 055801 (2013)
71. Cardoso, W.B., Zeng, J., Avelar, A.T., Bazeia, D., Malomed, B.A.: Bright solitons from the nonpolynomial Schrödinger equation with inhomogeneous defocusing nonlinearities. Phys. Rev. E **88**, 025201 (2013)
72. Driben, R., Kartashov, Y.V., Malomed, B.A., Meier, T., Torner, L.: Soliton gyroscopes in media with spatially growing repulsive nonlinearity. Phys. Rev. Lett. **112**, 020404 (2014)
73. Kartashov, Y.V., Malomed, B.A., Shnir, Y., Torner, L.: Twisted toroidal vortex-solitons in inhomogeneous media with repulsive nonlinearity. Phys. Rev. Lett. **113**, 264101 (2014)
74. Driben, R., Dror, N., Malomed, B., Meier, T.: Multipoles and vortex multiplets in multidimensional media with inhomogeneous defocusing nonlinearity. New J. Phys. **17**, 083043 (2015)
75. Kartashov, Y.V., Malomed, B.A., Vysloukh, V.A., Belić, M.R., Torner, L.: Rotating vortex clusters in media with inhomogeneous defocusing nonlinearity. Opt. Lett. **42**, 446–449 (2017)
76. Zeng, J., Malomed, B.A.: Localized dark solitons and vortices in defocusing media with spatially inhomogeneous nonlinearity. Phys. Rev. E **95**, 052214 (2017)
77. Zhong, R., Chen, Z., Huang, C., Luo, Z., Tan, H., Malomed, B.A., Li, Y.: Self-trapping under the two-dimensional spin-orbit-coupling and spatially growing repulsive nonlinearity. arXiv:1712.01430
78. Huang, C., Ye, F., Kartashov, Y.V., Malomed, B.A., Chen, X.: $\mathcal{PT}$ symmetry in optics beyond the paraxial approximation. Opt. Lett. **39**, 5443–5446 (2014)
79. Liang, C.H., Scott, D.D., Joglekar, Y.N.: $\mathcal{PT}$ restoration via increased loss and gain in the $\mathcal{PT}$-symmetric Aubry-André model. Phys. Rev. A **89**, 030102(R) (2014)
80. Lumer, Y., Plotnik, Y., Rechtsman, M.C., Segev, M.: Nonlinearly induced $\mathcal{PT}$ transition in photonic systems. Phys. Rev. Lett. **111**, 263901 (2013)
81. Yang, J.: Nonlinear waves in integrable and nonintegrable systems. SIAM, Philadelphia (2010)

Krein Signature in Hamiltonian and $\mathcal{PT}$-Symmetric Systems

A. Chernyavsky, P. G. Kevrekidis, and D. E. Pelinovsky

Abstract We explain the concept of Krein signature in Hamiltonian and $\mathcal{PT}$-symmetric systems on the case study of the one-dimensional Gross–Pitaevskii equation with a real harmonic potential and an imaginary linear potential. These potentials correspond to the magnetic trap, and a linear gain/loss in the mean-field model of cigar-shaped Bose–Einstein condensates. For the linearized Gross–Pitaevskii equation, we introduce the real-valued Krein quantity, which is nonzero if the eigenvalue is neutrally stable and simple and zero if the eigenvalue is unstable. If the neutrally stable eigenvalue is simple, it persists with respect to perturbations. However, if it is multiple, it may split into unstable eigenvalues under perturbations. A necessary condition for the onset of instability past the bifurcation point requires existence of two simple neutrally stable eigenvalues of opposite Krein signatures before the bifurcation point. This property is useful in the parameter continuations of neutrally stable eigenvalues of the linearized Gross–Pitaevskii equation.

Keywords Krein signature · Gross–Pitaevskii equation · Hamiltonian systems · $\mathcal{PT}$-symmetry · Instability bifurcations

A. Chernyavsky
Department of Mathematics and Applied Mathematics, University of Cape Town, Rondebosch, South Africa
e-mail: alexandr.chernyavsky@uct.ac.za

P. G. Kevrekidis
Department of Mathematics and Statistics, University of Massachusetts, Amherst, MA, USA
e-mail: kevrekid@math.umass.edu

D. E. Pelinovsky (✉)
Department of Mathematics and Statistics, McMaster University, Hamilton, Canada
e-mail: dmpeli@math.mcmaster.ca

D. Christodoulides, J. Yang (eds.), *Parity-time Symmetry and Its Applications*, Springer Tracts in Modern Physics 280,
https://doi.org/10.1007/978-981-13-1247-2_16

1 Introduction

We consider the prototypical example of the one-dimensional Gross-Pitaevskii (GP) equation arising in the context of cigar-shaped Bose–Einstein (BEC) condensates [42, 43]. The model takes the form of the following defocusing nonlinear Schrödinger (NLS) equation with a harmonic potential [9, 28]:

$$i\partial_t u = -\partial_x^2 u + V(x)u + |u|^2 u, \tag{1}$$

where u represents the complex wave function and V characterizes the external potential. The probability density of finding atoms at a given location and time is characterized by $|u|^2$.

In the case of magnetic trapping of the BECs [42, 43], the potential V is real-valued and is given by

$$V(x) = \Omega^2 x^2, \tag{2}$$

where Ω is the ratio of longitudinal to transverse confinement strengths of the parabolic trapping. The NLS equation (1) with the potential (2) is a Hamiltonian system written in the symplectic form

$$i\frac{\partial u}{\partial t} = \frac{\delta H}{\delta \bar{u}}, \tag{3}$$

where $\bar{u}$ stands for the complex conjugate u and H is the following real-valued Hamiltonian function

$$H(u) = \int_{\mathbb{R}} \left[|\partial_x u|^2 + V(x)|u|^2 + \frac{1}{2}|u|^4 \right] dx. \tag{4}$$

When quantum particles are loaded in an open system, the external potential V may be complex-valued [10, 18]. The intervals with positive and negative imaginary part of V correspond to the gain and loss of quantum particles, respectively. If the gain and loss are modeled by linear functions and the gain matches loss exactly, the external potential is given by

$$V(x) = \Omega^2 x^2 + 2i\gamma x, \tag{5}$$

where γ is the gain-loss strength. The NLS equation (1) with the potential (5) can still be cast to the form (3) but the Hamiltonian function H in (4) is now complex-valued. The complex-conjugate equation to (3) is determined by $\bar{H}$ with $\bar{H} \neq H$. Hence, the NLS equation (1) with the potential (5) is not a Hamiltonian system.

Although V in (5) is not real-valued, it satisfies the following condition

$$V(x) = \overline{V(-x)}, \quad x \in \mathbb{R}. \tag{6}$$

Let us introduce the parity operator $\mathcal{P}$ and the time reversal operator $\mathcal{T}$ acting on a function $u(x,t)$ as follows:

$$\mathcal{P}u(x,t) = u(-x,t), \quad \mathcal{T}u(x,t) = \overline{u(x,-t)}. \tag{7}$$

Then, we can see that V satisfying (6) is $\mathcal{PT}$-symmetric under the simultaneous action of operators (7). We say that the NLS equation (1) with the potential (5) is $\mathcal{PT}$-symmetric. For any solution $u(x,t)$,

$$\widetilde{u}(x,t) = \mathcal{PT}u(x,t) = \overline{u(-x,-t)}$$

is also a solution to the same NLS equation (1) with the potential (5).

Such $\mathcal{PT}$-symmetric models have attracted substantial attention over the past two decades. They were initially proposed in the context of a (non-Hermitian) variant of quantum mechanics [6, 7] (see also review in [4]). However, their experimental realization in both low-dimensional (e.g., dimer) [45] and high-dimensional (e.g., lattice) [52] settings has been confirmed in nonlinear optics. This direction has also inspired an extensive volume of theoretical activity and even experiments in other areas, including mechanical [5] and electrical [46] systems. Two recent reviews on the subject can be found in [32, 50].

The concept of Krein signatures was introduced by MacKay [34] for the finite-dimensional linear Hamiltonian systems, although the idea dates back to the works of Weierstrass [51]. In the setting of the NLS equation (1) with the potential (2), the linear Hamiltonian system can be formulated as the spectral problem

$$J\mathcal{L}v = \lambda v, \tag{8}$$

where $\mathcal{L}$ is a self-adjoint unbounded operator in the space of square-integrable functions $L^2(\mathbb{R})$ with a dense domain in $L^2(\mathbb{R})$ and J is a skew-adjoint bounded operator in $L^2(\mathbb{R})$. The operators $\mathcal{L}$ and J are assumed to satisfy $J^2 = -I$ and $J\mathcal{L} + \bar{\mathcal{L}}\bar{J} = 0$, thanks to the Hamiltonian symmetry.

If $\lambda_0 \in \mathbb{C}$ is an eigenvalue of the spectral problem (8), then it is neutrally stable if $\mathrm{Re}(\lambda_0) = 0$ and unstable if $\mathrm{Re}(\lambda_0) > 0$. Thanks to the Hamiltonian symmetry of $\mathcal{L}$ and J, the eigenvalues appear in symmetric pairs relative to the axis $\mathrm{Re}(\lambda) = 0$. Indeed, if v is an eigenvector of the spectral problem (8) for the eigenvalue λ, then $w = -J\bar{v}$ is an eigenvector of the same spectral problem (8) with the eigenvalue $-\bar{\lambda}$, which follows from the following equivalent transformations of the spectral problem (8) with $v = \bar{J}\bar{w}$:

$$J\mathcal{L}\bar{J}\bar{w} = \lambda\bar{J}\bar{w} \quad \Leftrightarrow \quad \bar{\mathcal{L}}\bar{w} = \lambda\bar{J}\bar{w} \quad \Leftrightarrow \quad \bar{J}\bar{\mathcal{L}}\bar{w} = -\lambda\bar{w} \quad \Leftrightarrow \quad J\mathcal{L}w = -\bar{\lambda}w.$$

For a nonzero eigenvalue $\lambda_0 \in \mathbb{C}$ of the spectral problem (8) with the eigenvector v_0 in the domain of $\mathcal{L}$, we define the Krein quantity $K(\lambda_0)$ by

$$K(\lambda_0) := \langle \mathcal{L}v_0, v_0 \rangle, \tag{9}$$

where $\langle \cdot, \cdot \rangle$ is the standard inner product in $L^2(\mathbb{R})$. The Krein quantity in (9) satisfies the following properties:

Main properties of the Krein quantity:

(1) $K(\lambda_0)$ is real if $\lambda_0 \in i\mathbb{R}$.
(2) $K(\lambda_0)$ is nonzero if $\lambda_0 \in i\mathbb{R}\backslash\{0\}$ is simple.
(3) $K(\lambda_0)$ is zero if $\lambda_0 \in \mathbb{C}\backslash\{i\mathbb{R}\}$.

The Krein signature is defined as the sign of the Krein quantity $K(\lambda_0)$ for a simple neutrally stable eigenvalue $\lambda_0 \in i\mathbb{R}\backslash\{0\}$. If parameters of the NLS equation (1) change, parameters of the spectral problem (8) change, however, the simple eigenvalue $\lambda_0 \in i\mathbb{R}$ remains on the axis $\mathrm{Re}(\lambda) = 0$ unless it coalesces with another eigenvalue or a part of the continuous spectrum, thanks to the preservation of its multiplicity and the Hamiltonian symmetry of eigenvalues. In this case, the eigenvalue λ_0 and its Krein quantity $K(\lambda_0)$ are at least continuous functions of the parameters of the NLS equation (1).

It is quite typical in the parameter continuations of the spectral problem (8) to see that the simple eigenvalue $\lambda_0 \in i\mathbb{R}$ coalesces at a bifurcation point with another simple eigenvalue $\lambda_0' \in i\mathbb{R}$ and that both eigenvalues split into the complex plane as unstable eigenvalues past the bifurcation point. The Krein signature is a helpful tool towards predicting this instability bifurcation from the following necessary condition.

Necessary condition for instability bifurcation. *Under some non-degeneracy constraints, the double eigenvalue $\lambda_0 = \lambda_0' \in i\mathbb{R}$ of the spectral problem (8) with a bifurcation parameter $\varepsilon \in \mathbb{R}$ splits into a pair of complex eigenvalues symmetric relative to $\mathrm{Re}(\lambda) = 0$ for $\varepsilon > 0$ only if there exist two simple eigenvalues $\lambda_0, \lambda_0' \in i\mathbb{R}$ with the opposite Krein signature for $\varepsilon < 0$.*

In other words, if two neutrally stable eigenvalues of the same Krein signature move towards each other in the parameter continuation of the spectral problem (8), then their coalescence will not result in the onset of instability, whereas if the two neutrally stable eigenvalues have the opposite Krein signature, their coalescence is expected to result in the onset of instability, subject to technical non-degeneracy constraints.

The concept of Krein signature in the infinite-dimensional setting, e.g. for the NLS equation, was introduced independently in works [23, 37]. It was justified in a number of mathematical publications [14, 24] and it remains a practical tool to trace instability bifurcations in physically relevant Hamiltonian systems [41, 47] (see review in [31]). The following completeness result is available for the Hamiltonian systems.

Hamiltonian–Krein Theorem. *If $\mathcal{L}$ has finitely many negative eigenvalues $n(\mathcal{L}) < \infty$ and the rest of its spectrum is strictly positive, then eigenvalues of the spectral problem (8) satisfy the completeness relation*

$$n(\mathcal{L}) = N_{\text{real}} + N_{\text{comp}} + N_{\text{imag}}^{-},$$

where N_{real} is the number of real positive eigenvalues λ, N_{comp} is the number of complex eigenvalues λ with $\text{Re}(\lambda) > 0$, and N_{imag}^{-} is the number of purely imaginary eigenvalues λ with negative Krein signature. All numbers are accounted in their algebraic multiplicity.

In the context of the NLS equation (1) with the potential (2), the phase invariance introduces a symmetry and a kernel of the operator $\mathcal{L}$. In this case, the negative index $n(\mathcal{L})$ has to be recomputed in a subspace of $L^2(\mathbb{R})$ which is J-orthogonal to the kernel of $\mathcal{L}$. See monographs [25, 39] for further mathematical details.

It was only very recently that the concept of Krein signature was extended to the non-Hamiltonian $\mathcal{PT}$-symmetric systems. The linear Schrödinger equation with a complex-valued $\mathcal{PT}$-symmetric potential was considered in [35], where the indefinite $\mathcal{PT}$-inner product with the induced $\mathcal{PT}$-Krein signature was introduced in the exact correspondence with the Krein signature for the Hamiltonian spectral problem (8). Coupled non-Hamiltonian $\mathcal{PT}$-symmetric systems were considered in [2, 3] (see also [48]), where the linearized problem was block-diagonalized to the form for which the Krein signature of eigenvalues can be introduced. A Hamiltonian version of the $\mathcal{PT}$-symmetric system of coupled oscillators was considered in [11, 12], where the Krein signature of eigenvalues was introduced by using the corresponding Hamiltonian. Finally, Krein signature of eigenvalues was defined in [13] for the spectral problem related to the linearization of the NLS equation with complex-valued potentials.

Compared to the Hamiltonian case in [23, 37] and to the linear $\mathcal{PT}$-symmetric Schrödinger equation in [35], it was shown in [13] that the Krein signature of eigenvalues in the linearization of the $\mathcal{PT}$-symmetric NLS equation cannot be computed just from the eigenvectors in the spectral problem. This is because the adjoint eigenvectors need to be computed separately and the sign of the adjoint eigenvector needs to be chosen by a continuity argument. This limits practical applications of the Krein signature in nonlinear $\mathcal{PT}$-symmetric systems. Nevertheless, the main properties of the Krein quantity listed above for the Hamiltonian NLS equation are extended to the case of the $\mathcal{PT}$-symmetric NLS equation. Moreover, the necessary condition for the instability bifurcation is extended to the $\mathcal{PT}$-symmetric NLS equation but not the Hamiltonian–Krein Theorem.

The purpose of this chapter is to explain definitions and properties of the Krein signature on the prototypical example of the NLS equation (1) with either the potential (2) or the potential (5).

We also address the Krein signature in the linear $\mathcal{PT}$-symmetric Schrödinger equation as the one introduced in [35], where we discuss differences from the Krein signature in the linearized $\mathcal{PT}$-symmetric NLS equation introduced here. We will show that the linear Schrödinger equation with a real even potential (2) admits two equivalent Hamiltonian formulations and hence two equivalent definitions of the Krein signatures. The standard Hamiltonian formulation leads to eigenvalues of only positive Krein signature, whereas the non-standard Hamiltonian formulation leads to infinitely many eigenvalues of opposite Krein signature. It is the latter Hamiltonian formulation that can be extended to the case of the $\mathcal{PT}$-symmetric potential (5).

This chapter is organized as follows. Section 2 addresses nonlinear stationary states bifurcating from simple eigenvalues of the quantum harmonic oscillator and describes Krein signature in the linearized NLS equation with the potential (2). Section 3 describes Krein signature for the $\mathcal{PT}$-symmetric NLS equation with the potential (5), where we highlight the differences between the Hamiltonian and the $\mathcal{PT}$-symmetric cases. Section 4 contains discussion of the linear $\mathcal{PT}$-symmetric Schrödinger equation. Section 5 summarizes the results and lists further directions.

2 Krein Signature for the NLS Equation

In the context of the NLS equation (1) with the potential (2), we consider the nonlinear stationary states of the form $u(x,t) = e^{-i\mu t}\phi(x)$, where $\mu \in \mathbb{R}$ is referred to as the chemical potential [18] and the real-valued function ϕ satisfies the differential equation

$$\mu\phi(x) = -\phi''(x) + x^2\phi(x) + \phi(x)^3, \tag{10}$$

where we have set $\Omega = 1$ without loss of generality. In the linear (small-amplitude) limit, we obtain the quantum harmonic oscillator with the eigenvalues $\mu_n = 1 + 2n$, $n \in \mathbb{N}_0 := \{0, 1, 2, \ldots\}$ and the L^2-normalized eigenfunctions

$$\varphi_n(x) = \frac{1}{\sqrt{2^n n!\sqrt{\pi}}} H_n(x) e^{-x^2/2},$$

where H_n is the Hermite polynomial of degree n, e.g., $H_0(x) = 1$, $H_1(x) = 2x$, $H_2(x) = 4x^2 - 2$, etc.

Each eigenfunction φ_n for a simple eigenvalue μ_n generates a branch of solutions bifurcating in the stationary problem (10). This follows from the general Crandall–Rabinowitz bifurcation theory [16] and is generally used in physics community, see, e.g., [20, 54]. Each branch can be approximated by the following expansion in terms of the small parameter ϵ:

$$\begin{cases} \mu = \mu_n + \epsilon^2 \mu_n^{(2)} + \ldots, \\ \phi = \epsilon \varphi_n + \epsilon^3 \varphi_n^{(3)} + \ldots, \end{cases} \tag{11}$$

where (μ_n, φ_n) is the n-th eigenvalue–eigenfunction pair, $(\mu_n^{(2)}, \varphi_n^{(3)})$ are the next-order correction terms to be found, and the dots denote the higher-order corrections terms. The n-th branch of the nonlinear stationary states is smooth with respect to the small parameter ϵ, which parameterizes both μ and ϕ, whereas it has a square-root singularity when it is written in terms of the parameter $\mu - \mu_n$.

The formal solvability condition for the correction terms $(\mu_n^{(2)}, \varphi_n^{(3)})$ yields

$$\mu_n^{(2)} = \int_{\mathbb{R}} \varphi_n(x)^4 dx > 0, \tag{12}$$

which implies that the branch of nonlinear stationary states extends towards $\mu > \mu_n$. The limit $\mu \to \infty$ can be rescaled as the semi-classical limit. Each n-th branch of the nonlinear stationary states is uniquely extended to the limit $\mu \to \infty$, where it is approximated asymptotically as a bound state of n dark solitons on the background of the harmonic potential V in (2) [15, 38].

When considering the stability of the nonlinear stationary state of the form $u(x,t) = e^{-i\mu t}\phi(x)$, we linearize the NLS equation (1) with the expansion

$$u(x,t) = e^{-i\mu t}\left[\phi(x) + \delta\left(a(x)e^{-\lambda t} + \bar{b}(x)e^{-\bar{\lambda} t}\right) + \ldots\right], \tag{13}$$

where δ is a formal small parameter. To the leading order in δ, the eigenvalue–eigenvector pair (λ, v) with $v = (a, b)^T$ is found from the spectral problem

$$\mathcal{L} v = -i\lambda \sigma_3 v, \tag{14}$$

where $\sigma_3 = \mathrm{diag}(1, -1)$ and the linear operator $\mathcal{L}$ is written in the differential form:

$$\mathcal{L} = \begin{bmatrix} -\partial_x^2 + x^2 - \mu + 2\phi(x)^2 & \phi(x)^2 \\ \phi(x)^2 & -\partial_x^2 + x^2 - \mu + 2\phi(x)^2 \end{bmatrix}. \tag{15}$$

The operator $\mathcal{L}$ is extended to a self-adjoint operator in $L^2(\mathbb{R})$ with the domain $H^2(\mathbb{R}) \cap L^{2,2}(\mathbb{R})$ (see [22], Ch. 4, p.37), where $H^2(\mathbb{R})$ is the Sobolev space of square integrable functions and their second derivatives and $L^{2,2}(\mathbb{R})$ is the space of square integrable functions multiplied by $(1 + x^2)$. The spectrum of $\mathcal{L}$ is purely discrete (see [44], Ch. XIII, Theorem 16 on p.120).

The spectral problem (14) takes the abstract form (8) with the self-adjoint operator $\mathcal{L}$ given by (15) and the skew-symmetric operator $J = i\sigma_3$. The Hamiltonian symmetry $J^2 = -I$ and $J\mathcal{L} + \bar{\mathcal{L}}\bar{J} = 0$ (or, equivalently, $\sigma_3 \mathcal{L} = \bar{\mathcal{L}}\sigma_3$) is satisfied. The eigenvalues are symmetric relative to the imaginary axis. To be precise, if λ_0 is an eigenvalue with the eigenvector $v_0 = (a, b)^T$, then $-\bar{\lambda}_0$ is another

eigenvalue with the eigenvector $\sigma_3\bar{v}_0 = (\overline{a}, -\overline{b})^T$ by the Hamiltonian symmetry $\sigma_3\mathcal{L} = \bar{\mathcal{L}}\sigma_3$.

In addition to the Hamiltonian symmetry, the operator $\mathcal{L}$ in (15) satisfies $\sigma_1\mathcal{L} = \bar{\mathcal{L}}\sigma_1$, where $\sigma_1 = \text{antidiag}(1, 1)$. This symmetry implies that the eigenvalues are symmetric relative to the real axis. Indeed, if λ_0 is an eigenvalue with the eigenvector $v_0 = (a, b)^T$, then $\bar{\lambda}_0$ is another eigenvalue with the eigenvector $\sigma_1\bar{v}_0 = (\bar{b}, \bar{a})$. Hence, the unstable eigenvalues with $\text{Re}(\lambda_0) > 0$ occur either as pairs on the real axis or as quadruplets in the complex plane, whereas the neutrally stable eigenvalues with $\text{Re}(\lambda_0) = 0$ occur as pairs on the imaginary axis.

For each nonzero eigenvalue $\lambda_0 \in \mathbb{C}$ of the spectral problem (14) with the eigenvector $v_0 = (a, b)^T \in H^2(\mathbb{R}) \cap L^{2,2}(\mathbb{R})$, the Krein quantity $K(\lambda_0)$ introduced in (9) can be written explicitly as follows:

$$K(\lambda_0) = \langle \mathcal{L}v_0, v_0\rangle = -i\lambda_0\langle\sigma_3 v_0, v_0\rangle = -i\lambda_0 \int_{\mathbb{R}} \Big[|a(x)|^2 - |b(x)|^2\Big]\, dx. \quad (16)$$

If $K(\lambda_0)$ is nonzero and real, the sign of $K(\lambda_0)$ is referred to as the Krein signature. In what follows, we only consider eigenvalues with $\lambda_0 \in i\mathbb{R}_+$, for which $-i\lambda_0 > 0$.

Let us verify the main properties of the Krein quantity $K(\lambda_0)$.

(1) If $\lambda_0 \in i\mathbb{R}$, then $(-i\lambda_0) \in \mathbb{R}$. The integral in (16) is also real. Hence, $K(\lambda_0)$ is real.

(2) Let us write the eigenvalue problem (15) for the generalized eigenvector v_g:

$$(\mathcal{L} + i\lambda_0\sigma_3)v_g = \sigma_3 v_0. \quad (17)$$

If $\lambda_0 \in i\mathbb{R}\backslash\{0\}$, then v_0 is in the kernel of the adjoint operator $(\mathcal{L}+i\lambda_0\sigma_3)^*$, and the Fredholm solvability condition of the above equation is $\langle\sigma_3 v_0, v_0\rangle = 0$. If $K(\lambda_0) = 0$, then there exists a solution to the nonhomogeneous equation (17), so that λ_0 is not simple. Hence, $K(\lambda_0) \neq 0$.

(3) Using the self-adjoint property of $\mathcal{L}$, one can write

$$\langle \mathcal{L}v_0, v_0\rangle = \langle v_0, \mathcal{L}v_0\rangle,$$

which can be expanded as

$$-i\lambda_0\langle\sigma_3 v_0, v_0\rangle = i\bar{\lambda}_0\langle v_0, \sigma_3 v_0\rangle,$$

where the equality holds either for $\lambda_0 \in i\mathbb{R}$ or $\langle\sigma_3 v_0, v_0\rangle = 0$. Hence $K(\lambda_0) = 0$ for $\lambda_0 \notin i\mathbb{R}$.

Let us now illustrate how the Krein signatures can be used to predict instability bifurcations from multiple neutrally stable eigenvalues of the spectral problem (14). We restrict consideration to the small-amplitude limit. If $\epsilon = 0$ and $\mu = \mu_n$, the linear operator (15) becomes diagonal:

$$\mathcal{L}_0 = \begin{bmatrix} -\partial_x^2 + x^2 - \mu_n & 0 \\ 0 & -\partial_x^2 + x^2 - \mu_n \end{bmatrix}$$

and the eigenvalues are located at $\sigma(\mathcal{L}_0) = \{2(m-n), \quad m \in \mathbb{N}_0\}$, where $n \in \mathbb{N}_0$ is fixed. Because of the skew-symmetric operator $J = i\sigma_3$ in the right-hand side of the spectral problem (14), these eigenvalues are mapped to the imaginary axis in the pairs $\lambda \in \pm i\{2(m-n), \ m \in \mathbb{N}_0\}$.

If $n = 0$, the ground state branch (11) leads to a double zero eigenvalue and a set of simple eigenvalues in pairs $\lambda \in \pm i\{2m, \quad m \in \mathbb{N}_0 \backslash \{0\}\}$. The double zero eigenvalue is preserved in ϵ due to gauge symmetry, whereas the simple neutrally stable eigenvalues are preserved on the imaginary axis due to Hamiltonian symmetry (at least for small ϵ). Moreover, each eigenvalue has a positive Krein signature, therefore, by the necessary condition for instability bifurcations, no complex eigenvalue quartets can arise in parameter continuations of solutions to the spectral problem (14) in ϵ (or equivalently, in μ). These spectral stability properties are natural for the ground state solution.

If $n = 1$, the first excited state branch (11) associated with a single dark soliton [15, 38] leads to a double zero eigenvalue, a pair of double eigenvalues $\lambda = \pm 2i$, and a set of simple eigenvalues in pairs $\lambda \in \pm i\{2(m-1), \ m \in \mathbb{N}_0 \backslash \{0, 1, 2\}\}$. The double zero eigenvalue is again preserved in ϵ due to gauge symmetry but the pair of nonzero double eigenvalues $\lambda = \pm 2i$ may split if $\epsilon \neq 0$. Note that two linearly independent eigenvectors exist for $\lambda_0 = 2i$:

$$v_1 = \begin{bmatrix} \varphi_2 \\ 0 \end{bmatrix}, \quad v_2 = \begin{bmatrix} 0 \\ \varphi_0 \end{bmatrix}. \tag{18}$$

The two eigenvectors induce opposite Krein signatures for the coalescent double eigenvalue since $K(\lambda_0) > 0$ for v_1 and $K(\lambda_0) < 0$ for v_2. Therefore, by the necessary condition on the splitting of the double eigenvalues, we may anticipate unstable eigenvalues for small ϵ.

Similarly, if $n = 2$, the second excited state branch (11) associated with two dark solitons [15, 38] leads to a double zero eigenvalue, two pairs of double eigenvalues $\lambda = \pm 2i$ and $\lambda = \pm 4i$, and a set of simple eigenvalues in pairs $\lambda \in \pm i\{2(m-2), m \in \mathbb{N}_0 \backslash \{0, 1, 2, 3, 4\}\}$. The double zero eigenvalue is again preserved in ϵ due to gauge symmetry but the pairs of nonzero double eigenvalues $\lambda = \pm 2i$ and $\lambda = \pm 4i$ may split if $\epsilon \neq 0$. Note that two linearly independent eigenvectors exist as follows:

$$\lambda_0 = 2i: \quad v_1 = \begin{bmatrix} \varphi_3 \\ 0 \end{bmatrix}, \quad v_2 = \begin{bmatrix} 0 \\ \varphi_1 \end{bmatrix} \tag{19}$$

and

$$\lambda_0 = 4i: \quad v_1 = \begin{bmatrix} \varphi_4 \\ 0 \end{bmatrix}, \quad v_2 = \begin{bmatrix} 0 \\ \varphi_0 \end{bmatrix}. \tag{20}$$

Again, the two eigenvectors induce opposite Krein signatures for each coalescent double eigenvalue, hence by the necessary condition on the splitting of the double eigenvalues, we may anticipate unstable eigenvalues for small ϵ.

In order to compute definite predictions whether or not the double eigenvalues produce instability bifurcations for the first and second excited states, we shall proceed using perturbation theory arguments. We substitute expansion (11) into the spectral problem (14) and expand it into powers of ϵ^2 as follows:

$$(\mathcal{L}_0 + \epsilon^2 \mathcal{L}_1 + \dots)v = -i\lambda\sigma_3 v, \tag{21}$$

where

$$\mathcal{L}_1 = \begin{bmatrix} 2\varphi_n(x)^2 - \mu_n^{(2)} & \varphi_n(x)^2 \\ \varphi_n(x)^2 & 2\varphi_n(x)^2 - \mu_n^{(2)} \end{bmatrix}.$$

Let $-i\lambda = \omega_0 + \epsilon^2\omega_1 + \dots$, where ω_0 is a coalescent double eigenvalue and ω_1 is a correction term. Representing $v = c_1 v_1 + c_2 v_2 + \dots$ and projecting the perturbed spectral problem (21) to the eigenvectors v_1 and v_2 yield the matrix eigenvalue problem

$$M \begin{bmatrix} c_1 \\ c_2 \end{bmatrix} = \omega_1 \sigma_3 \begin{bmatrix} c_1 \\ c_2 \end{bmatrix}, \tag{22}$$

where $M_{ij} = \langle \mathcal{L}_1 v_i, v_j \rangle$, $1 \le i, j \le 2$, and the L^2 normalization of eigenvectors has been taken into account.

Let us consider the first excited state $n = 1$ bifurcating from $\mu_1 = 3$. For $\epsilon = 0$, the eigenvalue at $\omega_0 = 2$ is double with two eigenvectors (18). However, there exists a linear combination of v_1 and v_2 which produces the so-called dipolar oscillation (also known as the Kohn mode, see explicit solutions in [29]) and thus the eigenvalue at $\omega_0 = 2$ related to this linear combination is independent of the variations of the chemical potential in ϵ. The shift of the eigenvalue for another linear combination of v_1 and v_2 has been the subject of intense scrutiny as it is associated with the oscillation frequency of the dark soliton in the parabolic trap [8, 40].

By using (12) for $n = 1$, we find $\mu_1^{(2)} = 3/(4\sqrt{2\pi})$. The matrix M in the matrix eigenvalue problem (22) is computed explicitly as

$$M = \begin{bmatrix} \frac{1}{8\sqrt{2\pi}} & \frac{1}{8\sqrt{\pi}} \\ \frac{1}{8\sqrt{\pi}} & \frac{1}{4\sqrt{2\pi}} \end{bmatrix}.$$

Computations of eigenvalues of the matrix eigenvalue problem (22) yield 0 and $-1/(8\sqrt{2\pi})$. The zero eigenvalue corresponds to the dipolar oscillations. The nonzero eigenvalue near $\omega_0 = 2$ is given by the following expansion:

$$\omega = 2 - \frac{1}{6}(\mu - 3) + \dots$$

Numerical results on the top left panel of Fig. 1 confirm this prediction. The smallest nonzero eigenvalue remains below $\omega_0 = 2$ and approaches $\omega \to \sqrt{2}$ as $\mu \to \infty$, in agreement with the previous results [8, 40].

It is relevant to indicate that the asymptotic limit of the eigenfrequencies of the ground state solution with $n = 0$ can be computed in the limit of large μ [49] (see also [29] for a recent account of the relevant analysis). These modes include the so-called dipolar oscillation, quadrupolar oscillation, etc. (associated, respectively, to $m = 1$, $m = 2$, etc.) and the corresponding eigenfrequencies are given by the analytical expression in the limit $\mu \to \infty$:

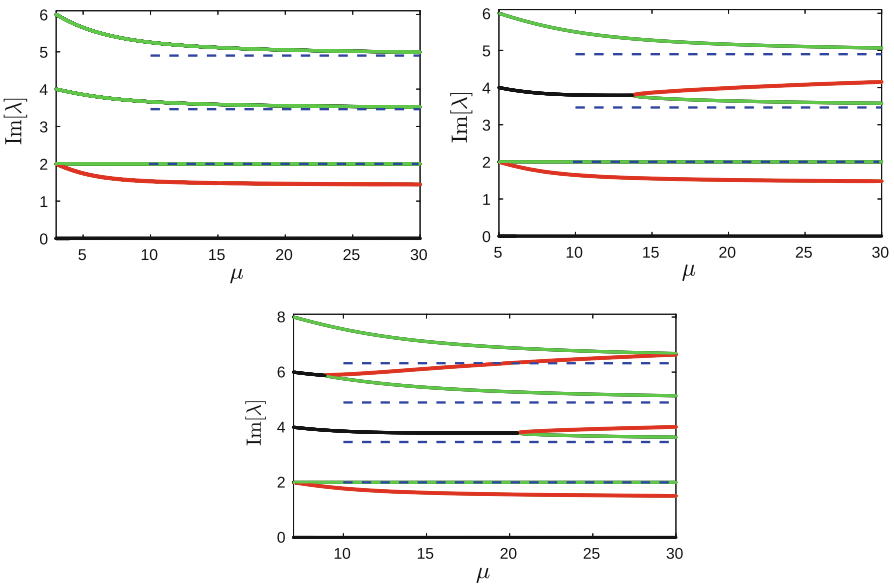

Fig. 1 The top left panel corresponds to the case of the first excited state, the top right one corresponds to the second excited state, while the bottom panel corresponds to the third excited state. Eigenvalues of negative (positive) Krein signature are shown in red (green), complex eigenvalues are shown in black. Asymptotic values in (23) are shown using blue dashed lines. For the first excited state, only the lowest nonzero eigenfrequency has a negative Krein signature (but its linear degeneracy with a symmetry mode yields no instability). For the second excited state, there are two degenerate modes at 2 and 4. Only the latter yields the quartet of complex eigenvalues. For the third excited state, there are three degenerate modes at 2, 4, and 6; the last two yield quartets of complex eigenvalues

$$\omega_m = \sqrt{2m(m+1)}, \quad m \in \mathbb{N}. \tag{23}$$

These asymptotic values are also shown on Fig. 1 by using blue dashed lines. From the top left panel, we can see that these frequencies of the ground state solution are present in the linearization of the first excited state in addition to the eigenfrequency $\omega_* = \sqrt{2}$, which corresponds to the oscillation of the dark soliton inside the trap.

While the example of the first excited state is instructive, it does not show any instability bifurcations due to coalescence of eigenvalues of the opposite Krein signatures. This is because although the eigenfrequency at $\omega_0 = 2$ is double, the dipolar oscillations do not allow the manifestation of an instability as a result of resonance. However, the onset of instability can still be found for the other excited states, e.g. for the second excited state $n = 2$ bifurcating from $\mu_2 = 5$.

By using (12) for $n = 2$, we find $\mu_2^{(2)} = 41/(64\sqrt{2\pi})$. At $\epsilon = 0$, the eigenvalue at $\omega_0 = 2$ is double with the two eigenvectors (19). The dipolar oscillation mode is present again and corresponds to the eigenvalue at $\omega_0 = 2$ independently of the variations of the chemical potential in ϵ. The other eigenvalue at $\omega_0 = 2$ is shifted for small ϵ. The matrix M in the matrix eigenvalue problem (22) is computed explicitly as

$$M = \begin{bmatrix} \frac{5}{32\sqrt{2\pi}} & \frac{15}{64\sqrt{3\pi}} \\ \frac{15}{64\sqrt{3\pi}} & \frac{15}{64\sqrt{2\pi}} \end{bmatrix}.$$

Computations of eigenvalues of the matrix eigenvalue problem (22) yield 0 and $-5/(64\sqrt{2\pi})$. The nonzero eigenvalue near $\omega_0 = 2$ is given by the following expansion:

$$\omega = 2 - \frac{5}{41}(\mu - 5) + \ldots \tag{24}$$

While the degeneracy at $\omega_0 = 2$ does not lead to the onset of instability, let us consider the double eigenvalue at $\omega_0 = 4$ with the two eigenvectors (20). The matrix M in the matrix eigenvalue problem (22) is computed explicitly as

$$M = \begin{bmatrix} \frac{1}{512\sqrt{2\pi}} & \frac{9}{128\sqrt{3\pi}} \\ \frac{9}{128\sqrt{3\pi}} & \frac{7}{64\sqrt{2\pi}} \end{bmatrix}.$$

The complex eigenvalues of the matrix eigenvalue problem (22) are given by $(-55 \pm 3\sqrt{23}i)/(2048\sqrt{2\pi})$. The complex eigenvalues near $\omega_0 = 4$ are given by the following expansion:

$$\omega = 4 + \frac{-55 \pm 3\sqrt{23}i}{656}(\mu - 5) + \ldots \tag{25}$$

The eigenvalues remain complex for values of $\mu \gtrsim 5$ but coalesce again on the imaginary axis at $\mu \approx 13.75$ and reappear as pairs of imaginary eigenvalues of the opposite Krein signatures. This reversed instability bifurcation takes place in a complete agreement with the necessary condition for the instability bifurcations.

In the large chemical potential limit, the eigenfrequencies of the linearization at the excited state with $n = 2$ include the same eigenfrequencies of the linearization at the ground state with $n = 0$ given by (23), see the top right panel of Fig. 1. In addition, two modes with negative Krein signature appear due to the dynamics of the two dark solitary waves on the ground state. One mode represents the in-phase oscillation of the two dark solitons and it is continued from the eigenvalue expanded by (24) to the limit $\mu \to \infty$, where it approaches $\omega_* = \sqrt{2}$. The other mode represents the out-of-phase oscillation of the two dark solitons and it appears from the complex pair (25) which reappears back on the imaginary axis for higher values of the chemical potential μ. Asymptotic approximation of the out-of-phase oscillation in the limit $\mu \to \infty$ is obtained in [15].

This pattern continues for other excited states with $n \geq 3$. The bottom panel on Fig. 1 shows the case $n = 3$. For every $n \geq 3$, there are n double eigenvalues with opposite Krein signature at $\epsilon = 0$. If $\epsilon \neq 0$, the lowest double eigenvalue does not lead to instability due to its linear degeneracy with the dipolar symmetry mode. The remaining $n - 1$ double eigenvalues may yield instability bifurcations with complex eigenvalues. For large μ, these eigenvalues reappear on the imaginary axis after the reversed instability bifurcations in agreement with the necessary condition for the instability bifurcation. The n eigenvalues of negative Krein signature characterize n dark solitons on top of the ground state solution. As such, they provide a rather lucid example of the nature and relevance of the negative Krein signature concept. Further details can be found in [15] for the large μ case and in [27] for the small μ case.

3 Krein Signature for the Nonlinear $\mathcal{PT}$-Symmetric Schrödinger Equation

Next, we consider the $\mathcal{PT}$-symmetric NLS equation (1) with the potential (5). Taking the nonlinear stationary states in the form $u(x,t) = e^{-i\mu t}\phi(x)$ with $\mu \in \mathbb{R}$, we obtain the following differential equation for the complex-valued ϕ:

$$\mu\phi(x) = -\phi''(x) + (x^2 + 2i\gamma x)\phi(x) + |\phi(x)|^2\phi(x), \tag{26}$$

where we have set $\Omega = 1$ again without loss of generality. We say that ϕ is a $\mathcal{PT}$-symmetric stationary state of the $\mathcal{PT}$-symmetric NLS equation if ϕ satisfies the $\mathcal{PT}$-symmetry condition:

$$\phi(x) = \mathcal{PT}\phi(x) = \overline{\phi(-x)}, \quad x \in \mathbb{R}. \tag{27}$$

In the linear (small-amplitude) limit, we can convert the linear spectral problem to the quantum harmonic oscillator by using the complex variable $z = x + i\gamma$. Then, the eigenvalues occur at $\mu_n = 1 + 2n + \gamma^2$, $n \in \mathbb{N}_0$ and the $\mathcal{PT}$-symmetric eigenfunctions are given by

$$\varphi_n(x) = \frac{i^n}{\sqrt{2^n n! \sqrt{\pi}}} H_n(x + i\gamma) e^{-(x+i\gamma)^2/2}. \tag{28}$$

Note that φ_n in (28) satisfies the $\mathcal{PT}$-symmetry condition (27). The eigenfunction φ_n is normalized by the condition

$$\langle \varphi_n, \varphi_n \rangle_{\mathcal{PT}} = (-1)^n,$$

where the modified inner product is used in the form

$$\langle \psi, \varphi \rangle_{\mathcal{PT}} := \int_{\mathbb{R}} \psi(x) \overline{\varphi(-x)} dx. \tag{29}$$

The inner product in the form (29) is used for all linear $\mathcal{PT}$-symmetric systems [4] and the alternating sign of $\langle \varphi_n, \varphi_n \rangle_{\mathcal{PT}}$ is taken in [35] as the Krein signature of the eigenvalue μ_n, see discussion in Sect. 4.

By the same Crandall-Rabinowitz bifurcation theory [16], each $\mathcal{PT}$-symmetric function φ_n for a simple eigenvalue μ_n generates a branch of solutions, which can also be approximated by the same expansion (11). Bifurcations of such nonlinear stationary states in the $\mathcal{PT}$-symmetric systems from simple real eigenvalues are considered in [19, 30], where it is proven that the bifurcating branch of the stationary states satisfies the $\mathcal{PT}$-symmetry (27) and the chemical potential μ is real (at least for small ϵ).

The formal solvability condition for the correction terms $(\mu_n^{(2)}, \varphi_n^{(3)})$ of the expansion (11) yields

$$\mu_n^{(2)} = \frac{\int_{\mathbb{R}} \varphi_n(x) |\varphi_n(x)|^2 \overline{\varphi_n(-x)} dx}{\int_{\mathbb{R}} \varphi_n(x) \overline{\varphi_n(-x)} dx} = (-1)^n \int_{\mathbb{R}} \varphi_n(x) |\varphi_n(x)|^2 \overline{\varphi_n(-x)} dx.$$

Although it is obvious that $\mu_n^{(2)}$ is real, the sign of this quantity is less explicit than in (12). At least for small γ, we know that $\mu_n^{(2)} > 0$ by continuity of $\mu_n^{(2)}$ in γ. Continuation of branches of the nonlinear stationary states in the limit $\mu \to \infty$ is a highly non-trivial problem (see [55, 56] for numerical results and [21] for partial analytical results on the ground state branch).

In our numerical experiments, we fix $\mu = 12$ and continue in γ the first four branches from the Hamiltonian case $\gamma = 0$. The resulting continuations are shown on the left panel of Fig. 2. Branches with stable nonlinear states are shown by using blue solid curves and branches with unstable states are shown in dashed red. The power curves represent the power of the mode:

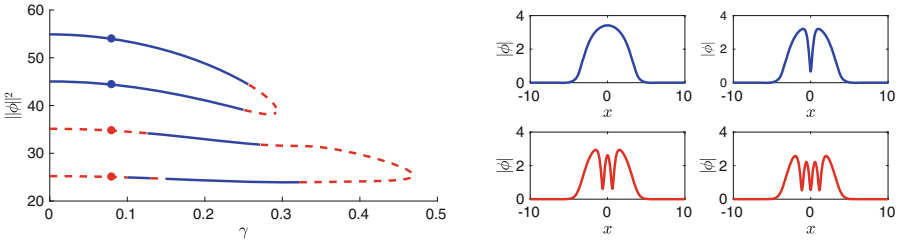

Fig. 2 Left: Power curves for branches of nonlinear states for $\mu = 12$ and $\gamma > 0$. Solid blue (dashed red) curves indicate stable (unstable) states. Right: Sample profiles for nonlinear states that correspond to the points shown on the power curves, from the top to the bottom branches

$$\|\phi\|^2 = \int_{\mathbb{R}} |\phi(x)|^2 dx.$$

The right panel of Fig. 2 shows the mode profiles corresponding to the points shown on the power branches on the left panel. Analyzing branches reveals two saddle-node bifurcations: the first branch meets the second one at $\gamma \approx 0.292$, whereas the third and fourth branches meet at $\gamma \approx 0.469$. Profiles of the nonlinear states for the merging branches at the saddle-node bifurcation become very similar, and after the bifurcation point both branches disappear. Such bifurcations are typical in the defocusing case, whereas branches of nonlinear states are extended for all γ in the focusing case [55, 56].

Linearizing the $\mathcal{PT}$-symmetric NLS equation with the same expansion (13) yields the same spectral problem as in (14):

$$\mathcal{L}(\gamma)v = -i\lambda\sigma_3 v, \tag{30}$$

with $\sigma_3 = \text{diag}(1, -1)$, but $\mathcal{L}(\gamma)$ is no longer a self-adjoint linear operator. The operator $\mathcal{L}(\gamma)$ is still defined in $L^2(\mathbb{R})$ with the domain $H^2(\mathbb{R}) \cap L^{2,2}(\mathbb{R})$ and is now given by

$$\mathcal{L}(\gamma) = \begin{bmatrix} -\partial_x^2 + x^2 + 2i\gamma x - \mu + 2|\phi(x)|^2 & \phi(x)^2 \\ \overline{\phi(x)^2} & -\partial_x^2 + x^2 - 2i\gamma x - \mu + 2|\phi(x)|^2 \end{bmatrix}.$$

This operator does not satisfy the Hamiltonian symmetry, $\sigma_3\mathcal{L}(\gamma) \neq \bar{\mathcal{L}}(\gamma)\sigma_3$ but instead, it satisfies the $\mathcal{PT}$-symmetry $\mathcal{P}\mathcal{L}(\gamma) = \bar{\mathcal{L}}(\gamma)\mathcal{P}$. In addition, it satisfies the symmetry $\sigma_1\mathcal{L}(\gamma) = \bar{\mathcal{L}}(\gamma)\sigma_1$, the same as in the Hamiltonian case. The quadruple symmetry of eigenvalues still exists due to these two symmetries. Indeed, if λ_0 is an eigenvalue with the eigenvector $v_0 = (a, b)^T$, then $-\bar{\lambda}_0$ is also an eigenvalue with the eigenvector $\mathcal{PT}v_0$, that is $(\overline{a(-x)}, \overline{b(-x)})^T$ for $x \in \mathbb{R}$, whereas $\bar{\lambda}_0$ is another eigenvalue with the eigenvector $\sigma_1\bar{v}_0 = (\bar{b}, \bar{a})$. Hence, eigenvalues of the $\mathcal{PT}$-symmetric spectral problem (30) still occur either in real or purely imaginary pairs or as quadruplets in the complex plane.

Besides the spectral problem (30), we also introduce the adjoint spectral problem with the adjoint eigenvector denoted by $v^{\#}$:

$$\mathcal{L}^*(\gamma)v^{\#} = -i\lambda\sigma_3 v^{\#}, \tag{31}$$

where $\mathcal{L}^*(\gamma)$ is the adjoint linear operator to $\mathcal{L}(\gamma)$ given by

$$\mathcal{L}^*(\gamma) = \begin{bmatrix} -\partial_x^2 + x^2 - 2i\gamma x - \mu + 2|\phi(x)|^2 & \phi(x)^2 \\ \overline{\phi(x)^2} & -\partial_x^2 + x^2 + 2i\gamma x - \mu + 2|\phi(x)|^2 \end{bmatrix}.$$

Unfortunately, the main limitation towards the Krein signature theory in the $\mathcal{PT}$-symmetric case $\gamma \neq 0$ is that the adjoint eigenvector $v^{\#}$ of the adjoint spectral problem (31) cannot be related to the eigenvector v of the spectral problem (30) for the same eigenvalue λ. Neither $\mathcal{L}^*(\gamma) = \mathcal{L}(\gamma)$ nor $\mathcal{L}^*(\gamma) = \mathcal{P}\mathcal{L}(\gamma)\mathcal{P}$ is true.

Let us now consider a simple isolated eigenvalue $\lambda_0 \in \mathbb{C}\backslash\{0\}$ of the spectral problems (30) and (31) with the eigenvector $v_0 \in H^2(\mathbb{R}) \cap L^{2,2}(\mathbb{R})$ and the adjoint eigenvector $v_0^{\#} \in H^2(\mathbb{R}) \cap L^{2,2}(\mathbb{R})$, respectively. If $\lambda_0 \in i\mathbb{R}$, then there exists a choice for the eigenvectors v_0 and $v_0^{\#}$ to satisfy the $\mathcal{PT}$-symmetry constraint:

$$v_0(x) = \overline{v_0(-x)}, \quad v_0^{\#}(x) = \overline{v_0^{\#}(-x)}, \quad x \in \mathbb{R}. \tag{32}$$

For each nonzero eigenvalue $\lambda_0 \in \mathbb{C}$ of the $\mathcal{PT}$-symmetric spectral problem (30) with the eigenvector $v_0 = (a, b) \in H^2(\mathbb{R}) \cap L^{2,2}(\mathbb{R})$ and the adjoint eigenvector $v_0^{\#} = (a^{\#}, b^{\#}) \in H^2(\mathbb{R}) \cap L^{2,2}(\mathbb{R})$, we define the Krein quantity $K(\lambda_0)$ as follows:

$$K(\lambda_0) := \langle \sigma_3 v_0, v_0^{\#} \rangle = \int_{\mathbb{R}} \left[a(x)\overline{a^{\#}(x)} - b(x)\overline{b^{\#}(x)} \right] dx. \tag{33}$$

If $\gamma = 0$, then $\mathcal{L}^*(0) = \mathcal{L}(0)$ and the adjoint spectral problem (31) becomes equivalent to the spectral problem (30). Therefore, the adjoint eigenvector $v_0^{\#}$ can be related to the eigenvector v_0 by $v_0^{\#} = v_0$. In this Hamiltonian case, the definition (33) represents the integral in the right-hand-side of the definition (16). The signs of $K(\lambda_0)$ defined for $\gamma = 0$ by (16) and $K(\lambda_0)$ defined for $\gamma \in \mathbb{R}$ by (33) are the same if $-i\lambda_0 > 0$ and $\gamma = 0$.

If $\gamma \neq 0$, the adjoint eigenvector $v_0^{\#}$ satisfying the $\mathcal{PT}$-symmetry condition (32) is defined up to an arbitrary sign. As a result, the Krein quantity $K(\lambda_0)$ in (33) is defined up to the sign change. In the continuation of the NLS equation (1) with respect to the parameter γ from the Hamiltonian case $\gamma = 0$, the sign of the Krein quantity $K(\lambda_0)$ in (33) is chosen so that it matches the sign of $K(\lambda_0)$ in (16) for every $-i\lambda_0 > 0$ and $\gamma = 0$, hence we choose $v_0^{\#} = v_0$ at $\gamma = 0$. After this choice is made for $\gamma = 0$, the eigenvector v_0, the adjoint eigenvector $v_0^{\#}$, and the Krein quantity $K(\lambda_0)$ are extended continuously with respect to the parameter γ.

Let us verify the main properties of the Krein quantity $K(\lambda_0)$ defined by (33).

(1) If f and g satisfy the $\mathcal{PT}$-symmetry condition (32), then the standard inner product $\langle f, g\rangle$ is real-valued. Indeed, this follows from

$$\langle f, g\rangle = \int_{\mathbb{R}} f(x)\overline{g(x)}dx = \int_0^{+\infty} \big(f(x)\overline{g(x)} + f(-x)\overline{g(-x)}\big)dx$$
$$= \int_0^{+\infty} \big(f(x)\overline{g(x)} + \overline{f(x)}g(x)\big)dx.$$

By (32), v_0 and $v_0^{\#}$ are $\mathcal{PT}$-symmetric if $\lambda_0 \in i\mathbb{R}$, hence $K(\lambda_0)$ is real if $\lambda_0 \in i\mathbb{R}$.

(2) Let us write the spectral problem for the generalized eigenvector v_g:

$$(\mathcal{L}(\gamma) + i\lambda_0\sigma_3)v_g = \sigma_3 v_0. \tag{34}$$

If $\lambda_0 \in i\mathbb{R}\backslash\{0\}$, then $v_0^{\#}$ is in the kernel of the adjoint operator $(\mathcal{L}(\gamma) + i\lambda_0\sigma_3)^*$, and the Fredholm solvability condition of the above equation is $\langle \sigma_3 v_0, v_0^{\#}\rangle = 0$. If $K(\lambda_0) = 0$, then there exists a solution to the nonhomogeneous equation (34), so that λ_0 is not simple. Hence, $K(\lambda_0) \neq 0$.

(3) Taking inner products of the spectral problems (30) and (31) with the corresponding eigenvectors yields

$$\left\langle \mathcal{L}v_0, v_0^{\#} \right\rangle = -i\lambda_0 \left\langle \sigma_3 v_0, v_0^{\#} \right\rangle$$

and

$$\left\langle v_0, \mathcal{L}^* v_0^{\#} \right\rangle = i\overline{\lambda}_0 \left\langle v_0, \sigma_3 v_0^{\#} \right\rangle,$$

hence

$$i(\lambda_0 + \overline{\lambda}_0)K(\lambda_0) = 0.$$

If $\lambda_0 \notin i\mathbb{R}$, then $\lambda_0 + \overline{\lambda}_0 \neq 0$ and $K(\lambda_0) = 0$.

Let us now illustrate how the Krein signatures can be used to predict instability bifurcations from multiple neutrally stable eigenvalues of the spectral problem (30). Recall that the eigenvalue is called *semi-simple* if algebraic and geometric multiplicities coincide and *defective* if the algebraic multiplicity exceeds the geometric multiplicity. In Sect. 2, we continued a semi-simple double eigenvalue with respect to parameter ϵ. Here we continue a defective double eigenvalue with respect to parameter γ.

Let γ_0 denote the bifurcation point where two neutrally stable eigenvalues coalesce: $\lambda_0 = \lambda_0' \in i\mathbb{R}\backslash\{0\}$. Near $\gamma = \gamma_0$, we expand the linear non-self-adjoint operator $\mathcal{L}(\gamma)$ as follows:

$$\mathcal{L}(\gamma) = \mathcal{L}_0 + (\gamma - \gamma_0)\mathcal{L}_1 + \ldots, \tag{35}$$

where

$$\mathcal{L}_1 = \begin{bmatrix} 2ix + 2\partial_\gamma |\phi(x)|^2|_{\gamma=\gamma_0} & \partial_\gamma \phi^2(x)|_{\gamma=\gamma_0} \\ \partial_\gamma \overline{\phi^2(x)}|_{\gamma=\gamma_0} & -2ix + 2\partial_\gamma |\phi(x)|^2|_{\gamma=\gamma_0} \end{bmatrix},$$

and ∂_γ denotes a partial derivative with respect to the parameter γ. We assume that there exists a defective double eigenvalue $\lambda_0 \in i\mathbb{R}\backslash\{0\}$ of the spectral problems (30) and (31) with the eigenvector v_0, the generalized eigenvector v_g, the adjoint eigenvector $v_0^\#$, and the adjoint generalized eigenvector $v_g^\#$, respectively. We will show that under the following non-degeneracy condition

$$\langle \mathcal{L}_1 v_0, v_0^\# \rangle \neq 0, \tag{36}$$

the necessary condition for instability bifurcation applies to the spectral problem (30). Thanks to the decomposition (35), we are looking for an eigenvalue $\lambda(\gamma)$ of the perturbed spectral problem

$$(\mathcal{L}_0 + (\gamma - \gamma_0)\mathcal{L}_1 + \ldots)\, v(\gamma) = -i\lambda(\gamma)\sigma_3 v(\gamma), \tag{37}$$

such that $\lambda(\gamma) \to \lambda_0$ as $\gamma \to \gamma_0$. Since λ_0 is a defective eigenvalue of geometric multiplicity *one* and algebraic multiplicity *two*, we apply Puiseux expansions [26]:

$$\begin{cases} \lambda(\gamma) = \lambda_0 + (\gamma - \gamma_0)^{1/2}\lambda_g + (\gamma - \gamma_0)\tilde{\lambda} + \ldots, \\ v(\gamma) = v_0 - i(\gamma - \gamma_0)^{1/2}\lambda_g v_g + (\gamma - \gamma_0)v_1 + \ldots, \end{cases} \tag{38}$$

where λ_g, $\tilde{\lambda}$, and v_1 are correction terms. To define v_1 uniquely, we add the orthogonality condition $\langle \sigma_3 v_1, v_0^\# \rangle = \langle \sigma_3 v_1, v_g^\# \rangle = 0$. The coefficient $-i\lambda_g$ comes in front of v_g thanks to the nonhomogeneous Eq. (34) arising at the order of $(\gamma - \gamma_0)^{1/2}$ from the perturbed spectral problem (37).

Plugging (38) into (37) yields at the order of $(\gamma - \gamma_0)$:

$$(\mathcal{L}_0 + i\lambda_0\sigma_3)\, v_1 = -\mathcal{L}_1 v_0 - \lambda_g^2 \sigma_3 v_g - i\tilde{\lambda}\sigma_3 v_0. \tag{39}$$

Fredholm solvability condition is satisfied if the right-hand side of the nonhomogeneous equation (39) is orthogonal to the kernel of adjoint operator $(\mathcal{L}_0 + i\lambda_0\sigma_3)^*$ spanned by $v_0^\#$. This orthogonality condition yields the constraint:

$$\langle -\mathcal{L}_1 v_0 - \lambda_g^2 \sigma_3 v_g - i\tilde{\lambda}\sigma_3 v_0, v_0^\# \rangle = 0. \tag{40}$$

Since $K(\lambda_0) = 0$ for the defective eigenvalue $\lambda_0 \in i\mathbb{R}$, $\tilde{\lambda}$ is not determined by equation (40). On the other hand, λ_g is defined by equation (40), which can be rewritten as follows:

$$(-i\lambda_g)^2 = \frac{\langle \mathcal{L}_1 v_0, v_0^\# \rangle}{\langle \sigma_3 v_g, v_0^\# \rangle}. \tag{41}$$

The denominator of (41) is nonzero because of the following argument. If λ_0 is a double eigenvalue, then the solution of the nonhomogeneous equation

$$(\mathcal{L}_0 + i\lambda_0\sigma_3)\tilde{v}_g = \sigma_3 v_g,$$

does not exist in $L^2(\mathbb{R})$. Hence $\langle \sigma_3 v_g, v_0^\# \rangle \neq 0$. Since v_0, $v_0^\#$, v_g, and $\mathcal{L}_1$ satisfy the $\mathcal{PT}$-symmetry conditions, both the nominator and the denominator of (41) are real-valued. By the assumption (36), the numerator of (41) is nonzero. Thus, $(-i\lambda_g)^2$ is either positive or negative.

Let us assume that $(-i\lambda_g)^2 > 0$ without loss of generality and fix $-i\lambda_g > 0$. If $\gamma > \gamma_0$, then $i(\gamma - \gamma_0)^{1/2}\lambda_g \in \mathbb{R}$ and we obtain the following expansions for the two simple purely imaginary eigenvalues λ_1 and λ_2 given by

$$\begin{aligned}
\lambda_1 &= \lambda_0 + (\gamma - \gamma_0)^{1/2}\lambda_g + \ldots, \\
\lambda_2 &= \lambda_0 - (\gamma - \gamma_0)^{1/2}\lambda_g + \ldots
\end{aligned}$$

The corresponding eigenvectors are expanded by

$$\begin{aligned}
v_1(\gamma) &= v_0 - i(\gamma - \gamma_0)^{1/2}\lambda_g v_g + \ldots, \\
v_2(\gamma) &= v_0 + i(\gamma - \gamma_0)^{1/2}\lambda_g v_g + \ldots,
\end{aligned}$$

whereas the adjoint eigenvectors for the same eigenvalues are expanded by

$$\begin{aligned}
v_1^\#(\gamma) &= v_0^\# - i(\gamma - \gamma_0)^{1/2}\lambda_g v_g^\# + \ldots, \\
v_2^\#(\gamma) &= v_0^\# + i(\gamma - \gamma_0)^{1/2}\lambda_g v_g^\# + \ldots
\end{aligned}$$

The leading order of Krein quantities for eigenvalues λ_1 and λ_2 is given by

$$\begin{aligned}
K(\lambda_1) = \langle \sigma_3 v_1(\gamma), v_1^\#(\gamma) \rangle &= -i(\gamma - \gamma_0)^{1/2}\lambda_g \langle \sigma_3 v_g, v_0^\# \rangle \\
&\quad + i\overline{(\gamma - \gamma_0)^{1/2}\lambda_g}\langle \sigma_3 v_0, v_g^\# \rangle + \ldots, \\
K(\lambda_2) = \langle \sigma_3 v_2(\gamma), v_2^\#(\gamma) \rangle &= +i(\gamma - \gamma_0)^{1/2}\lambda_g \langle \sigma_3 v_g, v_0^\# \rangle \\
&\quad - i\overline{(\gamma - \gamma_0)^{1/2}\lambda_g}\langle \sigma_3 v_0, v_g^\# \rangle + \ldots
\end{aligned}$$

Since

$$\langle \sigma_3 v_g, v_0^\# \rangle = \langle v_g, \sigma_3 v_0^\# \rangle = \langle v_g, (\mathcal{L}_0 + i\lambda_0\sigma_3)^* v_g^\# \rangle = \langle (\mathcal{L}_0 + i\lambda_0\sigma_3) v_g, v_g^\# \rangle = \langle \sigma_3 v_0, v_g^\# \rangle,$$

the two expansions for $K(\lambda_1)$ and $K(\lambda_2)$ can be rewritten in the case of $i(\gamma - \gamma_0)^{1/2}\lambda_g \in \mathbb{R}$ as

$$K(\lambda_1) = -2i(\gamma - \gamma_0)^{1/2}\lambda_g \langle \sigma_3 v_g, v_0^{\#} \rangle + \ldots,$$
$$K(\lambda_2) = 2i(\gamma - \gamma_0)^{1/2}\lambda_g \langle \sigma_3 v_g, v_0^{\#} \rangle + \ldots$$

Since $\langle \sigma_3 v_0, v_g^{\#} \rangle \neq 0$, $K(\lambda_1)$ has the opposite sign to $K(\lambda_2)$.

If $\gamma < \gamma_0$, then $i(\gamma - \gamma_0)^{1/2}\lambda_g \in i\mathbb{R}$, so that $\lambda_1, \lambda_2 \notin i\mathbb{R}$, whereas $K(\lambda_1) = K(\lambda_2) = 0$. Thus, the necessary condition for the instability bifurcation holds under the nondegeneracy assumption (36).

Note in passing that if the non-degeneracy assumption (36) is not satisfied, then $\lambda_g = 0$ follows from (41) and the perturbation theory must be extended to the next order with a characteristic equation to be derived for the correction term $\tilde{\lambda}$. In this case, the double defective eigenvalue $\lambda_0 \in i\mathbb{R}$ may split safely along $i\mathbb{R}$ both for $\gamma > \gamma_0$ and $\gamma < \gamma_0$.

Figures 3 and 4 show eigenvalues of the $\mathcal{PT}$-symmetric spectral problem (30) for the first four branches of the nonlinear stationary states with $\mu = 12$ shown on Fig. 2.

Figure 3 shows that the first branch is stable until $\gamma \approx 0.27$, whereas the second branch is stable until $\gamma \approx 0.25$. For the first branch (left panel), eigenvalues of the positive Krein signature coalesce at the origin, whereas for the second branch (right panel), eigenvalues of the negative Krein signature coalesce at the origin. The instability of the first branch is unusual, since it plays the role of the 'ground state' in analogy to Hamiltonian case. Nonetheless, this is no surprise since similar behavior was observed in [55], where the first two branches lost their stability very close to each other.

Figure 4 (left panels) shows seven bifurcations among eigenvalues of the third branch of the stationary states that occur at $\gamma_1 \approx 0.126$, $\gamma_2 \approx 0.271$, $\gamma_3 \approx 0.304$, $\gamma_4 \approx 0.316$, $\gamma_5 \approx 0.335$, $\gamma_6 \approx 0.338$, and $\gamma_7 \approx 0.393$. Bifurcations at γ_2, γ_5, and γ_7 occur when eigenvalues on the imaginary axis coalesce at the origin, resulting in pairs of eigenvalues on the real axis. The necessary condition for instability

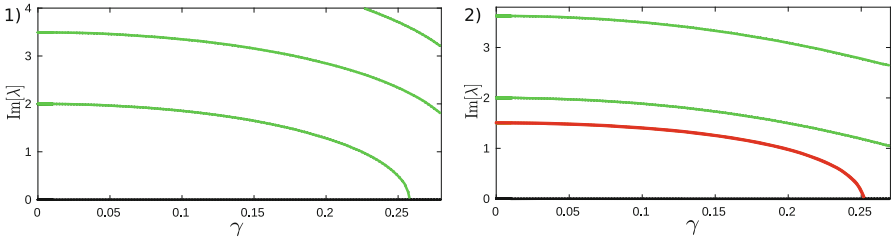

Fig. 3 Purely imaginary eigenvalues λ of the $\mathcal{PT}$-symmetric problem (30) for the first two stationary states with $\mu = 12$. Eigenvalues of negative (positive) Krein signature are shown in red (green), complex eigenvalues are shown in black

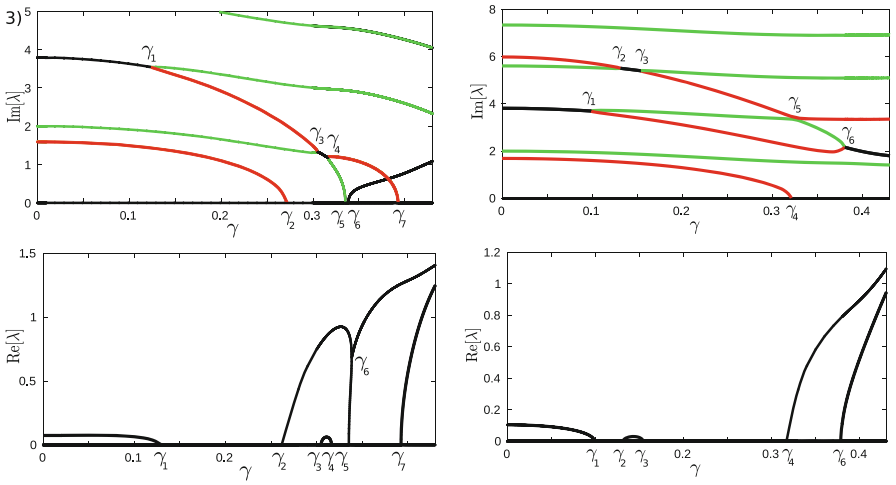

Fig. 4 The same as Fig. 3 but for the third (left panels) and fourth (right panels) branches of the stationary states. Top panels show imaginary parts and the bottom panels show real parts of the eigenvalues λ

bifurcations is not applicable if the double defective eigenvalue is located at the origin. The bifurcation at γ_6 occurs when real eigenvalues formed after bifurcations at γ_2 and γ_5 coalesce and transform into a quadruplet of complex eigenvalues.

At γ_1, complex quadruplets continued from the case $\gamma = 0$ coalesce and bifurcate into the imaginary eigenvalues with opposite Krein signatures, which provides an excellent example for the necessary condition of the reverse instability bifurcation. At γ_3 and γ_4, we have more examples of the instability bifurcation and the reverse instability bifurcation, in which the two eigenvalues before γ_3 and after γ_4 on the imaginary axis have opposite Krein signatures.

Figure 4 (right panels) shows six bifurcations among eigenvalues of the fourth branch of the stationary states at $\gamma_1 \approx 0.099$, $\gamma_2 \approx 0.131$, $\gamma_3 \approx 0.154$, $\gamma_4 \approx 0.322$, $\gamma_5 \approx 0.326$, and $\gamma_6 \approx 0.380$. The bifurcation at γ_1 is similar to the one for the third branch: a complex pair of eigenvalues coming from the Hamiltonian case coalesces on the imaginary axis and splits along the imaginary axis into two eigenvalues with opposite Krein signatures moving away from each other. Bifurcations at γ_2 and γ_3 occur when two imaginary eigenvalues with opposite Krein signatures continued from $\gamma = 0$ coalesce and bifurcate off into the complex plane at γ_2, after which the complex eigenvalues coalesce again on the imaginary axis at γ_3 and emerge as a pair of purely imaginary eigenvalues with opposite Krein signatures.

At γ_4, a pair of purely imaginary eigenvalues of negative Krein signature coalesces at the origin and they bifurcate into real eigenvalues. At γ_5, the purely imaginary eigenvalues nearly coalesce, but the numerical results are somewhat inconclusive. Figure 5 shows the squared norm of the difference of eigenvectors for the corresponding eigenvalues. As we can see, the difference between eigenvectors

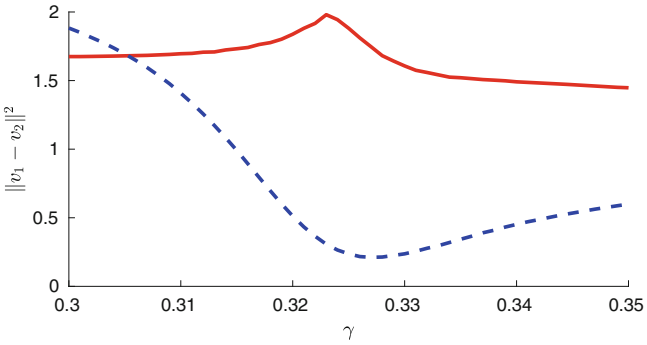

Fig. 5 Distance between eigenvectors (red solid curve) and adjoint eigenvectors (dashed blue curve) for the fourth branch in Fig. 4 near γ_5

does not vanish, which rules out the possibility of a double defective eigenvalue at the bifurcation point γ_5.

Finally, bifurcation at γ_6 shows coalescence of two eigenvalues with opposite Krein signatures after which they bifurcate into a complex quadruplet. Bifurcations at γ_1, γ_2, γ_3, and γ_6 agree with the necessary condition for the instability bifurcation.

Stability of nonlinear stationary states of the $\mathcal{PT}$-symmetric NLS equation (26) was studied numerically in [55] for fixed values of γ. The recent study in [13] was applied to a modified potential V where the imaginary part of V had a Gaussian decay; see also the earlier study of [1]. The instability bifurcations were found to be very similar to the present study. In addition to the bifurcations visible on Fig. 4, there was also the case when two eigenvalues with opposite signatures coalesce into a defective eigenvalue but not bifurcating into the complex plane. This may happen when the non-degeneracy condition (36) is not satisfied, so that the two eigenvalues of opposite Krein signature can pass each other on the imaginary axis without generating complex quadruplets.

4 Krein Signature for the Linear $\mathcal{PT}$-Symmetric Schrödinger Equation

Here we discuss the concept of Krein signature in the linear $\mathcal{PT}$-symmetric Schrödinger equation introduced in [35]. For the potential (5) with $\Omega = 1$, we can write the linear spectral problem in the form:

$$\mu\psi(x) = -\psi''(x) + x^2\psi(x) + 2i\gamma x\psi(x), \tag{42}$$

which is related to the non-self-adjoint $\mathcal{PT}$-symmetric Schrödinger operator $\mathcal{H} = -\partial_x^2 + x^2 + 2i\gamma x$ defined on the domain $H^2(\mathbb{R}) \cap L^{2,2}(\mathbb{R})$ in $L^2(\mathbb{R})$. The adjoint operator $\mathcal{H}^* = -\partial_x^2 + x^2 - 2i\gamma x$ satisfies $\mathcal{H}^* = \mathcal{PHP}$, where $\mathcal{P}$ is the parity operator. Because of this relation, if ψ_0 is an eigenfunction of $\mathcal{H}$ for the eigenvalue μ_0, then $\psi_0^\# = \mathcal{P}\psi_0$ is an eigenfunction of $\mathcal{H}^*$ for the same eigenvalue μ_0. By using the relation $\psi_0^\#(x) = \psi_0(-x)$, the Krein quantity of the eigenvalue μ_0 in the spectral problem (42) can be defined by the inner product in (29):

$$K(\mu_0) := \langle \psi_0, \psi_0 \rangle_{\mathcal{PT}} = \langle \psi_0, \psi_0^\# \rangle = \int_{\mathbb{R}} \psi_0(x) \overline{\psi_0(-x)} dx. \tag{43}$$

This definition was used in [35] to verify the main properties of the Krein quantity and the necessary condition for instability bifurcation.

The spectral problem (42) can be written in the Hamiltonian form (8), or explicitly,

$$i\mathcal{P}(\mathcal{PH})\psi = i\mu\psi, \tag{44}$$

where $\mathcal{L} = \mathcal{PH}$ is self-adjoint, $J = i\mathcal{P}$ is skew-adjoint and invertible, and $\lambda = i\mu$ is a new eigenvalue. By using the definition (9) of the Krein quantity for the Hamiltonian spectral problem (8), we obtain

$$\tilde{K}(\mu_0) = \langle \mathcal{PH}\psi_0, \psi_0 \rangle = \mu_0 \langle \psi_0, \mathcal{P}\psi_0 \rangle = \mu_0 K(\mu_0), \tag{45}$$

which is only different from the definition (43) by the factor μ_0. However, $\mu_0 > 0$ since the spectral problem (42) admits only positive eigenvalues. Thus, the Krein signature introduced in (43) coincides with the Krein signature introduced in (45).

The only difference between the Hamiltonian spectral problem (14) for the linearized NLS equation and the spectral problem (44) for the linear Schrödinger equation is that the eigenvalues λ of the spectral problem (14) on the imaginary axis occur in pairs thanks to the symmetry $\sigma_1 \mathcal{L} = \bar{\mathcal{L}} \sigma_1$, whereas the eigenvalues $\lambda = i\mu$ of the spectral problem (44) are located on the positive imaginary axis.

In the limit $\gamma \to 0$, eigenfunctions of the Schrödinger operator $\mathcal{H}_0 = -\partial_x^2 + x^2$ for the quantum harmonic oscillator are either even or odd. Eigenvalues $\mu_{2N} = 4N + 1$, $N \in \mathbb{N}_0$ with even eigenfunctions have positive Krein signature in (43), whereas eigenvalues $\mu_{2N-1} = 4N - 1$, $N \in \mathbb{N}$ with odd eigenfunctions have negative Krein signature. This seems to be surprising at first glance, since all eigenvalues are strictly positive and the operator $\mathcal{H}_0$ is self-adjoint in $L^2(\mathbb{R})$.

It is more natural in the Hamiltonian case $\gamma = 0$ to define the Krein quantity of an eigenvalue μ_0 by

$$K_H(\mu_0) := \langle \mathcal{H}_0 \psi_0, \psi_0 \rangle = \mu_0 \langle \psi_0, \psi_0 \rangle = \mu_0 \int_{\mathbb{R}} |\psi_0(x)|^2 dx, \tag{46}$$

which is strictly positive for every eigenvalue $\mu_0 > 0$. Rewriting the spectral problem $\mathcal{H}_0\psi = \mu\psi$ in the Hamiltonian form

$$i\mathcal{H}_0\psi = i\mu\psi, \tag{47}$$

with $\mathcal{L} = \mathcal{H}_0$, $J = i$, and $\lambda = i\mu$, we obtain the same sequence of eigenvalues on the positive imaginary axis but associated with the positive Krein quantity (46).

The apparent confusion is resolved by observing that the Schrödinger operator $\mathcal{H}_0$ admits two equivalent Hamiltonian formulations (44) and (47), where only the former is extended continuously with respect to the parameter $\gamma \neq 0$. In the former formulation (44) with $\gamma = 0$, the self-adjoint operator $\mathcal{L} = \mathcal{P}\mathcal{H}_0$ has now two sequences of real eigenvalues: positive eigenvalues $\mu_{2N} = 4N + 1$, $N \in \mathbb{N}_0$ for the even eigenfunctions and negative eigenvalues $-\mu_{2N-1} = -4N + 1$, $N \in \mathbb{N}$ for the odd eigenfunctions. This explains why the Krein quantity (43) is sign-alternating even at $\gamma = 0$, whereas the Krein quantity (46) is always positive.

5 Summary and Further Directions

We have extended the concept of the Krein signature beyond Hamiltonian systems and applied it to $\mathcal{PT}$-symmetric systems. We have reviewed the Hamiltonian theory, including the necessary condition for instability bifurcation as a result of the collision of two eigenvalues of opposite Krein signature. An instructive case example from the area of Bose–Einstein condensation provides a countable sequence of nonlinear states bifurcating from eigenstates of a quantum harmonic oscillator. The Krein signature was defined for the linearized NLS equation at each of these nonlinear states both in the Hamiltonian and $\mathcal{PT}$-symmetric cases. The standard properties of the Krein signature were explicitly confirmed and the necessary condition for instability bifurcation was verified. An illustrative (and rich in terms of bifurcations) example was given in the form of a linear gain/loss term in the NLS with a parabolic trap.

One can envision numerous extensions of the present theory. On the practical side of specific applications, it would be especially relevant to consider two-dimensional problems involving vorticity in settings such as the one of [1]. Also, more recently partially $\mathcal{PT}$-symmetric settings have been introduced in [17, 53] where one dimension retains the symmetry and the other dimension does not. Considering the applicability of the ideas herein in such systems or in systems with complex, yet non-$\mathcal{PT}$-symmetric potentials with families of solutions [33, 36] would also be of interest. Finally, from a more mathematical perspective, an understanding of whether ideas related to the Hamiltonian-Krein theorem can be adapted to the $\mathcal{PT}$-symmetric setting would be an especially intriguing task.

References

1. Achilleos, V., Kevrekidis, P.G., Frantzeskakis, D.J., Carretero-González, R.: Dark solitons and vortices in $\mathcal{PT}$-symmetric nonlinear media: from spontaneous symmetry breaking to nonlinear $\mathcal{PT}$ phase transitions. Phys. Rev. A **86**, 013808 (7pp) (2012)
2. Alexeeva, N.V., Barashenkov, I.V., Sukhorukov, A.A., Kivshar, Yu.S.: Optical solitons in $\mathcal{PT}$-symmetric nonlinear couplers with gain and loss. Phys. Rev. A **85**, 063837 (13pp) (2012)
3. Alexeeva, N.V., Barashenkov, I.V., Kivshar, Yu.S.: Solitons in $\mathcal{PT}$-symmetric ladders of optical waveguides. New J. Phys. **19**, 113032 (30pp) (2017)
4. Bender, C.M.: Making sense of non-Hermitian Hamiltonians. Rep. Prog. Phys. **70**, 947–1018 (2007)
5. Bender, C.M., Berntson, B.K., Parker, D., Samuel, E.: Observation of $\mathcal{PT}$ phase transition in a simple mechanical system. Am. J. Phys. **81**, 173–179 (2013)
6. Bender, C.M., Boettcher, S.: Real spectra in non-Hermitian Hamiltonians having $\mathcal{PT}$ Symmetry. Phys. Rev. Lett. **80**, 5243–5246 (1998)
7. Bender, C.M., Brody, D.C., Jones, H.F.: Complex extension of quantum mechanics. Phys. Rev. Lett. **89**, 270401 (4pp) (2002)
8. Busch, Th., Anglin, J.R.: Motion of dark solitons in trapped Bose-Einstein condensates. Phys. Rev. Lett. **84**, 2298–2301 (2000)
9. Carretero-González, R., Frantzeskakis, D.J., Kevrekidis, P.G.: Nonlinear waves in Bose–Einstein condensates: physical relevance and mathematical techniques. Nonlinearity **21**, R139–R202 (2008)
10. Cartarius, H., Wunner, G.: Model of a PT-symmetric Bose-Einstein condensate in a δ-function double-well potential. Phys. Rev. A **86**, 013612 (5pp) (2012)
11. Chernyavsky, A., Pelinovsky, D.E.: Breathers in Hamiltonian $\mathcal{PT}$-symmetric chains of coupled pendula under a resonant periodic force. Symmetry **8**, 59 (26pp) (2016)
12. Chernyavsky, A., Pelinovsky, D.E.: Long-time stability of breathers in Hamiltonian PT-symmetric lattices. J. Phys. A Math. Theor. **49**, 475201 (20pp) (2016)
13. Chernyavsky, A., Pelinovsky, D.E.: Krein signature for instability of $\mathcal{PT}$-symmetric states. Phys. D **371**, 48–59 (2018)
14. Chugunova, M., Pelinovsky, D.: Count of eigenvalues in the generalized eigenvalue problem. J. Math. Phys. **51**, 052901 (19pp) (2010)
15. Coles, M.P., Pelinovsky, D.E., Kevrekidis, P.G.: Excited states in the large density limit: a variational approach. Nonlinearity **23**, 1753–1770 (2010)
16. Crandall, M.G., Rabinowitz, P.H.: Bifurcation from simple eigenvalues. J. Funct. Anal. **8**, 321–340 (1971)
17. D'Ambroise, J., Kevrekidis, P.G.: Existence, stability, and dynamics of nonlinear modes in a 2D partially $\mathcal{PT}$ symmetric potential. Appl. Sci. **7**, 223 (10pp) (2017)
18. Dast, D., Haag, D., Cartarius, H., Main, J., Wunner, G.: Eigenvalue structure of a Bose–Einstein condensate in a $\mathcal{PT}$-symmetric double well. J. Phys. A Math. Theor. **46**, 375301 (19pp) (2013)
19. Dohnal, T., Siegl, P.: Bifurcation of eigenvalues in nonlinear problems with antilinear symmetry. J. Math. Phys. **57**, 093502 (18pp) (2016)
20. Feder, D.L., Pindzola, M.S., Collins, L.A., Schneider, B.I., Clark, C.W.: Dark-soliton states of Bose-Einstein condensates in anisotropic traps. Phys. Rev. A **62**, 053606 (11pp) (2000)
21. Gallo, C., Pelinovsky, D.E.: On the Thomas–Fermi approximation of the ground state in a $\mathcal{PT}$-symmetric confining potential. Stud. Appl. Math. **133**, 398–421 (2014)
22. Heffler, B.: Spectral Theory and its Applications. Cambridge Studies in Advanced Mathematics, vol. 185. Cambridge University Press, Berlin (2013)
23. Kapitula, T., Kevrekidis, P.G., Sanstede, B.: Counting eigenvalues via the Krein signature in infinite-dimensional Hamiltonian systems. Phys. D **195**, 263–282 (2004)
24. Kapitula, T., Promislow, K.: Stability indices for constrained self-adjoint operators. Proc. Am. Math. Soc. **140**, 865–880 (2012)

25. Kapitula, T., Promislow, K.: Spectral and dynamical stability of nonlinear waves. Appl. Math. Sci. vol. 185. Springer, Berlin (2013)
26. Knopp, K.: Theory of Functions, Part II. Dover, New York (1947)
27. Kevrekidis, P.G., Carretero-González, R., Frantzeskakis, D.J.: Stability of single and multiple matter-wave dark solitons in collisionally inhomogeneous Bose-Einstein condensates. Int. J. Mod. Phys. B **31**, 1742013 (12pp) (2017)
28. Kevrekidis, P.G., Frantzeskakis, D.J., Carretero-González, R.: The Defocusing Nonlinear Schrödinger Equation: From Dark Solitons to Vortices and Vortex Rings. SIAM, Philadelphia (2015)
29. Kevrekidis, P.G., Pelinovsky, D.E.: Distribution of eigenfrequencies for oscillations of the ground state in the Thomas-Fermi limit. Phys. Rev. A **81**, 023627 (5pp) (2010)
30. Kevrekidis, P.G., Pelinovsky, D.E., Tyugin, D.Y.: Nonlinear stationary states in PT-symmetric lattices. SIAM J. Appl. Dynam. Syst. **12**, 1210–1236 (2013)
31. Kollár, R., Miller, P.: Graphical Krein signature theory and Evans–Krein functions. SIAM Rev. **56**, 73–123 (2014)
32. Konotop, V.V., Yang, J., Zezyulin, D.A.: Nonlinear waves in $\mathcal{PT}$-symmetric systems. Rev. Mod. Phys. **88**, 035002 (59pp) (2016)
33. Konotop, V.V., Zezyulin, D.A.: Families of stationary modes in complex potentials. Opt. Lett. **39**, 5535–5538 (2014)
34. MacKay, R.S.: Stability of equilibria of Hamiltonian systems. In: Sarkar S (ed.) Nonlinear Phenomena and Chaos (Malvern, 1985). Malvern Physics Series. Hilger, Bristol (1986)
35. Nixon, S., Yang, J.: Nonlinear wave dynamics near phase transition in $\mathcal{PT}$-symmetric localized potentials. Phys. D **331**, 48–57 (2016)
36. Nixon, S.D., Yang, J.: Bifurcation of soliton families from linear modes in Non-$\mathcal{PT}$-symmetric complex potentials. Stud. Appl. Math. **136**, 459–483 (2016)
37. Pelinovsky, D.E.: Inertia law for spectral stability of solitary waves in coupled nonlinear Schrödinger equations. Proc. R. Soc. A **461**, 783–812 (2005)
38. Pelinovsky, D.: Asymptotic properties of excited states in the Thomas-Fermi limit. Nonlinear Anal. **73**, 2631–2643 (2010)
39. Pelinovsky, D.E.: Localization in Periodic Potentials: From Schrödinger Operators to the Gross–Pitaevskii Equation. Cambridge University Press, Cambridge (2011)
40. Pelinovsky, D.E., Frantzeskakis, D., Kevrekidis, P.G.: Oscillations of dark solitons in trapped Bose-Einstein condensates. Phys. Rev. E **72**, 016615 (12pp) (2005)
41. Pelinovsky, D.E., Yang, J.: Instabilities of multihump vector solitons in coupled nonlinear Schrödinger equations. Stud. Appl. Math. **115**, 109–137 (2005)
42. Pethick, C.J., Smith, H.: Bose-Einstein Condensation in Dilute Gases. Cambridge University Press, Cambridge (2008)
43. Pitaevskii, L., Stringari, S.: Bose–Einstein Condensation. International Series of Monographs on Physics, vol. 116. Oxford University Press, New York (2003)
44. Reed, M., Simon, B.: Methods of Modern Mathematical Physics. vol. 4: Analysis of Operators. Academic Press, New York (1978)
45. Rüter, C.E., Makris, K.G., El-Ganainy, R., Christodoulides, D.N., Segev, M., Kip, D.: Observation of parity-time symmetry in optics. Nat. Phys. **6**, 192–195 (2010)
46. Schindler, J., Lin, Z., Lee, J.M., Ramezani, H., Ellis, F.M., Kottos, T.: $\mathcal{PT}$-symmetric electronics. J. Phys. A Math. Theor. **45**, 444029 (15pp) (2012)
47. Skryabin, D.V.: Instabilities of vortices in a binary mixture of trapped Bose-Einstein condensates: Role of collective excitations with positive and negative energies. Phys. Rev. A **63**, 013602 (10pp) (2000)
48. Stanislavova, M., Stefanov, A.: On the stability of standing waves for $\mathcal{PT}$ symmetric Schrödinger and Klein-Gordon equations in higher space dimensions. Proc. AMS **145**, 5273–5285 (2017)
49. Stringari, S.: Collective excitations of a trapped Bose-condensed gas. Phys. Rev. Lett. **77**, 2360–2363 (1996)

50. Suchkov, S.V., Sukhorukov, A.A., Huang, J., Dmitriev, S.V., Lee, C., Kivshar, Yu.S.: Nonlinear switching and solitons in PT-symmetric photonic systems. Laser Photonics Rev. **10**, 177–213 (2016)
51. Weierstrass, K.: Mathematische Werke, vol. 1. Johnson Reprint, New York (1967)
52. Wimmer, M., Regensburger, A., Miri, M.-A., Bersch, C., Christodoulides, D.N., Peschel, U.: Observation of optical solitons in PT-symmetric lattices. Nature Commun. **6**, 7782 (9pp) (2015)
53. Yang, J.: Partially $\mathcal{PT}$ symmetric optical potentials with all-real spectra and soliton families in multidimensions. Opt. Lett. **39**, 1133–1136 (2014)
54. Zezyulin, D.A., Alfimov, G.L., Konotop, V.V., Pérez-García, V.M.: Stability of excited states of a Bose-Einstein condensate in an anharmonic trap. Phys. Rev. A **78**, 013606 (12pp) (2008)
55. Zezyulin, D.A., Konotop, V.V.: Nonlinear modes in the harmonic $\mathcal{PT}$-symmetric potential. Phys. Rev. A **85**, 043840 (6pp) (2012)
56. Zezyulin, D.A., Konotop, V.V.: Small-amplitude nonlinear modes under the combined effect of the parabolic potential, nonlocality and $\mathcal{PT}$-symmetry. Symmetry **8**, 72 (19pp) (2016)

Integrable Nonlocal PT Symmetric and Reverse Space-Time Nonlinear Schrödinger Equations

Mark J. Ablowitz and Ziad H. Musslimani

Abstract In this chapter a review of recent advances related to the emerging field of integrable nonlocal nonlinear PT symmetric, reverse space-time and reverse time only equations is presented. Starting from the well-known AKNS theory, it is shown how to obtain a host of nonlocal integrable equations previously discovered by the authors. Included are the nonlocal PT symmetric $(1+1)$D nonlinear Schrödinger (NLS) equation and its multi-component generalization; the reverse space-time and reverse time only NLS equations along with their vector versions. The inverse scattering transform associated with the nonlocal NLS hierarchy is briefly summarized and one soliton solutions corresponding to each of the above case are presented. The discrete nonlocal PT symmetric, reverse space-time and reverse time only NLS equations are also discussed. Starting from the Ablowitz-Ladik scattering problem, it is shown that all these discrete models arise from simple symmetry reductions.

1 Introduction

Integrable systems have a rich and long history that dates back to the nineteenth century. Their impact spans many areas of the mathematical sciences including mathematical analysis, solutions of differential equations and differential geometry to name a few. Some integrable models find important applications in physics including classical and quantum physics; e.g. water waves, nonlinear optics, elasticity, lattice dynamics, quantum statistical mechanics and quantum field theory.

M. J. Ablowitz
Department of Applied Mathematics, University of Colorado, Boulder, CO, USA
e-mail: Mark.Ablowitz@colorado.edu

Z. H. Musslimani (✉)
Department of Mathematics, Florida State University, Tallahassee, FL, USA
e-mail: musslimani@math.fsu.edu

D. Christodoulides, J. Yang (eds.), *Parity-time Symmetry and Its Applications*, Springer Tracts in Modern Physics 280,
https://doi.org/10.1007/978-981-13-1247-2_17

Originally, integrable systems were studied in the framework of classical finite dimensional Hamiltonian mechanics. In this regard, the concept of integrability refers to the existence of a canonical transformation from generalized coordinates (position and momenta) to action-angle variables. Alternatively, an autonomous Nth order dynamical system is said to be integrable if there exists $N - 1$ constant of motions that help reduce the order of the system to one.

The discovery of solitons by Zabusky and Kruskal in 1965 [1] opened the door and created an opportunity to extend the theory of integrable finite-dimensional Hamiltonian systems to infinite-dimensions. Indeed, in 1967, Gardner, Greene, Kruskal and Miura [2] used methods of direct and inverse scattering associated with the time independent Schrödinger operator to solve the Cauchy problem associated with the KdV equation. This together with the results of [3, 4] established the integrability of the KdV in terms of an infinite number of conserved quantities and action angle variables of an associated Hamiltonian system.

Inspired by these findings, Lax proposed in 1968 [5] a novel approach to solve the initial value problem associated with the KdV equation by reformulating it as a compatible set of two first order PDEs later known in the literature as Lax pairs. This new method was used by Zakharov and Shabat [6]. They introduced a Lax type compatible system, one of which was the Dirac system, and used it to solve the Cauchy problem associated with the nonlinear Schrödinger equation. They showed it was an integrable Hamiltonian system. In 1974, AKNS [7] introduced a method to generate evolution equations both in one and multi dimensions whose outcome is a single or set of PDEs that are guaranteed to be (i) integrable and (ii) solvable by the inverse scattering transform. Soon thereafter, intense research activity related to integrable soliton equations emerged, covering wide spectrum of research ranging from pure to applied to computational mathematics and to theoretical and experimental physics [8–16].

Towards the end of the nineteen nineties, it was believed that most relatively simple and physically relevant integrable evolution equations were already classified and their analytic and solution properties well understood. In this regard, research interest shifted towards understanding special solutions, asymptotics, symmetries, related aspects of integrability, perturbations as well as a more general nonlinear waves phenomena governed often by non-integrable PDEs.

In 2013 a new nonlocal symmetry reduction for the AKNS scattering problem was discovered [17] giving rise to a new type of integrable nonlocal nonlinear Schrödinger equation that preserves PT symmetry, i.e., it is invariant under the combined action of space reflection and time reversal symmetry. This surprising result ignited a renewed interest in integrable systems with emphasis on analysis of its underlying mathematical structure and physical applications [18–29]. Further unexpected results followed soon thereafter where additional (previously unknown) symmetry reductions for the AKNS system were found by the authors [30]. They belong to the so-called reverse space-time and reverse time only type reductions and give rise to numerous new integrable continuous and discrete equations. Examples include the reverse space-time and reverse time only NLS, mKdV, Davey-Stewartson, multi wave interactions, sine-Gordon equations to name a few. These

findings have also been extended to the discrete domain where new PT, reverse space-time and reverse time only symmetry reductions to the well-known Ablowitz-Ladik [31, 32] scattering problem have been identified and new discrete evolution systems have been derived [30, 33].

The focus of this book chapter is on reviewing recent progress in the emerging area of nonlocal PT symmetric and reverse space-time integrable systems. The emphasis is going to be on how to obtain a host of new integrable evolution equations, list a few of their integral of motions and present some of their soliton solutions.

2 Continuous Models

To outline the derivation of the nonlocal PT symmetric, reverse space-time and reverse time only NLS equations we start from the well-known AKNS scattering problem given by [8, 34]

$$\mathbf{v}_x(x,t) = \mathsf{X}\mathbf{v}(x,t)\ , \tag{1}$$

where subscript denotes partial derivative, $\mathbf{v}(x,t) \equiv (v_1(x,t), v_2(x,t))^T$ and $q(x,t)$, $r(x,t)$ are complex valued functions of the real variables x and t that are assumed to vanish rapidly as $|x| \to \infty$. The 2×2 matrix X depends on the functions $q(x,t)$ and $r(x,t)$ as well as on the spectral parameter k

$$\mathsf{X} = \begin{pmatrix} -ik & q(x,t) \\ r(x,t) & ik \end{pmatrix}\ . \tag{2}$$

Associated with the scattering problem (1) is the time evolution of the eigenfunctions $v_j(x,t)$, $j = 1, 2$ which is given by

$$\mathbf{v}_t(x,t) = \mathsf{T}\mathbf{v}(x,t)\ , \tag{3}$$

with

$$\mathsf{T} = \begin{pmatrix} \mathsf{A} & \mathsf{B} \\ \mathsf{C} & -\mathsf{A} \end{pmatrix}\ . \tag{4}$$

Here, the quantities A, B and C are scalar functions of $q(x,t), r(x,t)$ and the spectral parameter k. Depending on the choice of A, B and C one finds an evolution equation for the potential functions $q(x,t)$ and $r(x,t)$ which, under a certain symmetry restriction, leads to a single evolution equation for either $q(x,t)$ or $r(x,t)$. In the case where the quantities A, B and C are second order polynomials in the isospectral parameter k with coefficients depending on $q(x,t), r(x,t)$, i.e.,

$$\mathsf{A} = 2ik^2 + iq(x,t)r(x,t)\ , \tag{5}$$

$$\mathsf{B} = -2kq(x,t) - iq_x(x,t)\ , \tag{6}$$

$$\mathsf{C} = -2kr(x,t) + ir_x(x,t)\ , \tag{7}$$

the compatibility condition of system (1) and (3) leads to

$$iq_t(x,t) = q_{xx}(x,t) - 2r(x,t)q^2(x,t)\ , \tag{8}$$

$$-ir_t(x,t) = r_{xx}(x,t) - 2q(x,t)r^2(x,t)\ . \tag{9}$$

Equations (8) and (9) are known in the literature as the general q, r system. As we shall see later, depending on the choice between the potentials q and r an integrable evolution equation for either q or r can be derived.

2.1 Classical Local NLS

The classical NLS equation is obtained from system (8) and (9) by imposing the following relation between the potential functions $q(x,t)$ and $r(x,t)$

$$r(x,t) = \sigma q^*(x,t), \quad \sigma = \mp 1\ , \tag{10}$$

that gives rise to the classical NLS equation

$$iq_t(x,t) = q_{xx}(x,t) - 2\sigma|q(x,t)|^2 q(x,t)\ . \tag{11}$$

It should be pointed out that relation (10) is well-known in the literature for over forty years. The first few conserved quantities associated with Eq. (11) are given by (conservation of mass, momentum and energy respectively)

$$\int_{\mathbb{R}} |q(x,t)|^2 dx = \text{constant}, \tag{12}$$

$$\int_{\mathbb{R}} q_x^*(x,t)q(x,t)dx = \text{constant}, \tag{13}$$

$$\int_{\mathbb{R}} \left(\sigma|q_x(x,t)|^2 + |q(x,t)|^4\right) dx = \text{constant}. \tag{14}$$

2.2 Nonlocal PT Symmetric NLS

In 2013 a new symmetry reduction of the AKNS scattering problem was identified that leads to a new nonlocal NLS type equation that preserves PT symmetry, i.e., invariance under space reflection and time reversal symmetry (complex conjugation). Indeed, under the symmetry reduction

$$r(x,t) = \sigma q^*(-x,t)\ , \quad \sigma = \mp 1, \tag{15}$$

system (8) and (9) are compatible and leads to the nonlocal nonlinear Schrödinger equation first introduced in [17]:

$$iq_t(x,t) = q_{xx}(x,t) - 2\sigma q^2(x,t)q^*(-x,t), \tag{16}$$

where star denotes complex conjugation. The corresponding Lax pairs given by

$$\mathsf{X} = \begin{pmatrix} -ik & q(x,t) \\ \sigma q^*(-x,t) & ik \end{pmatrix}\ , \tag{17}$$

$$\mathsf{T} = \begin{pmatrix} 2ik^2 + i\sigma q(x,t)q^*(-x,t) & -2kq(x,t) - iq_x(x,t) \\ -2\sigma kq^*(-x,t) - i\sigma q_x^*(-x,t) & -2ik^2 - i\sigma q(x,t)q^*(-x,t) \end{pmatrix}. \tag{18}$$

The important symmetry reduction (15) was first discovered in [17] and leads to a novel class of nonlocal integrable nonlinear evolution equations including a nonlocal NLS hierarchy. This is a special and remarkably simple reduction of the more general AKNS system [7] which had not been previously found. A list of few important properties of Eq. (16) are given below [19]:

- Time-reversal symmetry: If $q(x,t)$ is a solution so is $q^*(x,-t)$.
- Invariance under the transformation $x \to -x$: If $q(x,t)$ is a solution so is $q(-x,t)$.
- Gauge invariance: If $q(x,t)$ is a solution so is $e^{i\theta_0}q(x,t)$ with real and constant θ_0.
- Complex translation invariance: If $q(x,t)$ is a solution so is $q(x+ix_0,t)$ for any constant and real x_0.
- Equation (16) is a Hamiltonian dynamical system and is obtained using the variational formulation

$$iq_t(x,t) = \frac{\delta H}{\delta q^*(-x,t)}, \tag{19}$$

where $\frac{\delta H}{\delta q^*(-x,t)}$ is the variational derivative of the Hamiltonian with respect to $q^*(-x,t)$ and is given by

$$H = \int_{-\infty}^{+\infty} \left[-q_x(x,t)q_x^*(-x,t) - \sigma q^2(x,t)q^{*2}(-x,t) \right] dx\ , \quad \sigma = \mp 1. \tag{20}$$

- PT symmetry: If $q(x,t)$ is a solution so is $q^*(-x,-t)$. Define the quantity

$$V(x,t) = \pm 2q(x,t)q^*(-x,t), \tag{21}$$

which, in classical optics is referred to as a self-induced potential, implies

$$V^*(-x,t) = V(x,t). \tag{22}$$

With this at hand, Eq. (16) is rewritten in the new form

$$iq_t(x,t) = q_{xx}(x,t) + V(x,t)q(x,t). \tag{23}$$

This equivalent formulation allows one to connect Eq. (16) with PT symmetric optics for which $V(x,t)$ represents a "waveguide" and the resulting equation remains invariant under the joint transformation of $x \to -x, t \to -t$ and a complex conjugate. Thus, the nonlocal equation (16) is PT symmetric [35]. We remark that wave propagation in PT symmetric coupled waveguides or photonic lattices has been observed in experiments in classical optics [36–51].

The PT symmetric NLS equation (16) is an integrable Hamiltonian dynamical systems admitting infinite number of conservation laws, the first few are given by

$$\int_{\mathbb{R}} q(x,t)q^*(-x,t)dx = \text{constant}, \tag{24}$$

$$\int_{\mathbb{R}} \left[q_x(x,t)q^*(-x,t) + q(x,t)q_x^*(-x,t)\right]dx = \text{constant}, \tag{25}$$

$$\int_{\mathbb{R}} \left[q_x(x,t)q_x^*(-x,t) - \sigma q^2(x,t)q^{*2}(-x,t)\right]dx = \text{constant}. \tag{26}$$

2.3 Reverse Space-Time NLS

Recently, new additional symmetry reductions associated with the AKNS scattering problem were found [30]. Unlike the previous ones (the classical and PT symmetric) the new ones are of the so-called reverse space-time type in which a reflection in both space and time is performed. The system of Eqs. (8) and (9) are compatible under the symmetry condition

$$r(x,t) = \sigma q(-x,-t), \quad \sigma = \mp 1, \tag{27}$$

that leads to the so-called reverse space-time nonlocal nonlinear Schrödinger equation

$$iq_t(x,t) = q_{xx}(x,t) - 2\sigma q^2(x,t)q(-x,-t). \tag{28}$$

The new symmetry condition (27) gives rise to a new class of nonlocal (in both space and time) integrable evolution equations including a nonlocal reverse space-time NLS hierarchy. Equation (28) is another special and remarkably simple reduction of the more general q, r system mentioned above. For completeness, we give the compatible pair associated with Eq. (28):

$$\mathsf{X} = \begin{pmatrix} -ik & q(x,t) \\ \sigma q(-x,-t) & ik \end{pmatrix}, \tag{29}$$

$$\mathsf{T} = \begin{pmatrix} 2ik^2 + i\sigma q(x,t)q(-x,-t) & -2kq(x,t) - iq_x(x,t) \\ -2\sigma kq(-x,-t) - \sigma iq_x(-x,-t) & -2ik^2 - i\sigma q(x,t)q(-x,-t) \end{pmatrix}. \tag{30}$$

It is well-known that the compatible pair (2)–(3) with (5)–(7) lead to an infinite number of conservation laws and conserved quantities cf. [8]. The first few conserved quantities associated with Eq. (28) are given by

$$\int_{\mathbb{R}} q(x,t)q(-x,-t)dx = \text{constant}, \tag{31}$$

$$\int_{\mathbb{R}} q_x(x,t)q(-x,-t)dx = \text{constant}, \tag{32}$$

$$\int_{\mathbb{R}} \left(\sigma q_x(x,t)q_x(-x,-t) + q^2(x,t)q^2(-x,-t)\right) dx = \text{constant}. \tag{33}$$

In the context of PT symmetric linear/nonlinear optics, the analogous quantity in Eq. (31) is referred to as the "quasipower." We also note that Eq. (28) is an integrable Hamiltonian system with Hamiltonian given by equation (33). It should be pointed out that Eq. (28) breaks time and space translation symmetry, i.e., if $q(x,t)$ is a solution to Eq. (28) then $q(x+x_0, t+t_0)$ with constants x_0, t_0 (generally speaking) is not. Another interesting observation is that Eq. (28) breaks gauge invariance symmetry as well, i.e., if $q(x,t)$ is a solution to Eq. (28) then $q(x,t)e^{i\theta}$ with constant are real θ (again generally speaking) is not. Despite the lack of these important symmetries, Eq. (28) is still invariant under time reversal symmetry, i.e., if $q(x,t)$ is a solution to Eq. (28) so is $\tilde{q}(x,t) = q^*(x,-t)$.

2.4 Reverse Time Only NLS

Another interesting nonlocal symmetry reduction that system (8) and (9) admits is given by

$$r(x,t) = \sigma q(x,-t), \quad \sigma = \mp 1, \tag{34}$$

which, in turn, leads to the following new *reverse-time* only nonlocal nonlinear Schrödinger equation

$$iq_t(x,t) = q_{xx}(x,t) - 2\sigma q^2(x,t)q(x,-t). \tag{35}$$

Again, the condition (34) is remarkably simple and was noticed first by the authors [30] and leads to a nonlocal in time NLS hierarchy. Furthermore, since this equation arises from the above AKNS scattering problem, it is an integrable Hamiltonian evolution equation that admits an infinite number of conservation laws /conserved quantities. The first few are listed below:

$$\int_{\mathbb{R}} q(x,t)q(x,-t)dx = \text{constant}, \tag{36}$$

$$\int_{\mathbb{R}} q(x,t)q_x(x,-t)dx = \text{constant}, \tag{37}$$

$$\int_{\mathbb{R}} \Big(\sigma q_x(x,t)q_x(x,-t) + q^2(x,t)q^2(x,-t)\Big)\, dx = \text{constant}. \tag{38}$$

The Lax pairs associated with Eq. (35) are thus given by

$$\mathsf{X} = \begin{pmatrix} -ik & q(x,t) \\ \sigma q(x,-t) & ik \end{pmatrix}, \tag{39}$$

$$\mathsf{T} = \begin{pmatrix} 2ik^2 + i\sigma q(x,t)q(x,-t) & -2kq(x,t) - iq_x(x,t) \\ -2\sigma kq(x,-t) \pm iq_x(x,-t) & -2ik^2 - i\sigma q(x,t)q(x,-t) \end{pmatrix}. \tag{40}$$

Similar to the reverse space-time case, here Eq. (35) breaks only time translation symmetry. This implies if $q(x,t)$ is a solution to Eq. (35) then $q(x,t+t_0)$ with real or complex constant t_0 (generally speaking) is not. Equation (35) breaks gauge invariance as well but not time reversal symmetry.

2.5 Multi-component Case

The extension to the matrix or vector (multi component) reverse space-time or reverse time only nonlocal NLS system can be carried out in a similar fashion. Indeed, if we start from the matrix generalization of the AKNS scattering problem then the compatibility condition generalizing the one given in system (8) and (9) now reads

$$i\mathbf{Q}_t(x,t) = \mathbf{Q}_{xx}(x,t) - 2\mathbf{Q}(x,t)\mathbf{R}(x,t)\mathbf{Q}(x,t), \tag{41}$$

$$-i\mathbf{R}_t(x,t) = \mathbf{R}_{xx}(x,t) - 2\mathbf{R}(x,t)\mathbf{Q}(x,t)\mathbf{R}(x,t), \tag{42}$$

where $\mathbf{Q}(x,t)$ is an $N \times M$ matrix; $\mathbf{R}(x,t)$ is an $M \times N$ matrix of the real variables x and t and super script T denotes matrix transpose. Under the symmetry reduction

$$\mathbf{R}(x,t) = \sigma\mathbf{Q}^T(-x,-t), \quad \sigma = \mp 1, \tag{43}$$

system (41) and (42) are compatible and this leads to the reverse space-time nonlocal matrix nonlinear Schrödinger equation

$$i\mathbf{Q}_t(x,t) = \mathbf{Q}_{xx}(x,t) - 2\sigma\mathbf{Q}(x,t)\mathbf{Q}^T(-x,-t)\mathbf{Q}(x,t). \tag{44}$$

In the special case where $\mathbf{Q}$ is either a column vector ($M = 1$) then Eq. (44) reduces to

$$i\mathbf{q}_t(x,t) = \mathbf{q}_{xx}(x,t) - 2\sigma[\mathbf{q}(x,t)\cdot\mathbf{q}(-x,-t)]\mathbf{q}(x,t), \tag{45}$$

where dot stands for the vector scalar product. As in the scalar case, we can generalize Eq. (35) to the matrix or vector multi component case. Indeed, we note that system (41) and (42) are compatible under the symmetry reduction

$$\mathbf{R}(x,t) = \sigma\mathbf{Q}^T(x,-t), \quad \sigma = \mp 1, \tag{46}$$

which in turn gives rise to the following nonlocal in time only matrix nonlinear Schrödinger equation

$$i\mathbf{Q}_t(x,t) = \mathbf{Q}_{xx}(x,t) - 2\sigma\mathbf{Q}(x,t)\mathbf{Q}^T(x,-t)\mathbf{Q}(x,t). \tag{47}$$

To obtain the multi-component analogue of Eq. (47) we restrict the matrix $\mathbf{Q}$ to a column vector ($N = 1$) giving rise to the following nonlocal evolution equation

$$i\mathbf{q}_t(x,t) = \mathbf{q}_{xx}(x,t) - 2\sigma[\mathbf{q}(x,t)\cdot\mathbf{q}(x,-t)]\mathbf{q}(x,t). \tag{48}$$

3 Discrete Models

In this section we show how to derive discrete analogues to the nonlocal PT symmetric, reverse space-time and reverse time only NLS equations first introduced in [30]. Since all these models originate from the Ablowitz-Ladik scattering problem they constitute integrable Hamiltonian systems and admit infinite number of conserved quantities.

The starting point is the well-known discrete scattering problem [31]

$$v_{n+1} = \begin{pmatrix} z & Q_n \\ R_n & z^{-1} \end{pmatrix} v_n, \tag{49}$$

$$\frac{dv_n}{dt} = \begin{pmatrix} \mathsf{A}_n & \mathsf{B}_n \\ \mathsf{C}_n & \mathsf{D}_n \end{pmatrix} v_n, \tag{50}$$

where $v_n = (v_n^{(1)}, v_n^{(2)})^T$, Q_n and R_n vanish rapidly as $n \to \pm\infty$ and z is a complex spectral parameter. Here,

$$\mathsf{A}_n = i\, Q_n R_{n-1} - \frac{i}{2}\left(z - z^{-1}\right)^2, \tag{51}$$

$$\mathsf{B}_n = -i\left(z Q_n - z^{-1} Q_{n-1}\right), \tag{52}$$

$$\mathsf{C}_n = i\left(z^{-1} R_n - z R_{n-1}\right) \tag{53}$$

$$\mathsf{D}_n = -i\, R_n Q_{n-1} + \frac{i}{2}\left(z - z^{-1}\right)^2. \tag{54}$$

The discrete compatibility condition $\frac{d}{dt} v_{n+1} = \left(\frac{d}{dt} v_m\right)_{m=n+1}$ yields

$$i\frac{d}{dt} Q_n(t) = \Delta_n Q_n(t) - Q_n(t) R_n(t)\left[Q_{n+1}(t) + Q_{n-1}(t)\right], \tag{55}$$

$$-i\frac{d}{dt} R_n(t) = \Delta_n R_n(t) - Q_n(t) R_n(t)\left[R_{n+1}(t) + R_{n-1}(t)\right], \tag{56}$$

where

$$\Delta_n F_n \equiv F_{n+1} - 2F_n + F_{n-1}. \tag{57}$$

As is the case with the continuum limit, any "consistent" relation between the two discrete potentials Q_n, R_n would lead to a discrete evolution equation that is integrable and solvable by the inverse scattering transform.

3.1 Ablowitz-Ladik Lattice

In [31, 32], it was shown that the system of Eqs. (55) and (56) are compatible under the symmetry reduction

$$R_n(t) = \sigma Q_n^*(t), \quad \sigma = \mp 1, \tag{58}$$

and gives rise to the Ablowitz-Ladik model [31, 32]

$$i\frac{dQ_n(t)}{dt} = \Delta_n Q_n - \sigma |Q_n(t)|^2 \left[Q_{n+1}(t) + Q_{n-1}(t)\right]. \tag{59}$$

3.2 PT Symmetric Discrete NLS

In 2014 an integrable discrete PT symmetric NLS model was introduced by the authors [33]. It arose from a new symmetry reduction to the Ablowitz-Ladik scattering problem given by

$$R_n(t) = \sigma Q_{-n}^*(t), \quad \sigma = \mp 1, \tag{60}$$

in which case the Q_n, R_n system reduces to a single nonlocal differential-difference equation

$$i\frac{dQ_n(t)}{dt} = \Delta_n Q_n - \sigma Q_n(t) Q_{-n}^*(t) \left[Q_{n+1}(t) + Q_{n-1}(t)\right]. \tag{61}$$

Importantly, Eq. (61) is an integrable system admitting an infinite number of conservation laws. The first two conserved quantities are given by

$$\sum_{n=-\infty}^{+\infty} Q_n(t)\ Q_{1-n}^*(t) = \text{constant}. \tag{62}$$

$$\sum_{n=-\infty}^{+\infty} \left[\sigma Q_n(t)\ Q_{2-n}^*(t) - \frac{1}{2}\left(Q_n(t)\ Q_{1-n}^*(t)\right)^2\right] = \text{constant}. \tag{63}$$

$$\prod_{n=-\infty}^{+\infty} \left[1 - \sigma\, Q_n(t)\; Q^*_{-n}(t)\right] = \text{constant}. \tag{64}$$

Note that Eq. (61) is a Hamiltonian dynamical system with $Q_n(t)$ and $Q^*_{-n}(t)$ playing the role of coordinates and conjugate momenta respectively. The corresponding Hamiltonian and (the non canonical) brackets are given by

$$H = -\sigma \sum_{n=-\infty}^{+\infty} Q^*_{-n}(t)\,(Q_{n+1}(t) + Q_{n-1}(t)) \tag{65}$$
$$-2 \sum_{n=-\infty}^{+\infty} \log\left(1 - \sigma\, Q_n(t)\; Q^*_{-n}(t)\right).$$

$$\left\{Q_m(t),\, Q^*_{-n}(t)\right\} = i\left(1 - \sigma\, Q_n(t)\; Q^*_{-n}(t)\right)\delta_{n,m}. \tag{66}$$

$$\{Q_n(t),\, Q_m(t)\} = \left\{Q_n(t),\, Q^*_{-m}(t)\right\} = 0. \tag{67}$$

A discrete soliton solution was derived in [33].

3.3 *Reverse Space-Time Discrete NLS*

Interestingly, the system of discrete Eqs. (55) and (56) are compatible under the symmetry reduction

$$R_n(t) = \sigma\, Q_{-n}(-t), \quad \sigma = \mp 1, \tag{68}$$

and gives rise to the reverse discrete-time nonlocal discrete NLS equation:

$$i\frac{dQ_n(t)}{dt} = \Delta_n Q_n - \sigma\, Q_n(t) Q_{-n}(-t)\left[Q_{n+1}(t) + Q_{n-1}(t)\right]. \tag{69}$$

The discrete symmetry constraint (68) was first noticed in [30]. Since Eq. (69) comes out of the Ablowitz-Ladik scattering problem, as such, it constitute an infinite dimensional integrable Hamiltonian dynamical system. The first two conserved quantities are given by

$$\sum_{n=-\infty}^{+\infty} Q_n(t)\; Q_{1-n}(-t) = \text{constant}. \tag{70}$$

$$\sum_{n=-\infty}^{+\infty}\left[\sigma\, Q_n(t)\; Q_{2-n}(-t) - \frac{1}{2}\left(Q_n(t)\; Q_{1-n}(-t)\right)^2\right] = \text{constant}. \tag{71}$$

$$\prod_{n=-\infty}^{+\infty}\left[1 - \sigma\, Q_n(t)\; Q_{-n}(-t)\right] = \text{constant}. \tag{72}$$

Importantly, Eq. (69) is a Hamiltonian dynamical system with $Q_n(t)$ and $Q_{-n}(-t)$ playing the role of coordinates and conjugate momenta respectively. The corresponding Hamiltonian and (the non canonical) brackets are given by

$$H = -\sigma \sum_{n=-\infty}^{+\infty} Q_{-n}(-t)\left(Q_{n+1}(t) + Q_{n-1}(t)\right) \tag{73}$$
$$-2\sum_{n=-\infty}^{+\infty} \log\left(1 - \sigma\, Q_n(t)\; Q_{-n}(-t)\right).$$

$$\{Q_m(t),\, Q_{-n}(-t)\} = i\left(1 - \sigma\, Q_n(t)\; Q_{-n}(-t)\right)\delta_{n,m}. \tag{74}$$

$$\{Q_n(t),\, Q_m(t)\} = \{Q_n(t),\, Q_{-m}(-t)\} = 0. \tag{75}$$

3.4 Reverse Time Only Discrete NLS

Equations (55) and (56) admit another important symmetry reduction given by

$$R_n(t) = \sigma\, Q_n(-t), \quad \sigma = \mp 1. \tag{76}$$

This symmetry reduction is called reverse time Ablowitz-Ladik symmetry and results in the following discrete reverse time nonlocal discrete NLS equation:

$$i\frac{dQ_n(t)}{dt} = \Delta_n Q_n - \sigma\, Q_n(t) Q_n(-t)\left[Q_{n+1}(t) + Q_{n-1}(t)\right]. \tag{77}$$

The discrete symmetry constraint (76) was first observed in [30]. As is the case with the complex discrete-time symmetry, Eq. (77) is also integrable and posses an infinite number of conservation laws. The first few conserved quantities are listed below

$$\sum_{n=-\infty}^{+\infty} Q_n(t)\; Q_{n-1}(-t) = \text{constant}. \tag{78}$$

$$\sum_{n=-\infty}^{+\infty} \left[\sigma\, Q_n(t)\; Q_{n-2}(-t) - \frac{1}{2}\left(Q_n(t)\; Q_{n-1}(-t)\right)^2\right] = \text{constant}. \tag{79}$$

$$\prod_{n=-\infty}^{+\infty} \left[1 - \sigma\, Q_n(t)\; Q_n(-t)\right] = \text{constant}. \tag{80}$$

Importantly, Eq. (77) is a Hamiltonian dynamical system with $Q_n(t)$ and $Q_{-n}(-t)$ playing the role of coordinates and conjugate momenta respectively. The corresponding Hamiltonian and (the non canonical) brackets are given by

$$H = -\sigma \sum_{n=-\infty}^{+\infty} Q_n(-t)\left(Q_{n+1}(t) + Q_{n-1}(t)\right) \tag{81}$$

$$-2 \sum_{n=-\infty}^{+\infty} \log\left(1 - \sigma\, Q_n(t)\; Q_n(-t)\right).$$

$$\{Q_m(t),\, Q_n(-t)\} = i\sigma\left(1 - \sigma\, Q_n(t)\; Q_{-n}(-t)\right)\delta_{n,m}. \tag{82}$$

$$\{Q_n(t),\, Q_m(t)\} = \{Q_n(t),\, Q_m(-t)\} = 0. \tag{83}$$

4 Single-Soliton Solutions

The inverse problem consists of constructing the potential functions $r(x,t)$ and $q(x,t)$ from the scattering data (reflection coefficients) as well as the soliton eigenvalues $k_j, \bar{k}_j$ in the upper, lower half plane, respectively and norming constants $C_j(t), \bar{C}_j(t)$. Using the Riemann-Hilbert approach, one can find equations governing the eigenfunctions of the associated scattering problem (cf. [34]) which in turn determines the potentials $q(x,t)$ and $r(x,t)$. For the one soliton solution, they are given by

$$q(x,t) = \frac{2ie^{-2i\bar{k}_1 x}\bar{C}_1(t)}{1 + \frac{C_1(t)\bar{C}_1(t)}{(k_1-\bar{k}_1)^2 e^{2i(k_1-\bar{k}_1)x}}}, \qquad r(x,t) = -\frac{2ie^{2ik_1 x}C_1(t)}{1 + \frac{C_1(t)\bar{C}_1(t)}{(k_1-\bar{k}_1)^2 e^{2i(k_1-\bar{k}_1)x}}}. \tag{84}$$

The time dependence of the potentials q and r in Eq. (84) is encoded in the eigenvalues and norming constants C_1 and $\overline{C}_1$. For the PT symmetric and reverse space-time as well as the reverse time only NLS problems we will be discussing here, following the derivation outlined in [34] for the temporal evolution one finds

$$C_1(t) = C_1(0)e^{-4ik_1^2 t}, \tag{85}$$

$$\overline{C}_1(t) = \overline{C}_1(0)e^{4i\bar{k}_1^2 t}. \tag{86}$$

Here, k_1 and $\bar{k}_1$ are often called the soliton eigenvalues and $C_1(0), \bar{C}_1(0)$ are termed norming constants. The corresponding well-known one soliton solution of the classical NLS Eq. (11) is obtained from Eq. (84) by letting $\sigma = -1, r(x,t) = -q^*(x,t)$ and $k_1 = \xi + i\eta$ and is given by

$$q_{NLS}(x,t) = 2\eta \text{sech}(2\eta(x - 4\xi t - x_0))e^{-2i\xi x + 4i(\xi^2 - \eta^2)t - i\psi_0}, \tag{87}$$

where $e^{2\eta x_0} = |C_1(0)|/(2\eta)$, $\psi_0 = arg(C_1(0)) - \pi/2$. Next, we provide one soliton solution for the PT symmetric and reverse time only nonlocal NLS equations.

4.1 Solitons for PT Symmetric NLS

As was shown in [17, 19], for the PT symmetric NLS equation, the soliton eigenvalues are on the imaginary axis: $k_1 = i\eta, \bar{k}_1 = -i\bar{\eta}, \eta > 0, \bar{\eta} > 0$ in which case we have $C_1(0) = i(\eta + \bar{\eta})e^{i\theta}, \bar{C}_1(0) = -i(\eta + \bar{\eta})e^{i\bar{\theta}}$. Thus, the one soliton solution of the PT symmetric nonlocal NLS Eq. (16) is given by

$$q_{PT}(x,t) = \frac{2(\eta + \bar{\eta})e^{i\bar{\theta}}e^{-2\bar{\eta}x - 4i\bar{\eta}^2 t}}{1 - e^{i(\theta+\bar{\theta})}e^{-2(\eta+\bar{\eta})x + 4i(\eta^2 - \bar{\eta}^2)t)}}. \tag{88}$$

An alternative form of writing the above 1-soliton solution (88) is

$$q_{PT}(x,t) = \frac{(\eta + \bar{\eta})e^{i(\bar{\theta} - \theta - \pi)/2}e^{-(\bar{\eta} - \eta)x}e^{-2i(\eta^2 + \bar{\eta}^2)t}}{\cosh\left[(\eta + \bar{\eta})x - 2i(\eta^2 - \bar{\eta}^2)t - i(\theta + \bar{\theta} + \pi)/2\right]}. \tag{89}$$

Next, some remarks are in order.

- The solution $q_{PT}(x,t)$ given in (88) is doubly periodic in time with periods given by $T_1 = \frac{\pi}{2\bar{\eta}^2}$ and $T_2 = \frac{\pi}{2(\eta^2 - \bar{\eta}^2)}$.
- The intensity $|q_{PT}(x,t)|^2$ breathes in time with period given by $T = \frac{\pi}{2(\eta^2 - \bar{\eta}^2)}$.
- The solution (88) can develop a singularity in finite time. Indeed, at the origin ($x = 0$) the solution (89) becomes singular when

$$t_n = \frac{2n\pi - (\theta + \overline{\theta})}{4(\eta^2 - \overline{\eta}^2)}, n \in \mathbb{Z}. \tag{90}$$

- The solution (88) is characterized by two important time scales: the singularity time scale and the periodicity of breathing.
- A feature of this solution of (88) (and other singular solutions discussed in this paper) is that it can be defined after singularity has developed; i.e. it has a pole in time and it can be avoided in the complex time plane; i.e. the solution is of Painlevé type.
- We recall that not all members of the one-soliton family develop a singularity at finite time. Indeed, if one let $\eta = \bar{\eta} \equiv \eta$ in (88) then we arrive at the well behaved soliton solution of the nonlocal PT symmetric NLS equation

$$q(x,t) = 2\eta \text{sech}[2\eta x - i\theta_*]e^{-4i\eta^2 t}e^{i(\theta_* - \theta)}, \ \theta_* \neq n\pi, n \in \mathbb{Z}, \tag{91}$$

where $\theta_* = \theta + \bar{\theta} + \pi/2$ and η is an arbitrary real constant.

4.2 Solitons for Reverse Time NLS

With the symmetries between the soliton eigenvalues and norming constants given by $\bar{k}_1 = -k_1$ and $\bar{C}_1(0) = C_1(0)$ and using the above time dependence for $C_1(t), \bar{C}_1(t)$ the nonlocal reverse time only NLS equation has the following one soliton solution

$$q(x,t) = \frac{2iC_1(0)e^{2ik_1x}e^{4ik_1^2t}}{1 + \frac{C_1^2(0)}{4k_1^2}e^{4ik_1x}}, \tag{92}$$

$$r(x,t) = -\frac{2iC_1(0)e^{2ik_1x}e^{-4ik_1^2t}}{1 + \frac{C_1^2(0)}{4k_1^2}e^{4ik_1x}}. \tag{93}$$

One can see that the symmetry condition $r(x,t) = -q(x,-t)$ is automatically satisfied. With $k_1 = \xi + i\eta$ another form of the solution is

$$q(x,t) = \frac{2iC_1(0)e^{2i\xi x}e^{4i(\xi^2-\eta^2)t}e^{-2\eta x}e^{-8\xi\eta t}}{1 + \frac{C_1^2(0)}{4k_1^2}e^{4i\xi x}e^{-4\eta x}}. \tag{94}$$

Note that as $|x| \to \infty$, $q(x,t) \to 0$, but as $\xi t \to -\infty$, $q(x,t) \to \infty$ so in general it is an unstable solution. If we write $\frac{C_1(0)}{2k_1} = e^{2\eta x_0}e^{-2i\psi_0}$ then a singularity can occur when

$$1 + e^{4i(\xi x - \psi_0)}e^{-4\eta(x - x_0)} = 0,$$

or when

$$x = x_0, \;\; 4(\xi x_0 - \psi_0) = (2n+1)\pi, \;\; n \in \mathbb{Z}.$$

When we take a special case $\xi = 0$ the solution is stable and can be singular depending on $C_1(0)$. But if we further take $C_1(0) = |C_1(0)|$ so that $\psi_0 = 0$, and call $|C_1(0)|/(2\eta) = e^{-2\eta x_0}$ we find

$$q(x,t) = 2\eta \text{sech}[2\eta(x - x_0)]e^{4i\eta^2 t}, \tag{95}$$

which is not singular. We note that from Eq. (87) the one soliton solution of NLS with $\xi = 0$ is given by

$$q(x,t) = 2\eta \text{sech}(2\eta(x - x_0))e^{-4i\eta^2 t - i\psi_0}, \tag{96}$$

which is the same solution as given above in Eq. (95) but with $\psi_0 = 0$. Indeed, $\psi_0 = 0$ is necessary for this to be a solution of the reverse time only equation. Indeed any solution to the classical NLS that satisfies the property

$$q^*(x,t) = q(x,-t), \tag{97}$$

automatically satisfies the corresponding nonlocal (in time) NLS equation. This holds when the solution (96) obeys $\psi_0 = 0$. In this regard, we also note that the solution

$$q(x,t) = \eta \tanh(\eta x)e^{2i\eta^2 t}, \tag{98}$$

with nonzero boundary conditions $q(x,t) \sim \pm\eta e^{2i\eta^2 t}$ as $x \to \pm\infty$, which is a "dark" soliton solution of the classical NLS, solves the reverse-time NLS equation Eq. (35) with $\sigma = 1$.

5 Conclusions

In this chapter we reviewed recent progress related to the exciting field of integrable nonlocal nonlinear PT symmetric, reverse space-time and reverse time only equations. Starting from the well-known AKNS theory, we showed how to derive various nonlocal integrable equations previously discovered by the authors. Among them are the nonlocal PT symmetric (1+1)D nonlinear Schrödinger (NLS) equation and its multi-component generalization; the reverse space-time and reverse time only NLS equations along with their vector versions. The inverse scattering transform associated with the nonlocal NLS hierarchy is briefly summarized and one soliton solutions corresponding to each of the above case are presented. The discrete

nonlocal PT symmetric; reverse space-time and reverse time only NLS equations are also discussed. Starting from the Ablowitz-Ladik scattering problem, it is shown that all these discrete models arise from a simple symmetry reductions.

Acknowledgements MJA was partially supported by NSF under Grant No. DMS-1712793.

References

1. Zabusky, N.J., Kruskal, M.D.: Interactions of solitons in a collisionless plasma and the recurrence of initial states. Phys. Rev. Lett. **15**, 240–243, (1965)
2. Gardner, C.S., Greene, J.M., Kruskal, M.D., Miura, R.M.: Method for solving the Korteweg-deVries equation. Phys. Rev. Lett. **19**, 1095–1098 (1967)
3. Miura, R.M., Gardner, C.S., Kruskal, M.D.: Korteweg-deVries equation and generalizations II. Existence of conservation laws and constants of motion. J. Math. Phys. **9**, 1202–1204 (1968)
4. Zakharov, V.E., Faddeev, L.D.: Korteweg-deVries equation, a completely integrable Hamiltonian system. Funct. Anal. Appl. **5**, 280–287 (1971)
5. Lax, P.D.: Integrals of nonlinear equations of evolution and solitary waves. Commun. Pure. Appl. Math. **21**, 467–490 (1968)
6. Zakharov, V.E., Shabat, A.B.: Exact theory of two-dimensional self-focusing and one-dimensional self-modulation of waves in nonlinear media. Sov. Phys. JETP **34**, 62–69 (1972)
7. Ablowitz, M.J., Kaup, D.J., Newell, A.C., Segur, H.: Inverse scattering transform – Fourier analysis for nonlinear problems. Stud. Appl. Math. **53**, 249–315 (1974)
8. Ablowitz, M.J., Segur, H.: Solitons and Inverse Scattering Transform. SIAM Studies in Applied Mathematics, vol. 4. SIAM, Philadelphia (1981)
9. Ablowitz, M.J., Clarkson, P.A.: Solitons, Nonlinear Evolution Equations and Inverse Scattering. Cambridge University Press, Cambridge (1991)
10. Novikov, S.P., Manakov, S.V., Pitaevskii, L.P., Zakharov, V.E.: Theory of Solitons: The Inverse Scattering Method. Plenum, New York (1984)
11. Calogero, F., Degasperis, A.: Spectral Transform and Solitons I. North Holand, Amsterdam (1982)
12. Chen, Z., Christodoulides, D.N., Segev, M.: Optical spatial solitons: historic overview and recent advances. Rep. Prog. Phys. **75**, 086401 (2012)
13. Lederer, F., Stegeman, G.I., Christodoulides, D.N., Assanto, G., Segev, M., Silberberg, Y.: Discrete solitons in optics. Phys. Rep. **463**, 1–126 (2008)
14. Kivshar, Y.S., Luther-Davies, B.: Dark optical solitons: physics and applications. Phys. Rep. **298**, 81–197 (1998)
15. Kevrekidis, P.G., Frantzeskakis, D.J., Carretero-González, R.: Emergent Nonlinear Phenomena in Bose-Einstein Condensates: Theory and Experiment. Springer, Berlin/Heidelberg (2007)
16. Yang, J.: Nonlinear Waves in Integrable and Non integrable Systems. SIAM Mathematical Modeling and Computation. Society for Industrial and Applied Mathematics, Philadelphia (2010)
17. Ablowitz, M.J., Musslimani, Z.H.: Integrable nonlocal nonlinear Schrödinger equation. Phys. Rev. Lett. **110**, 064105 (2013)
18. Gadzhimuradov, T.A., Agalarov, A.M.: Towards a gauge-equivalent magnetic structure of the nonlocal nonlinear Schrödinger equation. Phys. Rev. A **93**, 062124 (2016)
19. Ablowitz, M.J., Musslimani, Z.H.: Inverse scattering transform for the integrable nonlocal nonlinear Schrödinger equation. Nonlinearity **29**, 915–946 (2016)
20. Fokas, A.S.: Integrable multidimensional versions of the nonlocal nonlinear Schrödinger equation. Nonlinearity **29**, 319–324 (2016)

21. Yang, B., Yang, J.: Transformations between nonlocal and local integrable equations. arXiv:1705.00332 [nlin.PS] (2017)
22. Ablowitz, M.J., Musslimani, Z.H.: Inverse scattering transform for the nonlocal nonlinear Schrödinger equation with nonzero boundary conditions. J. Math. Phys. **59**, 011501 (2018)
23. Lou, S.Y.: Alice-Bob systems, $P_s - T_d - C$ principles and multi-soliton solutions. https://arxiv.org/abs/1603.03975 (2016)
24. He, J.S., Qiu, D.Q.: Mirror symmetrical nonlocality of a parity-time symmetry system. Private Communication (2016)
25. Zhang, Y., Qiu, D., Cheng, Y., He, J.: Rational solution of the nonlocal nonlinear Schrödinger equation and its application in optics. Rom. J. Phys. **62**, 108 (2017)
26. Lou, S.Y.: Alice-Bob Physics: Coherent Solutions of Nonlocal KdV Systems. https://arxiv.org/abs/1606.03154 (2016)
27. Yan, Z.: Integrable PT symmetric local and nonlocal vector nonlinear Schrödinger equations: a unified two-parameter model. Appl. Math. Lett. **47**, 61 (2015)
28. Yan, Z.: Nonlocal general vector nonlinear Schrödinger equations: integrability, PT symmetribility, and solutions. Appl. Math. Lett. **62**, 101 (2016)
29. Rao, J., Cheng, Y., He, J.: Rational and Semirational Solutions of the Nonlocal Davey–Stewartson Equations. Stud. Appl. Math. https://doi.org/10.1111/sapm.12178 (2017)
30. Ablowitz, M.J., Musslimani, Z.H.: Integrable nonlocal nonlinear equations. Stud. Appl. Math. **139**, 7–59 (2017)
31. Ablowitz, M.J., Ladik, J.F.: Nonlinear differential-difference equations. J. Math. Phys. **16**, 598–603 (1975)
32. Ablowitz, M.J., Ladik, J.F.: Nonlinear differential-difference equations and Fourier-analysis. J. Math. Phys. **17**, 1011–1018 (1976)
33. Ablowitz, M.J., Musslimani, Z.H.: Integrable discrete PT symmetric model. Phys. Rev. E **90**, 032912 (2014)
34. Ablowitz, M.J., Prinari, B., Trubatch, A.D.: Discrete and Continuous Nonlinear Schrödinger Systems. Cambridge University Press, Cambridge (2004)
35. Bender, C.M., Boettcher, S.: Real spectra in non-Hermitian Hamiltonians having PT symmetry. Phys. Rev. Lett. **80**, 5243–5246 (1998)
36. Makris, K.G., El-Ganainy, R., Christodoulides, D.N., Musslimani, Z.H.: Beam dynamics in PT symmetric optical lattices. Phys. Rev. Lett. **100**, 103904 (2008)
37. El-Ganainy E., Makris, K.G., Christodoulides, D.N., Musslimani, Z.H.: Theory of coupled optical PT symmetric structures. Opt. Lett. **32**, 2632 (2007)
38. Musslimani, Z.H., Makris, K.G., El-Ganainy, R., Christodoulides, D.N.: Optical solitons in PT periodic potentials. Phys. Rev. Lett. **100**, 030402 (2008)
39. Ruter, C.E., et al.: Observation of parity-time symmetry in optics. Nat. Phys. **6**, 192 (2010)
40. Guo, A., et. al.: Observation of PT symmetry breaking in complex optical potentials. Phys. Rev. Lett. **103**, 093902 (2009)
41. Regensburger, A. et al., Parity-time synthetic photonic lattices. Nature **488**, 167 (2012)
42. Regensburger A, Miri, M.A., Bersch, C., Näger, J., Onishchukov, G., Christodoulides, D.N., Peschel, U.: Observation of defect states in PT-symmetric optical lattices. Phys. Rev. Lett. **110**, 223902 (2013)
43. Weimann, S., Kremer, M., Plotnik, Y., Lumer, Y., Nolte, S., Makris, K.G., Segev, M., Rechtsman, M.C., Szameit, A.: Topologically protected bound states in photonic parity-time-symmetric crystals. Nat. Mater. **16**, 433–438 (2017)
44. Makris, K.G., Musslimani, Z.H., Christodoulides, D.N., Rotter, S.: Constant-intensity waves and their modulation instability in non-Hermitian potentials. Nat. Commun. **6**, 7257 (2015)
45. Makris, K.G., Ge, L., Tureci, H.E.: Anomalous transient amplification of waves in non-normal photonic media. Phys. Rev. X **4**, 041044 (2014)
46. Hodaei, H., Hassan, A.U., Wittek, S., Garcia-Gracia, S., El-Ganainy, R., Christodoulides, D.N., Khajavikhan, M.: Enhanced sensitivity at higher-order exceptional points. Nature **548**, 187–191 (2017)

47. Hodaei, H., Miri, M.A., Heinrich, M., Christodoulides, D.N., Khajavikhan, M.: Parity-time symmetric microring lasers. Science **346**, 975 (2014)
48. Lazarides, N., Tsironis, G.P.: Gain-driven discrete breathers in PT-symmetric nonlinear metamaterials. Phys. Rev. Lett. **110**, 053901 (2013)
49. Lumer, Y., Plotnik, Y., Rechtsman, M.C., Segev, M.: Nonlinearly induced PT transition in photonic systems. Phys. Rev. Lett. **111**, 263901 (2013)
50. Konotop, V.V., Yang, J., Zezyulin, D.A.: Nonlinear waves in PT-symmetric systems. Rev. Mod. Phys. **88**, 035002 (2016)
51. Nixon, S., Ge, L., Yang, J.: Stability analysis for solitons in PT-symmetric optical lattices. Phys. Rev. A **85**(2), 023822 (2012)

Construction of Non-$\mathcal{PT}$-Symmetric Complex Potentials with All-Real Spectra

Jianke Yang

Abstract We review recent work on the generalization of $\mathcal{PT}$ symmetry. We show that, in addition to $\mathcal{PT}$-symmetric complex potentials, there are also large classes of non-$\mathcal{PT}$-symmetric complex potentials which also feature all-real spectra. In addition, some classes of these non-$\mathcal{PT}$-symmetric potentials allow phase transitions which do or do not go through exceptional points. These non-$\mathcal{PT}$-symmetric potentials are constructed by a variety of methods, such as the symmetry and supersymmetry methods and the soliton theory. A generalization of $\mathcal{PT}$ symmetry in multi-dimensions is also reviewed.

1 Introduction

Linear paraxial propagation of light in an optical waveguide is governed by the Schrödinger equation [1–3]

$$\mathrm{i}\Psi_z + \Psi_{xx} + V(x)\Psi = 0, \tag{1}$$

where z is the distance of propagation, x is the transverse coordinate, $V(x)$ is a complex potential whose real part is the index of refraction and the imaginary part represents gain and loss in the waveguide. This same equation also arises in non-Hermitian quantum mechanics [4, 5] and Bose-Einstein condensates [6], in which case z is the time variable. Looking for eigenmodes of the form $\Psi(x, z) = \mathrm{e}^{\mathrm{i}\mu z}\psi(x)$ we arrive at the eigenvalue problem

$$L\psi = \mu\psi, \tag{2}$$

where $L = \partial_{xx} + V(x)$ is a Schrödinger operator, and μ is an eigenvalue.

J. Yang (✉)
Department of Mathematics and Statistics, University of Vermont, Burlington, VT, USA
e-mail: jyang@math.uvm.edu

D. Christodoulides, J. Yang (eds.), *Parity-time Symmetry and Its Applications*, Springer Tracts in Modern Physics 280,
https://doi.org/10.1007/978-981-13-1247-2_18

All-real spectrum for this Schrödinger operator with a complex potential is a sought-after property not only in non-Hermitian quantum mechanics, but also in optics and Bose-Einstein condensates. In quantum mechanics, μ is the energy level, which must be real in order for the system to be physically meaningful. In optics and Bose-Einstein condensates, an all-real spectrum of a complex potential is significant because it allows a dissipative optical system with gain and loss to behave like a conservative system.

Bender and Boettcher [4] first observed that, if the Schrödinger operator L is parity-time ($\mathcal{PT}$) symmetric, i.e., it is invariant under the joint transformations of $x \to -x$ and complex conjugation, then its spectrum can be all-real. This $\mathcal{PT}$ symmetry is equivalent to the condition on the complex potential that

$$V^*(x) = V(-x), \tag{3}$$

where the asterisk * represents complex conjugation. In optics, this condition means that the refractive index needs to be an even function in space, and the gain-loss profile needs to be an odd function in space. A simple reason for this all-real spectrum of a $\mathcal{PT}$-symmetric potential is that its eigenvalues always appear in complex conjugate pairs. This is because for such potentials, if μ is an eigenvalue with eigenfunction $\psi(x)$, then by taking the complex conjugate of Eq. (2) and switching $x \to -x$, we see that μ^* would also be an eigenvalue with eigenfunction $\psi^*(-x)$. This eigenvalue symmetry restricts the appearance of complex eigenvalues and facilitates the realization of an all-real spectrum. But this $\mathcal{PT}$ symmetry does not necessarily guarantee an all-real spectrum, and phase transition can occur when conjugate pairs of complex eigenvalues appear in the spectrum [2, 4, 7].

$\mathcal{PT}$ symmetry has found many optical applications, such as unidirectional reflectionless metamaterials [8], $\mathcal{PT}$ lasers [9, 10], and non-reciprocity in $\mathcal{PT}$-symmetric whispering-gallery microcavities [11]. In these optical applications, the refractive index and gain-loss profiles of the waveguide were carefully designed so as to respect $\mathcal{PT}$ symmetry. In a $\mathcal{PT}$ setting, the gain-loss profile must be anti-symmetric, which could be restrictive. The pursuit of non-$\mathcal{PT}$-symmetric potentials with more flexible gain-loss profiles and all-real spectra is thus an interesting question. In recent years, various techniques have been developed to construct non-$\mathcal{PT}$-symmetric potentials with all-real spectra, and they will be reviewed in this article (a brief review on some of these results could also be found in [12]).

2 Non-$\mathcal{PT}$-Symmetric Potentials with All-Real Spectra and Exceptional-Point-Mediated Phase Transition

To derive non-$\mathcal{PT}$-symmetric complex potentials with all-real spectra, one strategy is to impose an operator symmetry in order to guarantee conjugate-pair eigenvalue symmetry [13]. Like the case of $\mathcal{PT}$-symmetric potentials, this conjugate-pair eigenvalue symmetry guarantees that either the spectrum of L is all-real, or a phase transition occurs when pairs of complex eigenvalues appear.

To execute this strategy, we observe that if there exists an operator η such that L and its complex conjugate L^* are related by a similarity relation

$$\eta L = L^* \eta, \tag{4}$$

then the eigenvalues of L would come in conjugate pairs if the kernel of η is empty [13]. This operator relation resembles the condition for pseudo-Hermiticity [5], but we do not require η to be invertible here.

If we let $\eta = \mathcal{P}$, where $\mathcal{P}$ is the parity operator $x \mapsto -x$, then this η operator has an empty kernel, and the similarity condition (4) yields $V(-x) = V^*(x)$, which recovers the well-known class of $\mathcal{PT}$-symmetric potentials. However, when branching out to different choices of η, a completely real spectrum can be obtained for an arbitrary choice of the gain-loss distribution by a judicious construction of the index of refraction. This will be demonstrated below where η is chosen as a differential operator.

2.1 Type-I Potentials

First, we consider the simplest choice of a differential η operator,

$$\eta = \partial_x + a(x). \tag{5}$$

Substituting this η and operator L into the similarity condition (4), we get the following two equations

$$a_x = \mathrm{i}\,\mathrm{Im}(V), \qquad a_{xx} - V_x = (a^2)_x. \tag{6}$$

The second equation can be integrated once, and we get

$$a_x - V = a^2 + \xi_0, \tag{7}$$

where ξ_0 is a constant. Utilizing (6), this equation becomes

$$\mathrm{Re}(V) = -a^2 - \xi_0. \tag{8}$$

Equations (6), (7), and (8) show that $a(x)$ is a purely imaginary function, and ξ_0 is a real constant. Denoting $a(x) = \mathrm{i}g(x)$, where $g(x)$ is an arbitrary real function, we get $\mathrm{Re}(V) = g^2(x) - \xi_0$ and $\mathrm{Im}(V) = g'(x)$, with the prime representing the derivative. The constant ξ_0 can be eliminated by a gauge transformation to Eq. (1), and thus the resulting complex potential is

$$V(x) = g^2(x) + \mathrm{i}g'(x). \tag{9}$$

These potentials were called type-I potentials in [13]. They generalized the potentials of the same form in [14, 15], where special choices of the $g(x)$ function were taken (see Sects. 2.3 and 5 for reviews).

Compared to $\mathcal{PT}$-symmetric potentials, a distinctive feature of these type-I potentials is that the gain-loss profile $g'(x)$ is now arbitrary since $g(x)$ is arbitrary. But due to the symmetry relation (4), the spectra of these potentials can still be all-real, just like $\mathcal{PT}$-symmetric potentials. This possibility of all-real spectra for arbitrary gain-loss profiles is made possible by a judicious choice of refractive indices in relation to the gain-loss profiles.

As an example, we take

$$g(x) = \tanh[2(x + 2.5)] - \tanh(x - 2.5) + c_0, \tag{10}$$

where c_0 is a real constant. In Fig. 1, we show two potentials of the form (9), with the c_0 value taken as 0 and -0.3 respectively. In the upper row, the potential with $c_0 = 0$ has a completely real spectrum, and increasing c_0 will maintain the reality of the spectrum as more discrete eigenvalues bifurcate off the edge of the continuous spectrum. However, as c_0 is decreased, the spectrum will undergo a phase transition at $c_0 \approx -0.181$, where a pair of real eigenvalues and their eigenfunctions coalesce and form an exceptional point at $\mu \approx 0.056$. This exceptional point then bifurcates off the real axis and creates a pair of complex eigenvalues afterwards. This can be seen in the lower row of Fig. 1 with $c_0 = -0.3$. We stress that this phase transition is induced by going through an exceptional point, which is a common scenario for phase transition [4, 7].

2.2 Type-II Potentials

Type-I potentials (9) come from taking the simplest form of a differential η operator [i.e., a first-order operator (5)]. By increasing the order of this differential operator, more families of potentials arise. Let η now be a second-order operator,

$$\eta = \partial_{xx} + a(x)\,\partial_x + b(x). \tag{11}$$

Inserting this η into the similarity condition (4) and collecting coefficients of the same order of derivatives on the two sides of this condition, we get

	ηL	$L^*\eta$
∂_x^4	1	1
∂_x^3	a	a
∂_x^2	V	$V^* + 2a'$
∂_x^1	$Va + 2V'$	$V^*a + a'' + 2b'$
∂_x^0	$Vb + V'a + V''$	$V^*b + b''$

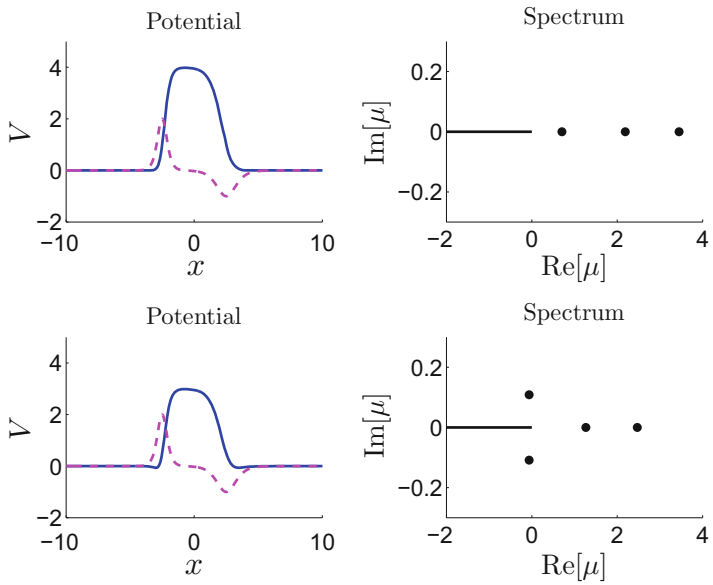

Fig. 1 Spectra of type-I potentials (9) with $g(x)$ given in (10). Upper row: $c_0 = 0$; lower row: $c_0 = -0.3$. In the potentials, the solid blue line is $\mathrm{Re}(V)$, and the dashed pink line is $\mathrm{Im}(V)$. (Adapted from [13])

Setting these coefficients in ηL and $L^*\eta$ to match each other, we get a system of equations which can be solved from top to bottom. From the ∂_x^2 coefficients, we get $a'(x) = \mathrm{i}\,\mathrm{Im}(V)$. Setting $a(x) = \mathrm{i}g(x)$, where $g(x)$ is a real function, we obtain $\mathrm{Im}(V) = g'(x)$. Inserting this $a(x)$ formula into the ∂_x^1 equation and integrating once, we get

$$b = \mathrm{Re}(V) - \frac{1}{2}g^2 + \frac{\mathrm{i}}{2}g' + c_1,$$

where c_1 is a constant.

Now we insert these $a(x)$ and $b(x)$ solutions into the ∂_x^0 equation. After simple algebra, this equation becomes

$$[\mathrm{Re}(V)g^2]' = g^3 g' - \frac{1}{2}g'''g - 2c_1 g'g,$$

from which we can solve the refractive index $\mathrm{Re}(V)$ as

$$\mathrm{Re}(V) = \frac{1}{4}g^2 + \frac{g'^2 - 2g''g + c_2}{4g^2} - c_1,$$

where c_2 is a real constant. The overall constant c_1 can be removed without loss of generality.

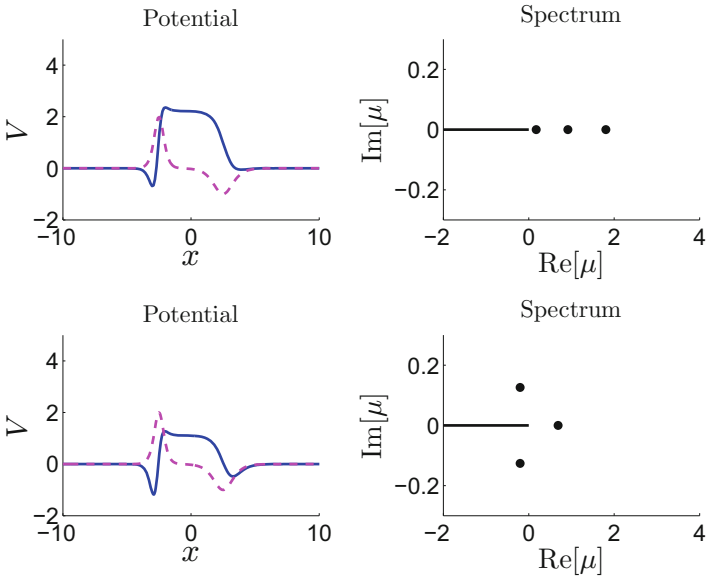

Fig. 2 Spectra of type-II potentials (12) with $g(x)$ given in (10). Upper row: $c_0 = 1$ and $c_2 = -1$; lower row: $c_0 = 1$ and $c_2 = 4$. (Adapted from [13])

Putting the above results together, we get potentials

$$V(x) = \frac{1}{4}g^2 + \frac{g'^2 - 2g''g + c_2}{4g^2} + \mathrm{i}g', \tag{12}$$

where $g(x)$ is an arbitrary real function, and c_2 is an arbitrary real constant. These potentials were called type-II potentials in [13], and they generalized potentials of the same form but with $c_2 \leq 0$ in [16] (see Sects. 2.3 and 4 for reviews).

Like type-I potentials, the gain-loss profile $g'(x)$ of these type-II potentials is also arbitrary, but their spectra can still be all-real due to the symmetry relation (4).

As an example, we take the same function $g(x)$ as in (10). The spectrum of this potential with $c_0 = 1$ and $c_2 = -1$ is completely real, see Fig. 2 (upper row). Fixing c_0 and decreasing c_2 will maintain the all-real spectrum. If c_2 is increased above a certain threshold (which is approximately 2.535), a phase transition occurs, where a pair of real eigenvalues coalesce and form an exceptional point, which then bifurcates off the real axis and creates a pair of complex eigenvalues afterwards. This can be seen in the lower row of Fig. 2 for $c_2 = 4$. In this lower row, an overall real constant $(c_0^2 + c_2/c_0^2)/4$ has been subtracted from the potential (12) so that the refractive index drops to zero at infinity. Again, the phase transition here is induced by going through an exceptional point.

2.3 Potentials with Strictly All-Real Spectra

For the two types of potentials (9) and (12), an exceptional-point-mediated phase transition is in general possible (see Figs. 1 and 2). But under certain restrictions on these potentials, all-real spectra can be guaranteed.

For type-I potentials (9), it was shown by Tsoy et al. [14] that, if $g(x)$ is a single-humped localized real function, then its spectrum is strictly real. This result was based on an observation by Wadati [15] that the Zakharov-Shabat (ZS) spectral problem [17]

$$v_{1x} + \mathrm{i}\zeta v_1 = g(x)v_2, \quad v_{2x} - \mathrm{i}\zeta v_2 = -g(x)v_1, \tag{13}$$

with ζ being a spectral parameter, can be transformed into the Schrödinger eigenvalue problems

$$\psi_{xx} + V(x,t)\psi = \mu\psi, \quad \phi_{xx} + V^*(x,t)\phi = \mu\phi,$$

with $V(x)$ being the type-I potential (9) and $\mu = -\zeta^2$, through the transformation

$$\psi = v_2 - \mathrm{i}v_1, \quad \phi = v_2 + \mathrm{i}v_1. \tag{14}$$

This means that, in order for the type-I potential (9) to have all-real μ spectrum, the necessary and sufficient condition is that the ζ spectrum of the ZS spectral problem (13) is either real or purely imaginary (note that the continuous spectrum of the ZS problem is the real ζ axis). It was shown by Klaus and Shaw [18] that when $g(x)$ is a single-humped localized real function, then all discrete eigenvalues of the ZS problem are purely imaginary, and thus type-I potentials (9) have all-real spectra.

For type-II potentials (12), it was shown by Andrianov et al. [16] that if $c_2 \leq 0$, then the spectrum is strictly real. The proof is based on supersymmetry (see Sect. 4). Specifically, when $c_2 = -\epsilon^2 \leq 0$, with ϵ being a real parameter, then we have the following intertwining operator relation,

$$[-\partial_x + W(x)]\,[\partial_{xx} + V(x)] = [\partial_{xx} + V_0(x)]\,[-\partial_x + W(x)]\,, \tag{15}$$

where $V(x)$ is the complex type-II potential (12),

$$W(x) = \frac{g' + \epsilon}{2g} - \frac{1}{2}\mathrm{i}g,$$

and V_0 is a real potential,

$$V_0(x) = \frac{1}{4}g^2 + \frac{2gg'' - 3g'^2 - 4\epsilon g' - \epsilon^2}{4g^2}.$$

The intertwining relation (15) shows that the Schrödinger operators $\partial_{xx} + V(x)$ and $\partial_{xx} + V_0(x)$ are related by a similarity transformation, and thus they share the same spectrum. Since the spectrum of the real potential V_0 is all-real, the spectrum of the type-II potential (12) is then all-real as well. Note that for $c_2 > 0$, such an intertwining operator relation does not exist, and the supersymmetry approach does not apply. In such cases, phase transition can occur in type-II potentials as Fig. 2 shows.

3 Non-$\mathcal{PT}$-Symmetric Potentials with All-Real Spectra and Exceptional-Point-Free Phase Transition

Extending the symmetry approach of the previous section, additional new types of complex potentials with all-real spectra can be constructed [19]. More interestingly, these potentials exhibit exceptional-point-free phase transition, which is very novel.

In this construction, instead of choosing η in Eq. (4) as pure differential operators, we now take η to be a combination of the parity operator $\mathcal{P}$ and differential operators. In the simplest case, we take η to be a combination of the parity operator and a first-order differential operator, i.e.,

$$\eta = \mathcal{P}\left[\partial_x + h(x)\right], \tag{16}$$

where $h(x)$ is a complex function to be determined. Substituting this η into the similarity condition (4), we get the following two equations

$$V(x) - V^*(-x) = 2h'(x), \tag{17}$$

$$\left[V(x) - V^*(-x)\right]h(x) = h''(x) - V'(x). \tag{18}$$

From the first equation, we see that $\left[h^*(-x)\right]_x = h'(x)$; thus

$$h^*(-x) = h(x) + c_1, \tag{19}$$

where c_1 is a constant. Substituting Eq. (17) into (18) and integrating once, we get

$$V(x) = h'(x) - h^2(x) + c_2, \tag{20}$$

where c_2 is another constant. Lastly, inserting (19) and (20) into Eq. (17), we obtain

$$c_1^2 + 2c_1 h(x) + c_2 - c_2^* = 0. \tag{21}$$

In order for the potential $V(x)$ in (20) not to be a constant, the function $h(x)$ should not be identically zero. Thus, Eq. (21) dictates that $c_1 = 0$ and c_2 is real. The former condition means that the complex function $h(x)$ is $\mathcal{PT}$-symmetric in view of Eq. (19). Regarding the latter condition, since a real constant in a potential can be easily removed by a simple shift of the eigenvalue, we can set $c_2 = 0$ without loss of generality. In the end, we find that for new complex potentials of the form

$$V(x) = h'(x) - h^2(x), \tag{22}$$

where $h(x)$ is a $\mathcal{PT}$-symmetric complex function, i.e., $h^*(x) = h(-x)$, the Schrödinger operator L satisfies the similarity condition (4) with η given in (16). Because of this, the eigenvalues of L exhibit complex-conjugate symmetry. Hence, the spectrum of L can be all-real, but phase transition may also occur, similar to $\mathcal{PT}$-symmetric potentials as well as non-$\mathcal{PT}$-symmetric potentials of the previous section.

In these new potentials, $h(x)$ is an arbitrary $\mathcal{PT}$-symmetric function. Because of this, simple algebra shows that these potentials can accommodate any arbitrary gain-loss profile [19], analogous to type-I and type-II potentials of the previous section.

A peculiar property of this new class of non-$\mathcal{PT}$-symmetric potentials is that, if these potentials are localized, then they will not admit any discrete real eigenvalues. This contrasts the previous non-$\mathcal{PT}$-symmetric potentials (9) and (12), where discrete real eigenvalues are very common (see Figs. 1 and 2).

To prove this statement, we recall that for any localized potential, the continuous spectrum of the Schrödinger operator L is the semi-infinite interval $-\infty \le \mu \le 0$; and discrete real eigenvalues, if any, are positive numbers. Suppose $\mu = k^2$, with $k > 0$, is a discrete real eigenvalue in the localized potential (22). Since L is a second-order differential operator, its discrete eigenvalue μ can only have geometric multiplicity one, meaning that the corresponding eigenfunction ψ is unique (up to a constant multiple). Applying the operator η to the eigenvalue equation $L\psi = k^2\psi$ and recalling the symmetry relation (4), we get $L^*(\eta\psi) = k^2(\eta\psi)$. Taking the complex conjugate of this equation, we get $L(\eta\psi)^* = k^2(\eta\psi)^*$. This means that $(\eta\psi)^*$ is also an eigenfunction of L at the same eigenvalue μ. Thus, $(\eta\psi)^*$ and ψ must be linearly dependent on each other, i.e., $(\eta\psi)^* = \alpha\psi$, where α is a complex constant. In view of the expression of η in Eq. (16), this relation can be rewritten as

$$[\partial_x + h(x)]\psi(x) = \alpha^*\psi^*(-x). \tag{23}$$

Now we examine this relation as $x \to \pm\infty$. Since the potential $V(x)$ is localized, $h(x)$ is localized as well. From the eigenvalue equation (2), we see that the large-x asymptotics of $\psi(x)$ is

$$\psi(x) \to a_\pm e^{-k|x|}, \quad x \to \pm\infty,$$

where $a_\pm$ are complex constants which cannot be both zero. Since $h(x)$ is localized, as $x \to \pm\infty$, the contribution of the $h(x)$ term in Eq. (23) is subdominant and will be ignored. Then, inserting the above ψ-asymptotics into (23), we get two parameter conditions

$$-ka_+ = \alpha^* a_-^*, \quad ka_- = \alpha^* a_+^*.$$

Dividing these two equations and rearranging terms, we get

$$|a_+|^2 + |a_-|^2 = 0,$$

which is impossible since $a_\pm$ cannot be both zero. Thus, localized potentials (22) do not admit discrete real eigenvalues.

The fact of localized potentials (22) not admitting discrete real eigenvalues is a distinctive property, and it has important implications. Since there are no discrete real eigenvalues, a phase transition in these potentials clearly cannot be induced from collisions of such eigenvalues through an exceptional point. Instead, complex eigenvalues will have to bifurcate out from the continuous spectrum. Below, we will use an example to show that this is exactly the case. In this example, we take

$$h(x) = d_1 \operatorname{sech} x + \mathrm{i} d_2 \operatorname{sech} x \tanh x, \tag{24}$$

which is $\mathcal{PT}$-symmetric for real constants d_1 and d_2. We also fix $d_1 = 1$. Then for two different d_2 values of 1 and 2, the resulting non-$\mathcal{PT}$-symmetric localized potentials and their spectra are plotted in Fig. 3. We see that neither spectrum contains discrete real eigenvalues, which corroborates our analytical result above. When $d_2 = 1$, the spectrum is all-real (see the upper right panel). But when $d_2 = 2$, a conjugate pair of discrete eigenvalues $\mu \approx -0.7067 \pm 0.4961\mathrm{i}$ appear (see the lower right panel). The phase transition occurs at $d_2 \approx 1.385$. Closer examination reveals that the two complex eigenvalues bifurcate out from $\mu_0 \approx -0.8062$, which is in the interior of the continuous spectrum. It is also noticed that the discrete (localized) eigenfunctions of the two complex eigenvalues bifurcate out from two different continuous (nonlocal) eigenfunctions of the real eigenvalue μ_0, rather than from a single coalesced eigenfunction. This reveals two facts: (1) these discrete eigenmodes bifurcate out from continuous eigenmodes, rather than embedded isolated eigenmodes, in the interior of the continuous spectrum; (2) this phase transition does not go through an exceptional point. The second fact is particularly significant, because all phase transitions reported before in both finite- and infinite-dimensional non-Hermitian systems occurred either due to a collision of real eigenvalues forming an exceptional point, where different eigenvectors or eigenfunctions coalesce [4, 7, 13], or through an exotic singular scenario, where complex eigenvalues bifurcate out from infinity of the real axis [20]. This is the first instance where a phase transition occurs without an exceptional point or a singular point. Very recently, an analytical explanation of this mysterious bifurcation was given by Konotop and Zezyulin [21] through the splitting of self-dual spectral singularity.

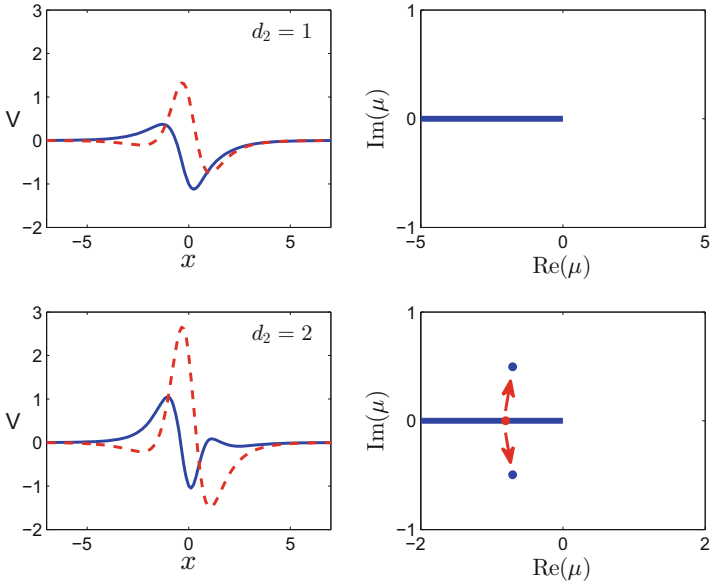

Fig. 3 Spectra of localized potentials (22) with $h(x)$ given in (24) and $d_1 = 1$ (the d_2 values are shown inside the panels). Left column: real (solid blue) and imaginary (dashed red) parts of the complex potentials. Right column: spectra of potentials in the left column (the red arrows in the lower panel indicate that the two complex eigenvalues in the spectrum bifurcate out from the red dot in the interior of the continuous spectrum when a phase transition happens). (Adapted from [19])

4 Construction of Non-$\mathcal{PT}$-Symmetric Potentials with All-Real Spectra Using Supersymmetry

The concept of supersymmetry (SUSY) was first introduced in quantum field theories and high-energy physics (see [22] and the references therein). Subsequently, SUSY was utilized in quantum mechanics to construct analytically solvable potentials. This construction is based on the factorization of the Schrödinger operator into the product of two first-order operators. Switching the order of these two first-order operators gives another Schrödinger operator with a new potential (called the *partner potential*) which shares the same spectrum as the original potential (except possibly a single discrete eigenvalue). SUSY can establish perfect phase matching between modes in the partner potentials, which has motivated applications such as mode converters in SUSY optical structures [23]. Extending the idea of SUSY, parametric families of complex potentials with all-real spectra can be constructed [16, 24–27].

Let us employ the idea of SUSY to construct complex potentials with all-real spectra, following [24, 27, 28].

Suppose $V_1(x)$ is a potential with all-real spectrum, and $\mu^{(1)}$ is an eigenvalue of this potential with eigenfunction $\psi^{(1)}$, i.e.,

$$\left[\frac{d^2}{dx^2} + V_1(x) - \mu^{(1)}\right]\psi^{(1)} = 0. \tag{25}$$

We first factorize the linear operator in this equation as

$$-\frac{d^2}{dx^2} - V_1(x) + \mu^{(1)} = \left[-\frac{d}{dx} + W(x)\right]\left[\frac{d}{dx} + W(x)\right]. \tag{26}$$

The function $W(x)$ in this factorization can be obtained by requiring $\psi^{(1)}$ to annihilate $d/dx + W(x)$, and this gives $W(x)$ as

$$W(x) = -\frac{d}{dx}\ln(\psi^{(1)}). \tag{27}$$

It is easy to directly verify that this $W(x)$ does satisfy the factorization equation (26).

Now we switch the two operators on the right side of the above factorization, and this leads to a new potential $V_2(x)$,

$$-\frac{d^2}{dx^2} - V_2(x) + \mu^{(1)} = \left[\frac{d}{dx} + W(x)\right]\left[-\frac{d}{dx} + W(x)\right], \tag{28}$$

where

$$V_2 = V_1 - 2W_x. \tag{29}$$

This V_2 potential is referred to as the partner potential of V_1. It is known that for any two operators A and B, AB and BA share the same spectrum in general (except for a possible difference in the zero eigenvalue when the kernel of A or B is non-empty). Then, in view of the two factorizations (26) and (28), we see that the spectrum of V_2 is that of V_1, but with $\mu^{(1)}$ generically removed.

The new potential V_2, however, is only real or $\mathcal{PT}$-symmetric if V_1 is so. In order to derive non-$\mathcal{PT}$-symmetric potentials, we build a new factorization for the V_2 potential,

$$-\frac{d^2}{dx^2} - V_2(x) + \mu^{(1)} = \left[\frac{d}{dx} + \widetilde{W}(x)\right]\left[-\frac{d}{dx} + \widetilde{W}(x)\right]. \tag{30}$$

The function $\widetilde{W}$ in this new factorization can be derived as follows [24, 27]. Equating this new factorization with the previous one in (28), we get

$$\widetilde{W}_x + \widetilde{W}^2 = W_x + W^2.$$

Denoting $\widetilde{W} = W + \phi$, we see ϕ satisfies a Ricatti equation

$$\phi_x + 2W\phi + \phi^2 = 0.$$

Through the standard variable transformation $\phi = q'/q$, the function q is found to satisfy a linear homogeneous equation

$$q'' + 2Wq' = 0.$$

Utilizing the W expression in (27), we obtain the general q solution as

$$q = \hat{c}\left[c + \int_0^x [\psi^{(1)}(\xi)]^2 d\xi\right],$$

where c and $\hat{c}$ are arbitrary complex constants. In view of the variable transformation $\phi = q'/q$, we see the constant $\hat{c}$ does not contribute to the ϕ solution. Putting all the above results together, we find the general function $\widetilde{W}(x)$ as

$$\widetilde{W}(x) = -\frac{d}{dx}\ln(\widetilde{\psi}^{(1)}), \tag{31}$$

where

$$\widetilde{\psi}^{(1)}(x) = \frac{\psi^{(1)}(x)}{c + \int_0^x [\psi^{(1)}(\xi)]^2 d\xi}.$$

For the new V_2 factorization (30), its partner potential, defined through

$$-\frac{d^2}{dx^2} - \widetilde{V}_1(x) + \mu^{(1)} = \left[-\frac{d}{dx} + \widetilde{W}(x)\right]\left[\frac{d}{dx} + \widetilde{W}(x)\right],$$

is

$$\widetilde{V}_1 = V_2 + 2\widetilde{W}_x.$$

Utilizing the V_2 and $\widetilde{W}$ formulae (29) and (31), this $\widetilde{V}_1$ potential is then found to be

$$\widetilde{V}_1(x) = V_1(x) + 2\frac{d^2}{dx^2}\ln\left[c + \int_0^x [\psi^{(1)}(\xi)]^2 d\xi\right]. \tag{32}$$

For generic values of the complex constant c, this $\widetilde{V}_1$ potential is complex and non-$\mathcal{PT}$-symmetric. In addition, its spectrum is identical to that of V_1. Indeed, even though $\mu^{(1)}$ may not lie in the spectrum of V_2, it is in the spectrum of $\widetilde{V}_1$ with eigenfunction $\widetilde{\psi}^{(1)}$. Hence, if V_1 has an all-real spectrum, so does $\widetilde{V}_1$. Notice that this $\widetilde{V}_1$ potential, referred to as the superpotential below, is actually a family of potentials due to the free complex constant c.

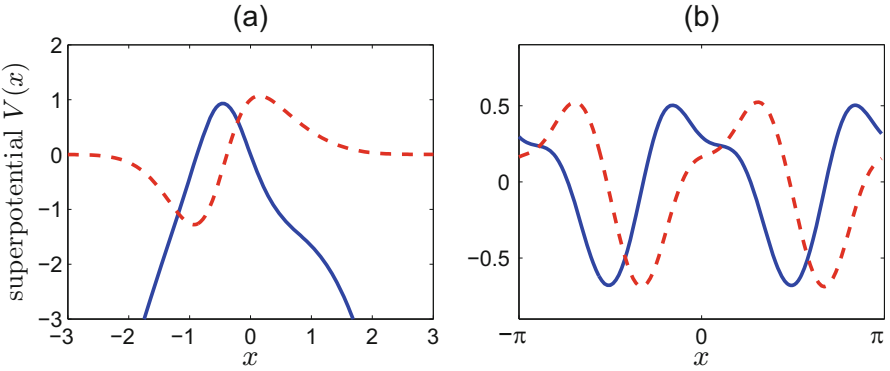

Fig. 4 (**a**) Superpotential (33) with $c = 1 + \mathrm{i}$; (**b**) Periodic superpotential (34) with $V_0 = 1$ and $c = 0.5 - 2\mathrm{i}$. The solid blue curve is Re(V), and the dashed red curve is Im(V). (Adapted from [28])

Now we give two explicit examples of non-$\mathcal{PT}$-symmetric superpotentials (32) with all-real spectra. The first one is constructed from the parabolic potential $V(x) = -x^2$ and its first eigenmode of $\mu_1 = -1$ with $\psi_1 = e^{-x^2/2}$. Then the superpotential (32) reads

$$V(x) = -x^2 + 2\frac{d^2}{dx^2} \ln\left[c + \int_0^x e^{-\xi^2} d\xi\right]. \tag{33}$$

This potential with $c = 1 + \mathrm{i}$ is shown in Fig. 4a. The spectrum of this potential (for any complex c value) is $\{-1, -3, -5, \ldots\}$, i.e., is all-real.

In the second example, the superpotential (32) is built from the $\mathcal{PT}$-symmetric periodic potential $V(x) = V_0^2 e^{2\mathrm{i}x}$ and its Bloch mode $\psi^{(1)} = I_1(V_0 e^{\mathrm{i}x})$ with eigenvalue $\mu_1 = -1$. Here V_0 is a real constant, and I_1 is the modified Bessel function. The resulting periodic superpotential (32) reads

$$V(x) = V_0^2 e^{2\mathrm{i}x} + 2\frac{d^2}{dx^2} \ln\left[c + \int_0^x I_1^2(V_0 e^{\mathrm{i}\xi}) d\xi\right]. \tag{34}$$

For $V_0 = 1$ and $c = 0.5 - 2\mathrm{i}$, this potential is shown in Fig. 4b. The diffraction (dispersion) relation of this superpotential (for all c values) is the same as that of the original potential $V(x) = V_0^2 e^{2\mathrm{i}x}$, i.e., $\mu = -(k + 2m)^2$, where the wavenumber k is in the first Brillouin zone, $k \in [-1, 1]$, and m is any non-negative integer.

If $V(x)$ is a localized real potential, then SUSY allows to construct localized complex superpotentials (32) with all-real spectra [27, 28].

A related technique to construct complex potentials with all-real spectra was proposed by Cannata, et al. [25]. This technique is based on the formulae (27) and (29). But instead of choosing $\mu^{(1)}$ as an eigenvalue of the potential $V_1(x)$ and $\psi^{(1)}$ as the corresponding eigenfunction, one chooses $\mu^{(1)}$ as an arbitrary

real number and the function $\psi^{(1)}$ as a complex linear combination of the two fundamental solutions to the Schrödinger equation (25) [here we do not require $\psi^{(1)}$ to be square-integrable]. For instance, if $V_1(x)$ is a real potential and $\mu^{(1)}$ is an arbitrary real number, then we can choose $\psi^{(1)}$ as a linear combination $c_1 f_1(x) + c_2 f_2(x)$, where f_1, f_2 are the two real fundamental solutions to Eq. (25), and c_1, c_2 are complex constants. With such choices of $\mu^{(1)}$ and $\psi^{(1)}$, it is easy to see that the potential $V_1(x)$ and the complex potential $V_2(x)$ [as given by Eq. (29)] still share the same spectrum in general. The only possible exception is regarding $\mu^{(1)}$. If $1/\psi^{(1)}$ is square-integrable, then since

$$\left[-\frac{d}{dx} + W(x)\right] \frac{1}{\psi^{(1)}} = 0,$$

$\mu^{(1)}$ is in the discrete spectrum of V_2; but it may not be in the discrete spectrum of V_1. Using this construction, non-$\mathcal{PT}$-symmetric complex potentials with all-real spectra can also be obtained. For examples, see [25].

One more variation of SUSY is based on the following observation. It can be seen from Eqs. (26) and (28) that, for any complex functions $W(x)$ and a complex constant c, the two potentials

$$-V_1(x) = W^2(x) - W'(x) + c, \quad -V_2(x) = W^2(x) + W'(x) + c,$$

form partner potentials which share the same spectrum (with the possible exception of a single bound state). Thus, if we choose $W(x)$ so that $V_1(x)$ is real, then the resulting complex potential $V_2(x)$ will have an all-real spectrum. These complex potentials $V_2(x)$ turn out to be type-II potentials (12) described in Sect. 2.2 but with $c_2 \leq 0$. An equivalent derivation of this result was given by Andrianov et al. [16] and reviewed in the end of Sect. 2.3.

5 Construction of Non-$\mathcal{PT}$-Symmetric Potentials with All-Real Spectra Using Soliton Theory

Another technique to construct complex potentials with all-real spectra is to use the soliton theory. This technique was proposed by Wadati [15] for the construction of $\mathcal{PT}$-symmetric potentials with all-real spectra, but it apparently can be extended to construct non-$\mathcal{PT}$-symmetric potentials with all-real spectra, as we will demonstrate below.

Let us consider the modified Korteweg-de Vries (mKdV) equation

$$u_t + 6u^2 u_x + u_{xxx} = 0 \tag{35}$$

for the real function $u(x,t)$, where x is the spatial coordinate, and t is time. We will consider localized solutions, $\lim_{|x|\to\infty} u(x,t) = 0$. Equation (35) is the compatibility condition between the Zakharov-Shabat (ZS) spectral problem [17]

$$v_{1x} + \mathrm{i}\zeta v_1 = u(x,t)v_2, \quad v_{2x} - \mathrm{i}\zeta v_2 = -u(x,t)v_1, \tag{36}$$

and the linear system

$$\begin{aligned} v_{1t} &= 2\mathrm{i}\zeta(u^2 - 2\zeta^2)v_1 + (2\mathrm{i}\zeta u_x - 2u^3 - u_{xx} + 4\zeta^2 u)v_2, \\ v_{2t} &= (2\mathrm{i}\zeta u_x + 2u^3 + u_{xx} - 4\zeta^2 u)v_1 - 2\mathrm{i}\zeta(u^2 - 2\zeta^2)v_2. \end{aligned}$$

Here, ζ is a spectral parameter.

The ZS spectral problem (36) can be transformed into Schrödinger eigenvalue problems through the transformation (14). Under this transformation, we get

$$\psi_{xx} + V(x,t)\psi = \mu\psi, \quad \phi_{xx} + V^*(x,t)\phi = \mu\phi, \tag{37}$$

where

$$V(x,t) = u^2(x,t) + iu_x(x,t), \tag{38}$$

and $\mu = -\zeta^2$. Here, time t plays the role of a parameter. If $u(x,t)$ is an even function of x, then the potential $V(x,t)$ is $\mathcal{PT}$ symmetric; for general $u(x,t)$ solutions, this potential is complex and non-$\mathcal{PT}$-symmetric.

Discrete eigenvalues of the ZS problem (36) appear as quadruples $(\zeta, \zeta^*, -\zeta, -\zeta^*)$ if ζ is complex and as complex-conjugate pairs (ζ, ζ^*) if ζ is purely imaginary. The continuous spectrum of the ZS problem is the real-ζ axis. In view of the above connection between the ZS and Schrödinger eigenvalue problems, we see that from *any* solution $u(x,t)$ of the mKdV equation (35) that possesses purely imaginary discrete ZS eigenvalues, one can obtain a complex potential $V(x,t)$, defined by (38), with strictly real spectrum. Further, we notice that while $u(x,t)$ depends on the parameter t, its ZS spectrum does not since $u(x,t)$ satisfies the mKdV equation. This means that t can be considered as a "deformation" parameter, and $u(x,t)$ generates a family of deformable potentials $V(x,t)$ with the same real spectrum. Since the solution $u(x,t)$ is asymmetric in general, the resulting complex potential $V(x,t)$ is then non-$\mathcal{PT}$-symmetric.

Analytical solutions $u(x,t)$ with purely imaginary discrete ZS eigenvalues can be derived by the soliton theory. Indeed, through the inverse scattering method, N-solitons of the mKdV equation with purely imaginary discrete eigenvalues $\{\pm\zeta_n, 1 \le n \le N\}$ were found as [29]

$$u(x,t) = -2\frac{\partial}{\partial x}\arctan\frac{\mathrm{Im}\det(I+A)}{\mathrm{Re}\det(I+A)}, \tag{39}$$

where I is the $N \times N$ identity matrix, Re and Im represent the real and imaginary parts, A is the $N \times N$ matrix whose elements are

$$A_{nm}(x,t) = -\frac{c_n}{\zeta_n + \zeta_m} e^{\mathrm{i}(\zeta_n+\zeta_m)x + 8\mathrm{i}\zeta_n^3 t},$$

$\zeta_n = \mathrm{i}\eta_n$, $\eta_n > 0$, and c_n are real constants. The corresponding complex potential $V(x,t)$ from Eq. (38) then would have all-real spectrum, with discrete eigenvalues as $-\zeta_n^2 = \eta_n^2$ $(1 \le n \le N)$ and the continuous spectrum as $(-\infty, 0]$.

As an example, we present non-$\mathcal{PT}$-symmetric potentials obtained from the two-soliton solution of the mKdV equation. These two solitons are found from the above general formula by taking $N = 2$ and can be written as [29]

$$u(x,t) = 4\frac{\eta_1 + \eta_2}{\eta_2 - \eta_1}\frac{G(x,t)}{F(x,t)}, \tag{40}$$

where

$$G(x,t) = \epsilon_1\eta_1 \cosh\left[2\eta_2 x + \delta_2(t) + \frac{1}{2}\gamma_{12}\right] + \epsilon_2\eta_2 \cosh\left[2\eta_1 x + \delta_1(t) - \frac{1}{2}\gamma_{12}\right],$$

$$\begin{aligned} F(x,t) = {} & \cosh[2(\eta_1+\eta_2)x + \delta_1(t) + \delta_2(t)] + \tfrac{4\eta_1\eta_2\epsilon_1\epsilon_2}{(\eta_1-\eta_2)^2} \\ & + \left(\tfrac{\eta_1+\eta_2}{\eta_1-\eta_2}\right)^2 \cosh[2(\eta_2-\eta_1)x + \delta_2(t) - \delta_1(t) + \gamma_{12}], \end{aligned}$$

$$\epsilon_1 = \pm 1, \quad \epsilon_2 = \pm 1, \quad \eta_1 > 0, \quad \eta_2 > 0,$$

$$\delta_1(t) = \delta_1 - 8\eta_1^3 t, \quad \delta_2(t) = \delta_2 - 8\eta_2^3 t, \quad \gamma_{12} = \ln(\eta_2/\eta_1),$$

and δ_1, δ_2 are real constants. To illustrate, we take

$$\eta_1 = 1, \quad \eta_2 = 2, \quad \delta_1 = \delta_2 = 0, \quad \epsilon_1 = \epsilon_2 = 1. \tag{41}$$

The soliton $u(x,t)$, the complex potential $V(x,t)$ and its spectrum at times $t = 0$ and 0.1 are displayed in the upper and lower rows of Fig. 5 respectively. Both complex potentials are non-$\mathcal{PT}$-symmetric and differ from each other significantly, but they have identical real spectra.

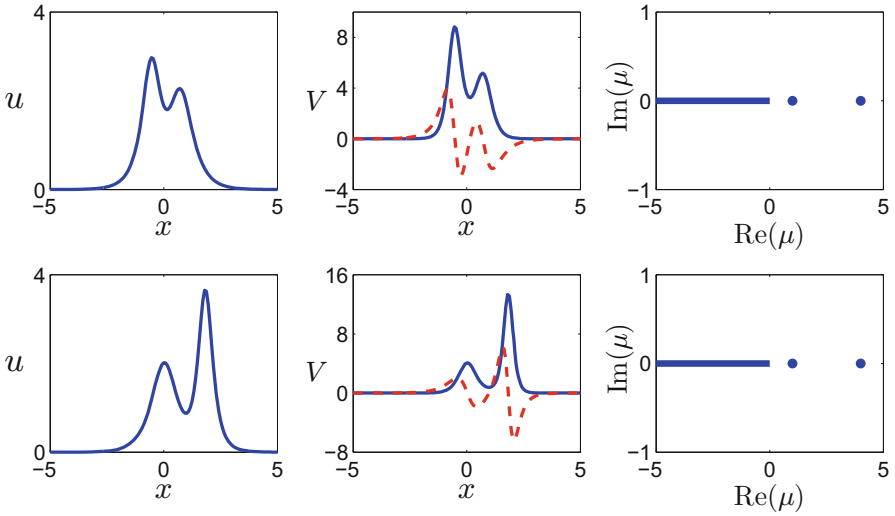

Fig. 5 Non-$\mathcal{PT}$-symmetric potentials with real spectra from the soliton theory. Left column: the two-soliton solution (40) with parameters (41); middle column: the corresponding complex potential $V(x,t)$ from Eq. (38); right column: spectrum of this $V(x,t)$ potential. Upper row: $t=0$; lower row: $t=0.1$

6 Partially-$\mathcal{PT}$-Symmetric Potentials in Multi-dimensions

In this section, we consider the generalization of $\mathcal{PT}$ symmetry to higher spatial dimensions. Let us consider a $(2+1)$-dimensional generalization of the paraxial linear beam propagation equation (1),

$$\mathrm{i}\Psi_z + \Psi_{xx} + \Psi_{yy} + V(x,y)\Psi = 0, \tag{42}$$

where z is the propagation direction, and (x,y) is the transverse plane. Looking for eigenmodes of the form $\Psi(x,y,z) = \mathrm{e}^{\mathrm{i}\mu z}\psi(x,y)$ we arrive at the eigenvalue problem

$$(\partial_{xx} + \partial_{yy} + V)\psi = \mu\psi, \tag{43}$$

where μ is the eigenvalue and ψ the eigenfunction.

The usual $\mathcal{PT}$ symmetry of the complex potential $V(x,y)$ is defined as

$$V^*(x,y) = V(-x,-y), \tag{44}$$

i.e., the potential is invariant under complex conjugation and simultaneous reflections in both x and y directions. For these potentials, the spectrum can be all-real, with a possibility of phase transition, just like one-dimensional $\mathcal{PT}$-symmetric potentials.

However, this usual concept of $\mathcal{PT}$ symmetry can be generalized. Indeed, if the potential is invariant under complex conjugation and reflection in a *single* spatial direction, i.e.,

$$V^*(x, y) = V(-x, y), \quad \text{or} \quad V^*(x, y) = V(x, -y), \tag{45}$$

its spectrum can still be all-real with a possibility of phase transition. These potentials were introduced in [30] and termed partially-$\mathcal{PT}$-symmetric potentials.

The fundamental reason these partially-$\mathcal{PT}$-symmetric potentials can also feature all-real spectra is that, their eigenvalues also come in complex conjugate pairs (μ, μ^*). This eigenvalue symmetry is a common feature of $\mathcal{PT}$-symmetric potentials, partially-$\mathcal{PT}$-symmetric potentials, and complex potentials derived in Sects. 2 and 3, which results in the possibility of all-real spectra for all these potentials.

The complex-conjugate-pair eigenvalue symmetry for these partially-$\mathcal{PT}$-symmetric potentials is easy to prove. Indeed, if $V^*(x, y) = V(-x, y)$ or $V^*(x, y) = V(x, -y)$, then by taking the complex conjugate of Eq. (43) and switching $x \to -x$ or $y \to -y$, we see that μ^* would also be an eigenvalue with eigenfunction $\psi^*(-x, y)$ or $\psi^*(x, -y)$.

As an example, we take the partially-$\mathcal{PT}$-symmetric complex potential $V(x, y)$ to be localized at four spots:

$$\begin{aligned} V(x, y) = 3 &\left(e^{-(x-x_0)^2-(y-y_0)^2} + e^{-(x+x_0)^2-(y-y_0)^2}\right) \\ &+2\left(e^{-(x-x_0)^2-(y+y_0)^2} + e^{-(x+x_0)^2-(y+y_0)^2}\right) \\ &+\mathrm{i}\beta\left[2\left(e^{-(x-x_0)^2-(y-y_0)^2} - e^{-(x+x_0)^2-(y-y_0)^2}\right)\right. \\ &\left.+\left(e^{-(x-x_0)^2-(y+y_0)^2} - e^{-(x+x_0)^2-(y+y_0)^2}\right)\right], \end{aligned} \tag{46}$$

where x_0, y_0 control the separation distances between these four spots, and β is a real constant. For definiteness, we set $x_0 = y_0 = 1.5$. This potential is not $\mathcal{PT}$-symmetric, but is partially-$\mathcal{PT}$-symmetric with symmetry $V^*(x, y) = V(-x, y)$. For $\beta = 0.1$, this potential is displayed in Fig. 6 (top row). It is seen that $\mathrm{Re}(V)$ is symmetric in x, $\mathrm{Im}(V)$ anti-symmetric in x, and both $\mathrm{Re}(V)$, $\mathrm{Im}(V)$ are asymmetric in y. The spectrum of this potential is plotted in Fig. 6c. It is seen that this spectrum contains three discrete eigenvalues and the continuous spectrum, which are all-real.

For potential (46) with varying β, we have found that its spectrum is all-real as long as $|\beta|$ is below a threshold value of 0.214. Above this threshold, a phase transition occurs, where pairs of real eigenvalues coalesce and then bifurcate off into the complex plane. This phase transition is illustrated in Fig. 6d, where the spectrum at $\beta = 0.3$ is shown.

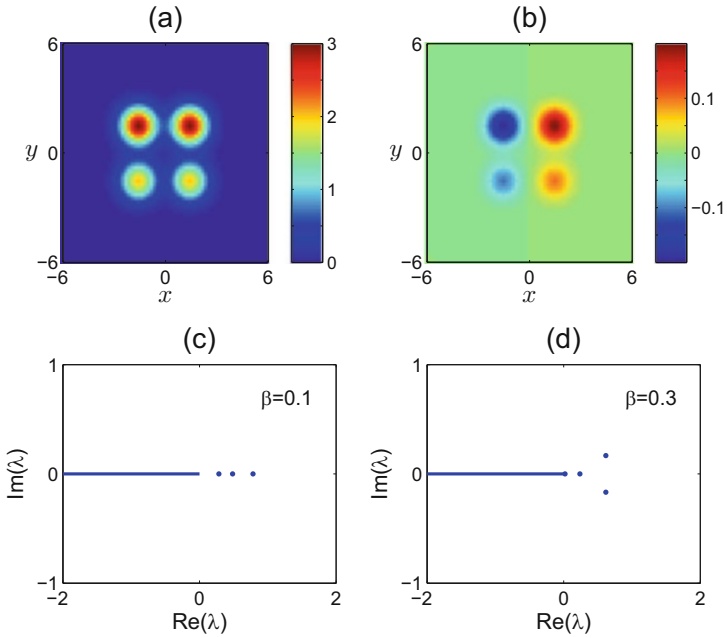

Fig. 6 (**a**, **b**) Real and imaginary parts of the partially-$\mathcal{PT}$-symmetric potential (46) for $\beta = 0.1$; (**c**, **d**) spectrum of this potential for $\beta = 0.1$ and 0.3 respectively. (Adapted from [30])

7 Summary and Discussion

In this article, we have reviewed various approaches to generalize $\mathcal{PT}$ symmetry. We have shown that large classes of non-$\mathcal{PT}$-symmetric complex potentials can also feature all-real spectra. These potentials are constructed by a variety of techniques, such as the symmetry method, the supersymmetry method, the soliton theory and partial $\mathcal{PT}$ symmetry. Of these non-$\mathcal{PT}$-symmetric potentials, the ones derived from the symmetry condition (4) in Sects. 2 and 3 allow for arbitrary gain-loss profiles. In addition, as free parameters and functions in those potentials vary, the spectrum could change, and phase transition (either through exceptional points or without) can occur. In non-$\mathcal{PT}$-symmetric potentials derived from supersymmetry and the soliton theory, on the other hand, the gain-loss profile is not totally free; and as free parameters in those potentials vary, the spectrum stays exactly the same.

The focus of this article was the spectrum of non-$\mathcal{PT}$-symmetric complex potentials, which is inherently a linear theory. When the spectrum of the complex potential is all-real, then wave propagation in the linear evolution equations (1) and (42) would show features which resemble those in real potentials (without gain and loss). When nonlinearity arises in these complex potentials, where nonlinear terms appear in the evolution equations (1) and (42), the interplay between nonlinearity and these complex potentials is an interesting question. In $\mathcal{PT}$-symmetric potentials and other $\mathcal{PT}$-symmetric systems, this interplay between nonlinearity and $\mathcal{PT}$ symmetry has

been reviewed in [12, 31]. In non-$\mathcal{PT}$-symmetric potentials, it was shown that the evolution equation (1) with Kerr nonlinearity could admit continuous families of solitons in type-I potentials (9), but not in other types of complex potentials [14, 28, 32, 33]. How other types of nonlinearities interact with these complex potentials is a worthy question for study in the future.

Acknowledgements This material is based upon work supported by the Air Force Office of Scientific Research under award number FA9550-18-1-0098, and the National Science Foundation under award number DMS-1616122.

References

1. Kivshar, Y.S., Agrawal, G.P.: Optical Solitons: From Fibers to Photonic Crystals. Academic Press, San Diego (2003)
2. Musslimani, Z.H., Makris, K.G., El-Ganainy, R., Christodoulides, D.N.: Optical solitons in $\mathcal{PT}$ periodic potentials. Phys. Rev. Lett. **100**, 030402 (2008)
3. Yang, J.: Nonlinear Waves in Integrable and Nonintegrable Systems. SIAM, Philadelphia (2010)
4. Bender, C.M., Boettcher, S.: Real spectra in non-Hermitian Hamiltonians having $\mathcal{PT}$ symmetry. Phys. Rev. Lett. **80**, 5243–5246 (1998)
5. Mostafazadeh, A.: Pseudo-Hermitian representation of quantum mechanics. Int. J. Geom. Methods Mod. Phys. **7**, 1191–1306 (2010)
6. Pitaevskii, L.P., Stringari, S.: Bose–Einstein Condensation. Oxford University Press, Oxford (2003)
7. Ahmed, Z.: Real and complex discrete eigenvalues in an exactly solvable one-dimensional complex $\mathcal{PT}$-invariant potential. Phys. Lett. A **282**, 343–348 (2001)
8. Feng, L., Xu, Y.L., Fegadolli, W.S., Lu, M.H., Oliveira, J.E.B., Almeida, V.R., Chen, Y.F., Scherer, A.: Experimental demonstration of a unidirectional reflectionless parity-time metamaterial at optical frequencies. Nat. Mater. **12**, 108–113 (2013)
9. Feng, L., Wong, Z.J., Ma, R., Wang, Y., Zhang, X.: Single-mode laser by parity-time symmetry breaking. Science **346**, 972–975 (2014)
10. Hodaei, H., Miri, M.-A., Heinrich, M., Christodoulides, D.N., Khajavikhan, M.: $\mathcal{PT}$-symmetric micro-ring laser. Science **346**, 975–978 (2014)
11. Peng, B., Özdemir, S.K., Lei, F., Monifi, F., Gianfreda, M., Long, G.L., Fan, S., Nori, F., Bender, C.M., Yang, L.: Parity-time-symmetric whispering-gallery microcavities. Nat. Phys. **10**, 394–398 (2014)
12. Konotop, V.V., Yang J., Zezyulin, D.A.: Nonlinear waves in $\mathcal{PT}$-symmetric systems. Rev. Mod. Phys. **88**, 035002 (2016)
13. Nixon, S., Yang, J.: All-real spectra in optical systems with arbitrary gain and loss distributions. Phys. Rev. A **93**, 031802(R) (2016)
14. Tsoy, E.N., Allayarov, I.M., Abdullaev, F.K.: Stable localized modes in asymmetric waveguides with gain and loss. Opt. Lett. **39**, 4215–4218 (2014)
15. Wadati, M.: Construction of parity-time symmetric potential through the soliton theory. J. Phys. Soc. Jpn. **77**, 074005 (2008)
16. Andrianov, A.A., Ioffe, M.V., Cannata, F., Dedonder, J.P.: SUSY quantum mechanics with complex superpotentials and real energy spectra. Int. J. Mod. Phys. A **14**, 2675–2688 (1999)
17. Zakharov, V.E., Shabat, A.B.: Exact theory of two-dimensional self-focusing and one-dimensional self-modulation of waves in nonlinear media. Zh. E'ksp. Teor. Fiz. **61**, 118 (1971) [Sov. Phys. JETP **34**, 62–69 (1972)]

18. Klaus, M., Shaw, J.K.: Purely imaginary eigenvalues of Zakharov-Shabat systems. Phys. Rev. E **65**, 036607 (2002)
19. Yang, J.: Classes of non-parity-time-symmetric optical potentials with exceptional-point-free phase transitions. Opt. Lett. **42**, 4067–4070 (2017)
20. Kartashov, Y.V., Konotop, V.V., Zezyulin, D.A.: $\mathcal{CPT}$-symmetric spin-orbit-coupled condensate. Europhys. Lett. **107**, 50002 (2014)
21. Konotop, V.V., Zezyulin, D.A.: Phase transition through the splitting of self-dual spectral singularity in optical potentials. Opt. Lett. **42**, 5206–5209 (2017)
22. Cooper, F., Khare, A., Sukhatme, U.: Supersymmetry and quantum mechanics. Phys. Rep. **251**, 267–385 (1995)
23. Heinrich, M., Miri, M.-A., Stützer, S., El-Ganainy, R., Nolte, S., Szameit, A., Christodoulides, D.N.: Supersymmetric mode converters. Nat. Commun. **5**, 3698 (2014)
24. Khare, A., Sukhatme, U.: Phase-equivalent potentials obtained from supersymmetry. J. Phys. A **22**, 2847–2860 (1989)
25. Cannata, F., Junker, G., Trost, J.: Schrödinger operators with complex potential but real spectrum. Phys. Lett. A **246**, 219–226 (1998)
26. Bagchi, B., Mallik, S., Quesne, C.: Generating complex potentials with real eigenvalues in supersymmetric quantum mechanics. Int. J. Mod. Phys. A **16**, 2859 (2001)
27. Miri, M., Heinrich, M., Christodoulides, D.N.: Supersymmetry-generated complex optical potentials with real spectra. Phys. Rev. A **87**, 043819 (2013)
28. Yang, J.: Necessity of $\mathcal{PT}$ symmetry for soliton families in one-dimensional complex potentials. Phys. Lett. A **378**, 367–373 (2014)
29. Wadati, M., Ohkuma, K.: Multiple-pole solutions of the modified Korteweg-de Vries equation. J. Phys. Soc. Jpn. **51**, 2029–2035 (1982)
30. Yang, J.: Partially $\mathcal{PT}$-symmetric optical potentials with all-real spectra and soliton families in multi-dimensions. Opt. Lett. **39**, 1133–1136 (2014)
31. Suchkov, S.V., Sukhorukov, A.A., Huang, J., Dmitriev, S.V., Lee, C., Kivshar, Y.S.: Nonlinear switching and solitons in $\mathcal{PT}$-symmetric photonic systems. Laser Photonics Rev. **10**, 177–213 (2016)
32. Konotop, V.V., Zezyulin, D.A.: Families of stationary modes in complex potentials. Opt. Lett. **39**, 5535–5538 (2014)
33. Nixon, S., Yang, J.: Bifurcation of soliton families from linear modes in non-$\mathcal{PT}$-symmetric complex potentials. Stud. Appl. Math. **136**, 459–483 (2016)

Constant-Intensity Waves in Non-Hermitian Media

Konstantinos G. Makris, Andre Brandstötter, and Stefan Rotter

Abstract When waves propagate through a non-uniform potential landscape their interference typically gives rise to a complex intensity pattern. In this chapter we review our work on how to entirely suppress these intensity variations by adding system-specific gain and loss components to the potential. The resulting constant-intensity (CI) waves are entirely free of interference fringes and get perfectly transmitted across any such non-Hermitian scattering landscape that is put in their way. We discuss how to generalize this concept to more than one dimension and to the non-linear regime where these special wave states open up the way to study the phenomenon of modulation instability in non-uniform potentials. Experimental implementations of these unique wave states are envisioned not just in optics, but also in other fields of wave physics such as in acoustics.

1 Introduction

Waves play an important role in many fields of science and in all of them the plane wave solution is the one that solves the corresponding wave equation in the most straightforward way. When placing a spatially varying potential in the way of such a plane wave, however, the problem becomes immediately less trivial as potentials typically reflect and scatter the wave, leading to interference and a non-uniform wave intensity that is strongly position-dependent. Such a potential could be an electrostatic field for an electronic matter wave, a non-uniform distribution of a dielectric medium for an electromagnetic wave or a wall that reflects an acoustic pressure wave. All of these cases lead to diffraction and wave interference,

K. G. Makris (✉)
Department of Physics, University of Crete, Heraklion, Greece
e-mail: makris@physics.uoc.gr

A. Brandstötter · S. Rotter
Institute for Theoretical Physics, Vienna University of Technology (TU Wien), Vienna, Austria
e-mail: andre.brandstoetter@tuwien.ac.at; stefan.rotter@tuwien.ac.at

D. Christodoulides, J. Yang (eds.), *Parity-time Symmetry and Its Applications*, Springer Tracts in Modern Physics 280,
https://doi.org/10.1007/978-981-13-1247-2_19

resulting in the highly complex variation of a wave's spatial profile that we are all very familiar with. Engineering these effects at one's will is a challenging task – think here, e.g., of the search for a cloaking device [1] or of the entire field of adaptive optics [2]. New strategies in this direction are thus in high demand and could establish a fertile ground in many of the different disciplines of science and technology in which wave propagation is a key element.

The starting point for our endeavor is the insight, that very unconventional phenomena arise in the situation where waves propagate and diffract in a suitably chosen spatial refractive index distribution that combines both gain and loss [3]. Such non-Hermitian potential regions [4, 5], which serve as sources and sinks for waves, respectively, can give rise to novel wave effects that are impossible to realize with conventional, Hermitian potentials. Examples of this kind, that were meanwhile also realized experimentally [6–10], are the uni-directional invisibility of a gain-loss potential [11], devices that can simultaneously act as a laser and as a perfect absorber [12–14] and resonant structures with unusual features like non-reciprocal light transmission [10] or loss-induced lasing [15–17]. In particular, systems with a $\mathscr{P}\mathscr{T}$-symmetry [18], where gain and loss are carefully balanced, have recently attracted enormous interest [19–24]. All these activities that were initially driven by the introduction of the counter-intuitive concept of $\mathscr{P}\mathscr{T}$-symmetry [18] in the realm of waveguide optics theoretically [19, 20] and experimentally [6, 7], opened a new area of research, that of non-Hermitian photonics or parity-time symmetric optics.

In the research presented below we extend the above concepts in a significant way. Specifically, we show here that for a general class of potentials that spatially combine gain and loss, it is possible to eliminate the intensity variations in wave scattering entirely, and create constant-intensity waves [25–28]. In particular, we present new solutions for a whole class of waves that have constant intensity even in the presence of a very irregular potential landscape. Quite surprisingly, these waves are solutions to both the paraxial equation of diffraction, the discrete and continuous non-linear Schrödinger equation, and the scalar Helmholtz scattering wave equation. In the linear regime, such constant-intensity waves resemble Bessel beams in free space [29] in that they carry infinite energy and propagate without distortion (depending on the truncation). In the non-linear regime, they provide the only background where the best known symmetry breaking instability, the so-called modulational instability (MI) [30–35] can be analyzed for the first time in inhomogeneous non-Hermitian potentials. Using these solutions for studying the phenomenon of MI, we find that, in the self-defocusing case, unstable finite size and periodic modes appear and cause the wave to disintegrate and to generate a train of complex solitons.

This book chapter follows in part our previously published manuscripts on the above subjects – see, in particular, the following three references [25, 26, 28] where also more details can be found.

2 Constant-Intensity Waves and Modulation Instability in Inhomogeneous Continuous Media

Following [25], we start from the well known non-linear Schrödinger equation (NLSE). This scalar wave equation encompasses both the physics of matter waves as well as many aspects of optical wave propagation. Specifically, we will consider the NLSE with a general, non-Hermitian potential $V(x)$ and a Kerr non-linearity,

$$i\,\partial_z \psi + \partial_x^2 \psi + V(x)\psi + \sigma|\psi|^2\psi = 0\,. \tag{1}$$

The scalar, complex valued function $\psi(x, z)$ describes the wave function of a matter wave as it evolves in time or the electric field envelope along a scaled propagation distance z. The non-linearity can either be self-focusing or de-focusing, depending on the sign of σ. For this general setting, we now introduce a whole family of potentials $V(x)$ which are determined by the following simple relation,

$$V(x) = W^2(x) + i\frac{dW(x)}{dx}, \tag{2}$$

where $W(x)$ is a given real generating function to which no further constraints apply (apart from smoothness). In the special case where $W(x)$ is an even function of x, the actual optical potential $V(x)$ turns out to be $\mathscr{P}\mathscr{T}$-symmetric, since $V(x) = V^*(-x)$. We emphasize, however, that our analysis is valid for all confined or periodic functions $W(x)$, which do not necessarily lead to a $\mathscr{P}\mathscr{T}$-symmetric form of $V(x)$. Rather, we can prove for the entire non-Hermitian family of potentials that are determined by Eq. (2), that the following analytical and stationary constant-intensity wave is a solution to the NLSE in Eq. (1),

$$\psi(x, z) = Ae^{i\sigma A^2 z + i\int W(x)dx}, \tag{3}$$

with a notably constant and real amplitude A. We emphasize here the surprising fact, that this family of solutions exists in the linear regime ($\sigma = 0$) as well as for arbitrary strength of non-linearity ($\sigma = \pm 1$). An interesting point to observe is that the above solutions exist only for non-Hermitian potentials, since for $W(x) \to 0$ we also have $V(x) \to 0$. Therefore, these families of counterintuitive solutions are the direct outcome of the non-Hermitian nature of the involved potential $V(x)$ and as such exist only for these complex structures.

In order to better understand and highlight the properties of such constant-intensity solutions we consider one-dimensional potentials that are generated by Hermite polynomials choosing $W(x) = H_n(x)e^{-Bx^2}$. The results for vanishing non-linearity ($\sigma = 0$) are illustrated in Fig. 1. Here, the localized optical potential $V(x)$ is not $\mathscr{P}\mathscr{T}$-symmetric (see Fig. 1a) and corresponds physically to a waveguide-coupler with lossy arms and optical gain in the evanescent region. If the initial beam is not designed to have the correct phase (as given by Eq. (3)), then the light diffracts

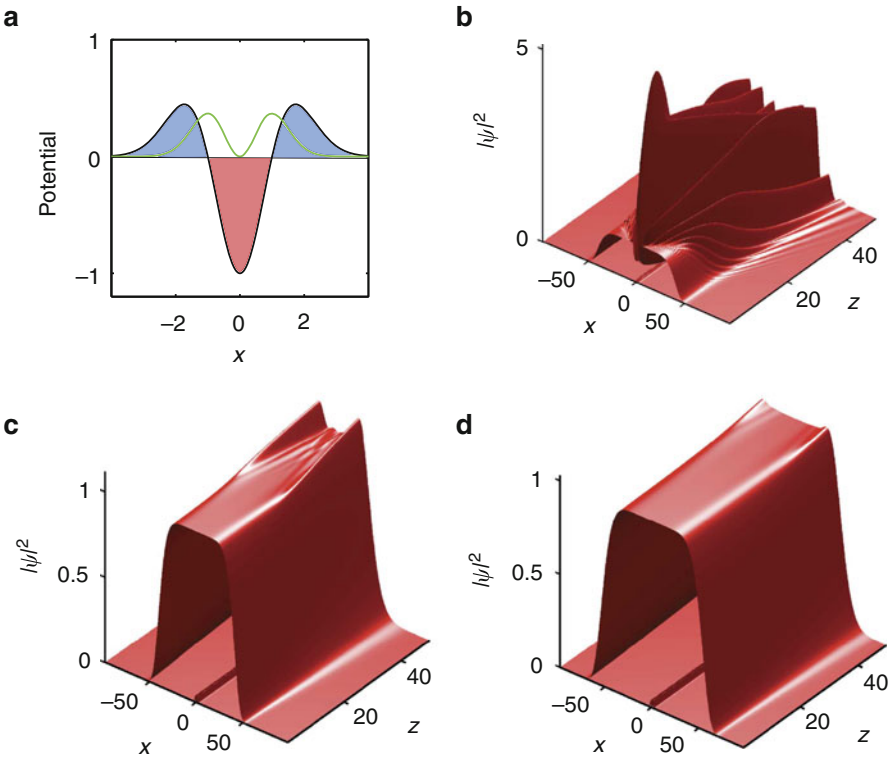

Fig. 1 (**a**) Real part (green line) and imaginary part (black line) of the complex potential $V(x)$ satisfying Eq. (2) (blue filled regions depict loss, whereas the red one depicts gain). (**b**) Evolution of a constant amplitude without the correct phase at the input at $z = 0$. (**c**, **d**) Spatial diffraction of the truncated constant-intensity solution satisfying the correct phase relation of Eq. (3). Two different input truncations are shown for comparison. The lines in the $x - z$ planes of (**b**, **c**, **d**) around $x = 0$ depict the real refractive index of the potential as shown in (**a**). Note the different vertical axis scale in (**b**)

fast to the gain region as we can see in Fig. 1b. The effects of truncation of the constant-intensity solution are shown in Figs. 1c, d. Similar to the diffraction-free beams [29], we find that the wider the width of the truncation aperture is, the larger is the propagation distance after which the beam starts to diffract. In the case of no truncation (i.e., infinitely wide aperture) diffraction is fully suppressed for an infinitely long propagation distance.

In a next step we demonstrate that the above concepts are not restricted to a single spatial dimension x (apart from the propagation distance z), but can easily be generalized to two spatial dimensions x, y. The family of these complex potentials $V(x, y)$ and the corresponding constant-intensity solutions $\psi(x, y, z)$ of the two-dimensional NLSE $i\frac{\partial\psi}{\partial z} + \frac{\partial^2\psi}{\partial x^2} + \frac{\partial^2\psi}{\partial y^2} + V(x, y)\psi + \sigma|\psi|^2\psi = 0$ are given as follows:

$$V(x, y) = |\mathbf{W}|^2 - i\nabla \cdot \mathbf{W}\,, \tag{4}$$

$$\nabla \times \mathbf{W} = 0\,, \tag{5}$$

$$\psi(x, y, z) = Ae^{i\sigma A^2 z + i\int_C \mathbf{W} d\mathbf{x}}\,, \tag{6}$$

where $\mathbf{W} = \mathbf{x}W_x + \mathbf{y}W_y$ with W_x, W_y being real functions of x, y and C being any smooth open curve connecting an arbitrary point (a, b) to any different point (x, y). As in the one-dimensional case, these solutions are valid in both linear and non-linear domains. For the particular case of $W_x = \cos(x)\sin(y)$, $W_y = \cos(y)\sin(x)$, the resulting periodic potential $V(x, y)$ is that of an optical lattice with alternating gain and loss waveguides. The imaginary part of such a lattice is illustrated in Fig. 2a. In Fig. 2b, we display the diffraction of a constant-intensity beam with the correct phase (as in Eq. (6)) launched onto such a linear lattice ($\sigma = 0$) through a circular aperture. As we can see, the beam maintains its constant intensity over a remarkably long distance. The transverse Poynting vector defined as $\mathbf{S} = (i/2)(\psi\nabla\psi^* - \psi^*\nabla\psi)$, is presented in Fig. 2c and the light always flows following complicated stream line patterns from the gain regions to the loss regions in a symmetric fashion. Once the finite beam starts to diffract this balanced flow is disturbed and all the light is concentrated only in the gain regions.

These unique diffraction-free and constant-intensity waves are also solutions of the NLSE for both the self-focusing and defocusing cases. As a result, we can study now for the first time their modulation instability under small perturbations. In other words, we want to investigate how perturbations of the exact CI solutions get reinforced by the non-linearity leading to a break up of the waveform into a complex pattern. Specifically, we are interested in understanding the linear stability of the solutions of Eq. (1) of the form $\psi(x, z) = [A + \varepsilon F_\lambda(x)e^{i\lambda z} + \varepsilon G^*_\lambda(x)e^{-i\lambda^* z}]e^{i\theta(x,z)}$, where the phase function is $\theta(x, z) = \sigma A^2 z + \int W(x)dx$. Here, $F_\lambda(x)$ and $G_\lambda(x)$ are the perturbation eigenfunctions with $\varepsilon \ll 1$ and the imaginary part of λ measures the instability growth rate of the perturbation. To leading order in ε, we obtain the following linear eigenvalue problem for the two-component perturbation eigenmodes $\boldsymbol{\varphi_\lambda}(x) \equiv [F_\lambda(x)G_\lambda(x)]^T$, the eigenvalues of which are λ, i.e., $\overleftrightarrow{M}(\hat{L}_\pm)\cdot\boldsymbol{\varphi_\lambda}(x) = \lambda\boldsymbol{\varphi_\lambda}(x)$. The operator matrix $\overleftrightarrow{M}$ is defined by the following expression:

$$\overleftrightarrow{M}(\hat{L}_\pm) = \begin{pmatrix} \hat{L}_+ & \sigma A^2 \\ -\sigma A^2 & -\hat{L}_- \end{pmatrix}. \tag{7}$$

Here the appearing linear operators are defined by the following relationships:

$$\hat{L}_\pm = \hat{L}_0 \pm i\hat{L}_1 \tag{8}$$

$$\hat{L}_0 = \sigma A^2 + d^2/dx^2 \tag{9}$$

$$\hat{L}_1 = 2W(x)d/dx \tag{10}$$

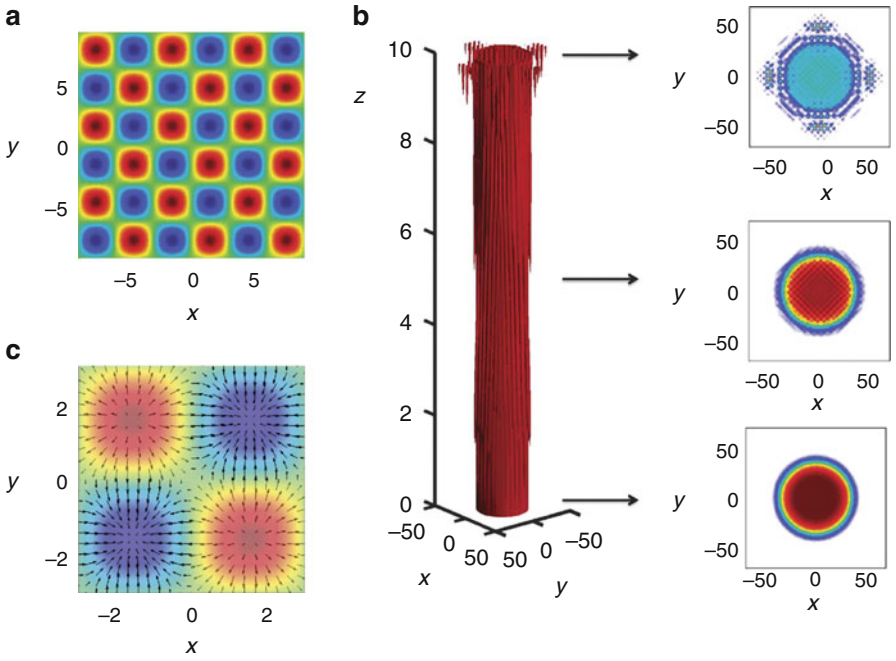

Fig. 2 Imaginary part of the complex potential $V(x, y)$ discussed in the text. Red and blue regions correspond to gain and loss, respectively. (**b**) Iso-contour of the beam intensity launched onto the potential in (**a**) through a circular aperture of radius $\sim 40\lambda_0$, where λ_0 is the free space wavelength. Also shown are three transverse intensity plots (from bottom to top) at $z = 0$, $z = 5$, $z = 10$. (**c**) Transverse power flow pattern (indicated by arrows) of the beam at $z = 5$

So far the above discussion is general and applies to any smooth function W (periodic or not) that is real. The eigenspectrum analysis of the above eigenvalue problem determines whether the constant-intensity solution is stable ($\lambda \in \mathbb{R}$) or unstable ($\lambda \in \mathbb{C}$). We now apply this analysis to study the modulation instability of constant-intensity waves in $\mathscr{P}\mathscr{T}$-symmetric optical lattices [19, 20] assuming that $W(x)$ is a periodic potential with period α. In particular, we consider the example of a $\mathscr{P}\mathscr{T}$-symmetric photonic lattice where $W(x) = \frac{V_0}{2} + V_1 \cos(x)$ and the resulting optical potential is $V(x) = [\frac{V_0^2}{4} + V_1^2 \cos^2(x) + V_0 V_1 \cos(x)] + i V_1 \sin(x)$. The corresponding constant-intensity solution, whose modulation instability we want to study is given by $\psi(x, z) = A \exp[i\sigma A^2 z + i\frac{V_0 x}{2} + i V_1 \sin(x)]$. In order for this constant-intensity solution to be periodic in x with the same period as the lattice, the constant term V_0 must be quantized, namely $V_0 = 0, \pm 2, \pm 4, \ldots$. For all the subsequent results we will always assume that $V_0 = 4$ and $V_1 = 0.2$ (without loss of generality). It is important to note here, that for our $\mathscr{P}\mathscr{T}$-lattice V(x) is in the so-called 'unbroken $\mathscr{P}\mathscr{T}$-symmetric phase' with only real propagation constants.

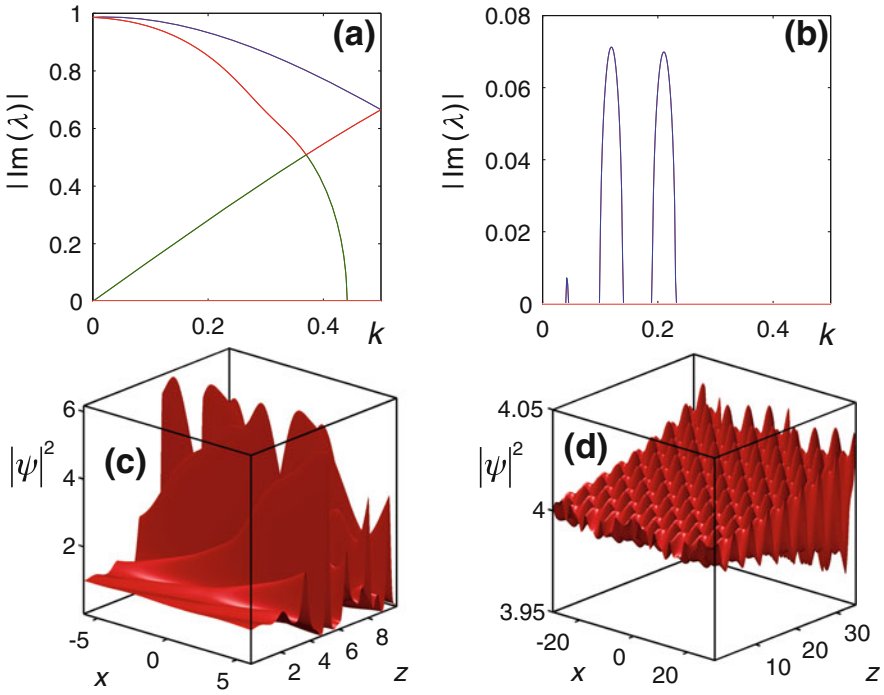

Fig. 3 (**a**, **b**) Modulation instability growth rate as a function of the Bloch momentum (half of first Brillouin zone), for (**a**) self-focusing non-linearity ($\sigma = 1$) and amplitude $A = 1$, and for (**b**) defocusing non-linearity ($\sigma = -1$) and amplitude $A = 2$. Different colors in (**a**), (**b**) denote different instability bands. (**c**, **d**) Numerical results for the intensity evolution of a constant-intensity wave for (**c**) a self-focusing non-linearity with parameters $k = 0$, $A = 1$, $\varepsilon = 0.01$, and (**d**) for a defocusing non-linearity with parameters $k = 0.22$, $A = 2$, $\varepsilon = 0.001$. The peak values are indicated on the vertical axes and match very well with the results of our perturbation analysis

In the broken phase some of these eigenvalues are complex and the instabilities are physically expected. Since $W(x)$ is periodic we can expand the perturbation eigenvectors $\boldsymbol{\varphi_\lambda(x)}$ in a Fourier series and construct numerically the bandstructure of the stability problem. So at this point we have to distinguish between the physical band-structure of the problem and the perturbation band-structure of the stability problem. Based on the above, the Floquet-Bloch theorem implies that the eigenfunctions $\boldsymbol{\varphi_\lambda(x)}$ can be written in the form $\boldsymbol{\phi_\lambda(x)} = \phi(x,k)e^{ikx}$, where $\phi(x,k) = \phi(x+\alpha,k)$ with k being the Bloch momentum of the stability problem. The results are illustrated in the following Fig. 3a for a self-focusing non-linearity ($\sigma = 1$) and for the amplitude $A = 1$. More specifically, we show the instability growth rate $|\mathrm{Im}\{\lambda(k)\}|$ as a function of the perturbation eigenvector k in the first half Brillouin zone, and we can see that the constant-intensity waves are linearly unstable for any value of Bloch momenta of the imposed perturbation.

The situation is different for the defocusing case ($\sigma = -1$) where the results are presented in Fig. 3b. For some values of k the constant-intensity solutions are linearly stable and their instability dependence forms bands reminiscent of the bands appearing in conventional MI results for bulk or periodic potentials [30, 33, 34], but quite different and profoundly more complex. In order to understand the physical outcome of such instabilities and how they lead to filament formation, we have performed direct numerical simulations for the dynamics of the constant-intensity solutions against specific perturbations. The results are presented in Fig. 3c, d. More specifically, we examine the intensity evolution of a constant-intensity solution when it is perturbed by a specific Floquet-Bloch mode. In other words, at the input of the lattice at $z = 0$, we have $\psi(x, z = 0) = [A + \varepsilon F_\lambda(x) + \varepsilon G^*_\lambda(x)]e^{i\theta(x,0)}$, and we are interested to see if the linear stability analysis captures the exponential growth of the imposed perturbations. For the considered $\mathscr{P}\mathscr{T}$-lattice with self-focusing non-linearity, we examine the non-linear dynamics of the constant-intensity solution and the result is presented in Fig. 3c. For a perturbation eigenmode with Bloch momentum $k = 0$ and $A = 1$, $\varepsilon = 0.01$, we can see from Fig. 3a that $\mathrm{Im}\{\lambda(0)\} \sim 1$. Therefore, we can estimate the growth for a propagation distance of $z = 5$ to be around $|1+0.01\cdot e^{1\cdot 5}|^2 \sim 6.1$, which agrees very well with the dynamical simulation of Fig. 3c. Similarly, for the defocusing non-linearity, and for parameters $k = 0.22$ and $A = 2$, $\varepsilon = 0.001$, we estimate the growth for a propagation distance $z = 35$ to be around $|2+0.001\cdot e^{0.046\cdot 35|^2} \sim 4.02$, which matches exactly with the propagation dynamics result of Fig. 3d.

We would like to mention here that the above MI analysis can be extended to vectorial non-linear Schrödinger equations for which multi-component constant intensity solutions exist [27].

3 CI-Waves in Discrete Disordered Lattices

Engineering a continuous distribution of gain and loss that perfectly matches the requirements of our theoretical analysis is a challenging task experimentally. To facilitate an experimental implementation, we thus also study whether our concepts can be applied to discrete rather than to continuous potential landscapes (see Fig. 4a,b for an illustration of these two cases). Consider, for this purpose, a lattice of coupled non-Hermitian single-mode waveguides as depicted in Fig. 4a extending along the positive z-direction. The propagation of light in such a lattice can be described using coupled mode theory. Specifically, the beam evolution is governed by the following normalized paraxial equation of diffraction for N coupled optical elements (waveguides or cavities),

$$i\frac{dU_n}{dz} + c(U_{n+1} + U_{n-1}) + (\beta_n + ig\gamma_n)U_n = 0\,, \tag{11}$$

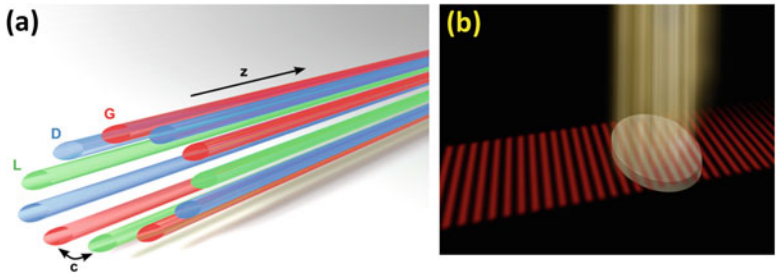

Fig. 4 (**a**) Schematics of a non-Hermitian lattice of coupled optical waveguides, that supports constant-intensity modes. The waveguides form a ring, corresponding to periodic boundary conditions. The labels D, L, G, c stand for a dielectric, loss, gain element, and for the coupling constant, respectively. (**b**) One of the envisioned goals to realize constant-intensity waves: by shining light through a spatial light modulator from the top, one can non-uniformly pump the gain medium inside a material to obtain a spatially varying gain-loss profile that makes the medium invisible for an incident wave from one side

where $U_n(z)$ represents the amplitude of the electric field envelope, z is the propagation distance, c is the coupling between adjacent neighbors (here taken to be equal to one, without any loss of generality) and $n = 1, \ldots N$ the waveguide index. Each channel is characterized by either gain ($\gamma_n < 0$) or loss ($\gamma_n > 0$) and by its real refractive index β_n. The gain-loss amplitude is described by the parameter g. For $g = 0$ the system is obviously Hermitian. The main question we will address for the case of an optical non-Hermitian lattice is if and under which conditions constant-intensity waves exist [26]. Specifically, we are looking for stationary constant-intensity solutions of the form:

$$U_n(z) = e^{i\theta_n} e^{i\lambda z}\,, \tag{12}$$

where θ_n is a given phase distribution over all waveguide channels and λ is the propagation eigenvalue. It is important to understand that in order for such CI-modes to exist, periodic boundary conditions must be imposed at the end points of the lattice. In particular, the Born-Von Karman periodic boundary conditions must be valid for the field, namely:

$$U_0 = U_N, U_{N+1} = U_1\,. \tag{13}$$

We can see that the complex refractive index must satisfy (for any given phase distribution):

$$\beta_n = \lambda - \cos(\theta_{n+1} - \theta_n) - \cos(\theta_{n-1} - \theta_n)\,, \tag{14}$$

$$\gamma_n = -\sin(\theta_{n+1} - \theta_n) - \sin(\theta_{n-1} - \theta_n)\,. \tag{15}$$

Since the constant-intensity wave of Eq. (12) must satisfy the periodic boundary conditions, it is also true that the phase distribution must satisfy the relations:

$$\theta_0 = \theta_N, \theta_{N+1} = \theta_1 . \tag{16}$$

Physically speaking, the periodic boundary conditions correspond to an optical ring-lattice of coupled optical elements (waveguides or cavities), as schematically depicted in Fig. 4a. The given phase distribution θ_n determines the real and imaginary parts of the refractive index (through Eqs. (14) and (15)) and the eigenvalue λ (which can be removed by a gauge transformation) affects only the real part of the index of refraction. An important difference between the solutions found in the continuum case studied in the previous chapter and those found here is the following: The CI-waves in the continuous and infinite case are radiation eigenmodes, while in the discrete and periodic problem at hand they are true eigenmodes (more precisely supermodes) of the entire system. We have also to note that for $\lambda = 0$, the CI-mode is unidirectionally invisible, since the wave propagates without any additional phase change and only in one propagation direction (for the opposite direction the complex conjugate potential must be used).

We have thus found that for system configurations satisfying Eq. (11) the complex refractive index can always be engineered to yield a CI solution. This is particularly remarkable in view of the fact that disordered waveguide lattices without any gain and loss give rise to Anderson localization – a well-studied phenomenon in condensed matter physics [36–40]. The existence and properties of localized modes in linear random systems has meanwhile been thoroughly investigated. The majority of the theoretical and experimental studies have, however, been concentrated on Hermitian media (with the exception of the random laser literature) where Anderson localization is now well understood. Adding gain and loss to the medium makes the fundamental question of localization generally more complicated [41]. In this context our results now provide the interesting insight that any disordered medium that gives rise to Anderson localization (without gain and loss) can also produce extended modes of uniform intensity (CI-supermodes) when a suitable combination of gain and loss is added.

In Fig. 5 such a random system of 100 coupled waveguides is considered. The real and imaginary part of the refractive index distribution is depicted for a particular realization of the lattice in Fig. 5a, b, respectively. As we can see, adding gain and loss to such a system alters the Anderson localized modes of the Hermitian lattice to extended delocalized modes, one of which is a CI-supermode (Fig. 5c) with a real eigenvalue (Fig. 5d).

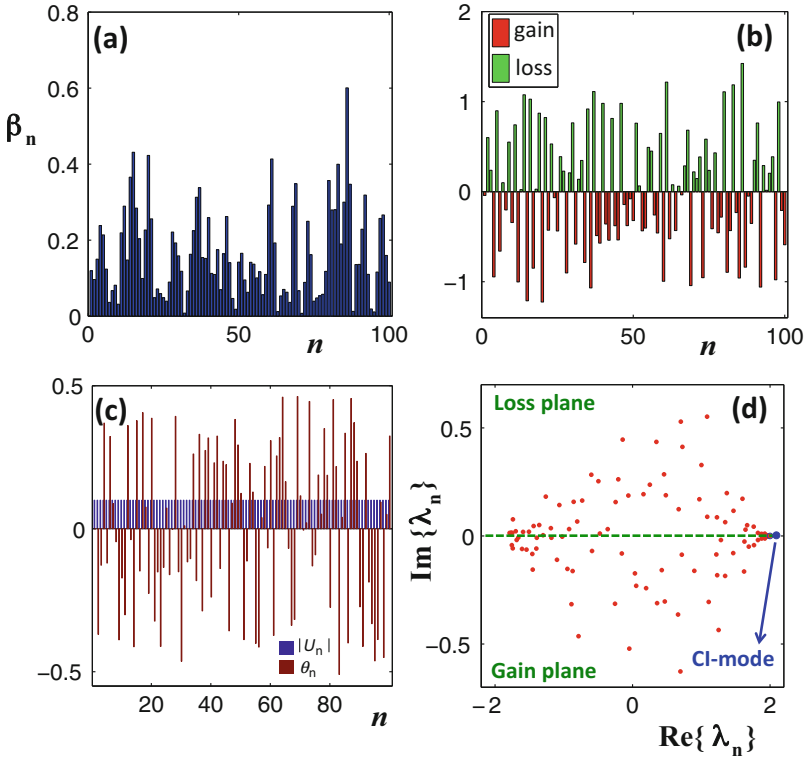

Fig. 5 CI-mode (with $\lambda = 2$, $g = 1$) in a disordered lattice of $N = 100$ waveguides with a random phase. In particular, (**a**) real part and imaginary parts of the refractive index per waveguide, (**b**) gain and loss per channel, (**c**) the amplitude and phase of the CI-supermode, and (**d**) eigenvalue spectrum in the complex plane. The eigenvalue of the CI-supermode is denoted with a blue circle

4 CI-Waves in the Scattering Regime

In all of the above considerations, the variation of the refractive index or of the potential was considered only in the direction transverse to the propagation direction. The question we want to address in the following is, whether CI waves also exist for the case that the potential variation occurs in the direction along which a wave is propagating. In particular, it would be very exciting to see if we can create in this way a "scattering state" that perfectly penetrates a disordered medium with constant intensity. The scattering of waves through disordered media has, in fact,

captured the interest of various communities for quite some time now [42–44]. While much work has been invested into understanding the *statistical* properties of the corresponding wave transport [45] there has recently been a surge of interest in controlling the scattering of waves through *individual* systems for specific purposes such as detection, imaging, and efficient transmission across disordered materials [46, 47]. Remarkable progress in these endeavors has recently been made in the optical domain, largely due to the availability of spatial light modulators and new concepts for how to apply them on turbid media [48, 49]. In a first generation of corresponding experiments the focus was laid on shaping the input wave front impinging on an immutable disordered sample such as to achieve a desired output, like a spatial or temporal focus behind the medium [50–53]. More recent studies concentrated instead on controlling the medium itself, e.g., through the material fabrication process [54] or through a spatially modulated pumping [55], leading, e.g., to a versatile control of random and micro-cavity lasers [56–60].

Here we will build on these advances and shall combine them with our insights on how to construct CI waves [28]. Specifically, we show that for a general disordered medium, given by a distribution of the real part of the refractive index $n_R(x)$, a corresponding distribution of its imaginary part $n_I(x)$ can be found, such that a wave propagating through this continuous medium will feature a constant intensity throughout the entire non-uniform scattering landscape. In other words, we demonstrate that adding a judiciously chosen distribution of gain and loss to a disordered medium will make waves lose all their interference fringes including perfect transmission through the disorder.

The solution strategy that we explore for this purpose is based on the one-dimensional normalized Helmholtz equation that describes time-independent scattering of a linearly polarized electric field $\psi(x)$ both in forward and in backward direction,

$$\left[\partial_x^2 + \varepsilon(x)\, k^2\right] \psi(x) = 0\,. \tag{17}$$

Here $\varepsilon(x)$ is the dielectric function varying along the spatial coordinate x and $k = 2\pi/\lambda$ is the wavenumber (with λ being the wavelength). The dielectric function is complex thus $\varepsilon(x) = [n_R(x) + i n_I(x)]^2$, where $n_R(x)$, $n_I(x)$ denote the real and imaginary parts of the refractive index. In general, when a plane wave is incident on a spatially varying distribution $\varepsilon(x)$, interference takes place between the waves propagating forward and backward. As a result, a complex interference pattern is produced with fringes on its intensity. As we will now show, this fundamental physical picture can be quite different in the case of non-Hermitian media with loss and/or gain.

To jump right to the heart of the matter, we start with an ansatz for a constant-intensity (CI) wave with unit amplitude, $\psi(x) = \exp[iS(x)]$, where $S(x)$ is a real valued function. Due to the obvious relation to WKB-theory [61], we will derive the CI solution of the Helmholtz Eq. (17) in the bulk, by demanding that the ansatz $\psi(x) = \exp[iS(x)]$ has to be exact in the first order WKB-

approximation. Expanding the function $S(x)$ in powers of a small parameter δ, $S(x) = \frac{1}{\delta}\sum_{n=0}^{\infty}\delta^n S_n(x)$, and inserting it into the Helmholtz Eq. (17) to leading order, we can show that in the limit of $\delta \to 0$, δ scales with $1/k$. Setting $\delta = 1/k$ and collecting terms with the same power of k, we can write down the two dominant terms:

$$k^2 = \tfrac{1}{\delta^2} : \mathrm{Re}[\varepsilon(x)] + i\,\mathrm{Im}[\varepsilon(x)] - [S_0'(x)]^2 = 0 \tag{18}$$

$$k^1 = \tfrac{1}{\delta^1} : i\,S_0''(x) - 2\,S_0'(x)\,S_1'(x) = 0 \tag{19}$$

The exactness requirement of our ansatz necessitates that all terms $S_{n>0}$ are zero and the demand for constant intensity of $\psi(x)$ calls for a real-valued $S_0(x)$. Both conditions can be fulfilled by choosing $\mathrm{Im}[\varepsilon(x)] = -S_0''(x)/k$ such that the term $\mathrm{Im}[\varepsilon(x)]$ moves from Eqs. (18) to (19) leading to $\mathrm{Re}[\varepsilon(x)] = [S_0'(x)]^2$ and $S_1'(x) = 0$. As a result $S_1(x) = const.$ and all higher terms are constant as well. Setting $S_0'(x) = W(x)$, we finally obtain the non-Hermitian dielectric function (relative permittivity),

$$\varepsilon(x) = W^2(x) - \frac{i}{k}\,\partial_x W(x)\,, \tag{20}$$

with a corresponding CI solution $\psi(x) = \exp[ik\int W(x')dx']$ that is an exact solution of the Helmholtz equation and valid for the whole bulk space and all wavelengths. In other words, we identify a general class of refractive index distributions where real and imaginary parts are connected through the generating function $W(x)$, for which the fringes in the interference pattern vanish entirely. The fact that $W(x)$ can be chosen arbitrarily, with no limitations on its spatial complexity (apart from smoothness), is a key asset of this approach, making it very generally applicable. For the special case that the generating function is left-right symmetric, $W(x) = W(-x)$, the dielectric function is $\mathscr{P}\mathscr{T}$-symmetric since $\varepsilon(x) = \varepsilon^*(-x)$. Independently, however, of whether $\varepsilon(x)$ is $\mathscr{P}\mathscr{T}$-symmetric or not it can be shown that CI waves can also be found for all dielectric functions that are described by Eq. (20) in a finite domain $x \in [-D, D]$, bordering on free space for $x < -D$ and $x > D$. In this case, the scalar Helmholtz equation (17) admits the following exact CI wave solutions $\psi(x)$:

$$\exp[ik\,(x + D)], \quad x < -D\,, \tag{21}$$

$$\exp[ik\int_{-D}^{x} W(x')dx'], \; -D \le x \le D\,, \tag{22}$$

$$\exp[ik\,(x - D + c)], \quad x > D\,, \tag{23}$$

with c being a constant that is determined by the definite integral of W over the entire scattering region, in order for the field continuity relations to be satisfied.

Most importantly, the above solution does not only feature a constant intensity $|\psi(x)|^2 = 1$ in the asymptotic regions $x \leq -D$ and $x \geq D$, where $\varepsilon(x) = 1$ and simple plane wave propagation is realized, but also inside the finite region of length $2D$ in which the dielectric function varies and the phase-evolution is non-trivial. Regarding the appropriate boundary conditions at $x = \pm D$, it can be shown that the perfect transmission boundary conditions (zero reflection) [24] $\partial_x \psi(\pm D) = ik\psi(\pm D)$ imply the following conditions for the generating function, $W(\pm D) = 1$. From this result it is also clear that for vanishing imaginary part, the dielectric function, as defined in Eq. (20), reduces to $\varepsilon(x) = 1$, in which limit our CI wave solution is just a plane wave in free space.

It is also important to note that the wavenumber k appearing in the dielectric function $\varepsilon(x)$ of Eq. (20) is the same as the wavenumber k in the CI wave solution given in Eq. (21). In other words, for any value of k for which a CI scattering state is desired, the dielectric function $\varepsilon(x)$ has to be engineered correspondingly. Once $\varepsilon(x)$ is fixed and plane waves with varying values of k are impinging on this dielectric structure, a perfectly transmitting CI solution in general only occurs at the predetermined k value inherent in the design of $\varepsilon(x)$, whereby no issue arises with the Kramers-Kronig relations.

To elucidate the above ideas, we consider now one specific example of an index distribution and study the CI-waves it gives rise to. We assume $W(x)$ to be a parabolic function modulated with a cosine, namely $W(x) = [1 - 0.2\cos(15\pi x/2)](2 - x^2)$. The corresponding real part of the refractive index distribution $n_R(x)$ is shown as the gray shaded area in Fig. 6. A wave impinging on this dielectric structure composed of only $n_R(x)$ is partly reflected and features a highly oscillatory profile, see Fig. 6a. Quite in contrast, when adding also the gain and loss inherent in the imaginary index component $n_I(x)$ derived from $W(x)$ (see green and red regions in Fig. 6b), the resulting scattering state is fully

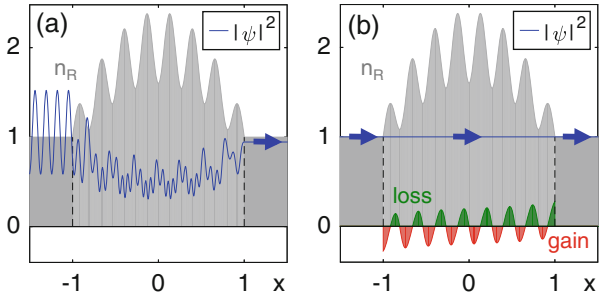

Fig. 6 (**a**) Scattering wave function intensity (blue line) in a Hermitian refractive index distribution for an incident plane wave (from the left) with a specific normalized wavenumber $k = 2\pi/0.26 = 24.15$. (**b**) Intensity of the CI-wave for the corresponding non-Hermitian refractive index $n(x)$ and the same incident plane wave. The real part of the refractive index is shown in gray, whereas its imaginary part is colored in green (loss) and red (gain). For illustration purposes the imaginary part in (**b**) was multiplied by a factor of 2. The calculations were performed using the transfer matrix approach

transmitted and features a constant intensity. Because of the boundary conditions, $W(x)$ must be symmetric at the end points of the cavity, resulting in an anti-symmetric distribution of $n_I(x)$. Our example shows that for a plane wave at an arbitrary incident wavenumber k, we can find the corresponding gain-loss landscape (from Eq. (20)), such that this wave will fully penetrate the scattering medium without forming any spatial variations in its intensity pattern.

Fixing a refractive index through Eq. (20) that leads to a CI wave at the specific wavenumber k_0, one can ask the question what happens to incident plane waves with detuned wavenumbers $k \neq k_0$. Naively, one may expect that the emergence of CI waves is a sharp resonance phenomenon, so that waves with a slight detuning in the wavenumber k should show a completely different behavior as, e.g., around a resonance in a Fabry-Perot interferometer [62]. This picture turns out to be misleading on several levels: Since the CI wave function at position x, $\psi(x) = \exp[ik\int_{-D}^{x} W(x')dx']$, only depends on the generating function $W(x')$ evaluated at values $x' < x$, one can easily truncate the system at any point x and still get a CI wave – provided one continues the system for all $x' > x$ with a constant generating function that has the same value as at the point of truncation. This behavior indicates that a refractive index profile that supports CI waves is not only reflectionless in total, but also unidirectional at any point inside a given structure. Perfect transmission in such systems is thus not a resonance phenomenon, suggesting that CI waves are stable against changes of the incident wavelength. To check this explicitly, we numerically calculated the average resonance width of the transmission spectrum $|t(k)|$ of the Hermitian system in Fig. 6, $\langle \Delta k_{Herm} \rangle = 0.84$, in an interval $k \in [\frac{2\pi}{0.5} - 3, \frac{2\pi}{0.5} + 3]$, with minimum transmission $|t(k)_{min}| = 0.77$. The transmission of the corresponding CI system (that of Fig. 6 but for the slighlty different wavenumber $k_0 = \frac{2\pi}{0.5}$) stays larger than 0.9 over the entire k-interval (not shown), confirming our prediction.

Another important point to make is that one can easily achieve a transmission equal to one in a non-Hermitian system just by adding enough gain to it. In a CI system, however, the net average amplification is zero, since $\int_{-D}^{D} \mathrm{Im}[\varepsilon(x)]dx = 0$ and the intensity is equally distributed everywhere. Additionally, the material gain corresponding to the potentials examined for $\lambda = 1.5\,\mu\mathrm{m}$ is around a realistic value of $80\,\mathrm{cm}^{-1}$ for $\max(n_I) = 10^{-3}$. Moreover, these uniform intensity waves are still valid for any slowly varying or rapidly fluctuating (subwavelength) optical potential (as exact solutions of Helmholtz equation). For these reasons the aforementioned physical values depend on the size of the scattering region, and on the operation wavelength.

The most striking application of CI waves occurs for the case of scattering through disordered environments. From the discussion above on the disordered lattices we already know that in strongly scattering disordered media Anderson localization occurs. For scattering states like the ones considered here, Anderson localization results in an exponential decrease of the transmittance $T = |t|^2$ for structures with sizes greater than the localization length $\xi = -2D\langle \ln[T(D)] \rangle^{-1}$. For a given real and disordered index of refraction in the localized regime close

to unit transmittance is thus very unlikely and occurs only at well-isolated, sharply resonant wave numbers that are difficult to achieve experimentally [63, 64]. Our approach now allows to turn this behavior upside down – not only in the sense that we can engineer unit transmission at any predetermined value of the wavenumber k, but also that we can create scattering states that have constant intensity in a strongly disordered environment which would usually give rise to the most dramatic intensity fluctuations known in wave physics.

We illustrate our results for the disordered one-dimensional slab shown in Fig. 7, where a refractive index distribution following Eq. (20) is considered with a tunable imaginary component, $\varepsilon(x) = [n_R(x) + i\, a\, n_I(x)]^2$ (the tunable parameter a controls the overall amplitude of gain and loss). More specifically, the generating function $W(x)$ is a superposition of 99000 Gaussian functions of the same amplitude and width, but centered around random positions. For $a = 0$ the refractive index is Hermitian, whereas for $a = 1$ CI waves exist. The refractive index distribution of such a non-Hermitian disordered medium is depicted in Fig. 7a, and the localization length ξ of the Hermitian refractive index ($a = 0$) is depicted in Fig. 7b. Without the gain and loss distribution, the system reflects almost all waves due to localization. Adding first only the gain part of the CI refractive index distribution (see Fig. 7c) still results in highly oscillatory scattering wave functions with finite reflectance for all values of the gain amplitude a (from 0 to 1), see Fig. 7d. Quite counterintuitively, adding also the loss part of the CI index distribution leads to perfect and fringe-free transmission for $a = 1$, see Fig. 7e. By varying the gain-loss amplitude a, as in Fig. 7e, we can also see the smooth transition from the Anderson localization regime (at $a = 0$) to perfect transmission with constant intensity (at $a = 1$).

Another important aspect of CI waves is their experimental realization, with the most challenging part being the fabrication of a specific index distribution with gain and loss [65]. In order to overcome such inherent difficulties, we study here also the existence of CI scattering states in a system of discrete elements, see Fig. 8. Such a set-up is composed of many discrete sites (cavities) with gain or loss and a specific real refractive index distribution. Translating the analytic solution of Eq. (20) to a finite-difference model, yields the following discrete solution that satisfies the discrete version of the Helmholtz equation with the discrete dielectric elements ε_m and the CI scattering state ψ_m:

$$\varepsilon_m = b^{-2}\left\{2 - e^{\frac{ik\Delta x}{2}(W_m+W_{m+1})} - e^{-\frac{ik\Delta x}{2}(W_m+W_{m-1})}\right\} \tag{24}$$

and

$$\psi_m = \exp\left[\frac{ik\Delta x}{2}\left(W_1 + W_m + 2\sum_{n=2}^{m-1} W_n\right)\right], \tag{25}$$

where $b = \omega\Delta x$, $\omega^2 = 2\,[1-\cos(k\Delta x)]/\Delta x^2$, and $m = 1, \ldots, M$. Additionally, perfect transmission boundary conditions imposed at the endpoints of the discrete chain of the scatterers $\psi_0 = \psi_1 \exp(-ik\Delta x)$, and $\psi_{M+1} = \psi_M \exp(ik\Delta x)$ as

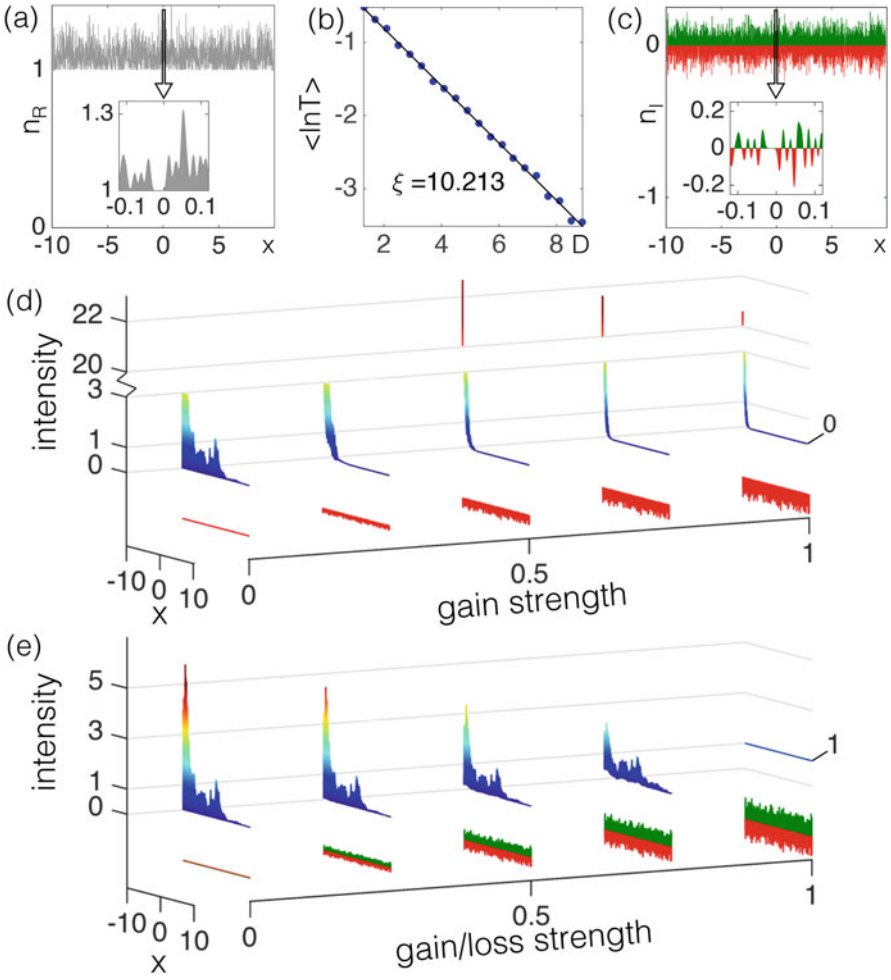

Fig. 7 A strongly disordered potential consisting of $N = 99000$ Gaussian scatterers is considered. (**a**) The corresponding refractive index distribution $n_R(x)$ in a small interval of x is shown. (**b**) Exponential suppression of the transmittance T with localization length ξ in this system for variable length of the disordered region D. (**c**) Imaginary part of the refractive index $n_I(x)$ following from the CI design principle ($n_I(x)$ is matched to the real index distribution in (**a**)). (**d**, **e**) Scattering wave functions for the disordered region as a function of the gain-loss strength parameter a, for the gain-only and gain-loss potential, respectively. In both cases, an incident plane wave is considered (from left to right). The CI-wave can be clearly seen for the full gain-loss strength ($a = 1$) in (**e**)

well as the relation $\omega \Delta x < 2$ must always hold. We consider a specific example in Fig. 8 of M-elements that form a one-dimensional disordered chain. By adding gain or loss onto the sites as prescribed by Eq. (24), an incoming wave from the left will have the same constant intensity on all of these sites.

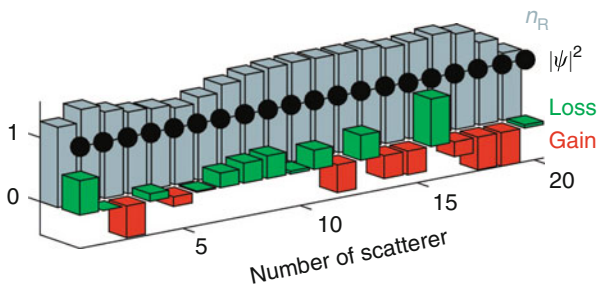

Fig. 8 Disordered chain of discrete scatterers with an incoming plane wave from the left. The real part (gray) as well as the gain (red) and loss (green) components of the refractive index are shown for each scatterer. The corresponding discrete CI-wave is depicted with black dots. The normalized parameters used are $M = 20$, $\omega = 12$, $L = 2$ and $\Delta x = L/(M - 1)$

5 Future Directions and Outlook

In conclusion, we have presented an overview of recent results related to constant-intensity waves in non-Hermitian systems such as synthetic media with gain and loss. The central idea of this line of research is to spatially engineer the imaginary part of the index of refraction in order to obtain a desired field pattern (constant-intensity in this case). A possible next step in this context is to generalize CI scattering states to more than one dimension. It is currently still an open question, however, whether this is possible at all or under which constraints this can work. A second direction that we are currently pursuing is to use our design principle not only to create waves with a constant intensity, but rather with any desired intensity profile inside a given medium [66, 67]. In preliminary calculations we find, e.g., that it is readily possible to create states that have a pronounced focus deep inside a disordered medium – a property that is very desirable for various applications in biophotonics and imaging. Last, but not least, we have also recently found [68] that a medium that supports CI scattering states can be made unidirectionally invisible. In this way we uncover a general design principle for unidirectional invisibility that goes far beyond the periodic structure with PT-symmetry discussed so far [11]. At this point we have to emphasize that these types of phenomena are based on complex wave interference and are therefore expected to exist in various areas of wave physics (optics, microwaves, acoustics, etc). As far as the experimental demonstration of such CI-waves is concerned, we have recently observed perfect transmission of acoustic CI-waves in disordered media [69]. These findings demonstrate that CI-waves have considerable potential for new exciting applications.

Acknowledgements This project was supported by the People Programme (Marie Curie Actions) of the European Union's Seventh Framework Programme (FP7/2007-2013) under REA Grant Agreement No. PIOFGA-2011-303228 (Project NOLACOME). K.G.M. is also supported by the European Union Seventh Framework Programme (FP7-REGPOT-2012-2013-1) under grant agreement 316165. S.R. acknowledges financial support by the Austrian Science Fund (FWF) through Project SFB NextLite (F49-P10) and Project GePartWave (I1142).

References

1. Leonhardt, U.: Optical conformal mapping. Science **312**, 1777–1780 (2006)
2. Tyson, R.K.: Principles of Adaptive Optics, 3rd edn. CRC Press, Boca Raton, London/New York (2001)
3. El-Ganainy, R., Makris, K.G., Khajavikhan, M., Musslimani, Z.H., Rotter, S., Christodoulides, D.N.: Non-Hermitian physics and PT symmetry. Nat. Phys. **14**, 11 (2018)
4. Moiseyev, N.: Non-Hermitian Quantum Mechanics. Cambridge University Press, Cambridge (2011)
5. Bender, C.M.: Making sense of non-Hermitian Hamiltonians. Rep. Prog. Phys. **70**, 947–1018 (2007)
6. Guo, A., Salamo, G.J., Duchesne, D., Morandotti, R., Volatier-Ravat, M., Aimez, V., Siviloglou, G.A., Christodoulides, D.N.: Observation of PT-symmetry breaking in complex optical potentials. Phys. Rev. Lett. **103**, 093902 (2009)
7. Rüter, C.E., Makris, K.G., El-Ganainy, R., Christodoulides, D.N., Segev, M., Kip, D.: Observation of parity–time symmetry in optics. Nat. Phys. **6**, 192–195 (2010)
8. Regensburger, A., Bersch, C., Miri, M.-A., Onishchukov, G., Christodoulides, D.N., Peschel, U.: Parity-time synthetic photonic lattices. Nature **488**, 167–171 (2012)
9. Feng, L., Xu, Y.-L., Fegadolli, W.S., Lu, M.-H., Oliveira, J.E.B., Almeida, V.R.,Chen, Y.-F., Scherer, A.: Experimental demonstration of a unidirectional reflectionless parity-time metamaterial at optical frequencies. Nat. Mater. **12**, 108–113 (2013)
10. Peng, B., Özdemir, Ş.K., Lei, F., Monifi, F., Gianfreda, M., Long, G.L., Fan, S., Nori, F., Bender, C.M., Yang, L.: Parity-time-symmetric whispering-gallery microcavities. Nat. Phys. **10**, 394–398 (2014)
11. Lin, Z., Ramezani, H., Eichelkraut, T., Kottos, T., Cao, H., Christodoulides, D.N.: Unidirectional invisibility induced by PT-symmetric periodic structures. Phys. Rev. Lett. **106**, 093902 (2011)
12. Chong, Y.D., Ge, L., Cao, H., Stone, A.D.: Coherent perfect absorbers: time-reversed lasers. Phys. Rev. Lett. **105**, 053901 (2010)
13. Wan, W., Chong, Y., Ge, L., Noh, H., Stone, A.D., Cao, H.: Time-reversed lasing and interferometric control of absorption. Science **331**, 889–892 (2011)
14. Sun, Y., Tan, W., H.-Q. Li, Li, J., Chen, H.: Experimental demonstration of a coherent perfect absorber with PT phase transition. Phys. Rev. Lett. **112**(14), 143903 (2014)
15. Liertzer, M., Ge, L., Cerjan, A., Stone, A.D., Türeci, H.E., Rotter, S.: Pump-induced exceptional points in lasers. Phys. Rev. Lett. **108**, 173901 (2012)
16. Brandstetter, M., Liertzer, M., Deutsch, C., Klang, P., Schöberl, J., Türeci, H.E., Strasser, G., Unterrainer, K., Rotter, S.: Reversing the pump dependence of a laser at an exceptional point. Nat. Commun. **5**, 4034 (2014)
17. Peng, B., Özdemir, Ş.K., Rotter, S., Yilmaz, H., Liertzer, M., Monifi, F., Bender, C.M., Nori, F., Yang, L.: Loss-induced suppression and revival of lasing. Science **346**, 328–332 (2014)
18. Bender, C.M., Brody, D.C., Jones, H.F.: Complex extension of quantum mechanics. Phys. Rev. Lett. **89**, 270401 (2002)
19. Makris, K.G., El-Ganainy, R., Christodoulides, D.N., Musslimani, Z.H.: Beam dynamics in PT symmetric optical lattices. Phys. Rev. Lett. **100**, 103904 (2008)
20. Musslimani, Z.H., Makris, K.G., El-Ganainy, R., Christodoulides, D.N.: Optical solitons in PT periodic potentials. Phys. Rev. Lett. **100**, 030402 (2008)
21. Chong, Y.D., Ge, L., Stone, A.D.: PT -symmetry breaking and laser-absorber modes in optical scattering systems. Phys. Rev. Lett. **106**, 093902 (2011)
22. Kottos, T.: Optical physics: broken symmetry makes light work. Nat. Phys. **6**, 166–167 (2010)
23. Makris, K.G., Ge, L., Türeci, H.E.: Anomalous transient amplification of waves in non-normal photonic media. Phys. Rev. X **4**, 041044 (2014)
24. Ambichl, P., Makris, K.G., Ge, L., Chong, Y., Stone, A.D., Rotter, S.: Breaking of PT-symmetry in bounded and unbounded scattering systems. Phys. Rev. X **3**, 041030 (2013)

25. Makris, K.G., Musslimani, Z.H., Christodoulides, D.N., Rotter, S.: Constant-intensity waves and their modulation instability in non-Hermitian potentials. Nat. Commun. **6**, 8257 (2015)
26. Makris, K.G., Musslimani, Z.H., Christodoulides, D.N., Rotter, S.: Constant intensity supermodes in non-Hermitian lattices. IEEE J. Sel. Top. Quantum Electron. **22**, 42–47 (2016)
27. Cole, J., Makris, K., Musslimani, Z., Christodoulides, D., Rotter, S.: Modulational instability in a PT-symmetric vector nonlinear Schrödinger system. Physica D Nonlinear Phenom. **336**, 53–61 (2016)
28. Makris, K.G., Brandstötter, A., Ambichl, P., Musslimani, Z.H., Rotter, S.: Wave propagation through disordered media without backscattering and intensity variations. Light Sci. Appl. **6**, e17030 (2017)
29. Durnin, J., Miceli, J.J., Eberly, J.H.: Diffraction-free beams. Phys. Rev. Lett. **58**, 1499–1501 (1987)
30. Tai, K., Hasegawa, A., Tomita, A.: Observation of modulational instability in optical fibers. Phys. Rev. Lett. **56**, 135–138 (1986)
31. Malendevich, R., Jankovic, L., Stegeman, G., Aitchison, J.S.: Spatial modulation instability in a Kerr slab waveguide. Opt. Lett. **26**, 1879 (2001)
32. Kip, D.: Modulation instability and pattern formation in spatially incoherent light beams. Science **290**, 495–498 (2000)
33. Meier, J., Stegeman, G.I., Christodoulides, D.N., Silberberg, Y., Morandotti, R., Yang, H., Salamo, G., Sorel, M., Aitchison, J.S.: Experimental observation of discrete modulational instability. Phys. Rev. Lett. **92**, 163902 (2004)
34. Lumer, Y., Plotnik, Y., Rechtsman, M.C., Segev, M.: Nonlinearly induced PT transition in photonic systems. Phys. Rev. Lett. **111**, 263901 (2013)
35. Zakharov, V.E., Gelash, A.A.: Nonlinear stage of modulation instability. Phys. Rev. Lett. **111**, 054101 (2013)
36. Schwartz, T., Bartal, G., Fishman, S., Segev, M.: Transport and Anderson localization in disordered two-dimensional photonic lattices. Nature **446**, 52–55 (2007)
37. Lahini, Y., Avidan, A., Pozzi, F., Sorel, M., Morandotti, R., Christodoulides, D.N., Silberberg, Y.: Anderson localization and nonlinearity in one-dimensional disordered photonic lattices. Phys. Rev. Lett. **100**, 013906 (2008)
38. Billy, J., Josse, V., Zuo, Z., Bernard, A., Hambrecht, B., Lugan, P., Clément, D., Sanchez-Palencia, L., Bouyer, P., Aspect, A.: Direct observation of Anderson localization of matter waves in a controlled disorder. Nature **453**, 891–894 (2008)
39. Lagendijk, A., Tiggelen, B.V., Wiersma, D.S.: Fifty years of Anderson localization. Phys. Today **62**, 24–29 (2009)
40. Segev, M., Silberberg, Y., Christodoulides, D.N.: Anderson localization of light. Nat. Photonics **7**, 197–204 (2013)
41. Basiri, A., Bromberg, Y., Yamilov, A., Cao, H., Kottos, T.: Light localization induced by a random imaginary refractive index. Phys. Rev. A **90**, 043815 (2014)
42. Lagendijk, A., van Tiggelen, B.A.: Resonant multiple scattering of light. Phys. Rep. **270**, 143–215 (1996)
43. Akkermans, E., Montambaux, G.: Mesoscopic Physics of Electrons and Photons. Cambridge University Press, Cambridge (2007)
44. Sebbah, P.: Waves and Imaging Through Complex Media. Springer, Netherlands/Dordrecht (2001) OCLC: 863932944
45. Beenakker, C.W.J.: Random-matrix theory of quantum transport. Rev. Mod. Phys. **69**, 731–808 (1997)
46. Mosk, A.P., Lagendijk, A., Lerosey, G., Fink, M.: Controlling waves in space and time for imaging and focusing in complex media. Nat. Photonics **6**, 283–292 (2012)
47. Rotter, S., Gigan, S.: Light fields in complex media: mesoscopic scattering meets wave control. Rev. Mod. Phys. **89**, 015005 (2017)
48. Vellekoop, I.M., Mosk, A.P.: Focusing coherent light through opaque strongly scattering media. Opt. Lett. **32**, 2309 (2007)

49. Popoff, S.M., Lerosey, G., Carminati, R., Fink, M., Boccara, A.C., Gigan, S.: Measuring the transmission matrix in optics: an approach to the study and control of light propagation in disordered media. Phys. Rev. Lett. **104**, 100601 (2010)
50. Vellekoop, I.M., Lagendijk, A., Mosk, A.P.: Exploiting disorder for perfect focusing. Nat. Photonics **4**, 320–322 (2010)
51. Katz, O., Small, E., Bromberg, Y., Silberberg, Y.: Focusing and compression of ultrashort pulses through scattering media. Nat. Photonics **5**, 372–377 (2011)
52. McCabe, D.J., Tajalli, A., Austin, D.R., Bondareff, P., Walmsley, I.A., Gigan, S., Chatel, B.: Spatio-temporal focusing of an ultrafast pulse through a multiply scattering medium. Nat. Commun. **2**, 447 (2011)
53. Yaqoob, Z., Psaltis, D., Feld, M.S., Yang, C.: optical phase conjugation for turbidity suppression in biological samples. Nat. Photonics **2**, 110–115 (2008)
54. Riboli, F., Caselli, N., Vignolini, S., Intonti, F., Vynck, K., Barthelemy, P., Gerardino, A., Balet, L., Li, L.H., Fiore, A., Gurioli, M., Wiersma, D.S.: Engineering of light confinement in strongly scattering disordered media. Nat. Mater. **13**, 720–725 (2014)
55. Bruck, R., Vynck, K., Lalanne, P., Mills, B., Thomson, D.J., Mashanovich, G.Z., Reed, G.T., Muskens, O.L.: All-optical spatial light modulator for reconfigurable silicon photonic circuits. Optica **3**, 396 (2016)
56. Bachelard, N., Gigan, S., Noblin, X., Sebbah, P.: Adaptive pumping for spectral control of random lasers. Nat. Phys. **10**, 426–431 (2014)
57. Hisch, T., Liertzer, M., Pogany, D., Mintert, F., Rotter, S.: Pump-controlled directional light emission from random lasers. Phys. Rev. Lett. **111**, 023902 (2013)
58. Schönhuber, S., Brandstetter, M., Hisch, T., Deutsch, C., Krall, M., Detz, H., Andrews, A.M., Strasser, G., Rotter, S., Unterrainer, K.: Random lasers for broadband directional emission. Optica **3**, 1035 (2016)
59. Ge, L., Malik, O., Türeci, H.E.: Enhancement of laser power-efficiency by control of spatial hole burning interactions. Nat. Photonics **8**, 871–875 (2014)
60. Liew, S.F., Redding, B., Ge, L., Solomon, G.S., Cao, H.: Active control of emission directionality of semiconductor microdisk lasers. Appl. Phys. Lett. **104**, 231108 (2014)
61. Bender, C.M., Orszag, S.A.: Advanced Mathematical Methods for Scientists and Engineers. 1: Asymptotic Methods and Perturbation Theory. Springer, New York (2009). OCLC: 837310111
62. Yeh, P.: Optical Waves in Layered Media. Wiley-Interscience, Hoboken (2005)
63. Wang, J., Genack, A.Z.: Transport through modes in random media. Nature **471**, 345–348 (2011)
64. Peña, A., Girschik, A., Libisch, F., Rotter, S., Chabanov, A.A.: The single-channel regime of transport through random media. Nat. Commun. **5**, 3488 (2014)
65. Szameit, A., Nolte, S.: Discrete optics in femtosecond-laser-written photonic structures. J. Phys. B Atomic Mol. Phys. **43**(16), 163001 (2010)
66. Brandstötter, A., Makris, K.G., Rotter, S.: Non-Hermitian focusing deep inside strongly disordered scattering media. In: IEEE, CLEO Europe, European Quantum Electronics Conference, EJ_P_1, June 2017, pp. 1–1
67. Makris, K.G., Brandstötter, A., Rotter, S.: Wave control in non-Hermitian disordered media. IEEE, Photonics Conference (IPC), Oct. 2017, pp. 391–392
68. Brandstötter, A., Makris, K., Rotter, S.: Non-Hermitian invisibility based on constant-intensity waves, p. FM4B.4. Frontiers in Optics, OSA (2017)
69. Rivet, E., Brandstötter, A., Makris, K. G., Lissek, H., Rotter, S., Fleury, R.: Constant-pressure sound waves in non-Hermitian disordered media. Nat. Phys. Published online at https://doi.org/10.1038/s41567-018-0188-7

Nonlinear Beam Propagation in a Class of Complex Non-$\mathscr{P}\mathscr{T}$-Symmetric Potentials

J. Cuevas-Maraver, P. G. Kevrekidis, D. J. Frantzeskakis, and Y. Kominis

Abstract The subject of $\mathscr{P}\mathscr{T}$-symmetry and its areas of application have been blossoming over the past decade. Here, we consider a nonlinear Schrödinger model with a complex potential that can be tuned controllably away from being $\mathscr{P}\mathscr{T}$-symmetric, as it might be the case in realistic applications. We utilize two parameters: the first one breaks $\mathscr{P}\mathscr{T}$-symmetry but retains a proportionality between the imaginary and the derivative of the real part of the potential; the second one, detunes from this latter proportionality. It is shown that the departure of the potential from the $\mathscr{P}\mathscr{T}$-symmetric form does not allow for the numerical identification of exact stationary solutions. Nevertheless, it is of crucial importance to consider the dynamical evolution of initial beam profiles. In that light, we define a suitable notion of optimization and find that even for non $\mathscr{P}\mathscr{T}$-symmetric cases, the beam dynamics, both in 1D and 2D – although prone to weak growth or decay– suggests that the optimized profiles do not change significantly under propagation for specific parameter regimes.

Keywords Solitons · Nonlinear Schrödinger equation · Stability · $\mathscr{P}\mathscr{T}$-symmetry · Unbalanced gain and loss · Symmetry breaking

J. Cuevas-Maraver
Departamento de Física Aplicada I, Escuela Politécnica Superior, Grupo de Física No Lineal, Universidad de Sevilla, Sevilla, Spain

Instituto de Matemáticas de la Universidad de Sevilla (IMUS), Sevilla, Spain
e-mail: jcuevas@us.es

P. G. Kevrekidis (✉)
Department of Mathematics and Statistics, University of Massachusetts, Amherst, MA, USA
e-mail: kevrekid@math.umass.edu

D. J. Frantzeskakis
Department of Physics, National and Kapodistrian University of Athens, Athens, Greece

Y. Kominis
School of Applied Mathematical and Physical Science, National Technical University of Athens, Athens, Greece

D. Christodoulides, J. Yang (eds.), *Parity-time Symmetry and Its Applications*, Springer Tracts in Modern Physics 280,
https://doi.org/10.1007/978-981-13-1247-2_20

1 Introduction

The original suggestion of Bender and collaborators [1, 2] of a new class of systems that respect parity and time-reversal (so-called $\mathscr{P}\mathscr{T}$-symmetric systems) was motivated by the consideration of the foundations of quantum mechanics and the examination of the need of Hermitianity within them. The argument of Bender and collaborators was that such systems, even if non-Hermitian and featuring gain and loss, could give rise to real spectra, thus presenting a candidacy for being associated with measurable quantities.

This proposal found a fertile ground for its development in areas, arguably, different than where it was originally proposed. In particular, the work of Christodoulides and co-workers in nonlinear optics a decade later, spearheaded an array of experimental realizations of such media (capitalizing on the ubiquitous in optics loss and on controllable gain) [3–8]. Other experiments swiftly followed in areas ranging from electronic circuits [9–11] to mechanical systems [12], bringing about not only experimental accessibility, but also an intense theoretical focus on this theme. These threads of research have now been summarized in two rather comprehensive recent reviews [7, 8].

While $\mathscr{P}\mathscr{T}$-symmetric variants of other nonlinear wave models have more recently been proposed, including the $\mathscr{P}\mathscr{T}$-symmetric variants of the Dirac equations [13] and of the nonlinear Klein-Gordon models [14], the main focus of associated interest has been on models of the nonlinear Schrödinger (NLS) type. This is natural given the relevance at the paraxial approximation level of such a model in applications stemming from nonlinear optics and related themes [7, 8]. In this important case, the $\mathscr{P}\mathscr{T}$-invariance is consonant with complex external potentials $\tilde{V}$, of the form $\tilde{V} = V + iW$, subject to the constraint that $\tilde{V}^*(x) = \tilde{V}(-x)$. This implies that the real part, V, of the potential needs to be even, while the imaginary part, W, of the potential needs to be odd to ensure $\mathscr{P}\mathscr{T}$-symmetry. The expectation, thus, has been that typically Hamiltonian and $\mathscr{P}\mathscr{T}$-symmetric systems featuring gain and loss will possess continuous families of soliton solutions; otherwise, the models will possess solutions for isolated values within the parameter space.

However, more recent investigations have started to challenge this belief. On the one hand, work on complex, asymmetric so-called Wadati potentials has produced mono-parametric continuous families of stationary solutions [15, 16]. On the other hand, the notion of partial $\mathscr{P}\mathscr{T}$-symmetry has been explored, e.g., with models that possess the symmetry in one of the directions but not in another [17, 18]. In fact, in the recent work of [19, 20] that motivated the present study, it was shown that to identify critical points one can localize a soliton[1] in a way such that its intensity has a vanishing total overlap with the imaginary part of the potential, assuming that the real part of the potential is proportional to the anti-derivative of the imaginary part (but without making any assumptions on the parity of either).

[1] Below, we use the term "soliton" in a loose sense, without implying complete integrability [21].

In the present work, we revisit these considerations. In particular, we discuss the results of the important contribution of [22]. This work suggests (and indeed conjectures) that the *only* complex potentials that could feature continuous families of stationary solutions although non-$\mathscr{P}\mathscr{T}$-symmetric are the ones of the Wadati type. In our case, we have considered potentials that depart from this form and either satisfy – or controllably depart from – the simpler mass and momentum balance conditions of [19, 20]. We observe that in such settings, waveforms "optimizing" the vector field (which we define as bringing it *very* – but not arbitrarily – close to vanishing) may exist, but still are not true solutions, in line with the above conjecture. We develop diagnostics that explore how these optimized beams behave dynamically, and identify their slow growth or decay. We do this for two different broad multi-parametric families of potentials to showcase the generality of our conclusions. We then extend relevant considerations also to 2D settings, showing how symmetry breaking bifurcation scenarios can be traced via our optimized beam approach.

Our presentation will be structured as follows. In Sect. 2, we introduce the model, connect our considerations to those of [22] and justify the selection of the complex potential. In Sect. 3, we explore the optimized beams and the associated dynamics of the relevant waveforms numerically. Then, in Sect. 4, we generalize these notions in a two-dimensional setting. In Sect. 5, we proceed to summarize our findings and propose a number of directions for future study. Finally, in the Appendix, details of the numerical method used to optimize the dynamical beams are presented.

2 The One-Dimensional Potential

As explained in the previous section, motivated by the development in the analysis of NLS models with complex potentials, we consider the rather broad setting of the form:

$$i\psi_t = -\psi_{xx} + [V(x) + iW(x)]\psi - |\psi|^2\psi, \tag{1}$$

with subscripts denoting partial derivatives. In the context of optics, $\psi(x,t)$ represents the complex electric field envelope, t is the propagation distance, x corresponds to the transverse direction, while the variation of the dielectric permittivity plays the role of the external potential, with $V(x)$ and $W(x)$ being its real and imaginary parts, respectively [7, 8]. In the recent analysis of [19, 20], assuming the existence of bright solitons (as is natural in the focusing nonlinearity setup under consideration), dynamical evolution equations were obtained for the soliton mass and velocity. Here, we use as our motivating point for constructing standing wave structures of Eq. (1) the stationary form of these equations, which read (cf. Eqs. (5)–(6) of Ref. [20]):

$$\int_{-\infty}^{\infty} |\psi(x)|^2 W(x+x_0)dx = \int_{-\infty}^{\infty} |\psi(x)|^2 V'(x+x_0)dx = 0, \tag{2}$$

where x_0 denotes the soliton center. The first one among these equations, corresponds to a "power-balance" (or mass balance) condition, implying that the soliton has a transverse profile such that it experiences gain and loss in an overall balanced fashion across its spatial extent. The second equation corresponds to a "momentum-balance" condition, i.e., the total force exerted on the solitary wave vanishes, hence the coherent structure is at an equilibrium.

This pair of stationarity conditions in Eq. (2) reduces to a single one, provided that $V' = -CW$, with C being a constant. In that context, the resulting condition posits the following: if a soliton can be placed relative to the gain/loss profile so that its intensity has an overall vanishing overlap with the imaginary part of the potential, then the existence of a fixed point (and thus a stationary soliton solution) may be expected.

However, it should be kept in mind that these conditions are *necessary but not sufficient* for the existence of a stationary configuration. In particular, a recent ingenious calculation sheds some light on this problem for a general potential in the work of [22]. Using a standing wave decomposition

$$\psi = r(x)e^{i\int^x \theta(x')dx'}e^{i\mu t}$$

in Eq. (1), the following ordinary differential equations were derived:

$$r_{xx} - \mu r - Vr + r^3 - \theta^2 r = 0, \tag{3}$$

$$(r^2\theta)_x = Wr^2. \tag{4}$$

It was then realized that, in the absence of external potential, two quantities, namely $J_1 = r^2\theta$ (the "angular momentum" in the classical mechanical analogy of the problem) and $J_2 = r_x^2 - \mu r^2 + r^4/2 + r^2\theta^2$ (the "first integral" or energy in the classical analogue) are conserved, i.e., $dJ_i/dx = 0$. For J_1, Eq. (4) yields its evolution in the presence of the potential while for J_2, direct calculation shows:

$$\frac{dJ_2}{dx} = V(r^2)_x + 2Wr^2\theta = S_x - r^2V_x - 2(r^2\theta)_x \int Wdx, \tag{5}$$

with $S = Vr^2 + 2r^2\theta \int Wdx$. Combining the last terms, upon substitution of $(r^2\theta)_x$ from Eq. (4) allows us to infer that this pair of terms will vanish if the coefficient multiplying r^2, namely $V_x - 2W\int Wdx$, vanishes; this occurs if the potential has the form:

$$V + iW = -[g^2 + ig'(x)] + c,$$

where c is a constant. A shooting argument presented in [22] suggests that there are 3 real constants (2 complex ones, yet one of them can be considered as real due to the phase invariance) in order to "glue" two complex quantities, namely ψ and ψ_x at some point within the domain. This can only be done when a conserved

quantity exists, which requires the type of potential suggested above, in the form $-[g^2 + ig'(x)]$. However, if additional symmetry exists, such as $\mathscr{P}\mathscr{T}$-symmetry, the symmetry alone may impose conditions such as $\mathrm{Im}(\psi(0))=\mathrm{Re}(\psi_x(0)) = 0$, which in turn allows for the shooting to go through (and thus solutions to exist) for a continuous range of μ's.

Nevertheless, a natural question is: suppose that the potential is not of this rather non-generic form, yet it deviates from the $\mathscr{P}\mathscr{T}$-symmetric limit, possibly in ways respecting the above mass and/or momentum balance conditions of Eq. (2); then what is the fate of the system? Do stationary states perhaps exist or do they not, and what are the dynamical implications of such conditions? It is this class of questions that we will aim to make some progress towards in what follows.

To test relevant ideas, we will use two different potentials $\tilde{V}_j(x) = V_j(x) + iW_j(x)$, with $j = 1, 2$. In the first one, W is of the form:

$$W_1(x) = A_1 k_1 \mathrm{sech}(x - x_d - \delta_1)\tanh(x), \tag{6}$$

where A_1, k_1, x_d and δ_1 are constants, with the latter two controlling the breaking of the $\mathscr{P}\mathscr{T}$-symmetry. We then use a real potential V_1 given by the form:

$$V_1(x)=-2A_1\left[\arctan\left(\tanh\left(\frac{x_d - x}{2}\right)\right)\coth(x_d)-\arctan\left(\tanh\left(\frac{x}{2}\right)\right)\mathrm{csch}(x_d)\right], \tag{7}$$

which, in the limit $x_d \to 0$, transforms into $V_1(x) = -A_1\mathrm{sech}(x)$. The motivation behind this selection is that if $\delta_1 = 0$ in Eq. (6) then V_1 is proportional to the anti-derivative of W_1 (hence ensures that the pair of conditions of Eq. (2) degenerate to a single one). In addition, for $\delta_1 = 0$ and in the limit $x_d \to 0$, the potential is $\mathscr{P}\mathscr{T}$-symmetric. In short, the two parameters x_d and δ_1 both control the departure from $\mathscr{P}\mathscr{T}$-symmetry, while the latter affects the departure from proportionality of V_1' and W_1. This selection and these parameters thus allow us to tailor the properties of the potential, controlling its departure from the $\mathscr{P}\mathscr{T}$-symmetric limit, but also from the possible degeneracy point of the conditions (2).

The second potential is given by

$$W_2(x) = A_2 k_2 x \mathrm{sech}^2(x - \delta_2 - 1), \tag{8}$$

and

$$V_2(x) = -A_2(\log[\cosh(1 - x)] + x\tanh(1 - x)), \tag{9}$$

where A_2, k_2 and δ_2 are constants. Contrary to the $\tilde{V}_1$ case, this potential does not possess a $\mathscr{P}\mathscr{T}$-symmetric limit.

For both $\tilde{V}_1(x)$ and $\tilde{V}_2(x)$ potentials, if $\delta_j = 0$ $(j = 1, 2)$ then $V_j'(x) = -C_j W_j(x)$ and, as shown in Ref. [19], rendering a topic of interest the exploration of the potential existence of stationary solutions in the vicinity of the interface between the lossy and amplifying parts when Eq. (2) applies. In our particular case, the proportionality factor C_j is $C_j = 1/k_j$.

3 Numerical Results

3.1 Stationary States

We start by seeking stationary localized solutions, of the form $\psi(x,t) = \mathrm{e}^{i\mu t}u(x)$ with $u(x) \in \mathbb{C}$, which will thus satisfy:

$$F[u] \equiv \mu u - u_{xx} + [V(x) + iW(x)]u - |u|^2 u = 0. \tag{10}$$

In what follows, we fix $A_1 = 0.1$ and $A_2 = 1$, and consider stationary solutions of frequency $\mu = 1$. We will make use of periodic boundary conditions.

Notice that the potentials of [22] $\tilde{V}(x) = -[g^2(x) + ig'(x)]$ would, in the present notation, necessitate:

$$[V'(x)]^2 = -4V(x)W^2(x). \tag{11}$$

It is important to note that the potentials studied in our chapter do not fulfill this relation *for any set of parameters* $(A_1, k_1, x_d, \delta_1)$ or (A_2, k_2, δ_2) – except for the "trivial" $\mathscr{P}\mathscr{T}$-limit – as it can be easily demonstrated. As a result then, presumably because of the above calculation, the standard fixed point methods that we have utilized fail to converge away from the $\mathscr{P}\mathscr{T}$-symmetric limit. For this reason, we make use of minimization algorithms in order to obtain optimized profiles of localized waveforms. With these methods, one can seek for local minima of the norm of $F[u]$ instead of zeros of that function. In our problem, we have made use of the Levenberg–Marquardt algorithm (see Appendix A for more details), which has been successfully used for computing solitary gravity-capillary water waves [23], and established a tolerance of $||F[u]|| < 10^{-3}$ with $||F[u]||$ being the L^2-norm of $F[u]$:

$$||F[u]|| = \sqrt{\int |F[u(x)]|^2 \mathrm{d}x}. \tag{12}$$

In the particular case of potential $\tilde{V}_1(x)$, we have studied the stability of solitons in the $\mathscr{P}\mathscr{T}$-symmetric limit $x_d = \delta_1 = 0$ as a function of k_1, observing that solitons are stable whenever $k_1 < k_c$, with $k_c = 8.28$. At this point, the soliton experiences a Hopf bifurcation. In order to avoid any connection of the findings below with the effect of such instability, we have fixed in what follows a value of k_1 far enough from k_c. Moreover, since the minimal value attained for $||F[u]||$ increases with k_1, we have restricted consideration to relatively small values of k_1 and more specifically will report results in what follows for $k_1 = 1/2$.

Figures 1 and 2 show the potential profile for two different (x_d,δ_1) and (k_2,δ_2) parameter sets. These figures also show the profile of the waveforms minimizing $||F[u]||$ for such potentials, which will be considered further in what follows.

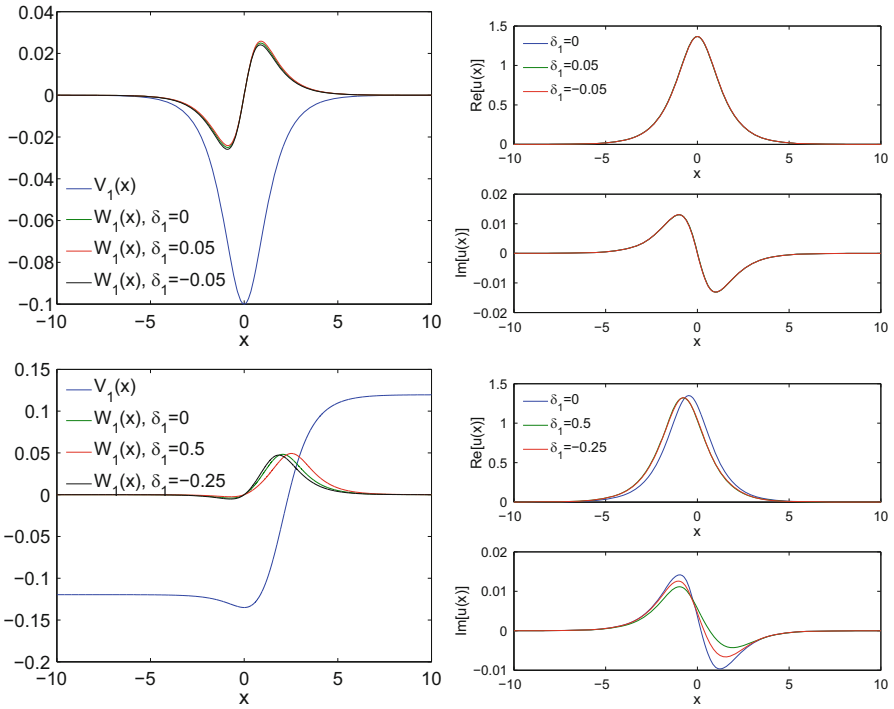

Fig. 1 Left panels: Real and imaginary part of the potential $\tilde{V}_1(x)$ for $A_1 = 0.1$, $k_1 = 1/2$ and $x_d = 0$ (top) and $x_d = 1$ (bottom); green line corresponds to the imaginary part for $\delta_1 = 0$, whereas red (black) line corresponds to the imaginary part for $\delta_1 = 0.05$ ($\delta_1 = -0.05$). Right panels: Beam profiles minimizing $||F[u]||$ (real and imaginary parts) for $A_1 = 0.1$, $k_1 = 1/2$ and $x_d = 0$ (top) and $x_d = 1$ (bottom); the blue line corresponds to $\delta_1 = 0$, and the green (red) line corresponds to $\delta_1 = 0.5$ ($\delta_1 = -0.25$)

These beam profiles will be referred to as "optimized" in the sense of the above minimization. In particular, their real part is nodeless, while their imaginary part features a zero crossing. Naturally, the profiles are asymmetric mirroring the lack of definite parity of the potentials' real and imaginary part. It is interesting to see that, despite the breaking of both the $\mathscr{P}\mathscr{T}$-symmetry and the violation of conditions such as the one in Eq. (11), there still exist spatially asymmetric structures almost satisfying the equations of motion. This naturally poses the question of the dynamical implications of such profiles in the evolution problem of Eq. (1), as we will see below.

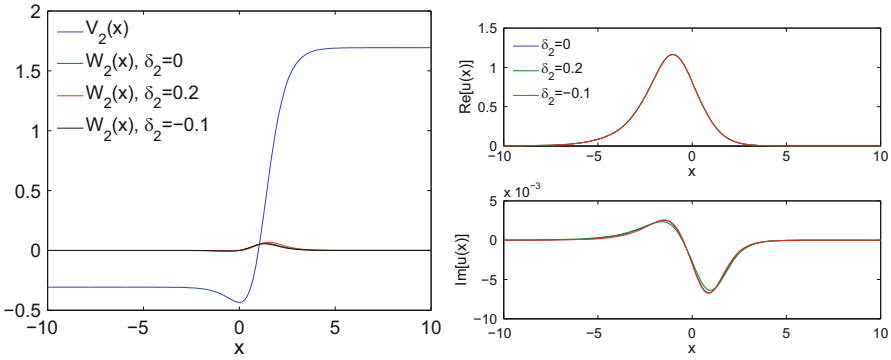

Fig. 2 Left panel: Real and imaginary part of the potential $\tilde{V}_2(x)$ for $A_2 = 1$, and $k_2 = 0.05$; the green line corresponds to the imaginary part for $\delta_2 = 0$, whereas the red (black) line corresponds to the imaginary part for $\delta_2 = 0.2$ ($\delta_2 = -0.1$). Right panels: optimized beam profiles (real and imaginary parts) for $A_2 = 1$, and $k_2 = 0.01$; the blue line corresponds to $\delta_2 = 0$, and the green (red) line corresponds to $\delta_2 = 0.2$ ($\delta_2 = -0.1$)

3.2 Dynamics

We now analyze the dynamics of several case examples for the NLS equation with potential $\tilde{V}_1(x)$, using as initial condition the optimized beam profiles found by the Levenberg-Marquardt algorithm. Figures 3 and 4 show the outcome of the simulations for $x_d = 1$ and $x_d = -1$, respectively, when $\delta_1 = 0$ is fixed; on the other hand, Figs. 5 and 6 correspond, respectively, to $\delta_1 = -0.1$ and $\delta_1 = 0.1$, when $x_d = 1$ is fixed. In these figures, we show the density $|\psi(x)|^2$ at different time instants (top left), the real and imaginary part of $F[u]$ (top right), a space-time contour plot of the evolution of the localized beam density $|\psi(x,t)|^2$ (bottom left), and the (squared) L^2-norm (power/mass in optics/atomic physics), $N(t)$ (bottom right), defined as

$$N(t) = \int |\psi(x,t)|^2 \mathrm{d}x. \tag{13}$$

One can observe a clear correlation between the qualitative shape of $\mathrm{Im}\{F[u]\}$ and the growing/decaying character of the dynamics. In other words, in the growing case, this quantity is predominantly positive, whereas for the decaying case, it is predominantly negative.

Moreover, it seems that a larger growth rate (i.e., a faster increase or decrease of N) is associated to a larger $||F[u]||$. In order to showcase this fact, we have depicted in Fig. 7 the dependence of diagnostic quantities λ and σ, that we have accordingly defined as

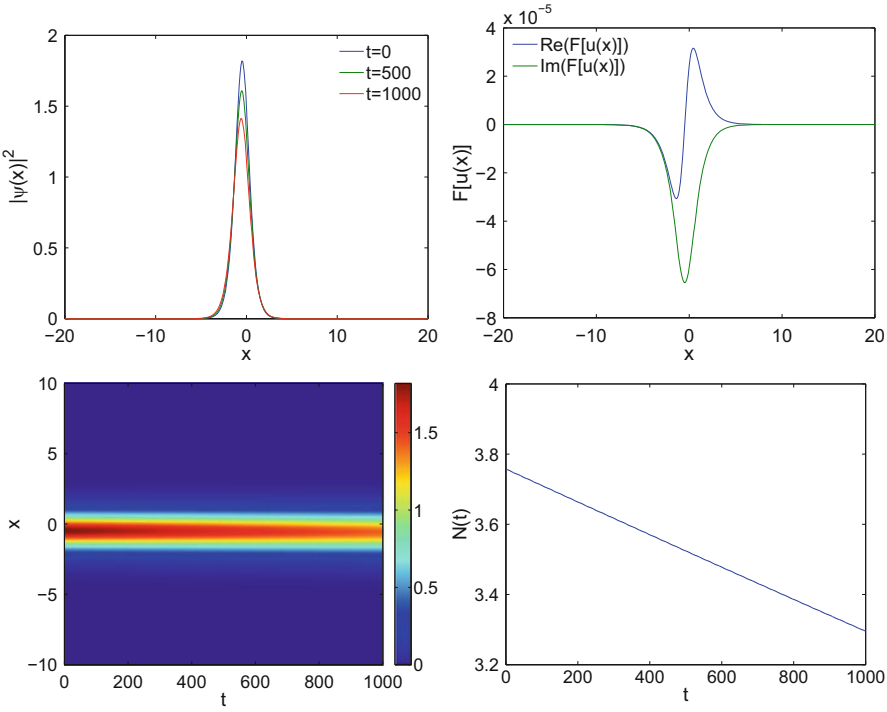

Fig. 3 Optimized beam dynamics in the potential $\tilde{V}_1(x)$ for $A_1 = 0.1$, $k_1 = 1/2$, $x_d = 1$ and $\delta_1 = 0$. The top left panel shows the density profile at $t = 0$, $t = 500$ and $t = 1000$, while the top right panel shows the real and imaginary part of $F[u]$. The bottom left panel shows the space-time contour plot of the density evolution, and the bottom right panel shows the evolution of the norm $N(t)$. The values of diagnostic quantities are $\lambda = -3.63 \times 10^{-3}$ and $\sigma = -1.07 \times 10^{-4}$

$$\lambda = \left.\frac{\mathrm{d}N}{\mathrm{d}t}\right|_{t=0}. \tag{14}$$

$$\sigma = S||F[u]||, \tag{15}$$

with

$$S = \mathrm{sgn}\left\{\int \mathrm{Im}\{F[u(x)]\}\mathrm{d}x\right\}$$

The quantity σ takes into account both the (minimized) norm of $||F[u]||$ and the form of $\mathrm{Im}\{F[u(x)]\}$ through S – that is, if the imaginary part of $F[u(x)]$ is chiefly positive or negative. Notice that the blank regions correspond to solutions for which $||F[u]||$ is higher than the prescribed tolerance of 10^{-3}. On the other hand, λ characterizes the rate of "departure" from the optimized beam profile obtained from this minimization procedure.

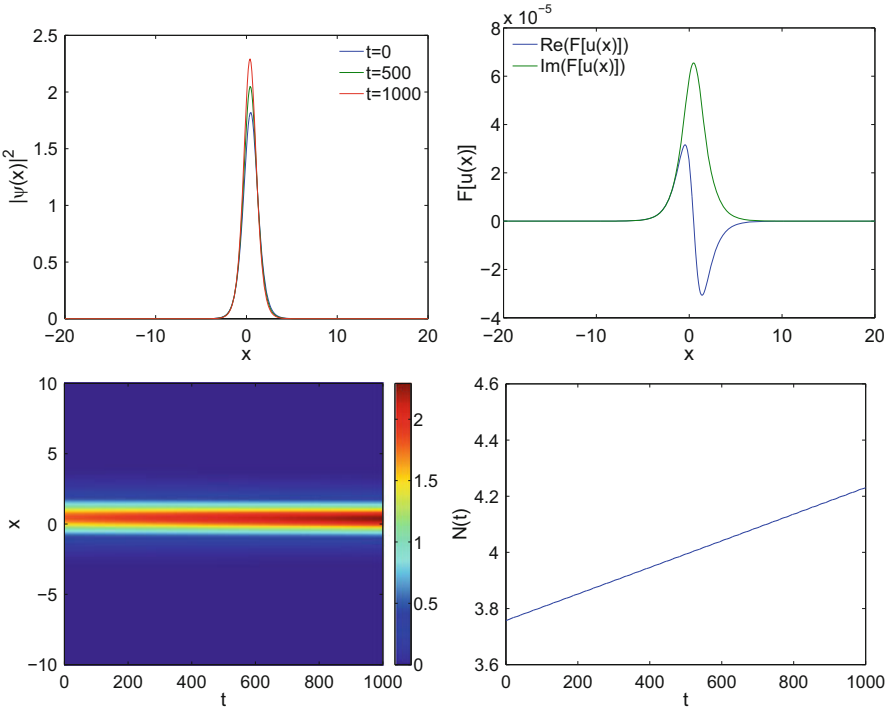

Fig. 4 Same as Fig. 3, but for $x_d = -1$. The values of diagnostic quantities are $\lambda = 3.63 \times 10^{-3}$ and $\sigma = 1.07 \times 10^{-4}$

Figure 7 shows a clear correlation between σ and λ. Notice the symmetry between the outcomes when the transformation $(x_d, \delta_1) \to (-x_d, -\delta_1)$ is applied, which is also manifested in the values of λ and σ displayed in the captions of Figs. 3 and 4. From this figure it is also clear that, roughly speaking, when $x_d\delta_1 < 0$, $N(t)$ grows with time, whereas the opposite takes place when $x_d\delta_1 > 0$. This is not always true, as there is a critical value δ_{1c} (close to zero) separating the growing ($\lambda > 0$) and decaying ($\lambda < 0$) dynamics, which is tantamount to the separation of the regions with $\sigma > 0$ and $\sigma < 0$. The dependence of δ_{1c} versus x_d is also depicted in Fig. 7; having in mind the continuous dependence of σ and λ with x_d and δ_1, it is clear that $\sigma = 0$ just at the curve $\delta_{1c}(x_d) = 0$, so one can find stationary soliton solutions. This is manifested in Fig. 8, where, for a set of parameters very close to the curve $\delta_{1c}(x_d) = 0$ (in particular, $x_d = 1$ and $\delta_1 = 0.014038$), the decay is very slow (with $\lambda \lesssim 10^{-7}$), but not identically zero, as $||F[u]|| \sim 10^{-8}$. Interestingly, as shown in the bottom left panel of the figure, the relation (11) is not fulfilled. Consequently, there is a range of parameter values for which states with a very small value of $||F[u]||$ can be obtained *even if* the potential is not of the form $-(g^2 + ig')$.

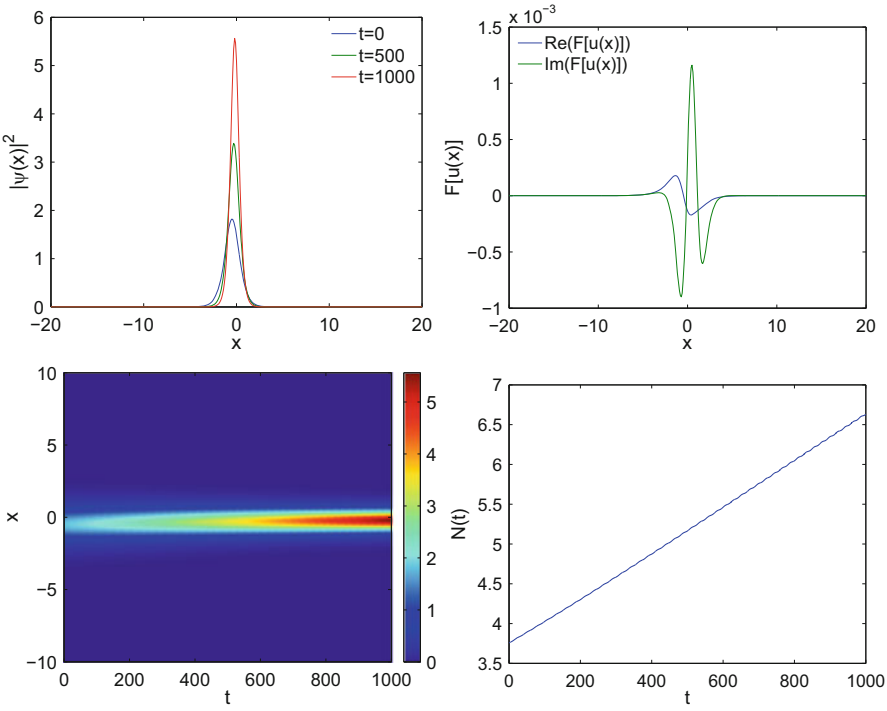

Fig. 5 Same as Fig. 3, but for $\delta_1 = 0.1$. The values of diagnostic quantities are $\lambda = 2.07 \times 10^{-2}$ and $\sigma = 6.07 \times 10^{-4}$

In the case of the NLS equation with potential $\tilde{V}_2(x)$, we only focus on the dependence of λ and σ with respect to parameters k_2 and δ_2, as the outcome of simulations is essentially the same as in the previous case. Namely, for non-vanishing values of λ and σ, a growth or decay of the solutions is identified for typical values of δ_2, as shown in Fig. 9. However, this growth or decay is quite slow, as achieved by the optimization of the beam via the Levenberg–Marquardt algorithm. Notice there is an anti-symmetry in the outcome when the transformation $k_2 \to -k_2$ is applied. In addition, both σ and λ are equal to zero at $k_2 = 0$ as at that point the potential is real and the solutions are stationary. Once again, the nearly parabolic curve in the (δ_2, k_2) plane where $\lambda = \sigma = 0$ enables us to identify parameter values in the vicinity of which states with particularly small $||F[u]||$ appear to exist.

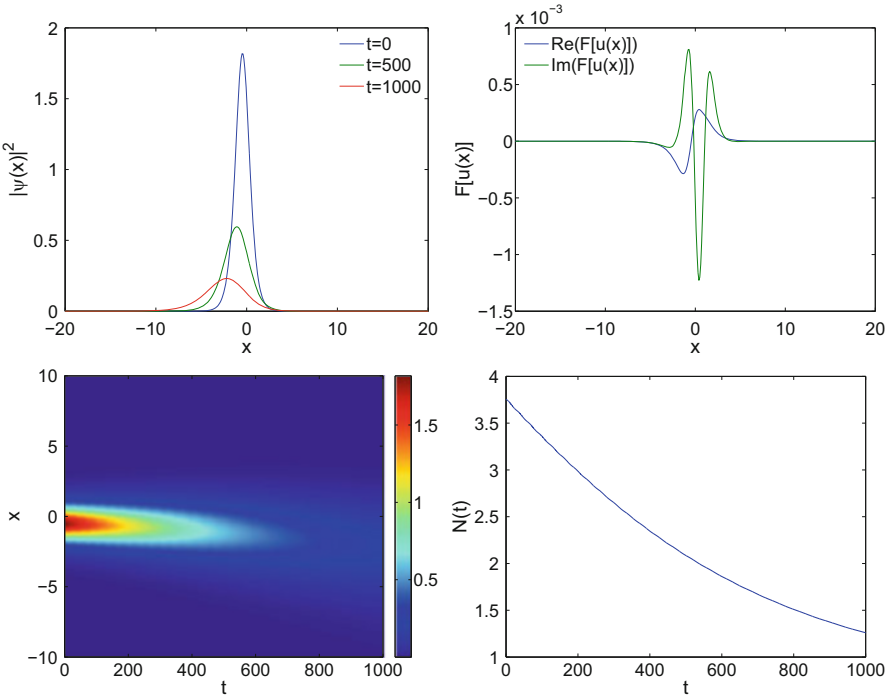

Fig. 6 Same as Fig. 3 but for $\delta_1 = -0.1$. The values of diagnostic quantities are $\lambda = -3.15 \times 10^{-2}$ and $\sigma = -9.40 \times 10^{-4}$

4 Symmetry Breaking in Two-Dimensional Potentials

It is of particular interest to extend the above one-dimensional considerations towards the emergence of asymmetric optimized beam families in the 2D version of Eq. (1) that reads:

$$i\psi_t = -(\psi_{xx} + \psi_{yy}) + [V(x, y) + iW(x, y)]\psi - |\psi|^2\psi. \tag{16}$$

In this case, stationary solutions, $\psi(x, y, t) = \mathrm{e}^{i\mu t}u(x, y)$ with $u(x, y) \in \mathbb{C}$, will satisfy:

$$F[u] \equiv \mu u - (u_{xx} + u_{yy}) + [V(x, y) + iW(x, y)]u - |u|^2 u = 0. \tag{17}$$

In Ref. [24], it is shown that not only symmetric solitons exist but also symmetry breaking is possible if the potential $\tilde{V}(x, y) = V(x, y) + iW(x, y)$ is of the form

$$\tilde{V}(x, y) = -[g^2(x) + \alpha g(x) + ig'(x) + h(y)] \tag{18}$$

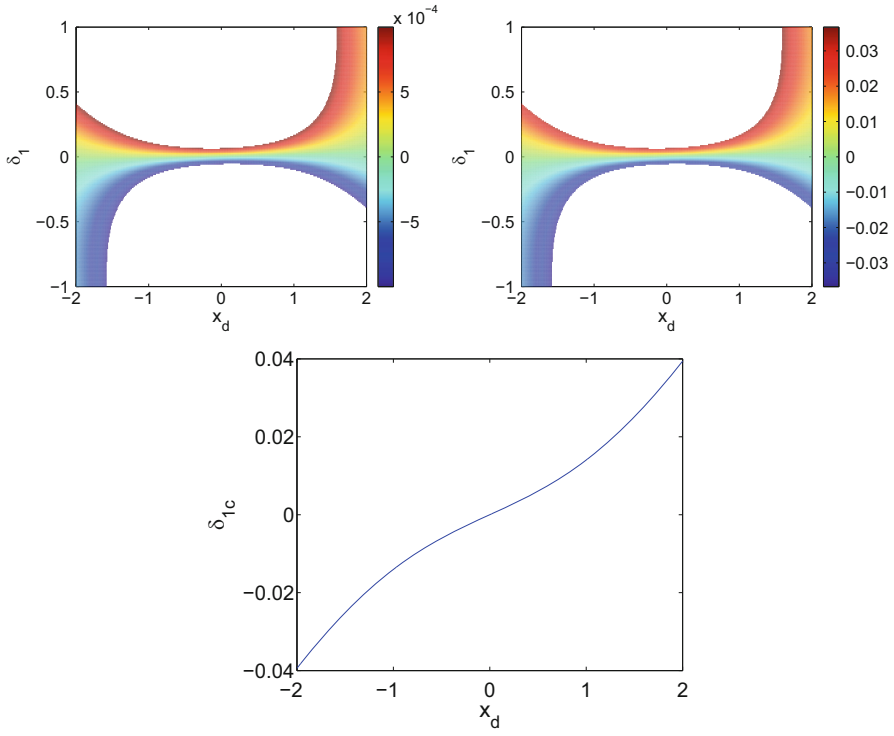

Fig. 7 Top panels: Dependence of diagnostic quantities σ (left) and λ (right) as a function of x_d and δ_1 for the potential $\tilde{V}_1(x)$ with $A_1 = 0.1$ and $k_1 = 1/2$. The bottom panel depicts the curve $\delta_{1c}(x_d)$ at which both σ and λ vanish

with $g(x)$ being a spatially even real function, $h(y)$ being a real function and α a real constant. Notice that this potential is partially-$\mathscr{P}\mathscr{T}$-symmetric (denoted also as P$\mathscr{P}\mathscr{T}$-symmetric), i.e.,

$$\tilde{V}^*(x, y) = \tilde{V}(-x, y) \tag{19}$$

The linear spectrum of this potential can be purely real. In this case, a family of $\mathscr{P}\mathscr{T}$-symmetric solitons can emerge from the edge of the continuous spectrum; two degenerate branches of asymmetric solitons, which do not respect the P$\mathscr{P}\mathscr{T}$ symmetry, bifurcate from the symmetric soliton branch through a pitchfork bifurcation. It is worthwhile to note that we consider such P$\mathscr{P}\mathscr{T}$-symmetric as a first step into the two-dimensional settings. Nevertheless (and in line with the title of this Chapter), extending considerations to a non-$\mathscr{P}\mathscr{T}$-symmetric 2D setting constitutes an important open question for future considerations.

The symmetry breaking bifurcation can also be observed either if the potential possesses double P$\mathscr{P}\mathscr{T}$ symmetry

$$\tilde{V}^*(x, y) = \tilde{V}(-x, y) \qquad \text{and} \tilde{V}^*(x, y) = \tilde{V}(x, -y) \tag{20}$$

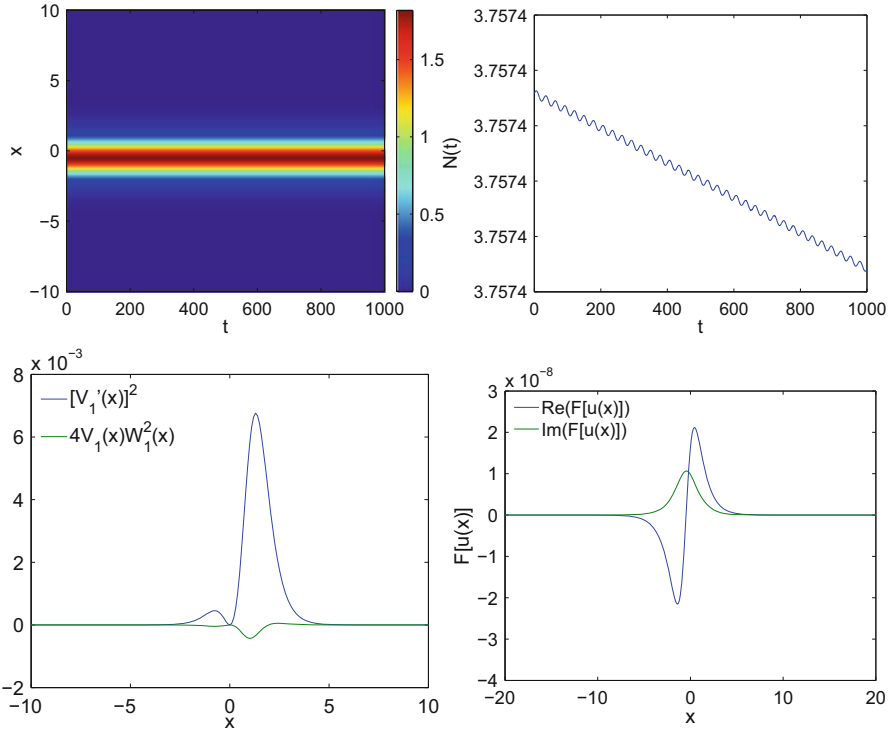

Fig. 8 Optimized beam dynamics with almost zero $||F[u]||$ in the potential $\tilde{V}_1(x)$ for $A_1 = 0.1$, $k_1 = 1/2$, $x_d = 1$ and $\delta_1 = 0.014038$. The top left panel shows the space-time contour plot of the density evolution, while the top right panel shows the evolution of the norm $N(t)$. The bottom left panel compares $[V_1'(x)]^2$ and $4V(x)W^2(x)$, showing that Eq. (11) does not hold. The bottom right panel depicts the real and imaginary part of $F[u]$. The values of the diagnostic quantities are $\lambda = -6.09 \times 10^{-8}$ and $\sigma = -3.87 \times 10^{-8}$

or $\mathscr{P}\mathscr{T}$- and one P$\mathscr{P}\mathscr{T}$-symmetry simultaneously

$$\tilde{V}^*(x, y)=\tilde{V}(-x, -y) \quad \text{and} \quad \tilde{V}^*(x, y)=\tilde{V}(-x, y) \text{or} \tilde{V}^*(x, y) = \tilde{V}(x, -y). \tag{21}$$

In such cases of double symmetries, there is no need for the potential to have a special form as in Eq. (18). In addition, the soliton branch that emerges from the spectrum edge possesses both symmetries whereas the bifurcating branch loses one of the symmetries although it retains the other.

A later work [25] reports the existence of the same branching behaviour in a $\mathscr{P}\mathscr{T}$-symmetric potential which also features a partial $\mathscr{P}\mathscr{T}$-symmetry along the x-direction. More specifically, the potential used in [25] is given by

$$V_3(x, y) = -[G^2(x, y) + G(x, y)], \quad W_3(x, y) = k_3 \partial_x G(x, y) \tag{22}$$

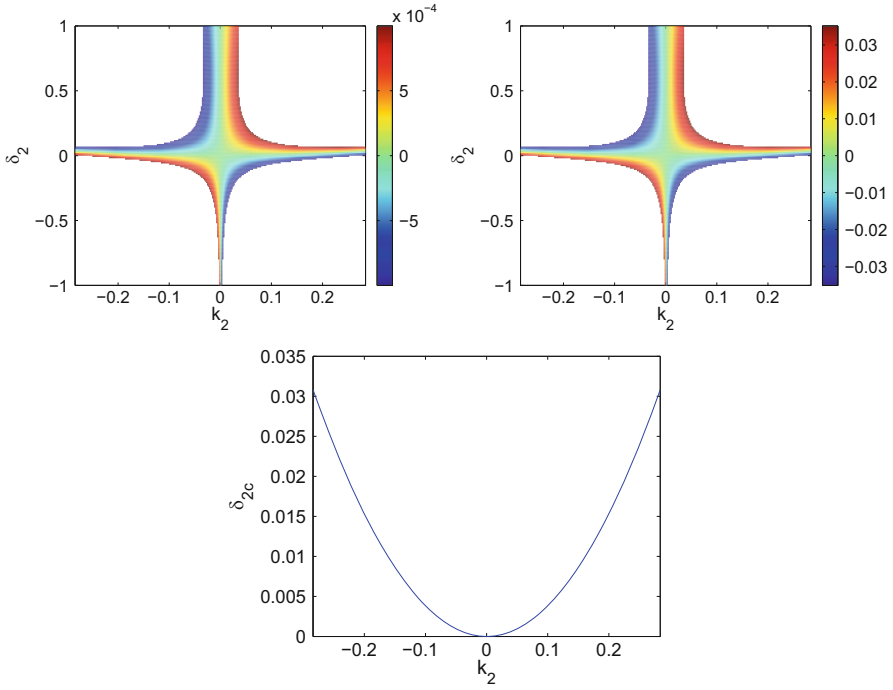

Fig. 9 Top panels: Dependence of diagnostic quantities σ (left) and λ (right) as a function of k_2 and δ_2 for the potential $\tilde{V}_2(x)$ with $A_2 = 1$. Bottom panel depicts the curve $\delta_{2c}(x_d)$ at which both σ and λ vanish

with

$$G(x, y) = A_3 \mathrm{e}^{-y^2}(\mathrm{e}^{-(x-1)^2} + \mathrm{e}^{-(x+1)^2}). \tag{23}$$

Notice that the symmetries mentioned above are applicable as a result of the even nature of the $G(x, y)$.

To give an associated example of the resulting symmetry breaking, we use, as in [25], $A_3 = 3$ and $k_3 = 1$. The resulting profile of the potential is shown in Fig. 10. $\mathscr{P}\mathscr{T}$-symmetric solitons are calculated by means of the Newton–Raphson method and the corresponding branch emerges from $\mu = 5.810$; asymmetric solitons (actually, optimized beams) are attained by using the Levenberg-Marquardt algorithm, with a tolerance of $||F[u]|| < 10^{-2}$. Now, the L^2-norm is defined as

$$||F[u]|| = \sqrt{\int |F[u(x)]|^2 \mathrm{d}x\mathrm{d}y}. \tag{24}$$

Figure 11 represents $P \equiv N(t = 0)$ versus μ for the symmetric and asymmetric soliton branches; notice that $N(t)$ is now defined as

$$N(t) = \int |\psi(x, y, t)|^2 \mathrm{d}x\mathrm{d}y. \tag{25}$$

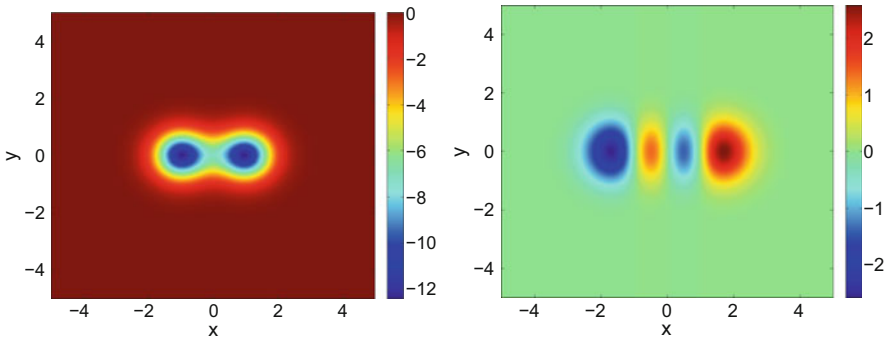

Fig. 10 Real (left) and imaginary (right) part of the 2D potential $\tilde{V}_3(x, y)$ for $A_3 = 3$ and $k_3 = 1$

One can observe that the asymmetric branches exist for $\mu \geq 6.3837$. The figure also shows the profile of solitons at $\mu = 7$, the same value that was taken in [25]. Notice that all the soliton profiles are symmetric with respect to the y-axis; the symmetric solitons present a couple of humps at $(x = \pm x_1, y = 0)$ whereas the asymmetric solitons only possess a single hump at $(x = x_2, y = 0)$. We have only shown solitons with $x_2 > 0$ as the solutions with $x_2 < 0$ are attained simply by making the transform $u(x, y) \to u(-x, y)$.

We have also computed the diagnostic quantities λ and σ [see (14) and Eqs. (15), with S adapted to 2D domains] for the asymmetric soliton and depicted them in Fig. 12. Again, we have considered asymmetric solitons branches centred at $x = x_2 > 0$. In that case, the norm grows with time, as corresponds to $\sigma > 0$ and $\lambda > 0$ whereas the opposite takes place if $x_2 < 0$. We can observe, as in the 1D case, a clear correlation between the two quantities.

Finally, we show in Figs. 13 and 14 the dynamics of the asymmetric and $\mathscr{P}\mathscr{T}$-symmetric solitons with $\mu = 7$. As it was pointed out in [25], the $\mathscr{P}\mathscr{T}$-symmetric solitons are unstable past the "bifurcation" point, i.e. when they coexist with the asymmetric branch; as we have shown in Fig. 14, they tend to a state similar to the asymmetric soliton, although displaying some density oscillations. However, it was claimed in the same reference that the asymmetric solitons were stable. For the optimized beam profiles that we have obtained, as shown in Fig. 13, the dynamical evolution does not dramatically alter the shape of the beam, yet it leads to slow growth of $N(t)$.

We also considered the stability of the $\mathscr{P}\mathscr{T}$-symmetric branch past the relevant bifurcation point. A spectral stability analysis shows that for $\mu \gtrsim 6.40$, the solitons become exponentially unstable as an eigenvalue pair becomes real. Interestingly, although the asymmetric solitons are actually optimized beams (i.e. solutions with minimal $||F(u)||$ but not exact solutions), they might be more robust than the exact solutions of the NLS equation corresponding to the $\mathscr{P}\mathscr{T}$-symmetric branch, past the corresponding destabilization point; compare the associated dynamics of Fig. 14 with those of Fig. 13.

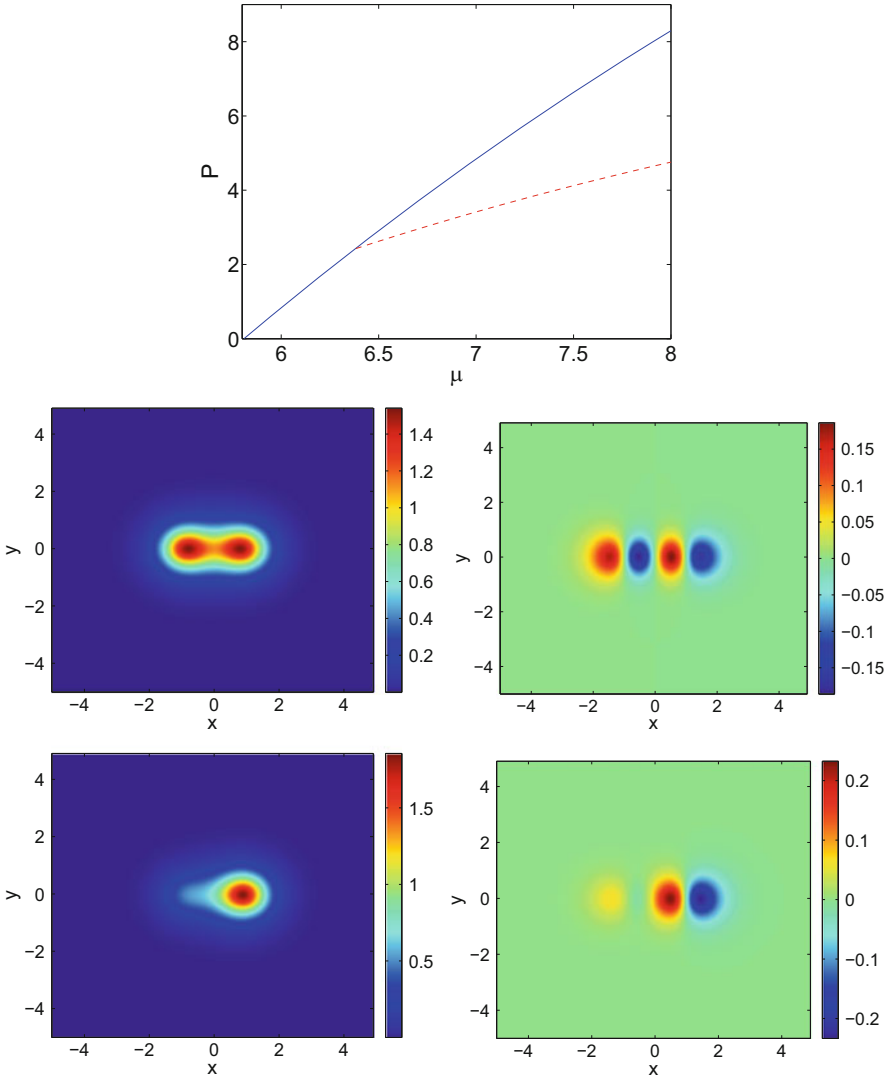

Fig. 11 Top row: dependence of the squared L^2-norm P of $\mathscr{P}\mathscr{T}$-symmetric solitons (blue full line) and asymmetric solitons/optimized beams (red dashed line) with respect to μ at the 2D potential $\tilde{V}_3(x, y)$ for $A_3 = 3$ and $k_3 = 1$. Middle row: real (left panel) and imaginary (right panel) of the $\mathscr{P}\mathscr{T}$-symmetric soliton with $\mu = 7$. Bottom row: same as middle panel but for the asymmetric soliton with the same value of μ

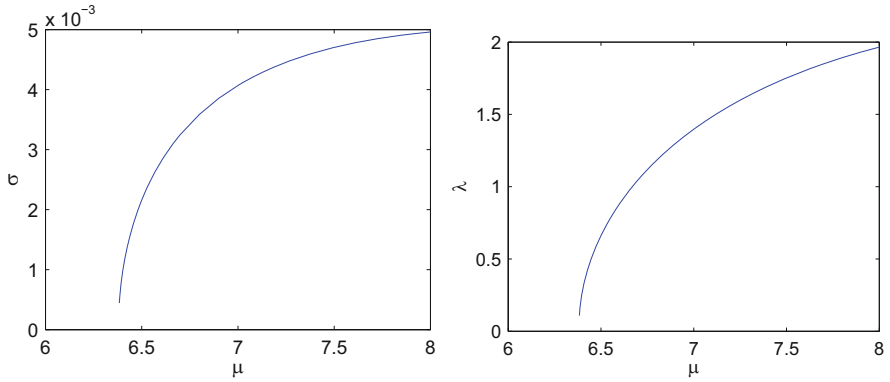

Fig. 12 Dependence of diagnostic quantities σ (left) and λ (right) as a function of μ for optimized beams at the 2D potential $\tilde{V}_3(x, y)$ with $A_3 = 3$ and $k_3 = 1$

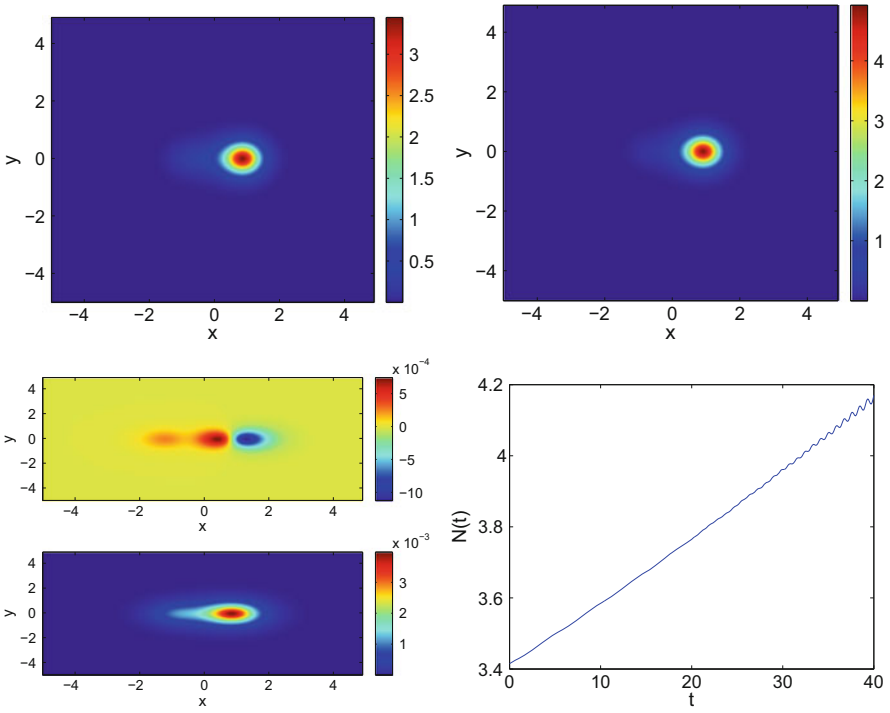

Fig. 13 Optimized beam dynamics in the 2D potential $\tilde{V}_3(x, y)$ for $A_3 = 3$, $k_3 = 1$ and $\mu = 7$. The top panels show the density profile at $t = 0$ (left) and $t = 40$ (right). The bottom left panel shows the real and imaginary part of $F[u]$ and the bottom right panel shows the evolution of the norm $N(t)$. The values of diagnostic quantities are $\lambda = 1.39$ and $\sigma = 4.07 \times 10^{-3}$

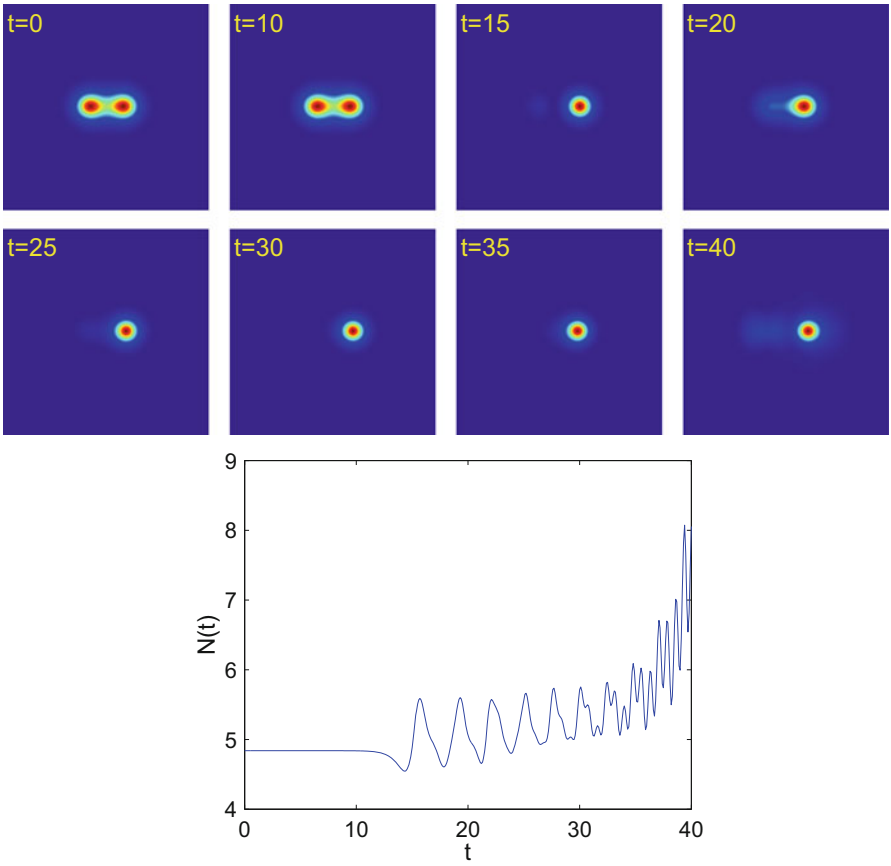

Fig. 14 Unstable $\mathscr{P}\mathscr{T}$-symmetric solitons dynamics in the 2D potential $\tilde{V}_3(x, y)$ for $A_3 = 3$, $k_3 = 1$ and $\mu = 7$. The top panels show snapshots of the density profile evolution. The bottom shows the evolution of the norm $N(t)$

5 Conclusions and Future Work

In the present work, we have revisited a variant of $\mathscr{P}\mathscr{T}$-symmetric systems. In particular, we have examined multi-parametric potentials whose parameters control, on the one hand, the potential departure from the $\mathscr{P}\mathscr{T}$-symmetric case (such as x_d herein), and on the other hand, the potential degeneracy of the conditions (2) for stationary solutions – motivated by the recent works of [19, 20]. We have confirmed the results of the important recent contribution of [22], suggesting that in the absence of a special form of the complex potential, no true stationary solutions are found to exist. On the other hand, that being said, we have identified beams that come very close to satisfying the stationary equations. The dynamics of these beams indicate a *slow* departure from such a configuration. In fact, diagnostics identifying the rate of

this growth and connecting it to the proximity of the profiles to a stationary solution (via $||F[u]||$) were developed and numerically evaluated, both in 1D and in 2D.

Naturally, this work poses a number of questions for the future. A notable one concerns the most general conditions (on, say, a complex potential) under which one may expect to find (or not) families of stationary solutions. $\mathscr{P}\mathscr{T}$-symmetry is a sufficient but not a necessary condition for such existence and extending beyond it seems of particular interest. The conjecture of [22] that the potentials $V + iW = -(g^2 + ig'(x)) + c$ represent the generic scenario is plausible, but it would be particularly interesting to produce a proof, perhaps revisiting more systematically the relevant shooting argument. It is also important to highlight that such shooting arguments are *only* valid in one spatial dimension. Hence, examining generalizations of the present setting to higher dimensions is of particular interest in their own right. We have briefly touched upon this aspect here, based on the earlier works of [24, 25], but clearly further efforts are necessary to provide a definitive reply in this direction. In particular, while an interesting class of partially-$\mathscr{P}\mathscr{T}$-symmetric potentials has been examined herein, it is particularly relevant to attempt to understand the phenomenology in non-$\mathscr{P}\mathscr{T}$-symmetric settings, constituting an important extension of our 1D considerations herein.

Appendix: The Levenberg–Marquardt Algorithm

Classical fixed-point methods like Newton–Raphson cannot be used for solving the problem $F[u(x)] = 0$ in the setting considered in the context of this Chapter, essentially because there might not exist a $u(x)$ that fulfils this relation (to arbitrarily prescribed accuracy). However, it is possible to find a function $u(x)$ that can minimize $F[u(x)]$. To this aim, an efficient method is the Levenberg–Marquardt algorithm (LMA, for short), which is also known as the damped least-square method. This method is also used to solve nonlinear least squares curve fitting [26, 27]. LMA is implemented as a black box in the Optimization Toolbox of Matlab ™ and in MINPACK library for Fortran, and can be considered as an interpolation between the Gauss-Newton algorithm and the steepest-descent method or viewed as a damped Gauss-Newton method using a trust region approach. Notice that LMA can find exact solutions, in case that they exist, as it is the case of the results presented, e.g., in Ref. [23].

Prior to applying LMA, we need to discretize our Eq. (10). Thus, we take a grid $x_n = -L/2 + nh$ with $n = 0, 1, 2 \ldots M$ and L being the domain length, and denote $u_n \equiv u(x_n)$ and $F_n \equiv F[u(x_n)]$. With this definition u_{xx} can be cast as $(u_{n+1} + u_{n-1} - 2u_n)/h^2$. In order to simplify the notation in what follows, let us call $\mathbf{u} \equiv \{u_n\}_{n=1}^M$ and $\mathbf{F}(\mathbf{u}) \equiv \{F_n\}_{n=1}^M$. We will also need to define the Jacobian matrix $\mathbf{J}(\mathbf{u}) \equiv \{J_{n,m}\}_{n,m=1}^M$ with $J_{n,m} = \partial_{u_m} F_n$. In the presently considered optimization framework, $\mathbf{F}(\mathbf{u})$ is also knows as the residue vector.

Let us recall that fixed point methods typically seek a solution by performing the iteration $\mathbf{u}_{j+1} = \mathbf{u}_j + \boldsymbol{\delta}_j$ from the seed $\mathbf{u}_0$ until the residue norm $||\mathbf{F}(\mathbf{u})||$ is below the prescribed tolerance; here $\boldsymbol{\delta}_j$ is dubbed as the search direction. In the Newton–Raphson method, the search direction is the solution of the equation system $\mathbf{J}(\mathbf{u}_j)\boldsymbol{\delta}_j = -\mathbf{F}(\mathbf{u}_j)$. If the Jacobian is non-singular, the equation system can be easily solved (as a linear system); however, if this is not the case, one must look for alternatives like the linear least square algorithm. It was successfully used for some of the authors for solving the complex Gross–Pitaevskii equation that describes the dynamics of exciton-polariton condensates [28–30]. This technique also allowed us to find optimized beams in the present problem, but presented poor convergence rates, as we were unable to decrease the residue norm controllably below the order of unity.

As fixed point methods are unable to give a reasonably small residue norm, we decided to use a trust-region reflective optimization method. Such methods consist of finding the search direction that minimizes the so called merit function

$$m(\boldsymbol{\delta}) = \frac{1}{2}\mathbf{F}(\mathbf{u})^{\mathrm{T}}\mathbf{F}(\mathbf{u}) + \boldsymbol{\delta}^{\mathrm{T}}\mathbf{J}(\mathbf{u})^{\mathrm{T}}\mathbf{F}(\mathbf{u}) + \boldsymbol{\delta}^{\mathrm{T}}\mathbf{J}(\mathbf{u})^{\mathrm{T}}\mathbf{J}(\mathbf{u})\boldsymbol{\delta}. \tag{26}$$

In addition, $\boldsymbol{\delta}$ must fulfill the relation

$$||\mathbf{D}\cdot\boldsymbol{\delta}|| < \Delta, \tag{27}$$

where $\mathbf{D}$ is a scaling matrix and Δ is the radius of the trust region where the problem is constrained to ensure convergence. There are several trust-region reflective methods, with the LMA being the one that has given us the best results for the problem at hand. This is a relatively simple method for finding the search direction $\boldsymbol{\delta}$ by means of a Gauss-Newton algorithm (which is mainly used for nonlinear least squares fitting) with a scalar damping parameter $\lambda > 0$ according to:

$$(\mathbf{J}(\mathbf{u}_j)^{\mathrm{T}}\mathbf{J}(\mathbf{u}_j) + \lambda_j\mathbf{D})\boldsymbol{\delta}_j = -\mathbf{J}(\mathbf{u}_j)^{\mathrm{T}}\mathbf{F}(\mathbf{u}_j) \tag{28}$$

with $\mathbf{D}$ being the scaling matrix introduced in Eq. (27). There are several possibilities for choosing such a matrix. In the present work, we have taken the simplest option, that is $\mathbf{D} = \mathbf{I}$ (the identity matrix), so (27) simplifies to $||\boldsymbol{\delta}_j|| < \Delta$. Notice that for $\lambda_j = 0$, (28) transforms into the Gauss-Newton equation, while for $\lambda_j \to \infty$ the equation turns into the steepest descent method. Consequently, the LMA interpolates between the two methods. Notice also the subscript in λ_j: this is because the damping parameter must be changed in each iteration, with the choice of a suitable λ_j constituting the main difficulty of the algorithm.

The scheme of the LMA is described in a quite easy way in the Numerical Recipes book [31, Chapter 15.5.2] and is summarized below:

1. Take a seed $\mathbf{u}_0$ and compute $||F(\mathbf{u}_0)||$
2. Choose a value for λ_0. In our particular problem, we have taken $\lambda_0 = 0.1$.
3. Solve the equation system (28) in order to get $\boldsymbol{\delta}_0$ and compute $||\mathbf{F}(\mathbf{u}_0 + \boldsymbol{\delta}_0)||$

4. • If $||F(\mathbf{u}_0 + \boldsymbol{\delta}_0)|| \geq ||\mathbf{F}(\mathbf{u}_0)||$, then take $\lambda_1 = 10\lambda_0$ and $\mathbf{u}_1 = \mathbf{u}_0$, as with this choice of λ_0 the residue norm has not decreased.
   • If $||F(\mathbf{u}_0 + \boldsymbol{\delta}_0)|| < ||\mathbf{F}(\mathbf{u}_0)||$, then take $\lambda_1 = \lambda_0/10$ and $\mathbf{u}_1 = \mathbf{u}_0 + \boldsymbol{\delta}_0$, as with this choice of λ_0 has succeeded in decreasing the residue norm.
5. Go back to step 3 doing $\lambda_0 = \lambda_1$ and $\mathbf{u}_0 = \mathbf{u}_1$

This algorithm is repeated while $||\mathbf{F}(\mathbf{u})||$ is above the prescribed tolerance.

Acknowledgements J.C.-M. thanks financial support from MAT2016-79866-R project (AEI/FEDER, UE). P.G.K. gratefully acknowledges the support of NSF-PHY-1602994, the Alexander von Humboldt Foundation, the Stavros Niarchos Foundation via the Greek Diaspora Fellowship Program, and the ERC under FP7, Marie Curie Actions, People, International Research Staff Exchange Scheme (IRSES-605096). The authors gratefully acknowledge numerous valuable discussions with and input from Professor Jianke Yang during the course of this work.

References

1. Bender, C.M., Boettcher, S.: Real spectra in non-hermitian Hamiltonians having $\mathscr{P}\mathscr{T}$ symmetry. Phys. Rev. Lett. **80**, 5243–5246 (1998)
2. Bender, C.M., Brody, D.C., Jones, H.F.: Complex extension of quantum mechanics. Phys. Rev. Lett. **89**, 270401 (2002)
3. Ruter, C.E., Makris, K.G., El-Ganainy, R., Christodoulides, D.N., Segev, M., Kip, D.: Observation of parity-time symmetry in optics. Nat. Phys. **6**, 192–195 (2010)
4. Peng, B., Ozdemir, S.K., Lei, F., Monifi, F., Gianfreda, M., Long, G.L., Fan, S., Nori, F., Bender, C.M., Yang, L.: Parity-time-symmetric whispering-gallery microcavities. Nat. Phys. **10**, 394–398 (2014)
5. Peng, B., Ozdemir, S.K., Rotter, S., Yilmaz, H., Liertzer, M., Monifi, F., Bender, C.M., Nori, F., Yang, L.: Loss-induced suppression and revival of lasing. Science **346**, 328–332 (2014)
6. Wimmer, M., Regensburger A., Miri, M.-A., Bersch, C., Christodoulides, D.N., Peschel, U.: Observation of optical solitons in PT-symmetric lattices. Nat. Commun. **6**, 7782 (2015)
7. Suchkov, S.V., Sukhorukov, A.A., Huang, J., Dmitriev, S.V., Lee, C., Kivshar, Yu.S.: Nonlinear switching and solitons in PT-symmetric photonic systems. Laser Photon. Rev. **10**, 177–213 (2016)
8. Konotop, V.V., Yang, J., Zezyulin, D.A.: Nonlinear waves in $\mathscr{P}\mathscr{T}$-symmetric systems. Rev. Mod. Phys. **88**, 035002 (2016)
9. Schindler, J., Li, A., Zheng, M.C., Ellis, F.M., Kottos, T.: Experimental study of active LRC circuits with $\mathscr{P}\mathscr{T}$ symmetries. Phys. Rev. A **84**, 040101 (2011)
10. Schindler, J., Lin, Z., Lee, J.M., Ramezani, H., Ellis, F.M., Kottos, T.: $\mathscr{P}\mathscr{T}$-symmetric electronics. J. Phys. A Math. Theor. **45**, 444029 (2012)
11. Bender, N., Factor, S., Bodyfelt, J.D., Ramezani, H., Christodoulides, D.N., Ellis, F.M., Kottos, T.: Observation of asymmetric transport in structures with active nonlinearities. Phys. Rev. Lett. **110**, 234101 (2013)
12. Bender, C.M., Berntson, B., Parker, D., Samuel, E.: Observation of $\mathscr{P}\mathscr{T}$ phase transition in a simple mechanical system. Am. J. Phys. **81**, 173–179 (2013)
13. Cuevas-Maraver, J., Kevrekidis, P.G., Saxena, A., Cooper, F., Khare, A., Comech, A., Bender, C.M.: Solitary waves of a $\mathscr{P}\mathscr{T}$-symmetric nonlinear dirac equation. IEEE J. Select. Top. Quant. Electron. **22**, 5000109 (2016)

14. Demirkaya, A., Frantzeskakis, D.J., Kevrekidis, P.G., Saxena, A., Stefanov, A.: Effects of parity-time symmetry in nonlinear Klein-Gordon models and their stationary kinks. Phys. Rev. E **88**, 023203 (2013); see also: Demirkaya, A., Kapitula, T., Kevrekidis, P.G., Stanislavova M., Stefanov, A: On the spectral stability of kinks in some PT-symmetric variants of the classical Klein-Gordon field theories. Stud. Appl. Math. **133**, 298–317 (2014)
15. Tsoy, E.N., Allayarov, I.M., Abdullaev, F.Kh.: Stable localized modes in asymmetric waveguides with gain and loss. Opt. Lett. **39**, 4215–4218 (2014)
16. Konotop, V.V., Zezyulin, D.A.: Families of stationary modes in complex potentials. Opt. Lett. **39**, 5535–5538 (2014)
17. Yang, J.: Partially $\mathscr{P}\mathscr{T}$-symmetric optical potentials with all-real spectra and soliton families in multi-dimensions. Opt. Lett. **39**, 1133–1136 (2014)
18. D'Ambroise, J., Kevrekidis, P.G.: Existence, stability and dynamics of nonlinear modes in a 2D partially $\mathscr{P}\mathscr{T}$-symmetric potential. Appl. Sci. **7**, 223 1–10 (2017)
19. Kominis, Y.: Dynamic power balance for nonlinear waves in unbalanced gain and loss landscapes. Phys. Rev. A **92**, 063849 (2015)
20. Kominis, Y.: Soliton dynamics in symmetric and non-symmetric complex potentials. Opt. Commun. **334**, 265–272 (2015)
21. Ablowitz, M.J., Segur, H.: Solitons and the Inverse Scattering Transform. SIAM, Philadelphia (1981)
22. Nixon, S.D., Yang, J.: Bifurcation of soliton families from linear modes in non-$\mathscr{P}\mathscr{T}$-symmetric complex potentials. Stud. Appl. Math. **136**, 459 (2016)
23. Dutykh, D., Clamond, D., Durán, Á.: Efficient computation of capillary-gravity generalised solitary waves. Wave Motion **65**, 1 (2016)
24. Yang, J.: Symmetry breaking of solitons in two-dimensional complex potentials. Phys. Rev. E **91**, 023201 (2015)
25. Chen, H., Hu, S.: The asymmetric solitons in two-dimensional parity-time symmetric potentials. Phys. Lett. A **380**, 162 (2016)
26. Levenberg, K.: A method for the solution of certain non-linear problems in least squares. Q. Appl. Math. **2**, 164 (1944)
27. Marquardt, D.: An algorithm for least-squares estimation of nonlinear parameters. SIAM J. Appl. Math. **11**, 431 (1963)
28. Cuevas, J., Rodrigues, A.S., Carretero-González, R., Kevrekidis, P.G., Frantzeskakis, D.J.: Nonlinear excitations, stability inversions, and dissipative dynamics in quasi-one-dimensional polariton condensates. Phys. Rev. B **83**, 245140 (2011)
29. Rodrigues, A.S., Kevrekidis, P.G., Cuevas, J., Carretero-González, R., Frantzeskakis, D.J.: Symmetry-breaking effects for polariton condensates in double-well potentials. In: Malomed, B.A. (ed.) Spontaneous Symmetry Breaking, Self-Trapping, and Josephson Oscillations, pp. 509–529. Springer, Berlin/Heidelberg (2013)
30. Rodrigues, A.S., Kevrekidis, P.G., Carretero-González, R., Cuevas-Maraver, J., Frantzeskakis, D.J., Palmero, F.: From nodeless clouds and vortices to gray ring solitons and symmetry-broken states in two-dimensional polariton condensates. J. Phys. Condens. Matter **26**, 155801 (2014)
31. Press, W.H., Teukolsky, S.A., Vetterling, W.T., Flannery, B.P.: Numerical Recipes. The Art of Scientific Computing, 3rd edn. Cambridge University Press, Cambridge (2007)